Fusion Research

Principles, Experiments and Technology

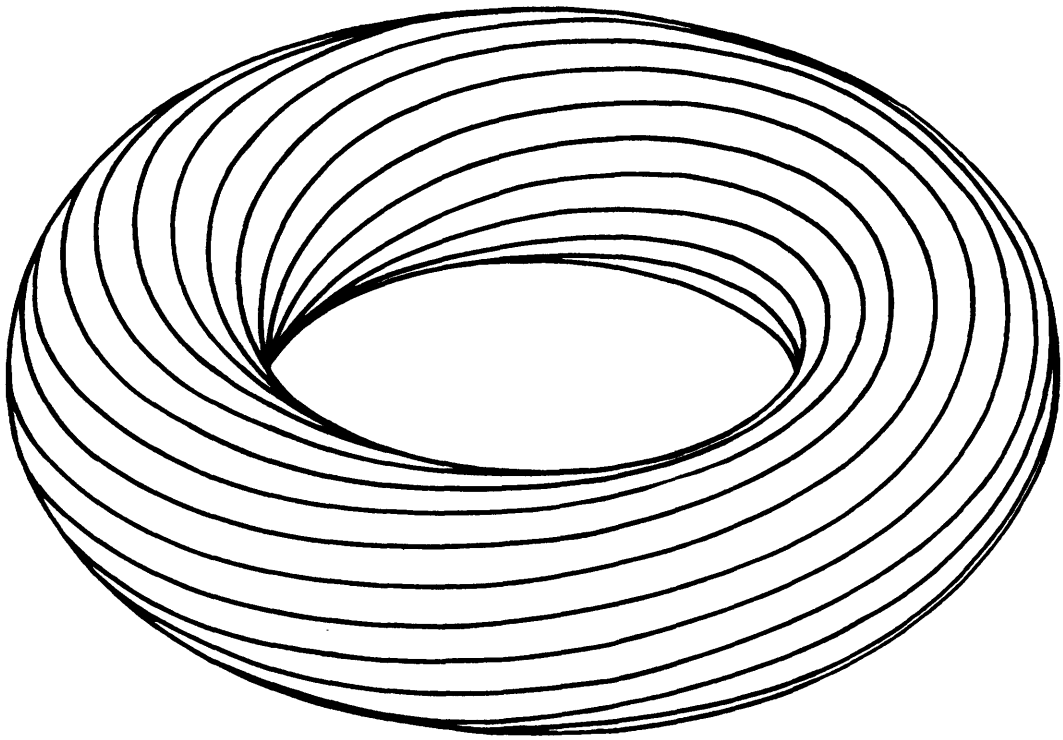

Dolan

Pergamon Press

Fusion Research

Principles, Experiments and Technology

Thomas James Dolan

Library of Congress Cataloging in Publication Data

Dolan, Thomas James, 1939-
Fusion research.

Includes indexes.
1. Nuclear fusion. I. Title.
QC791.D64 1980 539.7'64 80-18383
ISBN 0-08-025565-5

dedicated to

Charlou Baker Dolan
Virginia Fisher Dolan
Thomas James Dolan, Sr.

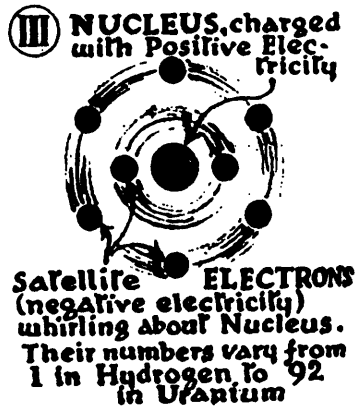

" The atomic weight of hydrogen is not exactly 1, but by careful measurement is found to be 1.0077 . Who could imagine that in this slight discrepancy -- which indeed needs some explanation to make intelligible,-- an immense store of possible energy is indicated, which some day, when we have learned how, may become accessible for good or ill to the human race ? ...

If then the whole of any perceptible portion of matter disappeared, the energy resulting would be prodigious. When hydrogen is packed into helium, the *whole* runs not the slightest risk of disappearing. But seven or eight parts in every 10,000 do disappear. The 1.0077 becomes one. And though the disappearing fraction is small, yet the total of which it is a fraction is so gigantic that the result would put all our other sources of energy to shame.

But we have not learned how to pack hydrogen into helium or into any other of the heavier atoms -- as yet. No, not yet. And yet it would appear that it must have been done, some time and somewhere; perhaps in the interior of stars, certainly in ways at present unknown...

And if ever the human race get hold of a means of tapping even a small fraction of the energy contained in the atoms of their own planet, the consequences will be beneficent or destructive according to the state of civilization at that time attained. "

from

Sir Oliver Lodge, F.R.S, "Putting the Atom to Work",
Scientific American, May 1924, pages 306-307, 358-359.

CONTENTS

In the paperback edition

Volume I: Principles includes chapters 1-10, pages 1-272

Volume II: Experiments includes chapters 11-17, pages 273-549

Volume III: Technology includes chapters 18-30, pages 550-855

PRINCIPLES

EXPERIMENTS

11. Mirrors and Cusps

12. Pinches and Compact Toroids

13. Tokamaks

14. Other Toroidal Devices

15. Inertial Confinement Fusion (ICF)

16. ICF Drivers and Chambers

17. Other Fusion Concepts

TECHNOLOGY

18. Fusion Engineering Problems

PREFACE

An abundant energy supply is necessary for feeding the world's hungry people. Agriculture and industry require great amounts of energy for fertilizers, irrigation, fuels, transportation, and manufacturing. Although technological prosperity cannot assure spiritual health, it can remove some causes of conflict, such as poverty and hunger, and thus alleviate some of the pressures leading to war. When nations prosper, a greater share of their resources can be devoted to solving other crucial problems, like disease.

Nuclear fusion reactions are the source of the enormous power radiated by the sun and other stars. The fossil fuels we consume now originally received their energy from sunlight, so fusion is called the *ultimate energy source*. However, the energy we receive from the sun is very diffuse. In order to provide more concentrated power, we will build miniature suns on earth, using deuterium fuel. When the deuterium extracted from one litre of water is burned in a fusion reactor, it will produce as much energy as burning 300 litres of gasoline. There is enough deuterium in the oceans to last mankind for millions of years. The difficulty is that the fuel must be heated to temperatures hotter than the sun and confined until a significant fraction burns.

Several fusion experiments will demonstrate plasma conditions equivalent to *breakeven* (fusion power output exceeding energy input) in the 1980's. Fusion research will become popular, funding and industrial participation will increase, and educational programs will be expanded to meet manpower needs.

The purpose of this book is to provide a general description of the methods and problems of fusion research, which will be useful to those entering the field and to those already engaged in fusion research, but specializing in one area. Each topic is simplified and condensed. The book has three main parts:

* *Principles (Chapters 1-10).* Chapter 4 describes the conditions under which fusion reactors can succeed, in terms of plasma parameters and efficiencies. It develops a set of fusion reactor power balance equations, applicable to either magnetic confinement or inertial confinement, to steady state or pulsed reactors, with or without direct conversion. Chapters 8-10 describe the fundamentals of plasma confinement, heating, and diagnostics. The other chapters in *Principles* provide background information for these chapters. Knowledge of modern physics and differential equations is assumed. Complex mathematical derivations important to plasma heating and stability have been included in a few cases (Sections 2E, 5E, 8D), but readers uninterested in such derivations may skip to the results without great loss. The book does not quantitatively describe some important plasma physics topics, such as the Fokker-Planck equation, wave-particle interactions, turbulence, and stochastic fields.

* *Experiments (Chapters 11-17).* About forty plasma confinement schemes and experiments are described. The history of who originated various concepts is not given. Some experimental parameters are cited to illustrate the state of the art as of 1981.

* *Technology (Chapters 18-29).* Various engineering problems associated with reactor design, vacuum and magnet systems, materials, plasma purity, fueling, blankets, neutronics, environment, and fusion-fission hybrids are discussed.

Readers more interested in engineering problems may begin reading the book at Chapter 18. Although some equations and concepts in *Technology* refer to previous chapters, most of the material can be understood independently.

Homework problems are provided in the *Principles* and *Technology* sections. The book uses Systeme Internationale (SI) units. The appendices provide units conversion factors, fundamental constants, mathematical functions, basic plasma equations, a table of symbols, and answers to homework problems. Since readers of technical literature often suffer from the Excessive Use of Abbreviations (EUA), a table of abbreviations is also provided.

The Bibliographies in each chapter provide starting places for further study, but the best places to find current information are in conference proceedings, laboratory reports, and journals, such as:

Plasma Physics and Controlled Nuclear Fusion Research (Brussels, 1980), IAEA, Vienna, 1981, and later conferences in the same series.

F. H. Tenney and C. C. Hopkins, Editors, *The Technology of Controlled Nuclear Fusion, Proceedings of the Fourth Topical Meeting (King of Prussia, PA, 1980)*, (CONF-801011), U. S. Department of Energy, 1981, and later conferences in the same series.

Fusion Energy Update (Abstracts, DOE)
IEEE Transactions on Plasma Science
Journal of Fusion Energy
Journal of Nuclear Materials
Journal of Plasma Physics
Nuclear Fusion
Nuclear Technology/Fusion
Physical Review Letters
Plasma Physics
Soviet Journal of Plasma Physics
The Physics of Fluids

The preponderance of descriptions of research performed in the USA is a consequence of the availability of literature, and does not properly indicate the great amount of research underway in other countries. The bibliographies cite only literature in English. Readers of German will be interested in J. Raeder, K. Borrass, R. Bünde, W. Dänner, R. Klingelhöfer, L. Lengyel, F. Leuterer, and M. Söll, *Kontrollierte Kernfusion*, B. G. Teubner, Stuttgart, 1981.

Please tell me about errors, and send suggestions for improvement of future editions.

ACKNOWLEDGEMENTS

Research at the national laboratories (such as ANL, Los Alamos, LLNL, BNL, ORNL, and PPPL) is performed "under the auspices of the U. S. Department of Energy" or its predecessors (ERDA, AEC). Los Alamos National Laboratory and LLNL are administered by the University of California, and PPPL, by Princeton University. Oak Ridge National Laboratory is operated by the Union Carbide Corporation. The journal *Nuclear Fusion* is published by the International Atomic Energy Agency. To save space, these credits are listed here instead of in the figure captions.

I am indebted to those listed below, who reviewed or wrote parts of the chapters indicated :

B.	Ahlborn	5	H. H.	Fleischmann	14,16	D. B.	Montgomery 20-22
I.	Alexeff	9	H. K.	Forsen	2	T.	Ohkawa 30
P. L.	Andrews	13	T. K.	Fowler	30	A. T.	Peaslee, Jr. 17
F. W.	Baity, Jr.	10	A. P.	Fraas	26	R. B.	Perkins 16
C. C.	Baker	18	H. P.	Furth	30	E. J.	Powers 6
S. J.	Barish	16	A. L.	Gardner	10,12	R. E.	Price many
W. L.	Barr	26	J. H.	Gardner	12	R. K.	Richards 10
G.	Bateman	8	G. A.	Gerdin	4,5	M.	Roberts 18
T. H.	Batzer	19	J. G.	Gilligan	8	F. C.	Rock 12
D. J.	Bender	26	J. C.	Glowienka	10,14	J. R.	Roth 14,17
F. M.	Bieniosek	10	R. A.	Gross	17	R. C.	Sanders 19,23
S. E.	Bodner	15	G. R.	Haste	14	T.	Sato 17
A. E.	Bolon	many	A. J.	Hatch	17	A. M.	Sessler 16
R. W.	Boom	22	R. S.	Hawke	17	S. R.	Seshadri 3,4,5,7
A. H.	Boozer	8	C. D.	Henning	22,23	J. L.	Shohet 14
K.	Brau	3	J. T.	Hogan	13	J. C.	Sprott 14
S. C.	Brown	3,5,6	J. P.	Holdren	28	D.	Steiner 4,18,27,28
G. A.	Carlson	18,28	G. R.	Hopkins	3	C. M.	Stickley 15,16
K. H.	Carpenter	14	D. P.	Hutchinson	10	B. S.	Tanenbaum 5
F. F.	Chen	many	E. L.	Kemp	21	F. H.	Tenney 9,13,25,29
B. E.	Cherrington	6	E. E.	Kintner	30	T.	Thomas 10
R. E.	Chrien	7	E. H.	Klevans	2,4,5	C. A.	Trachsel 18
J. A.	Cobble	10	H. E.	Knoepfel	21	A. W.	Trivelpiece 5
F. E.	Coffman	many	G. L.	Kulcinski	24	N.	Tsoulfanidis 27
R. J.	Colchin	10	O. A.	Lavrent'ev	17	P. J.	Turchi 17
D. N.	Cornish	22	M. S.	Lubell	22	J. T.	Verdeyen 10
A. W.	Culp, Jr.	1	R. L.	Martin	16	V. S.	Voitsenya 14
N. A.	Davies	13	J. G.	Martel	24	L. M.	Waganer 28
J. W.	Davis	24	R. H.	McFarland	3	S. E.	Walker 12
S. O.	Dean	many	A. T.	Mense	many	R. W.	Werner 18, 26
J. N.	Dimarco	12	P. A.	Miller	15,16	C. B.	Wharton 10
D. R.	Edwards	26	R. G.	Mills	18	F.	Winterberg 16, 17
G. A.	Emmert	4,5,8	S. L.	Milora	25	G.	Yonas 15,16,30
J.	File	22	R. W.	Moir	11,29	K. M.	Zwilsky 24
						M.	Schaffer 12

Many changes have been made since the reviews were received, so the reviewers are not responsible for errors. Many other scientists have contributed information on their research and permitted reprinting of figures and tables.

C. D. Croessmann and L. C. Cadwallader checked the example problems, and M. D. Carter, L. C. Cadwallader, and J. P. Head provided the homework problem solutions. A. E. Bolon and his students gave many helpful suggestions.

Acknowledgements

Charlou Dolan drew the figures, edited and proofread the manuscript, and supervised production of the camera-ready copy, typed by Sandy Shults and Margaret Schaefer. Jim Browning, Holly Stansfield, Bob Clark, Ramiz Ballou, Betty Volosin, Zak Dolan, and Mari Ann Edwall assisted with various production tasks.

Professors D. Ray Edwards and Der-Ling Tseng provided encouragement and support during writing of the book at the University of Missouri-Rolla and National Tsing Hua University, Taiwan.

Finally, I am grateful to Zak, Dan, Meg and Charlou for their patience and love during the long ordeal.

Fusion Research

CHAPTER 1
ENERGY SOURCES

1A. Forms of Energy

Energy may be described as "the ability to produce heat". *Power* is the rate of energy flow from one place or form to another. If no energy flows across the boundaries of a given region (an "isolated system"), then the total amount of energy inside remains constant, although many forms of energy may be present, in varying amounts. Some forms of energy are listed in Table 1A1, and units of energy are described in Appendix A. Strictly speaking, energy is not "the ability to do work", since thermal energy cannot be fully converted into work.

1B. Energy Demand

energy uses

Energy is needed in food production, transportation, communication, heating and cooling buildings, materials processing and manufacturing, and virtually all aspects of modern life. The distribution of energy usage in the United States is illustrated in Table 1B1.

The historical growth of energy input to the food system and of food energy consumed in the United States are shown in Fig. 1B1. More and more energy input is needed per calorie of food produced, as we attempt to grow food on arid lands, replenish exhausted soil nutrients, etc.

Great amounts of energy are needed to produce materials, such as lumber, cement, metals, and plastics, for construction and industry. The energy required to produce one kilogram of various materials is shown in Table 1B2, along with the fraction of the product price which is due to energy cost. As ores become scarce and depleted, more energy must be expended for mining, refining, and processing. Recycling of scarce materials also demands more energy consumption, for separation, transportation, and processing of materials.

relation to standard of living

The gross national product (GNP) per capita is one measure of the "standard of living" in a country. The relationship between the GNP per capita and the energy consumption per capita for various countries is shown in Fig. 1B2.

Table 1A1. Some forms of energy (mks units).

form	definition	variables	
rest-mass energy	$= m_0c^2$	m_0 = particle rest mass (kg) c = speed of light (m/s)	(1A1)
kinetic energy	$= mc^2-m_0c^2$	m = relativistic mass of particle (kg)	(1A2)
kinetic energy (nonrelativistic case)	$= mv^2/2$	m = mass (kg) v = speed (m/s) << c	(1A3)
electrostatic potential energy of 2 point charges	$= q_1q_2/4\pi\varepsilon_0 r$	q_1, q_2 = charges (C) ε_0 = permittivity of free space (F/m) r = distance between the charges (m)	(1A4)
thermal energy	$= m \int_0^T dT\, C_m$	m = mass (kg) C_m = heat capacity (J/kg-K) T = temperature (K)	(1A5)
potential energy of gravitation	$= Gm_1m_2/r$	G = constant ($J\text{-}m/kg^2$) m_1, m_2 = masses (kg) r = distance between the masses (m)	(1A6)
potential energy of spring	$= kx^2/2$	k = spring constant (J/m^2) x = extension of spring (m)	(1A7)
work	$= \int d\vec{s}\cdot\vec{F}$	$d\vec{s}$ = differential path length (m) $\vec{F}$ = force (N)	(1A8)
rotational kinetic energy	$= I\omega^2/2$	I = moment of inertia (Js^2) ω = angular speed (rad/s)	(1A9)
electric field energy	$= \int_{\text{volume}} d\vec{x}\ \varepsilon E^2/2$	E = electric field (V/m) $d\vec{x}$ = differential volume (m^3) ε = permittivity of the material (F/m)	(1A10)
magnetic field energy	$= \int_{\text{volume}} d\vec{x}\ B^2/2\mu$	B = magnetic induction (T) μ = permeability of medium (H/m)	(1A11)
energy stored in capacitor	$= C\phi^2/2$	C = capacitance (F) ϕ = voltage (V)	(1A12)
energy stored in inductance	$= LI^2/2$	L = inductance (H) I = current (A)	(1A13)

Table 1B1. Distribution of energy usage in the United States, 1968. From Stanford Research Institute, Patterns of Energy Consumption in the United States, U.S. Government Printing Office, Washington, 1972.

industrial	percent
primary metals	8.7
chemicals	8.2
petroleum refining	4.7
food and related products	2.2
paper	2.1
stone, clay, glass, concrete	2.1
other	13.3
	41.2
transportation	
gasoline	17.1
jet fuel	3.3
distillate and residual fuel	3.3
raw materials	0.3
other	1.2
	25.2
commercial	
space heating	6.9
air conditioning	1.8
asphalt and road oils	1.6
water heating	1.1
refrigeration	1.1
other	1.8
	14.4
residential	
space heating	11.0
water heating	2.9
refrigeration	1.1
cooking	1.1
other	2.4
	19.2

Table 1B2. Typical energy contents of materials and manufactured products. The actual values of a given product may vary considerably from these values. From The Technology of Efficient Energy Utilization, NATO Science Committee Conference (1973). Reprints available from Pergamon Press.

	energy input (MJ/kg)	ratio of energy cost to value of product
steel	25-30	0.3
copper	25-30	0.05
aluminum	60-270	0.4
magnesium	80-100	0.1
glass (bottles)	30-50	0.3
plastic	10	0.04
paper	25	0.3
inorganic chemicals (average)	12	0.2
cement	9	0.5
lumber	4	0.1

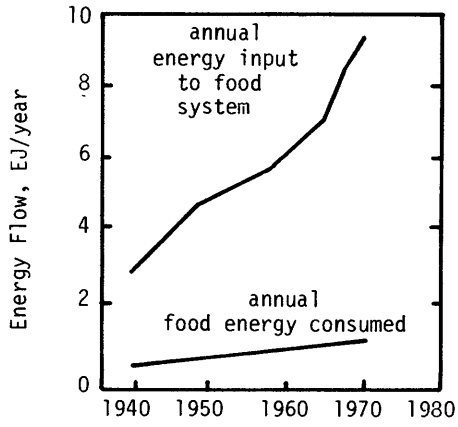

Fig. 1B1. Annual energy input to United States food system and annual food energy consumed in the United States for the period 1940-1970. 1 ExaJoule (EJ) = 10^{18} J. 1 EJ/year = 31.7 GW. Adapted from ENERGY: SOURCES, USE, AND ROLE IN HUMAN AFFAIRS, by Carol E. Steinhart and John S. Steinhart.

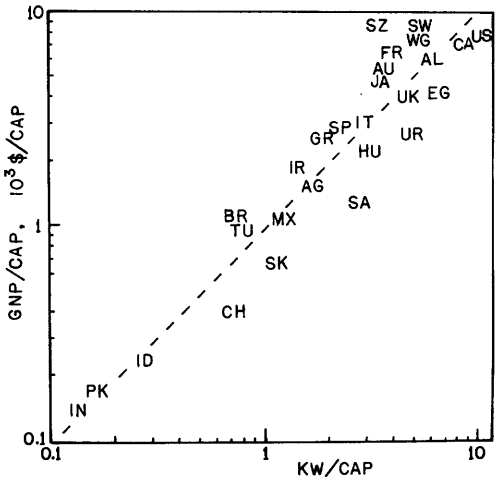

Fig. 1B2. Gross national product per capita vs. per-capita energy consumption rates for various countries, 1977-78 data. AG = Argentina, AL = Australia, AU = Austria, BR = Brazil, CA = Canada, CH = China, CZ = Czechoslovakia, EG = East Germany, FR = France, GR = Greece, HU = Hungary, ID = Indonesia, IN = India, IR = Iran, IT = Italy, JA = Japan, MX = Mexico, PK = Pakistan, SA = South Africa, SK = South Korea, SP = Spain, SW = Sweden, SZ = Switzerland, TU = Turkey, UK = United Kingdom, UR = USSR, US = USA, WG = West Germany.

predictions of demand

The total energy consumption rate of the world P_w may be written as the sum of the energy consumption rates of the various geographical regions:

$$P_w = \sum_k N_k p_k \qquad \text{(Watts)} \qquad (1B1)$$

where N_k is the population of region k and p_k is the average per-capita energy consumption rate of that region (W/person). Both N_k and p_k are increasing in almost every region of the world.

Estimates of the growth of populations and per-capita energy consumption rates for various geographical regions from 1975 to 2025 are shown in Table 1B3. The uncertainty in the 31 TW total is about ± 30%. (1 TW = 10^{12} W). Similarly, the world energy demands in 2000 and 2050 are estimated to be around 18 TW and 50 TW. World energy production rates must be greatly expanded to supply these needs, especially in developing nations.

1C. Energy Sources

power flows

Renewable energy sources, such as solar, geothermal, biomass, hydroelectric, wind, wave, and tidal power, are limited by the usable *power* they provide. Non-renewable fossil and nuclear fuels are limited by the total amount of *energy* they can provide.

About 178,000 TW of solar energy are incident on the earth, of which various amounts are reflected, reradiated, absorbed by evaporation and flow into wind, waves, and photosynthesis (Fig. 1C1). Geothermal heat flow and tidal power add about 35 TW to the balance. Although the solar and geothermal power flows are large, the useful fractions are small.

The rate of consumption of fossil fuels is limited by availability, transportation facilities, and environmental impact. An estimate of the complete cycle of world petroleum production is shown in Fig. 1C2. Production will probably decline after the year 2000. The restrictions of fossil fuel consumption necessary to

Table 1B3. Comparison of populations, per-capita power demands, and total power demands in 1975 and estimated for 2025. From R. M. Rotty, "Constraints on fossil fuel use", Interactions of Energy and Climate, Bach, Pankrath and Williams, editors, Reidel Publishing Co., 1980; and R. M. Rotty, Energy 4, 881-890 (1979).

REGION	populations N_k (millions)		p_k (thermal kW/cap)		total power demands $N_k p_k$ (TW = 10^{12} W)		
	1975	2025	1975	2025	1975	2025	growth ratio
N. America	237	315	11.5	15.0	2.72	4.74	1.7
W. Europe	305	447	5.6	5.5	1.70	2.47	1.5
E. Europe & USSR	359	480	5.3	13.6	1.90	6.54	3.4
Japan, Australia, N.Z.	128	320	4.3	6.3	0.55	2.02	3.7
Latin America	323	797	0.93	2.8	0.30	2.22	7.4
Africa	370	885	0.16	1.1	0.06	0.94	16
China & Indochina	1029	1714	0.61	2.0	0.63	3.43	5.4
South Asia	1170	2665	0.20	1.1	0.23	2.80	12
Mid-East	110	353	1.0	4.9	0.11	1.72	16
World average or total	4031	7976	2.0	3.4	8.20	26.9	3.3

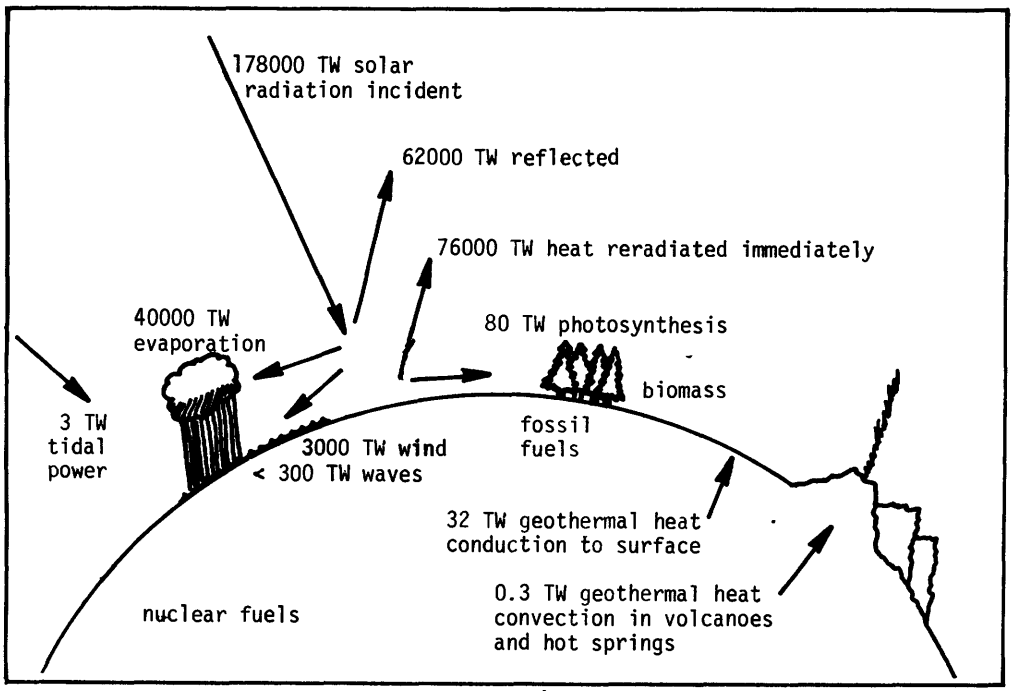

Fig. 1C1. Terrestrial power flows. Practically all incident energy is ultimately reradiated as heat (not shown). Based on data from M. K. Hubbert, "Energy resources of the earth", Scientific American (September, 1971), J. M. Weingart, "Global aspects of sunlight as a major energy source", Energy 4, 775-798 (1979), and J. M. Weingart, private communication, 1981.

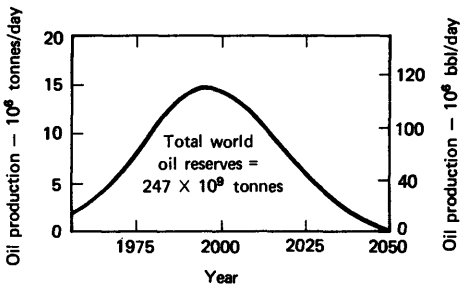

Fig. 1C2. Estimate of world crude oil production rates for the future. From Energy and Technology Review, March 1977, p. 6. Courtesy of LLNL.

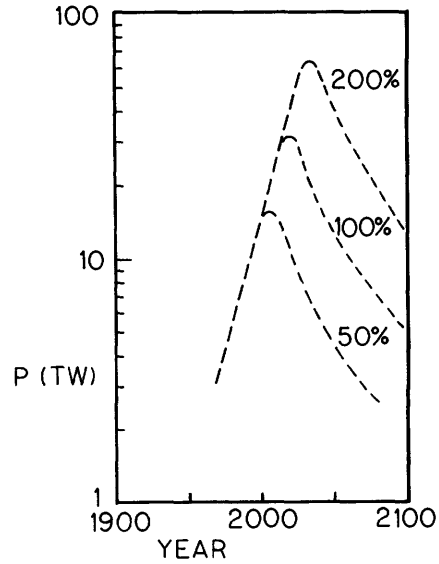

Fig. 1C3. Necessary limits on fossil fuel consumption, if the increases of atmospheric CO_2 concentration are to be kept below 50%, 100%, and 200%. What change can safely be tolerated is not yet known. From W. Haefele and W. Sassin, Energy strategies, Energy 1, 147 (1976). Copyright 1976, Pergamon Press, Ltd.

prevent various increases in atmospheric CO_2 concentrations are shown in Fig. 1C3.

If the CO_2 concentration becomes too high, then the resulting climate change could melt the polar ice caps, increasing the ocean levels and flooding major coastal cities. Therefore, not all of the available coal can be safely burned.

limits of usable energy

Estimates of the limits of various energy sources are listed in Table 1C1. Comparing these values with the estimated power demand of 50 TW in the year 2050, we see that only solar, fission, and fusion power can meet our long-term energy needs.

Nuclear fission power appears to be the most economical power source in the near future. It has an excellent safety record. Solutions to environmental problems, such as radwaste disposal, have been found, but political opposition is hindering its development.

Some estimates of solar power available in 2030 have been over 10 TW, but the 3 TW limit reflects the time it takes to manufacture and move enormous quantities of material and to "penetrate the market" economically (Haefele, 1979).

1D. Solar Energy

Solar heating and cooling of buildings is already economically competitive in some locations. Solar electric power, however, may take longer to be economically attractive. Four schemes are receiving wide attention: photovoltaic, satellite

Table 1C1. Limits of various energy sources. Data from Rotty (1976), Weingart (1979), Hubbert (1975), Haefele (1979), and Walton and Spooner (1976). These are rough estimates, but indicate the order of magnitude which can be expected.

	POWER LIMITS, TW	
renewable energy sources	by 2030	ultimately
solar electric, heating & cooling	∿ 3	∿100?
biomass	3	10
wind power	1	3
wave power & tidal power	.1	1
hydroelectric power	1.5	2.9
geothermal power	0.2	0.4
organic wastes	0.1	0.1

	ENERGY LIMITS	
practically recoverable fossil fuels	Joules	TW-years
coal & lignite (2.35×10^{12} tons)	53.2×10^{21}	1690
crude oil (2.1×10^{12} barrels)	12.4×10^{21}	390
natural gas (3.4×10^{14} m^3)	13.1×10^{21}	415
tar-sand oil (3×10^{11} barrels)	1.8×10^{21}	57
shale oil (1.9×10^{11} barrels)	1.1×10^{21}	35
total	81.6×10^{21}	2590

nuclear fission fuels	Joules	TW-years
U-235	10^{22}	300
U-238, Th-232	$> 10^{25}$	$> 3 \times 10^{5}$

nuclear fusion fuels	Joules	TW-years
lithium for DT reactors		
on land	2×10^{24}	6×10^{4}
in oceans, containing 0.17 ppm Li	2×10^{28}	6×10^{8}
deuterium in oceans	8×10^{30}	2×10^{11}

power stations, solar thermal, and ocean thermal power.

The simplest is photovoltaic panels (solar cells), which can be located on individual buildings. They cost about 10 $/peak Watt in 1980. Mass production may reduce the price by an order of magnitude or more, as it did for the manufacture of transistors. However, a storage system will more than double the initial cost, and the average power is about 1/4 the peak power, so the effective cost per average Watt is an order of magnitude higher than the peak-Watt cost.

Solar satellite power stations (SSPS) would collect power with photovoltaic panels on a satellite station in geosynchronous orbit (stationary over one point on earth) and transmit the power to earth via 2.45 GHz microwaves. While they appear to be technologically feasible, the SSPS can be economical only if major reductions in the cost of orbiting heavy payloads are achieved.

The most popular solar thermal electric conversion (STEC) schemes involve a central boiler heated by sunlight from an array of heliostats (reflectors). For example, a 10 MWe demonstration plant at Barstow, California, uses a central tower boiler surrounded by about 1800 heliostats, each with 40 m^2 area, and incorporates 3-4 hours of thermal energy storage in rock and heat-transfer oil (Caloria). Assuming that a 50% load factor were achieved with on-site thermal storage, commercial STEC plants of similar design operating under ideal solar conditions might cost 2000-3000 \$/kWe, if collector costs could be held to 100 \$/m^2 or less.

Ocean thermal electric conversion (OTEC) systems use a fluid with a low boiling temperature, such as ammonia, to run a Rankine cycle heat engine from ocean temperature gradients. For example, warm surface water at 300 K could evaporate ammonia in a boiler and drive a vapor turbine. Cool subsurface sea water at 278 K could cool the ammonia condenser to complete the cycle. Because the ΔT is so small (around 20 K), the cycle efficiency will be very low, necessitating high water flow rates and large, expensive heat exchangers. Other dominant cost items are the floating ocean platform, the cold water pipe, and the cable to carry the electricity to shore. Alternatively, the electricity could be used to produce hydrogen by electrolysis of water, and liquified hydrogen could be shipped as a fuel. Excluding the cable cost, a 250-400 MWe plant is expected to cost about 2000 \$/kWe (1978 \$).

It appears that various forms of solar power could produce electricity at costs of 70-100 mills/kWh, compared with about 20-40 mills/kWh for other sources (1 mill = .001 \$). Rapid deployment of solar electric power stations is limited by the huge surface areas which must be covered with collectors. The 24-hour average solar power flux in the Southern United States is on the order of 200-300 W/m^2. The flux is somewhat higher near the equator, and lower in northern latitudes. About 100 TW thermal energy might ultimately be collected by covering 10% of the earth's desert areas with collectors. This is the basis for the speculative figure of Table 1C1.

In spite of the advantages of solar power, it is still desirable to develop cheaper power stations which do not require a sunny climate, large collector areas, and large energy storage systems.

1E. Fusion Reactions

energy release

Nuclei with intermediate masses have the lightest average masses per nucleon, as shown in Fig. 1E1. When light elements are fused together or heavy elements are split apart, the resulting intermediate elements have less mass per nucleon. The excess mass ΔM is converted into kinetic energy :

$$W = \Delta Mc^2 = (\text{total inital mass} - \text{total final mass})c^2 \qquad (1E1)$$

where c is the speed of light.

EXAMPLE PROBLEM 1E1

Calculate the energy released by the reaction D + T → ^{4}He + n.

Using nuclear masses from App. B, we have

$$\Delta M = 2.013553 + 3.015501 - 4.001503 - 1.008665 = 0.018887 \text{ u} = 3.13631\times10^{-29} \text{ kg},$$

so $W = \Delta Mc^2 = 2.8188\times10^{-12}$ J = 17.593 MeV.

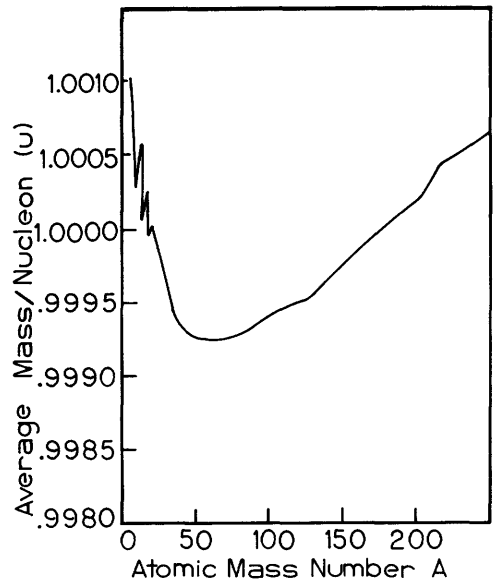

Fig. 1E1. Average mass per nucleon vs. atomic mass number. From R. D. Evans, The Atomic Nucleus, p. 295, copyright 1955, McGraw-Hill, New York. Used by permission of McGraw-Hill Book Company.

fusion fuels

Possible fusion reactor fuels include H, D, T, ^{3}He, ^{6}Li, and ^{11}B. Some nuclear reactions of interest are shown in Table 1E1. If the initial particles have energies <0.1 MeV, then the kinetic energy of the reaction products is divided up approximately in inverse proportion to their masses (to conserve momentum). For the DT reaction, the neutron gets 4/5 and the alpha particle (^{4}He) gets 1/5 of the kinetic energy.

The DT reaction is the most probable reaction at temperatures attainable in fusion reactors. (Reaction rates and probabilities will be discussed in Chapter 2.) Since deuterium constitutes 0.0153% of natural hydrogen, it is very abundant. The amount of tritium in nature is negligible, so it must be produced artificially. It can be produced by neutron absorption in lithium, as indicated in Table 1E1. (Seawater contains 0.17 ppm of Li and 0.003 ppm of U.)

The DT reaction has the following disadvantages:

* It is necessary to breed tritium from lithium (Chapter 27).
* The 14.1 MeV neutrons cause radiation damage and make walls radioactive (Chapter 24).
* Precautions are needed to minimize release of radioactive tritium (Chapter 28).
* Only 1/5 of the reaction energy is carried by charged particles and can be directly converted into electricity (Chapter 26).

The two branches of the DD reaction (DDn, DDp) have roughly equal probabilities. If the T and ^{3}He produced by these reactions react with more deuterium, then the net reaction is

$$6D \rightarrow 2H + 2n + 2^4He + 43.2 \text{ MeV} \qquad (1E2)$$

Table 1E1. Nuclear Reactions of Interest. Numbers in parentheses are approximate energies of reaction products, MeV. The exact energies vary with angle and incident particle energies. The symbols p, d, t, n, and α represent ^1_1H, ^2_1H, ^3_1H, ^1_0n, *and* ^4_2He.

name	fusion reactions	abbreviated form	energy yield MeV	Joule
DT:	$D + T \rightarrow {}^4_2He$ (3.54) + ^1_0n (14.05)	$T(d,n)^4He$	17.59	2.818×10^{-12}
DDn:	$D + D \rightarrow {}^3_2He$(.82) + ^1_0n(2.45)	$D(d,n)^3He$	3.27	5.24×10^{-13}
DDp:	$D + D \rightarrow T$(1.01) + p(3.02)	$D(d,p)T$	4.03	6.46×10^{-13}
TT:	$T + T \rightarrow {}^1_0n + {}^1_0n + {}^4_2He$	$T(t,2n)^4He$	11.3	1.81×10^{-12}
D-^{3}He:	$D + {}^3_2He \rightarrow {}^4_2He$(3.66) + p(14.6)	$^3He(d,p)^4He$	18.3	2.93×10^{-12}
p-^{6}Li:	$p + {}^6_3Li \rightarrow {}^4_2He + {}^3_2He$	$^6Li(p,\alpha)^3He$	4.02	6.44×10^{-13}
p-^{11}B:	$p + {}^{11}_5B \rightarrow 3({}^4_2He)$	$^{11}B(p,2\alpha)^4He$	8.68	1.39×10^{-12}
reactions for breeding tritium (Natural lithium is 7.5% ^{6}Li, 92.5% ^{7}Li.)			7.42	92.58
n-^{6}Li:	$^6_3Li + {}^1_0n$(thermal) $\rightarrow {}^4_2He$(2.05) + T(2.73)	$^6Li(n,\alpha)T$	4.78	7.66×10^{-13}
n-^{7}Li:	$^7_3Li + {}^1_0n$ (fast) $\rightarrow T + {}^4_2He + {}^1_0n$	$^7Li(n,n',\alpha)T$	-2.47 (endothermic)	-3.96×10^{-13}

which is called the "catalyzed DD reaction", since the high-probability DT reaction has the effect of a catalyst. The average yield per deuteron is 7.2 MeV, which is an energy yield of 3.44×10^{14} J/kg. The "catalyzed DD" fuel cycle eliminates the need to breed tritium from lithium, but it requires higher temperatures and has lower power densities than the DT reaction. Because of the more advanced technology required for the DD and D-^{3}He reactors, these are called "advanced fuel" reactors.

The ^{3}He produced in a DD reactor could either be burned in the same reactor or burned in a "satellite reactor" using primarily the D-^{3}He reaction. The advantage of D-^{3}He satellite reactors is that the neutron emission rate could be greatly reduced, resulting in much less wall activation and radiation damage.

The p-^{6}Li and p-^{11}B reactions are practically free of neutron emission, and all the reaction products are charged particles, amenable to direct conversion. However, these "exotic fuels" also have low power densities and require even higher temperature operation than the "advanced fuels", so it will be difficult to make an economical reactor using the exotic fuels.

1F. Fusion Reactors

The two main requirements for building a fusion reactor are to *heat* the fuel to ignition temperature and to *confine* it while it "burns".

Why is heating necessary before fusion reactions occur ? The positively charged nuclei repel each other, and cannot approach close enough for a nuclear reaction to occur unless they have high relative velocities.

Imagine trying to break an egg inside a foam rubber sphere by throwing other eggs in foam rubber spheres at it. They will merely bounce off unharmed unless you throw them at high velocity. In this analogy the egg is like the nucleus of deuterium or tritium, and the foam rubber represents the coulomb potential field surrounding the nucleus. Only when the ions have large relative velocities can they push through the coulomb barrier to produce a nuclear reaction.

In order to overcome the barrier, the ion's kinetic energy must almost equal the potential energy of repulsion of the two point charges. For example, the required energy for a deuteron and a triton to approach within a nuclear diameter (about 5×10^{-15}m) is found from Eq. (1A4) to be about 290 keV. Because of the quantum-mechanical "tunneling" effect and because some particles have much higher velocities than the average, the actual fuel temperatures required for the DT reactions are

$$T \gtrsim 10 \text{ keV} \simeq 10^8 \text{ K}. \qquad (1F1)$$

The required confinement time τ is given approximately by the "Lawson criterion"

$$n\tau \gtrsim 10^{20} \text{ m}^{-3} \text{ s}, \qquad (1F2)$$

where n is the plasma ion density (ions/m^3). If $n = 10^{20}$ m^{-3}, then the required confinement time is about 1 s.

The temperatures required to burn various fuels will become apparent from a study of nuclear reaction rates in Chapter 2. Following a discussion of radiation losses in Chapter 3, the confinement times required for various conditions will be derived in Chapter 4.

research progress

Fusion research experiments fall into two general categories: magnetic confinement and inertial confinement. Magnetic confinement employs strong magnetic fields to provide thermal insulation between the plasma and the chamber walls. Inertial confinement allows free plasma expansion and cooling, but relies on an extremely high density n to attain the Lawson criterion in the short expansion time (typically a few ns). The high density is attained by compressing a solid fuel pellet to over 1000 times its initial density, using laser beams or ion beams.

Fusion research experiments began in the 1950's, with hopes of rapid success, but plasma instabilities spoiled confinement. Ways to prevent various instabilities were found in the 1960's, as plasma theory made great progress. Many nations shifted experimental emphasis to tokamaks in the 1970's, following Soviet experimental success. Major experimental programs in inertial confinement fusion (ICF) were initiated in the 1970's, following optimistic predictions of attainable energy yields. In the late 1970's several other plasma confinement schemes have shown promise , including tandem mirrors, the field reversed pinch, ohmically-heated toroidal experiment, stellarators, Elmo bumpy torus, and compact toroids.

The magnetic confinement and ICF programs will both demonstrate *break-even* conditions (fusion power exceeding input power) in the mid-1980's, but many engineering problems remain. A Fusion Engineering Device will be constructed to demonstrate small-scale power production, to test reactor materials, and to develop various aspects of fusion technology.

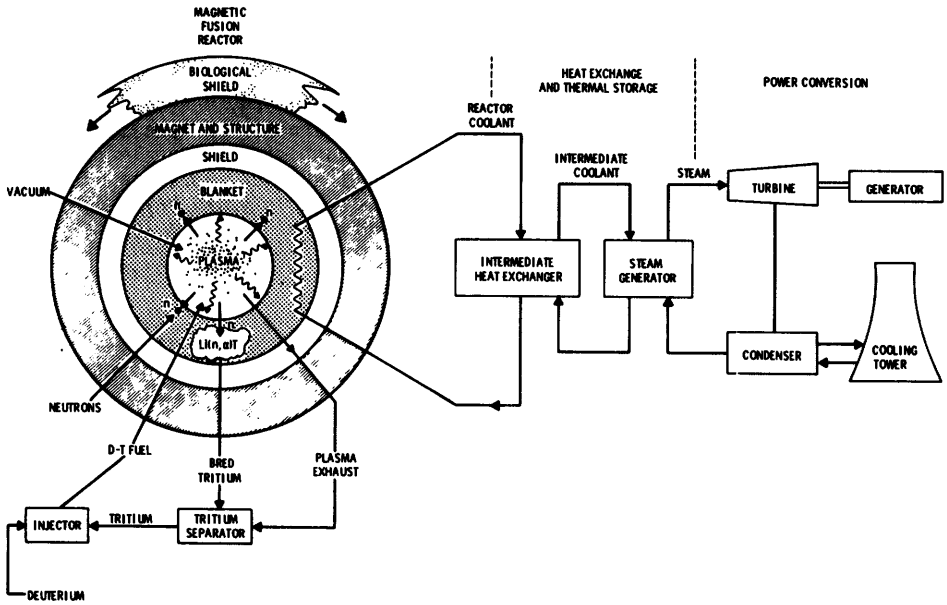

Fig. 1F1. Schematic diagram of a magnetic confinement fusion power plant. From H. J. Willenberg, T. J. Kabele, R. P. May, and C. E. Willingham, "Materials flow, recycle, and disposal for deuterium-tritium fusion", PNL-2830 (1978), Fig. 1, p.3.

power plants

Some elements of a fusion power plant are illustrated in Fig. 1F1. The plasma heating system is not shown. An ICF power plant will have similar components, but no magnet coils (unless the blast chamber walls are magnetically protected).

Potential applications of fusion power are shown in Fig. 1F2. Fusion reactor design studies estimate electrical power costs of about 35-40 mills/kWh (1980 constant $),which are comparable to costs of power from fission and fossil fuel plants. Estimated costs of solar electrical power are 70-100 mills/kWh (Weingart, 1979). Fusion power will be especially valuable if

* fuel imports are limited
* coal use cannot rapidly increase (due to mining, transportation, or environmental limitations)
* the LMFBR is not rapidly commercialized
* solar electric power costs do not become competitive
* discount (interest) rates are not too high
* fusion can be developed rapidly.

The development of fusion power will probably cost about 30 billion dollars.

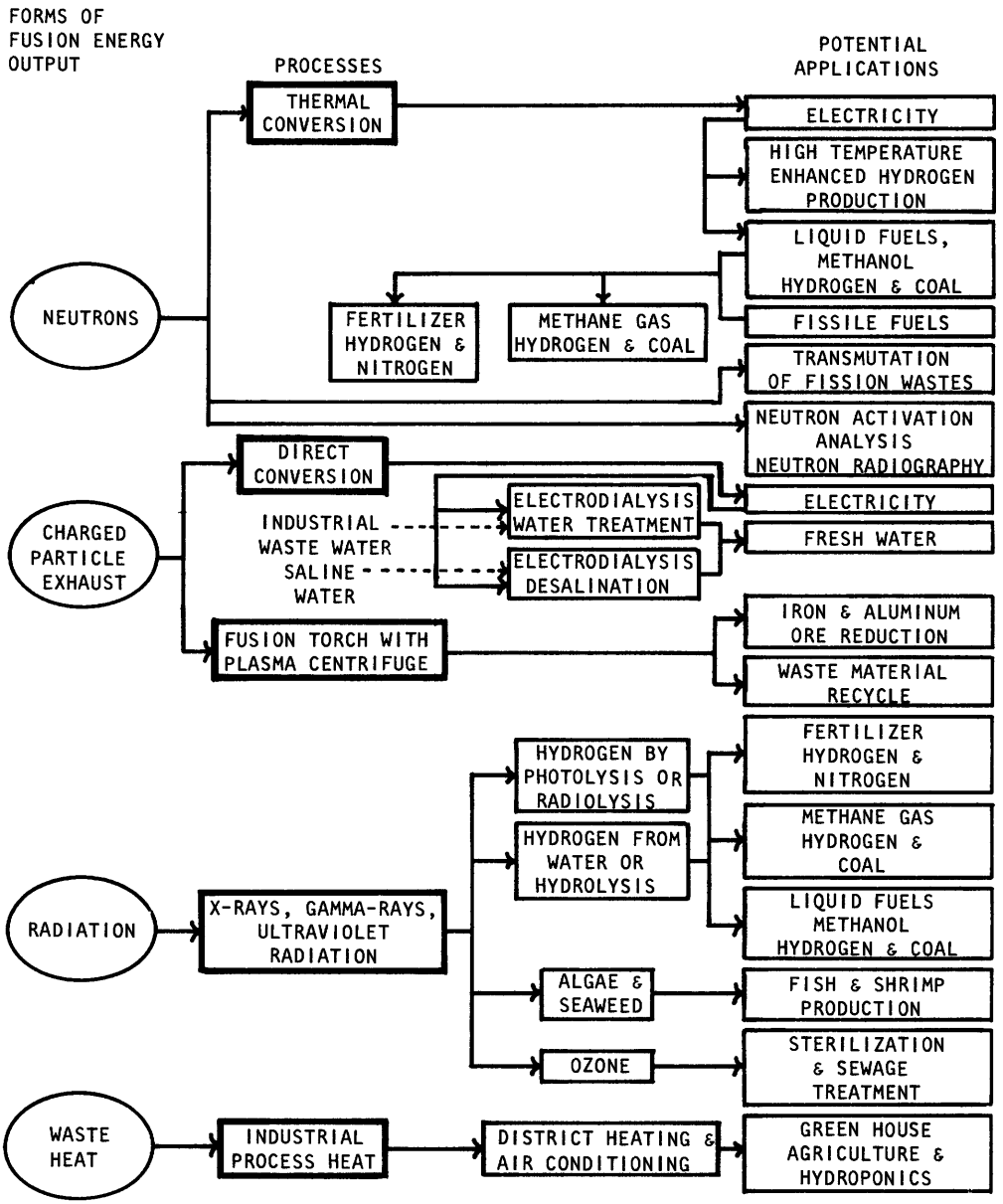

Fig. 1F2. Potential applications of fusion power. ("Magnetic Fusion Program Summary Document", Report HCP/T3168-01, prepared by TRW, Inc. for the U. S. Department of Energy, 1979.)

1G. Summary

The world power demand will rise to tens of TeraWatts in the 21st century. Most of the rise will be in developing nations, so efforts by industrialized countries to conserve energy will not prevent the power demand increase. Fossil fuels will be nearly exhausted by 2030, except for coal. Environmental problems, such as CO_2 accumulation in the atmosphere, may limit the allowable coal consumption. Tidal, wave, wind, hydroelectric, geothermal, biomass, and organic waste power together will be inadequate to meet the earth's long-term energy needs. Only fission, solar, and fusion power will be adequate.

Fission breeder reactors are already successful. The huge collector areas and energy storage systems required by solar electric power plants make it difficult to bring costs down. Fusion power plants offer the prospects of continuous operation and cheap, abundant fuel. However, there are still many problems to solve, and it will be many more years before the development of fusion power is complete.

Problems

1. If a person's body burns 2000 kcal/day of food energy, what is his average metabolism (Watts) ? How many TW food energy would be needed to feed eight billion people at this rate ? If each Joule of food energy required 8 J input to agriculture, how many TW would be required for agriculture ?

2. Calculate the energy yields of the DDn and DDp reactions.

3. Estimate the energy costs of the following forms of energy ($/MJ) :
   a. 1 liter of gasoline at $ 0.50 (heat of combustion 47 MJ/kg, and density 705 kg/m^3).
   b. 1 slice of apple pie (300 kcal) at $ 0.90 .
   c. electricity at 50 mills/kWh.
   d. energy storage in a lead-acid battery storing 80 Amp-hr at 12 V and costing $ 50 .
   e. work by a draft horse laboring 8 hours/day at a power of 1 kW, and costing $ 15/day for care.

4. A 3 GWth (GigaWatts thermal power) fusion reactor operates at full power 70 % of the time for a year, burning catalyzed DD fuel. How many kg of deuterium will be consumed ? How many cubic metres of water are needed to extract this much deuterium ?

5. How many litres of gasoline are required to produce the same energy as the energy of deuterium from 1 liter of water burned in a catalyzed DD reactor ? (Data on gasoline is given in Problem 3a.)

6. A fusion reactor has a cylindrical coil with B = 5 T inside and B ≃ 0 outside. The coil current is 10 kA, and the internal volume is 500 m^3. Estimate the approximate stored energy of the magnetic field (Table 1A1) and the coil inductance.

7. Assuming that the world power consumption grows at 6 %/year from P_0= 8 TW in 1980, and that 80 % of the power comes from fossil fuels, in what year would the fossil fuels be exhausted ? [$W = \int dt\, P(t)$].

Bibliography

energy

A. W. Culp, *Principles of Energy Conversion*, McGraw-Hill, New York, 1979.

I. G. C. Dryden, Editor, *The Efficient Use of Energy*, IPC Science and Technology Press, Surrey, England, 1975, p. 16.

W. P. Elliott and L. Machta, "Workshop on the global effects of carbon dioxide from fossil fuels", CONF-770385 (1977).

W. Haefele, Global perspectives and options for long-range energy strategies, *Energy 4*, 745-760 (1979).

W. Haefele and W. Sassin, Energy strategies, *Energy 1*, 147 (1976).

M. K. Hubbert, Survey of world energy resources, *Perspectives on Energy*, Edited by L. C. Ruedisili and M. W. Firebaugh, Oxford University Press, New York, 1975, p. 114.

J. H. Krenz, *Energy Conversion and Utilization*, Allyn and Bacon, Boston, 1976.

R. S. Pindyck, *The Structure of World Energy Demand*, MIT Press, Cambridge, MA, 1979.

R. M. Rotty, Growth in global energy demand and contribution of alternative supply systems, *Energy 4*, 881-890 (1979).

C. Starr, Energy and Power, *Scientific American 225*, 37 (1971).

J. S. Steinhart and C. E. Steinhart, Energy use in the United States food system, *Science 184*, 305-316 (April 19, 1974).

N. Tsoulfanidis, "Energy analysis of coal, fission, and fusion power plants", *Nuclear Technology/Fusion 1*, 238-254 (1981).

N. Walton and E. Spooner, "Lithium and nuclear Fusion", *Nature 261*, 533-535 (1976).

solar energy

P. E. Glaser, G. M. Hanley, R. H. Nanson, and R. L. Kline, First steps to the solar power satellite, *IEEE Spectrum*, May, 1979, p. 52-58.

A. Lavi and G. H. Lavi, Ocean thermal energy conversion (OTEC): social and environmental issues, *Energy 4*, 833-840 (1979).

J. M. Weingart, Global aspects of sunlight as a major energy source, *Energy 4*, 775-798 (1979).

fusion

C. C. Baker, G. A. Carlson, and R. A. Krakowski, "Trends and developments in magnetic fusion reactor concepts", *Nuclear Technology/Fusion 1*, 5-78 (1981).

H. P. Furth, "Progress toward a tokamak fusion reactor", *Scientific American 241*, 50-61 (1979).

G. H. Miley and J. G. Gilligan, "A possible route to small, flexible fusion units", *Energy 4*, 163-170 (1979).

D. Steiner, W. R. Becraft, and P. H. Sager, "The engineering test facility", *Journal of Fusion Energy 1*, 5-48 (1981).

CHAPTER 2
NUCLEAR REACTIONS AND COULOMB COLLISIONS

2A. Distribution Functions and Averages

The description of collision processes involves a mathematical description of particles' positions and velocities. The six-dimensional space (x,y,z,v_x,v_y,v_z) of position and velocity is called *phase space*, and is abbreviated by the vectors $(\vec{x},\vec{v})$. Let $f(x,y,z,v_x,v_y,v_z,t)dxdydzdv_xdv_ydv_z$ represent the number of particles having positions between x and x + dx; y and y + dy; z and z + dz; and velocities between v_x and $v_x + dv_x$; v_y and $v_y + dv_y$; and between v_z and $v_z + dv_z$ at time t. In other words, the distribution function f represents the number of particles per unit volume located simultaneously in both boxes of the six-dimensional volume element (Fig. 2A1).

Let $n(x,y,z,t)dxdydz$ be the number of particles per unit volume in dxdydz at point (x,y,z) and time t. The particle density n is found by integrating f over all velocities:

$$n(x,y,z,t) = \int_{-\infty}^{\infty} dv_x \int_{-\infty}^{\infty} dv_y \int_{-\infty}^{\infty} dv_z \, f(x,y,z,v_x,v_y,v_z,t) \qquad (2A1)$$

For simplicity, we will abbreviate $dv_xdv_ydv_z$ by $d\vec{v}$ and dxdydz by $d\vec{x}$. For example, Eq. (2A1) may be written as

$$n(\vec{x},t) = \int d\vec{v} \, f(\vec{x},\vec{v},t) \qquad (2A2)$$

where it is understood that $d\vec{v}$ indicates a three dimensional integration over $dv_xdv_ydv_z$, with the limits of integration including all possible values.

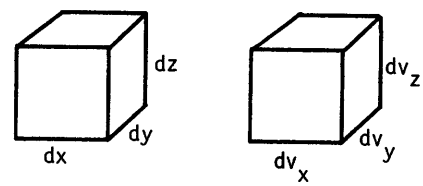

Fig. 2A1. A six-dimensional volume element of phase space.

By definition of a *mean* or *average value* of any function g(u) relative to a distribution function f(u),

$$\langle g(u) \rangle \equiv \frac{\int du\, f(u)\, g(u)}{\int du\, f(u)} \tag{2A3}$$

where the limits of integration should include all possible values of u. For example, u might represent the annual income of a family, and f might be the distribution function representing how many families have each value of income. If we set g(u) = u, then

$$\langle u \rangle \equiv \frac{\int du\, f(u)\, u}{\int du\, f(u)} \tag{2A4}$$

would represent the average income of the families considered. The denominator $\int du\, f(u) = N$, the total number of families.

Similar averages are useful in the theory of atomic and nuclear collisions. For example, the average velocity is

$$\langle \vec{v} \rangle \equiv \frac{\int d\vec{v}\, f(\vec{x},\vec{v},t)\, \vec{v}}{\int d\vec{v}\, f(\vec{x},\vec{v},t)} , \tag{2A5}$$

where the denominator equals the particle density $n(\vec{x},t)$; and the average value of kinetic energy $W \equiv mv^2/2$ (nonrelativistic) is

$$\langle W \rangle \equiv \frac{\int d\vec{v}\, f(\vec{x},\vec{v},t)\, mv^2/2}{\int d\vec{v}\, f(\vec{x},\vec{v},t)} . \tag{2A6}$$

At equilibrium, the distribution function of a group of particles has a Maxwellian distribution function given by

$$f_M(\vec{x},\vec{v},t) = n(\vec{x},t)\, (\beta/\pi)^{3/2} \exp(-\beta v^2) \tag{2A7}$$

where $\beta \equiv m/2kT$, m = particle mass, k = Boltzmann constant (Appendix B), T = temperature, and $v^2 = v_x^2 + v_y^2 + v_z^2$. The values of integrals involving Maxwellian distribution functions may be found using the integral tables of Appendix C. Thus, it can be verified that the Maxwellian distribution function of Eq. (2A7) satisfies Eq. (2A2).

EXAMPLE PROBLEM 2A1

Find the average values of v_x and $mv_x^2/2$ corresponding to a Maxwellian distribution function.

From Eq. (2A5),

$$\langle v_x \rangle = \frac{\int d\vec{v}\, f_M(\vec{x},\vec{v},t)\, v_x}{\int d\vec{v}\, f_M(\vec{x},\vec{v},t)}$$

$$= \frac{\int_{-\infty}^{\infty}dv_x \int_{-\infty}^{\infty}dv_y \int_{-\infty}^{\infty}dv_z\ n(\vec{x},t)\ (\beta/\pi)^{3/2}\exp[-\beta(v_x^2+v_y^2+v_z^2)]v_x}{\int_{-\infty}^{\infty}dv_x \int_{-\infty}^{\infty}dv_y \int_{-\infty}^{\infty}dv_z\ n(\vec{x},t)\ (\beta/\pi)^{3/2}\exp[-\beta(v_x^2+v_y^2+v_z^2)]} = 0$$

since $\int_{-\infty}^{\infty}dv_x \exp(-\beta v_x^2)v_x = 0$. Similarly,

$$\langle mv_x^2/2\rangle = \frac{\int_{-\infty}^{\infty}dv_x \int_{-\infty}^{\infty}dv_y \int_{-\infty}^{\infty}dv_z\ n(\vec{x},t)\ (\beta/\pi)^{3/2}\exp[-\beta(v_x^2+v_y^2+v_z^2)]mv_x^2/2}{\int_{-\infty}^{\infty}dv_x \int_{-\infty}^{\infty}dv_y \int_{-\infty}^{\infty}dv_z\ n(\vec{x},t)\ (\beta/\pi)^{3/2}\exp[-\beta(v_x^2+v_y^2+v_z^2)]}$$

$$\frac{\int_{-\infty}^{\infty}dv_x \exp(-\beta v_x^2)mv_x^2/2}{\int_{-\infty}^{\infty}dv_x \exp(-\beta v_x^2)} = kT/2.$$

Since the integrals over dv_y and dv_z are the same in numerator and denominator, they cancel out.

If we evaluated $\langle mv_y^2/2\rangle$ or $\langle mv_z^2/2\rangle$, the result would also be kT/2. Therefore,

$$\langle W\rangle = \langle m(v_x^2+v_y^2+v_z^2)/2\rangle = \langle mv_x^2/2\rangle + \langle mv_y^2/2\rangle + \langle mv_z^2/2\rangle$$

$$= 3kT/2. \qquad (2A8)$$

We can obtain the same result from Eq. (2A6). We know that an integral of the form $\int_{-\infty}^{\infty}dx \int_{-\infty}^{\infty}dy \int_{-\infty}^{\infty}dz\ f(r)$, where $r = (x^2+y^2+z^2)^{1/2}$, may be transformed to spherical geometry as $\int_{0}^{\infty}dr\ 4\pi r^2 f(r)$. Using the same transformation in velocity space, Eq. (2A6) becomes

$$\langle W\rangle = \frac{\int_0^{\infty} dv 4\pi v^2\ n(\vec{x},t)\ (\beta/\pi)^{3/2} e^{-\beta v^2}\ mv^2/2}{\int_0^{\infty} dv 4\pi v^2\ n(\vec{x},t)\ (\beta/\pi)^{3/2} e^{-\beta v^2}}$$

$$= \frac{(m/2)\ \int_0^{\infty}dv\ e^{-\beta v^2}\ v^4}{\int_0^{\infty}dv\ e^{-\beta v^2}\ v^2} = 3kT/2\ , \qquad (2A9)$$

in agreement with Eq. (2A8). The distribution function can also be written in terms of kinetic energy W by setting

$$F_M(\vec{x},W,t)dW = f_M(\vec{x},\vec{v},t)4\pi v^2 dv \qquad (2A10)$$

Since $v = (2W/m)^{1/2}$, $dv = (2/m)^{1/2}dW/2W^{1/2}$, and Eq. (2A10) becomes

$$F_M(\vec{x},W,t)dW = 2\pi^{-1/2}(kT)^{-3/2}n(\vec{x},t)W^{1/2}\exp(-W/kT)dW. \qquad (2A11)$$

This function is illustrated in Fig. 2A2 as a function of W/kT. We can also find averages with respect to $F_M(\vec{x},W,t)$. For example, the average value of particle speed $v = (2W/m)^{\frac{1}{2}}$ is

$$\langle v \rangle = \frac{\int_0^\infty dW\, 2\pi^{-\frac{1}{2}}(kT)^{-3/2} n(\vec{x},t) W^{\frac{1}{2}} \exp(-W/kT)\, (2W/m)^{\frac{1}{2}}}{\int_0^\infty dW\, 2\pi^{-\frac{1}{2}}(kT)^{-3/2} n(\vec{x},t) W^{\frac{1}{2}} \exp(-W/kT)}$$

$$= (8kT/\pi m)^{\frac{1}{2}}. \qquad (2A12)$$

The term "temperature" has no meaning for an individual particle. It is related to the average energy of particles having a Maxwellian distribution, since $kT = 2\langle W \rangle/3$. Using this relation, we can also define a fictitious temperature for non-Maxwellian distributions. The temperature has units of degrees Kelvin (K), kT has units of Joules (J), and kT/e has units of electron Volts (eV), where e is the electronic charge. It is common to speak of a "temperature" T in units of eV, however. A temperature of 1 eV corresponds to a temperature of (e/k) = 11604.9 K, and 1 keV = 1000 eV = 1.160×10^7 K.

Using the concepts of distribution functions and averages, the nuclear fusion reaction rates can be calculated and averaged over Maxwellian distributions of fuel ions.

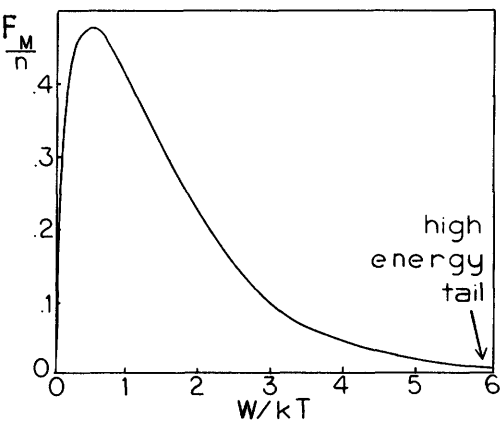

Fig. 2A2. The Maxwellian energy distribution function $F_M(\vec{x},W,t)/n(\vec{x},t)$ vs. W/kT. The total area under this curve = 1.

2B. Cross Sections and Reaction Rates

monoenergetic beam on stationary target

Consider the case of a monoenergetic particle beam from an accelerator incident upon a stationary target, as shown in Fig. 2B1. Let $n_1(x)$ be the density of *uncollided* beam particles, those which have not yet had a collision. The number of collisions which the incident particles have in going a small distance dx will be proportional to n_1 and to the target particle density n_2. Calling the proportionality constant σ, we can write

$$dn_1/dx = -\sigma n_1(x) n_2 \qquad (2B1)$$

where the minus sign indicates that the density of uncollided beam particles is decreasing as a result of collisions. The proportionality constant σ, defined by this equation, is called a *cross section*. Rearranging Eq. (2B1),

$$\sigma = \left[-\frac{dn_1}{n_1}\right]\left[\frac{1}{n_2 dx}\right]$$

$$= \begin{bmatrix}\text{fractional attenuation}\\ \text{of beam in distance dx}\end{bmatrix}\left[\frac{1}{\begin{matrix}\text{target particles per unit}\\ \text{area in distance dx}\end{matrix}}\right]$$

$$= \text{(collision probability)}\ \ \text{(area per target particle)}$$

$$= \begin{bmatrix}\text{effective area per target particle}\\ \text{for causing collisions}\end{bmatrix} . \qquad (2B2)$$

For *nuclear* collisions, the target diameter is $\sim 10^{-14}$ m, so a special unit has been defined for nuclear cross sections:

1 barn = 10^{-28} m^2. (The symbol $\sim$ means "on the order of".) For *atoms*, on the other hand, the diameters and cross sections are $\sim 10^{-10}$ m and $\sim 10^{-20}$ m^2.

The *reaction rate* per unit volume is defined to be

$$r(\vec{x},t) = -\frac{dn_1(\vec{x},t)}{dt} = n_1(\vec{x},t)n_2\sigma\frac{dx}{dt} =$$

$$n_1(\vec{x},t)n_2\sigma v . \qquad (2B3)$$

If the accelerator voltage is ϕ and the particle charge is q, then the resultant beam speed for a nonrelativistic case is

$$\tfrac{1}{2}mv^2 = q\phi,$$

$$v = (2q\phi/m)^{\frac{1}{2}} . \qquad (2B4)$$

The total beam current I is given by

$$I = \int d\vec{A}\cdot\vec{J} \qquad (2B5)$$

where $d\vec{A}$ is a differential cross sectional area, $\vec{J}$ is the beam current density (A/m^2), found from

$$\vec{J} = n_1 q\vec{v} , \qquad (2B6)$$

and n_1 is the beam density incident on the target. For a uniform circular beam of radius a

$$I = \pi a^2 J = \pi a^2 n_1 q v, \quad \text{or}$$

$$n_1 = I/\pi a^2 q v . \qquad (2B7)$$

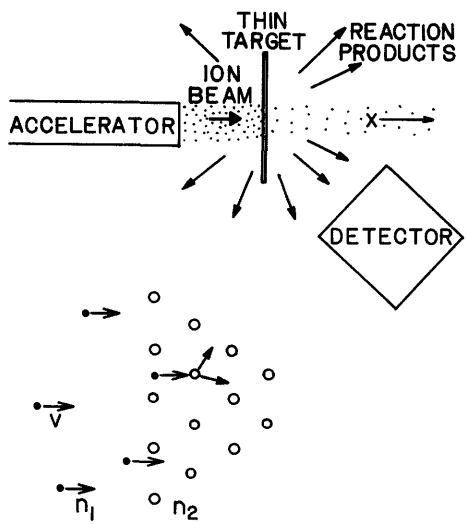

Fig. 2B1. A beam of monoenergetic ions with density n_1 and speed v incident on a stationary target with atomic density n_2 (top), and a microscopic view of the beam-target interaction region (bottom).

If the target is very thin, then n_1 changes very little as the beam passes through the target, and n_1 in the target can be estimated from Eq. (2B7), since the other parameters of that equation are all known from experimental measurements. Using a detector to measure the emission rate of reaction products (Fig. 2B1), the reaction rate in the target can be estimated. Dividing by the volume of the interaction region then gives the reaction rate per unit volume, r. The volume of the interaction region is equal to the target thickness times the beam-target interaction area. (If the beam is smaller than the target, the interaction area equals the beam area πa^2.)

The target atom density is given by

$$n_2 = \rho N_A N_a / M \qquad \text{(atoms/m}^3\text{)} \qquad \text{(2B8)}$$

where ρ is the target mass density (kg/m^3), the Avogadro number $N_A = 6.022 \times 10^{23}$ molecules/mole, M is the molecular weight of the target (kg/mole), and N_a is the number of target atoms per target molecule. (For example, $N_a = 2$ atoms/molecule for hydrogen in water.)

Now, all the quantities in Eq. (2B3) except σ are known from experimental measurements, so σ can be calculated.

EXAMPLE PROBLEM 2B1

A 100 keV, 1 mA deuteron beam is incident on a thin target of tritiated polyethylene with mass density 930 kg/m^3 and thickness 10^{-4} m. The beam radius is 10^{-3} m, and from neutron emission rates it is determined that the total fusion reaction rate is 2.92×10^{13} reactions per second. Estimate the cross section.

For tritiated polyethylene, $N_a = 4$ tritium atoms/molecule, and M = 24 g/mole = 0.024 kg/mole. Therefore, using Eq.(2B8),

$$n_2 = 930(6.022 \times 10^{23})\ 4/.024 = 9.33 \times 10^{28} \text{ atoms/m}^3.$$

From Eq. (2B4),

$$v = (2q\phi/m)^{\frac{1}{2}}$$

$$= 3.10 \times 10^6 \text{ m/sec.}$$

From Eq. (2B7),

$$n_1 = I/\pi a^2 q v$$

$$= 6.41 \times 10^{14} \text{ beam atoms/m}^3.$$

The target interaction volume is

$$V = \pi a^2\, \Delta x = \pi 10^{-6}\text{m}^2 (10^{-4}\text{m}) = 3.14 \times 10^{-10} \text{ m}^3.$$

and the reaction rate per unit volume is

$$r = 2.92 \times 10^{13} \text{ sec}^{-1}/3.14 \times 10^{-10} \text{ m}^3 = 9.30 \times 10^{22} \text{ reactions/m}^3\text{sec.}$$

Finally, from Eq. (2B3),

$$\sigma = r/n_1 n_2 v = 9.30\times10^{22}\text{sec}^{-1}/(6.41\times10^{14}\text{m}^{-3}9.33\times10^{28}\text{m}^{-3}3.10\times10^{6}\text{m/sec})$$

$$= 5.02 \times 10^{-28}\ \text{m}^2 = 5.02\ \text{barns}.$$

In using Eq. (2B7) it was assumed that n_1 changed very little in the target. We can check this approximation by estimating the fractional attentuation in the target

$$\Delta n_1/n_1 \simeq n_2\sigma\Delta x = 9.33\times10^{28}\text{m}^{-3}5.02\times10^{-28}\text{m}^2 10^{-4}\text{m} = .0047.$$

(In an actual experiment, scattering collisions would reduce the beam energy as the deuterons go through the target.)

Such experiments can be done at various beam energies to derive a plot of σ vs. beam energy.

moving target

In a plasma, both the incident and "target" particles will be moving, and the speed v of equation (2B3) must be replaced by the magnitude of the relative velocity

$$v = |\vec{v}| = |\vec{v}_1 - \vec{v}_2| \tag{2B9}$$

where $\vec{v}_1$ and $\vec{v}_2$ are the velocities of incident and "target" particles. The differential densities of particles having velocities $\vec{v}_1$ and $\vec{v}_2$ are

$$dn_1 = f(\vec{x},\vec{v}_1,t)d\vec{v}_1$$

$$dn_2 = f(\vec{x},\vec{v}_2,t)d\vec{v}_2 \quad , \tag{2B10}$$

and the cross section depends only upon the relative speed v. Therefore, the differential reaction rate due to particles dn_1 interacting with particles dn_2 is

$$d^2r = dn_1 dn_2 \sigma(v)v \tag{2B11}$$

The total reaction rate per unit volume at a given position and time is the integral of d^2r over all velocities $\vec{v}_1$ and $\vec{v}_2$:

$$r(\vec{x},t) = \int d\vec{v}_1 \int d\vec{v}_2\ f(\vec{x},\vec{v}_1,t)f(\vec{x},\vec{v}_2,t)\sigma(v)v \ . \tag{2B12}$$

This general relation will now be evaluated for various particular cases.

two Maxwellian distributions

Consider the case of two species of particles, such as deuterons and tritons, each having Maxwellian distributions, characterized by $\beta_1 = m_1/2kT_1$ and $\beta_2 = m_2/2kT_2$. For this case, Eq. (2B12) becomes

$$r = n_1(\vec{x},t)n_2(\vec{x},t)(\beta_1/\pi)^{3/2}(\beta_2/\pi)^{3/2} \int d\vec{v}_1 \int d\vec{v}_2 \; v\sigma(v)\exp(-\beta_1 v_1^2 - \beta_2 v_2^2). \quad (2B13)$$

It is convenient to change variables using $\vec{v}_1 = (\vec{v}+\vec{v}_2)$, $d\vec{v}_1 = d\vec{v}$ (holding $\vec{v}_2$ constant during this integration) so that

$$r = n_1(\vec{x},t)n_2(\vec{x},t)\ (\beta_1\beta_2/\pi^2)^{3/2} \int d\vec{v} \int d\vec{v}_2 \; v\sigma(v)\exp(-\beta_1(\vec{v}+\vec{v}_2)^2 - \beta_2 v_2^2). \quad (2B14)$$

The argument of the exponential function may be rearranged as follows:

$$-\beta_1 v^2 - 2\beta_1 \vec{v}_2\cdot\vec{v} - \beta_1 v_2^2 - \beta_2 v_2^2 =$$

$$= -\beta_1\beta_2 v^2/(\beta_1+\beta_2) - (\beta_1+\beta_2)[\vec{v}_2 + \beta_1\vec{v}/(\beta_1+\beta_2)]^2 \quad . \quad (2B15)$$

The terms involving only $\vec{v}$ may be taken outside the integral over $\vec{v}_2$, so that the reaction rate becomes

$$r = n_1(\vec{x},t)n_2(\vec{x},t)\ (\beta_1\beta_2/\pi^2)^{3/2} \int d\vec{v}\; v\sigma(v)\exp[-\beta_1\beta_2 v^2/(\beta_1+\beta_2)]$$

$$\int d\vec{v}_2 \exp\{-(\beta_1+\beta_2)[\vec{v}_2 + \beta_1\vec{v}/(\beta_1+\beta_2)]^2\} \quad . \quad (2B16)$$

To evaluate the integral over v_2, we can use the substitution $\vec{u} \equiv \vec{v}_2+\beta_1\vec{v}/(\beta_1+\beta_2)$. Since $\vec{v}$ is constant during this integration, $d\vec{v}_2 = d\vec{u}$. Let $\beta \equiv \beta_1\beta_2/(\beta_1+\beta_2)$. Then

$$r = n_1(\vec{x},t)n_2(\vec{x},t)\ (\beta_1\beta_2/\pi^2)^{3/2} \int d\vec{v}\; v\sigma(v)\exp(-\beta v^2) \int d\vec{u} \exp[-(\beta_1+\beta_2)u^2]$$

$$= n_1(x,t)n_2(x,t)\ (\beta_1\beta_2/\pi^2)^{3/2} \int d\vec{v}\; v\sigma(v)\exp(-\beta v^2)\ \pi^{3/2}(\beta_1+\beta_2)^{-3/2}$$

$$= n_1(x,t)n_2(x,t)\ (\beta/\pi)^{3/2} \int d\vec{v}\; v\sigma(v)\exp(-\beta v^2) \quad . \quad (2B17)$$

Let $\langle\sigma v\rangle$ be the average value of $\sigma(v)v$ over a Maxwellian distribution characterized by the parameter β. Then

$$\langle\sigma v\rangle = \frac{\int d\vec{v}\; n(\vec{x},t)\ (\beta/\pi)^{3/2}\exp(-\beta v^2)\sigma(v)v}{\int d\vec{v}\; n(\vec{x},t)\ (\beta/\pi)^{3/2}\exp(-\beta v^2)}$$

$$= (\beta/\pi)^{3/2} \int d\vec{v} \exp(-\beta v^2)\sigma(v)v \quad . \quad (2B18)$$

Comparing Eqs. (2B17) and (2B18), we see that

$$r(\vec{x},t) = n_1(\vec{x},t)n_2(\vec{x},t)\langle\sigma v\rangle \qquad (m^{-3}s^{-1}) \ , \quad (2B19)$$

which is similar to Eq. (2B3). The quantity $\langle\sigma v\rangle$ is called the *reaction rate parameter*. For the common case in which $T_1 = T_2$, β reduces to

$$\beta = m_r/2kT. \quad (2B20)$$

where $m_r \equiv m_1 m_2/(m_1+m_2)$ is the "reduced mass".

The reaction rate calculated from Eq. (2B19) is useful for many phenomena with interacting Maxwellian distributions, including nuclear reactions, atomic collisions, and galactic interactions. Once the cross section is known as a function of relative speed, the reaction rate parameter may be calculated from Eq. (2B18)

$$\langle\sigma v\rangle = (\beta/\pi)^{3/2} 4\pi \int_0^\infty dv\ v^3 \sigma(v) \exp(-\beta v^2). \tag{2B21}$$

Then,

$$\langle\sigma v\rangle \simeq (\beta/\pi)^{3/2} 4\pi \sum_j \Delta v_j\ v_j^3 \sigma(v_j) \exp(-\beta v_j^2) w_j\ , \tag{2B22}$$

where the integral is replaced by a summation over finite elements with weighting factors w_j. For example, using "Simpson's Rule" with equal Δv_j, the weighting factors w_j = 1/3, 4/3, 2/3, 4/3, 2/3, 4/3, ... , 2/3, 4/3, 1/3.

interactions among like particles

Consider the problem of calculating how many handshakes N there could be among different people in a large room containing n men. The number can be found by counting the number of x's in Table 2B1. It can be represented mathematically as

$$N = n(n-1)/2 \simeq n^2/2 \quad \text{if } n >> 1 \tag{2B23}$$

TABLE 2B1. Estimation of the number of handshakes between different people which could occur in a room containing n men.

	Al	Ben	Dan	Ed	Frank	George	Herb	Igor
Al		X	X	X	X	X	X	X
Ben			X	X	X	X	X	X
Dan				X	X	X	X	X
Ed					X	X	X	X
Frank						X	X	X
George							X	X
Herb								X
Igor								

Now consider the alternative problem of counting the number of possible handshakes between n_1 men and n_2 women in the room. For this case

$$N = n_1 n_2 \quad . \tag{2B24}$$

Since the fusion reaction rates in a plasma are proportional to the number of possible interactions which can occur, a similar reasoning applies. For unlike particles, the interaction rate is proportional to $n_1 n_2$, but for like par-

ticles, the interaction rate is proportional to $n^2/2$. Therefore, to avoid counting the same possible interaction twice (equivalent to filling in x's in the bottom half of Table 2B1), we must insert a factor of ½ in the reaction rate formula (2B19) to calculate reaction rates among *indistinguishable* like particles. Thus, for reactions among deuterons, Eq. (2B19) becomes

$$r(\vec{x},t) = \tfrac{1}{2}\, n^2(\vec{x},t)\langle\sigma v\rangle \tag{2B25}$$

The factor of ½ is not needed for beam-plasma interactions or beam-target interactions, because then the two species have separate identities and densities. The result of Eq. (2B25) could have been derived more rigorously by varying the limits of intergration of Eq. (2B13) so as to avoid counting the same interaction between v_1 and v_2 twice.

beam and Maxwellian

Consider the case of a monoenergetic beam injected into a Maxwellian plasma. For this case the relative velocity is

$$\vec{v} = \vec{v}_b - \vec{v}_2 \tag{2B26}$$

where $\vec{v}_b$ is the beam velocity and $\vec{v}_2$ is the velocity of the plasma ions. Taking $\vec{v}_b$ = constant, only $f(\vec{x},\vec{v}_1,t)$ depends upon $\vec{v}_1$, and the reaction rate equation (2B12) may be rearranged as follows:

$$r(\vec{x},t) = \int d\vec{v}_1 \int d\vec{v}_2 \;\; f(\vec{x},\vec{v}_1,t) f(\vec{x},\vec{v}_2 t)\sigma(|\vec{v}_b-\vec{v}_2|)|\vec{v}_b-\vec{v}_2|$$

$$= \int d\vec{v}_2 \; f(\vec{x},\vec{v}_2,t)\sigma(|\vec{v}_b-\vec{v}_2|)|\vec{v}_b-\vec{v}_2| \int d\vec{v}_1 \; f(\vec{x},\vec{v}_1,t). \tag{2B27}$$

The integral over $d\vec{v}_1$ yields the beam density $n_1(x,t)$, so the reaction rate is

$$r(\vec{x},t) = n_1(\vec{x},t) \int d\vec{v}_2 \; f(\vec{x},\vec{v}_2,t)\sigma(v)v \quad , \tag{2B28}$$

where $v = |\vec{v}_b-\vec{v}_2|$. For a Maxwellian distribution of plasma ions, this becomes

$$r(\vec{x},t) = n_1(\vec{x},t)n_2(\vec{x},t)(\beta_2/\pi)^{3/2} \int d\vec{v}_2 \; \exp(-\beta_2 v_2^2)\sigma(v)v. \tag{2B29}$$

If we define

$$\langle\sigma v\rangle_b = (\beta_2/\pi)^{3/2} \int d\vec{v}_2 \; \exp(-\beta_2 v_2^2)\sigma(v)v \quad , \tag{2B30}$$

then

$$r(\vec{x},t) = n_1(\vec{x},t)n_2(\vec{x},t)\langle\sigma v\rangle_b \quad . \tag{2B31}$$

The integrals of Eq. (2B30) can be further evaluated analytically, replacing $\vec{v}_2$ by $\vec{v}_b-\vec{v}$, $d\vec{v}_2$ by $d\vec{v}$, and using spherical velocity coordinates in which $d\vec{v} = v^2 dv \sin\theta d\theta d\phi$. Since $v_2^2 = v_b^2 + v^2 - 2vv_b\cos\theta$, the integrals over $d\phi$ and $d\theta$ can be evaluated to give

$$\langle\sigma v\rangle_b = \frac{\beta_2^{1/2}}{\pi^{1/2} v_b} \int_0^\infty dv\, v^2\sigma(v)\,\{\exp[-\beta_2(v-v_b)^2] - \exp[-\beta_2(v+v_b)^2]\}\ . \qquad (2B32)$$

The remaining integral must be done numerically. [For some forms of $\sigma(v)$, $\langle\sigma v\rangle_b$ can be expressed in terms of tabulated functions.]

two colliding beams

In like fashion, the reaction rate due to two monoenergetic beams with velocities v_{b1} and v_{b2} intersecting at an angle θ is found to be

$$r(\vec{x},t) = n_1(\vec{x},t)n_2(\vec{x},t)\sigma(v_{bb})v_{bb} \qquad (2B33)$$

where

$$v_{bb} = |\vec{v}_{b1}-\vec{v}_{b2}| = (v_{b1}^2 + v_{b2}^2 - 2v_{b1}v_{b2}\cos\theta)^{1/2}\ . \qquad (2B34)$$

collision frequency and mean free path

The mean time between reactions for particles of type 1 is equal to their density divided by the reaction rate:

$$\tau_1 = n_1(\vec{x},t)/r(\vec{x},t) \qquad (s) \qquad (2B35)$$

for any type of collision described by r, and the reciprocal of τ_1 is called the *collision frequency:*

$$\nu_1 = 1/\tau_1 = r(\vec{x},t)/n_1(\vec{x},t) \qquad (s^{-1}). \qquad (2B36)$$

The *mean free path* length travelled by a particle of type 1 between collisions is equal to its average speed times the mean collision time

$$\lambda_1 = \langle v_1\rangle\tau_1 = \frac{n_1(\vec{x},t)\langle v_1\rangle}{r(\vec{x},t)} = \frac{\langle v_1\rangle}{n_2\langle\sigma v\rangle} \qquad (m) \qquad (2B37)$$

For a monoenergetic beam on a stationary target, this reduces to $\lambda_1 = 1/n_2\sigma$. In these equations the subscripts 1 designate the particle species whose properties we wish to estimate. Similarly, values of ν_2 and λ_2 could be calculated for the other species of particles, and usually $\nu_2 \neq \nu_1$, $\lambda_2 \neq \lambda_1$, since the different species will have different densities and average speeds.

2C. Nuclear Fusion Reaction Rates

The cross sections of fusion reactions are functions of the relative speed between the two colliding particles. It is common practice to describe them in terms of particle energy, however, instead of speed. The cross sections for deuterons bombarding a tritium target and for tritons bombarding a deuterium target will be the same when the speed of approach is the same. For that case, the beam kinetic energies would have the ratio

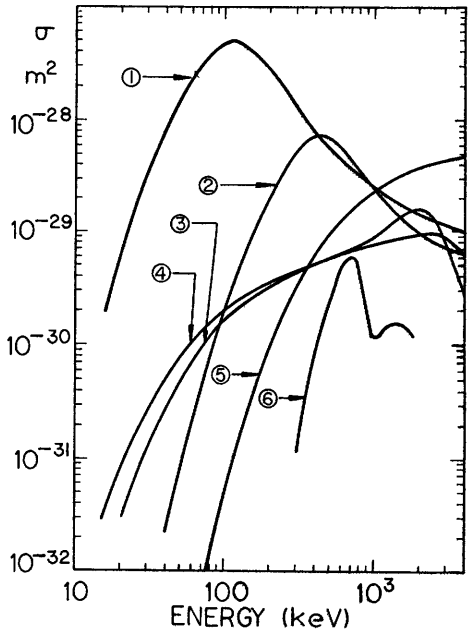

Fig. 2C1. Cross section vs. energy for monoenergetic beams on stationary targets. (1) D bombarding T, (2) D bombarding ^3He, (3) D + D → H + T, (4) T + T → ^4He + 2n, (5) ^3He bombarding T, (6) H bombarding ^{11}B. The cross section for D + D → ^3He + n is about the same as curve (3). From G. H. Miley, H. Towner, and N. Ivich, U. of Illinois Nucl. Eng. Report COO-2218-17 (1974).

Fig. 2C2 (below). Beam-plasma fusion reaction rate parameters $\langle\sigma v\rangle_b$ as functions of beam injection energy, for various plasma ion temperatures. (a) deuterons injected into tritium plasma, (b) tritons into deuterium plasma, (c) DDn reactions from deuterons into deuterium plasma, (d) DDp reactions from deuterons into deuterium plasma. From G. H. Miley et al, op. cit.

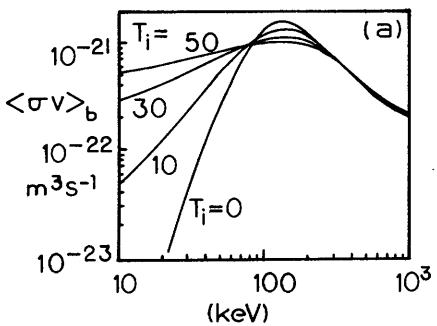

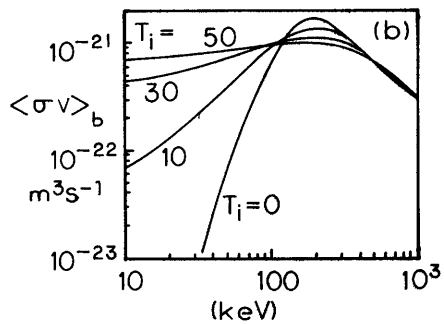

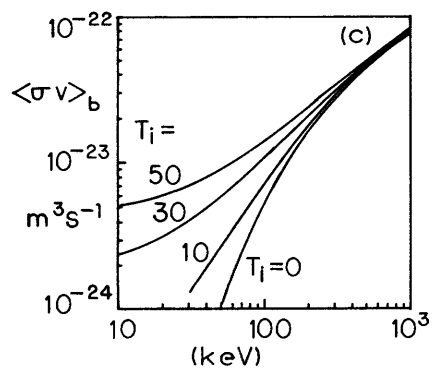

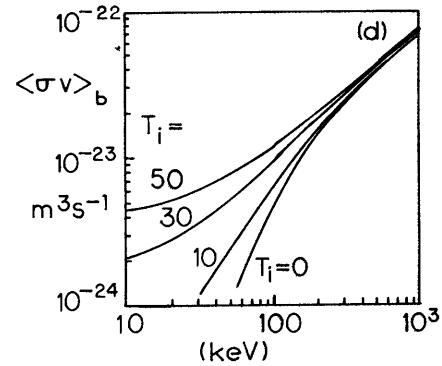

$$\frac{W_d}{W_t} = \frac{m_d v_d^2/2}{m_t v_t^2/2} = \frac{m_d}{m_t} = \frac{2}{3} \quad . \tag{2C1}$$

The cross section for monoenergetic deuterons bombarding a tritium target is shown as a function of deuteron kinetic energy W_d in Fig. 2C1, along with other reaction cross sections. Other possible fusion reactions have very low cross sections below 100 keV.

Values of $\langle\sigma v\rangle_b$ for monoenergetic tritons bombarding a Maxwellian deuterium plasma, and for monoenergetic deuterons incident on a Maxwellian tritium plasma or a Maxwellian deuterium plasma are shown in Fig. 2C2, for various plasma ion temperatures.

Maxwellian plasma reaction rate parameters $\langle\sigma v\rangle$ are listed in Table 2C1 for various reactions as functions of plasma ion temperature. Corresponding graphs

Table 2C1. Maxwellian reaction rate parameters, $m^3 s^{-1}$. (E-26 means 10^{-26}, etc.) From G. H. Miley, H. Towner, and N. Ivich, U. of Illinois Nucl. Eng. Report COO-2218-17 (1974).

T,keV	T(d,n)^{4}He	D(d,n)^{3}He	D(d,p)T	^{3}He(d,p)^{4}He	T(t,2n)^{4}He
1	.548 E-26	.692 E-28	.830 E-28	.302 E-31	.328 E-27
1.5	.589 E-25	.647 E-27	.729 E-27	.132 E-29	.218 E-26
2	.263 E-24	.260 E-26	.282 E-26	.142 E-28	.709 E-26
3	.171 E-23	.145 E-25	.150 E-25	.275 E-27	.303 E-25
4	.558 E-23	.423 E-25	.424 E-25	.177 E-26	.746 E-25
5	.129 E-22	.894 E-25	.877 E-25	.666 E-26	.140 E-24
6	.242 E-22	.157 E-24	.152 E-24	.183 E-25	.226 E-24
7	.398 E-22	.246 E-24	.235 E-24	.409 E-25	.329 E-24
8	.594 E-22	.355 E-24	.335 E-24	.796 E-25	.447 E-24
9	.826 E-22	.482 E-24	.451 E-24	.140 E-24	.579 E-24
10	.109 E-21	.626 E-24	.582 E-24	.227 E-24	.722 E-24
15	.265 E-21	.156 E-23	.141 E-23	.127 E-23	.156 E-23
20	.424 E-21	.273 E-23	.243 E-23	.379 E-23	.251 E-23
25	.559 E-21	.403 E-23	.357 E-23	.818 E-23	.351 E-23
30	.665 E-21	.541 E-23	.476 E-23	.145 E-22	.454 E-23
35	.745 E-21	.683 E-23	.598 E-23	.227 E-22	.557 E-23
40	.803 E-21	.826 E-23	.721 E-23	.323 E-22	.660 E-23
45	.843 E-21	.969 E-23	.844 E-23	.430 E-22	.763 E-23
50	.871 E-21	.111 E-22	.966 E-23	.544 E-22	.865 E-23
60	.897 E-21	.139 E-22	.121 E-22	.782 E-22	.107 E-22
70	.900 E-21	.166 E-22	.144 E-22	.102 E-21	.128 E-22
80	.890 E-21	.193 E-22	.167 E-22	.124 E-21	.148 E-22
90	.871 E-21	.218 E-22	.190 E-22	.144 E-21	.169 E-22
100	.849 E-21	.243 E-22	.212 E-22	.161 E-21	.191 E-22
150	.728 E-21	.358 E-22	.317 E-22	.220 E-21	.305 E-22
200	.628 E-21	.462 E-22	.414 E-22	.244 E-21	.424 E-22
250	.552 E-21	.559 E-22	.503 E-22	.251 E-21	.536 E-22
300	.495 E-21	.650 E-22	.585 E-22	.250 E-21	.631 E-22
energy yield W(J)	2.818E-12	5.24E-13	6.46E-13	2.93E-12	1.81E-12

are shown in Fig. 2C3. Some empirical equations fit to these data are listed in Table 2C2. Such expressions are useful for computer applications.

A simple formula for the D-T reaction rate parameter is

$$\langle \sigma v \rangle_{DT} \simeq 5.1 \times 10^{-22} \, [\ln(T_i) - 2.1] \; (m^3/s), \qquad (2C2)$$

which has ± 6% accuracy in the range $10 < T_i < 50$ KeV.

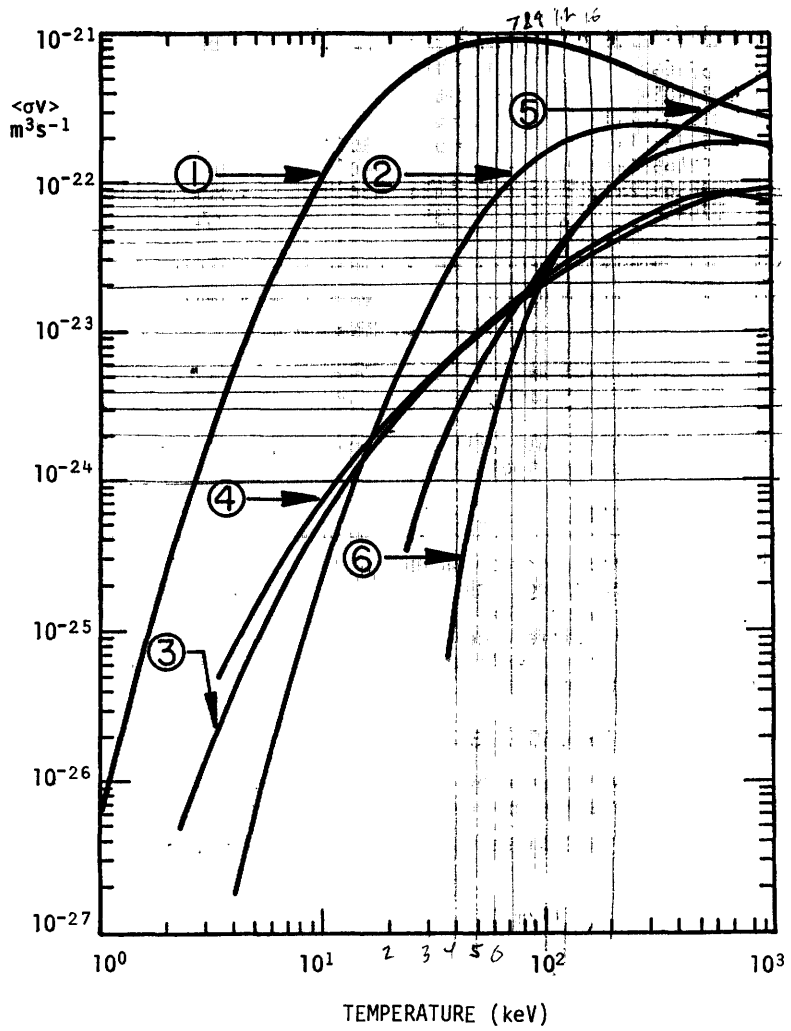

Fig. 2C3. Reaction rate parameters for mixtures of Maxwellian distributions at the same temperature. (1) D + T → n + ^{4}He, (2) D + ^{3}He → H + ^{4}He, (3) D + D → H + T, (4) T + T → ^{4}He + 2n, (5) T + ^{3}He → (various products), (6) H + ^{11}B → 3(^{4}He). The curve for D + D → ^{3}He + n is about the same as curve (3). From G. H. Miley, H. Towner, and N. Ivich, U. of Illinois Nucl. Eng. Report COO-2218-17 (1974).

$$\langle \sigma v \rangle_{DT} \simeq 1.7537 \times 10^{-22} \left(-1 + .16126\,T + 9.5843 \times 10^{-6}\,T^2\right)$$

$$\pm 10\% \text{ for } 8 \le T \le 35 \text{ keV}$$

Table 2C2. Empirical equations for fusion reaction rate parareters for Maxwellian distributions of ions at temperatures $1 \leq T \leq 80$ keV. These equations have accuracy $\lesssim 1$ % compared with precise computations of $\langle\sigma v\rangle$, but the basic cross section measurements have uncertainties up to 5 %. From L. M. Hively, "Convenient computational forms for Maxwellian reactivities", Nuclear Fusion 17, 873-876 (1977), Tables I-IV.

$\langle\sigma v\rangle = 10^{-6}\exp[a_1/T^r + a_2 + a_3T + a_4T^2 + a_5T^3 + a_6T^4]$ (m^3/s), T in keV.

	$T(d,n)^4He$	$D(d,p)T$	$D(d,n)^3He$	$^3He(d,p)^4He$
a_1	-21.377692	-15.511891	-15.993842	-27.764468
a_2	-25.204054	-35.318711	-35.017640	-31.023898
a_3	-7.1013427×10^{-2}	-1.2904737×10^{-2}	-1.3689787×10^{-2}	2.7889999×10^{-2}
a_4	1.9375451×10^{-4}	2.6797766×10^{-4}	2.7089621×10^{-4}	-5.5321633×10^{-4}
a_5	4.9246592×10^{-6}	-2.9198685×10^{-6}	-2.9441547×10^{-6}	3.0293927×10^{-6}
a_6	-3.9836572×10^{-8}	1.2748415×10^{-8}	1.2841202×10^{-8}	-2.5233325×10^{-9}
r	.2935	.3735	.3725	.3597

EXAMPLE PROBLEM 2C1

Calculate the neutron emission rate from a pure deuterium plasma with T = 30 KeV and $n = 10^{20}$ m^{-3}, ignoring secondary reactions of fusion products.

The neutron emission rate will equal the $D(d,n)He^3$ reaction rate. Using Eq. (2B25) with data from Table 2C1,

$$r = (10^{20}m^{-3})^2(.541\times10^{-23}m^3sec^{-1})/2 = 2.71 \times 10^{16} \text{ neutrons/m}^3\text{s}.$$

In this problem the average ion energy is 45 keV. If we consider a beam-target case with 45 keV beam energy, the $D(d,n)^3He$ reaction rate parameter $\sigma v = 3.8\times10^{-31}m^2(2.08\times10^6 \text{ m/s}) = 8\times10^{-25}$ m^3/s, which is much lower than for the 30 keV Maxwellian case. The difference is caused by the high reactivity of ions in the high-energy tail of the Maxwellian distribution function, and by the possibility of head-on collisions at high relative speeds.

2D. Power Density and Pressure

The power density produced by a given fusion reaction of type j is equal to the reaction rate r_j times the energy W_j released by the reaction. The total power density released by several reactions is the sum of their individual power densities:

$$P_f(\vec{x},t) = \sum_j r_jW_j \qquad (W/m^3) \quad , \tag{2D1}$$

where the subscript f indicates fusion power per unit volume. The total fusion power of the reactor, denoted by the subscript F, is the integral of P_f over the reactor volume:

$$P_F(t) = \int d\vec{x}\ P_f(\vec{x},t) \qquad (W). \tag{2D2}$$

We can define a volume-averaged power density

$$\langle P_f(t)\rangle \equiv \frac{\int d\vec{x}\, P_f(\vec{x},t)}{\int d\vec{x}} = \frac{P_F(t)}{V} \qquad (W/m^3) \quad , \tag{2D3}$$

where V is the plasma volume. Since the reactor cost increases with $V = P_F/\langle P_f\rangle$, it is economically desirable to use the largest possible value of $\langle P_f\rangle$. However, large values of P_f (time-averaged over a burn cycle) can cause radiation damage and overheating problems, shortening wall lifetime. For a long cylinder with length L, wall radius r_w, and plasma radius r_p, the average power flux on the walls F_p (W/m^2) may be found from the equation

$$2\pi r_w L F_p = P_F = \pi r_p^2 L \langle P_f\rangle \quad . \tag{2D4}$$

Materials problems (Chapter 24) will probably limit wall lifetimes to power fluences $\sim$ 10-20 MW-years/m^2. Thus, for a wall lifetime of 5 years, F_p would be limited to values $\sim$ 2-4 MW/m^2.

EXAMPLE PROBLEM 2D1

A cylindrical, steady-state reactor with uniform densities of deuterium and tritium $n_D = n_T = 10^{20}\ m^{-3}$, plasma radius = 1 m, and wall radius = 1.2 m has an estimated maximum wall fluence of 12 MW-years/m^2. Assuming that the first wall lifetime should be at least 4 years, find (a) the optimum fusion power density and (b) the corresponding required plasma temperature.

From the wall fluence and replacement time, F_p = (12 MW-years/m^2)/4 years = 3 MW/m^2. Then, from Eq. (2D4) we find

$$\langle P_f\rangle = 2r_w F_p/r_p^2 = 2(1.2)3/(1)^2 = 7.2\ MW/m^3 \ .$$

From Eq. (2D1), assuming the plasma to be uniform

$$P_f = \langle P_f\rangle = n_D n_T \langle\sigma v\rangle_{DT} W_{DT} + \tfrac{1}{2} n_D^2 (\langle\sigma v\rangle_{DDp} W_{DDp} + \langle\sigma v\rangle_{DDn} W_{DDn}) + \tfrac{1}{2} n_T^2 \langle\sigma v\rangle_{TT} W_{TT} \ .$$

Using reaction energies from Table 1E1, this becomes

$$\begin{aligned} 7.2\times10^6\ W/m^3 = {} & 10^{40} m^{-6} (2.818\times10^{-12} J)\langle\sigma v\rangle_{DT} \\ & + 5\times10^{39} m^{-6} (6.46\times10^{-13} J)\langle\sigma v\rangle_{DDp} \\ & + 5\times10^{39} m^{-6} (5.24\times10^{-13} J)\langle\sigma v\rangle_{DDn} \\ & + 5\times10^{39} m^{-6} (1.81\times10^{-12} J)\langle\sigma v\rangle_{TT} \end{aligned}$$

This equation can be solved for ion temperature. Since the DT reaction rate parameter is much larger than the others, we divide by its coefficient and solve for it:

$$\langle\sigma v\rangle_{DT} = 2.56\times10^{-22} - .1146\langle\sigma v\rangle_{DDp} - .0930\langle\sigma v\rangle_{DDn} - .321\langle\sigma v\rangle_{TT} \ .$$

From Table 2C1 it can be seen that the required temperature is $T_i \simeq 15$ keV. We

then use this approximate temperature to evaluate the other $\langle\sigma v\rangle$ terms

$$\langle\sigma v\rangle_{DT} = 2.56\times10^{-22} - 1.62\times10^{-25} - 1.45\times10^{-25} - 5.01\times10^{-25} = 2.55\times10^{-22}\ m^3s^{-1}.$$

Interpolating in Table 2C1, $T_i = 10 + 5(2.55-1.09)/(2.65-1.09) = 14.7$ keV. Higher T_i would increase $\langle P_f\rangle$ and shorten wall lifetime. Higher T_i would be permissible if the densities n_D and n_T were lowered, but then longer confinement times would be needed to satisfy the breakeven condition (Lawson criterion, Section 1F).

Thus, if the time-average of $\langle P_f\rangle$ is too low, the plasma volume required for a given total power will be very large, and if the time-averaged $\langle P_f\rangle$ is too large, the wall lifetime will be very short, both of which are uneconomical.

The pressure p exerted by a plasma is equal to the sum of the partial pressures of its constituents, each of which may be found approximately from the Ideal Gas Law

$$p = \sum_j p_j = n_e kT_e + n_i kT_i + n_\alpha kT_\alpha + \ldots \qquad (2D5)$$

where the subscripts e, i, and α denote electrons, fuel ions, and alpha particles. The pressure is thus equal to (2/3) the sum of the average 3-dimensional energy densities

$$p = (2/3)(n_e\langle W_e\rangle + n_i\langle W_i\rangle + n_\alpha\langle W_\alpha\rangle + \ldots) \qquad (Pa) \qquad (2D6)$$

In a magnetic field, the pressure varies with direction.

For a fusion reactor with equal electron and fuel ion densities $n_e = n_i = n$ and negligible alpha pressure, the density is

$$n = p/(kT_e + kT_i) \quad . \qquad (2D7)$$

Consider the case of a D-T plasma with $n_D = n_T = n/2$. At temperatures below 100 keV the fusion power densities of DD and TT reactions are much smaller than the D-T power density, so from Eqs. (2B19) and (2D1) we find that

$$P_f = \tfrac{1}{4}n^2\langle\sigma v\rangle_{DT}W_{DT} = \frac{p^2\langle\sigma v\rangle_{DT}W_{DT}}{4(kT_i)^2(1 + T_e/T_i)^2} \qquad W/m^3\ . \qquad (2D8)$$

For a catalyzed DD reactor, the corresponding equation is

$$P_f = \tfrac{1}{2}n^2\langle\sigma v\rangle_{DD}W_{DD} = \frac{p^2\langle\sigma v\rangle_{DD}W_{DD}}{2(kT_i)^2(1 + T_e/T_i)^2} \qquad W/m^3\ , \qquad (2D9)$$

where $\langle\sigma v\rangle_{DD} \equiv \langle\sigma v\rangle_{DDn} + \langle\sigma v\rangle_{DDp}$, and $W_{DD} = 21.6$ MeV $= 3.46\times10^{-12}$ J (from consumption of 3 deuterons per primary DD reaction).

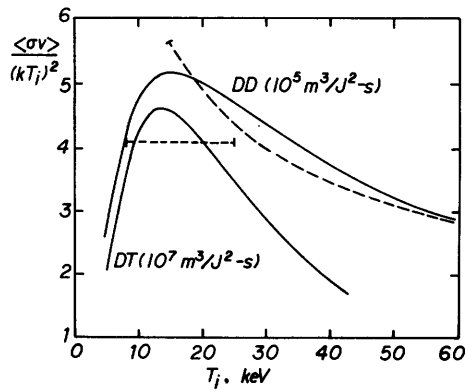

Fig. 2D1. Values of the parameter $\langle\sigma v\rangle/(kT_i)^2$ vs. T_i for DD and DT reactions (smooth curves).

Values of $\langle\sigma v\rangle/(kT_i)^2$ are shown in Fig. 2D1 for DD and DT reactions. The approximate formulas

$$\frac{\langle\sigma v\rangle_{DT}}{(kT_i)^2} \simeq 4.1 \times 10^7 \ \text{m}^3/\text{J}^2\text{-s} \qquad (\pm 15\ \%\ \text{for}\ 8 \leqq T_i \leqq 25\ \text{keV})$$

4.32×10^7 $\pm 6\%$ for $9 < T_i < 20$ (2D10)

$$\frac{\langle\sigma v\rangle_{DD}}{(kT_i)^2} \simeq 4.0 \times 10^5 \left(\frac{30\ \text{keV}}{T_i}\right)^{\frac{1}{2}} \text{m}^3/\text{J}^2\text{-s} \qquad (\pm 10\ \%\ \text{for}\ 15 \leqq T_i \leqq 70\ \text{keV}) \quad (2D11)$$

are indicated by dashed curves in the Figure. Substitution of these equations into Eqs. (2D8) and (2D9) yields

$$\textit{DT reactions}: \quad P_f \simeq \frac{2.9 \times 10^{-5} p^2}{(1 + T_e/T_i)^2} \ \text{W/m}^3 \qquad (8 \leqq T_i \leqq 25\ \text{keV}) \quad (2D12)$$

$$\textit{catalyzed DD reactions}: \quad P_f \simeq \frac{6.9 \times 10^{-7} p^2}{(1 + T_e/T_i)^2} \left(\frac{30\ \text{keV}}{T_i}\right)^{\frac{1}{2}} \text{W/m}^3 \qquad (15 \leqq T_i \leqq 70\ \text{keV}) \quad (2D13)$$

A reactor operating in the *hot-ion mode* ($T_e \ll T_i$) can thus have a fusion power density almost four times larger than one with $T_e = T_i$. Let us define a volume-averaged value of p^2 :

$$\langle p^2 \rangle \equiv \frac{\int d\vec{x}\ p^2}{V} \qquad (2D14)$$

where the integral is over the plasma volume V. We will integrate Eqs. (2D12) and (2D13) over the plasma volume and divide by V to find $\langle P_f \rangle$. Usually the

radial variation of p^2 will be much stronger than the variations of the other terms on Eqs. (2D12) and (2D13) , so it is a fair approximation to take them outside the integral sign, evaluating them at the plasma center. This will result in a slight underestimate of $\langle P_f \rangle$ for the DD case, since $(30/T_i)^{\frac{1}{2}}$ increases with radius. The magnetic field exerts an effective pressure of $B^2/2\mu_0$ (Section 8B). Let the ratio of rms plasma pressure to magnetic field pressure be defined as

$$\beta_* \equiv \frac{\langle p^2 \rangle^{\frac{1}{2}}}{B^2/2\mu_0} \qquad or \qquad \langle p^2 \rangle = \frac{\beta_*^2 B^4}{(2\mu_0)^2} \ . \tag{2D15}$$

The magnetic field value at any convenient reference point may be used in this definition. Then the approximate volume-averaged fusion power densities are

$$\textit{DT reactions:} \quad \langle P_f \rangle \simeq \frac{4.6\ \beta_*^2 B^4}{(1 + T_e/T_i)^2} \quad MW/m^3 \quad (8 \leq T_i \leq 25\ keV) \tag{2D16}$$

$$\textit{catalyzed DD reactions:} \quad \langle P_f \rangle \simeq \frac{0.11\ \beta_*^2 B^4}{(1 + T_e/T_i)^2} \left(\frac{30\ keV}{T_i}\right)^{\frac{1}{2}} MW/m^3 \quad (15 \leq T_i \leq 70\ keV) \tag{2D17}$$

where the temperatures are evaluated at the plasma center. If $T_e \simeq T_i$, these reduce to

$$\textit{DT reactions:} \quad \langle P_f \rangle \simeq 1.1\ \beta_*^2 B^4 \quad MW/m^3 \quad (8 \leq T_i \leq 25\ keV) \tag{2D18}$$

1.2 $\qquad 9 < T_i < 20 \quad \pm 6\%$

$$\textit{catalyzed DD reactions:} \quad \langle P_f \rangle \simeq 0.027\ \beta_*^2 B^4 \left(\frac{30\ keV}{T_i}\right)^{\frac{1}{2}} MW/m^3 \quad (15 \leq T_i \leq 70\ keV) \tag{2D19}$$

EXAMPLE PROBLEM 2D2

A given magnetic confinement system can sustain a plasma with $\beta_* = 0.1$ relative to the magnetic field at the center of the plasma. Assume that $T_e \simeq T_i$. What value of central magnetic field is needed to produce a volume-average fusion power density of 1 MW/m^3 with DT reactions ? with catalyzed DD reactions (taking $T_i \simeq 30$ keV) ?

Solving Eqs. (2D18) and (2D19) for B, we find B = 3.09 T for DT reactions and B = 7.80 T for catalyzed DD reactions. The inaccuracies of these equations are reduced in solving for B, since we take the fourth root of the equations. If higher values of β_* were attainable, then lower magnetic fields would suffice, and substantial cost savings would result in the magnet coils and structural supports.

2E. Coulomb Collisions

basic equations

Consider a *test particle* with mass m, velocity $\vec{v}$, charge q, and momentum $\vec{p} = m\vec{v}$ interacting with *field particles* having mass m_*, velocity $\vec{v}_*$, charge q_*, and momentum $\vec{p}_* = m\vec{v}_*$. By definition, let

$$\textit{relative velocity} \qquad \vec{u} \equiv \vec{v} - \vec{v}_* \tag{2E1}$$

$$\textit{reduced mass} \qquad m_r \equiv \frac{mm_*}{m + m_*} \tag{2E2}$$

$$\textit{center-of-mass velocity} \qquad \vec{v}_c \equiv \frac{m\vec{v} + m_*\vec{v}_*}{m + m_*} \quad . \tag{2E3}$$

The rate of change of test particle momentum may be written

$$\frac{d\vec{p}}{dt} = (\text{collision frequency})(\text{change in } \vec{p} \text{ per collision}) \; . \tag{2E4}$$

In a small differential volume dv_* of field particle velocity space, this may be written

$$\text{differential } \frac{d\vec{p}}{dt} = (dn_* u \, d\sigma)(\delta\vec{p}) \tag{2E5}$$

where $dn_* = f(\vec{v}_*)d\vec{v}_*$ is the number of field particles per unit volume, $d\sigma$ is the differential cross section for Coulomb scattering, and $\delta\vec{p}$ is the change in momentum per collision. The differential scattering cross section is a function of scattering angle and relative velocity u. Expressing the cross section in terms of differential solid angle $d\Omega$

$$d\sigma = \frac{d\sigma}{d\Omega} d\Omega \quad , \tag{2E6}$$

we can find the total rate of change of momentum by integrating over all field particle velocities and scattering angles:

$$\frac{d\vec{p}}{dt} = \int d\vec{v}_* \int d\Omega \;\; f(\vec{v}_*) \; u \, \frac{d\sigma}{d\Omega} \, \delta\vec{p} \tag{2E7}$$

Similarly, the rate of change of test particle kinetic energy is given by

$$\frac{dW}{dt} = \int d\vec{v}_* \int d\Omega \;\; f(\vec{v}_*) \; u \, \frac{d\sigma}{d\Omega} \, \delta W \tag{2E8}$$

where δW is the change due to a single collision. These are the basic equations for momentum and energy change due to Coulomb collisions. We will derive expressions for $\delta\vec{p}$, δW, and the Coulomb scattering cross section $d\sigma/d\Omega$, then evaluate the integrals. Those not interested in mathematical derivations may skip to the subsection "results", p. 40.

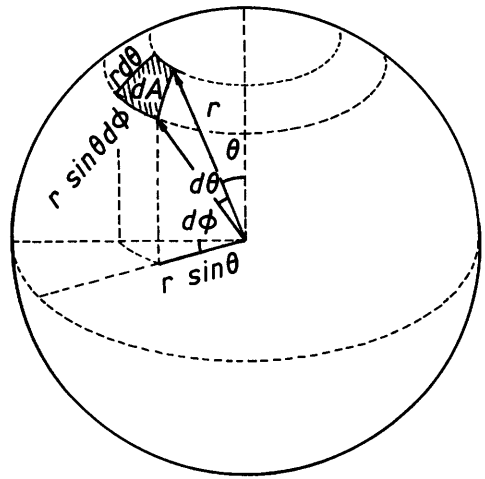

Fig. 2E1. A differential area on the surface of a sphere subtended by the differential angle dθ .

From Fig. 2E1 we can evaluate the differential area dA on the surface of the sphere and use it in the definition of differential *solid angle:*

$$d\Omega \equiv \frac{dA}{r^2} = \frac{(r\sin\theta d\phi)(rd\theta)}{r^2} = \sin\theta\, d\theta d\phi \qquad (2E9)$$

If azimuthal symmetry exists, then $\int d\phi = 2\pi$, and $d\Omega = 2\pi \sin\theta\, d\theta$.

evaluation of $\delta\vec{p}$ and δW

After a collision, the final velocities of the test particle and field particle will be $(\vec{v} + \delta\vec{v})$ and $(\vec{v}_* + \delta\vec{v}_*)$. From *momentum conservation*

$$m\vec{v} + m_*\vec{v}_* = m(\vec{v} + \delta\vec{v}) + m_*(\vec{v}_* + \delta\vec{v}_*) \quad \rightarrow \quad m\delta\vec{v} = -\, m_*\delta\vec{v}_* \quad . \qquad (2E10)$$

Consider a coordinate system in which m_* is at rest. In this system, the velocity of the test particle is equal to $\vec{u}$, the relative velocity. From *conservation of kinetic energy*

$$\tfrac{1}{2}mu^2 = \tfrac{1}{2}m(\vec{u} + \delta\vec{u})^2 \quad \rightarrow \quad \vec{u}\cdot\delta\vec{u} + \tfrac{1}{2}\delta\vec{u}\cdot\delta\vec{u} = 0 \qquad (2E11)$$

which shows that the magnitude of u remains unchanged, although its direction changes during the collision, as illustrated in Fig. 2E2.

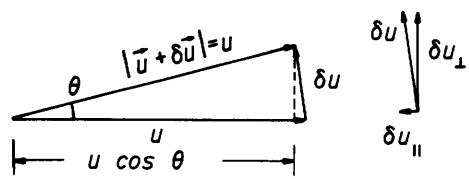

Fig. 2E2. During a collision the relative velocity $\vec{u}$ changes direction, but not magnitude.

From Eqs. (2E1) and (2E10), we find

$$\delta\vec{u} = \delta\vec{v} - \delta\vec{v}_* = \delta\vec{v}(1 + m/m_*) = \delta\vec{v}(m/m_r) \quad \rightarrow \quad \delta\vec{v} = (m_r/m)\delta\vec{u} \qquad (2E12)$$

Then

$$\delta\vec{p} = m\delta\vec{v} = m_r\delta\vec{u} \; . \qquad (2E13)$$

Let the subscripts $\parallel$ and $\perp$ denote components parallel and perpendicular to the original direction of motion. Because the scattering is symmetric in azimuthal angle, the $\delta p_\perp$ component will average to zero during integration over $d\phi$, and we only need to find $\delta p_\parallel$. From Fig. 2E2,

$$\delta u_\parallel = u\cos\theta - u = -\, u(1 - \cos\theta) = -\, 2u \sin^2(\tfrac{1}{2}\theta) \; . \qquad (2E14)$$

From Eqs. (2E13) and (2E14)

$$\delta\vec{p}_{\parallel} = -\,2m_r\vec{u}\,\sin^2(\tfrac{1}{2}\theta)\ . \tag{2E15}$$

The change in kinetic energy is

$$\delta W = \tfrac{1}{2}m(\vec{v}+\delta\vec{v})^2 - \tfrac{1}{2}mv^2 = m\vec{v}\cdot\delta\vec{v} + \tfrac{1}{2}m\delta\vec{v}\cdot\delta\vec{v}$$

$$= \frac{m(m\vec{v}+m_*\vec{v}_*)\cdot\delta\vec{v} + mm_*(\vec{v}-\vec{v}_*)\cdot\delta\vec{v}}{m+m_*} + \tfrac{1}{2}m\delta\vec{v}\cdot\delta\vec{v}$$

$$= m\vec{v}_c\cdot\delta\vec{v} + m_r\vec{u}\cdot\delta\vec{v} + \tfrac{1}{2}m\delta\vec{v}\cdot\delta\vec{v}$$

$$= m\vec{v}_c\cdot\delta\vec{v} + (m_r^2/m)(\vec{u}\cdot\delta\vec{u} + \tfrac{1}{2}\delta\vec{u}\cdot\delta\vec{u})$$

$$= m\vec{v}_c\cdot\delta\vec{v}$$

$$\delta W = \vec{v}_c\cdot\delta\vec{p} \tag{2E16}$$

where Eqs. (2E1), (2E2), (2E3), (2E12), (2E11), and (2E13) have been used. Since $\vec{v}_c$ is independent of scattering angle, it may be taken outside of the $d\Omega$ integral sign in Eq. (2E8). As before, the $\delta p_{\perp}$ component averages to zero, and only $\delta p_{\parallel}$ needs to be taken into account.

Coulomb scattering cross section

Consider the coordinate system in which m_* is at rest, as illustrated in Fig. 2E3.

The differential scattering cross section for scattering into angles between θ and $\theta+d\theta$ is simply the target area of the ring between b and b+db :

$$d\sigma = 2\pi b\ db \tag{2E17}$$

In view of the azimuthal symmetry,

$$\frac{d\sigma}{d\Omega} = \left|\frac{2\pi b\ db}{2\pi\sin\theta\ d\theta}\right| = \left|\frac{b\ db}{\sin\theta\ d\theta}\right|. \tag{2E18}$$

The absolute value signs have been added to keep $\frac{d\sigma}{d\Omega}$ positive, since $\frac{db}{d\theta} < 0$. Now we will derive a relation between the impact parameter b and the scattering angle θ. From Newton's Law (nonrelativistic) and the Coulomb force

$$m\frac{d\vec{v}}{dt} = \frac{qq_*\vec{r}}{4\pi\epsilon_0 r^3} = -\,m_*\frac{d\vec{v}_*}{dt} \tag{2E19}$$

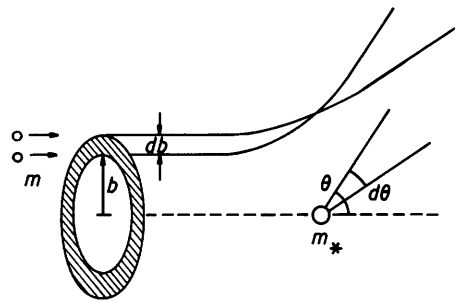

Fig. 2E3. Hyperbolic trajectories of test particles incident at impact parameters b and b+db, in a coordinate system with m_* at rest. Particles incident at larger radii are scattered through smaller angles θ.

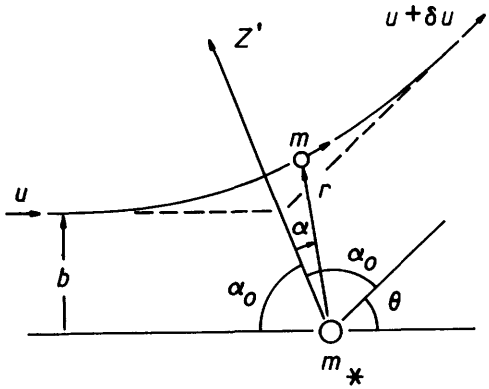

Fig. 2E4. Definition of radius vector $\vec{r}$, angle α, symmetry direction z', scattering angle θ, and limiting values of α equal to $\pm \alpha_0$.

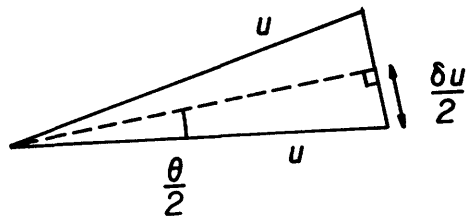

Fig. 2E5. Vector diagram relating $\delta\vec{u}$ to $\vec{u}$ and θ.

where r is defined in Fig. 2E4. Then

$$\frac{d\vec{u}}{dt} = \frac{d\vec{v}}{dt} - \frac{d\vec{v}_*}{dt} = \frac{qq_*\vec{r}}{4\pi\epsilon_0 r^3}\left[\frac{1}{m} + \frac{1}{m_*}\right] = \frac{qq_*\vec{r}}{4\pi\epsilon_0 m_r r^3} \quad . \tag{2E20}$$

By symmetry, $\delta\vec{u}$ is in the z' direction, and we only need to consider components of the Coulomb force in that direction to calculate $\delta\vec{u}$. Then

$$\delta u = \int dt\left[\frac{du}{dt}\right]_{z'} = \int_{-\alpha_0}^{\alpha_0} d\alpha \frac{dt}{d\alpha}\frac{du}{dt}\cos\alpha \quad . \tag{2E21}$$

From *conservation of angular momentum* around the point m_*

$$mub = mr^2\frac{d\alpha}{dt} \quad \rightarrow \quad \frac{dt}{d\alpha} = \frac{r^2}{ub} \quad . \tag{2E22}$$

Using Eqs. (2E22) and (2E20) in (2E21), we find

$$\delta u = \int_{\alpha_0}^{\alpha_0} d\alpha \frac{r^2}{bu}\frac{qq_*}{4\pi\epsilon_0 m_r r^2}\cos\alpha = \frac{qq_*}{4\pi\epsilon_0 m_r bu} 2\sin\alpha_0 \quad . \tag{2E23}$$

From Fig. 2E4,

$$2\alpha_0 + \theta = \pi \quad \rightarrow \quad \alpha_0 = \frac{\pi}{2} - \frac{\theta}{2} \quad . \tag{2E24}$$

With the aid of a trigonometric identity, Eq.(2E23) becomes

$$\delta u = \frac{qq_*}{4\pi\epsilon_0 m_r bu} 2\cos(\tfrac{1}{2}\theta) \quad . \tag{2E25}$$

From Fig. 2E5,

$$\tfrac{1}{2}\delta u = u\sin(\tfrac{1}{2}\theta) \quad \rightarrow \quad \delta u = 2u\sin(\tfrac{1}{2}\theta) \quad . \tag{2E26}$$

From Eqs. (2E25) and (2E26) we find

$$b = \frac{qq_* \cot(\frac{1}{2}\theta)}{4\pi\epsilon_0 m_r u^2} \quad , \qquad db = \frac{-\, qq_* d\theta}{8\pi\epsilon_0 m_r u^2 \sin^2(\frac{1}{2}\theta)} \quad . \tag{2E27}$$

After substituting these values into Eq. (2E18) and using the identity $\sin\theta = 2\sin(\frac{1}{2}\theta)\cos(\frac{1}{2}\theta)$, we obtain the *Rutherford scattering cross section*

$$\frac{d\sigma}{d\Omega} = \left[\frac{qq_*}{8\pi\epsilon_0 m_r u^2 \sin^2(\frac{1}{2}\theta)}\right]^2 \quad . \tag{2E28}$$

Coulomb logarithm

By symmetry, $d\Omega = 2\pi\sin\theta\, d\theta$. Substituting Eqs. (2E15) and (2E28) into (2E7), we have

$$\frac{d\vec{p}}{dt} = \int d\vec{v}_* \int_{\theta_{min}}^{\pi} 2\pi\sin\theta\, d\theta\, f(\vec{v}_*)\, u \left[\frac{qq_*}{8\pi\epsilon_0 m_r u^2 \sin^2(\frac{1}{2}\theta)}\right]^2 [-2m_r \vec{u} \sin^2(\tfrac{1}{2}\theta)]$$

$$= \frac{-\, q^2 q_*^2}{4\pi\epsilon_0^2 m_r} \int d\vec{v}_* \frac{f(\vec{v}_*)\vec{u}}{u^3} \int_{\theta_{min}}^{\pi} d(\tfrac{1}{2}\theta)\, \cot(\tfrac{1}{2}\theta)$$

$$= \frac{-\, q^2 q_*^2}{4\pi\epsilon_0^2 m_r} \int d\vec{v}_* \frac{f(\vec{v}_*)\vec{u}}{u^3} \ln \frac{1}{\sin(\frac{1}{2}\theta_{min})} \quad . \tag{2E29}$$

The minimum scattering angle corresponds to the maximum impact parameter. From Eq.(2E27)

$$\tan(\tfrac{1}{2}\theta_{min}) = \frac{qq_*}{4\pi\epsilon_0 m_r u^2 b_{max}} \simeq \sin(\tfrac{1}{2}\theta_{min}) \tag{2E30}$$

since the angle is very small. It will be shown in Section 5F that the electrostatic potential in a plasma is self-shielded by charged particle motions and decays exponentially with a characteristic scale length called the *Debye length* λ_D . Therefore, it is logical to choose

$$b_{max} \simeq \lambda_D \, . \tag{2E31}$$

Because of the logarithm function, the numerical result would vary little if we chose $2\lambda_D$ instead of λ_D. The logarithmic function is called the *Coulomb logarithm* :

$$L \equiv \ln \frac{1}{\sin(\frac{1}{2}\theta_{min})} \simeq \ln\left[\frac{4\pi\epsilon_0 m_r u^2 \lambda_D}{qq_*}\right] . \tag{2E32}$$

Many authors call this $\ln\Lambda$ instead of L . Since the logarithm's dependence on v_* is weak, we can take L outside the velocity integral, and use an average value for $u^2 \simeq 3kT/m_r$. At high energies, a quantum mechanical correction is needed in L. Formulas for computing L are listed in Table 2E1. In general,

Table 2E1. Values of the Coulomb Logarithm L. Here n_* is the field particle density (m^{-3}) and T_e and T_i are the electron and ion temperatures (eV). Typically L ≈ 18 ± 4 for fusion plasmas, so L ≈ 18 may be used in rough calculations. From Sivukhin (1966).

Low temperatures	all collisions:	$L = 30.0 - \frac{1}{2}\ln(n_*) + 1.5\ln(T_e)$ (Use T_i for ion-ion collisions).
Higher temperatures		
electron-electron collisions,	$T_e > 7$ eV:	$L = 31.0 - \frac{1}{2}\ln(n_*) + \ln(T_e)$
electron-ion collisions,	$T_e > 13$ eV:	$L = 31.3 - \frac{1}{2}\ln(n_*) + \ln(T_e)$
ion-ion collisions	$T_i > 24$ keV:	$L = 35.1 - \frac{1}{2}\ln(n_*) + \ln(T_i)$

there may be several species of field particles, and the total momentum change is found by summing the contributions of interactions with all species :

$$\frac{d\vec{p}}{dt} = -\sum_* \frac{q^2 q_*^2 L}{4\pi\epsilon_0^2 m_r} \int d\vec{v}_* \frac{f(\vec{v}_*)\vec{u}}{u^3} \quad . \tag{2E33}$$

Changing $\delta\vec{p}$ to δW transforms Eq.(2E7) into (2E8). According to Eq. (2E16), multiplying by $\vec{v}_c$ will accomplish this transformation. Therefore

$$\frac{dW}{dt} = -\sum_* \frac{q^2 q_*^2 L}{4\pi\epsilon_0^2 m_r} \int d\vec{v}_* \frac{f(\vec{v}_*)\vec{u}\cdot\vec{v}_c}{u^3} \quad . \tag{2E34}$$

Usually the field particle distribution function will be nearly Maxwellian:

$$f(\vec{v}_*) \simeq n_* b_*^3 \pi^{-3/2} \exp(-b_*^2 v_*^2) \qquad b_* \equiv (m_*/2kT_*)^{\frac{1}{2}} \quad . \tag{2E35}$$

results

For the case of Maxwellian field particles, the velocity integrals in Eqs. (2E33) and (2E34) can be evaluated, with the results

$$\frac{dp_{\parallel}}{dt} = -\sum_* \frac{n_* q^2 q_*^2 b_*^2 L}{4\pi\epsilon_0^2 m_r} \frac{H(x,0)}{x} \tag{2E36}$$

$$\frac{dW}{dt} = -\sum_* \frac{n_* q^2 q_*^2 b_* L}{4\pi\epsilon_0^2 m_*} H(x, m_*/m) \tag{2E37}$$

where

$$x \equiv b_* v = (m_* W/mT_*)^{\frac{1}{2}} \tag{2E38}$$

$$H(x, m_*/m) \equiv \mathrm{erf}(x)/x - 2\pi^{-\frac{1}{2}}(1 + m_*/m)\exp(-x^2) \tag{2E39}$$

[Sivukhin (1966) and Miyamoto (1980). Our $H(x,m_*/m)$ = their $F(x,\beta)/x$.] Although $dp_\perp/dt$ integrates to zero, $dp_\perp^2/dt$ is finite. Since

$$p^2 = p_\parallel^2 + p_\perp^2 = 2mW$$

we can evaluate

$$\frac{dp_\perp^2}{dt} = \frac{dp^2}{dt} - \frac{dp_\parallel^2}{dt} = 2m\frac{dW}{dt} - 2p_\parallel\frac{dp_\parallel}{dt} = \sum_* \frac{n_* q^2 q_*^2 b_* L}{4\pi\epsilon_0^2}\,\frac{2\mathrm{erf}(x)}{x} \qquad (2E40)$$

where the final value results from substitution of Eqs. (2E36) and (2E37). The error function erf(x) is described in Appendix E.

For *small x (x < 1)*

$$\mathrm{erf}(x) = \frac{2}{\pi^{\frac{1}{2}}}\left[\, x - \frac{x^3}{3\cdot 1!} + \frac{x^5}{5\cdot 2!} - \frac{x^7}{7\cdot 3!} + \ldots \,\right] \qquad (2E41)$$

$$H(x,m_*/m) = \frac{2}{\pi^{\frac{1}{2}}}\left[\, \frac{2x^2}{3} - \frac{2x^4}{5} + \ldots - \frac{m_*}{m}\left(1 - x^2 + \tfrac{1}{2}x^4 - \ldots\right) \right] \qquad (2E42)$$

For *large x (x > 2)*, $\mathrm{erf}(x) = 1$ and $\exp(-x^2) < 0.02$. If $x > 2$, then

$$H(x,m_*/m) = \frac{1}{x} \qquad (2E43)$$

unless $m_*/m \gg 1$. Values of $H(x,m_*/m)$ are shown in Fig. 2E6.

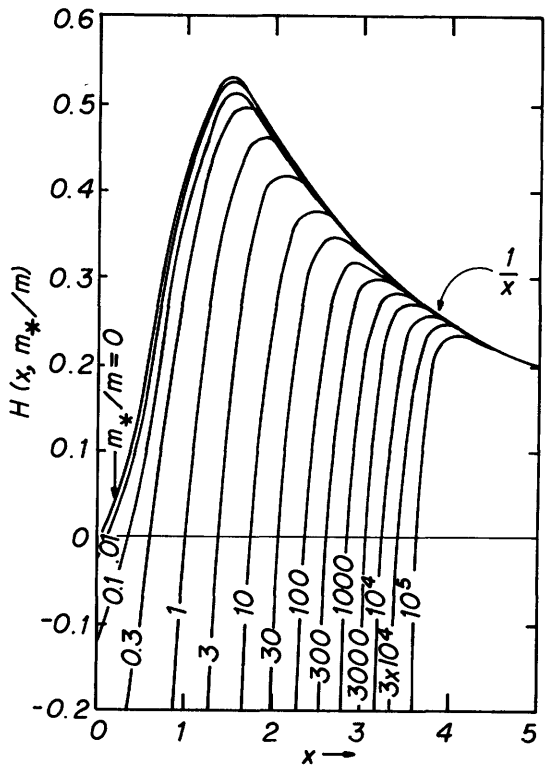

Fig. 2E6. Graph of the function $H(x,m_*/m)$ vs. x, for various values of m_*/m . (By J. J. Browning).

The equation for $dp_\parallel/dt$ represents slowing down of the test particle; dW/dt represents heating of the plasma by the test particle; and $dp_\perp^2/dt$ represents the rate of angular deflection of the test particle by Coulomb collisions with the plasma.

Sometimes the *test particles* will also have a *Maxwellian* distribution, characterized by a temperature T. We can average over that distribution to find the rate of energy transfer between the two Maxwellian distributions. If we define an *equilibration time* τ_{eq} by the equation

$$\frac{dT}{dt} \equiv \frac{T_* - T}{\tau_{eq}} \tag{2E44}$$

then the result is

$$\tau_{eq} = \frac{(2\pi^3)^{\frac{1}{2}} 3\varepsilon_0^2 m m_* \left[\frac{kT}{m} + \frac{kT_*}{m_*}\right]^{\frac{3}{2}}}{n_* q^2 q_*^2 L} \quad (s) \tag{2E45}$$

For the case of electron-ion interactions, if $\frac{kT_e}{m_e} >> \frac{kT_i}{m_i}$, then

$$\tau_{eq} = 9.99\times10^{18}(m_i/m_p)T_{ek}^{3/2}/nL \quad (s) \tag{2E46}$$

where m_i is the ion mass, m_p is the proton mass, T_{ek} is the electron temperature in keV, and n is the plasma density (m^{-3}). If the density were constant, and no other heating or cooling mechanism were present, then the two temperatures would gradually approach a common average temperature, as illustrated in Fig. 2E7. The value of τ_{eq} is not a constant during this process, which is called *energy relaxation, temperature relaxation,* or *equilibration.* In a real case, various other heating and cooling processes may keep the two species at different temperatures. A strong magnetic field tends to reduce the effective value of τ_{eq} (Ichimaru, 1973).

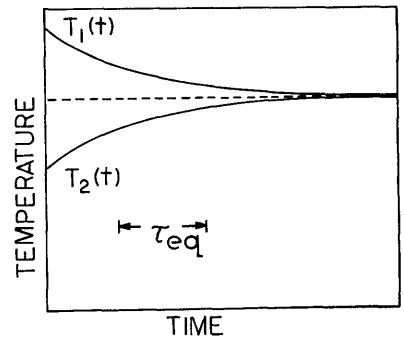

Fig. 2E7. Variation of plasma component temperatures T_1 and T_2 with time during equilibration.

We can define characteristic *momentum relaxation times* in the directions parallel and perpendicular to the initial test-particle velocity with the equations

$$\frac{dp_{\parallel}}{dt} \equiv -\frac{p_{\parallel}}{\tau_{\parallel}} \tag{2E47}$$

$$\frac{dp_{\perp}^2}{dt} \equiv \frac{p^2}{\tau_{\perp}} . \tag{2E48}$$

The *slowing-down time* $\tau_{\parallel}$ is the characteristic time for decrease of the test particle velocity, and the *deflection time* $\tau_{\perp}$ is the characteristic time for change of direction by large angles ($\sim 90^{\circ}$) by multiple small-angle Coulomb scattering collisions. From Eqs. (2E36) and (2E40) we find

$$\tau_{\parallel} = \frac{4\pi\varepsilon_0^2 m v}{\sum_* n_* q^2 q_*^2 b_*^2 L\ H(x,0)/m_r x} \simeq \frac{4\pi\varepsilon_0^2 m v^3}{\sum_* n_* q^2 q_*^2 L/m_r} \tag{2E49}$$

$$\tau_{\perp} = \frac{4\pi\varepsilon_0^2 m^2 v^2}{\sum_* n_* q^2 q_*^2 b_* L\ 2\mathrm{erf}(x)/x} \simeq \frac{2\pi\varepsilon_0^2 m^2 v^3}{\sum_* n_* q^2 q_*^2 L} \tag{2E50}$$

where the approximations assume $x > 1$. We can find characteristic relaxation times between the test particles and each species of field particles separately, then sum these times reciprocally to obtain the total relaxation times $\tau_{\parallel}$ and $\tau_{\perp}$. For example, if the test particles are electrons, then

$$\frac{1}{\tau_{\parallel e}} = \frac{1}{\tau_{\parallel ee}} + \frac{1}{\tau_{\parallel ei}} \tag{2E51}$$

in a two-component plasma, where the second letter designates the field particle species. When the test particles have a Maxwellian distribution, we can use a velocity corresponding to the average energy:

$$\tfrac{1}{2}mv^2 = \frac{3}{2}kT \quad .$$

Then the characteristic collision time for electrons is

$$\tau_e \equiv \frac{3^{\frac{1}{2}} 6\pi\varepsilon_0^2 m_e^{\frac{1}{2}} (kT_e)^{3/2}}{n_e e^4 L} = \frac{7.5\times10^{15} T_{ek}^{3/2}}{nL} = \tau_{\parallel ee} = \tau_{\perp ee} = Z^2\tau_{\perp ei} = \tfrac{1}{2}Z^2\tau_{\parallel ei} \tag{2E52}$$

where the ionic charge $q_i \equiv Ze$, and T_{ek} is in keV. The self-collision time for ions is

$$\tau_i \equiv \frac{3^{\frac{1}{2}} 6\pi\varepsilon_0^2 m_i^{\frac{1}{2}} (kT_i)^{3/2}}{n_i Z^4 e^4 L} = \tau_{\parallel ii} = \tau_{\perp ii} \tag{2E53}$$

These definitions follow those of Sivukhin (1966) and Miyamoto (1980). Spitzer (1962) used $x = (3/2)^{\frac{1}{2}}$ in evaluating erf(x) and H(x,0), with resulting relaxation times about 30 % larger than these. For collisions of ion test particles with electron field particles, usually $x \ll 1$, and only the first terms of Eqs.(2E41) and (2E42) need to be used. The ion-electron relaxation time may be defined as

$$\tau_{ie} \equiv \frac{3\pi(2\pi)^{\frac{1}{2}}\varepsilon_0^2 m_i (kT_e)^{3/2}}{n_e Z^2 e^4 L\, m_e^{\frac{1}{2}}} = \tfrac{1}{2}\tau_{\parallel ie} = \frac{T_e}{T_i}\tau_{\perp ie} \tag{2E54}$$

The ratios of these three relaxation times are

$$\tau_e : \tau_i : \tau_{ie} = 1 : \frac{1}{Z^4}\left(\frac{m_i}{m_e}\right)^{\frac{1}{2}}\left(\frac{T_i}{T_e}\right)^{3/2} : \frac{1}{Z^2}\left(\frac{\pi}{6}\right)^{\frac{1}{2}}\frac{m_i}{m_e} \tag{2E55}$$

or $\tau_e \ll \tau_i \ll \tau_{ie}$. Values of the energy relaxation time τ_{eq} for electron-

electron, ion-ion, and ion-electron collisions are almost the same as the above momentum relaxation times τ_e, τ_i, and τ_{ie}, respectively. The *mean free paths* of electrons and ions are

$$\lambda_{ei} = (3kT_e/m_e)^{\frac{1}{2}}/\nu_{ei} = \frac{1.9\times10^{16}\,T_{eV}^2}{Z^2 n}$$

$$\lambda_e = (3kT_e/m_e)^{\frac{1}{2}}\tau_e$$

$$\lambda_i = (3kT_i/m_i)^{\frac{1}{2}}\tau_i \quad . \tag{2E56}$$

The times τ_e and τ_i are also called *thermalization times*, because they are the characteristic time scales over which electrons or ions with initially non-Maxwellian distribution functions tend to become Maxwellian. In studying plasma resistivity and diffusion, the electron-ion momentum-transfer collision frequency

$$\nu_{ei} \equiv \frac{1}{\tau_{\|ei}} = \frac{Z^2}{2\tau_e} = \frac{nZ^2e^4\,L}{3^{\frac{1}{2}}12\pi\varepsilon_0^2 m_e^{\frac{1}{2}}(kT_e)^{3/2}} = \frac{6.7\times10^{-17}nZ^2L}{T_{ek}^{3/2}} \tag{2E57}$$

is useful, where T_{ek} is in keV.

Coulomb interactions define the *maximum values* of relaxation times. Wave-particle interactions can greatly accelerate momentum and energy transfer processes, resulting in much shorter time scales.

applications

These results will be illustrated by a few examples.

EXAMPLE PROBLEM 2E1

A 1 MeV alpha particle is slowing down in a deuterium plasma with $n = 10^{20}$ m^{-3}, $T_e = T_i = 10$ keV. Find the energy loss rates to electrons and to ions. What fraction of the alpha particle heating is going to the ions ?

Energy loss to electrons:

$m_*/m = m_e/m_\alpha = 1.36\times10^{-4}$

$x = (m_e W/m_\alpha T_e)^{\frac{1}{2}} = 0.117$

From Eq.(2E42), $H(x, m_*/m) = 0.0102$

$b_e = (m_e/2kT_e)^{\frac{1}{2}} = 1.686\times10^{-8}$ s/m

$L = 31.3 - \frac{1}{2}\ln(10^{20}) + \ln(10^4) = 17.5$

$q_\alpha = 2e$

From Eq.(2E37) $\left[\frac{dW}{dt}\right]_e = 8.71\times10^{-13}$ W

Energy loss to ions:

$m_*/m = 0.5032$

$x = (m_i W_\alpha/m_\alpha T_i)^{\frac{1}{2}} = 7.07$

$L = 30.0 - \frac{1}{2}\ln(10^{20}) + 1.5\ln(10^4) = 20.8$

$b_i = (m_i/2kT_i)^{\frac{1}{2}} = 1.02\times10^{-6}$ s/m

From Eq.(2E37) $\left[\frac{dW}{dt}\right]_i = 2.40\times10^{-13}$ W

The fraction going to the ions is $2.40/(2.40+8.71) = 0.22$.

The net fraction of the alpha particle energy transferred to ions during slowing down from initial energy W_0 = 3.5 MeV to final energy W_f is

$$f_i = \frac{\text{energy to ions}}{\text{total energy loss}} = \frac{1}{W_0 - W_f} \int_{W_f}^{W_0} dW \, \frac{\left[\frac{dW}{dt}\right]_i}{\left[\frac{dW}{dt}\right]_i + \left[\frac{dW}{dt}\right]_e} \qquad (2E58)$$

The resulting values of f_i are shown in Fig. 2E8 as a function of T_e. In the range $20 \leq T_e \leq 60$ keV, the formula

$$f_i \simeq 0.29 \ln(T_{ek}) - 0.5 \qquad (2E59)$$

has ± 5 % accuracy, with T_{ek} in keV.

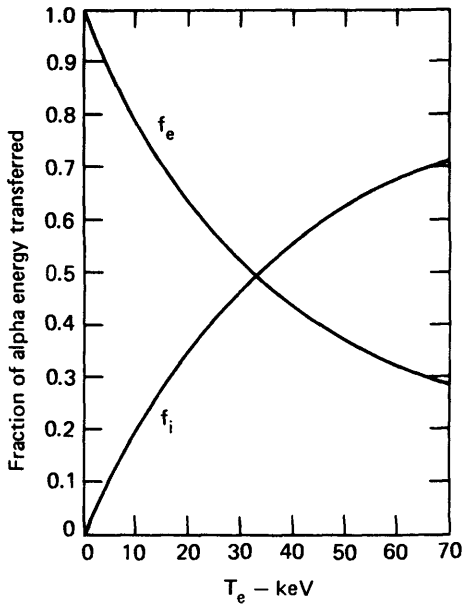

Fig. 2E8. Net fraction of alpha particle energy transferred to plasma electrons. (f_e) and plasma ions (f_i) during alpha slowing down from 3.5 MeV to plasma energy, as functions of electron temperature. From D. J. Rose, Nucl. Fusion 9, 183-203 (1969) and R. W. Moir et al, UCRL-52302 (1977).

EXAMPLE PROBLEM 2E2

In a "magnetic mirror" plasma confinement system (Section 8A), ions are usually lost after they have been deflected by a large angle from Coulomb scattering collisions. Approximately how long does this take in a deuterium plasma with $n = 10^{20}$ m^{-3} and T_i = 100 keV ?

From Table 2E1, $L = 35.1 - \frac{1}{2}\ln(10^{20}) + \ln(10^5) = 23.6$
(For rough estimates, as we are making here, it would suffice to set L = 18).
From Eq. (2E53) τ_i = 0.2 s . Thus, ions will be lost in about this length of time. The product $n\tau_i = 2 \times 10^{19}$ $m^{-3}s$ is less than the Lawson criterion (Section 1F), which shows the inadequacy of simple magnetic mirrors. Longer confinement times could be obtained at higher T_i, but the required heating power may be larger than the fusion power output.

EXAMPLE PROBLEM 2E3

A deuterium plasma has $n = 10^{20}$ m^{-3}, average electron energy = 6 keV, average ion energy = 3 keV, and non-Maxwellian distributions of electrons and ions. Approximately how long will it take for the electrons and ions to attain Maxwellian distributions ? How long will it take for the electron and ion temperatures to come to a common value ? For simplicity, assume that the plasma is in a perfect confinement system, with n = constant and no heating or cooling.

The temperatures will be 2/3 of the average energies, so T_e = 4 keV, T_i = 2 keV. We will set L = 18.
From Eq.(2E52), $\tau_e = 7.5\times10^{15}\ T_{ek}^{3/2}/nL = 3.3\times10^{-5}$ s.
From Eq.(2E53), $\tau_i = 7.2\times10^{-4}$ s.
Thus, it will take the electrons about 30-100 μs to attain a Maxwellian distribution, and it will take the ions about 0.7-2 ms.
From Eq.(2E46) with $m_i/m_p = 2$ and T_e = 4 keV, τ_{eq} = 0.09 s.
Thus, it will take a longer time, about 90-300 ms, for the electron and ion temperatures to arrive at a common average value of 3 keV.

Problems

1. Find $\langle v_x^3 \rangle$ and $\langle v_x^4 \rangle$ for a Maxwellian distribution.

2. A monoenergetic 60 keV deuteron beam is shot through a target containing tritium with density 10^{25} m^{-3}. (a) Ignoring scattering and slowing down in the target, what fraction of the deuterons will undergo fusion reactions in the first 0.1 mm of the target? (b) If a 60 keV triton beam were shot through a deuterated target with $n_D = 10^{25}$ m^{-3}, what fraction of the tritons would undergo fusion reactions in the first 0.1 mm? [See Eq. (2C1).]

3. A deuteron beam with velocity 10^6 m/s and density 10^{14} ions/m^3 is incident on a single-element target with volume 10^{-9} m^3 and atomic density 1.5×10^{28} m^{-3}. From measurements with a movable neutron detector it is determined that the total neutron emission rate is 2×10^8 neutrons/s. (a) Assuming that each reaction produces one neutron, and that only one type of reaction is occurring, estimate the reaction cross section. (b) Assuming that the beam has current uniformly distributed over a 1 mm^2 cross sectional area, estimate the required accelerator voltage and current to produce the beam.

4. A uniform plasma contains deuterons with density 10^{20} m^{-3} and ^{3}He ions with density 8×10^{19} m^{-3}. If the ion temperature is 35 keV, find (a) the fusion power density, (b) the neutron emission rate, and (c) the plasma pressure, assuming $T_e = T_i$ and $n_e = n_D + 2n_{He}$.

5. Derive Eq. (2B32) from (2B30).

6. Let $p(x)dx$ = probability of an incident particle traveling a distance x without a collision and then having a collision in the distance dx = (probability of traveling distance x without an interaction) (probability of having an interaction while traveling a distance dx) $=[\exp(-n_2\sigma x)][n_2\sigma dx]$. Using p(x) as a distribution function for collision probability, find the mean value of x which a particle travels to its first collision. This is an alternative way of evaluating the mean free path for monoenergetic incident particles.

7. (a) Find the mean free path of deuterons before undergoing a fusion reaction in a deuterium plasma with T_i = 20 keV, $n_i = 10^{20}$ m^{-3}. (b) For this same plasma, what is the mean free path before fusion of an injected 40 keV triton beam? (c) What fraction of the tritons would be consumed by fusion reactions in the first second after injection, ignoring slowing down?

8. Consider a D-^{3}He plasma with $n_D = n_{He}$, $n_e = n_D + 2n_{He}$, $p = n_e kT_e + n_D kT_i + n_{He} kT_i$. Derive an equation of the form

$$\langle P_f \rangle = \frac{\beta_*^2 B^4 F(T_i)}{(2\mu_0)^2(1 + 3T_e/2T_i)^2}$$ and plot $F(T_i)$ vs. T_i. If $T_e \simeq T_i$ and $\beta_* = 0.2$, what value of B is needed to make $\langle P_f \rangle$ = 1 MW/m^3 ? If $r_p/r_w = 0.8$, how large should r_w be to make F = 1 MW/m^2 ?

9. A proton-^{11}B plasma has $T_e = T_i = T$, $n_e = n_p + 5n_B$, $p = (n_p + n_B + n_e)kT$, and $P_f = n_p n_B \langle \sigma v \rangle_{pB} W_{pB}$. For a given pressure, what ratio n_B/n_p maximizes P_f ? What minimum pressure is required to attain P_f = 1 MW/m^3 at T = 120 keV ?

10. Estimate the instantaneous fraction of 3 MeV alpha particle energy loss to ions in a deuterium plasma with $n_i = n_e = 10^{20}$ m^{-3}, $T_e = T_i$ = 20 keV, and the alpha particle energy loss rate (keV/s).

11. Electron and ion guns inject 10 kA of monoenergetic 100 keV electrons and 10 kA of monoenergetic 20 keV deuterons for 10^{-6} s into a perfect confinement system with volume .01 m^3. (a) What will the final densities be? (b) What will the electron and ion temperatures be before equilibration and after equilibration? (c) How long will it take the electrons and ions to thermalize? (d) How long will it take for equilibration of electron and ion temperatures? Assume that wave-particle interactions and energy losses are negligible. (The number of particles injected N = It/e, where I = current, t = time, e = electronic charge.)

Bibliography

nuclear reactions

S. Glasstone and R. H. Lovberg, *Controlled Thermonuclear Reactions*, Van Nostrand, Princeton, NJ 1960.
T. Kammash, *Fusion Reactor Physics*, Ann Arbor Science, Ann Arbor, MI, 1975.
G. H. Miley, H. Towner, and N. Ivich, "Fusion cross sections and reactivities", U. of Illinois Nucl. Eng., Report COO-2218-17, 1974.
G. H. Miley, *Fusion Energy Conversion*, American Nuclear Society, LaGrange Park, IL, 1975.
D. J. Rose and M. Clark, Jr., *Plasmas and Controlled Fusion*, MIT Press, Cambridge, MA, 1961.

Coulomb collisions

S. Ichimaru, *Basic Principles of Plasma Physics, A Statistical Approach*, Benjamin, Reading, MA 1973.
K. Miyamoto, *Plasma Physics for Nuclear Fusion*, The MIT Press, Cambridge, MA, 1980, Chapter 4.
G. Schmidt, *Physics of High Temperature Plasmas, Second Edition*, Academic Press, New York, 1979, Chapter 11.
I. P. Shkarofsky, T. W. Johnston, and M. P. Bachynski, *The Particle Kinetics of Plasmas*, Addison-Wesley, Reading, MA 1966.
D. V. Sivukhin, "Coulomb collisions in a fully ionized plasma", *Reviews of Plasma Physics*, Vol. 4, Consultants Bureau, New York, 1966.
L. Spitzer, Jr., *Physics of Fully Ionized Gases*, 2nd Ed., Interscience, New York, 1962.

CHAPTER 3

ATOMIC COLLISIONS AND RADIATION

3A. Types of Collisions

Atomic collision phenomena play important roles in many aspects of fusion research: production of plasma, loss of hot ions by charge exchange, penetration of neutral atoms and impurities into plasma, production of high-power neutral beams for plasma heating, generation of laser beams for plasma heating and diagnostics, loss of electron energy by radiation, and others.

Some types of atomic and molecular collision phenomena are listed in Table 3A1. Impurity atoms in a fusion plasma (C, O, Fe, Ni, Mo, etc.) will absorb electron energy via excitation and ionization, then emit line and recombination radiation, most of which is lost to the walls. The result is rapid heat loss from the electrons.

Table 3A1. Some atomic and molecular collision phenomena of interest in fusion research. (Only a few examples are given.)

H = neutral atom of hydrogen, deuterium, or tritium
H^+ = ion
H* = atom in excited state
$h\nu$ = photon
e^- = electron
H_2 = molecule of hydrogen, deuterium, or tritium or combinations of them
$\underline{H}$, $\underline{H}_2$ = energetic atom, molecule

heavy particle collisions (atoms, ions, and molecules)	
heavy particle scattering	$\underline{H} + H \rightarrow H + \underline{H}$
excitation by heavy particle impact	$\underline{H} + H \rightarrow H + \underline{H}^*$
	$\underline{H}_2 + H \rightarrow H_2 + H^*$
	$\underline{H} + H_2 \rightarrow H + H_2^*$
dissociation	$\underline{H} + H_2 \rightarrow H + H + H$
	$\underline{H} + H_2^+ \rightarrow H + H + H^+$
molecular recombination	$H + H + H_2 \rightarrow H_2 + H_2$
electron capture and charge exchange	$\underline{H}^+ + H \rightarrow \underline{H} + H^+$
(N_2 = nitrogen molecule)	$\underline{H} + N_2 \rightarrow \underline{H}^- + N_2^+$

	$\underline{H}^+ + H_2 \rightarrow \underline{H} + H_2^+$
ionization and stripping by heavy particles	$\underline{H}^+ + H \rightarrow H^+ + H^+ + e^-$
	$\underline{H}^+ + H_2 \rightarrow H^+ + H_2^+ + e^-$
heavy particle slowing down in gases and metals	
recombination of positive and negative ions	$H^+ + H^- \rightarrow H + H$
ion-molecule and atom-molecule interchange:	$H_2^+ + H_2 \rightarrow H_3^+ + H$
<u>photon interactions</u>	
photoabsorption or photoexcitation	$h\nu + H \rightarrow H^*$
photoionization	$h\nu + H^* \rightarrow H^+ + e^-$
	$h\nu + H \rightarrow H^+ + e^-$
photodissociation	$h\nu + H_2^+ \rightarrow H + H^+$
	$h\nu + H_2^* \rightarrow H + H$
photodetachment	$h\nu + H^- \rightarrow H + e^-$
<u>electron collisions</u>	
elastic scattering	$e^- + H \rightarrow e^- + H$
inelastic scattering, excitation	$e^- + H \rightarrow e^- + H^*$
	$e^- + H_2 \rightarrow e^- + H_2^*$
dissociation (The resultant 1 to 10 eV neutral atoms are called "Franck-Condon" neutrals.)	$e^- + H_2^+ \rightarrow e^- + \underline{H} + \underline{H}^+$
	$e^- + H_2^* \rightarrow e^- + \underline{H} + \underline{H}$
ionization of atoms, molecules, and ions	$e^- + H \rightarrow e^- + e^- + H^+$
	$e^- + H_2 \rightarrow e^- + e^- + H_2^+$
	$e^- + He^+ \rightarrow e^- + e^- + He^{++}$
attachment	$e^- + H_2 \rightarrow H^- + H + h\nu$
radiative recombination	$e^- + H^+ \rightarrow H + h\nu$
dissociative recombination	$e^- + H_2^+ \rightarrow H^* + H^*$ (doubly excited)
dielectronic recombination	$O^{++} + e^- \rightarrow O^{+**} \rightarrow O^+ + h\nu_1 + h\nu_2$
autoionization	$O^{++} + e^- \rightarrow O^{+**} \rightarrow O^{++} + e^-$
<u>surface phenomena</u>	
sputtering, blistering (to be discussed in Chapter 24)	
secondary electron emission by electron and ion impact	
electron and ion reflection	
adsorption, desorption	
<u>transport phenomena</u>	
electron drift velocities and diffusion	
ion drift velocities, mobility, and diffusion	
neutral particle diffusion	

We can define reaction rates, collision frequencies, and mean free paths for atomic collisions:

$$r(\vec{x},t) = n_1(\vec{x},t)n_2(\vec{x},t)\langle\sigma v\rangle \quad (3A1)$$

$$\nu_1(\vec{x},t) = r(\vec{x},t)/n_1(\vec{x},t) = n_2(\vec{x},t)\langle\sigma v\rangle \quad (3A2)$$

$$\lambda_1(\vec{x},t) = n_1(\vec{x},t)\langle v_1\rangle/r(\vec{x},t) = \langle v_1\rangle/n_2(\vec{x},t)\langle\sigma v\rangle \quad (3A3)$$

where $\langle\sigma v\rangle$ is the rate parameter for the particular type of interaction considered.

The data to be presented here are mostly for ordinary hydrogen. Cross sections and reaction rate parameters for deuterium and tritium vary slightly from those of ordinary hydrogen at the same relative velocities.

3B. Scattering and Momentum Transfer

If the internal energy of an atom or molecule changes during a collision (either through excitation or de-excitation of energy levels), then the collision is called "inelastic". If the internal energy does not change during a collision, then the total kinetic energy of the two particles remains constant, and the collision is called "elastic". The total scattering cross section is the sum of the elastic and inelastic cross sections.

When electrons collide with heavy particles, they may be deflected by an angle θ, as illustrated in Fig. 3B1, with little change in speed. The change of momentum in the x direction is equal to $mv\cos\theta - mv = -mv(1-\cos\theta)$. Thus, for the purpose of studying electron motion by diffusion, it is common to define a "momentum transfer" cross section

$$\sigma_{en} = \langle\sigma_{el}(1-\cos\theta)\rangle \quad (3B1)$$

where σ_{el} is the elastic scattering cross section, and $\langle\ \rangle$ represents an average over all scattering angles. The momentum-transfer cross section of electrons in H_2 is shown in Fig. 3B2. At higher energies, the cross section decreases roughly as 1/v, so the collision frequency varies slowly. A scattering resonance occurs at the electron energy where the De-Broglie wavelength equals the radial extent of the potential, resulting in the observed peak. Numerous scattering data and references are given by Barnett et al (1977).

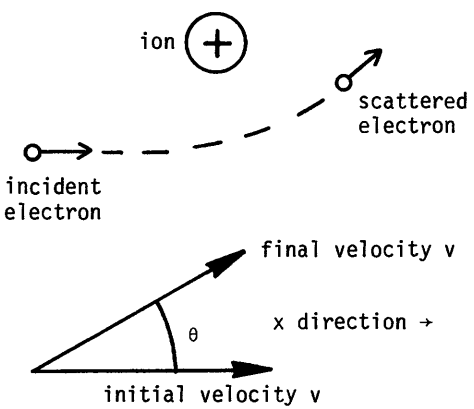

Fig. 3B1. Deflection of electrons by elastic scattering. The x-component of the electron momentum changes by an amount mv(1-cosθ)

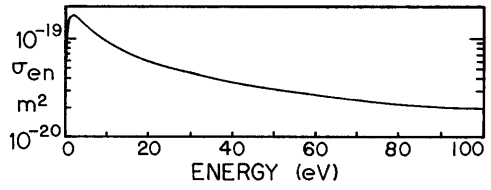

Fig. 3B2. Momentum-transfer cross section of electrons in H_2 as a function of electron energy. (Barnett et al, 1977).

EXAMPLE PROBLEM 3B1

Estimate the momentum-transfer collision frequency for electrons with H_2 molecules at T_e = 10 eV, $n_2 = 10^{18}\ m^{-3}$. This problem illustrates a numerical technique for computing $\langle\sigma v\rangle$ from cross section data.

The neutral molecule speeds will be negligible, so $\int d\vec{v}_2\ f_2(\vec{x},\vec{v},t) = n_2(\vec{x},t)$, and $r(\vec{x},t) = n_2(\vec{x},t) \int d\vec{v}_e f(\vec{x},\vec{v}_e,t)\sigma(v_e)v_e$. For Maxwellian electrons, this becomes $r(\vec{x},t) = n_2(\vec{x},t) \int_0^\infty dv_e 4\pi v_e^2(\beta_e/\pi)^{3/2} n_e(\vec{x},t)\exp(-\beta_e v_e^2)\sigma(v_e)v_e$

$$= n_2(\vec{x},t)n_e(\vec{x},t)(2/kT)^{3/2}\ (m\pi)^{-\frac{1}{2}} \int_0^\infty dW\ W\exp(-W/kT)\sigma(W)\ ,$$

where $W = \frac{1}{2}m_e v_e^2$. Approximating the integral by a sum,

$$r(\vec{x},t) \simeq n_2(\vec{x},t)n_e(\vec{x},t)\ (2/kT_e)^{3/2}(\pi m_e)^{-\frac{1}{2}}\ \Delta W \sum_j W_j\exp(-W_j/kT)\sigma(W_j)w_j$$

where w_j are numerical integration weighting factors, as in (2B22). Using Simpson's rule with ΔW = 5 eV and data of Fig. 3B2,

W_j,eV	W_j/kT	$\sigma(W_j)$	w_j	$W_j\exp(-W_j/kT)\sigma(W_j)w_j$ (with W_j in J)
0	0	0	1/3	0
5	.5	1.4E-19	4/3	9.07E-38
10	1	9.1E-20	2/3	3.58E-38
15	1.5	7.0E-20	4/3	5.00E-38
20	2	5.9E-20	2/3	1.71E-38
25	2.5	5.0E-20	4/3	2.19E-38
30	3	4.4E-20	2/3	7.02E-39
35	3.5	3.9E-20	4/3	8.80E-39
40	4	3.7E-20	2/3	2.90E-39
45	4.5	3.3E-20	4/3	3.52E-39
50	5	3.0E-20	2/3	1.08E-39
55	5.5	2.8E-20	4/3	1.34E-39
60	6	2.7E-20	1/3	2.14E-40
				sum = 2.40E-37 Jm^2

From Eq. (3A2) $\nu_{en} = r(\vec{x},t)/n_e(\vec{x},t) = n_2(2/kT_e)^{3/2}(\pi m_e)^{-\frac{1}{2}}\Delta W$ (sum)

$\nu_{en} = 10^{18}m^{-3}(2/1.60\times10^{-18}J)^{3/2}(\pi 9.11\times10^{-31}kg)^{-\frac{1}{2}}8.0\times10^{-19}J(2.40\times10^{-37}Jm^2)$

$\nu_{en} = 1.6 \times 10^5\ s^{-1}$, and $\langle\sigma v\rangle_{en} = 1.6\times10^{-13}\ m^3s^{-1}$.

Better accuracy could be attained by taking finer increments ΔW and extending the integration to higher energies.

3C. Molecular Collisions

The hydrogen molecule has energy states corresponding to electronic configuration, molecular vibration, and molecular rotation. Electronic motion is much more rapid than motion of the nuclei, so electronic energy states may be calculated in first approximation assuming that the nuclei are stationary. The curves of Fig. 3C1 represent the potential energy vs. nuclear separation for various electronic energy levels. The vibrational energy levels corresponding to each of these electronic energy states may be calculated relative to these curves, and the rotational motion of the molecule causes splitting of the vibrational levels.

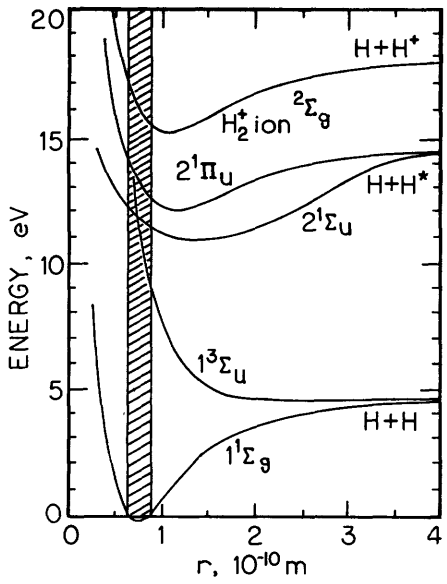

Fig. 3C1. Potential energy of hydrogen molecule vs. separation distance between nuclei. Only a few electronic energy states are shown. The shaded region represents the normal vibrational range of the nuclei in the electronic ground state ($^1\Sigma_g$). Based on H. S. W. Massey and E. H. S. Burhop, Electronic and Ionic Impact Phenomena, Clarendon Press, Oxford, 1952, p. 230.

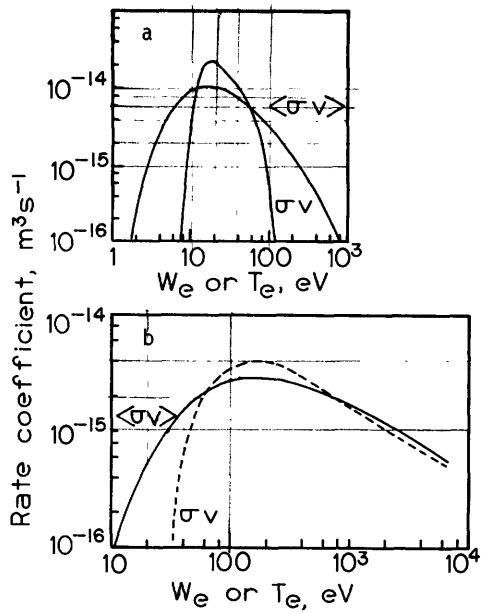

Fig. 3C2. Rate coefficients for dissociation of H_2 molecules. (a) $H_2 + e^- \rightarrow 2H + e^-$; (b) $H_2 + e^- \rightarrow H + H^+ + 2e^-$. <σv> curves for Maxwellian electrons, σv curves are for monoenergetic electrons. (Jones, 1977).

If about 4.4 eV or more is supplied to a ground state molecule by heavy particle impact, dissociation may occur directly. In order to produce electron impact dissociation or photodissociation, however, electronic excitation must occur first. According to the "Franck-Condon principle", electronic excitation occurs at constant separation r in Fig. 3C1, since it occurs much more rapidly than motion of the nuclei. The first electronic state above ground is the $^3\Sigma_u$ state, which requires a minimum energy of 8.9 eV to be supplied. The $^3\Sigma_u$ state is repulsive, and quickly dissociates into two H atoms, each having a few eV energy, called "Franck-Condon neutrals". The few eV energies of such neutrals enable them to penetrate much farther into a plasma than "cold" neutrals (having energies $\sim$ 0.03 eV) can.

Electron impacts providing over 15.4 eV can ionize the ground-state molecule, producing the stable H_2^+ ion. If more than 18 eV is supplied by electron excitation to the ground state molecule, both ionization and dissociation may be produced at once, resulting in $H + H^+$ as reaction products.

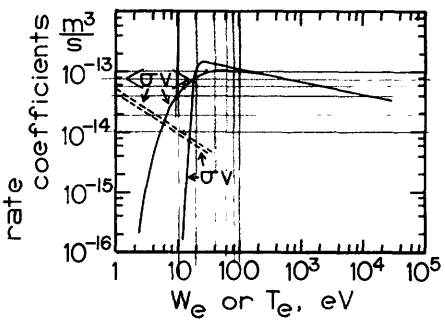

Fig. 3C3. Rate coefficients for dissociation of H_2^+ ions by electrons. Smooth curves: $H_2^+ + e^- \rightarrow \begin{cases} H + H^+ + e^- \\ 2H^+ + 2e^- \end{cases}$. *Dashed curves:* $H_2^+ + e^- \rightarrow H + H$. $\langle\sigma v\rangle$ *curves are for Maxwellian electrons,* σv *curves are for monoenergetic electrons. (Jones, 1977).*

Rate coefficients for dissociation of H_2 molecules and H_2^+ ions are shown in Figs. 3C2 and 3C3, as functions of electron temperature (Maxwellian) or energy (monoenergetic). Some of these processes also produce additional ionization.

Hydrogen leaving the chamber walls by thermal desorption comes off as H_2 molecules. As the molecules impinge on the plasma, some of them become dissociated

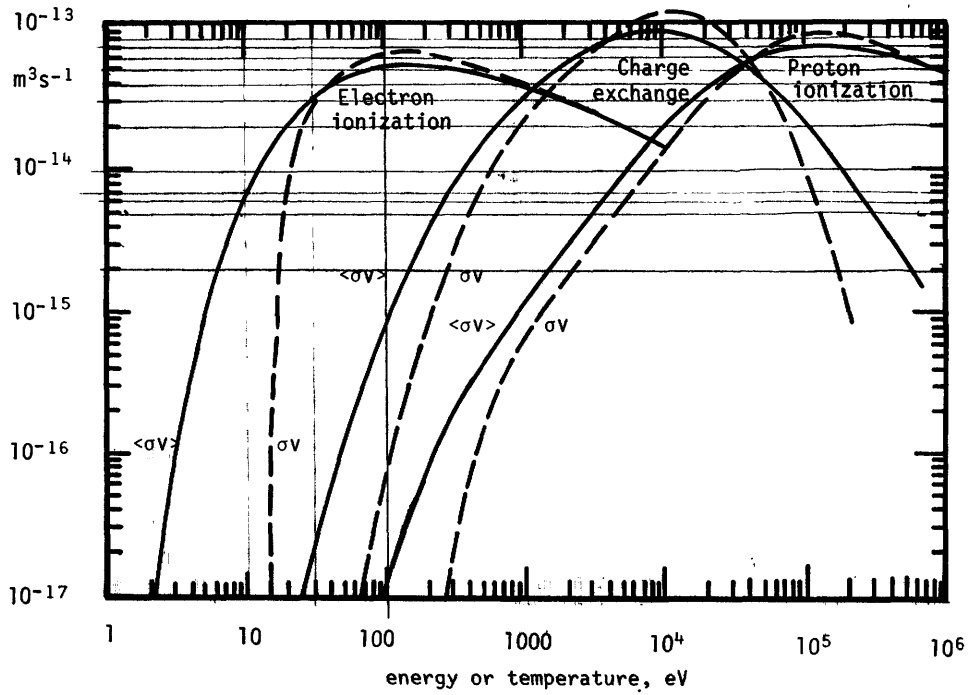

Fig. 3C4. Reaction rate parameters for charge exchange of protons in molecular hydrogen and for ionization of molecular hydrogen by impact of protons and by electron impact. The H_2 molecules are considered to be stationary target particles. (Freeman and Jones, 1974).

and ionized, forming H atoms, H_2^+ molecular ions, and H^+ ions. It is important to know the densities of each of these species, because hot ion loss by charge exchange occurs at different rates with atomic and molecular hydrogen.

Rate coefficients for charge exchange, electron impact ionization, and proton impact ionization of H_2 molecules are shown in Fig. 3C4 as functions of incident particle energy or temperature.

EXAMPLE PROBLEM 3C1

Consider H_2 molecules incident on a plasma with speed v_n = 1000 m/s. Estimate their mean free paths (a) against dissociation by electron impact, (b) against ionization to H_2^+, in a plasma with $n_e = 10^{19}$ m^{-3}, T_e = 100 eV. (c) What fraction of the incident H_2 will form H_2^+ instead of immediately dissociating? (d) What is the mean free path for dissociation of the resultant H_2^+ ions?

The H_2 speed is negligible in comparison with the plasma electron speeds, so we can use Maxwellian plasma data for $\langle\sigma v\rangle$.

(a) From Fig. 3C2 (a) and (b) the total dissociation rate parameter is $3.3\times10^{-15} + 2.7\times10^{-15} = 6.0\times10^{-15}$ m^3s^{-1}. Then $\lambda = v/n_2\langle\sigma v\rangle = 0.017$ m for dissociation, where $n_2 = n_e$.

(b) From Fig. 3C4, $\langle\sigma v\rangle = 5.3 \times 10^{-14}$ m^3s^{-1}, and so $\lambda = 0.0019$ m for ionization.

(c) The fraction ionized $= \dfrac{r(\text{ionization})}{r(\text{ionization}) + r(\text{dissociation})}$

$$= \frac{n_1 n_2 \langle\sigma v\rangle_i}{n_1 n_2 \langle\sigma v\rangle_i + n_1 n_2 \langle\sigma v\rangle_d} = 0.90 .$$

About 90% become ionized first, then dissociated, and 10% are dissociated first, then ionized.

(d) From Fig. 3C3, for dissociation of H_2^+, $\langle\sigma v\rangle = 1.0\times10^{-13}$, and $\lambda = 1000/10^{19}(1.0\times10^{-13}) = 10^{-3}$ m

Thus, most of the incident molecules are first ionized to H_2^+ in a distance of about 2 mm, then dissociated in a distance of about 1 mm.

3D. Atomic Collision Phenomena

Rate coefficients for charge exchange and ionization of atomic hydrogen are shown in Fig. 3D1. Ionization by protons is not effective until high proton energies are reached. Even though an energy of 13.6 eV is needed to ionize hydrogen atoms, electron impact ionization is significant at T_e = 2 eV, because there are a few electrons in the high energy tail of the Maxwellian distribution with enough energy to do the job. The charge exchange rate coefficients stay large even at low proton energies, in marked contrast to the case of molecular hydrogen (Fig. 3C4). The proton-atom charge exchange reaction is said to be "resonant" because they both have the same mass and available electronic energy levels, which facilitates electron transfer at low energies.

Excitation cross sections by electron impact rise very steeply from the threshold energy (10.2 eV in hydrogen) to a region of maximum, then decrease at high

$1 < T_e < 1000$ eV

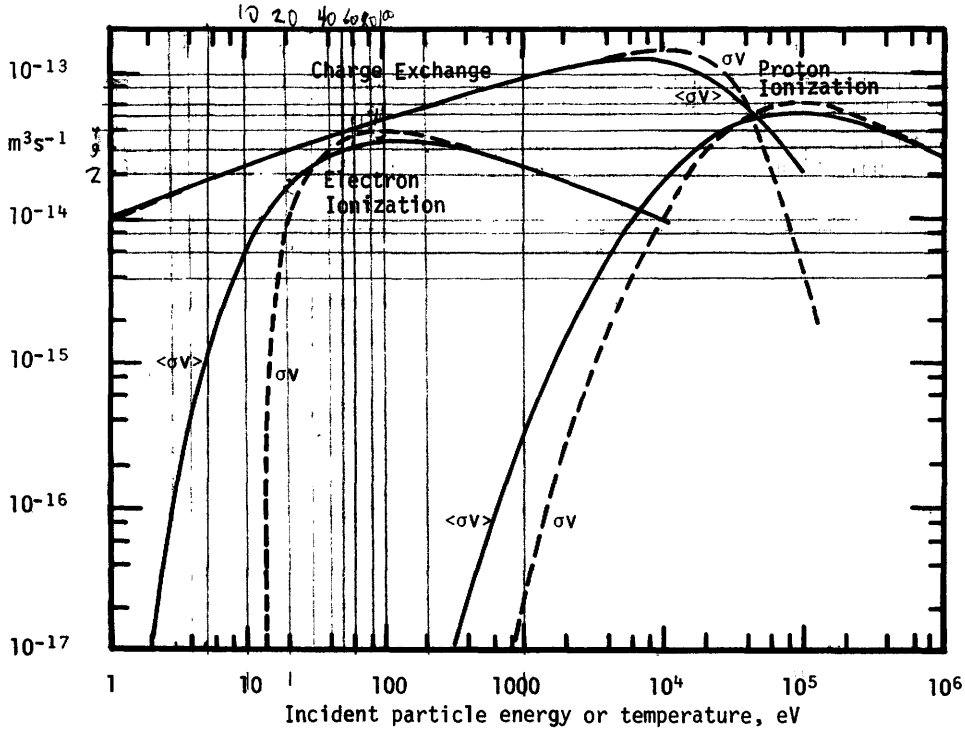

Fig. 3D1. Rate coefficients for charge exchange with protons, ionization by proton impact, and ionization by electron impact of atomic hydrogen, as functions of incident particle energy (monoenergetic, σv) or temperature (Maxwellian, <σv>). The hydrogen atoms are considered to be stationary target particles. (Freeman and Jones, 1974).

energies, as shown in Fig. 3D2. Atoms in excited states are much easier to ionize than those in the ground state, so stepwise ionization may be significant at low energies in high-density plasmas, even though most excited state lifetimes are short ($\sim 10^{-7}$ s).

Ionization may also be produced by energetic photons. The photon energy W is related to its frequency ν and wavelength λ by

$$W = h\nu = hc/\lambda = \frac{1240 \text{ eV}}{\lambda(\text{nm})} \qquad (3D1)$$

where h is Planck's constant and c is the speed of light. In hydrogen, photons below the threshold energy of 13.6 eV cannot cause photoionization from the ground state. Above this energy the photoionization cross section drops off rapidly, as shown in Fig. 3D3. Photoexcitation and ionization may significantly reduce the mean free path of wall-originated impurities incident on the plasma.

Electron attachment is useful in production of high-energy negative ion beams. The additional electron of H^- negative ions has a binding energy of only 0.75 eV, so it is easily removed after the ion has been accelerated to high energy. The

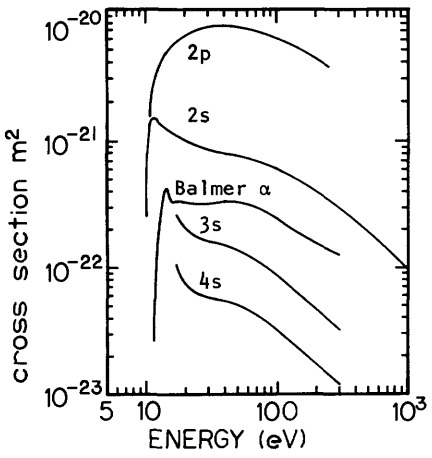

Fig. 3D2. Cross sections for excitation of various energy levels in atomic hydrogen by electron impact, as functions of electron energy. (Barnett et al, 1977).

resultant high-energy neutral beams are useful for plasma heating. The cross section for dissociative attachment in hydrogen is shown in Fig. 3D4. Radiative attachment ($e+H \rightarrow H^- + h\nu$) has cross sections on the order of $2\text{-}6 \times 10^{-28}$ m^2.

The rate coefficients of Fig. 3D5 represent ionization and charge exchange rates of monoenergetic neutral deuterium atom beams incident on a Maxwellian deuterium plasma due to interaction with plasma ions. Similar rate coefficients have been derived for non-Maxwellian distributions, such as occur in magnetic mirror devices (Miller and Miley, 1975). If the average electron speed $(8kT_e/\pi m_e)^{\frac{1}{2}}$ is large compared with the incident atom speed, then the atom is effectively at rest relative to the electrons, and Maxwellian electron ionization rate coefficients (Fig. 3D1) may be used.

Since neutral atoms are attenuated by ionization as they penetrate into a plasma, the neutral atom density drops off steeply away from the plasma edge. Neutrals causing charge exchange result

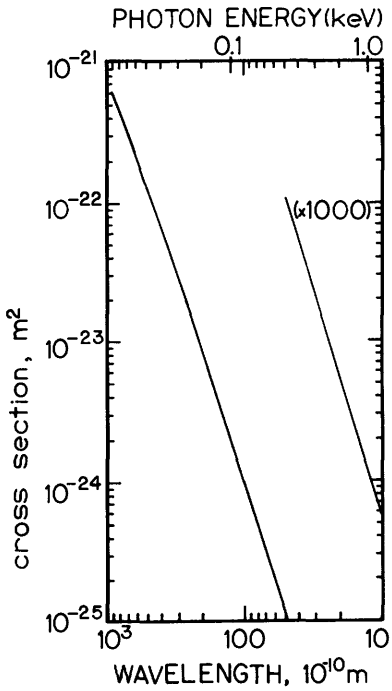

Fig. 3D3. Cross section for photoionization of atomic hydrogen vs. photon wavelength. (Barnett et al, 1977).

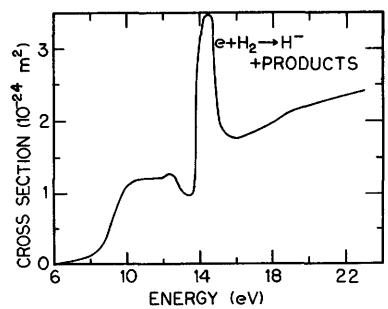

Fig. 3D4. Cross section for dissociative attachment of electrons in molecular hydrogen, as a function of electron energy. (Barnett et al, 1977).

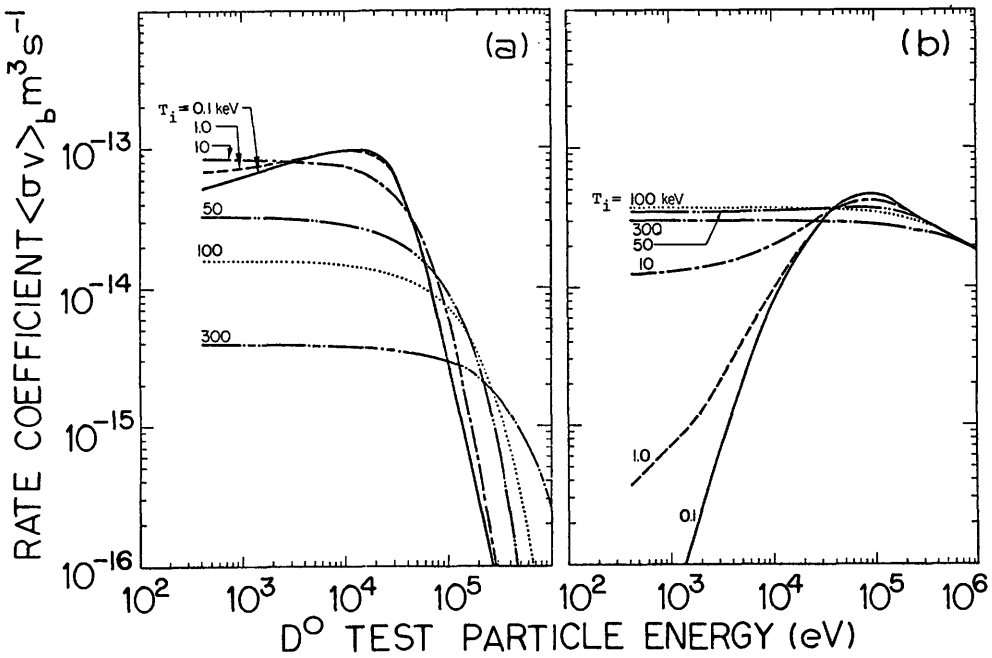

Fig. 3D5. Rate coefficients for (a) charge exchange and (b) ionization of monoenergetic deuterium atom beams D^o incident on a Maxwellian deuterium plasma by plasma ions, at various plasma ion temperatures. (Miller and Miley, 1975).

in plasma ions becoming neutralized. If these secondary neutrals are directed inwards, they may penetrate further towards the center before they undergo charge exchange or ionization. Thus, neutrals have a diffusion-like movement inwards, with charge-exchange processes perpetuating the existence of a neutral particle, but changing its velocity, and ionizations destroying the neutral. In a high-density plasma with a large radius, very few neutrals reach the plasma central region. Under these conditions, neutral atom production by electron-ion recombination may become significant.

In a high-temperature hydrogen plasma, radiative recombination is the dominant recombination process. The rate coefficient for radiative recombination in a hydrogen plasma is shown in Fig. 3D6 as a function of electron temperature.

Empirical equations for cross sections and rate coefficients of various atomic and molecular collision phenomena are given by Freeman and Jones (1974) and Jones (1977).

EXAMPLE PROBLEM 3D1

Monoenergetic 20 keV protons pass through a gas cell 1 m long containing H_2 at 0.1 Pa, 300 K. What fraction of the protons become neutralized as they pass through the cell, ignoring re-ionization? (This is a method of producing

$\langle \sigma v \rangle_{rec} = 1.13 \times 10^{-18} T_e^{-1.15}$ $\quad 5 < T_e < 3000$ eV

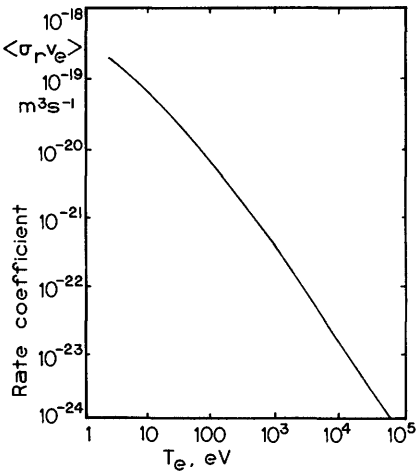

Fig. 3D6. Radiative recombination rate coefficient in hydrogen vs. electron temperature. Based on data of Yu. S. Gordeev, A. N. Zinov'ev, and M. P. Petrov, JETP Letters 25, No. 3, 205 (1977).

energetic neutral atom beams for plasma heating.)

The velocities of the H_2 molecules may be ignored. From Eq. (2B1), $dn_1/dx = -n_1(x)n_2\sigma$. Integrating, we get $n_1(x) = n_1(0)\exp(-n_2\sigma x)$ for the number of uncollided protons at x. Ignoring processes other than charge exchange, the fraction which have become neutralized is equal to $(n_1(0) - n_1(x))/n_1(0) = 1 - \exp(-n_2\sigma x)$.

The proton speed is $v = (2W/m)^{\frac{1}{2}} = 1.96 \times 10^6$ m/s. From Fig. 3C4 for charge exchange of H_2 by monoenergetic proton impact, $\sigma v = 1.2 \times 10^{-13}$ $m^3 s^{-1}$, so $\sigma = 6.1 \times 10^{-20}$ m^2 . $n_2 = p/kT = 2.41 \times 10^{19}$ m^{-3}. For x = 1 m, the fraction neutralized is $1 - \exp(-2.41 \times 10^{19}\ 6.1 \times 10^{-20}\ 1) = 0.77$. Re-ionization could be accounted for by writing rate equations for production and destruction of H^+ and H and solving them simultaneously. According to Fig. 3C4, the cross section for charge exchange drops off rapidly at higher energies. Then, neutralization of H^+ by charge exchange cells becomes inefficient, because of competing re-ionization processes.

EXAMPLE PROBLEM 3D2

(a) Estimate how far 20 keV neutral deuterium atom beams can go into a deuterium plasma with $n = 3 \times 10^{19}$ m^{-3}, $T_e = T_i = 1$ keV before undergoing either charge exchange or ionization. (b) What fraction becomes ionized?

From Fig. 3D5 the rate coefficients for charge exchange and ionization by ions are $\langle \sigma v \rangle_{bx} = 9 \times 10^{-14}$ $m^3 s^{-1}$, $\langle \sigma v \rangle_{bi} = 2.1 \times 10^{-14}$ $m^3 s^{-1}$. The beam speed $v = (2W/m_i)^{\frac{1}{2}} = 1.38 \times 10^6$ m/s, and the average electron speed is $(8kT_e/\pi m_e)^{\frac{1}{2}} = 2.12 \times 10^7$ m/s, so we can use the Maxwellian rate coefficient $\langle \sigma_e v_e \rangle = 2.3 \times 10^{-14}$ m^3/s from Fig. 3D1 for ionization by electrons. The total rate coefficient for all three processes is $\langle \sigma v \rangle = 1.34 \times 10^{-13}$ m^3/s. (a) The mean free path of the beam atoms is $\lambda = v/n_2\langle \sigma v \rangle = 0.34$ m. (b) The fraction of beam atoms

$$\text{ionized} = \frac{r(\text{ionization})}{r(\text{total})} = \frac{n_1 n_2(\langle \sigma_e v_e \rangle + \langle \sigma v \rangle_{bi})}{n_1 n_2(\langle \sigma_e v_e \rangle + \langle \sigma v \rangle_{bi} + \langle \sigma v \rangle_{bx})} = 0.33$$

3E. Equilibrium Degree of Ionization

equilibrium conditions

If plasma confinement times are long enough compared to collision times, then some sort of equilibrium may occur. In hot, low-density plasmas, like the solar corona, the populations of excited levels are determined by balancing the rates of collisional excitation and ionization with the rates of *radiative* de-excitation and recombination. For this case, called *coronal equilibrium* , the various state populations depend on many rate coefficients $\langle\sigma v\rangle$. In high-density plasmas, on the other hand, *collisional* processes may dominate de-excitation and recombination, and the relative populations in *local thermodynamic equilibrium* (LTE) are governed by the Boltzmann and Saha equations, depending only on the temperature. Sometimes the upper energy levels are dominated by collisional processes (LTE), while the lower levels are dominated by radiative de-excitation (coronal equilibrium). Conditions for existence of LTE and coronal equilibrium are discussed by Griem (1964) and Marr (1968). We will compute the equilibrium degree of ionization for the high-density case (Saha equation), and then estimate the neutral atom concentration in the center of a plasma in the low-density (coronal) case.

Saha equation

According to the Maxwell-Boltzmann distribution law for excited states, the ratio of atom densities n_a in state a and n_b in state b at thermal equilibrium is

$$\frac{n_a}{n_b} = \frac{g_a}{g_b} \exp\left[\frac{-(U_a-U_b)}{kT}\right] \tag{3E1}$$

where U_a and U_b are the energies of states a and b, T is the temperature, k is the Boltzmann constant, and g_a and g_b are "degeneracy factors" of states a and b. If the internal degrees of freedom are neglected for the case in which state b is a neutral atom and state a is an electron-ion pair, then

$$\frac{g_a}{g_b} = \left[\frac{2\pi m_e kT}{h^2}\right]^{3/2} \frac{1}{n_a} \tag{3E2}$$

where h is the Planck constant and m_e is the electron mass. Let $U \equiv U_a - U_b$ = the ionization potential of the gas (for hydrogen, U = 13.59 eV), n_i = ion density = n_a, and n_n = neutral atom density = n_b. Then these equations may be combined as

$$\frac{n_i^2}{n_n} = \left[\frac{2\pi m_e kT}{h^2}\right]^{3/2} \exp(-U/kT). \tag{3E3}$$

Let $n_t = n_n + n_i$ = total heavy particle density. Eliminating n_n in Eq. (3E3),

we obtain a quadratic equation for n_i with the solution

$$\frac{n_i}{n_t} = \frac{(1+4x)^{\frac{1}{2}} - 1}{2x} \quad , \quad \text{or} \quad x = \frac{1 - n_i/n_t}{(n_i/n_t)^2} \tag{3E4}$$

where $x = \dfrac{n_t h^3 \exp(U/kT)}{(2\pi m_e kT)^{3/2}}$. If T is expressed in eV, then $x = 3.313 \times 10^{-28} n_t T^{-3/2} \exp(U/T)$. For $x \ll 1$, Eq. (3E4) simplifies to

$$n_i/n_t \simeq 1 - x \quad . \tag{3E5}$$

Eqs. (3E3) to (3E5), called the *Saha Equation* , can be used to predict the equilibrium degree of ionization of gases such as hydrogen. More complicated sets of equations can be formulated in a similar fashion to predict the equilibrium densities of multiple ionization states of plasma impurity atoms, such as carbon and oxygen.

EXAMPLE PROBLEM 3E1

Estimate the fractional ionization of hydrogen gas at T = 1 eV, p = 10^{-3} atm.

The total heavy particle density is
$n_t = p/kT = 6.323 \times 10^{20}$ m^{-3}(p must be expressed in Pa, and kT in J).
$x = 3.313 \times 10^{-28} 6.323 \times 10^{20} (1)^{-3/2} \exp(13.59/1) = .1672$. From Eq. (3E4), $n_i/n_t = 0.873$. Therefore, the gas is 87% ionized.

The fractional ionization of hydrogen vs. temperature is shown in Fig. 3E1 for several values of n_t. The gas becomes highly ionized at T << U, because there are a few electrons in the high-energy tail of the Maxwellian distribution with sufficient energy to cause excitation and ionization. Ionization potentials for other elements range from 3.87 eV (Cs) to 24.46 eV (He). The Saha equation and Fig. 3E1 are based upon the assumption of *thermal equilibrium* .

coronal case

The fractional concentration of neutral atoms in the core of a high-temperature plasma may be estimated by balancing the rates of ionization and recombination.

$$n_e n_i \langle \sigma_r v_e \rangle \simeq n_e \langle \sigma_e v_e \rangle n_n + n_i \langle \sigma_i v_i \rangle n_n \tag{3E6}$$

where $\langle \sigma_r v_e \rangle$ is the recombination rate coefficient (Fig. 3D6) and $\langle \sigma_e v_e \rangle$, $\langle \sigma_i v_i \rangle$ are the rate coefficients for ionization by electrons and ions. Taking $n_e = n_i$, this equation may be solved for n_n/n_i, the equilibrium neutral atom fraction in the absence of neutral influx from outside. The results of such a calculation are shown in Fig. 3E2.

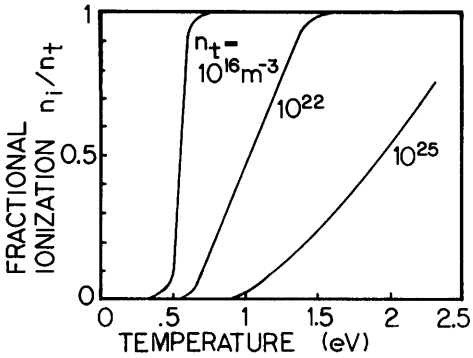

Fig. 3E1. Degree of ionization of hydrogen as a function of gas temperature, for various total heavy-particle densities n_t. Based on Fig. 1.5, Plasma Physics, by B. S. Tanenbaum. Copyright 1967, McGraw-Hill. Used with the permission of McGraw-Hill Book Company.

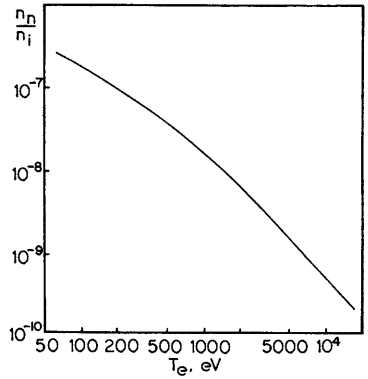

Fig. 3E2. Ratio of neutral atom density to plasma density in plasmas where influx of neutrals from outside is negligible. Based on data of Yu. S. Gordeev, A. N. Zinov'ev, and M. P. Petrov, JETP Letters 25, No. 3, 205 (1977).

3F. Radiation Losses

radiation processes

The fusion power density is primarily a function of ion temperature (Eq. 2D8), T_i is strongly coupled to T_e by Coulomb collisions (Eq. 2E46), and T_e is limited by radiative power losses. Therefore, radiation losses strongly influence the fusion power density and attainability of ignition (Section 4B).

Radiation power loss processes include radiative recombination P_R, dielectronic recombination P_D, bremsstrahlung radiation P_B, line radiation P_L, and cyclotron radiation P_C (also called synchrotron or betatron radiation). The total radiative power loss per unit volume is

$$P_{rad} = P_R + P_D + P_L + P_B + K_C P_C \qquad (W/m^3), \qquad (3F1)$$

where K_C is the fraction of cyclotron radiation which is absorbed in the walls and not reabsorbed in the plasma. Reabsorption of the other types of radiation is negligible.

Radiative recombination involves capture of a free electron by an ion, with the binding energy subsequently released by emission of radiation as the resultant atom or ion de-excites to its ground state. For example, the triply charged oxygen ion O^{+++} may capture an electron to become O^{++}

$$O^{+++} + e^- \rightarrow O^{++*} \rightarrow O^{++} + h\nu \qquad (3F2)$$

We will use the subscript j to denote the charge state of an ion. Thus O^{+++} has j = 3.

Dielectronic recombination involves capture of a free electron with simultaneous excitation of another orbital electron, so that two electrons are both in excited states. The doubly excited state may return to the original state by autoionization in a time $\sim 10^{-13}$ s, or it may de-excite by photon emission, with a slower time constant. The latter process, resulting in stable capture of the incident electron, is called dielectronic recombination. For example

$$O^{+++} + e^- \rightarrow O^{++**} \rightarrow \begin{cases} O^{++} + h\nu_1 + h\nu_2 & \text{dielectronic recombination} \\ O^{+++} + e^- & \text{autoionization} \end{cases} \qquad (3F3)$$

where ** denotes double excitation. Other recombination processes, such as dissociative recombination and three-body recombination, will probably be negligible in a fusion reactor plasma.

When an atom or ion is raised to an excited level by electron impact (or other process) it usually de-excites by emission of line radiation in about 10^{-7} s. For example

$$O^{+++} + e^- \rightarrow O^{+++*} + e^- \rightarrow O^{+++} + h\nu + e^- \qquad (3F4)$$

After ions have been completely stripped of orbital electrons, line radiation is impossible. (For example, H^+ and O^{8+} cannot emit line radiation).

Whenever a charged particle is accelerated, it will emit some radiation. For a given force, electrons will have large accelerations, because of their light mass, and ions will have small accelerations. Therefore, radiation by acceleration of ions is generally negligible.

Electrons are accelerated by electric and magnetic fields. The $q\vec{v}x\vec{B}$ force produces Larmor rotation around the magnetic field lines (Chapter 7) and consequent emission of cyclotron radiation. The Coulomb force $q\vec{E}$ from ions and other electrons during Coulomb collisions produces deflections and consequent emission of bremsstrahlung radiation. ("Bremsstrahlung" is German for "braking radiation".)

approach to coronal equilibrium

Let n_{kj} represent the concentration of atoms or ions of species k and ionization state j. For example, k = 8 represents oxygen, and j = 3 would represent O^{+++} (5 bound electrons). Let I_{kj} represent the rate coefficient for ionization of n_{kj} and R_{kj} be the rate coefficient for recombination of n_{kj} with an electron, including both radiative and dielectronic recombination. The rate of change of n_{kj} is given by

$$\frac{dn_{kj}}{dt} = n_e \left[n_{k,j+1} R_{k,j+1} + n_{k,j-1} I_{k,j-1} - n_{kj}(R_{kj} + I_{kj}) \right] . \qquad (3F5)$$

The recombination coefficients are functions only of T_e. For temperatures of a few keV or less, electron impact ionization is dominant (Fig. 3D1), and the ionization rates also are functions only of T_e.

We will write particle balance equations to compute the population of each ionization state, from which the radiative power losses can be calculated. Consider the case of atoms of a single impurity species incident on a plasma with constant T_e. Assuming that the atoms are initially neutral, the initial conditions are $n_{kj} = 0$ for all j except j = 0. For example, the equations for helium are

$$\textit{neutral He:}\quad \frac{dn_{20}}{dt} = n_e(n_{21}R_{21} - n_{20}I_{20}), \qquad n_{20}(0) = n_0$$

$$He^{+}:\quad \frac{dn_{21}}{dt} = n_e[n_{22}R_{22} + n_{20}I_{20} - n_{21}(R_{21}+I_{21})\,], \quad n_{21}(0) = 0$$

$$He^{++}:\quad \frac{dn_{22}}{dt} = n_e(n_{21}I_{21} - n_{22}R_{22}), \qquad n_{22}(0) = 0. \tag{3F6}$$

(There may also be a source of n_{22} from fusion reactions.) This set of coupled ordinary differential equations may be solved by use of Laplace transforms, or by integration on a digital computer. For higher-Z impurities, the transform method gets too complicated. If we assume n_e = constant and divide by n_e, then the left sides of the equations may be written

$$\frac{1}{n_e}\frac{dn_{kj}}{dt} = \frac{dn_{kj}}{d(n_e t)} \tag{3F7}$$

and the solution becomes a function of the new variable $n_e t$.

After a long time, coronal equilibrium is established and the time derivatives go to zero. If the temperature is high enough, most of the low Z ions will be completely stripped at equilibrium.

Fig. 3F1 shows the variation of fractional concentrations of oxygen ions with 0, 1, and 2 bound electrons with time during approach to equilibrium. In this case equilibrium is reached in about 200 ms, with about 72% of the ions fully stripped, 23% with 1 bound electron, and 5% with 2 bound electrons. Since the fully stripped ions do not emit line radiation, the power lost by radiation decreases as equilibrium is reached.

Each of the radiation power terms in Eq. (3F1) except P_C is proportional to the electron density and to the density of impurity atoms $n_k = n_{k0} + n_{k1} + \ldots + n_{kk}$, so we can define a *radiation power parameter* for species k

$$Q_k = (P_R + P_D + P_L + P_B)_k/n_e n_k \qquad (\text{W-m}^3), \tag{3F8}$$

which varies with time during approach to equilibrium and is also a function of T_e. The time variation of Q_k for oxygen is shown in Fig. 3F2, for various T_e. Equilibrium is attained when $n_e t \sim 10^{18}$ $m^{-3}s$, and the power radiated during approach to equilibrium is about an order of magnitude higher than the equilibrium value.

If spatial transport of impurities can be ignored and $n_e t > 10^{18}$ $m^{-3}s$, then we can assume that coronal equilibrium exists, and calculate the concentrations from equations of the form of (3F6) with the time derivatives set equal to zero. (Spatial transport of impurities will be discussed in Example Problem 5D1.)

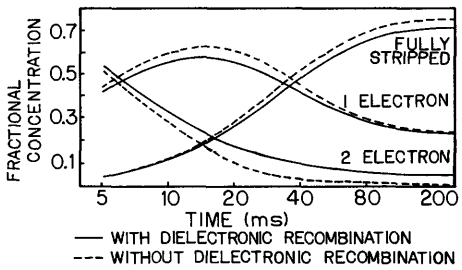

Fig. 3F1. Fractional concentrations of oxygen ions with 0, 1, and 2 bound electrons as functions of time during approach to equilibrium in plasma with $n_e = 10^{19}$ m^{-3} *and* $T_e = 300$ *eV. From G. R. Hopkins and J. M. Rawls, Nuclear Technology 36, 171 (1977), Fig. 2.*

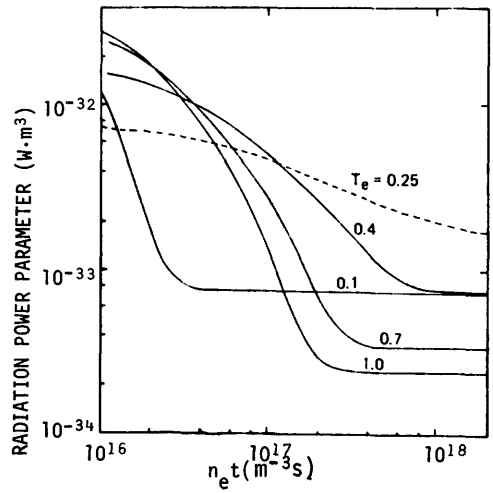

Fig. 3F2. Variation of the radiative power loss per electron per impurity atom from oxygen as a function of electron density times time during approach to coronal equilibrium, for various electron temperatures (keV). From G. R. Hopkins and J. M. Rawls, Nuclear Technology 36, 171 (1977), Fig. 1.

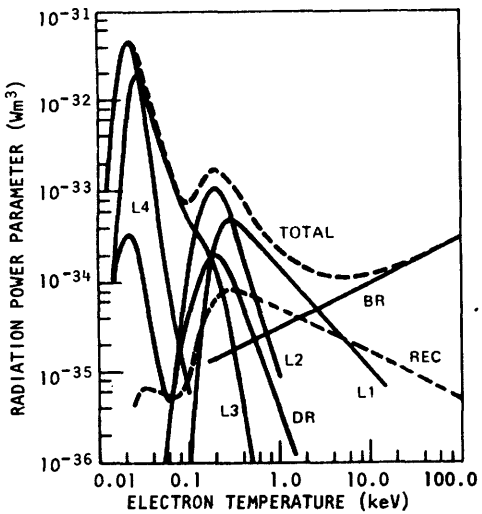

Fig. 3F3. The contributions to the radiation per oxygen atom per electron from line radiation (L1-L4), recombination radiation (REC), dielectronic recombination (DR), and bremsstrahlung radiation (BR). From G. R. Hopkins and J. M. Rawls, Nuclear Technology 36, 171 (1977), Fig. 5.

coronal equilibrium case

At coronal equilibrium, the relative contributions of the four terms in Eq. (3F8) vary with T_e, as shown in Fig. 3F3 for oxygen. At low temperatures, line radiation is the dominant process. As fewer bound electrons remain at higher temperatures, recombination and bremsstrahlung become significant, and the total radiated power decreases. At very high temperatures, the radiation power parameter is dominated by bremsstrahlung, and increases as $T_e^{\frac{1}{2}}$.

The radiation power parameter Q_k for various elements is shown in Fig. 3F4. The big differences in the shapes of curves for Li and He at low temperatures are related to differences in their ionization potentials and energy levels. The

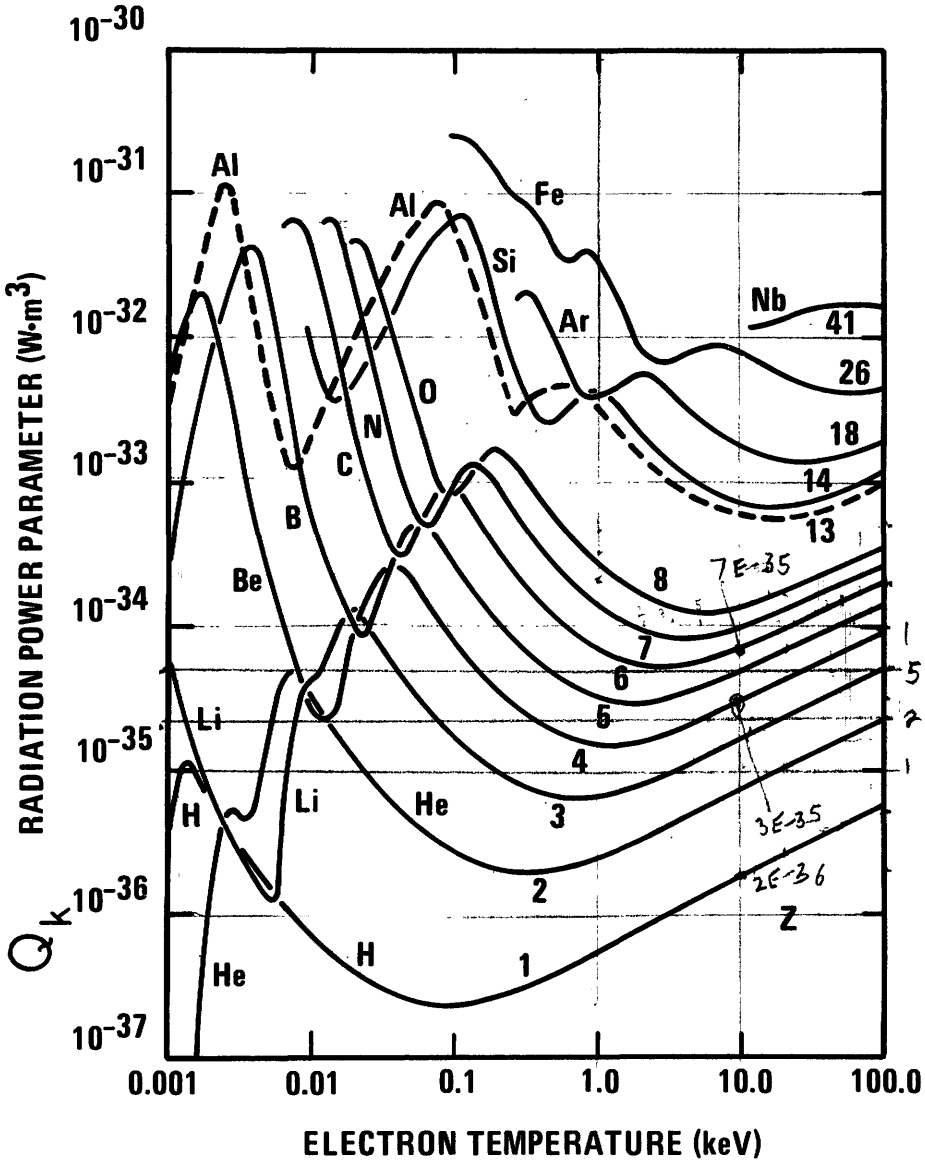

Fig. 3F4. The radiation power parameter as a function of electron temperature for various elements. (Cyclotron radiation losses must be computed separately.) From G. R. Hopkins and J. M. Rawls, Nuclear Technology 43, 382 (1979), Fig. 1.

total radiation power lost from the plasma is found by summing Eq. (3F8) over impurity species and combining with Eq. (3F1):

$$P_{rad} = \sum_k n_e n_k Q_k + K_C P_C \qquad (W/m^3). \qquad (3F9)$$

For a given impurity species, the average values of ionic charge and charge squared are given by

$$\langle Z \rangle_k = \frac{\sum_j n_{kj} Z_{kj}}{\sum_j n_{kj}}$$

$$\langle Z^2 \rangle_k = \frac{\sum_j n_{kj} Z_{kj}^2}{\sum_j n_{kj}} \qquad (3F10)$$

where $Z_{kj} = j$. As T_e increases, more electrons become stripped off the ion, and $\langle Z \rangle_k \to Z$, the atomic number of the nucleus. The variations of $\langle Z \rangle_k$ and $\langle Z^2 \rangle_k$ with T_e are shown in Fig. 3F5.

The total density of heavy particles in the plasma is

$$n_t = \sum_k n_k. \qquad (3F11)$$

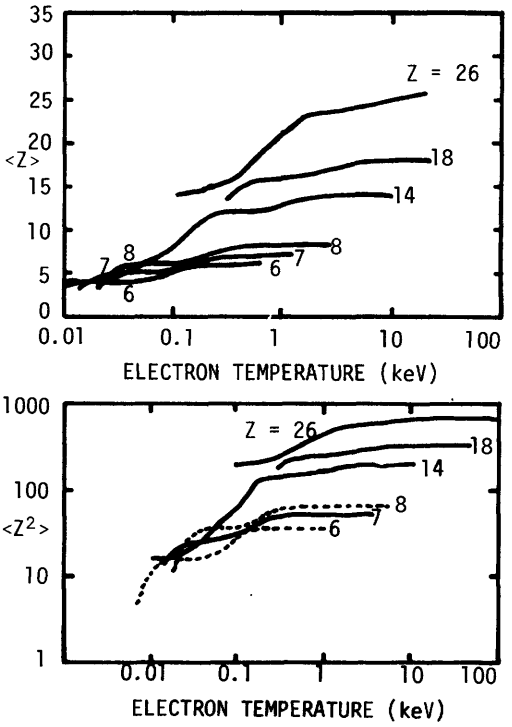

Fig. 3F5. The average values of nuclear charge and nuclear charge squared for various impurities in plasma at coronal equilibrium, as functions of electron temperature. From G. R. Hopkins and J. M. Rawls, Nuclear Technology 36, 191 (1977), Figs. 10,11.

According to the principle of "quasineutrality" (Chapter 5), the electron density equals the density of positive charges per unit volume

$$n_e = \sum_k n_k \langle Z \rangle_k \qquad (3F12)$$

We can define an effective value of Z for the plasma as a whole by

$$Z_{eff} = \frac{\sum_k n_k \langle Z^2 \rangle_k}{\sum_k n_k \langle Z \rangle_k} = \frac{\sum_k n_k \langle Z^2 \rangle_k}{n_e} = \left(1 - f_1 Z_1 - f_2 Z_2\right) + f_1 Z_1^2 + f_2 Z_2^2 \qquad (3F13)$$

$$\simeq 1 + f_1 Z_1 (Z_1 - 1) + f_2 Z_2 (Z_2 - 1)$$

Z_{eff} is useful in estimating plasma resistivity and bremsstrahlung losses.

To facilitate computations of power losses by line radiation, recombination radiation, and bremsstrahlung radiation, approximate equations for the radiation power parameter, $\langle Z \rangle_k$ and $\langle Z^2 \rangle_k$ as functions of T_e are given by Hopkins and Rawls

(1977 and 1979) for various elements, and a simplified formula for the radiation power parameter is given by Vernickel and Bohdansky (1978).

An approximate equation for the bremsstrahlung power loss is

$$P_B = 5 \times 10^{-37} Z_{eff} n_e^2 T_e^{\frac{1}{2}} \qquad (W/m^3), \tag{3F14}$$

where T_e is in keV. At temperatures high enough that line radiation and recombination radiation are negligible (the linear portion at the right of Fig. 3F4), the $\sum_k n_e n_k Q_k$ term of Eq. (3F9) may be replaced by P_B from Eq. (3F14).

cyclotron radiation

Cyclotron radiation is emitted at frequencies which are integer multiples of the fundamental frequency

$$\nu_c = \frac{eB}{2\pi m_e} = 2.80 \times 10^{10} B \qquad (Hz), \tag{3F15}$$

where e is the electronic charge (C) and B is the magnetic induction (T). For example, radiation at a frequency $\nu = 10\nu_c$ is called the "tenth harmonic". The total power emitted from the fundamental and all harmonics is given approximately by

$$P_C = \frac{e^4 B^2}{3\pi\varepsilon_0 m_e^2 c}\left[\frac{n_e k T_e}{m_e c^2}\right]\left[1 + \frac{3.5 k T_e}{m_e c^2} + \ldots\right] \qquad (W/m^3), \tag{3F16}$$

where ε_0 is the permittivity of free space and c is the speed of light. Expressing T_e in keV, this becomes

$$P_C = 6.21 \times 10^{-17} n_e T_e B^2 (1 + T_e/146 + \ldots) \qquad (W/m^3). \tag{3F17}$$

The magnetic field is reduced inside the plasma by plasma currents. The resultant magnetic field is a function of the parameter

$$\beta = \frac{\text{plasma pressure}}{\text{vacuum magnetic field pressure}} = \frac{p}{B^2/2\mu_0}, \tag{3F18}$$

where B is the magnetic induction without plasma.

The fraction K_C of cyclotron power absorbed in the walls of a cylindrical plasma is a function of T_e and the "plasma depth"

$$D \equiv \frac{2 n_e a}{B^{3/2} \eta^{\frac{1}{2}} (1-\beta)^{3/4}}, \tag{3F19}$$

where a is the plasma radius (m) and η is the electrical resistivity (Ohm-m), as shown in Fig. 3F6. Values of resistivity for some metals of interest are shown in Fig. 3F7.

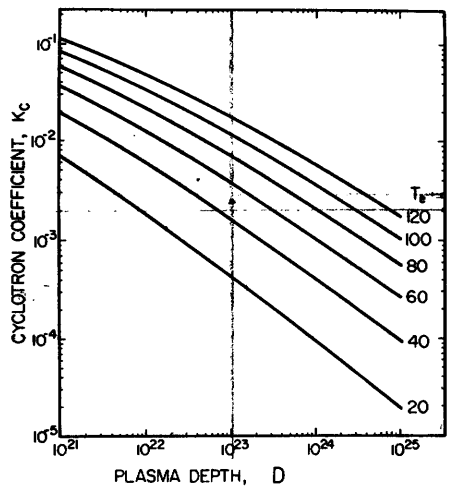

Fig. 3F6. Cyclotron radiation coefficient K_C vs. "plasma depth" D, for a cylindrical plasma with various T_e (keV). From G. H. Miley, Fusion Energy Conversion, American Nuclear Society, LaGrange Park, IL, 1975.

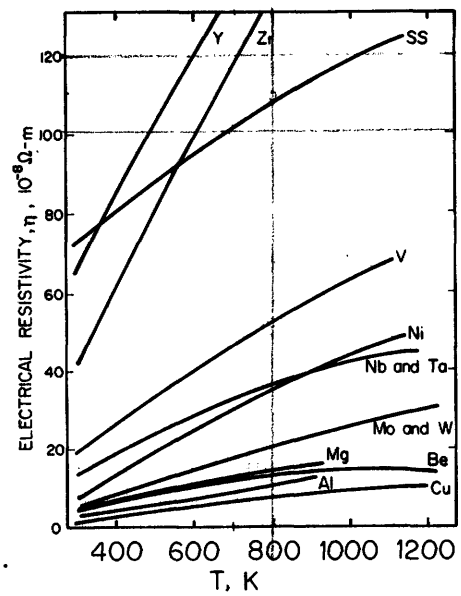

Fig. 3F7. Electrical resistivity vs. temperature for various metals. From G. H. Miley, Fusion Energy Conversion, American Nuclear Society, LaGrange Park, IL, 1975.

EXAMPLE PROBLEM 3F1

Assume that a toroidal DT fusion reactor with major radius R = 6 m, minor radius a = 2 m, and stainless steel walls at 700 K has a uniform edge plasma region Δr = 0.3 m thick with $n_e = 5\times10^{19}$ m^{-3}, $T_e = T_i$ = 100 eV, B = 3 T, and a 0.2% Fe impurity (meaning $n_{Fe}/n_e = 0.002$). Estimate Z_{eff} and the radiation power losses in the edge plasma region, assuming coronal equilibrium and ignoring spatial variation of B.

From Fig. 3F5, <Z> = 14 for iron. From Eq. (3F12) $n_e = n_i + 14\, n_{Fe}$, where n_i = fuel ion density. Thus, $n_i = n_e\left[1 - 14(.002)\right] = .972\, n_e$. The plasma pressure $p = n_e kT_e + n_i kT_i + n_{Fe} kT_{Fe} = n_e(1 + .972 + .002)\, kT = 1580$ Pa and $\beta = 2\mu_0 p/B^2 = 4.4\times10^{-4}$. From Fig. 3F7, $\eta = 10^{-6}$ Ohm-m. From Eq. (3F19), D = 3.9×10^{22}. From Fig. 3F6 with T_e = 0.1 keV, we estimate that $K_C < 10^{-5}$. From Eq. (3F17), $P_C = 2.8\times10^4$ W/m^3, so $K_C P_C$ is negligible for this case. From Fig. 3F4, $Q_{Fe} = 2.7\times10^{-31}$ W-m^3 and $Q_H = 2.3\times10^{-37}$ W-m^3. From Eq. (3F9), P_{rad} = 1.4 MW/m^3. The edge region volume is approximately $4\pi^2 aR\Delta r$ = 142 m^3, so the total power radiated from this region is about 200 MW. From Fig. 3F5, $\langle Z^2\rangle \simeq 180$. Then, from Eq. (3F13), $Z_{eff} = n_e\left[.972(1) + .002(180)\right]/n_e = 1.33$.

EXAMPLE PROBLEM 3F2

Estimate the cyclotron power loss from a cylindrical plasma with a = 2 m, $T_e = T_i = 50$ keV, B = 10 T, $n_i = n_e = 10^{20}$ m^{-3}, and stainless steel walls at 700 K.

For this case we find p = 1.6 MPa and $\beta = 0.040$. From Eq. (3F19) and Fig. 3F6, $D = 1.3 \times 10^{22}$ and $K_C = 0.009$. From Eq. (3F17), $P_C = 41.7$ MW/m^3, and $K_C P_C = 0.38$ MW/m^3.

For such cases, accurate computation of K_C becomes important. The large power loss by cyclotron radiation is a major limitation on temperatures attainable in fusion reactors.

Problems

1. If $n_e = 10^{19}$ m^{-3} and $T(H_2) = 400$ K in example problem 3B1, what is the mean free path of the electrons relative to momentum-transfer collisions with H_2? What is the mean free path of the neutrals relative to this type of collision? How does ν_{en} compare with ν_{ei} for this case? Are the neutrals and the plasma in thermal equilibrium?

2. Franck-Condon neutral H atoms with 3 eV energy are incident on a hydrogen plasma with $n_e = 10^{19}$ m^{-3}, $T_e = T_i = 1$ keV. What processes will be significant? About how far will the atoms penetrate before having any kind of reaction? About what fraction of the atoms will cause charge exchange?

3. A beam of monoenergetic electrons with current density 30 mA/cm^2 passes through H_2 gas at 7 Pa pressure, 340 K. How long does it take until half the gas is either ionized or dissociated if the beam energy is (a) 100 eV, (b) 10 keV?

4. A flux of 10^4 W/m^2 of photons at 30 eV is coming from a fusion plasma. How many photons/m^2s does this represent? What ionization rate will this flux produce in atomic hydrogen at 0.1 Pa, 900 K? What is the corresponding mean free path of the H atoms?

5. Monoenergetic 80 keV protons pass through a gas cell 0.8 m long containing H_2 gas at 0.2 Pa, 320 K. Ignoring re-ionization, what fraction become neutralized as they pass through the cell?

6. It is desired that neutral deuterium atom beams be able to penetrate at least 1.0 m (mean free path) into a reactor plasma with $n = 10^{20}$ m^{-3}, $T_e = T_i = 17$ keV. What energy must the beam have?

7. What temperatures are needed to produce 99% ionization (a) of helium, (b) of cesium, if $n_t = 10^{22}$ m^{-3}?

8. Estimate the fractional concentration of neutral H atoms in the core of a hydrogen plasma at $T_e = 1000$ eV using Eq. (3E6), and compare the result with Fig. 3E2.

9. A hydrogen tokamak plasma with $n_e = 6 \times 10^{19}$ m^{-3}, $T_e = T_i = 2$ keV, $K_c = 10^{-5}$, and B = 3 T has an oxygen fraction $n_0/n_e = 0.01$ at t = 200 ms. (a) If impurity transport rates are negligible, is the plasma likely to be at coronal equilibrium? (b) Estimate the power losses (W/m^3) due to line radiation, radiative recombination, dielectronic recombination, bremsstrahlung, cyclotron radiation, and total from oxygen and hydrogen. (c) What concentration of aluminum (instead of the oxygen) would it take to produce the same total radiation loss? (d) What would be the values of Z_{eff} for the two cases? (e) At what temperature would a pure hydrogen plasma have the same total radiation loss?

10. Consider a deuterium plasma with a 0.3% carbon impurity, a = 1.5 m, $n_e = 10^{20}$ m^{-3}, $T_e = T_i$, B = 8 T, and stainless steel walls (450 K). (a) At what plasma temperature will the power loss per m^3 exceed 1 MW/m^3? (Try various temperatures, such as 100 keV). (b) At what temperature will the cyclotron losses exceed the bremsstrahlung losses? (By 0.3% impurity, we mean $n_C/n_e = 0.003$.)

11. A given tokamak confinement system is limited to values of $\beta \leq 0.10$. Given $T_e = T_i$, $n_e = 10^{20}$ m^{-3}, B = 6 T, and a = 2m, and vanadium walls at 800 K, find (a) the maximum T_e (from plasma pressure) and (b) the corresponding cyclotron radiation power loss (W/m^3).

12. The energy confinement time in plasma devices is roughly defined as $\tau_E \simeq \frac{\text{energy content of plasma}}{\text{energy loss rate by radiation and transport}}$, where the energy content $\simeq 3nk(T_e+T_i)/2$. Ignoring transport losses and cyclotron radiation losses, estimate the energy confinement time for a plasma with $n = 2 \times 10^{19}$ m^{-3}, $T_e = T_i = 2$ keV and a 2% oxygen impurity ($n_0/n_e = 0.02$).

Bibliography

atomic and molecular collisions

C. F. Barnett, J. A. Ray, E. Ricci, M. I. Wilker, E. W. McDaniel, E. W. Thomas, and H. B. Gilbody, "Atomic data for controlled fusion research", ORNL-5206, Vols. 1 & 2, 1977.

R. L. Freeman and E. M. Jones, "Atomic collision processes in plasma physics experiments", Culham Laboratory Report CLM-R-137, 1974.

E. M. Jones, "Atomic collision processes in plasma physics experiments: analytic expressions for selected cross-sections and Maxwellian rate coefficients II", CLM-R-175, 1977.

E. W. McDaniel, *Collision Phenomena in Ionized Gases*, Wiley, New York, 1974.

M. R. C. McDowell and A. M. Ferendeci, Editors, *Atomic and Molecular Processes in Controlled Thermonuclear Fusion*, Plenum Press, New York, 1980.

R. L. Miller and G. H. Miley, "Ionization and charge exchange rate coefficients for CTR calculations", COO-2218-26, University of Illinois, 1975.

radiation

H. R. Griem, *Plasma Spectroscopy*, McGraw-Hill, New York, 1964.

G. R. Hopkins and J. M. Rawls, "Impurity radiation from medium density plasmas", *Nuclear Technology 36*, 171 (1977).

G. R. Hopkins and J. M. Rawls, "Addendum to 'Impurity radiation from medium density plasmas'", *Nuclear Technology 43*, 382 (1979).

G. V. Marr, *Plasma Spectroscopy*, Elsevier, New York, 1968.

D. M. Meade, "Effect of high-Z impurities on the ignition and Lawson conditions for a thermonuclear reactor", *Nuclear Fusion 15*, 289 (1975).

G. H. Miley, *Fusion Energy Conversion*, American Nuclear Society, 1975.

D. J. Rose and M. Clark, Jr., *Plasmas and Controlled Fusion*, MIT Press, Cambridge, MA, 1961.

H. Vernickel and J. Bohdansky, "A general formula for impurity radiation loss of fusion plasmas in corona equilibrium", *Nuclear Fusion 18*, 1467 (1978).

CHAPTER 4

FUSION REACTOR POWER BALANCE

4A. Conservation Equations

The simplest model of a fusion reactor treats the plasma as if it were uniform and quasineutral, characterized by electron, fuel ion, and alpha particle densities and temperatures n_e, n_i, n_α, T_e, and T_i.

Instead of solving momentum-conservation equations for motion of particles across the magnetic confinement system, we simply use characteristic times τ_p and τ_E for losses of particles and energy (with subscripts e, i, or α for the three species). Thus, τ_p denotes the loss time for fuel ions, while τ_{Ei} denotes their energy loss time. Ions are lost rapidly from the plasma edge region, but very slowly from a hot plasma core. Methods for calculating particle and energy loss times (called *confinement times*) will be discussed in Section 8G.

According to the principle of "quasineutrality" (Chapter 5), there will be equal concentrations of positive and negative charges per unit volume, so that

$$n_e = n_i + 2n_\alpha + \sum_k n_k \langle Z_k \rangle \tag{4A1}$$

where the summation includes all ion species except fuel ions and alpha particles, and $\langle Z_k \rangle$ was defined in Eq. (3F10).

For simplicity, assume equal densities of deuterons and tritons, $n_D = n_T = n_i/2$. The rate at which ions are destroyed by fusion reactions will be $2r_{DT}$, since each reaction consumes two ions. Using Eq. (2B19) for r_{DT}, a particle conservation equation for fuel ions may be written

$$\frac{dn_i}{dt} = (\text{source}) - (\text{loss from confinement system}) - (\text{loss by fusion})$$
$$= S_i - \frac{n_i}{\tau_p} - \tfrac{1}{2} n_i^2 \langle \sigma v \rangle_{DT} \, . \tag{4A2}$$

For temperatures of interest, the DD and TT fusion reaction rates are negligible in comparison with the DT reaction rate. Let τ_α denote the particle confinement time for alpha particles. A particle conservation equation for alpha particles is

$$\frac{dn_\alpha}{dt} = \tfrac{1}{4}n_i^2\langle\sigma v\rangle_{DT} - \frac{n_\alpha}{\tau_\alpha} \quad , \tag{4A3}$$

since each DT fusion reaction produces one alpha particle.

According to Eq. (2A8), the average energy per particle in a Maxwellian distribution is 3kT/2. Therefore, the average energy densities of electrons and fuel ions will be $1.5n_eT_e$ and $1.5n_iT_i$, where the Boltzmann constant is omitted for simplicity, with the temperature in energy units.

The energy conservation equation for the ions is

$$\begin{aligned}\frac{d(1.5n_iT_i)}{dt} &= (\text{external heating of ions}) + (\text{heating by alphas}) \\ &\quad + (\text{heating by electrons}) - (\text{energy loss rate}) \\ &= P_i + f_i f_r W_{\alpha 0} n_i^2\langle\sigma v\rangle_{DT}/4 + 1.5n_i(T_e-T_i)/\tau_{eq} - 1.5n_iT_i/\tau_{Ei}\end{aligned} \tag{4A4}$$

where P_i is the external heating power to the ions, f_r is the fraction of alpha energy deposited in the plasma, f_i is the fraction of their energy which goes to the ions (Fig. 2E8 and Eq. 2E59), $W_{\alpha 0}$ = 3520 keV = $5.64\text{x}10^{-13}$ J is the initial fusion product alpha energy, τ_{eq} is the equilibration time (Eq. 2E46), and the energy loss term includes losses by heat conduction, convection (including charge exchange losses), and destruction of ions by fusion reactions. Radiative loss of ion kinetic energy is negligible. Eq. (4A4) may be cast in units of keV/m^{3}s or in units of W/m^3. In order to study the effects of radiation separately, we will define a *nonradiative* electron energy loss time τ'_{Ee}. An electron energy conservation equation may be written

$$\begin{aligned}\frac{d(1.5n_eT_e)}{dt} &= (\text{external heating of electrons}) + (\text{heating by alphas}) \\ &\quad - (\text{cooling by fuel ions}) - (\text{radiation losses}) \\ &\quad - (\text{losses by conduction and convection}) \\ &= P_e + f_e f_r W_{\alpha 0} n_i^2\langle\sigma v\rangle_{DT}/4 - 1.5n_i(T_e-T_i)/\tau_{eq} \\ &\quad - P_{rad} - 1.5n_eT_e/\tau'_{Ee} \quad ,\end{aligned} \tag{4A5}$$

where $f_e = 1 - f_i$ is the fraction of the alpha energy given to the electrons (Fig. 2E8), and P_{rad} is the radiation power loss (Eq. 3F1 or 3F9). If $T_e < T_i$, then the τ_{eq} term in Eqs. (4A4) and (4A5) changes sign, and the ions tend to heat the electrons.

Since some alpha particles are lost after partial slowing down, the effective value of f_i may be less than that given in Fig. 2E8 for complete thermalization.

The external heating terms include heating by electrical current (Ohmic heating), heating by compression, heating by injection of energetic particle

beams, and heating by electromagnetic waves (Chapter 9).

Assuming that the confinement times, alpha retention fraction f_r, and impurity concentrations are known, Eqs. (4A1)-(4A5) constitute a complete set for finding the time variations of n_e, n_i, n_α, T_i, and T_e. How to calculate confinement times theoretically (Chapter 8) and prolong them experimentally (Chapters 11-17) have been major problems of fusion research.

Even without knowing the confinement times, we can use these conservation equations to find the consequences of various values of confinement times. In particular, we can estimate (1) equilibrium values of densities and temperatures, (2) conditions under which alpha heating of electrons and ions can sustain the plasma temperatures (the "ignition" condition), and (3) conditions under which the fusion power produced exceeds the input power for heating and confinement ("break-even" conditions).

4B. Equilibrium and Ignition

equal temperatures and no fuel depletion

The term "equilibrium" means that conditions are varying so slowly in time that the time derivative terms are negligible. For example, the equilibrium alpha particle density is found from Eq. (4A3) to be

$$n_\alpha = n_i^2 \langle \sigma v \rangle_{DT} \tau_\alpha / 4 \ . \tag{4B1}$$

To simplify the study of equilibrium and ignition conditions, we will first consider the case in which $T_e \simeq T_i \equiv T$, and impurity density $n_k \ll n_\alpha \ll n_i$, so that Eq. (4A1) reduces to $n_i \simeq n_e$. For simplicity, we will drop the subscript on n_e, letting $n \equiv n_e$. By definition, let the total external heating power

$$P_{ext} \equiv P_e + P_i \ , \tag{4B2}$$

the alpha heating power

$$P_h \equiv \tfrac{1}{4} f_r W_{\alpha 0} n_i^2 \langle \sigma v \rangle_{DT} \qquad (W_{\alpha 0} = 5.64 \times 10^{-13} \text{ J}), \tag{4B3}$$

and the plasma *non-radiative* energy confinement time

$$\frac{1}{\tau_E} \equiv \frac{1}{2}\left(\frac{1}{\tau_{Ei}} + \frac{1}{\tau_{Ee}}\right) \ . \tag{4B4}$$

Adding Eqs. (4A4) and (4A5), the result is

$$d(3nT)/dt = P_{ext} + P_h - 3nT/\tau_E - P_{rad} \ . \tag{4B5}$$

When the heating powers exceed the energy loss rates, the temperature will rise, and vice versa. At *equilibrium*,

$$P_{ext} + P_h = 3nT/\tau_E + P_{rad} \ . \tag{4B6}$$

The *ignition condition* is that the alpha heating power equal or exceed the energy loss rates:

$$P_h \geq 3nT/\tau_E + P_{rad} \quad . \qquad (4B7)$$

The variations of the terms of this equation with temperature are illustrated in Fig. 4B1. When $P_{ext} = P_1$, the equilibrium temperature determined from Eq. (4B6) will be T_1. This is a case of sub-ignition operation. When P_{ext} is raised to P_2, the new temperature is raised to the point where Eq. (4B7) is satisfied, and ignition occurs. Then, the heating terms in Eq. (4B5) exceed the cooling terms, and the plasma temperature will rise up to the equilibrium temperature T_{eq}, even if P_{ext} is turned off. If the temperature rose above T_{eq}, the cooling terms would exceed the heating terms, and the plasma would cool back down to T_{eq}. Thus T_{eq} is a stable operating temperature.

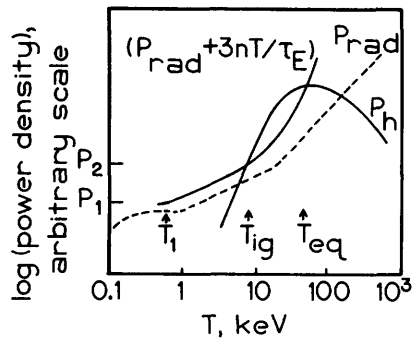

Fig. 4B1. Qualitative variation of power densities with plasma temperature, assuming plasma density held constant. The shape and height of the radiation curve depends strongly upon the concentrations and species of impurities in the plasma. The shape of the $3nT/\tau_E$ curve depends upon the type of confinement system and regime of operation.

The shape of the curve representing the right side of Eq. (4B7) depends strongly on the temperature variation of τ_E. For the case of a pressure-limited confinement system, it is desirable for the nonradiative loss rate to rise steeply with increasing temperature, in order to keep T_{eq} low, since the optimum T is about 13 keV (Fig. 2D1). If the nonradiative loss rate is low at high temperature, T_{eq} will tend to have very high values ($\sim$ 100 keV), making the plasma pressure very high and difficult to confine.

Solving for $n\tau_E$, the ignition condition may be written

$$n\tau_E \geq \frac{3T}{\frac{P_h}{n^2} - \frac{P_{rad}}{n^2}} \qquad (m^{-3}s), \qquad (4B8)$$

The right side of this equation is relatively insensitive to plasma density n. As impurity concentrations are increased, P_{rad} increases, and the required $n\tau_E$ for ignition becomes infinite or negative, meaning that ignition is impossible. For DT reactions, P_h is given by Eq. (4B3).

catalyzed DD reactor ignition

For the case of catalyzed DD fuel (Eq. 1E2), the same ignition conditions apply, but the equation for P_h must be modified to account for different charged particle energies heating the plasma.

Let n_3 and n_T be the densities of the ^{3}He and T nuclei. These densities will vary approximately as

$$dn_3/dt = S_3 + .5n_D^2\langle\sigma v\rangle_{DDn} - n_3 n_D \langle\sigma v\rangle_{D^3He} - n_3/\tau_p \quad (4B9)$$

$$dn_T/dt = S_T + .5n_D^2\langle\sigma v\rangle_{DDp} - n_T n_D \langle\sigma v\rangle_{DT} - n_T/\tau_p \quad (4B10)$$

where S_3 and S_T are injected particle sources, n_D is the deuteron density, τ_p is the ion confinement time, and $\langle\sigma v\rangle$ are the reaction rate parameters (Table 2C1). Ignoring slight unrecoverable losses, we can assume that all the ^{3}He and T ions lost to the walls are reinjected, so that $S_3 \simeq n_3/\tau_p$ and $S_T \simeq n_T/\tau_p$. Then, at equilibrium, these equations indicate that the secondary reactions (D-^{3}He and DT) will proceed at the same rates as the primary reactions (DDn and DDp). (Although such an equilibrium might not occur during one pulse of a short-pulsed reactor, it might hold true, on the average, for a large number of pulses.) Referring to Table 1E1, we can write the two branches of the catalyzed DD fuel cycle as

DDn and D-^{3}He :

$$D + D \rightarrow n + {}^3He + 3.27\ MeV$$
$$D + {}^3He \rightarrow p + {}^4He + 18.3\ MeV$$

net:

$$3D \rightarrow n + p + {}^4He + 21.6\ MeV \quad (4B11)$$

DDp and DT :

$$D + D \rightarrow p + T + 4.03\ MeV$$
$$D + T \rightarrow n + {}^4He + 17.59\ MeV$$

net:

$$3D \rightarrow n + p + {}^4He + 21.6\ MeV \quad (4B12)$$

Since the energies carried away by the neutrons in the DDn and DDp branches are 2.45 MeV and $\geq$ 14.1 MeV, respectively, the remaining charged-particle energies available to heat the plasma are W_{nc} = 19.2 MeV and $W_{pc} \leq$ 7.5 MeV. (The < sign applies when the tritons react before slowing down to thermal energies, enabling the neutrons to carry away more than 14.1 MeV energy). If f_r is the fraction of charged-particle energy retained in the plasma for heating, the heating power of the catalyzed DD fuel cycle may be written

$$P_h = \tfrac{1}{2}n_i^2 f_r(\langle\sigma v\rangle_{DDn} W_{nc} + \langle\sigma v\rangle_{DDp} W_{pc}) \quad (4B13)$$

where $W_{nc} = 3.07\times10^{-12}$ J and $W_{pc} = 1.20\times10^{-12}$J .

impurity effects

We will refer impurity fraction f_k to the electron density

$$f_k \equiv n_k/n \quad (4B14)$$

Then the quasineutrality condition (4A1) may be written

$$n = n_i + nf_1Z_1 + nf_2Z_2 + \ldots \quad (4B15)$$

where f_1, f_2, ... represent impurity fractions and Z_1, Z_2, ... represent the average charge states of the impurity ions, including helium. Thus

$$n_i/n = 1 - f_1Z_1 - f_2Z_2 - \ldots \tag{4B16}$$

which indicates the depletion in fuel ion density by accumulation of impurities. Impurities also change the plasma energy loss term $3nT/\tau_E$ in Eq. (4B5). If impurity effects are included, this term becomes

$$3nT/\tau_E \to 1.5(nT_e + n_iT_i + n_1T_1 + n_2T_2 + \ldots)/\tau_E$$

$$3T \to 1.5(T_e + n_iT_i/n + f_1T_1 + f_2T_2 + \ldots) \tag{4B17}$$

where τ_E is an average value for the whole plasma. We will usually assume that the impurity temperatures T_1, T_2, ... are equal to T_i (except for alpha particles slowing down from 3.5 MeV). Thus, impurities have three effects: decreasing fuel ion density n_i, increasing radiation losses P_{rad}, and changing the plasma energy loss term. Impurities also affect τ_E.

EXAMPLE PROBLEM 4B1

Estimate the confinement parameter $n\tau_E$ required for ignition of a DT plasma with a 0.5% oxygen impurity at $T_e = T_i = 10$ keV, assuming $f_r = \frac{1}{2}$ and cyclotron radiation is negligible.

From Fig. 3F5, the oxygen is fully stripped, and $\langle Z\rangle = 8$, $\langle Z^2\rangle = 64$. From Fig. 3F4, $Q_k = 1.6\times10^{-34}$ Wm^3 for oxygen and 1.8×10^{-36} Wm^3 for hydrogen (DT). Using Eq. (4B16), $n_i/n = 0.96$. Eq. (3F9) gives $P_{rad}/n^2 = 0.96(1.8\times10^{-36}) + 0.005(1.6\times10^{-34}) = 2.53\times10^{-36}$ Wm^3. From Eq. (4B3), $P_h/n^2 = 0.25(0.5)5.64\times10^{-13}(0.96)^2 1.09\times10^{-22} = 7.08\times10^{-36}$ Wm^3. From Eq. (4B17), $3T \to 1.5T_e(1 + n_i/n + f_1 + \ldots) = 29.5$ keV $= 4.72\times10^{-15}$ J. From Eq. (4B8), $n\tau_E \geq 1.04\times10^{21}$ m^{-3}s.

EXAMPLE PROBLEM 4B2

Estimate the maximum possible concentration of iron ($Z = 26$) for ignition of a DT plasma with $T_e = T_i$ at any temperature, assuming bremsstrahlung radiation is dominant. (This assumption is satisfactory for iron at $T_e \gtrsim 40$ keV, Fig. 3F4.)

Under optimum conditions, cyclotron radiation is negligible, $f_r = 1$, and $\tau_E = \infty$. From Eq. (4B7), $P_{rad}/n^2 \leq P_h/n^2$. Using Eqs. (4B3), (4B16), and (3F14), this becomes $5\times10^{-37}Z_{eff}T_e^{\frac{1}{2}} \leq .25(5.64\times10^{-13})(1-fZ)^2\langle\sigma v\rangle_{DT}$. or $Z_{eff} \leq 2.82\times10^{23}(1-fZ)^2\langle\sigma v\rangle_{DT}/T_e^{\frac{1}{2}}$. The maximum value of the right side is found by trying several temperatures.

T, keV	$\langle\sigma v\rangle_{DT}$	$2.82\times10^{23}\langle\sigma v\rangle_{DT}/T^{\frac{1}{2}}$
30	.665E-21	34.2
35	.745E-21	35.5
40	.803E-21	35.8
45	.843E-21	35.4
50	.871E-21	34.7

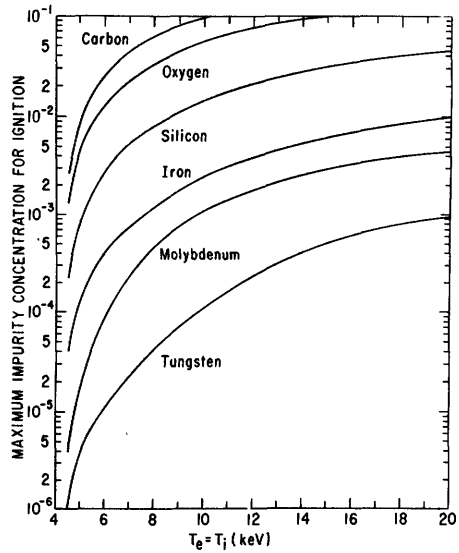

Fig. 4B2. Maximum tolerable impurity concentrations for ignition of a DT plasma vs. temperature, for various impurity species. From R. V. Jensen, D. E. Post, and D. L. Jassby, "Critical Impurity Concentrations for Power Multiplication in Beam-Heated Toroidal Fusion Reactors", Nucl. Sci. and Eng. 65, 282-289 (1978), Fig. 6, p. 288.

Thus, the optimum T_e is about 40 keV, for which $Z_{eff} \leq 35.8(1-fZ)^2$. From Fig. 3F5, the iron is fully stripped, and $\langle Z \rangle = 26$, $\langle Z^2 \rangle = 676$. From Eq. (3F13), $Z_{eff} \equiv \frac{n_i(1) + n_Z(676)}{n} = (1-26f) + 676f = 1 + 650f \leq 35.8(1-26f)^2$. The solution of this equation is $f \leq 0.0165 = 1.6\%$. Thus, an iron fraction over 1.6% will prevent ignition at any temperature.

The maximum tolerable impurity concentrations for ignition of a DT plasma are shown in Fig. 4B2. For a catalyzed DD reactor, the tolerable impurity fractions are lower.

When the effects of other radiation losses, nonradiative energy losses, and alpha energy losses ($f_r < 1$) are considered, the tolerable impurity fractions are significantly lower than the above value. Similar estimates can be made for plasmas with multiple impurity species.

4C. Energy Cycle

simple cycle

Consider a fusion power plant which can convert thermal energy into electricity with efficiency η_e. Let the symbol W represent the energy flows *per pulse* (J) of a pulsed reactor or *per unit time* (W) of a steady state reactor. Some pertinent parameters are defined in Table 4C1.

The energy incident on the reactor wall and blanket is equal to the input energy plus the fusion energy ($W_{in}+f_cW_f+f_nW_f$). The neutrons induce nuclear reactions in the blanket, producing additional energy. By definition of M, the energy deposited in the blanket by the neutrons, including the induced reactions, is equal to f_nW_fM. Thus, the total thermal energy flowing from the blanket to the heat engine is ($W_{in} + f_cW_f + f_nW_fM$), and the gross electrical power is

$$W_g = \eta_e(W_{in} + f_cW_f + f_nW_fM) \quad . \tag{4C1}$$

The energy flows per pulse (or per unit time) are illustrated in Fig. 4C1. If the definition of η_{in} is used to eliminate W_g in Eq. (4C1), we have

Table 4C1. Parameters of fusion reactor energy balance.

W_g = gross electrical energy output

W_f = fusion energy produced (for DT, W_f = 17.59 MeV)

W_{in} = energy input to heat or sustain plasma

ε = *recirculating energy fraction* or *recirculating power fraction*

η_e = efficiency of converting thermal into electrical energy

$\eta_{in} = W_{in}/\varepsilon W_g$

$Q = W_f/W_{in}$ = *energy gain ratio* or *power gain ratio*

f_n = fraction of fusion energy carried by neutrons (for DT reactors, f_n = 0.8; for catalyzed DD, f_n = 0.383)

Ψ_R = fraction of fusion energy leaving the plasma as charged particles
= fraction of W_f available for direct conversion

η = *plant efficiency*
= (net electrical energy out)/(nuclear reaction energy)

η_t = efficiency of converting thermal energy into electricity with a heat engine

$\eta_3 = \varepsilon\eta_e\eta_{in}$

$M = \dfrac{(\text{energy deposited in blanket by neutron kinetic energy plus neutron-induced nuclear reactions})}{(\text{energy deposited in blanket by neutron kinetic energy})}$
= *blanket energy gain ratio*

$(M-1)f_nW_f$ = energy from neutron-induced reactions in blanket

W_{rad} = energy leaving plasma as radiation

η_{dc} = efficiency of converting charged particle energy into electricity in a direct convertor

$f_c = 1-f_n$ = fraction of fusion energy carried by charged particles (for DT reactors, f_c = 0.2; for catalyzed DD, f_c = 0.617)

$$W_{in}/\varepsilon\eta_{in} = \eta_e(W_{in} + f_cW_f + f_nW_fM) \quad . \tag{4C2}$$

If we divide both sides by η_eW_{in} and use the definition of $Q = W_f/W_{in}$, the result is

$$(f_c+f_nM)Q + 1 = \frac{1}{\varepsilon\eta_e\eta_{in}} \quad . \tag{4C3}$$

For a given desired recirculating fraction ε, this equation tells the required value of Q; or for a given attainable Q, it tells the attainable value of ε.

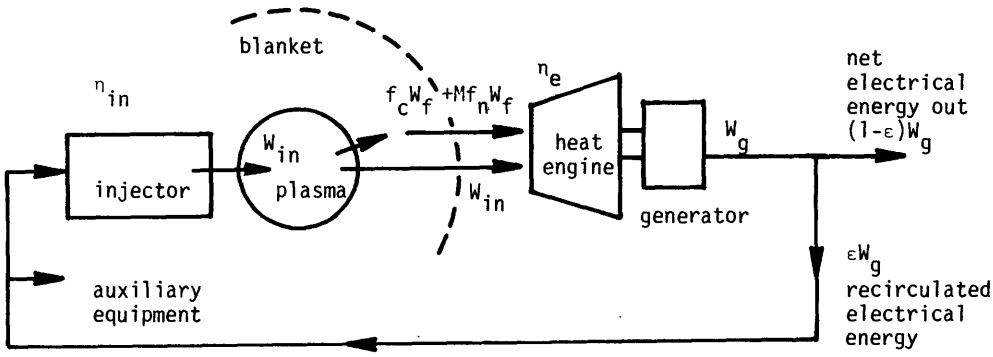

Fig. 4C1. Energy flows per pulse (or per unit time) for a fusion reactor without direct conversion.

The energy produced by nuclear reactions is equal to $(f_c W_f + f_n W_f M)$, and the net electrical energy output is $(1-\varepsilon)W_g$, so the "plant efficiency" is

$$\eta = \frac{(1-\varepsilon)W_g}{(f_c W_f + f_n W_f M)} = \frac{(1-\varepsilon)W_{in}/\varepsilon\eta_{in}}{(f_c + f_n M)Q W_{in}} = \frac{\eta_e(1-\varepsilon)[1 + (f_e + f_n M)Q]}{(f_c + f_n M)Q} \tag{4C4}$$

Using Eq. (4C3) to eliminate $(f_c + f_n M)Q$, this becomes

$$\eta = \frac{\eta_e(1-\varepsilon)}{1-\varepsilon\eta_e\eta_{in}} \qquad \text{or} \qquad \varepsilon = \frac{1 - \eta/\eta_e}{1 - \eta\eta_{in}} \quad . \tag{4C5}$$

Eliminating ε between Eqs. (4C5) and (4C3) gives a relation for the required value of Q to attain a given plant efficiency:

$$(f_c + f_n M)Q = \frac{1 - \eta_e\eta_{in}}{\eta_e\eta_{in}(1 - \eta/\eta_e)} \quad \text{or} \quad \frac{\eta}{\eta_e} = 1 - \frac{1 - \eta_e\eta_{in}}{\eta_e\eta_{in}(f_c + f_n M)Q} \quad . \tag{4C6}$$

For an economical power plant, we desire $\eta \gtrsim 0.3$. For the *break-even* case, $\varepsilon = 1$ and $\eta = 0$ (all the electrical energy is recirculated to keep the reactor running.) Typical values of conversion efficiency and blanket gain are $\eta_e \sim 0.35 \pm 0.5$ and $M = 1.2 \pm 0.2$. Higher M may be obtained by adding a neutron multiplier like beryllium to the blanket ($M \sim 1.7$) or by adding uranium to produce fast fissions ($M \sim 10$). The parameters which vary most from one reactor to another are Q and η_{in}. After ignition, W_{in} becomes very small. Even if $W_{in} \to 0$ and $Q \to \infty$, however, the ratio $W_f/\varepsilon W_g = \eta_{in} Q$ appearing in Eqs. (4C4) and (4C6) stays finite, because some energy is always needed for coolant pumping, refrigeration, etc.

EXAMPLE PROBLEM 4C1

Assume that an ignited DT reactor producing 2060 MW_{th} of fusion power recirculates 90 MW_e to keep the reactor running, with $\eta_e = 0.34$ and $M = 1.20$. Find η and ε, assuming that (a) 16 MW of recirculated energy goes into the plasma; (b) none goes in.

(a) By definition, $Q = W_f/W_{in} = 2060/16 = 129$. $\eta_{in} = 16/90 = 0.178$. From Eq. (4C6) $\eta/\eta_e = 0.896$, so $\eta = 0.305$. From Eq. (4C5), $\varepsilon = 0.110$. (b) Now $\eta_{in} = 0$ and $Q = \infty$, but $\eta_{in}Q = W_f/\varepsilon W_g = 2060/90 = 22.9$. From Eq. (4C6), $\eta/\eta_e = 0.889$, so $\eta = 0.302$. From Eq. (4C5), $\varepsilon = 0.111$. Thus, there is little difference between the two cases, although Q varies from 129 to infinity.

EXAMPLE PROBLEM 4C2

A pulsed DT reactor expends 1 GJ of stored energy each pulse for plasma confinement and heating, of which 20% goes into plasma energy. The fusion energy output per pulse is 4 GJ. (a) Assuming $\eta_e = 0.34$ and $M = 1.2$, find η. (b) If less than 4 GJ were produced by fusion reactions, what value of W_f would be required to break even, and what is the corresponding Q?

(a) $\varepsilon W_g = 1$ GJ and $W_f = 4$ GJ, so $\eta_{in}Q = W_f/\varepsilon W_g = 4.0$, $Q = \eta_{in}Q/\eta_{in} = 20$. From Eq. (4C6) $\eta/\eta_e = 0.409$, so $\eta = 0.14$. (b) For breakeven, $\varepsilon = 1$. Solving Eq. (4C3) for Q: $Q = (1/\varepsilon\eta_e\eta_{in} - 1)/(.2 + .8M) = 11.8$. $W_f = QW_{in} = Q\eta_{in}(\varepsilon W_g)$ $= 11.8(.20)10^9$ J $= 2.36\times10^9$ J.

The situation can be improved by direct conversion of some of the plasma energy and magnetic field energy into electricity; and by recovery of some of the energy expended in plasma heating systems (as in neutral beam injectors).

cycles with direct conversion

Direct conversion of charged particle energy into electricity permits higher efficiencies to be attained (Chapter 26). It is convenient to let Ψ_R be the fraction of fusion energy leaving the plasma in the form of charged particles:

$$\Psi_R = \frac{f_c W_f - W_{rad}}{W_f} = \textit{radiation parameter} \qquad (4C7)$$

where W_{rad} is the energy leaving the plasma as radiation. For pulsed plasmas $W_{rad} = \int dt\, P_{rad}$ over one pulse, and for a steady-state plasma $W_{rad} = P_{rad}$. Values of Ψ_R for DT and catalyzed DD reactors are shown in Fig. 4C2 as functions of ion temperature, for various values of cyclotron radiation parameter K_C (Fig. 3F6) and beta (Eq. 3F18). Negative values of Ψ_R mean that charged particle energy is insufficient to make up for radiation losses.

If we define an effective conversion efficiency

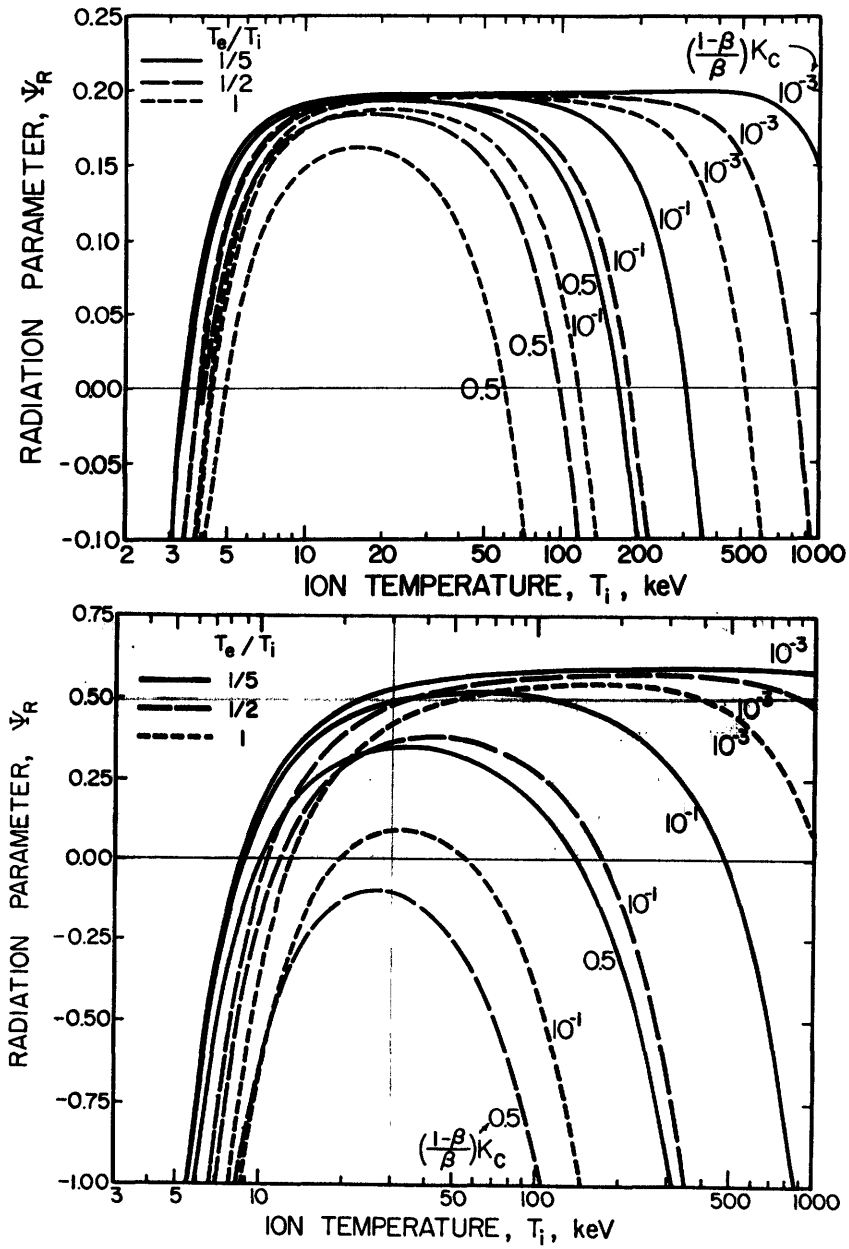

Fig. 4C2. Values of the radiation parameter Ψ_R vs. T_i for DT fuel (top) and catalyzed DD fuel (bottom), for various ratios T_e/T_i and $(1-\beta)K_c/\beta$, where K_c = cyclotron radiation parameter and β = (plasma pressure)/(magnetic field pressure). At high T_i, DD reactions become important in the DT fuel. From G. H. Miley, Fusion Energy Conversion, American Nuclear Society, LaGrange Park, IL, 1975, Fig 2.12 a&b.

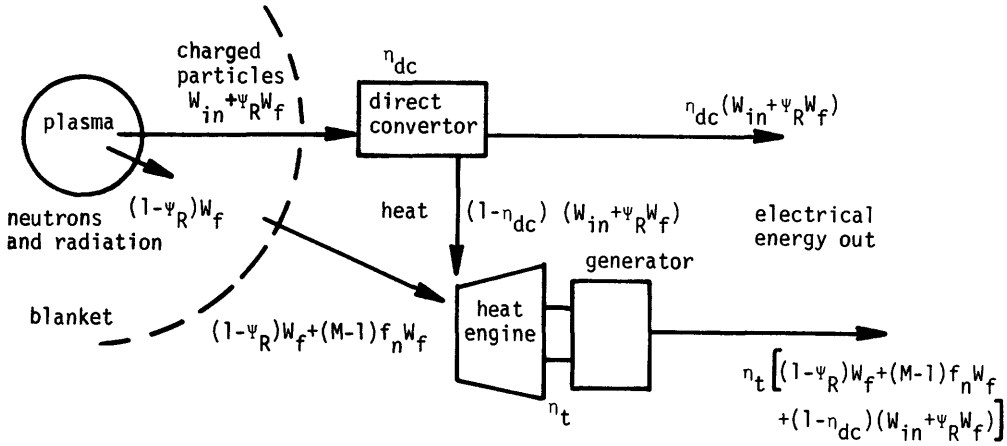

Fig. 4C3. Energy flow diagram for a reactor with direct convertor and heat engine. The charged particles emerging from the plasma are channeled into the direct convertor. A fraction η_{dc} of their energy is transformed directly into electricity, and the remaining fraction $(1-\eta_{dc})$ is converted into heat, which flows via a coolant to the heat engine. The neutron and radiation energy is absorbed in the first wall and blanket, with additional energy produced by neutron absorption reactions.

$$\eta_e = \frac{\text{gross electrical energy out}}{\text{total thermal energy out}} \tag{4C8}$$

then we can use this value of η_e in the simple cycle equations (4C1)-(4C6). The denominator is equal to $(W_{in} + f_c W_f + f_n W_f M)$. From the energy flow diagram Fig. 4C3, we can see that the numerator is equal to

$$W_g = \eta_{dc}(W_{in} + \psi_R W_f) + \eta_t[(1-\psi_R)W_f + (M-1)f_n W_f + (1-\eta_{dc})(W_{in} + \psi_R W_f)], \tag{4C9}$$

where $(M-1)f_n W_f$ is the energy gained by neutron absorption reactions in the blanket.

Combining Eqs. (4C8) and (4C9), using the definition $Q = W_f/W_{in}$, and rearranging, the effective energy conversion efficiency may be written

$$\eta_e = \eta_t + \frac{\eta_{dc}(1-\eta_t)(1 + Q\psi_R)}{1 + (f_c + f_n M)Q} \tag{4C10}$$

Similar results can be derived for more complex cases, such as when two heat engines with different efficiencies take heat from different parts of the system.

EXAMPLE PROBLEM 4C3

A tandem mirror reactor has $M = 1.2$, $\eta_t = 0.34$, $(1-\beta)K_c/\beta = 10^{-3}$, $\eta_{in} = 0.7$, and $\eta_{dc} = 0.65$. Find the plant efficiency and recirculating power

fraction (a) for a DT plasma with Q = 10, $T_e = T_i$ = 30 keV, (b) for a catalyzed DD plasma with Q = 3.5, $T_e = T_i$ = 100 keV.

(a) From Fig. 4C2, Ψ_R = 0.19. From Eq. (4C10),

$$\eta_e = .34 + \frac{.65(1-.34)\ (1+10(.19))}{1 + (.2 + .8(1.2))10} = 0.439$$

from Eq. (4C6), η/η_e = 0.806, so η = 0.354. From Eq. (4C5), ε = 0.280.
(b) From Fig. 4C2, $\Psi_R \simeq 0.5$. From Eq. (4C10)

$$\eta_e = .34 + \frac{.65(1-.34)\ (1 + 3.5(.5))}{1 + (.617 + .383(1.2))3.5)} = .587.$$

η_e is higher for catalyzed DD, because of its larger Ψ_R. For this case, Eq. (4C6) gives η/η_e = 0.620, so η = 0.364. From Eq. (4C5), ε = 0.510.

The lower assumed value of Q for the DD reactor makes its recirculating power fraction ε larger than for the DT reactor. For comparable plasma conditions, a DT reactor tends to have higher fusion power density and Q.

4D. Required Values of $n\tau_E$

steady state reactors

For steady state or long-pulse reactors, the input power is equal to the equilibrium value of $P_{ext}V$, and the fusion power is P_fV, so with Eq. (4B6) the power gain ratio

$$Q = \frac{P_f}{3nT/\tau_E + P_{rad} - P_h} \tag{4D1}$$

where common factors of volume V have cancelled out. (Beyond ignition, the denominator becomes negative, and Q also appears to be negative. However, $W_f/\varepsilon W_g = \eta_{in}Q$ stays finite and positive, since W_f, ε, and W_g are all > 0.) Solving for $n\tau_E$, we find

$$n\tau_E = \frac{3T}{P_f/n^2Q + P_h/n^2 - P_{rad}/n^2} \tag{4D2}$$

We can rewrite Eq. (4C3) as

$$Q = \frac{1 - \eta_3}{\eta_3(f_c + f_n M)}\ , \qquad \eta_3 \equiv \varepsilon\eta_e\eta_{in} \tag{4D3}$$

In evaluating these equations, we can find P_h from Eq. (4B3) for DT and (4B13) for catalyzed DD. To account for impurity effects, use Eq. (4B16) for n_i/n and Eq. (4B17) for 3T. The fusion power densities are

$$P_f/n^2 = \tfrac{1}{2}(n_i/n)^2(\langle\sigma v\rangle_{DDn} + \langle\sigma v\rangle_{DDp})W_{DD} \text{ (catalyzed DD)}$$
$$P_f/n^2 = \tfrac{1}{4}(n_i/n)^2\langle\sigma v\rangle_{DT}W_{DT} \qquad (4D4)$$

where W_{DD} = 21.6 MeV = 3.46×10^{-12} J (since each DD reaction leads to consumption of 3 deuterons and release of 21.6 MeV), W_{DT} = 17.6 MeV = 2.82×10^{-12} J, and we have assumed equal densities of deuterons and tritons.

If P_{rad} is too large, the denominator of Eq. (4D2) becomes negative, indicating that there is no value of $n\tau_E$ (even ∞) which can satisfy the power balance condition. In other words, more input power would be needed to sustain the reactor than is produced ($\varepsilon>1$) regardless of $n\tau_E$. Cyclotron radiation losses may cause this problem at high temperatures ($T \gtrsim 50$ keV). As $Q \to \infty$, Eq. (4D2) reduces to the ignition condition (4B8). For the case M = 1.2, $P_{rad} = P_B$ (Eq. 3F14), $Z_{eff} = 1$, $\eta_3 = 1/3$ (very optimistic), $f_r = 1$, T = 20 keV, the required $n\tau_E = 4\times10^{19}m^{-3}s$ from Eq. (4D3). More realistic assumptions give $n\tau_E \sim 10^{20}m^{-3}s$ for DT and $n\tau_E \sim 10^{21}$ $m^{-3}s$ for catalyzed DD fuel. Such required values of $n\tau_E$ are called *Lawson criteria*, after an early calculation (Lawson, 1957).

pulsed reactors

We can estimate the maximum Q for a pulsed reactor by setting W_{in} = (plasma thermal energy at ignition) and evaluating P_f at an "effective burn temperature" T_b:

$$Q \leqq \frac{P_f(T_b)\tau_b}{3nT_{ig}} \qquad (4D5)$$

where τ_b is the fuel burn time. The required $n\tau_b$ is

$$n\tau_b \geqq \frac{3T_{ig}Q}{P_f(T_b)/n^2} = \frac{(1-\eta_3)3T_{ig}}{\eta_3(f_c + f_n M)P_f(T_b)/n^2}, \quad \eta_3 \equiv \varepsilon\eta_e\eta_{in} \quad . \qquad (4D6)$$

If $P_h \simeq P_{rad}$, Eq.(4D2) resembles (4D6).

Usually η_e, η_{in} and M will be known. For the *break-even* case, all the electrical power is recirculated to keep the plant running, so ε = 1 and η = 0. For an economical *power plant*, we desire $\eta \gtrsim 0.3$, which determines ε via Eq. (4C5). Then the required $n\tau_E$ or $n\tau_b$ may be found from Eqs. (4D3) or (4D6).

burnup fraction

We can estimate the fraction of the fuel ions which undergo fusion reactions. If all the ions are either lost by convection or destroyed by fusion reactions, then f_b = burnup fraction = $\dfrac{\text{ions lost by fusion}}{(\text{ions lost by fusion}) + (\text{ions lost by convection})}$.

For a steady state DT reactor, from Eq. (4A2)

$$f_b = \frac{n_i^2 \langle\sigma v\rangle_{DT}/2}{n_i^2 \langle\sigma v\rangle_{DT}/2 + n_i/\tau_p} \tag{4D7}$$

Similarly, for a steady state catalyzed DD reactor, where 3 deuterons are consumed for each DD reaction:

$$f_b = \frac{3n_i^2 \langle\sigma v\rangle_{DD}/2}{3n_i^2 \langle\sigma v\rangle_{DD}/2 + n_i/\tau_p} \tag{4D8}$$

where $\langle\sigma v\rangle_{DD} \equiv \langle\sigma v\rangle_{DDn} + \langle\sigma v\rangle_{DDp}$. For pulsed reactors the smaller of (τ_i, τ_b) should be used in estimating f_b.

When defining a particle confinement time τ_p and calculating fractional burnup, one must be careful. If τ_p is averaged over the entire plasma volume, it will be relatively short, since edge particles recycle rapidly. A short τ_p would then give a small f_b. However, if τ_p is defined as the particle confinement time in the central region where most of the fusion reactions occur, then it will be comparatively long, and f_b will be comparatively high.

EXAMPLE PROBLEM 4D1

A steady-state DT reactor with a 1% helium impurity and 0.05% iron impurity has $\eta_e = 0.35$, $M = 1.2$, $f_r = 0.9$, $\eta_{in} = 0.6$, $T_z = T_i = 20$ *keV*, $T_e = 18$ *keV. Estimate the required values of Q and non-radiative energy confinement time (a) for breakeven, (b) for a power plant with* $\eta = 0.3$.

(a) Cylotron radiation will be negligible. From Fig. 3F5, the impurities will be completely stripped. From Fig. 3F4, $Q_k \simeq 10^{-35}$ Wm^3 for He, 3×10^{-36} Wm^3 for hydrogen, and 5×10^{-33} Wm^3 for iron.

From Eq. (4B16) $n_i/n = (1 - .01(2) - .0005(26)) = .967$

From Eq. (3F9) $P_{rad}/n^2 = .01\,(10^{-35}) + .0005(5\times10^{-33}) + .967(3\times10^{-36})$
$= 5.5\times10^{-36}$ Wm^3.

From Eq. (4D3), $\eta_3 = 1(.35).6 = .21$, $Q = 3.24$.

From Eq. (4D4), $P_f/n^2 = \frac{1}{4}(.967)^2 4.24\times10^{-22}(2.82\times10^{-12}) = 2.80\times10^{-34}$ Wm^3.

From Eq. (4B3), $P_h/n^2 = \frac{1}{4}(.967)^2 0.9(4.24\times10^{-22})5.6\times10^{-13} = 5.00\times10^{-35}$ Wm^3.

From Eq. (4B17), $3T = 1.5[18 + .967(20) + .01(20) + .0005(20)]1.60\times10^{-16}$
$= 0.90\times10^{-14}$ J.

From Eq. (4D2), $n\tau_E = 0.7\times10^{20}$ m^{-3}s for "break even".

(b) For the power plant with $\eta = 0.3$, Eq. (4C5) gives $\varepsilon = 0.1742$.
From Eq. (4D3), $\eta_3 = 0.0366$, $Q = 22.7$. From Eq. (4D2), $n\tau_E = 1.6\times10^{20}$ m^{-3}s.

EXAMPLE PROBLEM 4D2

A steady-state catalyzed DD reactor with a 1% helium impurity and a 0.05% iron impurity has $\eta_e = 0.35$, $M = 1.2$, $f_r = 0.9$, $\eta_{in} = 0.6$, $T_z = T_i = 60$ *keV*, T_e

= 50 keV, B = 10 T, K_c = .01, and n = 3×10^{20} m^{-3}. Find (a) $n\tau_E$ for breakeven, (b) $n\tau_E$ for a power plant with η = 0.3, (c) the value of β which the confinement system must be able to contain.

(a) From Eq. (3F17), $K_c P_c/n^2 = 1.39\times10^{-35}$ Wm^3. From Fig. 3F4, $Q_k = 5\times10^{-33}$ Wm^3 (Fe), 1.5×10^{-35} Wm^3 (He), and 5×10^{-36} Wm^3 (hydrogen). From Eq. (4B16), $n_i/n = 1 - .01(2) - .0005(26) = 0.967$.

From Eq. (3F9), $P_{rad}/n^2 = .967(5\times10^{-36}) + .01(1.5\times10^{-35}) + .0005(5\times10^{-33}) + 1.39\times10^{-35} = 2.14\times10^{-35}$ Wm^3.

For "break-even" ε = 1. For catalyzed DD, f_c = .617, f_n = .383.

From Eq. (4D3), $\eta_3 = 0.21$, Q = 3.49.

From Eq. (4D4), $P_f/n^2 = \frac{1}{2}(.967)^2(1.39\times10^{-23} + 1.21\times10^{-23})\ 3.46\times10^{-12} = 4.21\times10^{-35}$ Wm^3.

From Eq. (4B13), $P_h/n^2 = \frac{1}{2}(.967)^2 0.9[1.39\times10^{-23}(3.07\times10^{-12}) + 1.21\times10^{-23}(1.20\times10^{-12})] = 2.41\times10^{-35}$ Wm^3.

From Eq. (4B17), $3T = 1.5[50 + .967(60) + .01(60) + .0005(60)]\ 1.60\times10^{-16} = 2.61\times10^{-14}$ J.

From Eq. (4D2), $n\tau_E = 1.8\times10^{21}$ $m^{-3}s$.

(b) For a power plant with η = 0.3, Eq. (4C5) gives ε = .1742. From Eq. (4D3), η_3 = .0366, Q = 24.4. From Eq. (4D2), $n\tau_E = 5.9\times10^{21} m^{-3}s$. These $n\tau_E$ values are much higher than for DT because of the lower reactivity of DD fuel and because of cyclotron radiation losses at high T_e.

(c) $p = 3\times10^{20}[50 + .967(60) + .0105(60)]\ 1.60\times10^{-16} = 5.22$ MPa, $\beta = 2\mu_0 p/B^2 = 0.13$. If the attainable β were lower, then B would have to be increased to sustain the plasma pressure, and cyclotron radiation losses would be more severe.

EXAMPLE PROBLEM 4D3

Are the power plant cases of example problems 4D1 and 4D2 ignited? If not, how much heating power P_{ext} is required? (Take n = 10^{20} m^{-3} for the DT case.)

For example problem 4D1, Eq. (4B6) gives $P_{ext}/n^2 = 3T/n\tau_E + P_{rad}/n^2 - P_h/n^2 = 1.2\times10^{-35}$ $Wm^3 > 0$ so it is not ignited. If $n = 10^{20}$ m^{-3}, then P_{ext} = 0.12 MW/m^3.

For example problem 4D2, we find $P_{ext}/n^2 = 1.74\times10^{-36}$ Wm^3. Since $n = 3\times10^{20}$ m^{-3}, P_{ext} = 0.16 MW/m^3.

EXAMPLE PROBLEM 4D4

A pulsed DT reactor ignites at T_{ig} = 6 keV, and burns at T_b = 40 keV for 0.03s. Assume $n = 2\times10^{22}$ m^{-3}, M = 1.2, η_e = 0.34, ε = 0.21, and no impurities. Estimate Q and η.

From Eq. (4D4), $P_f = \frac{1}{4}(2\times10^{22})^2 8.03\times10^{-22}(2.82\times10^{-12}) = 2.26\times10^{11}$ W/m^3. From Eq. (4D5) $Q \leq 118$. From Eq. (4C4), η = 0.27.

EXAMPLE PROBLEM 4D5

Estimate the burnup fractions for the break-even and power plant cases of Example Problem 4D1, assuming that $n = 10^{20} m^{-3}$ *and* $\tau_p/\tau_E \simeq 1.5$.

From Eq. (4D7), with parameters of example problem 4D1, $f_b \simeq .022$ for breakeven $f_b \simeq .048$ for the power plant.

Assuming uniform plasmas, we have derived simple conditions for plasma equilibrium, ignition, energy balance, required $n\tau_E$, and burnup fraction in steady-state and pulsed reactors. Next we will consider special cases of mirror reactors, subignition toroidal reactors, and non-uniform plasmas.

4E. Mirror Reactors

For a simple "magnetic mirror" plasma confinement system (to be described in Chapter 11) the maximum attainable confinement time is

$$n_i\tau_E \simeq 2.7\times10^{16}\ W_0^{3/2}\log_{10} R \tag{4E1}$$

where W_0 is the neutral atom beam injection energy (keV) and R is the "mirror ratio" (ratio of maximum to minimum magnetic fields in the plasma confinement region). For mirrors $P_{ext} \simeq nW_0/\tau_E$. An approximate value of Q for a simple DT mirror reactor is given by

$$Q \simeq \frac{P_f}{nW_0/\tau_E} = \frac{n\tau_E\langle\sigma v\rangle_m W_{DT}}{4W_0} \tag{4E2}$$

where $\langle\sigma v\rangle_m$ is the value of $\langle\sigma v\rangle_{DT}$ for the non-Maxwellian distribution of a mirror device, shown in Fig. 4E1. (However, the Maxwellian values of $\langle\sigma v\rangle_{DT}$ from Chapter 2 may be used for the central cell of a Tandem Mirror.)

To illustrate the difficulty of using simple mirrors for fusion reactor power plants, we will estimate the maximum Q attainable by a simple mirror device at $W_0 = 100$ keV.

Taking R = 10 in Eq. (4E1), we find $n\tau_E = 2.7\times10^{19}\ m^{-3}s$. From Fig. 4E1, $\langle\sigma v\rangle_m = 9.5\times10^{-22}\ m^3s^{-1}$. Then, from Eq. (4E2)

$$Q = \frac{2.7\times10^{19}(9.5\times10^{-22})17{,}600}{4(100)} = 1.1.$$

This increases slightly at higher injection energies, but $\langle\sigma v\rangle_m$ decreases, and high-energy neutral beam injection systems are still under development.

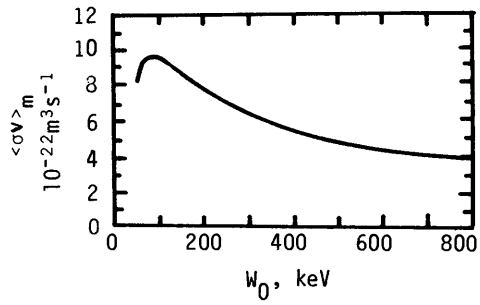

Fig. 4E1. Reaction rate parameter for DT plasma in a simple magnetic mirror. From A. H. Futch, Jr., J. P. Holdren, J. Killeen, and A. A. Mirin, Plasma Physics 14, 211 (1972), Fig. 2.

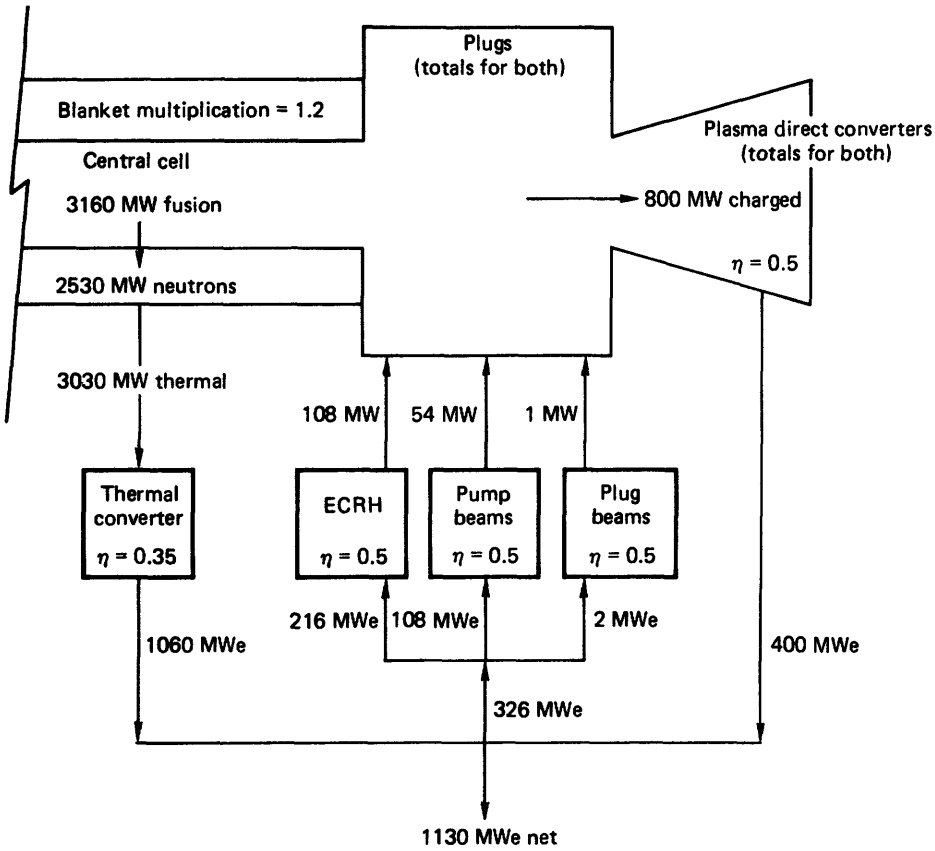

Fig. 4E2. Power flow diagram for a tandem mirror reactor with central cell length 100 meters, Q = 19.4. From G. A. Carlson et al, Tandem Mirror Reactor with Thermal Barriers, UCRL-52836, 1979, Fig. 1-3.

Furthermore, experimental values of confinement times are less than given by Eq. (4E1). Since

$$\varepsilon = 1/\eta_e\eta_{in}(Q' + 1),\ Q' \equiv (f_c + f_n M)Q \tag{4E3}$$

low Q values will result in high recirculating power fractions and low plant efficiencies. To make mirror reactors economical, larger values of Q are needed. Values of $Q \sim 10$ may be attainable with "field-reversed mirrors" or with "tandem mirrors" (Chapter 11). A power flow diagram for a hypothetical tandem mirror reactor is shown in Fig. 4E2.

The injected energy is 108 + 54 + 1 = 163 MW, so η_{in} = 163/326 = 0.50. (This is a consequence of assumed values of 0.5 for all injection efficiencies). The effective conversion efficiency is η_e = (1060 + 400)/(3030 + 800) = 0.381. [If

the 400 MW of rejected heat from the direct convertor were converted into electricity at 35% efficiency, then the gross electrical output would be (1060 + 400 + 140) = 1600 MW, yielding $\eta_e = 0.417$, in agreement with Eq. (4C10).] The recirculating power fraction $\varepsilon = 326/1460 = 0.223$, which is consistent with Eq. (4C3). The plant efficiency $\eta = 1130/(3030 + 800 - 163) = 0.308$, which is consistent with Eq. (4C5). For an actual reactor, about 30 MW would be needed for auxiliary systems (coolant pumping, refrigeration, etc.), so the net electrical output would be close to 1100 MW. Mirror devices will be discussed more in Chapter 11.

4F. Beam-driven Toroidal Reactors

Toroidal fusion devices like Tokamaks (Chapter 13) and Stellarators (Chapter 14) may either be ignited or operated at sub-ignition temperatures, driven by neutral beam injection. Beam-driven reactors can attain high fusion power densities, due to large values of $\langle\sigma v\rangle_b$ (Fig. 2C2), so $Q \geq 1$ conditions may be attained at lower values of $n\tau_E$ than for Maxwellian plasmas alone. The neutral beams provide a continuous fuel supply, so long-pulse or steady-state operation is feasible, if impurity buildup can be controlled.

However, beam-driven reactors are limited to low values of Q, since considerable energy must be given to each injected fuel atom. Let p_f be the probability that an injected ion will undergo a fusion reaction before slowing down to the plasma thermal energy, and I be the injected beam current (A). Then the fusion power from beam-plasma reactions may be expressed as $W_{DT}p_f f_t I/e$ where e is the electronic charge, and f_t is the fraction of I trapped. The power gain ratio is

$$Q = \frac{W_{DT}p_f f_t I/Ve + n_D n_T \langle\sigma v\rangle_{DT} W_{DT}}{W_0 I/Ve} \tag{4F1}$$

where W_0 is the neutral beam injection energy, V is the plasma volume, and n_D and n_T are densities of D and T in the Maxwellian target plasma. If the beam-plasma power density is much greater than the Maxwellian plasma thermonuclear power density and $f_t = 1$, then

$$Q \simeq \frac{p_f W_{DT}}{W_0} \quad . \tag{4F2}$$

The *fusion probability* can be expressed as the time integral of the beam-plasma collision frequency for fusion reactions while slowing down:

$$p_f = \int_0^{t_1} dt\ \nu_b(t) \tag{4F3}$$

where t_1 is the time it takes to slow down to thermal energy. We can use the change of variables

$$dt = \frac{dW}{\left(\frac{dW}{dt}\right)} \tag{4F4}$$

in Eq. (4F3), along with Eqs. (2B36) and (2B31) to obtain

$$P_f = n_2 \int_{W_{th}}^{W_0} \frac{dW\langle\sigma v\rangle_b}{-\left(\frac{dW}{dt}\right)} \tag{4F5}$$

where the limits of integration are the final and initial ion energies during the slowing down process and n_2 is the target ion density. (If the beam is deuterium, then $n_2 = n_T$, and vice-versa). The value of (dW/dt) is found from Eq. (2E37).

The values of Q attainable by injecting deuterium atoms into a cold-triton target plasma are shown as functions of injection energy in Fig. 4F1 for various plasma electron temperatures. These values correspond to Eqs. (4F2) and (4F5). If $T_e \lesssim 15$ keV, then $Q \lesssim 2$, and the optimum $W_0 \sim 200$ keV.

The value of Q can be optimized by varying the composition of the target plasma $n_i = n_D + n_T$. For short confinement times a pure tritium plasma is optimum with deuteron injection, and for long confinement times thermonuclear reactions can become significant, so that the optimum composition approaches 50% each (D and T) as ignition is approached. The variation of such a composition-optimized Q with energy confinement time is shown in Fig. 4F2, for a case with $T_e = T_i = 8$ keV, plasma pressure 0.66 MPa. At low $n\tau_E$, the fusion power density from beam-plasma reactions is high, but Q is low. As $n\tau_E$ increases, thermonuclear reactions of the Maxwellian plasma raise Q but n_T is decreased (to optimize Q), so beam-plasma fusion reactions are fewer, and P_f drops. This graph illustrates the transition from the beam-driven subignition regime to the thermonuclear regime.

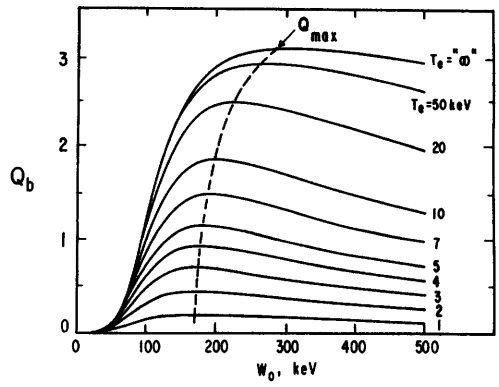

Fig. 4F1. Fusion power gain Q as a function of deuteron energy W_0 for various electron temperatures in a cold-triton target plasma, assuming $n_T = n_e$. From D. L. Jassby, "Optimization of fusion power density in the two-energy-component tokamak reactor", Nucl. Fusion 15, 453 (1975). Fig. 3.

In practice, the situation of Fig. 4F1 would be difficult to achieve, since deuterons would gradually accumulate in the pure tritium target plasma. It would be easier to operate with $n_D \simeq n_T$ in both the plasma and injected beams. For this case there will be fusion reactions from beam deuterons and plasma tritons, beam tritons and plasma deuterons, beam-beam interactions, and thermonuclear

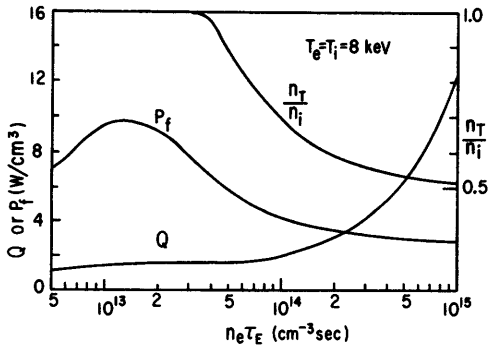

Fig. 4F2. Variation of fusion power density P_f and Q with confinement parameter $n_e\tau_E$. The power gain Q is optimized by varying the tritium fraction n_T/n_i. Total pressure = 0.655 MPa. W_0 = 200 keV (deuterium atoms). From D. L. Jassby, Optimization of fusion power density in the two-energy-component tokamak reactor, Nucl. Fusion 15, 453 (1975). Fig. 10.

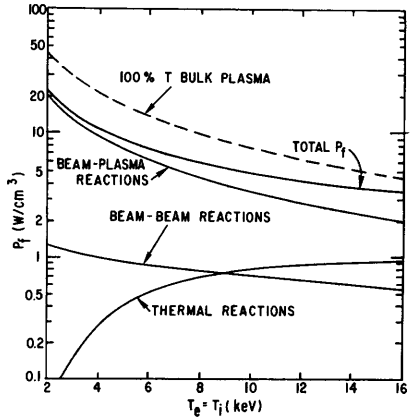

Fig. 4F3. Contributions to fusion power density P_f from various reactions in a 50% D-T plasma with equal-density beams of D and T ions injected at 200 and 300 keV, respectively. pressure = 0.655 MPa. The dashed curve is for a pure tritium plasma heated by a 200 keV D beam. From D. L. Jassby, Optimization of fusion power density in the two-energy-component tokamak reactor, Nucl. Fusion 15, 453 (1975). Fig. 12.

reactions in the Maxwellian plasma. The relative contributions of these various reactions to P_f are shown in Fig. 4F3.

In a pulsed device, the beams can be maintained at high energies for longer times by compressing the plasma as the beams slow down ("clamping"), with the result that Q may be increased by about a factor of two.

EXAMPLE PROBLEM 4F1

Estimate the fusion probability of a 200 keV deuteron slowing down in a pure tritium plasma with T_e = 10 keV.

From Fig. 4F1, Q = 1.8. From Eq. (4F2), $p_f = QW_0/W_f$, so p_f = 0.2 MeV(1.8)/17.6 MeV = 0.020 = 2.0% probability. p_f could also be estimated from Eq. (4F5), with $\langle\sigma v\rangle_b$ values from Fig. 2C2, and numerical quadrature.

4G. Non-uniform and Time-varying Plasmas

spatial variations

Real plasmas will not be uniform, as assumed in the simple energy balance equations. We need to find the volume-averaged values of fusion power density, radiation power, etc., and use these values in the energy balance equations.

For example, the volume -averaged fusion power density of a DT plasma is given

by

$$\langle P_f \rangle \equiv \frac{\int d\vec{x}\, n_i^2 \langle\sigma v\rangle_{DT} W_{DT}/4}{\int d\vec{x}} \tag{4G1}$$

where the denominator $\int d\vec{x} = V$, the plasma volume.

Consider a cylindrical plasma with a parabolic density distribution

$$n(r) = n_0(1 - r^2/r_p^2) \tag{4G2}$$

where r_p is the plasma radius. If the temperature were uniform, then $\langle P_f \rangle = \langle\sigma v\rangle_{DT} W_{DT} \langle n^2\rangle/4$. For the parabolic profile $\langle n^2\rangle = n_0^2/3$, while $(\langle n\rangle)^2 = n_0^2/4$. Thus, we cannot evaluate P_f at the average density and get accurate results. The radial variations of T and $\langle\sigma v\rangle_{DT}$ should also be taken into account.

EXAMPLE PROBLEM 4G1

Estimate the volume-averaged fusion power density for a cylindrical plasma with parabolic density and temperature profiles, $n_0 = 10^{20}$ m^{-3}, $T_0 = 20$ keV, and a 50% DT mixture. Compare with P_f evaluated at the average density and temperature, defining $\langle T\rangle = \int d\vec{x} nT / \int d\vec{x} n$.

$$\langle P_f \rangle \equiv \langle n^2 \langle\sigma v\rangle_{DT} W_{DT}/4\rangle = \frac{1}{\pi r_p^2 L} \int_0^{r_p} dr\, 2\pi r L\, n_0^2 \left(1 - \frac{r^2}{r_p^2}\right)^2 \langle\sigma v\rangle_{DT} W_{DT}/4$$

$$= \frac{n_0^2 W_{DT}}{2} \int_0^1 dx\, x(1-x^2)^2 \langle\sigma v\rangle_{DT}\Big|_x$$

where $x = r/r_p$. Using numerical quadrature with equal Δx, we have

$$\langle P_f \rangle \simeq \frac{n_0^2 W_{DT} \Delta x}{2} \sum_j x_j (1-x_j^2)^2 \langle\sigma v\rangle_{DTj} w_j$$

For simplicity, we will use Simpson's rule weights w_j with $\Delta x = \frac{1}{4}$.

x_j	$T_j = T_0(1-x_j^2)$	$\langle\sigma v\rangle_{DTj}$	w_j	$x_j(1-x_j^2)^2\langle\sigma v\rangle_{DTj} w_j$
0	20 keV	.424E-21	1/3	0
.25	18.75	.384E-21	4/3	11.25×10^{-23}
.5	15	.265E-21	2/3	4.97×10^{-23}
.75	8.75	.768E-22	4/3	1.47×10^{-23}
1.	0	0	1/3	0
				sum = 1.77×10^{-22} m^3s.

$$\langle P_f \rangle = \frac{10^{40} 17.6 (1.60\times10^{-13}) .25}{2} \; 1.77\times10^{-22} = 6.2\times10^5 \text{ W/m}^3$$

Better accuracy could be obtained by using finer Δx and an equation for $\langle\sigma v\rangle_{DT}$, instead of linear interpolation in Table 2C1. For parabolic distributions, $\langle n\rangle = \frac{1}{2}n_0$, $\langle T\rangle = (1/3)T_0$, and $P_f(\langle n\rangle, \langle T\rangle) = \frac{1}{4}(5\times10^{19})^2 3.5\times10^{-23}(2.82\times10^{-12})$ $= 6\times10^4$ W/m^3.

For Tokamak plasmas, peaked density and temperature profiles are found to have a strong effect on the fusion power density, fractional burnup, particle containment time, and ignition conditions (Kesner and Conn, 1976).

For the case of pulsed plasmas, the fusion power and radiation losses must be integrated in time over the burn time to get the energies per pulse used in the equations of Section 4C. Thus, the fusion energy released per pulse is

$$W_f = V \int_{\text{pulse}} dt \langle P_f\rangle . \tag{4G3}$$

For example, consider the case in which the plasma is heated up to ignition temperature, followed by a rapid rise up to equilibrium temperature described approximately by the equations

$$T(r,t) = [T_{ig} + (T_{eq}-T_{ig})\ (1 - e^{-t/\theta})]\ f(r) \tag{4G4}$$

where θ is the characteristic time for self-heating of the plasma ($\theta \sim$ alpha particle slowing-down time) and $f(r)$ describes the radial variation of temperature. At the same time, the plasma density may be escaping with a particle loss time τ_p

$$n(r,t) = n_0 g(r) e^{-t/\tau_p}. \tag{4G5}$$

If we assume that the required input energy per pulse is equal to $V\langle 3nT_{ig}\rangle$ (the spatially averaged energy density at ignition times the volume), then

$$Q = \frac{\int dt \langle P_f\rangle}{\langle 3nT_{ig}\rangle}, \tag{4G6}$$

which is similar to Eq. (4D2). Combining Eqs. (4G4)-(4G6), and assuming spatial variations of n and T, we can find the Q values corresponding to various values of τ_p and θ. Alternatively, we can find the value of $n\tau_i$ required to produce a given Q. Such required $n\tau$ to make Q = 9 are shown in Fig. 4G1 as functions of T_{eq}, for various values of θ, assuming parabolic radial profiles of n and T. For comparison, the values which would be found from Eq. (4D2), assuming uniform plasma with n and T constant for a time $\tau_b = \tau_p$, are shown by the dashed curve.

Because the required values of $n\tau_E$ vary strongly with the shapes of the plasma density and temperature profiles and with their time variations, curves based on a constant, uniform plasma are inaccurate, like the dashed curve of Fig. 4G1.

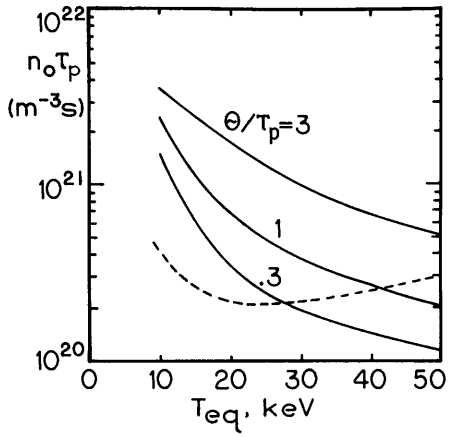

Fig. 4G1. Required $n_0\tau_p$ as a function of equilibrium temperature to achieve Q = 9, for various rate of temperature rise θ, assuming parabolic radial distributions of plasma density and temperature, with T_{ig} = 6 keV. The dashed curve is for the case of uniform, constant plasma density and temperature. From T. J. Dolan and K. F. Keller, Energy balance for a pulsed D-T reactor, Nucl. Fusion 13, 875 (1973).

The effect of varying spatial profiles on the volume-average fusion power density in a catalyzed DD reactor is illustrated in Fig. 4G2.

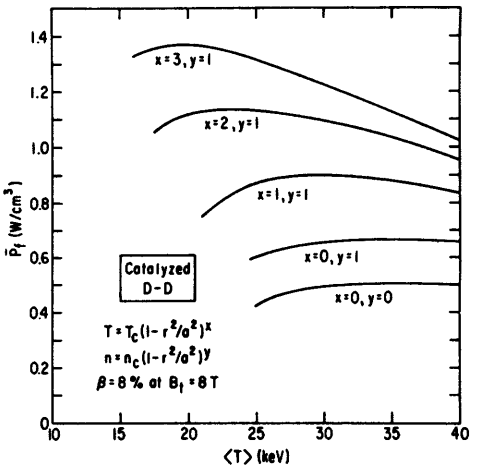

Fig. 4G2. Spatially-averaged fusion power density for various temperature and density profiles, with a constant spatially-averaged plasma pressure: 2.1 MJ/m , or <β>= 8 % at B_t = 8.0 T. (Energetic ions are not included in <β>). The minimum ignition temperature is at the left end of each curve. From D. L. Jassby and H. H. Towner, "Optimization of plasma profiles for ignited low-beta toroidal plasmas utilizing 'advanced fuels' ", Proceedings of the Review Meeting on Advanced-Fuel Fusion, EPRI ER-536-SR (1977), Fig. 6, p. 281.

4H. Comparison of Reactor Types

Various proposed fusion reactor schemes differ widely in the required values of Q and $n\tau_E$, mainly because of great differences in the energy input fraction η_{in}. For the purpose of comparison we will assume that the power plants all have thermal conversion efficiencies η_t = 0.35 and blanket multiplication factors M = 1.2. Higher η_t may be attained by using high-temperature cycles (Chapter 26), but, due to uncertainties in materials properties, early fusion power plants will probably use conventional materials like stainless steel, which limits the power plant to temperatures around 800 K and $\eta_t \lesssim 0.35$.

We will assume that reactors based upon pinch devices will have $\eta_{in} \sim 0.2$, as for the Reference Theta Pinch Reactor (Krakowski et al, 1974), and $\eta_e \simeq .5$ (using direct conversion via magnetic induction).

Table 4H1. Comparison of required values of Q and $n\tau_E$ for various potential fusion reactor types, assuming DT fuel, M = 1.2, Z_{eff} = 1.5, f_r = .9, $\langle\sigma v\rangle_{DT}$ = $6.7\times10^{-22} m^3 s^{-1}$ (T = 30 keV), T_{ig} = 6 keV. These values are only approximate, for purpose of comparison.

	tandem mirror reactor	beam-driven toroidal reactor	ignited toroidal reactor	high-β pinch reactor	inertial confinement reactor (laser-driven)
assumed values					
η_e	.5	.35	.35	.5	.35
η_{in}	.7	.6	.6	.2	.01
n, m^{-3}	10^{20}	10^{20}	10^{20}	2×10^{22}	5×10^{31}
calculated values (required values of Q, $n\tau_E$, f_b) breakeven case (η = 0, ε = 1)					
Q	1.6	3.2	3.2	7.8	245
$n\tau_E$	3.8×10^{19}	1.6×10^{20} (Fig. 4F2)	6.4×10^{19}	4.7×10^{19}	1.5×10^{21}
power plant (η = .3)					
ε	.51	.17	.17	.43	.14
Q	4.0	23	23	19	1720
$n\tau_E$	7.3×10^{19}	unattainable	1.4×10^{20}	1.2×10^{20}	1.1×10^{22}
τ_E, s	0.7		1.4	.006	2.1×10^{-10}
f_b	.024		.046	.038	.78
attainable values					
Q	$\sim$ 10	<3	>> 10	> 10	>> 10

For laser fusion reactors

$$\eta_{in} \sim 0.01 \ .$$

Some representative values of η_e, η_{in}, and plasma density n for various potential fusion reactors are listed in Table 4H1, along with calculated values of the required Q and $n\tau_E$ for breakeven and power plant cases. The values of ε and Q were calculated from Eqs. (4C5) and (4C3), the required $n\tau_E$ were found from Eqs. (4D6) (taking $\tau_b = \tau_E$) and (4D2) (for the tandem mirror and ignited toroidal reactor cases), and f_b was found from Eq. (4D7). The values in the table are only approximate, but serve to illustrate salient differences between some alternate approaches to fusion power. There are also other approaches, which will be discussed in Chapters 11-17.

For other fuels, like catalyzed DD, the required values of Q would be almost the same, but the required $n\tau_E$ would be much higher, due to the lower $\langle\sigma v\rangle$.

Taking into account fuel depletion effects and the spatial and time variations of plasma parameters would alter the relations between Q and $n\tau_E$, but not effect the values of Q required to match a given combination of η_e, η_{in}, M, and η.

summary

We have used a simple point model to describe the main features of reactor power balance. Ignition occurs when $P_h \geq 3nT/\tau_E + P_{rad}$. The power balance condition is $(f_c + f_n M)Q + 1 = 1/\varepsilon\eta_e\eta_{in}$. The confinement times required to attain a given Q may be estimated from

$$n\tau_E = \frac{3T}{P_f/n^2Q + P_h/n^2 - P_{rad}/n^2} \quad \text{(steady-state reactor)}$$

$$n\tau_E \geq \frac{3T_{ig}Q}{P_f(T_b)/n^2} \quad \text{(pulsed reactor)} .$$

Fractional fuel burnup is typically 3-10% for a reactor. Beam-driven toroidal reactors have high fusion power densities, but low Q. Plasma power balance depends strongly upon the radial density and temperature profiles and their time variations. The main differences between alternate approaches are their values of η_{in} and fusion burn times (pulse lengths). Devices which have low η_{in} usually require higher Q and $n\tau_E$.

Problems

1. Estimate the maximum possible concentration of oxygen for ignition of a DT plasma with $T_e = T_i$. Compare the result with Fig. 4B2.

2. Estimate the required $n\tau_E$ for ignition of a catalyzed DD reactor with 0.2% carbon, no cyclotron radiation, $f_r = .9$, at $T_e = T_i = 40$ keV.

3. A pulsed DT reactor with $\eta = 0.27$ expends 780 MJ of energy each pulse for running the reactor. Of this 15% goes into plasma energy. M = 1.2 and $\eta_e = 0.35$. Find ε, Q, and the net electrical energy output per pulse.

4. It is desired to have $\eta = 0.31$ in a catalyzed DD tandem mirror reactor with M = 1.2, $\eta_t = 0.35$, $\eta_{dc} = 0.68$, $\eta_{in} = 0.7$, $T_e = T_i = 80$ keV, and $(1-\beta)K_c/\beta = 10^{-3}$. Find the required values of Q and ε.

5. A steady-state DT reactor with a 2% helium impurity and a 0.7% carbon impurity has $\eta_e = 0.35$, M = 1.2, $f_r = 0.84$, $K_c \simeq 0$, $\eta_{in} = 0.57$, $T_z = T_i = 25$ keV, $T_e = 21$ keV. Estimate the required $n\tau_E$ for a reactor with $\eta = 0.32$.

6. A steady-state catalyzed DD reactor with a 2% helium impurity and a 0.7% carbon impurity has $\eta_e = 0.35$, $M = 1.2$, $f_r = 0.84$, $\eta_{in} = 0.57$, $T_z = T_i = 70$ keV, $T_e = 58$ keV, $B = 9$ T, $K_c = .01$, and $\beta = 0.17$. Find (a) the plasma pressure, (b) n_e, (c) the plant efficiency if $n\tau_E = 4\times10^{21}$ $m^{-3}s$, (d) f_b, assuming $\tau_p/\tau_E = 2$.

7. A pulsed DT reactor with $\eta = .3$ ignites at 6 keV, with burn occurring at an equilibrium $T_e = T_i = 35$ keV, and $\eta_{in} = 0.2$. The plasma density is 3×10^{22} m^{-3} and impurities are negligible. $M = 1.2$ and $\eta_e = 0.35$. Find the required values of recirculating energy fraction, plasma burn time, and f_b.

8. Calculate the effect of removing the direct convertor from the power flow diagram of Fig. 4E2, with all the thermal energy converted to electricity at $\eta_e = \eta_t = 0.35$. Holding the gross electrical power (1460 MWe), injection efficiencies , Q, and M constant, find the new values of P_{net}, ε, and η.

9. A deuteron beam is slowing down in a tritium plasma with $T_e = 7$ keV, $T_i \simeq 0$. When the beam ions have energies of 210 keV (initial energy), 160 keV, 110 keV, 50 keV, and 10 keV, their energy loss rates are found from Eq.(2E37) to be $20.9\times10^{-34}n$, $17.8\times10^{-34}n$, $15.2\times10^{-34}n$, $13.9\times10^{-34}n$, and $24.5\times10^{-34}n$ Watts (n = density), respectively. Estimate the fusion probability during slowing down to 10 keV, using Simpson's Rule with $\Delta W = 50$ keV. Compare your result with a value of p_f derived from Fig. 4F1 and Eq. (4F2).

10. Calculate a volume-average P_{rad} for the parameters of Example Problem 4G1, assuming only bremsstrahlung radiation with $Z_{eff} = 1.7$. Compare the result with P_{rad} evaluated at the average temperature and density.

11. Referring to the parameters of Table 4H1, estimate
    (a) the minimum n_e for a tandem mirror which could keep $Q \leq 10$.
    (b) how large M should be to reduce the required Q for a beam-driven toroidal reactor to 2.
    (c) the effect of reducing η_{in} by a factor of 2 in an inertial confinement reactor, keeping other input parameters constant.

Bibliography

ignition, energy cycle, required $n\tau_E$

S. Glasstone and R. H. Lovberg, *Controlled Thermonuclear Reactions*, Van Nostrand Reinhold Co., New York, 1960.

R. V. Jensen, D. E. Post, and D. L. Jassby, "Critical impurity concentrations for power multiplication in beam-heated toroidal fusion reactors, *Nuclear Science and Engineering* 65, 282 (1978).

T. Kammash, *Fusion Reactor Physics*, Ann Arbor Science, Ann Arbor, MI, 1975.

J. D. Lawson, "Some criteria for a power producing thermonuclear reactor, *Proceedings of the Physical Society (London)* B70, 6 (1957).

J. R. McNally, Jr., "The ignition parameter $Tn\tau$ and the energy multiplication factor k for fusioning plasmas", *Nuclear Fusion* 17, 1273 (1977).

D. M. Meade, "Effect of high-Z impurities on the ignition and Lawson conditions for a thermonuclear reactor", *Nuclear Fusion* 14, 289 (1974).

G. H. Miley, *Fusion Energy Conversion*, American Nuclear Society, LaGrange Park, IL, 1975.

P. J. Persiani, W. C. Lipinski, and A. J. Hatch, "Power-balance parameters Q and ε as measures of performance for fusion power reactors", *Technology of Controlled Thermonuclear Fusion Experiments and the Engineering Aspects of Fusion Reactors*, CONF-721111, USAEC, 1974, p. 347.

D. J. Rose and M. Clark, Jr., *Plasmas and Controlled Fusion*, MIT Press, Cambridge, MA, 1961.

W. M. Stacey, Jr., *Fusion Plasma Analysis*, Wiley, New York, 1981.

mirrors and beam-driven toroidal reactors

G. A. Carlson, B. Arfin, W. L. Barr, B. M. Boghosian, J. L. Erickson, J. H. Fink, G. W. Hamilton, B. G. Logan, J. O. Myall, and W. S. Neef, Jr., "Tandem mirror reactor with thermal barriers", UCRL-52836, 1979.

A. H. Futch, Jr., J. P. Holdren, J. Killeen, and A. A. Mirin, "Multispecies Fokker-Planck calculations for D-T and D-^{3}He mirror reactors", *Plasma Physics* 14, 211 (1972).

D. L. Jassby, "Optimization of fusion power density in the two-energy-component tokamak reactor", *Nuclear Fusion* 15, 453 (1975).

D. L. Jassby, "Neutral-beam-driven tokamak reactors", *Nuclear Fusion 17*, 309-365 (1977). Review Paper.

R. W. Moir, et al, "Preliminary design study of the Tandem Mirror Reactor (TMR)", UCRL-52302 (1977).

effects of spatial and time variations

T. J. Dolan and K. F. Keller, "Energy balance for a pulsed D-T reactor", *Nuclear Fusion* 13, 875 (1973).

J. Kesner and R. W. Conn, "Space-dependent effects on the Lawson and ignition conditions and thermal equilibria in Tokamaks", *Nuclear Fusion* 16, 397-404 (1976).

comparison of reactor types

R. A. Krakowski, F. L. Ribe, T. A. Coultas, and A. J. Hatch, "An engineering design of a reference theta pinch reactor", ANL-8019/LA-5336 (1974).

M. Nozawa and D. Steiner, "An assessment of the power balance in fusion reactors", ORNL-TM-4421, 1974.

CHAPTER 5
PLASMA FUNDAMENTALS

5A. Introduction

This chapter introduces some plasma phenomena and equations which will be of use in later chapters. This introductory material omits some important topics, which are covered in standard plasma physics texts (Bibliography).

background

Plasma occurs in stars, the earth's ionosphere, lightning, flames, gas-filled electronic tubes, arcs, laboratory devices, and in fluorescent lights and neon signs. Over 95% of the universe is in the plasma state. The densities and temperatures of some types of plasma are plotted in Fig. 5A1.

Some events in the history of plasma studies are listed in Table 5A1.

fourth state of matter

The state of matter (solid, liquid, gas, or plasma) is determined mainly by its temperature. At very high temperatures, gases become ionized, with the equilibrium degree of ionization described by the Saha equation (3E4). The resulting group of charged particles has properties markedly different from those of gases, including electrical conductivity, diamagnetism, self-shielding from applied electric fields, and unusual wave propagation phenomena.

Because gas molecules are electrically neutral, they experience only short-range forces. Therefore, they have straight-line trajectories punctuated by binary collisions, resulting in zig-zag paths. Charged particles, on the other hand, experience long-range Coulomb forces from thousands of surrounding particles, so their trajectories are constantly curving, as illustrated in Fig. 5A2. The Coulomb force between two particles with charges q_1 and q_2 separated by a distance r is

$$F = \frac{q_1 q_2}{4\pi\varepsilon_0 r^2} \quad (N), \tag{5A1}$$

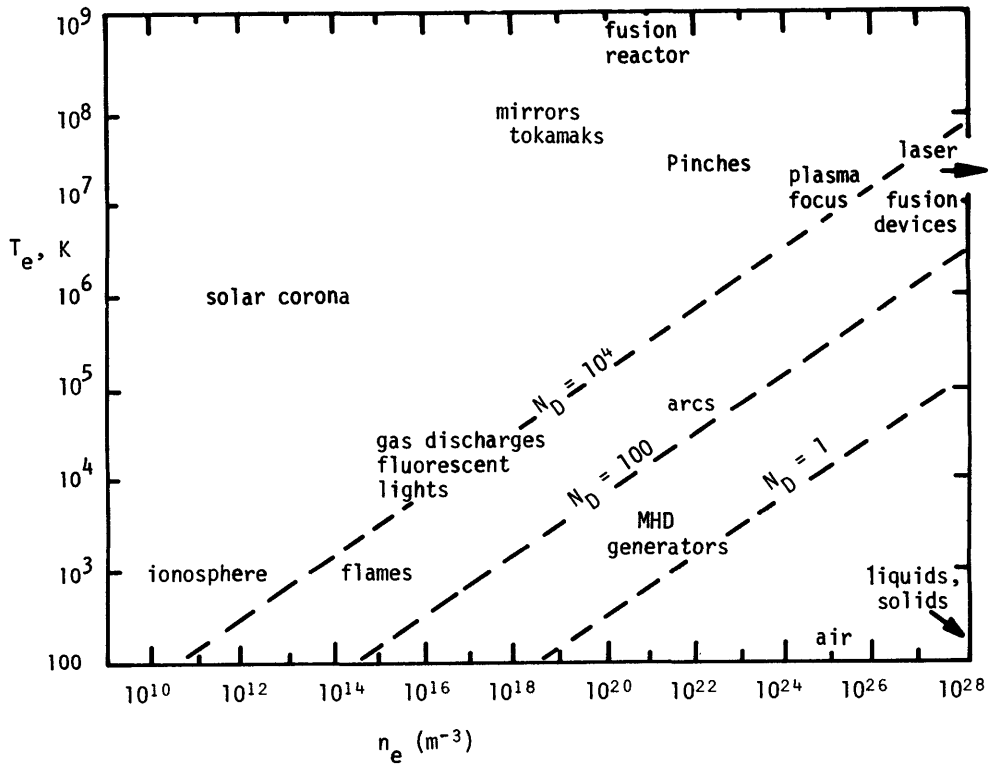

Fig. 5A1. Typical electron temperatures and densities in various gases and plasmas. For comparison, the densities of molecules in air, liquids and solids are also shown. N_D is the number of particles in a sphere with radius equal to a Debye length (Eq. 5F8).

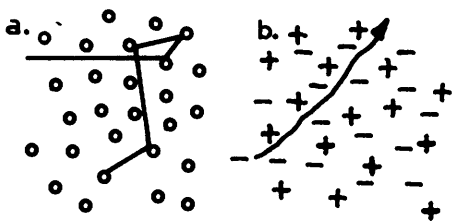

Fig. 5A2. Illustration of typical particle trajectories. (a) molecules in a gas, (b) charged particles in a plasma. In a plasma large-angle deflections are rare.

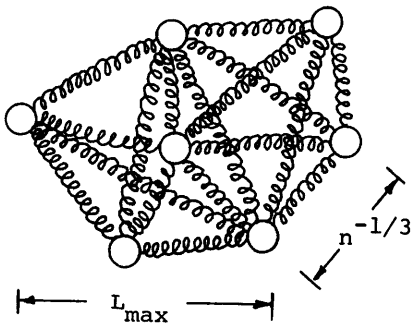

Fig. 5A3. The Analogy of balls connected by springs, with long springs weaker than short springs, and no springs longer than L_{max}.

Table 5A1. Some events in the history of plasma physics.

600-300 BC	Although much of ancient natural philosophy was wild speculation mixed with mythology, a few of the concepts were remarkably similar to present scientific beliefs. Anaximenes (Ionia) stated that every state of matter can be changed into every other state by establishing appropriate conditions. Democritus stated that everything is composed of tiny atoms. Thales (Miletus) studied static electricity, rubbing amber rods with fur, etc. The word "electron" comes from the Greek word for amber. Empedocles (Agrigentum) stated that there are four states of matter: earth, water, air and fire (which may be interpreted as solid, liquid, gas, plasma).
1785	Coulomb published experiments on electrical forces between charged particles.
1879	Sir William Crookes observed electrical discharges in gases and described an apparent "fourth state of matter".
1912	Debye and Hückel described the shielding effect around charged particles in an electrolyte.
1920's	I. Langmuir and L. Tonks studied gas discharges and plasma oscillations, and originated the term "plasma" to describe ionized gases.
1929	F. Houtermanns and R. Atkinson suggested that the fusion of light elements is the source of stellar energy.
1930's	Expanding studies of gas discharges and plasma theory.
1940's	Development of hydrogen bomb (inertial confinement fusion).
1950's	Plasma confinement and heating experiments begun, but troubled by instabilities.
1960's	Successful control of some types of instabilities in mirrors, Tokamaks, and multipole devices.
1970's	Larger experiments approach fusion reactor parameters.

where $\varepsilon_0 = 8.854 \times 10^{-12}$ F/m is the permittivity of free space.

The average spacing between particles in a plasma with density n is $n^{-1/3}$, so the approximate force between adjacent deuterons in a plasma with $n = 10^{20}$ m^{-3} is found from Eq. (5A1) to be $F = 5 \times 10^{-15}$ N. The forces of many other deuterons at slightly greater distances will also be significant.

Imagine a large number of balls connected by springs, as illustrated in Fig. 5A3, with long springs being weaker than short springs (in contrast to Hooke's Law), and no springs at all between balls spaced further apart than L_{max}. The springs tend to make the balls move together. If the average interparticle spacing $n^{-1/3} \ll L_{max}$, then each ball will have many springs attached to it, and *collective interactions* (group motion effects) will be dominant. In a plasma L_{max} corresponds roughly to the "Debye length", and collective Coulomb interactions give rise to plasma oscillations, Debye shielding, and quasineutrality (Sections 5E, 5F, 5G).

The main problem of plasma theory is to determine the electromagnetic fields and particle motions in a plasma. The *fields* can be found from Maxwell's

Equations, if the particle densities and velocities are known. From the electric and magnetic fields the *forces* on the charged particles can be calculated. From the forces, the plasma behavior can be computed. The new plasma parameters determine the new electromagnetic fields, and so on, in a cycle (Fig. 5A4). For self-consistency, the sets of equations describing fields, forces, and plasma behavior must be solved simultaneously.

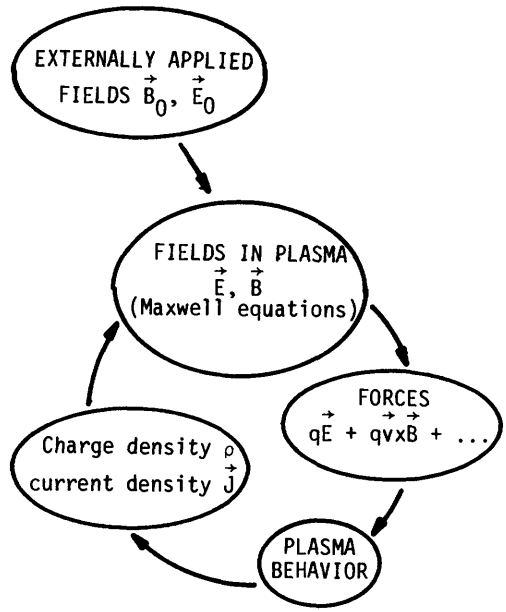

Fig. 5A4. The cycle of computing fields, forces and particle motions in a plasma.

5B. Electromagnetic Fields and Forces

charge and current densities

The charge desnity ρ and the current density $\vec{J}$ are defined by the equations

$$\rho = \sum_k q_k \int d\vec{v} f_k(\vec{x},\vec{v},t)$$
$$= n_i q_i - n_e e + \ldots \quad (C/m^3) \qquad (5B1)$$

$$\vec{J} = \sum_k q_k \int d\vec{v} f_k(\vec{x},\vec{v},t)\vec{v}$$
$$= n_i q_i \vec{u}_i - n_e e\vec{u}_e + \ldots \quad (A/m^2) \qquad (5B2)$$

where the subscripts k denote different species of charge (electrons and ions), $f_k(\vec{x},\vec{v},t)$ is their distribution function, n represents particle density (m^{-3}), q represents the charge of the particles (C), e is the electronic charge, and $\vec{u}$ is the average velocity. For a hydrogen plasma in which $u_e >> u_i$, these equations reduce to the form

$$\rho = e(n_i - n_e) \qquad (C/m^3) \qquad (5B3)$$

$$\vec{J} \simeq - n_e e\vec{u}_e \qquad (A/m^2). \qquad (5B4)$$

EXAMPLE PROBLEM 5B1

A uniform, cylindrical hydrogen plasma 2 cm in diameter has an axial current I = 50 mA, $n_e = 10^{18}\ m^{-3}$, and n_i one part per million larger. Find the charge density, current density, and average electron flow speed.

From Eq. (5B3) we find that $\rho = 1.6\times10^{-7}$ C/m^3. The current density $J = I/\pi r^2$ = 160 A/m^2. Then, from Eq. (5B4), $u_e = J/n_e e$ = 1000 m/s.

Maxwell Equations

Once the charge density and current density are known, the electric field $\vec{E}$ (V/m) and the magnetic induction $\vec{B}$ (T) can be found from Maxwell's Equations:

$$\vec{\nabla}\cdot\vec{E} = \rho/\varepsilon_0 \qquad (V/m^2) \qquad (5B5)$$

$$\vec{\nabla}\cdot\vec{B} = 0 \qquad (T/m) \qquad (5B6)$$

$$\vec{\nabla}\times\vec{E} = -\partial\vec{B}/\partial t \qquad (V/m^2) \qquad \textit{(Faraday's Law)} \qquad (5B7)$$

$$\vec{\nabla}\times\vec{B}/\mu_0 = \varepsilon_0(\partial\vec{E}/\partial t) + \vec{J} \qquad (A/m^2) \qquad \textit{(Ampere's Law)} \qquad (5B8)$$

where $\mu_0 = 4\pi\times10^{-7}$ H/m is the permeability of free space. Vector identities useful with these equations are listed in Appendix F. The latter two equations may be transformed to other forms by integrating over a surface area dS, and using Stokes Theorem, which states

$$\oint d\vec{S}\cdot\vec{\nabla}\times\vec{E} = \int d\vec{\ell}\cdot\vec{E} \qquad (5B9)$$

surface boundary

where $\vec{E}$ is any vector and the line integral is along the closed path bounding the surface integral. The integral forms of Eqs. (5B7) and (5B8) are

$$\oint d\vec{\ell}\cdot\vec{E} = -\int d\vec{S}\cdot(\partial\vec{B}/\partial t) \qquad (V) \qquad \textit{(Faraday's Law)} \qquad (5B10)$$

$$\oint d\vec{\ell}\cdot\vec{B} = \varepsilon_0\mu_0\int d\vec{S}\cdot(\partial\vec{E}/\partial t) + \mu_0\int d\vec{S}\cdot\vec{J}$$

$$= \varepsilon_0\mu_0\int d\vec{S}\cdot(\partial\vec{E}/\partial t) + \mu_0 I \qquad (Vs/m), \quad \textit{(Ampere's Law)} \qquad (5B11)$$

where I is the total current passing through the surface of integration.

EXAMPLE PROBLEM 5B2

Find the steady-state magnetic field at the surface of the plasma of the previous example problem.

In Ampere's Law the $\partial\vec{E}/\partial t$ term will be zero at steady state. By symmetry, B is constant around the circumference of the plasma. Both $\vec{B}$ and $d\vec{\ell}$ are in the azimuthal direction, so

$$\oint d\vec{\ell}\cdot\vec{B} = B\oint d\ell = 2\pi rB = \mu_0 I$$

Thus, $B = \mu_0 I/2\pi r = 10^{-6}$ T

In fusion experiments with high currents the resultant magnetic field can be very strong ($\sim$ 1 T).

The direction of the magnetic field produced by a current I can be found from the right-hand rule, Fig. 5B1.

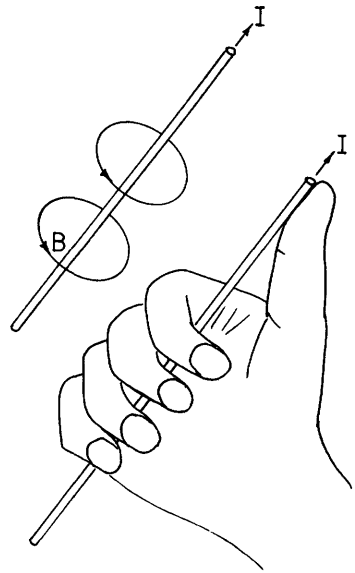

Fig. 5B1. The "right hand rule" for determining the direction of magnetic field lines around a current-carrying conductor. If the thumb points in the direction of the current I, then the other fingers curl in the direction of the magnetic field lines $\vec{B}$.

EXAMPLE PROBLEM 5B3

A toroidal plasma forms the secondary winding of an iron-core transformer, as shown in Fig. 5B2. When the primary coil of the transformer is pulsed on, a changing magnetic induction $\partial B/\partial t$ is induced in the iron core, which has a cross-sectional area of 0.85 m^2. If it is desired to induce an electric field of 122 V/m in the plasma at radius R = 1 m, how large must $\partial B/\partial t$ be?

Very little magnetic flux leaks out of the iron, so $\partial\vec{B}/\partial t$ in the air is negligible, and $\int d\vec{S}\cdot(\partial\vec{B}/\partial t) \simeq A(dB/dt)$, where A is the iron core area. $\vec{E}$ and $d\vec{\ell}$ are both in the direction shown, and by symmetry $\vec{E}$ is constant around the loop, so $\oint d\vec{\ell}\cdot\vec{E} = 2\pi RE$. From Faraday's Law, we have

$$2\pi RE = -A(dB/dt)$$

$$-dB/dt = 2\pi RE/A = 902 \text{ T/s}.$$

---

vector and scalar potentials

In calculating $\vec{B}$ and $\vec{E}$ from ϕ and $\vec{J}$, it is sometimes convenient to first calculate the electrostatic scalar potential ϕ and the magnetic vector potential $\vec{A}$ from the equations

$$\phi = \frac{1}{4\pi\varepsilon_0}\int\frac{d\vec{x}\,\rho}{r} \quad \text{(V)} \qquad (5B12)$$

$$\vec{A} = \frac{\mu_0}{4\pi}\int\frac{d\vec{x}\,\vec{J}}{r} \quad \text{(T-m)} \qquad (5B13)$$

where the volume integrals include all space and r is the distance from a volume element dxdydz to the point where ϕ and $\vec{A}$ are to be calculated. (These equations

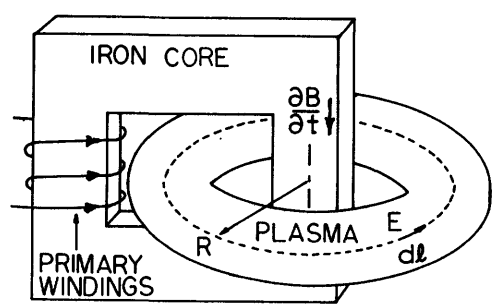

Fig. 5B2. Electric field induced in plasma by changing magnetic induction in transformer.

must be modified if the potentials vary significantly during the time r/c, where c is the speed of light.) The vector potential $\vec{A}$ has physical significance and can be measured even in regions where $\vec{B} = 0$ (Shadowitz, 1975). The fields are then found from the relations

$$\vec{B} = \vec{\nabla}\times\vec{A} \tag{5B14}$$

$$\vec{E} = -\vec{\nabla}\phi - \partial\vec{A}/\partial t \quad . \tag{5B15}$$

When $\partial\vec{A}/\partial t \simeq 0$, $\vec{E} = -\vec{\nabla}\phi$, and Eq. (5B5) becomes

$$\nabla^2\phi = -\rho/\varepsilon_0 \quad , \tag{5B16}$$

which is called the *Poisson Equation.*

EXAMPLE PROBLEM 5B4

If the potential at the outside of the plasma of example problem 5B1 is zero, calculate the potential at the center.

From App. F, the Poisson equation in cylindrical coordinates is

$$\nabla^2\phi = \frac{1}{r}\frac{d}{dr}\left(r\,\frac{d\phi}{dr}\right) = -\rho/\varepsilon_0 \tag{5B17}$$

By symmetry, $d\phi/dr = 0$ at $r = 0$. The other boundary condition is $\phi(a) = 0$, where a is the plasma radius. Eq. (5B17) may be integrated twice, yielding

$$\phi(r) = -\frac{\rho r^2}{4\varepsilon_0} + C_1 \ell n(r) + C_2 \quad ,$$

where C_1 and C_2 are integration constants. Using the boundary conditions to evaluate the constants, the result is

$$\phi(r) = \frac{\rho(a^2-r^2)}{4\varepsilon_0} \quad . \tag{5B18}$$

The potential at the plasma center ($r = 0$) is $\rho a^2/4\varepsilon_0 = 0.45$ V.

---

forces on individual particles

The Lorentz force

$$\vec{F} = q\vec{E} + q\vec{v}\times\vec{B} \qquad (N) \tag{5B19}$$

describes the effects of electric and magnetic fields on a single particle with charge q and velocity $\vec{v}$. The force $m\vec{g}$ of gravity is usually negligible in comparison with the Lorentz force in plasmas. Particles moving along a curved path with radius of curvature r experience a centrifugal force

$$\vec{F} = mv^2\hat{r}/r \qquad (N) \tag{5B20}$$

where $\hat{r}$ is a unit vector outwards. Let the velocity vector be divided into components $v_\perp$ perpendicular to $\vec{B}$ and $v_\parallel$ parallel to $\vec{B}$. If $E \simeq 0$, the Lorentz force

$qv_\perp B$ balances the centrifugal force $mv_\perp^2/r$ to yield circular motion with the "Larmor" radius $\rho = mv_\perp/qB$. The centrifugal force $mv_\parallel^2/R_c$ of motion along magnetic field lines with curvature radius R_c is balanced by tension in the magnetic field lines. The resultant ion (or electron) trajectory is a spiral, as illustrated in Fig. 5B3.

fluid forces

In the fluid model of plasma behavior, additional forces arise from particle interactions. Particle species j with pressure $p_j = n_j kT_j$ (Eq. 2D5) experiences an effective pressure-gradient force per particle of

$$\vec{F} = -\vec{\nabla}p_j/n_j \qquad (N) \tag{5B21}$$

and an effective frictional drag force from particles of species k with average velocity $\vec{u}_k$ equal to

$$\vec{F} = -m_j\nu_{jk}(\vec{u}_j - \vec{u}_k) \quad (N) \tag{5B22}$$

where m_j and u_j are the mass and average velocity of particles j, and ν_{jk} is the momentum-transfer collision frequency between species j and k.

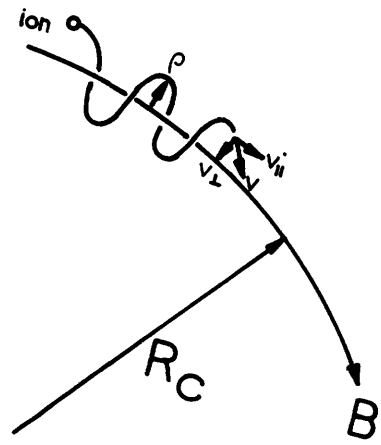

Fig. 5B3. Spiral path of an ion along a magnetic field line B. The radius of curvature of the magnetic field line is R_c, and the radius of the spiral is ρ. The ion velocity v may be resolved into components $v_\parallel$ parallel to B and $v_\perp$ perpendicular to B.

EXAMPLE PROBLEM 5B5

Assume that a longitudinal magnetic field B = 0.01 T is applied to the uniform cylindrical plasma of example problem 5B4. Estimate the Lorentz force on a proton moving radially outwards at the surface of the plasma with v = 10^4 m/s.

The electric field at the surface of the plasma is found to be

$$\vec{E} = -\vec{\nabla}\phi = -(d\phi/dr) = \rho r/2\varepsilon_0 = 90 \text{ V/m}$$

in the positive radial direction.

Since $\vec{v}$ is in the radial direction and $\vec{B}$ is in the z direction, the cross product $\vec{v}\times\vec{B}$ is in the negative θ direction. The Lorentz force on a proton is then

$$\vec{F} = e\vec{E} + e\vec{v}\times\vec{B} = (1.4\times10^{-17}\text{ N})\hat{r} - (1.6\times10^{-17}\text{ N})\hat{\theta}$$

where $\hat{r}$ and $\hat{\theta}$ are unit vectors in the r and Θ directions. The force of gravity is only 1.6×10^{-26} N.

When the forces acting on the plasma are known, the plasma behavior can be calculated. There are three main approaches: kinetic theory, the fluid approximation, and study of individual particle trajectories.

5C. Kinetic Theory

Of the methods commonly used for describing plasma behavior, kinetic theory is the most general and accurate. The plasma is described in terms of distribution functions $f(\vec{x},\vec{v},t)$. As discussed in Section 2A, the distribution function f represents the average number of particles per unit volume and per unit of velocity-space volume having position $\vec{x}$ and velocity $\vec{v}$ at time t. The main equation of kinetic theory, the Boltzmann equation, states that df/dt is equal to the rate of change of f due to collisions $(\partial f/\partial t)_{col}$. Applying the chain rule for differentiation of a function of several variables, we have

$$\begin{aligned} df/dt &= \partial f/\partial t + (\partial f/\partial x)\,(\partial x/\partial t) + (\partial f/\partial y)\,(\partial y/\partial t) + (\partial f/\partial z)\,(\partial z/\partial t) \\ &\quad + (\partial f/\partial v_x)\,(\partial v_x/\partial t) + (\partial f/\partial v_y)\,(\partial v_y/\partial t) + (\partial f/\partial v_z)\,(\partial v_z/\partial t) \\ &= (\partial f/\partial t)_{col}. \end{aligned} \tag{5C1}$$

This may be condensed by using a subscript j to represent the x, y, and z components of vectors and summing over j:

$$\partial f/\partial t + \sum_j (\partial x_j/\partial t)\,(\partial f/\partial x_j) + \sum_j (\partial v_j/\partial t)\,(\partial f/\partial v_j) = (\partial f/\partial t)_{col}. \tag{5C2}$$

Usually the summation signs are omitted for simplicity. Since $(\partial x_j/\partial t) = v_j$ and $(\partial v_j/\partial t)$ = acceleration = F_j/m (for the nonrelativistic case), this equation may be written in the forms

$$\partial f/\partial t + v_j(\partial f/\partial x_j) + (F_j/m)\,(\partial f/\partial v_j) = (\partial f/\partial t)_{col} \tag{5C3}$$

and

$$\partial f/\partial t + \vec{v}\cdot(\partial f/\partial \vec{x}) + (\vec{F}/m)\cdot(\partial f/\partial \vec{v}) = (\partial f/\partial t)_{col}. \tag{5C4}$$

Usually only the Lorentz force is needed for $\vec{F}$. Pressure-gradient effects are accounted for by the $(\partial f/\partial \vec{x})$ term, and frictional drag effects by the collision term. For the case of binary collisions in a neutral gas (Fig. 5A2) an accurate expression may be written for $(\partial f/\partial t)_{col}$; but in a plasma the particles are continuously interacting with thousands of surrounding particles, and it is difficult to do so. In spite of this difficulty, the *Fokker-Planck* expression for $(\partial f/\partial t)_{col}$, which represents long-distance binary collisions, has yielded successful results in many cases (Schmidt, 1979; Krall and Trivelpiece, 1974).

The Boltzmann equation may be written once for electrons and once for ions. The particle densities and average velocities, defined by Eqs. (2A1) and (2A4), determine the charge density and current density via Eqs. (5B1) and (5B2). Then the Maxwell equations can be solved for $\vec{E}$ and $\vec{B}$. These equations form a complete set, which should be solved simultaneously. Since kinetic theory accounts for the velocity distribution of the particles, it can describe the interaction of parti-

cles having velocity $\vec{v}$ with a plasma wave having phase velocity $\vec{v}_\phi \simeq \vec{v}$. Kinetic theory is needed for studying resonant wave-particle interactions, but its mathematical complexity makes analytic solution of the full set of non-linear equations impractical. Various simplifying assumptions may be made to facilitate solution:

(a) assuming spatial symmetry to reduce the number of spatial dimensions from three (x,y,z) to zero, one, or two.

(b) assuming symmetry in velocity space, to reduce the number of velocity variables from three (v_x, v_y, v_z) to one or two,

(c) assuming $(\partial f/\partial t)_{col} \simeq 0$, which is valid at high temperatures and low densities. The resulting equation is called the *Vlasov equation.*

(d) assuming steady state equilibrium, so that $\partial f/\partial t = 0$.

(e) assuming that the ions are at rest, and uniformly distributed in space, so that the Boltzmann equation for ions may be omitted. This assumption is valid for motions at high frequencies, since the ions' comparatively heavy masses prevent them from responding rapidly to applied fields.

(f) assuming that the magnetic field produced by plasma currents is negligible in comparison with the magnetic field produced by external coils (valid for low-pressure plasmas.)

(g) assuming that the plasma contains equal densities of positive and negative charges, so $\rho \simeq 0$ (quasineutrality), which is invalid only in small, low-density plasmas.

(h) assuming that $f(\vec{x},\vec{v},t) = f_0(\vec{v}) + f_1(\vec{x},\vec{v},t)$, where $f_0(\vec{v})$ is an equilibrium distribution and $f_1 << f_0$; and that $\vec{E}(\vec{x},t) = \vec{E}_0(\vec{x}) + \vec{E}_1(\vec{x},t)$, with $E_1 << E_0$. When these are substituted into the Boltzmann equation, the nonlinear term $(q\vec{E}_1/m)\cdot(\partial f_1/\partial \vec{v})$ may be dropped, since it involves the product of two small quantities (E_1 and f_1). The resulting "linearized" equation is more amenable to analytical solution, though the validity of the solution is restricted to small amplitudes of the perturbations f_1 and E_1.

(i) assuming that $f_1(\vec{x},\vec{v},t) = f_1(\vec{v})\exp(i\vec{k}\cdot\vec{x} - i\omega t)$ and $\vec{E}_1(\vec{x},t) = \vec{E}_1\exp(i\vec{k}\cdot\vec{x} - i\omega t)$, where $i = (-1)^{\frac{1}{2}}$, ω is a wave frequency (radians/s), and $\vec{k}$ is a vector pointing in the direction of wave propagation and having magnitude $k = 2\pi/\lambda$, where λ is the wavelength. These assumptions facilitate study of plasma waves, and have the advantage that the time and space derivatives in the Boltzmann and Maxwell Equations are replaced by algebraic multipliers. For example, $\partial f_1/\partial t \rightarrow -i\omega f_1$ and $\partial \vec{E}_1/\partial z \rightarrow ik_z\vec{E}_1$. (This assumption is similar to use of Fourier-Laplace transforms.)

Kinetic theory is needed for studying resonant wave-particle interactions and microinstabilities, which will be discussed qualitatively in Chapter 8. However, many problems can be solved by using the simpler fluid equations, which describe the plasma in terms of particle densities, average velocities, and temperatures.

5D. Fluid Equations

two-fluid theory

The fluid equations represent conservation of particles, momentum, and energy for electrons and for ions. They may be derived by considering the transport of particles, momentum, or energy across the surfaces of a small volume element dxdydz. Alternatively, they may be derived by multiplying the Boltzmann equation by 1, $m\vec{v}$, and $m(\vec{v}-\vec{u})(\vec{v}-\vec{u})$, where u is the average velocity, and integrating

over all velocities. (Equations based on higher-order integrals of the Boltzmann equation have also been used for improved accuracy.)

The particle conservation equation for ions states that $\partial n_i/\partial t$ = (production by ionization) - (loss by recombination) - (loss by outflow), where n_i is the ion density (m^{-3}). The loss by outflow is equal to

$$\vec{\nabla}\cdot(n_i\vec{u}_i) = \partial(n_iu_{ix})/\partial x + \partial(n_iu_{iy})/\partial y + \partial(n_iu_{iz})/\partial z.$$

Putting the outflow term on the left side, the equation may be written

$$\partial n_i/\partial t + \vec{\nabla}\cdot(n_i\vec{u}_i) = n_nn_i\langle\sigma_iv_i\rangle + n_nn_e\langle\sigma_ev_e\rangle - n_en_i\langle\sigma_rv\rangle, \qquad (5D1)$$

where n_n is the neutral atom density, $\langle\sigma_rv\rangle$ is the recombination rate, and $\langle\sigma_iv_i\rangle$ and $\langle\sigma_ev_e\rangle$ are the rates for ionization of neutrals by ions and by electrons. Similarly, the electron conservation equation is

$$\partial n_e/\partial t + \vec{\nabla}\cdot(n_e\vec{u}_e) = n_nn_i\langle\sigma_iv_i\rangle + n_nn_e\langle\sigma_ev_e\rangle - n_en_i\langle\sigma_rv\rangle. \qquad (5D2)$$

Additional source and loss terms may be needed in these *continuity equations* to account for neutral beam injection, fusion reactions, and electron beam injection. If the spatial variations of $n_i(\vec{x},t)$ are ignored and the outflow term replaced by by n_i/τ_i, then Eq. (4A2) is obtained.

EXAMPLE PROBLEM 5D1

Assume that the density of impurity ions is known at two points x_1 and x_2 from spectroscopic measurements, and that these ions have a constant velocity u_x. Solve the steady-state continuity equation to deduce the value of u_x, and estimate the time it takes them to flow from x_1 to x_2.

At steady state the time derivative term is zero. Taking $n_i = n_e$, the continuity equation becomes

$$u_x\frac{dn_z}{dx} = n_zn_e\langle\sigma_ev_e\rangle + n_zn_e\langle\sigma_iv_i\rangle - n_zn_e\langle\sigma_rv\rangle$$

We can divide both sides by n_z and integrate to obtain

$$u_x\ln\frac{n_z(x_2)}{n_z(x_1)} = \int_{x_1}^{x_2} dx\, n_e(\langle\sigma_ev_e\rangle + \langle\sigma_iv_i\rangle - \langle\sigma_rv\rangle).$$

Knowing n_e, T_e, and T_i from other measurements, we can evaluate the integral and solve this equation for u_x. Then the flow time is equal to $(x_2-x_1)/u_x$.

Transport of impurity ions alters the establishment of coronal equilibrium (Section 3F) in Tokamak plasmas.

The momentum-conservation equations are equivalent to Newton's Second Law $m(d\vec{u}/dt) = \vec{F}$, where $\vec{F}$ is the sum of the forces. Since the average velocity of the fluid is a function of $\vec{x}$ and t,

$$d\vec{u}/dt = \partial\vec{u}/\partial t + (\partial\vec{u}/\partial x)(\partial x/\partial t) + (\partial\vec{u}/\partial y)(\partial y/\partial t) + (\partial\vec{u}/\partial z)(\partial z/\partial t)$$
$$\equiv \partial\vec{u}/\partial t + (\vec{u}\cdot\vec{\nabla})\vec{u} \ . \qquad (5D3)$$

When multiplied by nm, the $(\vec{u}\cdot\vec{\nabla})\vec{u}$ term represents net outflow of momentum from a differential volume element. The *momentum conservation equations* for singly charged ions and electrons may be written

$$n_i m_i\left[\partial\vec{u}_i/\partial t + (\vec{u}_i\cdot\vec{\nabla})\vec{u}_i\right] = -\vec{\nabla}\cdot\underline{\underline{P}}_i + n_i e(\vec{E} + \vec{u}_i x\vec{B}) + \vec{R}_{ei} - n_i m_i \vec{u}_i \nu_{in} \qquad (5D4)$$

$$n_e m_e\left[\partial\vec{u}_e/\partial t + (\vec{u}_e\cdot\vec{\nabla})\vec{u}_e\right] = -\vec{\nabla}\cdot\underline{\underline{P}}_e - n_e e(\vec{E} + \vec{u}_e x\vec{B}) - \vec{R}_{ei} - n_e m_e \vec{u}_e \nu_{en} \qquad (5D5)$$

where n_i, n_e, m_i, m_e, $\vec{u}_i$, $\vec{u}_e$ represent the particle densities, masses, and average velocities of ions and electrons, e is the electronic charge, ν_{in} and ν_{en} are momentum transfer collision frequencies to neutral atoms, $\vec{E}$ and $\vec{B}$ are the electric and magnetic fields, $\vec{R}_{ei}$ is the rate of momentum transfer from electrons to ions, and $\vec{\nabla}\cdot\underline{\underline{P}}_i$, $\vec{\nabla}\cdot\underline{\underline{P}}_e$ are the divergences of the ion and electron pressure tensors, having components

$$\vec{\nabla}\cdot\underline{\underline{P}} = \hat{x}(\partial P_{xx}/\partial x + \partial P_{xy}/\partial y + \partial P_{xz}/\partial z) + \hat{y}(\partial P_{yx}/\partial x + \partial P_{yy}/\partial y + \partial P_{yz}/\partial z)$$
$$+ \hat{z}(\partial P_{zx}/\partial x + \partial P_{zy}/\partial y + \partial P_{zz}/\partial z) \qquad (5D6)$$

for either species. The components of the pressure tensors are defined by

$$P_{\alpha\beta}(\vec{x},t) \equiv \int d\vec{v}\ f(\vec{x},\vec{v},t)(\vec{v}-\vec{u})_\alpha(\vec{v}-\vec{u})_\beta \equiv nm\langle(\vec{v}-\vec{u})_\alpha(\vec{v}-\vec{u})_\beta\rangle \qquad (5D7)$$

for either species, where α and β represent x, y, or z; $\vec{v}$ is an individual particle velocity, and $\vec{u}$ is the average velocity for that species.

It is customary to let $\underline{\underline{\Pi}}_{\alpha\beta}$ be the anisotropic part of the pressure tensor:

$$\underline{\underline{\Pi}}_{\alpha\beta} \equiv \underline{\underline{P}}_{\alpha\beta} - p\delta_{\alpha\beta}, \quad \delta_{\alpha\beta} \equiv \begin{cases} 0, & \alpha \neq \beta \\ 1, & \alpha = \beta \end{cases} \qquad (5D8)$$

where $p = nkT$ is the scalar pressure. If the distribution is nearly isotropic and Maxwellian in a reference frame moving at the average velocity, then $\vec{\nabla}\cdot\underline{\underline{\Pi}}_{\alpha\beta} \simeq 0$, and

$$\vec{\nabla}\cdot\underline{\underline{P}}_e \simeq \vec{\nabla}P_e \equiv \vec{\nabla}(n_e kT_e)$$

$$\vec{\nabla}\cdot\underline{\underline{P}}_i \simeq \vec{\nabla}p_i \equiv \vec{\nabla}(n_i kT_i) \qquad (5D9)$$

The momentum transfer rate $\vec{R}_{ei}$ from electrons to ions is caused by friction and by a temperature-gradient force (Braginskii, 1965). For simplicity, we will

ignore the thermal force terms and use the approximate expression

plasma resistivity:

$$\vec{R}_{ei} \simeq -n_e(\eta_{\parallel}\vec{J}_{\parallel} + \eta_{\perp}\vec{J}_{\perp}) , \qquad \eta_{\parallel} = 2.4\times10^{-9}ZL/T_e^{3/2} \quad (\Omega\text{-m}), \tag{5D10}$$

where $\vec{J}_{\parallel}$ and $\vec{J}_{\perp}$ are the components of $\vec{J}$ parallel and perpendicular to $\vec{B}$, Z is the ionic charge, L is the Coulomb logarithm (Table 2E2), T_e is in keV, and $\eta_{\perp} \simeq 2\eta_{\parallel}$.

Frequently the "inertia" terms $(\vec{u}\cdot\vec{\nabla})\vec{u}$ appearing in these equations are negligibly small in comparison with the pressure gradient terms and may be discarded. To show that this is true, we can write

$$|\vec{\nabla}p_e/n_e| \sim p_e/L_p n_e = kT_e/L_p$$

$$|m_e(\vec{u}_e\cdot\vec{\nabla})\vec{u}_e| \sim m_e u_e^2/L_u \tag{5D11}$$

where L_p and L_u are characteristic scale lengths corresponding to the spatial derivatives of p_e and u_e. For example, in a one-dimensional case, $L_p = p_e/|dp_e/dx|$. The inertia term is negligible if

$$m_e u_e^2/L_u << kT_e/L_p \text{ , or}$$

$$u_e << (kT_e/m_e)^{\frac{1}{2}}(L_u/L_p)^{\frac{1}{2}} \sim (kT_e/m_e)^{\frac{1}{2}} \tag{5D12}$$

since $L_u/L_p \sim 1$. In other words, the inertia term is negligible if the average flow velocity is much less than the average speed of random thermal motions, which is often the case. (An exception is ion acceleration in a plasma sheath, where the accelerating voltage exceeds T_i).

The *energy conservation equations* for electrons and ions may be written

$$1.5n_e\left[\partial T_e/\partial t + (\vec{u}_e\cdot\vec{\nabla})T_e\right] = - p_e\vec{\nabla}\cdot\vec{u}_e - \vec{\nabla}\cdot\vec{q}_e + Q_e + Q_{ve} + P_e - P_{rad} \tag{5D13}$$

$$1.5n_i\left[\partial T_i/\partial t + (\vec{u}_i\cdot\vec{\nabla})T_i\right] = - p_i\vec{\nabla}\cdot\vec{u}_i - \vec{\nabla}\cdot\vec{q}_i + Q_i + Q_{vi} + P_i - P_{cx} \tag{5D14}$$

where P_{rad} and P_{cx} are power lost by radiation and charge exchange, P_e and P_i represent external heating (such as by radio waves or neutral beam injection), Q_{ve} and Q_{vi} represent heat generation by viscous forces, Q_e and Q_i represent heat generation by collisions between different species of particles, and $\vec{q}_e$ and $\vec{q}_i$ are the heat-flux vectors, defined by

$$\vec{q}_e \equiv \int d\vec{v}\ f_e(\vec{x},\vec{v}_e,t)m_e(\vec{v}_e-\vec{u}_e)^2\vec{v}_e/2 \equiv n_e m_e\langle(\vec{v}_e-\vec{u}_e)^2\vec{v}_e/2\rangle$$

$$\vec{q}_i \equiv \int d\vec{v}\ f_i(\vec{x},\vec{v}_i,t)m_i(\vec{v}_i-\vec{u}_i)^2\vec{v}_i/2 \equiv n_i m_i\langle(\vec{v}_i-\vec{u}_i)^2\vec{v}_i/2\rangle. \tag{5D15}$$

Additional terms may be needed in Eqs. (5D13) and (5D14) for self-heating by fusion reaction products, as in Eqs. (4A4) and (4A5).

When the heat fluxes and heats generated by collisions and viscosity are expressed in terms of the temperatures and average velocities, we have a complete set of equations for the unknowns n_e, n_i, $\vec{u}_e$, $\vec{u}_i$, T_e, T_i, $\vec{E}$, and $\vec{B}$. Solution of these *transport equations* will be discussed in Section 8F.

In the simplest case, if resistivity, viscosity, and all types of heat flow are negligible, the energy conservation equations reduce to the *adiabatic equations of state*

$$(\partial/\partial t + \vec{u}_e\cdot\vec{\nabla})(p_e/n_e^\gamma) \simeq 0,\ p_e/n_e^\gamma \simeq \text{constant},\ \vec{\nabla}p_e \simeq \gamma_e kT_e\vec{\nabla}n_e$$

$$(\partial/\partial t + \vec{u}_i\cdot\vec{\nabla})(p_i/n_i) \simeq 0,\ p_i/n_i^\gamma \simeq \text{constant},\ \vec{\nabla}p_i \simeq \gamma_i kT_i\vec{\nabla}n_i \quad , \tag{5D16}$$

where γ_e, γ_i are the specific heat ratios related to the "number of degrees of freedom" N by

$$\gamma = \frac{2+N}{N} \quad . \tag{5D17}$$

For example, if the electrons have effectively one-dimensional motion in a strong magnetic field, then $\gamma_e = 3$. If the magnetic field effects are negated by collisions, then the electrons may have three degrees of freedom and $\gamma_e = 5/3$ (as for a monoatomic gas). For an isothermal plasma (uniform T_e), $\gamma_e = 1$, and similarly for ions.

ambipolar motion

Multiplying Eq.(5D1) by e (the charge of hydrogen ions) and Eq.(5D2) by -e, and adding the two equations together, we find that the terms on the right side cancel, and the terms on the left may be expressed in terms of ρ and $\vec{J}$, with the result

$$\partial\rho/\partial t + \vec{\nabla}\cdot\vec{J} = 0 \ . \tag{5D18}$$

For steady-state cylindrical plasma with azimuthal symmetry, this becomes

$$(1/r)\partial(rJ_r)/\partial r + \partial J_z/\partial z = 0.$$

If $\partial J_z/\partial z = 0$, then $rJ_r = \text{constant} = 0$. For singly charged ions, $J_r = 0$ gives

$$n_i u_{ir} = n_e u_{er} \ . \tag{5D19}$$

Thus, the electron and ion particle fluxes must be equal. If one particle flux were larger, an excess of the opposite charge would accumulate in the plasma, creating a retarding electric field for the faster particles. The electric field adjusts itself to maintain the condition (5D19), which is called *ambipolar motion*.

The ambipolar flow condition (5D19) is only valid if $\partial J_z/\partial z = 0$, which is not always the case. Sometimes ion diffusion across the magnetic field (J_r) is balanced by rapid electron flow along the magnetic field (J_z) to conducting end walls.

transport coefficients

Since the particle velocities adjust to the forces very rapidly, it is often satisfactory to use the equilibrium values of $\vec{u}_e$ and $\vec{u}_i$ from the momentum conservation equations (5D4), (5D5) in solving the other transport equations. These velocities, and also $\vec{q}_e$, $\vec{q}_i$, and J, may be expressed in terms of gradients of density, temperature, and electrostatic potential, multiplied by appropriate *transport coefficients*.

To illustrate this method, we will consider the case of a long cylindrical plasma in a uniform axial magnetic field B, with all derivatives in the θ and z directions equal to zero, and solve for u_{er} and u_{ir}. We will assume that Eqs. (5D10) and (5D12) are valid and that $n_i = n_e \equiv n$, $\eta_\perp = m_e\nu_{ei}/ne^2$, and use the following definitions:

$$\nu_{ie} \equiv m_e\nu_{ei}/m_i$$

$$\nu_e \equiv \nu_{ei} + \nu_{en}$$

$$\nu_i \equiv \nu_{ie} + \nu_{in}$$

$$\omega_{ce} \equiv eB/m_e$$

$$\omega_{ci} \equiv eB/m_i \ . \qquad (5D20)$$

We will see in Chapter 7 that the "cyclotron frequencies" ω_{ce} and ω_{ci} are the frequencies at which the electrons and ions rotate around the magnetic field lines (rad/s). After dividing the ion and electron momentum conservation equations (5D4) and (5D5) by nm_i and nm_e, respectively, we can write their steady state r and θ components as

$$\begin{aligned}
u_{ir} \text{ equation:} \quad & -\nu_i u_{ir} + \omega_{ci}u_{i\theta} + \nu_{ie}u_{er} && = p_i'/nm_i - eE_r/m_i \\
u_{i\theta} \text{ equation:} \quad & -\omega_{ci}u_{ir} - \nu_i u_{i\theta} + \nu_{ie}u_{e\theta} && = 0 \\
u_{er} \text{ equation:} \quad & \nu_{ei}u_{ir} - \nu_e u_{er} - \omega_{ce}u_{e\theta} && = p_e'/nm_e + eE_r/m_e \\
u_{e\theta} \text{ equation:} \quad & \nu_{ei}u_{i\theta} + \omega_{ce}u_{er} - \nu_e u_{e\theta} && = 0
\end{aligned} \qquad (5D21)$$

where primes denote derivatives with respect to r.

In order for magnetic confinement to be effective, we need to have the charged particles rotate around magnetic field lines many times between collisions:

$$\omega_{ci} >> \nu_i, \ \nu_{ie}, \ \nu_{in} \qquad \omega_{ce} >> \nu_e, \ \nu_{ei}, \ \nu_{en} \qquad (5D22)$$

Using these conditions to simplify the algebra, we can write the solutions of

Eqs. (5D21) as

$$u_{ir} = \frac{-\nu_i}{m_i\omega_{ci}^2}\left[\frac{p_i'}{n} + \frac{\nu_{ie}}{\nu_i}\frac{p_e'}{n} - \frac{eE_r\nu_{in}}{\nu_i}\right]$$

$$u_{er} = \frac{-\nu_e}{m_e\omega_{ce}^2}\left[\frac{p_e'}{n} + \frac{\nu_{ei}}{\nu_e}\frac{p_i'}{n} + \frac{eE_r\nu_{en}}{\nu_e}\right] \qquad (5D23)$$

Since $p_i' = nkT_i' + kT_in'$ and $p_e' = nkT_e' + kT_en'$, we can express the particle fluxes as

$$nu_{ir} = -\left(\frac{\nu_i kT_i + \nu_{ie}kT_e}{m_i\omega_{ci}^2}\right)n' - \left(\frac{\nu_{ie}nk}{m_i\omega_{ci}^2}\right)T_e' - \left(\frac{\nu_i nk}{m_i\omega_{ci}^2}\right)T_i' + \left(\frac{-e\nu_{in}}{m_i\omega_{ci}^2}\right)nE_r$$

$$nu_{er} = -\left(\frac{\nu_e kT_e + \nu_{ei}kT_i}{m_e\omega_{ce}^2}\right)n' - \left(\frac{\nu_e nk}{m_e\omega_{ce}^2}\right)T_e' - \left(\frac{\nu_{ei}nk}{m_e\omega_{ce}^2}\right)T_i' + \left(\frac{e\nu_{en}}{m_e\omega_{ce}^2}\right)nE_r. \qquad (5D24)$$

The coefficients of n' are called *diffusion* coefficients $D_{\perp i}$, $D_{\perp e}$; the coefficients of T_i' and T_e' are called *thermal diffusion* coefficients; and the coefficients of nE_r are called *mobilities* $\mu_{\perp i}$, $\mu_{\perp e}$. (The symbol $\perp$ means perpendicular to the magnetic field.) If we had not assumed zero derivatives in the θ and z directions, additional terms containing those derivatives would appear in these equations.

If the conditions for *ambipolar flow* are met, we can set $u_{ir} = u_{er} \equiv u_r$ and solve Eqs. (5D23) for E_r and u_r, with the result

$$E_r = \frac{m_i\nu_{in}p_i' - m_e\nu_{en}p_e'}{ne(m_i\nu_{in} + m_e\nu_{en})}$$

$$nu_r = -\frac{(\nu_{in}\nu_{en} + \nu_{ie}\nu_{en} + \nu_{ei}\nu_{in})(p_e' + p_i')}{(m_e\omega_{ce}^2\nu_{in} + m_i\omega_{ci}^2\nu_{en})} \qquad (5D25)$$

For a *fully ionized* plasma, $\nu_{in} = \nu_{en} \simeq 0$, the particle flux reduces to

$$nu_r \simeq -\frac{\nu_{ei}(p_e' + p_i')}{m_e\omega_{ce}^2}, \qquad (5D26)$$

For *weakly ionized* plasma, on the other hand, $\nu_{ei} \ll \nu_{in}$, ν_{en}, and

$$nu_r \simeq -\frac{\nu_{in}\nu_{en}(p_e' + p_i')}{(m_e\omega_{ce}^2\nu_{in} + m_i\omega_{ci}^2\nu_{en})}. \qquad (5D27)$$

Coefficients of ambipolar diffusion and thermal diffusion may be identified by writing these equations in terms of n', T_e', and T_i', as before. (These equations would be modified if a more accurate expression were used for $\vec{R}_{ei}$.)

We can find the particle fluxes in the θ and z directions in a similar manner. Then the particle fluxes can be written as vector equations with tensor coefficients multiplying the gradients of density, temperature, and electrostatic potential. Similar expressions can also be derived for the heat fluxes $\vec{q}_i$ and $\vec{q}_e$. Since the current density $\vec{J} = ne(\vec{u}_i - \vec{u}_e)$, it can be written in terms of the gradients once $n\vec{u}_i$ and $n\vec{u}_e$ are known. The coefficients relating heat fluxes to temperature gradients are called *thermal conductivities* $\underline{\chi}$, and the coefficient relating $\vec{J}$ to $\vec{E}$ is called *conductivity* $\underline{\sigma}$. Thus,

$$\vec{J} = \underline{\sigma}\vec{E} + (\text{other terms})$$

$$\vec{q}_e = -\underline{\chi}_e \vec{\nabla} T_e + (\text{other terms})$$

$$\vec{q}_i = -\underline{\chi}_i \vec{\nabla} T_i + (\text{other terms}) \quad . \tag{5D28}$$

For example, the *classical* thermal conductivities perpendicular to B (due to Coulomb collisions only) are

$$\chi_{\perp i} \simeq \frac{\sqrt{2}nk^2(m_e m_i)^{1/2} T_e^{3/2} \nu_{ei}}{e^2 B^2 T_i^{1/2}}$$

$$\chi_{\perp e} \simeq 3\chi_{\perp i}(m_e T_i / m_i T_e)^{\frac{1}{2}} \sim nkD_{\perp e} \tag{5D29}$$

and $\sigma_\perp = 1/\eta_\perp$ (Eq. 5D10). Details of classical transport coefficients are reviewed by Braginskii (1965).

The classical estimates of radial transport due to collisions represent the *minimum* possible rates. Effects of magnetic curvature, MHD instabilities, and wave-particle interactions (microinstabilities) often increase the transport rates far above these values (Chapter 8). The main points to be made here are

* It is convenient to express particle fluxes, heat fluxes, and current density in terms of gradients of density, temperatures, and electrostatic potential multiplied by transport coefficients.

* The transport coefficients can be found by procedures similar to those used in deriving Eqs. (5D24), or directly from kinetic theory.

EXAMPLE PROBLEM 5D2

Consider a long, cylindrical hydrogen plasma in an axial magnetic field $B = 0.5$ T, with plasma radius $a = 0.05$ m, density distribution $n(r) = n_0(1 - .9r^2/a^2)$, $n_0 = 10^{17} m^{-3}$, uniform $T_e = 10$ eV, $T_i = 5$ eV. Assume $\nu_{in}/\nu_{en} \simeq (m_e/m_i)^{\frac{1}{2}}$, $\nu_{en} \simeq (2\times10^{-13} m^3 s^{-1}) n_n$, and that diffusion is ambipolar. Estimate the radial electric field and particle flux at $r = a$ (a) if $n_n = 10^{19}\ m^{-3}$, (b) if $n_n = 10^{15}\ m^{-3}$.

The pressure gradients at r = a are:
$p_e' = kT_e n' = -kT_e n_0(1.8r/a^2) = -5.77\ J/m^4$, $p_i' = -2.88\ J/m^4$. At r = a, $n = 10^{16} m^{-3}$
From Eq. (2E57), taking $L \simeq 18$, $\nu_{ei} = 6.7\times10^{-17} nL/T_{ek}^{3/2} \simeq 1.2\times10^4$, $\nu_{ie} \simeq 6.7\ s^{-1}$.

From Eqs. (5D20), $\omega_{ce} = 8.79\times10^{10}$ rads/s, $\omega_{ci} = 4.80\times10^{7}$ rad/s.
(a) $\nu_{en} = 2\times10^{6}\ s^{-1}$, $\nu_{in} = 4.67\times10^{4}\ s^{-1}$.
From Eqs. (5D25), $E_r \simeq 1700$ V/m, $nu_r \simeq 2.0\times10^{15}$ ions/m^{2}s (or electrons/m^{2}s).
(b) $\nu_{en} = 200\ s^{-1}$, $\nu_{in} = 4.7\ s^{-1}$.
From Eqs. (5D25), $E_r \simeq 1700$ V/m, $nu_r \simeq 1.2\times10^{13}$ ions/m^{2}s (or electrons/m^{2}s).
If we had used the approximate equations (5D27) and (5D26) for parts (a) and (b), we would have found $nu_r = 2.4\times10^{15}$ and 1.2×10^{13} m^{-2}s^{-1}, respectively.

Boltzmann relation

At high temperatures, the plasma is nearly collisionless. High thermal conductivity and rapid electron flow tend to make T_e uniform along magnetic field lines, establishing equilibrium quickly. Assuming that condition (5D12) is satisfied, the electron momentum conservation equation (5D5) component along the magnetic field reduces to

$$-kT_e(\partial n/\partial z) + ne(\partial\phi/\partial z) = 0.$$

where $n \equiv n_e$. If we choose $\phi = \phi_0$ where $n = n_0$, the result of integration is

$$\ln(n/n_0) = e(\phi-\phi_0)/kT_e,\quad n/n_0 = \exp[e(\phi-\phi_0)/kT_e] \quad . \tag{5D30}$$

Thus, the potential will tend to be high in regions where the density is high, and vice versa.

MHD equations

So far we have considered the ions and electrons as separate fluids. Treating the plasma as a *single fluid* results in somewhat simpler equations. Assuming that $n_i = n_e \equiv n$, we can define a mass density, average velocity, and pressure of the fluid as a whole:

$$\rho_m \equiv n_i m_i + n_e m_e = n(m_i + m_e) \simeq nm_i \tag{5D31}$$

$$\vec{u} \equiv (n_i m_i \vec{u}_i + n_e m_e \vec{u}_e)/\rho_m = (m_i u_i + m_e u_e)/(m_i + m_e) \simeq u_i + (m_e/m_i)u_e \tag{5D32}$$

since $m_e \ll m_i$, and

$$p \equiv p_e + p_i \quad . \tag{5D33}$$

We will assume that the plasma is *fully ionized*, so that terms containing ν_{en}, ν_{in}, and n_n drop out of the two-fluid equations. The single-fluid equations are derived by taking various sums and differences of the two-fluid equations. To obtain an equation relating $\vec{E}$ to $\vec{J} \equiv ne(\vec{u}_i - \vec{u}_e)$, we can multiply (5D4) by m_e, (5D5) by m_i, and subtract (5D5) from (5D4) to get

$$nm_e m_i(\partial\vec{u}_i/\partial t - \partial\vec{u}_e/\partial t) = \underline{nm_e e\vec{E}} + nm_i e\vec{E} + ne(m_e\vec{u}_i + m_i\vec{u}_e)x\vec{B}$$
$$- \underline{m_e\vec{\nabla}p_i} + m_i\vec{\nabla}p_e - \underline{(m_e} + m_i)n_e e(\eta_{\parallel}\vec{J}_{\parallel} + \eta_{\perp}\vec{J}_{\perp}) \qquad (5D34)$$

Since $m_e << m_i$, the underlined terms may be discarded. The magnetic field term may be rearranged by adding and subtracting $m_e\vec{u}_e$ and $m_i\vec{u}_i$:

$$ne(m_e\vec{u}_i + m_i\vec{u}_e)x\vec{B} = ne(m_e\vec{u}_i + m_i\vec{u}_e + m_i\vec{u}_i - m_i\vec{u}_i + m_e\vec{u}_e - m_e\vec{u}_e)x\vec{B}$$
$$= ne\Big[\underline{m_e(\vec{u}_i-\vec{u}_e)} - m_i(\vec{u}_i - \vec{u}_e) + (m_i\vec{u}_i + m_e\vec{u}_e)\Big]\ x\vec{B}$$
$$\simeq - m_i\vec{J}x\vec{B} + e\rho_m\vec{u}x\vec{B} \qquad (5D35)$$

where the underlined term is negligibly small.

Assuming the density to be slowly-varying,

$$\partial\vec{J}/\partial t = \frac{\partial(ne\vec{u}_i - ne\vec{u}_e)}{\partial t} \simeq ne(\partial\vec{u}_i/\partial t - \partial\vec{u}_e/\partial t). \qquad (5D36)$$

Dividing (5D34) by $nm_i e$, and using (5D35), (5D36), the result is

$$(m_e/ne^2)(\partial\vec{J}/\partial t) = \vec{E} + \vec{u}x\vec{B} - (\eta_{\parallel}\vec{J}_{\parallel} + \eta_{\perp}\vec{J}_{\perp}) + (\vec{\nabla}p_e - \vec{J}x\vec{B})/ne \quad . \qquad (5D37)$$

The $(\partial\vec{J}/\partial t)$, $\vec{\nabla}p_e$, and $\vec{J}x\vec{B}$ terms can often be discarded, when n, $\vec{u}$, and gradient scale lengths are large (discussed by Krall and Trivelpiece, 1973), so that (5D37) simplifies to

$$\vec{E} + \vec{u}x\vec{B} - (\eta_{\parallel}\vec{J}_{\parallel} + \eta_{\perp}\vec{J}_{\perp}) \simeq 0 \qquad (5D38)$$

The voltage drop per unit length along $\vec{B}$ equals the resistivity times the current density, which is reminiscent of Ohm's Law, so Eq. (5D38) is called the *generalized Ohm's Law.*

An *equation of motion* can be derived by multiplying Eqs. (5D4) and (5D5) by n, adding them together, dropping the electron inertia term, and using $(\vec{u}_i\cdot\vec{\nabla})\vec{u}_i \simeq (\vec{u}\cdot\vec{\nabla})\vec{u}$, to obtain

$$\rho_m(\partial\vec{u}/\partial t) + \rho_m(\vec{u}\cdot\vec{\nabla})\vec{u} = \vec{J}x\vec{B} - \vec{\nabla}p. \qquad (5D39)$$

A *mass conservation equation* is found by multiplying (5D1) by m_i, (5D2) by m_e, and adding them together

$$\partial\rho_m/\partial t + \vec{\nabla}\cdot(\rho_m\vec{u}) = 0 \quad , \qquad (5D40)$$

assuming recombination is negligible and n_n very small. From combination of Eqs. (5D16) we can derive an *energy conservation equation*

$$\Big[\partial/\partial t + (\vec{u}\cdot\vec{\nabla})\Big]\ (p/\rho_m^{\gamma}) = 0, \qquad p/\rho_m^{\gamma} = \text{constant} \qquad (5D41)$$

(5D38)-(5D41) together with the Maxwell Eqs. (5B7) and (5B8) form a complete set of *magnetohydrodynamic (MHD) equations* for the unknowns $\vec{J}$, $\vec{u}$, p, ρ_m, $\vec{E}$ and $\vec{B}$. The other two Maxwell Equations (5B5) and (5B6) are not needed.

The Maxwell Eq. (5B5) can be derived by taking the divergence of (5B8) and using (5D18); and (5B6) can be derived from the divergence of (5B7). Although Eqs. (5B5) and (5B6) are superfluous, they are often useful.

EXAMPLE PROBLEM 5D3

Find u_r and the effective diffusion coefficient for a steady-state, fully-ionized cylindrical plasma, as in example problem 5D2.

Ignoring the inertia term $(\vec{u}\cdot\vec{\nabla})\vec{u}$ in the equation of motion, and using Ohm's Law to eliminate $\vec{J}_\perp$, we find

$$\frac{\vec{E}\times\vec{B} + (\vec{u}\times\vec{B})\times B}{\eta_\perp} = \vec{\nabla}p \quad . \tag{5D42}$$

With the aid of vector identities, this may be written

$$\vec{E}\times\vec{B} - B^2\vec{u} + \vec{B}(\vec{B}\cdot\vec{u}) = \eta_\perp \nabla p \quad . \tag{5D43}$$

The radial component of this equation in cylindrical geometry is

$$E_\theta B - B^2 u_r = \eta_\perp (dp/dr), \tag{5D44}$$

from which

$$u_r = \frac{E_\theta}{B} - \frac{\eta_\perp}{B^2}\frac{dp}{dr} = \frac{E_\theta}{B} - \frac{m_e\nu_{ei}}{ne^2B}\frac{dp}{dr} = \frac{E_\theta}{B} - \frac{\nu_{ei}}{nm_e\omega_{ce}^2}\frac{dp}{dr} \quad , \quad D = \frac{\nu_{ei}kT}{m_e\omega_{ce}^2} \quad . \tag{5D45}$$

If derivatives are zero in the θ direction, then $E_\theta = 0$, and this result is identical to Eq. (5D26). The E_θ term was retained to show the potential effects of oscillating E_θ caused by drift waves (Section 8E) on radial particle losses.

The plasma motion is strongly affected by wave-particle interactions, with the effective diffusion rates frequently being much larger than the classical values derived here.

5E. Plasma Waves

cold plasma model

The wave equation is derived by taking the curl of Eq. (5B7) and eliminating $\vec{B}$ with (5B8):

$$\vec{\nabla}\times(\vec{\nabla}\times\vec{E}) = -\vec{\nabla}\times(\partial\vec{B}/\partial t) = -(\partial/\partial t)(\vec{\nabla}\times\vec{B})$$

$$\vec{\nabla}\times(\vec{\nabla}\times\vec{E}) = -(\partial/\partial t)[\mu_0\epsilon_0(\partial\vec{E}/\partial t) + \mu_0\vec{J}] \qquad (5E1)$$

To proceed further, we need a relation between $\vec{J}$ and $\vec{E}$, which involves solving either the Boltzmann equation or the fluid equations of motion. In general, $\vec{J}$ is equal to an integral over space and time of a function of $\vec{E}$.

The simplest model uses the fluid equations without the $(\vec{u}\cdot\vec{\nabla})\vec{u}$ (inertia) terms, pressure-gradient terms, or collision terms. In this case $\vec{J}$ varies linearly with $\vec{E}$, which greatly simplifies the analysis. Since setting the temperatures equal to zero would drop out the pressure gradient terms, this model is called the *cold plasma model*. While this model does not describe phenomena such as sound waves, particle bunching, collisionless damping of waves, or plasma shock waves, it correctly describes many of the common small-amplitude perturbations which occur in hot plasmas.

We will assume that the perturbations of $\vec{B}$ caused by plasma currents are negligible, and that

$$\vec{u}_i(\vec{x},t) = \vec{u}_i(\vec{k},\omega)\exp(i\vec{k}\cdot\vec{x}-i\omega t)$$

$$\vec{u}_e(\vec{x},t) = \vec{u}_e(\vec{k},\omega)\exp(i\vec{k}\cdot\vec{x}-i\omega t)$$

$$\vec{E}(\vec{x},t) = \vec{E}(\vec{k},\omega)\exp(i\vec{k}\cdot\vec{x}-i\omega t) \qquad (5E2)$$

where $i = (-1)^{\frac{1}{2}}$, ω is an angular wave frequency (rad/s), $\vec{k}$ is a *wave propagation vector* pointing in the direction of wave propagation and having magnitude $k = 2\pi/\lambda$, and λ is the wavelength. Since

$$\exp(i\vec{k}\cdot\vec{x}-i\omega t) = \cos(\vec{k}\cdot\vec{x}-\omega t) + i\sin(\vec{k}\cdot\vec{x}-\omega t) \qquad (5E3)$$

these equations represent sinusoidal waves. The vector dot product $\vec{k}\cdot\vec{x} = k_x x + k_y y + k_z z$. At a given time, $\vec{u}_i$, $\vec{u}_e$, and $\vec{E}$ vary sinusoidally with x, y, and z; and at a given position, they vary sinusoidally with time. The assumptions (5E2) simplify time derivatives and spatial derivatives. For example, $\partial\vec{u}_i/\partial t = -i\omega\vec{u}_i(\vec{k},\omega)$. [A more rigorous treatment would use Fourier transforms instead of assumptions (5E2).]

After dividing by m_i, the three components of the ion momentum conservation equation (5D4) may be written

$$-i\omega u_{ix} = eE_x/m_i + \omega_{ci}u_{iy}$$
$$-i\omega u_{iy} = eE_y/m_i - \omega_{ci}u_{ix}$$
$$-i\omega u_{iz} = eE_z/m_i \qquad (5E4)$$

where $\omega_{ci} \equiv eB/m_i$ is the *ion cyclotron frequency* (rad/s), and the z axis is taken to be in the direction of $\vec{B}$. Similarly, the components of the electron momentum conservation equation (5D5) are

$$\begin{aligned} -i\omega u_{ex} &= -eE_x/m_e - \omega_{ce}u_{ey} \\ -i\omega u_{ey} &= -eE_y/m_e + \omega_{ce}u_{ex} \\ -i\omega u_{ez} &= -eE_z/m_e \end{aligned} \tag{5E5}$$

where $\omega_{ce} \equiv eB/m_e$ is the *electron cyclotron frequency* (rad/s). The solutions of Eqs. (5E4) and (5E5) are:

$$u_{ix} = \frac{i\omega eE_x/m_i - e\omega_{ci}E_y/m_i}{\omega^2 - \omega_{ci}^2} \quad , \quad u_{ex} = \frac{-i\omega eE_x/m_e - e\omega_{ce}E_y/m_e}{\omega^2 - \omega_{ce}^2} \quad ,$$

$$u_{iy} = \frac{i\omega eE_y/m_i + e\omega_{ci}E_x/m_i}{\omega^2 - \omega_{ci}^2} \quad , \quad u_{ey} = \frac{-i\omega eE_y/m_e + e\omega_{ce}E_x/m_e}{\omega^2 - \omega_{ce}^2} \quad ,$$

$$u_{iz} = ieE_z/m_i\omega \quad , \qquad u_{ez} = -ieE_z/m_e\omega \quad . \tag{5E6}$$

Assuming $n_i = n_e \equiv n$, the components of the current density $\vec{J} = ne\vec{u}_i - ne\vec{u}_e$ are found to be

$$J_x = i\omega\varepsilon_0\left(\frac{\omega_{pi}^2}{\omega^2-\omega_{ci}^2} + \frac{\omega_{pe}^2}{\omega^2-\omega_{ce}^2}\right)E_x + \varepsilon_0\left(\frac{-\omega_{ci}\omega_{pi}^2}{\omega^2-\omega_{ci}^2} + \frac{\omega_{ce}\omega_{pe}^2}{\omega^2-\omega_{ce}^2}\right)E_y$$

$$J_y = \varepsilon_0\left(\frac{\omega_{ci}\omega_{pi}^2}{\omega^2-\omega_{ci}^2} - \frac{\omega_{ce}\omega_{pe}^2}{\omega^2-\omega_{ce}^2}\right)E_x + i\omega\varepsilon_0\left(\frac{\omega_{pi}^2}{\omega^2-\omega_{ci}^2} + \frac{\omega_{pe}^2}{\omega^2-\omega_{ce}^2}\right)E_y$$

$$J_z = i\varepsilon_0\left(\frac{\omega_{pi}^2}{\omega} + \frac{\omega_{pe}^2}{\omega}\right)E_z \tag{5E7}$$

where

$$\omega_{pi}^2 \equiv ne^2/m_i\varepsilon_0$$

$$\omega_{pe}^2 \equiv ne^2/m_e\varepsilon_0 \qquad (\omega_{pe} \simeq 56.4n^{\frac{1}{2}}\ \text{rad/s}) \tag{5E8}$$

are the ion and electron *plasma frequencies* (to be discussed later). Eqs. (5E7) have the form

$$\begin{aligned} J_x &= \sigma_{xx}E_x + \sigma_{xy}E_y + \sigma_{xz}E_z \\ J_y &= \sigma_{yx}E_x + \sigma_{yy}E_y + \sigma_{yz}E_z \\ J_z &= \sigma_{zx}E_x + \sigma_{zy}E_y + \sigma_{zz}E_z \quad , \end{aligned} \tag{5E9}$$

which may be written in matrix form as

$$\begin{bmatrix} J_x \\ J_y \\ J_z \end{bmatrix} = \begin{bmatrix} \sigma_{xx} & \sigma_{xy} & \sigma_{xz} \\ \sigma_{yx} & \sigma_{yy} & \sigma_{yz} \\ \sigma_{zx} & \sigma_{zy} & \sigma_{zz} \end{bmatrix} \begin{bmatrix} E_x \\ E_y \\ E_z \end{bmatrix}$$

($\sigma_{xz} = \sigma_{yz} = \sigma_{zx} = \sigma_{zy} = 0$). This equation may be abbreviated as

$$\vec{J} = \underline{\underline{\sigma}}\,\vec{E} \tag{5E10}$$

where $\underline{\underline{\sigma}}$ is called the *conductivity tensor*. Assuming that $\underline{\underline{\sigma}}$ is constant, $\partial\vec{J}/\partial t = \underline{\underline{\sigma}}(\partial\vec{E}/\partial t)$, and the wave equation (5E1) becomes

$$\vec{\nabla}\times(\vec{\nabla}\times E) = -\mu_0\varepsilon_0(\partial^2\vec{E}/\partial t^2) - \mu_0\,\underline{\underline{\sigma}}(\partial\vec{E}/\partial t)\ . \tag{5E11}$$

EXAMPLE PROBLEM 5E1

Show that, for E given by Eq. (5E2), $\vec{\nabla}\times\vec{E} = i\vec{k}\times\vec{E}$.

Consider the y component of the vector equation in Cartesian coordinates:

$$(\vec{\nabla}\times\vec{E})_y = (\partial/\partial z)E_x\exp(i\vec{k}\cdot\vec{x}-i\omega t) - (\partial/\partial x)E_z\exp(i\vec{k}\cdot\vec{x}-i\omega t)$$

Since $i\vec{k}\cdot\vec{x} = ik_x x + ik_y y + ik_z z$, this becomes

$$(\vec{\nabla}\times\vec{E})_y = ik_z E_x\exp(i\vec{k}\cdot\vec{x}-i\omega t) - ik_x E_z\exp(i\vec{k}\cdot\vec{x}-i\omega t)$$

where E_x and E_z are functions of $\vec{k}$ and ω, but not of $\vec{x}$ and t. The y component of $\vec{k}\times\vec{E}$ is

$$(\vec{k}\times\vec{E})_y = k_z E_x\exp(i\vec{k}\cdot\vec{x}-i\omega t) - k_x E_z\exp(i\vec{k}\cdot\vec{x}-i\omega t).$$

Therefore, $(\vec{\nabla}\times\vec{E})_y = i(\vec{k}\times\vec{E})_y$, and likewise for the x and z components.

In a similar fashion, we can show that $\partial\vec{E}/\partial t = -i\omega\vec{E}$ and $\partial^2\vec{E}/\partial t^2 = -\omega^2\vec{E}$. After inserting Eq. (5E2) into Eq. (5E11) and using these simplifications, we obtain

$$-\vec{k}\times(\vec{k}\times\vec{E}) = \mu_0\varepsilon_0\omega^2\vec{E} + i\mu_0\omega\underline{\underline{\sigma}}\,\vec{E} = \omega^2\mu_0\varepsilon_0\left(1 + \frac{i\underline{\underline{\sigma}}}{\omega\varepsilon_0}\right)\vec{E}. \tag{5E12}$$

It is convenient to define a *dielectric tensor* $\underline{\underline{\varepsilon}}$ equal to the quantity in parentheses:

$$\underline{\underline{\varepsilon}} \equiv \begin{bmatrix} i\sigma_{xx}/\omega\varepsilon_0 + 1 & i\sigma_{xy}/\omega\varepsilon_0 & i\sigma_{xz}/\omega\varepsilon_0 \\ i\sigma_{yx}/\omega\varepsilon_0 & i\sigma_{yy}/\omega\varepsilon_0 + 1 & i\sigma_{yz}/\omega\varepsilon_0 \\ i\sigma_{zx}/\omega\varepsilon_0 & i\sigma_{zy}/\omega\varepsilon_0 & i\sigma_{zz}/\omega\varepsilon_0 + 1 \end{bmatrix} \tag{5E13}$$

Since $\mu_0\varepsilon_0 = c^{-2}$, where c is the speed of light, Eq. (5E12) may be written

$$\vec{k}\times(\vec{k}\times\vec{E}) + (\omega^2/c^2)\underline{\underline{\varepsilon}}\vec{E} = 0,$$

or, using a vector identity (App. F) for the vector cross products

$$-k^2\vec{E} + \vec{k}(\vec{k}\cdot\vec{E}) + (\omega^2/c^2)\,\underline{\underline{\varepsilon}}\vec{E} = 0. \tag{5E14}$$

From comparison of Eqs. (5E7) and (5E8) we can determine the components of $\underline{\underline{\sigma}}$, and then use them in Eq. (5E13) to determine the components of $\underline{\underline{\varepsilon}}$. The result may be written in the form

$$\underline{\underline{\varepsilon}} = \begin{bmatrix} \varepsilon_1 & i\varepsilon_2 & 0 \\ -i\varepsilon_2 & \varepsilon_1 & 0 \\ 0 & 0 & \varepsilon_3 \end{bmatrix} \tag{5E15}$$

where

$$\varepsilon_1 = 1 - \frac{\omega_{pi}^2}{\omega^2-\omega_{ci}^2} - \frac{\omega_{pe}^2}{\omega^2-\omega_{ce}^2} \tag{5E16}$$

$$\varepsilon_2 = -\frac{\omega_{ci}\,\omega_{pi}^2}{\omega(\omega^2-\omega_{ci}^2)} + \frac{\omega_{ce}\omega_{pe}^2}{\omega(\omega^2-\omega_{ce}^2)} \tag{5E17}$$

$$\varepsilon_3 = 1 - \frac{\omega_{pi}^2+\omega_{pe}^2}{\omega^2} \tag{5E18}$$

dispersion relation

We can choose the direction of the x axis so that $\vec{k}$ lies in the xz plane. Let θ be the angle between the wave propagation direction $\vec{k}$ and the magnetic field $\vec{B}$ (Fig. 5E1). Then $k_x = k\sin\theta$, $k_y = 0$, and $k_z = k\cos\theta$. The components of the wave equation (5E14) are:

$$\begin{aligned} &\left[-k^2\cos^2\theta + (\omega^2/c^2)\varepsilon_1\right]E_x + i(\omega^2/c^2)\varepsilon_2 E_y + k^2\sin\theta\cos\theta E_z = 0 \\ &-i(\omega^2/c^2)\varepsilon_2 E_x + \left[(\omega^2/c^2)\varepsilon_1 - k^2\right]E_y = 0 \\ &k^2\sin\theta\cos\theta E_x + \left[-k^2\sin^2\theta + (\omega^2/c^2)\varepsilon_3\right]E_z = 0. \end{aligned} \tag{5E19}$$

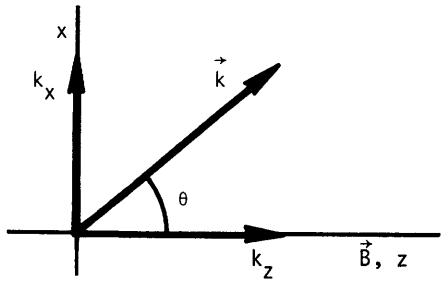

Fig. 5E1. Components of the wave propagation vector $\vec{k}$.

If we multiply these equations by (c^2/ω^2) and define the *refractive index*

$$\tilde{n} \equiv kc/\omega \tag{5E20}$$

then the equations may be written in matrix form as

$$\begin{bmatrix} \varepsilon_1-\tilde{n}^2\cos^2\theta & i\varepsilon_2 & \tilde{n}^2\sin\theta\cos\theta \\ -i\varepsilon_2 & \varepsilon_1-\tilde{n}^2 & 0 \\ \tilde{n}^2\sin\theta\cos\theta & 0 & \varepsilon_3-\tilde{n}^2\sin^2\theta \end{bmatrix} \begin{bmatrix} E_x \\ E_y \\ E_z \end{bmatrix} = 0 \tag{5E21}$$

In order for the equations to have a nontrivial solution, the determinant of the coefficient matrix must equal zero. Setting the determinant equal to zero yields a quadratic equation for $\tilde{n}^2$:

$$(\varepsilon_1\sin^2\theta+\varepsilon_3\cos^2\theta)\tilde{n}^4 - (\varepsilon_1\varepsilon_3 + \varepsilon_1^2\sin^2\theta + \varepsilon_1\varepsilon_3\cos^2\theta - \varepsilon_2^2\sin^2\theta)\tilde{n}^2$$

$$+ (\varepsilon_1^2\varepsilon_3 - \varepsilon_2^2\varepsilon_3) = 0 \quad . \tag{5E22}$$

The roots of this equation, called the *cold plasma dispersion relation*, express (k^2c^2/ω^2) as functions of ω, ω_{pi}, ω_{pe}, ω_{ci}, ω_{ci}, and θ.

The wave equation was derived from two of Maxwell's equations. The assumption of sinusoidally-varying $\vec{E}$ and $\vec{u}$ reduced the differential equations to algebraic equations. The momentum conservation equations were used to relate $\vec{J}$ to $\vec{E}$ and evaluate the components of $\underline{\underline{\sigma}}$ and $\underline{\underline{\varepsilon}}$. Then the three components of the wave equation were written in matrix form, and equating the determinant of the coefficient matrix to zero yielded an equation relating k to ω.

More accurate dispersion relations can be derived by keeping the pressure gradient and collision terms in Eqs. (5D4) and (5D5), or using the Boltzmann equation to relate $\vec{J}$ to $\vec{E}$. The kinetic theory technique is most accurate, but most complex, because $\vec{J}$ involves integrals of the distribution functions.

The remaining task is to try to make sense out of the dispersion relation. Some questions we might ask about plasma waves include:

* In what directions do they travel?
* How fast do they travel?
* Does their amplitude increase or decrease?
* Are they absorbed or reflected by the plasma?
* What types of waves exist in plasmas?
* How do the waves interact with particles and with each other?

The answers to these questions strongly influence the prospects for success of plasma confinement and heating techniques. We will discuss them in order.

Various waves can propagate in many directions at once. Each possible direction $\vec{k}$ at an angle θ relative to $\vec{B}$ has its own unique set of characteristics specified by the dispersion relation. Waves may be bent (diffracted) as they pass through plasma, just as light waves are diffracted in glass and water. Sometimes elaborate ray-tracing computations are needed to determine the paths of

microwaves incident on a plasma.

phase and group velocities

There are two velocities associated with plasma waves, as illustrated in Fig. 5E2. The motion of point A, located at the position cosine $(60^{o}) = \frac{1}{2}$ on the sinusoidal wave, is described by the real part of Eq. (5E4) for a one-dimensional case:

$$\cos(kx-\omega t) = \tfrac{1}{2}$$

As time passes, point A of the wave electric field moves so that $kx-\omega t$ = constant $= \pi/3$, or $x = (\pi/3 + \omega t)/k$. The "phase" of point A is $\pi/3$, and the velocity of point A is

$$v_{\phi} = dx/dt = \omega/k \ . \qquad (5E23)$$

Similarly, points with other phases would also move at velocity v_{ϕ}, which is called the *phase velocity*. This is the velocity at which ripples of the electric field move through the plasma; it is not the velocity of electron or ion motion. The particle velocities can never exceed the speed of light c, but the phase velocity of a plasma wave can. This does not mean that we could use plasma for communications exceeding the speed of light. Communications rely on the modulation of the amplitude of the wave, as indicated by the dashed curve in Fig. 5E1; and the envelope of the modulation may move at a much slower velocity than the phase velocity, never exceeding the speed of light. The velocity of the modulation envelope is called the *group velocity* v_g. During the time that point A moves a large distance, point B on the envelope of modulation only moves a short distance. The group velocity is related to ω and k by

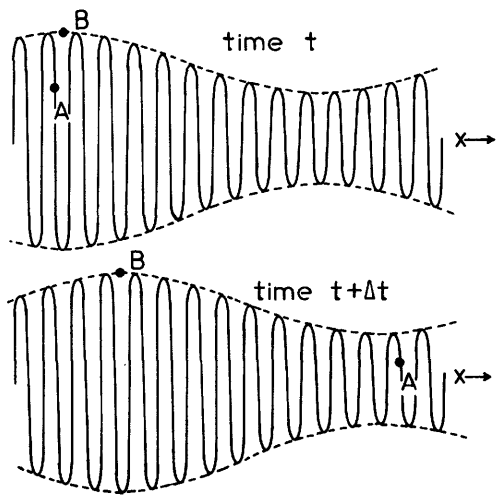

Fig. 5E2. Wave electric field amplitude vs. x at time t and at a later time t+Δt. Point A moves at the phase velocity, while point B on the envelope of modulation moves at the group velocity.

$$v_g = \partial\omega/\partial k. \qquad (5E24)$$

For any given set of plasma conditions, we can find v_{ϕ} and v_g from the dispersion relation.

wave growth and damping

The plasma may act upon the wave to amplify it (increase its amplitude) or damp it (decrease the amplitude). Either the frequency ω or the wave propagation vector $\vec{k}$ may be represented as complex numbers, having both real and imaginary parts, which can be determined from the roots of the dispersion relation. For example, let the real and imaginary parts of ω be designated ω_r and γ. Then

$$\omega = \omega_r + i\gamma \ . \qquad (5E25)$$

Inserting this into Eq. (5E3), we have

$$\vec{E}(\vec{x},t) = \vec{E}(\vec{k},\omega)\exp(i\vec{k}\cdot\vec{x} - i\omega_r t + \gamma t). \tag{5E26}$$

If $\gamma > 0$, the wave grows exponentially in time (instability), while for $\gamma < 0$ the wave damps exponentially. Similarly, the imaginary part of k leads to spatial growth or damping. Momentum-transfer collisions (ignored in the cold-plasma model) cause damping.

cutoffs and resonances

At *cutoff* frequencies, $\tilde{n} = kc/\omega \to 0$ in Eq. (5E22), and the wave cannot propagate. For a given species of ion, ω_{ci} and ω_{ce} depend only on B; and ω_{pi} and ω_{pe} depend only on plasma density n. Therefore, the frequencies at which cutoff occurs are functions of n, B, and direction angle θ. For example, a wave incident on a high density plasma may be cutoff (and reflected) at the place where the plasma density exceeds a certain critical value (the cutoff density n_c). Cutoff is observed in radio wave propagation around the earth (reflection by the ionospheric plasma), in plasma diagnostics, and in the interaction of laser beams with target pellets.

At *resonance* frequencies, $\tilde{n} = kc/\omega \to \infty$ in Eq. (5E22), both $v_\phi \to 0$ and $v_g \to 0$. The wave energy is generally absorbed at a resonance, so resonances are useful in plasma heating. For example, electrons and ions tend to spiral around magnetic fields with angular frequencies of rotation ω_{ce} and ω_{ci}. If microwaves or radiowaves are incident at these frequencies, then the particles will be accelerated by the waves, as in a cyclotron. If the energy is thermalized by collisions or wave-particle interactions, then plasma heating results.

Waves are classified as *longitudinal* if the oscillating electric field is parallel to the direction of propagation ($\vec{E} \parallel \vec{k}$) or *transverse* if the electric field of the wave is perpendicular to the direction of propagation ($\vec{E} \perp \vec{k}$). Longitudinal waves are *electrostatic*, involving only the electric field, while transverse waves are *electromagnetic*, involving an oscillatory magnetic field as well. In general, a wave propagates at an angle θ relative to B (Fig. 5E1). We will consider the special limiting cases $\theta = 0$ and $\theta = \pi/2$.

propagation along $\vec{B}$

For the case of propagation along $\vec{B}$ ($\theta = 0$), the dispersion relation (5E22) reduces to

$$\varepsilon_3(\tilde{n}^4 - 2\varepsilon_1\tilde{n}^2 + \varepsilon_1^2 - \varepsilon_2^2) = 0$$

with possible solutions $\varepsilon_3 = 0$ and $\tilde{n}^2 = \varepsilon_1 \pm \varepsilon_2$. The first case $\varepsilon_3 = 0$ yields

$$\omega^2 = \omega_{pi}^2 + \omega_{pe}^2 \simeq \omega_{pe}^2 \quad . \tag{5E27}$$

These are oscillations at the electron plasma frequency. From the wave Eq. (5E19) it can be shown that $E_x = E_y = 0$ for this mode, so the electric field is in the z direction, as is $\vec{k}$. [If the $\vec{\nabla}p_e$ term is retained in the equation of motion, a more accurate dispersion relation $\omega^2 = \omega_{pe}^2 + \gamma_e k^2(kT_e/m_e)$ is obtained, giving

finite v_ϕ and v_g.] A simple picture of the origin of these oscillations may be based on Fig. 5E3. Imagine an infinite one-dimensional plasma with fixed ions and mobile electrons. If the electrons were pulled away from the origin a distance z, the positive charge density left behind would create a potential in accordance with the Poisson equation (5B16)

$$d^2\phi/dz^2 = -ne/\epsilon_0 \tag{5E28}$$

where n is the ion density. Integrating once and using the symmetry boundary condition $d\phi/dz = 0$ at $z = 0$ gives

$$d\phi/dz = -nez/\epsilon_0 \tag{5E29}$$

The equation of motion for electrons at position z is

$$m_e d^2z/dt^2 = -eE_z = -ne^2z/\epsilon_0 \tag{5E30}$$

since $E_z = -d\phi/dz$. This may be written in the form

$$d^2z/dt^2 = -\omega_{pe}^2 z \tag{5E31}$$

which has oscillatory solutions of the form $\cos(\omega_{pe}t)$. As the electrons move away, the Coulomb force of the positive ions draws them back. As the electrons rush into the gap, their inertia carries them past the equilibrium position, producing an electric field in the opposite direction. The proportionality of the restoring force $-eE_z$ in (5E30) to the displacement is analogous to the oscillations of a mass m on a spring. According to (5E30), E_z oscillates at the same frequency as the electrons do. These *Langmuir plasma oscillations* are longitudinal waves, having the electric field and particle velocities both parallel to the direction of propagation.

The other roots of the dispersion relation $\tilde{n}^2 = \epsilon_1 \pm \epsilon_2$ yield

$$\frac{k^2c^2}{\omega^2} = 1 - \frac{\omega_{pi}^2}{\omega(\omega-\omega_{ci})} - \frac{\omega_{pe}^2}{\omega(\omega+\omega_{ce})} \quad (R) \tag{5E32}$$

and

$$\frac{k^2c^2}{\omega^2} = 1 - \frac{\omega_{pi}^2}{(\omega+\omega_{ci})} - \frac{\omega_{pe}^2}{(\omega-\omega_{ce})} \quad (L). \tag{5E33}$$

Analysis of the wave equation shows that these waves represent transverse electromagnetic waves, with $E_z = 0$, and E_x and E_y varying sinusoidally in such a way that their sum is a vector rotating at an angular frequency ω. The vector of the right-hand circularly polarized (R) wave rotates in the same direction as the ion motion, hence has a resonance at $\omega = \omega_{ci}$; and the left-hand circularly

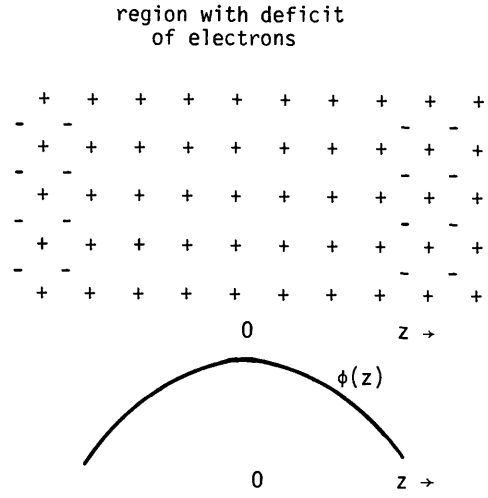

Fig. 5E3. Potential distribution caused by departure of electrons from center of plasma.

polarized (L) wave rotates in the direction of electron motion, and has a resonance at $\omega = \omega_{ce}$. The sum of the two counter-rotating vectors is a plane-polarized wave, with the plane of polarization gradually rotating (Faraday rotation), since the R and L waves propagate at slightly different v_ϕ.

In the low frequency limit ($\omega << \omega_{ci} << \omega_{ce}$), both the R and L waves reduce to

$$\frac{k^2c^2}{\omega^2} \simeq 1 + \frac{nm_i}{\varepsilon_0 B^2} = 1 + \frac{\mu_0 nm_i c^2}{B^2} \equiv 1 + \frac{c^2}{v_A^2} \simeq \frac{c^2}{v_A^2} \qquad (5E34)$$

where $v_A \equiv (B^2/\mu_0 nm_i)^{\frac{1}{2}}$ is the *Alfven velocity*. The phase velocity of Alfven waves is low, due to ion inertia. The ions tied to magnetic field lines act like beads on a string, with B^2 being analogous to tension in the string.

The *ion acoustic wave*, similar to ordinary sound waves, has $\omega/k = c_s \equiv ((kT_e + \gamma_i kT_i)/m_i)^{\frac{1}{2}}$ where c_s is the "ion sound speed". This relation can be derived by keeping the pressure gradient terms in the equations of motion and using the continuity equations for the density.

propagation perpendicular to $\vec{B}$

For the case of propagation across $\vec{B}$ ($\theta = \pi/2$), the dispersion relation (5E22) has the solutions $\tilde{n} = \varepsilon_3$, giving

$$\frac{k^2c^2}{\omega^2} = 1 - \frac{\omega_{pi}^2 + \omega_{pe}^2}{\omega^2} \qquad \text{(ordinary wave)} \qquad (5E35)$$

and $\tilde{n} = (\varepsilon_1 + \varepsilon_2)(\varepsilon_1 - \varepsilon_2)/\varepsilon_1$, giving

$$\frac{k^2c^2}{\omega^2} = \frac{(\omega^2 - \omega_R^2)(\omega^2 - \omega_L^2)}{(\omega^2 - \omega_{LH}^2)(\omega^2 - \omega_U^2)} \qquad \text{(extraordinary wave)} \qquad (5E36)$$

where terms proportional to m_e/m_i have been neglected, and

$$\omega_R \simeq \tfrac{1}{2}\omega_{ce} + (\tfrac{1}{4}\omega_{ce}^2 + \omega_{pe}^2)^{\frac{1}{2}}$$

$$\omega_L \simeq -\tfrac{1}{2}\omega_{ce} + (\tfrac{1}{4}\omega_{ce}^2 + \omega_{pe}^2)^{\frac{1}{2}} \qquad (5E37)$$

$$\omega_{LH}^2 = \left(\frac{1}{\omega_{ci}^2 + \omega_{pi}^2} + \frac{1}{\omega_{ci}\omega_{ce}}\right)^{-1} \qquad \text{(lower hybrid frequency)} \qquad (5E38)$$

$$\omega_U^2 = \omega_{pe}^2 + \omega_{ce}^2 \qquad \text{(upper hybrid frequency)} \qquad (5E39)$$

These waves have $\vec{k}$ in the x direction with $\vec{B}$ in the z direction.

If $\vec{E}$ is parallel to $\vec{B}$, we have the *ordinary wave*, which is unaffected by the magnetic field. This mode is commonly used for microwave interferometer measurements

of plasma density (Chapter 10), but it has a cutoff at $\omega \simeq \omega_{pe}$, and cannot propagate at lower frequencies.

If $\vec{E}$ is in the y direction (perpendicular to $\vec{B}$), then we have the *extraordinary wave*, which has cutoffs at ω_L and ω_R and resonances at the upper and lower hybrid frequencies. The lower hybrid resonance is useful for plasma heating, and has the advantage of a lower frequency than the electron cyclotron frequency ω_{ce}, for which high-power microwave generators are still under development.

EXAMPLE PROBLEM 5E2

Make a phase diagram of ω vs. k for the extraordinary wave in a plasma with $(\omega_{pe}/\omega_{ce}) \sim 1$, and discuss where the waves are cutoff, resonant, $v_\phi \to 0$, $v_\phi \to c$, $v_\phi \to \infty$, $v_g \to 0$, $v_g \to c$, and regions of no propagation.

From (5E37)-(5E39), $\omega_R^2 > \omega_U^2 > \omega_L^2 > \omega_{LH}^2$

We know that $k \to 0$ at ω_1 and ω_2, and that $k \to \infty$ at ω_U and ω_{LH}, and that $\omega/k \to c$ as $\omega \to \infty$. Thus, the plot of Fig. 5E4 is derived. Cutoffs occur at ω_L and ω_R, and resonances at ω_{LH} and ω_U. $v_\phi \to 0$ at resonances; $v_\phi \to c$ at very large ω; and $v_\phi \to \infty$ at cutoffs. $v_g \to 0$ at ω_L and ω_R, and $v_g \to c$ for very large ω. No propagation can occur for $\omega_L < \omega < \omega_L$ and for $\omega_U < \omega < \omega_R$, as $k^2c^2/\omega^2 < 0$ there.

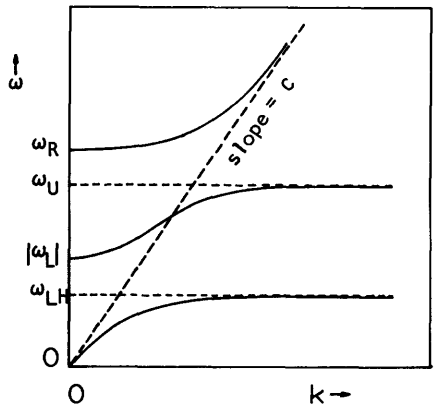

Fig. 5E4. Plot of ω vs. k for the extraordinary mode at $\theta = \pi/2$, assuming $\omega_{pe}/\omega_{ce} \sim 1$. Some waves have $\omega/k > c$, but no wave has $\partial\omega/\partial k > c$.

Propagation at an arbitrary angle θ in an inhomogeneous plasma is more complicated than the simplified cases described here. Wave-particle interactions will be discussed qualitatively in Chapters 8 and 15.

5F. Debye Shielding and Plasma Sheaths

screening of potential from point charge

The electrostatic potential surrounding a point charge q in a vacuum is given by

$$\phi(r) = \frac{q}{4\pi\epsilon_0 r} \tag{5F1}$$

where r is the distance from the charge. In a plasma the situation is changed by the response of the surrounding electrons and ions which tend to group themselves according to the Boltzmann relation (5D21)

$$n_e(r) = n\exp(e\phi/kT_e) \simeq n(1 + e\phi/kT_e + \ldots), \quad e\phi/kT_e \ll 1$$

$$n_i(r) = n\exp(-e\phi/kT_i) \simeq n(1 - e\phi/kT_i + \ldots), \quad e\phi/kT_i \ll 1 \tag{5F2}$$

assuming that the magnitude of the potential is much less than the particle temperatures, and that $\vec{B} = 0$. Let us find the potential $\phi(r)$ caused by a test charge q in a plasma. According to Eq. (5B3) the surrounding charge density is $\rho = e(n_i - n_e)$, so the Poisson Eq. (5B16) in spherical coordinates becomes

$$\frac{1}{r^2}\frac{d^2}{dr^2}(r^2\phi) = \frac{-e}{\epsilon_0}\left[n(1-e\phi/kT_i + \ldots) - n(1 + e\phi/kT_e + \ldots)\right]$$

$$\simeq \frac{2\phi}{\lambda_D^2} \tag{5F3}$$

where

$$\frac{1}{\lambda_D^2} \equiv \frac{ne^2}{2\epsilon_0}\left(\frac{1}{kT_i} + \frac{1}{kT_e}\right) \simeq \frac{ne^2}{\epsilon_0 kT_e}, \ (T_i \simeq T_e), \quad \lambda_D \equiv \textit{Debye Length} \tag{5F4}$$

[If $T_e \gg T_i \simeq 0$, then $n_i \simeq n$, and $\nabla^2\phi \simeq \phi/\lambda_D^2$, where $\lambda_D^2 \equiv \epsilon_0 kT_e/ne^2$.] The boundary conditions are $\phi(r\to 0) = q/4\pi\epsilon_0 r$, and $\phi(r\to\infty) \neq \infty$. Letting $u \equiv r^2\phi$, we have

$$\frac{d^2u}{dr^2} = \frac{2u}{\lambda_D^2} \tag{5F5}$$

with the solution

$$u(r) = C_1\exp(-\sqrt{2}r/\lambda_D) + C_2\exp(\sqrt{2}r/\lambda_D). \tag{5F6}$$

From the second boundary condition, $C_2 = 0$, and from the first, $C_1 = q/4\pi\epsilon_0$; so the electrostatic potential around the test charge q in a plasma is

$$\phi(r) = \frac{q\exp(-\sqrt{2}r/\lambda_D)}{4\pi\epsilon_0 r} \tag{5F7}$$

This is equal to the vacuum potential reduced by the exponential factor, as illustrated in Fig. 5F1. Thus, at distances of a few Debye lengths from the "test charge", its potential is greatly reduced by rearrangement of the surrounding electrons and ions. In order for this Debye shielding effect to occur, there must be many plasma particles in a sphere with radius λ_D;

$$N_D \equiv 4\pi\lambda_D^3 n_0/3 \gg 1 \quad , \qquad N_D = \textit{Debye Number}. \tag{5F8}$$

Lines for $N_D = 1$, 100, and 10^4 are shown in Fig. 5A1. The electron-ion momentum transfer collision frequency may be written in terms of N_D as

$$\nu_{ei}/\omega_{pe} = (2/\pi)^{\frac{1}{2}}\ln(9N_D)/9N_D \tag{5F9}$$

potential variation near wall or probe

For similar reasons, the potential in a plasma near a wall or probe immersed in the plasma varies exponentially, with a scale length $\sim \lambda_D$. In the presence of an electrostatic potential, the Maxwellian distribution function (2A7) may be modified to read

$$f(\vec{x},\vec{v}) = n_0(\beta/\pi)^{3/2}\exp[-\beta v^2 - q(\phi-\phi_0)/kT], \quad (\beta \equiv m/2kT). \tag{5F10}$$

where ϕ_0 is the potential where $n = n_0$. It can be verified by direct substitution that this distribution function satisfies the steady-state Vlasov equation (collisionless Boltzmann Eq. 5C4) for motion along the magnetic field:

$$v_z(\partial f/\partial z) - (q/m)(d\phi/dz)(\partial f/\partial v) = 0 \tag{5F11}$$

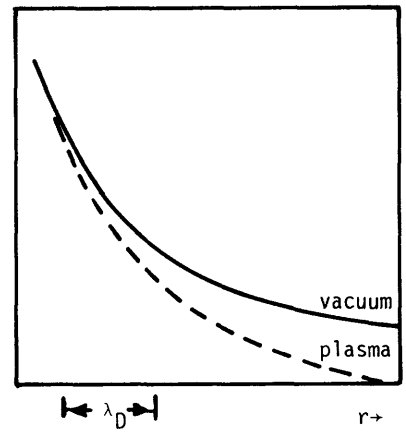

Fig. 5F1. Electrostatic potential due to a hypothetical test charge as a function of distance from that charge in a vacuum and in a plasma. In a plasma the rearrangement of the surrounding charges shields out the potential of the test charge over a distance of a few Debye lengths.

Consider the plasma-wall problem illustrated in Fig. 5F2. Ions stream out of the plasma towards the wall, with particle flux Γ_{i+}. As the ions approach the wall, they fall down a potential hill and are accelerated, but the particle flux remains constant, in accordance with the steady-state collisionless continuity Eq. (5D1), $\vec{\nabla}\cdot(n_i\vec{u}_i) = 0$. Evaluating Γ_{i+} in the plasma where $\phi = \phi_0$, we find

$$\Gamma_{i+} = \int_{v_z>0} d\vec{v}\, f_i(\vec{x},\vec{v})v_z$$

$$= \int_{-\infty}^{\infty} dv_x \int_{-\infty}^{\infty} dv_y \int_0^{\infty} dv_z\, n_0\,(\beta_i/\pi)^{3/2}\exp(-\beta_i(v_x^2 + v_y^2 + v_z^2))\, v_z$$

$$= n_0(kT_i/2\pi m_i)^{\frac{1}{2}} \tag{5F12}$$

The electrons, on the other hand, are repelled by the potential fall near the walls. Evaluating their particle flux at the wall where $\phi = 0$, we find

$$\Gamma_{e+} = \int_{v_z>0} d\vec{v}\, f_e(\vec{x},\vec{v})v_z$$

$$= \int_{-\infty}^{\infty} dv_x \int_{-\infty}^{\infty} dv_y \int_0^{\infty} dv_z\, n_0(\beta_e/\pi)^{3/2}\exp(-\beta_e(v_x^2 + v_y^2 + v_z^2) - e\phi_0/kT_e)v_z$$

$$= n_0(kT_e/2\pi m_e)^{\frac{1}{2}}\exp(-e\phi_0/kT_e). \tag{5F13}$$

The plasma potential adjusts itself so that the electron and ion particle fluxes to the wall are equal:

$$n_0(kT_i/2\pi m_i)^{\frac{1}{2}} = n_0(kT_e/2\pi m_e)^{\frac{1}{2}}\exp(-e\phi_0/kT_e) \quad (5F14)$$

from which the plasma potential ϕ_0 is estimated to be

$$\frac{e\phi_0}{kT_e} \simeq \frac{1}{2}\ln\left(\frac{m_i T_e}{m_e T_i}\right) . \quad (5F15)$$

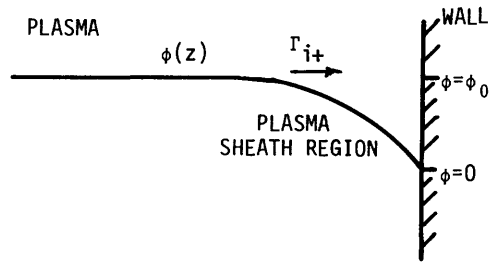

Fig. 5F2. Potential variation near a wall, for the case of motion along the magnetic field or in the absence of a magnetic field. Since electrons have higher thermal velocities, they initially leave the plasma faster, building up a net positive charge and plasma potential.

A more accurate calculation (Emmert et al, 1980) gives

$$\frac{e\phi_0}{kT_e} \simeq 0.37\ln\left(\frac{m_i T_e}{m_e T_i}\right) \quad (5F16)$$

valid if $T_i \gtrsim T_e$. For $T_i < T_e$, Eq. (5F16) overestimates ϕ_0. The maximum value of $e\phi_0/kT_e$, as $T_i \to 0$, is about 3.5 for a hydrogen plasma.

If we take z positive towards the plasma (z = 0 at the wall), then simultaneous solution of the Poisson equation with the equations of motion for ions and electrons yields the approximate potential profile

$$\phi(z) \simeq \phi_0[1 - \exp(-z/\lambda_D)] \quad . \quad (5F17)$$

In deriving this equation it was assumed that $e|\phi-\phi_0|/kT << 1$, so this equation is not valid close to the wall. This roughly exponential variation of potential over a scale length λ_D is similar to that of Eq. (5F7), and is expected for cases with plasma flow along $\vec{B}$ or with $\vec{B} = 0$. However, particle sources (by ionization) change the shape of $\phi(z)$, giving it considerable curvature at large distances from the walls.

Plasma sheaths occur wherever plasma contacts a solid surface, such as a wall or probe. For the case of plasma flow across a strong magnetic field, the ion loss rate tends to be faster than the electron loss rate, which may set up a negative plasma potential and ambipolar electric field (Eq. 5D25). The resultant plasma potential and sheath structure depend upon a balance between flow rates along $\vec{B}$ and across $\vec{B}$, including effects of atomic collisions and wave-particle interactions.

5G. Quasineutrality

Assuming Eq. (5F17) to be valid for $z > \lambda_D$, we will use it to estimate the degree of charge neutrality in the plasma. Using Eq. (5B3) in the one-dimensional Poisson Equation (5B16) we have

$$d^2\phi/dz^2 = e(n_e - n_i)/\varepsilon_0 \quad (5G1)$$

From Eq. (5F17) we have

$$d^2\phi/dz^2 = -(\phi_0/\lambda_D^2)\exp(-z/\lambda_D) \tag{5G2}$$

Using Eq. (5F4) for λ_D, and combining (5G1) and (5G2), we can solve for the fractional difference in electron and ion densities:

$$\frac{n_i - n_e}{n_0} = \frac{e\phi_0}{kT_e}\ \exp(-z/\lambda_D) \simeq -2\ \exp(-z/\lambda_D) \tag{5G3}$$

Thus, for $z/\lambda_D > 5$, the departure from charge neutrality becomes less than 1%. For $T_i \simeq T_e$, the Debye length is given by

$$\lambda_D \simeq 7434(T_e/n)^{\frac{1}{2}} \tag{5G4}$$

where T_e is in eV. Thus, for a laboratory plasma with T_e = 100 eV and $n = 10^{18}\ m^{-3}$, $\lambda_D = 7.4 \times 10^{-5}$ m, and the plasma is quasineutral at distances greater than about $5\lambda_D$ = 0.4 mm from the wall. If the plasma were not quasineutral, according to the Poisson equation enormous voltages would develop between the plasma and the wall, which would prevent one species from leaving and rapidly accelerate the other species until quasineutrality was re-established.

Thus, the condition (4A1) requiring equal concentrations of positive and negative charges is valid whenever the size of the plasma $r_p >> \lambda_D$.

plasma behavior

A plasma is distinguished by *collective Coulomb interactions*, which cause shielding, plasma oscillations, and unusual wave propagation phenomena. A group of charged particles will behave as a plasma when

* the plasma is hot enough for Debye shielding ($N_D >> 1$)
* neutral atoms do not rapidly damp Langmuir plasma oscillations. ($\omega_{pe} >> \nu_{en}$) (5G5)

The coupled, nonlinear differential equations of plasma physics are difficult to solve, even with simplifying approximations, so computer techniques are often needed.

5H. Computer Methods

finite difference equations

One technique for solving differential equations is to approximate the derivatives by finite differences. For example, consider a problem with one spatial dimension x and a time variable t. The region to be studied may be divided up into discrete locations $x_1, x_2, x_3, \ldots x_j$ separated by intervals Δx and discrete time steps $t_1, t_2, t_3, \ldots t_n$ separated by intervals Δt. The dependent variables, such as ϕ in the Poisson equation, may be given subscripts to denote the values of x and t:

$$\phi_{jn} \equiv \phi(x_j, t_n). \tag{5H1}$$

Their derivatives may be represented by finite differences between neighboring values:

$$\frac{\partial\phi}{\partial x} \simeq \frac{\phi_{j+1,n} - \phi_{j,n}}{\Delta x} \tag{5H2}$$

$$\frac{\partial^2\phi}{\partial x^2} \simeq \frac{(\partial\phi/\partial x)_{j,n} - (\partial\phi/\partial x)_{j-1,n}}{\Delta x}$$

$$= \frac{\phi_{j+1,n} - 2\phi_{j,n} + \phi_{j-1,n}}{\Delta x^2} \tag{5H3}$$

$$\frac{\partial\phi}{\partial t} \simeq \frac{\phi_{j,n+1} - \phi_{j,n}}{\Delta t}, \tag{5H4}$$

and so on. These approximations become exact in the limits $\Delta x \to 0$, $\Delta t \to 0$.

EXAMPLE PROBLEM 5H1

A square plasma 4 cm on a side has $\rho_A = 10^{-6}$ *C/m*^{3} *at the center,* $\rho_B = 0.7\ \rho_A$, *and* $\rho_C = 0.5\ \rho_A$, *and the plasma is surrounded by grounded walls (Fig. 5H1). Find the electrostatic potential at points A, B, and C, taking* $\Delta x = \Delta y = 1$ *cm.*

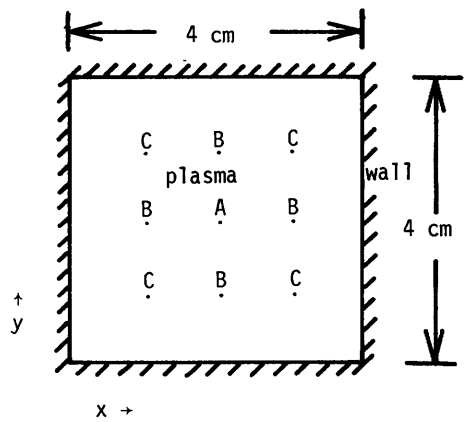

Fig. 5H1. Diagram of plasma and walls for example problem 5H1.

Let $\phi_{ij} = \phi(x_i, y_j)$. The Poisson equation

$$\frac{\partial^2\phi}{\partial x^2} + \frac{\partial^2\phi}{\partial y^2} = -\frac{\rho}{\varepsilon_0}$$

may be written in finite difference form

$$\frac{\phi_{i+1,j} - 2\phi_{i,j} + \phi_{i-1,j}}{\Delta x^2} + \frac{\phi_{i,j+1} - 2\phi_{i,j} + \phi_{i,j-1}}{\Delta y^2} = -\frac{\rho_{i,j}}{\varepsilon_0} \tag{5H5}$$

At points A, B, and C this becomes

$$4\phi_B - 4\phi_A = -\rho_A \Delta x^2/\varepsilon_0 = -11.3 \text{ V}$$

$$\phi_A + 2\phi_C - 4\phi_B = -\rho_B \Delta x^2/\varepsilon_0 = -7.91 \text{ V}$$

$$2\phi_B - 4\phi_C = -\rho_C \Delta x^2/\varepsilon_0 = -5.65 \text{ V}$$

The solution of these equations is $\phi_A = 9.61$ V, $\phi_B = 6.78$ V, $\phi_C = 4.80$ V. A coarse 4x4 grid with 3x3 = 9 unknown points was used here for simplicity. By symmetry, only 3 of the points are independent. Greater accuracy can be obtained by using an nxn grid, where n is a large number, for which there are

$(n-1)^2$ unknown points, of which $n(n+2)/8$ are independent. For example, a 32x32 grid would have 136 simultaneous equations.

Instead of using matrix inversion techniques, large numbers of equations are usually solved by assuming initial values of ϕ_{ij} and gradually adjusting the ϕ_{ij} values to reduce the residuals R_{ij} to zero, where

$$R_{ij} \equiv \phi_{i+1,j} + \phi_{i-1,j} + \phi_{i,j+1} + \phi_{i,j-1} - 4\phi_{i,j} + \Delta x^2 \rho_{i,j}/\varepsilon_0 \quad . \tag{5H6}$$

The gradual reduction of R_{ij} is called *relaxation*.

Using finite difference techniques, the Boltzmann equation may be solved to find the variation of the distribution function with various parameters; the fluid equations may be integrated in time to find the evolution of the density and temperature profiles; the MHD equations may be solved to find plasma equilibrium configurations; and the stability of various equilibria may be investigated.

Linear second-order differential equations may be written in the general form

$$A(\partial^2\phi/\partial x^2)+2B(\partial^2\phi/\partial x\partial y)+C(\partial^2\phi/\partial y^2) = D(\partial\phi/\partial x)+E(\partial\phi/\partial y)+G\phi+H. \tag{5H7}$$

where A, B, C, D, E, G, and H are functions of x and y. The equations are classified according to the value of $(B^2 - AC)$. If $B^2 < AC$, as in the Poisson equation, the equation is called "elliptic". If $B^2 = AC$, as in the diffusion equation $\partial n/\partial t = D\partial^2 n/\partial x^2$ (here t takes the place of y, and B and C are both zero), the equation is called "parabolic". If $B^2 > AC$, as in the wave equation, the equation is called "hyperbolic".

The relaxation technique mentioned in example problem 5H1 is useful with elliptic equations only. Equations like the diffusion equation and wave equation often represent initial value problems, which must be integrated in time from some given initial conditions. In solving such problems, the finite difference scheme must be chosen carefully to avoid *numerical instability*, which is a rapid growth of errors from one time step to another.

quasiparticle methods

Another method of simulating plasma behavior is to follow the trajectories of about 10^4 *quasiparticles*, each representing about a billion ions or electrons. A quasiparticle would then have mass $M = 10^9$ (m_i or m_e) and a charge = $\pm 10^9 e$. One way of handling the quasiparticles is the "particle in cell" (PIC) method. The 2- or 3-dimensional physical space to be studied is divided up into small cells with sides Δx, Δy, Δz. The particles are started out with initial positions and velocities. From these particle positions and velocities, ρ and $\vec{J}$ are calculated and smoothed out among the mesh points at the corners of the cells. Then Maxwell's equations are solved to find $\vec{E}$ and $\vec{B}$. Next, the equations of motion are solved for all the particles for one time step to find out what their new $\vec{x}$ and $\vec{v}$ will be after time Δt, and the particles are moved accordingly. (The time step Δt is chosen small enough that few particles travel more than one cell length in a time step). Then, using the new $\vec{x}$ and $\vec{v}$ of all the particles, ρ and $\vec{J}$ are computed, and the cycle of Fig. 5A4 is repeated for as many time steps as desired. Various parameters of interest, such as n, $\vec{u}$, $\vec{E}$, $\vec{B}$ are stored in memory for later display and analysis. Motion pictures may be made to show the particle

motions.

Quasiparticle methods have been successful in predicting various types of plasma pinches and wave-particle interactions, as in Fig. 12A3.

Problems

1. A fully-ionized toroidal plasma, as in Fig. 5B2, is to have its current maintained by a gradually changing magnetic induction. It is desired to maintain a current of 1 MA approximately uniformly distributed over a plasma cross sectional area of 0.3 m^2 at R = 1 m, with T_e = 1.1 keV, n = $4x10^{19}$ m^{-3}. Estimate the plasma resistivity and required dB/dt which must be provided in a transformer with core area 0.85 m^2. (Hint: Use Ohm's Law and Faraday's Law.) Assume Z = 1.

2. It is desired to build a cylindrical device which contains a cloud of electrons, with negligible ion density. If the radius of the cylinder is 5 cm, and the walls are grounded, how high can the electron density be without the voltage at the plasma center exceeding - 1000 V? Assume that $n_e(r) = n_0(1 - r^2/a^2)$, where a is the wall radius. [Solve the Poisson Eq. (5B17)].

3. Using assumptions (a), (b), (c), (e), (h), and (i) in Eq. (5C4), show that for a one-dimensional case (f dependent only on x and v_x) the linearized Vlasov equation for electrons becomes $-i\omega f_1 + ikv_x f_1 = (eE_x/m_e)(\partial f_0/\partial v_x)$. Assuming that the charge density $\rho = -e\int dv_x f_1$, combine this with Eq. (5B5) to obtain a dispersion relation for electron plasma waves:

$$1 = \frac{\omega_{pe}^2}{k^2 n_0} \int_{-\infty}^{\infty} \frac{dv_x(\partial f_0/\partial v_x)}{v_x - (\omega/k)}$$

4. Estimate the number of ions lost per metre length per second from a 10 cm diameter plasma by radial ambipolar diffusion, assuming that the plasma is weakly ionized, with B = 0.1 T, n_0 = $3x10^{17}$ m^{-3}, T_e = 10 eV, T_i = 3 eV, n_n = $2x10^{18}$ m^{-3}, $n(r) = n_0\exp(-r^2/b^2)$, where b = 2 cm, and negligible axial flow losses.

5. In a tandem mirror experiment, plasma with density 10^{19} m^{-3} is produced in the end plug regions by neutral beam injection. The central plasma density is 10^{18} m^{-3}. If the electron temperature is 1 keV everywhere and the electrons obey the "Boltzmann relation" what is the potential difference between the end plugs and the central plasma? Where is the potential higher? What energy ions can be confined by this potential barrier?

6. Find the ambipolar diffusion coefficients for a weakly ionized plasma and for a fully ionized plasma from Eqs. (5D26), (5D27).

7. Assume $\vec{R}_{ei} \simeq -n_e m_e \vec{u}_e \nu_{ei}$ in Eq.(5D5), and that $\vec{u}_i \simeq 0$. Show that the z component of (5E5) becomes $-i\omega u_{ez} = -eE_z/m_e - \nu_{ei}u_{ez}$ when the $\vec{R}_{ei}$ term is kept. Assume that $\nu_{ei}/\omega \ll 1$. Find ε_3, and show that the dispersion relation for ordinary waves becomes $\omega^2 \simeq \omega_0^2 - i\omega_{pe}^2\nu_{ei}/\omega$, where $\omega_0^2 \equiv k^2c^2 + \omega_{pe}^2$. [A series expansion of a term such as $(1 + i\nu_{ei}/\omega)^{-1}$ may be helpful.] Use $\omega \simeq \omega_0$ on the right side of

the dispersion relation, and take the square root, to show that $\exp(-i\omega t) \approx \exp[i\omega_0 t - \frac{1}{2}(\omega_{pe}^2/\omega_0^2)\nu_{ei}t]$. Thus, collisions produce exponential damping of the wave.

8. Draw a phase plot (ω vs. k) of the electron plasma wave $\omega^2 = \omega_{pe}^2 + 3k^2(kT_e/m_e)$ and find the limiting values of phase and group velocity at long and short wavelengths.

9. Estimate the electron plasma frequency associated with electrons in a TV picture tube beam with diameter 1 mm, current 1 mA, voltage 10 kV. What is this frequency in H_z? ($1\ H_z = 2\pi$ rad/s)

Bibliography

fundamentals of plasma physics

F. F. Chen, *Introduction to Plasma Physics*, Plenum, New York, 1974.
E. W. Holt and R. E. Haskell, *Foundations of Plasma Dynamics*, Macmillan, New York, 1965.
W. B. Kunkel, *Plasma Physics in Theory and Application*, McGraw-Hill, New York, 1966.
S. R. Seshadri, *Fundamentals of Plasma Physics*, Elsevier, New York, 1973.
J. L. Shohet, *The Plasma State*, Academic Press, New York, 1971.
L. Spitzer, Jr., *Physics of Fully Ionized Gases*, Interscience, New York, 1956.
W. M. Stacey, Jr., *Fusion Plasma Analysis*, Wiley, New York, 1981.
B. S. Tanenbaum, *Plasma Physics*, McGraw-Hill, New York, 1967.

more-advanced books on plasma physics

P. C. Clemmow, J. P. Daugherty, *Electrodynamics of Particles and Plasmas*, Addison-Wesley, Reading, MA, 1969.
G. Ecker, *Theory of Fully Ionized Plasmas*, Academic, New York, 1972.
S. Ichimaru, *Basic Principles of Plasma Physics: A Statistical Approach*, Addison-Wesley, Reading, MA, 1973.
N. A. Krall and A. W. Trivelpiece, *Principles of Plasma Physics*, McGraw-Hill, New York, 1973.
M. A. Leontovich, Editor, *Reviews of Plasma Physics, Vols. 1-8*, Consultants' Bureau, New York, 1966-1979.
K. Miyamato, *Plasma Physics for Nuclear Fusion*, MIT Press, Cambridge, MA, 1980.
D. C. Montgomery and D. A. Tidman, *Plasma Kinetic Theory*, McGraw-Hill, New York, 1964.
Plasma Physics, International Atomic Energy Agency, Vienna, 1965.
M. N. Rosenbluth, Editor, *Advanced Plasma Theory*, Academic Press, New York, 1964.
B. J. Rye and J. C. Taylor (Editors), *Physics of Hot Plasmas*, Plenum, New York, 1970.
G. Schmidt, *Physics of High Temperature Plasmas*, 2nd Edition, Academic Press, New York, 1979.
I. P. Shkarofsky, T. W. Johnston, and M. P. Bachynski, *The Particle Kinetics of Plasmas*, Addison-Wesley, Reading, MA, 1966.
A. Simon and W. B. Thompson, Editors, Advances in Plasma Physics, Vols. 1-6, *Interscience*, New York, 1968-1976.
T. H. Stix, *The Theory of Plasma Waves*, McGraw-Hill, New York, 1962.
J. O. Thomas and B. J. Landmark, Editors, *Plasma Waves in Space and in the Laboratory, Vol. 1 and 2*, American Elsevier, New York, 1969.

computer simulation of plasmas

B. Adler, S. Fernbach, and M. Rotenberg, Editors, Methods of Computational Physics, Vol. 9, *Plasma Physics,* Academic Press, New York, 1970.
B. Adler, S. Fernbach, and M. Rotenberg, Editors, Methods in Computational Physics, Vol. 16, *Controlled Fusion,* Academic Press, New York, 1976.
C. K. Birdsall and J. M. Dawson, "Plasma Physics", Chapter 13, *Computers and Their Role in the Physical Sciences,* S. Fernback and A. Taub, Editors, Gordon and Breach, New York, 1970.
J. Kileen, "Computer models of magnetically confined plasmas", *Nuclear Fusion 16,* 841 (1976).

electrodynamics

D. R. Corson and P. Lorrain , *Introduction to Electromagnetic Fields and Waves,* Freeman, San Francisco, 1962.
J. D. Jackson, *Classical Electrodynamics,* Wiley, New York, 1962.
W. K. H. Panofsky and M. Phillips, *Classical Electricity and Magnetism,* Addison-Wesley, Reading, MA, 1955.
A. Shadowitz, *The Electromagnetic Field,* McGraw-Hill, New York, 1975.

other topics

S. I. Braginskii, "Transport Processes in a plasma", *Reviews of Plasma Physics, Vol. 1,* Ed. M. A. Leontovich, Consultants Bureau, New York, 1965, p. 205-311.
S. C. Brown, "A short history of gaseous electronics", Chapter 1, *Gaseous Electronics,* M. N. Hirsh and H. J. Oskam, Editors, Academic Press, 1978.
G. A. Emmert, R. M. Wieland, A. T. Mense, and J. N. Davidson, "Electric sheath and presheath in the collisionless, finite ion temperature plasma", *The Physics of Fluids 23,* 803 (1980).
D. G. Samaras, *Theory of Ion Flow Dynamics,* Prentice Hall, Englewood Cliffs, NJ, 1962.
W. P. Allis, S. J. Buchsbaum, and A. Bers, *Waves in Anisotropic Plasmas,* The MIT Press, Cambridge, MA, 1963.

CHAPTER 6

GAS DISCHARGES AND BREAKDOWN

6A. Background

Charged conductors gradually lose their charge. In the eighteenth century it was found that this "discharge" occurs by means of leakage current through the surrounding air. The term *gas discharge* gradually came to include any current passing through a gas. Gas discharges occur naturally as lightning, corona, and sparks. In the nineteenth century batteries were used to provide continuous currents, and arcs were produced by touching and then separating electrodes connected to a battery. Faraday and others studied discharges in gases at low pressures.

Since then, arcs have been used as intense sources of light and heat for illumination and welding; and glow discharges in low pressure gases have found wide use in fluorescent lights, neon signs, and laser tubes. An understanding of gas discharges and breakdown criteria is important in fusion research for several reasons.

* Unwanted electrical breakdown must be prevented in plasma devices.
* Switching devices for high voltages and currents involve high voltage breakdown and arc suppression problems.
* Plasma production and heating usually involves some kind of gas discharge.
* Ion sources for neutral beam production (for plasma heating) rely on gas discharges.
* Gas discharges are used in lasers for plasma heating and diagnostics.
* Near the walls of fusion reactors, electric fields may cause various types of gas discharge. For example, arc tracks have been observed in the walls of Tokamaks. It is desirable to minimize the wall erosion and plasma impurity sources produced by such discharges.

6B. Townsend Discharges

Consider a sealed glass tube containing gas at low pressure and electrodes at the ends connected to a battery, as illustrated in Fig. 6B1. The circuit equation for the tube is

$$\phi_b = \phi_t + IR \tag{6B1}$$

where ϕ_b is the power supply voltage and ϕ_t is the potential drop across the tube. The current I will be limited by the number of free electrons and ions available

in the gas, by their mobilities, by the mutual repulsion of the electrons ("space charge" effects, Section 6F), and by the external circuit resistance R. A few free electrons may be produced by external radiation (via the photoelectric effect at the cathode or ionization of the gas) and a small current will flow. However, if the external radiation is blocked, the electrons and ions will be lost, and the current will cease. Such a non-self-sustaining case is called a *Townsend discharge*.

The electrons in the discharge will have both random thermal motion characterized by a temperature T_e (although the distribution function may not be Maxwellian) and an average flow velocity $\vec{u}_e$ induced by the electric field $\vec{E}$. The electrons are continually accelerated by the electric field, but suffer frequent randomizing collisions with neutral gas molecules, so their speeds of random thermal motion will usually be much larger than their average flow speed u_e. (An exception occurs if E is large and the neutral gas density n_n is very low.)

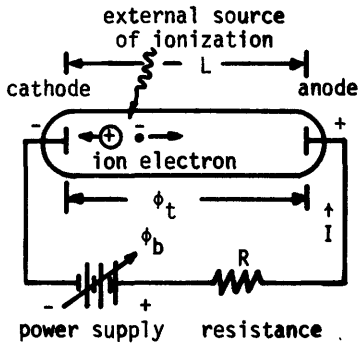

Fig. 6B1. A gas discharge tube.

The average flow velocity $\vec{u}_e$ may be estimated from the electron momentum conservation equation (5D5), keeping only the electric field and electron-neutral collision terms:

$$-e\vec{E} - m_e \nu_{en} \vec{u}_e \simeq 0, \tag{6B2}$$

$$\vec{u}_e \simeq (-e/m_e \nu_{en})\, \vec{E} \quad . \tag{6B3}$$

where the quantity in parentheses is the electron *mobility*. For the low electron densities and currents of a Townsend discharge, the applied electric field $E = \phi_t/L$ is fairly uniform along the tube, and so is u_e.

Ionization by ions is negligible, due to their low temperature. Assuming u_e is constant, the axial variation of electron density can be estimated from the steady-state, one-dimensional continuity equation (5D2) in the form

$$u_e\, (dn_e/dx) = n_n n_e \langle \sigma_e v_e \rangle - n_e n_i \langle \sigma_r v \rangle \tag{6B4}$$

Multiplying both sides by $dx/n_e u_e$, integrating from 0 to x, and taking the exponential of both sides, we find

$$n_e(x)/n_{e0} = \exp \int_0^x dx\, (n_n \langle \sigma_e v_e \rangle - n_i \langle \sigma_r v \rangle)/u_e \tag{6B5}$$

where n_{e0} is the electron density at x = 0 (the cathode). For low degrees of ionization ($n_i \ll n_n$) the recombination term is negligible in comparison with the ionization term, and Eq. (6B5) simplifies to

$$n_e(x)/n_{e0} \simeq \exp \int_0^x dx\, \alpha\, (x) \tag{6B6}$$

where the *first Townsend coefficient* $\alpha \equiv n_n \langle \sigma_e v_e \rangle / u_e$. The first Townsend coefficient may be represented approximately by the equation

$$\alpha \simeq Ap \exp(-Bp/E) \ (m^{-1}) \qquad (6B7)$$

where the coefficients A and B are listed in Table 6B1 for various gases. As the electrons travel towards the anode, their density increases approximately exponentially due to the ionization they produce in the gas. This rapid density growth is called an *electron avalanche*.

Similar phenomena occur in transient discharges. Practical applications include ionization chambers and Geiger-Mueller tubes for detecting nuclear radiations (x-rays, gamma rays, electrons, alpha particles, or fission fragments). In such detectors the primary radiation causes the few ionizations, which are amplified by the *field intensified ionization* to produce measureable current pulses.

Townsend discharges are characterized by a fairly uniform electric field, very low currents, small charge density, and little or no luminosity. In order for the discharge current to be sustained when the external radiation source is removed, an independent means of producing free electrons at the cathode is needed.

Free electrons may be produced at the cathode by thermionic emission (from a heated cathode), by field emission (if the local electric field is very high), by photoemission, and by secondary emission.

Table 6B1. Coefficients for estimation of α. Adapted from E. Nasser, Fundamentals of Gaseous Ionization and Plasma Electronics, Wiley-Interscience, New York, 1971, Table 7.1, p. 203.

Gas	A ionization Pa-m	B V Pa-m	E/p validity Range V/Pa-m
Air	11	274	75-600
N_2	9.0	257	75-450
H_2	3.8	104	15-450
He	2.3	26	15-110
Ne	3.0	75	75-300
A	11	135	75-450
Kr	13	180	75-750
Xe	20	263	150-600

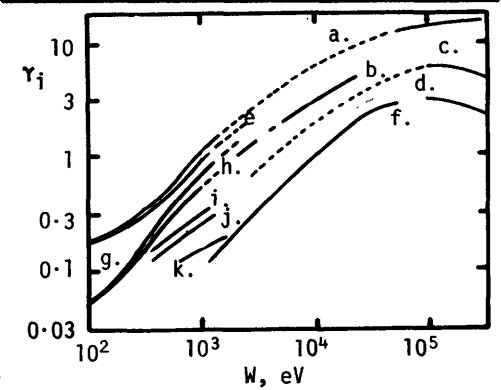

Fig. 6B2. Secondary emission coefficient γ_i for ions of energy W incident on the surfaces of various metals. a = He^+ – Mo, b = A^+ – Cu, c = H_2^+ – Mo, d = H^+ – Mo, e = He^+ – Ni, f = Li^+ – Ni, g = Ne^+ – Mo, h = Ne^+ – Ni, i = H_2^+ – Ni, j = D_2^+ – Ni, k = A^+ – Ni. (From A. von Engel, Ionized Gases, 2nd Ed., Oxford University Press, Oxford, 1965, p. 96).

Secondary emission is the process in which electrons are ejected from a surface by the impact of an incident atom, ion, or electron. The *secondary emission yield* γ is defined to be the average number of electrons ejected per incident particle. The secondary emission yield varies with incident particle energy, mass, charge, and angle of incidence, and with the surface material and condition. The variation of γ_i with incident ion energy for a few particular cases is shown in Fig. 6B2. Secondary emission is discussed further by Loeb and Brown (1959), Brown (1965), and von Engel (1965).

6C. Simplified Breakdown Condition

If each electron starting out at the cathode produced 50 ions by ionization of neutral atoms before it reached the anode, and if each of these ions had a secondary emission yield of 0.02, then one new electron would be born, on the average, for each one that had left the cathode, and the discharge would be self-sustaining. The onset of a self-sustaining discharge is called "breakdown". The condition for breakdown may be written

$$\left[\begin{array}{l}\text{Number of electrons}\\ \text{emitted at cathode}\\ \text{per incident ion}\end{array}\right] \left[\begin{array}{l}\text{Number of ions created}\\ \text{by each electron}\\ \text{emitted from cathode}\end{array}\right] \geq 1 \tag{6C1}$$

By definition, the first term is the secondary emission yield γ_i (also called the *second Townsend coefficient*). The total number of ions produced per second in the tube volume is

$$\text{(ion production rate)} = \int_0^L dx \int dA\ n_e n_n \langle \sigma_e v_e \rangle \tag{6C2}$$

$$= \int_0^L dx \int dA\ \alpha n_e u_e$$

where $\int dA$ is an integral over the tube cross sectional area. The number of electrons leaving the cathode per second is

$$\text{(electron emission rate)} = \int dA\ n_{e0} u_e \tag{6C3}$$

The second term in brackets in Eq. (6C1) is the ratio of Eqs. (6C2) and (6C3):

$$\text{(number of ions created per electron emitted)} = \frac{\int_0^L dx \int dA\ \alpha n_e u_e}{\int dA\ n_{e0} u_e} \tag{6C4}$$

If we make the simplifying assumption that radial variations of n_e, u_e, and α are negligible, then $\int dA = A$, the tube area, and Eq. (6C4) reduces to

$$\text{(number of ions created per electron emitted)} = \int_0^L dx\ \alpha n_e / n_{e0}$$

$$= \int_0^L dx\ \alpha \exp\left[\int_0^x dx'\ \alpha(x')\right] \tag{6C5}$$

where Eq. (6B6) has been used, and the dummy variable x' has been introduced to distinguish the two integrations. Thus, the breakdown condition (6C1) may be written approximately as

$$\gamma_i \int_0^L dx\ \alpha \exp\left[\int_0^x dx'\ \alpha(x')\right] \geq 1 \tag{6C6}$$

Let $y \equiv \int_0^x dx'\ \alpha(x')$. Then $dy = \alpha\, dx$, and (6C6) simplifies to

$$\gamma_i \int_0^{y(L)} dy\, e^y = \gamma_i \left[e^{y(L)} - 1 \right] \geq 1 \tag{6C7}$$

With the definition of the average value of α along the tube

$$\bar{\alpha} \equiv \frac{1}{L} \int_0^L dx'\, \alpha(x'), \tag{6C8}$$

Eq. (6C7) becomes

$$\gamma_i (e^{\bar{\alpha}L} - 1) \geq 1, \tag{6C9}$$

which may be rearranged to read

$$\bar{\alpha}L \geq \ln(1 + 1/\gamma_i) \tag{6C10}$$

Equation (6C10) is called the "breakdown condition", or the condition for the discharge to be self-sustaining when the external radiation is removed.

We will now show that the required breakdown voltage ϕ_t found from this equation is primarily a function of the parameter product $n_n L$.

Using the definition $\nu_{en} = n_n \langle \sigma v \rangle_{en}$ and $E = \phi_t/L$, the electron flow speed is found from Eq. (6B3) to be

$$u_e = e\phi_t / m_e \langle \sigma v \rangle_{en} n_n L \quad . \tag{6C11}$$

Since $\langle \sigma v \rangle_{en}$ is a slowly varying function of T_e, u_e depends primarily on ϕ_t and $n_n L$. For simplicity, consider the case in which α is uniform. Using the definition of α, Eq. (6C10) becomes

$$\frac{n_n L \langle \sigma_e v_e \rangle}{u_e} \geq \ln(1 + 1/\gamma_i) \tag{6C12}$$

At small $n_n L$, the left side of Eq. (6C12) becomes small (since $u_e \propto 1/n_n L$), and the equation cannot be satisfied. At large $n_n L$, $E/n_n = \phi_t/n_n L$ is small, and the electrons cannot gain much energy from the electric field between collisions, so T_e will be low, and $\langle \sigma_e v_e \rangle$ will approach zero, again preventing the equation from being satisfied. Thus, there is a narrow range of values of $n_n L$ for which the breakdown condition can be satisfied, and an optimum $n_n L$ at which the required ϕ_t is a minimum, as shown in Fig. 6C1 for hydrogen. The fact that the breakdown voltage is primarily a function of $n_n L$ is called *Paschen's Law*. (Instead of $n_n L$, the product pL appears in much of the literature, where $p = n_n k T_n$ is the neutral gas pressure. At $T_n = 293$ K, a value of pL = 1 Torr-cm corresponds to $n_n L = 3.3 \times 10^{20}$ m^{-2}.)

To the left of the U-shaped curve of Fig. 6C1, there are too few neutral atoms to have significant ionization occur as electrons travel from cathode to anode. To the right of the curve there are so many neutrals that the electron temperature and $\langle \sigma_e v_e \rangle$ are too low for significant ionization. Only in the central region are conditions right for field intensified ionization to sustain the discharge.

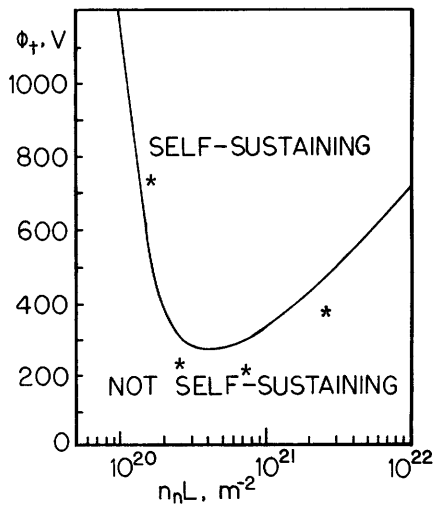

Fig. 6C1. Breakdown voltage vs. product of neutral density and electrode gap for hydrogen gas between plane, parallel nickel electrodes. This curve varies slightly for other electrode materials. Asterisks denote estimates of Example Problem 6C1.

EXAMPLE PROBLEM 6C1

Using the approximate equation for α, and assuming γ_i = 0.1 , T = 293 K, estimate the breakdown voltages of hydrogen at pL = 0.7 , 1 , 3, and 10 Pa-m, and compare with Fig. 6C1.

Combining $E = \phi_t/L$ with Eqs. (6C10) and (6B7) and solving for ϕ_t we find

$$\phi_t = \frac{BpL}{\ln \frac{ApL}{\ln (1 + 1/\gamma_i)}} \qquad (6C13)$$

Using values of A and B from Table 6B1 for H_2, we find $\phi_t = 104\ pL/\ln(1.58pL)$. At the specified values of pL, this yields ϕ_t = 723, 227, 200, and 377 V, respectively. The values of n_nL corresponding to the specified pL are 1.7×10^{20}, 2.5×10^{20}, 7.4×10^{20}, and 2.5×10^{21} m^{-2}, respectively. If we plot the calculated values of ϕ_t on Fig. 6C1, they lie fairly close to the curve (asterisks).

6D. Other Phenomena Influencing Breakdown

In predicting breakdown conditions for an experiment, we need to consider many additional factors.

* *electrodes.* The shape, material, and surface condition of the electrodes strongly affect γ_i, thus varying the breakdown voltage.
* *metastable states.* Some atomic energy levels have exceptionally long lifetimes against radiative decay. Such metastable states are easier to ionize, since much less energy is required than for ionization directly from the ground state. Thus, an atom may first be excited to a metastable state by one collision, then ionized by the second collision. Such stepwise ionization enhances the overall ionization rate. Metastable states may also interact with gases of other species. For example, helium metastables at a 16 eV energy

level can collide with other atoms having lower ionization potentials and ionize them.

* *attachment.* Electrons readily attach themselves to some gas molecules, such as SF_6. Such attachment depletes the supply of free electrons, making breakdown more difficult to attain. Therefore, gases in which attachment occurs rapidly make good insulators and are used to prevent breakdown in high voltage switches.
* *recombination.* Recombination of ions and electrons into neutral atoms also depletes the supply of free electrons, making breakdown more difficult.
* *diffusion.* Radial diffusion to the tube walls is another loss mechanism for charged particles.
* *photo-emission.* Ultraviolet and x-ray photons, produced by electron impact on electrode surfaces and gas molecules, can eject electrons from the cathode. Photo-emission is an important process in high-voltage switch tubes, such as vacuum spark gaps (Chapter 21).
* *field emission.* If the electrodes have rough or sharp surfaces, the local electric field at the surface may become large enough to pull electrons directly out of the surface. Such "field emission" is useful in generation of high-voltage electron and ion beams (Chapter 16), but it may cause undesired breakdown in other devices.
* *thermionic emission.* When the cathode becomes hot, some electrons may be boiled off, enhancing the electron supply, and lowering the voltage required to sustain the discharge.

6E. Glow and Arc Discharges

When breakdown occurs in a tube such as that shown in Fig. 6B1, the charge density near the cathode becomes large, due to accumulation of positive ions. Then the electric field is no longer uniform ($E \neq \phi_t/L$). Instead, most of the potential drop occurs near the cathode, and the discharge is called a "glow discharge". Glow discharges are common in fluorescent lights and neon signs. Several alternate light and dark regions occur in a glow discharge, due to various atomic processes (Cobine, p. 213) but they are not of direct interest to fusion research. The "positive column", a plasma, extends over most of the tube's length.

The operating point of a gas discharge is that point where the voltage-current characteristics of the discharge match the external circuit equation $\phi_b = \phi_t + IR$, as indicated in Fig. 6E1. As the power supply voltage is increased to ϕ_{b_1} and ϕ_{b_2}, a Townsend discharge occurs. When the voltage is increased to ϕ_{b_3}, breakdown occurs, and a glow discharge is observed. If the power supply voltage were now reduced to ϕ_{b_2}, the discharge would stay in the glow regime. Thus, there are two stable regimes of operation at ϕ_{b_2}, Townsend and glow discharges. (The intersection marked U is unstable, shifting operation to one of the stable points.) Whether the operation at ϕ_{b_2} occurs in the Townsend or glow discharge regime depends upon prior history of the discharge (direction of approach along the tube characteristic curve). Further increase in power supply voltage to ϕ_{b_5} results in a transition to an arc discharge. The tube could also be regulated by varying R, which changes the slope of the straight lines representing the circuit equation.

What happens physically during transition to an arc is that ion bombardment heats up a spot on the cathode enough that it emits electrons thermionically. The thermionic emission facilitates a great increase in discharge current with a low voltage ϕ_t across the tube. An arc may also be initiated by field emission from a

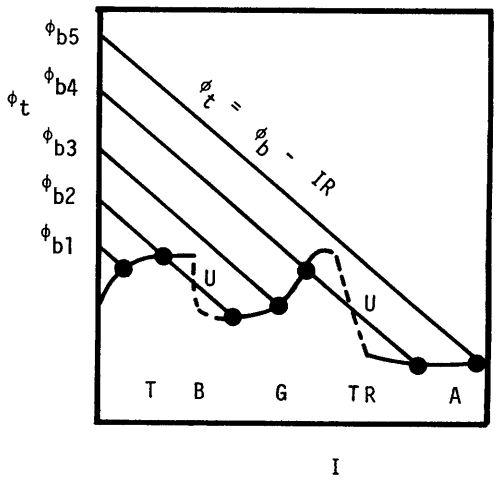

Fig. 6E1. Variation of discharge tube potential ϕ_t with current I in a low-pressure gas discharge (not to scale). Smooth curve represents discharge tube characteristics, which may vary considerably from one tube to another. Straight lines represent the external circuit equation for various external power supply voltages ϕ_{b1} to ϕ_{b5}. Solid points are stable operating points. U = unstable points, T = Townsend discharge, B = breakdown, G = glow discharge, TR = glow to arc transition, A = arc.

sharp cathode surface. Typical voltage drops ϕ_t for arcs range from 10-100 Volts, and for glow discharges, 100-1000 Volts. The voltage depends on type of gas, gas pressure, electrode material, surface conditions, etc. In general, higher gas pressures result in higher voltage drops.

The current at which the transition from Townsend to glow discharge occurs is typically about 10^{-5} A, and the glow-to-arc transition occurs around 0.1A, but these values may vary considerably. Arc currents are typically 1-100 A. At still higher currents, the magnetic field produced by the plasma current becomes appreciable. From Example Problem 5B2, the azimuthal field at radius r around an axial current I is

$$B_\theta = \mu_0 I/2\pi r \tag{6E1}$$

where μ_0 is the permeability of free space. Thus, a current I = 1000 A produces a magnetic induction B_θ = 0.01 T at r = 0.02 m. The plasma motion may be described by the MHD equation

$$\rho_m(\partial\vec{u}/\partial t) + \rho_m(\vec{u}\cdot\vec{\nabla})\vec{u} = \vec{J}\times\vec{B} - \vec{\nabla}p \tag{6E2}$$

With $\vec{J}$ in the axial (z) direction and $\vec{B}$ in the azimuthal (θ) direction, the $\vec{J}\times\vec{B}$ force is radially inwards, compressing the plasma. At very high currents ($\sim 10^5$A), the compression is very strong, "pinching" the plasma to small radii. The compression heats the plasma up to high temperatures, but the plasma is usually broken up quickly by instabilities (Chapter 8).

6F. Space Charge Limitation of Current

When plenty of electrons are available from the cathode, the negative charge of the cloud of electrons near the cathode tends to repel electrons just leaving the cathode, thus limiting the attainable current density. The variation of the potential near the cathode is illustrated in Fig. 6F1 for three cases. We shall consider case (b), with ϕ = 0 and $d\phi/dx$ = 0 at the cathode (x = 0). Assuming that electrons leave the cathode with negligible kinetic energies, and ignoring the effects of positive ions, the maximum attainable current density can be estimated from the energy conservation equation

$$\tfrac{1}{2}m_e v_e^2 = e\phi(x) \qquad (6F1)$$

and the Poisson equation

$$d^2\phi/dx^2 = -n_e e/\varepsilon_0 = J/v_e\varepsilon_0. \qquad (6F2)$$

Eliminating v_e, we have

$$d^2\phi/dx^2 = C_1\phi^{-\frac{1}{2}} \qquad (6F3)$$

where $C_1 \equiv (J/\varepsilon_0)\,(m/2e)^{\frac{1}{2}}$.

After multiplication by $2(d\phi/dx)$, Eq. (6F3) becomes

$$2\,(d^2\phi/dx^2)(d\phi/dx) = 2C_1\phi^{-\frac{1}{2}}(d\phi/dx). \qquad (6F4)$$

The left side is equal to $(d/dx)(d\phi/dx)^2$, so the equation may be integrated to obtain

$$(d\phi/dx)^2 = 4C_1\phi^{\frac{1}{2}} + C_2 \qquad (6F5)$$

where C_2 is an integration constant. From the boundary conditions, $C_2 = 0$. Taking the square root of both sides, we have

$$d\phi/dx = 2C_1^{\frac{1}{2}}\phi^{\frac{1}{4}} \qquad (6F6)$$

which may be rearranged as

$$\int \frac{d\phi}{\phi^{\frac{1}{4}}} = 2C_1^{\frac{1}{2}}\int dx + C_3 \qquad (6F7)$$

where C_3 is another integration constant. After integrating, we find

$$(4/3)\phi^{3/4} = 2C_1^{\frac{1}{2}}x + C_3 \qquad (6F8)$$

Since $\phi = 0$ at $x = 0$, $C_3 = 0$. Inserting the value of C_1, solving for J, and setting $\phi = \phi_t$ at $x = L$, we get the result

$$J = (4\varepsilon_0/9L^2)\,(2e/m_e)^{\frac{1}{2}}\phi_t^{3/2} \qquad (6F9)$$

which is called the "Child-Langmuir Law". For case (c) of Fig. 6F1, we could define $x = 0$ and $\phi = 0$ at the virtual cathode, and obtain the same result. Thus, the space charge of electrons leaving the cathode produces a region of low potential in front of the cathode, inhibiting electron flow from the cathode, and limiting the current density in accordance with Eq. (6F9). Similar results apply for other geometries, such as cylindrical or spherical: the maximum current den-

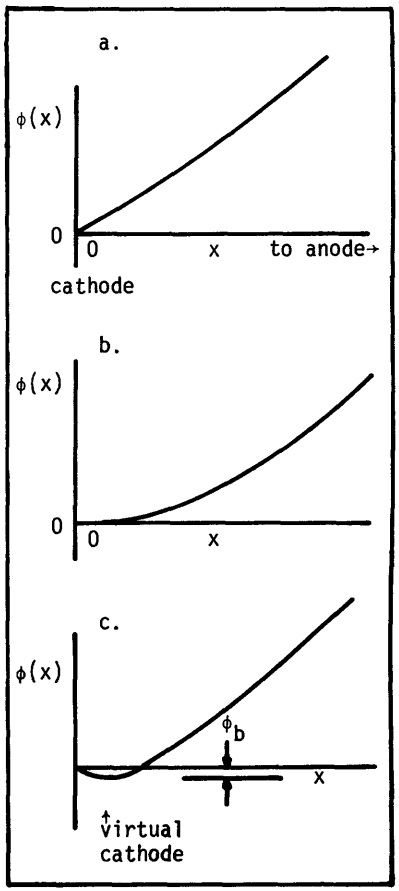

Fig. 6F1. Variation of electrostatic potential near the cathode for various space-charge conditions. (a) the usual emission-limited case, space charge effects insignificant, (b) electrons emitted copiously with near-zero kinetic energies, $d\phi/dx \approx 0$ at cathode, (c) electrons emitted copiously with kinetic energy $\approx e\phi_b$. Space-charge effects produce a "virtual cathode" tending to block electrons with energies less than $|e\phi_b|$.

sity which can be attained is proportional to $\phi_t^{3/2}/L^2$, where ϕ_t is the applied voltage and L is the interelectrode spacing. The steady-state limits of Eq. (6F9) may be exceeded temporarily during transient phenomena. This Equation also changes when ion density and collision effects between the electrodes are significant. If we write $J = G\phi_t^{3/2}$ the coefficient G is called the *perveance* of the diode.

summary

Plasma production usually involves some type of gas discharge. At low currents, a non-self-sustaining Townsend discharge occurs. Breakdown occurs when field intensified ionization and secondary emission become large enough to make the discharge self-sustaining. As current increases, a glow discharge becomes an arc when cathode heating makes thermionic emission significant. Finally, at very high currents, the self-magnetic field of the plasma current pinches the plasma to small diameter and high pressure, but plasma instability generally disrupts the current quickly. The current which can flow between cathode and anode is limited by space charge effects to a value $J \propto \phi_t^{3/2}/L^2$.

Problems

1. A 40-Watt fluorescent lamp tube has the following parameters: $n_e = n_i = 2\times10^{17}$ m^{-3}, p = 400 Pa (3 Torr) of Argon and 0.8 Pa (0.006 Torr) of Hg vapor, $T_i = T_n = 313$ K, $T_e = 11{,}000$ K, L = 1.5 m, J = 500 A/m^2, E = 75 V/m. Estimate (a) the average electron flow speed u_e from J, assuming ion current negligible, (b) the average speed of electron thermal motion $\langle v_e \rangle$, (c) the effective electron-neutral momentum-transfer collision frequency, (d) the first Townsend coefficient (Eq. 6C10), assuming $\gamma_i = 0.01$, (e) $\langle \sigma_e v_e \rangle$.

2. Estimate the breakdown voltage in air at p = 300 Pa, L = 1 m, assuming $\gamma_i = 0.05$.

3. A probe is inserted into a large plasma chamber containing hydrogen at 1 Pa, 300 K, and the magnetic field is turned off. Estimate the breakdown voltage from the probe (a) to a wall 1 cm away, (b) to an opposite wall 1 m away. Explain why the two values differ.

4. Assume that a lightning stroke carries a current of 200 kA uniformly distributed in a channel with radius 5 cm. Estimate the self-magnetic field around the channel, the inwards $\vec{J}\times\vec{B}$ force at the surface of the channel (N/m^3), and the pressure gradient which could be held at equilibrium (Pa/m and atm/cm), if instability did not occur.

5. Estimate the maximum current attainable from an electron gun with applied voltage of 1000V, electrode spacing of 1 cm, and cathode radius 0.5 cm. What electrode spacing would make I = 1A, assuming that emission is space-charge limited?

Bibliography

S. C. Brown, *Basic Data of Plasma Physics*, Wiley, New York, 1959.
S. C. Brown, *Introduction to Electrical Discharges in Gases*, Wiley, New York, 1966.
B. E. Cherrington, *Gaseous Electronics and Gas Lasers*, Pergamon Press, New York, 1979.
J. D. Cobine, *Gaseous Conductors*, Dover, New York, 1958.
M. N. Hirsh and H. J. Oskam, Editors, *Gaseous Electronics, Vol. 1, Electrical Discharges*, Academic Press, New York, 1978.
A. M. Howatson, *An Introduction to Gas Discharges*, Pergamon, New York, 1965.
L. B. Loeb, *Basic Processes of Gaseous Electronics*, University of California Press, Berkeley, 1955.
E. W. McDaniel, *Collision Phenomena in Ionized Gases*, Wiley, New York, 1964.
J. W. McGowan and P. K. John, Editors, *Gaseous Electronics, Some Applications*, North-Holland, Amsterdam, 1974.
J. M. Meek and J. D. Craggs, *Electrical Breakdown of Gases*, Oxford University Press, London, 1953.
E. Nasser, *Fundamentals of Gaseous Ionization and Plasma Electronics*, Wiley, New York, 1971.
A. von Engel, *Ionized Gases, Second Edition*, Oxford University Press, London, 1965.

CHAPTER 7

CHARGED PARTICLE TRAJECTORIES

7A. Guiding Center Approximation

The simplest description of particle motion ignores collisions and waves and considers only the effect of external forces on the particle motions. In spite of its simplicity, the study of charged particle trajectories can provide valuable information about the tendencies of particles to drift across magnetic field lines and escape, and about the reflection of particles by "magnetic mirrors".

We can choose the z axis parallel to $\vec{B}$, the magnetic field. Then the three components of the nonrelativistic equation of motion $d\vec{v}/dt = \vec{F}/m$ for an ion with mass m and charge q may be written

$$dv_x/dt = \omega_{ci} v_y + F_x/m \tag{7A1}$$

$$dv_y/dt = -\omega_{ci} v_x + F_y/m \tag{7A2}$$

$$dv_z/dt = F_z/m \tag{7A3}$$

where

$$\omega_{ci} \equiv qB/m \tag{7A4}$$

is called the *ion cyclotron frequency*, and $\vec{F} = q\vec{E} + m\vec{g} + \ldots$ represents the sum of the nonmagnetic forces. The equation for v_x contains v_y, and vice versa, so these two equations are coupled. They can be decoupled by differentiating Eq. (7A1) with respect to time and eliminating dv_y/dt with Eq. (7A2). A similar procedure can be used with Eq. (7A2), with the result

$$d^2v_x/dt^2 = -\omega_{ci}^2 v_x + \omega_{ci} F_y/m$$

$$d^2v_y/dt^2 = -\omega_{ci}^2 v_y - \omega_{ci} F_x/m \tag{7A5}$$

Here it has been assumed that $d\vec{F}/dt \simeq 0$ and $d\vec{B}/dt \simeq 0$, which means that the

analysis will be invalid if the external forces vary rapidly in time. The solution of the three velocity equations (7A3-7A5) may be written in the form

$$v_x(t) = v_{rot}\sin(\omega_{ci}t + \theta) + F_y/qB \tag{7A6}$$

$$v_y(t) = v_{rot}\cos(\omega_{ci}t + \theta) - F_x/qB \tag{7A7}$$

$$v_z(t) = v_{zo} + F_z t/m \tag{7A8}$$

where $v_{rot} \equiv [(v_{xo} - F_y/qB)^2 + (v_{yo} + F_x/qB)^2]^{1/2}$, $\theta \equiv \tan^{-1}[(v_{xo} - F_y/qB)/(v_{yo} + F_x/qB)]$, $v_{xo} = v_x(0)$, $v_{yo} = v_y(0)$, and $v_{zo} = v_z(0)$. The validity of these equations may be demonstrated by substituting them into the original differential equations. Since $v_x = dx/dt$, the x coordinate of the ion's position at any time may be found from the equation $\int_{x_0}^{x} dx = \int_{o}^{t} dt\, v_x$ where x_o is the ion's initial position. The y and z coordinates can be found similarly. The result of integrating Eqs. (7A6-7A8) is

$$x(t) = x_o - (v_{rot}/\omega_{ci})[\cos(\omega_{ci}t + \theta) - \cos\theta] + F_y t/qB \tag{7A9}$$

$$y(t) = y_o + (v_{rot}/\omega_{ci})[\sin(\omega_{ci}t + \theta) - \sin\theta] - F_x t/qB \tag{7A10}$$

$$z(t) = z_o + v_{zo}t + F_z t^2/2m \tag{7A11}$$

where x_o, y_o, z_o are the initial coordinates of the ion. These equations describe the ion's motion for any given initial position and velocity, and for any combination of forces $\vec{F}$. If $\vec{F} = 0$ and $v_{zo} = 0$, then the trajectory is simply a circle in the x-y plane centered at (x_o, y_o, z_o) with radius

$$\rho_i = v_{rot}/\omega_{ci} \tag{7A12}$$

where ρ_i is called the ion *Larmor radius, gyroradius,* or *cyclotron radius.* To write Eqs. (7A1)-(7A3) for electrons, we use the electron mass and replace ω_{ci} by $-\omega_{ce}$, where $\omega_{ce} \equiv eB/m_e$. Then the results of Eqs. (7A4)-(7A11) are applicable, using these replacements and $q \to -e$. The electron Larmor radius is

$$\rho_e = v_{rot}/\omega_{ce} \tag{7A13}$$

where v_{rot} for the electrons must be used. With the z axis parallel to B, positive ions rotate clockwise in the x-y plane, and electrons, counterclockwise (Fig. 7A1). The cyclotron frequencies ω_{ci} and ω_{ce} are angular frequencies (rad/s). The corresponding frequencies in cycles/s (Hz) are

$$\nu_{ce} = \omega_{ce}/2\pi = 28.0\ B\ (\text{GHz}) \qquad (1\ \text{GHz} = 10^9\ \text{Hz}) \tag{7A14}$$

$$\nu_{ci} = \omega_{ci}/2\pi = 7.63\ B\ (\text{MHz}) \tag{7A15}$$

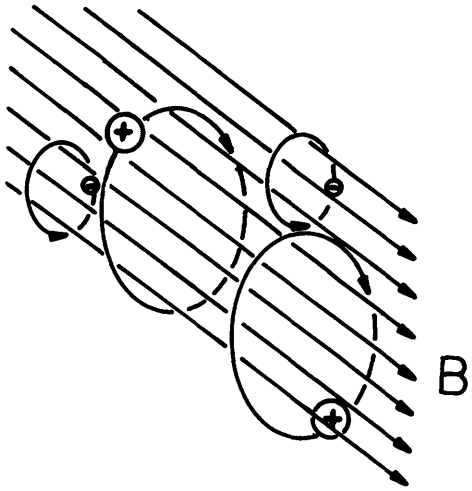

Fig. 7A1. Clockwise rotation of ions (+) and counterclockwise rotation of electrons (-) in a magnetic field. The self-magnetic fields of these little current loops are all in the opposite direction from the applied magnetic field $\vec{B}$.

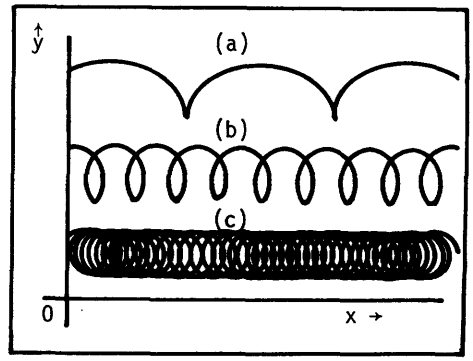

Fig. 7A2. Cycloidal trajectories of charged particles with a magnetic field in the z direction. (a) large F_y, *(b) intermediate* F_y, *(c) small* F_y. *Usually* $v_d << v_{rot}$, *and the trajectory resembles case (c).*

If $F = 0$ and $v_{zo} \neq 0$, then the trajectory is a helix with circular motion in the x-y plane and constant velocity in the z direction.

When $\vec{F} \neq 0$ there will be, in addition to the circular rotation in the x-y plane, a constant *drift velocity* in the x-y plane with components $v_{dx} = F_y/qB$, $v_{dy} = -F_x/qB$. The resultant trajectory is called a "cycloid", which is the same as the trajectory of a point on a rolling wheel. Some cycloidal trajectories are illustrated in Fig. 7A2.

A particle's velocity may be written vectorially as

$$\vec{v} = \vec{v}_{\parallel} + \vec{v}_{rot} + \vec{v}_d \quad , \tag{7A16}$$

where

$$\vec{v}_d = \vec{F}\times\vec{B}/qB^2 \quad . \tag{7A17}$$

Thus, the particle has three types of motion: motion along the magnetic field $\vec{v}_{\parallel}$, with possible acceleration by F_z; rotational motion around a magnetic field line v_{rot} at the cyclotron frequency; and a drift velocity $\vec{v}_d$ of the "guiding center of rotation", where $\vec{v}_d$ is perpendicular to both $\vec{F}$ and $\vec{B}$.

The above analysis, known as the *guiding center approximation*, may be applied to either electrons or ions. The guiding center approximation is valid if

* the plasma size $r_p >> \rho_i$
* collisions may be neglected ($\nu_{ei} << \omega_{ce}$, $\nu_{ie} << \omega_{ci}$)
* $dF/dt \simeq 0$ and $dB/dt \simeq 0$.
* spatial variations of $\vec{F}$ and $\vec{B}$ are slow ($dB/dx << B/\rho_i$, $dF/dx << F/\rho_i$, etc.)

The theory may be extended to cover special cases when some of these conditions are not satisfied.

7B. Diamagnetism

Let $\vec{v}_\perp = \vec{v}_{rot} + \vec{v}_d$ be the velocity component perpendicular to the magnetic field. Usually $v_{rot} >> v_d$, $v_\perp \simeq v_{rot}$. The average energy perpendicular to the magnetic field is $<W_\perp> = mv_\perp^2/2 = kT$, so $v_{rot} \simeq (2kT/m)^{\frac{1}{2}}$. The average Larmor radii are

$$\rho_e = (2m_e kT_e)^{\frac{1}{2}}/eB$$

$$\rho_i = (2m_i kT_i)^{\frac{1}{2}}/qB = (m_i/m_e)^{\frac{1}{2}}(T_i/T_e)^{\frac{1}{2}}\rho_e/Z \qquad (7B2)$$

where $q = Ze$ for the ions. Thus, the ions will have larger Larmor radii, due to their greater mass. Some values of the average electron Larmor radius are given in Fig. 7B1. The mass ratios for various ions are given in Table 7B1. For non-Maxwellian ions, $T_i \to W_{i\perp}$.

The gyration of ions and electrons produces little loops of electrical current (Fig. 7A1), which create small local magnetic fields. The direction of these self-magnetic fields inside each loop is opposite to that of the externally applied magnetic field $\vec{B}$. The consequent reduction of the applied magnetic field within the plasma is called *diamagnetism*. Complete cancellation of the external field is possible if the plasma has high enough density and kinetic energy. In such a case only the particles on the plasma boundary, where $\vec{B} \neq 0$ rotate; the particles inside, where $\vec{B} = 0$, follow almost straight paths, bouncing off the plasma boundary, as sketched in Fig. 7B2. Such trajectories are found in some pinch devices (Chapter 12). Diamagnetism is only significant when the plasma pressure is large (Chapter 8).

7C. Drift Velocities

A charged particle's *magnetic moment* is defined to be

$$\mu_m = W_\perp/B = mv_\perp^2/2B \qquad (J/T) \quad . \qquad (7C1)$$

In a spatially varying magnetic field, a charged particle experiences an effective force

$$\vec{F} = -\mu_m \vec{\nabla} B \qquad (N) \qquad (7C2)$$

where $\vec{\nabla}$ represents the gradient operator (Appendix F) and $B = |\vec{B}|$. For example,

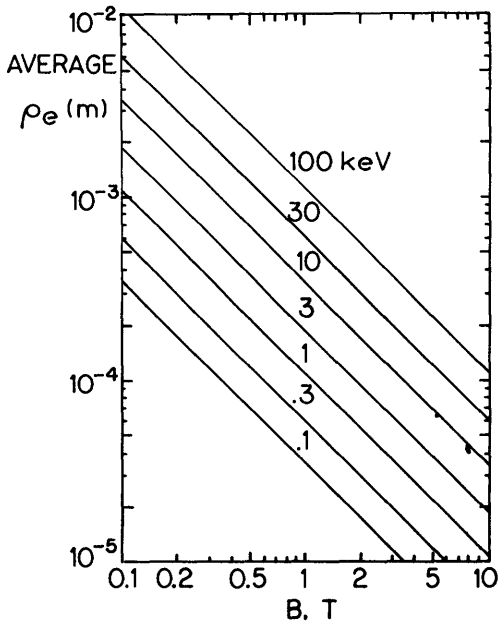

Fig. 7B1. Average Lamor radius for electrons vs. magnetic induction B, at various electron temperatures.

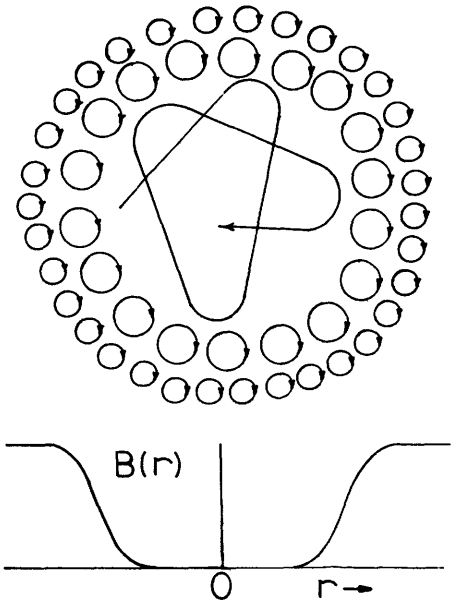

Fig. 7B2. Effect of diamagnetism on trajectories (top) and magnetic field vs. radius in a high-pressure plasma.

Table 7B1. Ratios of various ion masses to electron mass.

ion	m_i/m_e	$(m_i/m_e)^{\frac{1}{2}}$
proton	1836.15	42.8503
deuteron	3670.48	60.5845
triton	5496.92	74.1412
alpha (^{4}He)	7294.30	85.4066

the x component of this vector equation is $F_x = -\mu_m(\partial B/\partial x)$. If B is increasing with x, then the effective force is in the negative x direction. The magnetic field gradient force also produces a drift velocity, in accordance with Eq. (7A17)

$$\vec{v}_{\nabla B} = \frac{-\mu_m \vec{\nabla} B \times \vec{B}}{qB^2} \quad \text{(m/s)} \quad . \tag{7C3}$$

The centrifugal force $\vec{F} = mv_{\parallel}^2 \vec{R}_c/R_c^2$ produces a drift velocity

$$\vec{v}_c = \frac{mv_{\parallel}^2 \vec{R}_c \times \vec{B}}{qB^2 R_c^2} \quad \text{(m/s)} \tag{7C4}$$

where $\vec{R}_c$ is the radius of curvature of the magnetic field lines, Fig. 7C1. In a curved magnetic field with negligible plasma diamagnetism, $B \propto 1/R_c$,

so $\vec{\nabla}B/B = -\vec{R}_c/R_c^2$. Then Eqs. (7C3) and (7C4) may be combined to read

$$\vec{v}_{\nabla B} + \vec{v}_c = \frac{m\vec{R}_c \times \vec{B}}{qB^2R_c^2}\,(v_{\parallel}^2 + v_{\perp}^2/2) \quad (m/s)$$

$$= \frac{-m\vec{\nabla}B \times \vec{B}}{qB^3}\,(v_{\parallel}^2 + v_{\perp}^2/2) \quad (m/s) \qquad (7C5)$$

These equations apply to either ions or electrons, using the appropriate mass and charge. Because of the opposite signs of their charges, ions and electrons tend to drift in opposite directions, producing a slight separation of positive and negative charges, and hence an electric field. The force $q\vec{E}$ of an electric field results in a drift velocity

$$\vec{v}_E = \frac{\vec{E}\times\vec{B}}{B^2} \quad (m/s) \qquad (7C6)$$

which has the same direction for both ions and electrons, independent of charge. For the case of a toroidal magnetic field, these particle drifts are illustrated in Fig. 7C1.

The outward drift tendency of charged particles in a toroidal magnetic field can be compensated by adding a poloidal magnetic field. The resultant magnetic field lines are twisted into helical shapes (Fig. 7C2), and electrons flowing along field lines can neutralize the charge-separation electric field. This

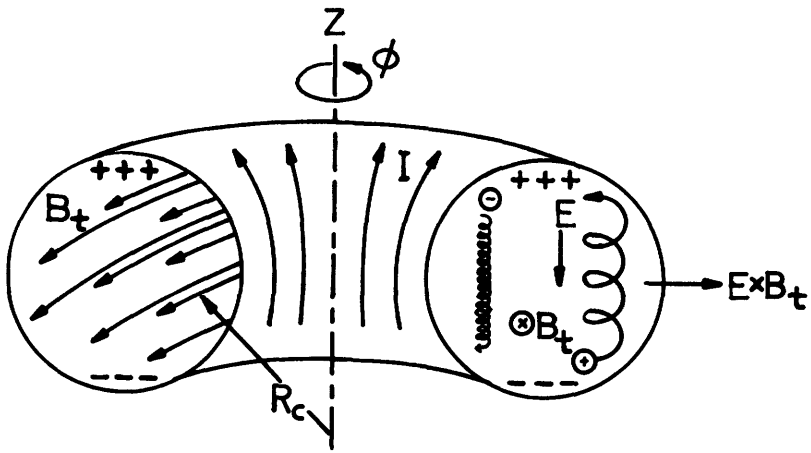

Fig. 7C1. Particle drifts in a toroidal magnetic field B_t. The magnetic field gradient and curvature drifts cause the electrons to move downwards and ions to move upwards. The resultant partial charge separation sets up an electric field E downwards. The charge-separation electric field then causes an $\vec{E}\times\vec{B}/B^2$ drift outwards. The coil currents producing the toroidal magnetic field are denoted by I. From D. L. Jassby, "Tokamak devices and reactors", Ch. 7, Proceedings of the Second IEEE Minicourse on Fusion, Ed. G. H. Miley, U. of Illinois Fusion Studies Laboratory, 1977.

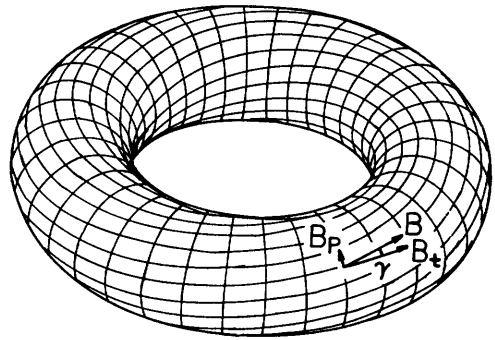

Fig. 7C2. Helical magnetic field lines. The total magnetic field $\vec{B}$ is the vector sum of the toroidal field B_t and the poloidal field B_p.

neutralization will reduce or eliminate the $\vec{v}_E$ drift. The twisting of the magnetic field lines is called *rotational transform*. The poloidal magnetic field can be produced either by a strong plasma current (as in tokamaks) or by external helical coils (as in stellarators).

Additional drift motions are produced by gravity, by spatial variation of the electric field, and by time-varying electric and magnetic fields. Because the force of gravity on ions and electrons is usually much less than the forces of electric or magnetic fields, the drift velocity $\vec{v}_g = m\vec{g}\times\vec{B}/qB^2$ is usually negligible for laboratory plasmas. In the case of a spatially varying electric field, Eq. (7C6) is modified to read

$$\vec{v}_E = \left(1 + \frac{\rho^2\nabla^2}{4}\right)\frac{\vec{E}\times\vec{B}}{B^2} \qquad \text{(m/s)} \qquad (7C7)$$

where ∇^2 is the Laplacian operater (Appendix F) and ρ is the particle's Larmor radius (Chen, 1974). For sinusoidal perturbations of the electric field, as in Eq. (5E2), $\nabla^2\vec{E} = -k^2\vec{E}$, where $k = 2\pi/\lambda$, and λ is the wavelength of the perturbation. Thus, short-wavelength perturbations produce the biggest effects. If the drift motions tend to increase the electric field, then a drift wave instability may result (Chapter 8).

Time-varying electric fields produce a polarization drift

$$\vec{v}_{pi} = \frac{1}{\omega_{ci}B}\frac{d\vec{E}}{dt} \quad \text{(ions)}$$

$$\vec{v}_{pe} = \frac{-1}{\omega_{ce}B}\frac{d\vec{E}}{dt} \quad \text{(electrons)} \qquad (7C8)$$

The resultant polarization current density is

$$\vec{j}_p = n_i q\vec{v}_{pi} - n_e e\vec{v}_{pe} \simeq n_i q\vec{v}_{pi} \qquad (7C9)$$

since $\omega_{ci} << \omega_{ce}$. This current is a consequence of ion inertia during oscillations of the electric field.

Time-varying magnetic fields induce electric fields in accordance with the Maxwell equation

$$\nabla\times\vec{E} = -\left(\partial\vec{B}/\partial t\right) \qquad (7C10)$$

as illustrated in Example Problem 5B3. If $\partial B/\partial t$ is very large, shock wave heating may be produced (Chapter 9). However, if B does not vary too rapidly in time or in space along the particle trajectory, its magnetic moment $\mu_m \equiv W_\perp/B$ remains constant.

7D. Adiabatic Invariants and Magnetic Mirrors

magnetic moment

To demonstrate the invariance of μ_m, we will estimate the change in $W_\perp$ during one period $\tau_c \equiv 2\pi/\omega_c$ of rotation around a magnetic field line, where ω_c represents either ω_{ci} or ω_{ce}. Let

$$\Delta W_\perp \equiv \int_0^{\tau_c} dt\ (dW_\perp/dt) = \oint d\vec{\ell}\cdot\vec{F} \quad , \tag{7D1}$$

where we have equated the change in kinetic energy to the work done by the force $\vec{F}$. The line integral is around one loop of rotation, assuming the loop to be nearly closed, which implies that $v_d \ll v_{rot}$. Using the Lorentz force for $\vec{F}$, we have

$$\Delta W_\perp = \oint d\vec{\ell}\cdot(q\vec{E} + q\vec{v}\times\vec{B}) \tag{7D2}$$

Since $d\vec{\ell} = \vec{v}dt$, $d\vec{\ell}\cdot(\vec{v}\times\vec{B}) = -dt\ \vec{v}\cdot(\vec{v}\times\vec{B}) = 0$. By convention $d\vec{\ell}$ is in a counterclockwise direction, opposite to the direction of $q\vec{v}$. According to Stokes' Theorem (Appendix F)

$$\oint d\vec{\ell}\cdot\vec{E} = \int d\vec{A}\cdot(\vec{\nabla}\times\vec{E}) \tag{7D3}$$

where $d\vec{A}$ is a unit of area in the opposite direction from $\vec{B}$, and the surface integral is over the area of the circle of rotation. Thus, using Eq. (7C10),

$$\Delta W_\perp = q\int d\vec{A}\cdot(\vec{\nabla}\times\vec{E}) = -q\int d\vec{A}\cdot(\partial\vec{B}/\partial t) \simeq \pi\rho^2 q(dB/dt) \tag{7D4}$$

Here ρ represents the Larmor radius ρ_i or ρ_e, and dB/dt is the time rate of change of B at the guiding center of rotation. Since $\rho \equiv v_{rot}/\omega_c \simeq mv_\perp/qB$, this becomes

$$\Delta W_\perp = \pi(mv_\perp/qB)^2 q(dB/dt) = \tau_c(W_\perp/B)\ (dB/dt) \quad . \tag{7D5}$$

If we assume that $W_\perp$ changes slightly during the period τ_c, then

$$dW_\perp/dt \simeq \Delta W_\perp/\tau_c = (W_\perp/B)\ (dB/dt) \quad . \tag{7D6}$$

The rate of change of the magnetic moment μ_m is

$$\frac{d\mu_m}{dt} = \frac{d(W_\perp/B)}{dt} = \frac{B(dW_\perp/dt) - W_\perp(dB/dt)}{B^2} \simeq 0 \quad , \tag{7D7}$$

so $\mu_m \simeq$ constant. Under adiabatic conditions (the absence of significant energy

transfer during a cycle of rotation or periodic motion) the magnetic moment tends to remain constant, so it is called an "adiabatic invariant". The magnetic moment is invariant when the following conditions are satisfied:

* energy is not transferred by collisions between particles (for electrons, $\nu_{ei} << \omega_{ce}$ and $\nu_{en} << \omega_{ce}$)
* B must vary slowly along the particle trajectory ($\partial B/\partial t << B/\tau_c$, $\partial B/\partial z << B/v_{\parallel}\tau_c$, $\partial B/\partial x << B/\rho$, $\partial B/\partial y << B/\rho$)
* $v_d << v_{rot}$
* B must not become very weak. (If B is weak, ρ and τ_c become large, and then conditions like $\partial B/\partial z << B/v_{\parallel}\tau_c$ will not be satisfied.)
* radiative energy loss is slow on time scales of interest.

magnetic mirrors

Under adiabatic conditions, the total energy of a particle is conserved:

$$W = \tfrac{1}{2}mv_{\parallel}^2 + \tfrac{1}{2}mv_{\perp}^2 + q\phi = \tfrac{1}{2}mv_{\parallel}^2 + \mu_m B + q\phi = \text{constant} \qquad (7D8)$$

where $q\phi$ is the electrostatic potential energy. Therefore,

$$\tfrac{1}{2}mv_{\parallel}^2 = W - \mu_m B - q\phi \quad . \qquad (7D9)$$

This equation shows that an increase of B can reduce $v_{\parallel}$ to zero, stopping the particle motion along the field line. Then the particle will start moving back towards the region of weaker B, because of the force $F_z = -\mu_m(\partial B/\partial z)$ (Eq. 7C2). Thus, the particle may be reflected from a region of increasing magnetic field, called a *magnetic mirror*. For $\phi = 0$, the reflection condition (7D9) is

$$\mu_m B = W \quad . \qquad (7D10)$$

If we evaluate μ_m and W at some reference location where $B = B_0$ and $v = v_0$, then $\mu_m = mv_{\perp 0}^2/2B_0$ and $W = \tfrac{1}{2}mv_0^2$, and the reflection condition may be rearranged to read

$$B/B_0 = v_0^2/v_{\perp 0}^2 = 1/\sin^2\alpha_0 \ , \qquad (7D11)$$

where α_0 is the *pitch angle* between $\vec{v}$ and $\vec{B}$ at the reference location, Fig. 7D1. This equation determines the

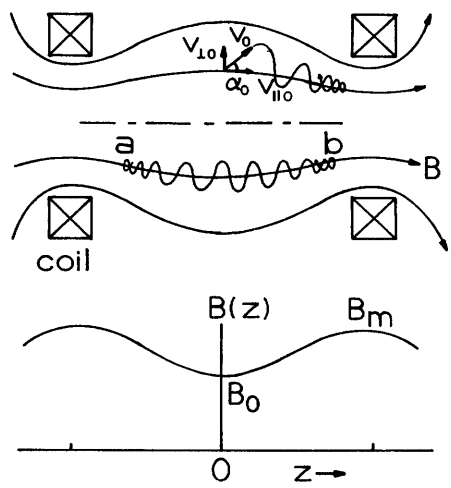

Fig. 7D1. Charged particle trajectories in a simple magnetic mirror (top) and variation of magnetic induction in the z direction (bottom). Trapped particles bounce back and forth between reflection points such as a and b.

value of B required to reflect a particle with initial pitch angle α_0, or what particles can be reflected by a magnetic field B. If the maximum value of B is B_m, then all particles having $\alpha_0 > \alpha_m$ will be reflected, with

$$\sin\alpha_m = (B_0/B_m)^{\frac{1}{2}} = (1/R)^{\frac{1}{2}} \tag{7D12}$$

where $R \equiv B_m/B_0$ is called the *mirror ratio* Thus, the angle α_m defines a cone in velocity space around $v_{\parallel 0}$. Particles with pitch angles outside the cone will be reflected, and those with pitch angles inside the *loss cone* will be transmitted through the magnetic mirror.

EXAMPLE PROBLEM 7D1

An ion starts out at the center of a magnetic mirror field ($B = B_0$) with $v_{\perp 0} = 2\times10^6$ m/s and $v_{\parallel 0} = 3\times10^6$ m/s. If the mirror ratio is 3, will it be reflected? What value of R would barely cause reflection?

Since $v_{\perp 0}/v_{\parallel 0} = \tan\alpha_0$, we find that $\alpha_0 = 33.69$ deg. For this case, $\sin\alpha_m = (1/3)^{\frac{1}{2}}$ and $\alpha_m = 35.26$ deg. Since $\alpha_0 < \alpha_m$, the ion will be transmitted through the mirror. (Its pitch angle is in the loss cone.) In order to reflect the ion, we must have $\alpha_m \leq \alpha_0 = 33.69$ deg. Then $R = 1/\sin^2\alpha_m \geq 3.25$.

The effects of electrostatic potential variations on particle reflection will be discussed in Chapter 11.

other adiabatic invariants

The particles trapped in a magnetic mirror bounce back and forth between turning points, such as a and b in Fig. 7D1. The magnetic field gradient drift $\vec{v}_{\nabla B}$ and curvature drift $\vec{v}_c$ gradually move the guiding center of rotation in the azimuthal direction, as shown in Fig. 7D2. Two other quantities tend to be adiabatically invariant, in addition to μ_m:

$$\textit{longitudinal invariant} \quad J \equiv \oint ds\, v_\parallel = \int_b^a ds\, v_\parallel + \int_a^{b'} ds\, v_\parallel \tag{7D13}$$

$$\textit{flux surface invariant} \quad \Phi \equiv \int_{r=0}^{r} d\vec{A}\cdot\vec{B} \tag{7D14}$$

where ds is a differential path length along the particle trajectory, and $d\vec{A}$ is an element of cross sectional area ($dA = 2\pi r dr$). The invariance of Φ and J is demonstrated by Lehnert (1964) and Sivukhin (1965).

If the magnetic mirrors are moved closer together, the path lengths from b to a and a to b' decrease. Then $v_\parallel$ must increase to maintain J constant. Moving magnetic mirrors can be used for plasma heating. (Motion of galactic magnetic mirrors is a possible acceleration mechanism for cosmic rays.)

The flux surface invariant indicates that, if B is slowly varied, the flux surface radius r (Fig. 7D2) varies so as to maintain $\pi r^2 B_{avg}$ = constant, where B_{avg} is the average value of magnetic induction passing through the circle of radius r.

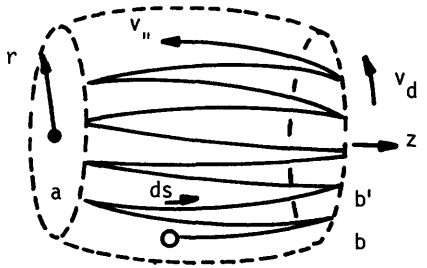

Fig. 7D2. Path of the guiding center of rotation of a charged particle trapped in a simple magnetic mirror. Rotational motion $\vec{v}_{rot}$ is not shown. As the particle bounces back and forth along field lines with velocity $\vec{v}_{\parallel}$, its guiding center gradually drifts in the azimuthal direction ($\vec{v}_d$), tracing out a barrel-shaped surface.

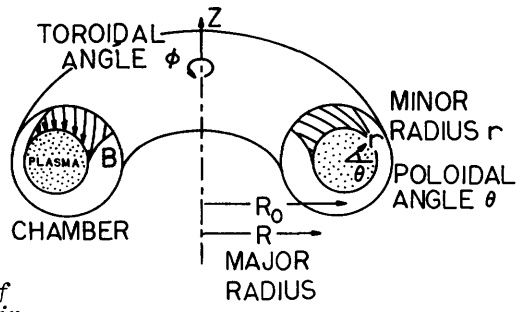

Fig. 7E1. Definition of toroidal coordinates. The magnetic field $\vec{B} = \vec{B}_t + \vec{B}_p + \vec{B}_v$, where B_t is the toroidal component (also called $B\phi$) B_p is the poloidal component (also called B_θ), and B_v is the vertical component (in the z direction).

7E. Particle Orbits in Tokamaks

The name "tokamak" stands for Russian words meaning "Toroidal Chamber with Magnet Coils". Toroidal coordinates are defined in Fig. 7E1. Tokamaks have a toroidal field B_t produced by external coils, a poloidal field B_p produced by a strong plasma current, and a weak vertical B_v for control of the major radius R, with $B_t >> B_p >> B_v$. The resulting magnetic field lines are helical, as shown in Fig. 7C2.

Let a be the value of r at the plasma edge. The *aspect ratio* R_0/a is typically 3-5, so the inverse aspect ratio $\epsilon \equiv a/R_0 \sim 1/4$. We will consider the trajectories of singly charged ions ($q = e$) or electrons with energy $W = mv^2/2$ and pitch angle α between $\vec{v}$ and $\vec{B}$. Hence,

$$v_{\parallel} = v\cos\alpha$$

$$v_{\perp} = v\sin\alpha \quad . \qquad (7E1)$$

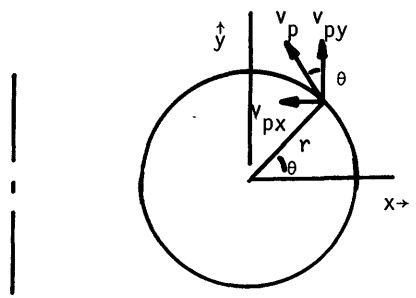

Fig. 7E2. Components of the poloidal velocity in a local Cartesian coordinate system.

Consider a local Cartesian coordinate system, as shown in Fig. 7E2, with $x = r\cos\theta$ and $y = r\sin\theta$. As a particle moves along its helical path, the magnetic field varies as

$$B(x) \simeq B_t(x) = \frac{B_0}{1 + x/R_0} \quad . \qquad (7E2)$$

Because of the invariance of the magnetic moment μ_m, the pitch angle α will vary with x in accordance with Eq. (7D9):

$$W\cos^2\alpha = W - \mu_m B(x) \quad , \qquad \sin^2\alpha = \mu_m B(x)/W \tag{7E3}$$

where we have assumed $\phi = 0$ to simplify the analysis.

The parallel velocity can be further divided into components in the toroidal and poloidal directions. Referring to Fig. 7C2,

$$v_p/v_\parallel = \sin\gamma = B_p/B \tag{7E4}$$

The velocity components of the particle guiding center are

$$dx/dt = -v_p\sin\theta = -(v_\parallel B_p/B)(y/r) \tag{7E5}$$

$$dy/dt = v_p\cos\theta + v_d = (v_\parallel B_p/B)(x/r) + v_d \tag{7E6}$$

where $\vec{v}_d = \vec{v}_{\nabla B} + \vec{v}_c$ is the vertical drift velocity caused by magnetic field gradient and curvature. Since it is primarily the toroidal curvature which causes this drift, $R_c \simeq R_0 + x$, and Eq. (7C5) may be written in the form

$$v_d B \simeq \frac{mv^2(1 - \frac{1}{2}\sin^2\alpha)}{e(R_0 + x)} \tag{7E7}$$

where v_d is upwards for ions. (For electrons, $e \to -e$, and the drift is downwards, Fig. 7C1.)

If Eqs. (7E5) and (7E6) are multiplied by x and y, respectively, and added, the sum is

$$x(dx/dt) + y(dy/dt) = v_d y \quad . \tag{7E8}$$

If Eq. (7E5) is solved for y and this value is inserted on the right side of Eq. (7E8), the result is

$$(xdx + ydy)/r = -(v_d B/v_\parallel B_p)dx \quad , \tag{7E9}$$

where dt has been cancelled. Since $r^2 = x^2 + y^2$, $rdr = xdx + ydy$, and Eq. (7E9) simplifies to

$$dr = -(v_d B/v_\parallel B_p)dx \quad . \tag{7E10}$$

It will be shown in Eq. (8B15) that $B_p = B_p(r)R_0/(R_0 + x)$. Inserting values of $V_d B$ from (7E7) and $v_\parallel$ from (7E1), we have

$$dr = \frac{-mv(1 - \frac{1}{2}\sin^2\alpha)dx}{eB_p(r)R_0\cos\alpha} \tag{7E11}$$

As particles move in the negative x direction, B increases in accordance with Eq. (7E2), and mirror trapping may occur at a point where $\alpha \to \pi/2$. From Eq. (7E3), the magnetic field required to produce reflection is

$$B_m = W/\mu_m \quad . \tag{7E12}$$

Using this equation to eliminate W in Eq. (7E3), we find

$$\cos\alpha = [1 - B(x)/B_m]^{\frac{1}{2}} \qquad \sin\alpha = [B(x)/B_m]^{\frac{1}{2}} \tag{7E13}$$

so (7E11) may be written

$$dr = \frac{-\, mv[1 - B(x)/2B_m]\, dx}{eB_p R_0 [1 - B(x)/B_m]^{\frac{1}{2}}} \tag{7E14}$$

$v_{\parallel} >> v_{\perp}$ case

For particles with large $v_{\parallel}$, the increase in magnetic field from $x = r$ (at $\theta = 0$) to $x = -r$ (at $\theta = \pi$) is not large enough to cause reflection. In other words, B_m is larger than the values of B encountered by the particles. For particles with $v_{\parallel} >> v_{\perp}$, $B/B_m << 1$, and Eq. (7E14) simplifies to

$$dr = \frac{-mv\, dx}{eB_p R_o} \quad . \tag{7E15}$$

We can take $r = r_0$ at $x = 0$ and integrate to obtain

$$r - r_0 \equiv -\lambda x = -\frac{mvx}{eB_p R_0} \tag{7E16}$$

where $\lambda \equiv mv/eB_p R_0$. For most particles, $\lambda << 1$. (The Larmor radius in the poloidal field would be $mv_{\perp}/eB_p$.) We can rearrange Eq. (7E16) and square both sides to get

$$(r_0 - \lambda x)^2 = r^2 = x^2 + y^2 \quad . \tag{7E17}$$

Except for very small terms proportional to λ^2, this is equivalent to the equation

$$(x + \lambda r_0)^2 + y^2 = r_0^2 \tag{7E18}$$

which represents a circle with its center slightly displaced in the x direction by a distance λr_0. Thus, the projections onto the x-y plane of the orbits of particles having $v_{\parallel} >> v_{\perp}$ are nearly circular, but with the centers slightly displaced. Particles which are not mirror reflected are called "free" or "passing".

$v_{\parallel} \sim v_{\perp}$ case

For particles with $v_{\parallel} \sim v_{\perp}$, reflection may occur at $x = x_m$, the position where $B = B_m$. Using $B(x) = B_0/(1 + x/R_0)$ and $B_m = B_0/(1 + x_m/R_0)$, we can write Eq. (7E14) in the form

$$dr = \frac{-mv[1 + (2x-x_m)/R_0](1 + x/R_0)^{-\frac{1}{2}}\,dx}{2eB_p R_0^{\frac{1}{2}}(x - x_m)^{\frac{1}{2}}} = \frac{-mv(1 + 3x/2R_0 - x_m/R_0 + \ldots)dx}{2eB_p R_0^{\frac{1}{2}}(x - x_m)^{\frac{1}{2}}} \tag{7E19}$$

For this case, let r_0 be the value of r at $x = x_m$. Integrating from (x_m, r_0) to (x,r), we find

$$r - r_0 = \frac{-mv(x - x_m)^{\frac{1}{2}}}{eB_p R_0^{\frac{1}{2}}}\left(1 + \frac{x}{2R_0} + \ldots\right) \quad . \tag{7E20}$$

When $v > 0$, $r < r_0$. After reflection, $v < 0$, and $r > r_0$. The resulting shape of the particle orbit is shown in Fig. 7E3. Trapped particles oscillate back and forth between $\pm\,\theta_m \equiv \cos^{-1}(x_m/R_0)$, gradually progressing in the ϕ direction. The projection of the guiding center orbit on the x-y plane has a "banana" shape, with $r < r_0$ when travelling in one direction and $r > r_0$ when going in the opposite direction. Since $(x - x_m) \sim r_0 \sim a$, the characteristic half-width of the bananas is

$$|r - r_0| \sim \frac{mv\varepsilon^{\frac{1}{2}}}{eB_p} \tag{7E21}$$

where $\varepsilon \equiv a/R_0 \sim 1/4$ is the inverse aspect ratio. Other types of orbits are illustrated in Fig. 7E4. The "bounce" frequency at which trapped particles oscillate back and forth between turning points is approximately

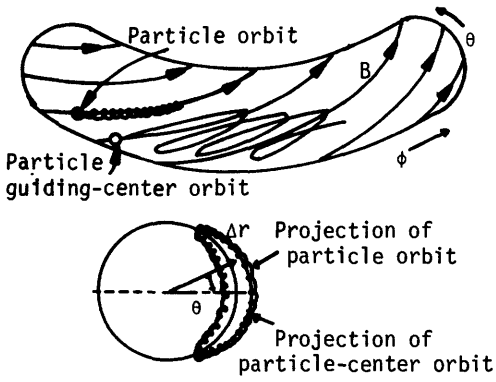

Fig. 7E3. Illustration of trapped particle orbits in a tokamak. From D. L. Jassby, "Tokamak devices and reactors", Ch. 7, Proceedings of the Second IEEE Minicourse on Fusion, Ed. G. H. Miley, U. of Illinois Fusion Studies Laboratory, 1977.

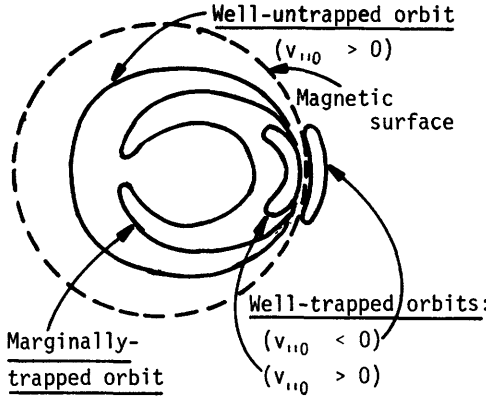

Fig. 7E4. Projections on the x-y plane of various types of particle orbits in tokamaks. Courtesy of F. L. Hinton.

$$\omega_b \simeq \frac{B_p \varepsilon^{\frac{1}{2}} (\mu_m B_t/m)^{\frac{1}{2}}}{aB_t} \qquad \text{(rad/s)} \tag{7E22}$$

For particles at $\theta = 0$, the effective mirror ratio is

$$R_m = \frac{R + r}{R - r} \simeq \frac{1 + \varepsilon}{1 - \varepsilon} \tag{7E23}$$

so the reflection condition (7D12) yields

$$\sin\alpha_m = \left(\frac{1 - \varepsilon}{1 + \varepsilon}\right)^{\frac{1}{2}} \quad . \tag{7E24}$$

Therefore, particles will be reflected if $\alpha > \alpha_m$, or

$$\left(\frac{v_\parallel}{v_\perp}\right)_{\theta=0} \equiv \cot\alpha \Big|_{\theta=0} < \cot\alpha_m = \left(\frac{2\varepsilon}{1 - \varepsilon}\right)^{\frac{1}{2}} \simeq (2\varepsilon)^{\frac{1}{2}} \tag{7E25}$$

For Maxwellian particle distributions, the fraction of particles satisfying this trapping condition is

$$f_t \simeq \left(\frac{2\varepsilon}{1 + \varepsilon}\right)^{\frac{1}{2}} \sim (2\varepsilon)^{\frac{1}{2}} \qquad \textit{trapped particle fraction} \; . \tag{7E26}$$

Thus, for $\varepsilon \sim 1/4$, $f_t \sim 60\%$.

It is not meaningful to speak of trapped-particle effects, however, unless

$$\omega_b >> \nu_{eff} \simeq \nu_{ei}/\varepsilon \tag{7E27}$$

where ν_{eff} is the effective collision frequency for changing the direction of v, and ν_{ei} is the electron-ion collision frequency. Otherwise, particles could be collisionally detrapped in a few bounce times. As plasma temperature is increased, ν_{ei} decreases until Eq. (7E27) is satisfied, and the *collisionless* or *banana regime* is entered. In this high-temperature regime the step size for collisional diffusion is on the order of the banana width (Eq. 7E21), and trapped particle interactions may lead to various instabilities (Chapter 8).

EXAMPLE PROBLEM 7E1

A tokamak has $R_0 = 1.2$ m, $a = 0.3$m, $T_e = T_i = 1$ keV, $B_t = 5$ T, $B_p(a) \simeq 0.5$ T, and $n_e = n_i = 3\times10^{19}$ m^{-3}. Estimate the characteristic banana widths and bounce frequencies for electrons and deuterons. Are the electrons and ions in the collisionless regime?

The average speeds $(8kT/\pi m)^{\frac{1}{2}}$ are 2.1×10^7 m/s for electrons and 3.5×10^5 m/s for deuterons. Using these values in Eq. (7E21), we find average banana half-widths of 0.12 mm for electrons and 7.3 mm for ions. Taking $\mu_m B_t = W_\perp \sim kT$ in Eq. (7E22), we find $\omega_{be} \sim 2.2\times10^6$ rad/s and $\omega_{bi} \sim 3.7\times10^4$ rad/s. Taking $L \simeq 18$ in Eq. (2E57), we find $\nu_{ei} \simeq 3.6\times10^4$ s^{-1}, so $\nu_{eff} \simeq 1.4\times10^5$ s^{-1}. Thus, the electrons are well into the collisionless regime, but the ions are not.

summary

Charged particles have motion along the field lines; Larmor rotation around a field line; and a gradual drift velocity across the field lines, produced by magnetic field gradients, curvature, electric fields, and other causes. In the absence of collisions, the magnetic moment $\mu_m = W_\perp/B$ tends to remain constant, causing particles to be reflected from high-field regions. Magnetic mirrors confine particles with large $v_\perp$, but lose those with large $v_\parallel$. Similar trapping can occur in toroidal devices like tokamaks, because of the higher magnetic field near $\theta = \pi$. Trapped particles have crescent-shaped orbits, while free particles have nearly circular orbits. In the collisionless regime trapped particle effects may strongly influence plasma behavior.

Analysis of individual charged particle trajectories can indicate ways in which plasma confinement systems will fail, but it cannot guarantee success. Even if individual particles are perfectly confined, collisional effects and a large number of plasma instabilities can reduce energy confinement times to unsatisfactory values (Chapter 8). Thus, single particle confinement is necessary, but not sufficient, for plasma confinement.

Problems

1. Demonstrate the validity of Eqs. (7A6-7A8) and (7A9-7A11).

2. Find the magnitude and direction of a proton's drift velocity in the ionosphere from the force of gravity in a magnetic induction of 10^{-5} T directed south.

3. A 15 keV deuteron with $W_\perp = 10$ keV is travelling along a magnetic field line bending counterclockwise in the xy plane with a radius of curvature of 1.2 m. What is the magnitude and direction of the drift velocity due to magnetic field curvature? Assume $B = 1.0$ T.

4. A plasma thruster for space propulsion accelerates plasma by applying an electric field in the y direction and a magnetic induction of 1 T in the x direction on a plasma. (a) In what direction will the plasma move? (b) How strong must the electric field be to produce an exhaust velocity of 10^4 m/s?

5. A magnetic field of 0.5 T is applied in the z direction and an electric field of 1000 V/m is applied in the x direction. Plot the trajectory of a deuteron with $v = 10^4$ m/s from $t = 0$ to $t = 2/\nu_{ci}$ if (a) it starts out in the x direction (b) it starts out in the y direction. Take $x_0 = y_0 = 0$.

6. In a certain mirror the coils are specially designed so that B increases linearly from 1 T to 3 T over a distance of one meter. (a) What is the effective force produced by this field on a 3 keV deuteron with $W_\perp = 2$ keV at the point where B = 1 T? (b) How far can the deuteron go towards the increasing magnetic field before the work done by the force $\int dz\, F_z$ is equal to its initial parallel energy $W_\parallel$? (c) Using magnetic mirror theory, calculate the magnetic induction at which the deuteron will be reflected, and compare with the result of part (b).

7. If the minimum magnetic induction of a magnetic mirror coil system is 0.8 T, how large must the maximum induction be to make the loss cone angle 30 degrees? to make it 5 degrees?

8. Particles are emitted isotropically from the center of a mirror device by the impact of a laser beam on a small pellet. What fraction of the particles will be in the loss cone if the mirror ratio is 3.5?

9. A long thin straight wire carries a current I_z, which produces an azimuthal magnetic induction $B_\theta = \mu_0 I/2\pi r$. (a) Find the drift velocities experienced by a particle with mass m, charge q, and initial velocity components v_{r0}, $v_{\theta 0}$, v_{z0} at a radius r. (This azimuthal field is similar to the toroidal field of toroidal confinement devices, such as tokamaks). (b) A deuteron starts out with $v_r = 10^4$ m/s, $v_\theta = 5000$ m/s with its guiding center of rotation at r = 1 m, $\theta = 0$, z = 0 in the magnetic field of a long, straight wire carrying a current of 1 MA in the z direction. Where is its guiding center 1 ms later? (Find r, θ, z).

Bibliography

elementary

F. F. Chen, *Introduction to Plasma Physics*, Plenum, New York, 1974, Ch. 2.
S. R. Seshadri, *Fundamentals of Plasma Physics*, American Elsevier, New York, 1973, Ch. 3.
B. S. Tanenbaum, *Plasma Physics*, McGraw-Hill, New York, 1967, Ch. 1.

more advanced

I. B. Bernstein, "The Motion of a Charged Particle in a Strong Magnetic Field", *Advances in Plasma Physics*, Vol. 4. (A. Simon and W. B. Thompson, Editors), Interscience, New York, 1971, p. 311-333.
N. A. Krall and A. W. Trivelpiece, *Principles of Plasma Physics*, McGraw-Hill, New York, 1973, App. I.
M. Kruskal, "Elementary orbit and drift theory", and "Advanced theory of gyrating particles", *Plasma Physics*, International Atomic Energy Agency, Vienna, 1965, p. 67-90.
B. Lehnert, *Dynamics of Charged Particles*, North-Holland Publishing Company, Amsterdam, 1964, Ch. 3, 4.
T. G. Northrup, "Adiabatic Charged-Particle Motion", *Plasma Physics in Theory and Application* (W. B. Kunkel, Editor), McGraw-Hill, New York, 1966, Ch. 2.
D. J. Rose and M. Clark, Jr., *Plasma and Controlled Fusion*, M. I. T. Press, Cambridge, Massachusetts, 1961, Ch. 10.
G. Schmidt, *Physics of High Temperature Plasmas*, Academic Press, New York, 1979, Ch. II.
D. V. Sivukhin, "Motion of charged particles in electromagnetic fields in the drift approximation", *Reviews of Plasma Physics, Vol. 1*, Consultants Bureau, New York, 1965, p. 1-104.

tokamak orbits

K. Miyamoto, *Plasma Physics for Nuclear Fusion*, M. I. T. Press, Cambridge, Massachusetts, 1980, Ch. 3.
W. M. Stacey, Jr., *Fusion Plasma Analysis*, Wiley, New York, 1981, Ch. 2.

CHAPTER 8
PLASMA CONFINEMENT

8A. Introduction

means of plasma containment

The purpose of a plasma containment system is to sustain the plasma pressure and to provide a long energy confinement time, in order to attain a high energy-gain ratio Q (Chapter 4). Plasma can be contained by:

* *solid walls.* Low-temperature plasmas, such as fluorescent lights, may be contained by glass or metal tubes. Hot plasma confinement in magnetic fields may be augmented by solid walls for brief periods of time, but prolonged contact cools the plasma rapidly by heat conduction and may overheat the wall.
* *gravity.* Although stellar plasmas, such as the sun, are confined by gravity, the mass of a laboratory plasma is many orders of magnitude too small for self-gravitational attraction to be significant.
* *inertia.* If a deuterium-tritium fuel pellet is compressed to high densities, significant fusion burn can occur before the compressed pellet expands. The inertia of the pellet limits the expansion rate of the internal plasma. At a plasma density $n \approx 10^{30} m^{-3}$, a confinement time $\tau > 10^{-10} s$ would satisfy the Lawson criterion (1F2). The compression may be produced by laser beams or by particle beams.

* *radiofrequency (rf) fields.* Radiofrequency and microwave fields can confine low-pressure plasma well, but enormous power inputs are required to confine high-pressure plasmas. Radiofrequency fields can augment magnetic confinement.
* *electrostatic fields.* Peaks of the electrostatic potential ϕ, which inhibit ion flow along magnetic field lines, may be established with high voltage electrodes, or by creating local regions of higher plasma density, in accordance with the Boltzmann relation $e(\phi-\phi_0) = kT_e \ln(n/n_0)$.
* *magnetic fields.* The present chapter will concentrate on magnetic confinement, because it is the most promising means for prolonged containment of high-pressure plasmas.

magnetic field shapes

Open magnetic confinement systems have many magnetic field lines leaving the plasma region and intersecting the chamber walls, so plasma may flow along the

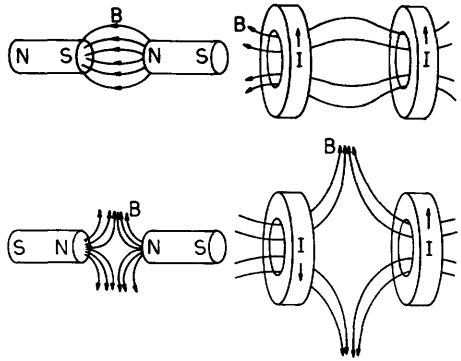

Fig. 8A1. Simple magnetic mirror fields (top) and spindle cusp fields (bottom) produced by bar magnets (left) and by a pair of circular magnet coils (right) with currents I. B = magnetic field lines. Plasmas could be confined in the central regions.

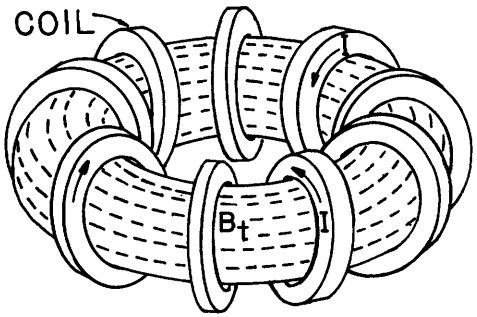

Fig. 8A2. A simple toroidal magnetic field produced by circular coils. The dashed curves represent magnetic field lines. (For clarity, only a few coils are shown. More coils would be needed to produce the smooth field lines shown.)

field lines to the walls. Open systems may be either "mirrors" or "cusps", as illustrated in Fig. 8A1, depending on the curvature of the magnetic field lines. The direction of the magnetic field lines produced by coils can be found from the right hand rule (Fig. 5B1). The magnetic fields $B \sim 0.5$ T produced by permanent magnets are probably too low to be useful for containment of high-pressure plasmas.

Closed magnetic confinement systems have magnetic field lines which stay within a specified volume, usually having a toroidal (donut) shape. A simple toroidal magnetic field produced by a group of circular magnet coils is shown in Fig. 8A2. Because of the effects of additional coils and plasma currents, the magnetic field lines will, in general, not be closed circles. Instead, they usually have spiral shapes, as shown in Fig. 7C2.

Various magnetic field geometries being studied for plasma confinement will be described in Chapters 11-14.

thermodynamic equilibrium and plasma equilibrium

Everything in nature tends towards a state of *thermodynamic equilibrium*, in which the temperatures of various bodies are uniform and equal to each other. Charged particles do not have an energy of interaction with a magnetic field, so there can be no pressure gradient at thermodynamic equilibrium. At thermodynamic equilibrium the DT fuel would be the same temperature as the chamber walls. Since we want to keep the chamber wall temperature $T_w \lesssim 1000$ K and the fuel ion temperature $T_i \sim 10^8$ K, the plasma confinement system must retard the establishment of thermodynamic equilibrium. In a plasma the slowest time scale for approach to thermodynamic equilibrium is that of Coulomb collisions (Chapter 2). Density gradients and temperature gradients provide sources of "free energy" to drive various types of plasma instabilities, which greatly accelerate the rate of approach to thermodynamic equilibrium and spoil plasma confinement.

8A. Introduction

The magnetic field and plasma currents must be designed to contain the plasma pressure and avoid instabilities. When the outward force of the plasma pressure is just balanced by the confining forces of the magnetic field and plasma current, we say that the plasma is in *equilibrium*. (This desirable force-balance condition should not be confused with the undesirable thermodynamic equilibrium.)

There are two general classes of plasma instabilities. Growing macroscopic distortions of the plasma shape are called *MHD instabilities*, after the MHD equations (5D38)-(5D41). Growing plasma waves caused by non-Maxwellian velocity distributions or by pressure gradients are called *microinstabilities*. The resultant plasma waves increase the rates of particle diffusion and heat conduction across the magnetic field.

energy loss mechanisms

Various energy loss mechanisms are listed in Table 8A1.

Table 8A1. Plasma energy loss mechanisms.

1. Particle and energy loss along magnetic field lines (Chapter 11).
   (a) simple mirrors. The loss time is roughly the characteristic time τ_i for Coulomb scattering of the ions into the loss cone
   (b) cusps. The loss time is roughly $a^2/\rho_i v_i$, where a = plasma radius, v_i = average ion speed, ρ_i = ion Larmor radius.
   (c) potential barriers. In devices with potential barriers restricting particle flow along field lines, the loss time is the time needed for the particle to gain enough energy by velocity space diffusion to overcome the barrier (the Coulomb collision time at the barrier energy).
2. drift motion $\vec{v}_d$ across the magnetic field, driven by $\vec{E}$, $\vec{\nabla}B$, and magnetic field curvature (Chapter 7). To minimize this loss, magnetic confinement systems are designed so that the drift motions of most particles carry them around inside the plasma volume and not to the walls.
3. MHD instabilities, driven by plasma expansion energy or magnetic field energy (Section 8D).
4. radiation losses, from line, recombination, bremsstrahlung, and cyclotron radiation (Chapter 3).
5. energy transport across the magnetic field by particle diffusion and heat conduction (Section 8F).
6. microinstabilities, increasing energy transport rates (Section 8E)
7. ion energy loss by charge exchange (Chapter 3).

Particle losses along field lines can be reduced by potential barriers or eliminated by using closed magnetic systems. Losses from drift motion can be minimized by proper design of the magnetic field. MHD instabilities can be controlled by proper magnetic field design and by keeping the plasma pressure below a limiting value. Radiation losses can be controlled by minimizing impurity concentrations and by keeping T_e low enough that cyclotron losses are not

excessive. If energy transport occurred at the "classical" rate governed by Coulomb collisions, long energy confinement times could be attained, but micro-instabilities often enhance transport rates to much larger values.

The goals of this Chapter are to describe
*plasma energy loss mechanisms
*general features of plasma confinement by magnetic fields
*plasma equilibrium in axisymmetric toroidal devices
*methods for studying MHD stability, and types of instabilities
*causes and effects of microinstabilities
*plasma transport equations and coefficients
*simple estimates of confinement times.

8B. Magnetic Confinement

Some terms used in describing magnetic confinement are defined in Table 8B1.

The simplest model for describing plasma confinement is the single-fluid (MHD) model. Plasma equilibrium may be described in terms of the equation of motion (5D39) and Ampere's Law (5B8), ignoring the $\partial\vec{E}/\partial t$ term:

$$\rho_m(\partial\vec{u}/\partial t) + \rho_m(\vec{u}\cdot\vec{\nabla})\vec{u} = \vec{J}\times\vec{B} - \vec{\nabla}p \qquad (8B1)$$

$$\vec{J} = \vec{\nabla}\times\vec{B}/\mu_0 \qquad (8B2)$$

[The assumption of scalar pressure used in Eq. (8B1) is not valid for anisotropic plasmas, as in magnetic mirrors.]

equilibrium conditions

At equilibrium, the forces $\vec{J}\times\vec{B}$ and $\vec{\nabla}p$ on the right side of the equation of motion (8B1) just balance each other, and

$$\vec{\nabla}p = \vec{J}\times\vec{B} \quad . \qquad (8B3)$$

This equation has three important consequences:

* The component of $\vec{\nabla}p$ along $\vec{B}$ is zero, so p is constant along a magnetic field line.
* In order to sustain a plasma pressure gradient $\vec{\nabla}p$, a current $\vec{J}_\perp$ must flow in a direction perpendicular to $\vec{B}$ and $\vec{\nabla}p$. If we multiply Eq. (8B3) vectorially by $\vec{B}\times$, we find

$$\vec{B}\times\vec{\nabla}p = \vec{B}\times(\vec{J}\times\vec{B}) = \vec{J}B^2 - \vec{B}(\vec{J}\cdot\vec{B}) = \vec{J}_\parallel B^2 + \vec{J}_\perp B^2 - \vec{B}(J_\parallel B) = \vec{J}_\perp B^2 \quad ,$$

$$\vec{J}_\perp = \vec{B}\times\vec{\nabla}p/B^2 \qquad (8B4)$$

where $\parallel$ and $\perp$ refer to components parallel and perpendicular to $\vec{B}$.

* If we multiply Eq. (8B3) by $\vec{B}\cdot$ and $\vec{J}\cdot$, the result is

$$\vec{B}\cdot\vec{\nabla}p = \vec{B}\cdot(\vec{J}\times\vec{B}) = 0$$

$$\vec{J}\cdot\vec{\nabla}p = \vec{J}\cdot(\vec{J}\times\vec{B}) = 0. \qquad (8B5)$$

Table 8B1. Plasma confinement terminology.

field line		A magnetic field line is a curve that is everywhere tangent to the direction of the magnetic field.
ergodic field line		An ergodic field line is one which will pass arbitrarily close to any point on a given surface (or in a given volume) if it is followed long enough. The field lines are said to fill the surface (or volume) ergodically.
magnetic surface		A magnetic surface is a surface which is covered ergodically by a magnetic field line. It is also a surface of constant magnetic flux.
magnetic flux		Magnetic flux is the integral over a surface of the magnetic field component perpendicular to that surface $\int d\vec{S}\cdot\vec{B}$
toroidal confinement		(See Figs. 7E1 and 8B1)
major axis	z	The major axis is perpendicular to the plane of the torus.
major radius	R	The major radius is the distance from the major axis.
plasma major radius	R_0	The major radius to the magnetic axis of the plasma.
minor radius	r	Distance from magnetic axis.
plasma minor radius	a	The value of r at the plasma surface.
toroidal angle	ϕ	Angle around major axis.
poloidal angle	θ	Angle around magnetic axis.
toroidal field	B_t	Magnetic field in toroidal direction (Fig. 7C2).
poloidal field	B_p	Magnetic field in poloidal direction (Fig. 7C2).
poloidal surface		A surface perpendicular to the major axis.
toroidal surface		A surface perpendicular to the toroidal field.
poloidal flux	ψ_p	The flux passing through a given poloidal surface $\psi_p \equiv \int_{\text{poloidal surface}} d\vec{S}\cdot\vec{B}_p$
toroidal flux	ψ_t	The flux passing through a given toroidal surface. $\psi_t \equiv \int_{\text{toroidal surface}} d\vec{S}\cdot\vec{B}_t$
axisymmetric		Symmetric in toroidal direction ϕ. Hence derivatives $(\partial/\partial\phi) = 0$.
magnetic axis		The magnetic axis is a line along which $B_p = 0$. A plasma may have more than one magnetic axis.
safety factor	q	$\equiv d\psi_t/d\psi_p$ is the amount of twist of the helical magnetic field lines. $q \simeq rB_t/R_0B_p$ (if $\beta<<1$, $\varepsilon<<1$)
rotational transform	ι	$= 2\pi/q$ (radians) is the amount of twist a field line makes in the θ direction while going once around the torus in the ϕ direction.
aspect ratio		R_0/a
inverse aspect ratio	ε	$\equiv a/R_0$.
magnetic shear		$r^2(d\iota/dr)/2\pi R_0 = -r^2(dq/dr)/q^2R_0$ = the change in direction of B from one surface to another.
shear length	L_s	$\equiv R_0q^2/r(dq/dr) = r/(\text{shear})$.

toroidal current density	J_t Component of current density in toroidal direction.
poloidal current density	J_p Component of current density in poloidal direction.

These equations indicate that both $\vec{B}$ and $\vec{J}$ are perpendicular to the pressure gradient, so $\vec{B}$ and $\vec{J}$ both lie on surfaces of constant pressure. [As shown in Eq. (8B4), $\vec{J}$ must have a component perpendicular to $\vec{B}$.] Thus, a toroidal magnetic surface traced out ergodically by a field line is also a surface of constant plasma pressure. It can be shown that the magnetic flux enclosed by the surface is a constant, so the surfaces can be labelled by the amount of flux they enclose. Such magnetic surfaces are illustrated in Fig. 8B2.

magnetic pressure

From Eqs. (8B2) and (8B3),

$$\vec{\nabla}p = \vec{J}\times\vec{B} = (\vec{\nabla}\times\vec{B})\times\vec{B}/\mu_0 = (\vec{B}\cdot\vec{\nabla})\vec{B}/\mu_0 - \vec{\nabla}B^2/2\mu_0 \quad ,$$

$$\vec{\nabla}(p + B^2/2\mu_0) = (\vec{B}\cdot\vec{\nabla})\vec{B}/\mu_0 \quad . \qquad (8B6)$$

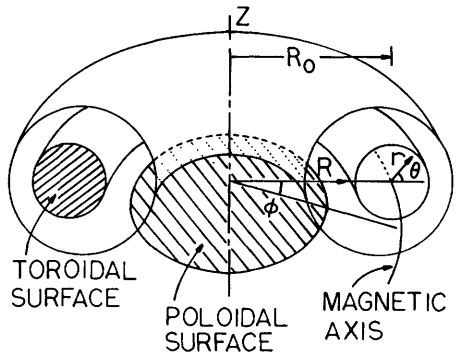

Fig. 8B1. Illustration of toroidal and poloidal surfaces, perpendicular to the toroidal and poloidal directions.

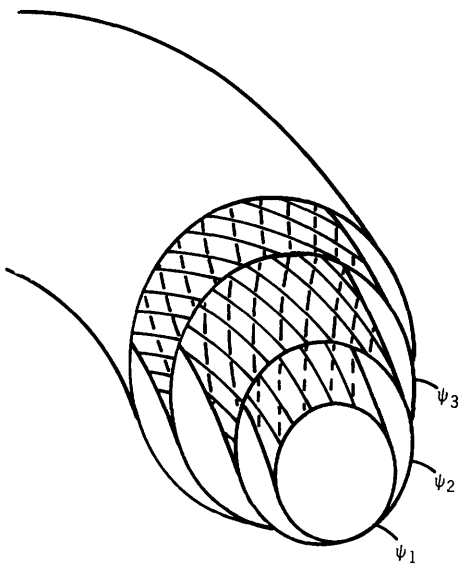

Fig. 8B2. Magnetic surfaces traced out by ergodic field lines (smooth curves). Dashed curves represent current density. Plasma pressure is uniform along each surface.

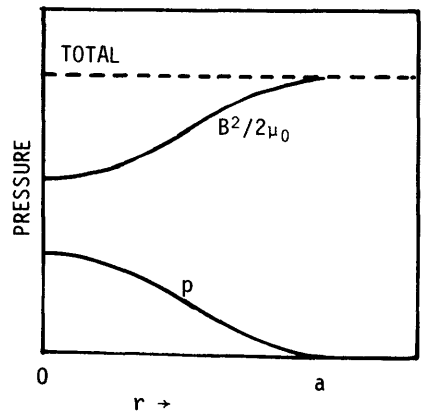

Fig. 8B3. Radial pressure variations for a straight cylindrical plasma, in which $p + B^2/2\mu_0$ = total pressure = constant.

The term on the right is related to the curvature of the magnetic field lines and it is zero if the field lines are straight, as for a uniform B_z in a cylinder.

There is an effective tension along the magnetic field lines, which tend to resist bending and stretching, and a magnetic pressure perpendicular to the field lines. The quantity $B^2/2\mu_0$ is called *magnetic pressure*. For field lines which have little curvature,

$$p + B^2/2\mu_0 \simeq \text{constant} \tag{8B7}$$

Consider the case of a straight, uniform B_z field. In the absence of plasma, $p = 0$ and the magnetic pressure is uniform. When plasma is introduced into the chamber, the magnetic field pressure will be reduced inside the plasma, due to plasma diamagnetism (Section 7B). The radial variations of plasma pressure and magnetic field pressure for such a case are illustrated in Fig. 8B3.

plasma beta

The *beta* value of a plasma is defined to be the ratio of the plasma pressure to the vacuum magnetic field pressure (the value of $B^2/2\mu_0$ with no plasma present). The *toroidal beta* β_t is defined relative to the value of B_t at the magnetic axis, and the *poloidal beta* β_p is defined relative to the value of B_p at $r = a$. If no field component is specified, then the total magnetic field is implied. Various pressures may also be used:

peak beta
$$\hat{\beta} \equiv \frac{p_{max}}{B^2/2\mu_0} \tag{8B8}$$

average beta
$$\langle\beta\rangle \equiv \frac{\langle p\rangle}{B^2/2\mu_0} \tag{8B9}$$

rms beta
$$\beta_* \equiv \frac{\langle p^2\rangle^{\frac{1}{2}}}{B^2/2\mu_0} \tag{8B10}$$

where the symbols $\langle\ \rangle$ denote a volume average. For the case of Fig. 8B3, $\hat{\beta} \simeq 0.3$ and $\langle\beta\rangle \sim 0.1$. The average fusion power density $\langle P_f\rangle$ is related to β_* by Eqs. (2D16)-(2D19). The vacuum magnetic field is zero at the center of a magnetic cusp system, so beta may be defined relative to the value of magnetic field along the plasma boundary. Other definitions of beta have also been used.

divergences

The Maxwell equation $\vec{\nabla}\cdot\vec{B} = 0$ may be written in cylindrical geometry as

$$\frac{1}{r}\frac{\partial}{\partial r}rB_r + \frac{1}{r}\frac{\partial B_\phi}{\partial \phi} + \frac{\partial B_z}{\partial z} = 0\ . \tag{8B11}$$

For a magnetic mirror field which is symmetric around the axis (Fig. 8A1) $B_\phi = 0$. This equation tells us that any change in the axial field B_z in the z direction must be accompanied by a change in the radial field B_r. If we integrate over a small cylindrical volume element $2\pi r dr dz$, we find

$$\partial\psi_r/\partial r = -\partial\psi_z/\partial z \tag{8B12}$$

where ψ_r and ψ_z are the magnetic fluxes in the r and z directions. Thus, this equation represents conservation of magnetic flux. All the field lines which enter the volume must leave it.

A similar relation applies to the current density. In view of vector relation (F25), the divergence of Eq. (8B2) yields

$$\vec{\nabla}\cdot\vec{J} = 0 \quad . \tag{8B13}$$

In a toroidal coordinate system with nearly circular flux surfaces

$$\vec{\nabla}\cdot\vec{B} \simeq \frac{1}{rR}\frac{\partial}{\partial r}(rRB_r) + \frac{1}{rR}\frac{\partial}{\partial\theta}(RB_p) + \frac{1}{R}\frac{\partial}{\partial\phi}B_t = 0 \tag{8B14}$$

and likewise for $\vec{J}$. By virtue of Eq. (8B5) B_r and J_r are zero for circular magnetic surfaces, and $(\partial/\partial\phi)$ is zero for an axisymmetric torus, so this equation reduces to

$$\frac{\partial}{\partial\theta}RB_p = 0, \quad RB_p = (\text{function of r}), \quad B_p = B_p(r)R_0/R$$

$$\frac{\partial}{\partial\theta}RJ_p = 0, \quad RJ_p = (\text{function of r}), \quad J_p = J_p(r)R_0/R \quad . \tag{8B15}$$

8C. Axisymmetric Toroidal Equilibrium

derivation of Grad-Shafranov Equation

The pressure balance equation (8B10) was derived from the force balance equation $\vec{\nabla}p = \vec{J}\times\vec{B}$ and the Maxwell equation $\vec{J} = \vec{\nabla}\times\vec{B}/\mu_0$. This equation can be re-derived, expressing $\vec{B}$ in terms of a magnetic flux function labelling the magnetic surfaces. The result is known as the Grad-Shafranov Equation.

Since $\vec{J}$ and $\vec{B}$ both lie along magnetic surfaces, they can be resolved into toroidal and poloidal components, with no component perpendicular to the surfaces:

$$\vec{J} = \vec{J}_p + \vec{J}_t$$

$$\vec{B} = \vec{B}_p + \vec{B}_t \tag{8C1}$$

For simplicity, we will consider only axisymmetric cases here, in which all derivatives in the toroidal direction ϕ are zero. Then from Eq. (5B14) the poloidal magnetic field may be written as

$$\vec{B}_p = \vec{\nabla}\times\vec{A}_\phi \tag{8C2}$$

where $\vec{A}_\phi$ is the magnetic vector potential in the toroidal direction. We will use the cylindrical coordinate system of Fig. 8B1. Let

$$\psi \equiv RA_\phi \quad . \tag{8C3}$$

From the definition of poloidal flux ψ_p (Table 8B1), it can be shown that

$$\psi = \psi_p/2\pi \quad . \tag{8C4}$$

Let $\hat{\phi}$ be a unit vector in the toroidal direction. Using the fact that $\vec{\nabla}\phi = \hat{\phi}/R$ and the relation $\vec{A}_\phi = \psi\hat{\phi}/R$, we can write Eq. (8C2) in the form

$$\vec{B}_p = \vec{\nabla}\times(\psi\hat{\phi}/R) = \vec{\nabla}\times(\psi\vec{\nabla}\phi) = \vec{\nabla}\psi\times\vec{\nabla}\phi = \vec{\nabla}\psi\times\hat{\phi}/R = -(\hat{R}/R)(\partial\psi/\partial z) + (\hat{z}/R)(\partial\psi/\partial R) \tag{8C5}$$

where $\hat{R}$ and $\hat{z}$ are unit vectors, and vector relations (F23), (F24), and (F32) have been used (Appendix F).

Using Eqs. (8C1) in the force-balance Eq. (8B7), we find

$$\vec{\nabla}p = \underline{\vec{J}_p\times\vec{B}_p} + \vec{J}_p\times\vec{B}_t + \vec{J}_t\times\vec{B}_p + \underline{\vec{J}_t\times\vec{B}_t} \quad , \tag{8C6}$$

where the underlined terms are equal to zero. The Maxwell equation (8B2) may be written

$$\vec{J} = \nabla\times(\vec{B}_p+\vec{B}_t)/\mu_0 = \vec{\nabla}\times\vec{B}_p/\mu_0 + \vec{\nabla}\times\vec{B}_t/\mu_0 \tag{8C7}$$

and we can identify

$$\vec{J}_p = \vec{\nabla}\times\vec{B}_t/\mu_0 \qquad \vec{J}_t = \vec{\nabla}\times\vec{B}_p/\mu_0 \quad . \tag{8C8}$$

After multiplying Eq. (8C6) by μ_0 and using (8C8), we have

$$\mu_0\vec{\nabla}p = (\vec{\nabla}\times\vec{B}_t)\times\vec{B}_t + (\vec{\nabla}\times\vec{B}_p)\times\vec{B}_p \quad . \tag{8C9}$$

With $\vec{B}_t = B_t\hat{\phi}$ and $\vec{B}_p$ given by various expressions in Eq. (8C5), this becomes

$$\mu_0\vec{\nabla}p = [\vec{\nabla}\times B_t\hat{\phi}]\times B_t\hat{\phi} + [\vec{\nabla}\times(-\frac{1}{R}\frac{\partial\psi}{\partial z}\hat{R} + \frac{1}{R}\frac{\partial\psi}{\partial R}\hat{z})]\times(\vec{\nabla}\psi\times\hat{\phi}/R)$$

$$= [-\frac{\partial B_t}{\partial z}\hat{R} + \frac{1}{R}\frac{\partial}{\partial R}(RB_t)\hat{z}]\times B_t\hat{\phi} - [\frac{\partial}{\partial R}(\frac{1}{R}\frac{\partial\psi}{\partial R}) + \frac{1}{R}\frac{\partial^2\psi}{\partial z^2}]\hat{\phi}\times(\vec{\nabla}\psi\times\hat{\phi}/R) \quad , \tag{8C10}$$

where (F34) has been used to evaluate the components of the vector curls in cylindrical coordinates (with $r \to R$). Since the parameter ψ is proportional to the poloidal flux [Eq. (8C4)] we can use it to label the magnetic surfaces, and write

$$p = p(\psi) \quad . \tag{8C11}$$

Then

$$\vec{\nabla}p = p'\vec{\nabla}\psi \tag{8C12}$$

where $p' \equiv dp/d\psi$. By definition, let

$$\Delta^*\psi \equiv R\frac{\partial}{\partial R}\left(\frac{1}{R}\frac{\partial\psi}{\partial R}\right) + \frac{\partial^2\psi}{\partial z^2} \quad . \tag{8C13}$$

Using Eq. (F16), Eq. (8C10) becomes

$$\mu_0 p'\vec{\nabla}\psi = -\frac{B_t}{R}\left[\frac{\partial}{\partial R}(RB_t)\hat{R} + R\frac{\partial B_t}{\partial z}\hat{z}\right] + \frac{1}{R^2}\Delta^*\psi\left[\vec{\nabla}\psi(\hat{\phi}\cdot\hat{\phi})\right) - \underline{\hat{\phi}(\vec{\nabla}\psi\cdot\hat{\phi})}\Big] \tag{8C14}$$

where the underlined term is zero, since $\vec{\nabla}\psi$ is perpendicular to the magnetic surfaces, hence orthogonal to $\hat{\phi}$. The product $\hat{\phi}\cdot\hat{\phi} = 1$. With the definition of the gradient in cylindrical geometry (F32), we can write Eq. (8C14) as

$$\mu_0 p'\vec{\nabla}\psi = -\frac{(RB_t)}{R^2}\vec{\nabla}(RB_t) - \frac{1}{R^2}\Delta^*\psi\,\vec{\nabla}\psi \quad . \tag{8C15}$$

Since this is a vector equation, $\vec{\nabla}(RB_t)$ must be parallel to $\vec{\nabla}\psi$, which means that RB_t is also a constant on each magnetic surface. Therefore, we can let

$$I(\psi) \equiv RB_t \quad . \tag{8C16}$$

From the definition of poloidal current density (Table 8B1), it can be shown that

$$I(\psi) = \mu_0 I_p/2\pi \quad , \qquad I_p \equiv \int_{\text{Poloidal Surface}} d\vec{S}\cdot\vec{J}_p \tag{8C17}$$

Now

$$\vec{\nabla}(RB_t) = I'\vec{\nabla}\psi \quad , \qquad I' \equiv \frac{dI}{d\psi} \tag{8C18}$$

and the vector $\vec{\nabla}\psi$ cancels out of Eq. (8C15), leaving

$$R^2\mu_0 p' = -II' - \Delta^*\psi \tag{8C19}$$

which is called the *Grad-Shafranov Equation*. The pressure gradient p' is balanced by the terms II' representing the $\vec{J}_p\times\vec{B}_t$ force and $\Delta^*\psi$ representing the $\vec{J}_t\times\vec{B}_p$ force. If the shape of the flux surfaces were known, then the poloidal current and pressure distributions $I(\psi)$ and $p(\psi)$ could be determined from the transport equations (Section 8F). Usually, some simple distributions $I(\psi)$ and $p(\psi)$ are assumed, and the Grad-Shafranov equation is solved for $\psi(R,z)$.

properties of the Grad-Shafranov equation

There are three simple limiting cases of Eq. (8C19) (Bateman, 1978):
(1) $II' \simeq 0$. In this case $J_p \simeq 0$ inside the plasma, and $B_t \propto 1/R$. The plasma pressure is balanced entirely by the $\vec{J}_t\times\vec{B}_p$ pinching force of the

self-magnetic field induced by the plasma toroidal current. For this case the poloidal beta $\beta_p \simeq 1$.

(2) Regions where $\vec{J}$ is parallel to $\vec{B}$. In such regions, the force $\vec{J}\times\vec{B} \simeq 0$, $p' \simeq 0$, and the pressure is uniform. If such a force-free region covers most of the plasma, then confinement is poor, and $\beta_p << 1$.

(3) $|II'| >> |\Delta^*\psi|$. In this case, the plasma pressure is balanced mainly by the $\vec{J}_p\times\vec{B}_t$ force, and $\beta_p > 1$.

Variations of B_t with R for these cases are shown in Fig. 8C1.

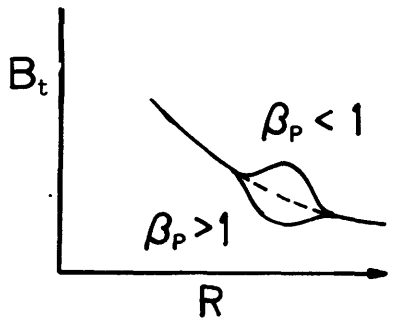

Fig. 8C1. Variations of toroidal magnetic field B_t with major radius R for three extreme cases of poloidal beta. Reprinted from MHD Instabilities by G. Bateman, Fig. 4.5, by permission of the MIT Press, Cambridge, Massachusetts. Copyright 1978 by the Massachusetts Institute of Technology.

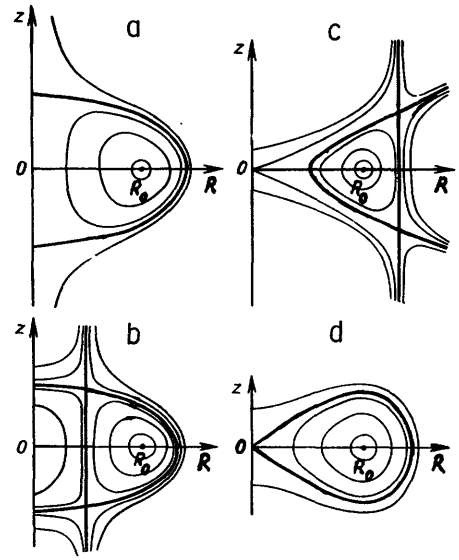

Fig. 8C2. Shapes of the magnetic surfaces ψ = constant for the simple equilibrium case of Eq. (8C21), for various values of b/a. (a) b/a = 0, (b) b/a = - 1/7, (c) b/a = -7, (d) b/a = 1. From L.S. Solov'ev, Hydromagnetic stability of closed plasma configurations, Reviews of Plasma Physics, Vol. 6, Consultants Bureau, New York, 1976, Fig. 2.

Copyright by Plenum. Used with permission of Plenum Publishing Corp.

The variation of the $\vec{J}_p\times\vec{B}_t$ force with R makes the plasma tend to move in the R direction. If a vertical magnetic field B_z is applied, the $\vec{J}_t\times\vec{B}_z$ force can be used to control this motion.

The Grad-Shafranov equation has been solved analytically only for a few simple cases. One such case is

$$p' = -a$$

$$II' = -bR_0^2 \tag{8C20}$$

where a and b are constants. The exact solution for this case is

$$\psi(R,z) = \frac{1}{2}(bR_0^2 + cR^2)z^2 + \frac{1}{8}(a - c)(R^2 - R_0^2)^2 \tag{8C21}$$

where R_0 is the radius of the magnetic axis and c is a constant. The shapes of the magnetic surfaces ψ = constant for this case are shown in Fig. 8C2 for various values of the ratio b/a.

It is usually not feasible to choose $\psi(R,z)$ and then try to find $p'(\psi)$ and $II'(\psi)$, because only a few flux functions $\psi(R,z)$ are suitable for MHD equilibria.

Since the flux function ψ is a natural coordinate of the plasma, it is often convenient to use a coordinate system based on (ϕ, ψ, θ) rather than the cylindrical coordinates (R, ϕ, z), where θ is a coordinate in the poloidal direction, similar to the angle θ of Fig. 7E1. It is possible to choose θ in such a way that the magnetic field lines appear as straight lines in the (ϕ,θ) plane. Such coordinates simplify visualization of MHD stability problems in toroidal devices.

8D. MHD Instabilities

Most of this Section follows the works of Schmidt (1979) and Bateman (1978),

the ball analogy

Consider the cases of a ball in a hole, on a level surface, and on a hill, Fig. 8D1. All three are equilibrium cases. If the ball on the hill is given a slight initial velocity, it will roll downhill and be accelerated as it goes, so the hilltop is an unstable equilibrium. If the ball in the hole is given a small initial velocity, it will oscillate about its initial position, with friction damping the oscillations until it comes to rest at its initial position. The tendency to return to its equilibrium condition is called *stability*.

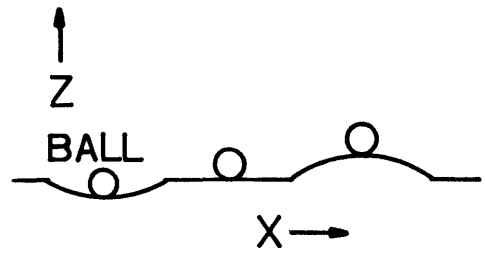

Fig. 8D1. The mechanical analogy of the stability of various equilibrium positions.

The stability depends upon the sign of the force experienced by the ball as it moves in the x direction. We use a Taylor series expansion for the force F around the initial position x_0, and write the equation of motion

$$m(d^2x/dt^2) = F(x) = F(x_0) + (x-x_0)(dF/dx) + (x-x_0)^2(d^2F/dx^2)/2! + \ldots \quad (8D1)$$

If x_0 is an equilibrium position, then $F(x_0) = 0$. By definition, let

$$\xi \equiv (x - x_0) \quad . \quad (8D2)$$

Considering only small displacements ξ, the nonlinear terms may be dropped from Eq. (8D1), which becomes

$$m\, d^2\xi/dt^2 = \xi(dF/dx) \tag{8D3}$$

We can express the force as the gradient of a potential energy function

$$F(x) = -(\partial U/\partial x) \tag{8D4}$$

with

$$U = mgz \tag{8D5}$$

where z is the elevation of the surface and g is the acceleration of gravity. Eq. (8D3) becomes

$$d^2\xi/dt^2 = -(\partial^2 U/\partial x^2)\xi/m \tag{8D6}$$

The second derivative $(\partial^2 U/\partial x^2) = mg(\partial^2 z/\partial x^2)$ represents the curvature of the surface in the x direction. If the ball is in the hole, the curvature is positive and oscillatory solutions

$$\xi(t) = \xi_0 \exp(\pm i\omega t), \qquad \omega^2 \equiv (\partial^2 U/\partial x^2)/m \tag{8D7}$$

are obtained. If the ball is on a hill, the curvature is negative $(\partial^2 U/\partial x^2 < 0)$ and solutions of the form

$$\xi(t) = \xi_0 \exp(\pm\gamma t) \quad , \qquad \gamma^2 \equiv -(\partial^2 U/\partial x^2)/m \tag{8D8}$$

are obtained. The $\exp(-\gamma t)$ solution damps out, but the $\exp(\gamma t)$ solution grows rapidly, and represents instability, with γ called the *growth rate*. For the ball on the level surface, $(\partial^2 U/\partial x^2) = 0$, so

$$d\xi/dt = \text{constant} \quad . \tag{8D9}$$

The ball does not return to its initial position, so the equilibrium is unstable, but with zero growth rate.

We can also define a displacement

$$\zeta \equiv (y - y_0) \tag{8D10}$$

in the y direction. It will obey the equation

$$d^2\zeta/dt^2 = -(\partial^2 U/\partial y^2)\zeta/m \quad . \tag{8D11}$$

If $(\partial^2 U/\partial y^2) > 0$, motion in the y direction is oscillatory, and if $(\partial^2 U/\partial y^2) < 0$, instability occurs. Thus, instability can occur in multidimensional systems if $(\partial^2 U/\partial x_i^2) < 0$ in any direction x_i.

In a plasma the principle is similar, but the equations are more complicated. Instead of a ball with mass m, we have a fluid with mass density ρ_m. Each fluid element may have a displacement vector $\vec{\xi}$ representing departure from its equilibrium position, and the potential energy for the whole plasma is

$$U = \int_{\text{volume}} d\vec{x}\, \left(\frac{p}{\gamma - 1} + \frac{B^2}{2\mu_0}\right) \tag{8D12}$$

where γ was defined in Eq. (5D17). (This is not the γ representing instability growth rate.) For 3-dimensional motion, $\gamma = 5/3$, and $p/(\gamma-1) = (3/2)nk(T_e+T_i)$ can be recognized as the average plasma energy density. The problem is to express U in terms of possible displacements $\vec{\xi}$ occurring in the plasma away from the equilibrium configuration. Let

$$\delta W \equiv U(\vec{\xi}) - U_0 \tag{8D13}$$

where $U_0 \equiv U(\vec{\xi}=0)$ is the equilibrium value. If any possible $\vec{\xi}$ produces a negative δW (a decrease in potential energy), then the plasma will be unstable to that type of perturbation. If the right side is expanded in a Taylor series, we find

$$\delta W = U_0 + (\vec{\xi}\cdot\vec{\nabla}U)_0 + (\text{second derivative terms}) + \ldots - U_0$$

$$= (\text{second derivative terms}) + \ldots \tag{8D14}$$

since $\vec{\nabla}U = 0$ at the equilibrium position (corresponding to zero slope in the ball analogy.) As in the ball analogy, a negative value of any second derivative term produces instability. Such an "energy principle" can predict whether instability occurs, but it does not predict the growth rates of the instabilities. To predict growth rates, we will use an equation of the form

$$\rho_m d^2\vec{\xi}/dt^2 = \vec{F}\{\vec{\xi}\} \tag{8D15}$$

where the "force" $\vec{F}$ is a differential operator (a function involving derivatives of $\vec{\xi}$). Such an equation can be found by "linearizing" the MHD equations.

The following sections deal with the mathematical techniques of stability analysis. Readers not interested in such techniques may skip to the subsection on "interchange instability", page 188.

linearized MHD equations

To linearize the MHD equations, we express the parameters ρ_m, $\vec{u}$, p and $\vec{B}$ in in terms of their equilibrium values (denoted by subscripts 0, with $\vec{u}_0=0$) plus a small perturbation (denoted by subscripts 1):

$$\rho_m = \rho_0 + \rho_1 \tag{8D16}$$

$$\vec{u} = \vec{u}_1 \tag{8D17}$$

$$p = p_0 + p_1 \tag{8D18}$$

$$\vec{B} = \vec{B}_0 + \vec{B}_1 \tag{8D19}$$

and consider only small departures from equilibrium: $\rho_1 << \rho_0$, $p_1 << p_0$, $B_1 << B_0$, and u_1 small. From Eq. (5D38).

$$\vec{E} = -\vec{u}\times\vec{B} + \eta_{\parallel}\vec{J}_{\parallel} + \eta_{\perp}\vec{J}_{\perp} \tag{8D20}$$

The "ideal" MHD equations assume that the plasma has perfect conductivity ($\eta\approx 0$). For convenience, we will add a "gravity" force $\rho\vec{g}$ to the equation of motion (5D32). With these modifications, the MHD equations (5D39)-(5D341)and Maxwell equation (5B7) may be written

$$(\rho_0+\rho_1)[\partial\vec{u}_1/\partial t + (\vec{u}_1\cdot\vec{\nabla})\vec{u}_1] = (1/\mu_0)[\vec{\nabla}\times(\vec{B}_0+\vec{B}_1)]\times(\vec{B}_0+\vec{B}_1) - \vec{\nabla}(p_0+p_1) + (\rho_0+\rho_1)\vec{g} \tag{8D21}$$

$$\partial(\rho_0+\rho_1)/\partial t = -\vec{\nabla}\cdot[(\rho_0+\rho_1)\vec{u}_1] \tag{8D22}$$

$$\partial(p_0+p_1)/\partial t = -\vec{u}_1\cdot\vec{\nabla}(p_0+p_1) - \gamma(p_0+p_1)\vec{\nabla}\cdot\vec{u}_1 \tag{8D23}$$

$$\partial(\vec{B}_0+\vec{B}_1)/\partial t = \vec{\nabla}\times[\vec{u}_1\times(\vec{B}_0+\vec{B}_1)] \tag{8D24}$$

These equations are linearized by dropping nonlinear terms containing products of two small quantities [such as $(\vec{u}_1\cdot\vec{\nabla})\vec{u}_1$] and by using the properties of the equilibrium solutions

$$\vec{\nabla}p_0 = (\vec{\nabla}\times\vec{B}_0)\times\vec{B}_0/\mu_0 + \rho_0\vec{g}$$

$$\partial\rho_0/\partial t = \partial p_0/\partial t = \partial\vec{B}_0/\partial t = 0 \tag{8D25}$$

With these simplifications, the *linearized MHD equations* are

$$\rho_0(\partial\vec{u}_1/\partial t) = (1/\mu_0)[(\vec{\nabla}\times\vec{B}_0)\times\vec{B}_1 + (\vec{\nabla}\times\vec{B}_1)\times\vec{B}_0] - \vec{\nabla}p_1 + \rho_1\vec{g} \tag{8D26}$$

$$\partial\rho_1/\partial t = -\rho_0\vec{\nabla}\cdot\vec{u}_1 - \vec{u}_1\cdot\vec{\nabla}\rho_0 \tag{8D27}$$

$$\partial p_1/\partial t = -\vec{u}_1\cdot\vec{\nabla}p_0 - \gamma p_0\vec{\nabla}\cdot\vec{u}_1 \tag{8D28}$$

$$\partial\vec{B}_1/\partial t = \vec{\nabla}\times(\vec{u}_1\times\vec{B}_0) \quad . \tag{8D29}$$

Since these equations are only valid for small values of ρ_1, $\vec{u}_1$, p_1, and $\vec{B}_1$, the instability growth rates predicted by them are only valid for the initial stages of growth. After a short period, the amplitudes of the perturbations become large enough that the nonlinear terms are no longer negligible. To assess later stages of instability, the nonlinear terms must be retained in the equations. In some cases, the instability may saturate (cease growing) without destroying plasma confinement. The advantage of linearized equations is that they can often be solved analytically, whereas nonlinear equations usually require numerical solution.

Let the displacement vector be defined by

$$\vec{\xi}(\vec{x},t) \equiv \int_0^t dt'\vec{u}_1(\vec{x},t') \quad . \tag{8D30}$$

We will assume that the initial conditions are

$$\vec{\xi}(\vec{x},0) = 0,\ (\partial\vec{\xi}/\partial t)_{t=0} \neq 0,\ \vec{B}_1(\vec{x},0) = 0,\ p_1(\vec{x},0) = 0 \quad . \tag{8D31}$$

The plasma is originally at equilibrium, but with a small velocity perturbation $(\partial\vec{\xi}/\partial t)$. With these initial conditions, we can integrate Eqs. (8D27)-(8D29) in time to obtain

$$p_1(\vec{x},t) = -\vec{\xi}\cdot\vec{\nabla}p_0 - \gamma p_0\vec{\nabla}\cdot\vec{\xi} \tag{8D32}$$

$$\vec{B}_1(\vec{x},t) = \vec{\nabla}\times(\vec{\xi}\times\vec{B}_0) \quad . \tag{8D33}$$

$$\rho_1(\vec{x},t) = -\rho_0\vec{\nabla}\cdot\vec{\xi} - \vec{\xi}\cdot\vec{\nabla}\rho_0 \tag{8D34}$$

Inserting Eq. (8D34) into Eq. (8D26) and replacing $\partial\vec{u}_1/\partial t$ by $\partial^2\vec{\xi}/\partial t^2$, we find

$$\rho_0\partial^2\vec{\xi}/\partial t^2 = \vec{F}\{\vec{\xi}\} \quad , \tag{8D35}$$

$$\vec{F}\{\vec{\xi}\} \equiv (1/\mu_0)\{(\vec{\nabla}\times\vec{B}_0)\times B_1 + (\vec{\nabla}\times\vec{B}_1)\times\vec{B}_0\} - \vec{\nabla}p_1 - [\rho_0\vec{\nabla}\cdot\vec{\xi} + \vec{\xi}\cdot\vec{\nabla}\rho_0]\vec{g} \quad .$$

This equation is the basic equation for linear stability analysis with $\vec{B}_1$ and p_1 given by Eqs. (8D32), (8D33). As a boundary condition we can require that the component of $\vec{\xi}$ perpendicular to an outer magnetic surface be zero, or that $\vec{\xi}$ be finite at an infinite distance away.

eigenvalues

Equation (8D35) can be solved by separation of variables. Assume that

$$\vec{\xi}(\vec{x},t) = \vec{\xi}(\vec{x})T(t) \quad . \tag{8D36}$$

Substituting this expression into (8D35) and dividing by $\vec{\xi}(\vec{x})T(t)\rho_0$, we find

$$\frac{1}{T}\frac{\partial^2 T}{\partial t^2} = \frac{\vec{F}\{\vec{\xi}(\vec{x})\}}{\vec{\xi}(\vec{x})\rho_0} \quad . \tag{8D37}$$

The left side depends only on t and the right side, only on $\vec{x}$, but both sides must be equal for all t and $\vec{x}$. Therefore, each side must be equal to a constant, which we will call $-\omega_j^2$. Equation (8D37) may be written as two separate equations:

$$\partial^2 T/\partial t^2 = -\omega_j^2 T$$

$$\vec{F}\{\vec{\xi}(\vec{x})\} = -\omega_j^2\rho_0\vec{\xi}(\vec{x}) \tag{8D38}$$

The first equation yields solutions of the form $\exp(\pm i\omega_j t)$. Solutions of the second equation can satisfy the boundary conditions only for certain values of ω_j. The situation is similar to that of a plucked string having only certain possible wavelengths of oscillation, such that $n(\lambda_n/2) = L$, where n is an integer, λ_n is the wavelength, and L is the length of the string. The possible values of wavelength, which satisfy the boundary condition of zero displacement at the ends of the string ($\lambda_n = 2L/n$), are called *eigenvalues*. The general solution of Eq. (8D36) is a sum of the solutions for all the possible eigenvalues ω_j:

$$\vec{\xi}(\vec{x},t) = \sum_j C_j \vec{\xi}_j(\vec{x}) \exp(\pm i\omega_j t) \tag{8D39}$$

where C_j are constants. If any of the eigenvalues $\omega_j^2 < 0$, the solution of the equation will grow proportional to $\exp(\pm\gamma_j t)$, where $\gamma_j^2 \equiv -\omega_j^2$. The positive exponential leads to instability with growth rate γ_j.

Thus, linear stability analysis can become a search for the possible eigenvalues ω_j^2 of Eq. (8D38). The corresponding *eigenfunctions* $\vec{\xi}_j(\vec{x})$ are called the normal modes. [In the case of the plucked string, the eigenfunctions are $\xi_n = \sin(n\pi x/L)$.]

example of normal mode analysis

The classical case of a heavy fluid supported by a lighter fluid, called the Rayleigh-Taylor instability, is illustrated in Fig. 8D2. The plasma analogy of this instability is a case in which the plasma is supported against a volumetric force by a magnetic field. Although this force will be called "gravity" $m\vec{g}$ in the equations, it can represent other forces as well, such as the centrifugal force and magnetic field gradient force.

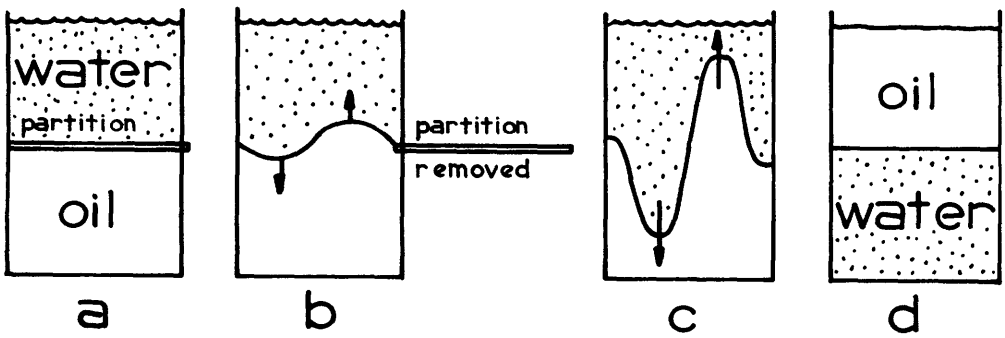

Fig. 8D2. Illustration of the Rayleigh-Taylor instability for the case of a heavy fluid (water) supported by a lighter fluid (oil). When the partition is removed, ripples along the interface grow rapidly, and the two fluids interchange places.

The problem is illustrated in Fig. 8D3. We take the z axis parallel to the magnetic field, and the y axis vertically, with gravity in the -y direction. For simplicity, we will assume that equilibrium quantities (B_0, p_0, ρ_0) vary only in the y direction, that nothing varies in the z direction, and that variations in the x direction of the perturbed quantities are periodic

$$\vec{\xi}(\vec{x}) = \vec{\xi}(y)e^{ikx}$$

$$p_1(\vec{x}) = p_1(y)e^{ikx} \quad . \tag{8D40}$$

Using Eq. (F27) in (8D33), we find

$$\vec{B}_1 = \vec{\nabla}\times(\vec{\xi}\times\vec{B}_0) = (\vec{B}_0\cdot\vec{\nabla})\vec{\xi} - (\vec{\xi}\cdot\vec{\nabla})\vec{B}_0 + \vec{\xi}(\vec{\nabla}\cdot\vec{B}_0) - \vec{B}_0(\vec{\nabla}\cdot\vec{\xi}) \quad . \tag{8D41}$$

We will assume that

$$\vec{\nabla}\cdot\vec{\xi} \simeq 0 \quad , \tag{8D42}$$

which is equivalent to the condition $\vec{\nabla}\cdot\vec{v}_1 \simeq 0$. This condition is valid if $p_0 \ll B^2/2\mu_0$ or if $\vec{k}\cdot\vec{v}_1 = 0$, where $\vec{k}$ is the wave propagation vector of the "ripples" of the perturbation. Since $\vec{B}$ is in the z direction and derivatives are zero in that direction, the operator $(\vec{B}\cdot\vec{\nabla}) = 0$, and the first term on the right side of Eq. (8D41) is zero. The fourth term is zero by (8D42), and the third term is zero by the Maxwell equation $\vec{\nabla}\cdot\vec{B} = 0$, so

$$\vec{B}_1 = -(\vec{\xi}\cdot\vec{\nabla})\vec{B}_0 = -\xi_y(\partial B_0/\partial y)\hat{z} \quad . \tag{8D43}$$

Since $\vec{B}_1$ is in the z direction, the curly-bracketed part of $\vec{F}$ in Eq. (8D35) may be simplified with (F29) as follows:

$$(\vec{\nabla}\times\vec{B}_0)\times\vec{B}_1 + (\vec{\nabla}\times\vec{B}_1)\times\vec{B}_0 = (\vec{B}_0\cdot\vec{\nabla})\vec{B}_1 + (\vec{B}_1\cdot\vec{\nabla})\vec{B}_0 - \vec{\nabla}(\vec{B}_0\cdot\vec{B}_1)$$

$$= -\vec{\nabla}(B_0B_1) \tag{8D44}$$

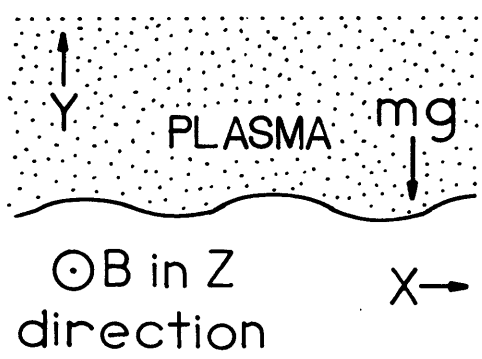

Fig. 8D3. The case of a plasma suspended against gravity by a uniform magnetic field.

Now Eq. (8D38) becomes

$$\vec{F}\{\vec{\xi}\} = -(1/\mu_0)\vec{\nabla}(B_0B_1) - \vec{\nabla}p_1 - (\vec{\xi}\cdot\vec{\nabla}\rho_0)\vec{g}$$

$$= -\omega_j^2\rho_0\vec{\xi} \quad . \tag{8D45}$$

The z component of this equation is zero. The x and y components are

$$-ik(B_0B_1/\mu_0 + p_1) = -\omega_j^2\rho_0\xi_x \tag{8D46}$$

$$-(\partial/\partial y)(B_0B_1/\mu_0 + p_1) + \xi_y g(\partial\rho_0/\partial y) = -\omega_j^2\rho_0\xi_y \tag{8D47}$$

where $(\partial/\partial x) \to ik$ by assumption (8D40). From Eq. (8D42)

$$ik\xi_x + \partial\xi_y/\partial y = 0 \quad . \tag{8D48}$$

If we eliminate $(B_0B_1/\mu_0 + p_1)$ between Eq. (8D46) and (8D47) and then eliminate ξ_x using (8D48), the result is

$$-\frac{\omega_j^2}{k^2}\frac{\partial}{\partial y}\left(\rho_0\frac{\partial\xi_y}{\partial y}\right) + \left(g\frac{\partial\rho_0}{\partial y} + \omega_j^2\rho_0\right)\xi_y = 0 \quad . \tag{8D49}$$

Letting primes denote y derivatives, this may be rearranged to read

$$\xi_y'' + (\rho_0'/\rho_0)\xi_y' - k^2(1 + g\rho_0'/\rho_0\omega_j^2)\xi_y = 0 \quad , \tag{8D50}$$

If ρ_0'/ρ_0 = constant (exponential density variation in the y direction), a possible bounded solution is ξ_y = constant $\neq 0$, $\xi_y'' = \xi_y' = 0$, for which (8D50) reduces to

$$1 + g\rho_0'/\rho_0\omega_j^2 = 0, \quad \omega_j^2 = -g\rho_0'/\rho_0 \quad . \tag{8D51}$$

Thus, if $\rho_0' > 0$ (density increasing upwards), $\omega_j^2 < 0$, and instability occurs with a growth rate

$$\gamma = (g\rho_0'/\rho_0)^{1/2} \quad . \tag{8D52}$$

Another simple case is that of $\rho_0 = 0$ below the boundary and ρ_0 = constant above the boundary. For $y > 0$, the equation is

$$\xi_y'' - k^2\xi_y = 0$$

with solutions

$$\xi_y(y) = Ae^{ky} + Ce^{-ky} \tag{8D53}$$

If the plasma extends upwards to large y, we must take A = 0 to avoid blowup of ξ_y. (Both terms would be kept if a wall were located a finite distance away.) At $y = 0$, $\rho_0' \to \infty$, and Eq. (8D50) becomes

$$\xi_y' - (k^2g/\omega_j^2)\xi_y = 0 \tag{8D54}$$

Using (8D53) to evaluate ξ_y and ξ_y' near y=0, we have

$$-kCe^{-ky} - (k^2g/\omega_j^2)Ce^{-ky} = 0 \quad ,$$

$$\omega_j^2 = -kg \to \gamma = (kg)^{1/2} \quad . \tag{8D55}$$

In this case perturbations with short wavelengths (large k) have the highest growth rates. For the simple (though unrealistic) case of exponential density variation in the y direction, only one eigenvalue was found (Eq. 8D51). For the discontinuous density case with an infinitely large plasma, a spectrum of eigenvalues was found, varying continuously with k (Eq. 8D55). If the plasma were bounded in the x direction, then only discrete values of λ_j would be possible in the x direction, yielding discrete values of k_j and ω_j^2. If dissipative effects like resistivity and viscosity were included, then γ would not become infinite as $k \to \infty$.

The force of gravity in the equation of motion may be replaced by the effective forces of magnetic field gradient and curvature

$$\rho_m\vec{g} \to -\rho_m v_\perp^2\vec{\nabla}B/B + \rho_m v_\parallel^2\vec{R}_c/R_c^2 \simeq (\rho_m\vec{R}_c/R_c^2)(v_\parallel^2 + v_\perp^2/2) \tag{8D56}$$

With this replacement, the growth rate for the sharp-boundary case (8D55) with $\vec{R}_c$ downwards is

$$\gamma = [k(v_\parallel^2 + v_\perp^2/2)/R_c]^{1/2} \sim (kp/\rho_m R_c)^{1/2} \sim c_s(k/R_c)^{1/2} \tag{8D57}$$

where $c_s = (\gamma p/\rho_m)^{1/2}$ is the speed of sound. If the direction of $\vec{R}_c$ is reversed, the instability is stabilized, as illustrated in Fig. 8D4.

If the linear growth rates are not needed, the "energy principle" may afford an easier way of testing for stability.

energy principle

The energy principle $\delta W < 0 \rightarrow$ instability (after Eq. 8D13) may be written in terms of the operator $\vec{F}\{\vec{\xi}\}$:

$$\delta W = -\tfrac{1}{2}\int d\vec{x}\ \vec{\xi}\cdot\vec{F}\{\vec{\xi}\}$$

$$\equiv (\delta W_F + \delta W_V + \delta W_S) < 0$$

$$\text{for instability} \quad , \qquad (8D58)$$

where δW_F, δW_V, and δW_S are changes in potential energy of the plasma, the vacuum magnetic field around the plasma, and the plasma surface, given by

$$\delta W_V = \tfrac{1}{2}\int_{\text{vacuum region}} d\vec{x}\ B_1^2/\mu_0 \qquad (8D59)$$

$$\delta W_S = \tfrac{1}{2}\int_{\text{plasma surface}} d\vec{S}\cdot[\vec{\nabla}(p_0 + B_0^2/2\mu_0)]\xi_\perp^2$$

$$= \tfrac{1}{2}\int_{\text{surface}} d\vec{S}\cdot[(\vec{B}_0\cdot\vec{\nabla})\vec{B}_0]\xi_\perp^2/\mu_0$$

$$= -\tfrac{1}{2}\int_{\text{surface}} d\vec{S}\cdot[\vec{R}_c B_0^2\xi_\perp^2/\mu_0 R_c^2] \qquad (8D60)$$

$$\delta W_F = \tfrac{1}{2}\int_{\text{plasma volume}} d\vec{x}\ [B_1^2/\mu_0 + \gamma p(\vec{\nabla}\cdot\vec{\xi})^2 + \underbrace{(\vec{\nabla}\cdot\vec{\xi})(\vec{\xi}\cdot\vec{\nabla}p)}_{\text{(interchange modes)}} + \underbrace{(\vec{\nabla}\times\vec{B})\cdot(\vec{\xi}\times\vec{B}_1)/\mu_0}_{\text{(kink modes)}}] \quad , \qquad (8D61)$$

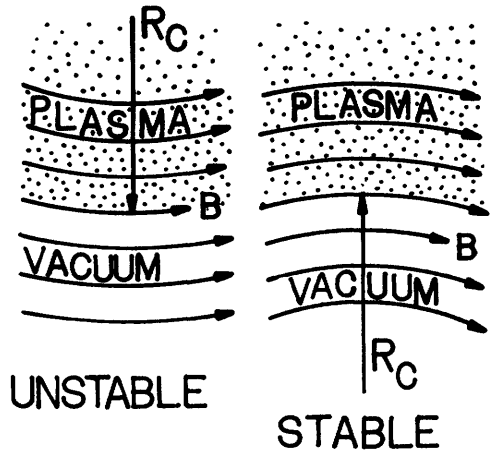

Fig. 8D4. Plasma supported by magnetic field with magnetic field radius of curvature R_c outwards (unstable) and inwards (stable).

where $\xi_\perp$ is the component of $\vec{\xi}$ perpendicular to the boundary surface, and $\vec{R}_c$ is the radius of curvature of the magnetic field lines. The vacuum term $\delta W_V > 0$, so it tends to be stabilizing. The quantity in brackets in Eq. (8D60) represents the change across the surface due to surface currents. This term will be negative (destabilizing) where the radius of curvature of the field lines points outwards, since $d\vec{S}$ is perpendicular to the surface and pointing outwards. The first term in δW_F represents the change in magnetic energy due to the displacement $\vec{\xi}$, the next two represent changes in plasma internal energy due to non-magnetic forces, and the last term, work done against magnetic forces. Only the last two can be negative, leading to interchange and kink instabilities,

respectively. The application of Eq. (8D58) to various cases is discussed by Bateman (1978), Schmidt (1979), and in Jeffrey and Taniuti (1966). We will discuss the interchange instability in light of a simpler version of the energy principle, then describe other instabilities qualitatively.

interchange instability

Consider the interchange of two adjacent magnetic flux tubes, illustrated in Fig. 8D5, with the rest of the plasma unchanged. We will assume that the flux tubes have equal magnetic fluxes

$$\Phi = B_1 A_1 = B_2 A_2 \tag{8D62}$$

where A_1, A_2 are the cross sectional areas of the tubes and B_1, B_2 are the magnetic fields, and that the plasma is adiabatic, so that

$$pV^{\gamma} = \text{constant} \tag{8D63}$$

where V is the volume occupied by a given quantity of plasma. After interchanging the flux tubes, the new pressures are

$$p_1' = p_1 (V_1/V_2)^{\gamma}$$

$$p_2' = p_2 (V_2/V_1)^{\gamma} \tag{8D64}$$

where p_1 and p_2 are the initial pressures of the two tubes, and V_1 and V_2 are the volumes of the two tubes. From Eqs. (8D12) and (8D13), the change in potential energy for the two tubes is

$$\delta W = (\text{final potential energy}) - (\text{initial potential energy})$$

$$= \frac{1}{\gamma - 1} \left[p_1 (V_1/V_2)^{\gamma} V_2 + p_2 (V_2/V_1)^{\gamma} V_1 - p_1 V_1 - p_2 V_2 \right] \tag{8D65}$$

Since we assumed that the fluxes in the two tubes were equal, the change in magnetic energy $B^2/2\mu_0$ is zero. Let

$$\delta p \equiv p_2 - p_1$$

$$\delta V \equiv V_2 - V_1 \quad . \tag{8D66}$$

Eliminating p_2 and V_2, Eq. (8D65) reduces to

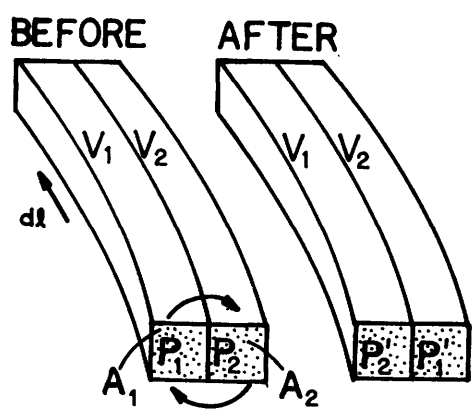

Fig. 8D5. Interchange of two adjacent flux tubes. Flux tube p_1, originally in tube volume V_1, moves to V_2 and changes pressure to p_1'. Tube p_2, originally in V_2, moves to V_1 and changes pressure to p_2'.

$$\delta W = \delta p \delta V + \gamma p (\delta V)^2 / V > 0 \text{ for stability.} \tag{8D67}$$

The last term is always positive. Near the plasma edge, p is small, so the last term may be ignored, and the requirement becomes

$$\delta p \delta V > 0 \quad \text{for stability} \quad . \tag{8D68}$$

In a confined plasma the pressure decreases outwards, and a flux tube moved outwards has $\delta p < 0$. Therefore, for stability, we require $\delta V < 0$, meaning that the volume of the flux tube should decrease as it is displaced outwards:

$$\delta V = \delta[\int d\ell\ A] = \Phi\ \delta[\int d\ell / B] < 0 \quad \text{for stability} \tag{8D69}$$

Thus, if $\int d\ell/B$ decreases as the flux tube is displaced outwards, the plasma will be locally stable against the interchange mode. This condition is called *minimum average B*.

Consider the magnetic mirror shown in Fig. 8D6. In the central region, the field lines bend outwards, and the magnetic field decreases with radius, so $\delta \int d\ell/B > 0$ as a flux tube is moved outwards, which tends to produce instability. Near the ends, the curvature is reversed, and $\delta \int d\ell/B < 0$ locally. The "good" curvature of the end regions, however, is not adequate to overcome the "bad" curvature of the central region, so that the value of $\delta \int d\ell/B$ for the whole flux tube is positive, and the plasma is prone to interchange instability. This interchange process usually has longitudinal ripples, resembling the flutes on a Greek column, hence the name "flute instability".

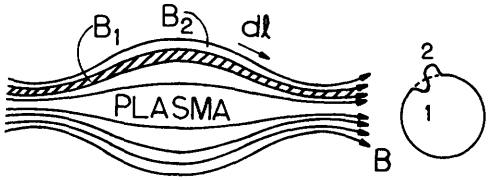

Fig. 8D6. Outward displacement of a flux tube in a magnetic mirror. In the central region B decreases with radius. When flux tube 1 interchanges with flux tube 2 containing vacuum, the surface becomes rippled and the potential energy decreases ($\delta W < 0$).

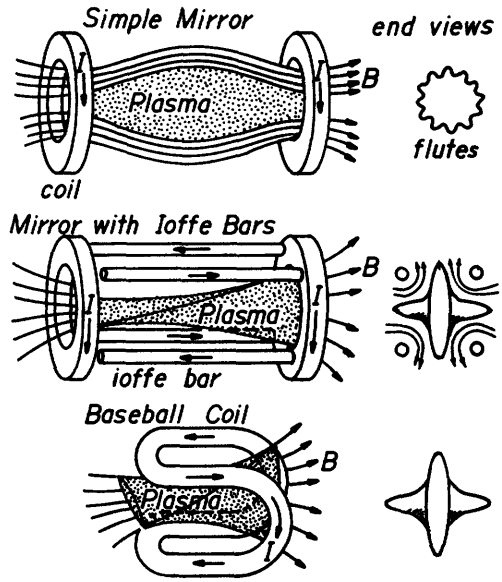

Fig. 8D7. Mirror field coil configurations. The simple mirror plasma is unstable to flute instabilities. The addition of four or more Ioffe bars carrying strong currents in alternate directions makes the magnetic pressure increase with radius, providing stability. The same stable plasma configuration can also be produced with a coil shaped like the seam of a baseball.

In contrast to mirrors, magnetic cusps have favorable curvature everywhere, and the plasma is stable against interchange modes. The instability tendency of mirrors can be eliminated by adding a cusp field around the edges, as illustrated in Fig. 8D7. The new magnetic field increases with distance from the plasma center in every direction, and is called *minimum B*. If the plasma begins to move in any direction, it encounters a region of increased magnetic pressure and is repelled back to its equilibrium position, so minimum B systems are always stable against MHD instabilities. Most minimum B systems, however, are in open magnetic confinement systems, suffering from rapid plasma loss along magnetic field lines. Cases where strong particle currents greatly change the magnetic field in the plasma region are exceptions (Chapters 11 and 14).

types of MHD instabilities

MHD Instabilities are classified according to cause (current-driven or pressure-driven), magnetic field geometry (cylinder, axisymmetric torus, etc.), type of theoretical methods used (ideal vs. finite resistivity, linear vs. nonlinear, finite Larmor radius, etc.), and shape of the deformations (mode numbers). The shape is described mathematically in terms of the functions

$$\exp(im\theta - ikz) \quad \text{cylinder}$$

$$\exp(im\theta - in\phi) \quad \text{torus} \tag{8D70}$$

where θ is the azimuthal angle in a cylinder or poloidal angle in a torus, and ϕ is the toroidal angle (Fig. 7E1). The shapes of plasma deformations in a cylinder corresponding to various mode numbers m are illustrated in Fig. 8D8. For the flute instability of Fig. 8D7, m = 12. The shapes of deformations corresponding to various toroidal mode numbers n are shown in Fig. 8D9.

The macroscopic instabilities observed so far in tokamaks and pinches are driven mainly by parallel current. It is not clear that pressure-driven instabilities, such as ballooning modes, have been observed in tokamaks.

The m = 0 sausage instability occurs in linear pinches, such as lighting bolts. It can be stabilized by a strong axial magnetic field. The m = 1 kink instability can be stabilized by keeping the plasma current low enough that the safety factor at the plasma surface q(a) > 1. For an axisymetric toroidal plasma, this means that

$$q(a) \simeq \frac{aB_t}{R_0 B_p} = \frac{2\pi a^2 B_t}{\mu_0 R_0 I(a)} > 1 \quad , \qquad I(a) < \frac{2\pi a^2 B_t}{\mu_0 R_0} \text{ for stability,} \tag{8D71}$$

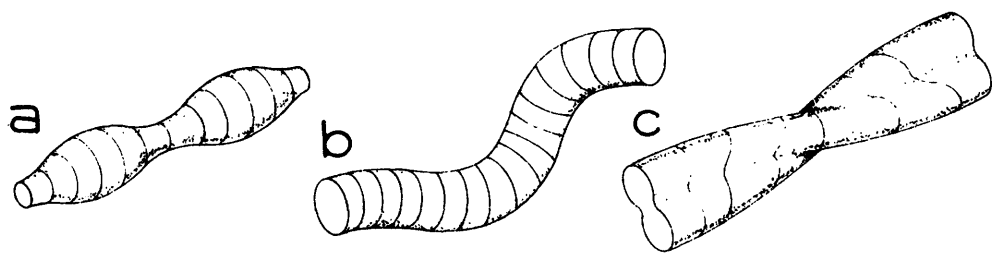

Fig. 8D8. Illustration of (a) m = 0 sausage instability, (b) m = 1 kink instability, (c) m = 2 instability in a straight circular cylindrical plasma. Cross sectional cuts are shown, not magnetic field lines. Reprinted from MHD Instabilities by G. Bateman, Fig. 1.1, by permission of The MIT Press, Cambridge Massachusetts. Copyright 1978 by the Massachusetts Institute of Technology.

where I(a) is the toroidal plasma current flowing inside r = a. This is called the *Kruskal-Shafranov limit*. For a plasma with a = 0.5 m, R = 2 m, and B_t = 4 T, the maximum plasma current is 2.5 MA. The kink deformations are stabilized by tension in the toroidal magnetic field lines, which resist stretching and bending. Values of q > 2 may be needed to ensure stability against both m = 1 and m = 2 modes.

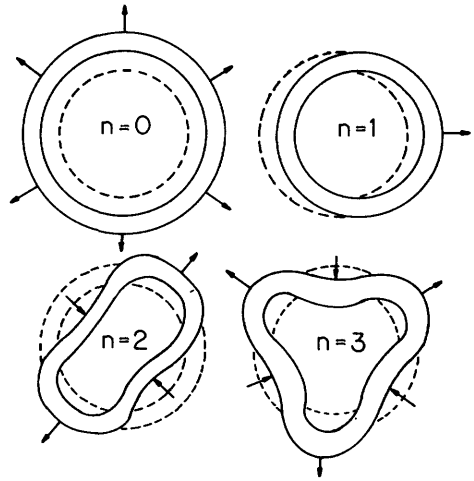

Fig. 8D9. Deformations corresponding to toroidal mode number n = 0 to 3.

ballooning modes

Ballooning modes are local bulges in the plasma surface, which expand as the plasma pushes outwards. They are high-mode-number interchange modes. These modes set a limit on the attainable value of β. They occur at the place where the curvature is the worst, such as at the outside of a torus (large R) or at the tips of a vertically elongated plasma. Stability against ballooning depends upon the magnitude of the curvature and on the *connection length* (distance between regions of good and bad curvature), which are related to q and R_0/a. For a circular plasma in an axisymmetric torus, a simplified theoretical estimate is

$$\beta \lesssim a/R_0 q^2 \qquad \text{for stability.} \tag{8D72}$$

For example, if q = 3 and R_0/a = 3, then $\beta \lesssim 0.04$. However, numerical calculations are needed for accurate predictions, and ballooning mode theories have not yet been verified experimentally.

tearing modes

If magnetic field lines break and reconnect to form magnetic islands, the local magnetic shear and potential energy are reduced. Island formation occurs near *rational surfaces* $q(\psi)$ = m/n, where m and n are the poloidal and toroidal mode numbers, Eq.(8D70), and ψ is the flux coordinate (replacing r) defined by Eqs. (8C3) and (8C4). Tearing modes are studied by retaining finite resistivity η in Eq. (8D20). In the limit $\eta \to 0$, tearing modes reduce to kink modes.

Following Boozer and Rechester (1978), we will consider magnetic surfaces described by $\Psi(\psi,\theta,\phi)$ and show how a magnetic field perturbation $\vec{B}_1$ leads to island formation at a rational surface. The toroidal angle ϕ and the poloidal angle θ were defined in Fig. 8B1.

The gradient $\vec{\nabla}\Psi$ is perpendicular to the magnetic surfaces, and therefore perpendicular to the magnetic field vector $\vec{B}$, which lies on the surface. The basic magnetic differential equation describing the shape of the magnetic

surfaces is

$$\vec{B}\cdot\vec{\nabla}\Psi = 0 . \tag{8D73}$$

We will linearize this equation with a technique similar to that of Eqs. (8D16)-(8D29). Let

$$\vec{B} = \vec{B}_0 + \vec{B}_1$$
$$\Psi = \Psi_0 + \Psi_1 \tag{8D74}$$

where the subscripts 0 and 1 denote the equilibrium solution and a small perturbation, respectively. The equilibrium quantities satisfy

$$\vec{B}_0\cdot\vec{\nabla}\Psi_0 = 0 . \tag{8D75}$$

Substituting Eqs.(8D74) into (8D73) , we find

$$\vec{B}_0\cdot\vec{\nabla}\Psi_0 + \vec{B}_0\cdot\vec{\nabla}\Psi_1 + \vec{B}_1\cdot\vec{\nabla}\Psi_0 + \vec{B}_1\cdot\vec{\nabla}\Psi_1 = 0. \tag{8D76}$$

The first term is zero by Eq.(8D75), and the last term may be neglected, since it is the product of two small quantities. Expanding the derivatives, this equation becomes

$$\frac{B_{0\phi}}{R}\frac{\partial\Psi_1}{\partial\phi} + \frac{B_{0\theta}}{r}\frac{\partial\Psi_1}{\partial\theta} + (\vec{B}_1\cdot\vec{\nabla}\psi)\frac{\partial\Psi_0}{\partial\psi} = 0 . \tag{8D77}$$

Since the safety factor $q(\psi) \simeq rB_{0\phi}/RB_{0\theta}$, this may be written

$$\frac{\partial\Psi_1}{\partial\phi} + \frac{1}{q}\frac{\partial\Psi_1}{\partial\theta} + \frac{R}{B_{0\phi}}(\vec{B}_1\cdot\vec{\nabla}\psi)\frac{\partial\Psi_0}{\partial\psi} = 0 . \tag{8D78}$$

The magnetic field perturbation may be represented by a Fourier series :

$$\frac{R}{B_{0\phi}}(\vec{B}_1\cdot\vec{\nabla}\psi) = e^{-in\phi}\sum_m b_m e^{im\theta} \tag{8D79}$$

where

$$b_m = \frac{e^{in\phi}}{2\pi}\int_{-\pi}^{\pi} d\theta\, \frac{R}{B_{0\phi}}\vec{B}_1\cdot\vec{\nabla}\psi\; e^{-im\theta} . \tag{8D80}$$

(Fourier series are explained by Arfken, 1973, Chapter 14.) Similarly, let

$$\Psi_1 = \sum_m \Psi_m e^{im\theta - in\phi} . \tag{8D81}$$

With these substitutions, Eq. (8D78) becomes

$$\sum_m \left[\left(-in + \frac{im}{q}\right)\Psi_m + b_m\frac{\partial\Psi_0}{\partial\psi}\right] e^{im\theta-in\phi} = 0 . \tag{8D82}$$

This equation must hold for all θ and ϕ , so

$$\Psi_m = \frac{iqb_m \frac{\partial \Psi_0}{\partial \psi}}{nq - m} \quad . \tag{8D83}$$

This equation gives infinite values of Ψ_m at rational surfaces where $q(\psi_m) = m/n$, unless $(\partial\Psi_0/\partial\psi) = 0$ there. Therefore, we will choose a functional relation for Ψ_0 which gives finite Ψ_m at the rational surfaces. One possible choice is

$$\frac{\partial \Psi_0}{\partial \psi} = \frac{\sin(n\pi q)}{n\pi q'} \tag{8D84}$$

where the prime denotes differentiation with respect to ψ. The factor $n\pi q'$ is put in the denominator to cancel a like factor which will arise in the numerator. Then

$$\Psi_m = \frac{iqb_m \sin(n\pi q)}{n\pi q'(nq - m)} \quad . \tag{8D85}$$

We will evaluate $\sin(n\pi q)$ near a rational surface. Expanding q in a Taylor series

$$q(\psi) = q(\psi_m) + q'(\psi - \psi_m) + \ldots \tag{8D86}$$

where $q(\psi_m) = m/n$. Then

$$\begin{aligned} \sin(n\pi q) &= \sin\{ n\pi \left[\frac{m}{n} + q'(\psi-\psi_m) + \ldots \right] \} \\ &= \sin(m\pi)\cos[n\pi q'(\psi-\psi_m)] + \cos(m\pi)\sin[n\pi q'(\psi-\psi_m)] \\ &= 0 + (-1)^m \sin[n\pi q'(\psi-\psi_m)] \\ &\simeq \pm n\pi q'(\psi-\psi_m) + \ldots \end{aligned} \tag{8D87}$$

assuming that $(\psi-\psi_m)$ is small. Inserting this value into Eq. (8D84), the factor of $n\pi q'$ cancels, and the result of integration is

$$\Psi_0(\psi) = \Psi_0(\psi_m) \pm \tfrac{1}{2}(\psi-\psi_m)^2 + \ldots \tag{8D88}$$

From Eqs. (8D85)- (8D87) we find

$$\Psi_m = \frac{\pm iqb_m[n\pi q'(\psi-\psi_m) + \ldots]}{n\pi q' \{ n \left[\frac{m}{n} + q'(\psi-\psi_m) + \ldots \right] - m\}} = \frac{\pm iqb_m}{nq'} \quad . \tag{8D89}$$

Since $e^{ix} = \cos x + i\sin x$, the real part of Ψ_1 is found from Eq. (8D81) to be

$$\Psi_1 = \pm \sum_m \frac{-qb_m \sin(m\theta - n\phi)}{nq'} \tag{8D90}$$

Inserting Eqs. (8D88) and (8D90) into (8D74), the result is

$$\Psi(\psi,\theta,\phi) = \Psi_0(\psi_m) \pm \left[\tfrac{1}{2}(\psi-\psi_m)^2 + \ldots - \sum_m \frac{qb_m \sin(m\theta-n\phi)}{nq'} \right] . \tag{8D91}$$

We can invert this to find how ψ varies along a magnetic surface of constant Ψ. For simplicity, assume that only one value of m is locally significant. Then

$$\psi = \psi_m \pm 2^{\frac{1}{2}} \left\{ [\Psi - \Psi_0(\psi_m)] + \frac{qb_m \sin(m\theta-n\phi)}{nq'} \right\}^{\frac{1}{2}} . \tag{8D92}$$

Let

$$\left(\frac{\Delta_m}{2}\right)^2 \equiv \frac{qb_m}{nq'} . \tag{8D93}$$

Then

$$\psi = \psi_m \pm 2^{\frac{1}{2}} \frac{\Delta_m}{2} \left\{ \frac{[\Psi - \Psi_0(\psi_m)]}{\Delta_m^2/4} + \sin(m\theta-n\phi) \right\}^{\frac{1}{2}} \tag{8D94}$$

If $4[\Psi - \Psi_0(\psi_m)]/\Delta_m^2 > 1$, then real solutions exist for all angles $(m\theta-n\phi)$.

If $4[\Psi - \Psi_0(\psi_m)]/\Delta_m^2 < 1$, then solutions exist only for certain ranges of $(m\theta-n\phi)$, and the flux surfaces form *magnetic islands*, as illustrated in Fig. 8D10. The boundary between continuous solutions and restricted ranges is

$$4[\Psi - \Psi_0(\psi_m)]/\Delta_m^2 = 1 . \tag{8D95}$$

This equation defines the separatrix

$$\psi_s = \psi_m \pm \Delta_m \left[\frac{1 + \sin(m\theta-n\phi)}{2} \right]^{\frac{1}{2}} \tag{8D96}$$

(dashed curve of Fig. 8D10). The maximum departure of the separatrix from ψ_m is $\psi_s = \psi_m \pm \Delta_m$, so Δ_m is the *half-width* of the magnetic islands. Thus,

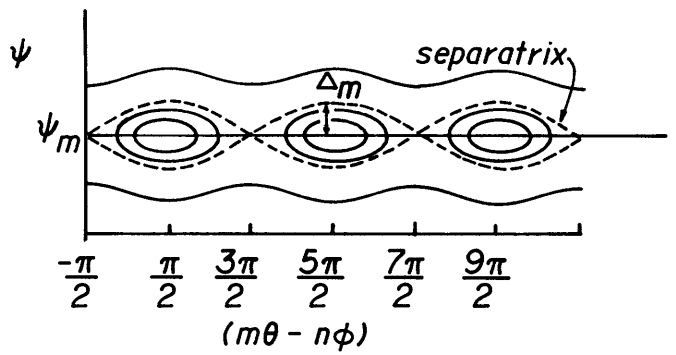

Fig. 8D10. A chain of magnetic islands, described by Eq. (8D94), centered on a rational surface where $q(\psi_m) = m/n$. (The flux coordinate ψ represents the minor radius r).

magnetic islands tend to form near rational surfaces , and the island half-widths are

$$\Delta_m = 2(qb_m/nq')^{\frac{1}{2}} \ . \tag{8D97}$$

The spacing between chains of islands with different m values can be estimated from

$$nq(\psi_{m+1}) = m + 1 = 1 + nq(\psi_m) \ ,$$

$$q(\psi_{m+1}) - q(\psi_m) = \frac{1}{n} \ . \tag{8D98}$$

Also, from Eq. (8D86),

$$q(\psi_{m+1}) = q(\psi_m) + q'(\psi_{m+1} - \psi_m) + \ldots \tag{8D99}$$

Combining these two equations, the result is

$$\psi_{m+1} - \psi_m \simeq \frac{1}{nq'} \ . \tag{8D100}$$

This represents the approximate spacing between adjacent island chains. The magnetic islands will *overlap* when the spacing between chains is less than the island width

$$\frac{1}{nq'} \leq 2\Delta_m = 4(qb_m/nq')^{\frac{1}{2}}$$

or

$$16nq'qb_m \geq 1 \ , \tag{8D101}$$

where b_m is known in terms of the magnetic field perturbation from Eq. (8D80). The perturbation amplitude $\vec{B}_1$ grows in time as magnetic field lines break and reconnect to form islands.

For simplicity, we will ignore anisotropy of the resistivity, assuming $\eta \equiv \eta_{\parallel} \simeq \eta_{\perp}$. From combination of Eqs. (5B6), (5B7), (8B2), (8D20), and (F30), we can find a diffusion equation for the magnetic field lines :

$$\partial\vec{B}/\partial t = -\vec{\nabla}\times\vec{E} = -\vec{\nabla}\times(-\vec{u}\times\vec{B} + \eta\vec{J}) = \vec{\nabla}\times(\vec{u}\times\vec{B}) - (\eta/\mu_0)\vec{\nabla}\times(\vec{\nabla}\times\vec{B})$$

$$= \vec{\nabla}\times(\vec{u}\times\vec{B}) + (\eta/\mu_0)\nabla^2\vec{B} \tag{8D102}$$

assuming that spatial variations of η are negligible. The first term represents plasma and magnetic field lines moving together (flux lines "frozen into the plasma"), and the second term represents diffusion of magnetic field lines through the plasma. We can approximate the derivatives as

$$\vec{\nabla}\times(\vec{u}\times\vec{B}) \sim uB/L_u$$

$$(\eta/\mu_0)\nabla^2\vec{B} \sim \eta B/\mu_0 L_B^2 \tag{8D103}$$

where L_u and L_B are characteristic scale lengths.
For plasma tied to magnetic field lines, $u \sim v_A$, the Alfven velocity of Eq. (5E34). By definition, let

$$\tau_A \equiv L_u/v_A = \textit{Alfven transit time}$$

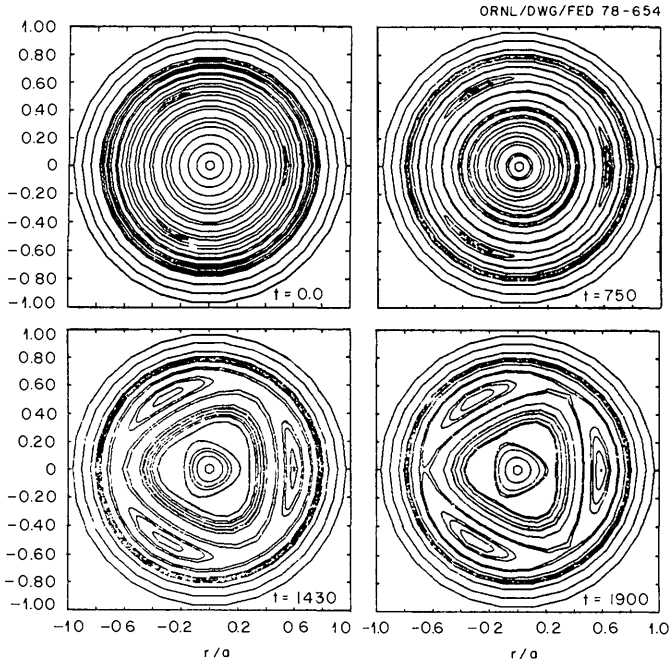

Fig. 8D11. Time evolution of the helical flux function ψ_* in a cylindrical plasma with a hollow current profile, showing the growth of magnetic islands associated with the m/n = 3/1 tearing mode. From B. Carreras, H. R. Hicks, and B. V. Waddell, Nuclear Fusion 19, 583-596 (1979), Fig. 14.

$$\tau_R \equiv \mu_0 L_B^2/\eta = \textit{resistive diffusion time} \quad . \tag{8D104}$$

The ratio of the magnitudes of the two terms on the right side of Eq. (8D102) is

$$S \equiv \frac{\tau_R}{\tau_A} = \textit{Magnetic Reynolds Number} \quad . \tag{8D105}$$

For the case of magnetic island formation, the scale length $L_B \sim \Delta_m$. For small values of Δ_m, τ_R will be short, and resistive diffusion will occur rapidly. As the island widths grow, τ_R increases, resistive diffusion slows down, and the island widths tend to saturate. The time evolution of magnetic islands with an m/n = 3/1 mode is illustrated in Fig. 8D11 .

Heat flows rapidly along magnetic field lines. When magnetic islands form, such flow can carry heat radially outwards around the islands, increasing the radial heat loss rate of the plasma. The variation of tearing modes in tokamaks with the magnetic Reynolds number will be discussed in Section 13A.

summary

The ball analogy indicates that instability occurs when any perturbation leads to a state of lower potential energy $\delta W < 0$. The linearized MHD equation of

motion leads to the relation

$$\rho_0 \frac{\partial^2 \vec{\xi}}{\partial t^2} = \vec{F}\{\vec{\xi}\} \qquad (8D106)$$

describing the possible growth of an infinitesimal displacement $\vec{\xi}$ of the plasma. Separation of variables leads to an eigenvalue equation

$$-\omega_j^2 \rho_0 \vec{\xi} = \vec{F}\{\vec{\xi}\} \quad . \qquad (8D107)$$

If any of the eigenvalues $\omega_j^2 < 0$, then instability occurs with a growth rate $\gamma = (-\omega_j^2)^{\frac{1}{2}}$. Using the normal mode analysis technique, the growth rate was estimated for the simple case of plasma supported against "gravity" (representing magnetic field gradient and curvature forces) by a magnetic field.

The energy principle in simplest form leads to the criterion $\delta \int d\ell/B < 0$ for stability against interchange modes, which shows the importance of magnetic field curvature. Interchange instabilities can be suppressed by using a minimum-B or minimum average B magnetic field.

The maximum plasma current is limited by the Kruskal-Shafranov condition $q > 1$ for stability against the kink mode, and the maximum plasma pressure may be limited by ballooning modes to values of $\beta \lesssim a/R_0 q^2$ in axisymmetric tori. Magnetic islands formed by tearing modes result in increased energy transport rates.

Even when MHD instabilities are suppressed, microinstabilities can still cause high plasma energy loss rates.

8E. Microinstabilities

types of interactions

MHD instabilities, driven by magnetic field energy or plasma expansion energy, involve macroscopic changes of the plasma-magnetic field configuration. All other types of instability are called *microinstabilities*.

Microinstabilities involve plasma wave growth and interaction with particles or other waves. Excluding the case of shock waves, wave-particle interactions are strongest for particles with velocity components in the direction of the wave near the wave phase velocity ω/k:

$$\vec{v} \cdot \vec{k} \simeq \omega \qquad (8E1)$$

where ω and k are the wave angular frequency and wave number. Such particles are called *resonant*. During an electrostatic wave-particle interaction, the rate of change of wave energy W_w is estimated from linear theory to be

$$\frac{dW_w}{dt} \simeq \frac{W_w \pi \omega \omega_p^2}{nk^2} \left(\frac{\partial f_0}{\partial v}\right)_{v=\omega/k} \qquad (8E2)$$

where $f_0(x,v,t)$ is a one-dimensional velocity distribution function for the electrons or ions, ω_p is their plasma frequency, and n is their density. Although this equation is only valid for the small perturbations described by linear theory,

it displays some general features of electrostatic wave-particle interactions:

*If the slope of the distribution function ($\partial f_0/\partial v$) at $v = \omega/k$ is positive, the wave can gain energy from the particles, leading to instability.

*If the slope is negative, the wave loses energy to the particles (Landau damping).

*Since $\omega_p^2 = ne^2/m\varepsilon_0$, the lighter mass of electrons makes them more responsive to wave-particle interactions, especially at high frequencies.

In a magnetic field, resonance can also occur when $\vec{k}\cdot\vec{v}$ differs from the wave frequency by an integer multiple of the particle's cyclotron frequency:

$$\vec{k}\cdot\vec{v} \simeq \omega - n\omega_c \quad , \qquad n = 0, \pm 1, \pm 2, \ldots \tag{8E3}$$

For a three-wave interaction, the resonance condition is

$$\vec{k}_0 = \vec{k}_1 + \vec{k}_2 \quad , \qquad \omega_0 = \omega_1 + \omega_2 \quad . \tag{8E4}$$

Since $\hbar\vec{k}$ = momentum and $\hbar\omega$ = energy, these equations represent conservation of momentum and energy during the wave-wave interaction. For example, an electron plasma wave can decay into an ion acoustic wave and another electron plasma wave in the opposite direction; or an incident electromagnetic wave can decay into an electron plasma wave and an ion acoustic wave. Wave-particle-wave interactions, such as scattering, also occur. Thus, many processes are occurring at once in the plasma, at a wide variety of frequencies and wavelengths.

From the Boltzmann relation (5D30), the fluctuation in electron density δn associated with fluctuations $\delta\phi$ of the electrostatic potential is estimated to be

$$\delta n/n \sim e\delta\phi/kT_e \quad . \tag{8E5}$$

Energy flows in a direction which proceeds towards thermodynamic equilibrium. For example, electron plasma waves generated by hot electrons might couple to ion acoustic waves, which could transfer energy to cold ions. The free energy to drive microinstabilities comes from various departures from thermodynamic equilibrium: non-Maxwellian distributions, anisotropic distributions, and gradients of density or temperature.

non-Maxwellian distributions

If an electron beam is injected into a plasma, the beam represents a bump on the high-energy tail of the electron velocity distribution function as shown in Fig. 8E1. The region where $(\partial f/\partial v)>0$ is highly unstable to generation and amplification of electron plasma waves with $k \sim \omega/v_b$, $\omega \simeq \omega_{pe}$. As the beam

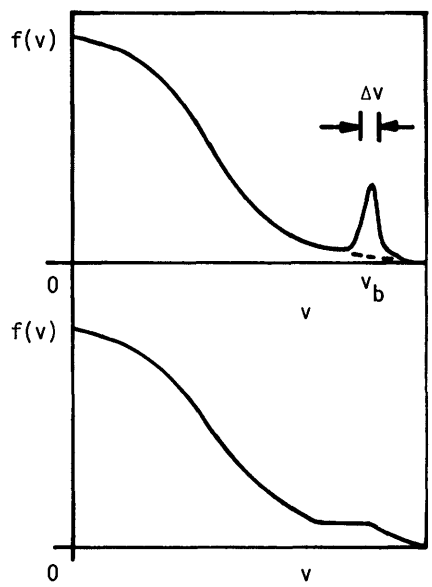

Fig. 8E1. A one-dimensional Maxwellian electron velocity distribution (top) with a bump due to an injected electron beam, and the formation of a plateau (bottom).

electrons travel through the plasma, they lose energy to the waves. The waves transfer the energy to other electrons, so that the distribution function smooths out, quickly forming a flat plateau where the bump had been. The beam-plasma instability facilitates much faster energy transfer than is possible by Coulomb collisions, enhancing the rate of plasma heating by electron beams. The steeper the slope ($\partial f/\partial v$), the faster the energy transfer to the wave, in accordance with Eq. (8E2). When the plateau stage is reached, wave growth ceases. The beam-plasma instability can also occur with ions.

At the outset of the instability, the electric field grows exponentially

$$E(t) = E_0 e^{\gamma t} \tag{8E6}$$

where E_0 is the initial value. Since the wave energy $W_w \propto E^2 = E_0^2 e^{2\gamma t}$, $dW_w/dt = 2\gamma W_w$. From Eq. (8E2) the initial growth rate is

$$\gamma \simeq \frac{\pi\omega\omega_p^2}{2nk^2}\left(\frac{\partial f_0}{\partial v}\right)_{v=\omega/k} \tag{8E7}$$

EXAMPLE PROBLEM 8E1

An electron beam with density, speed, and beam spread $n_b = 10^{15}\ m^{-3}$, $v_b = 10^8\ m/s$, $\Delta v = 10^7\ m/s$ is incident on a plasma with $n = 10^{18}\ m^{-3}$, $T_e = 10\ eV$. Estimate the characteristic time γ^{-1} for growth of the beam-plasma instability, and how far the beam travels during this time.

For simplicity, we will approximate the beam distribution function by a triangle with height f_b and base $2\Delta v$. To make $\int dv\, f = n_b$, we must set $f_b = n_b/\Delta v$. Since $v_b >> (kT_e/m_e)^{\frac{1}{2}}$, there are very few plasma electrons with velocities near v_b, and

$$(\partial f_0/\partial v)_{v=\omega/k} \simeq (\partial f/\partial v)_{beam} \simeq f_b/\Delta v = n_b/(\Delta v)^2 \tag{8E8}$$

From the resonance condition, $\omega/k \simeq v_b$, and $\omega \simeq \omega_{pe}$. Then the growth rate

$$\gamma \simeq \frac{\pi n_b v_b^2}{2n\Delta v^2}\omega_{pe} \qquad (s^{-1}) \quad . \tag{8E9}$$

The electron plasma frequency is found from Eq. (5E7)

$$\omega_{pe} = (ne^2/m_e\varepsilon_0)^{\frac{1}{2}} = 56.4\ n^{\frac{1}{2}} = 5.64 \times 10^{10} \qquad (rad/s)$$

The resulting value of $\gamma \simeq 9 \times 10^9\ s^{-1}$, so the characteristic growth time $\gamma^{-1} \simeq 0.1$ ns, and the distance travelled by the beam is about 1 cm.

If the plasma is hotter and the beam density lower, the bump produced by the beam may be so slight that no positive slope develops. Then, no instability will occur.

A similar instability occurs during the interaction of two oppositely-directed beams, as illustrated in Fig. 8E2. After the plateau stage is reached, the distribution evolves more slowly towards a final Maxwellian distribution.

If the electrons have a nonzero average velocity u_e, then their distribution is skewed to one side, as illustrated in Fig. 8E3. If the electron distribution has a positive slope and $T_e >> T_i$, then the electron plasma waves generated can couple to the ion acoustic wave, heating the ions. This ion acoustic instability can occur when

$$u_e > (kT_e/m_i)^{\frac{1}{2}} \quad \text{and} \quad T_e >> T_i . \tag{8E10}$$

anisotropic distributions

Sometimes the ions have distribution functions characterized by different pressures in the parallel and perpendicular directions, relative to the magnetic field. Radial compression and ion cyclotron resonance heating (Chapter 9) tend to add energy more in the perpendicular dimension. The mirror loss cone (Section 7D) makes mirror-confined plasmas inherently anisotropic. An approximate distribution function representing plasma in a simple mirror is

$$f(v_\parallel, v_\perp) \simeq C\, v_\perp^2 \exp(-\beta_\perp v_\perp^2 - \beta_\parallel v_\parallel^2) , \tag{8E11}$$

where C is a constant, $\beta_\parallel = m_i/2kT_\parallel$, and $\beta_\perp = m_i/2kT_\perp$. Such a distribution is illustrated in Fig. 8E4.

Instabilities tend to fill in the hole in the perpendicular distribution function by moving ions to smaller $v_\perp$ (arrow). Reduction of $v_\perp$ puts many of these ions into the loss cone, so that they are no longer confined. Unstable waves may grow at integer multiples of the ion cyclotron frequency ω_{ci}. These waves can couple energy to longitudinal electron plasma waves or to drift waves (described below). Such loss cone instabilities have hindered plasma density buildup in magnetic mirror experiments. Partially filling in the loss cone with warm flowing plasma (dashed curve) tends to stabilize the plasma. Instabilities in mirrors will be discussed further in Chapter 11.

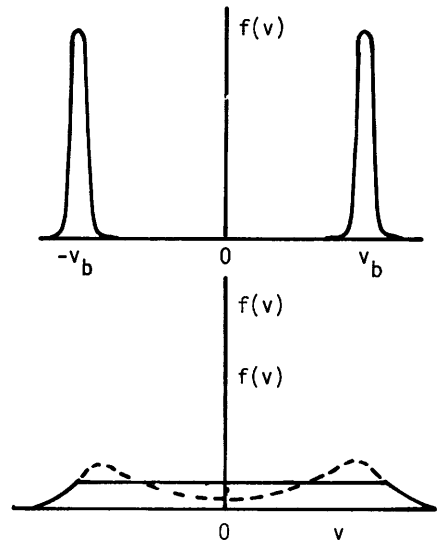

Fig. 8E2. The two-stream instability. Initial condition (top), intermediate stage (bottom, dashed curve), plateau (bottom, smooth curve).

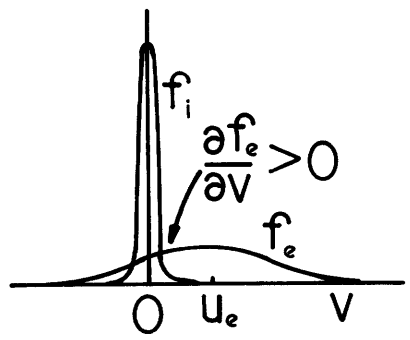

Fig. 8E3. Ion and electron velocity distribution functions for case in which ion acoustic instability may occur.

gradients and drift waves

Gradients of density or temperature in a cylindrical or toroidal plasma produce waves propagating around the plasma in the azimuthal (θ) direction. For simplicity, we will consider only the radial density gradient effect, and assume

*uniform T_e

*quasineutrality, $n_e = n_i$

*Electron flow along field lines enables them to obey the Boltzmann relation ;

$$n_e = n_0 \exp(e\phi/kT_e) \quad , \text{(taking } \phi_0 = 0\text{)} \tag{8E12}$$

*$\vec{B}$ is in the z direction (cylindrical geometry) and B is uniform.

*plasma is uniform in the z direction, so

$(\partial/\partial z) = 0$.

*The dominant contribution to ion perpendicular motion is the $\vec{E}x\vec{B}/B^2$ drift:

$$u_{ir} \simeq E_\theta/B = -(\partial\phi/\partial\theta)/Br \quad , \quad u_{i\theta} \simeq -E_r/B = (\partial\phi/\partial r)/B \quad . \tag{8E13}$$

*The rates of ionization and recombination are slow compared with wave phenomena, so these terms may be ignored in the ion continuity equation.

*$\partial n_0/\partial\theta = 0$.

Using Eq. (F33) for the divergence in cylindrical coordinates, the ion continuity equation (5D1) becomes

$$\partial n_i/\partial t + (1/r)(\partial/\partial r)(r n_i u_{ir}) + (1/r)(\partial/\partial\theta)(n_i u_{i\theta}) = 0 \tag{8E14}$$

We replace n_i by n_e, use Eq. (8E12) for n_e, and Eqs. (8E13) for u_{ir} and $u_{i\theta}$. When the derivatives are evaluated, the terms with $(\partial^2\phi/\partial r\partial\theta)$ and $(\partial\phi/\partial r)(\partial\phi/\partial\theta)$ cancel, and so does the $\exp(e\phi/kT_e)$ factor, leaving

$$(n_0 e/kT_e)(\partial\phi/\partial t) - (1/Br)(\partial n_0/\partial r)(\partial\phi/\partial\theta) = 0 \quad . \tag{8E15}$$

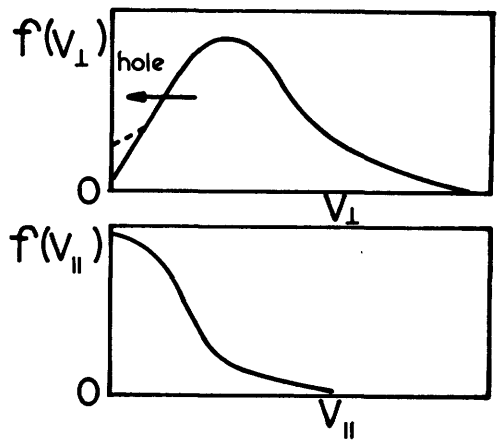

Fig. 8E4. A "mirror loss cone" distribution.

This equation is satisfied by waves of the form

$$\phi(\theta,t) = \phi_0 \exp(ik_\theta r\theta - i\omega t) \tag{8E16}$$

Substituting Eq. (8E16) into (8E15), we find the phase velocity of the wave

$$\frac{\omega}{k_\theta} = -\frac{1}{n_0}\frac{\partial n_0}{\partial r}\frac{kT_e}{eB} = -\frac{1}{n_0 eB}\frac{\partial p_e}{\partial r} \quad \text{(m/s)} \quad . \tag{8E17}$$

This is the same as the apparent velocity of electron flow in the azimuthal direction due to the electron pressure gradient. Taking the r component of the electron equation of motion (5D5) and considering only the $e\vec{u}_e x\vec{B}$ and $\vec{\nabla}p_e/n_e$ terms,

we have

$$-eu_{e\theta}B - (\partial p_e/\partial r)/n = 0$$

$$u_{e\theta} = -(\partial p_e/\partial r)/neB \equiv v_{de} \quad , \tag{8E18}$$

which is called the "electron diamagnetic drift velocity". This motion is not a guiding center drift, but an apparent flow, which is a manifestation of the existence of a pressure gradient perpendicular to the magnetic field. This average "flow" in the θ direction, caused by the pressure gradient, is illustrated in Fig. 8E5. Similarly, for the ions $v_{di} = (dp_i/dr)/neB$.

From simple assumptions about ions governed by the $\vec{E}\times\vec{B}/\vec{B}^2$ drift, electrons obeying the Boltzmann relation, and quasineutrality, we find that a density gradient causes *drift waves* with $\omega/k_\theta = v_{de}$ to flow in the azimuthal direction around the plasma. A temperature gradient has a similar effect. A fluctuation of ϕ affects u_{ir} via the ion equation of motion (8E13); the change of u_{ir} affects n_e via the ion continuity equation (8E14) and quasineutrality; and the change of n_e affects the electrostatic potential via the Boltzmann relation (8E12) to perpetuate the wave. Thus, drift waves involve an oscillating E_θ, which propagates in the θ direction and causes u_{ir} to oscillate. Electrons flow along the magnetic field to compensate for ion space charge. Every confined plasma will have a pressure gradient, and therefore have drift waves, driven by the plasma expansion energy. The drift waves can become unstable if they couple to some means of energy dissipation, such as plasma resistivity or other plasma waves having

$$\omega \simeq \omega_* \equiv k_\theta v_{de} \quad \text{(rad/s)}. \tag{8E19}$$

Other waves available for such coupling include ion acoustic waves, ion cyclotron waves, and Alfven waves. Interactions with trapped particles in Tokamaks may also drive drift waves unstable.

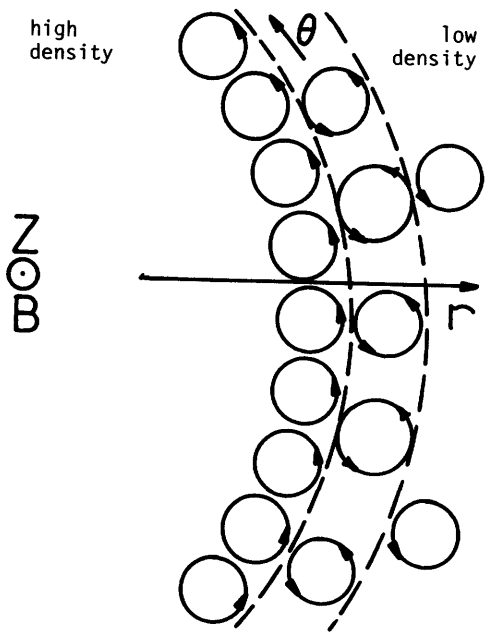

Fig. 8E5. Apparent electron flow due to electron density gradient. The magnetic field is out of the paper, and the circles represent electron Larmor rotation (counterclockwise). Along the dashed lines, it appears that there is more electron motion upward than downward, due to the density gradient.

The damping rate of the turbulent waves caused by microinstabilities is roughly $k_\perp^2 D$, where D is the effective diffusion coefficient. When this damping is comparable to the growth rate γ, the wave amplitude saturates. Hence, an estimate of the diffusion coefficient caused by the waves is

$$D \lesssim \gamma/k_\perp^2 \quad (m^2/s). \tag{8E20}$$

The electric field fluctuations caused by microinstabilities can greatly increase the rate of heat transport across the magnetic field. Such "anomalous" transport caused several fusion experiments to give disappointing results. Drift waves can be stabilized by a number of effects, including magnetic shear and favorable magnetic field gradients.

Table 8E1. Characteristics of some microinstabilities.

instability	frequency	process	effect	stabilization
NON-MAXWELLIAN DISTRIBUTIONS				
beam-plasma	ω_{pe}	Electron plasma oscillations excited by surplus of fast electrons.	Maxwellization	Use energy spread of injected beams
two stream	ω_{pe}	Counterstreaming beams excite plasma oscillations.	Maxwellization	
ion acoustic	kc_s	If $u_e > c_s$ and $T_e \gg T_i$, then streaming electrons excite ion acoustic oscillations.	ion heating	low u_e or T_e
ANISOTROPY				
ion cyclotron electrostatic	$\ell\omega_{ci}$ (ℓ=integer)	Perpendicular ion energy excites electron plasma oscillations when $\omega_{pe} > \ell\omega_{ci}$	reduction of ions' perpendicular energy	Avoid producing anisotropic distribution.
loss cone	$\ell\omega_{ci}$	(same)	scatters ions into loss cone	Use warm flowing plasma to partially fill in the loss cone.
GRADIENTS				
drift waves		When $\omega \sim \omega_*$ the drift energy is transferred to plasma waves by resonances or dissipated by collisions.	reduction of gradients by anomalous transport	minimum-B, magnetic shear
electrostatic drift	kc_s			
drift cyclotron	ω_{ci}			
electromagnetic drift	kv_A			
drift dissipative	ω_*			

c_s = ion sound speed $\simeq (kT_e/m_i)^{\frac{1}{2}}$

v_A = Alfven speed = $B/(\mu_0 n m_i)^{\frac{1}{2}}$

Table 8E1 summarizes a few aspects of the microinstabilities mentioned here. There are many other types of microinstabilities not discussed here. All of them are driven by some departure from thermodynamic equilibrium, and all accelerate the approach to thermodynamic equilibrium above the "classical" rate due to Coulomb collisions.

8F. Transport

The transport of particles, momentum, and energy across the magnetic field may be studied in a variety of ways. Usually kinetic theory is used to estimate the transport coefficients, such as the diffusion coefficient and thermal conductivity. Then, the transport for a given case may be studied using the fluid equations. The two-fluid equations are much simpler than kinetic theory (fewer independent variables), yet they retain a distinction between electrons and ions, which the single-fluid MHD equations do not. The transport rates for the two species can oe quite different, due to the different processes involved. There is also a set of equations to describe penetration of neutral atoms and impurities into the plasma from the walls.

To illustrate the equations used in transport calculations, we will consider confinement of plasma with circular cross section in an axisymmetric torus with large aspect ratio. By averaging the equations over a magnetic surface, the problem is reduced to one-dimensional variation with the minor radius r (or flux coordinate ψ). The resulting transport equations describe flow of particles and energy from one magnetic surface to the next.

transport equations

Some parameters used in transport equations are defined in Table 8F1. In a simple case there are nine unknown quantities (n, p_e, p_i, B_p, $J_\parallel$, Γ, q_e, q_i, and $E_\parallel$) to be found as functions of r and t.
If the temperatures T_e and T_i are expressed in energy units (J), the particle and energy conservation equations for n, p_e, and p_i may be written in the form (Hinton and Hazeltine, 1976)

$$\frac{\partial n}{\partial t} + \frac{1}{r}\frac{\partial}{\partial r} r\Gamma = S_n \quad , \quad (m^{-3}s^{-1}) \tag{8F1}$$

$$\frac{3}{2}\frac{\partial p_e}{\partial t} + \frac{1}{r}\frac{\partial}{\partial r} r\left(q_e + \frac{5}{2} T_e \Gamma\right) = -\frac{3m_e n(T_e - T_i)}{m_i \tau_e} + E_\parallel J_\parallel - \frac{\Gamma}{n}\frac{\partial p_i}{\partial r} + bA_i \frac{\partial T_i}{\partial r} + S_e \quad , \quad (W/m^3) \tag{8F2}$$

check these

$$\frac{3}{2}\frac{\partial p_i}{\partial t} + \frac{1}{r}\frac{\partial}{\partial r} r\left(q_i + \frac{5}{2} T_i \Gamma/Z\right) = \frac{3m_e n(T_e - T_i)}{m_i \tau_e} + \frac{\Gamma}{n}\frac{\partial p_i}{\partial r} - bA_i \frac{\partial T_i}{\partial r} + S_i \quad , \quad (W/m^3) \tag{8F3}$$

where S_n, S_e, and S_i represent additional (sources - losses) of particles, electron energy, and ion energy, from ionization, external heating, radiation, charge

Table 8F1. Parameters used in transport equations. Parameters averaged over a magnetic surface are indicated by "average". Temperatures are in Joules.

ionic charge	Z
electron collision time [similar to Eq. (2E52)]	$\tau_e \equiv 6\pi(2\pi m_e)^{\frac{1}{2}}\varepsilon_0^2 T_e^{3/2}/nZ^2e^4L = \frac{1.09\times10^{16}\, T_e^{3/2}}{nZ^2L}$
ion-ion collision time [similar to Eq. (2E53)]	$\tau_i \equiv 12\pi(\pi m_i)^{\frac{1}{2}}\varepsilon_0^2 T_i^{3/2}/nZ^4e^4L$
minor radius	r
major radius of magnetic axis	R_0
inverse aspect ratio	$\varepsilon \equiv r/R_0$
average poloidal magnetic field	B_p
poloidal gyroradius of electrons	$\rho_\theta \equiv (2m_eT_e)^{\frac{1}{2}}/eB_p$
average radial particle flux	$\Gamma \equiv n_e u_{er} = n_i u_{ir}$ (ambipolar flow)
parallel conductivity (units=A/v-m)	$\sigma_\parallel \equiv (ne^2\tau_e/m_e)(1.08 + Z)/(0.773 + 0.29Z)$
average radial electron heat flux	q_e
average radial ion heat flux	q_i
toroidal magnetic field	B_t
average parallel current density	$J_\parallel$
average parallel electric field	$E_\parallel$
average electron pressure	$p_e \equiv nT_e$
average ion pressure	$p_i \equiv nT_i$
ratio of effective electron collision frequency to electron bounce frequency	$\nu_{*e} \equiv \frac{r(B_t/B_p)}{\varepsilon^{3/2}\tau_e\,(T_e/m_e)^{\frac{1}{2}}}$
ratio of effective ion collision frequency to ion bounce frequency	$\nu_{*i} \equiv \frac{r(B_t/B_p)}{\varepsilon^{3/2}\tau_i\,(T_i/m_i)^{\frac{1}{2}}}$
particle density	$n \equiv n_e = n_i$ (quasineutrality)

exchange, fusion reactions, etc. The coefficients b, A_j are defined in Table 8F2. Equations (8F2) and (8F3) are equivalent to the two-fluid energy conservation equations (5D13) and (5D14), although they appear in different form here. The Maxwell Equations have the one-dimensional forms

$$\partial B_p/\partial t \simeq \partial E_\parallel/\partial r \qquad (T/s) \tag{8F4}$$

$$\mu_0 J_\parallel \simeq \frac{1}{r}\frac{\partial}{\partial r} rB_p \qquad (T/m) \quad . \tag{8F5}$$

The remaining four equations determine Γ, q_e, $J_\parallel$, and q_i in terms of transport coefficients multiplying gradients ;

Table 8F2. Neoclassical transport coefficients. These "neoclassical" values represent transport in toroidal geometry due to Coulomb collisions only, so they give the minimum transport rates. Coefficients for Z = 2 and Z = 4 are also available. From Hinton and Hazeltine, Reviews of Modern Physics 48, No. 2, Part 1, 239-308 (1976), Table III and Eqs. 6.132, 6.133, 6.135, and 6.136 .

(original equation numbers)

$$A_i = \Gamma/Z(1 + \nu_{*e}^2\varepsilon^3) \qquad (6.132)$$

$$b = \frac{\left(\frac{1.17 - 0.35\,\nu_{*i}^{1/2}}{1 + 0.7\,\nu_{*i}^{1/2}}\right)^{-2.1}\nu_{*i}^2\varepsilon^3}{1 + \nu_{*i}^2\varepsilon^3} \qquad (6.135,\ 6.136)$$

$$K_2 = \frac{0.66}{1 + 1.03\,\nu_{*i}^{1/2} + 0.31\,\nu_{*i}} + \frac{1.17\,\varepsilon^3\,\nu_{*i}}{1 + 0.74\,\nu_{*i}\varepsilon^{3/2}} \sim 0.55 \pm 0.1, \quad (\nu_{*i}<0.3) \qquad (6.133)$$

For m or n = 1 or 2,

$$K_{mn} = K_{mn}^{(o)}\left\{\frac{1}{1 + a_{mn}\nu_{*e}^{1/2} + b_{mn}\nu_{*e}} + \frac{\varepsilon^{3/2}(c_{mn}^2/b_{mn})\nu_{*e}\varepsilon^{3/2}}{1 + c_{mn}\nu_{*e}\varepsilon^{3/2}}\right\} . \qquad (6.125)$$

For n = 3,

$$K_{m3} = K_{m3}^{(o)}[1 + a_{m3}\nu_{*e}^{1/2} + b_{m3}\nu_{*e}]^{-1}[1 + c_{m3}\nu_{*e}\varepsilon^{3/2}]^{-1} . \qquad (6.126)$$

Z = 1 (Table III)

	mn	$K_{mn}^{(0)}$	a_{mn}	b_{mn}	c_{mn}
(Z=1)	11	1.04	2.01	1.53	0.89
	12	1.20	0.76	0.67	0.56
	22	2.55	0.45	0.43	0.43
	13	2.30	1.02	1.07	1.07
	23	4.19	0.57	0.61	0.61
	33	1.83	0.68	0.32	0.66

$$\Gamma = -(n\varepsilon^{1/2}\rho_\theta^2/\tau_e)(K_{11}A_e + K_{12}T_e'/T_e) - K_{13}n\varepsilon^{1/2}E_\parallel/B_p \quad (m^{-2}s^{-1}) \qquad (8F6)$$

$$(q_e + \tfrac{5}{2}T_e\Gamma) = -(nT_e\varepsilon^{1/2}\rho_\theta^2/\tau_e)(K_{12}A_e + K_{22}T_e'/T_e) - K_{23}nT_e\varepsilon^{1/2}E_\parallel/B_p \quad (W/m^2) \qquad (8F7)$$

$$J_\parallel = \sigma_\parallel E_\parallel - (nT_e\varepsilon^{1/2}/B_p)(K_{13}A_e + K_{23}T_e'/T_e) - K_{33}\varepsilon^{1/2}\sigma_\parallel E_\parallel \quad (A/m^2) \qquad (8F8)$$

$$q_i = -(n\varepsilon^{1/2}\rho_\theta^2 m_i/m_e\tau_i)K_2T_i' - bT_i\Gamma/Z(1 + \nu_{*e}^2\varepsilon^3) \quad (W/m^2) \qquad (8F9)$$

where

$$A_e \equiv p_e'/p_e - 2.5T_e'/T_e + (T_i/ZT_e)[p_i'/p_i - bT_i'/T_i(1 + \nu_e^{*2}\varepsilon^2)] \quad , \tag{8F10}$$

the primes denote radial derivatives, and the coefficients K_{mn} are defined in Table 8F2. Equation (8F6) is the toroidal analog of Eq. (5D26). Equations (8F1)-(8F9) constitute a complete set of equations for the nine unknowns. At each time step we can find B_p from Eq. (8F4), $J_\parallel$ from (8F5), and then solve (8F8) for $E_\parallel$. Values of $E_\parallel$, Γ, q_e, and q_i from (8F6)-(8F9) are used in (8F1)-(8F3) to advance n, p_e, and p_i in time. The new temperatures may be found from $T_e = p_e/n$, $T_i = p_i/n$.

additional considerations

For the case of non-circular plasmas, the transport equations are written in terms of the flux function ψ (or the volume V enclosed by a magnetic surface). The Grad-Shafranov Equation (8C19) can be solved simultaneously with the transport equations to determine the shapes of the magnetic surfaces as a function of time. The shapes are needed in order to average the plasma parameters over the magnetic surfaces.

A *neutral gas* transport code may be used to determine the neutral gas density distributions $n_n(\psi,\theta)$, which are needed to compute ionization rates and charge exchange rates in the S_n and S_i terms. Another code may be used to estimate production of *impurities* and their subsequent diffusion into the plasma, in order to compute P_{rad} for the S_e term and corrections to the transport coefficients. If neutral beam heating (Chapter 9) is used, another code is needed to compute the resultant ion *velocity distribution* $f_i(v_\parallel,v_\perp,t)$ from the Boltzmann Equation (5C4) with a Fokker-Planck collision term describing velocity diffusion due to long-range binary Coulomb collisions. A three-dimensional code may compute *drift orbits* of injected ions and fusion product alpha particles. An additional term may be needed in the $J_\parallel$ equation to account for the current of injected ions. Finally, many zero-dimensional equations are needed to calculate *plasma-wall interactions*, such as adsorption, desorption, and sputtering (Chapter 24). These equations help determine the outer boundary conditions for the transport equations. At the inner boundary (r = 0) the radial derivatives of the dependent variables may be set equal to zero. Numerical methods for solving plasma transport and impurity transport equations are discussed by Hogan (1976).

transport theories

There are a variety of theoretical predictions of transport coefficients for toroidally confined plasmas:

* *neoclassical*. The neoclassical transport coefficients (Table 8F1) represent transport in toroidal geometry due to Coulomb collisions only, so they give the *minimum* values of transport rates. From the transport equations (8F6) - (8F9) we can identify the neoclassical values of diffusion coefficient and thermal conductivity:

$$D = \varepsilon^{\frac{1}{2}}\rho_\theta^2 K_{11}/\tau_e \qquad (m^2/s)$$

$$\chi_e = n\varepsilon^{\frac{1}{2}}\rho_\theta^2 K_{22}/\tau_e \qquad (m^{-1}s^{-1}) \quad , \qquad \chi_i = n\varepsilon^{\frac{1}{2}}\rho_\theta^2 K_2 m_i/m_e\tau_{ie} \sim (m_i/m_e)^{\frac{1}{2}}\chi_e \tag{8F11}$$

Neoclassical predictions have been in rough agreement with experimental data for some plasmas which do not carry high currents, and for ion heat conduction in tokamaks, but they are much too low for electronic heat conduction and particle transport rates in tokamaks.

* *pseudoclassical.* The pseudoclassical transport coefficients are derived from considerations of drift wave turbulence. The electron thermal conductivity and diffusion coefficient are given by

$$D \sim 2\rho_\theta^2/\tau_e \quad (m^2/s)$$

$$\chi_e \sim 6n\rho_\theta^2/\tau_e \quad (m^{-1}s^{-1}) \tag{8F12}$$

These values are higher than neoclassical, and appear to be consistent with some experimental results.

* *trapped particle instabilities.* As the collision frequency decreases to $\nu_{*e} < 1$, the trapped electron instability may greatly increase transport rates. At lower collision frequencies, the trapped ion mode may occur. The diffusion coefficient associated with the trapped ion mode is

$$D \simeq \frac{\varepsilon^{5/2}}{\nu_{ei}} \left(\frac{T_i}{2neB}\right)^2 \left(\frac{dn}{dr}\right)^2 \propto T_i^{7/2} \tag{8F13}$$

assuming $T_e \simeq T_i$. Various effects tend to stabilize trapped particle instabilities, however.

* *Bohm diffusion.* The Bohm diffusion coefficient is defined to be

$$D = T_e/16eB \quad (m^2/s) \tag{8F14}$$

where T is again in energy units. Bohm diffusion is associated with drift waves. If we set $\gamma \simeq \omega_*$ in Eq. (8E20), we find

$$D \lesssim \omega_*/k_\perp^2 = k_\theta v_{de}/k_\theta^2 = (dp_e/dr)/neBk_\theta \simeq T_e\lambda_\theta/2\pi reB = T_e/NeB \tag{8F15}$$

where N is the number of wavelengths which fit around the circumference of the plasma. Bohm diffusion is probably the maximum diffusion rate perpendicular to the magnetic field to be expected in any plasma. It has been observed in a number of experiments, such as stellarators with low shear, and may occur when

$$R_0 q \rho_i / r^2 > 1 \quad , \tag{8F16}$$

where ρ_i is the ion gyroradius and q is the safety factor (Dean, 1974, p.26).

The variation of these various types of transport coefficients with collision frequency is illustrated in Fig. 8F1. A given plasma may be in different regimes at different radii. Transport codes attempt to account for instabilities phenomenologically by switching on higher local values of transport coefficients, such as thermal conductivity and resistivity, when conditions for instability occur. Results of some tokamak studies will be discussed in Chapter 13.

random walk model

A crude picture of diffusion processes is a random walk, in which steps are taken frequently in random directions. For such a process the diffusion coefficient is roughly equal to the step size squared times the step frequency. Classical diffusion of plasma across a magnetic field may be described by a step size equal to the electron Larmor radius and a step frequency equal to ν_{ei}:

$$D \simeq \rho^2 \nu_{ei} \ (m^2/s) \ \text{(classical)} \quad . \tag{8F17}$$

Neoclassical diffusion is essentially classical diffusion corrected for the effects of toroidal curvature. The step size is equal to the banana width (Eq. 7E21) and the step frequency is equal to the effective collision frequency of trapped particles multiplied by the fraction of trapped particles:

$$D \simeq (\Delta r)^2 \nu_{eff} f_t$$

$$\simeq (m_e v \varepsilon^{\frac{1}{2}}/eB_p)^2 (\nu_{ei}/\varepsilon)(2\varepsilon)^{\frac{1}{2}}$$

$$\simeq \nu_{ei} \rho^2 q^2 \varepsilon^{-3/2} \quad (m^2/s)$$

(banana regime) , (8F18)

where we have used $q = \varepsilon B_t/B_p$, $\rho = m_e v/eB_t$. For $q = 3$ and $\varepsilon = \frac{1}{4}$ this rate is about 70 times the classical rate.

The maximum value which the step frequency can have is the cyclotron frequency $\nu_{ce} = eB/2\pi m_e$. Using this value, we find

$$D_{max} \simeq \rho^2 \omega_{ce} \simeq (2m_e T_e/e^2 B^2)(eB/2\pi m_e)$$

$$= T_e/\pi eB \quad (m^2/s) \quad , \quad (8F19)$$

which differs from Bohm diffusion only in the numerical coefficient.

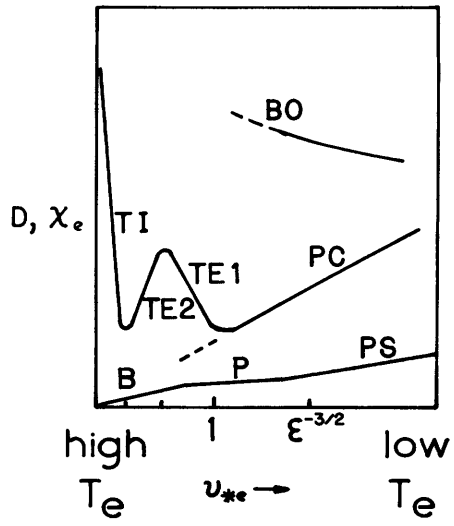

Fig. 8F1. Variation of transport coefficients with ratio of effective electron collision frequency to electron bounce frequency, according to various theories. The predictions of neoclassical theory are shown by the bottom curve: PS = Pfirsch-Schlueter (collisional) regime, P = plateau regime, B = banana (collisionless) regime. The middle curve shows the estimates for pseudoclassical theory (PC), trapped electron modes (TE1), (TE2), and trapped ion mode instabilities (TI). The top curve represents Bohm diffusion (BO).

EXAMPLE PROBLEM 8F1

A Tokamak plasma has $a = 1$ m, $R_0 = 4$ m, $T_{e0} = T_{i0} = 10$ keV, $B_t = 4$ T, $n_0 = 6\times10^{19}$ m^{-3}, $B_p = 0.4$ T, and $Z = 1$. Assuming edge plasma values 1/10 of central values, estimate the diffusion coefficients at the edge for cases of neoclassical, pseudoclassical, trapped ion mode, and Bohm diffusion.

At the edge, with T = 1 keV = 1.6×10^{-16} J and n = 6×10^{18}m^{-3}.

From Table 8F1, $\tau_e = 10^{-4}$s, $\rho_\theta^2 = 7.1\times10^{-8}$ m^2, and $\nu_{*e} = 0.06$.

Similarly, $\rho^2 = 2m_e T_e/e^2 B_t^2 = 7.1\times10^{-10}$ m^2

From Eq. (8F11) with $K_{11} \simeq 1.04$, neoclassical D = 3.7×10^{-4} m^2/s

Alternately, from Eq. (8F18), neoclassical D = 3.7×10^{-4} m^2/s.

From Eq. (8F12), pseudoclassical D = 1.4×10^{-3} m^2/s.

From Eq. (8F13) with $dn/dr \simeq -n_0/a$, trapped ion mode D = (4.9) m^2/s 6.7

From Eq. (8F14) Bohm D = 16 m^2/s

[Since condition (8F16) is not fulfilled, Bohm diffusion is unlikely.]

When the transport coefficients are known, the confinement times can be estimated.

8G. Confinement Times

definitions

We can define the particle confinement time for ions to be

$$\tau_p \equiv \frac{\text{(number of ions in plasma)}}{\text{(ion loss rate)}} \simeq \frac{\text{(number of ions in plasma)}}{\text{(ion production rate at equilibrium)}}, \tag{8G1}$$

where the production rate equals the loss rate if the plasma is at steady-state equilibrium. Due to the quasineutrality condition, these rates are the same for electrons as for ions, so the electron particle confinement time will be the same.

We can define an energy confinement time for electrons as

$$\tau_{Ee} \equiv \frac{\text{(electron energy in plasma)}}{\text{(electron energy loss rate)}} \simeq \frac{\text{(electron energy in plasma)}}{\text{(electron heating rate at equilibrium)}} \tag{8G2}$$

and a similar definition applies to ion energy confinement time. For the whole plasma, the energy confinement time is

$$\tau_E \equiv \frac{\text{(plasma energy)}}{\text{(energy loss rate)}} \simeq \frac{\text{(plasma energy)}}{\text{(plasma heating rate at equilibrium)}} \tag{8G3}$$

If the radiation power loss rate $\int d\vec{x}\, P_{rad}$ (over the plasma volume) is subtracted from the denominator, we have the "nonradiative" energy confinement times used in Chapter 4 to discuss ignition and power balance conditions.

Given the density and temperature profiles, the numerators of these equations are easy to calculate:

$$\begin{aligned}
\text{(number of ions in plasma)} &= \int d\vec{x}\, n \\
\text{(electron energy in plasma)} &= \tfrac{3}{2}\int d\vec{x}\, nT_e \\
\text{(plasma energy)} &= \tfrac{3}{2}\int d\vec{x}\, n(T_e+T_i)
\end{aligned} \tag{8G4}$$

Transport calculations give estimates of the denominators of these equations which depend strongly on the model used to determine the transport coefficients. We can estimate the particle and energy loss rates as

$$\text{(ion loss rate)} = \int_{\text{surface}} d\vec{S}\cdot\vec{\Gamma}$$

$$\text{(electron energy loss rate)} = \int_{\text{surface}} d\vec{S}\cdot(\vec{q}_e+2.5\vec{\Gamma}T_e) + \int_{\text{volume}} d\vec{x}\ P_{rad}$$

$$\text{(ion energy loss rate)} = \int_{\text{surface}} d\vec{S}\cdot(\vec{q}_i+2.5\vec{\Gamma}T_i) + \int_{\text{volume}} d\vec{x}\ n_n n_i\langle\sigma_x v_i\rangle 1.5T_i$$

$$\text{(plasma energy loss rate)} = \text{(ion energy loss rate + electron energy loss rate)} \qquad \text{(8G5)}$$

assuming that 1.5 T_i is the average energy of ions lost by charge exchange. The surface terms are determined by the values of Eqs. (8F6), (8F7), and (8F9) at the surface of the plasma in the neoclassical model, and methods for calculating the volume terms were discussed in Chapter 3. For open confinement systems, loss along field lines is calculated differently (Chapter 11).

experimental measurements

The denominators may be estimated from experimental measurements of input power for plasma heating, if the plasma reaches equilibrium. For example, ohmic heating power in Tokamaks is known from measurements of transformer voltage and current. The power of injected neutral beams is also known, and the fraction of that energy trapped in the plasma can be estimated. With radio wave heating, the fraction of input power absorbed by the plasma can also be estimated. Such estimates of the heating power input to the plasma yield experimental values of energy confinement time (or electron energy confinement time, if the fraction going to the electrons is known.)

Individual particle lifetimes are very short near the plasma edge, and very long at the plasma center. At equilibrium, the particle confinement time for the plasma as a whole can be estimated as

$$\tau_p \cong \frac{\int d^3\vec{x}\ n_i}{\int d^3\vec{x}\ n_e n_n(\langle\sigma_e v_e\rangle + \langle\sigma_i v_i\rangle)} \qquad \text{(8G6)}$$

The denominator can be estimated from spectroscopic measurements of $n_n(r)$ and laser beam scattering measurements of $n_e(r)$ and $T_e(r)$ (Chapter 10). An alternative technique for estimating the denominator is to measure the flux of ions leaving the plasma or the flux of neutrals incident on the plasma.

Diffusion coefficients and thermal conductivities can be inferred from experimentally measured profiles of n, n_n, T_e, and T_i, using the appropriate transport equations.

theoretical estimates

The equations for radial particle flux and heat fluxes may be written

$$\Gamma = -D(\partial n/\partial r) + (\text{other terms}) \qquad (m^{-2}s^{-1})$$

$$q_e = -\chi_e(\partial T_e/\partial r) + (\text{other terms}) \qquad (W/m^2)$$

$$q_i = -\chi_i(\partial T_i/\partial r) + (\text{other terms}) \qquad (W/m^2) \tag{8G7}$$

where the other terms depend on other gradients, etc, as in Eqs. (8F6), (8F7), and (8F9). Assuming that the other terms are negligibly small, we can use these relations to estimate confinement times. One method is to substitute these values into the conservation equations (8F1)-(8F3) and solve the resulting differential equations for $n(r,t)$, $T_e(r,t)$, and $T_i(r,t)$. However, variations of D, χ_e, and χ_i with n, T_e, and T_i make the equations nonlinear and difficult to solve analytically.

If the approximate shapes of the radial profiles $n(r)$, $T_e(r)$, and $T_i(r)$ are known, however, we do not need to solve the differential equations. Instead, we can substitute Eqs. (8G7) directly into Eqs. (8G5) and evaluate the surface integrals. For a long cylindrical plasma with radius a and length L, we find

$$\text{(ion loss rate)} = -2\pi aLD(\partial n/\partial r)\big|_{r=a} \qquad (m^{-2}s^{-1}) \quad ,$$

$$\text{(electron energy loss rate)} = -2\pi aL\chi_e(\partial T_e/\partial r)\big|_{r=a} - 5\pi aLT_eD(\partial n/\partial r)\big|_{r=a} + \int_{\text{volume}} d\vec{x}\, P_{rad} \qquad (W/m^2) \quad ,$$

$$\text{(ion energy loss rate)} = -2\pi aL\chi_i(\partial T_i/\partial r)\big|_{r=a} - 5\pi aLT_iD(\partial n/\partial r)\big|_{r=a} + \int_{\text{volume}} d\vec{x}\, n_n n\langle\sigma_x v_i\rangle 1.5T_i \qquad (W/m^2) \quad . \tag{8G8}$$

The particle confinement time and nonradiative electron energy confinement time become

$$\tau_p = \frac{\pi a^2 L\,\langle n\rangle}{-2\pi aLD(\partial n/\partial r)\big|_{r=a}} \qquad (s)$$

$$\langle n\rangle \equiv \frac{2\pi L\int_0^a dr\, rn}{\pi a^2 L} \qquad (m^{-3})$$

$$\tau'_{Ee} = \frac{\pi a^2 L\,\langle 1.5nT_e\rangle}{-2\pi aL\chi_e(\partial T_e/\partial r)\big|_{r=a} - 5\pi aLT_eD(\partial n/\partial r)\big|_{r=a}} \qquad (s) \tag{8G9}$$

$$\langle 1.5nT_e\rangle \equiv \frac{2L\int_0^a dr\, r\, 1.5nT_e}{\pi a^2 L} \qquad (J/m^3)$$

Let n_0 and T_{e0} be the values of n and T_e at r = 0. If we make the following rough estimates

$$(\partial n/\partial r)_{r=a} \sim -n_0/a \qquad (\partial T_e/\partial r)_{r=a} \sim -T_{e0}/a$$

$$\langle n \rangle \sim \tfrac{1}{2} n_0 \qquad \langle 1.5 n T_e \rangle \sim \tfrac{1}{4}(1.5 n_0 T_{e0})$$

$$\chi_e \sim 3 n_0 D \quad , \qquad T_e(r=a) \sim 0.1\, T_0 \qquad (8G10)$$

then the confinement times are found to be

$$\tau_p \sim 0.25\, a^2/D \quad (s) \quad ,$$

$$\tau'_{Ee} \sim 0.06\, a^2/D \quad (s) \quad , \qquad (8G11)$$

where D and the other terms in the denominator of Eqs.(8G9) are evaluated at r = a. However, the gradients producing drift wave turbulence depend upon a, so D could also be a function of a if such turbulence were dominant. The exact value of the numerical coefficients in Eqs. (8G11) depends upon the shape of the plasma density and temperature profiles. The main approximations made are those of Eqs. (8G10) and neglect of the "other terms" in Eqs. (8G7). For a torus with large aspect ratio, $L \to 2\pi R_0$, and the same results apply.

EXAMPLE PROBLEM 8G1

Estimate the particle confinement times for the cases of example problem 8F1.

Using the rough estimates of Eq. (8G11), we find

$\tau_p \sim a^2/4D = 690$ s (neoclassical)

$= 180$ s (pseudoclassical)

$= 0.05$ s (trapped ion mode)

$= 0.016$ s (Bohm) .

Thus, the different theories give widely different estimates of confinement times.

If the variations of D and χ with n and T are known, it is possible to solve the non-linear diffusion and heat transport equations analytically, using the method of Anderson and Lisak (1980).

Problems

1. A typical Tokamak has $B_t/B_p \sim 10$, $R_0/a = 4$. What is the rotational transform angle of its magnetic field lines? How many times does the field line go around the torus in the toroidal direction before it arrives back at its starting point?

2. A pulsed plasma with $\hat{\beta} = 1$ has B = 5 T, $T_i = 3T_e$, and peak density of 3×10^{22} m^{-3}. What is the peak ion temperature?

3. How many atmospheres of pressure can be confined in a magnetic field with B = 1 T? What electric field would be required to contain the same pressure? (The electric field pressure is $\epsilon_0 E^2/2$, Eq. 1A10).

4. Estimate $\langle\beta\rangle$ for a plasma with $\hat{\beta} = 1$ and $n/n_0 = T_e/T_{e0} = T_i/T_{i0} = (1 - r^2/a^2)^{\alpha}$ assuming B to be uniform.

5. Verify Eq. (8C4) by using the definition of ψ_p with $d\vec{S} = 2\pi R dR \hat{z}$ and Eq. (8C5).

6. A ball is at rest at the origin on the following surfaces. Which are stable equilibria? (a) $z = x^2+y^2$ (b) $z = x^2-2x^4+4$ (c) $z = x^2-y^2$ (d) $z = x^4 - 3x^2 + 2y^4$.

7. The simple toroidal magnetic field of Fig. 8A2 may be represented by the equation $B(R) = B_0 R_0/R$, where B_0 and R_0 are constants. Is plasma in this field stable according to the $\int d\ell/B$ criterion?

8. The volume and surface area of a torus may be estimated by approximating the torus as a cylinder with length $2\pi R_0$. It is desired to build a Tokamak with $q = 2.5$ (for stability) and aspect ratio of 4, to contain a plasma pressure of 10 atm in a volume of 500 m^3. Estimate (a) maximum attainable value of β (b) a and R_0, (c) required B, B_t, and B_p, (d) required plasma current, (e) stored energy of the magnetic field.

9. An electron beam with energy 10 keV, current density 10^4 A/m^2, and $\delta v/v = 0.1$ is incident on a plasma with density 10^{17} m^{-3} and temperature $T_e = 30$ eV. Estimate the phase velocity, wavelength, and growth rate of the plasma oscillations excited by the beam.

10. A deuterium plasma has $n(r)/n_0 = T_e(r)/T_{e0} = T_i(r)/T_{i0} = 1 - .9r^2/a^2$; $R_0/a = 4$; $q = 3$; $n_0 = 10^{19}$ m^{-3}, $T_{e0} = T_{i0} = 0.3$ keV, a = 0.1 m, B = 0.5 T. Estimate (a) v_{de} at r = a, (b) the wavelength of a drift wave with a frequency which matches the ion cyclotron frequency.

11. Estimate D and χ_e for the plasma of problem 10 at r = a assuming (a) neoclassical transport, (b) pseudoclassical, (c) Bohm diffusion (take $\chi_e \sim 3nD$). Which neoclassical regime is the plasma in, banana, plateau, or Pfirsch-Schlueter? (d) Estimate τ'_{Ee} for each case from (8G9).

12. For the plasma profiles of problem 10, estimate the ion energy loss time due to charge exchange alone, assuming that there is a uniform neutral density $n_n = 10^{17}$ m^{-3}. The integral in the denominator can be approximated by numerical integration with $\Delta r = \frac{1}{4}a$ and Simpson's Rule, as in example problem 4G1.

Bibliography

plasma confinement in general

F. E. Cap, *Handbook on Plasma Instabilities*, Academic Press, New York, Volume 1, 1976; Volume 2, 1978.

F. F. Chen, *Introduction to Plasma Physics*, Plenum, New York, 1974.

M. O. Hagler and M. Kristiansen, *An Introduction to Controlled Thermonuclear Fusion*, Lexington Books, Lexington, MA, 1977.

B. B. Kadomtsev, M. N. Rosenbluth, and W. B. Thompson, Directors, *Plasma Physics*, International Atomic Energy Agency, Vienna, 1965.

N. A. Krall and A. W. Trivelpiece, *Principles of Plasma Physics*, McGraw-Hill, New York, 1973.

M. A. Leontovich, Editor, *Reviews of Plasma Physics*, Vols. 1-7, Consultants Bureau, New York, 1965-1979.

K. Miyamoto, *Plasma Physics for Nuclear Fusion*, MIT Press, Cambridge, MA 1980.

D. J. Rose and M. Clark, Jr., *Plasmas and Controlled Fusion*, MIT Press, Cambridge, MA, 1961.

W. M. Stacey, Jr., *Fusion Plasma Analysis*, Wiley, New York, 1981.

equilibrium and MHD stability

G. Arfken, *Mathematical Methods for Physicists*, Academic Press, New York, 1973.

G. Bateman, *MHD Instabilities*, MIT Press, Cambridge, MA, 1978.

F. Bauer, O. Betancourt, and P. Garabedian, *A Computational Method in Plasma Physics*, Springer-Verlag, New York, 1978. (3-D equilibrium calculations.))

A. H. Boozer and A. B. Rechester, "Effect of magnetic perturbations on divertor scrape-off width", *The Physics of Fluids 21*, 682-689 (1978).

A. Jeffrey and T. Taniuti, *Magnetohydrodynamic Stability and Thermonuclear Containment*, Academic Press, New York, 1966.

B. McNamara, "Equilibria of magnetically confined plasmas", *Methods in Computational Physics*, Vol. 16, Academic Press, New York, 1976, p. 211-251.

G. Schmidt, *Physics of High Temperature Plasmas*, Academic Press, New York, 1979.

L. S. Solov'ev, " Hydromagnetic Stability of Closed Plasma Configurations", *Reviews of Plasma Physics*, Vol. 6, Consultants Bureau, New York, 1975.

J. A. Wesson, "Hydromagnetic stability of tokamaks", *Nuclear Fusion 18*, 87-132 (1978).

microinstabilities

H. R. Griem and R. H. Lovberg, *Methods of Experimental Physics*, Volume 9, Part A, Plasma Physics, Academic Press, New York, 1970, Chapters 7-9.

S. Ichimaru, *Basic Principles of Plasma Physics, A Statistical Approach*, W. A. Benjamin, Reading, MA, 1973.

W. M. Manheimer, "An introduction to trapped-particle instability in Tokamaks", TID-27157, 1977.

A. B. Mikhailovskii, *Theory of Plasma Instabilities*, 2 Volumes, Consultants Bureau, New York, 1974.

W. M. Tang, "Microinstability theory in Tokamaks", *Nuclear Fusion 18*, 1089-1160 (1978).

V. N. Tsytovich, *Theory of Turbulent Plasma*, Consultants Bureau, New York, 1977.

transport and confinement times

S. O. Dean, "Status and objectives of tokamak systems for fusion research", WASH-1295, U.S. Atomic Energy Commission, 1974.

F. L. Hinton and R. D. Hazeltine, "Theory of plasma transport in toroidal confinement systems", *Reviews of Modern Physics 48*, No. 2, Part 1, 239-308 (1976).

J. T. Hogan, "Multifluid Tokamak transport models", *Methods in Computational Physics*, Vol. 16, Academic Press, New York, 1976, p. 131-164.

B. R. Wienke, W. F. Miller, Jr., and T. J. Seed, "Hydrogen transport in a toroidal plasma using multigroup discrete-ordinates methodology",, *Nuclear Technology 42*, 272-288 (1979).

D. Anderson and M. Lisak, "Approximate solutions of some nonlinear diffusion equations", *Physical Review A 22*, 2761-2768 (1980).

CHAPTER 9
PLASMA HEATING

9A. Methods

An electric stove utilizes the I^2R ohmic heating power generated by flow of an electric current I through a heating element with resistance R. A diesel engine heats its fuel-air mixture to ignition temperature by compression. A microwave oven heats food by absorption of electromagnetic waves. Electron beam welders heat the metal to be welded by the impact of energetic electron beams. The principle methods of plasma heating are the same four methods: *ohmic heating, compression, wave heating,* and *particle beam injection.*

A plasma with $n_e = 10^{20}$ m^{-3}, T = 10 keV, and V = 200 m^3 would have a thermal energy $(3/2)nk(T_e + T_i)V \simeq 100$ MJ. A heating power on the order of 50 MW for a period of 3-10 s could be used to ignite such a DT plasma. A plasma heating method for a reactor should have the following characteristics:

* high power flux, so small ports may be used in the chamber walls
* high efficiency of generation, transmission, and coupling to the plasma
* large fraction of energy absorbed in plasma
* reliable operation and easy maintenance
* low cost ($/W).

9B. Ohmic Heating

Plasma currents and ExB drifts may be driven by magnetic induction or by metallic electrodes in contact with the plasma. The power dissipated per unit volume is

$$P = \vec{E}\cdot\vec{J} = E_{\parallel}J_{\parallel} + \vec{E}_{\perp}\cdot\vec{J}_{\perp} = \eta_{\parallel}J_{\parallel}^2 + \eta_{\perp}J_{\perp}^2 \qquad (W/m^3). \qquad (9B1)$$

By definition $\eta_{\parallel} \equiv |E_z/J_z| = E_z/neu_{ez}$. Equating the accelerating force of the electric field to the frictional force of electron-ion collisions, we find

$$-eE_z = -m_e u_{ez}\nu_{ei} \quad \rightarrow \quad u_{ez} = eE_z/m_e\nu_{ei} \ .$$

Then

$$\eta_{\parallel} = m_e\nu_{ei}/ne^2 = 2.38\times10^{-9}\, Z_{eff}\, T_{ek}^{-3/2} \qquad (\Omega\text{-m}) \qquad (9B2)$$

where Eq.(2E57) has been used for ν_{ei} . For Z = 1 and L ≃ 18, this becomes

$$\eta_{\parallel} \simeq 4\times10^{-8}\ T_{ek}^{-3/2} \quad (\Omega\text{-m}) \ . \tag{9B3}$$

For comparison, the resistivity of copper at room temperature is about 2×10^{-8} Ω-m. At temperatures of a few keV, a hydrogen plasma becomes a better conductor than copper. Ohmic heating becomes less effective at high temperatures.

increased resistivity

The resistivities given in Eq. (9B2) represent minimum values due to Coulomb collisions. If neutral atoms are present, the resistivity is increased by the ratio $(\nu_{en} + \nu_{ei})/\nu_{ei}$, where ν_{en} and ν_{ei} are the electron-neutral and electron-ion momentum-transfer collision frequencies. Impurity ions increase the effective value of Z, thus enhancing the resistivity. Effects of toroidal geometry and trapped particles result in "neoclassical" values of $\eta_{\parallel}$ (Section 13B).

Plasma turbulence can greatly increase the effective resistivity. *Turbulence* refers to a condition in which many random collective oscillations are excited by microinstabilities. The collective oscillations may be Langmuir plasma oscillations, ion acoustic waves, Alfven waves, etc. (Section 5E). Turbulence may increase the resistivity to a value

$$\eta_{\parallel} = m_e\nu_{eff}/ne^2 \tag{9B4}$$

where n, m_e, e, and ν_{eff} are the density, mass, charge, and effective collision frequency of the electrons, and ν_{eff} can be much larger than ν_{ei}. Although plasma turbulence increases resistivity and makes ohmic heating more effective, turbulence also increases plasma energy loss rates, and the high electric fields needed to drive plasma turbulence can lead to electron runaway.

electron runaway

The retarding force of electron-ion Coulomb collisions decreases at high relative velocities u, Eq. (2E33). For electrons with high velocities, this frictional force may be less than the force of the applied electric field, and they will be accelerated to even higher velocities, until they are lost or some other energy loss mechanism balances the applied electric field force. Such *runaway electrons* (Section 13E) may carry a substantial fraction of the plasma current. The energy they absorb from the electric field does not heat the plasma directly, and they may be poorly confined.

Ignition can be attained solely by ohmic heating at high magnetic fields (Wagner, 1981), but auxiliary heating methods are usually employed.

9C. Compression

If plasma is compressed slowly, energy losses during compression will prevent effective heating, and the compression is said to be *nonadiabatic*. If plasma is compressed on a time scale much less than the energy confinement time ($\tau \ll \tau_E$), then the compression can be *adiabatic*, meaning that energy flow across the boundary is negligible. Adiabatic heating is reversible : if the plasma were allowed to expand, it would return to its original temperature. Typical time scales for adiabatic compression are $\tau \sim 10^{-4} - 10^{-3}$ s. If compression occurs on a much shorter time scale $\tau \sim 1$ μs, then shock waves may form and produce intense irreversible heating.

shock heating

In an ordinary gas, a perturbation in density may propagate as a sound wave. The perturbation may be caused by rupturing a diaphragm between gases at different pressures, by detonation of an explosive, or by motion of a "piston", such as an airplane wing, through the gas. The speed of sound is larger at higher densities, as shown in Fig. 9C1a, which makes the velocity at point A larger than that at point B (Fig. 9C1c). The result is that the higher-density gas portion of the wave at point A catches up with points B and C, producing a very steep wave front, called a shock front (Fig. 9C1d). The discontinuity of density propagates through the gas, raising the density from n_C to n_A very rapidly, and heating the gas irreversibly. Further "overturning" of the wave is limited by heat conduction and viscosity, so that the shock front develops a certain thickness on the order of a few collisional mean free paths. Such a *hydrodynamic shock wave*, which propagates via molecular collisions, is not of interest for heating fusion reactor plasmas.

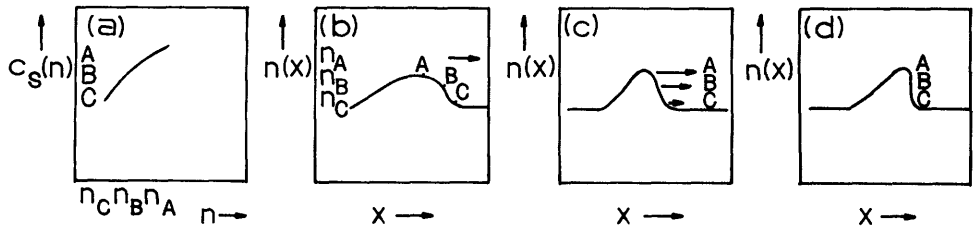

Fig. 9C1. Development of a shock wave. (a) Variation of the sound speed with density. (b) A density perturbation moving to the right. (c) Because the density at point A is higher, so is its velocity, and it tends to overtake points B and C resulting in a steep wave front (d).

In plasmas, shock waves are also caused by the increase of wave speed with density. The wave may be a large-amplitude MHD wave, instead of an ordinary sound wave; and wave propagation is facilitated by changing electromagnetic fields, instead of via collisions, although collisions may sometimes be significant. As in Fig. 9C1, a discontinuity of density and temperature develops and propagates through the plasma, leaving the plasma in its wake irreversibly heated.

In some cases a large current density flows in the wave front. This current-carrying "sheath" (different from the stationary sheath of Section 5F) acts as a *magnetic piston*, driving the plasma ahead of it like snow in front of a snowplow. The current may be driven by electrodes in contact with the plasma, or by the electric field induced by pulsed magnet coils. At high temperatures, the mean free path for collisions may be very large compared to the shock front thickness, which may be on the order of ρ_i (the ion Larmor radius). Such *collisionless shock waves* can result in ion temperatures $T_i \sim 10$ keV.

Shock heating is used in some pinch devices (Chapter 12). In order to work on microsecond time scales, shock heating coils must have low inductance and operate at high voltage, which leads to a number of technological problems (Chapter 21). Since very large coils would have high inductances, shock heating coils must be placed near the plasma, where they will be bombarded by an intense flux of fast neutrons, making them highly radioactive and difficult to replace. The fatigue problems associated with cyclic stresses limit the coil stress and magnetic field to values lower than those attainable in steady-state coils.

adiabatic compression

The adiabatic equation of state (5D16) is

$$p_i/n_i^\gamma = \text{constant} \quad , \tag{9C1}$$

where $p_i = n_i kT_i = (2/3)n_i\langle W_i\rangle$, (Eq. 2D6). Using $n_i \equiv N_i/V$, where N_i is the total number of ions (assumed constant) in plasma volume V, we can rearrange (9C1) to read

$$\langle W_i\rangle V^{\gamma-1} = \text{constant} \quad . \tag{9C2}$$

A similar relation applies to electrons. The paramater $\gamma = (N + 2)/N$, where N is the number of degrees of freedom during compression. For example, in a one-dimensional compression $\gamma = 3$. Halving the volume would quadruple the ion energy in the direction of compression. Often the average energies will be different in the parallel and perpendicular directions:

$$\langle W\rangle = \langle W_\parallel\rangle + \langle W_\perp\rangle$$

$$\langle W_\parallel\rangle = \tfrac{1}{2}kT_\parallel$$

$$\langle W_\perp\rangle = kT_\perp \tag{9C3}$$

Only the energy component in the direction of compression is affected by a compression. If the collision frequency is high enough to equalize $T_{\parallel}$ and $T_{\perp}$, then the system behaves three-dimensionally during any compression, and $\gamma = 5/3$. Toroidal plasma compression is illustrated in Fig. 9C2. Relations between dimensions and energies are summarized in Table 9C1.

Table 9C1. Relation of energies to dimensions during adiabatic compression.

	degrees of freedom	γ	equation
axial compression	1	3	$\langle W_{\parallel} \rangle L^2$ = constant
compression along major radius	1	3	$\langle W_{\parallel} \rangle R^2$ = constant
compression along minor radius (cylinder or torus)	2	2	$\langle W_{\perp} \rangle a^2$ = constant
three-dimensional compression, or any compression in which the collision rate is large enough to make energy distribution isotropic	3	5/3	$\langle W \rangle V^{2/3}$ = constant

In a *low-beta* plasma, the particles are tied to field lines, and

$$VB = \text{constant (radial compression)}$$

$$V/L = \text{constant (axial compression)} \qquad (9C4)$$

where L is the plasma length, and B is the magnetic field. (For a toroidal plasma $L \simeq 2\pi R_0$). For a *high-beta* plasma, the plasma pressure balances the magnetic field pressure:

$$2nkT = \beta B^2/2\mu_0 \ ,$$

$$TB^{-2}V^{-1} = \text{constant} \qquad (9C5)$$

For a given change in B (or L) the change of volume may be computed from Eq. (9C4) or (9C5), and then the corresponding energy change in the direction of compression may be computed from Eq. (9C2) or Table 9C1.

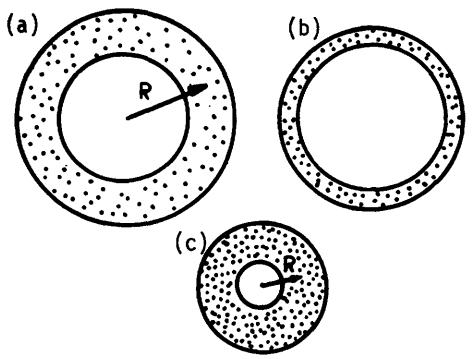

Fig. 9C2. Top view of compression of toroidal plasma. (a) initial state, (b) after compression along minor radius, (c) after compression along major radius.

In tokamaks, conservation of toroidal flux requires that $B_t a^2$ = constant. The toroidal field varies as $B_t = B_0 R_0/R$. If B_0 is not changed while the plasma is moved to smaller R, then

$$a^2/R = \text{constant} \qquad (9C6)$$

Thus, a decrease in major radius with B_0 constant automatically results in a decrease in minor radius, too.

EXAMPLE PROBLEM 9C1

A tokamak plasma is compressed by using the vertical field to move the plasma from R_0 = 1.5 m to R = 1.0 m, without changing B_0. If the initial temperatures are all 1 keV and $n_0 = 10^{19}$ m^{-3}, what are the final temperatures and density?

The compression of the major radius results in an increase in $T_{\parallel}$ in accordance with Table 9C1 of

$$T_{\parallel}/T_{\parallel 0} = \langle W_{\parallel}\rangle/\langle W_{\parallel 0}\rangle = R_0^2/R^2 = 2.25$$

and the compression of the minor radius (in accordance with Eq. 9C6) results in an increase of $T_{\perp}$ of

$$T_{\perp}/T_{\perp 0} = \langle W_{\perp}\rangle/\langle W_{\perp 0}\rangle = a_0^2/a^2 = R_0/R = 1.5 \quad .$$

Thus, the final parallel and perpendicular temperatures will be 2.25 keV and 1.5 keV, respectively, assuming that the compression is fast enough to neglect collisional effects. The density change is

$$n/n_0 = V_0/V = a_0^2R_0/a^2R = R_0^2/R^2 = 2.25,$$

so the final density is 2.25×10^{19} m^{-3}, assuming particle production and loss during compression are negligible.

In one fast plasma compression experiment the magnetic field penetrated anomalously fast into the plasma, resulting in strong heating. A simple theoretical model indicates that the average work done by the magnetic field was B_0^2/μ_0, of which half remained as magnetic energy and half appeared as plasma thermal energy, resulting in a final value of $\beta = 1/2$ (Alexeff, 1975).

If particles and energy are lost during compression, then the compression (no longer adiabatic) may be described using the transport equations.

Experiments with the Adiabatic Toroidal Compressor (ATC) tokamak demonstrated the effectiveness of this heating method. A tokamak could be compressed to ignition, then allowed to expand with its temperature maintained by alpha heating. However, control of plasma size and shape is not easy, and pulsed coils present technological problems, such as fatigue.

9D. Charged Particle Injection

charged particle beams

It is difficult to inject charged particles across magnetic field lines, because the $q\vec{v}\times\vec{B}$ force reflects them. It is easy to inject them into a magnetic cusp or mirror along magnetic field lines, but they tend to follow field lines out the other end. The mean free path for Coulomb collisions is usually orders of magnitude larger than the size of the magnetic bottle, so Coulomb collisions are not effective in trapping the beam energy. However, micro-

instabilities, such as the beam-plasma instability, can extract beam energy over short distances and heat the plasma via wave-particle interactions.

Plasmas in magnetic mirrors have been heated to keV temperatures by axial injection of electron beams. Electron beams have also been injected into toruses, by varying the magnetic field during injection. Powerful electron and ion beams may also be used to compress solid fuel pellets to very high densities, resulting in small thermonuclear explosions. (Chapters 15 and 16).

plasma guns

A coaxial plasma gun is illustrated in Fig. 9D1. When a high voltage is applied to the electrodes, breakdown occurs along the insulator. The $\vec{J}\times\vec{B}$ force accelerates the plasma outwards, then axially along the tube. Finally, the plasma momentum carries it off the end of the electrode as a blob of plasma moving along the chamber axis. Such plasma blobs, having keV temperatures, may be injected into plasma confinement systems. During injection across $\vec{B}$, the $q\vec{v}\times\vec{B}$ force produces a charge-separation electric field . This *polarization* field aids plasma penetration via the $\vec{E}\times\vec{B}/B^2$ drift.

In some cases the plasma blob leaving the end of the electrode collapses down to a very small diameter dense *plasma focus* (Section 12A). Detailed photographs of the plasma sheath sometimes reveal tiny plasma vortex filaments.

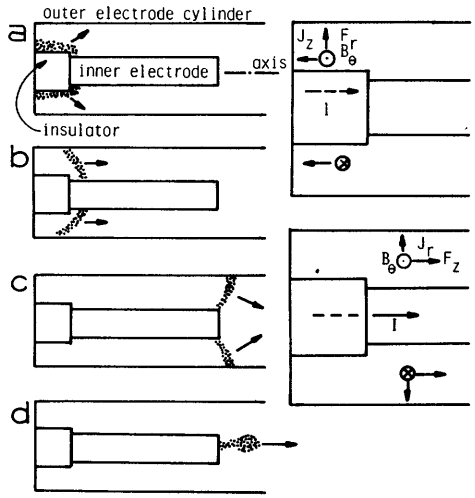

Fig. 9D1. Operation of a coaxial plasma gun. (a) breakdown along the insulator, (b) acceleration of the plasma sheath, (c) continued acceleration past the end of the inner electrode, (d) plasma blob leaving the end of the gun. The directions of the plasma current density, self-magnetic field, and resultant $\vec{J}\times\vec{B}$ force are indicated at the right.

Another type of plasma gun uses a stack of titanium washers impregnated with deuterium. When a high current is pulsed through the stack, the deuterium is emitted, ionized, and accelerated.

Plasma guns can introduce hot plasmas into confinement systems, but the number of particles injected per gun is limited, and the guns have short pulse lengths. Plasmas from guns make good target plasmas for trapping injected neutral atom beams.

9E. Neutral Beam Injection

penetration

Neutral atom beams can be injected across magnetic field lines, then trapped in the plasma by ionization. If the plasma is not dense enough, most of the fast neutrals will pass through the plasma without being ionized. If the plasma is too

dense, or the beam energy too low, then most of the beam will be stopped at the plasma edge, without penetrating to the center where it is needed. The resultant density peak at the plasma edge may lead to instability. Thus, beam penetration and trapping requirements are relative to plasma density and beam energy. The unattenuated beam density $n_b(x)$ is trapped at a rate

$$dn_b/dx \simeq - n_b/\lambda_a \qquad (9E1)$$

where x is the distance of penetration measured from the plasma edge, and λ_a is the attenuation length. [In a uniform plasma, $n_b \simeq n_{b0}\exp(-x/\lambda_a)$.] Values of the product $n_e\lambda_a$ for deuterium and tritium beams in a DT plasma are shown in Fig. 9E1 as functions of beam energy.

The ions trapped in distance dx at radius r will quickly spread out to fill the volume $(2\pi R_0)2\pi r dx$, for the case of circular flux surfaces in a torus with major radius R_0. This means that a few ions deposited at small r will provide a source density equal to that of many ions deposited at large r. If we let λ_{av} be the value of λ_a at the average values of n_e and T_e, then requiring that

$$\lambda_{av} > a/4 \qquad (9E2)$$

may give adequate penetration. For example, consider a case in which the average electron density $n_e = 8\times10^{19}$ m^{-3}, a = 1.25 m. For this case $n_e a = 10^{20}$ m^{-2}. To attain $n_e\lambda_{av} > 2.5\times10^{19}$ m^{-2}, the desired deuterium atom beam energy is about 100 keV.

It is possible to ignite large reactor plasmas without using much higher beam energies by keeping the plasma radius small until neutral beam heating has ignited the plasma, then allowing the plasma to expand to full size. For example, a tokamak reactor case with the following parameters was studied:

R_0 = 10 m, B_t = 4.2 T, plasma elongation (height/width) = 1.6, initial minor radius a = 1.4 m, $n_e \simeq 10^{20}$ m^{-3}, neutral beam energy = 150 keV, beam power = 130 MW, heating pulse length = 4 s, initial plasma current = 3 MA; final expanded radius a = 2.5 m, final current = 8 MA. The time variation of the ion temperature profiles for this case is shown in Fig. 9E2. These data illustrate the type of calculations needed for neutral beam energy deposition studies. They are not conclusive, because the results depend strongly on

* transport model assumed
* alpha particle confinement

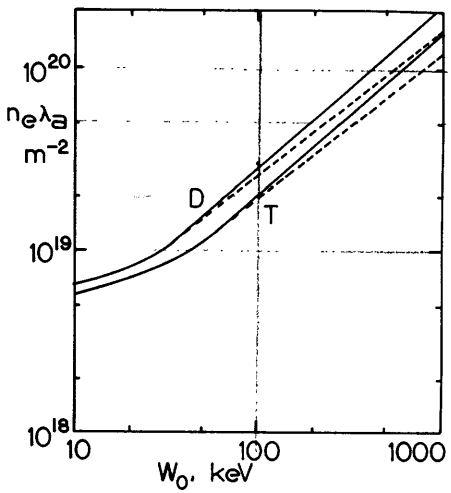

Fig. 9E1. Product of attenuation length λ_a and plasma density n_e vs. neutral beam energy, for deuterium and tritium beam injection. Smooth curve: T_e = 10 keV, dashed curve: T_e = 1 keV. Based on data of D. R. Sweetman, Nuclear Fusion 13, 157 (1973).

* alpha energy transfer to electrons and ions (collisional, as assumed in Fig. 9E2; or altered by microinstabilities).

Small ripples in the toroidal field ($\delta B_t/B_t \sim 1$ %) may help transport trapped ions inwards, permitting somewhat lower injection energies to be used, if instabilities do not interfere.

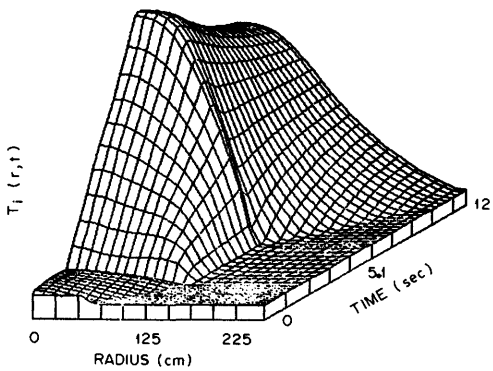

Fig. 9E2. Variation of ion temperature with radius and time for an expanding-radius tokamak reactor case. Neutral beam heating is on from t = 2 to t = 6 s, with radius a = 1.4 m. Then the plasma becomes ignited and is allowed to expand to a = 2.5 m, with T_i sustained by alpha heating. From W. A. Houlberg, A. T. Mense, and S. E. Attenberger, ORNL/TM-6730 (1979), Fig. 11.

neutral beam ion sources

Neutral atoms cannot be accelerated, since they are not affected by electromagnetic fields. However, ion beams can be accelerated and then partially neutralized by charge transfer in a gas cell. The unneutralized ions are magnetically separated, leaving the beam of fast neutral atoms to go across the magnetic field into the plasma, where the atoms are trapped by ionization.

Two main types of ion sources are used with neutral beam injectors: the LBL type with arc discharges from hairpin filaments, and the DuoPIGatron type (ORNL) using a Penning discharge.

A Penning discharge is a cylinder with negative end plates, one of which emits electrons, and an axial magnetic field. The electrons bounce back and forth between the end plates, gradually diffusing outwards to a cylindrical anode. A DuoPIGatron ion source is illustrated in Fig. 9E3. The cathode plasma created by the filaments supplies electrons to the Penning discharge. The source is designed to provide a nearly uniform plasma density in the extraction region. Ions are extracted through thousands of circular holes in the plasma grid. The magnetic field at the plasma grid is low, in order to reduce transverse ion energy and ion beam divergence angle.

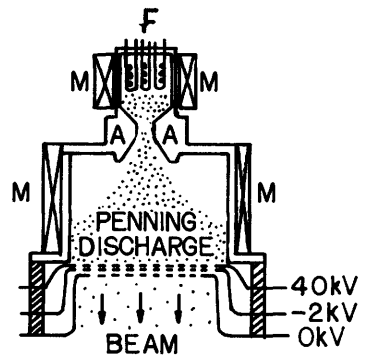

Fig. 9E3. Schematic of the DuoPIGatron ion source. Numerical values correspond to a 22 cm diameter source. A = anode, F = filaments, M = magnet coils, producing a vertical magnetic field.

An LBL ion source is shown in Fig. 9E4. Higher arc current is needed for this type of source than for the DuoPIGatron, because of the absence of the magnetic field, but the arc power is still only a small fraction of the total power requirements. The gas pressure in the source chamber is around 1 Pa (10^{-2} Torr). The *gas efficiency* (ratio of ion flow rate to flow rate of ions plus gas) is around 30% for the LBL source and 50% for the DuoPIGatron. A high neutral gas flow rate (low gas effiency) in the electrode region could cause trouble by electrode bombardment from secondary ions and electrons. Very powerful vacuum pumps are needed to minimize neutral gas flow into the plasma chamber, because cold

neutral gas causes ion cooling by charge exchange.

Rectangular slotted electrodes are used with the LBL source. The extracted ions will typically be about 70% D^+, 20% D_2^+, and 10% D_3^+. After acceleration by the same voltage, the D_2^+ and D_3^+ ions will have 1/2 and 1/3 of the D^+ energy per atom. The following discussion will be limited to the Tokamak Fusion Test Reactor (TFTR) neutral beam lines using LBL type sources with extraction areas of 10x40 cm (65 A at 120 keV).

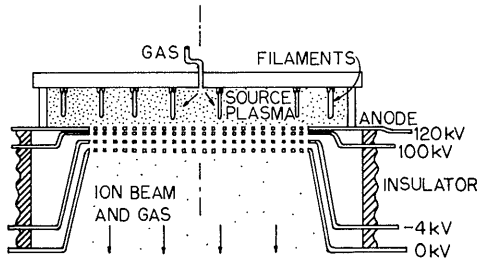

Fig. 9E4. The LBL type ion source. Discharges from the hairpin filaments to the anode create a dense, uniform source plasma without an applied magnetic field.

electrodes

To minimize beam divergence, the accelerating electrode is followed by a decelerating electrode. Electrode designs are analyzed to optimize beam flow, as shown in Fig. 9E5. Beam divergence is typically about half a degree in the plane parallel to the electrode slits and 1.3 deg. in the plane perpendicular to the electrodes (at 1/e = 37% of peak intensity). Grid rails are fastened at one end only, to allow for thermal expansion, and the grids are water-cooled. Current densities attainable by ion beam sources are typically around 3 kA/m^2 (0.3 A/cm^2). In the event of sparking, the high voltage must be rapidly disconnected to prevent arc damage to the electrodes.

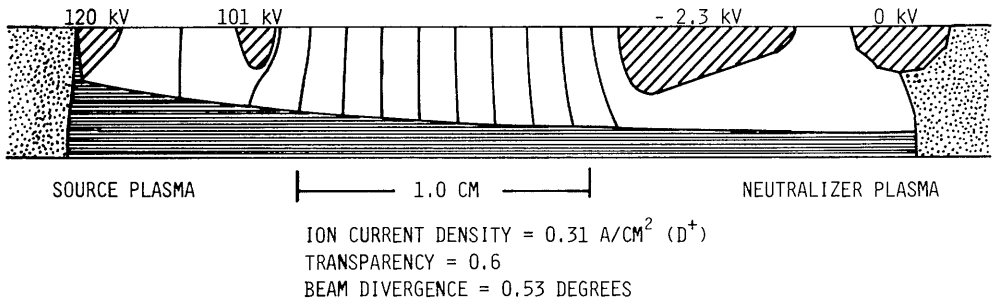

Fig. 9E5. Accel-decel electrode design of the TFTR neutral beam injection system. From PPPL-1475 (1978), Fig. 7-13. Vertical lines represent equipotential surfaces. Research at the Princeton Plasma Physics Lab is funded by the Dept. of Energy.

neutralizer and deflection magnet

The TFTR neutral beam line is shown schematically in Fig. 9E6. The D_2 gas pressure in the neutralizer region is on the order of 0.1 Pa (10^{-3} Torr). The fraction of the ion beam neutralized by charge exchange is

$$\eta = \frac{\sigma_{10}}{\sigma_{10}+\sigma_{01}} \left\{1 - \exp\left[-(\sigma_{10} + \sigma_{01}) \int_0^x dx\, n_n\right]\right\} \qquad (9E1)$$

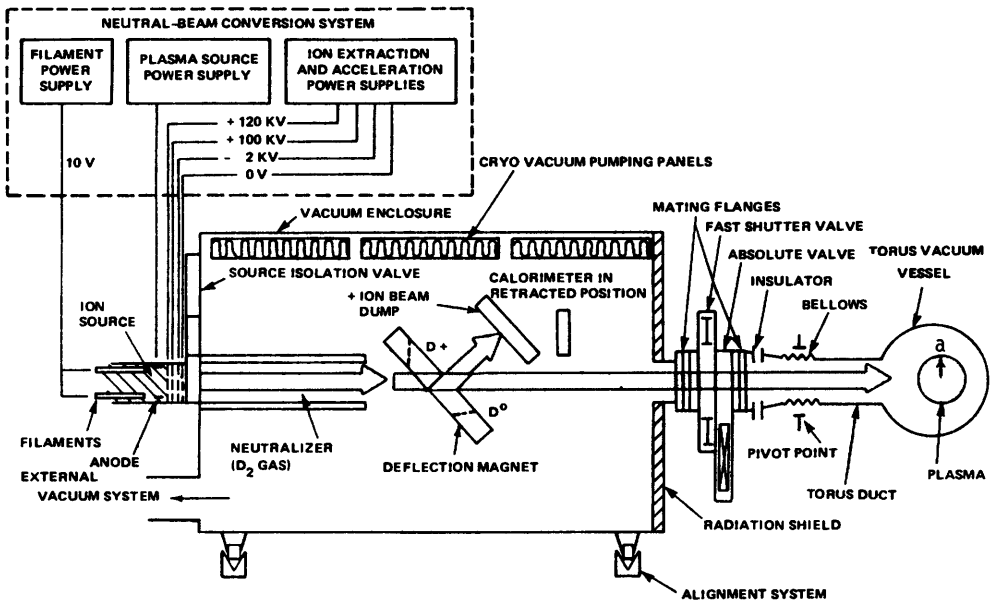

Fig. 9E6. Schematic of the TFTR neutral beam injection system. The vacuum enclosure is about 5 m high and 7 m long. From PPPL-1475 (1978), Fig. 7-1.

where x is the path length in the gas, n_n is the gas density, σ_{10} is the cross section for neutralization by charge exchange, and σ_{01} is the cross section for reionization of the neutrals. For values of $\int_0^x dx n_n \geq 2 \times 10^{20}$ m^{-2}, the exponential function is very small, and $\eta \simeq \sigma_{10}/(\sigma_{10} + \sigma_{01})$.

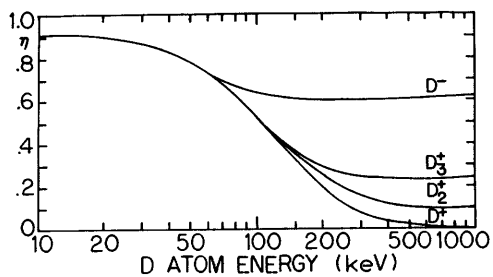

Fig. 9E7. Neutralization efficiency η vs. beam energy for deuteron beams in deuterium gas.

Since σ_{10} drops off at high energies, the neutralization of positive ions becomes inefficient there, as shown in Fig. 9E7. The rapid drop of the D^+ curve means that efficiency will be poor for neutralization of D^+ beams above 200 keV. Direct recovery of unneutralized ion energy can significantly improve the power efficiency of neutral beam production (Section 26G). Negative ion beam sources are being developed for production of high-energy neutral beams.

The TFTR neutral beam system has four or more units, providing a total of about 20 MW of 120 keV D^0 beams and 12-15 MW of partial-energy D^0 at 60 keV and 40 keV, with a pulse length up to 0.5 s. The unneutralized ions are deflected by a 0.22 T magnet into a beam dump, and the fast neutral beams flow through a duct into the torus. The magnet is shielded by a mild steel structure to prevent its field from interfering with plasma confinement. The beam power flows of various species, normalized to 1 MW D^0, are shown in Fig. 9E8. A calorimeter may be inserted into the beam path to measure beam power.

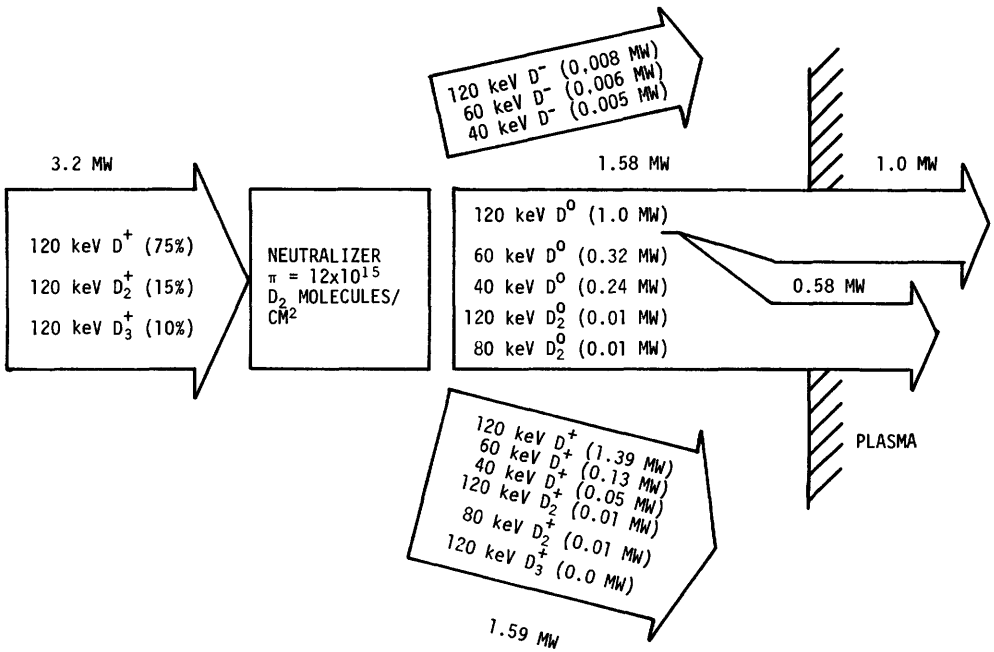

Fig. 9E8. Power flow of various species in the TFTR neutral beam system, per MW of D^0 beam. From PPPL-1475 (1978), Fig. 7-15. Here $\pi \equiv \int_0^x dx\, n_n$.

beam duct and pumping

The cryogenic vacuum pumping system must remove most of the neutral gas, to prevent it from flowing into the plasma region. (Cryopumps will be discussed in Chapter 19.) A fast shutter valve closes after the end of the beam pulse to prevent further gas flow. The entire injector may be pivoted around flexible bellows to vary the injection angle.

Buildup of neutral gas in the beam duct during injection may cause reionization of the beam, and prevent its penetration across the magnetic field. In order to prevent reionization from spoiling beam heating, the parameter $P_0 t \ell / C$ should be minimized, where P_0 is the desired beam power of primary D^0 (5 MW for TFTR beams), t is the pulse length (0.5 s), ℓ is the duct length (2.5 m), and C is the conductance of the vacuum system for deuterium leaving the beam duct (150 m^3/s). (Conductance is discussed in Chapter 19). Extending the pulse length to many seconds or continuous operation is a major challenge for neutral beam technology.

Some design considerations for neutral beam injectors are listed in Table 9E1. (There are also many other considerations related to mechanical design, vacuum system, cryogenics system, magnet system, electrical systems, etc.) From Fig. 9E8

Table 9E1. Some neutral beam injector design considerations.

* current density. To Maximize J in accordance with the Child-Langmuir Law, high accelerating voltages and narrow electrode gaps are desirable.
* high voltage breakdown. To avoid breakdown, smooth electrodes and large electrode gaps are desirable.
* beam divergence angle. To minimize divergence, use accel-decel electrodes, computer design, precise electrode dimension control and alignment, and allow for thermal expansion and contraction.
* beam blowup. To avoid transverse spreading of the beam caused by space charge, use narrow beamlets and place neutralization cell close to accelerating electrodes.
* overheating. To avoid electrode overheating, use cooling by water, helium, or liquid metal.
* arc damage. To prevent arc damage to electrodes, use computerized diagnostics and fast circuit-interrupters on power supplies.
* sputtering of electrodes. (Sputtering means surface erosion by ion bombardment, Chapter 24.) Minimize neutral gas pressure in electrode region.
* radiation damage. To reduce radiation damage, place electrodes far from reactor or out of line of sight of plasma (with bending magnet between electrodes and neutralizer). Shield insulators from neutrons.
* gas flow. To minimize gas flow into plasma, use a powerful cryogenic pumping system and fast-closing valve. Avoid reionization in beam duct.
* long-pulse or steady-state operation.
* high energy. For energies over 150 keV, develop high-current negative ion (D^-) sources.
* efficiency. To attain high electrical efficiency, convert unneutralized ion energy into electricity in beam dump (direct conversion, Chapter 26).

we can see that, without recovery of unneutralized beam energy, the efficiency of the TFTR beam system = (total beam power to plasma)/(input power) ≃ 1.58/32 = 49%. If the 1.59 MW of dumped beam energy were recovered at 30 or 60% efficiency, then the net efficiency would be raised to 58% or 70%, respectively.

Neutral beams have been very successful in heating tokamak plasmas (Chapter 13) and mirror plasmas (Chapter 11).

9F. Wave Heating

Plasma may be heated with various forms of electromagnetic waves, including radio waves, microwaves, and laser beams. Laser beams may be used to heat high density plasma ($n \gtrsim 10^{23}$ m^{-3}) and to compress solid fuel pellets (Chapter 15). However, absorption of laser light is ineffective at lower plasma densities.

stages of wave heating

The stages of electromagnetic wave heating are illustrated in Fig. 9F1. The problems of generation and transmission are fairly well resolved, except for high-power generation of waves at frequencies > 30 GHz. Coupling is most effective near resonances of the plasma or near resonant frequencies of the plasma-filled chamber. If the wave is reflected from the plasma, then it does not heat the plasma. If the wave is absorbed in the plasma surface layers, then the plasma core does not get heated, and the hot surface ions may cause severe sputtering of impurities from the walls and plasma instability. Thus, the waves, or modifications of them, must be able to penetrate to the plasma core for effective heating.

If the electric field of the wave is parallel to the magnetic field in the plasma (the "ordinary mode"), then the wave will be reflected from the plasma where the incident wave frequency $\omega = \omega_{pe}$. (For a fusion plasma with $n = 10^{20}$ m^{-3}, $\nu_{pe} = \omega_{pe}/2\pi = 90$ GHz.) However, the component of the wave with electric field perpendicular to the magnetic field (the "extraordinary mode") can penetrate further into the plasma.

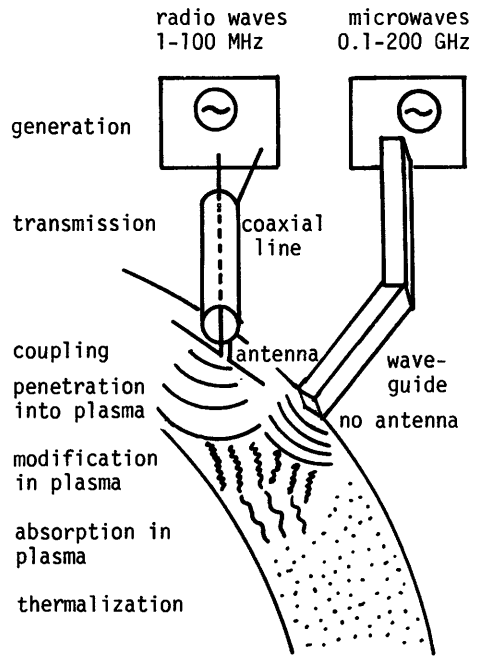

Fig. 9F1. Stages of wave heating. Adapted from T. H. Stix, "The physics of wave heating", MATT-929 (1972), Fig. 1.

plasma resonances

Electromagnetic wave absorption is strong at frequencies near natural resonance frequencies of the plasma, such as ω_{ce}, ω_{ci}, ω_{LH}, and ω_U (Section 5E), given by

$$\omega_{ce} \equiv eB/m_e$$

$$\omega_{ci} \equiv eB/m_i$$

$$\omega_{LH} \simeq \omega_{pi}(1 + \omega_{pe}^2/\omega_{ce}^2)^{-\frac{1}{2}}$$

$$\omega_U \equiv (\omega_{pe}^2 + \omega_{ce}^2)^{\frac{1}{2}} \qquad (9F1)$$

where $\omega_{pi}^2 \equiv ne^2/m_i\varepsilon_0$, $\omega_{pe}^2 \equiv ne^2/m_e\varepsilon_0$, and $\omega_{pe}^2/\omega_{ce}^2 = 1.03\times10^{-19}\ n/B^2$. These are angular frequencies (rad/s). The corresponding frequencies in Hz for electrons and deuterons are

$$\nu_{ce} = 28.0\ B \qquad \text{(GHz)}$$

$$\nu_{ci} = 7.63\ B \qquad \text{(MHz)} \qquad 15{,}3\ B \text{ for proton}$$

$$\nu_{LH} = 0.148 n^{\frac{1}{2}}(1 + 1.03\times10^{-19} n/B^2)^{-\frac{1}{2}} \qquad \text{(Hz)}$$

$$\nu_U = 28.0\ (1 + 1.03\times10^{-19} n/B^2)^{\frac{1}{2}} B \qquad \text{(GHz)} \qquad (9F2)$$

For example, when $n = 10^{20}$ m^{-3} and $B = 5$ T, these frequencies are $\nu_{ce} = 140$ GHz, $\nu_{ci} = 38.2$ MHz, $\nu_{LH} = 1.25$ GHz, $\nu_U = 166$ GHz.

Electromagnetic waves may undergo *mode conversion* (transformation to another type of plasma wave). The wave energy may be absorbed by Landau damping (Eq. 8E2) or other processes.

cavity resonances

An electromagnetic wave which is weakly absorbed by plasma can pass through the plasma many times, reflecting from the vacuum chamber walls. If the wave frequency is tuned to one of the natural resonant frequencies of the plasma-filled cavity, then the wave amplitude in the plasma can become very large, resulting in effective plasma heating in spite of the weak absorption. The cavity resonances are similar to resonances of musical instruments. Changes in plasma density profile alter the resonant frequencies of the toroidal cavity. For effective plasma heating, the radio wave generator frequency must follow the resonant frequency of the cavity and plasma. This frequency variation is called *mode tracking*.

Usually the impedance of the plasma and chamber is low compared to that of the radio wave transmission system and antenna. The impedance mismatch may result in ineffective coupling of the wave energy to the plasma. Near a resonance, the plasma impedance increases, and coupling becomes more efficient.

wave heating problems

Various frequency regimes and methods of wave heating are described in Table 9F1.

For effective fast-wave heating, $n_e a^2 > 5 \times 10^{19}/m$ is needed. For all types of heating, the antenna structure or waveguide array (*waveguide grill*) should be arranged so as to excite desired modes in the plasma. Otherwise, coupling may be inefficient, and required antenna voltages may become excessive, or waves may merely heat the surface plasma without penetrating to the core. A cavity-backed aperture antenna designed for ICRF heating in the NUWMAK tokamak reactor is shown in Fig. 9F2. This system is estimated to have a 97% coupling efficiency of transmission line and cavity. Combined with efficiences of 85% for the high voltage transformers, 95% for the dc power supplies, and 75% for the generator and high-power amplifier, this yields a net efficiency of 59% for the rf heating system in the NUWMAK design. ICRF can make $T_i >> T_e$, but it will fail if heated ions have bad drift orbits (intersecting the walls or limiter).

At the higher frequencies in Table 9F1 the attainable power per generator and transmission line drops, requiring a large number of ports to heat the plasma.

Wave heating may promote microinstabilities and increase energy transport rates in the plasma, in some cases. There is also danger of increased impurity sputtering, especially with ICRF heating. The resultant influx of impurities may cause MHD instability, in addition to increased radiation losses.

Table 9F1. Features of some wave heating methods (fusion reactor parameters).

type of wave	Shear Alfven Wave	Low-Frequency (Magnetosonic) Fast Wave	ICRF (Ion Cyclotron Range of Frequencies)	LHH (Lower Hybrid Resonance Heating)	ECRH (Electron Cyclotron Resonance Heating)
generation			$\sim 2\nu_{ci}$	$\geq \nu_{LH}$	$\geq \nu_{ce}$
frequency	1-2 MHz	1-10 MHz	50-100 MHz	1-5 GHz	50-200 GHz
attainable power per generator	10 MW	10 MW	1-2 MW	1 MW	0.2 MW (under development)
generation efficiency	90%	90%	70%	60%	40%
transmission					
means	coaxial line	coaxial line	coaxial line or ridged waveguide	waveguide	waveguide
power/line	10 MW	10 MW	2 MW	1 MW	0.2 MW
number of ports for 100 MW	10	10	50	100	500
coupling					
means	loop antenna modulating poloidal field $\delta B_p \sim 5 \times 10^{-4}$ T	loop antenna modulating toroidal field $\delta B_t \sim .005$ T	coil antenna or cavity-backed aperture antenna	flush-mounted waveguide array with specified phases	flush-mounted waveguide array
mode-tracking	no	yes	maybe	no	no
modification & absorption					
	mode conversion, damping by electrons	couple to cavity modes	couple to cavity modes, if feasible, damping by electrons or ions	mode conversion, electron damping	absorption by electron cyclotron resonance

High voltage breakdown must be avoided in the transmission line, vacuum window, and antenna. The radiofrequency voltages expected at high power are on the order of 30 kV. Cool plasma near the antenna may short out the antenna voltage, and arcs may develop at joints, windows, in waveguides, etc. The generators will be rapidly switched off if an arc persists for more than one cycle, to avoid damage to equipment.

In a reactor environment, radiation damage to rf antennas may be severe. Vacuum windows will be placed outside of the neutron shielding. Alloys retaining high electrical conductivity after neutron bombardment will be used for components requiring good electrical conductivity, such as waveguides. Waveguides will have several bends to reduce neutron streaming.

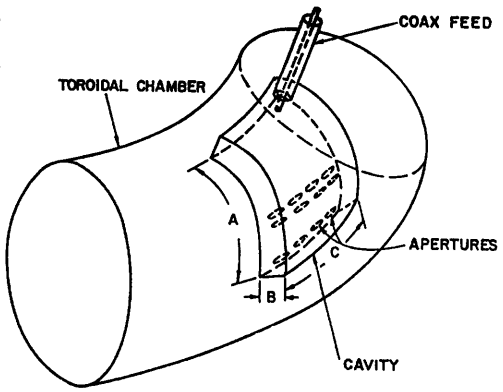

Fig. 9F2. A cavity-backed aperture antenna. The cavity impedance is designed to give efficient power transfer from the coaxial transmission line. Power flows from the cavity through elliptical holes into the plasma. From NUWMAK, A Tokamak Reactor Design Study, UWFDM-330 (1979), page V-52.

Radiofrequency heating may be used to drive plasma currents. In the Starfire Tokamak reactor design (ANL), lower hybrid heating is planned to maintain the toroidal plasma current, permitting steady-state reactor operation. Low currents have been driven by rf in plasma experiments (Section 13D).

If efficient generation, transmission, coupling, and absorption can be attained, electromagnetic wave heating offers some advantages in comparison with neutral beam heating:

* The problem of unwanted neutral gas inflow and the requirement for huge cryopumps are eliminated.
* The large neutral beam lines are replaced by smaller rf coaxial lines or waveguides, permitting easier access to the torus for maintenance.
* Capital costs of rf heating may be lower. Heating systems typically cost around 0.50 to 1 \$/W. For 100 MW of heating power, a cost difference of 0.1 \$/W is worth 10 M\$.

Problems

1. Estimate the ohmic heating power per unit volume in a tokamak plasma where $J_{\parallel} = 10^6$ A/m^2, $n = 5 \times 10^{19}$ m^{-3}, and B = 4 T, (a) if $T_e = 0.2$ keV, (b) if $T_e = 2$ keV.

2. A cylindrical low-beta plasma is compressed radially by tripling B. Initially $T_{\parallel} = T_{\perp} = 1$ keV. What are the final temperatures (a) if the plasma is collisionless, (b) if collisions are dominant?

3. A collisional, cylindrical high-beta plasma is compressed radially by tripling B. By what factor does the temperature increase?

4. A low-beta toroidal plasma is compressed by decreasing the major radius to 80% of its original value, with B_0 constant. If the plasma is collisional, by what factor does the temperature increase?

5. Assume that a plasma gun uses electrical energy from a 20 kJ capacitor bank to inject a plasma blob of 10^{18} ions with T_i = 0.8 keV, T_e = 0.1 keV. What is the efficiency = (plasma energy output)/(electrical energy input) of this heating device?

6. Estimate the required deuterium atom beam energy for effective penetration into a DT plasma with $n = 2 \times 10^{20}$ m^{-3}, T_e = 10 keV, and a = 2 m. What are the neutralization efficiencies of D^+ and D^- beams at this energy?

7. Estimate the minimum neutral hydrogen gas pressure which would cause breakdown between the 101 kV and the -2.3 kV electrodes of Fig. 9E5, assuming that $\gamma_i \sim 0.1$. (See Section 6C). (Breakdown can occur at lower pressures than this in a radiation environment.)

8. For the case of Fig. 9E6, estimate the required beam divergence angle in the vertical direction to have the beam aimed within a/2 of the magnetic axis.

9. Consider a laboratory plasma experiment with B_{max} = 0.5 T, $n = 3 \times 10^{18}$ m^{-3}. If you have generators at 1 MHz, 100 MHz, and 10 GHz available, what means might be used to couple the energy to the plasma?

Bibliography

general

H. S. Cullingford, Editor, "Plasma heating, fueling and maintenance, a technical assessment", US DOE Report HCP/T 1401-01 (1978).

T. Kammash, *Fusion Reactor Physics*, Ann Arbor Science, 1975.

K. Miyamoto, *Plasma Physics for Nuclear Fusion*, MIT Press, Cambridge, MA, 1980, Chapter 14.

Proceedings of the Third Topical Meeting on the Technology of Controlled Nuclear Fusion, CONF-780508, 1978.

W. M. Stacey, Jr., *Fusion Plasma Analysis*, Wiley-Interscience, New York, 1981, Chapter 9.

ohmic and beam heating

R. W. Conn et al, "UWMAK-III, a noncircular tokamak power reactor design", EPRI ER-368 (1976), Chapter IV-B.

D. A. Hammer, K. A. Gerber, and A. W. Ali, "Beam-plasma heating model", *IEEE Transactions on Plasma Science PS-7*, 83-93 (1979).

D. A. Hammer and K. Papadopoulos, "Tokamak heating by relativistic electron beams", *Nuclear Fusion 15*, 977-984 (1975).

C. E. Wagner, "Possibility of achieving ignition in a high-field ohmically-tokamak", *Physical Review Letters 46*, 654-657 (1981).

compression

I. Alexeff, "A theoretical predication of the observed plasma heating in the compression experiment at Ito's group at Osaka University", *IEEE Transactions on Plasma Science PS-3,* 15-17 (1975).

D. R. Cohn, D. L. Jassby, and K. Kreischer, "Neutral beam requirements for compression-boosted ignited tokamak plasmas", *Nuclear Fusion 18,* 1255-1262 (1978).

R. A. Gross and B. Miller, "Plasma heating by strong shock waves", *Methods of Experimental Physics,* Volume 9, Part A, Plasma Physics, Academic Press, New York, 1970, Chapter 5.

W. B. Kunkel, Editor, *Plasma Physics in Theory and Application,* McGraw-Hill, New York, 1966, Chapter 6.

D. A. Tidman and N. A. Krall, *Shock Waves in Collisionless Plasmas,* Wiley-Interscience, New York, 1971.

neutral beams

G. C. Barber et al, "Neutral beam injector research and development at ORNL and LBL/LLL in the United States", *8th International Conference on Plasma Physics and Controlled Nuclear Fusion Research (Brussels, 1980),* IAEA, Vienna, 1981.

J. D. Callen and J. A. Rome, "The plasma physics of intense neutral-beam heating in tokamaks", *Nuclear Fusion 20,* 501-505 (1980).

Equipe TFR, "High-power neutral injection and ion power balance in TFR", *Nuclear Fusion 18,* 1271-1303 (1978).

H. Eubank et al, "PLT neutral beam heating results", *Plasma Physics and Controlled Nuclear Fusion Research (Innsbruck, 1978),* Vol. I, IAEA, Vienna, 1979, p. 167-198.

J. H. Fink, W. L. Barr, and G. W. Hamilton, "Efficient high-power high-energy neutral beams for the Reference Mirror Reactor", *IEEE Transactions on Plasma Science PS-7,* 21-34 (1979).

J. A. Holmes, J. A. Rome, W. A. Houlberg, Y.-K. M. Peng, and S. J. Lynch, "Low-density ignition scenarios in injection-heated tokamaks", *Nuclear Fusion 20,* 59-67 (1980).

W. A. Houlberg, S. E. Attenberger, and A. T. Mense, "Neutral-beam energy and power requirements for expanding-radius and full-bore start-up of tokamak reactors", *Nuclear Fusion 20,* 811-820 (1980).

D. L. Jassby, "Neutral beam driven fusion reactors", *Nuclear Fusion 17,* 309-365 (1977).

Proceedings of the 4th ANS Topical Meeting on the Technology of Controlled Nuclear Fusion (King of Prussia, PA, 1980), DOE, 1981.

wave heating

B. Badger et al, "NUWMAK, a tokamak reactor design study", UWFDM-330 (1979), Chapter V.

C. C. Baker, M. A. Abdou, D. A. DeFreece, C. A. Trachsel, D. W. Graumann, et al, "STARFIRE - a commercial tokamak fusion power plant study", ANL/FPP (1980), Chapter 7.

J. Hosea et al, "Fast wave ion cyclotron heating in the Princeton Large Torus", *Plasma Physics and Controlled Nuclear Fusion Research (Brussels, 1980)*, IAEA, Vienna, 1981.

M. Porkolab, "Parametric processes in magnetically confined CTR plasmas", *Nuclear Fusion 18*, 367-413 (1978). Review Paper.

E. J. Powers, Editor, "Special issue on ray tracing in a plasmas for fusion research", *IEEE Transactions on Plasma Science PS-8*, Number 2 (June, 1980), p. 55-100.

R. Prater, R. Stambaugh, J. Wesley, D. Bhadra, K. Matsuda, and L. Rovner, "Fusion experimental power reactor (EPR) designs tasks", EPRI AP-1347 (1980), Chapters 2 and 3.

L. D. Smullin, Chairman, "Report of the ad hoc panel on RF heating in tokamaks", ERDA 76/115 (1976).

S. M. Wolfe, D. R. Cohn, R. J. Temkin, and K. Kreischer, "Characteristics of electron-cyclotron-resonance-heated tokamak power reactors", *Nuclear Fusion 19*, 389-399.

CHAPTER 10

PLASMA DIAGNOSTICS

10A. Introduction

The term *plasma diagnostics* refers to the measurement of plasma parameters, or to the devices used for their measurement. Some features desired in plasma diagnostics systems are listed in Table 10A1. Several techniques are available for measuring main parameters like n, T_e, and T_i. Some techniques, incapable of giving the desired resolution, are still useful to provide redundancy of measurements. Data acquisition and storage progressed from photography of a score of oscilloscope traces in the 1960's to use of on-line computers in the 1970's. New experimental techniques and equipment, such as high-power far-infrared (FIR) lasers, are being developed to meet unfulfilled needs.

Plasma diagnostic techniques may be grouped in the following categories:

* Electrical probes. The simplest example is a wire, with a variable voltage applied, inserted into the plasma. From the current drawn by the wire, the plasma density, temperature, and potential can be estimated.
* Magnetic flux measurements. Wire loops placed around the outside of the plasma (or immersed in the plasma) measure magnetic flux changes, from which magnetic field variations, plasma current, and plasma pressure can be deduced.
* Passive particle diagnostics. Detectors measure fluxes and energies of particles emitted by the plasma, from which plasma composition and energy distributions may be deduced.
* Active particle diagnostics. Particle beams are shot through the plasma. From their interactions with the plasma, parameters such as plasma density, potential, and internal magnetic field can be estimated.
* Passive wave diagnostics. Analysis of electromagnetic waves emitted by the plasma (x-rays, ultraviolet photons, visible light, infrared, microwaves, and radio waves) yields estimates of plasma density, impurity content, temperatures, magnetic field, etc.
* Active wave diagnostics. Electromagnetic waves, such as microwaves or laser beams, are sent into the plasma. From their transmission, reflection, scattering, refraction, change of polarization, and phase shift in the plasma, many plasma parameters can be deduced.

Table 10A1. Desirable features of plasma diagnostics systems.

parameters. Measure all important plasma parameters, including n, T_i or $f(v_i)$, T_e or $f(v_e)$, $\vec{B}$, $\vec{J}$, $\vec{E}$ or ϕ, n_n, impurity concentrations, drift velocity, MHD instabilities, plasma waves, and microinstabilities.

redundancy. Measure each parameter with more than one technique, if possible.

accuracy. Attain accuracy of measurements of a few percent.

spatial resolution. Attain spatial resolutions of about 1 cm for magnetically confined plasmas or 1 μm for inertially confined plasmas.

time resolution. Attain time resolutions of about 1 ms for magnetically confined plasmas like tokamaks and mirrors, 0.1 μs for pinches, and 0.01 ns (10 ps) for inertially confined plasmas.

completeness. Get a radial scan of important parameters at many times during the plasma pulse, so that a complete space-time mapping will be available.

computer analysis. Use a computer system to record, store, and analyze data.
* Use inversion techniques (such as Abel inversion) to convert data taken along a chord through the plasma into variations of the parameter with radius.
* Use analytical techniques like Fourier analysis to improve accuracy.
* Use statistical techniques to estimate magnitudes of errors.
* Use computer graphics to provide multidimensional displays of parameter space-time mappings, etc.

experimental techniques. Use experimental techniques which improve signal-to-noise ratios. For example, optical filters or gratings may be used to screen out photons at undesired wavelengths; and an incident wave may be modulated at a given frequency, with the detector electronics tuned to amplify only signals at that frequency.

The major techniques in these categories will be discussed briefly. The diagnostics used with a particular experiment will be described, and then the techniques used for measuring particular plasma parameters will be summarized. Some specialized techniques developed for inertial confinement fusion studies will be discussed in Section 15F.

10B. Electrical Probes

The simplest type of electrical probe is a wire inserted into the plasma. The wire, called a *Langmuir probe,* is insulated, except at its tip, as shown in Fig. 10B1. A variable voltage is applied to the probe, and the current drawn from the plasma as a function of probe voltage looks like the sketch of Fig. 10B2. In the central region, the current varies exponentially with the applied voltage

$$\ln I = e\phi + \text{constant, or}$$

$$\ln (I_2/I_1) = e(\phi_2 - \phi_1)/kT_e \qquad (10B1)$$

where 1 and 2 denote any two points along the exponential curve. This equation may be solved for T_e. When a large negative voltage is applied to the probe, all

the nearby ions will be drawn in to the probe from a sphere with radius on the order of a Debye length. The rate at which other ions wander into the sphere and replenish lost ions is called the *random ion current* or *ion saturation current* I_i. The ion density may be estimated from I_i using the relation

$$n_i \simeq 1.7\, I_i m_i^{\frac{1}{2}} / A_p e (kT_e)^{\frac{1}{2}} \quad (m^{-3}) \qquad (10B2)$$

where m_i is the ion mass (kg), and A_p is the area of the probe (m^2). The accuracy of probe results may be distorted, however, if the probe size is larger than either the electron mean free path for collisions or the electron cyclotron radius in a magnetic field.

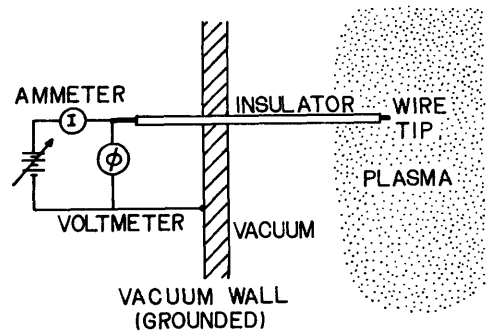

Fig. 10B1. A Langmuir probe.

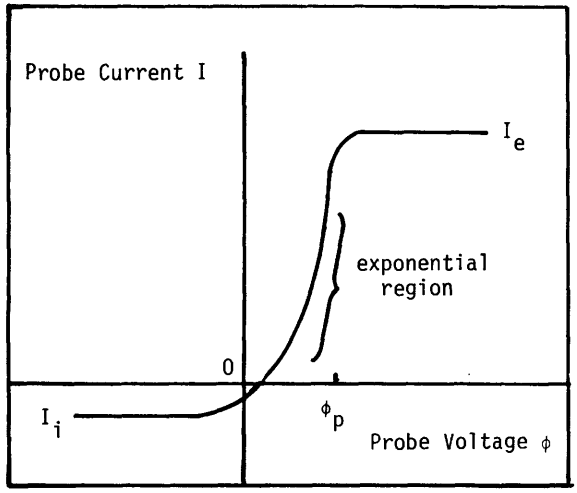

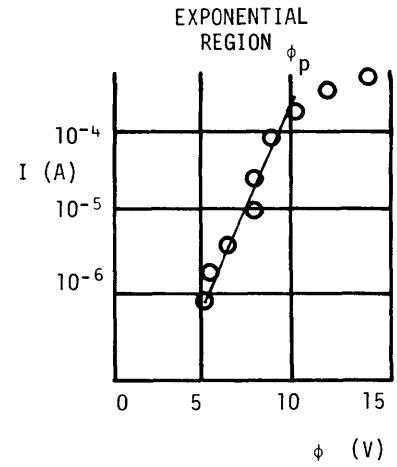

Fig. 10B2. Voltage vs. current for a simple Langmuir probe (left). I_i and I_e denote the ion and electron saturation current. The exponential region becomes a straight line on a semi-logarithmic plot (right). The plasma potential ϕ_p is approximately the voltage where the curvature changes.

The presence of the probe in the plasma also changes the plasma properties in its vicinity somewhat. The inaccuracy this causes may be overcome, to some extent, by using more sophisiticated probe techniques, such as double probes and resonance probes. A double probe is two probes located close together with voltage applied between them, and a resonance probe has a sinusoidal radiofrequency voltage applied to it.

In cases where plasma currents are induced by voltages on electrodes, such as gas discharges, arcs, and pinches, the electrode voltage and current can be monitored to give information about plasma current, resistivity, and inductance.

By placing probes at various positions along the plasma, the electric field can be determined from the differences in potentials. If the current density is known, the plasma resistivity can then be deduced from $E = \eta J$ and related to T_e, Z_{eff}, etc.

Fluctuations of density $\tilde{n}(\vec{x},t)$ and of potential $\tilde{\phi}(\vec{x},t)$ may be measured simultaneously at a given position using sophisticated probe techniques. Correlations of these quantities are important in the theory of plasma turbulence.

Since probes are melted by hot, dense plasmas, they are not used with high-temperature tokamak and mirror experiments. Their use is limited to plasmas with energy densities less than about 1 Pa, except for short pulses. (1 Pa ≡ 1 J/m^3. Tokamak experiments attain energy densities over 10^4 Pa). Probe techniques are described by Swift and Schwar (1969).

10C. Magnetic Flux Measurements

A changing magnetic flux will induce a voltage in a loop of wire in accordance with Faraday's Law

$$\oint d\vec{\ell}\cdot\vec{E} = -\oint d\vec{S}\cdot(\partial\vec{B}/\partial t) \quad . \tag{10C1}$$

For a small wire loop with area A_c and magnetic field B_n normal to the plane of the loop, the voltage induced in the loop is

$$\phi = A_c(\partial B_n/\partial t) \quad . \tag{10C2}$$

For a coil with N turns, the induced voltage is N times as great:

$$\phi = NA_c(\partial B_n/\partial t) \quad . \tag{10C3}$$

Such coils can be mounted around the outside of a plasma with various orientations, to measure changes in various components of $\vec{B}$. Some magnetic loop arrangements are illustrated in Fig. 10C1.

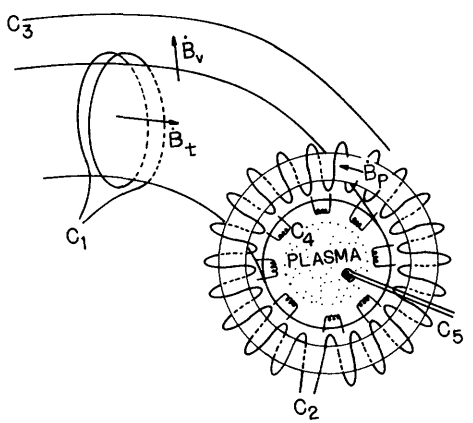

Fig. 10C1. Arrangement of coils for magnetic flux measurements on a toroidal plasma. Coil C_1 measures $\dot{B}_t \equiv \partial B_t/\partial t$, which is related to plasma pressure. Coil C_2 (called a Rogowski loop) measures $\dot{B}_p$, which is related to plasma current. Coil C_3 measures changes in vertical field $\dot{B}_v$. Coils C_4 measure azimuthal variations of $\dot{B}_p$ related to MHD instabilities. Coil C_5 measures variations of $\vec{B}$ inside the plasma region (useful only in vacuum, low-pressure plasmas, or for very short pulses).

Variations of magnetic field components with time can be determined by electronic integration of signals from such pickup coils.

The magnetic induction can be measured both with and without plasma present.

The change due to plasma diamagnetism can be related to plasma pressure. Plasma rotation and high-energy electrons complicate the interpretation of diamagnetic measurements.

In the case of a low-pressure plamsa or a short-pulsed plasma, small magnetic probe coils C_5 may be inserted into the plasma volume to measure radial variations of $\vec{B}$. However, such coils tend to be destroyed by high-pressure plasma, they tend to perturb the plasma configuration, and they are a source of impurities. The plasma current density can be estimated from Ampere's Law

$$\vec{J} = \vec{\nabla}x\vec{B}/\mu_0 \quad . \tag{10C4}$$

when $\vec{B}(r)$ is known.

Many small probe coils, such as C_4 in Fig. 10C1, can be placed at various locations around the plasma. When MHD instabilities occur, the signals at different coils will vary according to the mode numbers (n,m) of the instability. The mode numbers can be determined from analysis of the probe signals, even if two modes are occurring at the same time.

Magnetic probe techniques are described by Huddlestone and Leonard (1965) and by Equipe TFR (1978).

10D. Passive Particle Diagnostics

Many types of particles, including electrons, ions, charge-exchange neutral atoms, impurity atoms, alpha particles, and neutrons, will be emitted by a high-temperature plasma. Measurement of the particle fluxes can provide information about their concentrations and velocity distributions.

electrons and ions

Measurements of electron and ion fluxes across the magnetic field are difficult, due to their small Larmor radii and diffusive flows; but flow along magnetic field lines, as from the ends of a magnetic mirror, can be measured with gridded analyzers. Figure 10D1 illustrates a gridded electrostatic energy analyzer for measuring the ion velocity distribution. The repeller grid is negative to repel incident electrons. The bias grid repels incident ions, except for those with energies larger than $e\phi_b$, which can pass through to the collector. The screen grid and grounded case help avoid spurious currents from secondary electrons and inductive pickup. The current of ions reaching the collector is

$$I = eA\varepsilon_g^4 \int_{v_{min}}^{\infty} dv_{\parallel} f(v_{\parallel}) v_{\parallel} \tag{10D1}$$

where e is the electronic charge, A is the beam area entering the detector, ε_g is the grid transparency of each grid (assumed equal), $v_{\parallel}$ is the ion velocity component along the magnetic field, $f(v_{\parallel})$ is the ion distribution function at the collector, and $v_{min} = [2e(\phi_b - \phi_c)/m_i]^{\frac{1}{2}}$ is the velocity at the collector of ions which barely pass over the potential barrier. The current I can be measured as a function of ϕ_b. The distribution function at the collector $f(v_{\parallel})$ can be found in terms of $dI/d\phi_b$ by differentiating Eq. (10D1) with respect to ϕ_b. Then the ion distribution function in the plasma can be deduced from $f(v_{\parallel})$ at the collector, taking into account the difference in potentials $e(\phi_p - \phi_c)$. A similar technique may be used with electrons. Diagnostics for particle beams are described by Wharton (1979).

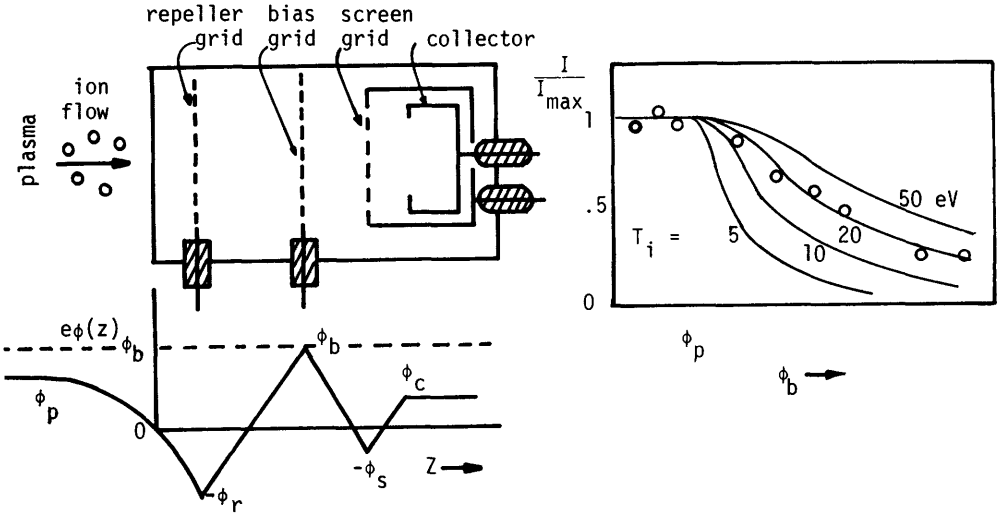

Fig. 10D1. A gridded electrostatic energy analyzer (top left) for measuring ion velocity distribution; the potential distribution produced by the grids (bottom left); and a graph of theoretical collector current vs. bias grid voltages for various ion temperatures (right). Circles represent hypothetical data, and ϕ_p is the plasma potential.

charge-exchange neutral atoms

The plasma ion energy spectrum can be estimated from the energy spectrum of charge-exchange neutral atoms leaving the plasma, measured by a system like that of Fig. 10D2. A sensitive type

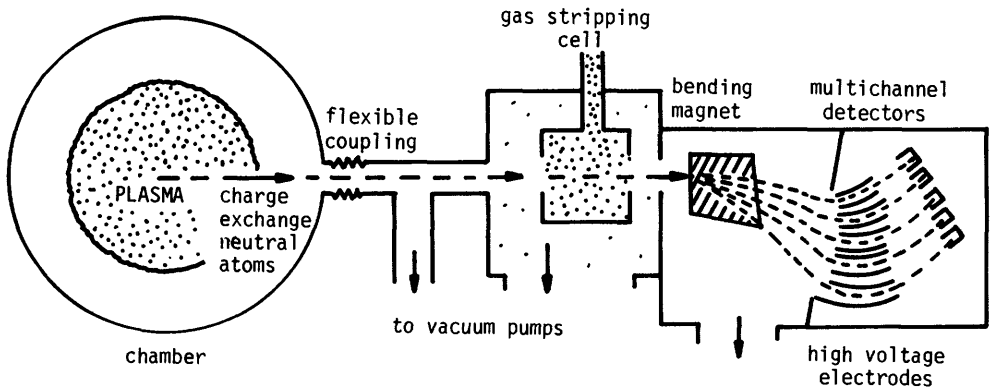

Fig. 10D2. An energy analyzer for charge-exchange neutral atoms. As the neutral atoms pass through the stripping cell, many of them become ionized. The ions are deflected by a bending magnet, deflected again by high-voltage electrodes, and measured by multichannel detectors. The assembly may be pivoted about the flexible coupling to observe other chords through the plasma.

of ion detector is illustrated in Fig. 10D3. The system can be calibrated by shooting in neutral atom beams of known energy and composition. By using both magnetic and electrostatic deflection, both the atomic species and energies can be determined. The bending magnet field and electrostatic deflection fields may be varied to map out desired particle species and energies. The device may be aimed at different chords through the plasma, or several such devices may be used simultaneously along different chords. Then the cord data are inverted mathematically to obtain $T_i(r,t)$. (Abel inversion will be illustrated in Eq. 10G7). Due to banana drifts in tokamaks, the radial distribution may appear to be asymmetric.

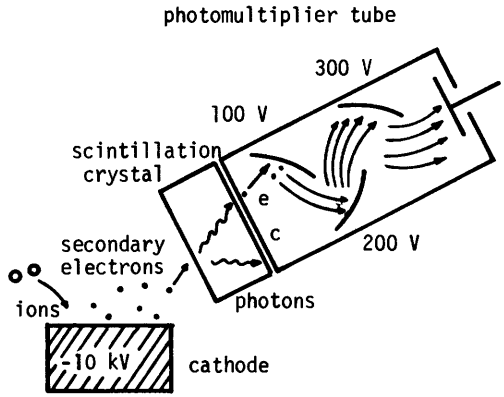

Fig. 10D3. The Daly system for detection of positive ions. Ions striking the cathode eject secondary electrons, which produce photons in the scintillation crystal. The photons eject photoelectrons e from the cathode c of the photomultiplier tube. The electrons are accelerated successively to dynodes at higher voltages, and the secondary electrons they eject greatly multiply the electronic current.

In analyzing the data, the distribution of neutral gas density $n_n(r)$ in the plasma must be known or assumed, since it appears in the charge exchange reaction rate $n_i n_n \langle \sigma_x v_i \rangle$. Cold neutral gas atoms may be ionized near the surface, but Franck-Condon neutrals, with energies near 2 eV, may penetrate further into the plasma. The neutral atoms resulting from charge exchange may gradually "diffuse" inwards, via successive charge exchange reactions, with the result that the central desntiy $n_n(0)$ may be on the order of 10^{13} - 10^{15} m^{-3}. In large tokamaks, the charge-exchange neutral atoms leaving the hot core are attenuated before they get to the surface of the plasma. Then particles reaching the analyzer come mainly from near the plasma surface, and it becomes difficult to measure $T_i(r)$ near the plasma center with this technique. Charge-exchange diagnostics are discussed by Eubank (1979) and Brusati (1979).

neutrons

Neutrons may be produced in fusion experiments by fusion reactions in the plasma; by energetic ions bombarding surfaces containing absorbed deuterium or tritium, such as walls and limiters; by electrodisintegration caused by high-energy runaway electrons; and by impact of gamma ray photons on heavy elements. (The gammas may be produced by impact of runaway electrons). The spurious neutron sources can be distinguished from neutrons originating in the plasma by their energy distributions and source locations.

There is uncertainty of the $D(d,n)^3He$ cross sections below 10 keV, but ion temperatures deduced from measurement of these 2.45 meV neutrons agree with other measurements of ion temperature.

Neutrons may be detected by several methods:

* *gas-filled proportional counters.* A gas-filled proportional counter is a cylindrical tube with an axial wire maintained at a positive voltage of about 500 V. When charged particles pass through the gas, they produced ionization, and the

resulting electrons produce a current pulse. (At higher voltages, field intensified ionization produces very large current pulses, and the device is called a Geiger-Müller tube.) For neutron detection, the gas will contain BF_3 or ^3He, which produce energetic alpha particles or protons via the reactions

$$^{10}B + n \rightarrow {}^4He(2.8\ MeV) + {}^7Li$$

$$^3He + n \rightarrow {}^1H(0.59\ MeV) + T \quad . \tag{10D2}$$

Since these reactions are most probable for thermal neutrons, a neutron moderator, such as paraffin, may be used to slow down the energetic fusion neutrons so that they can interact more effectively with the ^{10}B or ^3He (Fig. 10D4).

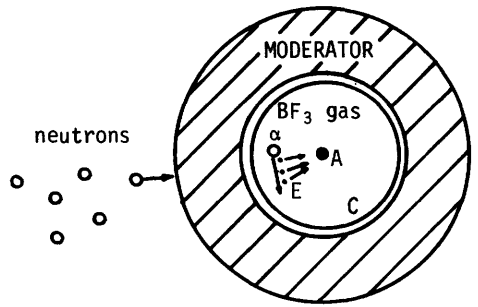

Fig. 10D4. A proportional counter for neutron detection (end view). Incident fast neutrons are slowed down in the moderator, some of them interact with ^{10}B to produce energetic alpha particles α, which ionize some gas atoms. The resultant free electrons E are accelerated to the anode A, producing a current pulse. The ions are collected at the cathode C.

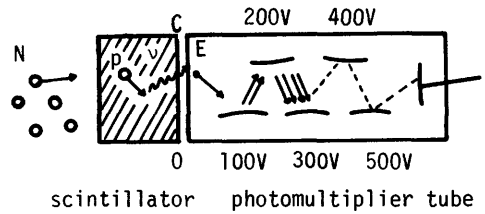

Fig. 10D5. A scintillation detector and photomultiplier tube. Incident fast neutrons N produce knock-on protons P, which cause the scintillator to emit photons ν. The photons eject photoelectrons E from the cathode C of the photomultiplier tube. The electrons are accelerated successively to dynodes at higher voltages, knocking off more secondary electrons at each stage. Thus, the electron current pulse is greatly amplified after many stages.

Gas-filled proportional counters containing CH_4 may be used without a moderator. Incident fast neutrons striking the gas produce knock-on protons with energies up to the neutron energy. Since the amount of ionization produced by the protons is proportional to their energy, the neutron energy spectrum may be deduced from analysis of the pulse amplitudes.

* *scintillation detectors.* Energetic neutrons incident on organic liquids and plastics produce energetic recoil protons by elastic collisions. The protons cause the scintillator to emit photons, which in turn eject photoelectrons from the cathode of a photomultiplier tube, which amplifies the current pulse, Fig. 10D5. Since the proton energy and light output increase with incident neutron energy, the pulse amplitudes may be analyzed to deduce the neutron energy spectrum.

Scintillation detectors are also sensitive to x-rays and gamma rays, so they must be shielded to prevent spurious pulses.

* *foil activation.* Foils of ^{109}Ag or other metals may be activated by neutron absorption. The resultant ^{110}Ag nucleus is radioactive, emitting beta rays (energetic electrons) with a half life of 24 s. From the number of beta rays emitted by the foil after activation, the number of neutrons emitted by the plasma can be calculated. Although this method lacks spatial and time resolution, it is insensitive to x-rays, and it can be used to check other neutron detectors.

Neutron detectors can be calibrated by using neutrons from a neutron source of known strength, such as ^{252}Cf.

The number of neutrons emitted by a DD plasma per second is

$$dN/dt = .5 \int d\vec{x}\, n_D^2 \langle\sigma v\rangle_{DDn} \quad . \tag{10D3}$$

If the density and ion temperature profiles are known, then dN/dt can be calculated and compared with measured neutron yields. Although good time resolution of neutron emission rates can be obtained with scintillation detectors and proportional counters, good spatial resolution is much more difficult to obtain, because neutrons are difficult to collimate and because neutron yields in many experiments have not been high enough to attempt collimation. Neutron diagnostics are discussed by Eubank (1979, p. 403-420).

A number of surface physics techniques have been developed to study particle fluxes leaving the plasma (Cohen, 1978).

10E. Active Particle Diagnostics

Electron beams have been used to probe plasmas in weak magnetic fields, in order to map out spatial variations of the electrostatic potential. Energy loss of electron beams passing through magnetic mirrors along the axis indicates the amount of heating produced by the beam, which may be correlated with plasma parameters. However, electron beams cannot be injected across strong magnetic fields, due to their small Larmor radii.

ion beam probes

A beam of singly-ionized heavy ions, such as Tl^+, Cs^+, I^+, Rb^+, or K^+ with an energy of 10-100 keV and a current of a few μA may be injected across the magnetic field.

Some of the beam ions will be further ionized by collisions in the plasma. The doubly charged ions will have half the Larmor radius of the primary beam ions, hence divergent trajectories. In Fig. 10E1 the Tl^{++} ions produced at point 1 will travel to the electrostatic analyzer and detector. The current of such ions is typically 10-100 nA. The electrostatic analyzer measures the energy of the Tl^{++} ions, from which the plasma potential at point 1 may be calculated.

As the primary beam ions enter the plasma, their kinetic energy is reduced to $e(\phi_0 - \phi)$, where ϕ_0 is the accelerating voltage and ϕ is the plasma potential. (If the plasma potential is negative, the ions gain kinetic energy.) After ionization, the doubly charged ions leaving the plasma gain $2e\phi$ of kinetic energy, so their kinetic energy at the electrostatic analyzer is

$$W_{++} = e(\phi_0 - \phi) + 2e\phi = e(\phi_0 + \phi) \quad . \tag{10E1}$$

For example, if the primary beam energy is $e\phi_0$ = 120 keV and the plasma potential at the ionization point ϕ = - 1.5 kV, then the kinetic energy of the doubly charged beam at the analyzer is W_{++} = 118.5 keV.

The electrostatic analyzer voltage ϕ_A may be feedback-controlled using signals from detectors D_1 and D_2. If the beam only hits D_1, ϕ_A is increased, and if it only strikes D_2, ϕ_A is decreased, until the two detector signals are equal. Then the beam energy is a known function of ϕ_A.

If the ion gun is tilted (dashed curve in Fig. 10E1), then the Tl^{++} ions produced at point 2 will be the ones entering the analyzer. In this way the variation of plasma potential with radius can be determined.

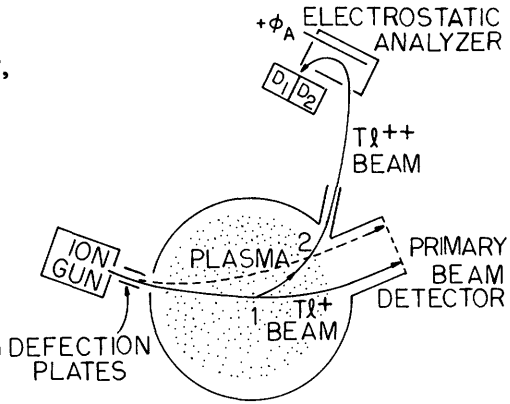

Fig. 10E1. A heavy ion beam probe system. By deflecting the primary beam (dashed curve), the interaction region viewed by the analyzer is moved from point 1 to point 2.

The poloidal magnetic field will cause the beam trajectories to bend out of the plane of the drawing. From the amount of deflection, the poloidal field can be estimated. The current of the secondary beam can be related to the electron density and temperature. By using two beams with different masses, the electron density and temperature profiles can both be determined. However, to probe large plasmas in high magnetic fields (a $\sim$ 1 m, B $\sim$ 5 T), very high beam energies ($\sim$ 1 MeV) are needed.

neutral beam probes

Production of high-current neutral atom beams was described in Section 9E. Low-current neutral beams may be used for plasma diagnostics, provided that:

* They do not perturb the plasma significantly.
* They can penetrate to the center of the plasma.
* They are narrow enough to provide good spatial resolution.

There are several ways in which neutral beams can be used for diagnostics, including:

* *attenuation measurements*. A neutral beam shot through a plasma will be attenuated by charge exchange and ionization . With several beam species, both n_e and T_e can be determined. Measurements along several chords through the plasma enable radial profiles to be determined by Abel inversion (Section 10G).

* *scattering measurements*. If beam atoms with mass m_b were scattered from cold ions with mass $m_i < m_b$, the maximum scatting angle would be $\theta_{lim} = \text{Arcsin}(m_i/m_b)$, which is 14 degrees for He beam atoms in an H^+ plasma. If the plasma ions are hot, however, larger scattering angles can occur. From the ratio of beam atoms scattered through angles $\theta > \theta_{lim}$ to those scattered at a smaller angle, the average ion temperature along the chord can be determined.

* *charge exchange measurements.* If the beam density $n_b \gtrsim n_n$ (the neutral atom density inside the plasma), then the beam produces enhanced charge exchange losses of plasma ions. The charge-exchange neutrals can be analyzed with a standard charge-exchange neutral energy analyzer (beam on vs. beam off) to determine T_i in the small volume intersected by the beam and the analyzer line-of-sight. Thus, good spatial resolution is attainable.

* *spectroscopic measurements.* As beam atoms pass through the plasma, they become excited by electron impact and emit light. From spectroscopic analysis of that light, the local plasma density and magnetic field can be determined. Spatial resolution is determined by the volume of the beam viewed by the spectroscopic equipment, and can be very good. Spectroscopy will be discussed in the next section. Beam probe diagnostics are described by Eubank (1979).

10F. Passive Wave Diagnostics

photography

The shape of the plasma can be determined by fast photography. For the case of pinch plasmas lasting only a few microseconds, very fast shutter speeds are needed, which cannot be attained with mechanical shutters. Figure 10F1 illustrates the use of an image convertor tube (vidicon tube). Light from the plasma

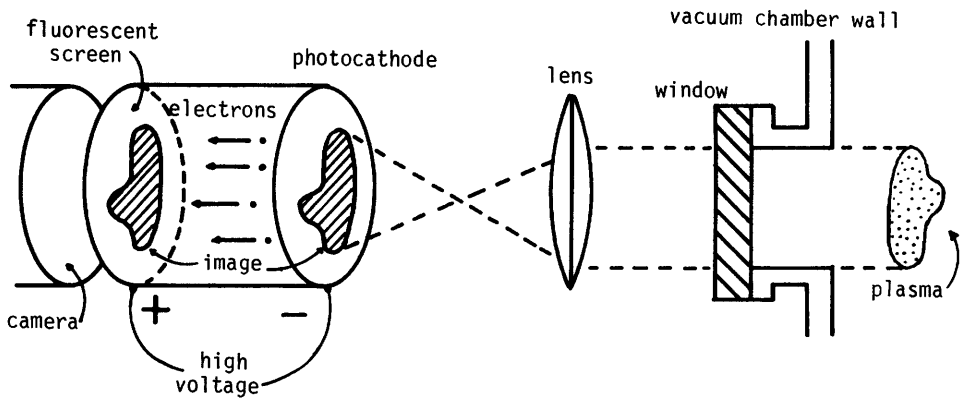

Fig. 10F1. Use of an image convertor tube as a fast shutter for photography. The image on the fluorescent screen is controlled by the high voltage, accelerating electrons from the photocathode.

is focussed onto the photocathode. Photoelectrons are accelerated onto the fluorescent screen to produce a glowing image, which is then photographed by an ordinary camera. If the high voltage is turned on for 0.1 μs, only light from the plasma during that time will be imaged on the fluorescent screen and photographed, so the high voltage pulse to the image convertor tube acts as an ultrafast electronic shutter. The tube can also make the image brighter, and the persistent glow of the fluorescent screen gives the camera a longer exposure time. Framing cameras have been developed which can take several pictures of the plasma about a microsecond apart and display them side by side.

A streak camera uses a rotating mirror to scan the plasma image across the film, as shown in Fig. 10F2. The plasma is viewed through a narrow slit, so only a vertical profile is seen. The resulting photograph shows how the plasma shape varied as a function of time, as illustrated at the bottom of the Figure.

At a given temperature the plasma luminosity increases with density, so the density distribution can sometimes be estimated from photographs such as an end view of a cylindrical plasma. Fast photography is useful in viewing the growth of MHD instabilities in pinch devices.

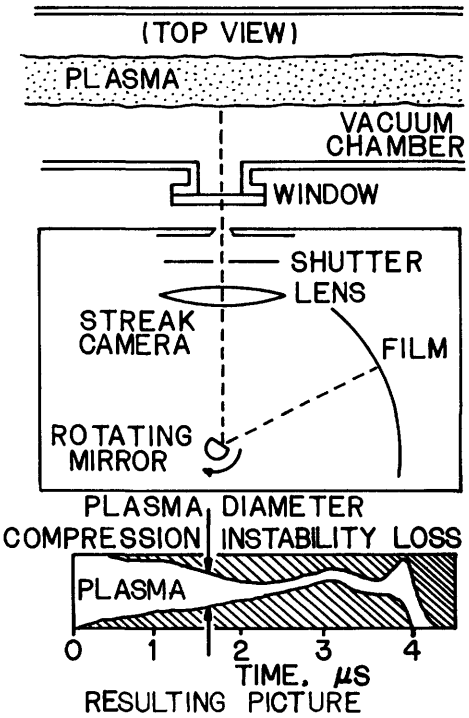

Fig. 10F2. Schematic diagram of a streak camera, and the resulting photograph, showing plasma position and diameter as a function of time.

spectroscopic analysis of hydrogen density

The concentration of neutral hydrogen atoms in a plasma can be determined from the absolute intensity of H_α or H_β radiation at wavelengths of 656.28 and 486.13 nm, using a photomultiplier tube with a monochromator or an interference filter to screen out other wavelengths. The absolute intensity measurements can be calibrated with a tungsten lamp of known intensity. Spatial resolution may be obtained by scanning the plasma with a rotating mirror or by the use of fiber optics light pipes. However, the brighter light from the plasma surface regions, where n_n is much larger, makes it difficult to make accurate measurements of the plasma core region.

impurity radiation

Multiply-ionized impurity atoms in plasmas with keV temperatures emit radiation in the far ultraviolet and soft x-ray regions of the spectrum. Because ultraviolet radiation at $\lambda < 185$ nm is strongly attenuated by the oxygen in air, spectroscopic equipment must operate in a vacuum, (or in a more transparent gas, like He), hence the name *vacuum ultraviolet (VUV) spectroscopy*. One type of VUV monochromator is illustrated in Fig. 10F3. As the grating is rotated, the recording device stores a record of intensity vs. wavelength. At wavelengths below 50 nm, the reflection coefficients of materials for normal incidence are very small, and a grazing incidence spectograph must be used.

To determine impurity concentrations, the absolute intensities of the spectral lines must be measured. Due to lack of readily available accurate standards, calibration of VUV spectrographs and monochromators is a problem. One method for calibration is to view the same plasma volume simultaneously with a calibrated visible-light spectrometer (or monochromator), and compare the apparent intensities of two spectral lines, one visible and one VUV, originating from the same upper energy level of an atom, such as the hydrogen lines at 410.2 and 93.7 nm, (caused by transitions from the n = 6 level to the n = 2 and n = 1 levels, respectively). When the two instruments are properly calibrated, the intensity ratio of these two lines should equal the ratio of their transition probabilities, which is 0.606 for the above example. This is called the *branching ratio method* of calibration. Uncertainty in the absolute intensities of VUV lines is usually at least ± 50%.

From VUV measurements along chords through the plasma, the radial profiles of various impurities and ionization states can be unfolded. For example, the radial distribution of various oxygen ionization states during the constant-current phase (plateau) of a tokamak are shown in Fig. 10F4. Here OIII means O^{++}, OIV means O^{+++}, etc. It appears that the oxygen atoms diffuse inwards with a speed of about 10 m/s, becoming more highly ionized as they go. Measurements of radiation from various ionization states of iron are described by Hinnov (1979).

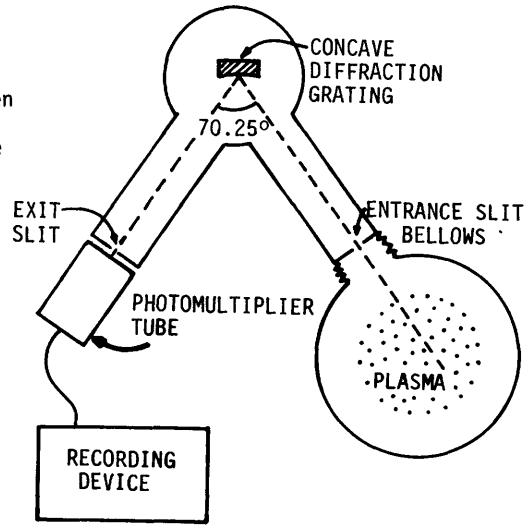

Fig. 10F3. Top view of a Seya mount VUV monochromator. Rotation of the diffraction grating about a vertical axis scans the wavelengths seen by the phototube. The instrument may be pivoted around the bellows to view different chords.

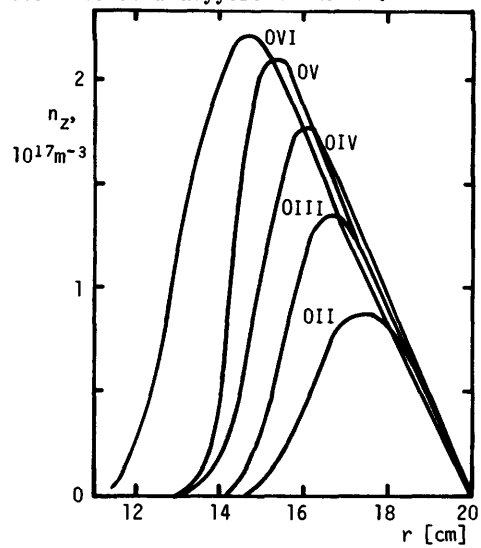

Fig. 10F4. Densities $n_z(r)$ of oxygen states during TFR tokamak current plateau. Reprinted with permission from Plasma Physics 20, TFR Group, "Space-resolved vacuum ultraviolet spectroscopy on TFR tokamak plasmas", p.735-747, Fig. 8, © 1978, Pergamon Press, Ltd.

spectral line broadening

If we plot the intensity of light emitted by an atom vs. wavelength, the spectral lines will appear as spikes with finite width. In the absence of broadening phenomena, the natural line widths are very narrow (10^{-14}m). However, there are several processes which cause the measured peaks to appear broader:

* *instrumental broadening.* The spectoscopic instrument will make the line appear broader than it really is, due to the finite width of the entrance and exit slits, imperfections of alignment, and so on. Wider slits produce greater instrumental broadening.

* *Doppler Broadening.* If an atom is moving away from an observer with velocity v_x, the wavelength of the light it emits appears to be longer:

$$\lambda = \lambda_0(1 + v_x/c) \qquad (10F1)$$

where λ_0 is the wavelength from an atom at rest and c is the speed of light. Similarly, if the atom is moving towards the observer, $v_x < 0$, and λ is shorter. A plasma has many atoms with various v_x, so the light intensity I seen at wavelength λ is proportional to the number of atoms having the appropriate v_x:

$$I(\lambda)d\lambda = Cf(v_x)dv_x \qquad (10F2)$$

$$I(\lambda_0)d\lambda = Cf(0)dv_x \qquad (10F3)$$

where $f(v_x)$ is the velocity distribution function and C is a proportionality constant. If we divide Eq. (10F2) by Eq. (10F3), use a one-dimensional Maxwellian velocity distribution function

$$f(v_x)dv_x = n(\beta/\pi)^{\frac{1}{2}}\exp(-\beta v_x^2) \quad , \quad \beta \equiv (m_i/2kT_i) \tag{10F4}$$

and use Eq. (10F1) to eliminate v_x, the result is

$$\frac{I(\lambda)}{I(\lambda_0)} = \exp\left[-\frac{m_i c^2(\lambda-\lambda_0)^2}{2kT_i\,\lambda_0^2}\right] \quad . \tag{10F5}$$

This is a Gaussian distribution centered at λ_0, as illustrated in Fig. 10F5b. At the wavelengths where $I(\lambda)/I(\lambda_0) = \frac{1}{2}$, the "full width at half maximum intensity" $\delta\lambda$ is found from Eq. (10F5) to be

$$\delta\lambda/\lambda_0 = (2/c)(2kT_i \ln 2/m_i)^{\frac{1}{2}} \tag{10F6}$$

or

$$T_i = \frac{m_i c^2(\delta\lambda)^2}{8k\ \ln 2\ \lambda_0^2} \quad . \tag{10F7}$$

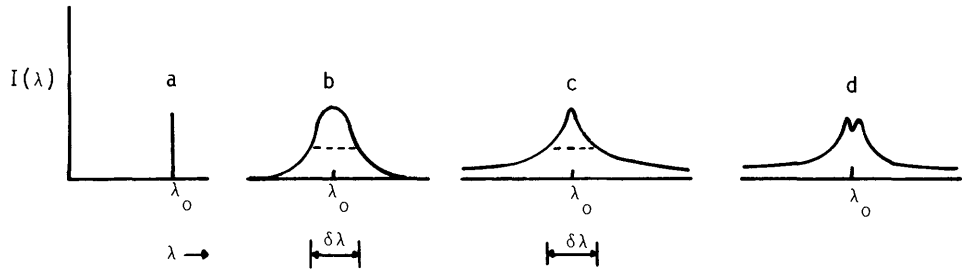

Fig. 10F5. Graphs of intensity vs. wavelength for an isolated spectral line. (a) unbroadened, (b) a Gaussian shape due to Doppler broadening, (c) and (d) Holtzmark profiles due to Stark broadening.

Thus, if Doppler broadening is dominant, the ion temperature can be calculated from the measured $\delta\lambda$. For carbon impurity ions at T_i = 1 keV, it is found from Eq. (10F6) that $\delta\lambda/\lambda_0 = 7\times10^{-4}$. For wavelengths $\lambda_0 \sim 200$ nm, $\delta\lambda \sim 0.14$ nm (1 nm = 10 Å). To observe this effect, the instrumental broadening should be significantly less than $\delta\lambda$.

* *pressure broadening.* Pressure broadening includes effects of collisions with neutral particles (van der Waals forces), resonance interactions between identical atoms, and collisions with charged particles (Stark broadening). The first two processes are not significant in highly ionized plasmas.

* *Stark broadening.* Strong electric fields produce splitting of atomic energy levels, so that the spectral lines resulting from transitions between the levels are also split (the Stark effect). Collisions with charged particles produce locally strong electric fields in high-density plasmas. Since the electric

fields have random direction and magnitude, the observed spectral lines appear broadened (Fig. 10F5c and d), rather than split into several thin lines. The line width due to Stark broadening is given approximately by

$$\delta\lambda \simeq A_s n^{2/3} \qquad (10F8)$$

where n is the electron density (m^{-3}) and A_s is a constant for a given spectral line. For the visible hydrogen lines H_α, H_β, H_γ, and H_δ at λ_0 = 656.3, 486.1, 410.2, and 397.0 nm, the values of A_s are 1.4, 2, 2.9, and 3.1×10^{-24} m^3, respectively. (For deuterium the values of λ_0 and A_s are slightly different.) For example, the Stark widths of H_β at $n = 10^{20}$ and 10^{23} m^{-3} (characteristic of tokamaks and pinches) are approximately 0.043 nm and 4.3 nm. If Stark broadening is dominant, measurement of $\delta\lambda$ gives an estimate of the plasma density. However, several regions of different density may be viewed by the spectroscopic instrument simultaneously, complicating the interpretation. In cases where both Stark and Doppler broadening are significant, the combination of the two processes produces a complicated expression for the line shape. If the Stark broadening is approximated by a Lorentzian shape $[1 + (\lambda-\lambda_0)^2/(.5\delta\lambda)^2]^{-1}$, then the convolution of the Gaussian (Doppler) and Lorentzian profiles leads to *Voigt profiles*, which can be compared with measured line shapes. From analysis of two or more different lines, estimates of both the Stark and Doppler widths can be obtained.

* *Zeeman effect.* Interaction of the magnetic moment of an atom with an applied magnetic field produces splitting of the atomic energy levels, and consequent splitting of the spectral lines. The magnitude of the Zeeman splitting is $\delta\lambda_z \sim 1000\ \lambda_0^2 B^2$, where the wavelengths are in meters and B is in Tesla. For example, a line at 500 nm in B = 1 T would have $\delta\lambda_z \sim 0.25$ nm. There is some problem in distinguishing the Zeeman effect from the effects of Doppler broadening, etc. and in obtaining good spatial resolution. One solution is to study the Zeeman splitting of an injected neutral beam of heavy atoms, such as barium. Spatial resolution is determined by the small volume where the viewing optics intersect the beam, and the line of sight may be rapidly scanned along the beam with a rotating mirror. By viewing at 90° relative to the beam direction, Doppler effects are minimized, and the Zeeman effect can be distinguished to determine the magnetic field inside the plasma.

spectral line intensities

Particle densities may be estimated from the absolute intensities of spectral lines or of the continuum of radiation emitted by free electron collisions (bremsstrahlung). From the ratios of various spectral line intensities, the electron temperature may sometimes be estimated, provided that the theoretical distribution of atomic states can be calculated, such as for the cases of local thermodynamic equilibrium and coronal equilibrium (Section 3E).

The total power radiated by a plasma can be measured with a foil heated by the radiation (a *bolometer*). The foil temperature can be related to the radiated power.

soft x-ray measurements

Electron impact on an atom may eject an inner shell electron, with emission of an x-ray at a characteristic wavelength as the shell is refilled. In addition to these discrete x-ray lines, a continuous spectrum of x-rays is emitted by

bremsstrahlung, as illustrated in Fig. 10F6. The peak of each curve is at $\lambda = 0.62/T_e$ nm, with T_e in keV. The relation between photon energy and wavelength is

$$W_\nu = hc/\lambda = 1.24 \text{ keV-nm}/\lambda \qquad (10F9)$$

so the peak corresponds to a photon energy $W_\nu \simeq 2T_e$. The power density may be expressed in terms of W_ν,

$$dP/dW_\nu = P_{br}\exp(-W_\nu/T_e)/T_e \qquad (10F10)$$

where P_{br} is the total radiated power (W/m^3). If dP/dW_ν is plotted on semi-logarithmic paper, the curve is a straight line, with a slope determined by T_e. The energy spectrum may be measured experimentally with solid state detectors, and T_e can be estimated from the slope of the curve. However, such detectors require low pulse rates and long counting times to avoid distortion caused by pile-up of pulses.

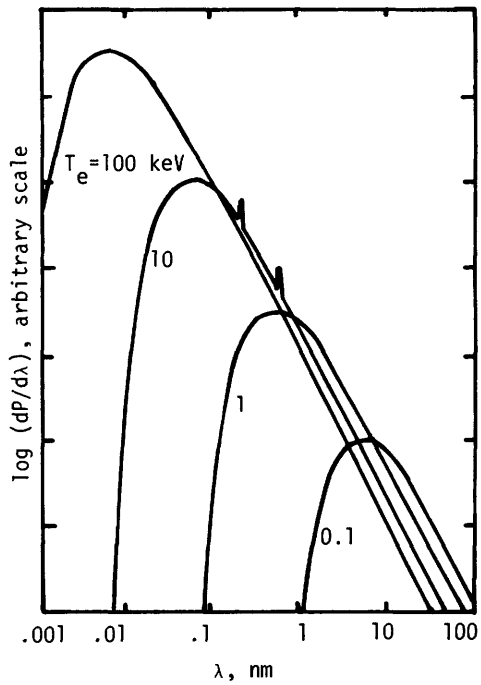

Fig. 10F6. Spectral power density dP/dλ of bremsstrahlung vs. wavelength, for various electron temperatures. The spikes on the 10 keV curve illustrate the appearance of discrete x-ray lines caused by electron impact on heavy atoms (plasma impurities or walls).

Another technique is to use absorber foils in front of scintillation detectors or silicon diodes. For example, two detectors may be covered with foils of different materials or thickness. From the ratio of the two signals (corrected for differences in detectors) T_e can be computed. This method gives good time resolution. Spatial resolution is determined by lead collimators placed between the plasma and detectors. Soft x-ray measurements are reviewed by von Goeler (1979).

hard x-ray measurements

Hard x-rays (hundreds of keV and above) are produced by runaway electrons in toroidal devices and by very hot electrons produced by electron cyclotron resonance heating (Chapter 9). The energy distribution and number of runaway electrons can be estimated from the hard x-ray spectrum, which can be measured with NaI(Tl) scintillation detectors. Groups of electrons with several MeV energies have been observed in tokamaks. Hard x-ray measurements are described by Knoepfel (1979).

far-infrared and microwave measurements

Cyclotron radiation is emitted by electrons at integer multiples of $\omega_{ce} \equiv eB/m_e$, with much of it being reabsorbed in the plasma. The theoretical frequency distribution of power leaving a plasma slab is illustrated in Fig. 10F7. Since $\nu_{ce} = \omega_{ce}/2\pi = 28.0B$ (GHz), where B is the magnetic field (T), typical values of ν_{ce} range from 50-200 GHz for reactors with B = 2-7 T. From Fig. 10F7 we see that

the power leaving the plasma is spread over frequencies from 1 to 30 times as high, corresponding to wavelengths $\lambda = c/\nu$ in the range of 50-5000 μm, which lies in the far-infrared region (10-1000 μm) and microwave region (λ>1000 μm).

In measuring cyclotron radiation, it is desirable to avoid viewing reflected radiation, because it would ruin the spatial resolution of the measurements. Reflected radiation can be minimized by selecting lower harmonics (such as $2\nu_{ce}$) and the proper polarization for good self-absorption by the plasma. It is also desirable to view along a direction, such as the major radius of a torus, where B varies strongly through the plasma. Then a particular frequency represents a fairly well-defined spatial location, so the measurements can be spatially resolved.

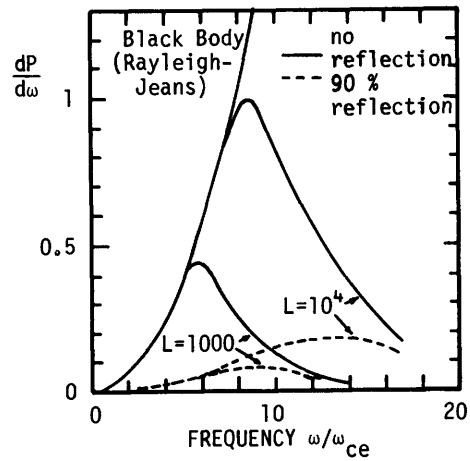

Fig. 10F7. Cyclotron radiation power spectrum $dP/d\omega$ leaving a plasma slab with T_e = 50 keV and thickness a, as a function of frequency, for two different values of $L = \omega_{pe}^2 a/\omega_{ce} c$, where ω_{pe} and ω_{ce} are the electron plasma frequency, and electron cyclotron frequency, and c is the speed of light. Reprinted from Plasmas and Controlled Fusion by D. J. Rose and M. Clark, Jr., Fig 11.6, p. 249, by permission of The MIT Press, Cambridge, Massachusetts. Copyright 1961 by The Massachusetts Institute of Technology.

If the plasma is optically thick to radiation at $2\nu_{ce}$, the radiated power near this frequency may be used to determine $T_e(r)$. The measurement can be made with a microwave system and high-gain antenna. A microwave heterodyne system combines the microwave signal from an external generator at a fixed frequency ν_0 with the plasma signal at ν_{ce} and measures power with beat frequency $(\nu_0 - \nu_{ce})$ less than $\Delta\nu_0$ < 125 MHz. By varying ν_0 the plasma can be scanned radially. If high-frequency generators are available, other harmonics can be scanned, too.

Electron cyclotron emissions can also be studied using far-infrared spectroscopy. Windows may be made of crystal quartz or polyethylene (ordinary glass absorbs infrared radiation). A variety of solid state detectors have been developed, including indium antimonide refrigerated to 4 K. Wavelength resolution may be obtained with a diffraction grating, wire mesh filters, a Fabry-Perot interferometer, or a Michelson interferometer, as described by Equipe TFR (1978). Such measurements have very good time resolution, but only fair spatial resolution and absolute accuracy. Therefore, they may be calibrated by other, more accurate techniques such as Thomson scattering (to be discussed).

Fluctuations of soft x-ray emission and electron cyclotron emission yield valuable information about plasma instabilities, as will be discussed in Chapter 13.

10G. Active Wave Diagnostics

Active wave techniques include *reflection* from the plasma, measurements of the plasma *refractivity* by wave transmission through the plasma (with resonant cavities, interferometers, or holography), *polarization* measurements, wave

scattering from plasma electrons and laser-induced *fluorescence*.

microwave reflection

Microwaves propagating across B in the ordinary mode ($\vec{E} \parallel \vec{B}$) will be reflected at the plasma layer where $\omega_{pe}^2 \geq \omega^2$, where ω is the angular frequency of the wave and $\omega_{pe}^2 \equiv ne^2/m_e\varepsilon_0$. Thus, reflection occurs where $n \geq n_c$ with

$$n_c \equiv m_e\varepsilon_0\omega^2/e^2 = m_e\varepsilon_0(2\pi\nu)^2/e^2 = 0.0124\ \nu^2 = 1.11\times10^{15}/\lambda_0^2\ (m^{-3}) \quad , \tag{10G1}$$

where ν is the wave frequency (Hz) and λ_0 is the vacuum wavelength (m). For example, if ν = 10 GHz, the cutoff density $n_c = 1.24\times10^{18}\ m^{-3}$. The phase shift of the reflected wave can be measured using a microwave interferometer (as described later). From the time variation of the phase shift, density fluctuations near the critical layer (where $n = n_c$) can be determined. Such information is useful for study of microinstabilities.

If the plasma column is moving, the reflected microwaves will also be Doppler shifted in frequency with $\Delta\nu/\nu \propto v_c/c$, where v_c is the velocity of the critical layer towards the microwave receiver/source antenna and c is the speed of light. Using several such reflection probes, the motions of the plasma can be detected, facilitating feedback control of the plasma position.

resonant cavity measurements

Metallic chambers have certain frequencies at which they are resonant, like musical instruments. When plasma is introduced, the resonant frequency shifts. If the shape of the density profile is known, the magnitude of the density can be calculated from the frequency shift. This technique is useful for very low-density plasmas (down to $10^{14}\ m^{-3}$) and for calibrating microwave interferometers.

plasma refractive index

The refractive index $\tilde{n} \equiv kc/\omega$ for the extraordinary wave varies with the magnetic field, Eq. (5E36), so it is preferable to use the ordinary wave, which does not. From Eq. (5E35)

$$\tilde{n} = (1 - \omega_{pe}^2/\omega^2)^{\frac{1}{2}} = (1 - n/n_c)^{\frac{1}{2}} \tag{10G2}$$

The phase of an electromagnetic wave propagating a distance ℓ is

$$\phi(x) = -\int_0^{\ell} dx\ k(x) = -(\omega/c)\int_0^{\ell} dx\ \tilde{n}(x) \tag{10G3}$$

where we have taken $\phi = 0$ at $x = 0$. The change in phase when the plasma is turned on is

$$\Delta\phi \equiv \phi(\text{plasma}) - \phi(\text{vacuum}) = (\omega/c)\int_0^{\ell} dx[1 - (1-n/n_c)^{\frac{1}{2}}] \quad \text{(radians)} \quad . \tag{10G4}$$

If $(n/n_c) << 1$, then $(1-n/n_c)^{\frac{1}{2}} \simeq 1 - \frac{1}{2}(n/n_c)$ and

$$\Delta\phi \simeq (\omega/2cn_c)\int_0^{\ell} dx\ n \quad , \qquad (n/n_c) << 1 \quad . \tag{10G5}$$

Consider the case of a wave propagating along a chord which passes a distance h from the plasma axis, Fig. 10G1. For this case

$$x = (r^2 - h^2)^{\frac{1}{2}}, \quad dx = rdr(r^2 - h^2)^{-\frac{1}{2}},$$

and

$$\Delta\phi = (\omega/2cn_c)\, 2 \int_h^a drr\, n(r)(r^2 - h^2)^{-\frac{1}{2}} \quad . \tag{10G6}$$

This is an integral equation from which n(r) may be determined if the variation of $\Delta\phi$ with h is known. Assuming symmetry in the θ direction, the solution of this integral equation is

$$n(r) = -(2cn_c/\pi\omega) \int_r^a dh\, (h^2-r^2)^{-\frac{1}{2}}\, (d\Delta\phi/dh), \tag{10G7}$$

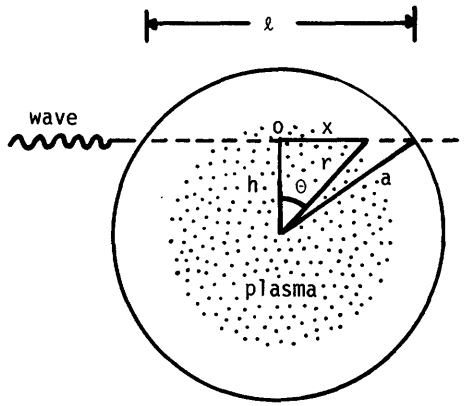

Fig. 10G1. Propagation of wave along a chord passing a distance h from the plasma axis. Based on Equipe TFR, Nuclear Fusion 18, 647 (1978), Fig. 15.

which is called an *Abel inversion*. Thus, from measurements of $\Delta\phi$ at several values of h, we can determine n(r). Methods of inversion for cases lacking θ symmetry are discussed by Sauthoff and von Goeler (1979). If the plasma density is *uniform*, Eq. (10G5) reduces to

$$n = 2cn_c\Delta\phi/\omega\ell = 1.18\times10^6\ \nu\ \Delta\phi/\ell = 3.55\times10^{14}\ \Delta\phi/\lambda_0\ell\ (m^{-3}) \quad , \tag{10G8}$$

where λ_0 is the wavelength in vacuum. The microwave or laser beam frequency should be chosen high enough that $(n/n_c) < 1$, yet low enough that (n/n_c) is large enough to make $\Delta\phi$ easily measureable. The remaining question is how to measure $\Delta\phi$.

microwave interferometers

A microwave interferometer is illustrated in Fig. 10G2. Let E and ϕ be the

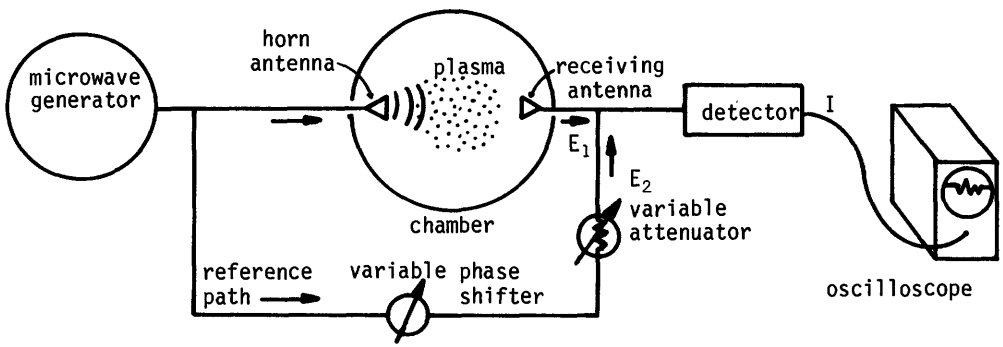

Fig. 10G2. A microwave interferometer. The combination of microwaves E_1 transmitted through the plasma with microwaves E_2 transmitted through the reference path produces an interference pattern, displayed on the oscilloscope.

amplitude and phase of the microwave electric fields at the detector, and let the subscripts 1 and 2 represent the plasma path and reference path, respectively. The detector signal I will be proportional to the time average over one wave period $2\pi/\omega$ of the square of the resultant electric field:

$$I = C(\omega/2\pi) \int_0^{(2\pi/\omega)} dt' \left[E_1\cos(\omega t' + \phi_1) + E_2\cos(\omega t' + \phi_2)\right]^2 \qquad (10G9)$$

where C is a constant. The variable attenuator in the reference path can be adjusted to make $E_2 \simeq E_1$. Using a trigonometric identity for the sum of two cosine functions, this equation simplifies to

$$I = C(\omega/2\pi)\, 4E_1^2\cos^2\left(\frac{\phi_1-\phi_2}{2}\right) \int_0^{(2\pi/\omega)} dt'\, \cos^2\left(\omega t' + \frac{\phi_1+\phi_2}{2}\right)$$

$$= C\, 4E_1^2\, \cos^2\left(\frac{\phi_1-\phi_2}{2}\right) = 2CE_1^2\,[1 + \cos(\phi_1-\phi_2)] \quad . \qquad (10G10)$$

The phase of the waves through the plasma may be written

$$\phi_1 = \phi_{1v} + \Delta\phi \qquad (10G11)$$

where ϕ_{1v} is the phase in vacuum, with no plasma present. The maximum signal strength is $I_{max} = 4CE_1^2$, so

$$I/I_{max} = \tfrac{1}{2}[1 + \cos(\phi_{1v} + \Delta\phi - \phi_2)] \qquad (10G12)$$

Since ϕ_{1v} and ϕ_2 remain constant during the plasma discharge, the phase shift $\Delta\phi$ produced by the plasma can be found from the measured variation of I/I_{max}. The variable phase shifter may be adjusted to give $(\phi_{1v} - \phi_2)$ any desired value.

If $\Delta\phi$ is small (a fraction of a radian) then the variation of I/I_{max} will be small. On the other hand, if $\Delta\phi$ is several cycles (multiples of 2π), then I/I_{max} will pass through several maxima and minima (called *fringes*), as illustrated in Fig. 10G3. Microwave interferometers are relatively sensitive to low plasma densities and provide good time resolution, but spatial resolution is not as good as that of laser interferometers.

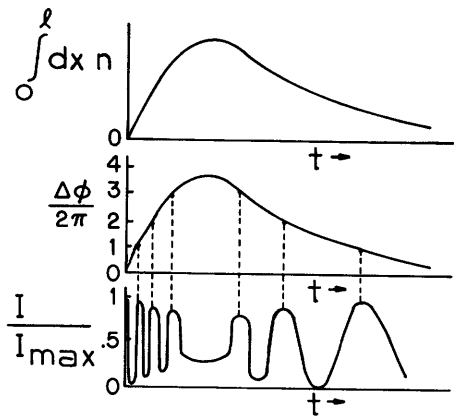

Fig. 10G3. Time variation of plasma density line integral, microwave phase shift, and interferometer signal for a case with $(\phi_{1v}-\phi_2) = 0$. Due to refractive effects, E_1 is not constant, so the signal is not a pure cosine curve, and I/I_{max} does not always reach the end points 0 and 1.

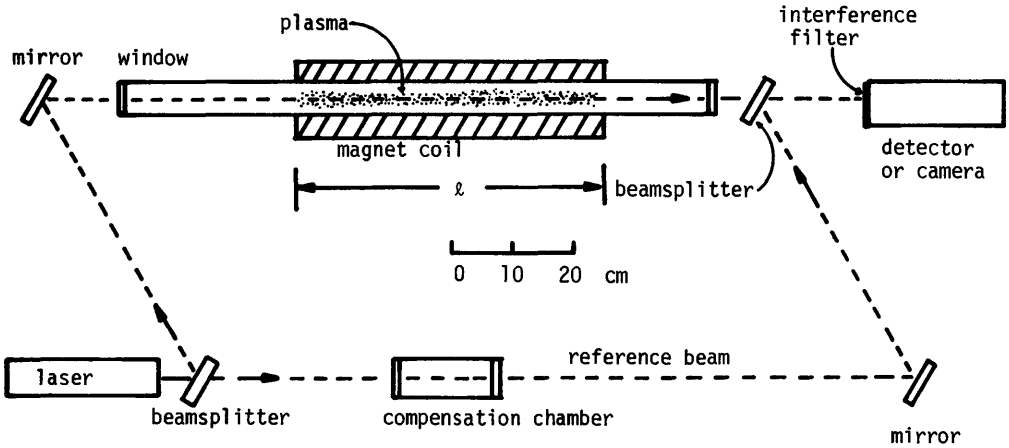

Fig. 10G4. Schematic diagram of a Mach-Zehnder interferometer for plasma diagnostics.

A "zebra stripe display" may be used to clarify interferometer data. Microwave techniques are described in Heald and Wharton (1978).

Mach-Zehnder laser interferometers

The same equations apply to laser interferometers, but the hardware is different. A Mach-Zehnder laser interferometer is illustrated in Fig. 10G4. The laser beam is divided into two paths by a partially silvered mirror (beamsplitter). One path goes through the plasma, and the reference path goes through a compensation chamber, to make the optical path lengths nearly equal. The beams are recombined by another beamsplitter and then impinge on the detector or camera. An interference filter may be used to screen out unwanted light. The optics are aligned so that the initial pattern at the camera is straight, parallel fringes (black and white stripes, representing places where $I/I_{max} = 0$ or 1). When the plasma is produced, the phase shifts created by the plasma density produce circular fringes, as shown in Fig. 10G5. Counting inwards from the outside, each fringe represents a phase difference of 2π radians, hence a density change Δn given by Eq. (10G8)

$$\Delta n\ell = 2.23\times10^{15}/\lambda_0 \quad (m^{-2}) \qquad \textit{per fringe} \qquad (10G13)$$

relative to the density at the previous fringe. Because the laser wavelengths are much shorter than microwave wavelengths, much better spatial resolution is possible with lasers.

Fig. 10G5. Fringe pattern of a theta pinch plasma, taken with a Mach-Zehnder interferometer. (Courtesy of Los Alamos National Laboratory.)

In spite of its good spatial and time resolution, a Mach-Zehnder interferometer with a ruby laser (λ_0 = 694.3 nm) has several disadvantages:

* *low sensitivity.* It takes a large $\Delta n\ell = 3.2 \times 10^{21}$ m^{-2} to produce 1 fringe.
* *sensitivity nulls.* The signal change from Eq. (10G12) is

$$dI/d(\Delta\phi) = -\tfrac{1}{2} I_{max} \sin(\phi_{1v} + \Delta\phi - \phi_2) \simeq 0 \text{ near } (\phi_{1v} + \Delta\phi - \phi_2) = 0, 2\pi, \ldots \quad (10G14)$$

* *ambiguous interpretation.* From signals like that of Fig. 10G3 (bottom curve) it is not always clear when the density is increasing and when it is decreasing.
* *calibration difficulties.* The values of signal corresponding to the maxima and minima of I/I_{max} must be known. They can be estimated from the envelope of the fringe signal (Fig. 10G3), but not if the phase change produced by the plasma is less than 2π (1 fringe). If the interferometer is calibrated before the plasma pulse, it may drift out of calibration, due to mechanical vibrations, etc.
* *refractive effects.* The plasma density gradient acts like a lens to bend the electromagnetic waves, changing the amplitude E_1 of the transmitted signal, and distorting the fringe envelope (Fig. 10G3).

Several techniques have been developed or proposed to improve the accuracy and sensitivity of laser interferometers.

Ashby-Jephcott interferometer

Fig. 10G6 shows an Ashby-Jephcott interferometer. In this scheme the He-Ne laser operates at two wavelengths simulatneously: 0.6328 μm(red) and 3.3923 μm (infrared). The germanium filter transmits the infrared but blocks the red beam. The infrared beam passes through the plasma, is reflected by the end mirror, M3, then returns through the filter and laser mirror M2 to the laser tube. This feedback from the external cavity, which is modulated by phase shifts in the plasma, affects the laser tube operation. Reinforcing feedback increases the laser infrared output, and decreases the red output, since both of these transitions come from the same upper energy level. Thus, a visible light detector may be used for an infrared interferometer. Instead of a sinusoidal signal modulation, as in the previous cases, this type of interferometer produces spike-shaped signals, because the external cavity is reinforcing only for a narrow region near $\Delta\phi = 2\pi N$ (where N is an integer). Sensitivity is improved by the longer wavelength and by the double pass of the laser beam through the plasma, so this system is about an order of magnitude more sensitive than an ordinary red laser interferometer. Further sensitivity increases can be made by using a concave mirror for M3 and aligning it so that the beam makes multiple passes (such as 8) through the plasma tube before returning to the laser cavity.

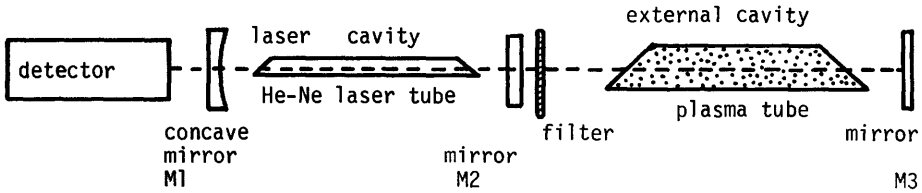

Fig. 10G6. An Ashby-Jephcott interferometer. (The tube windows are at the Brewster angle to minimize reflections.)

quadrature interferometers

The Mach-Zehnder interferometer in general has a signal of the form

$$I_1 = I_0(1 + k\cos\phi) \qquad (10G15)$$

where $\phi \equiv (\phi_{1v} + \Delta\phi - \phi_2)$ and k is a constant relating to the difference in amplitudes of E_1 and E_2. The cosine function brings in the problems of sensitivity nulls and ambiguity; and the constants bring in the problems of refractive effects and calibration. A quadrature interferometer eliminates these four problems by using two signals

$$I_1 = I_0(1 + k\cos\phi)$$

$$I_2 = I_0(1 + k\sin\phi) \quad . \qquad (10G16)$$

Solving for ϕ, we find

$$\phi = \text{Arctan}[(I_2 - I_0)/(I_1 - I_0)] + n\pi/2 \qquad (n = \text{interger}) \quad . \qquad (10G17)$$

The need to determine the constant k has disappeared, so calibration is easier and refractive effects insignificant. The differential sensitivity does not have nulls: $dI_1/d\phi$ and $dI_2/d\phi$ are not zero at the same place. Since either I_1 or I_2 is always finite, the signal can be interpreted without ambiguity, even after several fringes and reversals. The name *quadrature interferometer* refers to the fact that I_1 and I_2 are 90^o out of phase with each other. The experimental arrangement is similar to a Mach-Zehnder interferometer, but with a quarter-wave plate in the reference beam, two detectors instead of one, and a Wollaston prism in front of the detectors. [A quarter-wave plate is a crystal with $(\tilde{n}_x - \tilde{n}_y)t = \lambda_0/4$, where $\tilde{n}_x$ and $\tilde{n}_y$ are refractive indices in the x and y directions, propagation is in the z direction, t is the thickness, and λ_0 is the wavelength. Its effect is to convert a linearly polarized wave into a circularly polarized wave.] The quarter-wave plate makes the reference beam circularly polarized, and the Wollaston prism splits the combined reference beam and scene beam (from the plasma) into two signals, I_1 and I_2. The linearly-polarized scene beam is the same in I_1 and I_2, but, due to the Wollaston prism, the reference beams in I_1 and I_2 are 90^o out of phase, as in Eq. (10G16). This basic quadrature interferometer may be further modified so that only one detector is required, calibration is automatic during the plasma pulse, and accuracy of 1/40 fringe is attained. (Lowenthal and Hoffman, 1979).

far-infrared (FIR) interferometers

Interferometers using far-infrared lasers ($10\ \mu m \lesssim \lambda_0 \lesssim 1000\ \mu m$) are more sensitive to electron density changes than visible and infrared laser interferometers, and their wavelengths are still short enough to give excellent spatial resolution. Photographic film is not sensitive to FIR photons, so electrical detectors are used. The problems of calibration and accuracy may be solved by several techniques:

* *feedback stabilization.* A CO_2 laser interferometer ($\lambda_0 = 10.6\ \mu m$) can be used to measure fractional fringe shifts if its calibration can be maintained, avoiding drifts in the optical path lengths due to vibrations, thermal expansion, etc. To correct for such drifts, a mirror may be mounted on an electromechanical device like a loud speaker, so that its position is controlled by an electrical signal. Feedback from the detector on a slow time scale moves the mirror to maintain its calibration.

* *beam modulation.* An oscillating mirror in one beam path can produce a reference fringe pattern at the detector, which facilitates calibration and accuracy. The plasma then shifts the reference fringe pattern. For example, one HCN laser interferometer (λ_0 = 337 μm) used a configuration similar to the Ashby-Jephcott interferometer (Fig. 10G6) with mirror M3 moved in and out by a rotating wheel. Phase-shift sensitivity of 1/20 fringe was attained. The mirror modulation frequency of such interferometers is limited by mechanical forces, especially at long λ_0, where larger displacements are needed to produce 1 fringe.

* *frequency shifting.* A frequency-shift interferometer uses two laser beams, one with frequency ω and the other at (ω + Δω). The first beam is split into two paths: the reference beam and the scene beam (through the plasma). Then the reference beam (ω) is combined with the (ω + Δω) beam and observed by detector D_1 ; and the scene beam (ω) is combined with the (ω + Δω) beam and observed by detector D_2 (Fig. 10G7). When beams with frequencies (ω) and (ω + Δω) are combined, the resultant signal has the "beat frequency" Δω, which appears in the detectors. With this system the reference beam and scene beam are *not* recombined. No interference fringes are produced or needed. The phase information comes instead from comparison of the two detector signals, conveniently shifted to a lower frequency Δω ∿ 10 kHz - 1 MHz. (High Δω give better time resolution, but a resolution ∿ 0.1 ms is adequate for large tokamak plasmas). The phase shift produced by the plasma may be determined from the time difference Δt between zero crossings of the two detector signals, precisely measured with an electronic clock. The TFR tokamak system uses diffraction from a rotating blazed cylindrical grating to produce a frequency shift Δω = 10 kHz on a single 150 mW HCN laser beam. The Alcator experiment uses two alcohol lasers (λ_0 = 119 μm, 2 mW, optically pumped by a CO_2 laser), tuned so that Δω = 1 MHz.

The scene beam of the TFR interferometer is split into 8 paths to view 8 chords through the plasma simultaneously. Abel inversion on a computer yields plasma density profiles with good time resolution and spatial resolution, providing a space-time mapping of plasma density in the region viewed by the interferometer. Several other FIR lasers with pulsed powers of 0.1 - 1 W are available in the 300-1200 μm region (Grossman et al, 1979).

holographic interferometry

In one variant of holographic interferometry, a pulsed laser beam passing

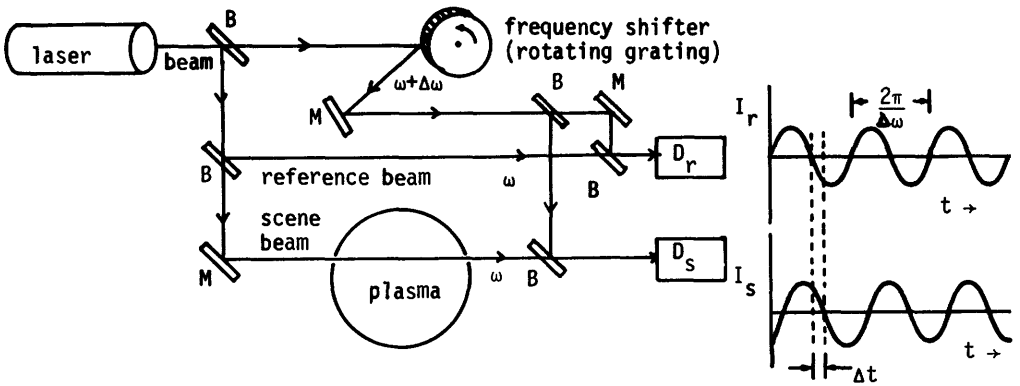

Fig. 10G7. The frequency-shifting FIR interferometer developed for the TFR tokamak. B = beamsplitter, M = mirror. From D. Veron, Optics Communications 10, 95-98 (1974).

through the plasma chamber without the plasma is recorded on film. Then during the plasma discharge the laser beam is pulsed again and recorded on the same film. If the superposition of the two laser beam phase patterns on the film is viewed later with coherent light from a continuous laser, an apparent three-dimensional image of the plasma may be seen, showing interference fringes representing contours of plasma refractive index (plasma density).

Holographic interferometry has been used with wavelengths from the ultraviolet to the infrared (3 μm), but not in the FIR region, due to technical difficulties, such as film sensitivity. It provides three-dimensional information with good spatial and time resolution, and avoids the phase errors of some interferometry methods. However, it requires high plasma densities ($n > 10^{22}$ m^{-3}), it does not provide a complete time mapping, and analysis of the data is less amenable to computerization than electrical signals from detectors. The principles of holographic interferometry are described by Vest (1979) and Quinn (1979).

Faraday rotation

A plane-polarized electromagnetic wave propagating in a magnetic field has its plane of polarization rotated by an angle

$$\theta_{rot} = \tfrac{1}{2}(\theta_R + \theta_L) = \tfrac{1}{2}\int_0^L dx\ (k_L - k_R) \qquad (10G18)$$

where

$$k_R = (\omega/c)[\,1 - \omega_{pe}^2/\omega(\omega + \omega_{ce})\,]^{\frac{1}{2}}$$

$$k_L = (\omega/c)[\,1 - \omega_{pe}^2/\omega(\omega - \omega_{ce})\,]^{\frac{1}{2}} \quad , \qquad (10G19)$$

are the wave propagation vectors of the right and left circularly polarized waves, found from Eqs. (5E32) and (5E33). (The ion terms are negligibly small at high frequencies.) Here $\omega_{ce} = eB_k/m_e$, where B_k is the component of the magnetic field parallel to the direction of wave propagation. Combining these equations in the high-frequency limit yields the result

$$\theta_{rot} \simeq \tfrac{1}{2}\int_0^\ell dx\ \omega_{pe}^2\omega_{ce}/c\omega^2 = (2.36\times10^4/\nu^2)\int_0^\ell dx\ n\ B_k\ (\text{rad}),\ \nu \equiv \omega/2\pi \qquad (10G20)$$

Thus, the amount of the *Faraday rotation* of the plane of polarization is proportional to nB_k along the wave path. If the plasma density is known, Faraday rotation measurements of an FIR laser beam can be used, with Abel inversion of the data, to determine the poloidal magnetic field $B_p(r)$ in tokamaks. Then the current density can be found from Ampere's Law (10C4).

Fig. 10G8 shows an arrangement for measuring Faraday rotation in a tokamak. The laser beam passes through a polarizing filter P1, then a ferrite modulator, actuated by a magnet coil driven by $\omega_m \sim 10$ kHz. The modulator rotates the plane of polarization $\theta_m(t)$ back and forth. After the beam passes through the plasma, the angle of rotation is $\theta_m + \theta_p$. The beam passes through another polarizing filter P2 into the detector. The detector signal is amplified by a lock-in amplifier tuned to ω_m, and the amplifier output signal voltage is

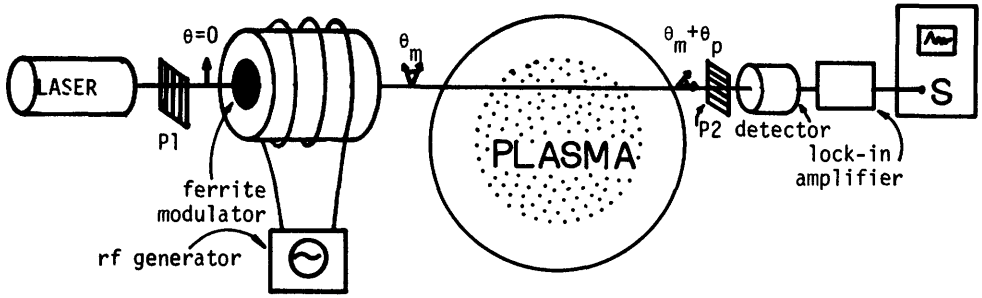

Fig. 10G8. Measurement of Faraday rotation with a FIR laser. (Instead of using the oscilloscope S, the data may be digitized and stored in a computer.)

$$\phi = \phi_0 \sin(2\theta_p) \simeq 2\phi_0\theta_p \qquad \text{(for small } \theta_p\text{)} \ , \tag{10G21}$$

where ϕ_0 is a constant determined by calibration, and θ_p is the rotation angle produced by the plasma. Thus, the amplifier eliminates the dependence on θ_m.

Thomson scattering

When a charged particle is accelerated, it radiates electromagnetic waves. If the acceleration is caused by an incident electromagnetic wave, the radiation process is called *Compton scattering* at high energies (x-rays and gamma rays) and *Thomson scattering* at low energies (visible and infrared). If $kT_e/m_ec^2 \ll 1$, then the power P_s scattered within the solid angle $d\Omega$ in the wavelength interval $d\lambda_s$ at λ_s by a ruby laser (λ_0 = 694.3 nm) is

$$P_s(\lambda_s)d\lambda_s d\Omega = d\Omega(d\lambda_s/\lambda_0)r_0^2\pi^{-\frac{1}{2}}nLP_0(c/v_0)y_1\exp[-(c/v_0)^2y_2] \tag{10G22}$$

where

$$y_1 = 2^{-\frac{1}{2}}(1 - 3.5x + 7.6x^2 - 13.3x^3)$$

$$y_2 = \tfrac{1}{2}x^2(1-x)$$

$$x = (\lambda_s - \lambda_0)/\lambda_0$$

$$v_0 = (2kT_e/m_e)^{\frac{1}{2}} \ .$$

r_0 = classical electron radius = 2.8178×10^{-15} m

n = electron density (m^{-3})

L = length of scattering volume (m)

P_0 = incident laser beam power (W).

The scattered power spectra given by this equation are shown in Fig. 10G9 as functions of scattering wavelength, for various T_e. At high temperatures the spectra are shifted to shorter wavelengths. The plasma density n can be calculated from the measured ratio of P_s/P_0 (the height of the curves of Fig. 10G9). The value of T_e can be determined from the shape of the scattered spectrum. One

simple way of estimating T_e is to plot log (P_s) vs. y_2. From the slope of the straight line, v_0 and T_e can be determined. Sometimes the scattered spectra differ from the anticipated shapes, however, which may be due to anisotrophy in the electron velocity distribution function.

The incident laser light will scatter incoherently from individual electrons if $\lambda_0 < 0.1[4\pi\lambda_D \sin(\theta/2)]$ and coherently from plasma density fluctuations if $\lambda_0 >> 0.1[4\pi\lambda_D \sin(\theta/2)]$, where λ_D is the Debye length and θ is the scattering angle. Ruby laser scattering usually views the incoherent scattering case, from which T_e and n can be found. Coherent scattering measurements, requiring small scattering angles and powerful FIR lasers (under development), yield estimates of T_i and n.

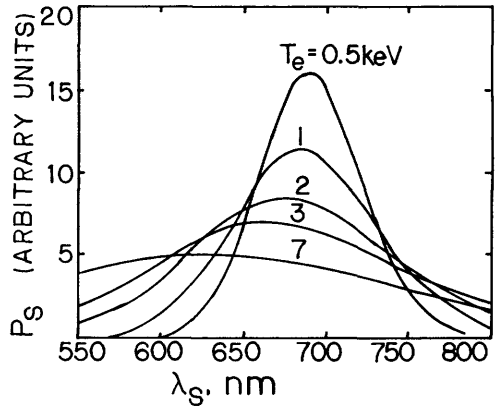

Fig. 10G9. Spectra of Thomson scattered ruby laser light (λ_0 = 694.3 nm) at $\theta = 90^\circ$ for various electron temperatures. From Equipe TFR, "Tokamak plasma diagnostics", Nuclear Fusion 18, 647-730 (1978), Fig. 41.

The required beam power and pulse duration are determined by the need for a satisfactory signal-to-noise ratio (SNR). There will be spurious signals (noise) from the detectors and electronic circuits; from plasma radiation; and from laser beam photons multiply-scattered by the walls, baffles, etc. (parasitic radiation).

Since P_s/P_0 is typically $<10^{-13}$ and there is much stray light (noise), laser beam powers over 100 MW are usually needed, except for continuous wave (cw) lasers, which can be modulated and synchronously detected. A typical ruby laser used in Thomson scattering has a beam energy $\sim$ 10 J, pulse length $\sim$ 20 ns, $P_0 \sim 2$ GW, wavelength spread $\Delta\lambda_0 \sim 10^{-3}$ nm, and beam divergence $\sim$ 1 mrad. CO_2 lasers (λ_0 = 10.6 μm) can attain comparable parameters, but with $\Delta\lambda_0 \sim 1$ nm. At longer wavelengths, HCN lasers (λ_0 = 337 μm) have much lower powers (kiloWatts), beam energies ($\lesssim$ .1 J), and larger beam divergences ($\sim$ 20 mrad) and wavelength spreads ($\sim$ 25 μm). A small divergence is desired to be able to focus the beam to a small diameter in the plasma region. If the incident beam is not monochromatic (if $\Delta\lambda_0$ is not $<< \Delta\lambda_s$) then interpretation of the scattered spectra is more difficult.

The PLT tokamak Thomson scattering equipment is illustrated in Fig. 10G10. Light scattered from various vertical positions along the laser beam path is focussed onto a vertical array of fiber optics light pipes, which concentrate the light and carry it to the relay lens and spectrometer. The diffraction grating separates out the various wavelengths, which are focussed onto an array of 20 different wavelength channels λ (horizontally) and 76 spatial channels y (vertically). This 20x76 channel array is intensified by a microchannel-plate intensifier and recorded by a vidicon tube. Thus, a graph of intensity vs. wavelength is obtained at each spatial position. An example of density and temperature profiles obtained with this system is shown in Fig. 10G11.

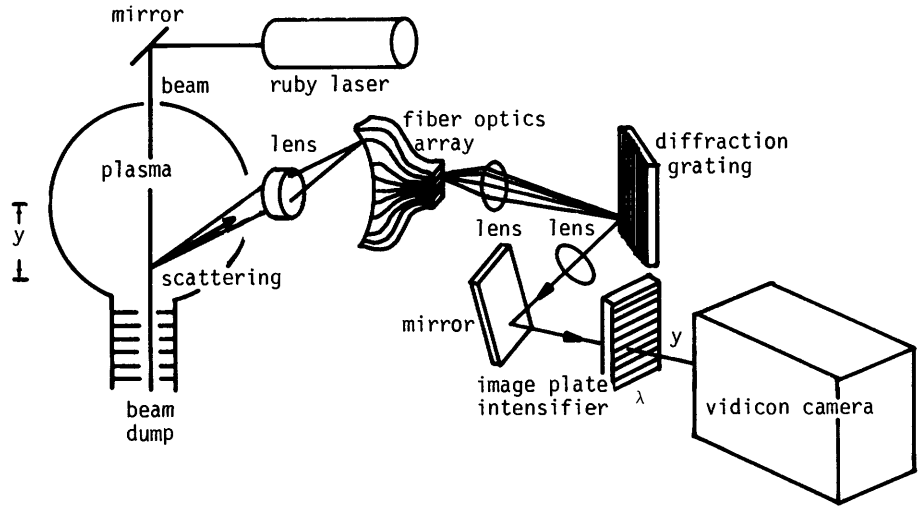

Fig. 10G10. The Thomson scattering system for the PLT tokamak. (For simplicity, various mirrors and lenses are not shown.)

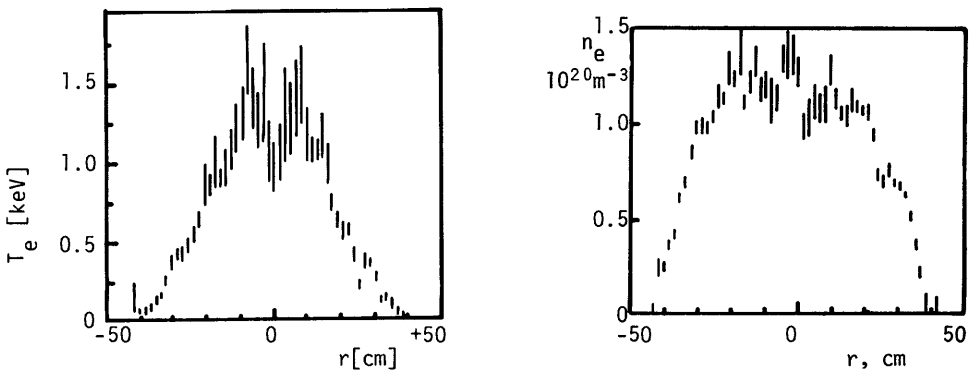

Fig. 10G11. Temperature and density profiles from Thomson scattering on a single PLT discharge. From Equipe TFR, "Tokamak Plasma Diagnostics", Nuclear Fusion 18, 692-731 (1978) Fig. 45. [Based on N. Bretz, D. Dimock, V. Foote, D. Johnson, D. Long, and E. Tolnas, Applied Optics 17, 192 (1978), Fig. 13.]

In order to have such data at several times during each discharge, it is necessary to develop a multiple-pulse high energy laser, to use many separate pulsed lasers, or to use a high-power cw laser.

The theory and practice of Thomson scattering are described by Sheffield (1975). Resonance fluorescence diagnostics are described by Razdobarin and Folomkin (1979).

10H. TFTR Diagnostics

The diagnostics for the Tokamak Fusion Test Reactor (TFTR) are designed to measure plasmas with $10^{19} \leq n \leq 4 \times 10^{20}$ m^{-3}, $0.3 \leq T \leq 15$ keV, with a

non-Maxwellian high-energy tail. In later experiments, high neutron and gamma fluxes will be encountered, so *hardening* of the diagnostic instruments (making them resistant to radiation damage) is important. The arrangement of some of the diagnostics around the torus is shown in Fig. 10H1, and the diagnostic systems are listed in Table 10H1. It is difficult to find space for all the desired equipment around a complex experiment like TFTR. Figure 10H2 shows the vertical access for some diagnostics from below the torus. The diagnostics are linked to the Central Instrumentation Control and Data Acquisition (CICADA) System.

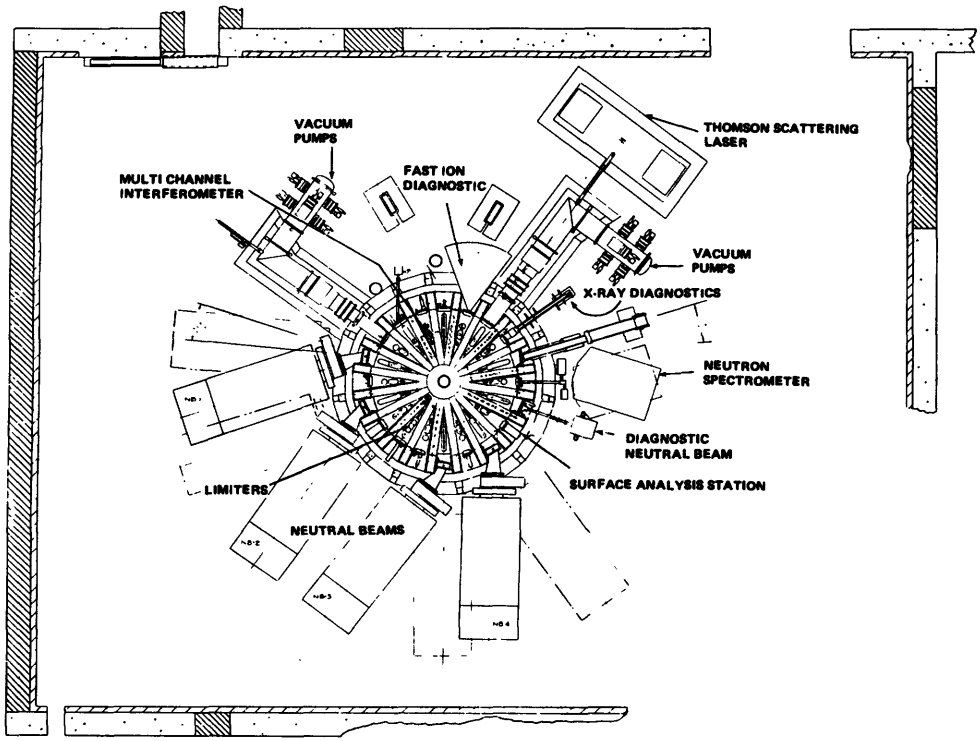

Fig. 10H1. Arrangement of some of the TFTR diagnostics. From TFTR Final Design Report, PPPL-1475 (1978), Fig. 8-1. (Research at the Princeton Plasma Physics Laboratory is funded by the Department of Energy.)

Table 10H1. TFTR Diagnostic Systems. From TFTR Final Design Report, PPPL-1475 (1978), Tables 8-1, 8-2, 8-3.

NAME	MEASUREMENT
group 1: control and basic information	
Electron beam	measurement of field alignment
Voltage loops	voltage around toroid (ohmic power, impedance)
Rogowski loops	plasma current
Diagmagnetic loops	plasma pressure
4 mm μ-wave interferometer	check effectiveness of initial breakdown (for control system)
2 mm μ-wave interferometer	check sufficient plasma density prior to beam injection (for control system)
Neutron activation detectors	neutron fluence from D-T reactions: symmetry and total yield
Epithermal neutron detectors	real-time neutron flux in test cell
group 2: physics studies	
Visible spectrometers	impurity content close to plasma surface
UV spectrometers	impurity content, power radiated, ion temperature
CH_3OH multichannel interferometer	radial, temporal behavior of electron density
Bolometer	energy loss distribution
Thomson scattering	spatial variation of electron temperature and density at several times
Cyclotron emission	continuous electron temperature
X-ray pulse height analysis	electron temperature, electron velocity distribution, impurity concentration
X-ray crystal monochromator	impurity concentration, ion temperature
X-ray wave detectors	location of internal plasma fluctuations
Hard x-ray detectors	runaway electron effects
Neutron spectroscopy	ion temperature, beam thermalization
Charge exchange neutral beam and analyzer	ion temperature, fast ion diagnostics
Calorimetry, duct diagnostic	neutral-beam input power and localization
Surface physics analysis stations	wall surface effects
Residual gas analyzers	evolving gas species
Plasma TV	view inside vacuum vessel during pulse
group 3: diagnostics under development	
CH_3OH multichannel system	$J_{\parallel}$ by Faraday rotation
Very soft x-ray detectors	power radiated in 100 eV - 1 keV range
CO_2 laser scattering	ion temperature, $J_{\parallel}$ distribution
D_2O laser scattering	ion temperature
CO_2 laser scattering	density fluctuations
Microwave scattering	density fluctuations
Heavy ion beam	plasma potential, density fluctuations
α-particle detectors	spatial distribution of α-particle loss
Triton detector	density of tritons in plasma
Pellet injection	impurity diffusion
Various	magnetic field distribution

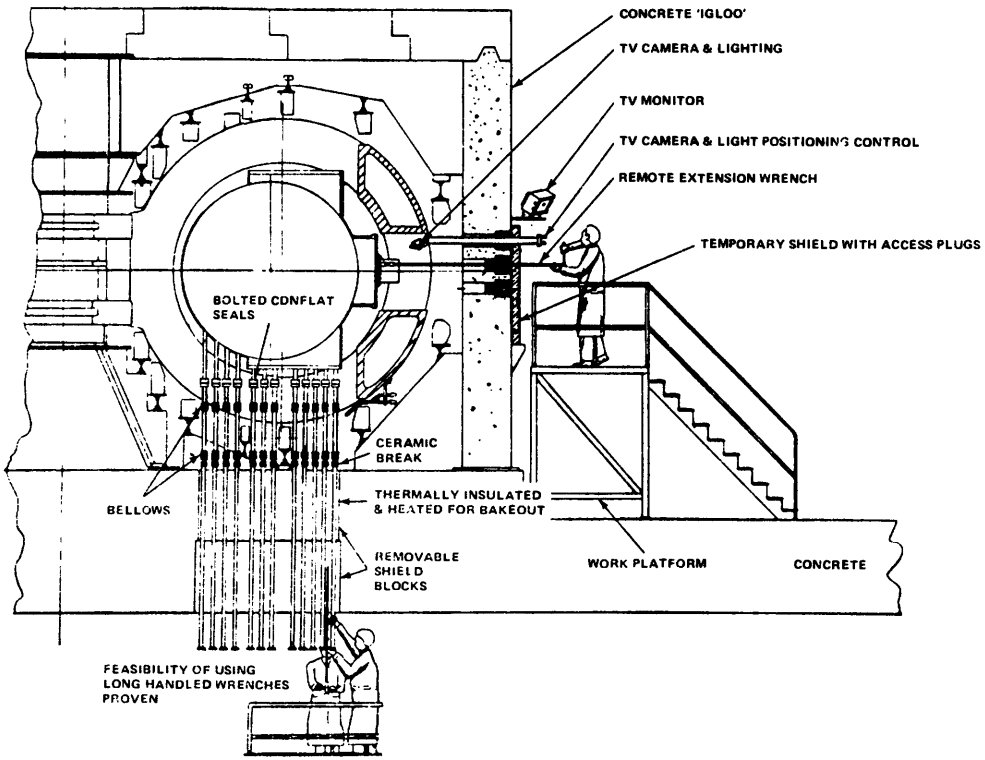

Fig. 10H2. Cross sectional view of TFTR diagnostic access. From TFTR Final Design Report, PPPL-1475 (1978), Fig. 8-2.

10J. Summary

Some diagnostic techniques available to measure various plasma parameters are summarized in Table 10J1. For brevity, several of these techniques have not been discussed in this Chapter. The desirable features of diagnostics systems are to measure all the important parameters with redundancy, accuracy, good spatial and time resolution, and completeness. There is still need of improvement in some of these areas, especially completeness.

Table 10J1. Some techniques for measuring various plasma parameters.

electrostatic potential and electric field
- electrical probes
- plasma conductivity from voltage-current measurements
- heavy-ion beam probe
- electron beam probe (weak magnetic field)
- Stark effect
- plasma impedance from applied oscillating electric field

magnetic field components (Peacock, 1979)
- magnetic flux measurements
- generation of microwave harmonics
- Zeeman effect
- heavy-ion beam probe
- neutral beam probe
- Faraday rotation

electron density or ion density
- Langmuir probe
- microwave, FIR, and optical interferometers
- microwave cavity resonance
- heavy-ion beam probe
- neutral atom beam probe
- Stark broadening
- holographic interferometry
- Thomson scattering
- rf conductivity probes
- Alfven wave and sound wave propagation
- charged particle collectors
- photography

electron temperature or velocity distribution
- gridded analyzers
- Thomson scattering
- heavy-ion beam probe
- x-ray measurements
- electron cyclotron radiation measurements (microwaves, FIR spectroscopy)
- spectral line intensity ratios
- intensities of bremsstrahlung and recombination radiation
- Langmuir probes (low-pressure plasmas)

ion temperature or velocity distribution
- charge-exchange neutral atom analyzer
- Doppler broadening
- neutron emission
- coherent Thomson scattering (FIR)
- gridded analyzers
- magnetic flux measurements of plasma diamagnetism
- calorimetry

neutral density and impurity concentrations
- optical, UV, VUV spectroscopy
- charge-exchange neutral analyzer
- mass spectrometer
- resonance absorption and scattering of light and infrared radiation
- ion cyclotron resonance absorption
- vacuum pressure gage

refractivity measurements (high density)
neutral beam probing

average velocities (drift, rotation, shock fronts, expansion)
time-of-flight from probes or photography
Doppler frequency shift of waves emitted
Doppler shift of reflected microwaves
magnetic flux measurements
runaway electrons from hard x-ray measurements

MHD instabilities and microinstabilities (turbulence) (Kawabe, 1979)
magnetic flux measurements
electrical probes
x-ray fluctuations
microwave reflection
electromagnetic wave scattering (microwaves and FIR)
density fluctuations by heavy-ion beam probe
temperature fluctuations by electron cyclotron emission
photography of plasma shape
plasma resistivity from external voltage-current measurements
neutron energy spectrum and isotropy

Problems

1. If Fig. 10B2 represents a hydrogen plasma with random ion current of 50 μA and probe area of 1 mm^2, estimate the plasma density and electron temperature.

2. A 100-turn magnetic probe coil 3 mm in diameter records a voltage of 2 V with no integrating circuit during the pulsing of a magnet coil. What is the rate of change of the magnetic field?

3. Assume that the poloidal field in an axisymmetric torus with large aspect ratio is found to be $B_p(r) = \frac{B_{po} r}{a+r}$. Find the variation of $J_t(r)$, approximating the torus as a long cylinder.

4. Assume that a ten-turn coil C_1 (Fig. 10C1) is very close to the plasma, so that its radius ≃ a = 0.6 m, the plasma surface radius. If the average plasma pressure increases linearly from 0 to 10^4 Pa in 5 ms, and B = 3 T, estimate the voltage induced in C_1. (Ignore the curvature term in Eq. 8B6, to relate $\partial B/\partial t$ to $\partial p/\partial t$.)

5. A uniform deuterium plasma with density 10^{21} m^{-3} and volume 0.01 m^3 is constant for 2 μs, during which time a detector counts 10^5 neutrons. If the detector measures 10^{-4} of the neutrons emitted by the plasma, what is the approximate ion temperature?

6. A 10 keV K^+ beam probes a plasma. The energy of the K^{++} ions arriving at the detector from one point in the plasma is 9.3 keV. What is the plasma potential at that point?

7. If the Doppler width of the helium spectral line at 468.6 nm is 0.17 nm, what is the approximate ion temperature?

8. If the measured line width of H_β is 2.0 nm, and the Doppler width is estimated to be << 2 nm what is the approximate plasma density? (Assume instrumental broadening and the Zeeman effect are negligible.)

9. From soft x-ray measurements it is determined that the power radiated at W_ν = 2, 4, and 6 keV is $dP/dW_\nu = 10^{-3}$, 10^{-4}, and 10^{-5} (relative units). What is the electron temperature?

10. A sensitive microwave interferometer operating at a wavelength of 1.5 cm measures a phase shift of 3.6 degrees across a plasma path length of 7 cm when the plasma is pulsed on. What is the average plasma density?

11. If L = 1 m and a ruby laser (694.3 nm) was used to make the fringe pattern shown in Fig. 10G5, compute the central plasma density.

12. How much rotation would be produced in an HCN laser beam (337 μm) propagating through a plasma with $n = 3 \times 10^{19}$ m^{-3} and B_k = 0.4 T over a path length of 0.7 m, assuming n and B_k are uniform along the path?

Bibliography

general

Equipe TFR, "Tokamak plasma diagnostics", *Nuclear fusion 18*, 647-731 (1978).

H. Eubank and E. Sindoni, Editors, *Course on Plasma Diagnostics and Data Acquisition Systems (Varenna, Italy, 1975)*, Pergamon Press, Elmsford, NY, 1975.

R. H. Huddlestone and S. L. Leonard, *Plasma Diagnostic Techniques*, Academic Press, New York, 1965.

T. Kawabe, "Fluctuations", p. 327-340 of Sindoni and Wharton (1979).

N. J. Peacock, "Measurements of magnetic fields in toroidal systems", p. 367-402 of Sidoni and Wharton (1979).

I. M. Podgornyi, *Topics in Plasma Diagnostics*, Plenum Press, New York, 1971.

E. Sindoni and C. Wharton, Editors, *Diagnostics for Fusion Experiments (Proceedings of the Course, Varenna, Italy, 1978)*, Pergamon Press, New York, 1979.

C. B. Wharton, "Plasma Diagnostics", *Proceedings of the Second IEEE Minicourse on Fusion*, Ed. G. H. Miley, U. of Illinois, Fusion Studies Laboratory, 1977, Chapter 6.

mathematical data inversion techniques

N. R. Sauthoff and S. von Goeler, "Techniques for the reconstruction of two-dimensional images from projections", *IEEE Transactions on Plasma Science PS-7*, 141-146 (1979).

electrical probes

J. D. Swift and M. J. R. Schwar, *Electrical Probes for Plasma Diagnostics*, American Elsevier, New York, 1969.

magnetic flux measurements

Equipe TFR, op. cit., pp. 650-658.

passive particle diagnostics

M. Brusati, "Charge-exchange measurements", p. 35-46 of Sindoni and Wharton (1979).
S. A. Cohen, "Tokamak plasma diagnostics by surface physics techniques", *Journal of Nuclear Materials 76 & 77*, 68-77 (1978).
H. P. Eubank, "Determination of plasma ion temperatures by analysis of charge-exchange neutrals", p. 7-16 of Sindoni and Wharton (1979).
H. P. Eubank, "Neutron diagnostics", p. 403-420 of Sindoni and Wharton (1979).
T. K. Mau, "Plasma diagnostics and nonlinear wave studies with a gridded electrostatic energy analyzer", *IEEE Transactions on Plasma Science PS-2*, 152-159, (1974).
M. P. Petrov, "Particle diagnostics of a quasisteady thermonuclear plasma", *Soviet Journal of Plasma Physics 2*, 201-211 (1977).
V. I. Tolok, Editor, "Corpuscular, correlation, bolometric, and other techniques", Volume 3, *Recent Advances in Plasma Diagnostics*, Consultants Bureau, New York, 1971.
C. B. Wharton, "Particle-beam-fusion experiments and diagnostics", p. 459-481 of Sindoni and Wharton (1979).

active particle diagnostics

J. A. Cobble and J. C. Glowienka,"Optical diagnostics using a barium ion beam for spatial resolution of plasma parameters", *IEEE Transactions on Plasma Science PS-7*, 147-150 (1979).
H. P. Eubank, "Particle Beams systems in plasma diagnostics", p. 17-35 of Sindoni and Wharton (1979).
K. Kadota, K. Tsuchida, Y. Kawasumi, and J. Fujita, "Plasma diagnostics by neutral beam probing", *Plasma Physics 20*, 1011-1023 (1978).
R. E. Reinovsky, J. C. Glowienka, W. C. Jennings, and R. L. Hickok, "Performance of a feedback controlled electrostatic energy analyzer for use with an ion beam probe diagnostic system", *IEEE Transactions on Plasma Science PS-3*, 194-200 (1975).

passive wave diagnostics

R. Cano, "Electron cyclotron emission as a diagnostic tool in tokamaks", p. 191-204 of Sindoni and Wharton (1979).
S. von Goeler, "Soft x-ray measurements", p. 79-110 of Sindoni and Wharton (1979)
H. R. Griem, *Plasma Spectroscopy*, McGraw-Hill, New York, 1964.
H. R. Griem, *Spectral Line Broadening by Plasmas*, Academic, New York, 1974.
E. Hinnov, "Iron radiation in tokamak discharges", p. 139-148 of Sindoni and Wharton (1979).
H. Knoepfel, "Hard x-ray measurements", p. 111-138 of Sindoni and Wharton (1979).
G. V. Marr, *Plasma Spectroscopy*, Elsevier, New York, 1968.
G. D. Tait, F. J. Stauffer, and D. A. Boyd, "Electron cyclotron radiation measurements on the PLT tokamak", *The Physics of Fluids 24*, 719-728 (1981).
A. P. Thorne, *Spectrophysics*, Chapman and Hall, London, 1974.

active wave diagnostics

C. J. Buchenauer and A. R. Jacobson, "Quadrature interferometer for plasma density measurements", *Review of Scientific Instruments 48*, 769-774 (1977).

R. Cano, "A review of microwave scattering on toroidal plasma", p. 177-190 of Sindoni and Wharton (1979).

J. G. Grossman, W. A. Peebles, M. C. Luhnann, Jr., and A. Semet, "Compact, pulsed low-pressure far infrared laser for use in plasma diagnostics", *Review of Scientific Instruments 50*, 1341-1343 (1979).

M. A. Heald and C. B. Wharton, *Plasma Diagnostics with Microwaves*, Krieger, New York, 1978.

F. C. Jahoda and G. A. Sawyer, "Optical refractivity of plasmas", *Methods of Experimental Physics*, Volume 9, Part B (H. R. Griem and R. H. Lovberg, Editors) Academic Press, New York, 1971, Chapter 11.

K. Kadota, K. Tsuchida, Y. Kawasumi, and J. Fujita, "Plasma diagnostics by neutral beam probing", *Plasma Physics 20*, 1011-1023 (1978).

R. J. Keys, Editor, *Optical and Infrared Detectors*, Topics in Applied Physics Volume 19, Springer-Verlag, Berlin, 1977.

W. Kunz, "First measurement of poloidal-field-induced faraday rotation in a tokamak plasma", *Nuclear Fusion 18*, 1729-1732 (1978).

A. Lesage, J. Richou, P. Charil, M. Combier, and J. L. Lebrun, "Optoelectronic modulation of a laser interferometer in the infrared for accurate electron density variation measurements", *Review of Scientific Instruments 50*, 1306-1308 (1979).

D. D. Lowenthal and A. L. Hoffman, "Quasi-quadrature interferometer for plasma density radial profile measurements", *Review of Scientific Instruments 50*, 835-843 (1979).

C. H. Ma, D. P. Hutchinson, and K. L. Vander Sluis, "A modulated submillimeter-laser polarimeter for the measurement of the Faraday rotation by a plasma", *Applied Physics Letters 34*, 218-220 (1979).

T. C. Marshall, "Microwave scattering from plasmas", *Methods of Experimental Physics*, Vol. 9, Part A (H. R. Griem and R. H. Lovberg, Editors), Academic Press, New York, 1970, Chapter 2.

R. W. Peterson and F. C. Jahoda, "A far-infrared coupled cavity interferometer", *Applied Physics Letters 18*, 440-442 (1971).

M. P. Petrov, "Particle diagnostics of a quasisteady thermonuclear plasma", *Soviet Journal of Plasma Physics 2*, 201-211 (1977).

W. E. Quinn, "Interferometric measurements of plasma density in high-β plasmas", "Measurement of plasma beta in high-β fusion experiments", and "Faraday rotation measurements in high-β fusion experiments", p. 421-458 of Sindoni and Wharton (1979).

G. T. Razdobarin and I. P. Folomkin, "Plasma diagnostics by the method of resonance fluorescence", p. 311-325 of Sindoni and Wharton (1979).

J. Schneider and S. Robertson, "Feedback-stabilized fractional fringe laser interferometer for plasma density measurements", *Review of Scientific Instruments 50*, 856-858 (1979).

J. Sheffield, *Plasma Scattering of Electromagnetic Radiation*, Academic Press, New York, 1975.

V. T. Tolok, Ed., "Optical Techniques", and "Microwave Techniques", Vol. 1 and 2, *Recent Advances in Plasma Diagnostics*, Consultants Bureau, New York, 1971.

D. Veron, "High sensitivity HCN laser interferometer for plasma electron density measurements", *Optics Communications 10*, 95-98 (1974).

C. M. Vest, *Holographic Interferometry*, Wiley, New York, 1979.

CHAPTER 11
MIRRORS AND CUSPS

11A. Coil Geometries

mirror coils

Plasma in simple mirrors is vulnerable to interchange instabilities. Stability may be achieved by several means:

* use of electron cyclotron resonance heating (ECRH) to produce a high-current ring of hot electrons, which alters the magnetic field geometry. (A "bumpy torus" comprised of simple mirrors connected end to end in a circle and stabilized by hot electron currents will be described in Section 14D).
* application of a radial electric field to induce strong plasma rotation (Section 11H)
* injection of high-current neutral beams to produce strong ion currents, which reverse the axial magnetic field ("Field-Reversed Mirrors", Section 11F)
*use of circular magnetic cusps at the plasma surface
*use of linear magnetic cusps at the plasma surface (Ioffe bars), baseball coils (Fig. 8D7), or Yin-Yang coils (Fig. 11A1) to produce a minimum-B field.

The shapes of the magnetic field lines and of the constant magnetic pressure surfaces of the MFTF Ying-Yang coils are shown in Fig. 11A2. If we define "coil efficiency" to be the ratio of peak vacuum magnetic field in the plasma region to peak magnetic field at the coil windings, then Yin-Yang coils are more efficient than a baseball coil.

The Tandem Mirror Experiment (TMX) involves a central solenoid with mirror "plugs" at its ends, as shown in Fig. 11A3. The octupole coils help stabilize the central region, and the transition coils guide the flux tube from the circular solenoid to the fan-shaped plug regions.

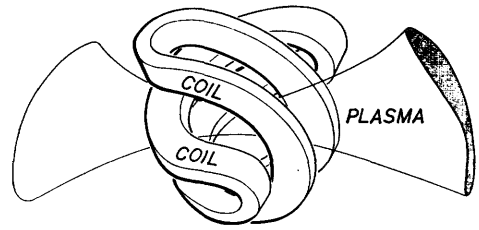

Fig. 11A1. A pair of Yin-Yang coils, and the corresponding plasma shape. Courtesy of LLNL.

cusp coils

Some magnetic cusp fields are illustrated in Fig. 11A4. The spindle cusp is produced by two circular coils with

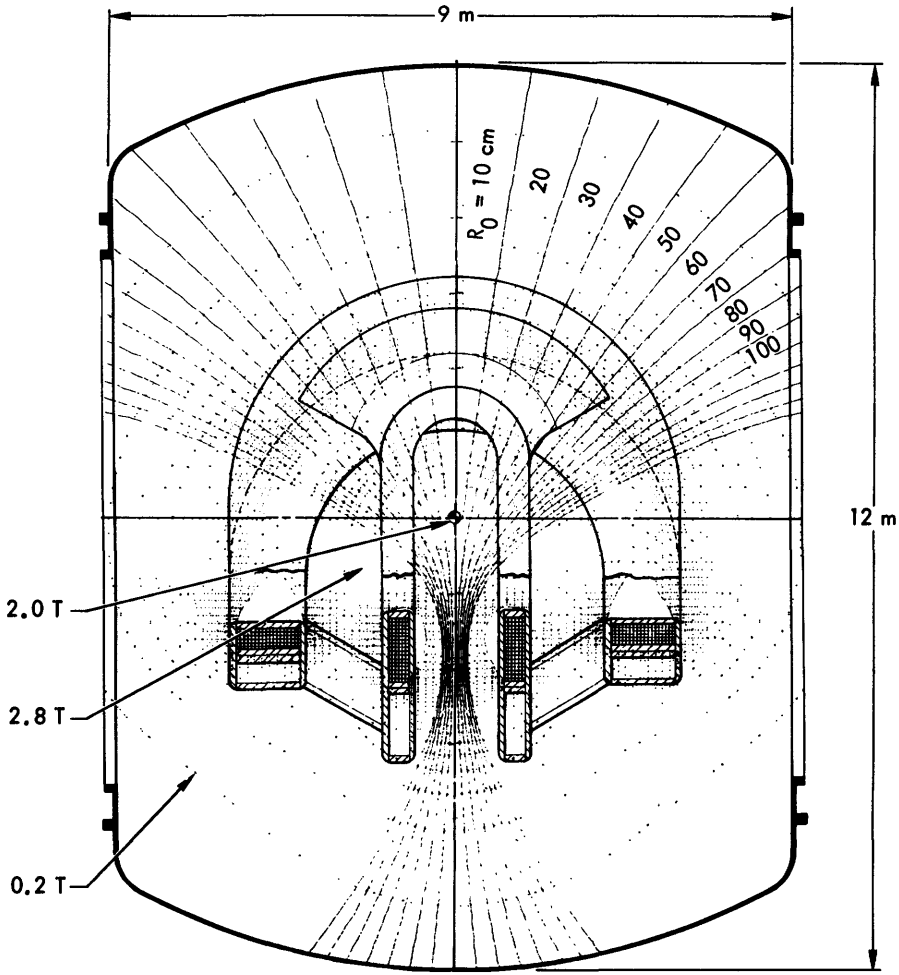

Fig. 11A2. Magnetic field lines (smooth curves) and contours of constant magnetic pressure (dotted curves) for the Yin-Yang coils of the MFTF experiment. R_0 represents the distance from a magnetic field line to the origin. The outermost closed magnetic isobar has B = 2.8 T, giving a radial well depth of 1.4 relative to the field minimum at the origin. Courtesy of LLNL.

opposite currents (see also Fig. 8A4).

Cusp fields have magnetic field nulls, near which the magnetic moment

$$\mu = W_\perp/B \qquad (11A1)$$

is not conserved (Section 7D). (Cusp fields are said to be *non-adiabatic*). Consequently, many of the particles are not mirror-trapped, and are lost after a few bounces inside the cusp device. However, various trapping mechanisms permit longer confinement times for some groups of particles (Section 11J).

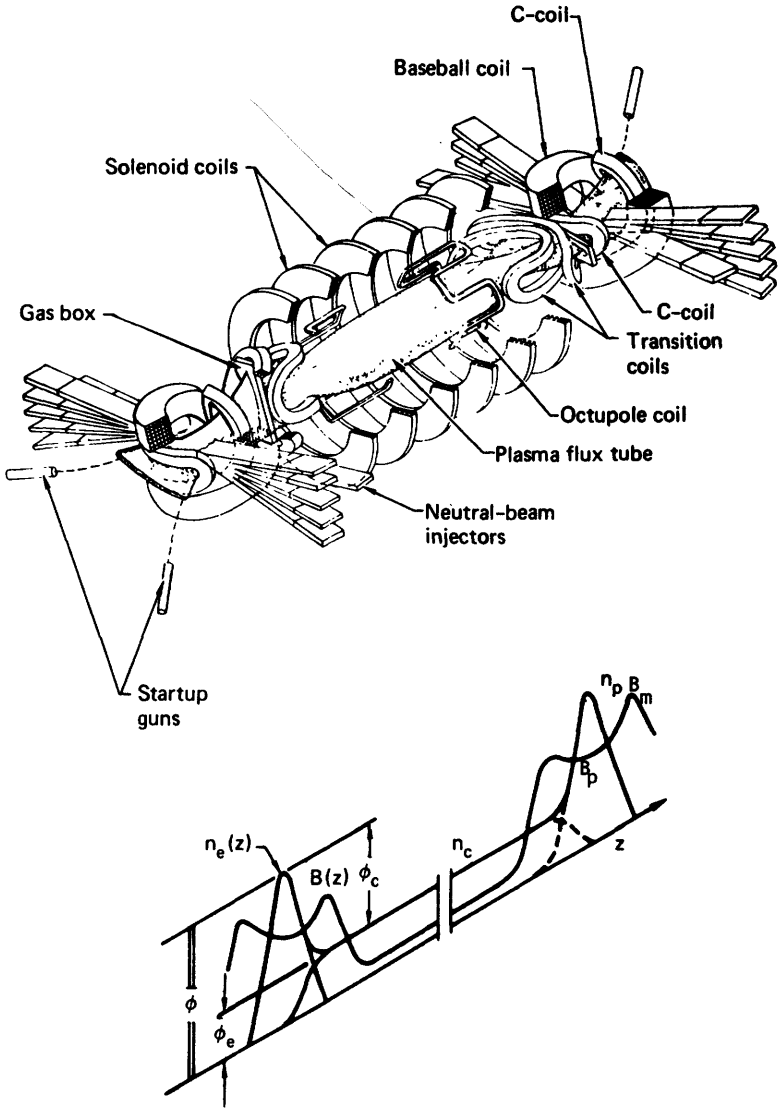

Fig. 11A3. Schematic drawing of the TMX magnet and neutral-beam system used to produce the tandem-mirror axial magnetic field, density, and potential profiles. From T. C. Simonen et al, "Plasma confinement experiments in the TMX tandem mirror", 8th International Conference on Plasma Physics and Controlled Nuclear Fusion Research (Brussels, 1980), IAEA, Vienna, 1981.

Cusp fields may be combined with mirror fields, as with the addition of Ioffe bars to a simple mirror (Fig. 8D7). The addition of a toroidal magnetic field to a toroidal multipole cusp (Fig. 11A4) produces a "Toroidal Magnetic Cusp (TORMAC)" geometry (Section 11J).

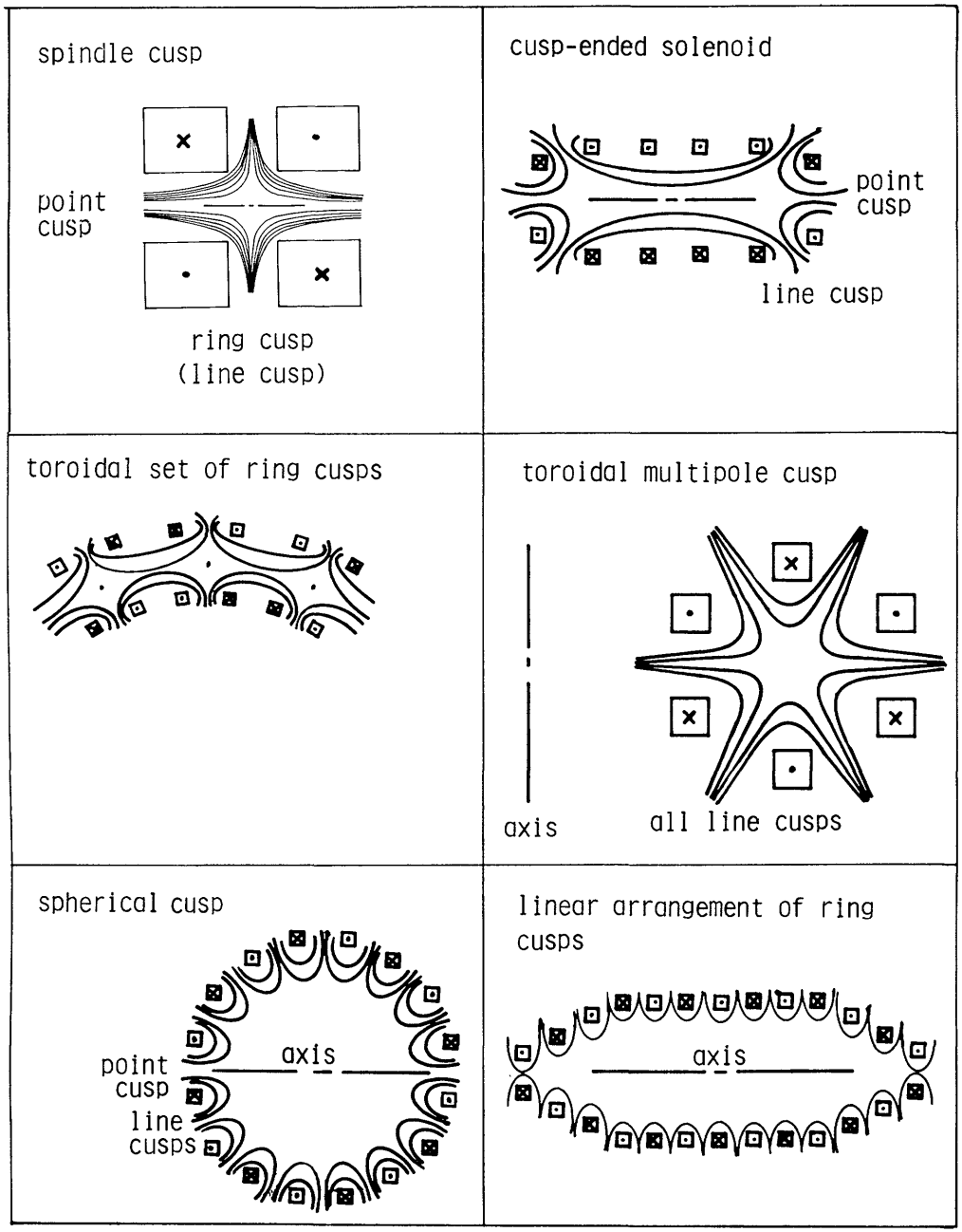

Fig. 11A4. Magnetic field lines (smooth curves) in some cusped geometries. The symbols × and • represent current into and out of the drawing, respectively.

11B. Mirror Loss Boundaries

Electrons tend to scatter into the mirror loss cone faster than ions. A rapid initial loss of electrons builds up a positive plasma potential, which accelerates ion loss and retards electron loss. At equilibrium, the plasma in a simple magnetic mirror has equal electron and ion loss rates and a large positive potential. According to the energy conservation equation (7D8)

$$\tfrac{1}{2}mv_{\parallel}^2 + \tfrac{1}{2}mv_{\perp}^2 + q\phi = \text{constant} = \tfrac{1}{2}mv_{\parallel 0}^2 + \tfrac{1}{2}mv_{\perp 0}^2 + q\phi_0 \qquad (11B1)$$

where the subscript 0 refers to a starting point near the plasma center. If the magnetic moment is conserved, then

$$v_{\perp}^2 = v_{\perp 0}^2 B/B_0 \quad . \qquad (11B2)$$

The loss boundary in velocity space is given by the values of $v_{\parallel 0}$ for which $v_{\parallel} = 0$ at the maximum field B_m. From Eqs. (11B1) and (11B2) we find

$$v_{\parallel 0}^2 = v_{\perp 0}^2(R - 1) - (2q/m)(\phi_0 - \phi_m) \qquad (11B3)$$

where the "mirror ratio" $R \equiv B_m/B_0$, and ϕ_m is the potential where $B = B_m$. The axial variations of magnetic field and electrostatic potential in a simple mirror are shown in Fig. 11B1, along with the hyperbolic loss boundaries computed with Eq. (11B3) for ions ($q = e$) and for electrons ($q = -e$). The asymptotes of the hyperbolas are identical to the "loss cone" of Eq. (7D12), computed for the simplified case in which potential variations were ignored.

When plasma is introduced, its diamagnetism reduces the vacuum magnetic field B_{0V} to a new value B_0. From Eq. (8B7),

$$p + B_0^2/2\mu_0 \simeq \text{constant} = B_{0V}^2/2\mu_0 \quad . \qquad (11B4)$$

Thus, the reduced magnetic field inside the plasma is found to be

$$B_0 = B_{0V}(1-\beta)^{\frac{1}{2}} \quad , \qquad (11B5)$$

where $\beta \equiv 2\mu_0 p/B_{0V}^2$, and the mirror ratio

$$R = R_V/(1-\beta)^{\frac{1}{2}} \quad . \qquad (11B6)$$

where the vacuum mirror ratio $R_V = B_m/B_{0V}$. This equation is suitable for a *long, thin plasma* where end effects and curvature are small. For a *short, thick plasma*, a better approximation is

$$R \simeq R_V/(1 - \tfrac{1}{2}\beta) \quad . \qquad (11B7)$$

However, the magnetic moment of high-energy ions is not always conserved, especially at high R, so they may not be adiabatically confined (Foote, 1972). Thus, the loss regions may be larger than those estimated from Eq. (11B3). The "adiabaticity limits" estimated for the MFTF end plugs are illustrated in Fig. 11B2. Since some plasma is well trapped in cusp devices and some plasma may be "nonadiabatic" in mirrors, high-β mirror confinement and cusp confinement are not completely different.

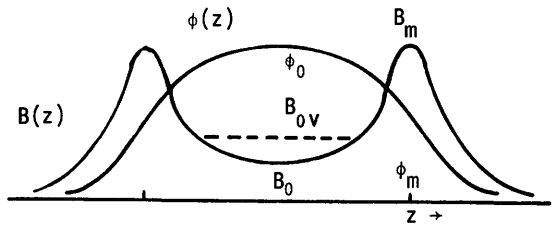

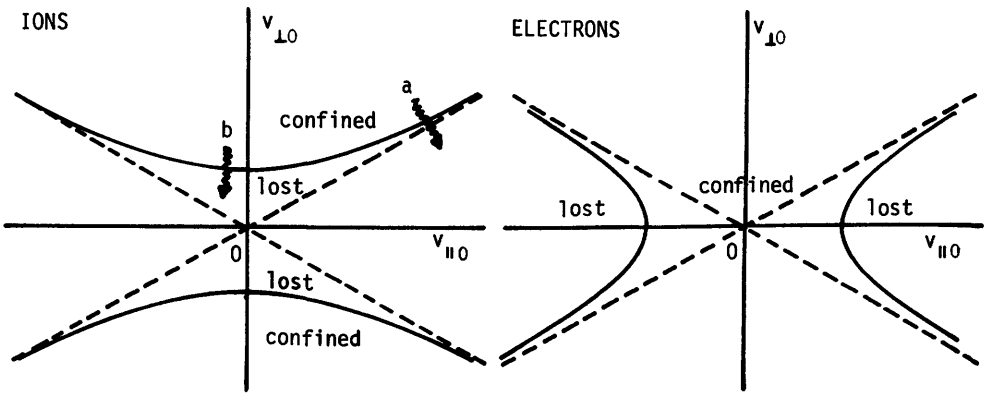

Fig. 11B1. Axial variation of magnetic field and plasma potential in a simple magnetic mirror, and the resulting loss boundaries for ions and electrons. The dashed curve B_{0v} indicates the vacuum magnetic field (in the absence of plasma). Ions are lost by (a) pitch angle scattering (ion-ion collisions) and (b) energy loss to electrons ("electron drag").

11C. Instabilities

Several instabilities can occur in mirror-confined plasmas, limiting the attainable plasma length, radius, and beta.

drift cyclotron loss cone (DCLC) mode

As discussed in Section 8E, electrons travelling azimuthally, with drift

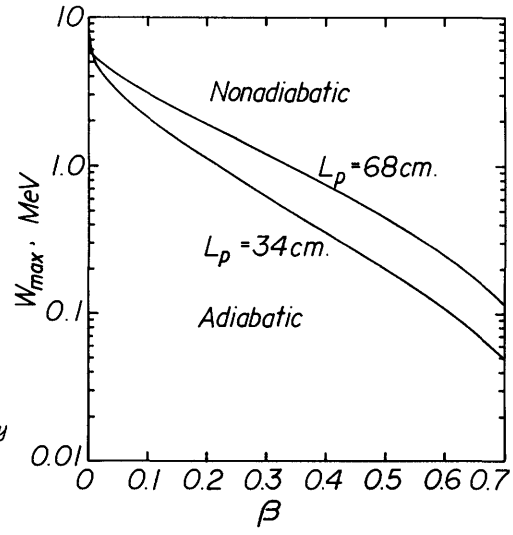

Fig. 11B2. Adiabaticity limits for ions in the MFTF experiment, as functions of plasma beta and length L_p. Ions with energies above W_{max} are not adiabatically confined. Courtesy of LLNL.

velocity $v_{de} = -(dp_e/dr)/neB$ can bunch up to form waves with wavelengths such that $i\lambda = 2\pi r_p$ (where i is an integer and r_p is the plasma radius) and frequency

$$\omega^* = k_\theta v_{de} = 2\pi v_{de}/\lambda = i v_{de}/r_p \qquad (11C1)$$

The gyrating ions tend to bunch up near the drift wave electron bunches, provided that the drift wave frequency $\omega^* \sim j\omega_{ci}$ where j is an integer and ω_{ci} is the ion cyclotron frequency. This wave coupling allows energy to flow from the high-energy ions via the ion cyclotron wave and electron drift wave to the cooler electrons. The interaction with the fluctuating electric field of the waves causes the ions to diffuse more rapidly in velocity space than they would by Coulomb scattering alone, greatly reducing the time it takes for them to be scattered into the loss hyperboloid of Fig. 11B1. It has been predicted that this instability can be stabilized by the presence of unconfined warm plasma, partially filling in the loss cone (dashed curve, Fig. 8E4), and by use of a large plasma radius r_p, which reduces the pressure gradient. These techniques reduce the sources of free energy driving the instability (non-Maxwellian distribution and gradients). The predicted densities of warm plasma and plasma radii required to stabilize the DCLC mode, illustrated in Fig. 11C1, are consistent with experimental results from the 2XIIB device.

mirror mode and Alfven ion cyclotron mode

The mirror mode is an electromagnetic instability which is driven by anisotropy of the velocity distribution in a mirror, that is, by the difference between the ion temperatures $T_{i\parallel}$ along the magnetic field and $T_{i\perp}$ perpendicular to the magnetic field. This mode occurs if

$$\beta_e = 2\mu_0 nkT_e/B^2 > \frac{0.5}{\left(\frac{T_{i\perp}}{T_{i\parallel}} - 1\right)} \qquad (11C2)$$

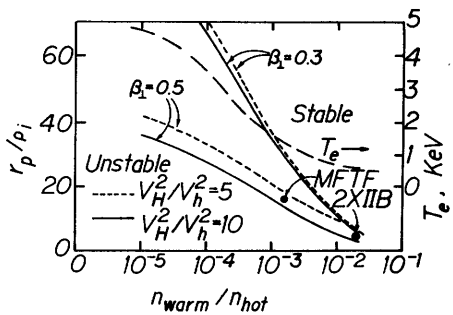

Fig. 11C1. Theoretical minimum plasma radius r_p for stability against the DCLC mode as a function of the ratio of warm flowing plasma density to hot plasma density. The theoretical electron temperature is also shown. Regions above and to the right of the curves are stable. For example, the 2XIIB experiment has a small r_p/ρ_i ratio, so it requires a large density n_{warm} of flowing plasma to maintain stability. The MFTF device has a larger r_p/ρ_i, so a much lower flowing plasma density is needed for stability, and the electron temperature will be much higher. Here $\beta_\perp = 2\mu_0 nk(T_{e\perp}+T_{i\perp})/B^2$, and V_H and V_h are ion velocities corresponding to $T_{i\perp}$ and $e(\phi_0-\phi_m)$. Courtesy of LLNL.

thus setting a limit on the electron pressure and degree of anisotropy. The Alfven ion cyclotron mode represents a coupling between ion cyclotron motion and an Alfven wave (Eq. 5E34). Theoretical limiting values of $\beta_\perp = 2\mu_0 nk(T_{e\perp} + T_{i\perp})$, are illustrated in Fig. 11C2.

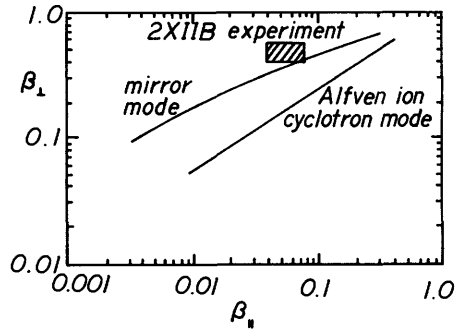

Fig. 11C2. Maximum value of $\beta_\perp$ for stability against the mirror and Alfven ion cyclotron modes, as a function of $\beta_\parallel$, based upon an assumed "Holdren" type of velocity distribution function. Simple theory indicates that the region above the curves is unstable. Values of $\beta_\perp$ observed in the 2XIIB experiment exceed these predictions. Courtesy of LLNL.

convective loss cone mode

The convective loss cone mode, also driven by anisotropy, has $\omega \simeq \omega_{pi}$ (the ion plasma frequency), and it propagates almost parallel to the magnetic field. According to theoretical estimates, this mode can be stabilized if

$$L/\rho_i < 45(R + 1)^{\frac{1}{2}} \text{ and}$$

$$\omega_{pe}^2/\omega_{ce}^2 \gtrsim 3 \qquad (11C3)$$

where L is the plasma length, R is the mirror ratio, ω_{pe} is the electron plasma frequency, and ω_{ce} is the electron cyclotron frequency. Another mode, called a "negative energy wave", may also limit the allowable plasma length in mirror machines to tens of ion Larmor radii. Such length restrictions hinder design of a large mirror fusion reactor. However, these modes have not been clearly identified experimentally, and they did not appear to disrupt confinement in the 2XIIB experiment, which had $L/\rho_i \sim 100$. (The warm flowing plasma in that experiment may have had a stabilizing effect on these modes.)

ballooning mode

The ballooning mode, described briefly in Section 8D, can occur in regions of bad magnetic field curvature, such as the transition regions between the central solenoid and the end plugs of a tandem mirror, Fig. 11A3. It limits the attainable values of beta, as illustrated in Fig. 11C3. Axisymmetric tandem mirrors can

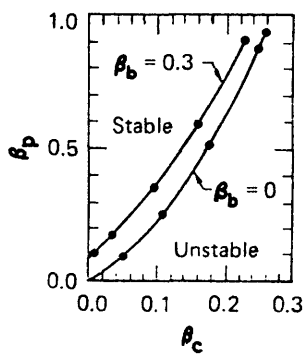

Fig. 11C3. Ballooning mode marginal stability boundaries in a tandem mirror with A-cell thermal barriers (thermal barriers will be discussed later). The values of beta in the central cell, end plugs, and barrier cells are denoted β_c, β_p, and β_b, respectively. From D. E. Baldwin et al., "Studies in tandem mirror theory", 8th Conference on Plasma Physics and Controlled Nuclear Fusion Research, Brussels, 1980, to be published by IAEA.

probably attain higher values of β_c than those indicated for the A-cell thermal barrier tandem mirror. Values of $\beta_c \gtrsim 0.4$ are desired for reactors.

Thus, instabilities may place limits on the maximum length and minimum radius of plasma in simple mirrors, limits on the amount of warm flowing plasma needed to reduce anisotropy-driven microinstabilities, and limits on the attainable values of plasma pressure (beta).

Plasma losses along magnetic field lines from cusp systems have generally been so rapid that instabilities were not identified.

11D. 2XIIB Experiment

The 2XIIB experiment originally involved injection of plasma from plasma guns into mirror coils which were pulsed to trap and compress the plasma. With the addition of powerful neutral beam injection systems, the gun plasma was used as a target plasma to ionize and trap the neutral beams. It was found that leaving the plasma guns on during neutral beam injection reduced instabilities at the ion cyclotron frequency, increased confinement time by a factor of six, and permitted buildup to higher plasma densities. Later, it was found that the plasma guns are not necessary at sufficiently high neutral beam currents. Flowing neutral gas can be used as the target for plasma buildup, and the flowing gas becomes ionized flowing plasma, which helps stabilize microinstabilities. However, the cold plasma reduces T_e, increasing the ion loss rate by electron drag.

Some parameters of the 2XIIB experiment (later renamed "Beta-II") are listed in Table 11D1.

Table 11D1. Parameters of the 2XIIB Experiment.

peak central field B_0	1.4 Tesla
axial mirror ratio R	2
distance between mirrors	1.5 m
plasma radius r_p	$\sim$ 0.08 m
neutral beam injection energy	20 keV
neutral beam current	$\sim$ 500 A-equiv.
n_i	$\sim 10^{20}$ m^{-3}
$\langle W_i \rangle$	$\sim$ 10 keV
T_e	$\sim$ 0.1 keV
$n\tau_E$	$\sim 5 \times 10^{16} m^{-3} s$
β	$\sim$ 1.

During neutral beam injection, much of the beam energy is lost by charge exchange, so very high currents are required. Once most of the background gas is ionized (called "burnout" of the neutral gas) the charge exchange rate greatly decreases and the plasma density increases exponentially in time up to a high-density equilibrium value, as illustrated in Fig. 11D1.

Figure 11D2 illustrates the stabilizing effect of flowing warm plasma on maintenance of plasma density. With the stream on, potential fluctuations at ω_{ci} (probably the DCLC mode) are suppressed, and the plasma density is not lost as rapidly as without the stream, but the electron temperature is also reduced by interaction with the cool plasma stream.

The effect of ion-cyclotron fluctuations on the plasma loss rate is shown in Fig. 11D3. When these fluctuations are suppressed by flowing plasma, the confinement time is governed primarily by electron drag and ion-ion scattering into the loss hyperboloids (Fig. 11B1). Then $n\tau$ increases roughly proportional to $W_i^{3/2}$, where W_i is the average ion energy, as shown in Fig. 11D4.

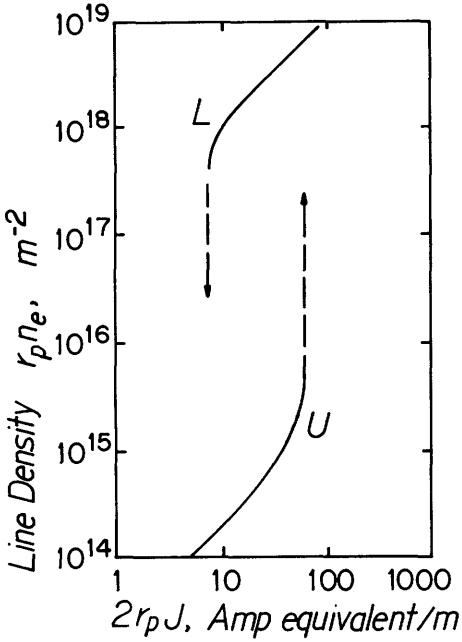

Fig. 11D1. Density regimes of mirror experiments sustained by neutral beam injection with current density J in a plasma with radius r_p. Along the lower smooth curve, neutral gas effects are dominant. Burnout occurs at the "upper critical current" U. Coulomb collision effects are dominant along the upper smooth curve. The plasma reverts to low density at the "lower critical current" L. From G. H. Miley, Editor, Proceedings of the Second IEEE Minicourse on Fusion, U. of Illinois Fusion Studies Laboratory, 1977, Chapter 8, Fig. 22.

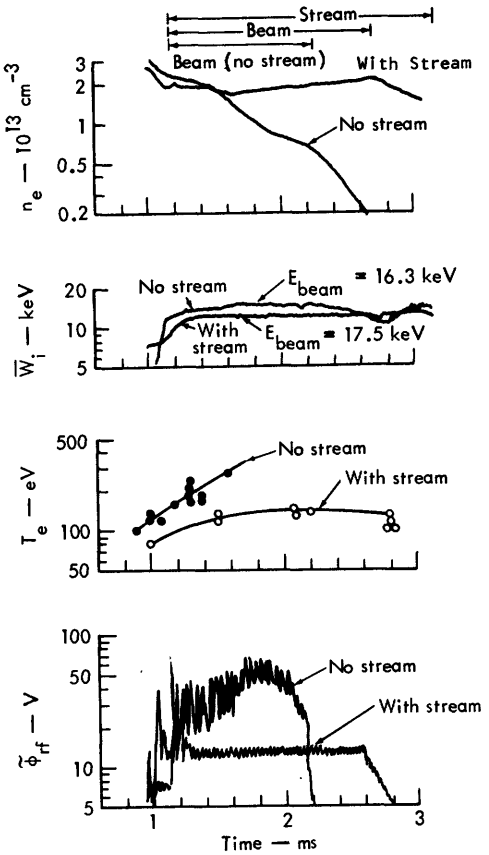

Fig. 11D2. The effect of the warm plasma stream on time variation of electron density (microwave measurements), mean ion energy (11-channel charge-exchange analyzer), electron temperature (by Thomson scattering), and ion-cyclotron fluctuation amplitude (probe rf envelope). Courtesy of LLNL.

The principal results of the 2XIIB experiment are

* surpassing the upper critical current and attaining high-density operation,
* stabilization of microinstabilities using warm flowing plasma,
* stabilization by flowing neutral gas,
* attaining high ion energy ($W_i \simeq 13$ keV),
* attaining $\beta \gtrsim 1$,
* verifying scaling of $n\tau$ with $W_i^{3/2}$ as predicted for electron drag and ion-ion scattering loss rates.

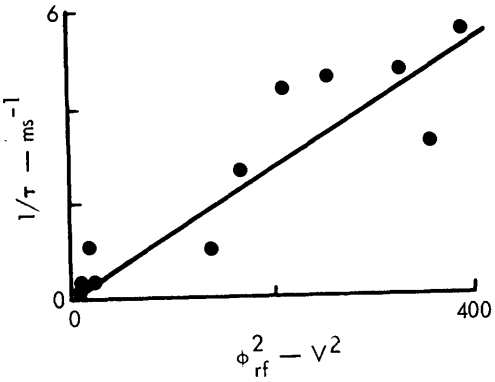

Fig. 11D3. Plasma loss rate (scattering into loss hyperboloid) vs. the square of the amplitude of the ion-cyclotron fluctuations. Courtesy of LLNL.

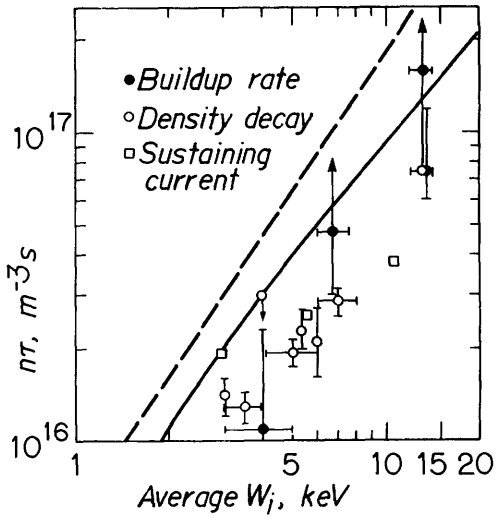

Fig. 11D4. Variation of confinement parameter $n\tau$ with average ion energy. The smooth curve is the theoretical value, and the dashed curve is the theoretical value if only ion-ion scattering is considered (ignoring electron drag). The different types of data refer to different measurement techniques. Courtesy of LLNL.

11E. Tandem Mirrors

potential barriers

The main problem with mirror confinement is rapid plasma loss along magnetic field lines. One way to impede such loss is to establish electrostatic potential hills at the ends of the plasma.

The steady-state momentum conservation equation (5D5) for collisionless, isothermal electron flow along the magnetic field reduces to

$$e(\partial\phi/\partial z) = kT_e(\partial n/\partial z)/n \quad , \tag{11E1}$$

which integrates to

$$\phi - \phi_0 = (kT_e/e)\ln(n/n_0) \quad , \tag{11E2}$$

where the subscript 0 denotes any convenient reference point. Thus, a density peak produces a corresponding potential hill, which can be used to confine ions electrostatically.

Establishment of such potential hills is the main idea of tandem mirrors, illustrated in Fig. 11A3. A long central cell with plasma density n_c has "plug" mirror cells at each end. Neutral beam injection into the end plug cells establishes high plasma densities n_p there. Since electron scattering into the loss region tends to be more rapid than ion scattering, the plasma potential in the plugs adjusts to a high positive value, at which the electron and ion loss rates are equal, as discussed with Fig. 11B1. Thus, the plug potential is fixed relative to the end walls.

The electrostatic potential of the central cell is established by the equality of electron and ion loss rates from that region as illustrated in Fig. 11E1. Potential curve 1 would have poorly confined ions, and very well-confined electrons. Curve 3 would have poorly confined electrons, but well-trapped ions. Curve 2, having about equal electron and ion loss rates, is the equilibrium potential shape.

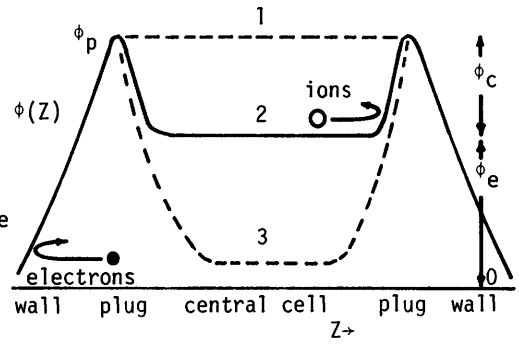

In accordance with Eq. (11E2), the potential barrier height ϕ_c is related to the plasma density ratio by

$$\phi_c = T_e \ln(n_p/n_c) \quad ,$$

$$n_p/n_c = \exp(\phi_c/T_e) \qquad (11E3)$$

where the potential and temperature are both expressed in keV.

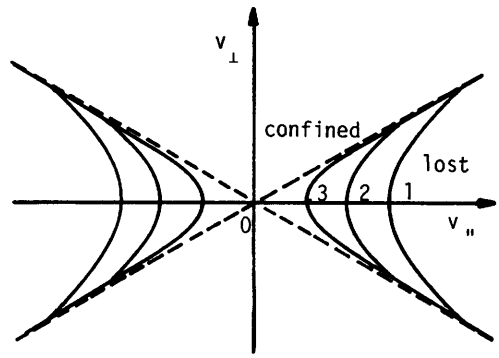

Fig. 11E1. Possible potential profiles in the central cell of a tandem mirror device, and the corresponding electron loss boundaries (bottom). The heights of the potential barriers confronting central cell ions and electrons are designated ϕ_c and ϕ_e, respectively.

plug ions

The loss boundaries for plug ions and central cell ions are shown in Fig. 11E2. The asymmetry of the plug ion curves is due to the different potentials on the two sides (wall side and central cell side) of the plugs. Plug ion confinement differs little from confinement in ordinary mirrors (Fig. 11B1), but central cell ion confinement is much better. Therefore, it is desirable to have small plug volumes and a large central cell volume, in order to take advantage of the long central cell ion confinement times.

In order to avoid rapid loss of injected ions, the injection energy W_0 must be large enough that

$$W_0 > (\phi_c + \phi_e)/(R_p - 1) \qquad \text{(keV)} \quad , \qquad (11E4)$$

where

$$R_p = B_m/B_p(1 - \beta_p)^{\frac{1}{2}} \quad . \qquad (11E5)$$

is the plug mirror ratio, and β_p is the plug beta. (Typically $\beta_p \sim 0.5$-0.7 may be expected in Yin-Yang plugs).

Consider the axial magnetic field distribution of Fig. 11E3. The plug ion confinement time τ_p may be estimated from the relation (Carlson et al, 1979)

$$\frac{1}{n\tau_p} = \frac{1}{n\tau_{ii}} + \frac{1}{n\tau_{ie}} \qquad (11E6)$$

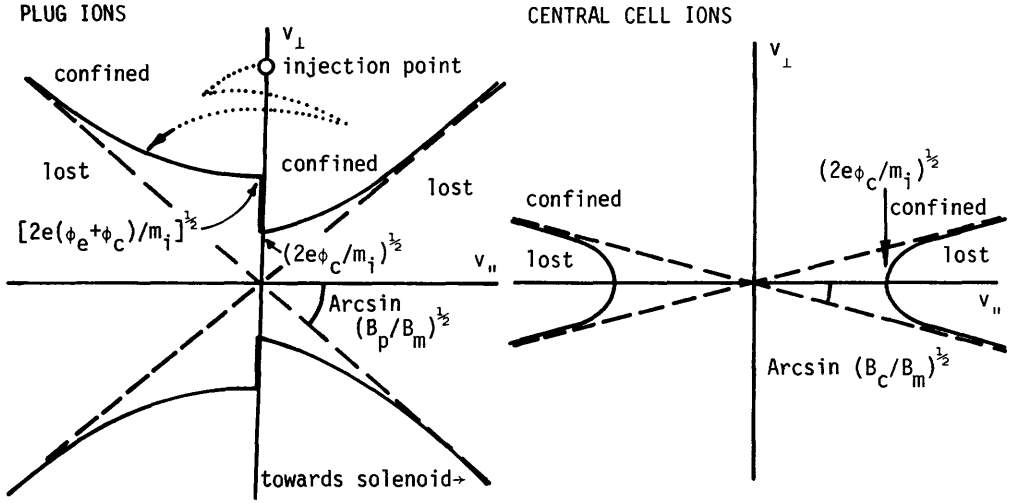

Fig. 11E2. Velocity space loss boundaries for tandem mirror plug ions and central cell ions. The dotted curve illustrates typical velocity-space diffusion of an injected plug ion.

where

$$n\tau_{ii} = 2.8\times10^{18}\, A_p^{1/2}\, W_0^{3/2} \log_{10} R_{eff}/L_{ii} \quad (m^{-3}s) \qquad (11E7)$$

represents loss by pitch-angle scattering,

$$n\tau_{ie} = 10^{19} A_p T_{ep}^{3/2} \ln(W_0/W_L)/L_{ie} \quad (m^{-3}s) \qquad (11E8)$$

represents loss by electron drag,

$$R_{eff} = \frac{R_p \sin^2\theta_i}{1 + (\phi_e + \phi_c)/W_0} \qquad (11E9)$$

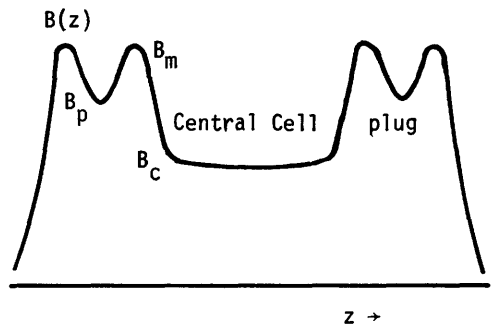

Fig. 11E3. Axial magnetic field profile for an ordinary tandem mirror.

is the effective plug mirror ratio, W_0 is the beam injection energy (keV), θ_i is the beam injection angle relative to B, A_p is the plug ion mass in atomic mass units (A_p = 2 for deuterons), T_{ep} is the plug electron temperature (keV), L_{ii} and L_{ie} are the Coulomb logarithms for ion-ion and ion-electron collisions, Table 2E1, and W_L is an average energy at which plug ions are lost [typically $\ln(W_0/W_L) \sim 1$].

The beam current needed to sustain each plug is

$$I_p = en_p^2 V_p/(n\tau_p) \quad (A) \qquad (11E10)$$

where V_p is the plug plasma volume (m^3) and e is the electronic charge (C). The total beam power needed for the two plugs is

$$P_p = 2I_p W_0 / f_t \qquad (kW) \quad , \tag{11E11}$$

where f_t is the fraction of the beam power trapped in the plug plasma, and W_0 is in keV.

central cell confinement

The particle and energy loss rates of central-cell particles of species a with density n_a, charge $z_a e$, temperature T_a, and collision time τ_a due to *Coulomb collisions* are given by the equations

$$(dn_a/dt) = -4Z_a n_a I(y_a)\exp(-y_a)/\pi^{1/2}\tau_a y_a G(RZ_a) \quad , \tag{11E12}$$

which represents a confinement time

$$\tau_{1,} = \pi^{1/2}\tau_a y_a G(RZ_a)\exp(y_a)/4Z_a I(y_a) \qquad (s) \quad , \tag{11E13}$$

and

$$1.5\, d(n_a T_a)/dt = z_a e\phi_m [1/I(y_a) + 1.5/y_a](dn_a/dt) \quad , \tag{11E14}$$

with

$$y_a \equiv z_a e\phi_m / T_a \quad , \tag{11E15}$$

$$G(RZ_a) \equiv 1 + \left(\frac{1}{RZ_a}\right)^{1/2} \ln\left[\frac{(1 + 1/RZ_a)^{1/2} + 1}{(1 + 1/RZ_a)^{1/2} - 1}\right] , \tag{11E16}$$

$$I(y_a) \equiv 1 + \tfrac{1}{2}(\pi/y_a)^{1/2}\exp(y_a)[1 + \mathrm{erf}(y_a^{1/2})] \simeq 1 + 1/2y_a - 1/4y_a^2 + 1/8y_a^3 + \ldots \tag{11E17}$$

where ϕ_m is the potential barrier confronting the particles (ϕ_c or ϕ_e), and R is the magnetic mirror ratio, which is assumed to be large (Cohen, Rensink, Cutler, and Mirin, 1978). In writing particle and energy balance equations, other sources and losses (ionization, equilibration, rf heating, radiation, charge exchange, etc.) must be added to these Coulomb collision loss rates. The Coulomb collision times for ions and electrons are given by (cf. Eq. 2E49)

$$1/\tau_i = (e^4/4\pi\varepsilon_0^2) \sum_j Z_i^2 Z_j^2 n_j L_{ij}/m_i m_j v_i^3 \qquad (s^{-1}) \tag{11E18}$$

$$\Sigma_i \equiv \Big(\sum_j z_j^2 n_j L_{ij}\Big)/2\sum_j z_j^2 n_j L_{ij}(m_i/m_j) \tag{11E19}$$

$$v_i \equiv (2kT_i/m_i)^{1/2} \qquad (m/s) \qquad (kT_i \text{ in J}) \tag{11E20}$$

$$1/\tau_e = e^4 n_e L_{ee}/4\pi\varepsilon_0^2 m_e^2 v_e^3 \qquad (s^{-1}) \tag{11E21}$$

$$Z_e \equiv \tfrac{1}{2} + (\sum_j z_j^2 n_j L_{ej})/2n_e L_{ee} \tag{11E22}$$

$$v_e \equiv (2kT_e/m_e)^{\frac{1}{2}} \qquad (m/s) \qquad (kT_e \text{ in J}) \tag{11E23}$$

where the L_{ab} are Coulomb logarithms, and the summations run over ion species only. For electrons, $z_e = -1$, and ϕ_m is negative. The mean energy of escaping particles is

$$\overline{W}_a = Z_a e\phi_m + T_a \qquad (keV) \quad . \tag{11E24}$$

For the case of a *single species* of hydrogen ions,

$$z_i = 1,\ Z_i = \tfrac{1}{2},\ z_e = -1,\ Z_e = 1 \quad , \tag{11E25}$$

$$\tau_i = 64\pi\ \varepsilon_0^2 m_i^2 v_i^3/e^4 n L_{ii} \qquad (s) \quad . \tag{11E26}$$

If $T_e = T_i$ and if the confining potentials ϕ_m had equal magnitudes for electrons and ions (if $\phi_e \simeq \phi_c$) then

$$\frac{dn_e/dt}{dn_i/dt} \simeq \frac{2G(R/2)}{G(R)} \simeq 2 \tag{11E27}$$

The electrons undergo significant angular scattering in collisions with both ions and electrons, but ions are scattered significantly only in collisions with other ions, so the electron loss rate (for equal confining potentials) tends to be about twice as large as the ion loss rate.

To illustrate this mass effect, consider a smooth floor with ping-pong balls and golf balls spaced at regular intervals about ¼ m apart. If you roll a ping-pong ball along the floor, it will be deflected by collisions with both ping-pong balls and golf balls; but if you roll a golf ball across the floor, it will not be deflected significantly by collisions with ping-pong balls (although it will gradually be slowed down, as by electron drag).

EXAMPLE PROBLEM 11E1

Consider a tandem mirror device containing a deuterium plasma with $n_c = 10^{20}\ m^{-3}$, $\beta_c = 0.4$, $T_{ec} = T_{ic} = 20$ *keV*, $\phi_c = 40$ *keV*, $R_c = 8$, $R_p = 2$, $W_0 = 300$ *keV*, $T_{ep} = W_0/15$, $f_t = 0.9$, $\theta_i = \pi/2$, $V_p = 0.3\ m^3$, $\beta_p = 0.6$, *and assume* $\ln(W_0/W_L) \simeq 1$, $\phi_e/T_{ec} \sim 6$. *Find the attainable ion loss time from the central cell along the magnetic field* ($\tau_{\parallel}$), *the required plug ion density and beam injection power, and the required values of* B_c, B_m, *and* B_p. ($R_c \equiv B_m/B_c$) .

Numbers in parentheses refer to equations:

(11E20) $v_i = 1.385\times10^6$ m/s

(11E25) $Z_i = \frac{1}{2}$

Table 2E2 $L_{ii} = 21.8$

(11E26) $\tau_i = 64\pi(8.854\times10^{-12})^2(3.344\times10^{-27})^2(1.385\times10^6)^3/(1.602\times10^{-19})^4 10^{20}(21.8)$

$= 0.326$ s

(11E15) $y_i = 2$

(11E17) $I(y_i) = 1.200$

$R_c Z_i = 4$

(11E16) $G(R_c Z_i) = 2.444$

(11E13) $\tau_{ii} = \pi^{\frac{1}{2}}(0.326)2(2.444)\exp(2)/4(\frac{1}{2})1.200$

$\tau_{ii} = 8.7$ s

(11E3) $n_p = 7.39\times10^{20}$ m^{-3}

(11E9) $R_{eff} = 2\sin(\pi/2)/[1 + (40+120)/300] = 1.30$

Table 2E2 (using $n_p = 7.39\times10^{20}$ and $T_i \sim 2\times10^5$ eV) $L_{ii} = 23.3$.

(using $T_e = 2\times10^4$ eV) $L_{ie} = 17.2$

(11E7) $n\tau_{ii} = 1.01\times10^{20}$ m^{-3}s

(11E8) $n\tau_{ie} \simeq 1.04\times10^{20}$ m^{-3}s

(11E6) $n\tau_p \simeq 5.1\times10^{19}$ m^{-3}s

(11E10) $I_p = 510$ A

(11E11) $P_p = 340$ MW

Central cell pressure $p = nk(T_{ec} + T_{ic}) = 6.41\times10^5$ Pa

$B_c = (2\mu_0 p/\beta_c)^{\frac{1}{2}} = 2.01$ T

(11B6) $B_m/B_c = R_{vc} = R_c(1-\beta_c)^{\frac{1}{2}} = 6.20$, $B_m = 12.5$ T

(11E5) $B_p = B_m/R_p(1-\beta_p)^{\frac{1}{2}} = 9.9$ T

Thus, high magnetic fields (> 12 T), beam injection energies (> 200 keV), and beam powers are needed to sustain the end plugs. Increasing W_0 would decrease the required injection power P_p a little, but the neutral beam injectors become increasingly complex as the voltage is raised. The thermal barrier concept has been invented in order to permit operation at lower values of B_m, W_0, and P_p.

thermal barriers

A region of minimum electrostatic potential acts like a potential hill for electrons, because they are negatively charged. Rapid electron flow normally keeps T_e nearly uniform along magnetic field lines. However, if potential valleys can be established between the central cell and the end plugs, then electron flow will be impeded, and we can use microwave heating in the plugs to make $T_{ep} >> T_{ec}$. High values of T_{ep} will then provide large ϕ_c without requiring high values of n_p, as will be shown later.

One means of establishing such thermal barriers is illustrated in Fig. 11E4. A neutral beam is injected perpendicular to the magnetic field lines at point B_p. The trapped ions bounce back and forth between turning points B_p and B_p'. Because the sloshing ions slow down near the turning points, their density is larger there, and a double-humped density distribution is established (dotted curve). The density minimum at n_b produces an electrostatic potential minimum ϕ_b relative to the central cell.

Coulomb collisions would gradually change the sloshing ions' energies and pitch angles, tending to fill in the region of minimum density and potential, so the ions trapped there must be continuously removed.

A second neutral beam (the *pump beam*) may be injected at point b at a small angle relative to the magnetic field direction. Some trapped ions will be neutralized by charge exchange with the pump beam and lost. The pump beam ions will not be mirror-trapped, but will pass through the central cell and be reflected by the potential barrier ϕ_c at the other end. Thus, the pump beams help to remove trapped ions and to preserve a region of minimum ion density n_b, which is a region of minimum potential. The potential valley ϕ_b constitutes the *thermal barrier* to electron flow between the central cell and the end plug.

The plug electrons can now be heated with ECRH near point B_a to make $T_{ep} >> T_{ec}$. ECRH may also be used at point b (at a lower resonant frequency) to depress the electron density n_b^* there below the ion density n_b. Then the potential barrier is found from the Boltzmann relation to be

$$\phi_b = T_{ec} \ln(n_c/n_b^*) \quad . \qquad (11E28)$$

Similarly, the barrier $(\phi_b+\phi_c)$ between points b and p is approximately

$$\phi_b + \phi_c \simeq T_{ep} \ln(n_p/n_b^*)$$

according to simple theory. A more accurate treatment results in the equation

$$\phi_b + \phi_c = T_{ep} \ln[(n_p/n_b^*)(T_{ec}/T_{ep})^{\frac{1}{2}}] \quad . \qquad (11E29)$$

Subtracting (11E28) from (11E29), we find

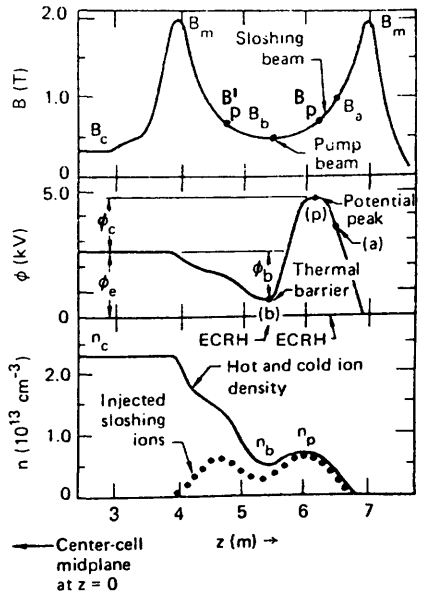

Fig. 11E4. Axial profiles of magnetic field (top), electrostatic potential (middle), and ion density (bottom) in the barrier and end plug regions with sloshing ions. From D. E. Baldwin et al, "Studies in Tandem Mirror Theory", 8th International Conference on Plasma Physics and Controlled Nuclear Fusion Research (Brussels, 1980), IAEA, Vienna, 1981, Fig. 1b.

$$\phi_c = T_{ep} \ln[(n_p/n_b^*)(T_{ec}/T_{ep})^{\frac{1}{2}}] - T_{ec} \ln(n_c/n_b^*) \quad . \tag{11E30}$$

EXAMPLE PROBLEM 11E2

If a thermal barrier is produced in the device of Example Problem 11E1 with $n_b^* = 10^{19}$ m^{-3} and T_{ep} = 100 keV, how large must n_p be to produce the same ϕ_c as before ? What is the new plug injection power ?

Solving Eq. (11E29) for n_p, we find

$$n_p = n_b^*(T_{ep}/T_{ec})^{\frac{1}{2}} \exp[(\phi_c/T_{ep}) + (T_{ec}/T_{ep}) \ln(n_c/n_b^*)] \quad . \tag{11E31}$$

which yields $n_p = 5.3 \times 10^{19}$ m^{-3}. This is a marked reduction from the original value of 7.4×10^{20} m^{-3}. Proceeding as before

Table 2E2 $L_{ii} = 24.6$, $L_{ie} = 20.1$

(11E7) $n\tau_{ii} = 9.53 \times 10^{19}$ m^{-3}s

(11E8) $n\tau_{ie} = 9.95 \times 10^{20}$ m^{-3}s (electron drag is small at high T_{ep})

(11E6) $n\tau_p = 8.7 \times 10^{19}$ m^{-3}s

(11E10) $I_p = 1.55$ A

(11E11) $P_p = 1.03$ MW.

Thus, the required beam current and power are greatly reduced by the thermal barrier.

---

power gain ratio

The main power inputs are now the powers required to maintain the thermal barrier (pump beam plus ECRH). Assuming that the pump beam power is dominant, the power gain ratio is

$$Q = \frac{P_f V_c}{2V_p P_p + 2V_p P_{ECRH} + 2V_b P_{pump}} \approx \frac{P_f V_c}{2V_b P_{pump}} \tag{11E32}$$

where P_f is the fusion power density in the central cell, V_c is its volume, and fusion reactions in the end plugs are ignored. The value of Q increases linearly with L_c, the central cell length, but for $L_c > 200$ m the total fusion power becomes enormous (over 10 GWth).

Taking $T_{ec} = T_{ic} = 30$ keV, central cell plasma radius $r_c = 1$ m, wall radius $r_w = 1.5$ m, and neutron wall loading = 3 MW/m^2, the plasma density is found to be $n_c = 1.4 \times 10^{20}$ m^{-3}. The required central cell magnetic field is then $B_c \simeq 2.1/\beta_c^{\frac{1}{2}}$ (T). Assuming $P_{pump} >> (P_p + P_{ECRH})$ and $B_m = 12$ T, Eq. (11E32) reduces to

$$Q \sim \frac{1}{[1.25(1-\beta_c)^{\frac{1}{2}} L_b/L_c \beta_c^{\frac{1}{2}} + 1/L_c]} \quad \text{(for DT fuel)} \quad . \qquad (11E33)$$

(Carlson et al, 1979). Estimates of Q from this equation are shown in Fig. 11E5 as functions of potential barrier length L_b and attainable β_c. The value of β_c has a strong influence on Q, so ballooning mode stability is an important issue. Values of Q from catalyzed DD fuel would be substantially lower.

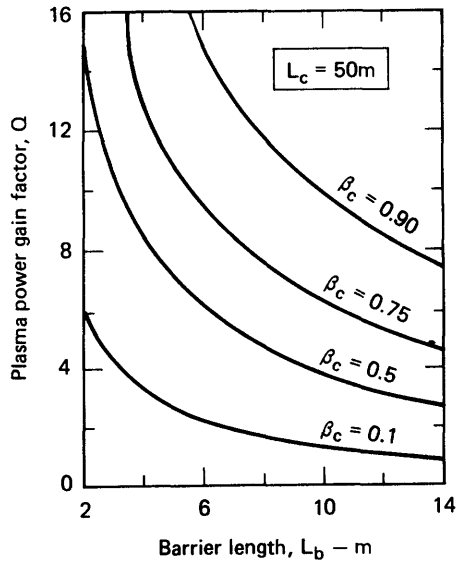

Fig. 11E5. Approximate power gain ratio Q attainable with DT fuel in a tandem mirror with thermal barriers, as a function of barrier length and central cell beta. From G. A. Carlson et al, "Tandem mirror reactor with thermal barriers", UCRL-52836 (1979), Fig. 2-2, p. 60.

If high central cell beta could be attained, DD fuel could be used in a tandem mirror reactor. With direct conversion of end-loss charged particle energy into electricity (Eq. 4C10) values of $Q \gtrsim 4$ would probably be satisfactory in view of the high values of Ψ_R for catalyzed DD reactions (Fig. 4C2).

Many other schemes are possible for establishing end plug plasmas and thermal barriers. Trapped ions may be pumped out of the barrier region by rf heating at the axial bounce frequency between mirrors (increasing $v_{\parallel}$). Ion cyclotron resonance heating (ICRH) may be used to help sustain end plug plasmas. Auxiliary mirror cells (A-cells) may be added at the ends to reduce losses from the plug mirrors by reducing the asymmetry of the plug ion loss boundaries (Fig. 11E2). Axisymmetric tandem mirrors based on a cusp ended solenoid, Fig. 11A4, may be used to attain higher β_c.

experiments

There are tandem mirror experiments at the University of Tsukuba, Japan; at Lawrence Livermore National Laboratory, Livermore, CA; at the University of Wisconsin, Madison; and at Novosibirsk, USSR.

Early studies with the Gamma 6 tandem mirror device at Tsukuba (B_c = 0.16 T, B_m = 1.0 T, B_p = 0.24 T, L_c = 2 m, W_0 = 10 keV, I_p = 3.5 A, ECRH at 2.45 GHz) demonstrated the following results:

* MHD stability
* potential increase in end plugs produced by neutral beam injection, consistent with the Boltzmann relation
* electron heating by axial injection of a 360 keV, 50 kA electron beam, increasing the plug potential
* enhancement of plug confinement by rf plugging (Section 17B).

The Tandem Mirror Experiment (TMX) at LLL has the parameters listed in Table 11E1. Thermal barriers are being added to TMX.

Table 11E1. Parameters of the Tandem Mirror Experiment (TMX) at Livermore.

central cell		*plasma*	
length L_c	= 5.5 m	duration	20-30 ms
field B_c	= 0.1 T	n_c	= 0.5-1x10^{19} m^{-3}
plasma volume V_c	= 0.4 m^3	$n\tau_c$	= 2-7x10^{16} $m^{-3}s$
end plugs		T_{ep}	= 0.1-0.26 keV
plug field B_p	= 1.0 T	T_{ec}	= slightly less than T_{ep}
maximum field B_m	= 2.0 T	n_p	= 1-4x10^{19} m^{-3}
plasma length L_p	= 0.4 m	average W_{ip}	= 11 keV
plasma radius r_p (at half-maximum density)	= 0.07 m	ϕ_c	= 0.1-0.3 keV
		ϕ_e	= 0.1-0.3 keV
plasma volume V_p	= 0.063 m^3	T_{ic}	= 0.04-0.25 keV
beam energy W_0	= 17 keV	β_c	~ 0.1
mean energy per beam atom	= 13 keV		
plug power P_p	= 5.2 MW		
trapped power $f_t P_p$	= 0.4 MW		

MFTF-B

The MFTF-B experiment at LLL, illustrated in Fig. 11E6, is to begin operation in 1984. Its axial magnetic field profile, plasma density, and electrostatic potential are illustrated in Fig. 11E7. The distance between A-cell maximum fields is about 50 m. A thermal barrier is produced by a sloshing ion distribution in the A-cell, combined with pump neutral beams to remove trapped ions by charge exchange, ECRH at 28 GHz to trap electrons in the center of the A-cell (reducing the potential), and ECRH at 60 GHz to heat electrons outboard of the thermal barrier. The high plasma density produced by neutral beam injection in the Yin-Yang cell at point B helps to ensure MHD stability of the system.

The device will be started up by 60 MW of 80 keV neutral beams lasting 0.5 s, and sustained by 28 MW of 80 keV beams lasting 30 s. The plasma duration of 30 s is a great increase over the 30 ms duration of the TMX plasmas (1979). Anticipated central cell plasma parameters are density $n_c \simeq 2\text{x}10^{19}$ m^{-3}, ion temperature $T_{ic} \simeq 15$ keV, and confinement time τ_c of several seconds (in contrast to several ms for TMX), and potential barriers as illustrated in Fig. 11E7. Thus, the MFTF-B plasma will be near break-even conditions.

Component reliability is an important problem, in view of the large numbers of components having finite failure probabilities. The goal is to attain 70 % overall availability, meaning that the facility should be able to operate 70 % of the 80 hours per week planned for experiments. Operations will be coordinated by computers with operator control by touch-sensitive panels and computer-graphics

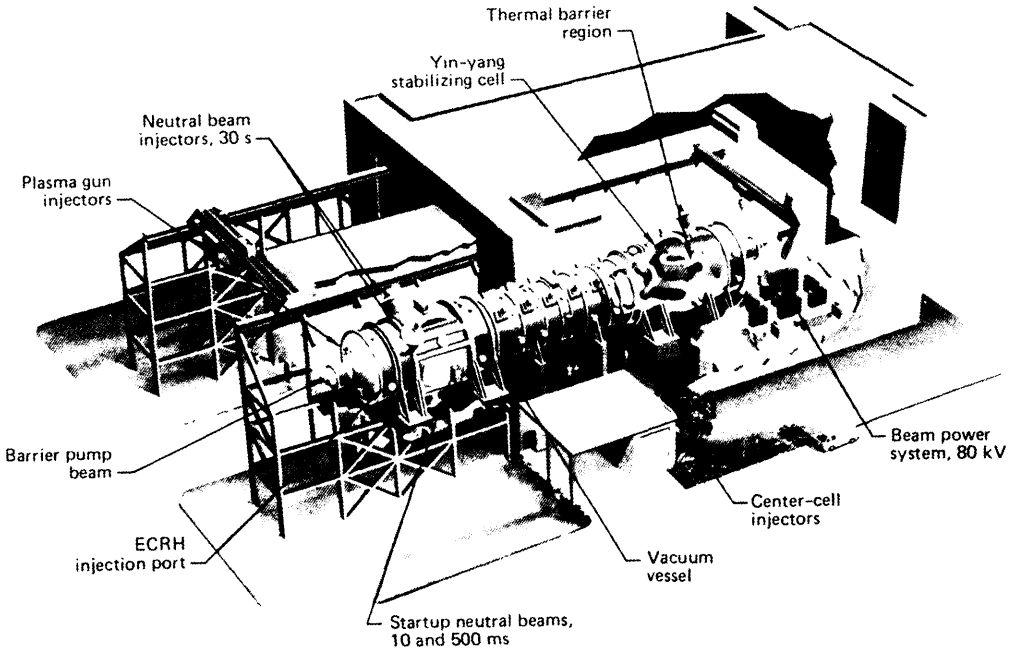

Fig. 11E6. Artist's rendering of the finished MFTF-B, showing necessary additions to the existing building. From Energy and Technology Review, LLNL, July, 1980, Fig. 4, p. 6.

color displays showing the status of equipment, with fiber optic communications between the device and the control building.

The main technological developments needed for MFTF-B are

* extension of neutral beam pulse lengths to 30 s
* beam dumps capable of handling sustained high power fluxes
* powerful 60 GHz gyrotrons for ECRH to produce the potential peaks
* coordination and reliability of large numbers of components.

Some ideas for *axisymmetric* tandem mirror plugs are shown in Fig. 11E8. Particles in axisymmetric devices have drift orbits which are confined better than those in devices lacking axisymmetry, such as tandem mirrors with Yin-Yang plugs. The circular coils of an axisymmetric device would be simpler to wind, and the coil forces would be easier to support.

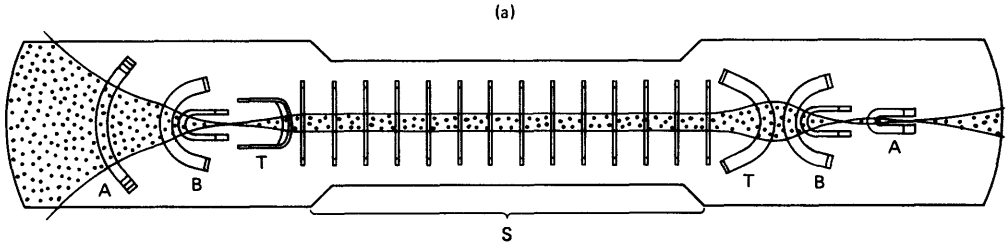

Fig. 11E7. ***Summary profiles of the MFTF-B fields, potentials, and plasma density in relation to the magnet array. (a) Plan view of the magnet array and magnetic regions. In addition to the solenoid (S) and the minimum-B mirrors (B), this array has transition coils (T) to flatten the cylindrical plasma from the solenoid to fit the yin-yang geometry. An auxiliary coil at either end (A) improves the confinement by heating electrons behind a thermal barrier. (b) The magnetic field, showing variations that form magnetic mirrors. (c) The electrostatic potential, showing a minimum in the A cell that separates electrons beyond the barrier from those in the central parts of the MFTF-B. The potential peak is created by electron-cyclotron resonance heating (ECRH) power applied at 60 GHz at the peak, and the minimum is enhanced by 28-GHz ECRH power there. (d) The ion density profile, showing the hot-ion peak in the yin-yang cell (required for MHD stability and maintained by neutral beam injection) and the relatively modest ion density in two peaks in the A cell. The trough between the two density peaks in the A cell creates the potential minimum that makes a thermal barrier. Beams of neutral atoms injected at A, B, and C interact with the plasma, heating it and making up losses.***

From Energy and Technology Review, LLNL, July, 1980, p. 4, Fig. 2.

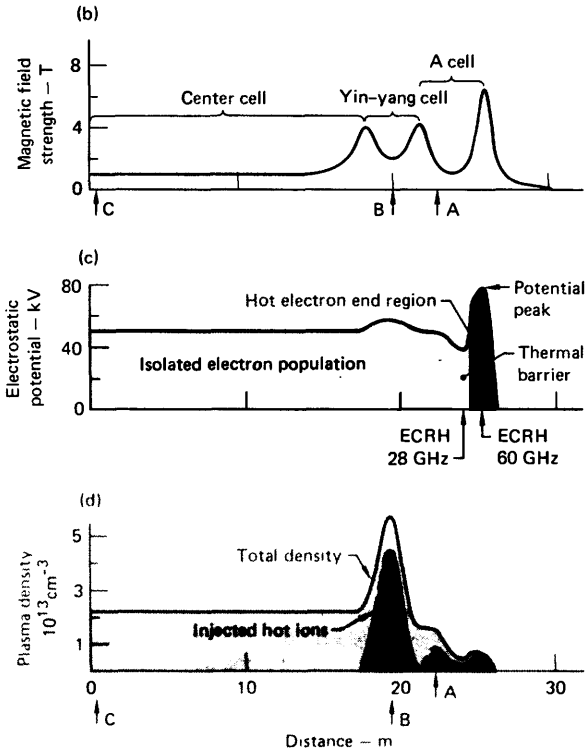

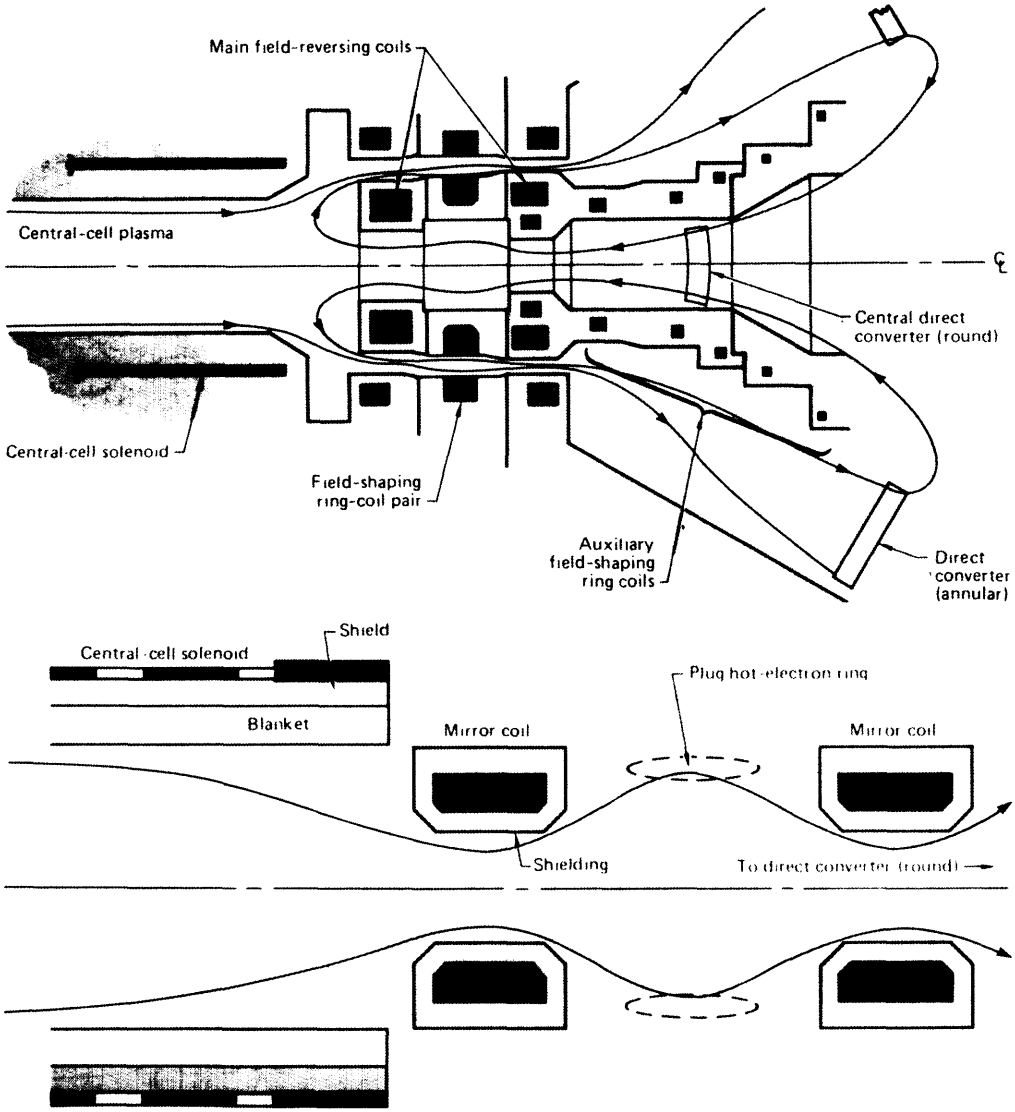

Fig. 11E8. An axisymmetric tandem mirror end plug with cusp fields (top), and one with a hot electron ring (bottom). The favorable magnetic curvature of the cusp fields (like a cusp-ended solenoid) enhances MHD stability, enabling higher values of beta to be sustained in the central cell. Pump neutral beams and ECRH (not shown) could establish thermal barriers. The simple mirror cell (bottom) uses ECRH to establish a ring of high-energy (MeV) electrons, which provides MHD stability and a potential barrier, as in EBT (Section 14D).From G. A. Carlson, Energy and Technology Review, June 1981, Fig. 2, p. 12-13.

11F. Field Reversed Mirrors

concept

The concept of a field-reversed configuration is illustrated in Fig. 11F1. If the plasma current is strong enough, the magnetic field direction along the axis will be reversed. A compact toroidal plasma configuration may result, but field reversal alone is not enough to ensure that the field lines are closed.

The plasma shape may be described in terms of a magnetic flux function $\psi \equiv rA_\theta$ where r is the minor radius and A_θ is the azimuthal component of the magnetic vector potential (Section 8C). The spherical Hill vortex

$$\psi = \begin{cases} (-3B_0 r^2/4a^2)(a^2-R^2) & R < a \\ (B_0 r^2/2)(1 - a^3/R^3) & R > a \end{cases} \qquad (11F1)$$

$R \equiv r^2 + Z^2$ is sometimes used to provide a simplified model of a field reversed plasma configuration. The flux surfaces for this case are illustrated in Fig. 11F2. There are null points at the intersection of the $\psi = 0$ surface with the z axis. Ion trajectories in a Hill vortex are described by Wang and Miley (1979). Typical paths are illustrated in Fig. 11F3. Usually the ion Larmor radii are smaller than the plasma minor radius ($\rho_i < a$).

production

One measure of field reversal is $\Delta B/B_{vac}$, where ΔB is the change in the magnetic field on the axis and B_{vac} is the vacuum magnetic field there. (A value $\Delta B/B_{vac} > 1$ would constitute field reversal.)

Field reversed plasma configurations may be produced by many means, including:

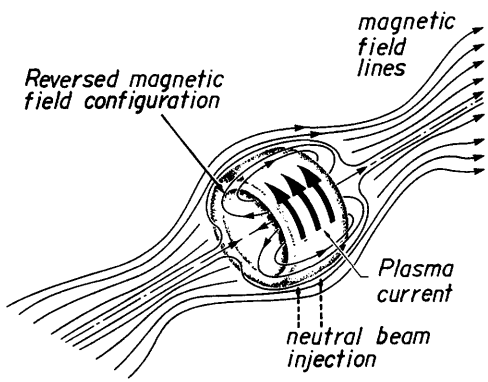

Fig. 11F1. Magnetic field lines in a field reversed mirror. External coils are not shown. From R. F. Post, "Physics of mirror fusion systems", Proceedings of 2nd ANS Topical Meeting on the Technology of Controlled Nuclear Fusion, CONF-760935 (1976).

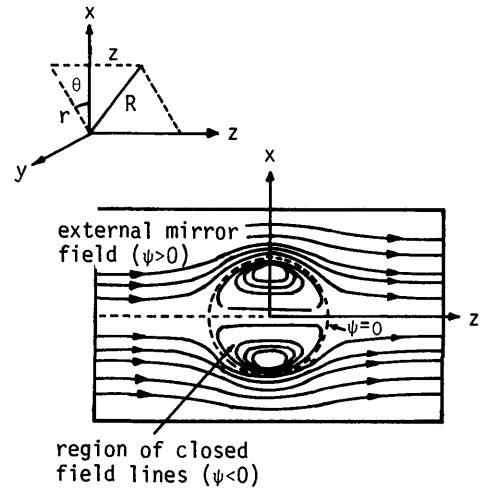

Fig. 11F2. Magnetic field lines of the Hill spherical vortex model of a field reversed mirror plasma. From M. Y. Wang and G. H. Miley, "Particle orbits in field-reversed mirrors", Nuclear Fusion 19, 39-49 (1979), Fig. 1.

* neutral beam injection into a target plasma
* coaxial plasma guns
* conical theta pinch plasma guns
* a theta pinch with reverse bias field (Chapter 12)
* injection and trapping of relativistic electron beams or ion beams in a magnetic mirror or cusp
* other magnetic pinch geometries.

In the Beta-II experiment at LLL, injection of up to 500 A of neutral beams into a target plasma produced values of $\Delta B/B_{vac} = 0.9$ at $B_{vac} = 0.44$ T, in agreement with predictions. However, at $B_{vac} = 0.67$ T, confinement was degraded by ion-cyclotron-frequency microinstabilities, and $\Delta B/B_{vac} = 0.6$.

Production of a field-reversed plasma ring by a coaxial plasma gun, illustrated in Fig. 11F4, has been done in the Beta-II device with $\Delta B/B_{vac} \sim 4$ and ring current $\sim$ 100-200 kA. In order to make the magnetic field lines break and reconnect around the plasma, a special electrode structure may be used. A computer simulation of a field-reversed ring produced by a coaxial plasma gun is illustrated in Fig. 11F5. It is desirable to heat and sustain the plasma ring by neutral beam injection. A computer study predicts significant plasma expansion during neutral beam heating, resulting in a decrease of plasma density. An analytical estimate of the energy confinement time of a Hill's vortex model plasma fueled at the null is

$$\tau_E \simeq 0.04(r_0/\rho_i)^2\tau_i \qquad (11F2)$$

where r_0 is the separatrix radius, ρ_i is the average ion Larmor radius at the plasma center, and τ_i is the ion-ion collision time (Anderson et al, 1980). Stability analyses, however, indicate that plasmas with small (r_0/ρ_i) tend to have better MHD stability.

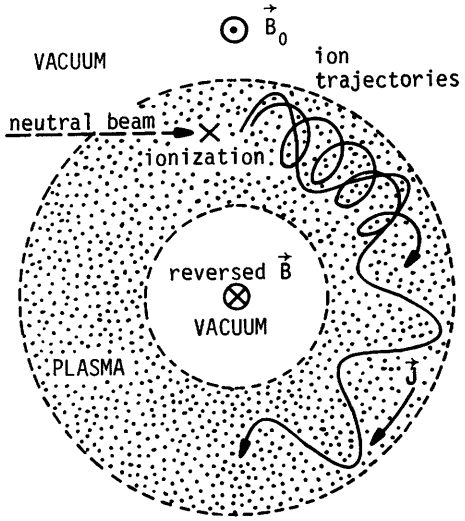

Fig. 11F3. Typical ion trajectories in a field reversed mirror plasma (end view).

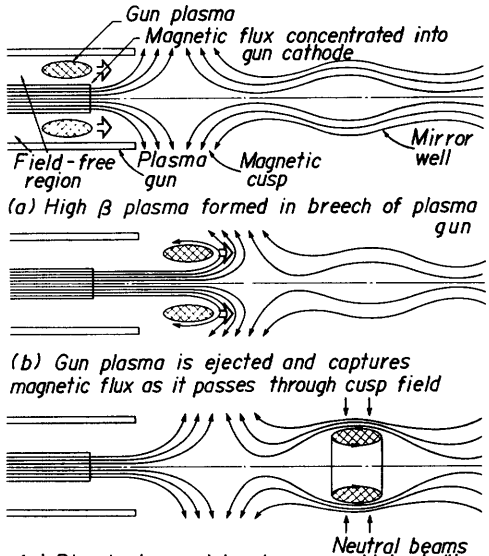

Fig. 11F4. Formation of a field reversed plasma by a coaxial plasma gun. From G. A. Carlson et al, "Conceptual design of the field-reversed mirror reactor", UCRL-52467 (1978), Fig. 3-6.

reactor concepts

A hypothetical reactor plasma has been studied using the model of Fig. 11F6 with the following assumptions:

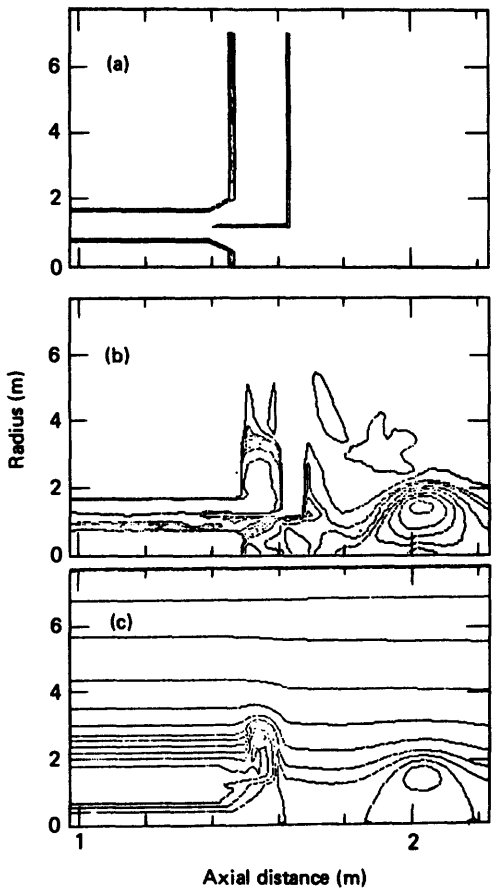

Fig. 11F5. MHD simulation calculation of production of a field-reversed ring by a modified plasma gun: (a) geometry of the gun and the auxiliary "divider" electrode in r - Z coordinates; (b) contour plot of plasma density at 17.0 μs; (c) contour plot of the poloidal flux function at the same time. From D. V. Anderson et al, "Theory of field-reversed mirrors and field-reversed plasma-gun experiments", Proceedings of the Eighth International Conference on Plasma Physics and Controlled Nuclear Fusion Research (Brussels, 1980), IAEA, Vienna, 1981.

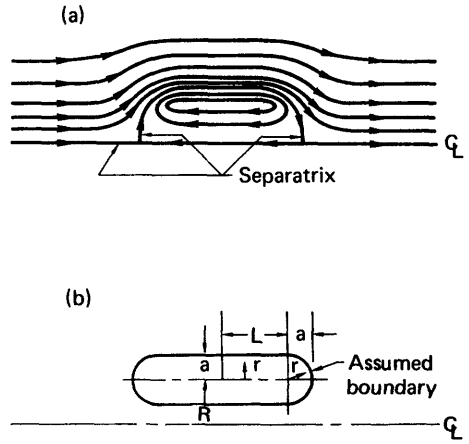

Fig. 11F6. Cross section of the model field-reversed plasma layer. From G. A. Carlson et al, UCRL-52467 (1978), Fig. 2-1.

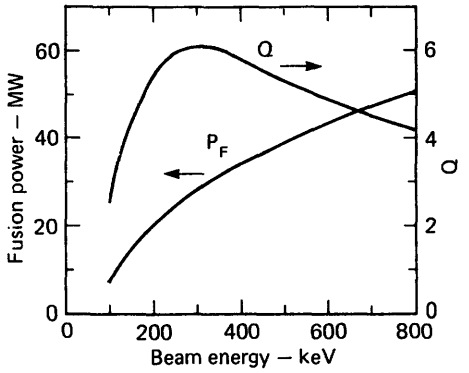

Fig. 11F7. Estimates of fusion power and Q for a field-reversed mirror. From G. A. Carlson et al, UCRL-52467 (1978), Fig. 2-5.

* $n = n_0[1 - (r/a)^3]$, where n_0 is the density at $r = 0$
* temperatures are nearly uniform and heat conduction is small
* $a/\rho_i \simeq 5$
* $L/a \simeq 6$
* $\beta = 1.5$
* transport processes occur on a τ_i scale (classical scaling was also studied)
* about 10 % of the alpha particle energy is retained in the plasma.

The resulting variations of fusion power and power gain ratio Q with neutral beam injection energy W_0 are shown in Fig. 11F7. At W_0 = 300 keV, the average ion and electron energies are W_i = 150 keV, W_e = 70 keV, and the required magnetic field is B_{vac} = 7 T. If

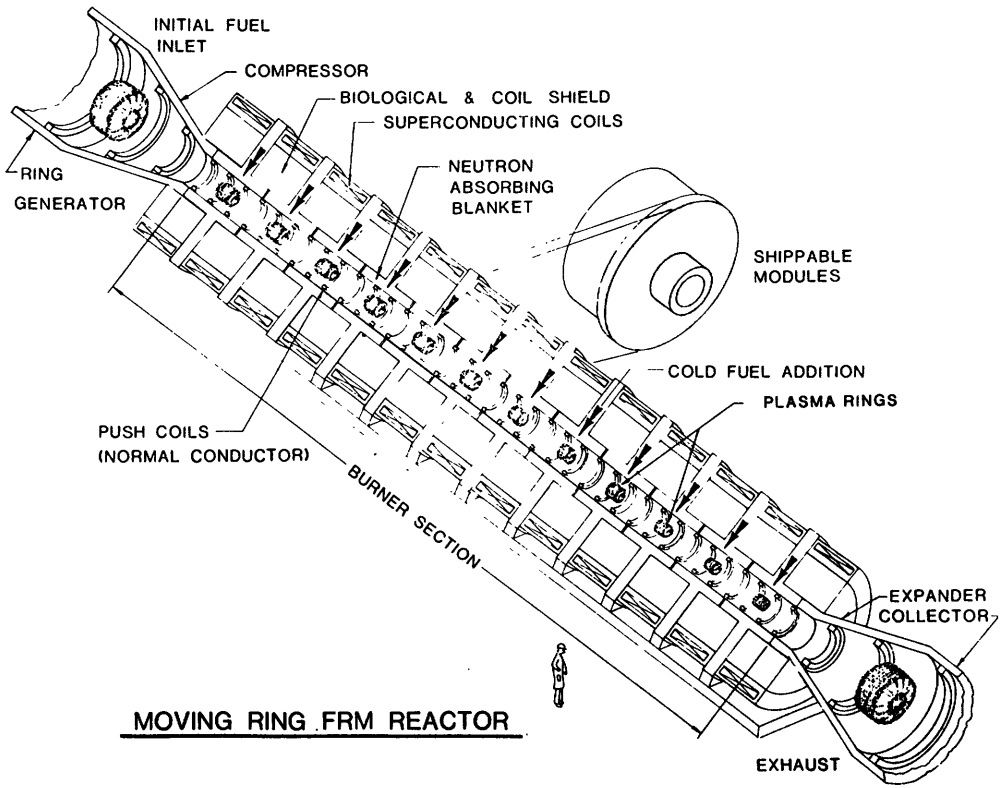

Fig. 11F8. A moving ring field-reversed mirror reactor. From G. A. Carlson, et al., EPRI ER-1045 (1979).

a cool plasma layer around the ring causes significant ion heat conduction losses, the peak Q value decreases by about 20 %; and Q also decreases if lower fractions of the alpha particle power are retained in the plasma. Higher Q values are feasible if confinement scaling is classical, or if $(a/\rho_i) > 5$ may be attained without MHD instability. Field reversed plasmas offer the hope of low power (20 - 50 MW), compact fusion reactors at reasonable direct capital costs.

The concept of a moving-ring field reversed mirror (FRM) reactor is illustrated in Fig. 11F8. The plasma rings may be compressed and heated by forcing them into an increasing (converging) magnetic field.

11G. Multiple Mirrors

configuration

A multiple mirror configuration is illustrated in Fig. 11G1. Consider the case of an ion starting out in the loss cone of one of the central mirror cells. There are three limiting cases, with regard to the size of the ion scattering mean free path λ_i, the mirror cell length L_c, the mirror ratio R, and the total device length L:

$\lambda_i > L$ Ions in the loss cone will flow freely out the ends of the device, just as for ordinary mirrors. Confinement times will be short, limited by ion scattering and electron drag.

$\lambda_i \sim RL_c$ Ions in the loss cone of one mirror cell may be scattered out of the loss cone as they pass through a neighboring cell. When scattering back into the loss cone, the ion could go either left or right. The axial motion has a random walk character (Section 8F), which may be described by a diffusion equation. Much longer confinement times are attainable.

$\lambda_i < L_c$ Ions undergo multiple scattering in each cell. The flow may be described by MHD equations.

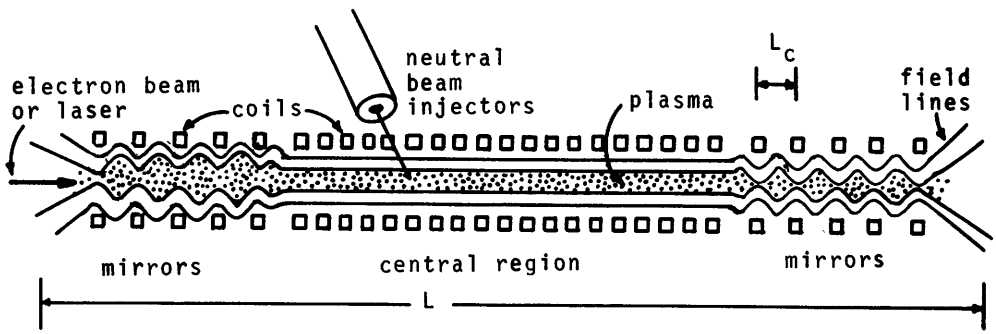

Fig. 11G1. A multiple mirror device. End losses from the central region are impeded by diffusive flow through multiple mirrors at the ends. Ioffe bars may be added to provide better MHD stability.

The intermediate regime ($\lambda_i \sim RL_c$) is desirable for multiple mirror operation. The mean free path for deuterons (Eq. 2E56) is

$$\lambda_i = \tau_i v_i \simeq 10^{22} T_i^{3/2}/n \quad (m) \qquad (11G1)$$

where v_i is the average ion speed (m/s), T_i is the ion temperature (keV), and n is the plasma density (m^{-3}). For example, if $n = 10^{20}$ m^{-3} and $T_i = 10$ keV, then $\lambda_i \simeq 3$ km. In order to use reasonable mirror cell lengths ($L_c \sim 3$-10 m) at thermonuclear temperatures, very high plasma densities $n \sim 10^{23}$-10^{24} m^{-3} are needed. These high plasma densities make the plasma pressure very high. For example, if $n \sim 10^{23}$ m^{-3} and $T_e = T_i = 10$ keV, then $p = 300$ MPa = 3000 atm. If $\beta = 1$, then the required magnetic field would be $B = (2\mu_0 p/\beta)^{1/2} = 28$ T. For a vacuum mirror ratio of 2, the peak field would be twice as high. The maximum practical steady-state magnetic field is on the order of 30 T. There are therefore two alternative modes of operation:

* steady state burn, with $n \sim 10^{23}$ m^{-3}, $T_i \lesssim 10$ keV, $\beta \sim 0.8$, and continuous refueling
* pulsed burn, with $n \sim 10^{24}$ m^{-3}, $T_i > 10$ keV, $\beta >> 1$, and refueling between pulses.

steady state mode

A steady-state reactor with $T \sim 5$ keV, $n \sim 0.8 \times 10^{23}$ m^{-3}, $L \sim 400$ m, $R \sim 3$, and $\beta \sim 0.8$, heated and fueled by neutral beams, could attain a power gain ratio $Q \sim 3$ (Yang and Lieberman, 1977). To have a net output power of 3 GWe, the required plasma radius would be 1.5 cm, and the peak magnetic field would be about 30 T. Multiple mirror experiments with $n \sim 10^{19}$ m^{-3}, $T \sim 0.01$ keV, $\lambda_i \sim RL_c \gtrsim 0.5$ m have demonstrated axial density profiles consistent with theory (Tuszewski, Lichtenberg, and Eylon, 1977).

pulsed mode

Values of $\beta >> 1$ may be used for pulsed plasmas. In this case the magnetic field does not fully confine the plasma pressure, but it reduces radial heat flow and slows plasma expansion as the field lines are compressed between the plasma and a conducting wall. The plasma density and magnetic field are highest at the wall, as shown in Fig. 11G2. The plasma may be heated up to ignition temperature by axial injection of a relativistic electron beam (1 MA, 1 MeV,

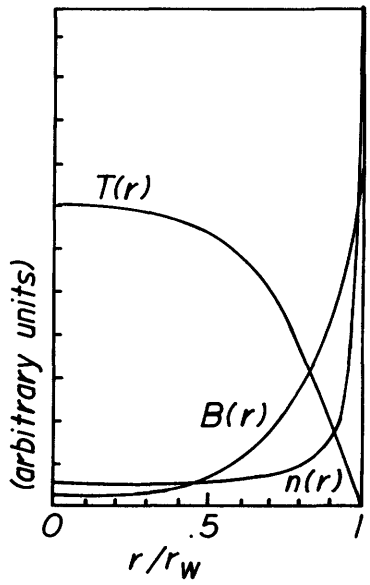

Fig. 11G2. Variation of plasma density and temperature and magnetic field with radius in a $\beta >> 1$ multiple-mirror confined plasma at the moment of ignition. Plasma expansion pushes the magnetic field lines outwards, compressing them and increasing B near the walls, since the field lines cannot penetrate quickly into the conducting liner.

100 μs) or CO_2 laser beam. Assuming transport at the Bohm rate, a reactor might have $n \gtrsim 3\times10^{23}$ m^{-3}, T ∿ 20 keV, L ∿ 20 m, plasma radius ∿ 0.05 m, β ∿ 100, and confinement time τ ∿ 0.5 ms. If radial transport were slower than the Bohm rate, then smaller radii and weaker magnetic fields would suffice.

11H. Rotating Plasmas

One scheme for producing a rotating plasma is illustrated in Fig. 11H1. Electrodes placed at the ends of a magnetic mirror establish a radial electric field, which causes a plasma rotation with velocity $\vec{v}_E = \vec{E}\times\vec{B}/B^2$. By flux conservation,

$$r_k^2/r_0^2 = B_0/B_m \equiv 1/R. \tag{11H1}$$

The rotational kinetic energy alters the loss boundary from the hyperboloid of Eq. (11B3) to

$$v_{\parallel 0}^2 = v_{\perp 0}^2(R - 1) - (2q/m)(\phi_0 - \phi_m) + V_{E0}^2(1 - r_k^2/r_0^2) \tag{11H2}$$

(magnetic mirror) (electrostatic) (rotational)

where the subscript 0 refers to the center of the device (z = 0), the subscript m refers to the region of maximum magnetic field, and R is the magnetic mirror ratio. (Bekhtenev et al, 1980). This loss boundary is illustrated in Fig. 11H2. The electrostatic potential in the plasma adjusts itself so that the electron and ion loss rates are equal. From this condition the potential barrier retarding ion escape is found to be

$$U_i \simeq (R - 1)T_i \tag{11H3}$$

The ion loss time along magnetic field lines increases (over that for a simple mirror) approximately as $\exp(U_i/T_i)$.

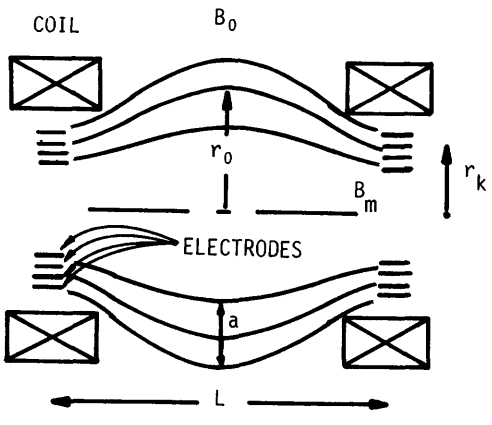

Fig. 11H1. A rotating plasma device. Ring electrodes at the ends establish a strong radial electric field.

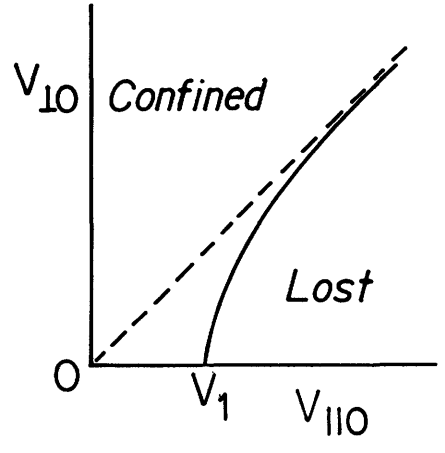

Fig. 11H2. Loss hyperboloid for ions in a rotating plasma.

$$V_1 = [-(\tfrac{2q}{m})(\phi_0-\phi_m) + V_{E0}^2(1 - 1/R)]^{\frac{1}{2}} .$$

A reactor could have $n \sim 3\times10^{19}$ m^{-3}, $T \sim 30$ keV, $\beta \sim 0.25$, $a/r_0 \sim 0.2$, $B_0 \sim 2$ T, $r_0 \sim 3$ m, and $L \sim 4r_0$. With total voltage drop across the electrodes of several MeV, power gain ratios $Q \gtrsim 10$ appear to be attainable, facilitated by recovery of part of the ion energy by the electrodes. The centrifugal force aids in removal of impurities.

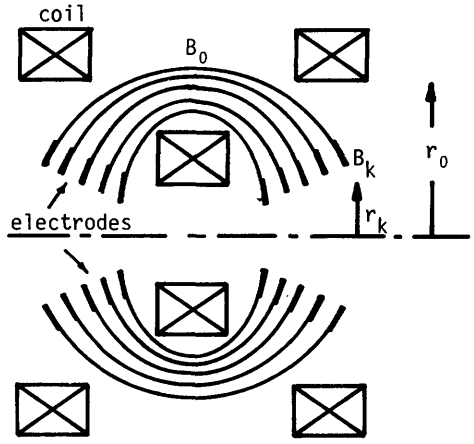

Fig. 11H3. A centrifugal trap.

The longitudinal current tends to stabilize the plasma against flute modes, but high current densities are required in small experiments. Plasma stability in large devices is uncertain. The high electric fields required at the electrodes ($\sim$ 100 kV/cm) may lead to high voltage breakdown problems. The centrifugal trap illustrated in Fig. 11H3 alleviates this problem somewhat by spreading the electrodes further apart. If successful, such reactors would have the advantage of being available in small sizes (P < 100 MWe).

11J. Cusps

confinement

The particle distribution functions may be expressed in terms of the Hamiltonian H, the angular momentum p_θ, and the magnetic moment μ:

$$f = f(H, p_\theta, \mu) \tag{11J1}$$

where

$$H \equiv \tfrac{1}{2}mv^2 + q\phi = \text{kinetic energy + potential energy} \tag{11J2}$$

$$p_\theta \equiv mrv_\theta + qrA_\theta \tag{11J3}$$

$$\mu \equiv \tfrac{1}{2}mv_\perp^2/B \quad , \tag{11J4}$$

in which m, q, and $\vec{v}$ are the particle's mass, charge, and velocity, ϕ and $\vec{A}$ are the scalar and vector potentials, and θ is the azimuthal direction. In the absence of collisions, H and p_θ are constants, and μ may be invariant if B is large. In terms of these variables we can distinguish several groups of particles:

* untrapped particles
* particles trapped magnetically by conservation of μ
* particles trapped electrostatically by conservation of H
* particles trapped by conservation of p_θ

In the case of large rf fields, a quasipotential term arises, permitting rf trapping, too. For a given magnetic field geometry and plasma potential, one can define loss boundaries similar to those for magnetic mirrors, but more complicated.

Because B is small inside a high-beta plasma, μ is less likely to be conserved there than around the edges, where B is large. Thus, many particles around the edges may be adiabatically trapped, while few near the center are. Loss times for magnetically trapped particles are essentially mirror loss times, as in Eq. (11E6). An orbit of a p_θ trapped particle is illustrated in Fig. 11J1.

Electrostatically trapped particles have loss times dependent upon the ratio of potential barrier height ϕ_m to their temperature, as in Eq. (11E13).

untrapped particles

Untrapped particles have confinement times limited by their flow rates and the effective cusp apertures.

The ion confinement time may be estimated from Eq. (8G1)

$$\tau = \frac{\text{(number of ions)}}{\text{(ion loss rate)}} = \frac{nV}{\Gamma A} \qquad \text{(11J5)}$$

where Γ is the loss flow rate (ions/m^{2}s), A is the area of the "hole" through which the ions are lost, n is the average plasma density, and V is the plasma volume. (The electron confinement time will be the same as the ion confinement time, by quasineutrality.) For free flow through an aperture,

$$\Gamma = \tfrac{1}{4}\, nu$$

where

$$u = (8kT_i/\pi m_i)^{1/2}$$

is the average ion speed. The loss area of a ring cusp is approximately

$$A_{ring} = (2\pi R)(2\delta) \qquad \text{(11J6)}$$

where R is the ring cusp radius and δ is the half-width of the ring gap, called the "sheath thickness". For a spindle cusp, let $\alpha \equiv A_{point}/A_{ring}$, where A_{point} is the effective loss area of the two point cusps. Assuming that $\alpha \simeq 1$, the expression for the confinement time in a spindle cusp becomes

$$\tau \simeq \frac{V}{2\pi u R \delta} \quad \text{(s)} \quad . \qquad \text{(11J7)}$$

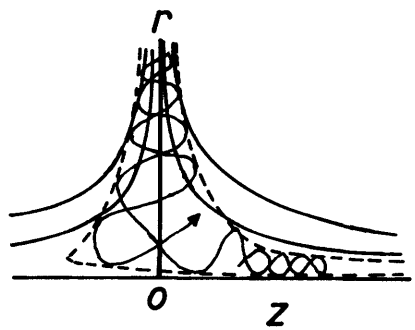

Fig. 11J1. Orbit of a trapped particle in a spindle cusp. Motion in the θ direction is not shown in this r-z plot. The dashed curve represents the boundary of the allowed region of space.

Similar estimates apply to other cusp geometries.

sheath thickness

Ion viscosity effects may be important in broadening the sheath. If the effect of ion viscosity is included and the time derivative and inertia terms are ignored, the MHD equation of motion (5D39) may be written

$$\vec{\nabla}p = \vec{J}\times\vec{B} + \tfrac{\mu}{3}\vec{\nabla}(\vec{\nabla}\cdot\vec{u}) \quad . \qquad \text{(11J8)}$$

where μ is the ion viscosity. Ignoring $E_\perp$ in Ohm's Law (5D38), we find

$$\vec{J}_\perp = \vec{u}\times\vec{B}/\eta_\perp \tag{11J9}$$

We can estimate the magnitude of the viscosity term by approximating the derivatives by $|\nabla| \simeq 1/\delta$. Thus, for very thin sheaths, the viscosity effect will be dominant. The sheath will broaden until the viscosity term is comparable in magnitude to the $\vec{J}\times\vec{B}$ term:

$$uB^2/\eta_\perp \simeq \frac{\mu u}{3\delta^2} \quad ,$$

from which

$$\delta^2 \simeq \frac{\mu\eta_\perp}{3B^2} \quad . \tag{11J10}$$

For the viscosity and resistivity we may substitute the expressions

$$\mu = nkT_i/\nu_i$$

$$\eta_\perp = m_e\nu_e/ne^2 \quad , \tag{11J11}$$

where ν_i and ν_e are effective collision frequencies of ions and electrons, m_e is the electron mass, and e is the electronic charge. For a turbulent sheath with electrostatic wave energy density W, the effective collision frequencies are given by

$$\nu_e = \frac{W}{nkT_e}\left(\frac{n_e^2}{m_e\varepsilon_0}\right)$$

$$\nu_i = \frac{W}{nkT_i}\left(\frac{n_e^2}{m_i\varepsilon_0}\right) \tag{11J12}$$

where ε_0 is the permittivity of free space (Haines, 1977). If we substitute Eqs. (11J11), (11J12) into (11J10) and use the definitions $\rho_e \equiv (2m_ekT_e)^{1/2}/eB$, $\rho_i \equiv (2m_ikT_i)^{1/2}/eB$, the resulting sheath thickness is

$$\delta \simeq \frac{1}{\sqrt{6}}\left(\frac{T_i}{T_e}\right)^{\frac{3}{4}}(\rho_i\rho_e)^{1/2} \quad . \tag{11J13}$$

Thus, this estimate yields a sheath thickness on the order of the *hybrid Larmor radius* $(\rho_e\rho_i)^{1/2}$. A similar result is obtained if classical Coulomb collision frequencies are used instead of the turbulent values. This estimate of the sheath thickness is probably not correct under all conditions, however. There have been theoretical estimates as small as ρ_e and as large as ρ_i. (The sheath thickness is probably influenced by the perpendicular electric field: large inward $E_\perp$ may tend to reduce δ by inhibiting ion penetration into the sheath, etc.)

From Eq. (11J7) with any kind of Larmor radius sheath thickness, it can be shown that

$$n\tau \propto nVB/RT^{3/2} \quad . \tag{11J14}$$

Thus, high temperature plasma is more rapidly lost (because of higher flow speed and wider gap widths), and confinement increases only linearly with B, in contrast to the B^2 dependence of toroidal confinement. Large-volume, high-density systems are advantageous.

EXAMPLE PROBLEM 11J1

Assuming $\delta \simeq (\rho_e \rho_i)^{\frac{1}{2}}$, *estimate the initial density decay time of deuterium plasma in a spindle cusp with R = 1 m, V = 0.1 m*^{3}, *B = 5 T,* $T_e = T_i = 10$ *keV.*

For this case, we find $\rho_e = 6.44 \times 10^{-5}$ m, $\rho_i = 4.09 \times 10^{-3}$ m, $\delta \simeq 5.13 \times 10^{-4}$ m. The average speed $u = (8kT_i/\pi m_i)^{\frac{1}{2}} = 1.10 \times 10^6$ m/s. Then, from Eq. (11J7) we find $\tau = 28$ μs. Since the untrapped plasma leaves first, this will be the initial density decay time scale. (Other cusp geometries could provide larger ratios of V/R, hence longer τ.)

Cusp confinement times may be improved by:

* application of an additional magnetic field component to avoid field nulls and make the plasma confinement adiabatic (conserving μ). For this case the free streaming losses are avoided, and particles on open field lines are lost at the mirror rate. There may be an interior region with better confinement in some geometries, such as TORMAC.
* application of electrostatic potential barriers, as in electromagnetic traps (Chapter 17) and axisymmetric tandem mirrors.
* application of rf potential barriers, as in rf plugging (Chapter 17).
* use of imploding metallic liners to attain ultrahigh magnetic cusp fields.

TORMAC

A couple of "Toroidal Magnetic Cusp" (TORMAC) geometries are illustrated in Fig. 11J2. Plasma ions in the sheath are confined in a mirror-like magnetic field, with a corresponding loss time $\sim \tau_i/2$. Plasma ions from the central plasma with volume V must move into the sheath with volume V_s in order to be lost. Therefore, the average confinement time can be estimated from the equation

$$n_i V/\tau \simeq n_i V_s/.5\tau_i \tag{11J15}$$

The thickness of the sheath region is assumed to be about $2\rho_i$, so the volume ratio is $V_s/V \simeq 2\pi r_p(2\rho_i)/\pi r_p^2 \simeq 4\rho_i/r_p$, where r_p is the radius of an equivalent circular plasma. Thus, the confinement time is roughly

$$\tau \simeq 0.1\, \tau_i\, r_p/\rho_i \simeq 5 \times 10^{17} r_p T_i B/n \tag{11J16}$$

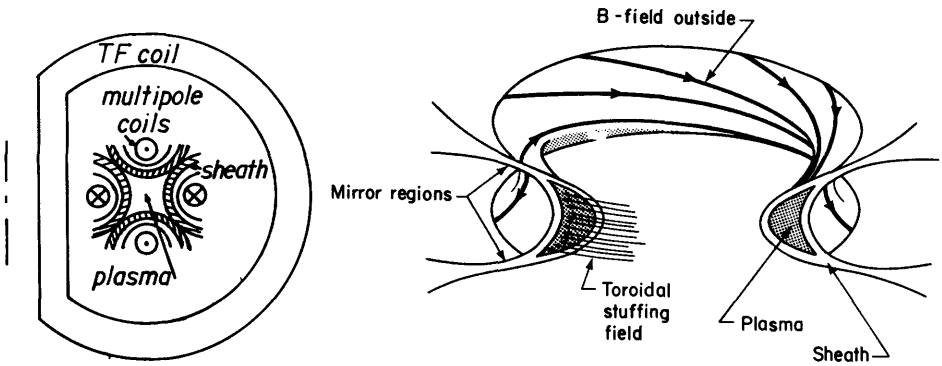

Fig. 11J2. Tormac geometries. a. Toroidal multipole cusp with added toroidal field. b. The bounding surface of a toroidal "bi-cusp" tormac plasma (coils not shown). From Brown, Kunkel, and Levine (1977), Fig. 1.

for deuterons, with T_i in keV and B in Tesla. A slightly more accurate expression is given by

$$n\tau \simeq 4\times10^{17}\ r_p B T_i \beta^{\frac{1}{2}} \qquad m^{-3}s \qquad (11J17)$$

(Brown, Kunkel, and Levine, 1977).

Tormac experiments have been pulsed devices, with $n \sim 10^{22}$ m^{-3}, $\tau \lesssim 10^{-4}$ s, $T_e \sim 1$ - 10 eV, $T_i \sim 10$ - 100 eV. The confinement scaling of Eq. (11J17), which would be favorable for reactors, has not yet been conclusively verified. There are questions regarding the possibility of more rapid mixing of core and sheath plasmas, and microinstabilities in the sheath, both of which would shorten the net confinement time.

There are many other cusp geometries, as indicated in Fig. 11A4. Cusp confinement theories, plasma stability, and experiments are reviewed by Haines (1977).

Bibliography

General

D. E. Baldwin, "End-loss processes from mirror machines", *Reviews of Modern Physics 49*, 317-339 (1977).

H. L. Berk, D.L. Correll, C. Gormezano, and M. E. Rensink, "Plasma energy confinement in conventional mirrors with externally heated electrons", *Nuclear Fusion 18*, 1379-1388 (1978).

B. Brunelli, Editor, *Driven Magnetic Fusion Reactors (Proceedings of the Course, Erice-Tripani, Italy, 1978)* Pergamon Press, New York, 1979.

D. L. Correll, J. H. Clauser, F. H. Coensgen, W. F. Cummins, R. P. Drake, J. H. Foote, A. H. Futch, R. K. Goodman, D. P. Grubb, G. M. Melin, W. E. Nexsen, T. C. Simonen, B. W. Stallard, and W. C. Turner, "Production of large-radius, high-beta, confined mirror plasmas", *Nuclear Fusion 20*, 655-664 (1980).

R. S. Devoto and D. J. Bender, "Plasma models for standard mirror reactors", *Nuclear Fusion 19*, 1151-1169 (1979).

J. H. Foote, "Nonadiabatic energy limit versus mirror ratio in magnetic-well geometry", *Plasma Physics 14*, 543-552 (1972).

C. Gormezano, "Reduction of losses in open-ended magnetic traps", *Nuclear Fusion 19*, 1085-1137 (1979). Review Paper.

S. Miyoshi, "Physics in open-ended fusion systems", *Nuclear Fusion 20*, 1047-1050. Conference report.

Proceedings of the Seventh International Conference on Plasma Physics and Controlled Nuclear Fusion Research, Innsbruck, August 1978, IAEA, Vienna, 1979, Volume II, p. 389-520.

D. D. Ryutov, "open traps", *Nuclear Fusion 20*, 1068-1072 (1980). A brief summary of historical developments.

tandem mirrors

D. E. Baldwin and B. G. Logan, "Improved tandem mirror fusion reactor", *Physical Review Letters 43*, 1318-1321 (1979).

G. A. Carlson et al, "Tandem mirror reactor with thermal barriers", UCRL-52836 (1979).

R. H. Cohen, "Time-dependent tandem mirror confinement studies", *Nuclear Fusion 19*, 1295-1305 (1979).

R. H. Cohen, M. E. Rensink, T. A. Cutler, and A. A. Mirin, "Collisional loss of electrostatically confined species in a magnetic mirror", *Nuclear Fusion 18*, 1229-1243 (1978).

R. H. Cohen, I. B. Bernstein, J. J. Dorning, and G. Rowlands, "Particle and energy exchange between untrapped and electrostatically confined populations in magnetic mirrors", *Nuclear Fusion 20*, 1421-1437 (1980).

G. I. Dimov, V. V. Zakaidakov, and M. E. Kishinevsky, *Soviet Journal of Plasma Physics 2*, 326-333 (1976).

R. P. Drake, T. A. Casper, J. F. Clauser, F. H. Coensgen, D. L. Correll, W. F. Cummins, J. C. Davis, J. H. Foote, A. H. Futch, R. K. Goodman, D. P. Grubb, R. S. Hornady, W. E. Nexsen, T. C. Simonen, and B. W. Stallard, "The effect of end-cell stability on the confinement of the central-cell plasma in TMX", *Nuclear Fusion 20*, 359-364 (1981).

J. Kesner, "ICRF fueling of tandem mirror end plugs", *Nuclear Fusion 19*, 108-112 (1979).

J. Kesner, "Axisymmetric sloshing-ion tandem-mirror plugs", *Nuclear Fusion 20*, 557-562 (1980).

B. G. Logan, A. A. Mirin, M. E. Rensink, and T. K. Fowler, "Calculation of the fusion power gain for a DD tandem mirror reactor", *Soviet Journal of Plasma Physics 4*, 301-305 (1978).

B. G. Logan, et al., "Tandem mirror reactors with thermal barriers"; D.E. Baldwin et al., "Studies in tandem mirror theory"; T. C. Simonen et al., "Plasma confinement experiments in the TMX tandem mirror"; Proceedings of the Eighth International Conference on Plasma Physics and Controlled Nuclear Fusion Research (Brussels, 1980) IAEA, Vienna, 1981.

T. D. Rognlien and T. A. Cutler, "Transition from Pastukhov to collisional confinement in a magnetic and electrostatic well", *Nuclear Fusion 20*, 1003-1001 (1980).

D. D. Ryutov, "Longitudinal plasma loss from nonaxisymmetric open systems", *Soviet Journal of Plasma Physics 5*, 665-672 (1980).

field reversed mirrors

D. V. Anderson et al, "Theory of field-reversed mirrors and field-reversed plasma-gun experiments", Proceedings of the Eighth International Conference on Plasma Physics and Controlled Nuclear Fusion Research, (Brussels, 1980) IAEA, Vienna, 1981.

A. H. Boozer, "Magnetic surfaces in reversed-field geometry", *Nuclear Fusion 18*, 1663-1669 (1978).

G. A. Carlson et al, "Definition and conceptual design of a small fusion reactor", EPRI ER-1045, Electric Power Research Institute, 1979.

G. A. Carlson et al, "Conceptual Design of the field-reversed mirror reactor", UCRL-52467 (1978).

E. C. Morse and G. H. Miley, "Stability of the field-reversed mirror", *Nuclear Fusion 21*, 473-479 (1981).

W. C. Turner et al, "Field-reversal experiments in a neutral-beam-injected mirror machine", *Nuclear Fusion 19*, 1011-1028 (1979).

M. Y. Wang and G. H. Miley, "Particle orbits in field-reversed mirrors", *Nuclear Fusion 19*, 39-49 (1979).

multiple mirrors

S. L. Musher and M. D. Spector, "Transverse confinement of a high-pressure plasma in a corrugated magnetic field", *Nuclear Fusion 20*, 149-157 (1980).

R. F. Post and X. Z. Li, "Particle confinement in asymmetric-cell multiple-mirror systems", *Nuclear Fusion 21*, 135-144 (1981).

J. C. Riordan, A.J. Lichtenberg, and M. A. Lieberman, "Minimum-average-B wells in linked magnetic mirror fields", *Nuclear Fusion 19*, 21-31 (1979).

M. Tuszewski, A. J. Lichtenberg, and S. Eylon, "Transient confinement of a high-density plasma in a multiple-mirror magnetic field configuration", *Nuclear Fusion 17*, 893-902 (1977).

S. T. Yang and M. A. Lieberman, "Power balance and impurities in two-component, multiple-mirror reactors", *Nuclear Fusion 17*, 697-712 (1977).

rotating plasma

A. A. Bekhtenev, V. I. Volosov, V. E. Pal'chikov, M.S. Pekker, and Yu. N. Yudin, "Problems of a thermonuclear reactor with a rotating plasma", *Nuclear Fusion 20*, 579-598 (1980).

cusps

I. G. Brown, W. B. Kunkel, and M. A. Levine, "TORMAC reactor considerations", *Nuclear Fusion 18*, 761-768 (1978).

K. W. Ehlers and K. N. Leung, "Characteristics of the Berkeley multicusp ion source", *Review of Scientific Instruments 50*, 1353-1361 (1979).

M. G. Haines, "Plasma containment in cusp-shaped magnetic fields", *Nuclear Fusion 17*, 811-858 (1977).

N. Hershkowitz, J. R. DeKock, and C. Chan, "The effect of picket-fence surface magnetic fields at the end of a magnetized plasma", *Nuclear Fusion 20*, 695-702 (1980).

A. Kitsunezaki, M. Tanimoto, and T. Sekiguchi, "Cusp confinement of high-beta plasmas produced by the laser pulse from a freely-falling deuterium ice pellet", *The Physics of Fluids 17*, 1895-1902 (1974).

K. N. Leung, N. Hershkowitz, and K. R. MacKenzie, "Plasma confinement by localized cusps", *The Physics of Fluids 19*, 1045-1053 (1976).

M. Sadowski, "Plasma containment in a spherical multipole magnetic trap", *Journal of Plasma Physics 4*, 1-12 (1970).

M. Sadowski, "Spherical Multipole magnets for plasma research", *The Review of Scientific Instruments 40*1545-1549 (1969).

G. Schmidt, "Nonadiabatic particle motion in axialsymmetric fields", *The Physics of Fluids 5*, 994-1002 (1962).

G. Schmidt, *Physics of High Temperature Plasmas, Second Edition*, Academic Press, New York, 1979, Chapter 2.

CHAPTER 12

PINCHES AND COMPACT TORUSES

12A. Types of Pinches

The pinch effect was first observed with a liquid metal in 1904. The history of fusion research with pinch devices is summarized by Bickerton (1980).

Z pinches

Assuming circular symmetry, an axial current density J_z induces an azimuthal magnetic field

$$B_\theta(r) = \mu_0 I(r)/2\pi r \qquad (12A1)$$

where

$$I(r) = 2\pi \int_0^r drrJ_z \qquad (12A2)$$

is the current enclosed by a circle at radius r (Example Problem 5B2). The interaction of the plasma current with this magnetic field produces a radially-inwards force per unit volume

$$\vec{F} = \vec{J}\times\vec{B} = -J_z B_\theta \hat{r} \quad (N/m^3) \quad , \qquad (12A3)$$

(Fig. 12A1), which tends to pinch the plasma down to smaller radii, if the current is strong. Since the current is in the z direction, this phenomenon is called a Z-pinch.

For a quasistatic equilibrium Eq. (5D39) becomes

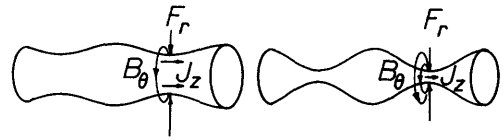

Fig. 12A1. Development of an m = 0 sausage instability in a Z pinch. The current density J_z and magnetic field B_θ are stronger where the plasma radius is smaller, so that region is compressed more rapidly.

$$- J_z B_\theta - dp/dr \simeq 0 \quad . \tag{12A4}$$

From Eq. (12A2)

$$dI/dr = 2\pi r J_z \quad . \tag{12A5}$$

Using Eqs. (12A1) and (12A5) in (12A4), we find

$$dr(2\pi r)^2 dp/dr = \mu_0 I(dI/dr)dr \quad . \tag{12A6}$$

The left side may be integrated by parts from r = 0 to r = a (the plasma boundary) to give

$$(2\pi r)^2 p \Big|_0^a - 4\pi \int_0^a 2\pi r dr\, p = \mu_0 I^2/2 \Big|_0^a \quad . \tag{12A7}$$

Assuming p(a) = 0, the first term is zero at both limits. If we define a volume-average pressure as

$$p_{av} = \frac{1}{\pi a^2} \int_0^a dr\, 2\pi r\, p \tag{12A8}$$

then Eq. (12A7) may be written

$$p_{av} = \mu_0 I_a^2 / 8\pi^2 a^2 \quad . \tag{12A9}$$

where I_a is the total current enclosed by radius a. This equation, derived by W. H. Bennett in 1934, is independent of the current density profile $J_z(r)$. For example, if $I_a = 10^6$ A and a = 0.01 m, then p_{av} = 160 MPa = 1600 atm, which could sustain an intense fusion power density. However, a simple Z pinch breaks up in microseconds by MHD instabilities, such as the m = 0 "sausage" instability (Section 8D). A lightning bolt is an example of a Z-pinch discharge.

Application of a strong external axial magnetic field B_z produces magnetic shear, which partially stabilizes the MHD instabilities, but the kink mode still limits the attainable current. High-pressure gas surrounding the plasma may also be used to stabilize MHD modes.

A Z-pinch operating at 600 kV and I = 100 kA in hydrogen at 500 Pa pinched from an initial radius of 5 mm down to a pinch radius a = 1.5 mm, and remained stable for 100 ns, with $n \sim 2\times10^{24}$ m^{-3} and $T_{max} \sim 0.8$ keV. (P. Choi et al, IAEA Conference, 1978). A set of parameters estimated to attain a Lawson parameter $n\tau \simeq 10^{20}$ m^{-3}s is: $n = 10^{27}$ m^{-3}, τ = 100 ns, a = 1 mm, I = 10 MA, V = 5.6 MV, stored energy W = 5.6 MJ.

Applications of Z-pinch phenomena include plasma focus devices, imploding foils, hard-core pinches, and toroidal Z-pinches.

plasma focus

Two common plasma focus geometries are illustrated in Fig. 12A2. The Mather type is like a coaxial plasma gun (Fig. 9D1). The plasma breaks down along the insulator and moves to the outer electrode at time t_1. Then the current-carrying

plasma sheath is accelerated axially (Mather type) or radially inwards (Filippov type), until it passes the end of the electrode at time t_2. Finally, the plasma collapses into a small-diameter Z-pinch, with $r \sim 1$ mm. Often, a second pinch follows the first about 50-100 ns later. If deuterium gas is used, intense neutron emission is observed. Yields up to 10^{12} neutrons/shot have been attained at capacitor bank energy W =340 kJ.

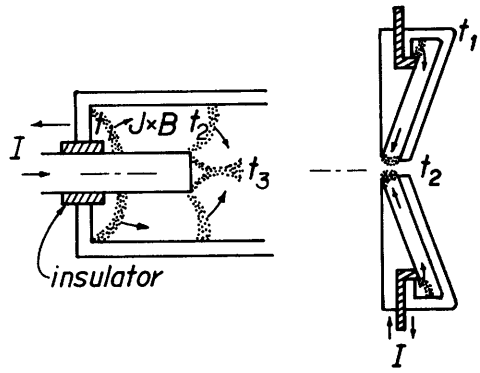

Fig. 12A2. Plasma focus devices of the Mather type (left) and Filippov type (right). The plasma current sheet is accelerated from t_1 to t_2 to the final Z-pinch collapse at t_3.

The very high electron current density generates plasma turbulence. The turbulent electric field accelerates some deuterons to very high energies (hundreds of keV), and these deuterons cause fusion reactions as they strike other deuterons and deuterium atoms. There is also some thermonuclear neutron emission from the bulk plasma distribution at T_i of several keV. A comparative study at $p \sim 200$ Pa has shown similar characteristics between the Mather and Filippov types of discharge, with regard to time variation of neutron emission, neutron yield, second compression, and current sheath structure (double-peaked with a width of about 2 cm).

Sometimes a second breakdown occurs across the insulator during the pinch. The current drain caused by such a "restrike" tends to spoil compression and neutron yield, so it must be avoided.

The capacitor bank voltage, energy, and electrode dimensions can be adjusted to maximize energy transfer from the capacitor bank to the pinch. Usually, the plasma sheath velocity and rate of change of inductance $\dot{L}$ are nearly constant during acceleration. If the initial rate of current rise is $\dot{I}_0$, then the optimum bank voltage, maximum plasma current, and current rise time are given by

$$U_{opt} = 2.12(W\dot{I}_0\dot{L}^2)^{1/3} \quad (V) \tag{12A10}$$

$$I_{m,opt} = 0.64(W\dot{I}_0/\dot{L})^{1/3} \quad (A) \tag{12A11}$$

$$\tau_{opt} = 1.5(W/\dot{L}\dot{I}_0^2)^{1/3} \quad (s) \tag{12A12}$$

(G. Decker et al., IAEA Conference, 1978, Vol. II, p. 136). If L_0 is the external circuit inductance and C is the capacitance, then the impedance matching condition for these optimum conditions is

$$L_0/C = (2.18\dot{L})^2 \quad (\Omega^2) \quad . \tag{12A13}$$

Dividing Eq. (12A10) by (12A11), we find

$$U_{opt} = 3.31\ I_{m,opt}\dot{L} \quad (V) \quad . \tag{12A14}$$

Assuming that $\dot{I}_0 \propto W$ and normalizing to 10^{12} A/s at 10^5 J, we have

$$\dot{I}_0 \sim 10^7 W \qquad \text{(A/s)} \quad . \tag{12A15}$$

Then, from Eq. (12A11), the required bank energy is

$$W \sim 6\times10^{-4}\, \dot{L}^{\frac{1}{2}}\, I_{m,opt}^{3/2} \qquad \text{(J)} \quad . \tag{12A16}$$

Typically, $\dot{L} \sim 0.02$ Ohm. For this case, to attain a maximum plasma current $I_{m,opt} = 1$ MA would require an optimum bank voltage $U_{opt} \simeq 70$ kV, and a bank energy $W \sim 85$ kJ.

If the bank voltage is optimized, at the time of maximum current 74 % of the bank energy is in magnetic energy, 17 % is in plasma kinetic energy, and 9 % is still in the bank.

The pinch current I_p is usually less than the total current. According to some experimental data, the maximum neutron yield Y_m varies as

$$Y_m \sim 2\times10^{11} I_p^4 \qquad \text{(neutrons/shot, deuterium fuel)} \tag{12A17}$$

where I_p is expressed in MA, but this scaling fails at high currents.

The goal of plasma focus research is to determine the neutron emission mechanisms and scaling laws, and to scale up the devices to higher bank energies and neutron yields. Acceleration of the current sheath is well understood, as illustrated in Fig. 12A3, but the turbulence and neutron emission phenomena are not. Increases in bank energy have not always produced the anticipated increases in neutron yield.

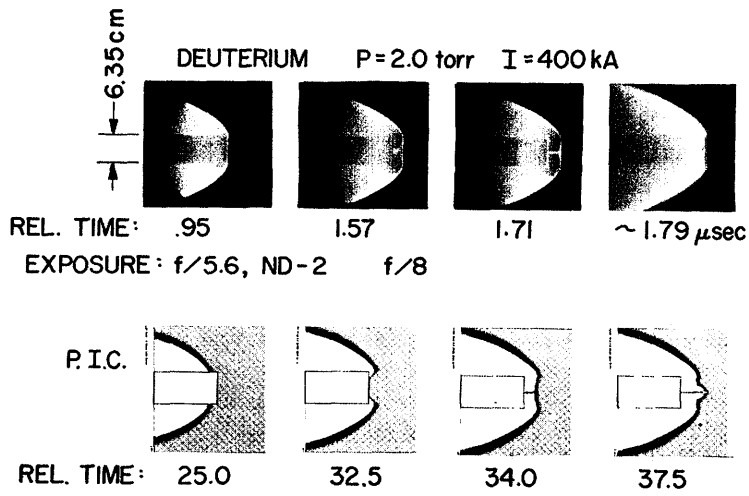

Fig. 12A3. Comparison of plasma light photographs (upper photos) with "particle in cell" computer simulations (lower pictures, arbitrary dimensionless times) for various stages of a plasma focus. From T. D. Butler, I. Henins, J. Marshall, and R. Morse, "Coaxial snowplow discharge", Proceedings of the APS Topical Conference on Pulsed High-Density Plasmas, LA-3770 (1967), Fig. 2, p. c7-4.

imploding liner

When a high current is passed axially through a thin metal tube, the $J_z B_\theta$ force will cause the tube to implode, like a Z-pinch. If a hot plasma and magnetic field are inside the tube, the internal magnetic field will be unable to diffuse through the metal liner as it implodes. The magnetic field and plasma will both be compressed to high pressures. An azimuthal field B_θ will inhibit both radial and axial plasma energy losses.

For a fusion reactor, the initial plasma would need to have $n_0 \sim 3\times10^{23}$ m^{-3}, $T_0 \sim 0.3$ keV, $B_{\theta 0} \sim 5$-10 T, and the liner implosion velocity should be $v \sim 10^4$ m/s. The attainable energy gain ratio is estimated to be

$$Q' = \frac{\text{fusion energy}}{\text{liner energy}} = 2.8(\rho_0 W_L/L)^{\frac{1}{2}} \qquad (12A18)$$

where ρ_0 is the initial liner density (g/cm^3) and W_L/L is the liner energy per unit length (GJ/m), assuming that the plasma energy loss rate during compression is small.

Experiments using aluminum liners 0.1 m long and 1 mm thick, Fig. 12A4, have attained implosion velocities of 0.5×10^4 m/s and 10^4 m/s at capacitor bank energies of 1.8 and 2.4 MJ. Plasma preparation experiments using a coaxial gun have produced plasmas with $n_0 \sim 3\times10^{22}$ m^{-3}, $T_0 \sim 40$ eV, and $B_{\theta 0} \sim 1$ T at $t = 2$ μs after injection.

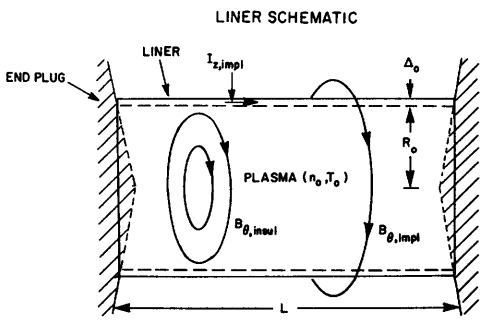

Fig. 12A4. Geometry of the Fast Liner experiment at Los Alamos. From A. R. Sherwood, E. L. Cantrell, I. Henins, H. W. Hoida, T. R. Jarboe, R. C. Malone, and J. Marshall, "The LASL fast liner experiment", Plasma Physics and Controlled Nuclear Fusion Research 1980 (Brussels), IAEA, Vienna, 1981.

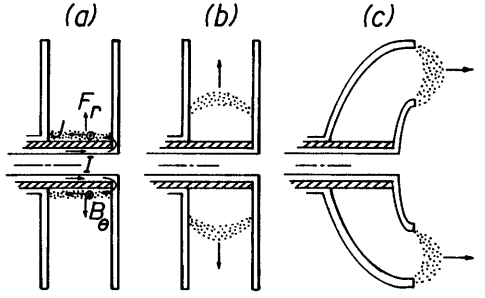

Fig. 12A5. An inverse pinch. (a) breakdown along insulator; (b) outward motion of plasma; (c) use of curved electrodes to produce axial motion.

inverse pinch and hard-core pinch

If an axial current flows inside the plasma with direction opposite to the plasma current, an inverse pinch is created, as shown in Fig. 12A5a. In this case the interaction of the B_θ produced by the current of the inner conductor with the plasma current drives the plasma outwards, Fig. 12A5b. Such devices have been used for accelerating blobs of plasma, as in Fig. 12A5c. This configuration is topologically similar to that of a coaxial plasma gun, Fig. 9D1.

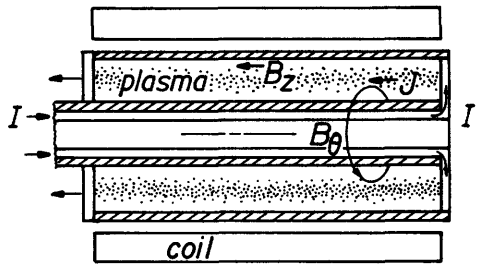

Fig. 12A6. A hard-core pinch.

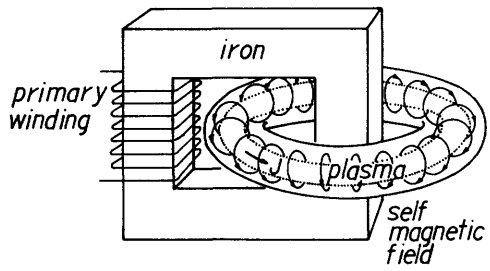

Fig. 12A7. A toroidal Z-pinch. The plasma is the secondary circuit of a transformer.

A hard-core pinch, Fig. 12A6, is similar to the inverse pinch. A central conductor creates a B_θ which decreases radially outwards, and an external solenoid creates a strong stabilizing B_z. The plasma forms along the central conductor and is pushed outwards by the inverse pinch force, compressing the B_z field. The plasma then is held in stable equilibrium between the internal B_θ pressure and the external B_z pressure, with fairly strong magnetic shear.

toroidal Z-pinch

All of the above pinches have plasma impurities emitted from electrodes in direct contact with hot plasma. In order to avoid this problem, the electric field can be induced by a transformer, in a toroidal device, as illustrated in Fig. 12A7. Instead of using an iron core, the primary windings can be wrapped directly around the toroidal vacuum chamber.

Although the electrode problem is alleviated, MHD instabilities are severe. Plasma stability can be improved by adding a strong toroidal magnetic field and by placing a conducting wall close to the plasma. If the toroidal magnetic field is comparable to the poloidal self-magnetic field of the plasma current ($B_t \sim B_p$, a *toroidal diffuse pinch*) instabilities persist, but if $B_t \gg B_p$, (a *tokamak*) stability is satisfactory. Wall stabilization is limited by the time it takes the magnetic field lines to diffuse into the wall (typically milliseconds). Another stabilization technique is to program the magnetic fields so that a toroidal magnetic field is trapped inside that plasma, and then a reversed B_t is applied on the outside of the plasma (or appears spontaneously). Such a *reversed-field toroidal pinch* will be described in Section 12D.

Another way of providing MHD stability is to levitate a current-carrying ring inside the plasma. The *levitron* is the toroidal analog of a hard-core pinch. Devices with internal current-carrying rings will be discussed in Section 14B.

linear theta pinch

In cylindrical geometry, a rapidly-changing axial field B_z will induce a plasma current in the theta direction (hence the name *theta pinch*), and a radially inwards force

$$F_r = -J_\theta B_z \tag{12A19}$$

will compress the plasma. In order to minimize inductance and maximize dB_z/dt, a single-turn coil is often used, as shown in Fig. 12A8. Such pulsed coil systems will be discussed in Chapter 21.

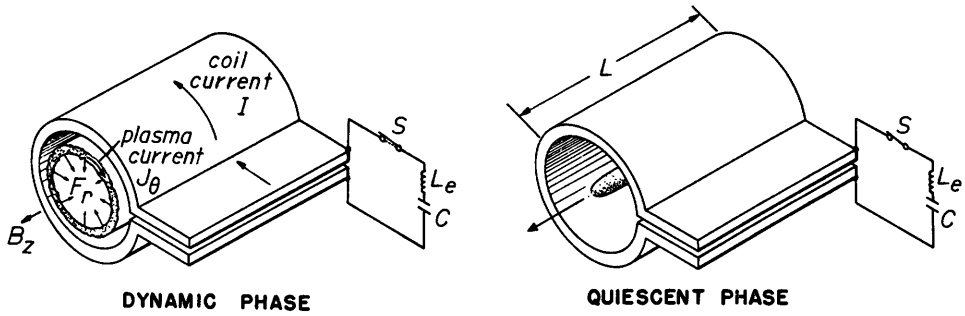

Fig. 12A8. Operation of a theta pinch. A capacitor bank C is charged up to high voltage (such as 60 kV). When switch S is closed, a high current I flows through the circuit, having inductance L_e. The rising coil current produces an increasing B_z, which induces a plasma current J_θ. The $J_\theta B_z$ force then compresses the plasma, heating it to a high temperature. From AEC Report TID-23277 (1966) Appendix 3.

Plasma confinement in the radial direction is very good, with nearly classical diffusion rates observed. The main problem is rapid plasma losses out the ends. Assuming $T_e = T_i = T$, the characteristic end loss time is

$$\tau \simeq 2.5L/v_{Ti} \quad , \qquad v_{Ti} \equiv (kT/m_i)^{\frac{1}{2}} \tag{12A20}$$

where L is the plasma length, m_i is the ion mass, k is the Boltzmann constant, and T is the plasma temperature [Ellis, 1975, Eq. (5) with $\eta_m \simeq 2$]. For DT ions at T = 10 keV, $v_{Ti} = 6.2\times10^5$ m/s. Usually $\beta \simeq 1$. From a pressure balance

$$2nkT = \beta B^2/2\mu_0 \tag{12A21}$$

we find

$$n \simeq 1.24\times10^{21}\, B^2/T \qquad (m^{-3}) \quad , \tag{12A22}$$

where T is expressed in keV, and B in Telsa. A practical maximum value of B is probably $B \lesssim 20$ T, due to coil stress problems (Sections 20C, 24D). If $T \sim 10$ keV, then $n \lesssim 5\times10^{22}$ m^{-3}. For a reactor with $n\tau = 5\times10^{20}$ m^{-3} s, the required confinement time would be 10 ms, corresponding to $L \simeq 0.4\, v_{Ti}\tau \simeq 2.5$ km.

In order to reduce the required reactor size, several methods have been proposed:

* *multiple mirrors*. The conditions for effective end plugging with multiple mirrors were discussed in Section 11G. In order to attain MHD stability, internal conducting rings or external Ioffe bars may be needed.
* *solid end plugs*. Solid material end plugs inhibit ion flow rates out the ends. Ablated material creates a high-Z cool-plasma region where energy is lost by line radiation, but electronic and ionic heat conduction are retarded. Solid end plugs were studied experimentally with the Scylla IV-P five-meter-long theta pinch. The best results were obtained with LiD plugs. The energy confinement with and without the solid end plugs is shown in Fig. 12A9. The plugs increase the energy confinement time by a factor of 3, which agrees with theoretical predictions.
* *re-entrant end plugs*. Two parallel linear theta pinches may be connected at their ends by curved tubes, in a "race-track" configuration, Fig. 12A10. Rapid heat loss would occur in the curved sections, probably at nearly the Bohm rate. Estimated confinement parameters attainable with and without re-entrant end plugs are shown in Fig. 12A11, assuming B = 20 T, T = 5 keV. At higher temperatures, the $n\tau$ vary proportional to T^{-1} (race-track) and $T^{-3/2}$ (unplugged). The line marked "brem" indicates the limitation of bremsstrahlung radiation losses on attainable $n\tau$: higher values are probably unattainable.

A hypothetical linear theta pinch reactor with re-entrant end plugs has the following parameters: length of straight sections = 100 m; wall radius = 0.5 m; shock heating with a fast rising field of 1.1 T; then adiabatic compression up to 10 T; plasma density $\sim 2\times10^{22}$ m^{-3}; $n\tau = 1.4\times10^{21}$ m^{-3} s; fuel burnup fraction f_b = 8 %; cycle time = 12 s; and recirculating power fraction ε = 0.21 [J. P. Friedberg et al, LA-UR-77-961 (1977), p. 89-92].

Helical windings or Tormac-like cusp coils may be used to aid MHD stability in the curved ends of a race-track configuration.

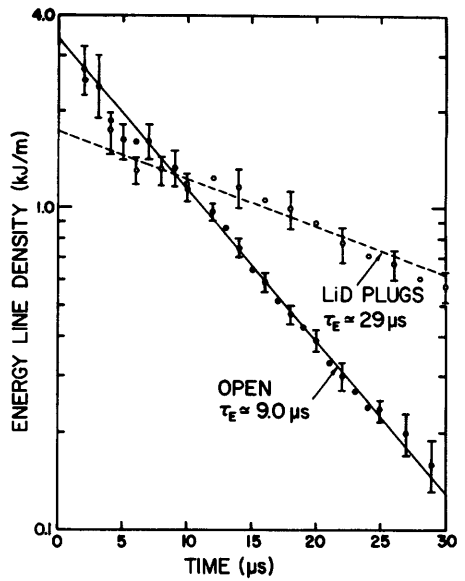

Fig. 12A9. The energy line density, inferred from diamagnetic loop measurements at the midplane of the Scylla IV-P theta pinch. The straight lines and time constants shown result from least squares fitting exponential decays to the data for times greater than six μs. *From K. S. Thomas and G. A. Sawyer, LA-7474-PR (1979), Fig. IV-18, p. 36.*

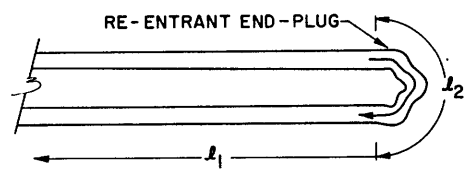

ELONGATED RACETRACK ($\ell_1 >> \ell_2$)

Fig. 12A10. Twin theta pinches connected by re-entrant end plugs. From J. P. Friedberg et al, "Review of the linear theta pinch (LTP) concept", LA-UR-77-961 (1977), Fig. 4, p. 44.

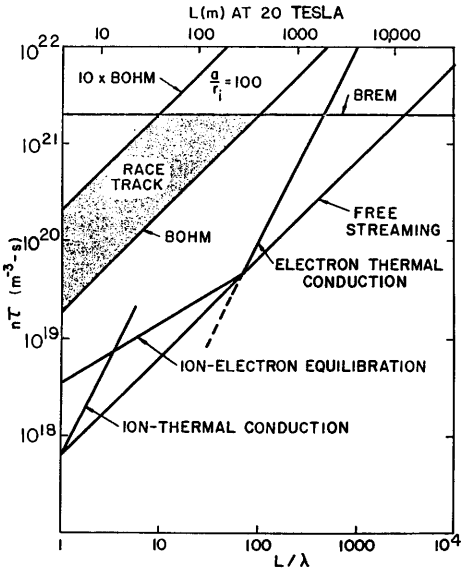

Fig. 12A11. Product of plasma density and confinement time vs. ratio of plasma length to ion mean free path λ, assuming T_i = 5 keV. The lower curves show losses of ordinary linear theta pinches, and the shaded region, for a "race-track" configuration with cross-field energy confinement times given by the Bohm value or 10 times the Bohm value (Section 8G). From J. P. Friedberg et al, LA-UR-77-967 (1977), Fig. 2, p. 34.

toroidal theta pinch

If the race-track-shaped theta pinch were rounded out into a circle, we would have a toroidal theta pinch. The main problem of a toroidal theta pinch is fast-growing MHD instabilities, such as the m = 1 kink mode. The Scyllac experiment (major radius R = 4 m, minor coil radius b ∿ 7 cm, B ∿ 9 T, n ∿ 3×10^{22} m^{-3}, T_i ∿ 2 keV) used helical "stellarator" type windings (Section 14A) to reduce the growth rates of MHD modes, but confinement times were limited to 10-50 μs. Feedback stabilization (with pulsed coils responding to plasma motion) increases confinement times, but it involves complex technology.

screw pinch and belt pinch

A combination of a Z-pinch with a theta pinch produces a plasma with currents induced in both the Z and θ directions. The helical shape of the magnetic field lines gives rise to the name *screw pinch*. A toroidal screw pinch is similar to a tokamak, but operating at high β ∿ 20 % , while tokamaks usually have β < 10 %.

For example, the parameters of the SPICA screw pinch (or high-beta tokamak) experiment at Jutphaas are R = 0.6 m, b = 0.2 m, B_t = 1.6 T, I_t = 300 kA, n = 5×10^{21} m^{-3}, and T = 50 eV. This device has attained β ∿ 20 % and stable equilibria for 200 μs, with a decay time of the toroidal current of 700 μs. Screw pinch discharges are usually stable if the safety factor q ≳ 2 (Table 8B1).

Toroidal screw pinches with highly elongated plasmas are called *belt pinches*. The advantage of an elongated plasma cross section is illustrated in Fig. 12A12. For example, the BPIIA experiment at Garching, West Germany, is illustrated in Fig. 12A13. It has a major radius R = 0.53 m, an elongated toroidal chamber with rectangular cross section 2.6 m high and 0.45 m wide, and a toroidal plasma current of 200 kA. Plasmas with n ∿ 10^{20} m^{-3}, T_i ∿ 50 eV, and $\langle\beta\rangle$ ∿ 60 % have been confined for times > 50 μs. Flux surface plots at 10 and 70 μs are shown in Fig. 12A14. Cross-field particle transport appears to be within a factor of 5 of the classical diffusion rate. Heat transport is masked by impurity line radiation, so accurate determination of the thermal conductivities is difficult (typical impurity fractions are O ∿ 0.4 %, C ∿ 0.6 %). Electron heat conduction is small, and ion heat conduction

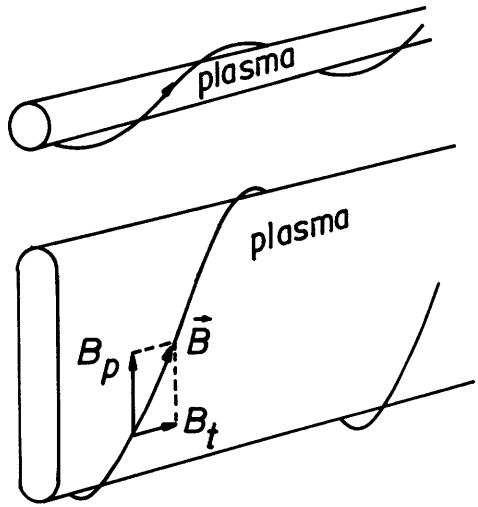

Fig. 12A12. Comparison of two plasmas having the same pitch q. The elongated plasma has a larger B_p, hence it may have better confinement. Courtesy of P. C. T. Van der Laan [Based on oral presentation, Bulletin of the American Physical Society 22, 1156 (1977)].

is within 10 times the classical value. Many other toroidal screw pinches and belt pinch experiments are operating in various laboratories.

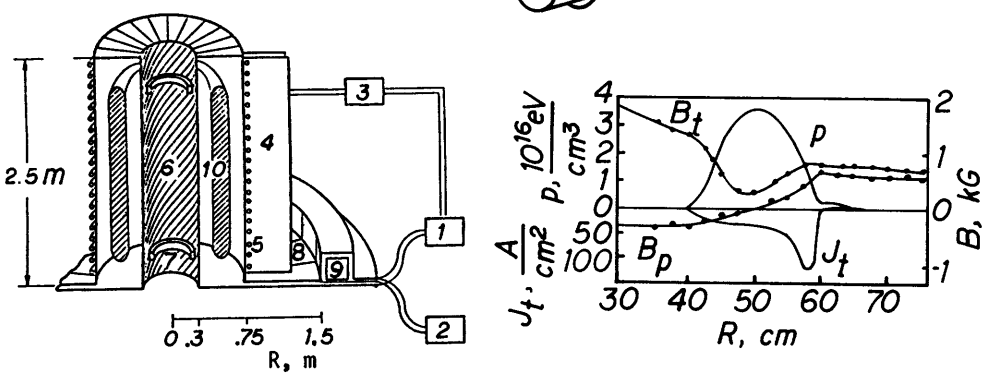

Fig. 12A13. Left: the BPIIA belt pinch experiment, at Garching, West Germany. (1), (2), (3) = power supplies, switches, transmission lines; (4), (5) = coils to induce toroidal current; (6) spiral coils on inside of torus; (7) control coils; (8), (9) headers for coils to induce poloidal current; (10) plasma. Right: radial variation of current density, plasma pressure, and magnetic field components. A = 4.5, β_p/A = 0.92, t = 10 μs. Courtesy of the Max-Planck-Institut für Plasmaphysik, Garching, FRG.

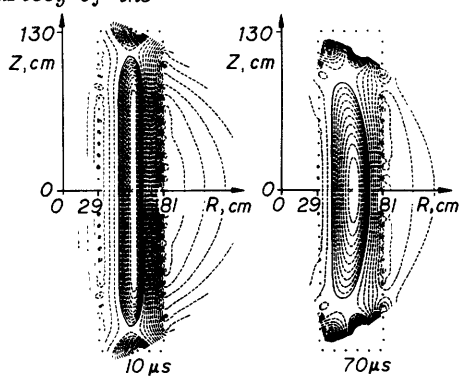

Fig. 12A14. Computer simulation of the poloidal magnetic flux surfaces of the BPIIA plasma, at times of 10 and 70 μs. From Max-Planck-Institut für Plasmaphysik Jahresbericht 1977, Fig. 6, p. 12.

EXTRAP

The extrap concept, illustrated in Fig. 12A15, is a high-beta toroidal pinch. Several poloidal field coils with parallel currents surround the plasma, which carries an antiparallel current. Closed magnetic surfaces are bounded by a single-null separatrix. The coil geometry is similar to that of a toroidal octupole (Section 14B), except that a strong plasma current alters the magnetic surfaces, and the coils are not surrounded by the plasma. The plasma current may be induced by varying the main coil currents, or by the use of separate ohmic heating coils. Although EXTRAP is a pulsed device, like tokamaks, various current drive mechanisms offer the hope of steady-state operation (Section 13D). A pure poloidal field may be used, as in Fig. 12A15, or a toroidal field may be added to provide magnetic shear.

A partially-ionized boundary layer separates the fully-ionized plasma core from the neutral gas layer next to the chamber wall. Plasma-gas interactions in the boundary layer may help to stabilize the plasma against some MHD modes. The simple coil geometry offers obvious reactor advantages, but the plasma equilibrium, stability, and beta limits for EXTRAP have not been thoroughly studied yet.

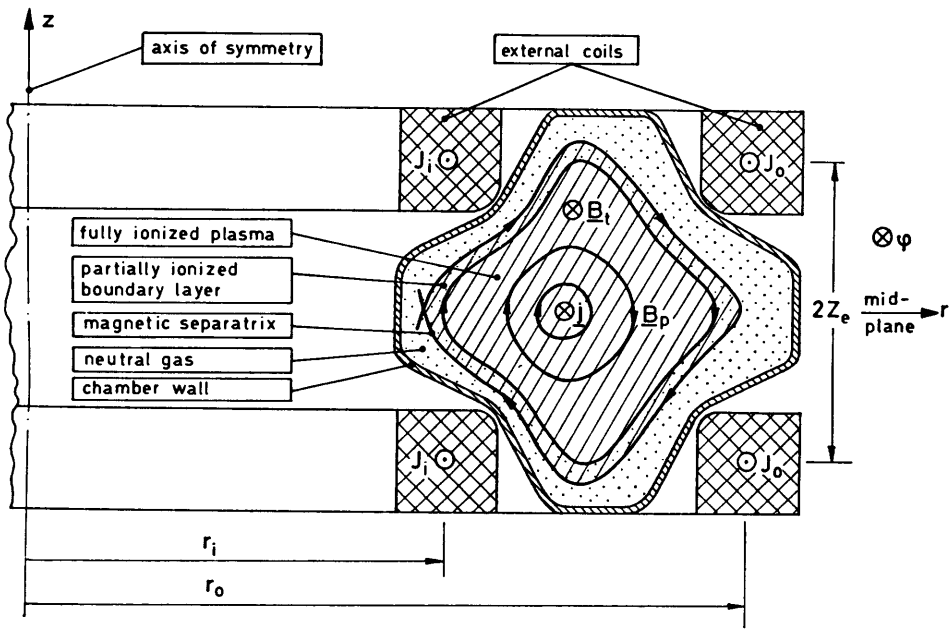

Fig. 12A15. One type of EXTRAP system, with a single-null separatrix defining the confined plasma boundary. Other numbers and spacings of coils may be used to produce similar confinement systems. From B. Lehnert, Physica Scripta 16, 147-155 (1977), Fig. 1.

compact toroids

The term *compact toroid (CT)* designates any toroidal device with no magnet coils passing through the hole in the torus. The absence of toroidal field coils greatly simplifies construction and maintenance.

Compact toroids may be *prolate* (elongated parallel to the major axis), or *oblate* (elongated perpendicular to the major axis), as shown in Fig. 12A16.

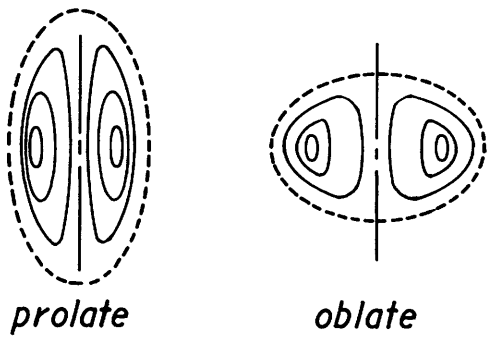

Fig. 12A16. Elongated toroids. The dashed curve is the separatrix, which is the boundary between closed magnetic surfaces and open field lines.

Compact toroids are classified according to the ratios B_p/B_t (the poloidal and toroidal magnetic fields) and ρ_p/a (the ion gyroradius in the poloidal field and the plasma minor radius). The field-reversed mirror has $B_p/B_t \gg 1$ and $\rho_p/a < 1$. Some other types of CT are listed in Fig. 12A17.

	$\rho_p/a < 1$	$\rho_p/a \geq 1$
$B_p/B_t \gg 1$	field-reversed mirror field-reversed theta pinch	E-layers P-layers
$B_p/B_t \sim 1$	spheromak or "null-field Z-pinch"	REB-injected toruses

Fig. 12A17. Types of compact toroids. From H. P. Furth, "The compact torus concept and the spheromak", Proceedings of the US-Japan Joint Symposium on Compact Toruses and Energetic Particle Injection, PPPL, 1979, p. 3-7, Fig. 4.

Field-reversed theta pinches and spheromaks will be described in Sections 12B and 12C, and charged particle rings (E-layers, P-layers, REB-injected toruses) will be discussed in Section 14C.

12B. Field-Reversed Theta Pinch

formation

The arrangement of the theta-pinch coil, discharge tube, and resulting compact toroid are shown in Fig. 12B1. The time sequence of producing such a configuration is illustrated in Fig. 12B2. First a reverse bias field B_i is applied to the plasma region. The plasma may be preionized by a preliminary theta pinch

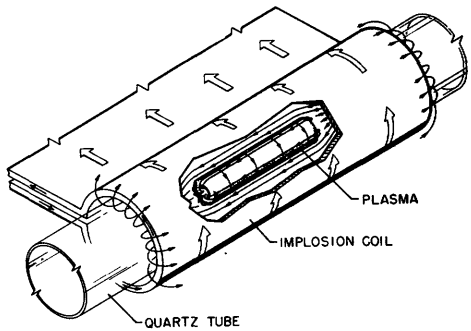

Fig. 12B1. Arrangement of theta-pinch coil, discharge tube, and compact toroid plasma configuration obtained with reversed bias field. From H. Dreicer and Los Alamos Staff, LA-8045-P (1979), Fig. 2, p. 12.

(damped sinusoid) discharge, by rf heating, by a Z-pinch discharge, by plasma gun injection, or by a combination of these means. It is important to maximize the degree of ionization without losing the reverse bias field.

Then the main capacitor bank is discharged through the theta pinch coil, imploding the plasma radially. The reverse bias field will be trapped inside the plasma and compressed, with the implosion field on the outside of the plasma in the opposite direction. At the end of compression the magnetic field lines at the plasma ends break and reconnect, forming closed poloidal field loops around the plasma. Then the prolate toroid contracts axially into its final equilibrium configuration, where it may exist stably for tens of microseconds.

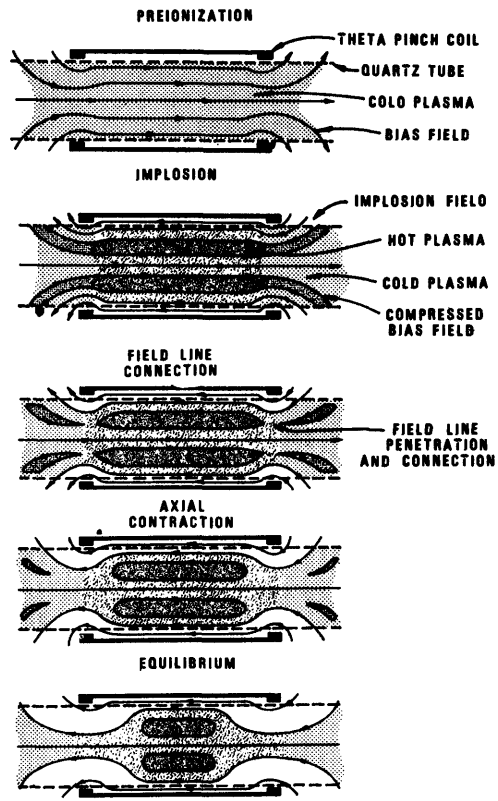

Fig. 12B2. Formation sequence of a compact toroid in a field-reversed theta pinch. From H. Dreicer and Los Alamos Staff, LA-8045-P (1979), Fig. 3, p. 13.

The variation of the magnetic field outside the plasma with time in the FRX-B experiment is shown in Fig. 12B3. In this case the CT exists for about 30 μs.

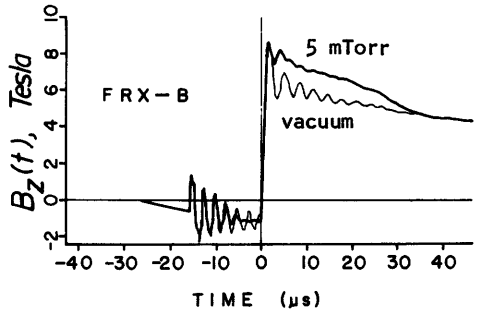

Fig. 12B3. Magnetic field time history obtained with a probe outside the discharge tube at the coil midplane in the FRX-B experiment. A negative bias field is first applied, followed by a ringing theta pinch preionization discharge. The main implosion field is applied at t = 0. The difference between traces with 5 mTorr and vacuum is due to the toroidal current of the CT. From H. Dreicer and Los Alamos Staff, LA-8045-P (1979), Fig. 4, p. 14.

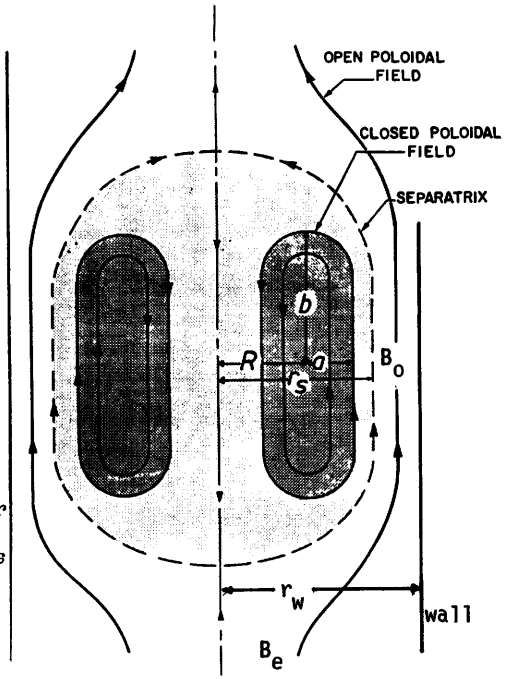

Fig. 12B4. Cross section of a prolate CT configuration showing the poloidal field geometry, the separatrix radius r_s, major radius R, minor radius a, and half-length b. The toroidal field is not shown. From W. T. Armstrong et al, Plasma Physics and Controlled Nuclear Fusion Research 1980 (Brussels), IAEA, Vienna, 1981.

equilibrium and stability

Some parameters of a prolate CT are defined in Fig. 12B4. Consider the cross sectional view of a given flux surface bounded inside and outside by radii r_i and r_0, Fig. 12B5. The flux between adjacent surfaces is

$$d\psi = 2\pi r_i dr_i B_i = 2\pi r_0 dr_0 B_0 \quad . \quad (12B1)$$

At the separatrix the plasma pressure is taken to be zero, and the magnetic field pressure is maximum. Moving inwards, the plasma pressure increases, and the magnetic field pressure decreases (Eq. 8B6). At equilibrium the plasma pressure p is constant along each flux surface, so $p(r_i) = p(r_0)$. Ignoring curvature effects, then, $B_i = -B_0$, and Eq. (12B1) reduces to

$$d\psi/2\pi B_0 = - r_i dr_i = r_0 dr_0 \quad . \quad (12B2)$$

Integrating from $\psi(R)$, we find

$$R^2 - r_i^2 = r_0^2 - R^2 \quad . \quad (12B3)$$

At the separatrix $r_0 = r_s$ and $r_i = 0$, from which

$$r_s/R = \sqrt{2} \quad , \quad (12B4)$$

independent of the pressure distribution $p(\psi)$.

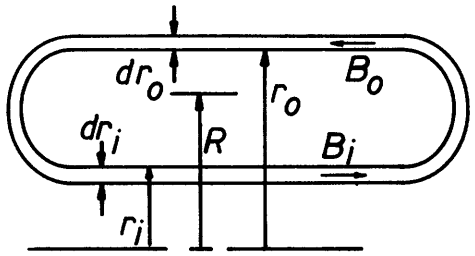

Fig. 12B5. Inside and outside radii r_i and r_0 bounding a given flux surface.

Magnetic field lines exert a positive pressure perpendicular to the field, but a negative pressure (tension) of $-B^2/2\mu_0$ along the magnetic field. We can write an axial force balance equation comparing forces at the midplane and end region (Fig. 12B4) :

$$\underset{\text{midplane}}{\int_0^{r_s} dr\, 2\pi r(\, p - B^2/2\mu_0)} + \underset{\text{midplane}}{\int_{r_s}^{r_w} dr\, 2\pi r(-\, B_0^2/2\mu_0)} = \underset{\text{end}}{\int_0^{r_w} dr\, 2\pi r(-\, B_e^2/2\mu_0)} \qquad (12B5)$$

where p is the plasma pressure, B is the magnetic field inside the plasma, B_0 is the field outside the plasma at the midplane, B_e is the magnetic field at the end of the plasma, and r_w is the wall radius. We can estimate B from a radial pressure balance, ignoring the curvature term in Eq. (8B6):

$$p + B^2/2\mu_0 = B_0^2/2\mu_0 \quad . \qquad (12B6)$$

The field at the ends can be related to the field B_0 around the plasma by magnetic flux conservation:

$$\pi r_w^2 B_e = \pi(r_w^2 - r_s^2)B_0 \quad . \qquad (12B7)$$

With the aid of Eqs. (12B6) and (12B7), Eq. (12B5) becomes

$$2\int_0^{r_s} dr\, 2\pi r\, p - \pi r_w^2 B_0^2/2\mu_0 = -\pi r_w^2[1 - (r_s/r_w)^2]^2 B_0^2/2\mu_0 \quad . \qquad (12B8)$$

With the definition

$$\langle\beta\rangle \equiv (2\mu_0/B_0^2\pi r_s^2)\int_0^{r_s} dr\, 2\pi r\, p \qquad (12B9)$$

this simplifies to

$$\langle\beta\rangle = 1 - \tfrac{1}{2}(r_s/r_w)^2 \quad , \qquad (12B10)$$

which is independent of the pressure profile. With a given internal pressure, a smaller value of r_s means a steeper pressure gradient, and more rapid particle and heat transport.

For non-rotating plasmas, the condition $r_s/r_w \gtrsim 0.4$ is predicted to help stabilize radial displacement MHD instability modes with $n \lesssim 3$. Stability against ballooning modes depends upon the fraction of ions which encircle the axis; larger fractions enhance stability (Finn, 1981). An n = 1 resistive axial mode (tilt) is expected from some calculations, but not observed experimentally. Plasma rotation at angular frequency ω_{rot} produces an n = 2 rotational flute mode which terminates plasma confinement when $-\omega_{rot}/\omega_* \gtrsim 1.5$, where ω_* is the diamagnetic drift frequency (Section 8E).

Plasma rotation may be induced by several mechanisms. One of these is conservation of total angular momentum as drifting ions diffuse across the separatrix and are lost. The predicted rotation for a rigid-rotor profile (uniform ω_{rot}) is

$$-\omega_{rot}/\omega_* = \left[2 + \frac{\beta}{1-\beta} - \frac{1}{2(1-\beta)^{\frac{1}{2}}\,\mathrm{sech}^{-1}(\beta^{\frac{1}{2}})}\right] F \quad , \tag{12B11}$$

where β is evaluated at the separatrix, and F is the fraction of particles which has been lost. For FRX-B, $\beta \simeq 0.65$, so a value of $F \gtrsim 0.57$ is predicted to terminate confinement. The experimental value of $F = 0.55 \pm 0.16$. Another mechanism causing rotation is end-shorting and viscous shear (Steinhauer, 1981).

parameter scaling

For a fixed plasma temperature, the particle-loss time is predicted to be proportional to R^2/ρ_i, where ρ_i is the ion Larmor radius. If τ_s is the stable period (time to onset of the rotational instability), then

$$\tau_s \propto R^2/\rho_i \quad . \tag{12B12}$$

Such a scaling is observed with experimental data, Fig. 12B6.

The stable period has also been correlated with the "compression ratio" B_f/B_i, where B_f is the external magnetic field produced by the implosion coil and B_i is the magnitude of the initial reverse bias field, as shown in Fig. 12B7. Thus, it is desirable to maximize B_i. The maximum value of B_i is

$$B_{imax} = k_B \dot{B}^{\frac{1}{2}} (\pi r_w^2 n_0)^{\frac{1}{4}} \quad \text{Tesla}, \tag{12B13}$$

where n_0 is the initial plasma density, $\dot{B}$ is the rate of increase of the implosion field (T/s), and $k_B \simeq 4.4\times10^{-9}\ T^{\frac{1}{2}} s^{\frac{1}{2}} m^{\frac{1}{4}}$. If the initial bias field were greater, then the plasma expansion during field reversal would cause too much flux loss. [An approximate derivation of this scaling is obtained from

$$\begin{aligned} \text{(field turn-on time)} &\ll \text{(Alfven wave transit time)} \\ B_i/\dot{B} &\ll r_w/v_A = r_w(n_0 m_i \mu_0)^{\frac{1}{2}}/B_i \\ B_i &\ll (r_w \dot{B})^{\frac{1}{2}} (n_0 m_i \mu_0)^{\frac{1}{4}} . \ ] \end{aligned} \tag{12B14}$$

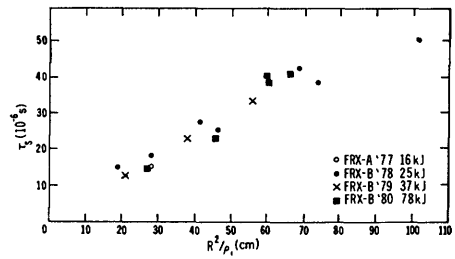

Fig. 12B6. Variation of stable period τ_s (time to the onset of the n = 2 rotational instability) with R^2/ρ_i, where R is the major radius of the compact toroid and ρ_i is an ion Larmor radius. This scaling is consistent with studies of anomalous transport. From J. Lipson, W. T. Armstrong, J. C. Cochrane, K. F. McKenna, E. G. Sherwood, and M. Tuszewski, "Scaling studies in field reversal experiments", Applied Physics Letters 39, No. 1, p. 43, (1981) Fig. 3.

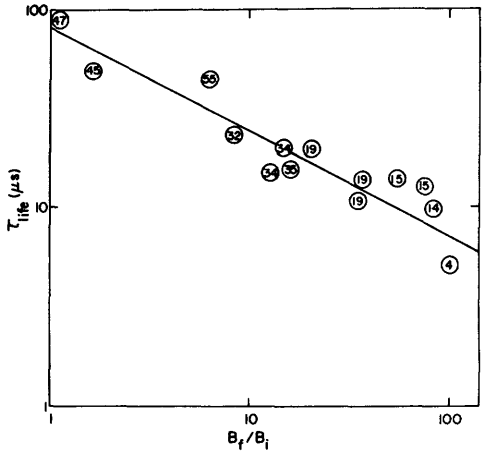

Fig. 12B7. Variation of compact toroid lifetime with ratio of final external magnetic field B_f to initial bias field B_i. From H. Dreicer and Los Alamos Staff, "Proposal for FRX-C and Multiple-Cell Compact Torus Experiments", LA-8045-P (1979), Fig. D-2, p. 94. Circled numbers refer to references cited in that report.

The ratio of plasma half-width a to ion Larmor radius $a/\rho_i \propto (\pi r_w^2 n_0)^{\frac{1}{2}}$. At very large values of $(\pi r_w^2 n_0)$, a/ρ_i is large, "finite Larmor radius" stabilizing effects are negligible, and MHD instabilities may occur. At low values of $(\pi r_w^2 n_0) \lesssim 10^{18}/m$, plasma resistivity is anomalously high, and implosion efficiency is poor. (The value of this lower limit depends upon effectiveness of preionization). The plasma temperature resulting from implosion heating scales as

$$kT \propto \frac{U_0 B_f}{(\pi r_w^2 n_0)^{\frac{1}{2}} B_i} \qquad (12B15)$$

where U_0 is the main capacitor bank voltage. To obtain long τ_s, small B_f/B_i are desirable, and to maximize kT, the minimum value of $(\pi r_w^2 n_0)$ should be used. Then further increases of temperature rely on increasing U_0 or using auxiliary heating.

experiments

Long plasma lifetimes can be promoted by maximizing the trapped flux fraction Φ_i/Φ_0, where Φ_i is the magnetic flux (reverse bias field) trapped in the plasma and $\Phi_0 = \pi r_w^2 B_i$ is the initial bias flux. In experiments with FRX-B, the initial value when implosion begins is $\Phi_i/\Phi_0 \sim 0.5$, due to the nature of the preionization process. The value of Φ_i/Φ_0 then decays by resistive diffusion to $\Phi_i/\Phi_0 \sim 0.14$ at the end of confinement. Better preionization could increase Φ_i/Φ_0.

Field-reversed theta pinch experiments are underway in several laboratories. Stable periods $\sim$ 100 μs have been observed (Es'kov et al, 1978). Some parameters of the FRX-B and FRX-C experiments at Los Alamos are listed in Table 12B1. Once formed, the CT's can be moved axially along the magnetic field into another chamber by means of moving magnetic mirrors. In a reactor, this would separate the fusion burn chamber from the implosion coil where the CT's are generated.

Table 12B1. Approximate parameters of the FRX-B and FRX-C experiments at Los Alamos. From H. Dreicer and Los Alamos Staff, LA-8045-P (1979), Table I, p. 18.

	FRX-B	FRX-C
main bank voltage U_0, kV	45	250
final magnetic field B_f, T	0.75	0.9
risetime, μs	1.8	1.8
decay time, μs	150	200
wall radius r_w, m	0.2	0.4
coil length, m	1.0	1.5
fill pressure, Torr	9	2 - 90
$\pi r_w^2 n_0$, m^{-1}	2×10^{19}	2×10^{19} - 2×10^{20}
bias field B_i, T	0.18	0.16 - 0.32
major radius of plasma R	0.04	0.06 - 0.09
minor radius a, m	0.017	0.017 - 0.034
plasma length 2b, m	0.36	0.36 - 0.54
electron temperature T_e, eV	100	20 - 500
ion temperature T_i, eV	240	40 - 1100
final density, m^{-3}	4×10^{21}	10^{21} - 3×10^{22}
a/ρ_i	4	5 - 11
τ_s, μs	35	(to be measured)

Another idea is multiple mirror cells, each containing a CT, as shown in Fig. 12B8. If the ion mean free path is comparable to a cell length, then improved confinement of ions on open field lines should result in higher plasma pressure at the separatrix, reduced pressure gradients inside the CT's, and prolonged particle confinement times and stable periods.

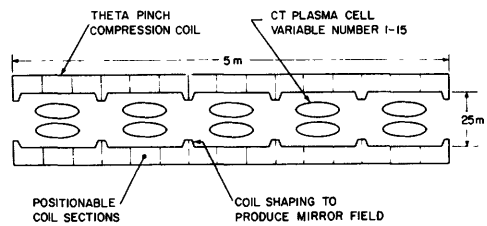

Fig. 12B8. Magnetic compression coil arrangement for the Scylla IV-P multiple-cell experiment. Shaped coils may be arranged in various patterns to produce up to 15 separate mirror cells. From H. Dreicer and Los Alamos Staff, LA-8045-P (1979), Fig. 10, p. 28.

The "triggered reconnection adiabatically compressed torus" (TRACT) concept is a field-reversed theta pinch with delayed field line reconnection, leading to shock heating during axial contraction, followed by adiabatic compression to ignition. The coil structures and firing sequence are illustrated in Fig. 12B9. The multipole barrier field prevents plasma-wall contact during field reversal, and permits bias fields greater than B_{imax} of Eq. (12B13) to be trapped. The combination of static cusp coils and pulsed trigger coils at the ends delays magnetic reconnection, so that the magnetic energy may be released suddenly after it has built up to a large value, producing an axial shock wave.

Fusion reactor design studies indicate that compact toroids offer the prospects of comparatively small, low-power, low-capital-cost reactors with recirculating power fractions $\lesssim$ 20 % (Hagenson and Krakowski, 1980; Willenberg, et al, 1980).

If an axial current is passed through a field-reversed theta pinch plasma during preionization, then a toroidal field will also be trapped inside the plasma, making the configuration akin to a spheromak.

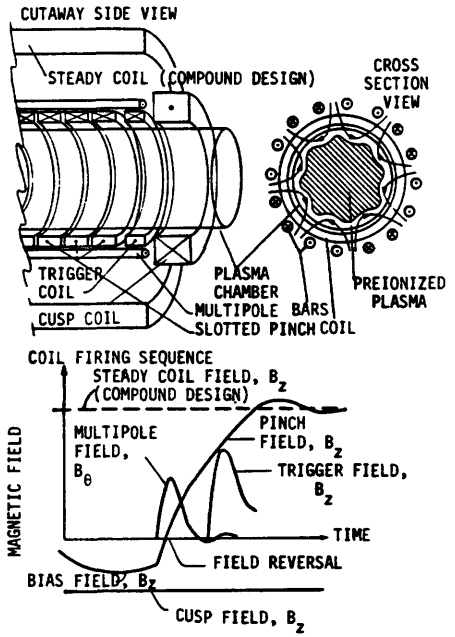

Fig. 12B9. Coil structures and firing sequence of TRACT. In the compound magnet design, the pinch field represents the sum of contributions from the steady outer coil and the pulsed pinch coil. B_z is the axial field component, and B_θ is the azimuthal field. From L. C. Steinhauer and H. J. Willenberg, "Technology issues of TRACT plasma engineering", Proceedings of the 4th ANS Topical Meeting on the Technology of Controlled Nuclear Fusion (King of Prussia, PA, 1980), DOE, 1981, Fig. 1.

12C. Spheromak

equilibrium and stability

In a plasma with high conductivity, the *magnetic helicity*

$$K \equiv \tfrac{1}{2}\int d\vec{x}\ \vec{A}\cdot\vec{B} = \text{constant} \qquad (12C1)$$

where $\vec{A}$ is the magnetic vector potential (Eq. 5B13), with the consequence that the energy of the system is minimized by current distributions of the form

$$\vec{\nabla}\times\vec{B} = \mu_0\vec{J} = \mu_0 k\vec{B} \qquad (12C2)$$

where k is a constant (Taylor, 1974). Since the force $\vec{J}\times\vec{B} = k\vec{B}\times\vec{B} = 0$, this is a *force-free equilibrium*. Taking the curl of Eq. (12C2) and using Eqs. (5B6) and (F30), we find

$$\nabla^2\vec{B} + k^2\vec{B} = 0 \quad . \qquad (12C3)$$

The solution of this equation in spherical coordinates (r,θ,ϕ) is

$$\vec{B}_n = \sum_{m=n}^{\infty} b_m^n e^{in\phi} \left\{ \left[m(m+1) p_m^n \frac{j_m(kr)}{kr} \right] \hat{r} + \left[\frac{in}{\sin\theta} p_m^n j_m - \sin\theta p_m^{n'} \frac{1}{kr} \frac{d}{dr} rj_m \right] \hat{\theta} \right.$$

$$\left. + \sin\theta \left[p_m^{n'} j_m + \frac{in}{\sin\theta} p_m^n \frac{1}{kr} \frac{d}{dr}(rj_m) \right] \hat{\phi} \right\} , \qquad (12C4)$$

where primes denote derivatives with respect to the argument of the function, $P_m^n \equiv P_m^n(\cos\theta)$ are Associated Legendre Functions, $j_m \equiv j_m(kr)$ are Spherical Bessel Functions, the b_m^n are constants (with $b_0^0 = 0$), and $\hat{r}$, $\hat{\theta}$, and $\hat{\phi}$ denote unit vectors (Rosenbluth and Bussac, 1979). [Spherical Bessel Functions and Associated Legendre Functions are described in M. Abramowitz and I. A. Stegun, *Handbook of Mathematical Functions*, National Bureau of Standards, Washington, DC, 1966.]

The b_1^0 term represents the "classical" spheromak shape illustrated in Fig. 12C1. If we take $b_1^0 = 1$, then $k = 4.493/d$. Adding the b_3^0 term makes the plasma oblate or prolate, depending on the ratio b_3^0/b_1^0.

For plasmas with significant resistivity, Eqs. (12C1) - (12C4) are not exact, but provide a fair approximation.

To evaluate the maximum stable values of beta, the Grad-Shafranov Equation (8C19) has been solved numerically for the model toroidal field distribution

$$I(\psi) = I_0 \left[\frac{\psi_e - \psi}{\psi_e - \psi_0} \right]^{\alpha} \qquad (12C5)$$

where ψ_0 and ψ_e are labelled in Fig. 12C1, I_0 is a normalizing factor (determined by a specified toroidal current), and α is a variable parameter. The separatrix surface is defined by an ellipse with $(x/d)^2 + (z/b)^2 = 1$ (Fig. 12C1). The flux at the plasma edge is defined by

$$\psi_e = \delta\psi_0 \quad . \qquad (12C6)$$

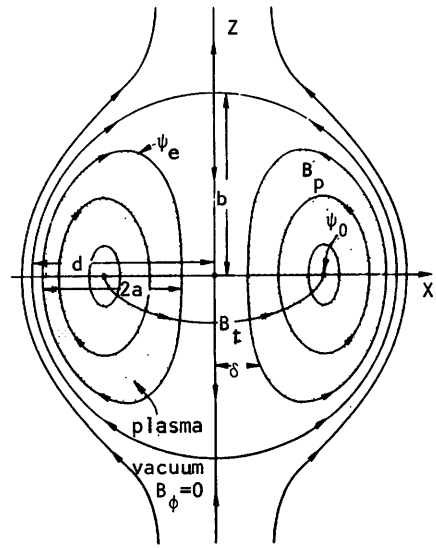

Fig. 12C1. The spheromak configuration. The "classical spheromak" has $\delta = 0$, and $b = d$. The major radius R is the value of the radius x at the magnetic axis. From M. Okabayashi and A. M. M. Todd, "A numerical study of MHD equilibrium and stability of the spheromak", Nuclear Fusion 20, 571-577 (1980), Fig. 1, p. 571.

The "classical spheromak" with $\delta = 0$ has safety factors $q(\psi_0) = 0.82$ and $q(\psi_e) = 0.72$, hence low magnetic shear (Table 8B1). A flux hole or vacuum region around the z axis represented by nonzero values of δ makes $q(\psi_e) = 0$, and

increases the shear, permitting higher values of plasma pressure to be sustained against interchange modes.

In the limit of zero plasma pressure, a value of $\alpha = 1$ corresponds to the force-free profile of Eq. (12C2), and a value of $\alpha = \frac{1}{2}$ corresponds to a constant-toroidal-current case (at large aspect ratio R/a). Larger values of α represent current profiles peaked near the magnetic axis.

The pressure profiles $p(\psi)$ were optimized for stability. Let

$$\beta_0 \equiv 2\mu_0 p_0 / B_0^2 \qquad (12C7)$$

$$\beta_e \equiv 2\mu_0 \langle p^2 \rangle^{\frac{1}{2}} / B_e^2 \qquad (12C8)$$

where the subscripts 0 and e denote values at the magnetic axis (ψ_0) and plasma edge (ψ_e), and < > denotes an average over the plasma volume. The maximum values of these betas for stability are shown as functions of ellipticity (b/d), of current profile shape α, and of flux hole size δ in Fig. 12C2. Values of $\alpha < 1$ may be difficult to attain. The shapes of the magnetic flux contours and radial variations of magnetic field components and poloidal current density

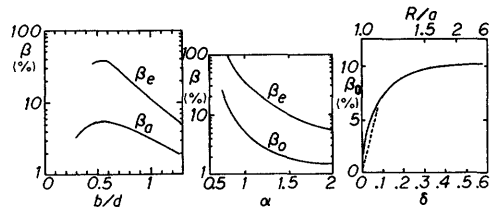

Fig. 12C2. Variations of maximum beta for stability with ellipticity (b/d), current profile parameter α, and flux hole size δ, about the nominal case $\alpha = 1$, (b/d) = 0.6, and $\delta = 0.05$. From M. Okabayashi and A. M. M. Todd, Nuclear Fusion 20, 571-577 (1980), Figs. 3, 4, 5.

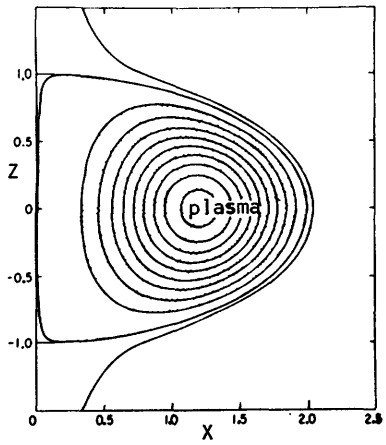

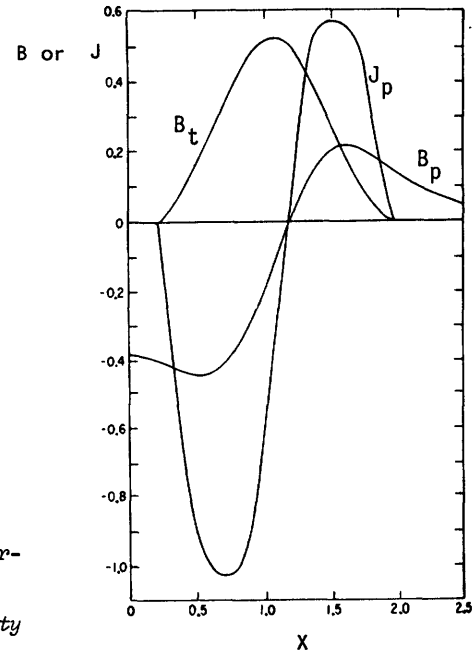

Fig. 12C3. Equilibrium magnetic flux contours and radial variations of magnetic field components and poloidal current density in the midplane for a spheromak with $\alpha = 1.3$, b/d = 0.6, and $\delta = 0.05$. (The toroidal current density profile $J_t(x)$ is not shown.) From M. Okabayashi and A. M. M. Todd, Nuclear Fusion 20, 571-577 (1980), Fig. 6.

are shown in Fig. 12C3 for a near-optimum case. For this case, the flux surfaces near the magnetic axis are nearly circular, and $B_p(x=2) \equiv B_e \simeq B_0/3$, where $B_0 \equiv B_\phi(x=1.2)$. Stability is improved if hollow current profiles occur (J_t minimum near the magnetic axis.)

Prolate spheromaks tend to be unstable to an n = 1 tilting mode (a rotation of the z axis). Oblate spheromaks are unstable to current-driven kink modes, but these can be stabilized by a nearby conducting wall ($r_w/d \sim 1.2$). Thus, given a suitable conducting wall, stable operation appears feasible with oblate plasmas ($b/d \sim 0.5$) at $\beta_e \sim 15$ %.

production by pinches and guns

Spheromak plasma configurations have been produced by several means, including theta pinches, plasma guns, and slow induction.

A spheromak can be produced in a field-reversed theta pinch, using an axial current I_z to induce a toroidal magnetic field, as illustrated in Fig. 12C4. Magnetic flux surfaces measured in the University of Maryland Paramagnetic Spheromak (PS-1) device are shown in Fig. 12C5. Initially two CT's are formed, but by 2 μs they have merged into one. Plasma parameters at t = 2 μs are $n \sim 3\times10^{21}$ m^{-3}, $T_e \sim 30$ eV, $T_i \sim 200$ eV, $\beta = 0.4$ at the plasma center. The spheromaks produced in this manner have remained stable for times up to 40 μs, with gradual decay by diffusion, but tilting occurs at late times.

Production of a field-reversed plasma by a coaxial plasma gun was illustrated in Fig. 11F4. Such plasmas are being injected into magnetic mirrors and vacuum tanks with conducting liners of various shapes to study their time evolution, stability against tilting, and the possibility of sustaining them by neutral beam injection or other means. Compact toroids injected into a cylindrical flux conserver were observed to rotate their axis by 90° so that it became perpendicular to the axis of the gun and flux conserver, but then they decayed gradually with time constants up to 100 μs.

slow induction technique

For reactor applications it is desirable to avoid pulsed high-power

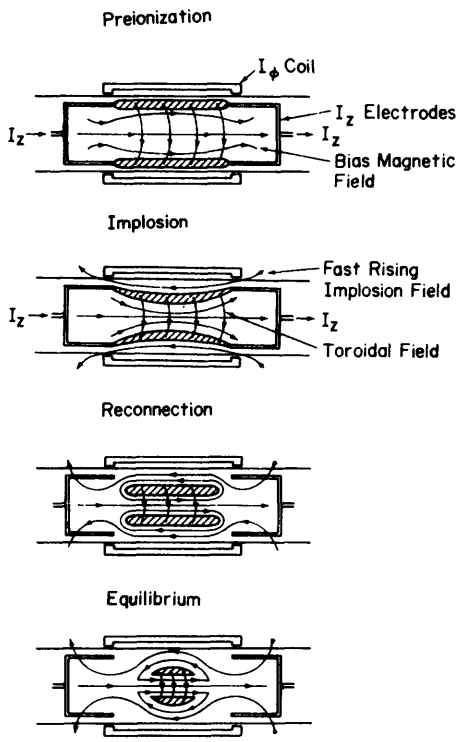

Fig. 12C4. Formation of a spheromak configuration by combination of a reversed-field theta pinch with an axial current. From G. C. Goldenbaum, J.H. Irby, Y.P. Chong, and G.W. Hart, "Formation of a spheromak plasma configuration", Physical Review Letters 44, 393-396 (1980), Fig.1.

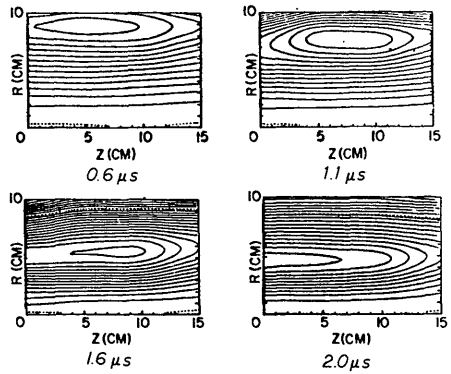

Fig. 12C5. Surfaces of constant magnetic flux in the PS-1 device after the start of the fast-rising main B_z field. These data were taken with a two-coil probe, which measured B_z and B_ϕ simultaneously and was moved between shots to map out half of the R-Z plane. The change in the flux function between adjacent curves is 10^{-4} T-m^2, and the dashed curve is the separatrix. From G. C. Goldenbaum, J. H. Irby, Y. P. Chong, and G. W. Hart, Physical Review Letters 44, 393-396 (1980), Fig. 2.

systems, with associated electrodes, impurities, high-voltage breakdown problems, and high stresses. An alternative scheme induces plasma poloidal and toroidal currents on a longer time scale τ such that $\tau_A << \tau < \tau_{dif}$, where $\tau_A \equiv R/v_A$ is the Alfven wave transit time and $\tau_{dif} \sim a^2/4D$ is the characteristic plasma diffusion time.

A toroidally-shaped flux core, Fig. 12C6, contains both toroidal field (TF) coils (a solenoid wound in the poloidal direction around the core) and poloidal field (PF) coils (wound in the toroidal direction inside the core). When these coils are pulsed, both poloidal and toroidal fields are induced in the plasma. A continuous vertical magnetic field is produced by external coils (not shown) to weaken the poloidal field on the small-major-radius side of the flux core.

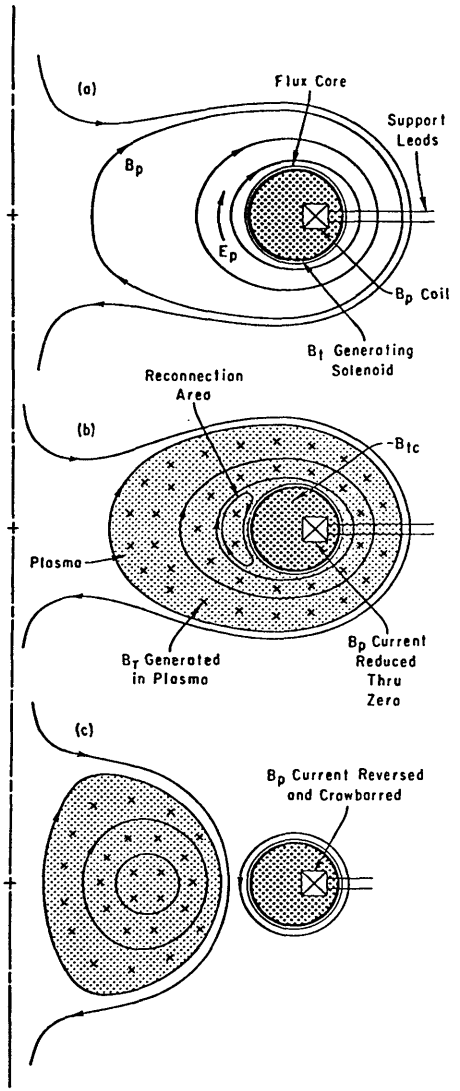

Fig. 12C6. Spheromak production by slow induction. From M. Yamada, H.P. Furth, W. Hsu, A. Janos, S. Jardin, M. Okabayashi, J. Sinnis, T.H. Stix, and K. Yamazaki, "Quasistatic formation of the spheromak plasma configuration", Physical Review Letters 46, 188-191 (1981), Fig.1.

First the PF coil is pulsed on, producing a poloidal field around the flux core, Fig. 12C6a. Next the TF coil is pulsed on, inducing a poloidal current in the sleeve-shaped plasma surrounding the flux core. The resultant field stretches the poloidal-field sleeve towards the magnetic axis, where the poloidal field is

weakest. Then the PF coil is reduced through zero to a negative value of current and maintained there (by "crowbarring" the capacitor bank, Section 21B). This large change of the poloidal field causes magnetic field lines to break and reconnect on the small-major-radius side of the flux core, Fig. 12C6b.

The time variations of the PF and TF coil currents and the plasma density in the Proto S-1 device are shown in Fig. 12C7. The desired spheromak configuration, Fig. 12C6c, is completely formed at t ≃ 16 μs. The toroidal and poloidal fields, highly reproducible from pulse to pulse, have been mapped out with magnetic probes. The experimental toroidal field contours at t = 16 μs are compared with theoretical simulation values in Fig. 12C8. After its formation, the spheromak persists

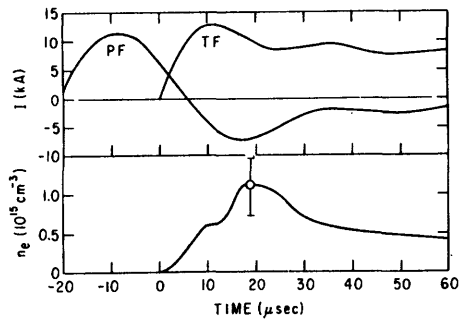

Fig. 12C7. Time evolution of the current in one turn of the PF (three-turn) and TF (40-turn) coils and of the plasma density at R = 6 cm and Z = 0 in the Proto S-1 device. The vacuum field outside the core is expected to be phase shifted by 6-7 μs (PF) and 2 μs (TF) because of induced liner currents. From M. Yamada et al, Physical Review Letters 46, 188-191 (1981), Fig. 2.

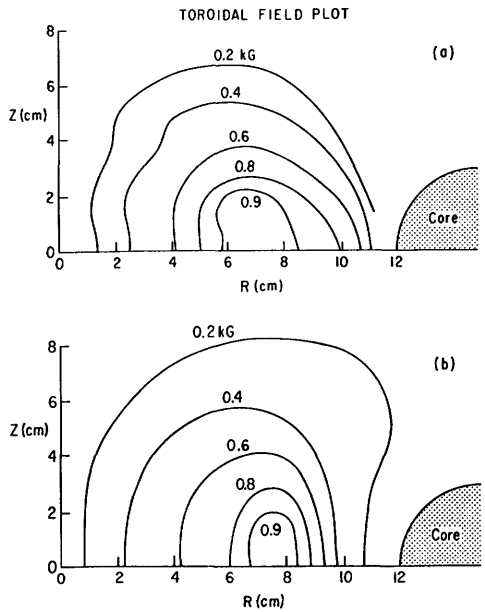

Fig. 12C8. Measured toroidal field contours at t = 16 μs in the Proto S-1 device (top), and the result of computer simulation (bottom). The symmetry around the major axis was checked and found to be satisfactory. From M. Yamada et al, Physical Review Letters 46, 188-191 (1981), Fig. 4.

for 15-20 μs, when it develops non-axisymmetric motion (perhaps a tilting instability). The Proto S-1 device is a 1/6 scale version of the S-1 device, Fig. 12C9, which will explore regimes of slower induction and longer plasma duration. The S-1 device will have a toroidal plasma current $I_t \sim 500$ kA, a formation time ∿ 0.1 ms, and an equilibrium vertical field of 0.2 T. The "pinch" coils of Fig. 12C9 enhance field line reconnection. Power loss to the toroidal flux core supports will limit T_e to low values initially, but after the toroidal plasma is formed this loss will become insignificant, and ohmic heating should raise T_e to the desired values (> 100 eV). In order to avoid microinstabilities, the electron streaming velocity will be kept below 3 % of the thermal velocity, by keeping

$$\beta_0^* n a^2 > 3 \times 10^{16} \text{ m}^{-1} \qquad (12C9)$$

where

$$\beta_0^* \equiv 2\mu_0 \langle p^2 \rangle^{\frac{1}{2}} / B_0^2 \qquad (12C10)$$

and B_0 is the field at the magnetic axis. With $n > 5 \times 10^{20}$ m^{-3} and $a \sim 0.2$ m, values of $\beta_0^* \gtrsim 2$ % will satisfy the requirement of Eq. (12C9).

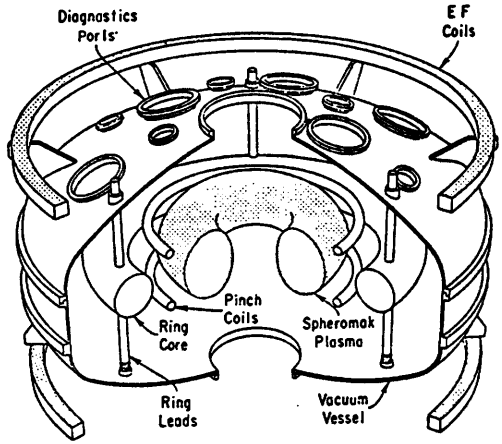

Fig. 12C9. The S-1 Spheromak device at Princeton. From M. Yamada, J. Sinnis, H.P. Furth, M. Okabayashi, G. Sheffield, T.H. Stix, and A.M.M. Todd, "Design and fabrication of the S-1 Spheromak device", Proceedings of the US-Japan Joint Symposium on Compact Toruses and Energetic Particle Injection, PPPL, 1979, p. 171-175, Fig. 7.

applications

Several schemes have been proposed for spheromak fusion reactors. In some the plasma is formed by a gun or pinch, and then translated into the burn chamber. In others the plasma is formed in the reaction chamber. The "Holomak" scheme uses an aluminum shell flux conserver to transmit the toroidal flux from outside the blanket into the plasma burn chamber, as in Fig. 12C10. The toroidal field lines generated by the transformer cannot penetrate quickly through the aluminum shell, so they are forced upwards into the reaction chamber. In this design ohmic heating coils are placed radially inside the plasma region for effective coupling to the plasma, as in a tokamak. The divertor coils are for control of plasma impurities (Chapter 25).

In the "Stellarmak" concept the spherical chamber is surrounded by helical windings, which create magnetic shear to enhance plasma stability and beta limits. The resultant field ripple and viscous effects would also aid in plasma current drive (Section 13D) by neutral beam injection (C.W. Hartmann, 1979 Symposium).

A compact torus plasma may be able to operate continuously, sustained by neutral gas feed through an ionization layer. The fresh fuel ions would be pulled towards the plasma center by the Nernst effect (a thermal force tending to move particles towards regions of higher temperatures). The principle advantage of spheromaks is their geometric simplicity, which facilitates assembly and maintenance.

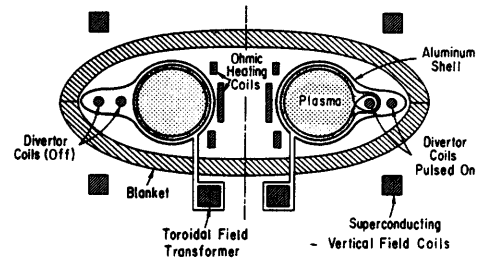

Fig. 12C10. A Holomak reactor. The spheroidal blanket encloses an aluminum stabilizing shell, which also serves as a one-turn toroidal field coil. The divertor is shown pulsed on (right side) and off (left side). The design is compatible with axial disassembly. From T.H. Stix and A.M.M. Todd, "The Holomak -- a toroidal spheromak", Proceedings of the US-Japan Joint Symposium on Compact Toruses and Energetic Particle Injection, PPPL, 1979, p. 204-207, Fig. 4.

12D. Reversed Field Pinch (RFP)

equilibrium and stability

The main idea of a reversed field pinch is to have the toroidal magnetic field in one direction inside the plasma and in the opposite direction outside the plasma, along with a poloidal field produced by a toroidal plasma current. This configuration can be produced by the magnetic field programming shown in Fig. 12D1. The equilibrium radial field distributions are shown in Fig. 12D2, and the resultant helical field lines are illustrated in Fig. 12D3. The high magnetic shear (rapid change in pitch angle with radius) gives the RFP good MHD stability.

The RFP equilibrium can be described using the Taylor-Woltjer minimum-energy condition (12C2)

$$\mu_0 \vec{J} = \vec{\nabla} \times \vec{B} = k\vec{B} \qquad (12D1)$$

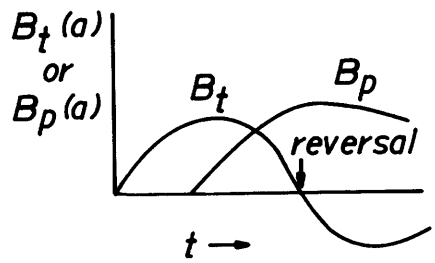

Fig. 12D1. Time variation of toroidal magnetic field B_t and poloidal field B_p at the plasma edge in a reversed field pinch. A toroidal plasma current is induced to create the poloidal field. The original positive toroidal field is trapped inside the plasma, and the external toroidal field is reversed. (It may reverse itself spontaneously). Other field programming sequences may be used to achieve the same effect.

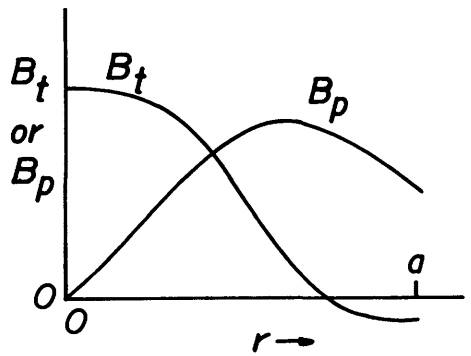

Fig. 12D2. Equilibrium radial distributions of toroidal and poloidal magnetic fields in a reversed field pinch.

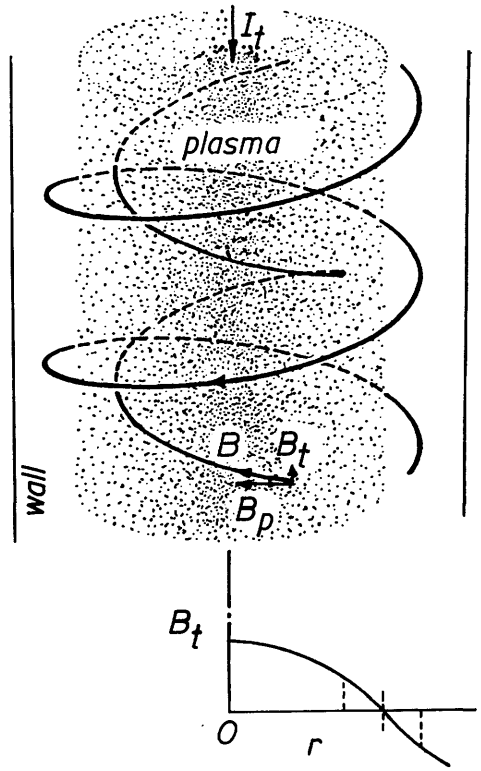

Fig. 12D3. Shape of magnetic field lines in a reversed field pinch. The toroidal field is positive on the inside and negative on the outside of the plasma. The plasma current I_t produces a poloidal field component B_p. The resultant magnetic field is helical, spiralling in different directions inside the plasma and outside the plasma. Courtesy of P.C.T. van der Laan, from oral presentation Bull. Am. Phys. Soc. 22, 1156 (1977).

in cylindrical coordinates (as an approximation to toroidal geometry). Assuming symmetry in the azimuthal and longitudinal directions ($\partial/\partial\theta = \partial/\partial z = 0$), the solution of this equation is

$$B_z = B_0 J_0(kr) \quad \textit{(represents } B_t\textit{)} \qquad J_z = kB_z/\mu_0$$

$$B_\theta = B_0 J_1(kr) \quad \textit{(represents } B_p\textit{)} \qquad J_\theta = kB_\theta/\mu_0 \qquad (12D2)$$

$$B_r = 0 \qquad J_r = 0$$

where J_0 and J_1 are Bessel functions and B_0 is a constant. These functions have radial profiles similar to those of Fig. 12D2. The reversed toroidal field configuration corresponds to a minimum energy state. Including finite plasma pressure (not accounted for by a force-free model) shifts the equilibrium $\vec{J}$ slightly from that of this *Bessel Function Model (BFM)*. The component of $\vec{J}$ parallel to $\vec{B}$ produces the desired magnetic field configuration, and the component perpendicular to $\vec{B}$ confines the plasma pressure via $\vec{\nabla}p = \vec{J}\times\vec{B}$.

It is convenient to describe RFP equilibria in terms of two parameters:

pinch parameter $\Theta \equiv B_\theta(a)/\langle B_z\rangle$ (12D3)

field-reversal ratio $F \equiv B_z(a)/\langle B_z\rangle$ (12D4)

where $\langle B_z\rangle$ is the volume average of $B_z(r)$. For BFM distributions, $\Theta = ka/2$. There is a single value of F corresponding to each value of Θ. Experimental equilibria tend to fall near a universal F-Θ curve, as illustrated in Fig. 12D4, provided that the experiment lasts long enough. Reversal of the B_z field occurs (F becomes negative) for values of $\Theta \gtrsim 1.3$. Thus, there is a minimum value of Θ for operation in the RFP mode. Experiments often deviate from the equilibrium F-Θ curve initially, but move towards it as the plasma approaches equilibrium. This approach to the minimum energy state may be hastened by MHD instabilities and plasma turbulence, and spontaneous reversal of B_z is often observed, as Θ exceeds 1.3.

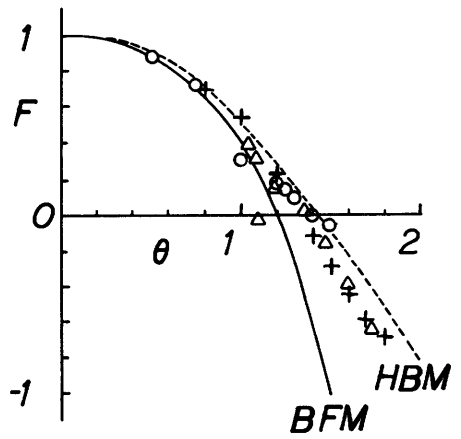

Fig. 12D4. An F-Θ diagram with points from three experiments (HBTX1, Alpha, and Zeta) operating in widely different conditions, illustrating a universal experimental F-Θ curve. The theoretical curves are for the Bessel Function Model (BFM) and a "high beta model" (HBM) with relatively high β (up to $\sim$ 20 %) corresponding better to the distributions found in experiments. From H.A.B. Bodin and A.A. Newton, "Reversed-field-pinch research", Nuclear Fusion 20, 1255-1324 (1980), Fig. 27.

In studying plasma stability, it is convenient to define

$$\textit{magnetic pitch} \equiv P \equiv rB_z/B_\theta = rB_t/B_p \simeq Rq \qquad (12D5)$$

where R is the plasma major radius and q is the safety factor (Table 8B1). Since $B_p \sim B_t$, $q < 1$. The ratio B_t/B_p is the tangent of the angle between B and B_p (Fig. 12D3).

RFP plasmas are stable to current-driven kink modes if a conducting wall is located near the plasma such that $r_w/a \lesssim 2\text{-}3$, where r_w is the wall radius. The ideal MHD stability criterion for pressure-driven modes is (Bodin and Newton, 1980)

$$\frac{rB_t^2}{8\mu_0}\left[\frac{1}{q}\frac{dq}{dr}\right]^2 \geq (1-q^2)\left(-\frac{dp}{dr}\right) \quad . \qquad (12D6)$$

Usually (-dp/dr) is positive. Tokamaks are stabilized by having $q > 1$. RFP have $q < 1$, but they can be stabilized by large magnetic shear. If $q \ll 1$, this reduces to

$$\frac{rB_t^2}{8\mu_0}\left[\frac{1}{q}\frac{dq}{dr}\right]^2 \geq \left(-\frac{dp}{dr}\right) \qquad (12D7)$$

which is called the *Suydam criterion*. This tells the maximum pressure gradient which can be sustained by a given magnetic pressure and shear. Stable values of β are shown in Fig. 12D5 as functions of Θ, according to ideal MHD theory.

Including finite resistivity in the MHD equations leads to tearing modes and resistive interchange modes. The tearing modes (current-driven) are relatively benign in RFP's, but the resistive interchange modes (pressure-driven) may reduce the allowable values of β to $\lesssim 10$ %. According to the model of Christiansen and Roberts (1978), an RFP has three regions: a turbulent inner region unstable to Suydam modes, with flat density and temperature profiles, an intermediate high-shear stable region sustains the plasma pressure, and an outer region where atomic collisions and wall interactions are important. The duration of stability depends upon how long it takes for the trapped positive B_t flux to diffuse outwards through the confinement region. RFP theory and experiments are reviewed by Bodin and Newton (1980).

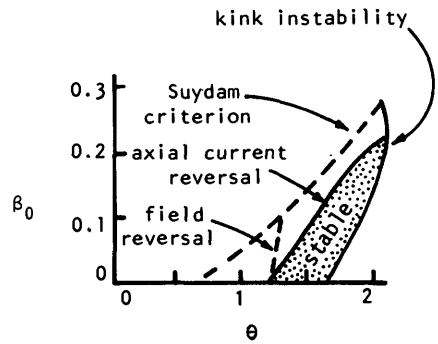

Fig. 12D5. Stability diagram showing the variation of limiting $\beta_0 \equiv 2\mu_0 p_0/B_{t0}^2$ *(0 denotes r = 0) with* Θ *for a modified minimum energy configuration. From H.A.B. Bodin and A.A. Newton, Nuclear Fusion 20, 1255-1324 (1980), Fig. 9.*

experiments

In the 1960's periods of low plasma fluctuations were observed in the Zeta device, lasting up to 3 ms (for $\Theta \sim 2.1$, $p_0 \sim 3$ Pa, and magnetic Reynolds number

S > 4000). These *quiescent periods*, indicative of good confinement, were associated with spontaneous toroidal field reversal, explained later by Taylor's minimum energy theory, Eqs. (12D1), (12D2).

Several small-bore devices with fast-rising magnetic fields have been built to study RFP phenomena with various field programming schemes (variants of Fig. 12D1). Most of them have been limited by radiation losses to $T_e \lesssim 20$ eV, at which the magnetic Reynolds number S is too low to observe quiescence.

There is a peak in the radiation power loss curve from oxygen impurities at $T_e \sim 25$ eV, Fig. 3F3. In order to reach higher temperatures, the heating power must be high enough to overcome this *radiation barrier*. We can define a parameter

$$\Sigma_0 \equiv \frac{\text{(approximate cooling rate by oxygen at T = 25 eV)}}{\text{(approximate ohmic heating rate at T = 25 eV)}}$$

$$\Sigma_0 = \frac{Q_0(T_0)\langle n_0\rangle\langle n_e\rangle}{\eta(T_0)\langle J\rangle^2} \sim 0.005 \left(\frac{10^7 A/m^2}{\langle J\rangle}\right)\left(\frac{\langle n_0\rangle}{10^{18}\ m^{-3}}\right)\left(\frac{\langle n_e\rangle}{10^{20}\ m^{-3}}\right) \qquad (12D8)$$

where $T_0 = 25$ eV, $Q_0 \sim 5\times10^{-32}$ Wm^3 (Fig. 3F3), η is the resistivity, n_0 is the oxygen concentration (m^{-3}), n_e is the electron density (m^{-3}), J is the current density (A/m^2), and $\langle\ \rangle$ denote a mass-weighted average (Caramana and Perkins, 1979 Joint Symposium). Since there will be other impurity species and other energy loss processes, it is required that $\Sigma_0 \lesssim 0.2$ in order to overcome the radiation barrier.

A second requirement is that the energy needed to heat the plasma to T $\sim$ 40 eV be a small fraction of the poloidal magnetic field energy W_p, in order to avoid a serious erosion of the confining field. Let

$$\tau \equiv \tfrac{1}{2}\ln[W_p(0)/W_p(t)]$$

$$\beta_D \equiv 2W_k/3W_p(0) \qquad (12D9)$$

where W_k is the internal kinetic energy content of the plasma at T = 40 eV. In order to keep $W_p(t)/W_p(0) \gtrsim 0.9$, $\tau \lesssim 0.05$. These requirements are summarized in Fig. 12D6. Thus, a small device like ZT-S ($r_w \simeq 8$ cm) cannot succeed in passing the radiation barrier, even with a very small oxygen fraction. The ZT-40 device can tolerate fractions up to about 1 %, and the larger RFX device can tolerate oxygen fractions over 2 %.

Parameters of some medium-sized RFP experiments are listed in Table 12D1. The ZT-40M device is shown in Fig. 12D7. When its original ceramic liner was replaced with a metal liner, dramatic improvements in confinement occurred: the plasma fluctuation level decreased from $\delta\phi/\phi \sim 15$ % to about 1 %; the toroidal current decay time increased from 0.3 ms to several ms; much higher T_e were obtained at a given toroidal current; and the high temperatures lasted much longer. With a "power crowbar" switch to keep coil currents flowing longer, the quiescent discharge duration is extended to about 8 ms, particle confinement times of 1.4 ms are attained, and $T_e > 150$ eV are observed at a toroidal current of 250 kA. Time variations of toroidal current and magnetic field are shown in Fig. 12D8.

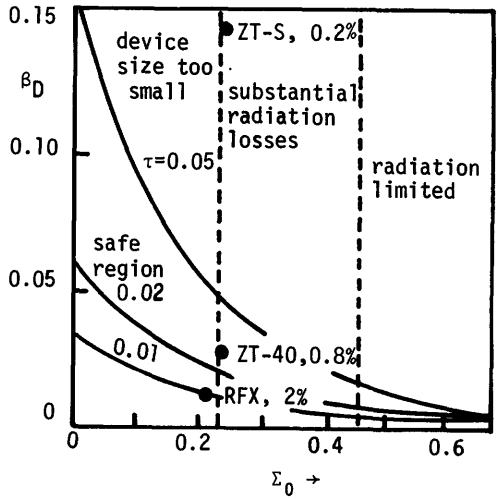

Fig. 12D6. A design guide for RFP plasmas. Plasmas in the central region will have difficulty in passing the radiation barrier, but may succeed. Those on the right side will fail by radiation losses. Those on the left side can succeed if β_D is small enough to keep $\tau \lesssim 0.05$. The solid points refer to experimental devices. The percentages refer to oxygen impurity content near the boundary line. From E. J. Caramana and F. W. Perkins, "Effects of impurity radiation on reversed-field pinch evolution", Nuclear Fusion 21, 23 (1981).

Table 12D1. Parameters of some RFP experiments. From H.A.B. Bodin and A.A. Newton, Nuclear Fusion 20, 1255-1324 (1980), Table VIII, p. 1313.

	R, m	a, m	I_t, MA	field rise time, ms	field duration, ms
Zeta, Culham (shut down)	1.5	0.48	0.3-1.05	0.8-2.4	3-20
Eta Beta II, Padua	0.65	0.12	0.2-0.3	0.12	1
HBTX1A, Culham	0.8	0.26	0.4	0.1-0.5	1-5
ZT-40M, Los Alamos	1.14	0.2	0.15-0.6	0.15-1	8
RFX, Culham (planned)	1.8	0.6	2.0	10-50	100

Reversed field pinch reactor studies indicate that $Q \sim 12$ can be attained with $I \sim 20$ MA, $a \sim 1.5$ m, $R \sim 13$ m, $T \sim 10$ keV, $n \sim 4 \times 10^{20}$ m^{-3}, $B \sim 2$ T, $\beta_p \sim 0.35$, burn time ~ 20 s, cycle time ~ 30 s, recirculating power fraction $\varepsilon \lesssim 20$ %, and gross thermal power $\sim$ 2-3 GW. Potential advantages of such a reactor include :

* possibly high beta, low magnetic field
* arbitrary aspect ratio
* high current density; ignition may be possible by ohmic heating alone.

On the other hand, a conducting shell is needed for plasma stabilization, and the attainable value of beta is uncertain; impurities from plasma-wall interactions may hinder ignition by ohmic heating; and pulsed magnetic fields create cyclic stress problems in the coils and chamber.

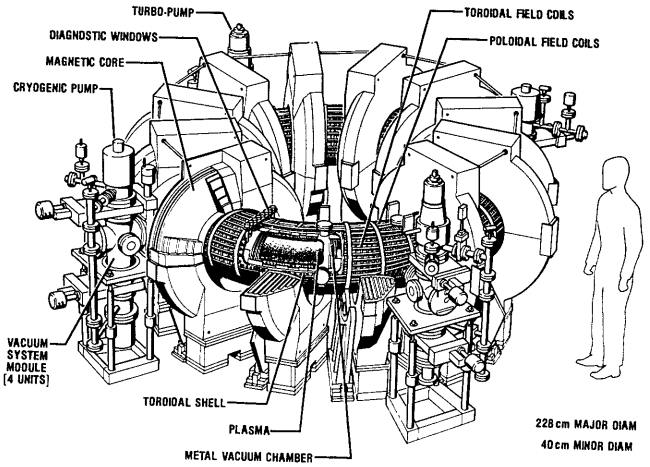

Fig. 12D7. The ZT-40M experiment at Los Alamos. From D.A. Baker et al, "LASL toroidal reversed-field pinch programme", Plasma Physics and Controlled Nuclear Fusion Research 1978 (Innsbruck), IAEA, Vienna, 1979, Volume II, p. 3-22, Fig. 8.

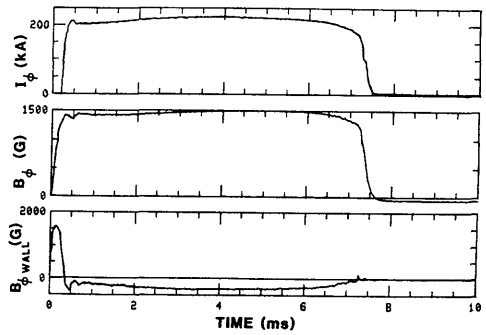

Fig. 12D8. Toroidal current, average toroidal magnetic field, and toroidal field at the wall in ZT-40M with power crowbars. From D. A. Baker et al, 10th European Conference on Controlled Fusion and Plasma Physics, Moscow, September 1981, Fig. 8.

12E. Pitch-Reversed Helical Pinch

equilibrium and stability

If two adjacent flux surfaces have the same pitch $P \equiv rB_t/B_p$, plasma fluctuations can interact resonantly and grow rapidly, resulting in plasma instability. For stability, the pitch profile must monotonically increase or decrease without a maximum or minimum (except at r = 0). The value q = P/R = 1 corresponds to a rotational transform angle (Table 8B1) of 2π, so that a field line closes on itself after going once around the torus. This situation can lead to rapid growth of fluctuations, so it must be avoided, too. Therefore, the q(r) profiles of toroidal devices must increase or decrease monotonically, without crossing q = 1 within the plasma. Pitch profiles of tokamaks, stellarators, and RFP are illustrated in Fig. 12E1. (Tokamaks and stellarators will be described in Chapters 13 and 14).

The RFP has *pitch reversal*, meaning that the pitch (or q) changes sign within the plasma. A pitch-reversed helical pinch has a similar q profile, but it is produced by helical windings, instead of by a programmed toroidal field. Poloidal plasma currents produce an internal B_t (paramagnetism), as in spheromaks. A

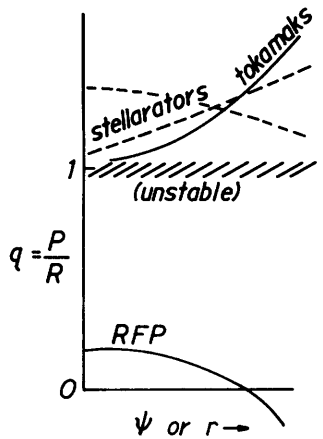

Fig. 12E1. Variation of safety factor with flux surface or radius, for tokamaks, stellarators, and RFP.

pitch-reversed helical pinch is essentially a toroidal Z-pinch stabilized by external helical windings, as shown in Fig. 12E2. A pitch-reversed helical pinch device is compared with some other toroidal confinement schemes in Fig. 12E3.

The equilibrium of a helical pinch may be described in terms of a long straight cylinder with helical symmetry. (Toroidal effects are small, since $q << 1$). The independent variables are reduced from (r, θ, z) to (r, v), where

$$v \equiv \theta - \alpha z \qquad (12E1)$$

and α is the inverse pitch of the helix. The magnetic field components may be expressed in terms of a magnetic

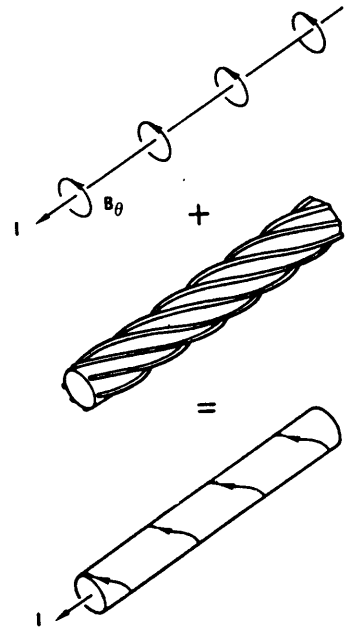

Fig. 12E2. Addition of helical windings ($\ell = 3$) to a cylindrical (or toroidal) Z-pinch having only an azimuthal magnetic field at its surface. The resulting field lines have an axial component, with a direction which can be made opposite to that of the internal pitch. This additional axial component is called axial translation or axial transform, and the resultant pitch reversal helps to stabilize the plasma. From T. Ohkawa, "Helical plasma configuration with pitch reversal", Nuclear Fusion 20, 1464-1469 (1980), Fig. 1.

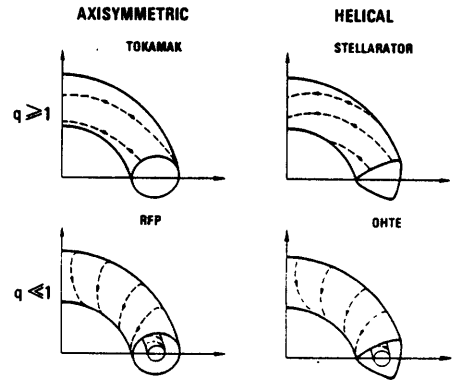

Fig. 12E3. A comparison of tokamak, stellarator, RFP, and OHTE (a pitch-reversed helical pinch). From T. Ohkawa and the OHTE Group, "Physics of the OHTE", Proceedings of the US-Japan Joint Symposium on Compact Toruses and Energetic Particle Injection, PPPL, 1979, p. 65-67, Fig. 1.

flux function $\psi(r, v)$ and a helical current function $f(\psi)$ as

$$B_r = -\frac{1}{r}\frac{\partial\psi}{\partial v}$$

$$B_\theta = \left(\frac{\partial\psi}{\partial r} + \alpha r f\right)/K$$

$$B_z = \left(-\alpha r \frac{\partial\psi}{\partial r} + f\right)/K \quad . \tag{12E2}$$

where

$$K \equiv 1 + \alpha^2 r^2 \quad .$$

The current density components may be found from $\mu_0\vec{J} = \vec{\nabla}\times\vec{B}$. Then the plasma equilibrium equation $\vec{\nabla}p = \vec{J}\times\vec{B}$ becomes

$$-\mu_0 p' = \frac{1}{r}\frac{\partial}{\partial r}\frac{r}{K}\frac{\partial\psi}{\partial r} + \frac{1}{r^2}\frac{\partial^2\psi}{\partial v^2} + \frac{2\alpha f}{K^2} + \frac{ff'}{K} \tag{12E3}$$

where $p = p(\psi)$ and primes denote derivatives with respect to ψ (Ohkawa et al, 1980). This equation is the helical analog of the Grad-Shafranov equation (8C19). For any assumed pressure profile $p(\psi)$ and current profile $f(\psi)$, it can be solved to find the equilibrium shape of the flux surfaces $\psi(r,v)$. Analytic solutions are possible in simple cases, such as $p' = 0$, $f = -\mu$ (where μ = constant), which leads to a force-free equilibrium with $\vec{J} = \mu\vec{B}$ and

$$\psi(r,v) = \sum_{m=0}^{\infty} a_m \left[\frac{\mu}{\alpha} J_m(y_m) - y_m J_m'(y_m)\right] e^{imv} \tag{12E4}$$

$$y_m \equiv \left[\mu^2 - m^2\alpha^2\right]^{\frac{1}{2}} r$$

where J_m is a Bessel Function, J_m' is its derivative, and the a_m are constants. (If $\mu^2 < m^2\alpha^2$, then the J_m are replaced by modified Bessel functions I_m.) For a case of order ℓ, we keep only the $m = 0$ and $m = \ell$ terms. For example, using three pairs of helical windings would produce an $\ell = 3$ helical equilibrium, as illustrated in Fig. 12E4. The parameter μ can be controlled experimentally by varying the plasma current I and the axial magnetic flux Φ, because $\mu = \vec{J}/\vec{B} = I/\Phi$.

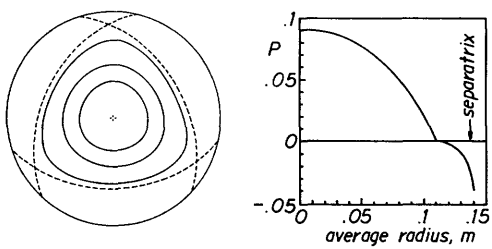

Fig. 12E4. Surfaces of constant ψ on the (r, ϕ) plane calculated for a force-free, free-boundary $\ell = 3$ helical equilibrium (left) and the resulting variation of pitch P with flux-surface-average radius (right). The dashed curve is the separatrix. Basic parameters for this case are: winding pitch = 0.215 m, separatrix vertex radius = 0.172 m, mean separatrix radius = 0.140 m, $f' = -22\ m^{-1}$ inside and $f' = 0$ outside the zero pitch surface, cylindrical boundary radius = 0.185 m. From T. Ohkawa, Nuclear Fusion 20, 1464-1469 (1980), Fig. 2.

Numerical calculations for cases with finite plasma pressure indicate stability to ideal interchange modes for values of poloidal beta over 30%, due to the large magnetic shear. Resistive interchange modes will probably lower the allowable beta, as for the RFP. Stability to kink and tearing modes is provided by the combination of shear and a conducting shell. The pitch reversal needed for stability is tolerant to moderate magnetic field errors.

In an RFP the pitch reversal is usually produced spontaneously by plasma turbulence, which temporarily impairs confinement, resulting in energy loss. The high current density near the walls may lead to significant influx of impurities. In a pitch-reversed helical pinch the reversal, aided by steady-state helical coils, may be produced with less turbulence, and the reversal will last as long as the current in the helical windings is maintained. A lower current density near the walls may result in lower impurity influx. In both pinches, the duration of the plasma is limited by decay of the plasma current.

experiments

A pitch-reversed helical pinch requires a set of helical windings, poloidal field coils or an ohmic heating transformer to induce the toroidal plasma current, and vertical field coils to maintain the desired plasma equilibrium position. (The vertical field could also be produced by varying the pitch of the helical windings.) The "Ohmic Heated Toroidal Experiment" (OHTE), shown in Fig. 12E5, consists of a stainless steel bellows vacuum chamber surrounded by a 1.5 cm thick aluminum shell (for plasma stabilization), around which a set of $\ell = 3$ helical windings is arranged. By imbalancing the currents in the helical windings, a net toroidal field up to 0.3 T can be produced, to provide the needed toroidal flux.

Table 12E1. Parameters of the OHTE.

R = 1.24 m

a = 0.19 m

E coils (ohmic heating)
flux swing = 2.8 V-s

E-coil energy = 3 MJ

plasma current $I \leq 0.6$ MA

helical coil power $\leq$ 16 MW

$B_t \leq 0.3$ T

$B_v \leq 0.16$ T

duration of experiment = 0.1 s

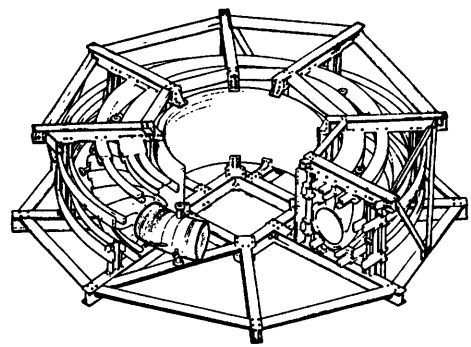

Fig. 12E5. The OHTE, showing vacuum chamber, helical windings, ohmic heating coils, and structural supports. From American Nuclear Society Fusion Energy Division Newsletter, January 1981, p. 2.

Other parameters are listed in Table 12E1. If the electron energy loss follows the "Alcator" scaling of tokamaks, $T \sim 1$ keV are anticipated. With such scaling, a reactor plasma with $a \sim 0.2$ m, $n \sim 3 \times 10^{21}$ m^{-3}, and $I \sim 6$ MA could achieve ignition by ohmic heating, if impurity concentrations were not too high.

12F. Topolotron

topological stability

The qualitative global discussion of the stability of a plasma differs greatly from the usual quantitative local analysis. The approach follows Poincaré who, after having shown the impossibility of proving the stability of the solar system by *any* quantitative method, revived the qualitative point of view in dealing with the problem (Abraham, 1967). His was a global geometric approach in which the dynamical problem was reduced to a geometric one by his introduction of the idea of a phase portrait. He then proceeded directly to the stability problem, which is a qualitative one, by qualitative (geometric) methods. This departed from the usual approach of first reducing the problem to an analytic one, obtaining approximate quantitative solutions and then attempting to deduce the qualitative properties from these approximate solutions. Following this lead, Andronov and Pontriagin (1937) rigorously formulated the problem in terms of the notion of structural stability.

Structural stability is thought to be the most comprehensive of the many different notions of stability (Abraham, 1967). In plasma confinement it requires that any nearby global vector magnetic field accessible to an equilibrium magnetic configuration by a small perturbation be qualitatively equivalent to it. Theorems giving necessary and sufficient conditions for a configuration to be structurally stable in a *volume* region are not known, though Peixoto (1962) and, independently, Pliss (1966) have been able to provide such conditions for a vector field confined to a toroidal surface. Since it is possible to produce high conductivity plasmas in a pinch having magnetic field exterior to and partially trapped in a relatively thin surface layer of the plasma it has been conjectured that the design of a toroidal pinch device using the criteria of Peixoto and Pliss might be structurally stable, or if not, might none-the-less be superior in its stability to other designs. The simplest magnetic field configuration satisfying these criteria is one in which the magnetic field lines on the surface are neither closed nor ergotic but are asymptotic to each of two limit cycles.

An axisymmetric toroidal plasma with no cusps or singularities can have three distinct topological configurations, as shown in Fig. 12F1: closed field lines, ergodic field lines (Table 8B1), or a limit cycle configuration. Plasma on closed field lines is highly vulnerable to resonant growth of fluctuations, such as interchange instability. Plasma on ergodic field lines can be stable, but the qualitative character of the field line configuration can often change from ergodic to closed (or vice-versa) during a discharge (such as when a q = 1 surface moves into the plasma). This danger of a qualitative change is called *topological instability*. The limit cycle configuration, which cannot easily change its topological character, is topologically stable.

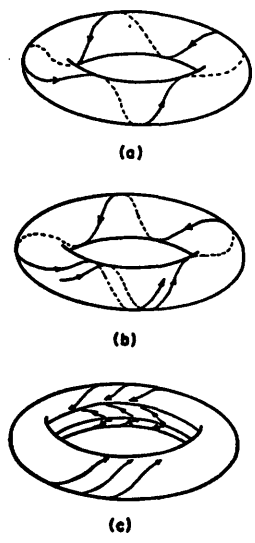

In the ball analogy (Section 8D), slight changes in the curvature of the hole and hill would still leave them as

Fig. 12F1. The three topologies for a high-beta axisymmetric toroidal magnetic field with no cusps or singularities, (a) closed field lines, (b) ergodic field lines, (c) a limit cycle configuration. From K. H. Brown, H. R. P. Ferguson, J. H. Gardner, L. V. Knight, and H. M. Nelson, IEEE Transactions on Plasma Science PS-4, 162-165 (1976), Fig. 1.

stable and unstable surfaces, respectively, so they are topologically stable. But a level surface is topologically unstable, since slight changes in its curvature could change it into either type of topological character.

If small changes of plasma parameters merely stretch or bend the field lines, then the plasma may be topologically stable. If such changes result in tearing or breaking the field lines, then the plasma is topologically unstable. The formation of magnetic islands by tearing modes is a manifestation of topological instability, which can result in a catastrophic change, such as a tokamak plasma disruption (Section 13A). Ordinary stability is necessary for good plasma confinement. The importance of topological stability is an open question, which is being studied experimentally.

experiment

The set of topologically stable toroidal magnetic field configurations, called the *topolotron*, is characterized by the following features:

* a smooth toroidal surface
* no magnetic field null points
* a nonconvex poloidal cross section (meaning that it is possible to pass a straight line through the surface which intersects it at more than two points)
* a zero rotational transform angle
* a finite, nonzero, even number (such as 2) of closed magnetic field lines, which are *limit cycles*. The other field lines on the toroidal surface converge towards one of these closed lines and diverge from the other, as illustrated in Fig. 12F2.

A set of coils for a topolotron with two limit cycles is shown in Fig. 12F3. The resultant poloidal flux surfaces are shown in Fig. 12F4. Tension of the poloidal field lines inhibits plasma motion outwards or vertically, and the toroidal magnetic field gradient impedes plasma motion inwards. The goals of the topolotron experiment ($R \sim 0.25$ m, $B \sim 0.8$ T, $n \sim 10^{22}$ m^{-3}) are to demonstrate

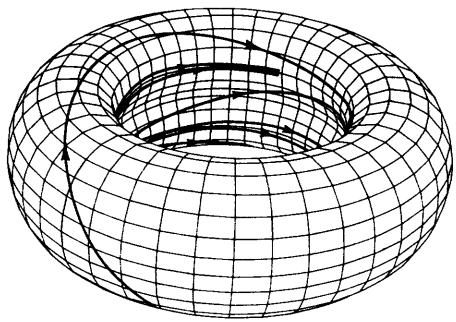

Fig. 12F2. A torus, showing asymptotic field lines on its surface approaching one limit cycle (closed circular field line on the inside of the torus) and diverging from the other. From H. M. Nelson, K. H. Brown, and C. A. Hart, The Physics of Fluids 19, 1810-1819 (1976), Fig. 1.

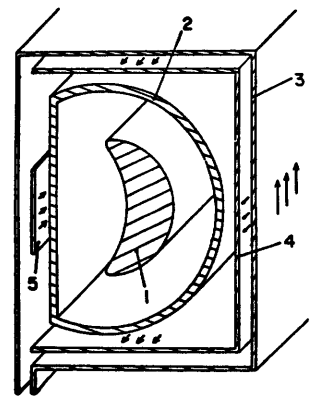

Fig 12F3. Cutaway view of a section of the torus of a topolotron device with two limit cycles. (1) the plasma during compression, (2) the vacuum envelope, (3) the theta coil (produces the toroidal magnetic field), (4) the C-coil, (5) the I-coil. Arrows indicate directions of coil currents. From K. H. Brown, H. R. P. Ferguson, J. H. Gardner, L. V. Knight, and H. M. Nelson, IEEE Transactions on Plasma Science PS-4, 162-165 (1976), Fig. 5.

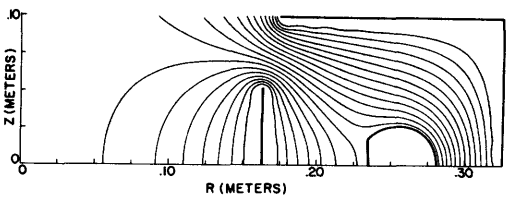

Fig. 12F4. Computed poloidal magnetic field lines around a compressed high-beta topolotron plasma, showing the I-coil and C-coil locations and the equilibrium plasma boundary shape. From H. M. Nelson, K. H. Brown, and C. A. Hart, The Physics of Fluids 19, 1810-1819 (1976), Fig. 6.

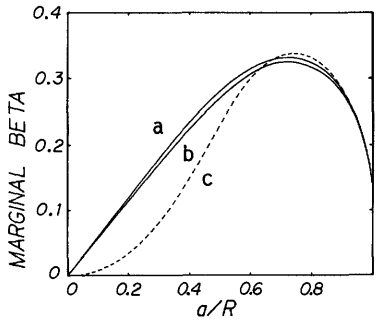

Fig. 12F5. Marginal beta vs. inverse aspect ratio marginal ($\varepsilon = \frac{a}{R}$) for sharp boundary model of (a) semi-stable, (b) stable, and (c) $\beta_p = 1$ configuration with b/a = 2. From Rock (1981).

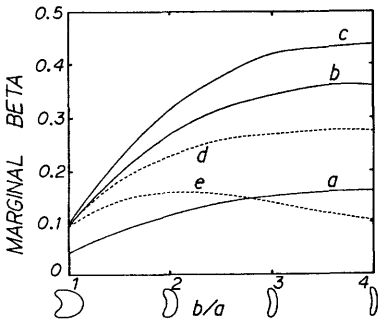

Fig. 12F6. Marginal β vs. elongation for (a) ε = 0.2, (b) ε = 0.5, (c) ε = 0.8 topolotrons. Curves (d) the $\beta_p = 1$ case for ε = 0.5 and (e) the ellipse for ε = 0.5 are shown for comparison. From Rock (1981).

the existence of a topologically stable plasma configuration and to study the importance of such stability for plasma confinement.

The results of a computational MHD stability analysis of the sharp boundary topolotron are shown in Fig. 12F5 and 12F6 (F. C. Rock, 1981). This model shows a distinct advantage for the non-convex poloidal cross section and limit cycles over the ellipse and $\beta_p = 1$ plasmas. Slightly above the topolotron curve in Fig. 12F5 is the topologically *semi-stable* case. The semi-stable case is the one in which the poloidal field component on the inside of the torus (Fig. 12F1c) is reversed from that of the topologically stable case. A comparison of semi-stable and stable configurations for diffuse equilibria are shown in Fig. 12F7. Further study will be necessary to sort out the stability differences between these two topological characters in the diffuse case. There are in fact large differences between the diffuse equilibria for these two cases.

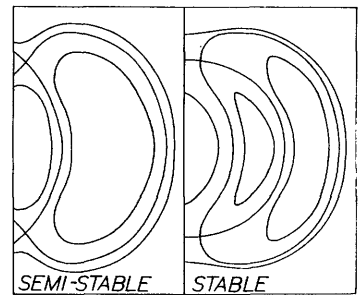

Fig. 12F7. Sketches of diffuse asymptotic equilibria. From Rock (1981).

(This Section was written largely by J. H. Gardner and F. C. Rock, Brigham Young University.)

Bibliography

types of pinches

R. J. Bickerton, "Pinch Research", *Nuclear Fusion 20*, 1072-1075 (1980).
W. R. Ellis, "CTR applications of the high-density linear theata pinch", *Nuclear Fusion 15*, 255-270 (1975).

R. A. Gerwin and R. C. Malone, "Adiabatic plasma heating and fusion-energy production by a compressible fast liner", *Nuclear Fusion 19*, 155-177 (1979).

Plasma Physics and Controlled Nuclear Fusion Research 1978 (Innsbruck), Volume II, IAEA, Vienna, 1979.

Plasma Physics and Controlled Nuclear Fusion Research 1980 (Brussels), IAEA, Vienna, 1981.

field-reversed theta pinch

W. T. Armstrong, D. C. Barnes, R. R. Bartsch, R. J. Commisso, C. A. Ekdahl, I. Henins, D. W. Hewett, H. W. Hoida, T. R. Jarboe, C. G. Lilliequist, R. K. Linford, J. Lipson, J. Marshall, K. F. McKenna, J. P. Mondt, D. A. Platts, C. E. Seyler, A. R. Sherwood, E. G. Sherwood, R. E. Siemon, D. V. Anderson, R. Christian, E. H. Klevans, S. Hamasaki, D. D. Schnack, J. M. Sayer, A. I. Shestakov, and J. Killeen, "Compact toroid experiments and theory", *Plasma Physics and Controlled Nuclear Fusion Research 1980 (Brussels)*, IAEA, Vienna, 1981.

A. G. Es'kov, R. Kh. Kurtmullaev, A. P. Kreshchuk, Ya. N. Laukhin, A. I. Malyutin, A. I. Markin, Yu. S. Martyushov, B. N. Mironov, M. M. Orlov, A. P. Proshletsov, V. N. Semenov, and Yu. B. Sosunov, "Principles of plasma heating and confinement in a compact toroidal configuration", *Plasma Physics and Controlled Nuclear Fusion Research 1978 (Innsbruck)*, Volume II, IAEA, Vienna, 1979, p. 187-204.

J. M. Finn, "Ballooning and interchange stability in axisymmetric field reversed equilibria", *The Physics of Fluids 24*, 274-283 (1981).

R. L. Hagenson and R. A. Krakowski, "A compact-toroid fusion reactor based on the field-reversed theta pinch: reactor scaling and optimization for CTOR", *Proceedings of the 4th ANS Topical Meeting on the Technology of Controlled Nuclear Fusion* (King of Prussia, PA, 1980), DOE, 1981.

Proceedings of the US-Japan Joint Symposium on Compact Toruses and Energetic Particle Injection, PPPL, 1979.

L. C. Steinhauer, "Plasma rotation in a reversed-field theta pinch", *The Physics of Fluids 24*, 328-338 (1981).

L. C. Steinhauer and H. J. Willenberg, "Technology issues of TRACT plasma engineering", *Proceedings of the 4th ANS Topical Meeting on the Technology of Controlled Nuclear Fusion* (King of Prussia PA, 1980), DOE, 1981.

H. J. Willenberg, L. C. Steinhauer, A. L. Hoffman, T. L. Churchill, and P. H. Rose, "TRACT fusion reactor studies", *Proceedings of the 4th ANS Topical Meeting on the Technology of Controlled Nuclear Fusion* (King of Prussia, PA, 1980), DOE, 1981.

reversed field pinch

D. A. Baker, C. J. Buchenauer, L. C. Burkhardt, J. N. Dimarco, J. N. Downing, A. Haberstich, R. B. Howell, J. C. Ingraham, A. R. Jacobson, K. A. Klare, E. M. Little, R. S. Massey, G. Miller, J. A. Phillips, A. E. Schofield, K. F. Schoenberg, K. S. Thomas, R. G. Watt, P. G. Weber, and R. Wilkins, "Initial reversed-field pinch experiments on ZT-40M with a metallic vacuum liner", 10th European Conference on Controlled Fusion and Plasma Physics, Moscow, September, 1981.

H. A. B. Bodin and A. A. Newton, "Reversed-field-pinch research", *Nuclear Fusion 20*, 1255-1324 (1980). Review Paper.

J. P. Christiansen and K. V. Roberts, "Evolution of the reversed-field pinch", *Nuclear Fusion 18*, 181-197 (1978).

S. Ortolani, "Reversed-field pinch (RFP) configuration", *Nuclear Fusion 19*, 535-544 (1979). (Report on International Workshop at Padua, 1978.)

Plasma Physics and Controlled Nuclear Fusion Research 1978 (Innsbruck), Volume II, IAEA, Vienna, 1979, p. 3-68.

Plasma Physics and Controlled Nuclear Fusion Research 1980 (Brussels), IAEA, Vienna, 1981.

Proceedings of the US-Japan Joint Symposium on Compact Toruses and Energetic Particle Injection, PPPL, 1979.

reversed-pitch helical pinch

T. Ohkawa, M. Chu, C. Chu, and M. Schaffer, "Helical plasma configuration with pitch reversal", *Nuclear Fusion 20*, 1465-1469 (1980).

T. Ohkawa and the OHTE Group, "Physics of the OHTE", *Proceedings of the US-Japan Joint Symposium on Compact Toruses and Energetic Particle Injection*, PPPL, 1979, p. 65-67.

spheromak

G. C. Goldenbaum, J. H. Irby, Y. P. Chong, and G. W. Hart, Formation of a spheromak plasma configuration", *Physical Review Letters 44*, 393-396 (1980).

W. H. Hugrass, I. R. Jones, K. F. McKenna, M. G. R. Phillips, R. G. Storer, and H. Tuczek, "Compact torus configuration generated by a rotating magnetic field: the Rotamak", *Physical Review Letters 44*, 1676-1679 (1980).

T. R. Jarboe, I. Henins, H. W. Hoida, R. K. Linford, J. Marshall, D. A. Platts, and A. R. Sherwood, "Motion of a compact toroid inside a cylindrical flux conserver", *Physical Review Letters 45*, 1264-1267 (1980).

S. C. Jardin and W. Park, "Two-dimensional modeling of the formation of spheromak configurations", *The Physics of Fluids 24*, 679-688 (1981).

M. Okabayashi and A. M. M. Todd, "A numerical study of MHD equilibrium and stability of the spheromak", *Nuclear Fusion 20*, 571-577 (1980).

Plasma Physics and Controlled Nuclear Fusion Research 1980 (Brussels), IAEA, Vienna, 1981.

Proceedings of the US-Japan Joint Symposium on Compact Toruses and Energetic Particle Injection, PPPL, 1979.

M. N. Rosenbluth and M. N. Bussac, "MHD stability of spheromak", *Nuclear Fusion 19*, 489-498 (1979).

J. B. Taylor, "Relaxation of toroidal plasma and generation of reverse magnetic fields", *Physical Review Letters 33*, 1139-1141 (1974).

D. R. Wells, E. Nolting, F. Cooke, Jr., J. Tunstall, P. Jindra, and J. Hirschberg, "Adiabatic compression of plasma vortex structures", *Physical Review Letters 33*, 1203 (1974).

M. Yamada, H. P. Furth, W. Hsu, A. Janos, S. Jardin, M. Okabayashi, J. Sinnis, T. H. Stix, and K. Yamazaki, "Quasistatic formation of the spheromak plasma configuration", *Physical Review Letters 46*, 188-191 (1981).

K. Yamazaki, "Internal tilting-mode stability of a slightly non-spherical spheromak", *Nuclear Fusion 20*, 1459-1461 (1980).

topolotron

R. Abraham, *Foundation of Mechanics*, p. 1-2, Benjamin (1967).

A. Andronov and L. Pontriagin, "Systems Grossiers", *Doklady Akademii Nauk SSSR 14*, (1937) 247-251.

K. H. Brown, H. R. P. Ferguson, J. H. Gardner, L. V. Knight, and H. M. Nelson, "The topolotron: a high beta device with topological stability", *IEEE Transactions on Plasma Science PS-4*, 162-165 (1976).

H. M. Nelson, K. H. Brown, and C. A. Hart, "Computer model of a fast toroidal plasma compression, with application to the topolotron", *The Physics of Fluids 19*, 1810-1819 (1976).

M. Peixoto,"Structural stability on 2-dimensional manifolds", *Topology 2* (1962) p. 101-121.

V. A. Pliss, *Nonlocal Problems in the Theory of Oscillations*, Academic Press (1966).

F. C. Rock, "Magnetohydrodynamic stability of structurally stable toroidal plasmas", (submitted to *The Physics of Fluids*, 1981).

CHAPTER 13

TOKAMAKS

13A. MHD Stability

introduction

Basic components of a tokamak are reviewed in Fig. 13A1. Particle orbits in tokamaks were discussed in Section 7E. About 70 tokamaks have been built. Table 13A1 lists the main parameters of some of them. The history of tokamak research is summarized by Rutherford (1980).

MHD instabilities are driven by the magnetic energy associated with the plasma current (tearing and kink modes) and by the plasma pressure gradient (interchange modes). The instabilities are characterized by mode numbers (m/n) in the (poloidal/toroidal) directions (Eq. 8D70). Most of the symbols used here have been defined in Section 8B.

Kink and tearing modes are basically the same instability (driven by magnetic energy) in different temperature regimes. At low temperatures, instability growth is impeded by the rate at which magnetic field lines break and reconnect to form magnetic islands, dependent on plasma resistivity. At high temperatures, resistivity is negligibly small, (the *ideal* case) , instability growth is limited by inertial effects, and the instability appears mainly as helical deformations ("kinks") of the plasma surface or localized "ballooning".

ideal kink modes

Consider the following distribution of toroidal current density:

$$J_t(r) = J_0(1 - r^2/a^2)^{\nu} \tag{13A1}$$

where r is the minor radius, a is the outer radius of a circular plasma, J_0 is the central current density, and ν is a variable parameter. The shapes of this distribution for various values of ν are shown in Fig. 13A2.

The safety factor q, defined in Table 8B1, may be written

$$q(r) = \frac{R_0 B_t}{2\pi} \oint \frac{d\ell}{B_p R^2} \tag{13A2}$$

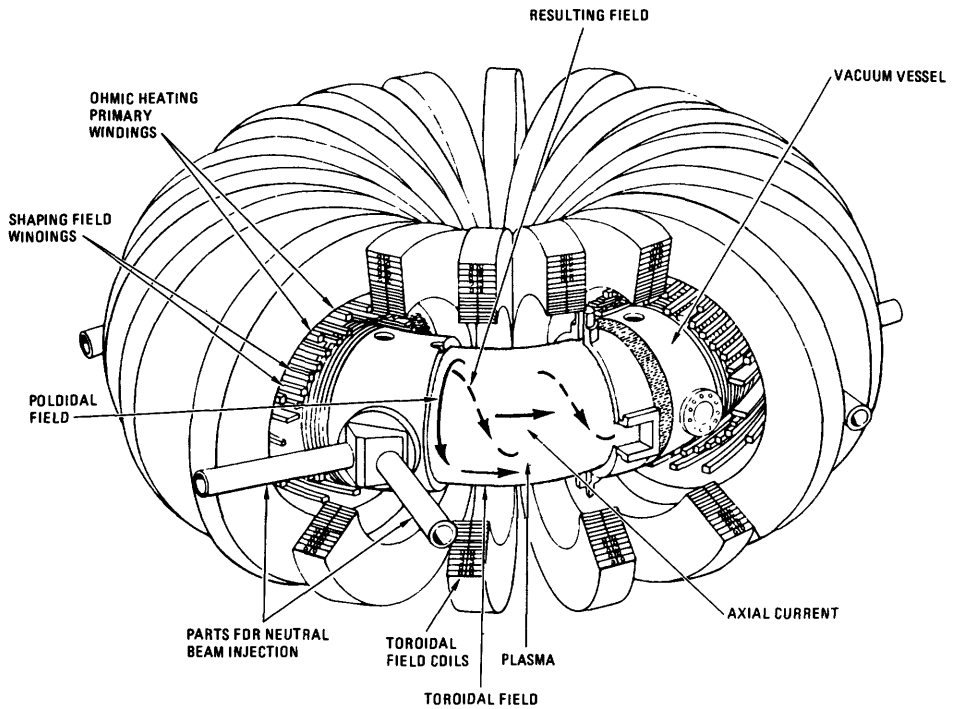

Fig. 13A1. Basic components of a tokamak. Some tokamaks also have an iron transformer core to improve magnetic coupling between the primary ohmic heating windings and the plasma current. From J. M. Rawls et al, "Status of tokamak research", DOE/ER-0034 (1979), Fig. 1-1.

which reduces to

$$q(r) \simeq rB_t/R_0B_p \qquad (13A3)$$

for a circular plasma with large aspect ratio (R_0/a).

Radial variation of the toroidal current density gives rise to a "torque" (Wesson, 1978, Eq. 12)

$$T_\phi = B_r(dJ_t/dr) \qquad (13A4)$$

where B_r is the radial component of the perturbed magnetic field. If $nq < m$, this torque twists the plasma so that B_r increases, which increases the torque, etc., as illustrated in Fig. 13A3. Nearby conducting walls and magnetic shear tend to stabilize these deformations. The

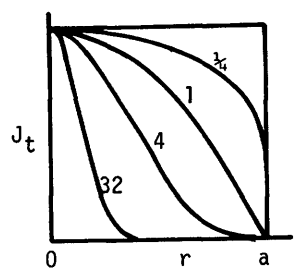

Fig. 13A2. Radial distributions of current density described by Eq. (13A1) with various values of the parameter ν. From J. A. Wesson, Nuclear Fusion 18, 87-132 (1978), Fig. 6.

Table 13A1. Parameters of some tokamaks. (Some of the values of B_t and I shown here are design values which have not yet been attained).

tokamak	location	R_0, m	a, m	B_t, T	I, kA	remarks
LT3	Australia	.4	.1	1.4	30	
Petula	France	.72	.16	2.7	100	
TFR-600	France	.98	.2	6.0	600	
Pulsator	W. Germany	.70	.12	2.8	300	
ASDEX	W. Germany	1.65	.4	2.8	500	poloidal divertor
FT	Italy	.83	.19	10.0	1000	$n_0\tau_E = 4\times10^{19}$ $m^{-3}s$
JFT-2	Japan	.90	.25	2.0	150	
JIPP-T-II	Japan	.90	.17	3.0	160	
DIVA	Japan	.6	.1	1.3	60	poloidal divertor
CLEO	UK	.90	.18	2.0	120	
DITE,	UK	1.17	.27	2.7	280	bundle divertor
Alcator A	MIT, USA	.54	.10	10.0	400	$n_0\tau_E > 3\times10^{19} m^{-3}s$, $Z_{eff}=1$
Alcator C	MIT, USA	.64	.17	14.0	1000	
PLT	PPPL, USA	1.3	.45	4.0	1400	T_{i0} = 7 keV, $\tau_E \sim 0.1$ s, $\nu_{i*} < 0.1$
ISX-B	ORNL, USA	.93	.2	1.8	180	$\beta_* = 4$ %
Doublet III	GA, USA	1.4	.45x1.5	4.0	2000	elongated plasma
PDX	PPPL, USA	1.45	.45	2.4	500	poloidal divertor
FT-1	USSR	.63	.15	1.0	30	
TM-3	USSR	.40	.13	4.0	80	ECRH, ICRH
T-4	USSR	.90	.23	4.5	200	ICRH
TO-1	USSR	.60	.18	2.0	30	feedback stabilization
T-6	USSR	.70	.25	1.5	100	
T-7	USSR	1.2	.35	3.0	400	superconducting TF coils
T-10	USSR	1.5	.40	5.0	1600	$\tau_E \sim 0.1$ s
Large tokamaks (1983-1988)						
JET	Europe	2.8	1.3x2.0	3.5	3000	D-shaped plasma
JT-60	Japan	3.0	1.0	5.0	3000	divertor
TFTR	USA	2.5	.85	5.2	2500	24 MW NBI
T-15	USSR	2.4	.7	3.5	1400	superconducting coils 5 MW NBI, 5 MW ICRF

peaking of the current profile may be represented by the ratio q_a/q_0, where the subscripts refer to r = a and r = 0. For the distribution of Eq. (13A1),

$$q_a/q_0 = \nu + 1 \quad . \tag{13A5}$$

Small values of q_a/q_0 (or small ν) correspond to large dJ_t/dr near the plasma boundary (Fig. 13A2) leading to instability. The results of kink mode stability theory are summarized as follows (Wesson, 1978):

* $J_t(a) \lesssim 0$ is necessary for stability.
* $q_a > m$ stabilizes perturbations with poloidal mode number m.
* Large m modes are stabilized by small $(dJ_t/dr)_a$, which corresponds to large q_a/q_0 (large ν).
* If substantial plasma pressures are to be contained (if $\beta \sim a^2/R_0^2$), then stabilization of kink modes by magnetic shear requires $q_a/q_0 > 2, (\nu > 1)$, which limits the total plasma current to $I < \frac{1}{2}\pi a^2 J_0$.
* A conducting wall near the plasma boundary tends to stabilize low-m modes.
* Stability requirements for non-circular cross sections appear to be similar to those for circular plasmas.

Although large values of

$$q_a \simeq aB_t/R_0B_p = 2\pi a^2 B_t/\mu_0 I R_0 \tag{13A6}$$

tend to stabilize kink modes, high values of B_t are uneconomical, so it is desirable to operate at the minimum stable values of q_a. In tokamaks without a conducting wall near the plasma, the minimum stable value is typically $q_a \sim 2.5$. In tokamaks with a copper liner, stable discharges with $q_a < 2$ have been produced. In DIVA, for example, discharges with $q_a \gtrsim 1.3$ have been stable.

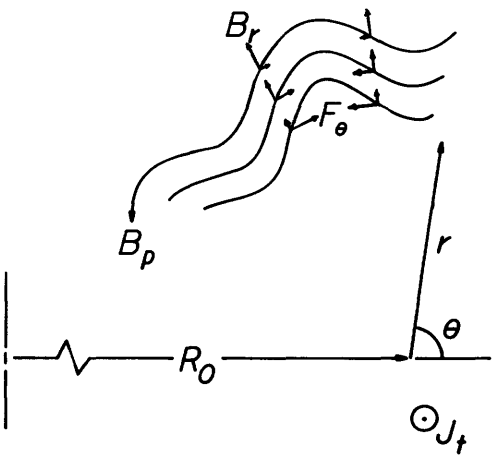

Fig. 13A3. Perturbations of the plasma boundary and the resulting forces. The values of B_r decrease inwards, but J_t increases inwards. The radial variation of $F_\theta = J_t B_r$ depends upon the size of nq/m. If nq/m < 1, then F_θ increases inwards, and the resulting torque causes the perturbations to grow.

ideal internal modes

Ideal internal modes occur near *resonant surfaces*, where q(r)=m/n. Values of $q_0 > 1$ tend to stabilize these modes for all values of m. Violation of this criterion may result in local instability near the magnetic axis, enhancing plasma transport and flattening the plasma pressure profile near the resonant surface. The regions of kink mode instability and internal mode instability are shown on a plane of (q_a/q_0) and q_a in Fig. 13A4. The stable region shrinks further when finite plasma resistivity is taken into account (resistive modes).

ideal axisymmetric (n = 0) modes

The plasma will theoretically be stable to axisymmetric modes if it has a circular cross section, or if a conducting wall is nearby. An elliptical plasma

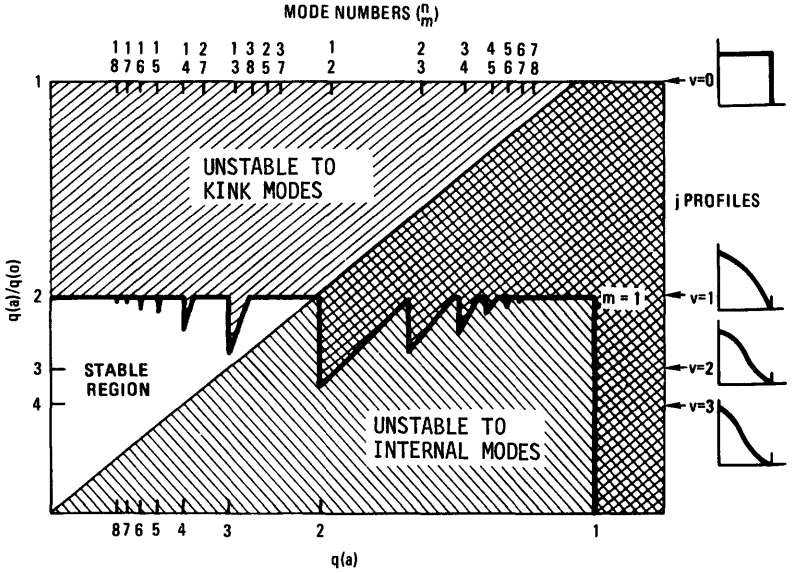

Fig. 13A4. Stability diagram for ideal kink and internal modes, for the current distribution of Eq. (13A1). Stability against internal modes requires $q_0 > 1$; stability against m = 1 kinks requires $q_a > 1$; and stability against m = 2 kink modes requires some peaking of the current profile ($\nu \geq 1$). From J. M. Rawls et al, DOE/ER-0034 (1979), Fig. 2-2, based on J. A. Wesson, Nuclear Fusion 18, 87-132 (1978), Fig. 8.

with no conducting wall may be unstable to vertical displacements (m = 1) in the direction of elongation. For large aspect ratio plasmas ($R_0/a >> 1$) the plasma will be stable against rigid displacements if the vertical field B_z satisfies the criterion

$$-(R/B_z)\,(dB_z/dR) > 0 \qquad (13A7)$$

Small aspect ratio plasmas tend to be more stable to such displacements. Passive feedback may be used to inhibit axisymmetric modes (Lipschultz et al, 1980).

resistive interchange modes

The resistive interchange mode, driven by the plasma pressure gradient, is the same as the ideal internal mode, but with finite plasma resistivity taken into account. The resistive interchange modes, which have growth rates proportional to $\eta^{1/3}$ (where η is the resistivity), are stabilized by sufficiently large values of q(r). At low β, the stability requirement is the same as for ideal internal modes. For circular plasmas, the requirement is q(r) > 1 for all r. Due to their slow growth rates and comparatively easy stabilization, resistive interchange modes are not a serious problem.

resistive tearing modes

Resistive tearing modes have growth rates proportional to $\eta^{3/5}$. The magnetic energy is reduced by formation of magnetic islands. Heat is transported radially along the magnetic field around the magnetic islands, enhancing the energy loss rate.

Tearing modes with m > 3 are stabilized by magnetic shear. The m = 2 and m = 3 modes are stabilized by certain $J_t(r)$ profiles, but at low β, $q_a > m$ is required for their stability (as for kink modes).

At higher values of β, these modes are stabilized by sufficiently large values of the parameter Λ, defined by

$$\Lambda \equiv \beta_p^{5/6}(a/R_0)^2 S^{1/2} \qquad (13A8)$$

$$\beta_p \equiv 2\mu_0 p/B_p^2$$

$S \equiv$ Magnetic Reynolds Number, Eq.(8D105)

where p is the plasma pressure (Pa), μ_0 is the permeability of free space, and B_p is the poloidal magnetic field (T). The Magnetic Reynolds Number S is a measure of how long it takes magnetic field lines to diffuse through the plasma, or to break and reconnect. At high temperatures, resistivity is low, field line diffusion is slow, S and Λ are very large, and tearing mode growth rates are slow. Assuming that $J_t(r)$ is described by Eq.(13A1), the variation of the plasma stability boundary with Λ is illustrated in Fig. 13A5 for the (2/1) resistive tearing mode. At $\Lambda > 30$, the stability region extends almost to the $q_0 = 1$ dashed line boundary, and for $\Lambda > 60$, there is little departure from the ideal MHD boundaries. Numerical modeling of tearing modes yields flux plots like those of Fig. 13A6. The flux surfaces are helical, not axisymmetric. When only one mode is present, its amplitude (the island width) may saturate, leading to benign Mirnov oscillations (to be discussed), but simultaneous growth of two or more modes can lead to plasma disruption.

disruptive instability

When $q_0 \lesssim 1$ and $q_a \lesssim 2.5$, the (2/1) tearing mode, driven to large amplitude at the q(r) = 2 surface, alters $J_r(r)$ so that neighboring modes (3/2) or (5/3) also become destabilized. The corresponding magnetic field topology is illustrated in Fig. 13A7. When the islands overlap, the path of a magnetic

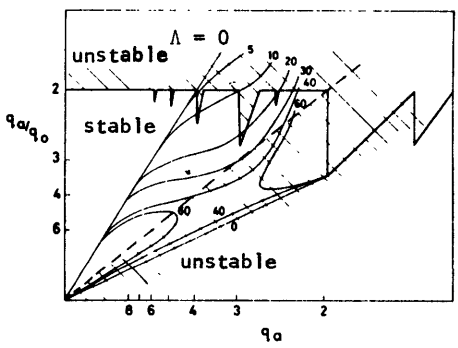

Fig. 13A5. Stability diagram for the (2,1) tearing mode with current profiles of Eq. (13A1) for various values of Λ. As Λ increases, the region of stability increases. From J. A. Wesson, Nuclear Fusion 18, 87-132 (1978), Fig. 36.

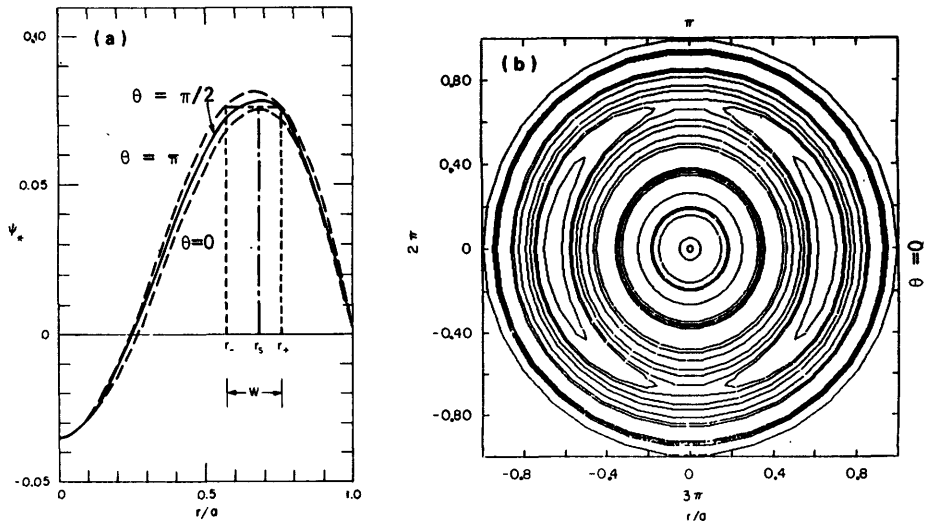

Fig. 13A6. Radial variation of the helical flux function (a) and contours of constant ψ_* on a plasma cross section for a (2/1) tearing mode. Here $q_a = 4$, the singular surface radius $r_2 = 0.68$ a, and the island width $w = 0.17a$. From J. D. Callen et al, "Magnetic 'islandography' in tokamaks", Plasma Physics and Controlled Nuclear Fusion Research 1978, Vol. 1, 415-431, Fig. 1, IAEA, Vienna, 1979.

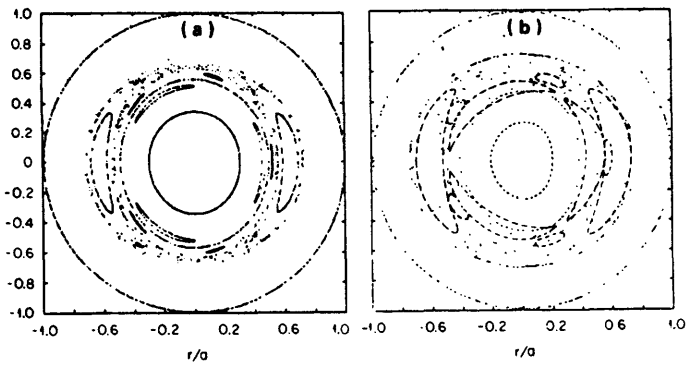

Fig. 13A7. Magnetic field topology in a plasma cross section. Dots represent the locations of a magnetic field line as it passes through the cross section, making many trips around the torus. At early times (a) there are prominent (2/1) and (3/2) magnetic islands and small (5/3) islands, and w/d = 0.88, where w is the island width and d is the radial separation between singular surfaces. Later w/d= 1.15 (case b), the magnetic islands overlap, and the magnetic field line trajectory becomes ergodic, filling practically the whole region near the singular surfaces. From J. D. Callen et al, Plasma Physics and Controlled Nuclear Fusion Research 1978, Vol. 1, 415-431, Fig. 2, IAEA, Vienna, 1979.

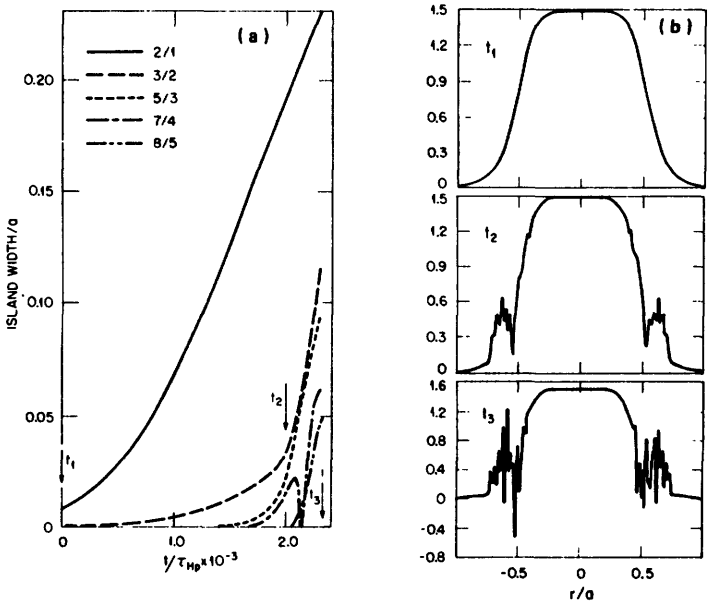

Fig. 13A8. Growth of magnetic islands in time (a) and the corresponding deformation of the current density profile (b) for a case where both the (2/1) and (3/2) tearing modes are unstable. For this case modelling a PLT disruption, $S = 10^6$ and $q(r) = q_0[1 + (r/r_0)^{2\lambda}]^{\lambda}$ with $q_0 = 1.34$, $r_0 = 0.56a$, and $\lambda = 3.24$, which corresponds to the measured $T_e(r)$ profile. From J. D. Callen et al, Plasma Physics and Controlled Nuclear Fusion Research 1978, Vol. 1, 415-431, Fig. 5, IAEA, Vienna, 1979.

field line becomes *stochastic* (random), the magnetic flux surfaces are destroyed, particles flowing along magnetic field lines may cross through the entire region, and confinement is spoiled. The growth of island widths and evolution of the current density profile are illustrated in Fig. 13A8. The experimental values of disruptive instability growth rates correlate well with the theoretical island-width growth rates, and a measurement of x-ray emission intensity during instability in PLT shows a clear m = 2 structure (Fig. 13A9).

There may be several small disruptions, or a major disruption terminating plasma confinement. A major disruption is characterized by

* flattening of the $J_t(r)$ profile
* expulsion of the poloidal flux
* a large negative voltage spike in the OH circuit
* a decrease of the major radius R_0
* rapid plasma expansion (< 1 ms)
* plasma energy dump onto the walls or limiter
* a burst of hard x-rays (> 100 keV).

The ohmic heating system must be protected against the large voltage spikes. Protection of the chamber walls is also a serious problem for a tokamak reactor. The dumping of 200 MJ thermal energy onto the walls could cause vaporization of several kg of metal, if the deposition were localized.

Techniques used for combatting disruptions include:

* minimizing impurity concentrations
* keeping plasma density and current within safe limits
* control of plasma current and dI/dt
* feedback-controlled neutral gas injection
* feedback-controlled helical coils to limit the (2/1) mode amplitude
* supplementary heating to raise T_e and Λ
* use of a close-fitting conducting wall.

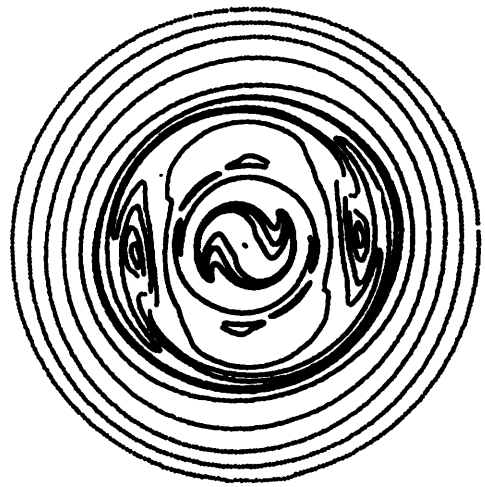

Fig. 13A9. Contours of equal x-ray emissivity in a minor cross section of PLT, depicting an m = 2 structure. From N. R. Sauthoff, S. Von Goeler, and W. Stodiek, Nuclear Fusion 18, 1445-1458 (1978), Fig. 7a.

There is a critical plasma density, above which disruptions occur. An empirical formula for this critical density in tokamaks using cold neutral gas to build up the density is

$$\bar{n}_{crit} \simeq 10^{20} B_t A_i^{\frac{1}{2}}/q_a Z_{eff} R_0 \qquad (m^{-3}) \qquad (13A9)$$

where A_i = (ion mass)/(proton mass) (Equipe TFR, 1980). Many tokamaks have $\bar{n} \propto B_t/R_0$ (Murakami, Callen, and Berry, 1976). For a reactor with B_t = 5 T, A_i = 2, Q_a = 2.5, Z_{eff} = 1, and R_0 = 5 m, this scaling would indicate $\bar{n}_{crit} = 6 \times 10^{19}$ m^{-3}, which is rather low. However, higher values may apply to a tokamak fueled by pellet injection.

ballooning modes and beta limits

Ballooning modes are local (high n) interchange modes at the plasma surface in regions of bad magnetic field curvature (Section 8D). Stability against ballooning modes is expected if

$$\langle\beta\rangle \lesssim a/R_0 q_a^2 \qquad (13A10)$$

If R_0/a = 3 and q_a = 3, this yields $\langle\beta\rangle \lesssim 4$ %. Higher values of beta can theoretically be obtained in plasmas with non-circular cross sections. The variation of maximum theoretically stable β_* with toroidal mode number n is shown in Fig. 13A10 for one specific case. Values of β_* = 4.4 % have been attained experimentally in ISX-B.

operating regimes

The stable operating regime of tokamaks in the I - n plane is illustrated in Fig. 13A11. At high current, $q_a = 2\pi a^2 B_t/\mu_0 I$ approaches Kruskal-Shafranov limit

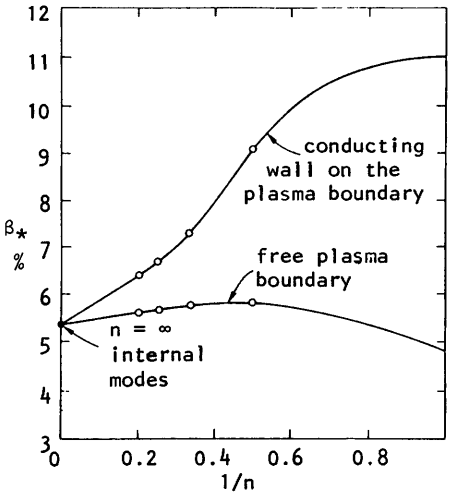

Fig. 13A10. Critical β_* vs. reciprocal toroidal mode number for a tokamak with R_0/a = 3.5, elongation K = 1.65, δ = 0.25 (slight triangularity of plasma cross section), 1<q<3, and p(ψ) = $[(\psi_b - \psi)/(\psi_b - \psi_a)]^{\alpha} p_a$, with α = 1.4 . From A. M. M. Todd et al, Nuclear Fusion 19, 743-752 (1979), Fig. 15.

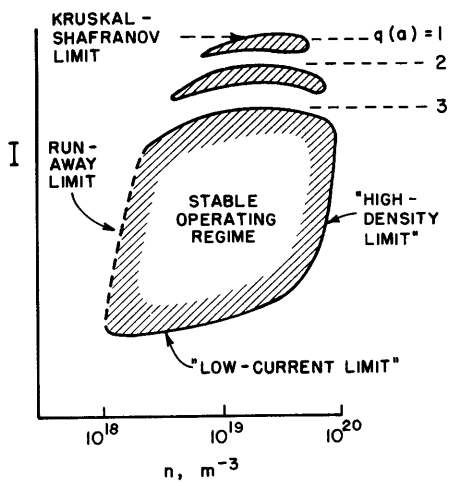

Fig. 13A11. Illustration of the stable operating regime in tokamaks. Electron runaway occurs at low density, and the disruptive instability occurs at high density and at both high and low currents. From S. O. Dean et al, WASH-1295 (1974), Fig. 7.

(q_a = 1), and a disruptive instability occurs. At low current, the discharge tends to shrink in diameter, which also makes q_a too small for stability. At high plasma density the shrinking/disruption problem occurs, and plasma pressure may exceed beta limits. At low densities, electron runaway is a serious problem. The boundaries shown in this figure are for illustrative purposes only, and vary considerably from one device to another. For example, Alcator plasmas have operated stably at $\bar{n} = 7 \times 10^{20}$ m^{-3}. Impurities tend to shrink the stable operating region, as shown in Fig. 13A12.

Mirnov oscillations

Helical perturbations of B_p, observed with magnetic probes, are called *Mirnov oscillations*. They are indicative of resistive tearing modes (or, in the high-temperature limit, kink modes). Initially, high-m modes (m $\sim$ 4 to 15) are observed, because the current is low and q_a is large, suppressing modes with m < q_a. As I increases, q_a decreases, and modes with lower m can become unstable. For example, the variation of m from 6 to 5 to 4 during the early phases of a tokamak discharge is shown in Fig. 13A13. Sometimes a mixture of harmonics is observed. These transient MHD modes perturb the plasma but do not terminate confinement. The more dangerous low-m modes may occur after the plasma has reached its current plateau.

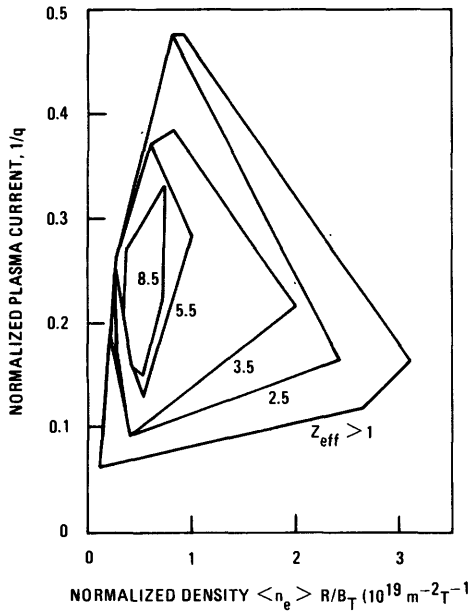

Fig. 13A12. The stable operating regime of tokamaks on a plane of normalized density and normalized current, for various impurity concentrations. From J. M. Rawls et al, DOE/ER-0034 (1979), Fig. 2-5.

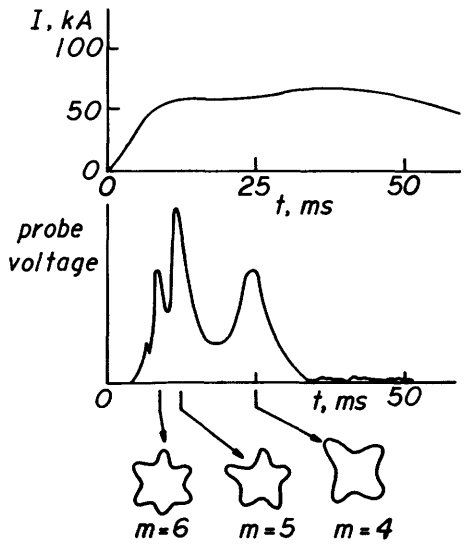

Fig. 13A13. Variation of plasma current, probe voltage, and shape of plasma boundary with time in a tokamak discharge. The boundary shape is determined by analysis of data from many probes mounted around the outside of the plasma. The "probe voltage" graph shows the data from one such probe. Based on data of L. A. Artsimovich, Nuclear Fusion 12, 215 (1972).

sawtooth oscillations

When q(r) drops below 1 at some radius r_1, the m = 1 internal mode occurs and causes flattening of the electron temperature profile out to $r \simeq 1.4 r_1$, as illustrated in Fig. 13A14. Plasma at $r < r_1$ has gradual heating, followed by sudden energy loss from the instability. Signals from $r > r_1$ have the opposite shape, as shown in the figure. Such *sawtooth oscillations* are often observed on the soft x-ray (2-20 keV) signals from the plasma. Similar, but smaller amplitude, sawtooth modulations may also be observed on the plasma density and ion temperature (neutron emission) signals. These *internal disruptions* enhance energy transport rates in the plasma core, but do not spoil confinement of the plasma as a whole.

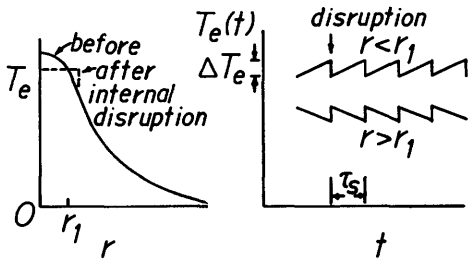

Fig. 13A14. Variation of electron temperature with radius and time during internal disruptions. At radii inside r_1 (the radius where q = 1), the temperature suddenly drops as energy is lost. This outwards flow of energy causes sudden increases in T_e at radii outside r_1.

The sawtooth amplitude $\Delta T_e/T_e \sim$ 10-20 % in ohmically-heated tokamaks, and it may reach 30 % with high-power neutral beam injection. The sawtooth period $\tau_s \sim$ 5-50 ms, increasing with size and heating power. Most tokamaks exhibit either sawtooth oscillations or strong (2/1) Mirnov oscillations, as illustrated in Fig. 13A15.

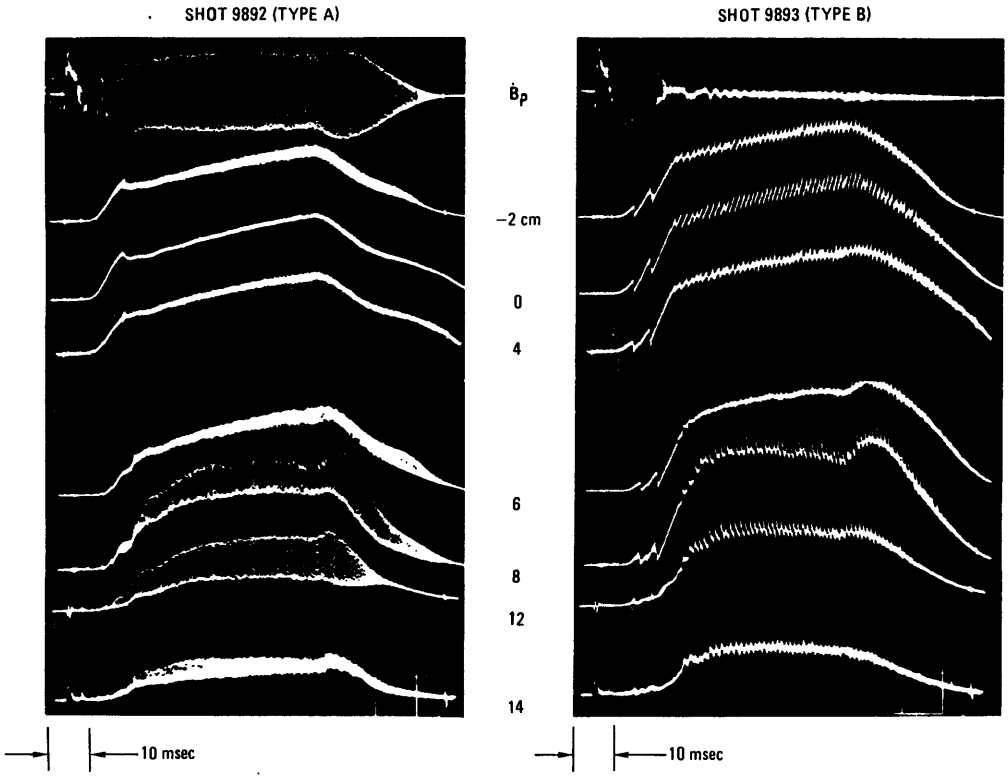

Fig. 13A15. Characteristic magnetic probe ($\dot{B}_p$) and soft x-ray signals from two ORMAK discharges (I = 155 kA, B_t = 2.16 T, q_a = 4.6, p = 4.1×10^{-4} Torr). The x-ray detectors were collimated to view along different chords of a minor cross section, with tangent radii from r = -2 to + 14 cm. The discharge on the left is dominated by (2,1) Mirnov oscillations (tearing mode). The discharge on the right is dominated by sawtooth oscillations (internal disruptions) with r_1 = 6 cm. From J. M. Rawls et al, DOE/ER-0034 (1979), Fig. 2-3.

effects of plasma shape

According to Eq. (13A2), for given values of q, R_0, and B_t, an increase of the plasma circumference permits a corresponding increase in B_p, which should increase confinement times and beta. The large shear of the Doublet shape (Fig. 13A16) should promote MHD stability. Stable equilibria with $\langle\beta\rangle \sim$ 5-10 % are predicted for Doublets and D-shaped plasmas.

13B. Transport

neoclassical transport

At high temperatures, the step size for neoclassical diffusion is roughly equal to a banana width Δr (Eq. 8F18). The variation of neoclassical transport coefficients with collision frequency was illustrated in Fig. 8F1. Neoclassical transport effects include the bootstrap current, the trapped particle pinch effect, electrical resistivity, magnetic field ripple effects, and transport of impurity ions.

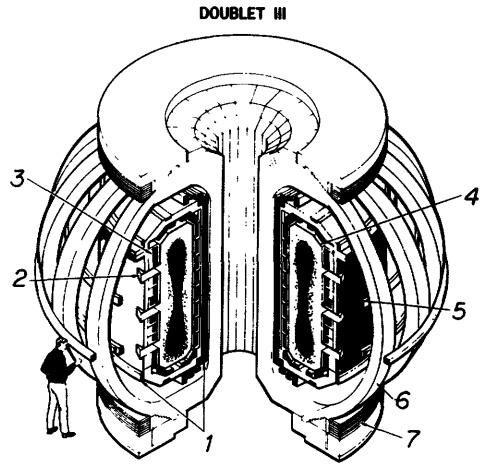

Fig. 13A16. The Doublet III tokamak at General Atomic Company. 1. OH and EF coils, 2. neutral beam ports, 3. field shaping coils, 4. hot liner, 5. vacuum tank, 6. toroidal field coils, 7. prestressing support ring. It can operate with plasma currents of 2-5 MA and neutral beam injection powers of 7-14 MW at 80 keV. From T. Ohkawa, EPRI 115-2 (1975), Fig. 1.

bootstrap current

The frictional force between trapped and untrapped particles can induce a current to flow in the plasma. In the collisionless regime the current can be very strong, even as large as the required ohmic heating current. It is possible that this *bootstrap current* may be able to sustain the plasma steady state, after initial startup by ohmic heating coils, provided that impurities are removed and fresh fuel is added. The name refers to the idea of "lifting yourself up by your bootstraps".

Ware pinch

In a Z-pinch (Chapter 12) the interaction of the axial electric field with the azimuthal magnetic field results in a radially inward drift velocity $v_r = -E_z B_\theta / B_\theta^2$ (cf. Eq. 7C6). In a diffuse toroidal pinch (tokamak) the frictional force between trapped and untrapped particles results in a similar, but faster, inward drift velocity. For a pure hydrogen plasma with $r/R_0 \sim 0.2$, the *trapped particle pinch* or *Ware pinch* velocity is

$$v_r \simeq -2.3(r/R_0)^{\frac{1}{2}} E_t / B_p (1+2\nu_{*e}) \qquad (13B1)$$

where E_t is the toroidal electric field (induced by the ohmic heating transformer), B_p is the poloidal magnetic field, r is the minor radius, R_0 is the major radius of the magnetic axis, and the collisionality parameter ν_{*e} was defined in Table 8F1. This effect may aid inward transport of cold ions produced by ionization of neutral gas at the plasma surface.

resistivity

Since trapped particles create additional friction for current-carrying untrapped particles but do not carry current themselves, the resistivity of a toroidal plasma is higher than that of a linear plasma. According to neoclassical theory, the parallel resistivity of a tokamak plasma is given by

$$\eta_{\parallel} = \frac{m_e \nu_e}{n_e e^2} G(Z_{eff}) \frac{1}{\left(1 - \frac{f_t}{1 + \xi\nu_{*e}}\right)\left(1 - \frac{C_R f_t}{1 + \xi\nu_{*e}}\right)} \qquad (13B2)$$

$$G(Z_{eff}) \equiv \frac{Z_{eff}(2.67 + Z_{eff})}{3.4(1.13 + Z_{eff})}$$

$$f_t = 1 - \frac{(1-\varepsilon)^2}{(1-\varepsilon^2)^{1/2}} \frac{1}{(1 + 1.46\varepsilon^{1/2})}$$

$$\varepsilon \equiv r/R_0$$

$$\xi \equiv 0.58 + 0.20\, Z_{eff}$$

$$C_R \equiv \frac{0.56(3.0 - Z_{eff})}{Z_{eff}(3.0 + Z_{eff})}$$

where f_t represents the fraction of trapped particles (Rawls, 1979).

ripple trapping and diffusion

The toroidal magnetic field will have some nonuniformity in the toroidal direction, called *ripple*, caused by gaps between toroidal field coils. The amount of ripple is represented by the parameter $\delta = \Delta B_t/B_t$, where ΔB_t is half the peak-to-peak variation of the toroidal magnetic field B_t. Particles with low parallel velocities $v_{\parallel}$ can become trapped in these ripples (not to be confused with the trapped particles having banana orbits, Fig. 7E3). Ripple-trapped particles are unable to complete a circular orbit, so they gradually drift out with the magnetic field gradient and curvature drift velocity $\vec{v}_d \equiv \vec{v}_c + \vec{v}_{\nabla B}$ (Eq. 7C5). If the effective collision frequency is ν_{eff}, then the diffusion step size is roughly v_d/ν_{eff}. The fraction of ripple-trapped particles is roughly $v_{\parallel}/v \sim \delta^{1/2}$. Since ν represents the frequency for scattering through an angle of 90 degrees, and only small scattering angles $\sim \delta$ are needed to detrap ripple-trapped particles, the effective collision frequency for detrapping is $\nu_{eff} \sim \nu/\delta$. Then, the resultant diffusion coefficient is

$$D \approx (\text{trapped particle fraction})(\text{collision frequency})(\text{step size})^2$$

$$\approx \delta^{1/2}\nu_{eff}(v_d/\nu_{eff})^2 \sim \delta^{3/2} v_d^2/\nu \sim \delta^{3/2}(kT_i/eBR_0)^2/\nu \quad . \qquad (13B3)$$

This process is sometimes called "superbanana diffusion". The main effect of ripple-trapping on plasma transport is enhancement of ion heat conduction. For a typical TFTR plasma with $\delta \sim 0.05$, χ_i is enhanced over the neoclassical value by a factor of about 3. For individual ions with energy W_i, $D \propto W^{7/2}$, so fast ions are preferentially lost, as illustrated in Fig. 13B1. This loss of high-energy ions can significantly reduce the fusion reaction rate.

impurity transport

Because of their higher charge states Z, impurity ions will have higher degrees of collisionality ν_{*i} than hydrogen ions. Thus, with hydrogen ions in the banana regime, the impurity ions may be in the plateau or Pfirsch-Schluter regimes (Fig. 8F1).

The impurity ions tend to diffuse up the hydrogen ion density gradient (towards the region of maximum ion density) and down the temperature gradient (away from the region of maximum temperature). The net motion is a balance of these and other effects, such as the Ware pinch. Impurity effects will be discussed further in Chapter 25.

anomalous transport

Ion heat transport in tokamaks is usually within a factor of five of the neoclassical rate, but electron heat transport is usually "anomalous" (much faster than the neoclassical rate). A variety of processes can cause accelerated transport: drift waves, trapped electron modes, tearing modes, drift-tearing modes, magnetic flutter, and stochastic magnetic fields. It is not clear yet which process is dominant, or how χ_e should vary with experimental parameters.

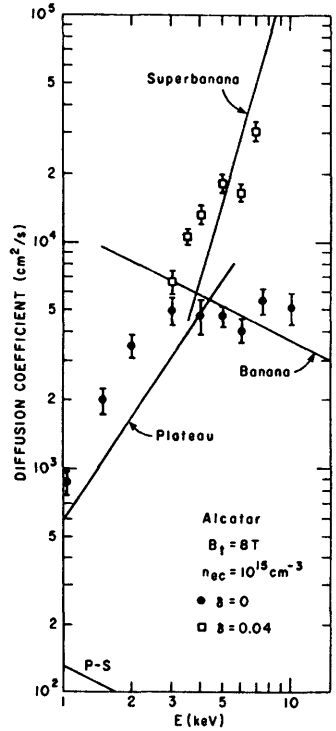

Fig. 13B1. Collisional diffusion coefficients for ions with energy E near the center of a high-density Alcator plasma, assuming uniform ripple. The points are the results of Monte Carlo guiding center calculations, with error bars representing standard deviations. The smooth curves are theoretical estimates with q = 1, a/R_0 = 0.05. (The Monte Carlo method will be described in Chapter 27.) From D.L. Jassby, H. H. Towner, and R. J. Goldston, Nuclear Fusion 18, 825-833 (1978), Fig. 3.

drift waves and trapped particle modes

Drift waves with phase velocities $\omega/k_\theta = -(1/n_0 eB)(dp_e/dr)$ will always be present in a magnetized plasma column. They may become unstable when some form of energy dissipation is present, such as plasma resistivity, friction with trapped particles, etc.

According to one estimate, the heat transport by electrons due to drift wave turbulence is

$$q_e \simeq -\alpha \frac{nT_e^2}{eB}\left(\frac{W_f}{nT_e}\right)\bar{k}_y r_n \left(\frac{1}{T_e}\frac{dT_e}{dr}\right) G_k^2 \qquad (13B4)$$

where T_e is the electron temperature in energy units, G_k^2 is a dimensionless numerical coefficient, $r_n = n/|dn/dr|$ is the density gradient scale length, $\bar{k}_y$ is

the wave number at the peak of the turbulent wave spectrum (typically $\bar{k}_y \sim 0.6/\rho_e$, ρ_e is the electron Larmor radius), and a small density-gradient term has been omitted, for simplicity (Horton and Estes, 1979). It is assumed that the actual fluctuation level is αW_f, where α is some fraction of the maximum possible turbulent energy density W_f, given by

$$W_f/nT_e = (\rho_e/r_n)^2(L_s/r_n) \qquad (13B5)$$

and the shear length L_s was defined in Table 8B1. By fitting this theory to data from various tokamaks, it is found that $\alpha \sim 0.15$. Trapped particle modes can cause transport coefficients to increase steeply with temperature. For example, the trapped ion mode diffusion coefficient $D \propto T_i^{7/2}$ (Eq. 8F13). Such a scaling would strongly limit plasma temperatures. However, the potency of the trapped ion mode is uncertain, because it was expected in PLT experiments ($\nu_{*i} << 1$) but not observed.

Drift waves and trapped particle modes are electrostatic perturbations. Perturbations of the magnetic field can also give rise to anomalous transport rates.

magnetic perturbations

Tearing modes, driven by magnetic energy, can lead to very rapid transport along magnetic field lines going radially around magnetic islands. Such rapid transport occurs near a mode rational surface (q = m/n).

The magnetic component of drift waves and shear-Alfven waves, called *magnetic flutter*, may lead to substantial anomalous transport. A small-scale drift-tearing mode may produce short-wavelength perturbations of the magnetic field. Such oscillating $\tilde{B}_r$ facilitate radial transport along magnetic field lines, which is qualitatively different from the $\tilde{E}xB/B^2$ drifts associated with electrostatic perturbations. Small values of $\tilde{B}_r/B \sim 10^{-4}$ could cause substantial anomalous transport.

transport codes

Transport codes are used to model many phenomena, including high-beta equilibria, non-circular plasmas, divertors, impurity production and transport, and magnetic compression of the plasma.

For many of these cases it is necessary to model the flux surfaces in at least two dimensions, by solving the Grad-Shafranov equation (8C19) on a two-dimensional grid. The transport equations, however, can be written as one-dimensional functions of the poloidal flux function ψ (or other equivalent label). Different sets of transport coefficients are used for electrons and ions in various spatial regions, to account for current estimates of their behavior in various regimes of collisionality.

Contours of constant pressure and current density calculated for the PDX tokamak are shown in Fig. 13B2. Parameters relating to plasma stability are monitored, in order to estimate and model the consequences of MHD instabilities. In some cases, values of $\langle\beta\rangle \sim 0.1$ have been simulated, but enhanced transport from ballooning modes is expected to become a serious problem.

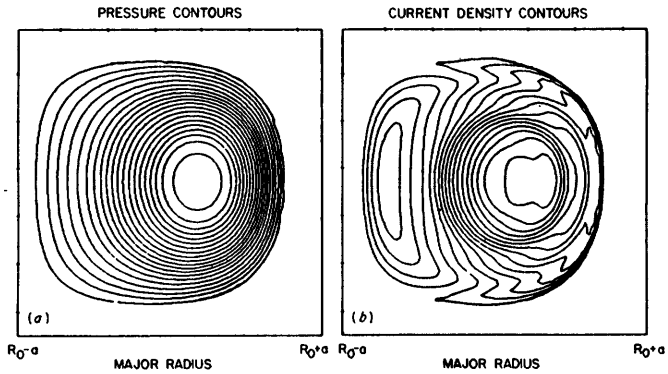

Fig. 13B2. Typical pressure and current density contours for the PDX "square" geometry case. The beam and thermal plasma pressure rise causes a compression of the plasma against the outer edge of the device. From J. T. Hogan, Nuclear Fusion 19, 753-776 (1979), Fig. 10.

experimental measurements

resistivity and current density

Voltage, current, and density measurements for an ohmically-heated discharge in PLT are illustrated in Fig. 13B3, and the evolutions of the electron temperature and density profiles for the same discharge are shown in Fig. 13B4.

Impurity concentrations are measured by ultraviolet spectroscopy. The values of Z_{eff} and $\eta_{\parallel}$ calculated from these measurements (Eq. 13B2) usually agree with values of $\eta_{\parallel}$ calculated from plasma current-voltage characteristics.

It is often assumed that E_t and Z_{eff} are independent of radius, so that the current density profile $J_t(r)$ can be estimated from the variation of resistivity $\eta_{\parallel}(r)$. Then $J_t(r) \propto T_e^{3/2}(r)$, which is known from Thomson scattering (Fig. 13B4) and from electron cyclotron emission measurements. Then $B_p(r)$ and $q(r)$ can be calculated from $J_t(r)$, and singular surfaces $q(r) = m/n$ can be compared with experimental data on MHD

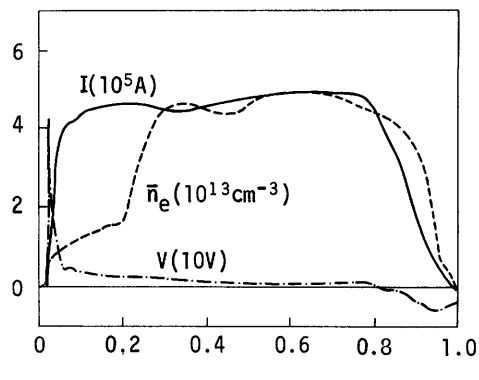

Fig. 13B3. Variations of plasma current, density, and voltage with time in an ohmically-heated PLT discharge (R_0 = 1.34 m, a = 0.40 m, B_t = 3.2 T). From J. M. Rawls, DOE/ER-0034 (1979), Fig. 2-14(A).

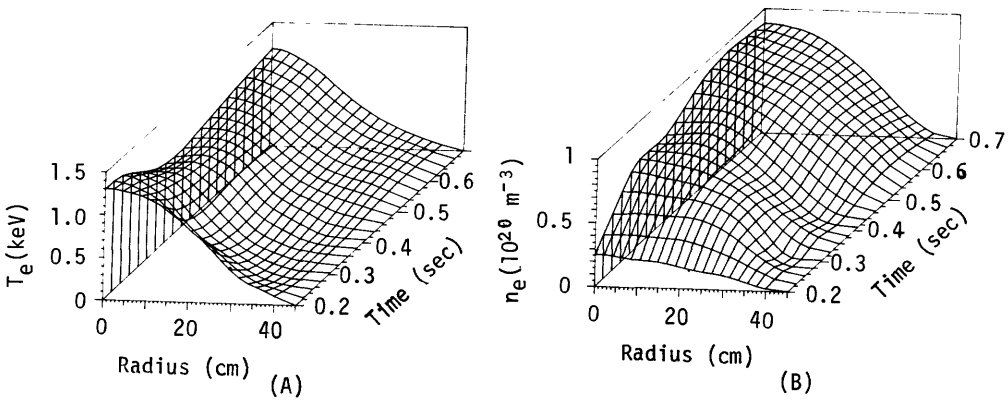

Fig. 13B4. Evolution of electron temperature and density profiles, measured by Thomson scattering, for the same PLT discharge as in Fig. 13B3. From J. M. Rawls, DOE/ER-0034 (1979), Fig. 2-15.

activity, such as sawtooth oscillations. Several diagnostic techniques are being developed to measure $B_p(r)$ or $J_t(r)$ directly: heavy-ion beam probing, Zeeman splitting of spectral lines from an injected neutral beam probe (such as Ba), and generation of harmonic microwaves.

particle flow

As particles diffuse to the walls, the plasma density will decrease, unless new fuel ions are added to the central region. If a puff of neutral gas is admitted to the outside of the plasma, a local density peak could occur, with some of the new ions diffusing towards the interior of the plasma. Often the inward motion has been so rapid that no density spike was observed at the plasma edge. Neutral gas puffing lowers the plasma edge temperatures and alters $J_t(r)$, as illustrated in Fig. 13B5. The improved confinement in the case on the right was due more to reduced plasma transport rates than to reduced radiation losses. [Hollow $T_e(r)$ profiles can also be produced late in a discharge by radiation losses from impurity accumulation in the plasma core.]

The duration of the plasma discharge may be much longer than the average lifetime of ions in the edge region. A typical ion will diffuse to the wall, return to the plasma as a neutral atom, become ionized (or charge exchanged), and then diffuse to the wall again several times during the discharge. Such recycling has an important effect on plasma density.

energy flow

The energy flows in a tokamak are illustrated in Fig. 13B6. The magnitudes of these energy flows can be determined experimentally and compared with transport code predictions. Transport coefficients can be inferred from experimentally measured density and temperature profiles and from sawtooth oscillations. For example, the central electron heat conductivity can be estimated from

$$\chi_{e0}/n_0 \simeq 3r_s^2/8\tau_s \qquad (13B6)$$

where n_0 is the central plasma density, r_s is the radius of the q = 1 singular

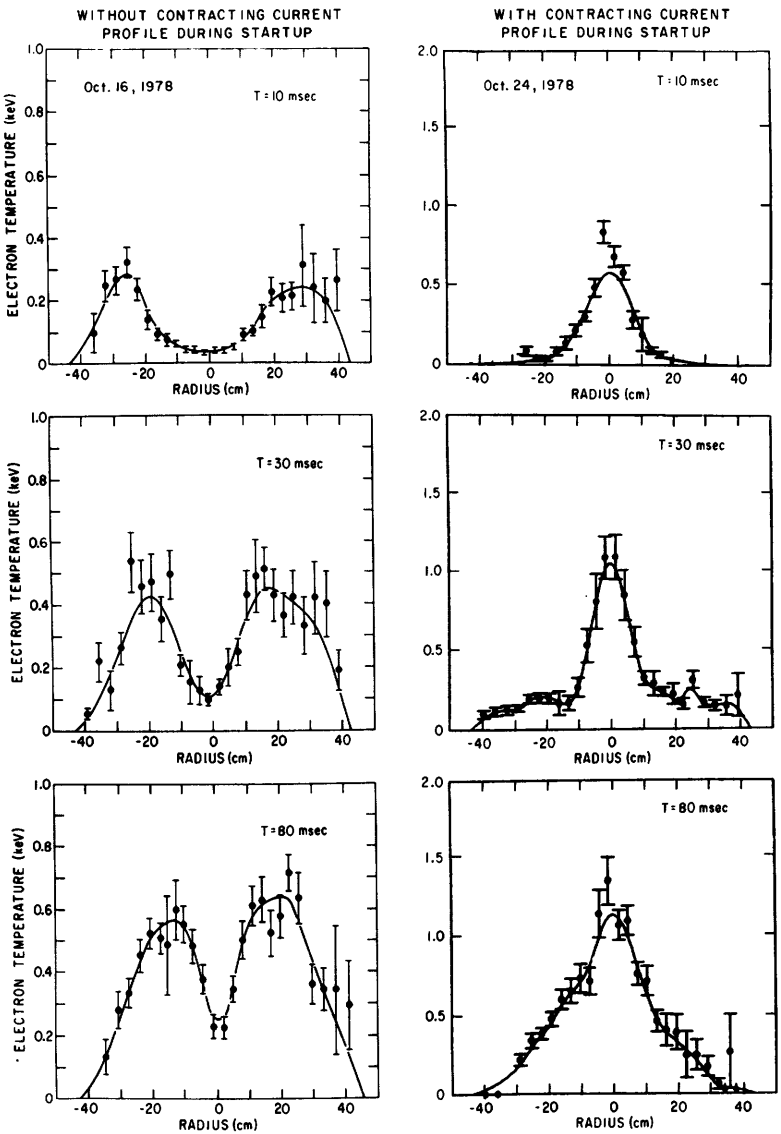

Fig. 13B5. The effect of gas puffing on electron temperature profiles during plasma startup. In the case on the left, a skin current induced near the plasma boundary heats up the outside, forming a hollow temperature profile. Plasma interaction with the limiter releases metallic impurities, which increase radiation losses and keep T_e low. In the case on the right, gas puffing causes the current channel to contract, reducing plasma-limiter interactions, and producing higher T_e (note the different temperature scales).

From R. J. Hawryluk et al, Nuclear Fusion 19, 1307-1317 (1979), Fig. 7.

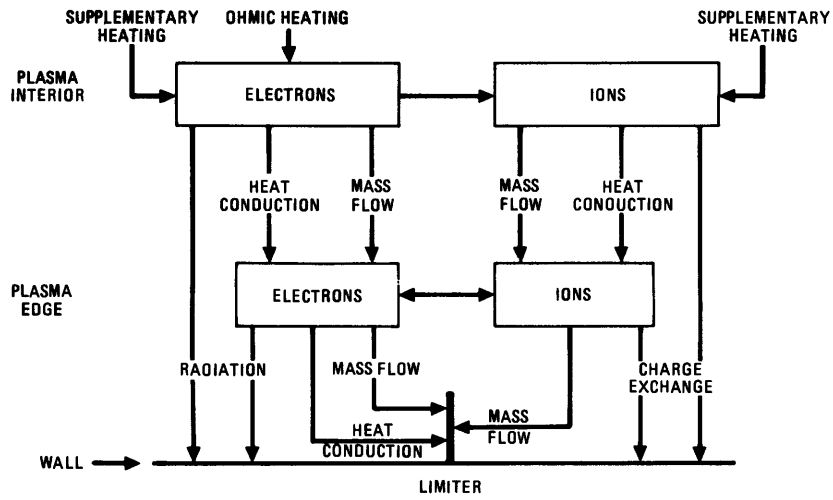

Fig. 13B6. Energy flow pattern in a tokamak. From J. M. Rawls, DOE/ER-0034 (1979), Fig. 2-16.

surface, and τ_s is the sawtooth pulse length (Fig. 13A11). A more exact formula for estimating χ_e at any location where $(\partial\tilde{T}/\partial r) = 0$ is

$$\chi_e(r) = \frac{3(\partial\tilde{T}/\partial t)n}{2(\partial^2\tilde{T}/\partial r^2)} \qquad \text{at } (\partial\tilde{T}/\partial r) = 0 \tag{13B7}$$

where $\tilde{T}(r,t) \equiv T_e(r,t) - T_0(r)$, and $T_0(r)$ is the "equilibrium" temperature profile just before a sawtooth disruption (Soler and Callen, 1979). Results of this method agree with other estimates of χ_e. From particle flow rates, it appears that $nD/\chi_e \sim 0.2\text{-}0.4$.

The electron energy flow may be divided into three regions, as illustrated in Fig. 13B7. In the outer region $r_2<r<a$ transport is dominated by atomic collision processes, such as ionization, line radiation, and charge exchange. In the inner region $r < r_1$, transport is dominated by internal disruptions (sawtooth oscillations). In the intermediate region, transport is dominated by electronic heat conduction (except at high densities, where ionic heat conduction may be significant). The *global* energy confinement time (for the plasma as a whole) is determined by a mixture of these processes. For example, the power flows of the TFR-600 tokamak are shown in Fig. 13B8 as functions of radius.

Ignoring heating by fusion reaction products, the power balance conditions (4A4), (4A5) may be written

$$1.5\ d(nT_e)/dt = P_e - 1.5nT_e/\tau'_{Ee} - P_{rad} - 1.5n(T_e-T_i)/\tau_{eq} \tag{13B8}$$

$$1.5\ d(nT_i)/dt = P_i + 1.5n(T_e-T_i)/\tau_{eq} - 1.5nT_i/\tau_{Ei} \tag{13B9}$$

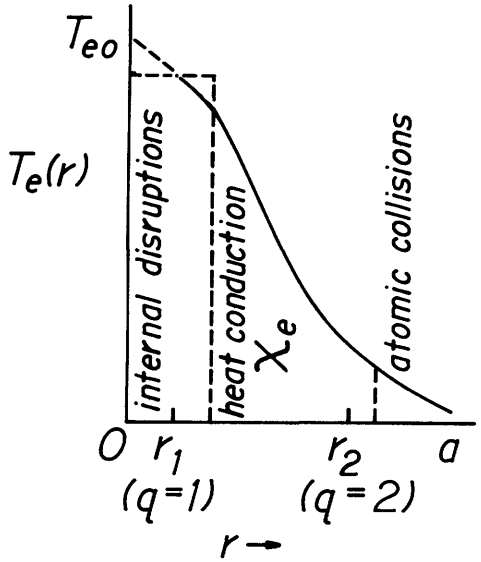

Fig. 13B7. Electron temperature profile, indicating dominant heat flow processes.

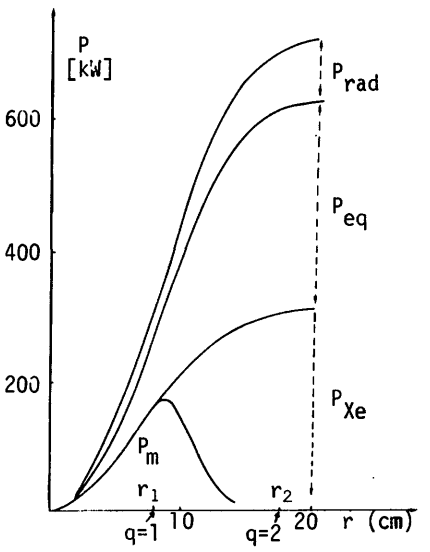

Fig. 13B8. Radial variations of power flows in the TFR-600 tokamak. Here P_{eq} represents heat flow from electrons to ions, P_m represents heat flow due to internal disruptions, and P_{Xe} represents electron heat conduction. From Equipe TFR, Nuclear Fusion 20, 1227-1245 (1980), Fig. 2b.

Estimates of τ'_{Ee}, τ_{Ei}, and τ_{eq} will be given in Section 13F. The equilibrium solutions are

$$T_e = \frac{P_i/\tau_{eq}+(P_e-P_{rad})/\tau_{hi}}{1.5n(1/\tau_{he}\tau_{hi}-1/\tau_{eq}^2)} \qquad (13B10)$$

$$T_i = \frac{P_i/\tau_{he}+(P_e-P_{rad})/\tau_{eq}}{1.5n(1/\tau_{he}\tau_{hi}-1/\tau_{eq}^2)} \qquad (13B11)$$

$$\tau_{he} \equiv \tau'_{Ee}\tau_{eq}/(\tau'_{Ee}+\tau_{eq}) = \tau'_{Ee}/(1+\tau'_{Ee}/\tau_{eq})$$

$$\tau_{hi} \equiv \tau_{Ei}\tau_{eq}/(\tau_{Ei}+\tau_{eq}) = \tau_{Ei}/(1+\tau_{Ei}/\tau_{eq}) \qquad (13B12)$$

In these equations P_e, P_i are the heating powers per unit volume delivered to the electrons and ions. In *low-density plasmas*, $\tau_{eq} >> \tau'_{Ee}$, τ_{Ei}, these equations reduce to

$$T_e \simeq P_i\tau'_{Ee}\tau_{Ei}/1.5n\tau_{eq} + (P_e-P_{rad})\tau'_{Ee}/1.5n \quad . \qquad (13B13)$$

$$T_i \simeq P_i\tau_{Ei}/1.5n + (P_e-P_{rad})\tau'_{Ee}\tau_{Ei}/1.5n\tau_{eq} \qquad (13B14)$$

In *ohmically-heated* tokamaks, $P_i = 0$,

$$P_e = P_{oh} = \eta_{\parallel} J^2 \quad , \tag{13B15}$$

$$T_i = T_e \tau_{hi}/\tau_{eq} = T_e/(1 + \tau_{eq}/\tau_{Ei}) \quad , \tag{13B16}$$

and

$$T_e = \frac{(P_{oh}-P_{rad})\tau'_{Ee}(\tau_{Ei}+\tau_{eq})}{1.5n(\tau'_{Ee}+\tau_{Ei}+\tau_{eq})} \tag{13B17}$$

Equations (13B8)-(13B17) can be applied to either volume-average temperatures or central temperatures, provided that appropriate values of the terms are used (volume-average P_{oh} or central P_{oh}, etc.). Use of these equations will be illustrated in Section 13F.

burn control

When ignition occurs, alpha heating tends to raise the plasma temperature up to a high equilibrium value (T_{eq}, Fig. 4B1), where the plasma pressure would exceed MHD stability limits. For example, if the maximum stable $\langle\beta\rangle = 6$ %, $B = 5$ T, and $n = 10^{20}$ m^{-3}, then the maximum (volume-averaged) pressure $p = \langle\beta\rangle B^2/2\mu_0 = 0.6$ MPa, corresponding to a temperature $T = p/2n = 3\times10^{-15}$ J = 19 keV. Thus, confinement would be lost unless some form of burn control could keep $T \lesssim 19$ keV.

One possibility is to let the temperature rise, but reduce the density, in order to maintain constant pressure. However, this would probably reduce the fusion power density to uneconomically low values, since P_f is a maximum at $T \sim 13$ keV in pressure-limited DT plasmas (Fig. 2D1). Fusion burn may be controlled by transport processes, radiation, fueling, subignition operation, or plasma motion.

* *transport.* Any transport process which increases rapidly with temperature, will tend to limit the temperature to moderate values. The trapped ion mode has not appeared experimentally, but ripple transport is promising. Since $\nu \propto T^{-3/2}$, it can be seen from Eq. (13B3) that $D \propto T^{7/2}$ for this process. Although only a fraction of the ions become ripple trapped, they are mainly high-energy ions, which strongly affect the fusion reaction rate. Reactor studies indicate that ripples of about 2 % are sufficient to maintain desirable temperatures without preventing ignition.

* *radiation.* Impurity gases, such as xenon, may be injected into the plasma to increase radiation losses in a controlled way. This would raise the (P_{rad} + $3nT/\tau_E$) curve of Fig. 4B1, moving T_{eq} to the left.

* *fueling.* Feedback control could be used on fuel injection systems to control the plasma parameters. Studies of this method for a tokamak reactor found that it is feasible to maintain the desired temperature by cutting back tritium injection when the temperature is too high, and vice-versa.

* *subignition operation.* If the reactor is operated below ignition, then the heating rate P_{ext} will control the plasma temperature. As T_{ig} is approached, the required heating power drops to zero, so high values of Q can be attained with subignition operation close to T_{ig}. The value of T_{ig} can be raised by injection of impurity gases, in order to operate in regimes of high fusion power density ($T \gtrsim 10$ keV).

* *plasma motion.* The plasma can be ignited in the main tokamak chamber, allowed to expand during burn so that pressure limits are not exceeded, then exhausted to an adjacent chamber, where it is cooled by expansion, neutralized, and pumped away. At the same time a new plasma is produced in the main chamber and heated to ignition.

13C. Heating

ohmic heating

If J_t is uniform at small r,

$$B_p(r) = \mu_0 J_t r/2 \quad , \tag{13C1}$$

$$q(r) \simeq \frac{rB_t}{R_0 B_p} = \frac{2B_t}{\mu_0 J R_0} \quad ,$$

and

$$J \simeq \frac{2B_t}{\mu_0 R_0 q} \tag{13C2}$$

Since MHD stability requires $q \gtrsim 1$, the maximum value of J is $2B_t/\mu_0 R_0$. For example, in Alcator C (R_0 = 0.64 m, B_t = 14 T), we find $J_{max} = 3.5\times10^7$ A/m^2 . At T_e = 2 keV and Z_{eff} = 1, $\eta_{\parallel} \simeq 1.4\times10^{-8}$ Ωm (Eq. 9B3), and the maximum ohmic heating power density $\eta_{\parallel} J_{max}^2 \simeq 17$ MW/m^3. Since $\eta_{\parallel}$ varies as $T_e^{-3/2}$, higher power densities are attainable at lower T_e. For a reactor with R = 5 m and B_t = 5 T, however, $J_{max} = 1.6\times10^6$ A/m^2, about a factor of 20 smaller than J_{max} for Alcator C. Temperatures obtained by high-power ohmic heating in Alcator are illustrated in Fig. 13C1. At high densities, τ_{eq} becomes small, and T_{i0} approaches T_{e0} (Eq. 13B16). At very high B_t, it is possible to attain ignition by ohmic heating (Wagner, 1981).

neutral beam injection

Neutral beam injection systems were described in Section 9E.

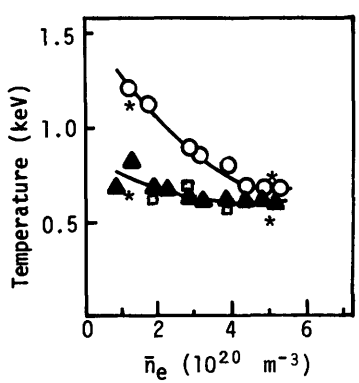

Fig. 13C1. Variation of central electron and ion temperatures with density in Alcator, showing nearly equal values at high density. These data were taken in deuterium at B_t = 6 T, I = 130-160 kA. Circles denote Thomson scattering data (T_e), squares are charge exchange data (T_i) and triangles are neutron data (T_i). Asterisks indicate predictions of Example Problem 13F1. From A.Gondhalekar et al, "A study of energy balance in Alcator", Plasma Physics and Controlled Nuclear Fusion Research (Innsbruck, 1978), Vol. I, IAEA, Vienna, 1979, Fig. 2, p. 200.

Ions trapped by neutral beam injection may be rapidly lost by several processes:

* *charge exchange* with neutral atoms present in the plasma. In PLT discharges, about 5-30 % of the injected beam power is lost by charge exchange.

* *bad drift orbits*. Particles injected tangentially (nearly parallel to the magnetic axis) will have nested circular drift surfaces with the centers of the circles shifted from the magnetic axis by a distance

$$\Delta = qv(1 + \zeta^2)/2\zeta\omega_{ci} \qquad (13C3)$$

where q is the safety factor, v is the injected ion speed, $\omega_{ci} = eB/m_i$ is the ion cyclotron frequency, and $\zeta \equiv v_{\parallel}/v$. [This equation may be derived from Eq. (7E11), integrating as in the derivation of Eq. (7E18) and using Eq. (13A3).] For ions injected parallel to the plasma current (*co-injection*) v is positive, and the shift is outwards, and for ions injected in the opposite direction (*counter-injection*) the shift is inwards. Thus counter-injected ions trapped near the plasma edge will have bad drift orbits, as illustrated in Fig. 13C2. Co-injected ions would have point C' to the right of point P, and much smaller drift orbit radii (dashed curve) staying inside the plasma. The fraction of particles lost depends upon the ratios Δ/a and λ_a/a, where the attenuation length λ_a is given in Fig. 9E1. Thus, co-injection provides better drift orbits. Some counter-injection may also be used, if toroidal rotation induced by co-injection becomes a problem. If the beams are injected nearly perpendicularly to the magnetic axis, then the resultant ions will be trapped in banana orbits. Counter injected beams will have bananas extending outside their ionization point, while co-injected beams will have bananas inside the ionization point (Fig. 7E4).

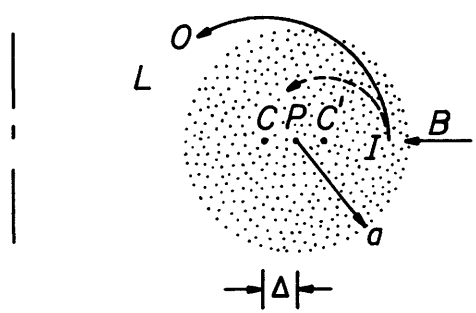

Fig. 13C2. Illustration of a bad drift orbit caused by counterinjection. Dots represent plasma. B = injected beam path, I = point of ionization of a given ion, C = center of that ion's drift orbit, P = center of the plasma, a = minor radius, Δ = shift of drift orbit center from plasma center, O = path of drift orbit, L = point where ion is lost to wall or limiter, C' = center of orbit of co-injected ion orbit (dashed curve).

* *ripple diffusion*. If injection is perpendicular to the magnetic flux surfaces, then some of the ions may become trapped in the toroidal field ripples and lost by "ripple diffusion" (Eq. 13B3).

On the other hand, the vertical drift of ripple-trapped ions may be used to make them drift through the plasma center, enhancing beam penetration. The ripples could be decreased on the other side of the plasma by special coils, so that the ions are detrapped as they pass through the center.

Variations of T_i, T_e, and n with time during neutral beam injection into PLT are shown in Figs. 13C3 and 13C4. The experimental data for $T_i(t)$ are consistent with predictions of the transport code (smooth curve), which assumes τ_p = 30 ms and neoclassical χ_i. The density rise is mostly due to neutral gas desorbed from the walls by ion bombardment. By turning off one of the counter-injected beams,

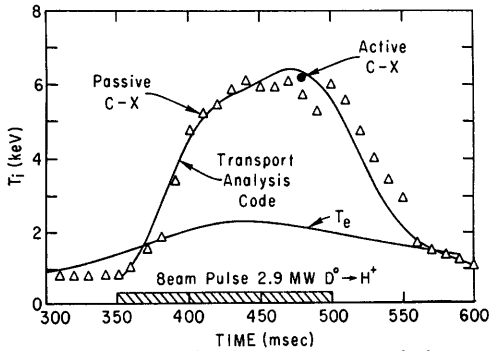

Fig. 13C3. Variations of central ion temperature and electron temperature with time during neutral beam injection into PLT, with B_t = 2.5 T, 2 co-injected deuterium beams and 2 counter-injected deuterium beams into a hydrogem plasma. Courtesy of PPPL. (Research at PPPL is supported to Princeton University and DOE under Contract # DE-AC-2-76-CH03073).

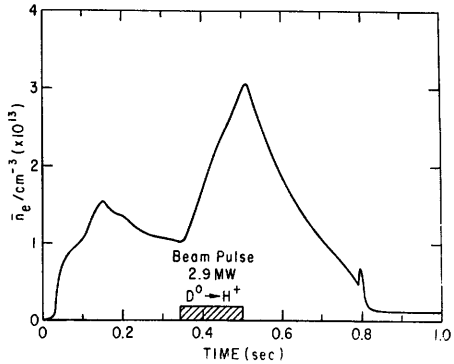

Fig. 13C4. Variation of average plasma density during neutral beam injection into PLT, same conditions as the previous figure. Courtesy of PPPL.

Fig. 13C5. Variation of ion temperature with ratio of beam power to average plasma density in PLT. From H. Eubank et al, Physical Review Letters 43, 270- 274 (1979), Fig. 2.

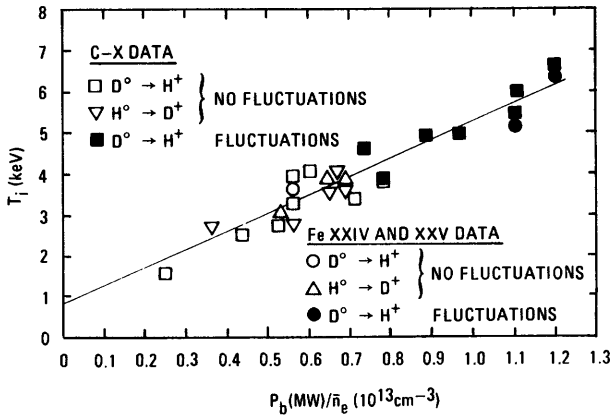

the impurity radiation and density rise were reduced ($\bar{n}$ = 1.5x10^{19} m^{-3}), and T_i = 7.1 keV was attained, even though P_i was reduced to 2.4 MW. The ratio of beam energy density to plasma energy density on the axis was about 3.8, without loss of stability or unusual turbulence. According to Eq. (13B11), T_i should increase approximately linearly with P_i/n. Such a linear rise is observed experimentally in PLT, Fig. 13C5. Electron heating is less than ion heating during neutral beam injection, because more power is deposited with the ions, and because the ohmic heating power P_{oh} decreases as T_e increases. Electron heating is also sensitive to Z_{eff}, since increasing Z_{eff} tends to increase both P_{rad} and P_{oh}

Methods which predominantly heat ions offer the opportunity for operation in the *hot ion mode*, with $T_i/T_e \sim 2$. The hot ion mode enables ignition at lower values of $n\tau_E$($\sim$5x10^{19} m^{-3}s) than other modes of operation (Clarke, 1980), but it is difficult to maintain a substantial temperature difference if $n > 10^{20}$ m^{-3}, because of the τ_{eq} term in Eqs. (13B8) and (13B9).

There is considerable agreement between theory and experimental data on slowing down of injected beams in the plasma:

* *energy spectra.* Fokker-Planck codes have been used to calculate the energy spectra of injected beam ions during slowing down. The results of such calculations agree with data from charge-exchange neutral analyzers (Eubank et al, 1979).
* *decay times.* After neutral beam cutoff, the decays of the charge-exchange neutral signals at various energies agree with theoretical predictions.
* *high energy tail.* The shape of the high-energy tail of the ion distribution function agrees with calculations.
* *neutron yields.* For injection of a deuterium beam into a deuterium plasma, the beam-plasma neutron yields agree with predictions.
* *diamagnetism.* The change of plasma diamagnetism produced by beam injection (measured by magnetic probes) is consistent with theoretical estimates based on density and temperature profiles.

Reactor ignition may be facilitated at low densities, with fueling by cold gas feed after ignition to increase the density up to the desired value (Holmes et al, 1980; Singer, Jassby, and Hovey, 1980).

rf heating

Some methods of wave heating were discussed in Section 9F. Reactor studies indicate that overall efficiencies of about 60 % could be attained with either fast magnetosonic wave heating or lower hybrid wave heating. Use of ECRH requires high-power generators at frequencies on the order of 100 GHz, which are not yet developed and will probably be more expensive than other wave heating techniques.

Ion cyclotron heating may be aided by heating a minority species in the plasma, such as 10 % protons in a deuterium plasma. Much of the energy is dissipated by ion-ion collisions, resulting in effective ion heating. (If only one species were present, self-ion collisions would be less effective in dissipating the energy, since most of the ions would be resonant with the wave.) Results obtained in PLT with proton and ^{3}He minority species in deuterium plasmas are shown in Fig. 13C6. The *heating rate* $\Delta T_i n_i / P_{rf}$ for these experiments is 3×10^{16} keV/m^{3}kW (H minority case) and 6×10^{16} keV/m^{3}kW (^{3}He minority case), where ΔT_i is the change in T_i caused by the wave heating.

Heating at ω_{ci} is done with half-turn loop antennas, which would be subject to severe radiation damage in a reactor. Heating at the second harmonic ($2\omega_{ci}$) has also been effective in PLT, with a heating rate of about 3.5×10^{16} keV/m^{3}kW, and mode tracking does not appear to be necessary. This frequency is high enough that waveguide coupling is possible (at $B \sim 5$ T, $2\omega_{ci} \sim 80$ MHz for deuterons and 100 MHz for $^3He^{++}$ ions). Third harmonic heating could permit the use of smaller waveguides.

Using a Faraday-shielded antenna in DIVA, about 80 % of the ICRF input power was absorbed by ions in the plasma core, raising T_i from 150 to 450 eV. Heating at the lower hybrid resonance ω_{LH} in tokamaks is also being studied.

compression

When a collisional plasma is compressed by decreasing the major radius R, the plasma ion temperature change is

$$\frac{T_{i2}}{T_{i1}} = \frac{\langle W_{i2}\rangle}{\langle W_{i1}\rangle} = \left(\frac{V_1}{V_2}\right)^{2/3}$$

$$= \frac{2\pi^2 R_1 a_1^2}{2\pi^2 R_2 a_2^2} = \left(\frac{R_1}{R_2}\right)^{4/3} \qquad (13C4)$$

where the subscripts 1, 2 denote before and after compression, and Table 9C1 and Eq. (9C6) have been used. Similarly, the ion density change is

$$\frac{n_{i2}}{n_{i1}} = \frac{V_1}{V_2} = \left(\frac{R_1}{R_2}\right)^2 . \qquad (13C5)$$

These density and temperature changes were verified experimentally with the ATC (adiabatic toroidal compressor) tokamak. For example, with a compression ratio of 2.2, T_i increased from 0.4 to 1.2 keV.

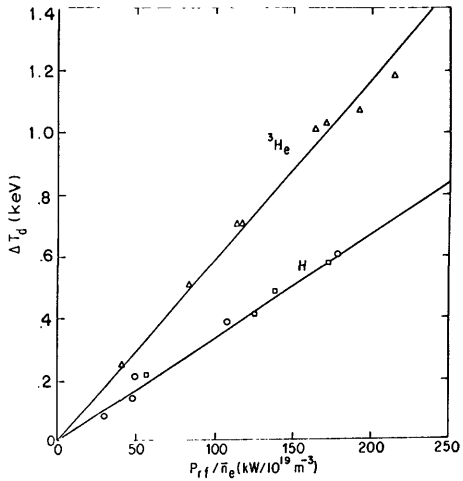

13C6. Deuteron temperature increase in PLT as a function of rf power normalized to the electron density. The rf power ranges from 30 to 600 kW over densities from $\bar{n}_e = 1.0$ *to* 4.5×10^{19} m^{-3}. *Heating is via ion-ion coupling with minority H or* ^{3}*He ions. From J. Hosea et al, "Fast wave ion cyclotron heating in the Princeton Large Torus", 8th International Conference on Plasma Physics and Controlled Fusion Research, 1980, IAEA, Vienna, 1981, Fig. 1.*

Minor-radius compression (by increasing B_t) was demonstrated in the TUMAN and TOSCA devices, with $T_{i2}/T_{i1} = (B_2/B_1)^{4/3}$ and $n_{i2}/n_{i1} = (B_2/B_1)^2$, in accord with theory. However, it is experimentally more difficult to increase B_t, and doing so results in a large aspect ratio (unfavorable for high-beta stability) and a small plasma volume.

other heating methods

Electron beam injection (Section 16E) can be very efficient, if good penetration and trapping can be attained.

Plasma guns can inject target plasmas into tokamaks, but they probably will not be hot enough to attain ignition without other heating methods. Turbulent heating experiments in tokamaks have failed, probably due to enhanced energy loss rates caused by the turbulence.

Another possibility is to form two or more plasma columns, then move them together. As they coalesce, some of the poloidal flux is annihilated, with the energy transformed into plasma thermal energy (Shafranov, 1979).

13D. Current Drive

There are several problems to be solved if tokamak reactors are to operate steady state (or with very long pulses):

current drive
burn control
plasma purity
fueling.

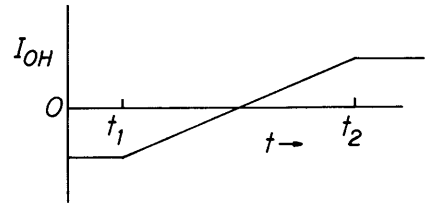

Fig. 13D1. Ohmic heating coil current vs. time. The pulse length is (t_2-t_1).

Burn control was discussed briefly in Section 13B, and plasma purity and fueling will be discussed in Chapter 25.

magnetic induction

According to Faraday's Law (Example Problem 5B3)

$$2\pi RE = -A(dB/dt) \quad , \tag{13D1}$$

so the induction of a toroidal electric field E (to drive the plasma current) requires a changing magnetic field dB/dt, which in turn requires changing the current in the ohmic heating (OH) coils. Thus, the inductive current drive ceases when the OH coils reach maximum current. The pulse length can be maximized by running the coils from negative current to positive current, as illustrated in Fig. 13D1.

The poloidal magnetic field is established by a combination of several coil systems:

* *Ohmic heating* (OH) coils provide enough Volt-seconds of induction to develop a strong plasma current.
* *Equilibrium field* (EF) coils (also called *vertical field* coils) control the plasma shape and position.
* *Divertor coils* are used in some designs to direct the outer magnetic surfaces away to another chamber, so that the outer layers of plasma can be scraped off, neutralized, and pumped away, in order to maintain plasma purity (Chapter 25).

Figures 13D2 and 13D3 show the Tokamak Fusion Test Reactor (TFTR) and its poloidal field coils. During initial operation, the OH coils will drive a plasma current of 2.5 MA with a flat-top (constant-current) period of 1 second. The EF coils will produce an equilibrium field up to 0.42 T. Parameters of the poloidal coils are listed in Table 13D1. The flat-top time may be extended to 3 seconds by use of additional power supplies.

For optimum performance, the OH coils should lie on a single flux surface or else be connected in parallel. Coil system interactions can be minimized by making the total EF coil current equal to the total OH coil current, and by minimizing the mutual inductance between the coil systems.

Placement of EF coils outside the TF coils simplifies coil winding and maintenance, but requires higher EF coil currents and loses the stabilizing effect of closely fitting coils. The OH and EF coils must be protected against voltage spikes and electromagnetic forces induced by plasma disruptions.

The use of an iron-core transformer, as in Fig. 5B2, decreases the energy required to drive the OH coils and reduces stray magnetic fields. However, in

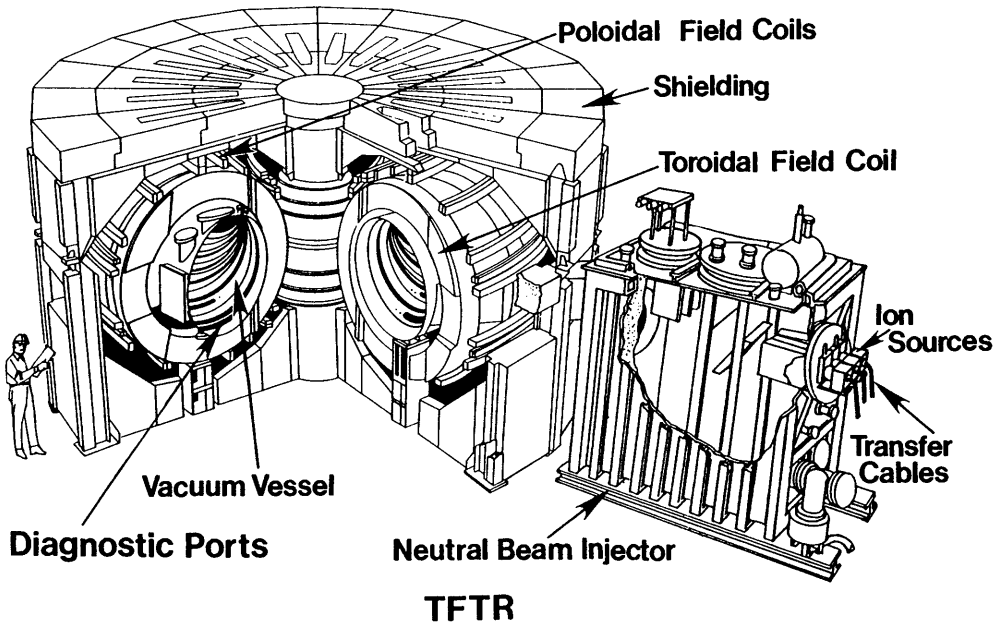

Fig. 13D2. The Tokamak Fusion Test Reactor. Courtesy of PPPL.

high-field devices saturation of the iron diminishes the energy savings, complicates the electrical behavior of the system, and causes field errors. The presence of an iron core reduces access space on the inside of the torus and reduces plasma stability against radial displacements.

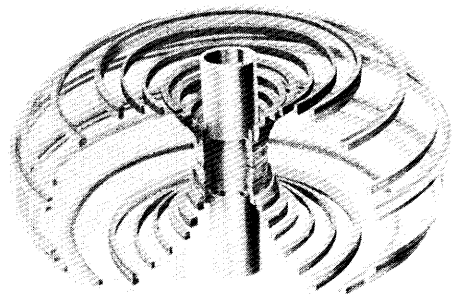

Fig. 13D3. Illustration of the poloidal field coils of TFTR. Courtesy of PPPL.

The voltage $\phi = 2\pi RE$ required from the OH coil system is determined by the electric field needed to start the discharge and drive the desired current. The maximum OH coil current limits the Volt-second (magnetic flux) capacity, hence the pulse length. Breakdown is usually initiated by microwave heating or ultraviolet radiation. ECRH is useful to reduce the loop voltage which the OH coils must provide. For example, in ISX-B the inductive component of the loop voltage (LdI/dt + IR) stayed constant at 16 V, but the resistive component decreased from 27 V to 9 V with ECRH preionization. Usually the discharge is initiated at low pressure, with cold gas added later to build up the density after the current is large enough for plasma confinement.

The OH power is limited by the attainable electric field ($P_{OH} = E^2/\eta_{\parallel}$), by the maximum attainable current density (Eq. 13C3), and by the allowable dI/dt in superconducting OH coils. Auxiliary heating systems are ineffective until a

Table 13D1. Parameters of TFTR poloidal field coils. From PPPL-1475 (1978), Table 3-8.

	ohmic heating (OH) and horizontal	equilibrium field (EF)	variable curvature (in series with EF)
Maximum flux, Volt-seconds	13	7	7
number of turns	498	196	98
current, kA	23	34	34
power consumed, MW	37	59	78
stored energy, MJ	36	50	44
mass of copper, tons	24	29	9

strong plasma current has been developed to provide good plasma confinement. The plasma current tends to peak at the edge and then gradually penetrate inwards, and the observed penetration rate is faster than expected from classical theory.

It is possible to operate tokamaks steady state, if a means of current drive other than magnetic induction can be provided. Steady-state operation would have the following advantages:

* steady power output, without thermal energy storage
* reduced complexity of OH coil system
* avoidance of pulsed coil stresses and fatigue
* avoidance of thermal cycling of materials and associated thermal stress fatigue problems
* avoidance of repeated energy losses during startup.

There are several ideas for steady-state current drive, including the bootstrap current, neutral-beam driven currents, and rf current drive.

bootstrap current

The bootstrap current is induced by outward diffusion of plasma particles, so it is not compatible with edge fueling by cold neutral gas. If fresh fuel could be continuously supplied to the plasma core, however, the bootstrap current might be able to sustain plasma confinement, or at least to reduce the required OH power. A selective counter-current loss of some alpha particles, combined with banana orbit effects, may act as a "seed current" for the bootstrap current.

neutral-beam-driven current

When a neutral beam is injected and trapped, the resultant flowing ions constitute an electrical current.

Beam ions colliding with background electrons will impart momentum to the electrons, tending to drag them along with the beam, and the resulting electronic current opposes the beam ion current. The electrons will also be retarded by friction with background plasma ions. When the frictional forces are in balance, the electronic current cancels the beam ion current. However, impurities and trapped electrons can increase the friction of streaming electrons with background plasma, so that the electronic current does not fully cancel the beam ion current. The net current density is approximately

$$J_{net} = J_{beam}[1 - 1/Z_{eff} + (1.5/Z_{eff})(1 + 0.7/Z_{eff})(r/R)^{\frac{1}{2}}] \quad (13D2)$$

where

$$J_{beam} \equiv 2\pi Re \int d^3\vec{v}\, f_{beam} v_{\shortparallel}$$

(Rawls, 1979). High neutral beam energies and powers may be required to attain satisfactory penetration.

electron-beam-driven current

Relativistic electron beams can be injected into a torus along $\vec{B}_t$ using vertical drift to carry them away from the electron gun. Calculations indicate that large currents could be sustained in tokamaks by repeated bursts of electrons from a pulsed gun. Beams with pulse lengths up to 20 transit times (around the torus) have been injected into a torus with trapping efficiencies on the order of 60 %. The main problems to be solved are:

beam energy transport into the chamber without introducing impurities
injection and trapping
pulse repetition rate and lifetime of beam generator.

rf current drive

Travelling waves have time-averaged energy densities W_{rf} and momenta $\vec{p}$ related by the expression

$$\vec{p} = (\vec{k}/\omega)W_{rf} \quad (13D3)$$

where $\vec{k}$ and ω are the wave propagation vector and angular frequency. Wave momentum is transferred to electrons and collisionally dissipated at a rate

$$\dot{p} = nmu_e\nu \quad (13D4)$$

where the dot represents a time derivative, n is the electron density, m is the electron mass, u_e is the average electron flow velocity, and ν is the momentum-transfer collision frequency. The current density

$$J = neu_e = (e/m\nu)\dot{p} = (e/m\nu)(k/\omega)\dot{W}_{rf} \quad . \quad (13D5)$$

Since the wave phase velocity $v_\phi = \omega/k$, the ratio of current density to rf power dissipated is

$$J/\dot{W}_{rf} = e/m\nu v_\phi \quad . \quad (13D6)$$

This ratio is a figure of merit for rf current drive schemes.

If the rf power is transferred to the electrons at $v_e \sim v_\phi$ and dissipated by electron-ion collisions with momentum-transfer collision frequency ν_e, then

$$J/\dot{W}_{rf} = \begin{cases} (e/m\nu_e v_{te})\, C_1 (v_\phi/v_{te})^2 & \text{if } v_\phi > v_{te} \\ (e/m\nu_e v_{te})\, C_2 (v_{te}/v_\phi) & \text{if } v_\phi < v_{te} \end{cases} \qquad (13D7)$$

where the electron thermal velocity $v_{te} \equiv (kT_e/m)^{1/2}$. The constants $C_1 \sim 0.2$ and $C_2 \sim 1$ are determined by Fokker-Planck codes describing collisional dissipation of wave energy. For the high-phase-velocity case (top line, Eq. 13D7), the resonant electrons will have high velocities $v_e \sim v_\phi >> v_{te}$, and therefore low collision frequencies, since $\nu_e \propto 1/v_e^3$. These low collision frequencies will tend to make the ratio $J/\dot{W}_{rf}$ large, as desired.

For the low-phase-velocity case $v_\phi << v_{te}$, the ratio (v_{te}/v_ϕ) appearing in the bottom line of Eq. (13D7) tends to make $J/\dot{W}_{rf}$ large, but trapped particle effects may invalidate this equation.

Assuming that the poloidal beta $\beta_p \simeq R_0/a$, that $Z_{eff} \simeq 1$, and that the fusion reaction rate parameter $\langle\sigma v\rangle_{DT} \propto T^2$, the ratio of required rf power to fusion power is estimated to be

$$\frac{P_{rf}}{P_F} = \begin{cases} \dfrac{2.5\times10^{10}}{(\bar{n}aR_0)^{1/2}(v_\phi/c)^2\bar{T}^{3/2}} & \text{if } v_\phi > v_{te} \\ \dfrac{2.8\times10^{12}(v_\phi/v_{te})}{(\bar{n}aR_0)^{1/2}\,\bar{T}^{5/2}} & \text{if } v_\phi < v_{te} \end{cases} \qquad (13D8)$$

where $\bar{T}$ is the average plasma temperature (keV), $\bar{n}$ is the average density (m^{-3}), and c is the speed of light (Rawls et al, 1979). In order to keep the recirculating power fraction low, large, hot plasmas are desirable. If $\bar{n} = 10^{20}$ m^{-3}, $\bar{T}$ = 20 keV, a = 1.2 m, R_0 = 6 m, and $v_\phi/c = 0.5$, then $P_{rf}/P_F \simeq 0.04$. For this same case, if $v_\phi/v_{te} = 0.3$, then $P_{rf}/P_F \simeq 0.02$.

Currents driven by rf power have been observed experimentally. About 10 A of plasma current was driven in the ACT-1 device by 500 W of rf power at the lower hybrid frequency (160 MHz). When the direction of the wave phase velocity was reversed, the plasma current also reversed. Theoretical estimates of the current and optimum vertical field B_v are consistent with the experimental results (Wong, Horton, and Ono, 1980). Rf current drive using other types of waves is also under study. Estimates for reactors driven by lower hybrid waves indicate that values of $Q \sim 30$ are attainable, which result in a recirculating power fraction $\varepsilon \sim 15$ % for typical conversion efficiencies $\eta_e \sim 0.35$, $\eta_{in} \sim 0.5$ and blanket gain $M \sim 1.2$ (Eq. 4C3). An alternative scheme is to drive runaway electrons (at energies of about 10 MeV) by rf to carry the bulk of the current needed for plasma confinement.

13E. Runaway Electrons

generation

Electrons in a tokamak will be accelerated by the applied electric field E and retarded by the frictional force of Coulomb collisions with ions and with other electrons. The magnitude of this frictional force on an electron with velocity v_e moving in a Maxwellian distribution with $T_e \simeq T_i$ is

$$F(x) = (A_e n_e/kT_e)[\ 2G(x) + (1/n_e m_e) \sum_j n_j m_j Z_j^2 G(x m_j^{1/2}/m_e^{1/2})\ ] \qquad (13E1)$$

$$A_e \equiv e^4 L/4\pi\varepsilon_0^2 \simeq 1.2\times10^{-53}\ J^2m^2 \text{ (for } L \simeq 18)$$

$$G(x) \equiv (1/2x^2)[\mathrm{erf}(x) - (2x/\pi^{1/2})\exp(-x^2)] = H(x,0)/2x \quad \text{(Eq. 2E39)}$$

$$x \equiv v_e/v_{te}$$

where n_e, m_e, T_e are the electron density, mass, and temperature, n_j, Z_j, and m_j are the density, charge, and mass of ion species j, k is the Boltzmann constant, e is the electronic charge, ε_0 is the permittivity of free space, and $v_{te} \equiv (kT_e/m_e)^{1/2}$ is the electron thermal velocity. The quantity in brackets for a fully ionized hydrogen plasma is plotted in Fig. 13E1. At low values of x, the frictional force is mainly due to electron-ion collisions, but when $x > 1$ the electron-electron collisions cause about twice as much friction as electron-ion collisions. The peak friction occurs at $x \sim (m_e/m_i)^{1/2}$.

The accelerating force on electrons is eE, independent of velocity, and the retarding frictional force drops off at high velocities (large x). There will be some critical velocity x_c where the forces just balance:

$$F(x_c) \equiv eE \qquad (13E2)$$

Electrons with $x > x_c$ will have $eE > F(x)$, and therefore they will be continuously accelerated. These *runaway electrons* may reach energies of several MeV. For $x > 0.04$, the function plotted in Fig. 13E1 may be represented in the form

$$(kT_e/A_e n_e)F(x) = [Z_{eff} + 2(1 - e^{-x^2})\ ]/2x^2 \quad , \quad (x > 0.04) \qquad (13E3)$$

where Z_{eff} was defined in Eq. (3F13). We can use this approximation in Eq. (13E2) to find the critical velocity x_c :

$$KT_e eE/A_e n_e = [Z_{eff} + 2(1 - e^{-x_c^2})\ ]/2x_c^2$$

$$\simeq (Z_{eff} + 2)/2x_c^2 \quad \text{if } x_c \gtrsim 2 \quad . \qquad (13E4)$$

For typical tokamak parameters $n_e = 3\times10^{19}\ m^{-3}$, $T_e = 1$ keV, $E = 0.5$ V/m, and $Z_{eff} = 1.5$, the solution of this equation is $x_c = 5.0$. For this case,

$v_{te} = 1.3 \times 10^7$ m/s, so electrons with velocities over $v_{ec} = 6.6 \times 10^7$ m/s will run away. This corresponds to a critical energy $W_c = \frac{1}{2} m_e v_{ec}^2 = 12$ keV.

An electric field which is so strong that electrons with $v_e = v_{te}$ will run away, called the *critical electric field* E_c, may be found from Eq. (13E4) by setting $x_c = 1$:

$$E_c = \frac{A_e n_e (Z_{eff} + 1.26)}{2ekT_e} \quad . \qquad (13E5)$$

For the same parameters as above, $E_c = 19$ V/m.

During initiation of the tokamak discharge, the plasma is only partially ionized. Since neutral molecules have less of a retarding force on the electrons than ions have, runaway is more probable then. The friction force may be represented by

$$F(x) = F_p(x) + F_m(x) \qquad (13E6)$$

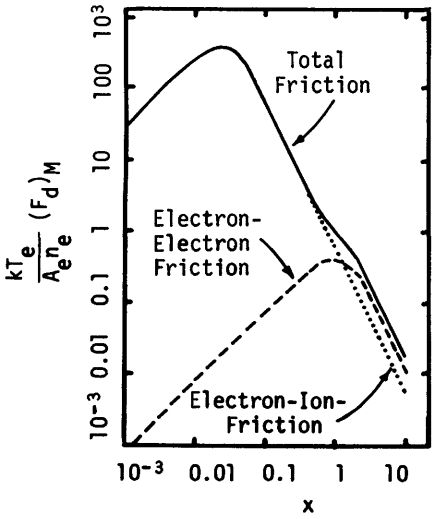

Fig. 13E1. Normalized dynamic friction force experienced by an electron moving in a fully ionized hydrogen plasma with $T_i = T_e$, as a function of the electron's normalized velocity $x = v_e/v_{te}$. From H. Knoepfel and D. A. Spong, Nuclear Fusion 19, 785-829 (1979), Fig. 1.

where F_p represents the force of the plasma (Eq. 13E1) and F_m represents the force of collisions with neutral gas, given approximately by

$$F_m \simeq e^4 n_m Z \ln(2W_e/U)/16\pi\varepsilon_0^2 W_e \qquad (13E7)$$

where n_m and Z are the density and charge number of the gas, $W_e = \frac{1}{2} m_e v_e^2$ is the electron energy, and U is the average excitation energy of the gas.

Electron runaway can be suppressed by using a high filling pressure of gas in the chamber, which tends to make n_m and n_e large, so that E_c is large. It can also be minimized by using the minimum electric field needed to start the discharge and build up the current.

limitations of runaway velocity

There are several phenomena which limit the degree of anisotropy which the electron distribution function can attain as a result of runaway. Electrons in the runaway beam may be rapidly scattered in pitch angle by oscillations caused by the *anomalous Doppler effect*, as illustrated in Fig. 13E2. This effect is likely to occur when the average velocity of the runaway beam u_b exceeds a threshold value

$$u_{bc} = 3v_{te}x_c(\omega_{ce}/\omega_{pe})^{3/2} \quad , \quad (13E8)$$

where $\omega_{ce} = eB/\gamma m_e$ is the electron cyclotron frequency and $\omega_{pe} = (n_e e^2/\gamma m_e \varepsilon_0)^{1/2}$ is the electron plasma frequency, with $\gamma \equiv (1 - u_b^2/c^2)^{-1/2}$. If B = 3T and $\gamma \sim 2$ in the previous example case, then $\omega_{ce} = 2.6\times10^{11}$ rad/s, $\omega_{pe} = 2.2\times10^{11}$ rad/s, and $u_{bc} = 2.6\times10^{8}$ m/s, which corresponds to an electron energy of about 0.5 MeV.

The rapid pitch-angle scattering caused by the anomalous Doppler effect is followed by a beam-plasma type instability, which spreads the electron energies and removes the bump from the $f(v_{\parallel})$ distribution at the top of Fig. 13E2, forming a plateau (as in Fig. 8E1). After these relaxation processes spread out the runaway beam in velocity space, acceleration by the electric field gradually builds up the distribution function towards the initial configuration of Fig. 13E2, and the cycle repeats.

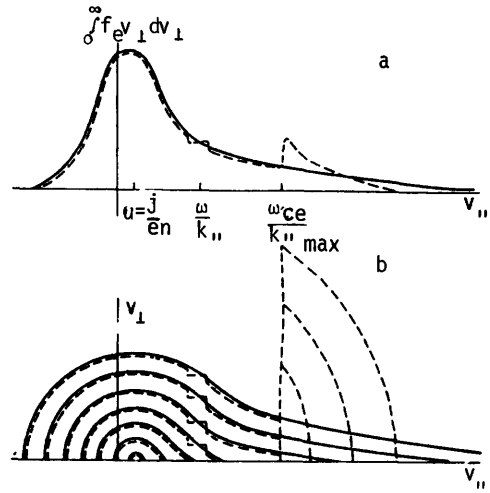

Fig. 13E2. Typical electron velocity distribution before (smooth curves) and after (dashed curves) the anomalous Doppler effect. Top: parallel velocity distribution. Bottom: contours of constant f on the $(v_\perp, v_\parallel)$ plane. From V. V. Parail and O. P. Pogutse, Soviet Journal of Plasma Physics 2, 125 (1976), Fig. 1 .

Phenomena influencing transport of runaway electrons include:

* instabilities driven by the runaways
* displacement of the orbits of relativistic electrons causing some of them to intersect the walls or limiter
* stray magnetic fields
* trapping in banana orbits or ripples and subsequent drifts
* stochastic magnetic fields caused by tearing modes
* magnetic flutter associated with drift waves.

experimental observations

When the runaway electron distribution suddenly changes, a number of phenomena are observed experimentally:

* The value of $\beta_\perp$, measured by diamagnetic loops, suddenly jumps.
* The plasma current suddenly decreases by a slight amount (a few percent in some cases).
* The loop voltage suddenly increases slightly.
* The plasma position shifts.
* There is a sharp increase in synchrotron radiation from the electrons in a period of less than 10 μs.
* Anomalous ion heating may occur.
* A burst of hard x-rays ($\gtrsim$ 100 keV) is observed.
* Nuclear reactions of the (γ,n), (γ,p) or (γ,α) type may be produced in the wall or limiter metals by hard x-rays.

* The limiter or chamber wall may be damaged.

Some of these observations are illustrated in Fig. 13E3.

Marked changes in the discharge are observed when

$$E/E_c \gtrsim 0.01\ Z_{eff}/T_e^{\frac{1}{2}} \qquad (13E9)$$

where T_e is in keV, E is the electric field, and E_c is the critical electric field of Eq. (13E5). For the previous example case, this gives $E/E_c > 0.015$. Tokamak discharges may be classified into several regimes, Table 13E1, depending upon the value of the streaming parameter

$$\xi \equiv u_e/v_{te} \qquad (13E10)$$

where $u_e \equiv J/n_e e$ is the average electron flow velocity, and J is the current density.

The following measures can be taken to control electron runaway:

* Control E and J (OH coils), Z_{eff} (Chapter 25), and n_e (filling pressure).
* Use auxiliary heating (such as ECRH) during startup to increase T_e.
* Use divertors or ripples to remove runaway electrons.
* Inject neutral gas into the discharge (increases n_e).
* Shift the plasma position to remove runaway electrons, especially during startup.

Runaway electron phenomena and dynamics are reviewed by Knoepfel and Spong (1979).

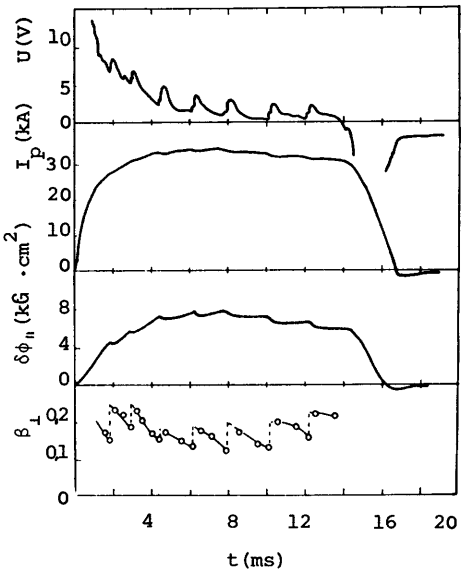

Fig. 13E3. Time variations of loop voltage U, plasma current I_p, longitudinal flux $\delta\phi_{\parallel}$, and $\beta_\perp$ in the T-6 tokamak (B_t = 0.75 T, p_0 = 1.5 mTorr). From V. S. Vlasenkov et al, Nuclear Fusion 13, 509-516 (1973), Fig. 2.

Table 13E1. Tentative classification of tokamak discharges. Typical values of ξ_c are 0.1 in the TM-3 tokamak and 0.2-0.4 in Alcator (hydrogen). The runaway beam discharge occurs instead of the slide-away type of discharge if there is a relatively large fraction of impurities in the plasma at breakdown. From H. Knoepfel and D. A. Spong, Nuclear Fusion 19, 785-829 (1979), Table II.

Discharge type	ω_{ce}/ω_{pe}	Typical phenomena
1. Nearly thermal $\xi < \xi_c$	< 1	Normal discharges Resistivity is higher than classical Very low or no hard X-ray activity
2. Intermediate $\xi < \xi_c$	> 1	Enhanced emission at $n\omega_{ce}$ and ω_{pe} (n = integer)
3a. Slide-away $\xi > \xi_c$	> 1	Resistivity is lower than classical Instabilities with enhanced emission at $n\omega_{ce}$, ω_{pi}, ω_{LH} Anomalous ion heating Piercing of vacuum vessel
3b. Runaway beam $\xi > \xi_c$	> 1	Large outward shift of discharge column Cold plasma Large X-ray activity, low MHD activity

13F. Scaling

energy confinement

Many empirical scaling laws have been formulated to describe how plasma density, temperature, and confinement times vary in tokamaks as functions of (R_0, a, q_a, B_t, I, Z_{eff}, etc.). The task is complicated by the fact that several phenomena occur simultaneously. For example, energy confinement is affected by electron heat transport (with various microinstabilities), ion heat transport, impurity radiation, charge exchange, and disruptions. Nevertheless, scaling laws fit the data from many experiments fairly well in specific regimes of operation.

If radiation losses are small, the plasma energy confinement time is given by Eq. (4B4)

$$\frac{1}{\tau_E} \equiv \frac{1}{2}\left(\frac{1}{\tau'_{Ee}} + \frac{1}{\tau_{Ei}}\right) \qquad (13F1)$$

where τ'_{Ee} represents heat transport by electrons and τ_{Ei} represents heat transport by ions and charge exchange losses. In noncircular plasmas, τ_E is expected to be a factor of $2K^2/(1+K^2)$ larger than for circular plasmas, where the "elongation" $K \equiv b/a$, and a, b are the half-width and half-height of the plasma.

Here we will describe some scaling laws based on data from *ohmically-heated* tokamak operation at low Z_{eff}, formulated by Equipe TFR (1980).

The nonradiative electron energy confinement time is given approximately by

$$\tau'_{Ee} = 2.5\times10^{-21}\ \bar{n}\ q_a^{\frac{1}{2}}\ a^2\ R_0 \quad . \tag{13F2}$$

In the limit $\tau'_{Ee} \ll \tau_{Ei}$, Eq. (13F1) reduces to

$$\tau_E \simeq 2\tau'_{Ee} = 5\times10^{-21}\ \bar{n}\ q_a^{\frac{1}{2}}\ a^2\ R_0 \quad . \tag{13F3}$$

This scaling is compared with experimental data in Fig. 13F1. If $q_a \sim 3$ and $R_0 \sim 0.7$ m, this reduces to the *Alcator scaling* $\tau_E \simeq 6\times10^{-21}\ \bar{n}\ a^2$.

When heat conduction is dominant (small charge exchange losses), the ion energy confinement time is given approximately by

$$\tau_{Ei} = 4\times10^{18} a^2 B_t^2/q_0^2\ n_0\ R_0 \tag{13F4}$$

As density increases, τ'_{Ee} increases, but τ_{Ei} decreases. Therefore, there is an average density at which τ_E in Eq. (13F1) is maximum. Equating τ'_{Ee} to τ_{Ei}, we find

$$\bar{n}_{\tau max} = \frac{4\times10^{19}\ B_t}{q_0 R_0 (q_a)^{\frac{1}{2}} (n_0/\bar{n})^{\frac{1}{2}}} \tag{13F5}$$

For example, in ISX-A, $B_t = 1.3$ T, $R_0 = 0.9$ m. Assuming that $q_0 = 1$, $q_a \simeq 4$, and $n_0/\bar{n} \simeq 2$, we find $\bar{n}_{\tau max} = 2.9\times10^{19}$ m^{-3}. The experimental value is about 3.5×10^{19} m^{-3}.

For deuterons with $L \simeq 18$, the equipartition time given by Eq. (2E46) becomes

$$\tau_{eq} = 1.1\times10^{18}\ T_e^{3/2} / \bar{n} \quad . \tag{13F6}$$

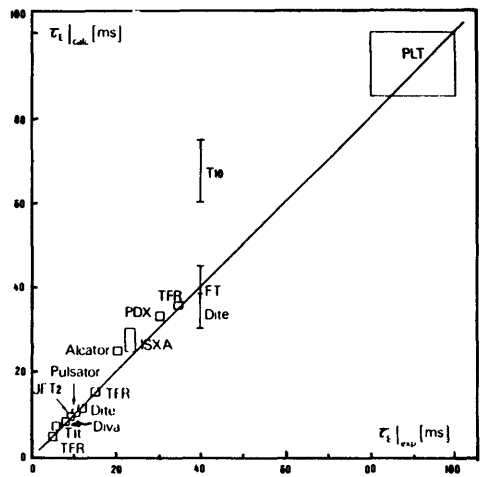

Fig. 13F1. Comparison of the theoretical values of energy confinement time from Eq. (13F3) with experimental values for various tokamaks. From Equipe TFR, "Tokamak scaling laws, with special emphasis on TFR experimental results", Nuclear Fusion 20, 1227-1245 (1980), Fig. 4.

temperatures in ohmically-heated tokamaks

From Eqs. (9B3) and (13C2) the central ohmic heating power is

$$P_{oh} = \eta_{\parallel} J^2 = 4\times10^{-8}\ T_e^{-3/2} (2B_t/\mu_0 R_0 q_0)^2 \tag{13F7}$$

If $P_{rad} << P_{oh}$, then Eq. (13B17) may be solved for T_{e0}, giving

$$T_{e0}^{5/2} = \frac{4\times10^{-8}(2B_t/\mu_0 R_0 q_0)^2 2.5\times10^{-21}\bar{n}\, a^2 q_a^{\frac{1}{2}} R_0 (\tau_{Ei} + \tau_{eq})}{(1.6\times10^{-16}\ \text{J/keV})\ 1.5\bar{n}\ (\tau_{Ei} + \tau_{eq} + \tau'_{Ee})}$$

from which

$$T_{e0} = \left(\frac{B_t a}{q_0}\right)^{4/5} \frac{q_a^{1/5}}{R_0^{2/5}} \left(\frac{\tau_{Ei} + \tau_{eq}}{\tau_{Ei} + \tau_{eq} + \tau'_{Ee}}\right)^{2/5} \text{keV} \qquad (13F8)$$

EXAMPLE PROBLEM 13F1

Estimate T_{e0} and T_{i0} for an Alcator A plasma with $n_0 = 1.5\ \bar{n}$, $B_t = 6$ T, $q_0 = 1$, $q_a = 4$, $Z_{eff} = 1$, (a) at $\bar{n} = 10^{20}$ m^{-3} (b) at $\bar{n} = 5\times10^{20}$ m^{-3}.

(a) From Table 13A1, $R_0 = 0.54$ m, $a = 0.10$ m.

As a first approximation, we take $T_{e0} \sim 1$ keV. From Eqs. (13F2), (13F4), and (13F6), we find $\tau'_{Ee} = 2.7$ ms, $\tau_{Ei} = 18$ ms, and $\tau_{eq} = 11$ ms. Then, from Eq. (13F8), $T_{e0} = 1.1$ keV. A revised value of τ_{eq} is $\tau_{eq} = 12$ ms, and a second estimate of T_{e0} is again 1.1 keV. From Eq. (13B16), $T_{i0} = 0.64$ keV.

(b) For the second case, $\tau_{Ei} = 3.6$ ms, $\tau_{eq} = 2.2$ ms, and $\tau'_{Ee} = 13$ ms. From Eq. (13F8), $T_{e0} = 0.7$ keV, and from Eq. (13B16) $T_{i0} = 0.5$ keV. These estimates are indicated by asterisks in Fig. 13C1.

---

ignition

The device parameters required for ignition can be estimated using the assumption that $\langle\sigma v\rangle_{DT} \propto T^2$, which has about 20 % accuracy for $8 < T < 25$ keV. For a case with parabolic n(r) and T(r), the result is

$$B^2 a_{eff} \geq \frac{1.34\ Z_{eff}^{1/3}}{\langle\beta\rangle f_p^{5/3}} \qquad (13F9)$$

where $f_p \equiv$ (fuel ion density)/n_e, and a_{eff} is the effective plasma radius (for a

circular plasma, $a_{eff} = a$). Thus, for $B \simeq 5$ T, $\langle\beta\rangle \simeq 0.05$, $Z_{eff} \simeq 2$, and $f_p \simeq 0.9$, the required $a_{eff} \simeq 1$ m.

large tokamaks

Operation of JET, JT-60, TFTR, and T-15 in the mid-1980's will help to clarify uncertainties about plasma transport processes and scaling laws. A larger "International Tokamak Reactor" (INTOR) with $R = 5.2$ m, $a = 1.3$ m, $K = 1.6$, $B_t = 5.5$ T, $I = 6.4$ MA, $\langle\beta\rangle = 5$ %, $n = 1.3 \times 10^{20}$ m^{-3}, $T_i = 10$ keV, and pulse length > 100 s, producing several hundred MW of thermal power, could be operational in the early 1990's.

Bibliography

general

Plasma Physics and Controlled Nuclear Fusion Research 1980, IAEA, Vienna, 1981.

Plasma Physics and Controlled Nuclear Fusion Research 1978, IAEA, Vienna, 1979.

J. M. Rawls, Editor, "Status of tokamak research", DOE/ER-0034 (1979), (a general review).

P. Rutherford, "The tokamak: 1955-1980", *Nuclear Fusion 20*, 1086-1092 (1980), (a history of tokamak research).

MHD stability

G. Bateman, *MHD Instabilities*, MIT Press, Cambridge, MA, 1978.

L. C. Bernard and R. W. Moore, "Systematic optimization of tokamaks for ideal magnetohydrodynamic stability", *Physical Review Letters 46*, 1286-1289 (1981).

B. Carreras, H. R. Hicks, and B. V. Waddell, "Tearing-mode activity for hollow current profiles", *Nuclear Fusion 19*, 583-596 (1979).

M. A. Dubois, D. A. Marty, and A. Pochelon, "Method of cartography of q = 1 islands during sawtooth activity in tokamaks", *Nuclear Fusion 20*, 1355-1361 (1980)

J. T. Hogan, "The accessibility of high-beta tokamak states", *Nuclear Fusion 19*, 753-776 (1979).

J. T. Hogan, "Beta limits in beam-heated tokamaks", *Nuclear Fusion 20*, 1119-1128 (1980).

B. Lipschultz, S. C. Prager, A. M. M. Todd, and J. Delucia, "Axisymmetric instability in a non-circular tokamak: experiment and theory", *Nuclear Fusion 20*, No. 6, p. 683-893 (1980).

M. Murakami, J. D. Callen, and L. A. Berry, "Some observations on maximum densities in tokamak experiments", *Nuclear Fusion 16*, 347-348 (1976).

D. C. Robinson and K. McGuire, "Magnetic islands and disruptions in the TOSCA tokamak", *Nuclear Fusion 19*, 115-119 (1979).

N. R. Sauthoff, S. Von Goeler, and W. Stodiek, "A study of disruptive instabilities in the PLT tokamak using x-ray techniques", *Nuclear Fusion 18*, 1445-1458 (1978).

A. M. M. Todd, J. Manickam, M. Okabayashi, M. S. Chance, R. C. Grimm, J. M. Greene, and J. L. Johnson, "Dependence of ideal-MHD kink and ballooning modes on plasma shape and profiles in tokamaks", *Nuclear Fusion 19*, 743-752 (1979).

A. A. Ware and J. C. Wiley, "Multiple equilibria and poloidal rotation instabilities in tokamak plasmas", *The Physics of Fluids 24*, 936-946 (1981).

J. A. Wesson, "Hydromagnetic stability of tokamaks", *Nuclear Fusion 18*, 87-132 (1978). Review article.

transport

A. H. Boozer, "Enhanced transport in tokamaks due to toroidal ripple", *The Physics of Fluids 23*, 2283-2290 (1980).

R. J. Hawryluk et al, "The effect of current profile evolution on plasma-limiter interaction and the energy confinement time", *Nuclear Fusion 19*, 1307-1317 (1979).

R. J. Hawryluk, S. Suckewer, and S. P. Hirshman, "Low-Z impurity transport in tokamaks", *Nuclear Fusion 19*, 607-632 (1979).

J. T. Hogan, "The accessibility of high-beta tokamak states", *Nuclear Fusion 19*, 753-776 (1979).

J. T. Hogan, "Neoclassical current effects in neutral-beam-heated tokamak discharges", *Nuclear Fusion 21*, 365-387 (1981).

W. Horton and R. D. Estes, "Anomalous drift-wave transport analysis of tokamak discharges", *Nuclear Fusion 19*, 203-222 (1979).

D. L. Jassby, H. H. Towner, and R. J. Goldston, "Reduced fusion-neutron production in non-axisymmetric tokamak devices", *Nuclear Fusion 18*, 825-833 (1978).

W. M. Manheimer, An Introduction to Trapped-Particle Instability in Tokamaks, TID-27157, Technical Information Center, ERDA, 1977.

J. J. Schuss, "Effect of magnetic field ripple on energetic ions in Alcator A", *Nuclear Fusion 20*, 1160-1164 (1980).

M. Soler and J. D. Callen, "On measuring the electron heat diffusion coefficient in a tokamak from sawtooth oscillation observations", *Nuclear Fusion 19*, 703-714 (1979).

W. M. Tang, "Microinstability theory in tokamaks", *Nuclear Fusion 18*, 1089-1160 (1978). Review article.

burn control

D. E. T. F. Ashby, M. H. Hughes, "Dynamic burn control of a tokamak reactor by fuel injection", *Nuclear Fusion 20*, 451-457 (1980).

L. Bromberg, J. L. Fisher, and D. R. Cohn, "Active burn control of nearly ignited plasmas", *Nuclear Fusion 20*, 203-207 (1980).

L. Bromberg and D. R. Cohn, "Effect of impurities and ripple upon power regulation in self-sustained tokamaks", Fourth Topical Meeting on the Technology of Controlled Nuclear Fusion (King of Prussia, PA, 1980), DOE, 1981.

L. M. Degtyarev, V. I. Pistunovich, and V. D. Shafranov, "Two-stroke tokamak reactor", *Nuclear Fusion 20*, 102-103 (1980).

Ya. I. Kolesnichenko, "The role of alpha particles in tokamak reactors", *Nuclear Fusion 20*, 727-789 (1980). Review paper.

M. H. Lipner, A. J. Impink, Jr., and F. M. Heck, "An analysis by hybrid computer simulation of a power level control system for a tokamak fusion reactor plasma", Fourth Topical Meeting on the Technology of Controlled Nuclear Fusion (King of Prussia, PA, 1980), DOE 1981.

T. W. Petrie and J. M. Rawls, "Burn control resulting from toroidal field ripple", *Nuclear Fusion 20*, 419-428 (1980).

heating

J. F. Clarke, "Hot-ion-mode ignition in a tokamak reactor", *Nuclear Fusion 20,* 563-570 (1980).

H. Eubank et al, "PLT neutral beam heating results", Plasma Physics and Controlled Nuclear Fusion Research 1978, Vol. 1, 167-198, IAEA, Vienna, 1979.

J. A. Holmes, J. A. Rome, W. A. Houlberg, Y.-K. M. Peng, and S. J. Lynch, "Low-density ignition scenarios in injection-heated tokamaks", *Nuclear Fusion 20,* 59-67 (1980).

J. Hosea et al, "Fast wave ion cyclotron heating in the Princeton Large Torus", 8th International Conference on Plasma Physics and Controlled Nuclear Fusion Research, (Brussels, 1980), IAEA, Vienna, 1981.

W. A. Houlberg, S. E. Attenberger, and A. T. Mense, "Neutral-beam energy and power requirements for expanding-radius and full-bore start-up of tokamak reactors", *Nuclear Fusion 20,* 811-820 (1980).

K. Odajima et al, "High-efficiency ICRF heating in DIVA", *Nuclear Fusion 20,* 1330-1334 (1980).

Y.-K. M. Peng, S. K. Borowski, and T. Kammash, "Microwave start-up of tokamak plasmas near electron cyclotron and upper hybrid resonances", *Nuclear Fusion 18,* 1489-1498 (1978).

V. D. Shafranov, "Mixing of plasma columns in a tokamak", *Nuclear Fusion 19,* 187-193 (1979).

C. E. Singer, D. L. Jassby, and J. Hovey, "Ignition of an overheated, underdense, fusioning tokamak plasma", *Nuclear Fusion 20,* 489-497 (1980).

C. M. Surko, R. E. Slusher, J. J. Schuss, R. R. Parker, I. H. Hutchinson, D. Overskei, and L. S. Scaturro, "Study of driven lower-hybrid waves in the Alcator tokamak using CO_2-laser scattering", *Physical Review Letters 43,* 1016-1019 (1979).

C. E. Wagner, "Possibility of achieving ignition in a high-field ohmically heated tokamak", *Physical Review Letters 46,* 654-657 (1981).

current drive

V. Bailey, J. Benford, R. Cooper, and V. L. Teofilo, "Electron-beam-driven, compact, steady-state tokamaks", Fourth Topical Meeting on the Technology of Controlled Nuclear Fusion (King of Prussia, 1980), DOE, 1981.

D. K. Bhadra, "Runaway electrons and current drive in a tokamak", *Nuclear Fusion 20,* 619-623 (1980).

D. A. Ehst, "Design constraints for steady-state tokamak reactors driven by lower hybrid waves", *Nuclear Fusion 19,* 1369-1378 (1979).

N. J. Fisch, "Current generation by minority-species heating", *Nuclear Fusion 21,* 15-22 (1981).

N. J. Fisch and C. F. F. Karney, "Current generation with low-frequency waves", *The Physics of Fluids 24,* 27-39 (1981).

R. W. Harvey, K. D. Marx, and M. G. McCoy, "Non-linear Fokker-Planck studies of rf current drive efficiency", *Nuclear Fusion 21,* 153-157 (1981).

Ya. I. Kolesnichenko, S. N. Reznik, and V. A. Yavorskij, "The current generated by alpha-particle loss in tokamak reactors", *Nuclear Fusion 20,* 1041-1046 (1980).

Ya. I. Kolesnichenko, "Steady-state current drive in tokamaks workshop summary", DOE/ET-0077 (1979).

V. B. Krapchev and A. K. Ram, "Adiabatic theory of current generation by non-linear waves in a Vlasov plasma", *Nuclear Fusion 20,* 1533-1541 (1980).

R. J. LaHaye, C. J. Armentrout, R. W. Harvey, C. P. Moeller, and R. D. Stambaugh, "Observation of radio-frequency-driven plasma current in the octopole tokamak", *Nuclear Fusion 20,* 218-222 (1980).

K.-L. Wong, R. Horton, and M. Ono, "Current generation by unidirectional lower hybrid waves in the ACT-1 toroidal device", *Physical Review Letters 45,* 117-120 (1980).

S. Y. Yuen, D. Kaplan, and D. R. Cohn, "Characteristics of lower-hybrid-wave-driven steady-state tokamak power reactors", *Nuclear Fusion 20,* 159-169.

electron runaway

H. Knoepfel and D. A. Spong, "Runaway electrons in toroidal discharges", *Nuclear Fusion 19,* 785-829 (1979). (Review Paper.)

scaling

A. P. Biddle, R. N. Dexter, R. J. Groebner, D. J. Holly, B. Lipschultz, M. W. Phillips, S. C. Prager, J. C. Sprott, "Initial results from the tokamak tokapole-II poloidal divertor device", *Nuclear Fusion 9,* No. 11, p. 1509-1518 (1979).

A. Hirose and H. M. Skarsgaard, "On the energy confinement times of tokamaks", *Nuclear Fusion 18,* 1737-1742 (1978).

Equipe TFR, "Tokamak scaling laws, with special emphasis on TFR experimental results", *Nuclear Fusion 20,* 1227-1245 (1980).

B. J. Green, "Large tokamak experiments", *Nuclear Fusion 19,* 515-534 (1979).

International Tokamak Reactor Zero Phase, Report of the INTOR Workshop (1979), IAEA, Vienna, 1980.

INTOR Group, "International tokamak reactor", *Nuclear Fusion 20,* 349-388 (1980).

W. Pfeiffer and R. E. Walz, "Empirical scaling laws for energy confinement in ohmically-heated tokamaks", *Nuclear Fusion 19,* 51-67 (1979).

CHAPTER 14

OTHER TOROIDAL DEVICES

14A. Stellarators and Torsatrons

The history of stellarator research is summarized by Shafranov (1980) and Miyamoto (1978).

stellarator magnetic fields

In a simple toroidal magnetic field, the magnetic field gradient and curvature drifts cause opposite vertical motions of ions and electrons, producing a charge separation electric field, which results in outward particle drifts to the wall, as in Fig. 7C1. Rotational transform may be used to reduce the charge separation electric field effects.

The rotational transform angle ι is the average poloidal angle of rotation which a field line makes as it goes once around the torus in the toroidal direction, Fig. 14A1. The arc length in the poloidal direction is $r\iota$, and the path length in the toroidal direction is approximately $2\pi R_0$. Therefore, the twist angle of the magnetic field lines (Fig. 7C2) is

$$\tan\gamma = \frac{B_p}{B_t} \simeq \frac{r\iota}{2\pi R_0} \quad ,$$

or

$$\frac{\iota}{2\pi} = \frac{1}{q} \simeq \frac{R_0 B_p}{r B_t} \qquad (14A1)$$

where q is the safety factor.

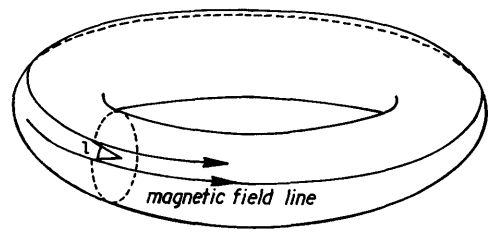

Fig. 14A1. Rotational transform. In passing once around the torus in the toroidal direction, the field line is rotated through an angle ι in the poloidal direction.

In a tokamak, the poloidal field is created mainly by the plasma current. In stellarators, the poloidal field is produced by external helical windings, or by twisting the chamber itself. Early stellarators were shaped like a figure eight, Fig. 14A2.

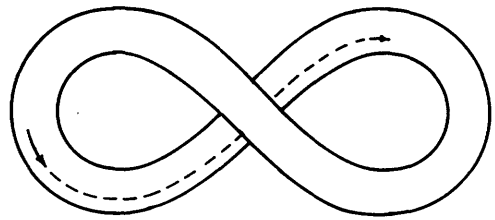

Fig. 14A2. A figure eight stellarator, (top view), and a charged particle trajectory along a magnetic field line (dashed curve). Ions tend to drift upwards at one end of the torus and downwards at the other end, with electron drifts in the opposite directions. Electron flow along the magnetic field lines can short out the electric field, which tends to be downwards at one end and upwards at the other. The twist of the tube thus reduces the charge-separation electric field effects.

A classical stellarator has toroidal field coils plus ℓ pairs of helical windings, as illustrated in Fig. 14A3 for the $\ell = 3$ case. The helical coil currents can be varied independently of the toroidal field coil currents, in order to control the rotational transform angle.

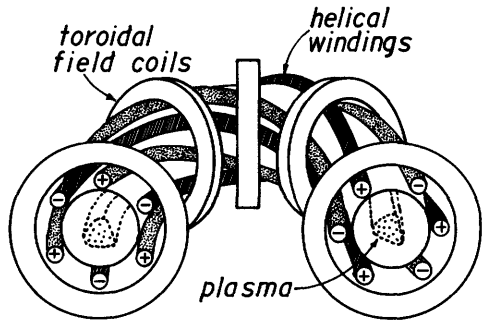

Fig. 14A3. Shape of coils and plasma for an $\ell = 3$ stellarator.

For simple estimates of the magnetic field shape, the torus may be approximated by a long cylinder of length $L = 2\pi R$, with cylindrical coordinates (r, θ, z) and helical symmetry such that the angular dependence is a function of $(\theta - \alpha z)$, where α is the pitch parameter. In vacuum, $\vec{\nabla} \times \vec{B} = 0$, and $\vec{B}$ may be represented as the gradient of a scalar magnetic potential

$$\vec{B} = -\vec{\nabla}\Phi_B \quad . \tag{14A2}$$

Since $\vec{\nabla} \cdot \vec{B} = 0$, the potential must satisfy the Laplace equation

$$\nabla^2 \Phi_B = 0 \quad . \tag{14A3}$$

The solution of this equation for the cylindrical case with helical symmetry is

$$\Phi_B = B_0 z + \frac{1}{\alpha} \sum_{\ell} b_\ell I_\ell(\ell\alpha r) \sin\ell(\theta - \alpha z) \tag{14A4}$$

where B_0 is the axial magnetic field, the I_ℓ are modified Bessel Functions, and the coefficients b_ℓ indicate the magnitude of the component with order ℓ (Miyamoto, 1978). (Bessel Functions are described by G. Arfken, *Mathematical Methods for Physicists*, Academic Press, New York, 1973, Chapter 11). From Eq. (14A2), the components of $\vec{B}$ are found to be

$$B_r = \sum_{\ell} \ell b_\ell I'_\ell(\ell\alpha r) \sin\ell(\theta - \alpha z)$$

$$B_\theta = \sum_{\ell} \left(\frac{1}{\alpha r}\right) \ell b_\ell I_\ell(\ell\alpha r) \cos\ell(\theta - \alpha z)$$

$$B_z = B_0 - \sum_{\ell} \ell b_\ell I_\ell(\ell\alpha r) \cos\ell(\theta - \alpha z) \quad . \tag{14A5}$$

where the prime denotes a derivative of the Bessel function with respect to its argument.

Magnetic surfaces may be traced out by following the path of a magnetic field line. For a single set of helical windings (such as $\ell = 3$ in Fig. 14A3), one b_ℓ is dominant.

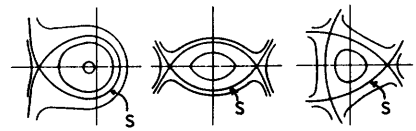

$\ell = 1$ $\ell = 2$ $\ell = 3$

Fig. 14A4. The magnetic surfaces of $\ell = 1$, $\ell = 2$, and $\ell = 3$ stellarator fields, found from the magnetic fields of Eqs. (14A5). From K. Miyamoto, Nuclear Fusion 18, 243-284 (1978), Fig. 2. s = separatrix.

Averaging along a field period in the z direction, the approximate equations for the r and θ variations of a magnetic surface are

$$r = r_0 + \frac{1}{\alpha}\frac{b_\ell}{B_0} I'_\ell \cos\ell(\theta-\alpha z)$$

$$\theta = \frac{\iota}{2\pi R} z - \frac{b_\ell}{B_0}\left(\frac{1}{\alpha r_0}\right)^2 I_\ell \sin\ell(\theta-\alpha z) \qquad (14A6)$$

where the rotational transform angle

$$\iota \equiv \pi\left[\frac{b_\ell}{B_0}\right]^2 \frac{R\ell^3}{r}\frac{d}{dx}\left[\frac{I_\ell I'_\ell}{x}\right]_{x=\ell\alpha r}$$

$$\underset{\sim}{\sim} 2\pi\left[\frac{b_\ell}{B_0}\right]^2\left[\frac{1}{2^\ell \ell!}\right]^2 \ell^5\alpha R(\ell\alpha r)^{2(\ell-2)}[(\ell-1)+(\ell\alpha r)^2/2+\ldots], \qquad (14A7)$$

$R \equiv L/2\pi$, and the argument of the Bessel Functions is the same as in the previous equations. (Miyamoto, 1978). These equations are valid for $r \underset{\sim}{<} \frac{1}{2}r_s$, where r_s is the separatrix radius. The resulting magnetic surfaces have shapes like those of Fig. 14A4. Effects of toroidal curvature and plasma currents will distort the magnetic surfaces from those shown here.

For good plasma confinement near the plasma center, it is necessary to have nonzero rotational transform there. According to Eq. (14A7), ι is nonzero at $r = 0$ if $\ell \leq 2$, but $\iota = 0$ at $r = 0$ if $\ell \geq 3$. The variation of ι with radius is illustrated in Fig. 14A5.

In a toroidal stellarator with major radius R_0 the application of a vertical field B_v causes a slight radial shift of the centers of the magnetic surfaces by an amount

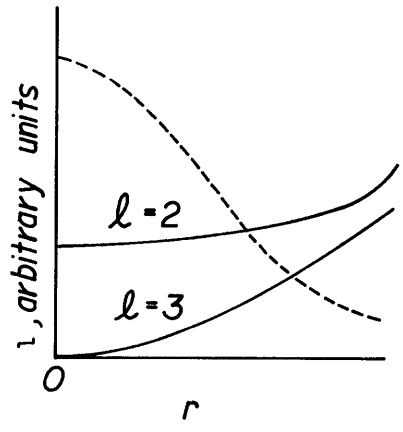

Fig. 14A5. Radial profiles of rotational transform angle ι in $\ell = 2$ and $\ell = 3$ stellarators. The curve shapes vary with pitch α and with plasma current distributions. For comparison, the dashed curve illustrates the profile in a tokamak.

$$\Delta(r) = \frac{2\pi R_0}{\iota(r)} \frac{B_v}{B_0} \quad . \tag{14A8}$$

The magnetic field varies roughly as $B(R) \simeq B_0 R_0/R$. We can define a parameter U as

$$\begin{aligned} U &\equiv \oint d\ell/B \\ &\simeq \oint d\ell (R/B_0 R_0) \qquad (d\ell \simeq R d\phi, \ R \simeq R_0 + \Delta) \\ &\simeq 2\pi (R_0+\Delta)^2/B_0 R_0 \\ &\simeq (2\pi R_0/B_0)[1 + 2\Delta(r)/R_0] \qquad \Delta << R_0 \quad . \end{aligned} \tag{14A9}$$

If $U(r) < U(0)$, the plasma is stable against the interchange mode, Eq. (8D69), and the fractional difference in U is called *magnetic well depth*:

$$\frac{U(0) - U(r)}{U(0)} \simeq \frac{2[\Delta(0) - \Delta(r)]}{R_0} = \frac{4\pi B_v}{B_0}\left[\frac{1}{\iota(0)} - \frac{1}{\iota(r)}\right] \quad . \tag{14A10}$$

Thus, if $\iota(r) > \iota(0)$, the application of a vertical field can produce a magnetic well. If two helical fields with the same pitch length and indices ℓ and $\ell+1$ are applied simultaneously, a similar magnetic well is produced. Plasma configurations with magnetic wells and strong shear can also be produced by high-order stellarators ($\ell \sim 7$) with non-circular cross section (Wang and Jensen, 1978).

torsatron magnetic fields

A torsatron has only ℓ helical windings (instead of 2ℓ) with currents all in the same direction, as illustrated in Fig. 14A6. The helical windings also produce the toroidal magnetic field, so no toroidal field coils are necessary.

The helical windings, magnetic surfaces, and coil current distributions of stellarators and torsatrons are compared in Fig. 14A7. The torsatron coils require higher currents, but the coil forces may be greatly reduced by proper choice of pitch angle (Section 20C).

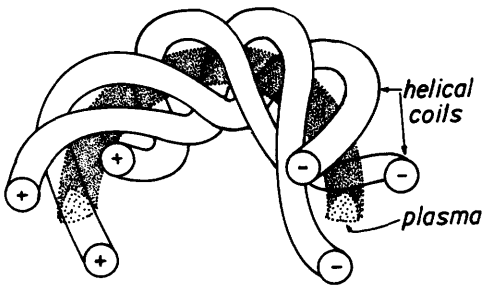

Fig. 14A6. An $\ell = 3$ torsatron configuration (vacuum chamber not shown).

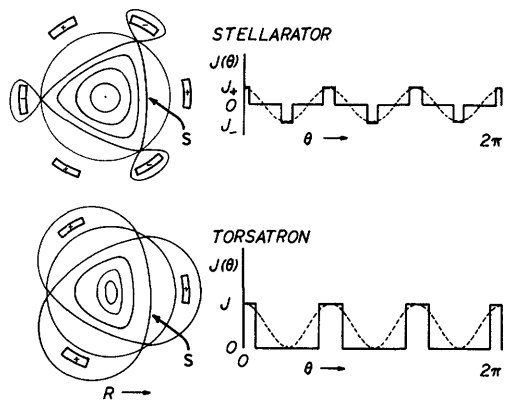

Fig. 14A7. Helical windings and magnetic surfaces in $\ell = 3$ stellarator and an ℓ torsatron, and the azimuthal variation of helical winding currents. s = separatrix.

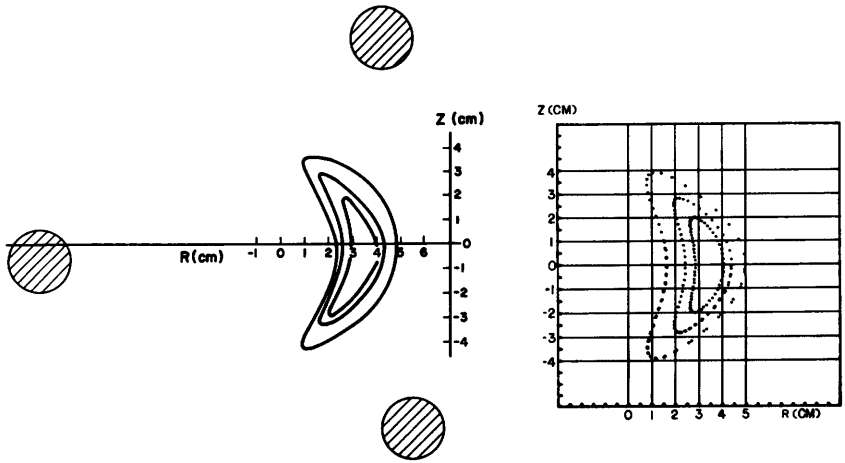

Fig. 14A8. Magnetic surfaces measured in the Proto-Cleo torsatron by electron beam injection (left) and the corresponding theoretical magnetic surfaces (right). Each surface measured experimentally corresponds to a different position of the electron gun. From E. S. Fairbanks and J. L. Shohet, "Electron-beam measurements of the magnetic surfaces in the Proto-Cleo Torsatron", IEEE Transactions on Plasma Science, PS-7 (1979) p. 98, Figs. 8 and 9. © *1979 IEEE.*

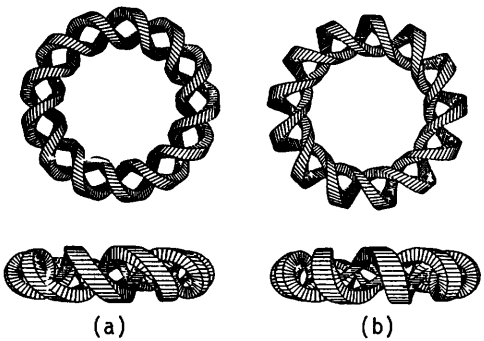

Fig. 14A9. The helical winding of a conventional thirteen-field-period, $\ell = 2$ torsatron with aspect ratio $R_0/a = 4.0$ (left) compared with a similar ultimate torsatron with a modulation of $\alpha_w = 0.63$ (right). From T. W. Kruckewitt and J. L. Shohet, Nuclear Fusion 20, 1375-1380 (1980), Fig. 1.

The magnetic surfaces can be measured experimentally by injecting an electron beam along a magnetic surface and detecting the electrons with a movable probe after they have made various numbers of transits around the torus, with results like those of Fig. 14A8.

Vertical field coils (not shown) are needed to counteract the vertical field of the helical windings. (In an ordinary stellarator, half of the helical windings have currents in each direction, so the net vertical field is nearly zero.) Alternatively, the pitch of the helical windings may be varied, in accordance with the winding rule

$$\theta = (m/\ell)\phi + \alpha_w \sin\theta \qquad (14A11)$$

where θ is the poloidal angle, ϕ is the toroidal angle, α_w is the "modulation" of the winding, and $m = \alpha_w \ell R_0$ determines the pitch of the windings, in order to produce the desired vertical field. Such an "ultimate torsatron" is illustrated in Fig. 14A9(b).

modular coils

It is desirable to design stellarators or torsatrons with modular coils, which can be easily disassembled for maintenance. There are several ideas for modular designs, including a spatial magnetic axis, elliptical coils, twisted coils, and zigzag coils.

The term *spatial magnetic axis* refers to designs with a magnetic axis twisted to provide rotational transform. For example, the figure eight stellarator of Fig. 14A2 is of this type. A helical magnetic axis is another possibility. Only circular (toroidal field) coils are needed for this type of stellarator, but the attainable shear and plasma beta are low.

Elliptical coils and twisted coils are illustrated in Fig. 14A10. Alternatively, circular coils could be used with shaped soft-iron inserts to produce the desired elliptical (ℓ = 2) boundary (Ikuta and Hirano, 1980).

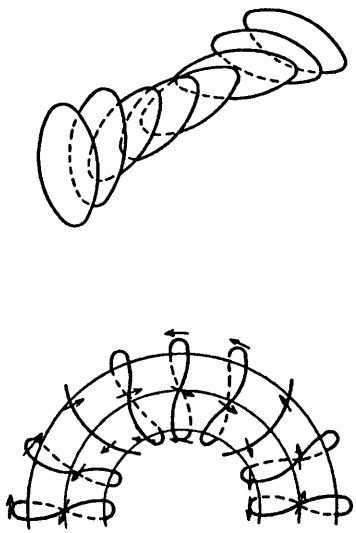

Fig. 14A10. Production of a stellarator-type of field with elliptical coils (above) or twisted coils (below). From K. Miyamoto, Nuclear Fusion 18, 243-284 (1978), Figs. 9 and 10.

If we imagine two sets of helical windings in opposite directions laid out on the (θ, ϕ) plane, then the coils may be broken and rejoined as shown in Fig. 14A11 to produce zigzag shaped coils.

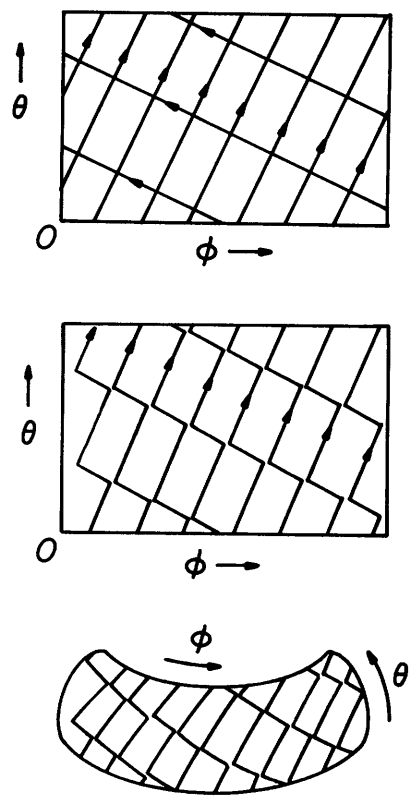

Fig. 14A11. Two sets of helical windings on the θ-ϕ plane (top), broken and reconnected to form zigzag coils (middle), and the resulting coils arranged around a section of a torus (bottom).

Another idea for a modular stellarator is shown in Figs. 14A12 and 14A13. The ℓ = 3 helical windings are cut and linked

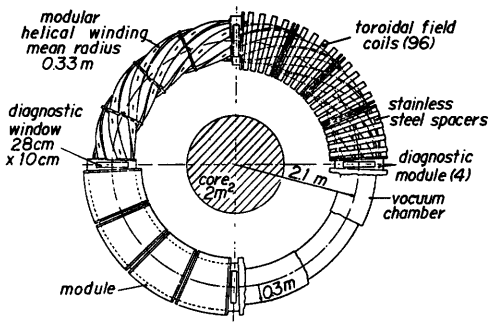

Fig. 14A12. Layout of the Canberra Modular Stellarator windings. The "diagnostics gaps" are 13 cm wide at the mean major radius and offer access to the plasma from all four directions. From S. M. Hamberger, L. E. Sharp, and L. F. Peterson, "A large stellarator based on modular coils", Ninth European Conference on Controlled Fusion and Plasma Physics, Oxford, September 1979, Fig. 1.

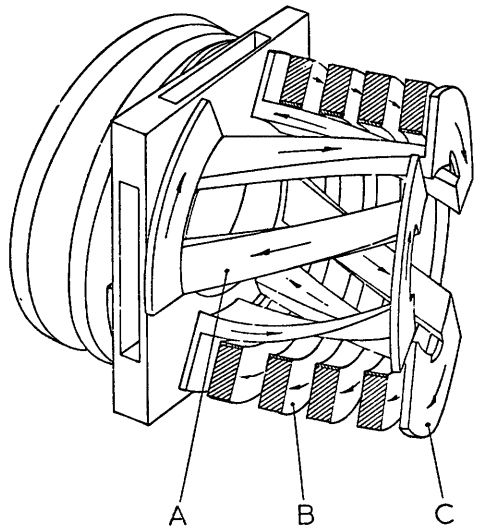

Fig. 14A13. Arrangement of windings on one module (external connections not shown). Two modules (of different types) form each field period. The conductor cross-sections and mean minor radii are: A = 17×6 cm, 33 cm; B = 20×7.5 cm, 48 cm; C = 3×20 cm, 48 cm. From S. M. Hamberger, L. E. Sharp, and L. F. Peterson, "A large stellarator based on modular coils", 9th European Conference on Controlled Fusion and Plasma Physics, Oxford, September 1979, Fig. 2.

at the ends of each module by segments carrying current in the same direction as the toroidal field coils.

equilibrium and stability

The rotational transform of a stellarator plasma may be approximated by

$$\iota = \iota_h + \iota_I - \iota_h\iota_I/mq\pi - \beta\pi(\ell/m)(R_0/a)^2 \qquad (14A12)$$

where ι_h is the transform due to the helical windings, ι_I is the transform due to plasma current (if present), and $\beta = 2\mu_0 p/B^2$. The third term represents the helical component of the force-free plasma current ($J_{\parallel}$), and the last describes the effect of plasma diamagnetism. If the plasma is initially produced by ohmic heating with a strong current, then ι_I will be large. As the plasma current decays, stability can be maintained by increasing the helical winding current (increasing ι_h) to compensate for the decrease in ι_I. In this way stable zero-current operation has been attained in the Wendelstein VIIa stellarator.

Some stability diagrams for stellarators are shown in Fig. 14A14. The stable regions are enhanced at low plasma currents (small ι_I). Such low-current operation is impossible in tokamaks. The attainable value of beta is limited by both

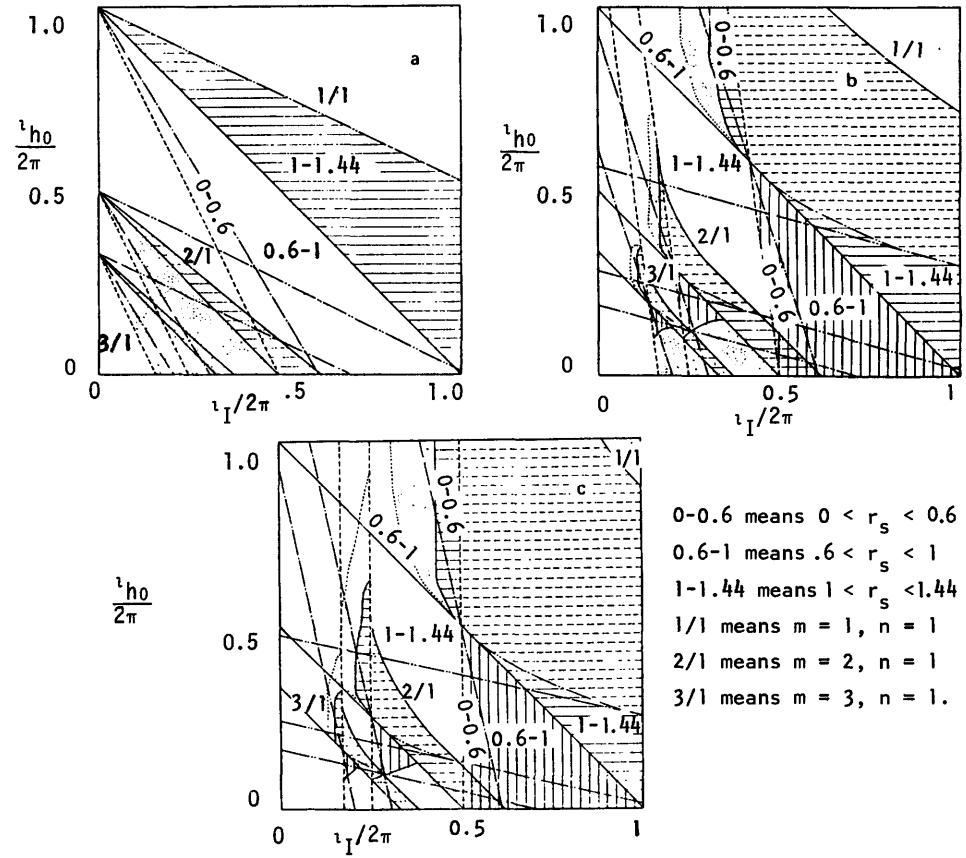

Fig. 14A14. Stability diagrams of rotational transform at r = a due to helical windings (ι_h) and plasma current (ι_I) for kink and tearing instabilities of plasma with a parabolic current distribution. (a) a long-pitch ℓ = 2 stellarator with $\iota_h(r) = \iota_{h0}$ = constant, (b) a short-pitch ℓ = 2 stellarator with $\iota_h(r) = \iota_{h0}[0.286+0.714(r/a)^2]$, (c) an ℓ = 3 stellarator, $\iota_h(r) = \iota_{h0}(r/a)^2$. Horizontally striped areas (by dashed lines) are unstable regions against an external kink mode which has no singular point in the region 0 < r < b. Horizontally striped areas (by solid lines) are unstable regions against an external kink mode which has a singular point. Vertically striped areas are unstable regions against an internal kink mode. Dotted regions are unstable against the resistive tearing mode. From K. Miyamoto, Nuclear Fusion 18, 243-284 (1978), Fig. 17.

equilibrium and stability considerations, as illustrated in Fig. 14A15. Analytic studies are limited to simplified conditions, and do not give reliable estimates of the attainable values of beta.

Numerical studies of 3-dimensional equilibria give more reliable estimates, but it is unfeasible to use fine mesh sizes, due to the large amount of computer time required to solve the equations. For example, a case with 10x18x234 mesh points took 2 hours of time on the CRAY computer at the MFECC for 2500 iterations. In order to predict the stability of various configurations, the growth rates are

predicted using several mesh sizes, and then extrapolated down to zero mesh size. Most stellarator configurations are limited to values of $\beta < 5$ %. Stable beta values of 5-10 % have been found for some cases involving a combination of $\ell = 2$ and $\ell = 3$ windings (Bauer, Betancourt, and Garabedian, 1980).

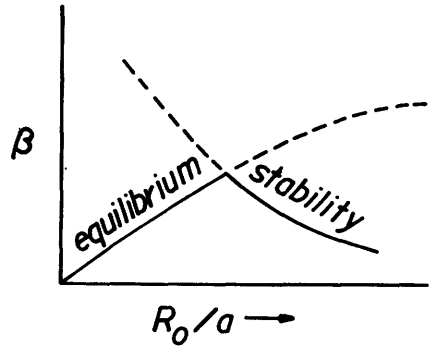

Fig. 14A15. The maximum value of beta vs. aspect ratio for stellarators, limited by equilibrium considerations at low aspect ratios and by stability considerations at high aspect ratios. From V. D. Shafranov, Nuclear Fusion 20, 1076-1083 (1980), Fig. 6.

transport

The variation of magnetic field strength along a given field line in a stellarator is illustrated in Fig. 14A16. Particles may be trapped in the helical field ripples ϵ_h, which causes them to have banana-shaped orbits. The centers of the banana orbits tend to precess in circles around the magnetic axis, unless the precession is impeded by collisions or by trapping in mirrors of the toroidal field. Mirroring of the banana orbits by the toroidal field gives rise to superbanana orbits, as illustrated in Fig. 14A17.

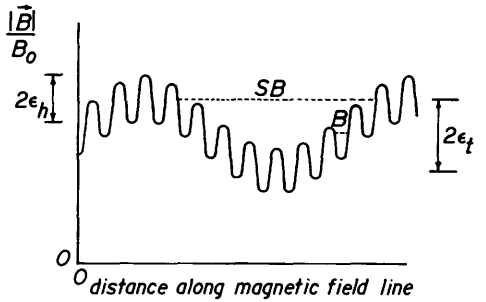

Fig. 14A16. Variation of magnetic field strength along a magnetic field line in a stellarator, showing modulations due to the helical fields (ϵ_h) and due to the variation of toroidal field with major radius (ϵ_t). Dashed lines indicate particles trapped in helical ripples leading to banana orbits (B) and possible trapping of these helical bananas by mirrors of the toroidal field, leading to "superbananas" (SB).

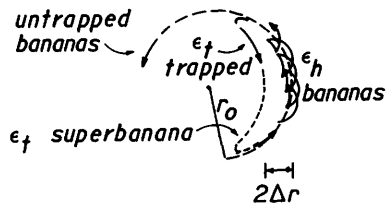

Fig. 14A17. Collisionless particle orbits in stellarators. Untrapped particles have nearly circular orbits (not shown). Helical trapping gives rise to bananas. The orbit of the banana center may be circular if it is untrapped, or it may have a "superbanana" shape, with $\Delta r/r_0 \approx (\epsilon_t/\epsilon_h)^{\frac{1}{2}}$, if it is trapped by the toroidal field ϵ_t.

If collisions prevent the untrapped helical bananas from precessing all the way around the magnetic axis, then the charge separation is not compensated, and the banana may diffuse out of the confinement region. The step size for this diffusion process is $(v_{\nabla B}/\nu_{ei})$, where $v_{\nabla B}$ is the grad-B drift velocity of Eq. (7C3) and ν_{ei}

is the effective electron-ion collision frequency. The diffusion coefficient can be estimated from

$$D_h \sim \left(\begin{matrix}\text{fraction of helically}\\ \text{trapped particles}\end{matrix}\right)(\text{step size})^2(\text{collision frequency})$$

$$\sim (\varepsilon_h^{3/2}\varepsilon_t^2)(v_{\nabla B}/\nu_{ei})^2\nu_{ei}$$

$$\sim \varepsilon_h^{3/2}\varepsilon_t^2(\omega_0/\nu_{ei})(kT/eB) \qquad (\nu_{ei} > \varepsilon_h^2\omega_0) \tag{14A13}$$

where

$$\omega_0 \equiv -kT/eB_0r^2 \tag{14A14}$$

is the approximate precession frequency of the bananas around the magnetic axis, B is the magnitude of the magnetic field, and B_0 is the value at the magnetic axis. This equation is equivalent to the ripple-trapping diffusion coefficient for tokamaks, Eq. (13B3), with the ripple parameter $\delta = \varepsilon_h$, and $\varepsilon_t = (r/R_0)$. Since $D_h \propto 1/\nu_{ei}$, trapping in helical ripples could lead to serious losses at high temperatures (small ν_{ei}).

The predictions of D vs. ν_{ei} in various regimes of collisionality are illustrated in Fig. 14A18. Predictions of χ_i have similar shapes. However, experimental values of D (such as from the Saturn stellarator) vary less rapidly with ν_{ei} than the predictions of the simple D_h formula, as indicated by the circles on the graph.

In order to compare with theories of ionic heat conduction, ion orbits in a torsatron were simulated by starting 360 ions out on a given flux surface (spaced 1° apart) randomly distributed according to an isotropic Maxwellian distribution. The ions were followed for 30 ms, recording their energy and position every 3 ms. Then the ion thermal conductivity was computed from the ion energy flow across the magnetic surfaces, with the results shown in Fig. 14A19. As in the case of experimentally measured values of D, the Monte Carlo simulation values of χ_i vary only slightly over a wide range of ν_{ei}

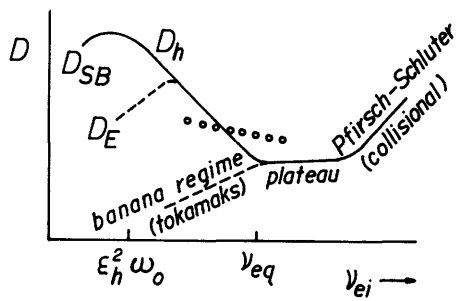

Fig. 14A18. Theoretical variation of diffusion coefficient with electron-ion collision frequency in stellarators. $\nu_{eq} \equiv \varepsilon_h^{3/2}\ell v_{Te}/2\pi R_0$, where $v_{Te} \equiv (kT_e/m_e)^{\frac{1}{2}}$. The D_h curve, Eq. (14A12), shifts upwards if ε_h is increased. D_{SB} represents effects of superbananas. The D_E curve represents possible reduction of D_h by electric fields in the plasma. Based on K. Miyamoto, Nuclear Fusion 18, 243-284 (1978) Figs. 15 and 16.

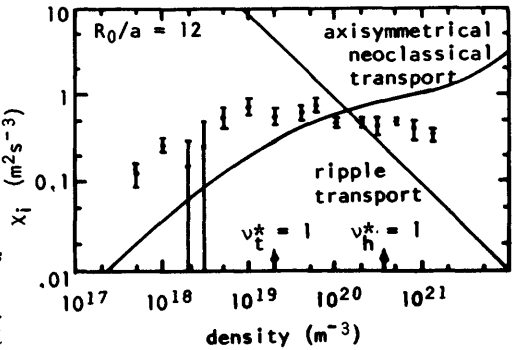

Fig. 14A19. Variation of ion thermal conductivity with plasma density in a torsatron with R_0 = 48 m, a_{coil} = 4 m, ℓ = 3, N = 32 field periods, B_0 = 5.5 T, ψ_{sep} = 82.8 Wb, $\langle r_{sep} \rangle$ = 2.1 m. Smooth curves represent theoretical predictions of ripple transport and neoclassical theory. Points represent a Monte Carlo simulation of ion motion. The parameters ν_h^* and ν_t^* represent the ratios of the effective collision frequency for detrapping to bounce frequencies in the helical ripples and toroidal mirrors, respectively. From R. E. Potok, P. A. Politzer, and L. M. Lidsky, Physical Review Letters 1328-1331 (1980), Fig. 1.

(proportional to density). This behavior may be due to resonances between the motion in the helical modulation and bounce motion in the toroidal modulation. The resonances would prevent conservation of the adiabatic invariant J [Eq. (7D13)], and lead to transport coefficients independent of ν_{ei} (Potok, Politzer, and Lidsky, 1980). Fluctuating electric fields could have a similar effect of reducing variations of D and χ_i with ν_{ei}.

The hypothesis that fluctuations untrap helically trapped particles was tested experimentally in the Saturn stellarator/torsatron. Application of broad-band rf power at f $\sim$ 1 MHz, which is roughly the bounce frequency for many of the trapped electrons, resulted in a 40 % increase in confinement time. No effect was observed if the plasma was not in the superbanana regime or if single-frequency rf was applied.

When the rotational transform $\iota/2\pi$ = 1/m, where m is an integer, (when the safety factor q = m), then a rational surface exists inside the plasma, meaning that a field line closes on itself after making m trips around the torus. This condition gives rise to resonant wave growth and enhanced transport rates, as illustrated in Fig. 14A20.

Electron energy transport rates in ohmically-heated stellarators are roughly consistent with pseudoclassical transport, Eq. (8F12). Ohmically-heated tokamaks and stellarators have similar energy confinement time scaling, but current-free stellarators have longer confinement times.

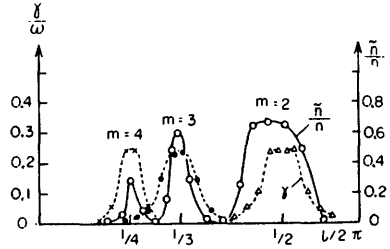

Fig. 14A20. Variation of the density fluctuation $\tilde{n}/n$ of Xe plasma in the JIPP Ib ℓ = 2 stellarator with rotational transform. The theoretical value of the growth rate of a resistive drift instability is also shown. From K. Miyamoto, Nuclear Fusion 18, 243-284 (1978), Fig. 20.

experiments

Parameters of some stellarator experiments are listed in Table 14A1. Altogether, about 30-40 stellarators have been built or planned. The stellarator minor radii a $\sim$ 5-20 cm are significantly smaller than tokamak minor radii a $\sim$ 10-100 cm (Table 13A1).

Table 14A1. Parameters of some stellarators. From Miyamoto (1978), Table I.

device (location)	R_0 cm	a cm	B T	ℓ	$\iota/2\pi$	remarks
Proto-Cleo (Wisconsin)	40	7	0.3	2 or 3	0.8	stellarator or torsatron helical coils in vacuum chamber
IMS (Wisconsin)	40	7	0.6	3	0.8	modular stellarator
Cleo (Culham)	90	10	2.0	3	0.5	NBI
Wendelstein VII-A (Garching)	200	10	4.0	2	0.23	NBI
JIPP T-II (Nagoya)	91	17	3.0	2	0.3	NBI
Heliotron D (Kyoto)	105	10	0.5	2	2	torsatron, helical coils in vacuum chamber
Heliotron E (Kyoto)	220	21x41*	2.0	2	2	torsatron, non-circular cross section of chamber, NBI
L-2 (Lebedev)	100	11.5	2.0	2	0.7	
Uragan 2 (Kharkov)	110	10*	2.0	3	1	race-track shape, 10.4 m circumference
Uragan 3 (Kharkov)	100	15-17	3.0	3	0.7	torsatron, helical coils in vacuum chamber, NBI

*vacuum chamber dimension; others are plasma radius.
NBI = neutral beam injection IMS = Interchangeable Module Stellarator

Almost all stellarators employ ohmic heating for initial plasma production. Most of them also use some form of wave heating, such as lower hybrid waves, Alfven waves, ECRH, and ICRH. Typical parameters attained with ohmic heating are $n \sim 5\times10^{18}$ - 5×10^{19} m^{-3}, $T_e \sim 200$-700 eV, $T_i \sim 20$-250 eV, $Z_{eff}(0) \sim 1$-1.5, and $\tau_E \sim 6$-10 ms. Some stellarators can also be operated as tokamaks. The density and temperature profiles tend to be flatter in the stellarator mode than in the tokamak mode, as illustrated in Fig. 14A21. The larger stellarators also use neutral beam injection.

When the drift parameter $\xi \equiv u_e/v_{te} \gtrsim 0.01$ [where $u_e \equiv J/ne$ and $v_{te} \equiv (kT_e/m_e)^{\frac{1}{2}}$], microinstabilities occur, causing enhanced transport rates, and reducing the plasma energy confinement times. For example, the variation of electron energy confinement time with ξ in the Cleo stellarator is shown in Fig. 14A22. Therefore, it is desirable to use ohmic heating only for initiating the discharge, and then to sustain the plasma by other heating techniques, letting current decay to zero.

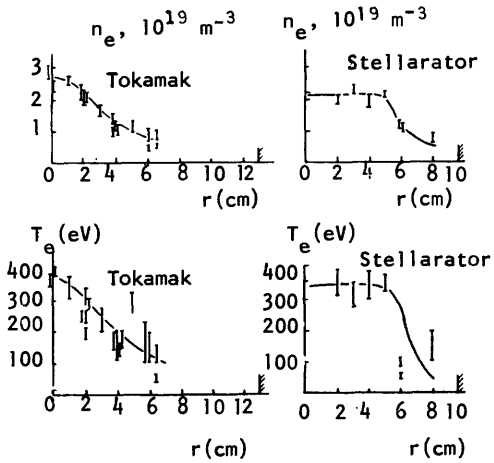

Fig. 14A21. Radial profiles of plasma density and electron temperature in the Cleo device for stellarator and tokamak modes of operation at B_0 = 1.27 T, I = 17 kA. From K. Miyamoto, Nuclear Fusion 18, 243-284 (1978), Fig. 31.

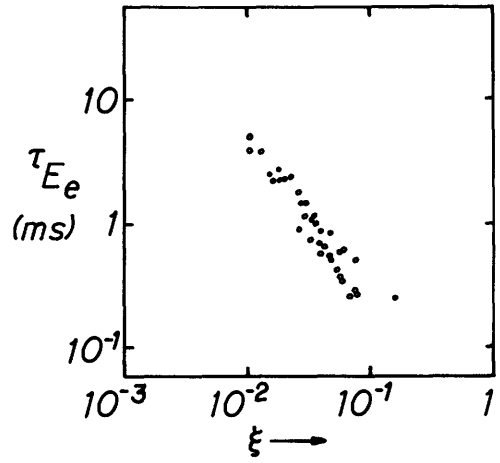

Fig. 14A22. Variation of electron energy replacement time with mean drift parameter in the Cleo stellarator. From D. W. Atkinson et al, Plasma Physics and Controlled Nuclear Fusion Research (Innsbruck 1978), Volume II, IAEA, 1979, p. 251-264, Fig. 1.

Current-free operation has been attained in the Wendelstein VII-A stellarator at $n \sim 10^{20}$ m^{-3}, $T_e \sim 700$ eV, using NBI to sustain the plasma. As the plasma current decayed, the current to the helical windings was increased, in order to maintain the total rotational transform nearly constant (Eq. 14A12). The energy confinement time increased from about 5 ms (current on) to over 20 ms (current off). The value of $n\tau_E \simeq 2 \times 10^{18}$ m^{-3} s is about five times higher than attained in tokamaks of comparable size.

Current disruptions are often observed in tokamaks (Section 13A) and stellarators at high current. These disruptions can be suppressed in the Wendelstein VII-A experiment by sufficiently large values of rotational transform, $\iota_h/2\pi \gtrsim 0.15$. The amplitude of the (2,1) tearing mode decreases to negligibly small values as ι_h is increased above this value. This stabilization is not produced by shear, because the $\ell = 2$ windings of that device produce very little shear. Instead, it is probably due to shifting the q = 2 resonant surface to a place where the current-density gradient dJ/dr is small (W VII-A Team, 1980).

In an $\ell = 3$ stellarator there are about six intersections of the separatrix with the walls, Fig. 14A7. Plasma outside the separatrix tends to flow to the walls at these locations, instead of crossing the separatrix and entering the hot plasma core. Thus, outer layers of plasma containing impurities from the walls can be "scraped off", neutralized at the wall, and pumped away by vacuum pumps. This is the principle of divertors (Section 25B). Measurements of particle fluxes with movable probes show sharp peaks along the separatrix, as expected. Particle fluxes to the outside of the torus (large R) may be greater than to the inside of the torus (small R), (Voitsenya et al, 1979).

reactors

Stellarator and torsatron reactor studies usually have $\ell = 2$ or $\ell = 3$ coils, a $\sim$ 2 m, $R_0 \sim$ 15-30 m, $\langle\beta\rangle \sim$ 3-6 %, $B_0 \sim$ 5 T, ignited steady-state operation, and plant efficiency $\eta \sim$ 30 %. Some important problem areas are:

* *maintenance*. Coils should allow easy blanket replacement, and it must be possible to replace failed coils.
* *plasma purity*. Maintenance of plasma purity in a reactor environment may require a magnetic divertor (Section 25B). Torsatrons are more compatible with divertors than tokamaks, and present experiments have low values of Z_{eff}.
* *beta*. It is not yet known what beta values are attainable. Coil costs decrease as beta increases.
* *transport*. Ripple diffusion could increase transport rates in reactors. High-density low-temperature operation may be desirable, in order to keep ν_{ei} high. (However, ripple diffusion is not a serious problem in present experiments).

Stellarators and torsatrons have the following potential advantages, in comparison with tokamaks:

* Steady state operation is feasible.
* During ohmic heating the (2,1) tearing mode and plasma disruptions can be controlled with the rotational transform of the helical windings.
* Ohmic heating is unnecessary, so the drift parameter ξ can be kept small, in order to maximize confinement time.
* Flatter density and temperature profiles give a larger region of high fusion power density.
* Simpler coil configurations than tokamaks.
* Natural poloidal divertors help maintain plasma purity.
* The confining fields are established before the plasma is turned on, minimizing plasma-wall contact. Feedback control of the plasma position is not necessary.

14B. Internal Rings

magnetic field configurations

Internal ring devices, described theoretically by Ohkawa and Kerst (1961), were the first toroidal devices to confine plasma quiescently (Dory et al, 1966). A toroidal magnetic field is not required for equilibrium and stability, except in the single-ring case. Thus, multipole plasmas are inherently high-beta over most of their volume and can be operated over an enormous range of plasma parameters, steady state or pulsed, with or without ohmic heating, and with or without the magnetic shear produced by the toroidal field. Therein lies their great utility for basic magnetic confinement studies as well as their undeserved reputation for low density, low temperature operation (J. C. Sprott, private communication, 1981).

In the mid-1960's almost every major laboratory had an internal ring device. Although these devices were originally conceived for pure research, it is now apparent that they are uniquely suitable for advanced fuels (lithium, boron) requiring high temperatures, because the magnetic field is low inside the plasma, and synchrotron radiation losses are tolerable. Structural activation problems

would be minimized with advanced fuels, which emit very few neutrons. With the increasing popularity of tokamaks in the 1970's, most multipole experiments were shut down, and those remaining (UW and UCLA) have been devoted to the assessment of multipoles as advanced fuel reactors, with a secondary emphasis on fundamental confinement studies (transport, heating, ballooning, plasma-wall interactions).

Toroidal multipole devices are illustrated in Fig. 14B1. The rings create a region with minimum average B, Eq.(8D69), promoting stability against interchange modes. The single-ring case is similar to a tokamak, with the toroidal current carried by the metal ring instead of by the plasma. Since the ring is rigid, it is not subject to kink instabilities. The ring currents, induced by pulsed external coils, are all in the same direction. The rings may be suspended on wires,

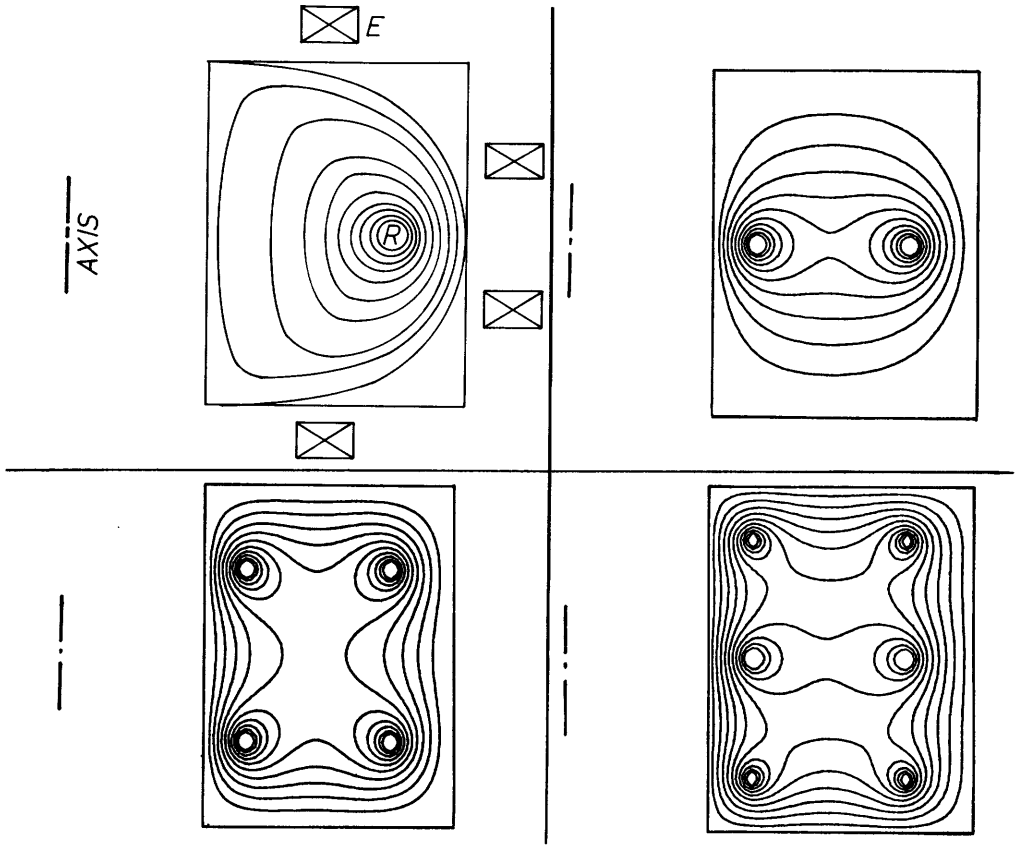

Fig. 14B1. Toroidal internal ring devices with a single ring (Levitron or Spherator), two rings (toroidal quadrupole), four rings (toroidal octupole), and six rings (duodecapole SURMAC). The ring (R), axis, and equilibrium field coils (E) are indicated for the single ring case only. Smooth curves represent magnetic surfaces in the presence of a low-beta plasma. For those with 2, 4, and 6 rings, β = 1 %, 3 %, and 6 %, respectively. The 2, 4, and 6 ring figures are from D. A. D'Ippolito, E. A. Adler, and Y. C. Lee, "Equilibrium and stability of high-β toroidal multipoles", The Physics of Fluids 23, 794-802 (1980), Figs. 2-4.

temporarily levitated by withdrawing mechanical supports, or magnetically levitated. Since plasma flows freely around the rings, wire supports enhance plasma losses and add impurities to the plasma. Strong currents in the support wires can provide "magnetic shielding" of the supports, reducing particle loss rates (Molvik, 1972; Lehnert, 1975). Pulsed mechanical supports allow only a few ms operation before the ring falls by gravity. In the FM-1 Spherator, a superconducting ring was levitated for hours , with position control by feedback control to external coils. Such rings must be periodically recharged with liquid helium to maintain superconductivity.

Most plasma confinement properties improve with increasing multipole order (number of rings), including:

total number of confined particles per unit magnetic flux
confinement time
magnetic well depth, Eq. (14A10) (quadrupole $\Delta U/U$ = 3 %, octupole $\Delta U/U$ = 10 %)
magnetic connection length (distance between regions of good and bad curvature, which should be small to impede growth of ballooning modes)
maximum theoretical beta
fraction of plasma which is in the low-magnetic-field region (low synchrotron losses).

For example, theoretical estimates for the 2, 4, and 6 ring cases with no toroidal field indicate maximum stable values of beta of about 1 %, 4 %, and 7 %, respectively (D'Ippolito, Adler, and Lee, 1980). However, increasing the number of rings tends to exacerbate engineering problems. The required current density to produce a given magnetic flux increases, and support problems, such as ring forces and stability, become more difficult.

If two of the internal rings of a toroidal octupole (with toroidal field) have their currents reversed, the field topology becomes a toroidal cusp, similar to Tormac (Fig. 11J2), but with plasma circulation around the cusp coils, as illustrated in Fig. 14B2. This scheme, called MIRICLE (for "mirrored ions, closed-loop electrons"), is like a magnetic mirror, in which the electrons escaping from one end are recirculated back in the other end. The diminished electron loss reduces the ambipolar potential and improves ion confinement. The high mirror ratio, minimum-B geometry, and deep magnetic well provide good MHD stability. The toroidal field makes the magnetic field nonzero everywhere inside the plasma, so that the adiabatic invariants (Section 7D) can be conserved. Ions escaping from the central region are not well confined, but can be shunted into a direct convertor, where part of their kinetic energy is directly converted into electricity (Section 26G). The MIRICLE concept offers the prospect of better Q values than a simple mirror (for which $Q \lesssim 1$), but it has not been tested experimentally.

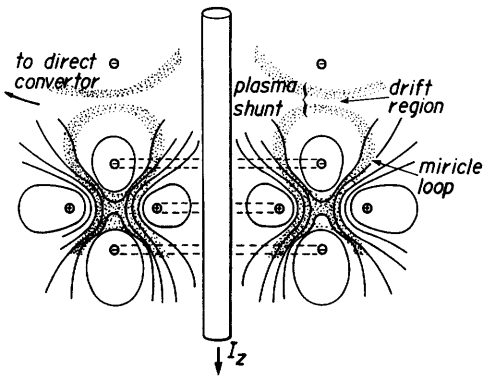

Fig. 14B2. A cross-sectional view of MIRICLE. The axial current I_z creates the toroidal magnetic field. Escaping electrons flow around the Miricle loop and return to the central region (shaded gray). Ring supports are not shown. From F. F. Chen, EPRI ER-429-SR (1977), Part A, p. 52, Fig. 18.

The separatrix of the spherator is nearly spherical. Devices with a spherical separatrix can also be created by means of helical conductors arranged on two concentric spheres, as illustrated in Fig. 14B3. The inner conductor should

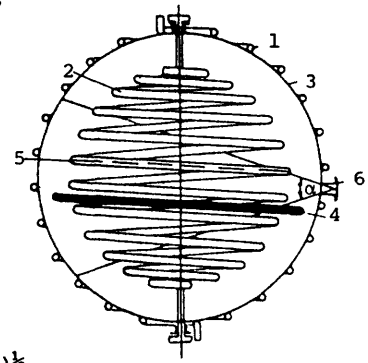

Fig. 14B3. The Tornado-650 magnetic trap. (1) outer helical conductor, (2) inner helical conductor, (3) vacuum chamber, (4) circular cathode to produce an E×B discharge for plasma rotation and heating, (5) anode (along one turn of the inner conductor, near the equator), (6) viewing angle of spectrograph. From B. P. Peregood and B. Lehnert, "Magnetic traps with a spherical separatrix: Tornado traps", Nuclear Instruments and Methods 180, 357-386 (1981), Fig. 31.

be designed so that its deflections under high magnetic forces do not spoil the magnetic confinement topology. If I_{in} and I_{out} are the currents in the inner and outer helices, with radii r_{in} and r_{out}, the ideal ratio is $I_{out}/I_{in}=(r_{in}/r_{out})^{\frac{1}{2}}$. Particle losses occur by cross-field diffusion and by drifts caused by non-ideal magnetic topology. At the above current ratio, the magnetic field inside the inner sphere is weak, and diffusion losses dominate. When $I_{out}/I_{in}\sim 0.7(r_{in}/r_{out})^{\frac{1}{2}}$, the two loss processes have nearly equal rates, and confinement times are maximized (for 8-turn spirals). An experiment with r_{in} = 0.8 m, r_{out} = 0.93 m, B = 2.5 T, and β = 0.1 could probably attain densities $n \sim 10^{20}$-10^{22} m^{-3}, rotational velocities $\sim$ 3-9x10^5 m/s (induced by an applied electric field), and T $\sim$ 0.3-3 keV (Peregood and Lehnert, 1981).

Quasistationary regions of electrostatic potential hills or valleys may form as the result of plasma turbulence from gun injection or of magnetic field perturbations caused by support wires, field errors, etc. A positive potential hill causes local $\vec{E}\times\vec{B}/B^2$ drifts in the clockwise direction. Because the circulating particle flows are similar to those observed during heat convection in fluids, they are called *convective cells*, Fig. 14B4. The resulting spatial-averaged particle flux is

$$\langle\Gamma_x\rangle = \langle nE_y\rangle/B_z \qquad (m^{-2}s^{-1}). \qquad (14B1)$$

Convective cells are often large, occupying the whole chamber, in contrast to the small cell shown in the Figure. They have been observed in multipoles and stellarators, and may also be present in other plasma confinement devices. Their effects can be minimized by viscosity (at high collisionality), by magnetic shear, by avoiding field errors, and by using quiescent methods of plasma production and heating (Navratil and Post, 1979).

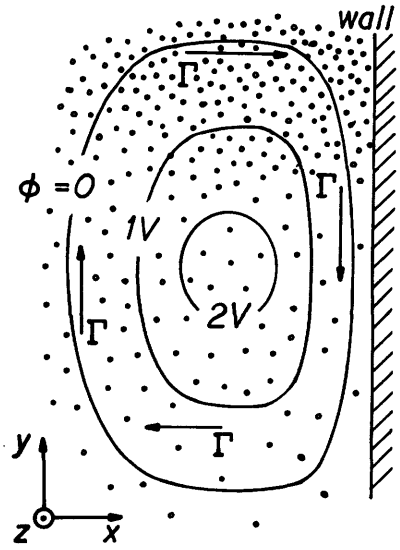

Fig. 14B4. A convective cell. The magnetic field is in the z direction. E×B drifts cause the particle drifts Γ .

experiments

A couple of internal ring experiments are illustrated in Figs. 14B5 and 14B6. Plasma may be produced in multipoles by ECRH, gun injection, or ohmic heating, and sustained by neutral beam injection or wave heating. Ring currents are tens of kA to MA, densities $n \sim 10^{16}$-10^{20} m^{-3}, and temperatures T $\sim$ 1-600 eV. Multipoles have attained low fluctuation levels and long confinement times, limited by convective cells or support losses (if wire supports are used). For example,

Fig. 14B5. The University of Wisconsin levitated octupole experiment. Courtesy of J. C. Sprott and S. C. Prager.

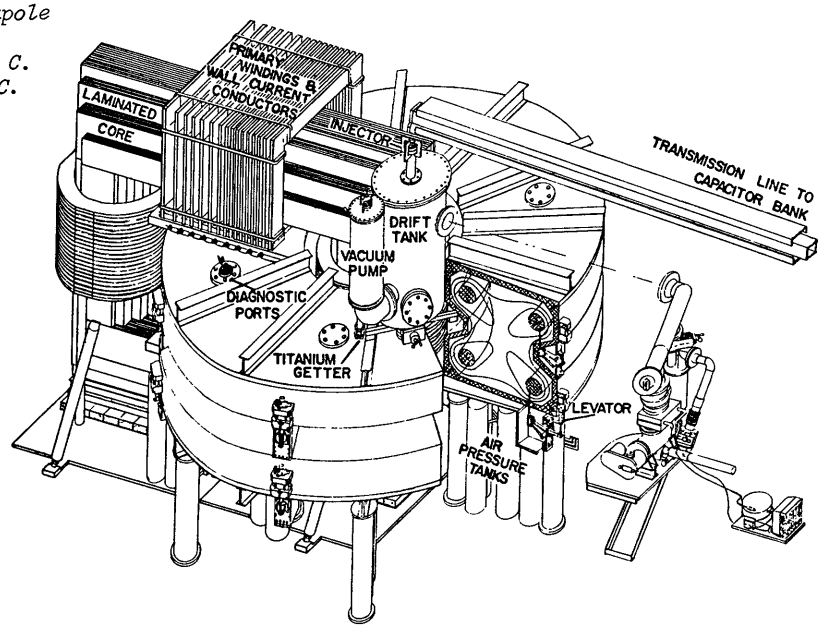

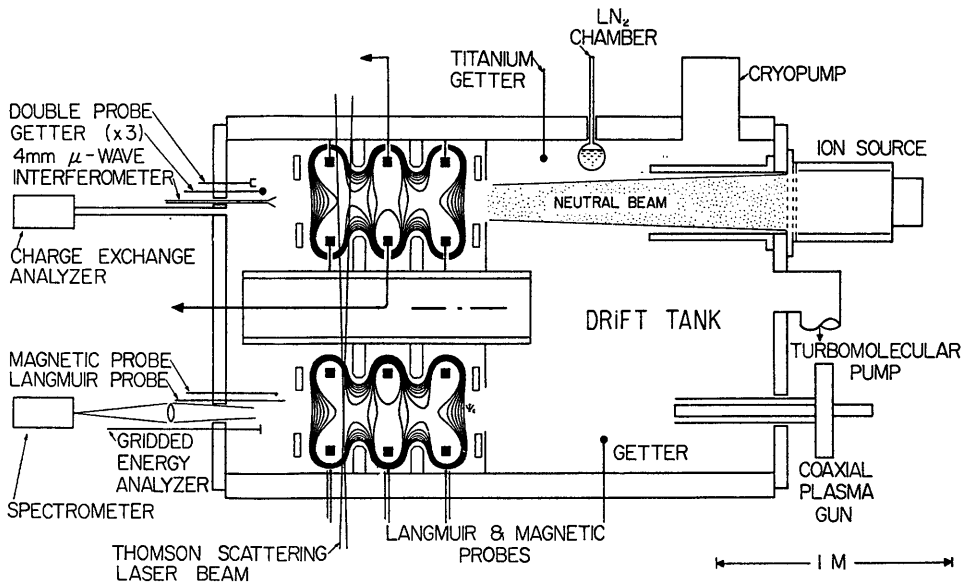

Fig. 14B6. The Dodecapole SURMAC (Surface Magnetic Confinement) experiment at UCLA. Courtesy of R. W. Schumacher and A. Y. Wong.

particle confinement times in the FM-1 Spherator experiment, using a levitated superconducting ring carrying about 200 kA current, ranged from 1 ms to 3 s. (A group of 100 keV electrons produced by ECRH had lifetimes of tens of seconds.) Confinement times in several internal ring devices have been within factors of 2-10 of the values predicted for classical diffusion. Unlike tokamaks, there is no lower density limit in multipoles. A tokamak with a poloidal divertor, such as PDX (Fig. 2585), is topologically similar to a toroidal multipole with added toroidal field, ohmic heating, and sufficient plasma current to generate closed flux surfaces which do not surround the rings.

Multipole experiments have confined plasmas with values of beta exceeding theoretical predictions for stability against ballooning modes. For example, the theoretical beta limit in the Wisconsin Levitated Octupole is about 4 %, but values of 8 % have been attained in bad curvature regions (between the rings and the wall), where ballooning is most likely. When the magnetic field is reduced (increasing ρ_i), values of beta $\beta \sim 35$ % have been confined (Halle et al, 1981). Values of $\beta \sim 8$ % have also been attained in the Dodecapole SURMAC at UCLA. There must be at least 2-3 ion Larmor radii ρ_i between the separatrix and the vacuum critical flux surface where $(\partial/\partial\psi) \oint d\vec{\ell}\cdot\vec{B} = 0$ for good confinement. Since $\rho_i \propto (T_i/B^2)^{\frac{1}{2}}$, the ion temperature tends to scale proportional to B (Schumacher et al, 1981).

Potential advantages of internal ring devices as fusion reactors include:
* long confinement times (nearly classical)
* magnetic wells promoting plasma stability
* availability of magnetic shear, if a toroidal field is applied
* low magnetic field inside the plasma, so synchrotron radiation losses are low, possibly enabling use of advanced fuels (lithium, boron).

The main problem is how to support the rings. One possibility is to replace metal rings with ring currents of electrons or ions.

14C. Electron and Ion Rings

field reversal

Production of relativistic electron beams (REB) and high-energy ion beams will be described in Chapter 16.

The original *Astron* concept of N. C. Christofilos involved transverse injection of an REB into a magnetic mirror, in order to produce a field-reversed configuration like that of the field-reversed mirror (Fig. 11F1), but with the REB encircling the axis. In experiments at LLL, 600 A, 6 MeV, 0.3 μs pulses were injected at 86° relative to the mirror axis in hydrogen gas at 30 Pa (0.2 Torr) pressure (Briggs et al, 1973). Beam axial motion was damped inductively by resistors mounted inside the chamber walls, but beam loss by various processes made it difficult to build up high ring currents.

Complete field reversal was attained in Relativistic Electron Coil Experiments (RECE) at Cornell by injecting single pulses of much higher current into a magnetic mirror or cusp. In RECE-CHRISTA 5 MeV electrons formed a ring which persisted for over 1 ms. Field-reversing rings have also been produced by injection of 1 MeV ions.

Ion rings should have longer lifetimes than electron rings, because synchrotron radiation from ions is negligible, and their heavier masses give the ring greater rigidity. An ion accelerator could produce a field reversing ion ring in a low-field region at one end of a reactor. Then the ring could be moved axially (by pulsed mirror fields) into a higher-field region, increasing the ring current and energy density, and igniting fusion burn in the toroidal plasma confined by the ring current, as shown in Fig. 14C1. The axial conductor carries a current of about 10 MA, creating a toroidal field to help suppress precessional instability of the ring. About one-fourth of the ion ring energy goes to heat the plasma. A 300 MeV ring could have a lifetime on the order of 5 s. For one reactor case a power gain ratio Q $\sim$ 2-3 was estimated, but higher Q values may be attainable. One way of attaining higher Q is to form many electron or ion rings inside a bumpy torus (Section 14D).

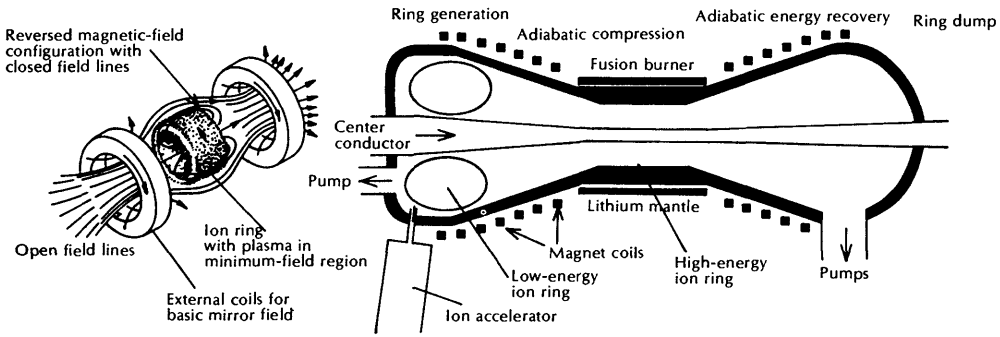

Fig. 14C1. A fusion reactor based on a reversed-field configuration (left) produced by injection and compression of an ion ring (right). Deuterons would be injected from an accelerator at about 30 MeV. An increasing magnetic field at the left would move the ion ring into the fusion burner region compressing the ring to an energy of about 300 MeV, and igniting fusion burn. After substantial fuel burnup, the ring would be moved into the ring dump and cooled by adiabatic expansion. The neutralized gases would then be pumped away by vacuum pumps, and another cycle begun. From H. H. Fleischmann, Engineering: Cornell Quarterly 12, No. 3, December 1977, p. 28.

Potential advantages of an ion ring compressor reactor are:

* The magnetic field is low, except in a small volume, so superconducting magnets are not necessary. Magnets would have low powers and stresses.
* No auxiliary plasma heating equipment is needed.
* Most of the ring energy comes from its compression, so the efficiencies of acceleration and injection are not crucial.
* Ring replacement time can be much shorter than the fusion burn time, so a duty cycle of 80-90 % is possible.
* Helium ash and other impurities are exhausted with each ring, to maintain purity of the next ring.

The main uncertainties are:

* attainable Q
* stability of the ion rings
* development of the ion beam accelerator, injection, and trapping mechanisms
* ring energy recovery system and plasma dump chamber.

injection into toruses

The metal ring of a Spherator/Levitron (or the toroidal plasma current of a tokamak) can be replaced with a high-current REB or ion beam. Several phenomena may be used to facilitate beam injection and trapping in toruses:

* The vertical drift caused by toroidal field curvature and gradient moves the beam away from the injector
* Decay of return current induced in the plasma increases the net current and the image current in the conducting walls, causing the ring current radius to contract
* The toroidal and vertical magnetic fields produced by external coils may be varied in time, and locally in space.

The SPAC-V experiment at Nagoya is illustrated in Fig. 14C2. A toroidal field is produced by a vertical conductor, and a vertical field by external coils (not shown). Plasma is injected into the torus before the REB is injected. When the cathode is pulsed negative, a plasma sheath forms around it, and the sheath ions serve as the anode of the electron gun. The negative potential of the cathode prevents the beam-induced return current in the plasma from flowing to the cathode, so the return current is forced to flow along field lines towards the chamber wall. (If the return current flowed to the electron gun, then the poloidal field of the REB would be masked, and plasma confinement impaired.) In the SPAC-VI experiment (similar to Fig. 14C2) about 100 kA of 1 MeV electrons were injected into a target plasma (from a plasma gun) with $n \sim 4 \times 10^{12}$ m^{-3}. The resulting electron ring current $\sim$ 40 kA lasted for 10 ms, during which the electrons travelled a distance of 3000 km. Peak ion temperatures $T_{imax} \sim 800$ eV were attained. Apparent plasma density and ion temperature decay times 0.5 ms after injection were 2 ms and 0.3 ms, respectively, and then the density became nearly constant for 8 ms.

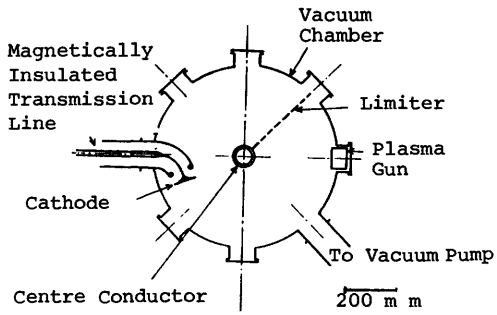

Fig. 14C2. Top view of the toroidal chamber of the SPAC-V experiment at Nagoya. From A. Mohri et al, Plasma Physics and Controlled Nuclear Fusion Research (1978, Innsbruck), Volume III, IAEA, Vienna, 1979, P. 311-320, Fig. 1.

In the "Electrostatic Tokamak Fusion Reactor" concept, an electron beam is injected into a torus under high vacuum while the magnetic field is increased, so that the beam spirals inwards. The beam space charge produces a very strong radial electric field of several MV/cm. Then an aerosol of DT particles (about 10 μm diameter) is injected, partly stripped, electrostatically trapped, and ionized. Ions are heated and confined by the deep negative potential well (tens of MV), which also traps alpha particles, facilitating ignition. The beam current provides the poloidal magnetic field for plasma confinement, as in conventional tokamaks. Once plasma forms between the central region and the walls, however, cross-field conductivity will greatly reduce the central potential (Chen, 1977).

Electron and ion injection schemes offer alternative means of establishing high currents in toroidal devices like tokamaks, with very low aspect ratios, high magnetic shear, simpler coil systems, and efficient heating.

14D. Elmo Bumpy Torus (EBT)

introduction

Electron cyclotron resonance heating (ECRH) experiments in mirror devices at ORNL and Nagoya showed that under certain conditions a stable *annulus* (ring) of relativistic electrons can be produced at the mirror midplane with temperatures of 50 - 1500 keV and betas of 5 - 100 %. The high-beta ring digs a local magnetic well, which enhances plasma stability, but bulk plasma confinement times are limited by mirror end-losses. In order to improve confinement, many mirror cells can be arranged end to end in a circle, forming a *bumpy torus*, Fig. 14D1.

The field lines in a bumpy torus are nominally closed, with zero rotational transform. The magnetic field gradient and curvature drifts in the mirrors induce a rapid poloidal drift motion of the plasma, which averages out the vertical drift and charge separation tendencies caused by toroidal curvature. Orbits of the mirror-trapped particles resemble the orbit of Fig. 7D2. However,

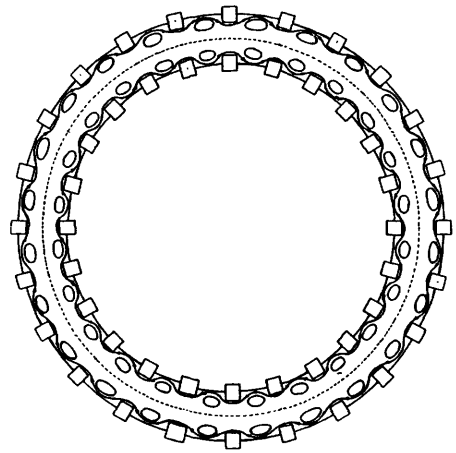

Fig. 14D1. A bumpy torus comprised of 24 mirror cells connected end to end in a circle. Squares represent circular coils, the wavy line represents an outer magnetic surface, and the ellipses represent the location of the hot electron rings in EBT. Courtesy of ORNL (ORNL-DWG 75-488R2).

the "bad" curvature of the mirror regions tends to promote interchange instabilities, as in Fig. 8D6.

Bumpy torus stability may be promoted by various means, including internal metal rings (Section 14B), electron and ion rings (Section 14C), and applied electric fields (Section 14E). The Elmo Bumpy Torus (EBT) and Nagoya Bumpy Torus (NBT) use electron rings produced by ECRH to provide plasma stability. Future devices may also use ion rings induced by ICRH. The key issues are ring stability and maintenance with moderate power input.

The electron ring and the toroidal plasma help to stabilize each other. The ring diamagnetism digs a magnetic well, which stabilizes the plasma interchange modes; and the toroidal plasma helps to stabilize instabilities driven by ring pressure anisotropy.

Three modes of operation are observed in EBT experiments (including NBT), depending on neutral gas pressure, as illustrated in Fig. 14D2.

* *collisional mode (C mode).* At high pressures, the plasma temperatures and potential are low, with evidence of drift wave turbulence
* *toroidal plasma mode (T mode).* At intermediate pressures $p \sim 1$ mPa (8×10^{-6} Torr), the plasma is comparatively quiescent, with high temperatures and a potential well in the center.

* *mirror mode (M mode).* At low pressures, the plasma temperature and ring energy density are high, but large-amplitude fluctuations spoil confinement, and the toroidal plasma density is low. Each ring behaves like an isolated mirror cell.

Only the T mode will be described here, because it is the only mode which provides good plasma confinement.

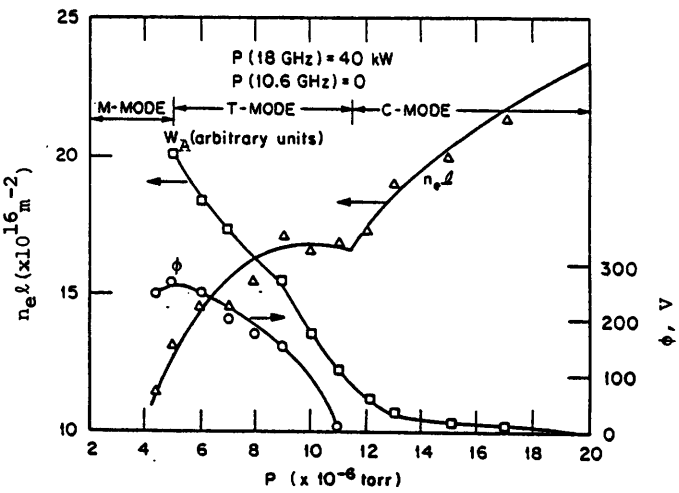

Fig. 14D2. Variation of plasma density $n_e\ell$ (ℓ = interferometer path length), ring stored energy W_A, and ambipolar potential ϕ in EBT-1 with neutral gas pressure, showing the three principle modes of operation. (The true chamber pressure probably differs from the gage pressure shown here.) From M. Fujiwara et al, "Experimental studies of plasma confinement in the bumpy torus", Plasma Physics and Controlled Nuclear Fusion Research (Brussels, 1980), IAEA, Vienna, 1981, Fig. 2.

particle orbits

For a particle with mass m, velocity v, and charge q, the vertical drift velocity due to the toroidal magnetic field gradient and curvature is (Eq. 7C5)

$$v_T = \frac{mv^2}{2qBR_t}\left[1 + \frac{v_{||}^2}{v^2}\right] \sim \frac{kT}{qBR_t} \tag{14D1}$$

and the poloidal precession velocity due to mirror curvature and to the radial ambipolar electric field E_r at radius r is (Eqs. 7C5, 7C6)

$$r\Omega = \frac{mv^2}{2qBR_c}\left[1 + \frac{v_{||}^2}{v^2}\right] + \frac{E_r}{B} \sim \frac{kT}{qBR_c}\left[1 + \frac{0.7e\phi}{kT_e}\right] \tag{14D2}$$

where ϕ is the ambipolar potential, R_t is the major radius of the torus, $v_{||}$ is the component of the v parallel to the magnetic field B, and $R_C = -B/\nabla_r B$ is the mirror radius of curvature. The longitudinal adiabatic invariant J [Eq. (7D13)] is fairly constant around each particle orbit. Most orbits are nearly circular, with the center of the orbit displaced from the minor axis by an amount v_T/Ω, as illustrated in Fig. 14D3. For certain values of $v_{||}$, the mirror curvature drift of an ion may be cancelled by a negative electric field (Eq. 14D2), and $\Omega \simeq 0$. These *resonant ions* have crescent-shaped drift orbits, leading to rapid diffusion.

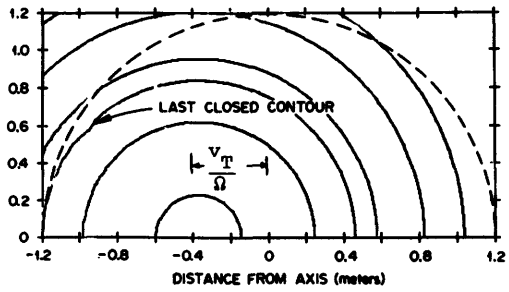

Fig. 14D3. Particle drift surfaces in the midplane (smooth curves). The magnetic field lines which intersect the wall are indicated by the dashed curve. Particles with drift orbits outside the "last closed contour" intersect the walls and are lost promptly. The particles shown here all have the same value of orbit displacement (v_T/Ω). Particles with other values of $v_{||}/v$ would have different values of (v_T/Ω). From D. G. McAlees et al, ORNL/TM-5669 (1976), Fig. B-9.

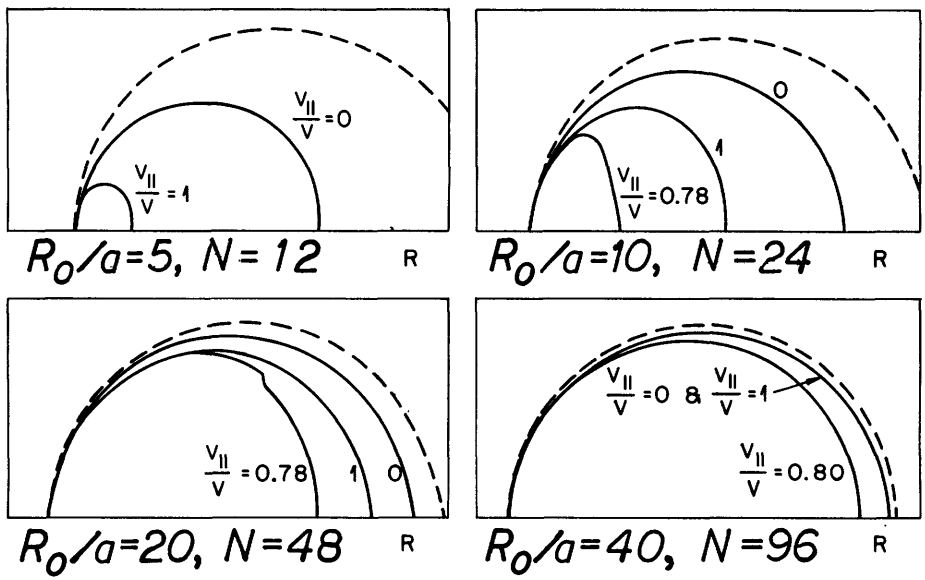

Fig. 14D4. Shapes of the last closed drift contours for various values of N (number of coils) and $v_{||}/v$, assuming ideal confinement in vacuum magnetic fields. Curves are shown for $v_{||}/v$ = 0, 1, and that value for which confinement is poorest. Courtesy of C. L. Hedrick, ORNL.

The size of the last closed drift contour (outermost confined orbit) increases with the number N of mirror cells in the torus, and varies strongly with $v_{||}/v$, as illustrated in Fig. 14D4. Confinement is poor for N = 12, and excellent for N = 96. The areas of the last closed drift contours can be increased by increasing N, or by using modified coil designs, such as aspect ratio enhancement (ARE) coils Fig. 14D5. The effect of ARE coils on drift orbit areas is shown in Fig. 14D6 for a case with N = 48. The drift surface areas with I_{ARE}/I_{TF} = 7.5 % are about as good as those for the N = 96 case. The curves shown in these figures also vary

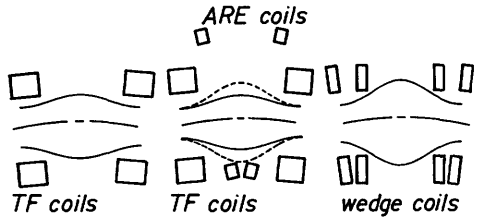

Fig. 14D5. EBT toroidal field coil schemes: ordinary coils (left); aspect ratio enhancement (ARE) coils (center); and wedge coils (right). The ARE coils have currents in the opposite direction from the TF coils, which makes the field lines bulge out more (dashed curves) when they are energized, increasing the mirror ratio, decreasing R_c, and increasing the poloidal drift velocity.

with the other parameters appearing in the equations for V_t and Ω, such as $e\phi/kT_e$.

equilibrium and stability

The total current is the sum of the plasma and electron ring currents:

$$\vec{J} = \vec{J}_p + \vec{J}_r \quad . \tag{14D3}$$

The plasma pressure p is nearly isotropic, but the ring pressure tensor $\underline{\underline{P}}_R$ is anisotropic. The equilibrium equations may be written

$$\begin{aligned} \vec{\nabla}\times\vec{B}/\mu_0 &= \vec{J}_p + \vec{J}_r \\ (\vec{J}_p + \vec{J}_r)\times\vec{B} &= \vec{\nabla}\cdot\underline{\underline{P}}_R + \vec{\nabla}p \\ \vec{\nabla}\cdot\vec{B} &= 0 \quad . \end{aligned} \tag{14D4}$$

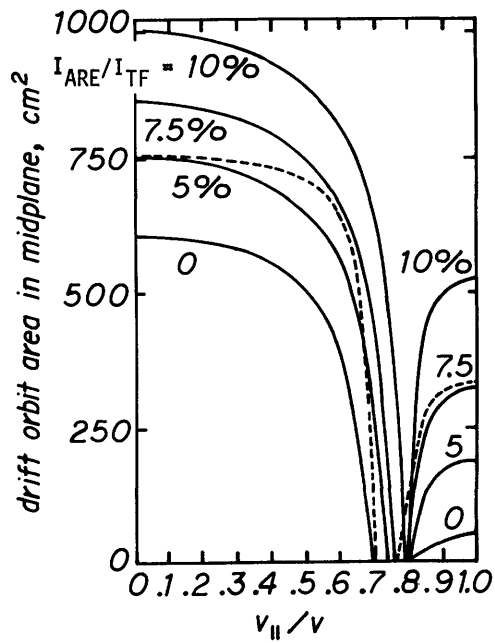

Fig. 14D6. Area of the last closed drift orbit vs. $v_{\parallel}/v$ for a device with N = 48 at various ARE coil currents, expressed as fractions of the TF coil current. The dashed curve is for N = 96 without ARE coils. From R. A. Dandl et al, ORNL/TM-5955 (1978), Fig. C.2.

These equations have been solved numerically. The resulting magnetic surfaces and surfaces of constant magnetic pressure are illustrated in Fig. 14D7. The radial variations of pressures, magnetic field, and $U \equiv \oint d\ell/B$ at the midplane of a mirror cell are shown in Fig. 14D8.

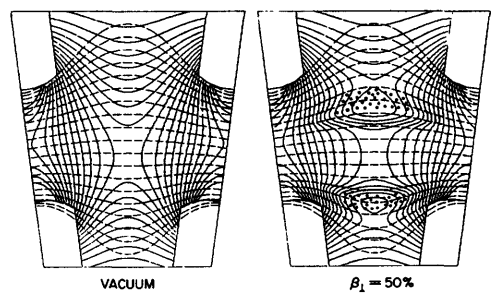

Fig. 14D7. Magnetic field configuration of EBT. The dashed lines represent magnetic field lines, and the solid lines represent surfaces of constant B. Dots represent the approximate location of the hot electron annulus. Courtesy of ORNL.

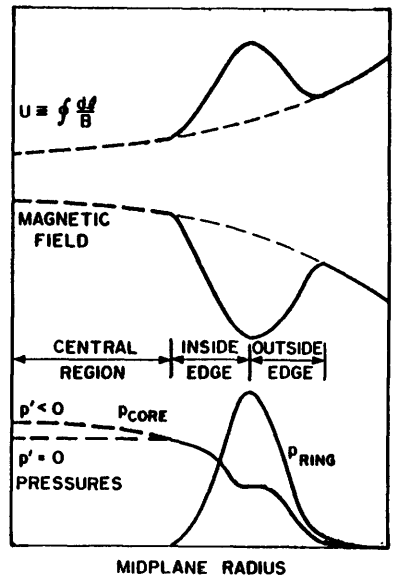

Fig. 14D8. Radial variations of pressures, magnetic field, and U in the midplane of an EBT mirror cell. Courtesy of N. A. Uckan, ORNL.

The MHD stability of an EBT plasma may be studied by treating it as a bumpy cylinder with toroidal effects as perturbations. For this case, the energy principle of Eqs. (8D58)-(8D61) may be written approximately as

$$\delta W = \int d\psi \left\{ \int \frac{d\ell}{B} \left[\left(\frac{1}{r} \frac{dX}{d\ell} \right)^2 + p' DX^2 \right] + \left(\frac{U^2}{I + U/\gamma p} \right) \langle DX \rangle^2 \right\} \geq 0 \qquad (14D5)$$

for stability, where

$$X \equiv \vec{\xi} \cdot \vec{\nabla} \psi$$

$$p' \equiv \partial p / \partial \psi$$

$$U \equiv \oint d\ell / B$$

$$I \equiv \oint d\ell / B^3$$

$$D \equiv p'/B^2 - J/rB^2 - (2/B)\, \partial B / \partial \psi \qquad (14D6)$$

$$\langle DX \rangle \equiv \frac{1}{q} \oint \frac{d\ell DX}{B}$$

(Nelson and Hedrick, 1979). Usually, p' is negative in confined plasma. If $D < 0$ everywhere, then $\delta W > 0$, and the plasma will be stable, because the other terms in δW are all positive. Thus, a large, positive $\partial B/\partial \psi$ (magnetic well) is good for stability. If a trial function X = constant is used in order to simplify Eq. (14D5), it becomes

$$\delta W \simeq X^2 \int d\psi \left[Up' \langle D \rangle + \frac{U^2 \langle D \rangle^2}{I + U/\gamma p} \right] \geq 0 \qquad (14D7)$$

for stability. It can be shown that

$$U \langle D \rangle = U' - p' I \qquad (14D8)$$

where $U' \equiv \partial U / \partial \psi$. For stability on each flux surface, the quantity in brackets in Eq. (14D7) must be positive, giving

$$U \langle D \rangle \left[\frac{p' I + p' U/\gamma p + U \langle D \rangle}{I + U/\gamma p} \right] \geq 0 \quad ,$$

which reduces to

$$(U' - p' I)(Up' + \gamma p U') \geq 0 \quad , \qquad (14D9)$$

since the denominator is positive. This equation is an approximate stability criterion for EBT plasmas. In the *central region* and *inside edge* (Fig. 14D8)

$U' > 0$ and $p' \lesseqgtr 0$ (core plasma), so Eq. (14D9) reduces to

$$\gamma p U' \gtreqless - Up' \tag{14D10}$$

for stability. Since U' is larger at the inside edge, larger pressure gradients can be sustained there than in the central region. In the *outside edge* region $p' < 0$ and $U' < 0$, so Eq. (14D9) reduces to

$$I|p'| \lesseqgtr |U'| \quad , \tag{14D11}$$

where $I \equiv \oint d\ell/B^3$. This equation limits the allowable pressure gradient in the outside edge region. This condition is equivalent to making <D> negative (Eq. 14D8), so $\partial B/\partial\psi > 0$ is desirable (a magnetic well). The minimum value of ring beta can be estimated from the condition $\partial B/\partial\psi \gtreqless 0$. From Eq. (8B6)

$$\vec{\nabla}_\perp p_\perp + \vec{\nabla}_\perp B^2/2\mu_0 = (\vec{B}\cdot\vec{\nabla})\vec{B}/\mu_0 \tag{14D12}$$

where $p_\perp$ is the perpendicular component of the ring pressure. In the outer edge region, the radial components of the derivatives may be approximated as

$$\vec{\nabla}_\perp p_\perp \simeq -p_\perp/\delta_A$$

$$\vec{\nabla}_\perp B^2/2\mu_0 \simeq (B/\mu_0)(\partial B/\partial r)$$

$$(\vec{B}\cdot\vec{\nabla})\vec{B}/\mu_0 \simeq -B^2/\mu_0 R_c \tag{14D13}$$

where δ_A is the half-width of the annulus and R_c is the radius of curvature of the magnetic field lines. Using these values in Eq. (14D12) and setting $(\partial B/\partial r) \gtreqless 0$, we find

$$\beta_\perp \equiv 2\mu_0 p_\perp/B^2 \gtreqless 2\delta_A/R_c \quad . \tag{14D14}$$

where B is the vacuum field at the ring. This is the value of ring beta needed to produce a magnetic well. A similar prediction, taking into account the length L_a of the electron annulus, is

$$\beta_\perp \gtreqless (\delta_A/R_c)(L/L_a)(M^2-1)/2\pi M \tag{14D15}$$

where $M = B_{max}/B_{min}$ is the axial magnetic mirror ratio and L is the length of a mirror cell (Sanuki and Fujiwara, EBT Ring Physics Workshop, 1979, p. 460). For $M = 2$ and $L/L_a \simeq 6$, this reduces to $\beta_\perp \gtreqless 1.5\ \delta_A/R_c$. Typically $\delta_A/R_c \sim 0.1$ so the required $\beta_\perp \sim 15$ % relative to B at the ring. [If $\beta_\perp$ were defined relative to the field on the axis (at the midplane), then the required $\beta_\perp \sim 5$ %.] However, there is considerable uncertainty in such estimates. Lower values of $\beta_\perp$ do not produce a magnetic well, leaving the outer edge region unstable. If the toroidal plasma pressure increases, the field lines bulge out more, decreasing R_c and increasing the required ring beta. If the annulus is located closer to the magnetic axis, then R_c is increased, decreasing the required beta. Similarly, a thin annulus (small δ_A) allows a smaller ring beta.

ring stability

Potential MHD instabilities of the electron ring include mirror modes and interchange modes. The *mirror modes*, driven by ring pressure anisotropy, are expected to be stable if

$$T_\perp/T_{\parallel} < 1 + (1/2\beta_\perp) \sim 3 \quad . \tag{14D16}$$

(D. A. Spong, in EBT Ring Physics Workshop, 1979, p. 89). In a simple mirror heated by ECRH,

$$T_\perp/T_{\parallel} \simeq (B_{res}/B_{mid} - 1)^{-1} \tag{14D17}$$

where res and mid refer to the location of the cyclotron resonance and the orbit midplane, Fig. 14D9. Although this may be modified in a bumpy torus, it illustrates the possibility of having some control over the temperature anisotropy by adjusting the magnetic field shape and microwave frequency. If $B_{res}/B_{mid} \gtrsim 1.2$, the plasma is usually free of instabilities driven by anisotropy. The temperature anisotropy can also be reduced by adding microwave heating at a frequency above the cyclotron resonance, called *upper off-resonant heating*.

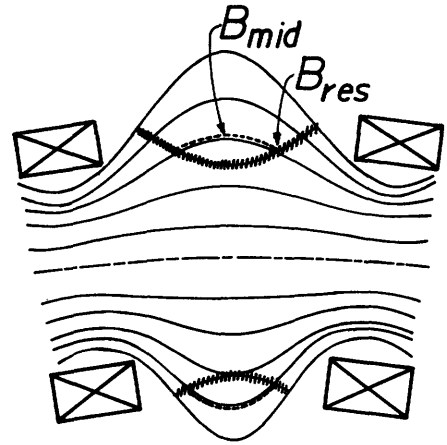

Fig. 14D9. One mirror sector, showing coils (rectangles), field lines (smooth curves), surface of constant $|\vec{B}|$ where resonance heating occurs (shaded curve), path of a heated electron (dotted line), and definitions of B_{mid} and B_{res}.

Interchange modes (flutes and ballooning) tend to be stabilized by the magnetic well and by cooler plasma electrons (density n_c) interacting with the hot ring electrons (density n_h). Various predictions indicate values of $n_c/n_h \sim$ 1-20 may be needed for stability. The required value decreases with increasing (Ω_A/ω_{ci}), the ratio of the hot electron precession frequency to the ion cyclotron frequency. The decrease in (n_c/n_h) resulting from a lowering of neutral gas pressure may cause instability and be responsible for the T-M transition (T mode to M mode).

The allowable $\beta \equiv 2\mu_0 p/B^2$ of the toroidal plasma is uncertain. Models treating the ring as a rigid body indicate that values of $\beta \lesssim \beta_\perp$ will be stable; but a model including plasma ring interactions in a simplified geometry indicates $\beta < 0.1$ for stability (J. W. Van Dam and J. C. Lee, EBT Ring Physics Workshop, 1979, p. 471).

Microinstabilities of the ring are classified as electrostatic and electromagnetic. "Timofeev half-harmonic" electrostatic modes have been observed in simple mirrors, but not in EBT. They are stabilized if $T_\perp/T_{\parallel} \lesssim 6$, which is easily satisfied by the use of upper off-resonant heating. Ring electrons may dissipate perpendicular energy by driving *whistler* waves, which are low-frequency electromagnetic R-mode waves, Eq. (5E32). (Audio-frequency noise initiated by lightning bolts propagates along the earth's magnetic field by this mode, with higher frequencies travelling at higher group velocities, so that an observer a great distance away hears a falling pitch, like a whistle.) The whistler wave extracts perpendicular energy from the ring electrons, so that they are no longer mirror trapped, and bursts of detrapped hot electrons have been observed in simple mirrors. The whistler instability is driven by ring pressure anisotropy, and it interacts primarily with lower-energy ring electrons, having energies $\lesssim 50$ keV. It is theoretically stabilized if

$$T_\perp/T_{\parallel} \lesssim (2/\beta_\perp)^{\frac{1}{2}} \sim 3 \quad , \tag{14D18}$$

which is similar to the mirror-mode condition (14D16).

heating

Formation of the hot electron ring is accomplished by ECRH, which also provides some heating of the toroidal plasma electrons. Although resonant zones exist in the plasma where $\omega = \omega_{ce}$, the incident microwaves may be reflected by the outer layers of plasma before they can penetrate to the resonant zones, so *accessibility* of the resonance is a problem. It is possible in principle to solve a 3-D boundary-value problem for the distribution of microwave power and heating rates in the plasma, but polarization-dependent phenomena, cutoffs, and resonances make this technique very difficult. If the microwave wavelength $\lambda << L_n$ (the density or magnetic field gradient scale length) the geometric optics approximation may be used. Then the paths of the microwave rays may be computed numerically (*ray tracing*) to determine where they are reflected and how much energy is deposited at each point along the way. (Special formulas are needed near cutoffs and resonances, where the geometric optics approximation is invalid.)

If s is the distance along the ray trajectory and S(s) is the wave power flux (W/m^2) at point s, then the rate of decrease of power flux may be written

$$dS/ds = - \alpha S \tag{14D19}$$

where $\alpha = 2k_i$ is the power absorption coefficient, and k_i is the imaginary part of the wave number. Let θ be the angle between $\vec{k}$ and $\vec{B}$, as in Fig. 5E1. The variations of α with θ for the ordinary mode ($\vec{E}$ in the $\vec{k}$-$\vec{B}$ plane) and for the extraordinary mode ($\vec{E}$ perpendicular to the $\vec{k}$-$\vec{B}$ plane) are shown in Fig. 14D10, assuming $T \sim 12$ keV and wave frequency ~ 120 GHz. At lower plasma temperatures and densities, such as $T \sim 200$ eV and $n \sim 10^{18}$ m^{-3} in EBT-1, damping of the ordinary wave is very weak.

Wave energy is also absorbed at *harmonics*

$$\omega = n\omega_{ce} + k_{\parallel}v_{\parallel} \tag{14D20}$$

where $v_{\parallel}$ and $k_{\parallel}$ are the components of $\vec{v}$ (electron velocity) and $\vec{k}$ parallel to $\vec{B}$, and n is an integer.

In general, the extraordinary (X) mode is strongly damped near the *fundamental* resonance (n = 1) with $k_i/k_r \sim 1$ for propagation nearly parallel to B ($\theta \sim 0$), but decreasing with increasing θ, where k_r is the real part of the wave number. Damping increases with temperature, but decreases with increasing plasma density. The ordinary (O) mode is weakly damped ($k_i/k_r \sim T_e/mc^2$), but damping increases with θ, temperature, and density. At the *second harmonic* ($\omega \sim 2\omega_{ce}$) both modes are weakly damped, with $k_i/k_r \sim T_e/mc^2$ for the X mode and $k_i/k_r \sim (T_e/mc^2)^2$ for

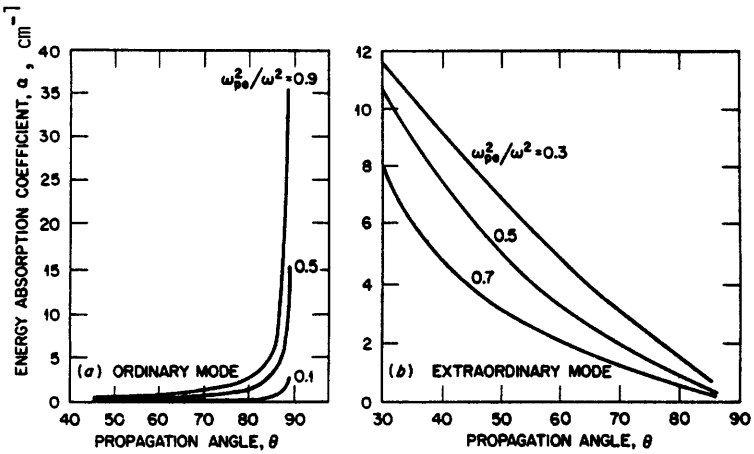

Fig. 14D10. Energy absorption coefficient α versus propagation angle for various values of ω_{pe}^2/ω^2 for the ordinary mode (left) and extraordinary mode (right). From N. A. Uckan and D. B. Batchelor, "Heating techniques for an EBT reactor", ORNL/TM-6346 (1978), Fig. 2.

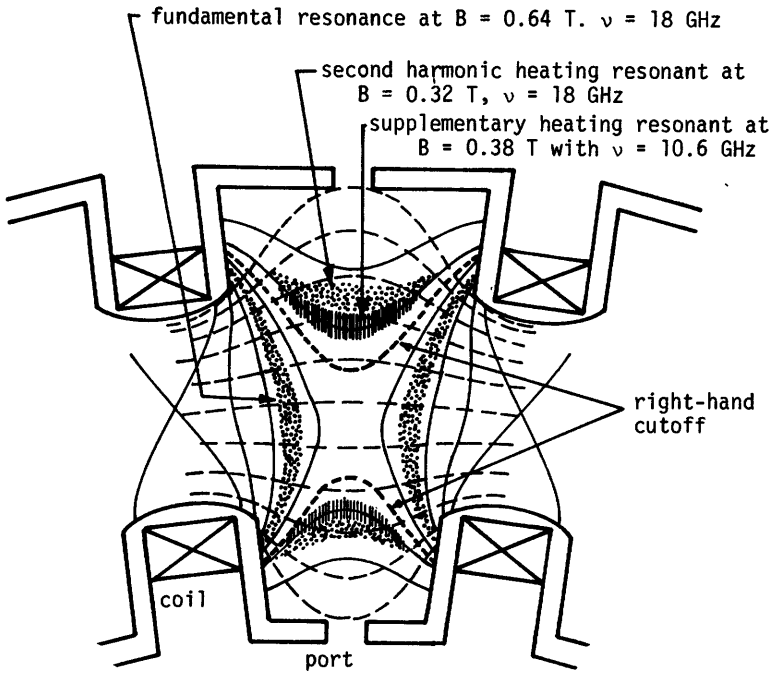

Fig. 14D11. Magnetic field lines (thin dashed curves) and surfaces of constant magnetic field strength (thin smooth lines) in EBT-1, showing regions of fundamental and second harmonic resonances, and the location of the right-hand cutoff (thick dashed curves). Supplementary heating at a lower frequency is resonant in the shaded zones. From N.A. Uckan and D.B. Batchelor, ORNL/TN-6346 (1978), Fig. 1.

the O mode. Absorption increases with temperature and plasma density. Damping of the X mode increases with θ, but damping of the O mode peaks at an oblique angle between 0 and $\pi/2$.

A given wave frequency ω may be used to heat toroidal plasma in the high-field regions near the mirror throats with the fundamental resonance and to heat ring electrons in the lower-field regions near the mirror midplane with the second harmonic resonance simultaneously, as illustrated in Fig. 14D11. In EBT-1, damping of ordinary waves is very weak, so only the extraordinary waves interact strongly with the resonance zones. If the plasma density is not too high ($\omega_{pe} < \omega$), then the entire core region is accessible to the ordinary mode. The extraordinary mode is reflected at the right-hand cutoff layer, and extraordinary waves from the port cannot directly reach the fundamental resonance zone. However, ordinary waves which have penetrated into the high-field region can be converted into extraordinary waves during reflection from the walls, so that effective heating can occur at the fundamental resonance zone.

For the case of rays incident on a perfectly conducting wall at the $z_1 = 0$ plane, let θ_w be the angle between the ray and the plane [$\tan \theta_w = k_z/(k_x^2 + k_y^2)^{\frac{1}{2}}$] and ϕ be an azimuthal angle [$\tan \phi = k_y/k_x$], with the magnetic field in the x direction. Then the fraction T_{OX} of the incident power which is converted from the ordinary (O) mode to the extraordinary (X) mode upon reflection is shown in Fig. 14D12. Typical values of T_{OX} range from 10 to 50 %, with an average value of 40 % for an isotropic distribution of incident rays. Thus, mode conversion during multiple reflections can be very effective at converting the ordinary mode to the extraordinary mode.

It is also possible for O→X mode conversion to occur within an inhomogeneous plasma, but this process is only effective in a narrow cone ($\sim \pm 1°$) around a critical propagation angle.

Absorption of microwaves in an EBT plasma has been studied with a three-dimensional ray-tracing code. The extraordinary mode incident from the low-field region (lower-left in Fig. 14D13) is reflected at the right-hand cutoff and unable to penetrate to the resonance zone, but waves propagating from the high-field region (upper right) are thoroughly absorbed near the resonance region. These waves could originate from mode conversion of ordinary mode waves during reflection at the wall. For EBT-1 parameters, the ordinary mode is very weakly damped in the plasma, and its rays travel in nearly straight lines. For reactor parameters, however, absorption of the ordinary mode can be significant, as illustrated in Fig. 14D14.

The absorption of microwaves at the second harmonic (to produce the hot electron annulus) is stronger than

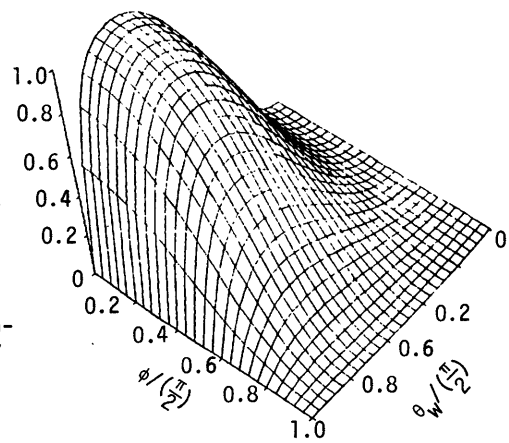

Fig. 14D12. Power conversion coefficient T_{OX} from ordinary to extraordinary mode versus angle of incidence, assuming surface plasma parameters characteristic of EBT-1. From D. B. Batchelor and R. C. Goldfinger, Nuclear Fusion 20, 403-418, (1980), Fig. 10.

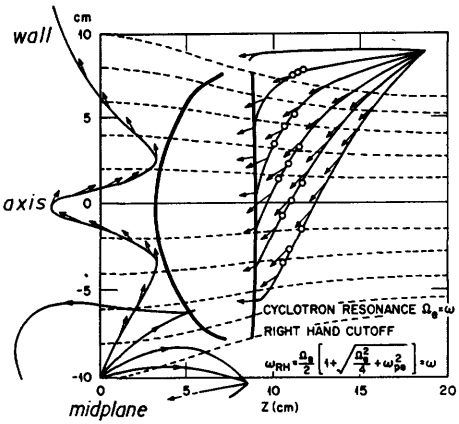

Fig. 14D13. Extraordinary mode rays propagating in a mirror plasma characteristic of EBT-I. Dashed curves represent magnetic field lines, and thin smooth curves represent microwave rays. Circles mark 1 %, 50 %, and 99 % absorption of the wave energy, and vectors indicate the direction of $\vec{k}$. *From D. B. Batchelor, "Status of the theoretical study of microwave heating in EBT", ORNL/TM-6320 (1978), Fig. 12.*

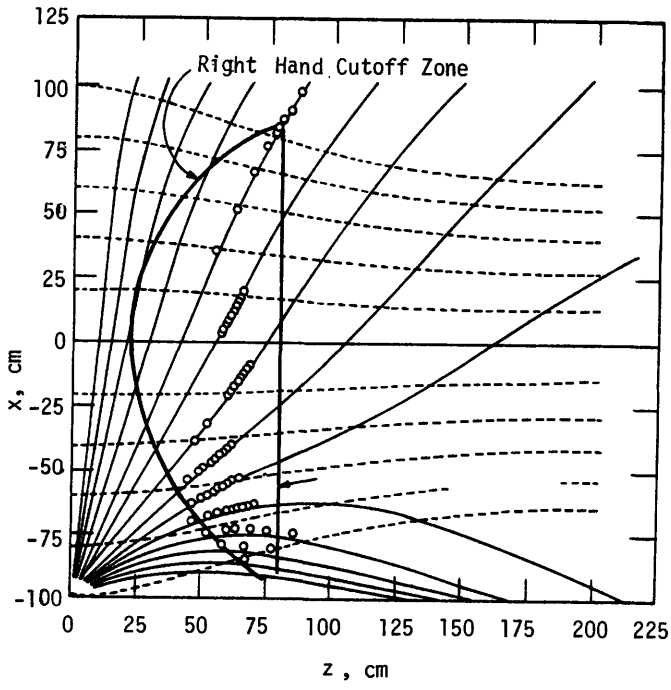

Fig. 14D14. Field lines in a magnetic mirror (dashed curves) and rays of microwaves (smooth curves) propagating from the lower left corner, calculated with three-dimensional ray tracing code for ordinary mode waves with $\nu = 120$ *GHz,* $n = 1.5\times10^{20}$ m^{-3} *(density decreasing radially outwards in the* $\pm$ x *direction), and* $T_e = 12$ *keV. Circles represent absorption of 10 % of the initial wave energy. From N. A. Uckan and D. B. Batchelor, ORNL/TM-6346 (1978), Fig. 3.*

predicted by simple analyses. To explain the enhanced absorption, various hypotheses are under study, including long-term, coherent motion of resonant electrons with large pitch angles (electrons which stay resonant for long times), and decay of the incident wave into two Bernstein waves (waves propagating near $\theta = \pi/2$ with $\vec{E}$ parallel to $\vec{k}$).

EBT plasmas can also be heated by *ion cyclotron resonance heating* (ICRH). Theoretical studies of ICRH in EBT plasmas use a bumpy cylinder model of the plasma and cavity shape, illustrated in Fig. 14D15. The resulting dispersion relation has several modes which can propagate at a given frequency, and frequencies with little or no propagation (stop bands), where electron Landau damping is effective. The spatial distribution of the wave poloidal electric field is illustrated in Fig. 14D16. The intensity peaks near the plasma center

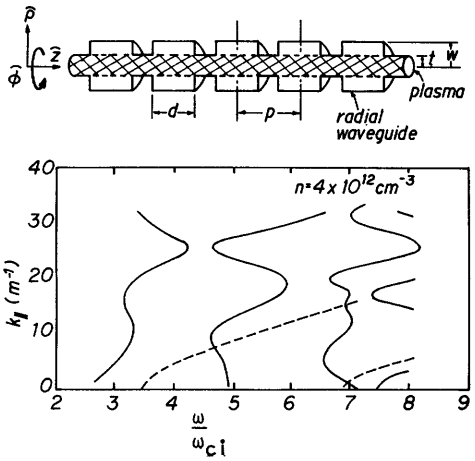

Fig. 14D15. Bumpy cylinder model of an EBT plasma (top) and resulting dispersion relation for TE_{11} excitation by waves with frequencies ω near the ion cyclotron frequency ω_{ci} (bottom, smooth curves). The dashed curves show the dispersion relation for a smooth cylinder, which is markedly different from that of the bumpy cylinder. From T. L. Owens, J. H. Mullen, and P. L. Huddleston, "Ion cyclotron resonance heating (ICRH) of an EBT with periodic boundary conditions", IEEE International Conference on Plasma Science, Madison, 1980.

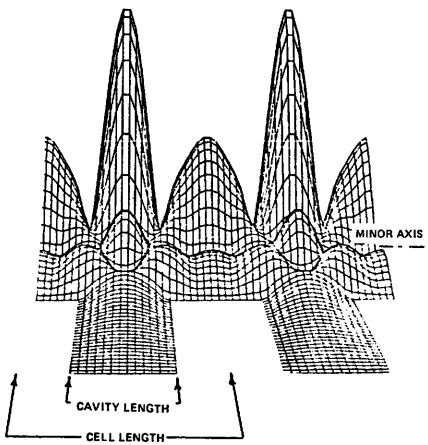

Fig. 14D16. Theoretical variation of poloidal wave electric field in 2 cells of EBT-P during ICRH heating. From T. L. Owens, J. H. Mullen, and P. L. Huddleston, IEEE Conference on Plasma Science, Madison, 1980.

indicate good wave penetration, which facilitates heating the plasma core region.

Auxiliary heating with ICRH is being studied on the EBT-S experiment. The coaxial line and ICRH antenna are shown in Fig. 14D17. The semicircular antenna is surrounded by a water-cooled aluminum shield (Faraday shield) to prevent direct contact with the plasma. The heat flux to the shield from the plasma is up to 10 W/cm^2. High-power ICRH can result in substantial increases in plasma temperatures and density, if sputtering from the shield does not introduce too many impurity atoms into the plasma.

Neutral beam injection can also be used for auxiliary heating of EBT plasmas. Particles with large $v_\perp$ are well confined, so perpendicular injection can be used. For a reactor, the plasma minor radius ($a \sim 1$ m) is small enough that neutral beams with energies $\sim$ 150 keV will probably have adequate penetration. However, the additional neutral gas flow will raise the chamber neutral pressure, which could make it difficult to maintain operation in the T mode, especially in small devices.

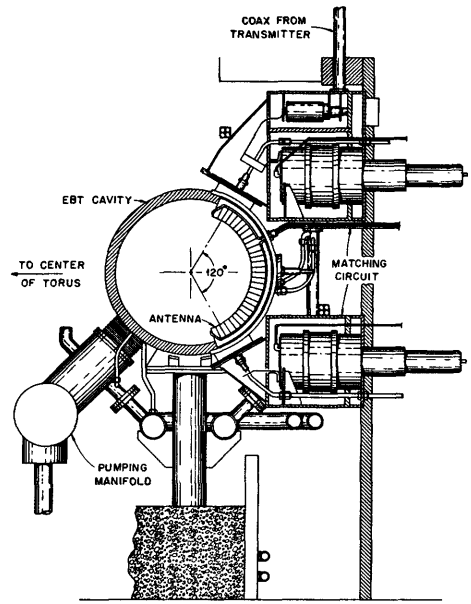

Fig. 14D17. The coaxial transmission line and antenna for ICRH heating on EBT-S. Courtesy of T. L. Owens, F. W. Baitty, Jr., ORNL, and J. H. Mullen, MDAC.

transport

The particle orbit displacement distance v_T/Ω (Fig. 14D3) acts as a step size for diffusion. The neoclassical diffusion coefficient may be written

$$D_n \sim \left\langle \frac{v_T^2 \nu}{\Omega^2 + \Omega_{eff}^2 + \nu_{eff}^2} \right\rangle \qquad (14D21)$$

where $\nu \equiv C_{ei} n/T_e^{3/2}$ is the electron-ion collision frequency, C_{ei} is a constant (Eq. 2E57), $\langle\ \rangle$ denotes an average over velocities,

$$\Omega_{eff} \equiv [2v_T d\Omega/dr]^{\frac{1}{2}} \qquad (14D22)$$

$$\nu_{eff} \equiv \Omega_0 (\nu/\Omega_0)^{1/3} \qquad (14D23)$$

and Ω_0 is the thermal value of Ω at $v_{\parallel} = 0$. If $\nu_{eff} = \Omega_{eff} = 0$, then $D_n \simeq \langle v_T^2\ \nu/\Omega^2 \rangle$ is dominated by those particles with $\Omega \sim 0$, hence the name "resonant particles". The Ω_{eff} and ν_{eff} terms have the effect of broadening the resonance (Berry, Hedrick, and Uckan, ORNL/TM-6743, 1979).

The particle and heat fluxes appearing in the transport equations may be expressed in terms of density gradients, temperature gradients, and the electric field:

$$\Gamma_r = - D_n \frac{\partial n}{\partial r} - D_T \frac{\partial T}{\partial r} + \mu_n n E_r$$

$$q_r = - K_n \frac{\partial n}{\partial r} - K_T \frac{\partial T}{\partial r} + \mu_T n E_r \quad . \qquad (14D24)$$

The coefficients μ_n, μ_T, D_T, K_n, and K_T may be expressed in terms of D_n (Jaeger, Hedrick and Spong, ORNL/TM-6806, 1979).

A simple, one-dimensional model of radial transport in an EBT plasma consists of conservation equations for particles, ion energy, and electron energy, and a radial component of Ampere's Law (averaged over poloidal angle) to determine E_r:

$$\frac{\partial n}{\partial t} = n_0 \langle \sigma v \rangle_i n - \frac{1}{r}\frac{\partial}{\partial r}(r\Gamma_r)$$

$$\frac{\partial}{\partial t}\left[\frac{3}{2} nkT_i\right] = Q_{ei} - \frac{1}{r}\frac{\partial}{\partial r}(rq_{ir}) - n_0 \langle \sigma v \rangle_{cx} \frac{3}{2} nk(T_i - T_0)$$

$$+ e\Gamma_{ir} E_r + n_0 \langle \sigma v \rangle_i \frac{3}{2} nkT_0 \qquad (14D25)$$

$$\frac{\partial}{\partial t}\left[\frac{3}{2} nkT_e\right] = 2m_e n \langle D_\mu \rangle - \frac{1}{r}\frac{\partial}{\partial r}(rq_{er}) - Q_{ei} - n_0 \langle \sigma v \rangle_i nE_I - e\Gamma_{er} E_r$$

$$\frac{\varepsilon_2}{e}\frac{\partial E_r}{\partial t} = \Gamma_{er} - \Gamma_{ir} = (D_{ni} - D_{ne})\frac{\partial n}{\partial r} + D_{Ti}\frac{\partial T_i}{\partial r} - D_{Te}\frac{\partial T_e}{\partial r} - n(\mu_{ni} - \mu_{ne}) E_r$$

where E_I is the ionization energy of atomic hydrogen, ε_2 is the perpendicular dielectric coefficient (Eq. 5E17), Q_{ei} is the electron-ion energy exchange rate, n_0 and T_0 are the neutral atom density and temperature, the $2m_e n\langle D_\mu \rangle$ term represents microwave heating of resonant electrons, and $\langle \sigma v \rangle_{cx}$ and $\langle \sigma v \rangle_i$ are rate coefficients for charge exchange and ionization.

If transport equations are derived by averaging the kinetic equation over two-dimensional magnetic surfaces, a set of equations like (14D25), but including geometrical form factors, is obtained. With parameters characteristic of EBT-1, steady state solutions of the transport equations yield radial profiles of density, temperatures, and electrostatic potential like those of Fig. 14D18. If a reflux boundary condition is used at the walls (incident neutral atom flux = outgoing ion flux), then the solutions for T_e may tend to grow without limit. Since most of the ions incident on the wall are implanted inside the wall and slowly diffuse back out, the flux of neutrals from the walls is nearly constant. Use of a constant neutral flux boundary condition avoids the thermal instability problem.

The energy confinement time may be estimated from equilibrium solutions of the transport equations. One result is

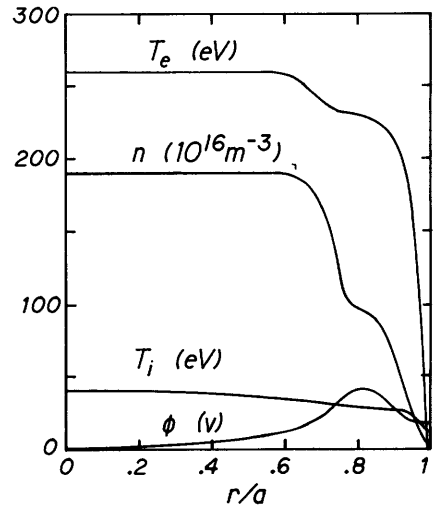

Fig. 14D18 Steady-state radial variations of density, temperatures, and electrostatic potential for EBT-1 parameters with 8 kW of microwave power and an edge neutral density of 2×10^{15} m^{-3}. Courtesy of E. F. Jaeger, ORNL.

$$\tau_E \simeq C \left[\frac{R_t}{R_c}\right]^2 \frac{B}{T_e}\left[\frac{\Omega}{\nu} + \frac{\nu}{\Omega}\right] \tag{14D26}$$

where C is a constant (Hiroe, Haste, and Dandl, ORNL/TM-6820, 1979). Since $e\phi/kT_e$ varies slowly with changes in T_e,

$$\nu/\Omega \simeq \frac{C_{ei} neBR_c}{T_{ek}^{3/2}\, kT_e(1 + .7e\phi/kT_e)} \propto nB/T_e^{5/2} \tag{14D27}$$

In collisional and collisionless regimes, then, the energy confinement time scales as

$$\tau_E \propto nB^2T_e^{-7/2} \quad , \qquad \nu/\Omega >> 1$$

$$\tau_E \propto T_e^{3/2}/n \quad , \qquad \nu/\Omega << 1 \quad . \tag{14D28}$$

ring power balance

Bremsstrahlung radiation losses from the hot electron ring will be negligible in comparison with other loss processes, unless Z_{eff} is very large, which is not a case of interest. The microwave power absorbed in the annulus per unit volume $P_{\mu A}/V_A$ (where V_A = annulus volume) is balanced by losses due to Coulomb collisions (drag and pitch-angle scattering) and due to synchrotron (cyclotron) radiation

$$P_{\mu A}/V_A = P_{Coulomb} + P_{synchrotron}$$

$$\simeq \underset{\text{drag}}{5\times10^{-38}} \frac{n_A n_p \gamma}{(\gamma^2 - 1)^{\frac{1}{2}}} \left[\underset{\text{drag}}{1} + \underset{\text{scattering}}{\frac{.5}{\gamma + 1}}\right] + \underset{\text{synchrotron}}{3.2\times10^{-20} n_A B_A^2(\gamma-1)[1 + 3.5(\gamma-1)]} \quad (MW/m^3) \tag{14D29}$$

where n_p is the plasma density at the ring (m^{-3}), n_A is the density of hot ring electrons (m^{-3}), B_A is the magnetic field at the ring (T), $\gamma = 1 + T_A/m_ec^2$, T_A is the annulus electron "temperature" (the distribution may be non-Maxwellian), and m_ec^2 = 511 keV is the electron rest-mass energy. The synchrotron radiation term is the same as Eq. (3F17). Coulomb logarithm values of 20 and 25 have been assumed in the drag and scattering terms [EBT Ring Physics Workshop Proceedings, 1980, p. 511-512]. [If the hot electrons scattered into the "loss cone" of the mirror cells are well confined, then their pressure will be nearly isotropic, they will become retrapped at approximately the same rate as they are detrapped, power losses due to pitch-angle scattering will be negligible, and the $.5/(\gamma+1)$ term should be set equal to 0.] The Coulomb drag term is dominant at low temperatures, but synchrotron radiation is important at T > 0.5 MeV (γ > 2).

The volume of N rings may be written

$$V_A = N\, 2\pi a \delta_A\, L_A \tag{14D30}$$

where a, δ_A, and L_A are the radius, thickness, and length of the annulus.

The power gain ratio Q of a nearly ignited reactor may be estimated from

$$Q = \frac{\text{fusion power output}}{\text{microwave power input to sustain the rings}}$$

$$= \frac{\langle \frac{1}{4} n_i^2 \langle \sigma v \rangle_{DT} W_{DT} \rangle V}{(P_{\mu A}/V_A) V_A} \tag{14D31}$$

where (P_μ/V_A) and V_A are given by the previous equations, V is the plasma volume, and the other terms in the numerator represent the volume-averaged fusion power density, Eq. (4D4).

A number of simplifications can be made to facilitate estimates of Q. Assume that the central plasma region has fairly flat density and temperature profiles (Fig. 14D18) characterized by $n_i \simeq n_e \equiv n$, $T_i \simeq T_e \equiv T$, $p = 2nkT$. Let

$$\beta_* \equiv \frac{2\mu_0 \langle p^2 \rangle^{\frac{1}{2}}}{B^2} = \frac{4\mu_0 \langle (nkT)^2 \rangle^{\frac{1}{2}}}{B^2} \rightarrow \langle (nkT)^2 \rangle = \frac{\beta_*^2 B^4}{16 \mu_0^2} \tag{14D32}$$

$$\beta_A \equiv \frac{2\mu_0 p_A}{B_A^2} = \frac{2\mu_0 n_A (\gamma-1) m_e c^2}{B_A^2} \rightarrow n_A = \frac{\beta_A B_A^2}{2\mu_0 m_c c^2 (\gamma-1)} \tag{14D33}$$

where $\langle\ \rangle$ denotes a volume average. Define a microwave cutoff plasma density at the annulus by $\omega_{pe}^2 = \omega_{ce}^2$ there:

$$\frac{n_c e^2}{m_e \varepsilon_0} = \frac{e^2 B_A^2}{m_e^2} \rightarrow n_c \equiv \frac{\varepsilon_0 B_A^2}{m_e} = 9.72 \times 10^{18}\ B_A^2 \quad (m^{-3}) \quad . \tag{14D34}$$

With these definitions we can express Eq. (14D29) in terms of B_A as

$$P_\mu/V_A = 2.4 \beta_A B_A^4 \left[\frac{n_p}{n_c}\right] \frac{\gamma}{(\gamma^2-1)^{\frac{1}{2}}(\gamma-1)} \left[1 + \frac{.5}{\gamma+1}\right] + 0.16 \beta_A B_A^4 [1+3.5(\gamma-1)] \quad (MW/m^3) \tag{14D35}$$

For values $1.4 \leq \gamma \leq 3$ ($0.2 < T_A < 1$ MeV) this may be approximated as

$$P_\mu/V_A \simeq \frac{4}{\gamma-1} \left[\frac{n_p}{n_c}\right] \beta_A B_A^4 \quad (MW/m^3) \quad . \tag{14D36}$$

If $n_p/n_c \geq \frac{1}{2}$ (smaller n_p would result in low n and low fusion power density), then this expression has accuracy typically $\sim$ 10 % (maximum error of 20 % at $n_p/n_c = \frac{1}{2}$, $\gamma = 3$). Assuming that $8 \leq T_i \leq 25$ keV, we can approximate the fusion power density with Eq. (2D18)

$$P_F \simeq 1.1\ \beta_*^2 B^4 V \quad (MW) \quad , \tag{14D37}$$

and Eq. (14D31) reduces to

$$Q \simeq 0.28 \frac{\beta_*^2}{\beta_A} \left[\frac{B}{B_A}\right]^4 \left[\frac{V}{V_A}\right]\left[\frac{n_c}{n_p}\right](\gamma-1) \quad . \tag{14D38}$$

For example, if $\beta_* \sim 0.2$, $\beta_A \sim 0.3$, $(B/B_A) \sim 1.5$, $(n_p/n_c) \sim 0.8$, and $(\gamma-1) \sim 1.5$, then

$$Q \sim 0.3 \frac{V}{V_A} \tag{14D39}$$

The volume ratio may be estimated as

$$\frac{V}{V_A} \simeq \frac{\pi a^2 2\pi R}{N 2\pi a \delta_A L_A} = \left[\frac{\pi R}{Na}\right]\left[\frac{a}{\delta_A}\right]\left[\frac{a}{L_A}\right] \tag{14D40}$$

In EBT-S, $R/a \sim 10$, $N/\pi \simeq 8$, $a/L_A \simeq 1$, $a/\delta_A \sim 5$, and $V/V_A \sim 6$. It is uncertain how δ_A will scale as the plasma size is increased. Some possible scalings are

Geometric scaling:	$\delta_A/a \sim 0.2$
Electron Larmor radius scaling:	$\delta_A \sim 10\,\rho_{eA}$
Ion Larmor radius scaling:	$\delta_A \gtrsim 5\rho_{iA}$

(14D41)

where ρ_{eA} and ρ_{iA} are the Larmor radii of the hot ring electrons and the plasma ions at the ring. For a reactor with $B_A = 2$ T, $\gamma = 2.5$ and $T_{iA} = 10$ keV, $\rho_{eA} = 2$ mm and $\rho_{iA} = 1$ cm (deuterons). If $a = 1$ m, the geometric scaling gives $a/\delta_A \sim 5$, the ion Larmor radius scaling gives $a/\delta_A \sim 20$, and the electron Larmor radius scaling gives $a/\delta_A \sim 50$. If $a/L_a \sim 1$ and $R/Na \sim 1$, then $V/V_A \sim 15$, 63, and 160 for the three scalings, respectively, and $Q \sim 5$, 20, and 50. More accurate calculations would include microwave power absorbed by the core and surface plasma in the denominator of Eq. (14D31), resulting in lower estimates of Q.

experiments

The EBT experiments at ORNL have usually heated the toroidal plasma at the fundamental resonance frequency and the ring electrons at the second harmonic. The fundamental frequency in the same chamber has been varied to 10.6 GHz to 18 GHz (EBT-1) to 28 GHz (EBT-S). In the Nagoya Bumpy Torus (NBT) the hot electron rings have been sustained by the fundamental resonance (FR) or by the second harmonic (SR). The larger EBT-P ("Proof of Principle") device at ORNL will operate at higher magnetic fields (2-3 T) and microwave frequencies (60-90 T). Some parameters of these experiments are listed in Table 14D1. In the EBT-S and NBT experiments, the heating powers are tens of kW, and the plasma dimensions are about the same. The NBT device is pulsed, and EBT-S operates continuously.

*Table 14D1. Approximate parameters of the NBT, EBT-1, EBT-S, and EBT-P experiments. These devices have mirror ratios ∿ 2 and operate at neutral gas densities $n_n \sim 10^{16}$ m^{-3}. * denotes predicted values.*

	NBT				
	SR	FR	EBT-1	EBT-S	EBT-P (1985)
number of sectors	24		24	24	36
major radius R_0, m	1.6		1.5	1.5	4.5
minor radius a, m	0.09		0.1	0.1	0.17
B_{res}, T	0.3	0.48	0.65	1	2
core heating frequency, GHz	8.5		18	28	60
total heating power, MW (ring ECRH, core ECRH, and core ICRH)	0.04	0.07	0.07	0.4	2.6
n, m^{-3}	5×10^{17}	10^{18}	10^{18}	2×10^{18}	3×10^{19}*
T_e, keV	0.1	0.02	0.2	0.5	3.5 *
T_i, keV			0.08	0.1	2 *
potential well depth ϕ, kV	0.06		0.19	0.25	3 *
τ_E, ms	0.4		1	3	75 *

$R_0/a \geq 26$

density and temperatures

Density profiles, measured by Thomson scattering and by a heavy ion beam probe, are fairly flat, with peak values $\sim 10^{18}$ m^{-3}, Fig. 14D19.

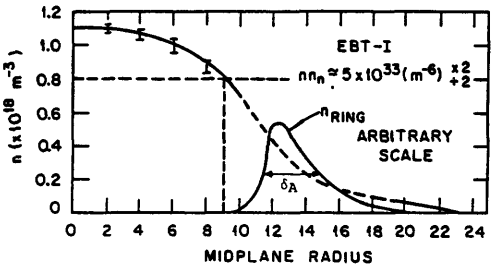

Fig. 14D19. Radial variation of plasma density, measured by a heavy ion beam probe in EBT-1 with P_μ = 50 kW (18 GHz) + 20 kW (10.6 GHz) and p = 0.8 mPa (6×10^{-6} Torr). The ring density n_A is about a factor of 3 below the average toroidal core plasma density, and the ring thickness $\delta_A \sim 3$ cm. Courtesy of N. A. Uckan, ORNL.

Plasma density in the FR mode is higher than in the SR mode (NBT). The annulus location and thickness have been estimated by moving a "skimmer" probe radially inwards and observing the destruction of ring stored energy (measured by diamagnetic loops), but there is considerable uncertainty in these estimates.

Electron temperature profiles, measured by Thomson scattering, are also fairly flat. The density and temperature vary as $n \propto P_\mu^{\frac{1}{2}}$ and $T_e \propto P_\mu^{3/2}$, Fig. 14D20. The electron temperature decreases with increasing neutral gas

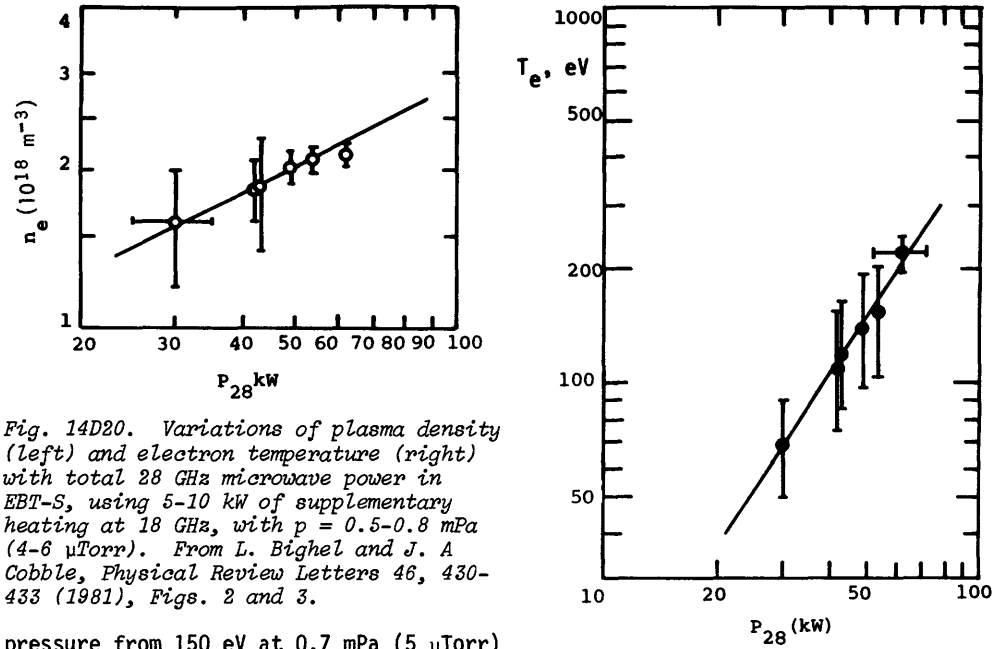

Fig. 14D20. Variations of plasma density (left) and electron temperature (right) with total 28 GHz microwave power in EBT-S, using 5-10 kW of supplementary heating at 18 GHz, with p = 0.5-0.8 mPa (4-6 μTorr). From L. Bighel and J. A Cobble, Physical Review Letters 46, 430-433 (1981), Figs. 2 and 3.

pressure from 150 eV at 0.7 mPa (5 μTorr) to 50 eV at 2.7 mPa (20 μTorr) in EBT-S. Electron density varies slightly with pressure. Central ion temperatures are typically 50-100 eV, decreasing with increasing pressure.

The "temperature" T_A of the hot electron annulus increases markedly with the the microwave frequency, as does the ring electron density n_A, Fig. 14D21.

potential

The spatial variation of the electrostatic potential $\phi(x)$, measured with a heavy ion beam probe, is illustrated in Fig. 14D22. The potential well in the center traps core ions, and the hill at the outside helps to repel impurity ions.

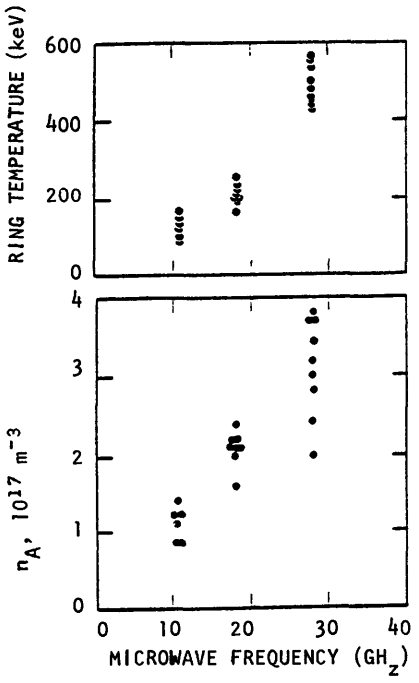

Fig. 14D21. Variations of electron ring temperature T_A (measured by hard x-ray spectra) and ring density n_A with microwave frequency, at various conditions in EBT-1 and EBT-S. From N. A. Uckan et al, "Physics of hot electron rings in EBT: theory and experiment", Plasma Physics and Controlled Nuclear Fusion Research (Brussels, 1980), IAEA, Vienna, 1981, Fig. 3.

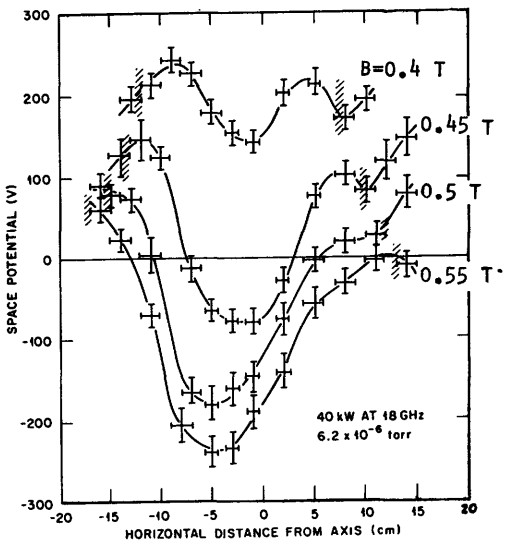

Fig. 14D22. Radial variation of electrostatic potential, measured by a heavy ion beam probe, for various magnetic field strengths on axis at the mirror midplane. Cross-hatched regions represent the locations of the second harmonic resonance. From J. C. Glowienka, Journal of Vacuum Science and Technology 18, 1088-1097 (1981), Fig. 4b.

The energy confinement time τ_E of the toroidal plasma may be estimated from the power balance equation

power input		power to rings		surface plasma		core plasma	
$\eta_\mu P_\mu$	=	W_A/τ_A	+	$n_s E_s V_s/\tau_s$	+	$(3/2)nk(T_e+T_i)V/\tau_E$	(14D42)

where P_μ and η_μ are the microwave power and transmission efficiency, W_A and τ_A are the total energy and decay time of the rings, V is the toroidal plasma volume, τ_s is the particle replacement time of the surface plasma region, n_s is the surface plasma density, and E_s is the average energy carried away per electron-ion pair, and V_s is the surface plasma volume. For a typical EBT-1 case, P_μ = 56 kW, $\eta_\mu \simeq 0.65$, $W_A \sim 0.3$-1 kJ, $\tau_A = 0.1$ s, $n_s = 3\times10^{17}$ m^{-3}, $E_s \sim 100$ eV, $\tau_s \sim 100$-300 μs, $V_s = 0.5$ m^3, $n \sim 10^{18}$ m^{-3}, $(T_e+T_i) \simeq 300$ eV, and V = 0.4 m^3. Of the 36 kW delivered, about 3-10 kW goes to the rings, 8-24 kW goes to the surface plasma, and the balance (2-25 kW) goes to the toroidal plasma. The value of τ_E from Eq. (14D42) is then $\tau_E \sim 4$ ms, with a factor of 4 uncertainty.

The variation of such experimental values of τ_E with collisionality (ν/Ω) is shown in Fig. 14D23, along with theoretical curves based on an equation like (14D26).

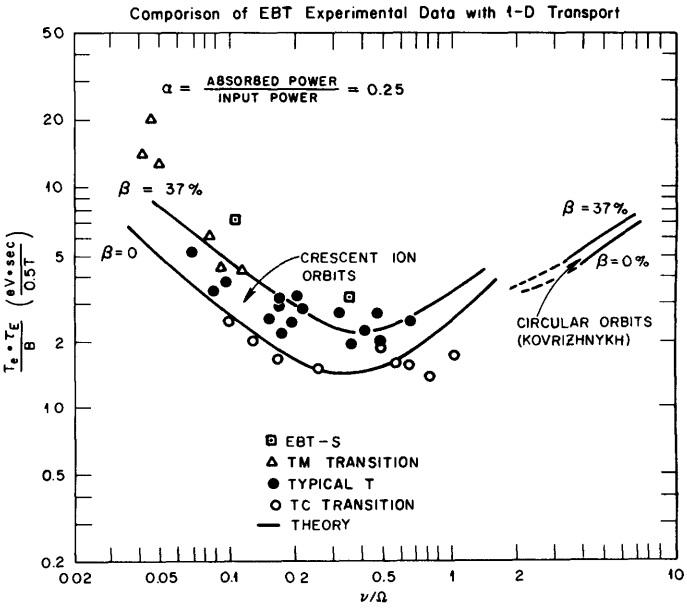

Fig. 14D23. Normalized energy confinement time vs. collisionality, for various operating conditions in EBT-1. The absolute error bars on these confinement times are quite large (not shown) but the relative variations with ν/Ω may be significant. The smooth curves represent predictions of neoclassical theory. From L. A. Berry, C. L. Hedrick, and N. A. Uckan, "ELMO Bumpy Torus", ORNL/TM-6743 (1979), Fig. 2.

Neutral atom density and impurity atom concentrations have been measured spectroscopically. The neutral hydrogen atom density in the toroidal core plasma is around 10^{16} m^{-3} (with $n_e = 2\times10^{18}$ m^{-3}). The impurity fractions of carbon and aluminum are less than 10^{-4} and 10^{-3} of n_e. The spatial variation of ultraviolet radiation emission from Al IV (Al^{+++}) is shown in Fig. 14D24.

Magnetic field errors δB give rise to a slight toroidal current in EBT-1, which can be nulled out by means of compensating coils wrapped the long way around the torus. According to theoretical estimates, magnetic field errors will not significantly enhance particle transport rates, provided that

$$\delta B/B < \rho_e/R_t \quad , \tag{14D43}$$

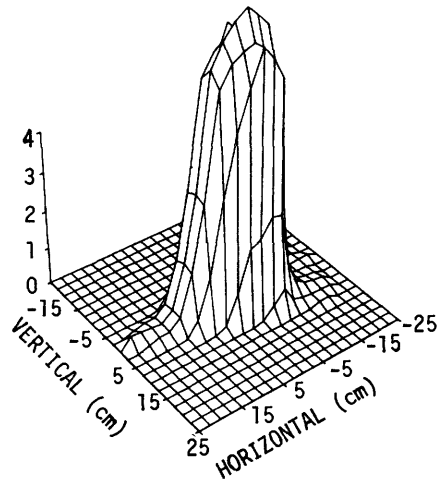

Fig. 14D24. Spatial distribution of the emission rate of the Al-IV 181.8 nm spectral line from the EBT-1 plasma reconstructed from data taken at two viewing angles. From N. H. Lazar, K. H. Carpenter, J. M. Tyson, E. S. Warden, and H. W. Moos, Nuclear Fusion 19, 571-581 (1979), Fig. 10.

where ρ_e is an electron Larmor radius.

reactors

Some design considerations for EBT reactors are:

* Match B_A to the ECRH heating frequency.
* Compute plasma parameters self-consistently.
* Maximize τ_E and Q via the parameters (R_t/R_c), β_*, (V/V_A), and drift surface areas.
* Provide impurity control and fueling.
* Provide heat removal, tritium breeding, and shielding.
* Design for ease of maintenance.
* Minimize cost of electricity.

One design study has N = 36 cells, a = 1 m, R_t = 35 m, average magnetic field B = 3.5 T, R_c = 1.5 m, and ARE coil current = 22 % of TF coil current. Assuming $\langle\beta\rangle$ = 18 %, it is estimated that $n \simeq 0.9\times10^{20}$ m^{-3}, T ~ 30 keV, Q ~ 80, $\nu/\Omega_e \simeq 0.2$, $\tau_E \simeq 2$ s, and the net electrical power P_e = 1.1 GW. About 43 MW of ECRH at 52 GHz would be required to sustain the electron rings at the fundamental resonance (B_A = 1.9 T), and about 40 MW of auxiliary rf heating (ICRH or lower hybrid heating) would be used to sustain the subignited plasma core temperature, with most of the core power losses made up by alpha heating (Bathke et al, 1981).

EBT reactors offer the following potential advantages:

* steady state operation
* simple, compact modules, with comparatively easy access and maintenance
* high-beta operation, comparatively low-cost magnets,

However, many uncertainties remain, including self-consistent plasma modeling, beta limits, alpha-particle effects, ring volume scaling, impurity control, and effects of magnetic field errors (for a reactor, $\delta B/B < \rho_e/R_t$ would be difficult to attain).

14E. Electric Field Bumpy Torus

If negative plates are placed at the ends of a magnetic mirror, electrostatically-trapped electrons will be reflected back and forth as they gradually diffuse outwards, and the radial electric field will produce high rotational drift velocities, (cf. Section 11H). Such a device, called a *Penning discharge*, can ionize low-pressure gas, so it is useful as a vacuum pump and in vacuum gages (Chapter 19).

A similar discharge can be produced by putting a positive (or negative) electrode around the midplane of the mirror. In such a modified Penning discharge, rotating "spokes" of ions and electrons were observed, accompanied by ion heating to temperatures up to 2 keV. In order to eliminate end losses, twelve mirrors were connected in a circle to form an electric field bumpy torus with superconducting coils producing peak fields of 3 T, as illustrated in Fig. 14E1. Plasmas with $n \sim 10^{16}$ - 10^{18} m^{-3} and ion temperatures up to 2 keV were produced, with $T_e << T_i$.

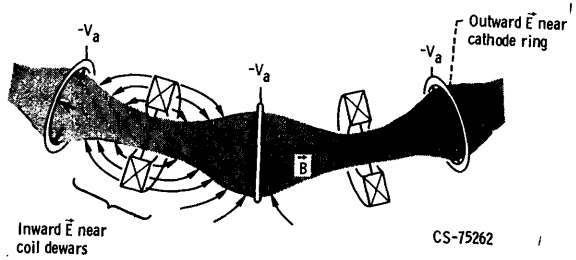

Fig. 14E1. Mirror coils, electrode rings ($-V_a$), and direction of the electric field in the electric field bumpy torus. From J. R. Roth et al, NASA Technical Paper 1411 (1979), Fig. 1. p. 3.

When the rings were biased negative, a radially inward electric field was produced in the mirrors, and radially *inward* ion transport was observed. The main limitation of the electric field bumpy torus was that plasma confinement times were comparable to the Bohm values (Sections 8F and 8G), with peak times of milliseconds. The use of electric fields is an economic means of producing hot ions, and the steady-state operation of such devices makes them useful for studying long-term plasma-wall interactions.

14. Bibliography

stellarators and torsatrons

D. T. Anderson, J. L. Shohet, S. Rehker, and J. A. Tataronis, "Neutral-beam injection calculations for torsatrons", *Nuclear Fusion 20*, 197-202 (1980).

F. Bauer, O. Betancourt, and P. Garabedian, "Numerical studies of new stellarator concepts", *Journal of Computational Physics 35*, 341-355 (1980).

T. K. Chu and Y. C. Lee, "Energy confinement comparison of ohmically heated stellarators to tokamaks", *Nuclear Fusion 20*, 803-809 (1980).

K. Ikuta and H. Hirano, "Helical magnetic configurations produced with the help of ferromagnetic materials - the Ferromak", *Nuclear Fusion 20*, 35-41 (1980).

T. W. Kruckewitt and J. L. Shohet, "Magnetic properties of ultimate torsatrons", *Nuclear Fusion 20*, 1375-1380 (1980).

K. Miyamoto, *Plasma Physics for Nuclear Fusion*, MIT Press, Cambridge, MA, 1980.

K. Miyamoto, "Recent stellarator research", *Nuclear Fusion 18*, 243-284 (1978), Review Paper.

Plasma Physics and Controlled Nuclear Fusion Research 1980 (Brussels), IAEA, Vienna, 1981.

Plasma Physics and Controlled Nuclear Fusion Research 1978 (Innsbruck), Volume II, IAEA, Vienna, 1979.

R. E. Potok, P. A. Politzer, and L. M. Lidsky, "Ion thermal conductivity in a helical toroid", *Physical Review Letters 45*, 1328-1331 (1980).

A. Pytte and A. H. Boozer, "Neoclassical transport in helically symmetric plasmas", *The Physics of Fluids 24*, 88-92 (1981).

V. D. Shafranov, "Stellarators", *Nuclear Fusion 20*, 1075-1083 (1980).

J. L. Shohet, "State of stellarator research", *Comments on Plasma Physics and Controlled Fusion 3*, 25-38 (1977).

J. L. Shohet, "Transport in toroidal stellarators and torsatrons", *Comments on Plasma Physics and Controlled Fusion 5*, 55-67, (1979).

H. R. Strauss and D. A. Monticello, "Limiting beta of stellerators with no net current", *The Physics of Fluids 24*, 1148-1155 (1981).

Plasma Physics and Controlled Fusion 5, 55-67 (1979).

V. S. Voitsenya, A. Yu Voloshko, P. M. Lats'ko, S. I. Solodovchenko, and A. F. Shtan', "Azimuthal distribution of divertor plasma fluxes in an $\ell = 3$ stellarator and torsatron", *Nuclear Fusion 19*, 1241-1244 (1979).

W VII-A Team, "Stabilization of the (2,1) tearing mode and of the current disruption in the W VII-A stellarator", *Nuclear Fusion 20*, 1093-1100 (1980).

T. S. Wang and T. H. Jensen, "Doublestar: a stellarator with three magnetic axes", *Nuclear Fusion 18*, 1459-1465 (1978).

internal rings

J. D. Barter and J. C. Sprott, "Ion cyclotron resonance heating in the Wisconsin supported toroidal octupole", *Plasma Physics 19*, 945-957 (1977).

F. F. Chen, "Status of Multipole-Surmacs as candidates for advanced fuel fusion reactors", Course on Unconventional Approaches to Fusion, Erice, Sicily, March, 1981, and UCLA PPG-553.

D. A. D'Ippolito, E. A. Adler, and Y. C. Lee, "Equilibrium and stability of high-β toroidal multipoles", *The Physics of Fluids 23*, 794-802 (1980).

R. A. Dory, D. W. Kerst, D. M. Meade, W. E. Wilson, and C. W. Erickson, "Plasma motion and confinement in a toroidal octupole magnetic field", *The Physics of Fluids 9*, 997-1009 (1966).

J. H. Halle, A. G. Kellman, R. S. Post, S. C. Prager, E. J. Strait, and M. C. Zarnstorff, "Observations of high-beta toroidal plasma", *Physical Review Letters 46*, 1394-1397 (1981).

B. Lehnert, "Plasma confinement in presence of magnetically shielded supports", *Plasma Physics 17*, 501-524 (1975).

B. Lehnert, "Power balance and stress problems of internal-conductor systems", *Nuclear Fusion 15*, 39-47 (1975).

A. W. Molvik, "Magnetic guarding of octupole hoop supports", *The Physics of Fluids 15*, 1128-1133 (1972).

G. A. Navratil and R. S. Post, "An interpretation of multipole confinement experiments", *Comments on Plasma Physics and Controlled Fusion 5*, 29 (1979).

T. Ohkawa and W. D. Kerst, "Multipole magnetic field configurations for stable plasma confinement", *Il Nuovo Cimento 22*, 784-799 (1961).

B. P. Peregood and B. Lehnert, "Magnetic traps with a spherical separatrix: Tornado traps", *Nuclear Instruments and Methods 180*, 357-386 (1981).

R. W. Schumacher, M. Fukao, A. Y. Wong, R. G. Suchannek, K. L. Lam, and K. Yatsu, "Stable confinement of high-beta collisionless toroidal plasma", *Physical Review Letters 46,* 1391-1394 (1981).

A. Y. Wong, R. W. Schumacher, M. Q. Tran, F. Fukao, P. Cheung, H. Stephanian, P. Lee, G. Skoczylas, and G. Hockney, "Surface magnetic confinement of fusion plasmas", EPRI RP 1043-1 (1980).

S. Yoshikawa, "Experiments on plasma confinement in internal-ring devices", *Nuclear Fusion 13,* 433-449 (1973). Review Paper.

electron and ion rings

R. J. Briggs, G. D. Porter, B. W. Stallard, J. Taska, and P. B. Weiss, "Efficient trapping of high-level E layers in a strong toroidal field", *The Physics of Fluids 16,* 1934-1938 (1973).

F. F. Chen, "Alternate concepts in controlled fusion", EPRI ER-429-SR (1977).

H. H. Fleischmann and T. Kammash, "System analysis of the ion-ring-compressor approach to fusion", *Nuclear Fusion 15,* 1143-1155 (1975).

S. Humphries, Jr., "Intense pulsed ion beams for fusion applications", *Nuclear Fusion 20,* 1549-1612 (1980). Review Paper.

A. Mohri, K. Narihara, Y. Tomita, T. Tsuzuki, M. Hasegawa, and K. Ikuta, "Experiment on plasma confinement by long-lived intense REB ring", *8th International Conference on Plasma Physics and Controlled Nuclear Fusion Research (Brussels, 1980),* IAEA, Vienna, 1981.

A. Mohri, K. Narihara, T. Tsuzuki, Y. Kubota, Y. Tomita, K. Ikuta, and M. Masuzaki, "Experiments on plasma confinement by relativistic-electron-beam ring", *Plasma Physics and Controlled Nuclear Fusion Research (Innsbruck, 1978),* IAEA, Vienna, 1979, Volume III, p. 311-320.

M. Tuszewski, D. J. Rej, and H. H. Fleischmann, "Adiabatic magnetic compression of field-reversing E layers", *Physical Review Letters 43,* 449-452 (1979).

EBT -- general

R. A. Dandl et al, "Experimental and theoretical studies of the Elmo Bumpy Torus (EBT)", *Plasma Physics and Controlled Nuclear Fusion Research (Innsbruck, 1978),* IAEA, Vienna, 1979, Volume II, p. 365-372.

J. C. Glowienka, "ELMO Bumpy Torus: an alternate concept to tokamaks and mirrors", *Journal of Vacuum Science and Technology 18,* 1088-1097 (1981).

D. B. Nelson, "Effects of hot electrons on magnetohydrodynamic modes in ELMO Bumpy Torus", *The Physics of Fluids 23,* 1850-1856 (1980).

N. A. Uckan, Editor, Proceedings of the EBT Ring Physics Workshop (1979) CONF-791228, 1980.

EBT equilibrium and stability

D. B. Batchelor and C. L. Hedrick, "A preliminary investigation of trapped-particle instabilities in EBT", *Nuclear Fusion 19,* 235-248 (1979).

J. P. Friedberg, "Toroidal MHD equilibrium of the Elmo Bumpy Torus", *Nuclear Fusion 20,* 673-682 (1980).

D. B. Nelson and C. L. Hedrick, "Macroscopic stability and beta limit in the Elmo Bumpy Torus", *Nuclear Fusion 19,* 283-292 (1979).

EBT Heating and ring physics

D. B. Batchelor and R. C. Goldfinger, "A theoretical study of electron-cyclotron absorption in Elmo Bumpy Torus", *Nuclear Fusion 20,* 403-418 (1980).

D. B. Batchelor, R. C. Goldfinger, and H. Weitzner, "Ray tracing near the electron cyclotron frequency with application to EBT", *IEEE Transactions on Plasma Science PS-8*, 78-89 (1980).

N. A. Uckan et al, "Physics of hot electron rings in EBT: theory and experiment", *Plasma Physics and Controlled Nuclear Fusion Research (Brussels, 1980)*, IAEA, Vienna, 1981.

N. A. Uckan and D. B. Batchelor, "Heating techniques for an EBT reactor", ORNL/TM-6346 (1978).

EBT transport, power balance, and reactor

C. C. Baker, G. A. Carlson, and R. A. Krakowski, "Trends and developments in magnetic confinement fusion reactor concepts", *Nuclear Technology/ Fusion 1*, 5-78 (1981).

C. G. Bathke, D. J. Dudziak, R. A. Krakowski, W. B. Ard, D. A. DeFreece, D. E. Driemeyer, R. E. Juhala, R. J. Kashuba, P. B. Stones, L. M. Waganer, D. S. Zuckerman, and D. W. Lieurance, "The Elmo Bumpy torus reactor", *Proceedings of the 4th ANS Topical Meeting on the Technology of Controlled Nuclear Fusion (King of Prussia, PA, 1980)*, DOE, 1981.

S. K. Borowski, N. A. Uckan, E. F. Jaeger, and T. Kammash, "A simple annulus power balance in EBT experiments", *Nuclear Fusion 20*, 177-188 (1980).

R. D. Hazeltine and P. J. Catto, "Bumpy torus transport in the low collision frequency limit", *The Physics of Fluids 24*, 290-306 (1981)

E. F. Jaeger and C. L. Hedrick, Jr., "Radial transport in the Elmo Bumpy Torus in collisional regimes", *Nuclear Fusion 19*, 443-453 (1979).

D. A. Spong, E. G. Harris, and C. L. Hedrick, "Kinetic transport properties of a bumpy torus with finite radial ambipolar field", *Nuclear Fusion 19*, 665-683 (1979).

U. S. Department of Energy, Proceedings of the EBT Transport Workshop, DOE/ET-0112 (1979).

EBT experiments

L. Bighel and J. A. Cobble, "Electron heating and confinement measurements in the EBT-S toroidal core plasma with Thomson scattering", *Physical Review Letters 46*, 430-433 (1981).

M. Fujiwara et al, "Experimental studies of plasma confinement in the bumpy torus", *Plasma Physics and Controlled Nuclear Fusion Research (Brussels, 1980)*, IAEA, Vienna, 1981.

N. H. Lazar, K. H. Carpenter, J. M. Tyson, E. S. Warden, and H. W. Moos, "Spatial distribution of impurities and H neutrals in Elmo Bumpy Torus (EBT)", *Nuclear Fusion 19*, 571-582 (1979).

electric field bumpy torus

J. R. Roth, "Effects of applied dc radial electric fields on particle transport in a bumpy torus plasma", *IEEE Transactions on Plasma Science PS-6*, 158-165 (1978).

J. R. Roth and G. Gerdin, "Characteristics of the NASA Lewis bumpy torus plasma generated with high positive or negative applied potentials", *Plasma Physics 19*, 423-446 (1977).

J. R. Roth, W. M. Krawczonek, E. J. Powers, J. Y. Hong, and Y. C. Kim, "Inward transport of a toroidally confined plasma subject to strong radial electric fields", *Physical Review Letters 40*, 1450-1453 (1978).

CHAPTER 15

INERTIAL CONFINEMENT FUSION (ICF)

15A. Introduction

ICF reactors

The general idea of an ICF reactor is illustrated in Fig. 15A1. A small target pellet several mm in diameter is injected into the chamber. As it passes through the center of the chamber, it is compressed and ignited by powerful laser beams or ion beams, producing a small thermonuclear explosion. Vacuum pumps remove gases and debris between explosions. New pellets are injected and ignited about 1-10 times/s. Heat from the thermonuclear explosions is deposited in the chamber walls and extracted by coolant to generate steam, which is used to drive turbine-generators (not shown) for production of electricity.

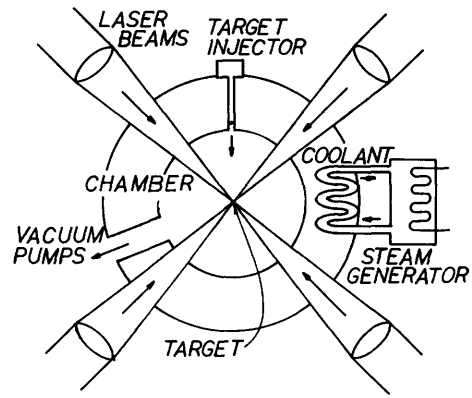

Fig. 15A1. The general idea of an ICF reactor (simplified for clarity).

Some important features of the ICF reactor concept include:

* *energy focusing.* The laser beam or ion beam *drivers* must focus a great amount of energy (1 - 10 MJ) onto a small target pellet in a short time ($\sim$ 10 ns).
* *target compression.* Ablation of matter from the outside of the target pellet causes an inward force, compressing the target to high densities. Final fuel densities $\rho \sim 1000$ g/cm^3 are needed to achieve high energy gains Q (fusion energy/driver energy). The energy required for such compression is much less than the energy which would be required to heat the whole target up to ignition temperature.
* *burn wave.* Spherical shock waves ignite the fuel at the center of the pellet. If the pellet density is high enough, the fusion product alpha particle energy will be trapped in surrounding fuel, heating it up to ignition temperature. Then a thermonuclear burn wave may propagate outwards through the fuel, until expansion decreases the fuel density

and quenches the burn. Only a small fraction of the fuel mass needs to be heated up to ignition.

Pure deuterium fuel can be ignited by fusion product alphas and neutrons from a central DT fuel region. Sufficient tritium can be produced by the DD reactions to compensate for that consumed in the DT core, so external breeding may be avoided, if this scheme is used, at the expense of higher input energy reguired for ignition. (Choi, Blue, and Miley, 1979).

Small fission explosions can also be ignited by compressing ^{235}U or ^{239}Pu fuel pellets (Winterberg, 1973; Seifritz and Ligou, 1975; Cole and Renken, 1975), but very high input energies are required.

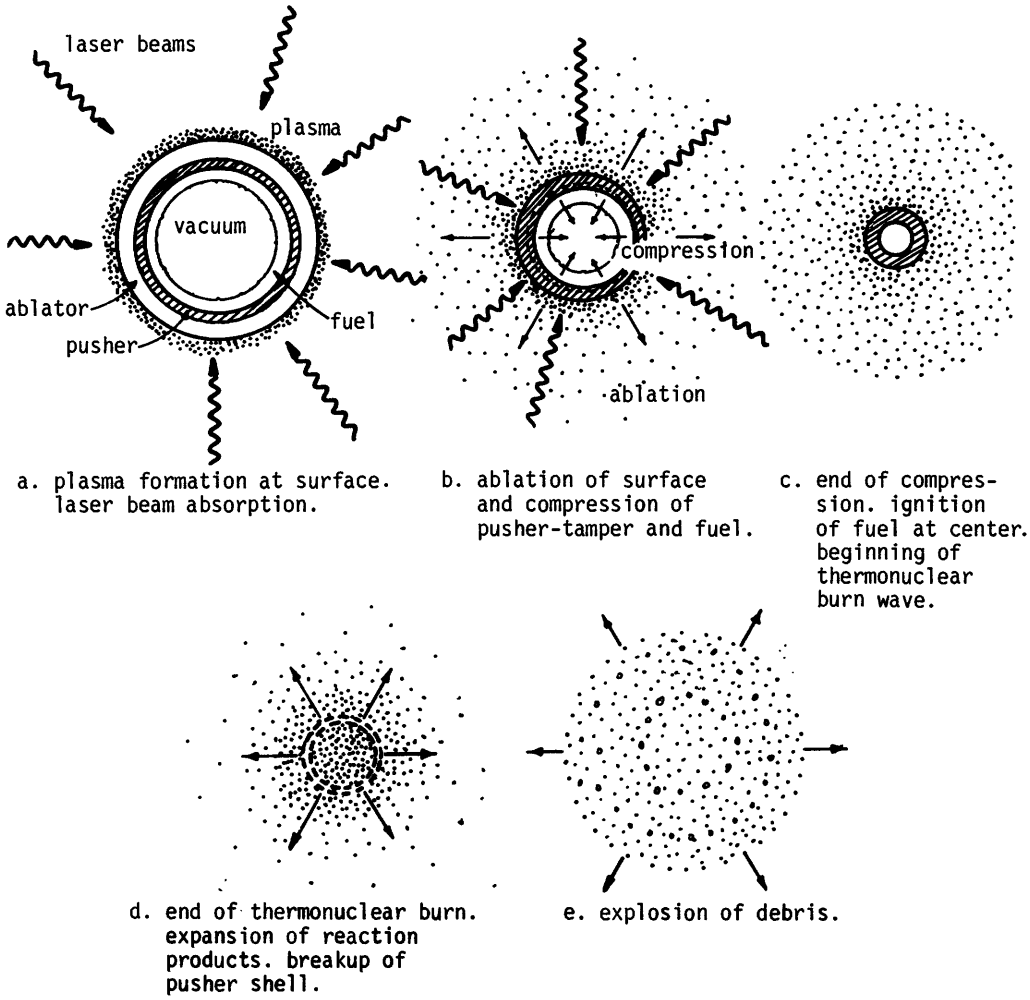

Fig. 15A2. Compression and burn of a spherical ICF target.

compression

When the laser or ion beams strike the target surface, some of the surface atoms will be vaporized and ionized, forming a plasma around the target. The laser beam energy will be partially reflected by this plasma, and partially absorbed by it. Heat conducted to the target surface will cause continuing *ablation* (erosion) of the surface. As matter ablates away from the surface, a reactive force is produced which compresses the shell inwards (similar to the thrust of a rocket produced by expelling matter). Ablative compression of a target shell by laser beams is illustrated in Fig. 15A2.

At the end of compression, the fuel at the pellet center may be ignited by spherical shock waves, resulting in a thermonuclear burn wave propagating outwards, if the density is high enough. The attainable energy gain will be discussed in Section 15B.

It is desirable to delay heating until compression is nearly complete. In some cases, high energy "suprathermal" electrons or shock waves travel inwards and heat the fuel before compression is complete. This *preheating* raises the internal fuel pressure, and prevents the attainment of high fuel densities. Thus, preheating must be avoided if compression is to be successful.

Breakup of the target shell by the *Rayleigh-Taylor instability*, as illustrated in Fig. 15A3, is another major problem to be avoided (Section 15D).

problems

The main problems to be solved in development of ICF reactors are listed in Table 15A1.

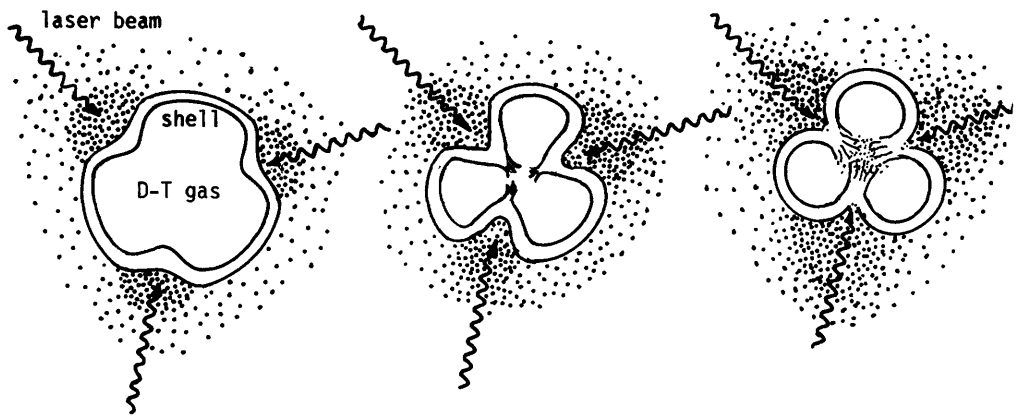

a. asymmetric irradiation.

b. growth of bumps on surface leads to spikes.

c. spikes lead to mixing of shell with fuel.

Fig. 15A3. Growth of the Rayleigh-Taylor instability, spoiling compression of the target shell.

Table 15A1. Problems of ICF reactor development.

theory	Understand the physics of energy absorption, reflection, heat transport, compression, instabilities ignition, and burn (Sections 15B, 15C, 15D).
experiments	Attain satisfactory values of the critical elements for high energy gain (Sections 15B, 15D): beam-to-fuel coupling efficiency compression along a cold-fuel isentrope implosion symmetry driver energy per unit fuel mass
target manufacture	Develop an automated system to manufacture high-gain spherical targets accurately and cheaply (cost $\lesssim$ 10¢ each) (Section 15E). Select target materials to avoid production of long-lived radioisotopes.
target injection	Develop a target injection and guidance system to ensure that the target is at the focus of the beams when the driver is fired.
diagnostics	Measure the parameters of experiments, such as implosion velocity, density distributions, energy distributions, ablated matter, laser beam reflection, implosion symmetry, and fusion reaction products, with good space and time resolution (Section 15F).
chambers	Develop reactor chambers to withstand repeated ($> 10^8$) explosions without failure (Section 16H). (A 1000 MJ yield has the explosive energy of 240 kg of TNT, but less momentum).
pumping	Remove debris and gases rapidly between explosions, in order to avoid scattering and attenuating the incident driver beams.
drivers	Develop laser or ion beams with high energy (1-10 MJ), high pulse repetition rate (1-10 Hz), proper pulse shape (duration 10-20 ns), suitable wavelength (lasers), and good efficiency ($\gtrsim$ 8 %).
reliability	Develop power supplies, power conditioning equipment, diodes, and optical components to operate reliably for $> 10^8$ shots.

15B. Energy Gain

required energy gain

The energy gain of an ICF target pellet is

$$Q \equiv \frac{\text{(fusion energy produced)}}{\text{(driver beam energy incident)}} \equiv \frac{W_F}{W_d} \quad . \tag{15B1}$$

(The symbol G is often used for gain, instead of Q.) The driver efficiency is defined to be

$$\eta_d \equiv \frac{\text{(driver beam energy incident on target)}}{\text{(electrical energy to driver)}} \tag{15B2}$$

Some of the recirculated electrical energy must be used to run coolant pumps, etc. If the fraction of recirculated electrical energy going to the driver is f_d, then the input efficiency of Chapter 4 becomes

$$\eta_{in} \sim f_d \eta_d \quad . \tag{15B3}$$

Typically $f_d > 0.95$, so

$$\eta_{in} \sim \eta_d \quad . \tag{15B4}$$

Assuming a blanket energy gain $M \sim 1.2$ with DT fuel, Eq. (4C3) becomes

$$1.16Q + 1 \simeq 1/\varepsilon\eta_e\eta_d \tag{15B5}$$

In order for a reactor to be economical, we require the recirculating power fraction $\varepsilon < 0.25$. Assuming a thermal conversion efficiency $\eta_e \simeq 0.35$, Eq. (15B5) simplifies to

$$\eta_d Q > 10 - 0.9\eta_d \quad .$$

Assuming that $\eta_d << 1$, this becomes

$$\eta_d Q > 10 \quad . \tag{15B6}$$

Thus, if a driver efficiency $\eta_d = 0.1$ is attainable, the required energy gain is $Q > 100$. (In a fusion-fission hybrid with $M \sim 10$, the required Q would be substantially less.) The attainable value of Q can be estimated in terms of the fuel burnup fraction f_b of the exploding pellet.

burnup fraction

After compression, a fusion burn wave propagates rapidly outwards through the fuel, igniting it, and raising it to an effective burn temperature T_b. The outer layers of the pellet expand, and a rarefaction wave propagates inwards at the ion sound speed

$$c_s = [(\gamma_e kT_e + \gamma_i kT_i)/m_i]^{1/2} = (10kT/3m_i)^{1/2} \tag{15B7}$$

where $m_i = 4.2\text{x}10^{-27}$ kg is the average mass of DT fuel ions. Thus, the time it takes for the pellet to disassemble is

$$\tau_s = R/c_s \tag{15B8}$$

where R is the fuel radius at the end of compression. The average time that the fuel ions are able to react before the rarefaction wave quenches burn is

$$\tau_b = \frac{\int_0^{\tau_s} dt\, m(t)}{m_0} = \frac{\int_0^{\tau_s} dt\, (4\pi\rho/3)(R-c_s t)^3}{(4\pi\rho/3)R^3} = \frac{R}{4c_s} \qquad (15B9)$$

where m_0 is the initial fuel mass, and m(t) is the mass remaining compressed. The fuel mass density is

$$\rho \equiv n m_i \quad , \qquad (15B10)$$

where n is the compressed ion density. Using Eqs. (15B9) and (15B10) in (4D7), we find the fuel burnup fraction

$$f_b \simeq \frac{\rho R}{\rho R + 8 c_s m_i / \langle\sigma v\rangle} \quad , \qquad (15B11)$$

where $\langle\sigma v\rangle$ is the reaction rate parameter of the compressed fuel. For $20 < T_b < 90$ keV, this becomes

$$f_b = \frac{\rho R}{\rho R + B} \qquad (15B12)$$

where $B \sim 110$ kg/m^2 = 11 g/cm^2 ($\pm$ 15 % for $20 \leqq T \leqq 90$ keV).

attainable energy gain

let

$m \equiv$ ~~initial~~ final fuel mass

$m_h \equiv$ mass of central "hot" fuel region heated to ignition

$w_F \equiv$ fusion energy released per unit mass burned = 3.37×10^{14} J/kg = 3.37×10^{11} J/g.

$w_c \equiv$ energy required per unit mass to compress the fuel to the desired density.

$w_h \equiv$ additional energy per unit mass needed to heat the central fuel up to ignition temperature ($\sim$ 5 keV) = 5.8×10^{11} J/kg = 5.8×10^{8} J/g.

$\eta_c \equiv$ coupling efficiency

$$\equiv \frac{\text{(energy going into pellet compression and heating)}}{\text{(incident driver beam energy)}} \quad .$$

Then

$$\eta_c W_d = m w_c + m_h w_h \qquad (15B13)$$

and

$$W_F = f_b m w_F \quad . \qquad (15B14)$$

Using these equations in (15B1), we find

$$Q = \frac{\eta_c f_b w_F}{w_c + (m_h/m)w_h} \tag{15B15}$$

Typical maximum values are $\eta_c \lesssim 0.15$ and $f_b \lesssim 0.4$. If *all* the fuel were heated ($m_h/m = 1$), then

$$Q < \eta_c f_b w_F / w_h \lesssim 35 \quad . \tag{15B16}$$

Therefore, it is desirable to minimize (m_h/m), in order to maximize the attainable Q.

The minimum energy needed for compression is the *Fermi energy*

$$w_f = w_{f0}(\rho/\rho_s)^{2/3} \tag{15B17}$$

where $w_{f0} = 1.1 \times 10^8$ J/kg $= 1.1 \times 10^5$ J/g and $\rho_s = 0.213$ g/cm^3 is the density of solid DT fuel at atmospheric pressure. (For a reactor $\rho \gtrsim 1000\rho_s$). If $w_c/w_f = 1$, the compression would be at constant entropy (isentropic), so we will call the ratio w_c/w_f the *isentrope* of the compression. (Other definitions of this term have been used.) One might expect to attain $w_c/w_f \sim 2$ - 10.

The range of fusion product alpha particles is

$$\rho R_\alpha \simeq \frac{0.104 T_e^{5/4}[1 + 0.3 \log_{10}(\rho/\rho_s)]}{1 + 0.0058\ T_e^{5/4}} \quad (\text{kg/m}^2) \tag{15B18}$$

where T_e is in keV. For $T_e \sim 10$ keV and $\rho/\rho_s \sim 1000$, this becomes $\rho R_\alpha \simeq 3$ kg/m^2 = 0.3 g/cm^2, or

$$R_\alpha \simeq \frac{0.3}{\rho_s}\frac{\rho_s}{\rho} = 1.4(\rho_s/\rho) \quad (\text{cm}) \quad .$$

Let R_h = the radius of the heated fuel region. In order to attain ignition, it is required that $R_h \geqq R_\alpha$. The minimum value of R_h is also limited by compression assymetry. If v_r is the radial compression velocity and δv is the tangential velocity of part of the shell (perpendicular to v_r), then

$$R_h \geqq (\delta v/v_r)R_0$$

where R_0 is the initial (uncompressed) fuel radius. Thus, the minimum radius of the heated region is

$$R_h \geqq \text{larger of} \begin{cases} 1.4\ \rho_s/\rho \quad (\text{cm}) \\ R_0 \delta v/v_r \end{cases} \tag{15B19}$$

The heated mass fraction is

$$\frac{m_h}{m} = \frac{(4\pi/3)\rho R_h^3}{(4\pi/3)\rho R^3} = \frac{(4\pi/3)\rho R_h^3}{4\pi\rho_0 R_0^2 \Delta R_0} = \frac{\rho R_h^3}{3\rho_0 R_0^2 \Delta R_0} \tag{15B20}$$

where ΔR_0 is the initial thickness of a thin spherical shell of fuel, and ρ_0 is the initial fuel density.

The compressed fuel radius is related to the initial radius by

$$(4\pi/3)R^3\rho = 4\pi R_0^2 \Delta R_0 \rho_s$$

$$R/R_0 = [3(\rho_s/\rho)(\Delta R_0/R_0)]^{1/3} \tag{15B21}$$

The driver energy may be related to the implosion velocity and to the final target density by energy conservation:

(coupled driver energy) = (kinetic energy of implosion) = (compression energy) + (heating energy)

$$\eta_c W_d = \tfrac{1}{2} m v_r^2 = m(w_c/w_f)w_f + m(m_h/m)w_h \quad , \tag{15B22}$$

from which the implosion velocity is estimated to be

$$v_r = (2\eta_c W_d/m)^{1/2} \quad . \tag{15B23}$$

Using Eqs. (15B20) and (15B17) in (15B22), we find

$$\frac{\eta_c W_d}{m} = \frac{v_r^2}{2} = w_{f_0}\left(\frac{w_c}{w_f}\right)\left(\frac{\rho}{\rho_s}\right)^{2/3} + \frac{\rho R_h^3 w_h}{3\rho_0 R_0^2 \Delta R_0} \tag{15B24}$$

where R_h can be estimated from (15B19). It is desirable to maximize the initial fuel density ρ_0, in order to minimize the required driver energy, so we will use $\rho_0 = \rho_s$. For a given value of $\eta_c W_d/m$, Eq. (15B24) can be used to estimate the *attainable compression ratio* ρ/ρ_s. It has been assumed that a small region of the fuel is heated up to ignition energy w_h. If $\eta_c W_d/m$ is too small, Eq. (15B24) cannot be satisfied for any value of ρ/ρ_s, meaning that ignition is impossible.

The gain is determined by the parameters specifying target size, driver energy, coupling, isentrope, and asymmetry, as illustrated in Fig. 15B1.

EXAMPLE PROBLEM 15B1

It is desired to attain $\rho R_h = 0.4$ g/cm^2 and $\rho/\rho_s = 1000$. If $\eta_c = 0.12$, $w_c/w_f = 4$, $\Delta R_0/R_0 = 0.1$, and $\delta v/v_r = 0.01$, estimate the attainable energy gain, the fuel mass, and the required driver energy and implosion velocity.

Since $\rho_s = 0.213$ g/cm^3, $\rho = 213$ g/cm^3 and $R_h = 1.88\times10^{-3}$ cm. Since $R_h \geq (\delta v/v_r)R_0$, we find $R_0 \leq 0.188$ cm. We take the largest value, in order to maximize R and f_b. Then $\Delta R_0 = 0.0188$ cm, and $m = 4\pi R_0^2 \Delta R_0 \rho_s = 1.77\times10^{-3}$ g. From Eq. (15B21), $R = 1.26\times10^{-2}$ cm. Then $m_h/m = (R_h/R)^3 = 3.32\times10^{-3}$. From Eq. (15B17) $w_f = 1.1\times10^{10}$ J/kg, so $w_c = 4.4\times10^{10}$ J/kg. With $\rho R = 2.68$ g/cm^2 in Eq. (15B12), we find $f_b = 0.196$. Then, from Eq. (15B15) $Q = 173$. The required driver energy is

$$W_d = (mw_c + m_h w_h)/\eta_c = 0.68 \text{ MJ} .$$

From Eq. (15B23), $v_r = 3.0\times10^5$ m/s .

More accurate analyses predict gains lower than estimated from this simple two-temperature model, partly because it is difficult to limit the heating strictly to the small region inside R_h. Some conservative estimates of attainable gain as a function of driver energy are shown in Fig. 15B2.

From Fig. 15B1, the key parameters affecting pellet gain are

target size	R_0, ΔR_0
driver energy	W_d
coupling efficiency	η_c
isentrope	w_c/w_f
compression asymmetry	$\delta v/v_r$.

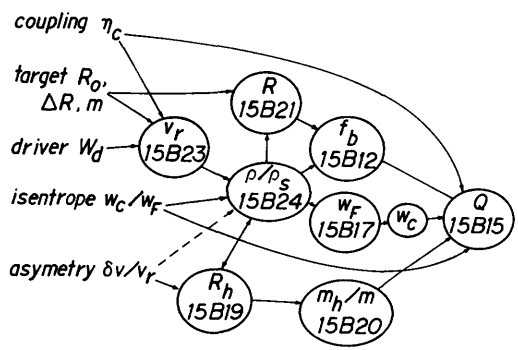

Fig. 15B1. Relation of parameters determining energy gain. For clarity, not all connecting lines have been shown. Numbers refer to equations. The dashed line indicates the possibility of Rayleigh-Taylor instability spoiling compression.

Higher gain can be attained by increasing target size and driver energy, but energy yields are probably limited to a few GJ by chamber structural problems (Section 16H), and large drivers entail high capital costs. Therefore, it is important to optimize the coupling efficiency, isentrope, and compression symmetry.

The coupling efficiency can be written

$$\eta_c = \eta_a \eta_h \eta_{tr} \qquad (15B25)$$

where η_a is the fraction of the beam energy absorbed by the target, η_h is the hydrodynamic efficiency (fraction of absorbed energy going into kinetic energy of implosion $\frac{1}{2}mv_r^2$), and η_{tr} is the transformation efficiency with which the kinetic energy is converted into compression and heating when the imploding shell converges at the center.

For ion beams the values of $n_a n_h$ can be high, but with laser beams substantial energy can be lost by backscattering or by conversion to energetic particles which do not couple well to target compression.

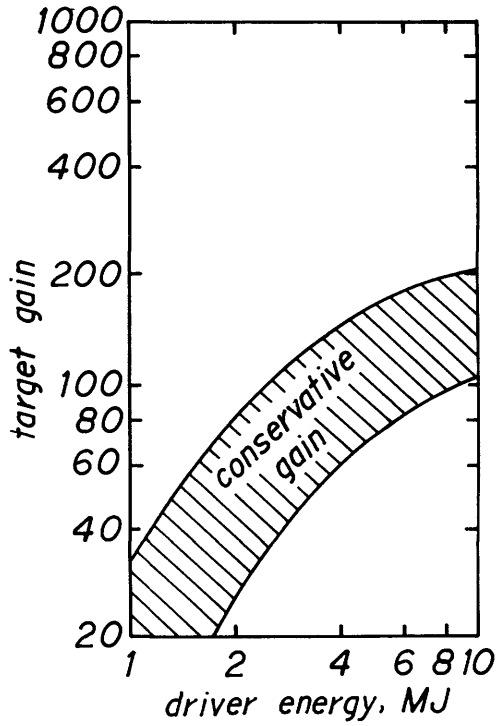

Fig. 15B2. Conservative estimates of energy gain as a function of driver energy. The upper limit of the band is anticipated for KrF lasers, and the lower limit, for CO_2 lasers, light ion beams, and heavy ion beams. From K. A. Brueckner et al, EPRI AP-1371 (1980), Fig. 2-1, p. 2-5.

15C. Laser-Plasma Interactions

plasma production

The laser beam intensity required to produce ionization and breakdown is approximately

$$I \gtrsim nT_e v_e \ . \qquad (15C1)$$

Thus, $I \sim 2\times10^{14}$ W/m^2(2×10^{10}W/cm^2) for $n \sim n_c = 1.1\times10^{15}/\lambda^2$ (Eq. 10G1), $T_e \sim 2$ eV (Fig. 3E1), $v_e \sim v_{Te} \equiv (kT_e/m_e)^{\frac{1}{2}}$, and $\lambda \sim 1$ μm. The beam intensity is related to the electric field E_0 of the wave by

$$I = \varepsilon_0 c E_0^2/2 \qquad (15C2)$$

where ε_0 is the permittivity of free space and c is the speed of light. At high laser beam intensities $\sim10^{19}$ W/m^2 (10^{15}W/cm^2) the wave electric field ($\sim 10^{11}$ V/m) is strong enough to strip electrons directly from atoms. Thus, when an intense laser beam strikes a target, the surface will be immediately ionized, producing an expanding plasma, with density decreasing radially outwards. The laser beam cannot penetrate beyond the plasma layer with $n = n_c$, where the beam is reflected, as illustrated in Fig. 15C1.

The initial target shell density $n_0 \sim 5\times10^{28}$ m^{-3}. For laser wavelengths of 0.25 μm (KrF laser), 1.06 μm (Nd glass laser), and 10.6 μm (CO_2 laser), the critical densities are $n_c = 1.8\times10^{28}$, 10^{27}, and 10^{25} m^{-3}, respectively. Therefore, only the short-wavelength lasers can penetrate near to the target surface. Long-wavelength laser beams must be absorbed very far from the surface, with the heat carried radially inwards by thermal conduction. The wave energy may be absorbed or scattered by several processes, including reflection from the critical density layer, collisional absorption, resonant absorption, parametric decay, stimulated Brillouin scattering, and stimulated Raman scattering.

collisional absorption

At the high frequencies of laser radiation, ion motion may be ignored. Adding an electron-ion collision term $-\nu_{ei}\vec{u}_e$ to Eqs. (5E5) and setting $B = 0$ ($\omega_{ce} = 0$), we find

$$\vec{J} = -ne\vec{u}_e = \frac{-i\varepsilon_0\omega_{pe}^2\vec{E}}{\omega + i\nu_{ei}} \quad . \qquad (15C3)$$

For this case the conductivity and dielectric tensor components become

$$\sigma_{xx} = \sigma_{yy} = \sigma_{zz} = \frac{-i\varepsilon_0\omega_{pe}^2}{\omega + i\nu_{ei}} \qquad (15C4)$$

$$\varepsilon_{xx} = \varepsilon_{yy} = \varepsilon_{zz} = 1 - \frac{\omega_{pe}^2}{\omega(\omega+i\nu_{ei})} \qquad (15C5)$$

and the other components are zero. For electromagnetic waves $\vec{k}\cdot\vec{E} = 0$, and Eq. (5E14) reduces to

$$-k^2\vec{E} + \frac{\omega^2}{c^2}\left[1 - \frac{\omega_{pe}^2}{\omega(\omega+i\nu_{ei})}\right]\vec{E} = 0 \qquad (15C6)$$

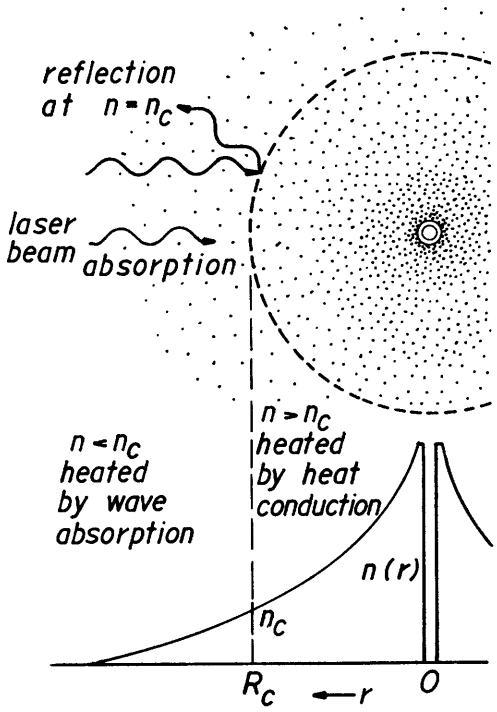

Fig. 15C1. The plasma cloud surrounding a target sphere, and radial variation of plasma density.

from which

$$\omega^2 = k^2c^2 + \omega_{pe}^2/(1+i\nu_{ei}/\omega) \simeq k^2c^2 + \omega_{pe}^2(1-i\nu_{ei}/\omega), \quad (\nu_{ei}/\omega << 1) \; . \qquad (15C7)$$

The real and imaginary parts of $\omega = \omega_r + i\gamma$ are

$$\omega_r = (k^2c^2 + \omega_{pe}^2)^{\frac{1}{2}} \quad , \qquad \gamma = -\nu_{ei}\omega_{pe}^2/2\omega^2 = -n\nu_{ei}/2n_c \quad . \qquad (15C8)$$

The wave intensity is

$$I(t) \propto E^2(t) = E_0^2\exp(-n\nu_{ei}t/n_c) = E_0^2\exp(-n\nu_{ei}x/n_cc) \qquad (15C9)$$

where x is the distance along the beam path in the plasma. The characteristic attenuation length of beam intensity is

$$\ell_a = n_c c/n\nu_{ei} \quad . \tag{15C10}$$

For example, if $\lambda \sim 1$ μm, $n \sim n_c \sim 10^{27}$ m^{-3} and $T_e = 1$ keV, then the Coulomb logarithm $L \sim 7.1$ (Table 2E2), $\nu_{ei} \sim 4.8\times10^{11}$ s^{-1} (Eq. 2E57), and $\ell_a \sim 630$ μm. Thus, collisional absorption (also called *inverse bremsstrahlung*) has a long scale length, especially at high temperatures or low plasma densities. Collisional absorption can be more significant for short-wavelength laser beams, since higher plasma densities are accessible to them. For example, if $\lambda \sim 0.25$ m, $n \sim n_c \sim 1.8\times10^{28}$ m^{-3}, and $T_e \sim 1$ keV, then $L \sim 5.7$, $\nu_{ei} \sim 6.9\times10^{12}$ s^{-1}, and $\ell_a \sim 44$ μm.

In addition to collisional absorption, wave energy may be absorbed by coupling to plasma waves, especially

* *electron plasma waves* $\omega^2 = \omega_{pe}^2 + 3k^2v_{Te}^2$ (high-frequency electron charge-density oscillations).
* *ion acoustic waves* $\omega^2/k^2 = c_s^2 \equiv (\gamma_e kT_e + \gamma_i kT_i)/m_i$ (low-frequency charge-density oscillations driven by electron pressure transmitted to ions via the self-consistent electric field).

resonance absorption

Consider a plasma with density increasing linearly in the z direction:

$$n(z) = n_c z/L_n \tag{15C11}$$

where n_c is the cutoff density and L_n is a scale length. Laser radiation may be incident on this inhomogeneous plasma at various angles θ relative to the z direction. If there is a component E_z of the wave electric field at the critical density layer $n = n_c$, electron plasma waves there will be driven to large amplitude, absorbing incident wave energy.

Ignoring collisions ($\nu_{ei} \simeq 0$) and setting $k^2 = k_x^2 + k_z^2$, Eq. (15C7) becomes

$$k_x^2c^2/\omega^2 + k_z^2c^2/\omega^2 = 1 - \omega_{pe}^2/\omega^2 \tag{15C12}$$

The momentum of the wave is $(h/2\pi)k$, where h is Planck's constant. There is nothing to change the x component of the wave momentum, so

$$k_x = \text{constant} = \omega\sin\theta/c \quad , \tag{15C13}$$

Since $\omega_{pe}^2/\omega^2 = n/n_c$ (Eqs. 10G1 and 5E8), Eq. (15C12) becomes

$$k_z^2c^2/\omega^2 = 1 - \sin^2\theta - n/n_c = \cos^2\theta - n/n_c \quad . \tag{15C14}$$

Therefore, k_z will drop to zero (the wave will be reflected) at the z position where

$$n(z)/n_c = \cos^2\theta \quad . \qquad (15C15)$$

Reflection of waves in accordance with Eq. (15C15) and the resultant variation of E_z^2 with z are illustrated in Fig. 15C2. Resonance absorption depends upon the magnitude of E_z at the critical layer ($n = n_c$). Beyond the reflection point, the wave decays exponentially. At small θ, enough of the wave can "tunnel" through to the critical layer to permit significant resonance absorption. The fractional absorption of the wave intensity by resonance absorption is given approximately by the formula

$$f_a \simeq 1.6\,\tau^2 \exp(-4\tau^3/3) \qquad (15C16)$$

(resonance absorption only)

$$\tau \equiv (2\pi L_n/\lambda_0)^{1/3}\sin\theta \quad ,$$

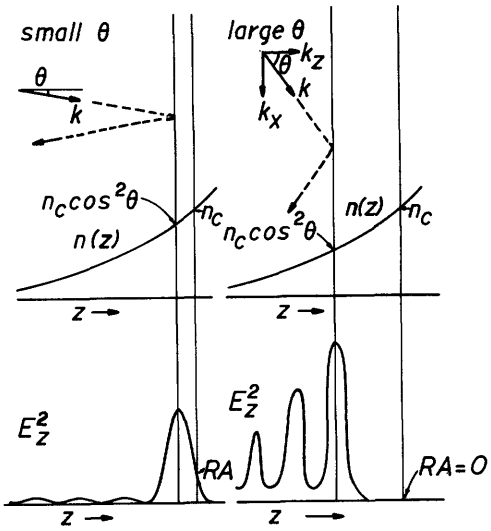

Fig. 15C2. Reflection of incident waves at $n = n_c\cos^2\theta$, and the resultant variation of E_z^2 with z. At small θ, E_z will be small, but the wave can penetrate close to n_c. At large θ, E_z will be large, but the wave cannot penetrate near n_c. (Not to scale.) RA denotes the wave amplitude available to drive resonance absorption.

where λ_0 is the vacuum wavelength of the incident laser beam (Kruer, 1980, normalized to a peak value of 0.5). This function is illustrated in Fig. 15C3 for various L_n/λ_0. The absorption is maximum at $\tau \sim 0.8$. Large values of L/λ_0 permit resonance absorption only for a narrow range of incident angles. If $L_n \sim 100$ μm, then resonance absorption would be significant at long wavelengths, such as $\lambda_0 \sim 10$ μm, and less effective at short wavelengths $\lambda_0 \lesssim 1$ μm. The general trends of collisional and resonance absorption processes with wavelength are illustrated in Fig. 15C4.

wave-coupling processes

Many processes of interest are based on the *ponderomotive force* on electrons

$$\vec{F}_{pm} = -\frac{\omega_{pe}^2}{\omega_0^2}\vec{\nabla}\langle\tfrac{1}{2}\varepsilon_0 E^2\rangle \qquad (15C17)$$

where ω_0 is the incident laser beam frequency. [For a concise derivation of this equation, see Chen, *Introduction to Plasma Physics*, Plenum Press, New York, 1974, p. 256-258]. The quantity $\langle\frac{1}{2}\varepsilon_0 E^2\rangle$ is the average energy density (pressure) of the electric field. Assuming that the wave pressure and the plasma pressure have comparable gradient scale lengths, the ratio of the ponderomotive force to the pressure gradient force is

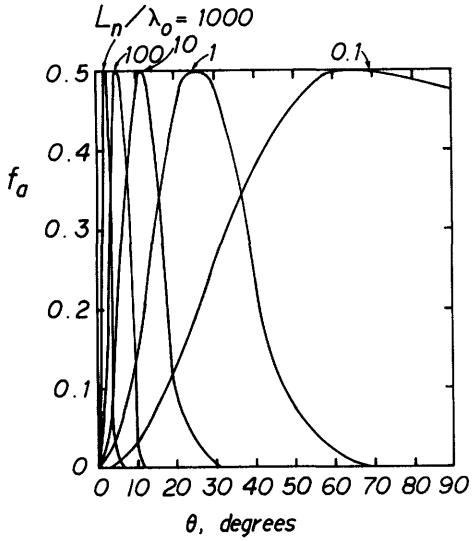

Fig. 15C3. Fractional absorption vs. angle of incidence for resonance absorption at various ratios of density gradient scale length to incident wavelength. The values of f_a have been normalized to a peak value of 0.5. The heights of the peaks may vary with experimental conditions, but the curve shapes should stay the same.

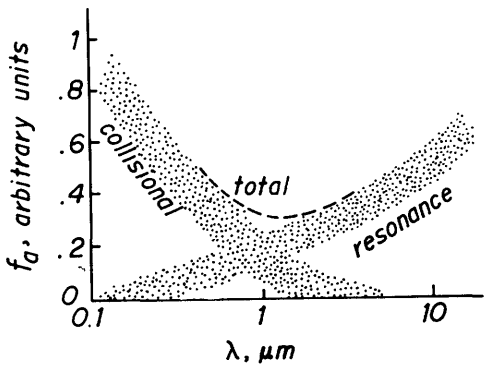

Fig. 15C4. Approximate variation of absorption fraction f_a with incident laser wavelength for collisional and resonance absorption processes. These processes vary significantly with I, T_e, etc., so these curves are only qualitatively correct.

$$\frac{F_{pm}}{F_{\nabla p}} = \frac{-(\omega_{pe}^2/\omega_0^2)\ \nabla\langle\tfrac{1}{2}\epsilon_0 E^2\rangle}{-\nabla(nkT_e)} \simeq \frac{v_0^2}{v_{Te}^2} \tag{15C18}$$

where $v_{Te}^2 \equiv kT_e/m_e$ and the "quiver velocity"

$$v_0^2 \equiv \frac{e^2E_0^2}{m_e^2\omega_0^2} \tag{15C19}$$

and E_0 is the incident wave amplitude. Thus, if $v_0/v_{Te} \ll 1$, the ponderomotive force effects will be relatively weak, while if $v_0/v_{Te} \sim 1$, they will be significant. Using Eq. (15C2) and $\omega = 2\pi c/\lambda$, Eq. (15C18) becomes

$$\frac{F_{pm}}{F_{\nabla p}} = \frac{v_0^2}{v_{Te}^2} = \frac{2e^2I\lambda_0^2}{(2\pi)^2\epsilon_0 kT_e mc^3}\ , \tag{15C20}$$

$$I\lambda_0^2 = \frac{(2\pi)^2 \varepsilon_0 kT_e mc^3}{2e^2} \left(\frac{v_0}{v_{Te}}\right)^2 \tag{15C21}$$

The product $I\lambda_0^2$ is directly related to the relative strength of the ponderomotive force. For example, to make $v_0/v_{Te} \sim 1$ with $T_e \sim 1$ keV and $\lambda_0 \sim 1$ μm requires $I \sim 3\times10^{19}$ W/m^2 (3×10^{15} W/cm^2).

The ponderomotive force tends to push electrons away from regions of high electric field. The resultant density perturbation δn can give rise to high-frequency electron plasma waves or to low-frequency ion acoustic waves, since the ions are tied to the electrons by the collective Coulomb force. Some wave-coupling processes are

$$\begin{aligned}
&\omega_0 \rightarrow \omega_{pe} + \omega_{ia} && \textit{parametric decay instability}\\
&\omega_0 \rightarrow \omega_{pe} + \omega_{pe} && \textit{two plasmon decay}\\
&\omega_0 \rightarrow \omega_t + \omega_{ia} && \textit{stimulated Brillouin scattering (SBS)}\\
&\omega_0 \rightarrow \omega_t + \omega_{pe} && \textit{stimulated Raman Scattering (SRS)}
\end{aligned} \tag{15C22}$$

where ω_{ia} represents an ion acoustic wave and ω_t represents an electromagnetic (transverse) wave.

The parametric decay instability and two-plasmon decay instability can absorb laser beam energy, while SBS and SRS reflect beam energy, hindering absorption. Since the wave energy and momentum are $(h/2\pi)\omega$ and $(h/2\pi)\vec{k}$, the energy and momentum conservation equations for wave-coupling processes may be written

$$\begin{aligned}
\omega_0 &= \omega_1 + \omega_2\\
\vec{k}_0 &= \vec{k}_1 + \vec{k}_2
\end{aligned} \tag{15C23}$$

where o denotes the incident wave (laser beam) and 1 and 2 denote the secondary waves (ω_{ia}, ω_{pe}, or ω_t). Taking the z direction parallel to $\vec{k}_0$, we can represent the (ω, k_z) as vectors with the equation

$$\begin{pmatrix}\omega_0\\ k_{z0}\end{pmatrix} = \begin{pmatrix}\omega_1\\ k_{z1}\end{pmatrix} + \begin{pmatrix}\omega_2\\ k_{z2}\end{pmatrix} \quad . \tag{15C24}$$

A vector diagram representing this equation can be drawn on the (ω, k_z) plane along with the dispersion relations for the appropriate waves, as illustrated in Fig. 15C5. Similar vector diagrams can be drawn for the other wave-coupling processes.

stimulated Brillouin scattering

The SBS instability can occur at $n << n_c$, as illustrated in Fig. 15C6. An ion acoustic wave is driven in the forward direction, and the electromagnetic wave is backscattered at a slightly lower frequency

$$\omega_1 = \omega_0 - \omega_{ia} \quad (\omega_{ia} << \omega_0) \qquad (15C25)$$

The backscattered light emerges at 180° relative to the incident light (optical ray retracing), and its intensity increases with L_n/λ_0. The theoretical variation of SBS reflectivity with incident wave intensity and a correlation with experimental data are shown in Fig. 15C7.

Since SBS increases with L_n/λ_0 and L_n increases with target size, SBS is expected to become a more serious problem with large targets. However, the ponderomotive force tends to steepen the plasma density profile, shortening L_n. SBS can also be limited by ion heating, and by using a spread of incident laser frequencies $\delta\omega_0$ around ω_0 (large bandwidth). When a prepulse preceeds the main laser pulse, the early plasma formation enhances SBS during the main laser pulse, reducing absorption. Some features of SBS are listed in Table 15C1.

The fraction f_a of beam energy *absorbed* varies with λ_0, L_n, I, T_e, target shape, focus, and surface conditions. Values of $f_a \sim 0.8$-0.9 have been observed with planar targets at low intensity ($I \sim 10^{17}$ W/m^2), but values for spherical targets are typically about a factor of 2 lower. SBS can drastically reduce f_a at high $I\lambda_0^2$ and large L_n/λ_0.

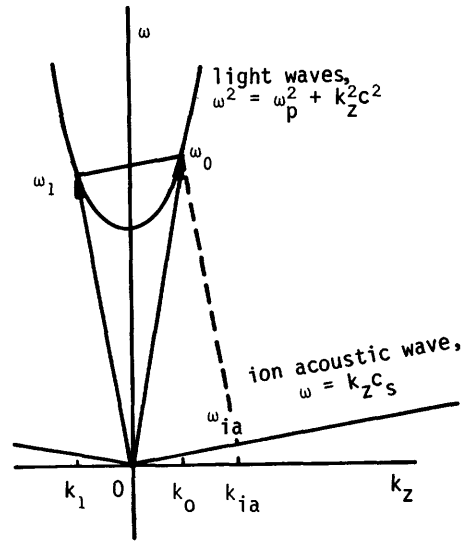

Fig. 15C5. Vector diagram representing stimulated Brillouin scattering on the ω-k_z plane.

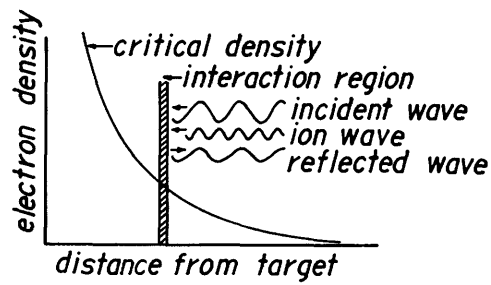

Fig. 15C6. Physical model for stimulated Brillouin scattering. From B. H. Ripin, "Absorption of laser light in laser fusion plasmas", NRL Memorandum Report 3684 (1977), Fig. 11, p. 23.

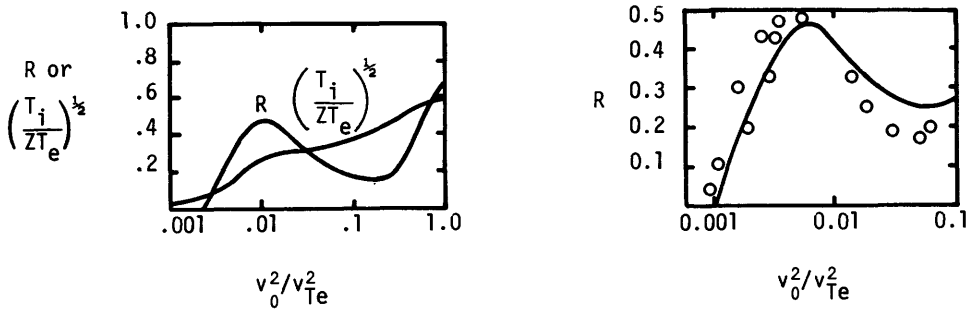

Fig. 15C7. Theoretical variations of SBS reflectivity R and the ion/electron temperature ratio $(T_i/ZT_e)^{1/2}$ with incident laser beam intensity, assuming $k_0L_n = 200$, $n/n_c = 0.1$ (left), and correlation of theory with experimentally measured reflectivity for the case $k_0L_n = 300$, $n/n_c = 0.1$, $T_e = 100$ eV (right). From K. Mima, J. J. Thomson, H. Azechi, and C. Yamanaka, "Limitation of stimulated Brillouin scattering", ICF '80, Topical Meeting on Inertial Confinement Fusion, Optical Society of America, 1980, Figs. 1 and 2 of paper TUD5, p. 27.

Table 15C1. Properties of stimulated Brillouin scattering. From B. H. Ripin, NRL Memorandum Report 3684 (1977) and H. G. Ahlstrom, UCRL-79819 (1977).

occurs in underdense plasma $n < n_c$

existence of a threshold near $v_0/v_{Te} \sim 0.1$

reflectivity increases with L_n/λ_0

insensitive to angle of incidence θ

optical ray retracing

scattered beam photons slightly red-shifted $\lambda_1 \sim \lambda_0 + 1.5$ nm

scattered intensity increases with pulse length and focal spot size.

preheating

Energetic electrons and x-rays produced in the plasma can penetrate into the target shell and heat the fuel before compression is completed. Such *preheating* raises the isentrope w_c/w_f (Section 15B), and makes it difficult to achieve high compression ratios or high energy gain. Sometimes two electron groups occur: "thermal" electrons with $T_e \sim 0.1 - 1$ keV, and "suprathermal" electrons, with $T_{es} \sim 10$-100 keV. Energetic electrons can be produced by resonance absorption, by the parametric decay instability near the critical density layer, and by the Raman instability or the two-plasmon decay instability in the underdense plasma near $\frac{1}{4}n_c$. Experimental measurements indicate that resonance absorption

is the dominant heating process in the case of $\lambda_0 \sim 1$ μm at high intensities $I \sim 10^{19}$-10^{20} W/m^2. The expanding cloud of hot electrons creates an outward electric field, which produces ambipolar flow, accelerating some ions to high energies (∿ 100 keV).

Preheating has been studied by measuring the temperature of the back sides of aluminum foils irradiated by 1 μm lasers. Very rapid heating by x-rays is followed at times of several ns by electron heat conduction, as indicated in Fig. 15C8.

Experimental measurements of T_{es}, x-ray spectra, and fast ion energy spectra give indications of the amount of preheat occurring in pellet irradiation experiments. For example, the variation of T_{es} with irradiance is shown in Fig. 15C9. At high $I\lambda_0^2$ preheat is a severe problem.

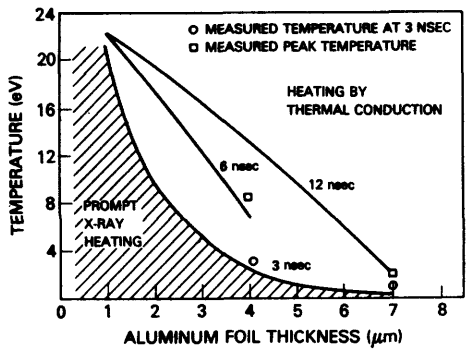

Fig. 15C8. Rear-surface temperature vs. aluminum foil thickness showing prompt x-ray heating at 3 ns, and prompt plus thermal conduction heating at 6 ns (4 μm foil) and at 12 ns (7 μm foil). From E. A. McLean et al, "Preheat studies for foils accelerated by ablation due to laser irradiation", Physical Review Letters 45, 1246-1249 (1980), Fig. 3.

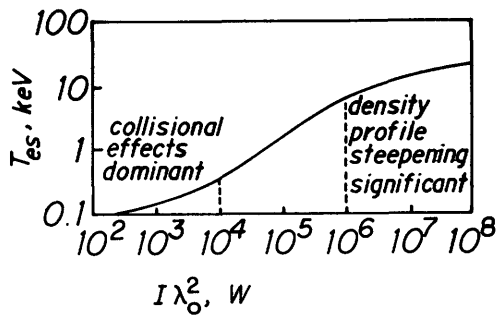

Fig. 15C9. Variation of suprathermal electron temperature with the product of laser intensity I and wavelength λ_0, based on experimental data at 1.06 and 10.6 μm. (Based on data from Physics Today, September, 1977, p. 19.)

Preheat can be reduced by the following procedures:

* Avoid strong shock waves ahead of the main compression, by avoiding sudden increases in surface pressure
* Keep T_{es} low by using low values of $I\lambda_0^2$
* Use a high-Z inner shell to attenuate x-rays and energetic electrons
* Avoid heat conduction by placing a vacuum gap between outer and inner shells.

At the end of compression, a mild shock wave will probably be adequate to heat the central region to ignition.

self-focusing

Self-focusing of a laser beam in a plasma is illustrated in Fig. 15C10. If a laser beam becomes split into several smaller self-focusing beams, the process is called *filamentation*. Filamentation causes non-uniform irradiation of the target, which can cause the Rayleigh-Taylor instability. Since this process is driven by the ponderomotive force, it can be significant when $v_0^2/v_{Te}^2 \gtrsim 0.1$.

magnetic fields

Laser-plasma interactions produce high plasma currents, which generate high magnetic fields. As a first approximation, all terms but the electric field and pressure gradient forces may be ignored in the electron momentum conservation equation (5D5) with scalar pressure (5D9):

$$-e\vec{E} - \frac{1}{n}\vec{\nabla}(nkT_e) \simeq 0 \qquad (15C26)$$

With Eq. (F21) this may be written

$$\vec{E} \simeq -\frac{k}{e}\vec{\nabla}T_e - \frac{kT_e}{ne}\vec{\nabla}n \quad . \qquad (15C27)$$

From Eqs. (5B7), (F24) and (F23) we find

$$\frac{\partial \vec{B}}{\partial t} = -\vec{\nabla}\times\left[\frac{k}{e}\vec{\nabla}T_e - \frac{kT_e}{ne}\vec{\nabla}n\right]$$

$$= \vec{\nabla}\left(\frac{kT_e}{ne}\right)\times\vec{\nabla}n = \frac{k}{ne}\vec{\nabla}T_e\times\vec{\nabla}n \quad . \qquad (15C28)$$

If we approximate the derivatives by $\partial B/\partial t \sim B/\tau$, $\nabla T_e \sim T_e/L_T$, and $\nabla n \sim n/L_n$, then

$$B \sim \frac{kT_e\tau}{eL_nL_T} \quad . \qquad (15C29)$$

If $kT_e/e \sim 1000$ eV, $L_n \sim L_T \sim 100$ μm, and $\tau \sim 10^{-9}$ s, then $B \sim 100$ T. Values of $B \sim 100$ T have been measured experimentally by Faraday rotation of probe laser beam polarization. [Even in a vacuum, high magnetic fields are associated with light waves at high intensities, with

$$\tilde{B}^2/2\mu_0 = I/c \quad . \qquad (15C30)$$

If $I \sim 10^{18}$ W/m^2, then $\tilde{B} \sim 90$ T.] High magnetic fields influence wave propagation, absorption, scattering, and heat transport. Three-dimensional modeling of laser-plasma interactions is thus very complicated.

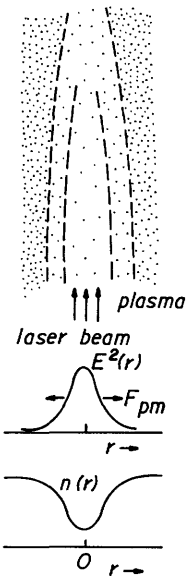

Fig. 15C10. Self-focusing of a laser beam in a plasma. The radial decrease of E^2 in the beam generates an outward ponderomotive force F_{pm}, which moves plasma outwards. The resultant hollow density profile creates a radial variation of refractivity $\tilde{n} = kc/\omega = (1-n/n_c)^{\frac{1}{2}}$. The radial decrease of refractivity acts like a convex lens, focusing the laser beam to a smaller diameter.

15D. Compression

rocket equation

If a rocket expels matter with a mass flow rate $\dot{M}$ and velocity u relative to the rocket, and the rocket velocity is v, then the velocity of the exhausted matter relative to the earth is (u-v), as illustrated in Fig. 15D1. In a brief time interval dt, the exhausted mass and momentum are $\dot{M}dt$ and $-\dot{M}dt(u-v)$. The total momentum change of the system is zero:

(momentum of exhausted matter) + (change of rocket momentum) = 0.

$$-\dot{M}dt(u-v) + d(Mv) = 0 \quad ,$$

where M is the rocket mass, so

$$d(Mv)/dt = \dot{M}(u-v) \quad . \tag{15D1}$$

Since $dM/dt = -\dot{M}$, this simplifies to

$$M(dv/dt) = -u(dM/dt) \quad . \tag{15D2}$$

If the mass is expelled with a spread of velocities $f(u,\theta)$ (Fig. 15D1c), then we can replace u in Eq.(15D2) by

$$u_{eff} \equiv \frac{\int du \int d\Omega \; f(u,\theta)\; u \cos\theta}{\int du \int d\Omega \; f(u,\theta)} \tag{15D3}$$

where $d\Omega = 2\pi \sin\theta d\theta$ is a differential solid angle [Eq. (2E9)], and azimuthal symmetry is assumed. For example, if

$$f(u, \theta) = Ce^{-\beta u^2} \cos^n\theta \tag{15D4}$$

where C is a constant, $\beta \equiv m_i/2kT$, and n is a variable parameter, then

$$u_{eff} = \bar{u}\,(n+1)/(n+2) \quad , \quad \bar{u} \equiv (8kT/\pi m_i)^{\frac{1}{2}} \quad . \tag{15D5}$$

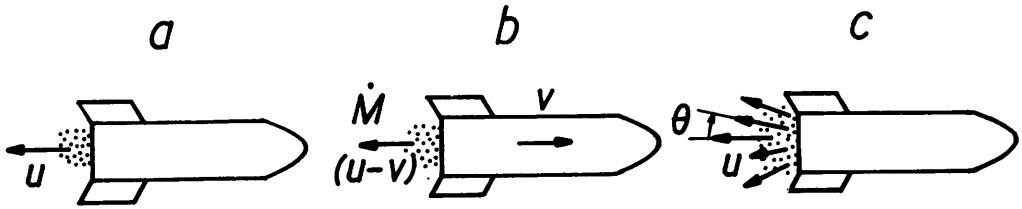

Fig. 15D1. Exhaust of matter with a mass flow rate $\dot{M}$ at velocity u relative to the rocket (a) in a reference frame moving with the rocket (b) in the earth reference frame (c) in the rocket reference frame with a spread of velocities u and angles θ .

The case n = 0 represents isotropic emission (in the range θ = 0 to θ = 90°), and the case $n \simeq \infty$ represents all the particles emitted at θ = 0°.

Assuming that u_{eff} is constant in time and that the initial velocity of the rocket is zero, Eq. (15D2) integrates to

$$v(t) = u_{eff} \ln(M_0/M) \quad , \tag{15D6}$$

where M is the mass of the rocket remaining at time t and M_0 is the initial rocket mass. The same equation applies to the acceleration of thin foils or target shells by laser-driven ablation, Fig. 15D2.

hydrodynamic efficiency

In the rocket's reference frame, Fig. 15D1a, kinetic energy of ablated material is produced at a rate $\frac{1}{2}\dot{M}\overline{u^2}$, where $\overline{u^2}$ is the average value of u^2. The rocket mass decreases at a rate

$$dM/dt = -\dot{M} \quad . \tag{15D7}$$

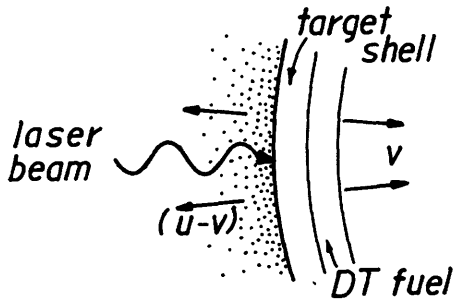

Fig. 15D2. Laser-driven ablation of a thin target shell.

By energy conservation

(laser power absorbed)

= (kinetic energy produced)

+ (losses)

$$P_{abs} = \tfrac{1}{2}\dot{M}\overline{u^2} + P_{loss} = -\tfrac{1}{2}(dM/dt)\overline{u^2} + P_{loss} \quad . \tag{15D8}$$

Integrating over time, we find

$$W_{abs} = \tfrac{1}{2}\overline{u^2}\,(M_0 - M) + W_{loss} \quad , \tag{15D9}$$

where

$$W_{abs} \equiv \int dt\, P_{abs} \quad , \quad W_{loss} \equiv \int dt\, P_{loss} \quad .$$

The hydrodynamic efficiency is

$$\eta_h = \frac{\text{rocket kinetic energy}}{\text{energy absorbed}} = \frac{\tfrac{1}{2}Mv^2}{\tfrac{1}{2}\overline{u^2}(M_0 - M) + W_{loss}} \tag{15D10}$$

Assuming an ablated ion distribution function of the form (15D4), we find

$$\overline{u^2} = 3kT/m_i \quad . \tag{15D11}$$

With the aid of Eqs. (15D5), (15D6), and (15D11), Eq. (15D10) becomes

$$\eta_h = \frac{\frac{M}{2}\left[\frac{8kT}{\pi m_i}\right]\left[\frac{n+1}{n+2}\right]^2 \ln^2\left[\frac{M_0}{M}\right]}{\left[\frac{3kT}{2m_i}\right](M_0 - M) + W_{loss}} \quad , \tag{15D12}$$

If the ablated matter has a cosine distribution (n = 1) and W_{loss} is negligible, then this reduces to

$$\eta_h \simeq \frac{0.4M\ \ln^2(M_0/M)}{(M_0 - M)} = \frac{0.4(v/u_{eff})^2}{\exp(v/u_{eff})-1} \quad . \qquad (15D13)$$

The variation of η_h with M/M_0 from this equation is shown in Fig. 15D3. The optimum value of $\eta_h \simeq 0.26$ occurs at $M/M_0 \simeq 0.2$, and at this optimum $v/u_{eff} \simeq 1.6$. These simplified equations have assumed u_{eff} = constant and ignored energy losses and the deceleration due to pellet internal pressure, so they give optimistic estimates of η_h. Nevertheless, they indicate that there exist some optimum values of M/M_0 and v/u_{eff} which experiments should try to match, in order to maximize η_h.

Experimental data from ablative acceleration of thin planar foils are consistent with this model, and values of $\eta_h \sim 0.2$ have been attained (Decoste et al, 1979; Ripin et al, 1980).

For effective compression, shell velocities $v_r \sim 3\times10^5$ m/s are needed (Example Problem 15B1). Near the maximum η_h, $v/u_{eff} \sim 1.5$, so $u_{eff} \sim 2\times10^5$ m/s. The required input energy is about

$$f_a W_d/\Delta M \gtrsim \tfrac{1}{2}\overline{u^2} = \tfrac{1}{2}\overline{u^2_{eff}}\ \frac{3\pi}{8}\left(\frac{n+2}{n+1}\right)^2$$

$$\sim 5\times10^{10}\ \text{J/kg} \qquad (15D14)$$

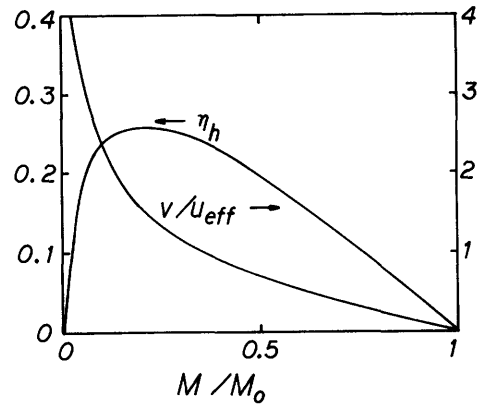

Fig. 15D3. Variations of hydrodynamic efficiency and normalized implosion velocity with unablated mass fraction.

where $\Delta M = M_0 - M$ is the ablated mass. For example, a pellet with fuel mass $m \sim 2$ mg might have an ablated mass $\Delta M \sim 10$ mg. If $f_a \sim 0.4$, then $W_d \gtrsim 1.3$ MJ would be required.

ablation pressure

We will estimate the ablation pressure required to attain a given radial implosion velocity, starting with Newton's Second Law

$$\frac{d}{dt}\left(M\frac{dR}{dt}\right) = -4\pi R^2 p_a \quad , \qquad (15D15)$$

where p_a is the ablation pressure, $4\pi R^2$ is the area on which it acts, M is the shell mass, and R is the shell radius. Due to ablation, the shell mass gets lighter as it moves inwards. We can get a conservative estimate of p_a by ignoring the mass change, and treating the shell as if M = constant. Multiplying both sides by (2/M)(dR/dt), we have

$$2\left(\frac{d^2R}{dt^2}\right)\frac{dR}{dt} = -\frac{8\pi p_a}{m} R^2 \frac{dR}{dt} \quad . \tag{15D16}$$

The left side may be rewritten in the form

$$\frac{d}{dt}\left(\frac{dR}{dt}\right)^2 = -\frac{8\pi p_a}{m} R^2 \frac{dR}{dt} \quad . \tag{15D17}$$

The initial conditions are $R = R_0$ and $(dR/dt) = 0$ at $t = 0$. Assuming p_a = constant, this equation may be integrated to obtain

$$v_r^2 \equiv \left(\frac{dR}{dt}\right)^2 = \frac{8\pi p_a}{3m}(R_0^3 - R^3) \simeq \frac{8\pi p_a R_0^3}{3m} \text{ when } R^3 << R_0^3 \quad . \tag{15D18}$$

Using $m = 4\pi R_0^2 \Delta R_0 \rho_0$, we find the required ablation pressure

$$p_a = \frac{3\Delta R_0 \rho_0 v_r^2}{2R_0} \quad . \tag{15D19}$$

For example, if $\Delta R_0/R_0 \sim 0.1$, $\rho_0 \simeq 300$ kg/m^3, and $v_r^2 \sim 2\text{-}3\times10^5$ m/s, then $p_a \sim 2\text{-}4\times10^{12}$ Pa.

shell stability

When a high-density material ρ_2 is pushed inwards with acceleration a (m^2/s) by a low-density material ρ_1, the Rayleigh-Taylor instability (Section 8D) can occur. For a target shell of radius r having sinusoidal surface ripples with wavelength λ_p

$$\ell\lambda_p = 2\pi r \quad , \tag{15D20}$$

where ℓ is an integer, as illustrated in Fig. 15D4 with $\ell = 8$. The wavenumber of the perturbation is

$$k \equiv 2\pi/\lambda_p = \ell/r \quad . \tag{15D21}$$

Let ξ designate the amplitude of the perturbations. For small values of ξ the instability growth is approximately exponential

$$\xi = \xi_0 e^{\gamma t} \tag{15D22}$$

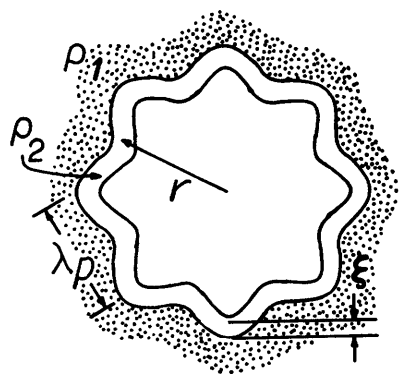

Fig. 15D4. Perturbations of a spherical shell surface with wavelength λ_p and amplitude ξ. Dots represent a low density region ρ_1, which may be the ablated plasma or a low-Z outer shell, surrounding a high-density shell ρ_2.

with growth rate

$$\gamma = [kg(\rho_2-\rho_1)/(\rho_2+\rho_1)]^{\frac{1}{2}} \quad . \tag{15D23}$$

[If $\rho_1 << \rho_2$ this reduces to Eq. (8D55).]

When $\xi > \lambda_p$, the growth rate is much slower, and no longer exponential. Perturbations with very large λ_p (small k) have slow growth rates, and those with $\lambda_p << \delta r$ (the shell thickness) tend to saturate at small amplitude. The most destructive perturbations have $\lambda_p \gtrsim \delta r$ and can lead to destruction of the shell.

Three different cases in which the Rayleigh-Taylor instability can occur are illustrated in Fig. 15D5.

The main causes of surface perturbations are

* pellet irregularities
  - non-spherical
  - non-uniform wall thickness
  - non-uniform shell density
  - surface roughness (leads to short λ_p perturbations)
* non-uniform irradiation
  - aiming
  - polarization-dependent absorption
  - self-focusing
  - non-uniform heat transport caused by local magnetic fields.

Figure 15D6 shows part of a computer simulation of an unstable shell implosion.

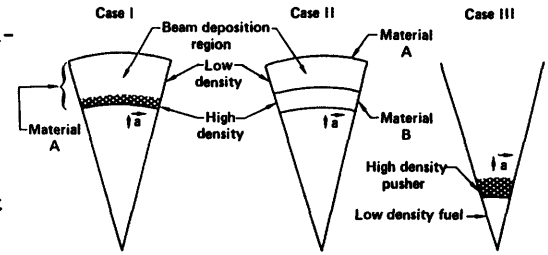

Fig. 15D5. Three cases in which the Rayleigh-Taylor instability can occur. (I) a high-density shell surrounded by a low-density plasma, (II) a density discontinuity between two shell layers, (III) low-density fuel surrounded by a high-density pusher near the end of compression. From R. O. Bangerter, "Fusion Target Design", Proceedings of the IEEE Minicourse on Inertial Confinement Fusion, Chapter 5, Edited by G. H. Miley, U. of Illinois Fusion Studies Laboratory, 1980, Fig. 8, p. 5-32.

If $p_a \propto I$ and the non-uniformity of the irradiation is δI, then the shell velocity is theoretically expected to have a velocity perturbation given by

$$\delta v/v_r \sim \delta I/I \quad . \tag{15D24}$$

The resulting radial perturbation near the end of compression is

$$\xi \sim R_0 \delta v/v_r \sim R_0 \delta I/I \quad , \tag{15D25}$$

where R_0 is the initial outer fuel radius, so the minimum final radius at the outside of the compressed fuel is

$$R_f > \xi \gtrsim R_0 \delta I/I \quad . \tag{15D26}$$

A simple estimate of the maximum "convergence ratio" is therefore

$$R_0/R_f \lesssim I/\delta I \tag{15D27}$$

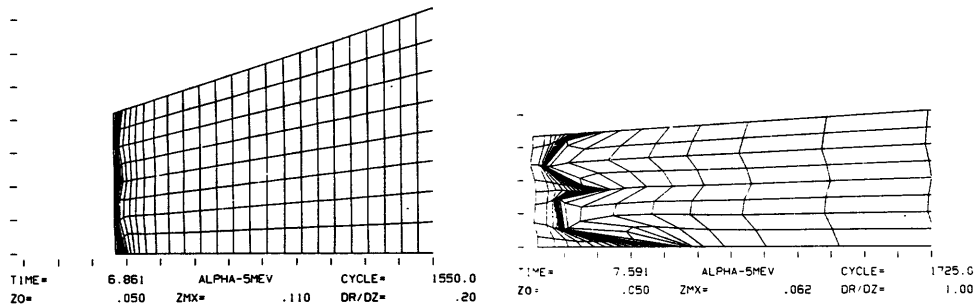

Fig. 15D6. Two frames of a movie showing the unsuccessful implosion of a shell driven by 5 MeV alpha particles. The perturbation has $\ell \simeq 200$. From R. O. Bangerter, Proceedings of the IEEE Minicourse on Inertial Confinement Fusion, Edited by G. H. Miley, U. of Illinois Fusion Studies Laboratory, 1980, Chapter 5, Figs. 12 and 13.

For example, if it is desired to attain $R_0/R_f \sim 20$, then $\delta I/I \lesssim 0.05$ may be necessary. However, effects of irradiation asymmetry are reduced by lateral heat flow around the target surface. In one experiment, an irradiation asymmetry of $\delta I/I \sim 0.4$ resulted in a velocity asymmetry of $\delta v/v_r \sim \pm 0.05$, in contradiction to Eq. (15D24) (Bodner, 1981).

If the laser intensity is too high, shock waves and suprathermal electrons cause excessive preheat and spoil compression, and plasma instabilities (such as filamentation) may be harmful. If the intensity is too low, the ablation pressure may be inadequate to attain the required implosion velocity, and the Rayleigh-Taylor instability may also be more serious. At $\lambda_0 \sim 1$ μm, the optimum intensity appears to be $I \sim 10^{18}$ W/m^2. These phenomena also depend on laser wavelength. Asymmetry problems are expected to be more severe at short wavelengths, and preheat problems, more severe at long wavelengths.

15E. Targets

exploding pushers

Some types of ICF targets are illustrated in Fig. 15E1. A hollow, spherical glass shell microballoon filled with DT gas is a typical exploding pusher target. The glass shell compresses the fuel somewhat, then disintegrates. Energetic particles and photons penetrate into the fuel gas and heat it effectively to high temperatures. These high temperatures result in fairly high fusion reaction rates and neutron yields.

Since exploding pushers do not compress the fuel efficiently (isentropically), it is impossible to attain high gains with such targets. They are primarily of interest for developing diagnostic techniques and checking predictions of computer codes.

Some of the processes considered by the LASNEX code are shown in Fig. 15E2. This code solves 10^5 coupled differential equations, each requiring 10^6 arithmetic operations. A typical run requires several hours of time on a CDC 7600 computer. Neutron yields observed from various targets (mostly exploding pushers) are compared with LASNEX predictions in Fig. 15E3.

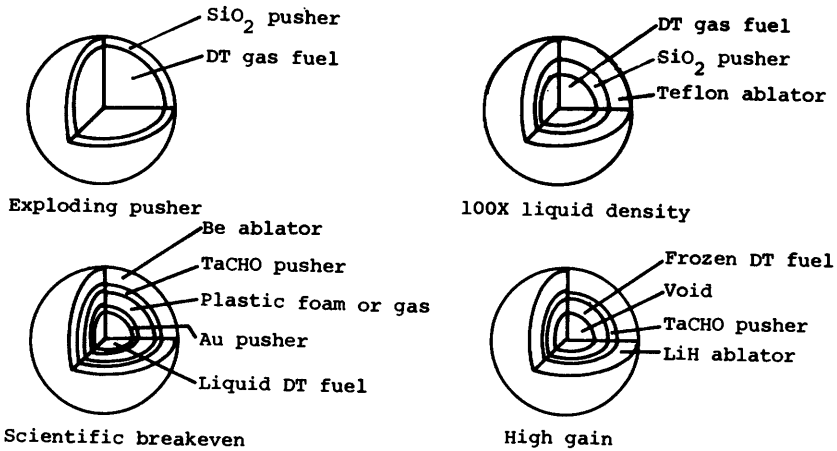

Fig. 15E1. Typical designs for laser fusion research pellets. From C. D. Hendricks, Journal of Nuclear Materials 85 & 86, 79-86 (1979), Fig. 1.

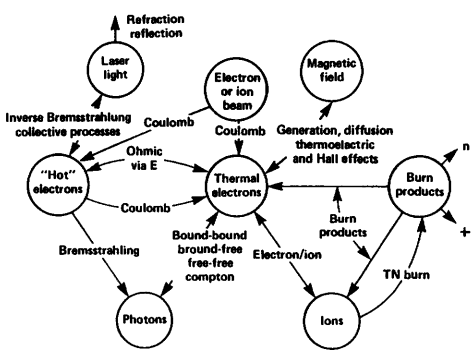

Fig. 15E2. Phenomena considered by the LASNEX computer code. From R. O. Bangerter, "Fusion Target Design", Chapter 5, Proceedings of the IEEE Minicourse on Inertial Confinement Fusion, Edited by G. H. Miley, U. of Illinois Fusion Studies Laboratory, 1980, Fig. 1, p. 5-25.

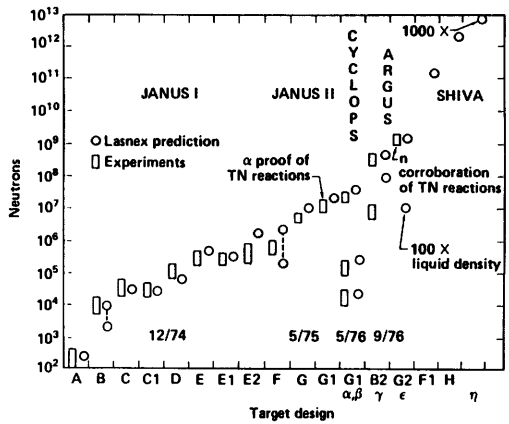

Fig. 15E3. Comparison of experimental and predicted neutron yield for a variety of targets, designated by symbols along the horizontal axis. Names at the top refer to laser systems, and numbers at the bottom are dates of measurements. From R. O. Bangerter, Proceedings of the IEEE Minicourse on Inertial Confinement Fusion, Chapter 5, Edited by G. H. Miley, U. of Illinois Fusion Studies Laboratory, 1980, Fig. 2, p. 5-26.

ablative compression

The goal of ablative compression is to maximize hydrodynamic efficiency η_h while maintaining a low isentrope and hydrodynamic stability. To achieve this goal, complex targets with multiple layers may be needed. The outer layer is typically a low-Z ablator material, such as polyethylene, teflon, LiH, or Be. Next comes a heavier pusher material. The pusher gathers inward momentum,

compresses the fuel, and (if it is thick) shields the fuel from hot electrons. A plastic pusher containing Ta (TaCHO) or W (CHOW) can be uniformly deposited onto a spherical shell, and the high-Z metal is effective at stopping energetic electrons (CHOW contains 32.3% C, 64.6% M, 2.2% O, and 0.88% W, atomic %). In some designs there may be a second pusher shell inside the first, separated from it by a void, gas, or plastic foam. It is easiest to manufacture pellets with gaseous DT fuel, but higher compression can be attained with liquid or frozen DT fuel.

The double-shell designs offer the possibility of velocity enhancement, when a heavy outer pusher with mass m_1 and speed u_1 strikes the lighter inner pusher with mass m_2 and zero initial velocity. If the collision were elastic, then from momentum and energy conservation

$$m_1 u_1 = m_1 u_{1f} + m_2 u_{2f}$$

$$\tfrac{1}{2} m_1 u_1^2 = \tfrac{1}{2} m_1 u_{1f}^2 + \tfrac{1}{2} m_2 u_{2f}^2 \qquad (15E1)$$

where the final velocities after the collision are denoted by f. Eliminating u_{1f}, we find the final inner shell velocity and the efficiency of energy transfer:

$$u_{2f} = 2m_1 u_1/(m_1+m_2) \qquad (15E2)$$

$$\text{efficiency} = \frac{\tfrac{1}{2} m_1 u_1^2}{\tfrac{1}{2} m_2 u_{2f}^2} = \frac{4 m_1 m_2}{(m_1+m_2)^2} \qquad (15E3)$$

(This efficiency of energy transfer should not be confused with the hydrodynamic efficiency η_h). For values of m_1/m_2 = 1, 2, 4, and 8, these equations indicate that u_{2f}/u_1 = 1, 4/3, 8/5, and 16/9, respectively, and that the efficiency is 1, 8/9, 16/25, and 32/81. These values are unrealistic, however. The collision will not be perfectly elastic, and asymmetry will further degrade the final velocity and efficiency. The effect of asymmetry on a double-shell target is illustrated in Fig. 15E4.

Another idea is to drive an inner pusher shell with ions from an exploding pusher outer shell. Such a double-shell exploding pusher target is less sensitive to irradiation asymmetries, but has comparatively poor coupling efficiency.

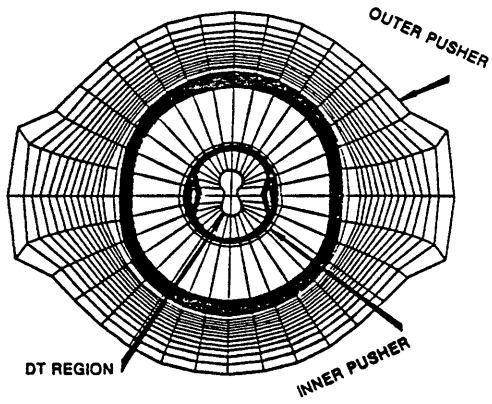

Fig. 15E4. Two-dimensional velocity multiplying target design with a large illumination asymmetry. From J. M. Kindel and M. A. Stroscio, Proceedings of the IEEE Minicourse on Inertial Confinement Fusion, Chapter 6b, Edited by G. H. Miley, U. of Illinois Fusion Studies Laboratory, 1980, Fig. 12, p. 6b-11.

Fuel densities and neutron yields attained with the Shiva (1.06 μm) experiments at LLNL are shown in Fig. 15E5. The ablative compression targets attain higher densities, but lower temperatures and neutron yields, due to the limited amount of energy available from the laser beams in those experiments.

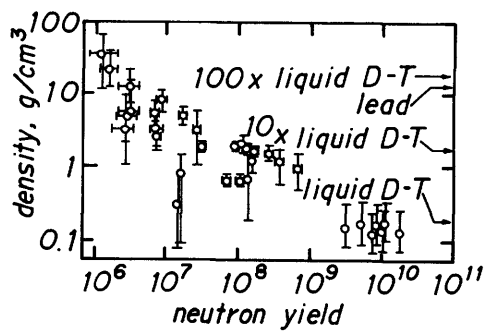

Fig. 15E5. "The Shiva laser facility can generate a wide range of thermonuclear fuel conditions. Operating Shiva in the 20- to 30-TW short-pulse (100-ps) regime, we can achieve neutron yields in excess of 10^{10} with ion temperatures of the order of 5 keV. However, because these targets operate in the exploding-pusher mode, the final D-T fuel density is only of the order of 0.2 g/cm³ (equivalent to the liquid density of D-T). Operating Shiva at the 10-kJ, 1-ns regime, we can drive target designs to final D-T fuel densities in the range of 10 to 20 g/cm³ (approximately 50 to 100 times the density of liquid D-T). With the limited energy available from Shiva, however, these high densities are accompanied by correspondingly low neutron yield and ion temperatures (of the order of 10^6 and 0.5 keV, respectively). By varying the target design and laser operating conditions, we can obtain final D-T fuel conditions spanning the range of these two extremes." From Energy and Technology Review, August, 1980, Fig. 17, p. 25.

ion beam targets

An ion beam target design is shown in Fig. 15E6. In this design, a low-density plastic (TaCOH) pusher is placed next to the fuel, to minimize the density difference which drives the Rayleigh-Taylor instability during the final stage of implosion (Case III, Fig. 15D5). The pusher thickness is large enough for slow growth of the perturbations, yet not too large for effective acceleration. A lead tamper is placed around the outside, to help contain the pressure. Since high-Z materials are less effective at stopping ions, little energy is lost in the lead tamper, Fig. 15E7. Some tantalum has been added to the plastic pusher to inhibit energy transport and preheat. The beam power should be low during initial stages of compression and high at the end, as in Fig. 15E8. During compression the pusher drives the fuel inwards, but the tamper stays at a relatively constant radius, as shown in Fig. 15E9. For the example case shown here, the maximum $v_r = 3.3 \times 10^5$ m/s, $W_d = 1.3$ MJ, $W_F = 113$ MJ, and Q = 88.

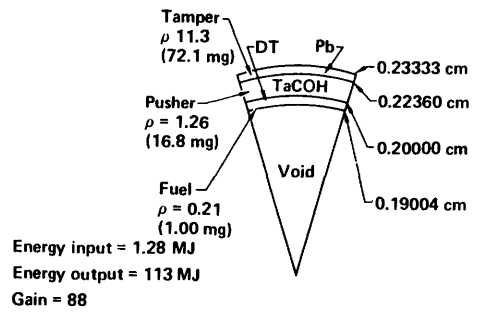

Fig. 15E6. Section of a spherical ion beam fusion target. From R.O. Bangerter, "Fusion Target Design", Chapter 5, Proceedings of the IEEE Minicourse on Inertial Confinement Fusion, Edited by G.H. Miley, U. of Illinois Fusion Studies Laboratory, 1980, Fig. A1, p. 5-41.

target specifications

Some target design considerations are listed in Table 15E1. Some compromises are required. Thick shells require too much energy input, while thin

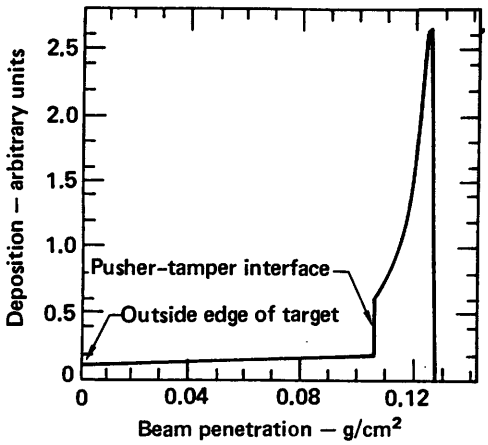

Fig. 15E7. Energy deposition by 6.5 MeV protons vs. depth in the previous target, at t = 18 ns. Ion energy is deposited mainly in the low-Z pusher. From R. O. Bangerter, 1980, Fig. A2, p. 5-42.

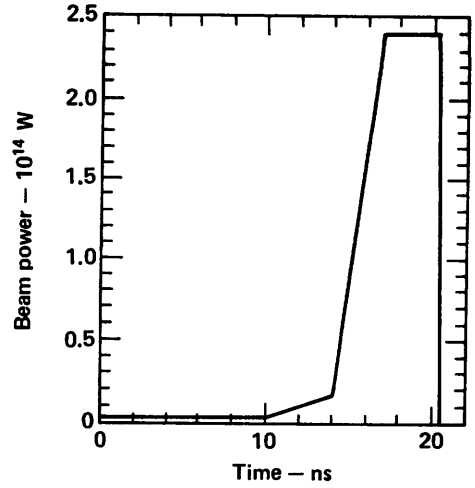

Fig. 15E8. Ion beam power vs. time for the example case. From R. O. Bangerter, 1980, Fig. A3, p. 5-43.

Table 15E1. ICF target design considerations.

high compression, hydrodynamic efficiency, and energy gain
tamper
multiple shells
hydrodynamic stability
good sphericity
smooth surfaces
uniform thickness shells
thick, low-Z pusher
large size (for ion beam targets, to ease focusing requirements)
low input energy
low mass
minimum preheat
high-Z material to stop electrons and x-rays
insulating gaps between shells
minimum production of long-lived radioisotopes
simple, inexpensive fabrication
single-shell design, if gain satisfactory
cheap materials, like plastics
easy handling and storage
(Avoid cryogenic targets, if high-gain can be attained without them.)

shells ($\Delta R_0/R_0 < 0.1$) may be unstable and allow preheat. Multiple shells reduce input energy, but are difficult to fabricate. Solid or liquid DT fuel has higher ρ_0 and can reach higher final densities than gaseous DT fuel, but very low temperatures are needed, making the pellets difficult to fabricate and handle. (At atmospheric pressure, hydrogen melts at 13.8 K and boils at 20.3 K.)

Specifications for two laser pellet designs are illustrated in Fig. 15E10.

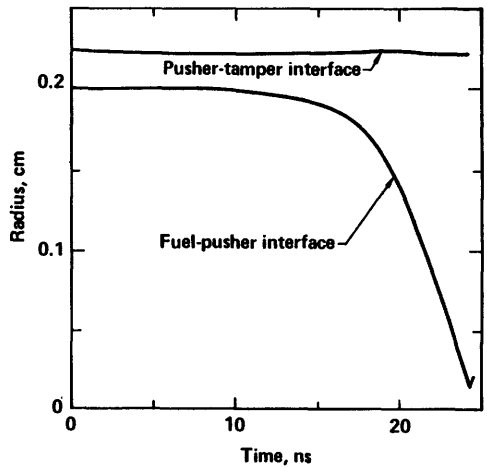

Fig. 15E9. Radius vs. time of the pusher-tamper and fuel-pusher interfaces for the example ion beam target. From R. O. Bangerter, 1980, Fig. A5, p. 5-45.

Glass microspheres meet the following types of specifications:

- sphericity better than 5%
- concentricity and wall uniformity better than 5%
- surface finish better than 0.2 μm
- able to contain gas pressures up to 10 MPa.

High-gain pellets require even higher standards. Similar specifications apply to other target shell materials, such as plastics.

fabrication

glass shells

Vibrations can be used to break up liquid jets into uniform droplets. In one process, uniform droplets of an aqueous solution of glass-forming chemicals flow through a vertical column at 570-770 K to remove the solvent. The dried pellets then pass through a high temperature region where they fuse into glass. Internal vapor pressure makes them hollow. Chemical composition, solute concentration, droplet size, temperature, and temperature gradients are all carefully controlled. About 80% of the finished microspheres meet the desired specifications. DT fuel gas can permeate the spheres at high pressures $\sim 10^7$ Pa

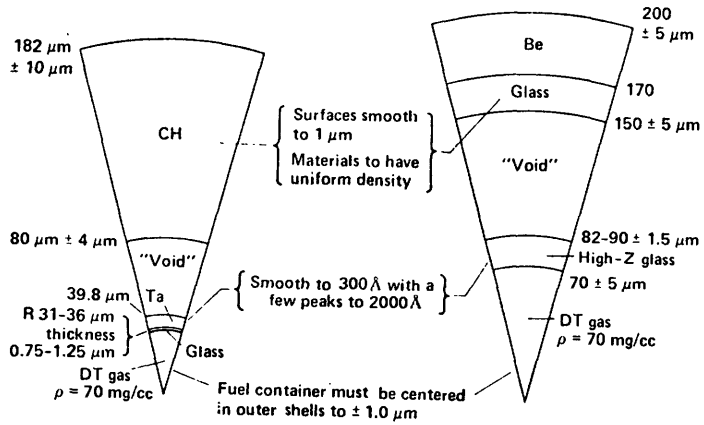

Fig. 15E10. Detailed specifications of small pellet designs. From C. D. Hendricks, "Fuel pellets and optical systems for inertially confined fusion", Journal of Nuclear Materials 85 & 86, 79-86 (1980), Fig. 2.

(100 atm) and temperatures ∿ 700 K. When the shells cool, the permeation coefficient is much lower, and the gas is trapped inside.

Trace quantities of heavier gases, such as Ar, are often desired in the pellets to facilitate diagnostics. Such gases cannot permeate into the finished spheres, but they can flow through the furnace column and be trapped in the spheres during fabrication.

coatings and layer deposition

During batch coating processes, spheres may be rolled around in a dish agitated by a piezoelectric crystal, or they may be levitated by gas flow, electrostatic repulsion, ac quadrupole fields, rf induction, or molecular beams. The levitation or agitation is necessary in order to achieve uniform thickness coatings. Plastic coatings may be applied by plasma polymerization: plastic-forming gases are activated by an electrical or microwave discharge, then flow over the spheres. Ion bombardment may be used to remove surface irregularities during coating. Metals may be sputter-deposited onto the spheres.

multiple shell targets

Figure 15E11 illustrates one technique for making multiple-shell targets. First two glass fibers (3 μm diameter) are mounted on a washer, and a glass microballoon (GMB) is epoxied onto the fibers. A paraffin ball is melted onto the GMB. Next the paraffin ball surface is melted quickly by lasers to smooth out the ripples. The glass fibers protruding from the paraffin ball are removed by chemical etching. Then the surface is further smoothed by rolling between two glass plates with a glycerol lubricant.

With the ball held in a vacuum chuck, a 15-20 μm diameter glass capillary tube is stuck lightly into the ball. Then a parylene (plastic) shell is deposited onto the ball by vapor phase pyrolysis. When the shell is heated in vacuum, the paraffin vaporizes and flows out through the capillary tube. Various gases can be inserted into the shell through the capillary tube. (The GMB is filled with DT fuel before mounting on the fibers). Outer shells 120-400 μm in diameter with 4-10 μm walls have been fabricated.

Multiple-shell targets are also made by cementing hemispheres together.

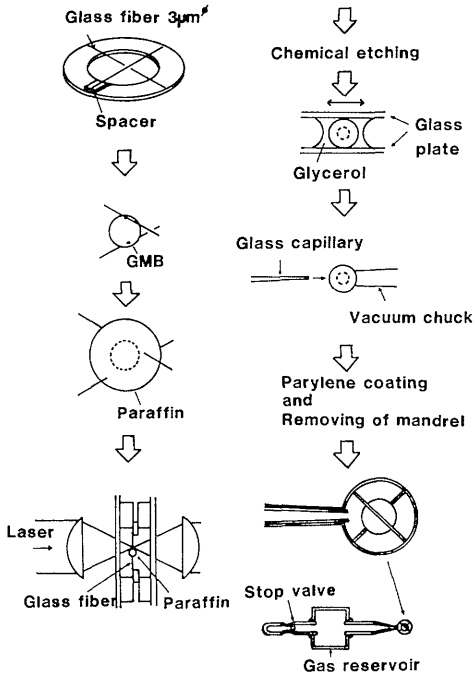

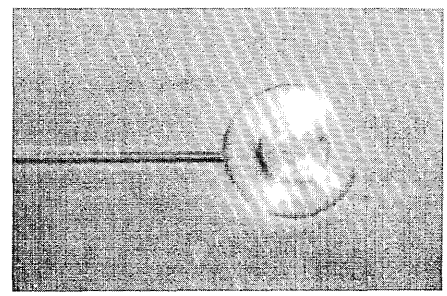

Fig. 15E11. A fabrication technique for multiple-shell targets (top), and a finished target (bottom). From T. Norimatsu, A. Furusawa, M. Yoshida, Y. Izawa, and C. Yamanaka, "Fabrication of double shell targets for laser fusion", Journal of Vacuum Science and Technology 18, 1288 (1981), Figs. 1 and 3.

mass production

Batch production techniques are being developed to form and process a continuous flow of microspheres. Microspheres can be filled with fuel during production. The spheres can then be charged and suspended in a toroidal quadrupole configuration, and moved in the toroidal direction by pulsed voltages applied to electrodes. Various coatings can be applied as they flow around the torus.

Cryogenic targets can be made continuously by freezing liquid DT droplets. As the fuel spheres fall vertically, they can be sprayed with gas coatings (such as Ne and Xe), which freeze to the spheres. The column walls can be maintained at low temperatures by liquid He coolant ($T \sim 4$ K).

target costs

For illustrative purposes, consider a power plant producing 1 GWe, with $\eta_e = 0.4$, $\varepsilon = 0.25$, $Q \sim 100\ W_L$(MJ) for $0.1 < W_L < 10$MJ and target fabrication costs 0.25 ¢/kwh. The fusion yield, the required number of shots per second for a 1000 MWe plant, the minimum allowable driver efficiency, and the maximum allowable target cost are shown as functions of W_L in Fig. 15E12. For a 2 MJ laser energy, a repetition rate of about 10 Hz is needed, the yield is about 300 MJ, the minimum driver efficiency is about 5 %, and the maximum allowable target cost is about 7 ¢/pellet.

characterization

After fabrication, the targets are inspected to ensure satisfactory quality. Many techniques have been developed to characterize the finished shells, including:

* optical microscopy, interferometry and holography of glass shells, to determine size, sphericity, wall thickness, uniformity.
* buoyancy and drag analysis, to determine diameter and wall thickness.
* scanning electron microscopy to determine surface uniformity and smoothness.
* quartz fiber microbalance, sensitive to 2 ng.
* x-ray radiography, to determine internal target parameters.
* micromanipulators, to hold and rotate targets for viewing all sides of them.
* computerization, to store and display the results.
* automated pattern recognition and processing, to decide whether a target meets specifications without the need for human viewing and judgement.
* glow discharge analysis, to measure type and pressure of confined gases.
* chemical analysis by Auger ion probe, fluorescence, and ir spectroscopy.

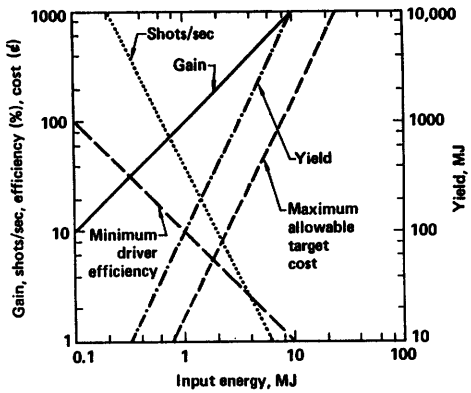

Fig. 15E12. Target yield, target gain, shot repetition rate, minimum allowable driver efficiency and maximum allowable target cost as a function of beam energy. These curves are for illustrative purposes and are very dependent on the assumptions stated in the text. From R. O. Bangerter, 1980, Fig. 16, p. 5-40.

For example, one x-ray technique records the x-ray image directly onto high-resolution film, with no magnification. The film is then scanned and analyzed by a digital image/memory processor, which plots image density vs. radius and fits a least-squares curve to the data. Data on diameter, wall thickness, and concentricity are obtained, with accuracy to within about 0.1 μm. Automatic measurements can be made on an array of 100 microspheres in less than 1 hour.

For a 10 Hz reactor pulse rate, 36000 targets would be injected per hour, creating a formidable inspection problem. However, if over 90 % of the spheres are satisfactory, it may suffice to inject all the targets without inspection, accepting 5-10 % low-yield shots.

positioning

Target spheres have been suspended from thin quartz fibers or held in place by thin plastic membranes. They are then manipulated microscopically into the focus of the lasers before each shot. Such positioning and alignment procedures are time consuming, requiring many minutes between shots.

For reactors, targets must be injected into the exact focus of the lasers at rates of 1-10 Hz, with accuracy of about 10 % of the pellet radius or better. The pellets may be injected into the chamber with $v \sim 10\text{-}1000$ m/s, and their trajectories monitored optically. The trajectories may be corrected by light pressure from weak pulsed laser beams.

In one scheme the pellet travels inside a hollow laser beam. When the pellet strays from the desired path, it strikes the laser beam "wall" and is reflected back into the channel. The success of such schemes depends upon avoiding significant preheat or loss of pellet symmetry during transit.

Another possibility is to use electro-optical means to move the location of the laser beams' foci to intersect the pellet trajectory.

15F. Diagnostics

Because of the extremely fine time resolution and spatial resolution needed, a variety of sophisticated diagnostic techniques have been developed. Studies of ICF targets include energy flow, optical emission, x-ray emission, x-ray probing, neutron emission, charged particle emission, and neutron activation of target materials.

laser-plasma interactions

Silicon pin diodes, plasma calorimeters, and bolometers measure the amount of ablated plasma and reflected laser beam energy leaving the target at various angles. From these measurements the amount of laser beam energy reflected at various angles can be determined, and the absorbed fraction estimated. Light reflected by stimulated Brillouin scattering is mainly at 180°, and light reflected back by Raman scattering is observed at wavelengths about twice the incident wavelength.

Holographic interferograms may be made with an ultraviolet laser beam, in order to penetrate inside the critical density surface. Such an interferogram and the resultant density profile data are shown in Fig. 15F1. The profile steepening by radiation pressure enhances resonance absorption and reduces SBS.

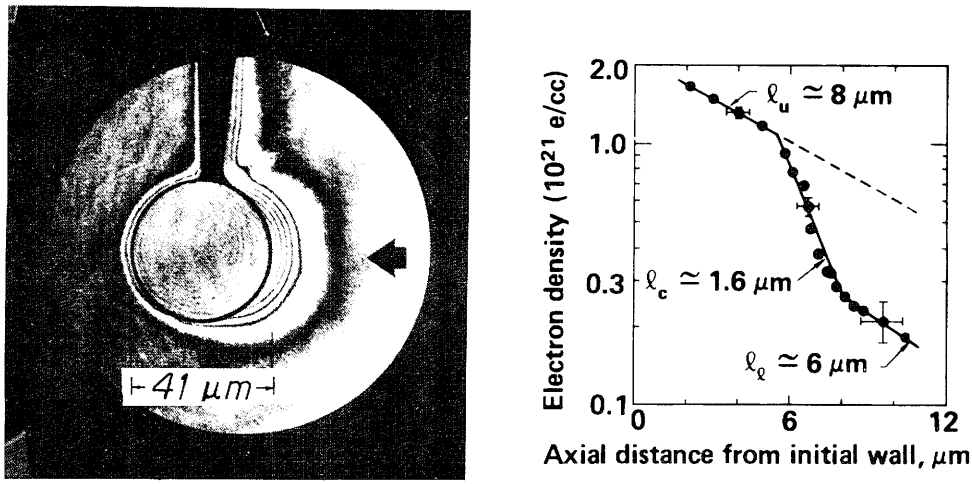

Fig. 15F1. Profile steepening due to radiation pressure is demonstrated in this target irradiation experiment $I \simeq 3\times10^{14}$ W/cm^2 at 1.06 μm, 15 ps. Probe beam λ = 266 μm. From D. T. Atwood, IEEE Journal of Quantum Electronics QE-14, 909-923 (1978), Fig. 10. © *1978 IEEE.*

Light emitted from the plasma may be monitored with optical streak cameras, to study the ablation process. Most of the radiation from the target and core, however, are at x-ray wavelengths.

x-ray measurements

Multichannel x-ray spectrometers have been developed. Each channel contains a mirror with grazing incidence reflection, which does not reflect x-rays above a certain cutoff energy. Then a thin-film filter screens out low-energy x-rays, providing an x-ray transmission "window" about 0.1-0.2 keV wide in each channel. Some typical channel responses are illustrated in Fig. 15F2. Each channel is connected to an x-ray detector. From the detector signals, the target x-ray spectra vs.time can be determined, as illustrated in Fig. 15F3. The spectra often show a two-temperature distribution, consisting of "thermal" and "supra-thermal" electrons. The suprathermal electron temperature, which is a main cause of preheat, follows the laser intensity in time.

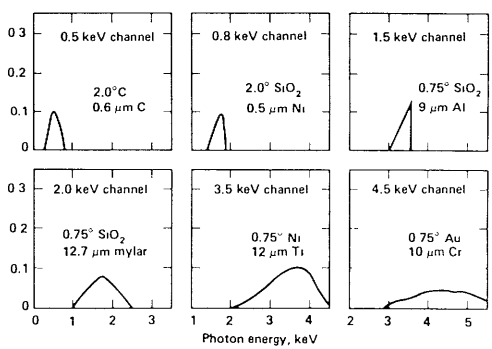

Fig. 15F2. Multichannel x-ray microscope spectral energy windows. From L. W. Coleman, "Laser fusion diagnostics", Chapter 7, Proceedings of the IEEE Mini-course on Inertial Confinement Fusion, Edited by G. H. Miley, U. of Illinois Fusion Studies Laboratory, 1980, Fig. 36, p. 7-69.

Space-time measurements of x-ray emission are provided by x-ray streak cameras. Instead of a rotating mirror, x-ray streak cameras use electronic sweeping of electrons from a photocathode, as illustrated in Fig. 15F4. The slit views x-rays emitted across a diameter through the target as a function of time. The resulting streak photographs provide a space-time mapping of x-ray intensity along that diameter, as illustrated in Fig. 15F5. From the rate at which the target edge moves inwards, the implosion velocity can be determined. Typical velocities are 1-4x10^5 m/s (0.1-0.4 μm/ps). X-ray pictures of the core region may be obtained by seeding the fuel with Argon and tuning a reflector to image an Argon x-ray line, with a spatial resolution < 10 μm .

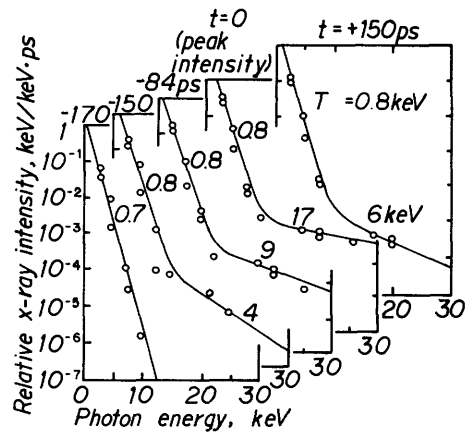

Fig. 15F3. Time resolved x-ray spectra from a laser irradiated gold alloy disk. The spectra beyond 8 keV show a suprathermal component which approximately follows the laser pulse. Shot #37101311: 284J/190 psec FWHM, 3x10^{15} W/cm^2. From D. T. Atwood, IEEE Journal of Quantum Electronics QE-14, 909-923 (1978), Fig. 23. © *1978 IEEE.*

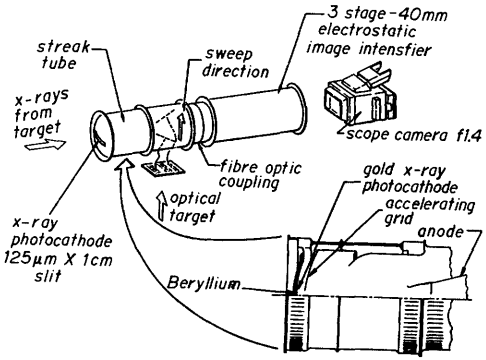

Fig. 15F4. An x-ray streak camera. From L. W. Coleman, 1980, Fig. 29, p. 7-62. Courtesy of LLNL and Univ. of California.

Two-dimensional spatial images can be obtained with an x-ray microscope using grazing-incidence mirrors and film. Although the microscope data are time-integrated, they indicate the degree of symmetry and degree of compression.

The target can be probed with a flash of x-rays from another source, such as a separate laser beam incident on a nearby metal disc. The image is recorded on an x-ray streak camera to portray the target shell radius vs. time, as illustrated in Fig. 15F6. This method gives a better picture of the shell interior

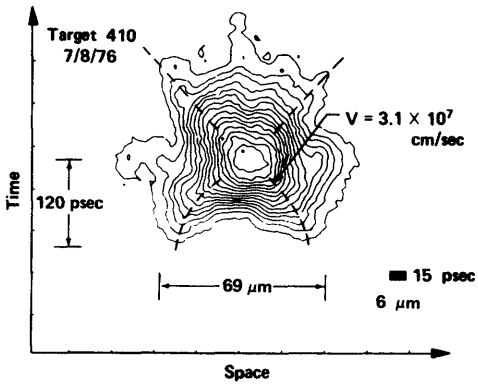

Fig. 15F5. Space-time isodensity contours for a two-sided target irradiation. Density contour interval is 0.2, monotonically increasing towards the target core. From D. T. Atwood, IEEE Journal of Quantum Electronics QE-14, 909-923 (1978) Fig. 19. © *1978 IEEE.*

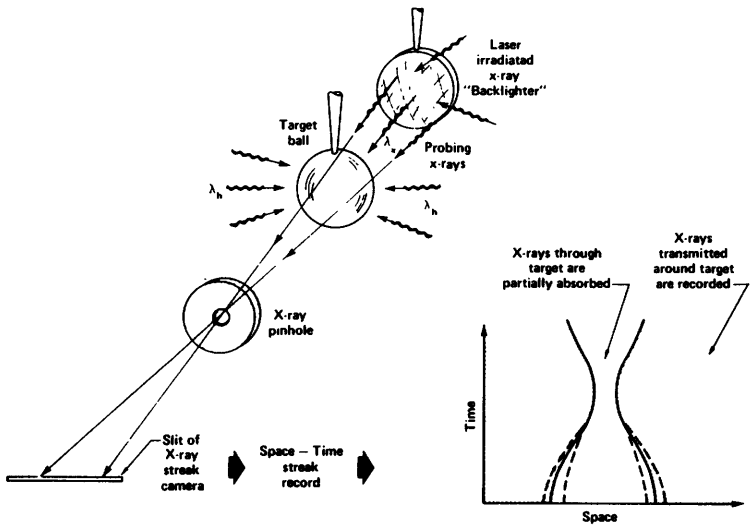

Fig. 15F6. Schematic diagram showing how a laser irradiated disk can provide necessary x-rays, λ_x, for diagnosing a relatively cold implosion. Target ball is shown being irradiated from two sides by laser heating pulse, λ_h. X-ray pinhole imaging is combined with streak camera to produce a space-time implosion history. Alternate schemes might use x-ray film with a short duration x-ray pulse for two-dimensional recording at a pre-selected time. Diffracting devices might be used for a multiplicity of images at differing x-ray wavelengths. From D. T. Atwood, IEEE Journal of Quantum electronics QE-14, 909-923 (1978), Fig. 28. © 1978 IEEE.

structure than other methods, especially with cool, high-density compressions. Interferometry and Thomson scattering with x-rays have also been proposed, but not yet developed.

charged particle measurements

Spatial resolution of alpha particles emerging from the core has been attained with Fresnel zone plates, as shown in Fig. 15F7. Such data give an estimate of the size of the burn region. However, this method fails at high ρR, because most of the alpha particles will be trapped inside the target.

If a deuterium fuel containing ^3He is used, 3 MeV protons will be produced by the DDp reactions, and 14.7 MeV protons, by the D-^3He reactions. The ratio of these reactions rates and proton yields is a strong function of ion temperature for $1 < T_i < 10$ keV, so the proton yield ratio may be measured to determine T_i.

It is also possible to measure the energetic knock-on deuterons and tritons produced by elastic scattering of the DT neutrons. The elastically scattered tritons and deuterons should have energy peaks near 3.5 and 6.3 MeV, respectively. Energy losses of the knock-on ions in the target distort the energy spectra. By measuring the energy losses of protons emitted by DDp or D-^3He reactions, this distortion can be taken into account. The resulting measurements then yield estimates of the ρR value for the compressed fuel.

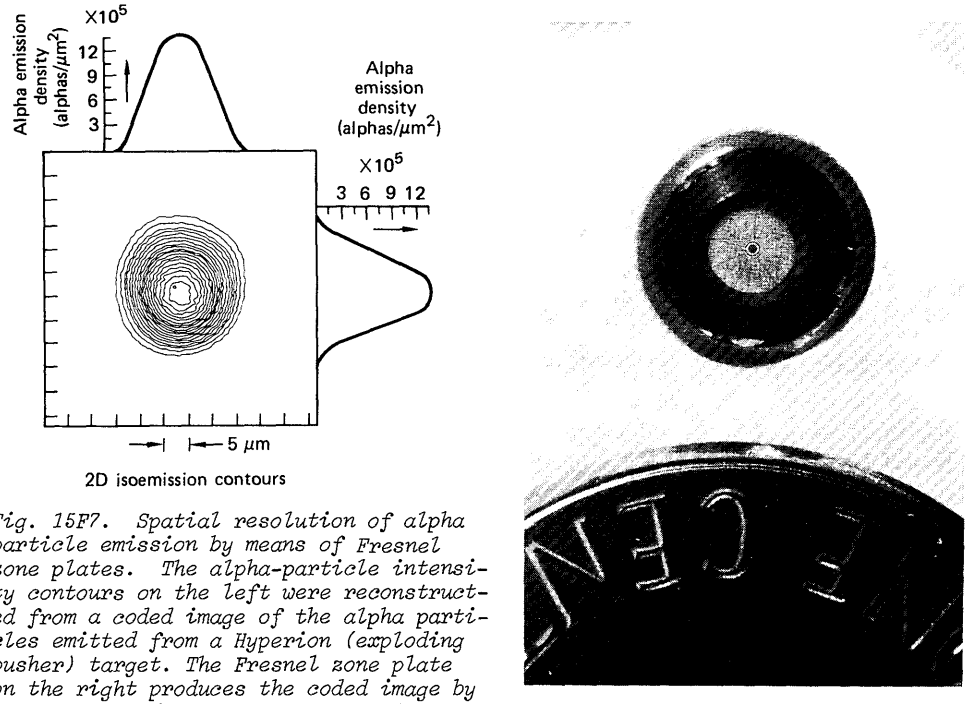

Fig. 15F7. Spatial resolution of alpha particle emission by means of Fresnel zone plates. The alpha-particle intensity contours on the left were reconstructed from a coded image of the alpha particles emitted from a Hyperion (exploding pusher) target. The Fresnel zone plate on the right produces the coded image by casting a shadow on an alpha-sensitive film located about 5 cm behind the zone plate. The zone plate, located about 1 cm from the target, is 2.5 mm in diameter with 100 zones, the smallest of which is only 5.3 μm wide. These plates are produced by ultraviolet photolithography and built up to the required 5 μm thickness by microelectroplating techniques. From "Diagnosis of laser fusion targets", Energy and Technology Review, August, 1977, p. 23-29, Fig. 2.

neutron measurements

The neutron yield vs. time can be measured with scintillation detectors. The time delay between the peak laser intensity and the peak neutron emission rate gives an estimate of the implosion speed.

A time-of-flight spectrometer may be used to measure the neutron energy spectrum. Neutrons from the target pass through a long tube to the detectors. High-energy neutrons arrive first, and low-energy neutrons, last. From the number of neutrons arriving at the detectors as a function of time after target compression, the energy distribution can be determined, as illustrated in Fig. 15F8. From the width of the neutron energy distribution, the fuel ion temperature can be estimated (4.8 keV in Fig. 15F8). The flight tube for the Shiva experiment is 125 m long, and provides an energy resolution of about 25 keV. With this tube length, the x-ray time of flight is about 417 ns, and the neutron flight time is about 2441 ns.

neutron activation analysis

Consider the case of monoenergetic neutrons passing through the target shell with slight attenuation and causing nuclear reactions with shell atoms having

density n_2 and cross section σ. The yield Y of activated atoms is found by integrating the nuclear reaction rate over time and space:

$$Y = \int dt \int_0^R 4\pi r^2 dr\, n_n n_2 \sigma v \exp(-\Sigma r) \qquad (15F1)$$

where n_n and v are the neutron density and speed, and Σ is a macroscopic cross section for neutron attenuation. The product $n_n v$ gives the neutron flux, and

$$Y_n = \int dt\, 4\pi r^2 n_n v \qquad (15F2)$$

is the total neutron yield. If the activated atoms have a mass fraction f_2 of the target density ρ and a mass m_2 per atom, then

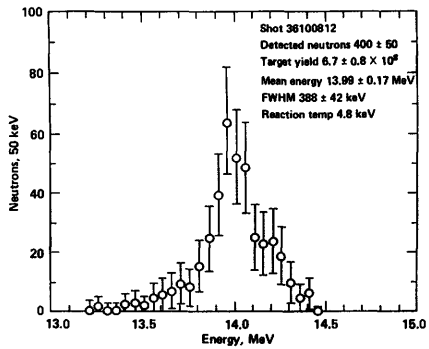

Fig. 15F8. Energy spectrum of DT neutrons measured by a time-of-flight spectrometer. From L. W. Coleman, 1980, Fig. 57, p. 7-90. Courtesy of LLNL, the University of California, and the Department of Energy.

$$n_2 = f_2 \rho / m_2 \quad . \qquad (15F3)$$

The activation yield may thus be written in the form

$$Y = (Y_n f_2 \sigma / m_2) \int_0^R dr\, \rho \exp(-\Sigma r) \qquad (15F4)$$

If $\Sigma R << 1$, then

$$Y/Y_n \simeq (f_2 \sigma / m_2) \rho\, \Delta R \qquad (15F5)$$

where ΔR is the thickness of the layer containing the atoms n_2. Thus, from measurements of the neutron yield and the yield of activated atoms, the $\rho \Delta R$ of compressed target layers can be estimated. (If the activated atoms are part of the fuel, then not all of the fusion neutrons pass through the atoms of n_2, and a correction factor is needed in these equations.)

Some nuclear reactions of interest include:

$^{28}Si(n,p)^{28}Al$	$^{28}Al \rightarrow \beta^- + {}^{28}Si + \gamma$	(2.24 min)	(15F6)
$^{63}Cu(n,2n)^{62}Cu$	$^{62}Cu \rightarrow \beta^+ + {}^{62}Ni$	(9.73 min)	(15F7)
$^{79}Br(n,2n)^{78}Br$	$^{78}Br \rightarrow \beta^+ + {}^{78}Se$	(6.5 min)	(15F8)

where the times in parentheses are decay half-lives. In order to improve the signal-to-noise ratio, the β^- and γ emitted by ^{28}Al are detected with two detectors connected with the coincidence logic: counts are only registered when the two occur at once. Similarly, the positrons emitted by ^{62}Cu and ^{78}Br are annihilated when they react with electrons, yielding two gamma rays, which can be detected with a coincidence system.

In practice, about half of the radioactive debris can be collected on a disc near the target and quickly transferred to the detector, where the decay products

are counted. By using different seed isotopes in the fuel and pusher, it is possible to determine their respective $\rho\Delta R$ values separately.

Bibliography

general

L. A. Booth, D. A. Freiwald, T. G. Frank, and F. T. Finch, "Prospects of generating power with laser-driven fusion", *Proceedings of the IEEE 64*, 1460-1482 (1976).

C. K. Choi, T. E. Blue, and G. H. Miley, "Advanced-fuel pellet approaches to inertial fusion", *Energy 4*, 157-162 (1979).

R. K. Cole, Jr., and J. H. Renken, "Analysis of the microfission reactor comcept", *Nuclear Science and Engineering 58*, 345-353 (1975).

ICF '80, Technical Digest of the Topical Meeting on Inertial Confinement Fusion, Optical Society of America, New York, 1980.

1978 Inertial Confinement Fusion, Technical Digest of the Topical Meeting on Inertial Confinement Fusion, Optical Society of America, IEEE, New York, 1977.

G. H. Miley, Editor, Proceedings of the IEEE Minicourse on Inertial Confinement Fusion, Montreal, 1979, U. of Illinois Fusion Studies Laboratory, 1980.

W. Seifritz and J. Ligou, "Laser-induced thermonuclear micro-explosions using fissionable triggers", *Nuclear Science and Engineering 56*, 301-303 (1975) (1975).

C. M. Stickley, "Laser fusion", *Physics Today*, May, 1978.

F. Winterberg, "The possibility of microfission explosions by laser or relativistic electron-beam high-density compression", *Lettere al Nuovo Cimento 6*, 407-411 (1973).

energy gain

S. E. Bodner, "Critical elements of high gain laser fusion", NRL Memorandum Report 4453, 1981.

G. S. Fraley, E. J. Linnebur, R. J. Mason, and R. L. Morse, "Thermonuclear burn characteristics of compressed deuterium-tritium microspheres", *The Physics of Fluids 17*, 474-489 (1974).

R. E. Kidder, "Energy gain of laser-compressed pellets: a simple analytical model calculation", *Nuclear Fusion 16*, 405-408 (1976).

laser-plasma interactions

C. M. Armstrong, B. H. Ripin, F. C. Young, R. Decoste, R. R. Whitlock, and S. E. Bodner, "Emission of energetic electrons from a Nd-laser-produced plasma", *Journal of Applied Physics 50*, 5233-5237 (1979).

F. F. Chen, *Laser Interaction and Related Plasma Phenomena, Vol. 3A*, H. Schwartz and H. Hora, Editors, Plenum Press, New York, 1974, p. 291-313.

R. Decoste and B. H. Ripin, "High-energy ion expansion in laser-plasma interactions", *Physical Review Letters 40*, 34-37 (1978).

T. P. Hughes, *Plasmas and Laser Light*, Wiley, New York, 1975, Chapter 2.

R. E. Kidder, "Hot-electron preheat of laser-driven targets", *Nuclear Fusion 21*, 145-151 (1981).

W. L. Kruer, "Laser-plasma coupling", Chapter 5 of *Proceedings of the IEEE Minicourse on Inertial Confinement Fusion*, Edited by G. H. Miley, U. of Illinois Fusion Studies Laboratory, 1980.

C. E. Max, C. F. McKee, and W. C. Mead, "A model for laser driven ablative implosions", *The Physics of Fluids 23*, 1620-1645 (1980).

S. P. Obenschain, R. H. Lehmberg, and B. H. Ripin, "Beam nonuniformity effects on laser ablatively accelerated targets", *Applied Physics Letters 37*, 903-906 (1980).

B. H. Ripin and E. A. McLean, "Brillouin backscatter dependence upon pulse amplitudes, timing, target material, and geometry", *Applied Physics Letters 34*, 809-811 (1979).

B. H. Ripin, R. R. Whitlock, F. C. Young, S. P. Obenschain, E. A. McLean, and R. Decoste, "Long-pulse laser-plasma interactions at 10^{12}-10^{15} W/cm^2", *Physical Review Letters 43*, 350 (1979).

J. A. Stamper, E. A. McLean, and B. H. Ripin, "Studies of spontaneous magnetic fields in laser-produced plasmas by Faraday rotation", *Physical Review Letters 40*, 1177-1181 (1978).

compression

R. Decoste, S. E. Bodner, B. H. Ripin, E. A. McLean, S. P. Obenschain, and C. M. Armstrong, "Ablative acceleration of laser-irradiated thin-foil targets", *Physical Review Letters 42*, 1673-1677 (1979).

R. E. Kidder, "Laser-driven isentropic hollow-shell implosions: the problem of ignition", *Nuclear Fusion 19*, 223-234 (1979).

R. C. Kirkpatrick and J. A. Wheeler, "The physics of DT ignition in small fusion targets", *Nuclear Fusion 21*, 389-401 (1981).

B. H. Ripin, R. Decoste, S. P. Obenschain, S. E. Bodner, E. A. McLean, F. C. Young, R. R. Whitlock, C. M. Armstrong, J. Grun, J. A. Stamper, S. H. Gold, D. J. Nagel, R. H. Lehmberg, and J. M. McMahon, "Laser-plasma interaction and ablative acceleration of thin foils at 10^{12} - 10^{15} W/cm^2", *The Physics of Fluids 23*, 1012-1030 (1980).

targets

R. O. Bangerter, "Fusion target design", Chapter 5; J. M. Kindel and E. L. Lindman, "Target designs for energetic ions", Chapter 6a; and J. M. Kindel and M. A. Stroscio, "Double-shell target designs for the Los Alamos Scientific Laboratory eight-beam laser system", Chapter 6b of Proceedings of the IEEE Minicourse on Inertial Confinement Fusion, G. H. Miley, Editor, U. of Illinois Fusion Studies Laboratory, 1980. (These articles were also printed as reports UCRL-82026, LA-UR-78-765, and LA-7167-MS, respectively.)

F. R. Chang, "Laser-guided pellets for inertial fusion", *Nuclear Fusion 20*, 537-545 (1980).

C. D. Hendricks, "Fuel pellets and optical systems for inertially confined fusion", *Fusion Reactor Materials, Part A*, Edited by F. W. Wiffen, J. H. DeVan, and J. O. Stiegler, North Holland, Amsterdam, 1979, p. 79-86. [Also published in *Journal of Nuclear Materials 85 & 86*, 79-86 (1979).]

R. C. Kirkpatrick, "An overview of design space for small fusion targets", *Nuclear Fusion 19*, 69-79 (1979).

M. A. Sweeney and A. V. Farnsworth, Jr., "High-gain, low-intensity ICF targets for a charged-particle beam fusion driver", *Nuclear Fusion 21*, 41-54 (1981).

diagnostics

D. T. Atwood, "Diagnostics of the laser fusion program - plasma physics on the scale of microns and picoseconds", *IEEE Journal of Quantum Electronics* Vol. QE-14, 12, 909-1309, (Dec. 1978).

T. E. Blue and D. B. Harris, "The ratio of D-T to D-D reactions as a measure of the fuel density-radius product in initially tritium-free inertial confinement fusion targets", *Nuclear Science and Engineering 77*, 463-469 (1981).

L. F. Chase, "Laser fusion power balance measurements (particle transmission diagnostics)", EPRI ER-591 (1978).

L. W. Coleman, "Laser fusion diagnostics", Proceedings of the IEEE Minicourse on Inertial Confinement Fusion, Edited by G. H. Miley, U. of Illinois Fusion Studies Laboratory, 1979, Chapter 7; and UCRL-81099 (1979).

ICF '80 Topical Meeting on Inertial Confinement Fusion Technical Digest, Optical Society of America, 1980, p. 106-112.

CHAPTER 16

ICF DRIVERS AND CHAMBERS

16A. Glass Lasers

fluence limitations

Laser operation and types of lasers are described by Lengyel (1971). Neodymium-doped glass lasers (λ = 1.05 μm) provide good energy storage and high gain. Very short pulse lengths (< 0.1 ns) are attainable.

The most powerful Nd-glass laser system will be the Nova facility at LLNL. It will be able to produce a 3 ns pulse of about 300 kJ (100 TW) or a 0.3 ns pulse of about 100 kJ (300 TW). A schematic illustration of one of the 20 beams is shown in Fig. 16A1. A small oscillator laser provides an initial pulse of photons to trigger stimulated emission in the amplifiers. The oscillator pulse is split into 20 paths by beam-splitters (partially transparent mirrors). The optical path length of each beam is adjusted so that it arrives at the target at the desired time. Then the beam passes through several amplifier stages.

As the power increases, the beam must be expanded, in order to prevent damage to optical components. Damage thresholds, shown in Table 16A1, are on the order of 10 J/cm^2. A laser beam producing $\sim$ 15 kJ, as each Nova beam will, needs to have an area $\sim$ 1500 cm^2, or a radius $\sim$ 22 cm. The radius of the final amplifier stage is 23 cm. The beam is further expanded to a radius of 37 cm before passing through the final focusing lens, in order to bring its fluence below the damage

Table 16A1. Surface damage threshold for anti-reflection-coated and uncoated optical surfaces (Nova performance at 12 kJ). From Energy and Technology Review, December, 1980, Table 1, p. 5.

	damage threshold, J/cm^2		
	0.1 ns	1.0 ns	3.0 ns
coated surfaces	2.5	8.0	8.5
bare polished surfaces	6.0	19	33

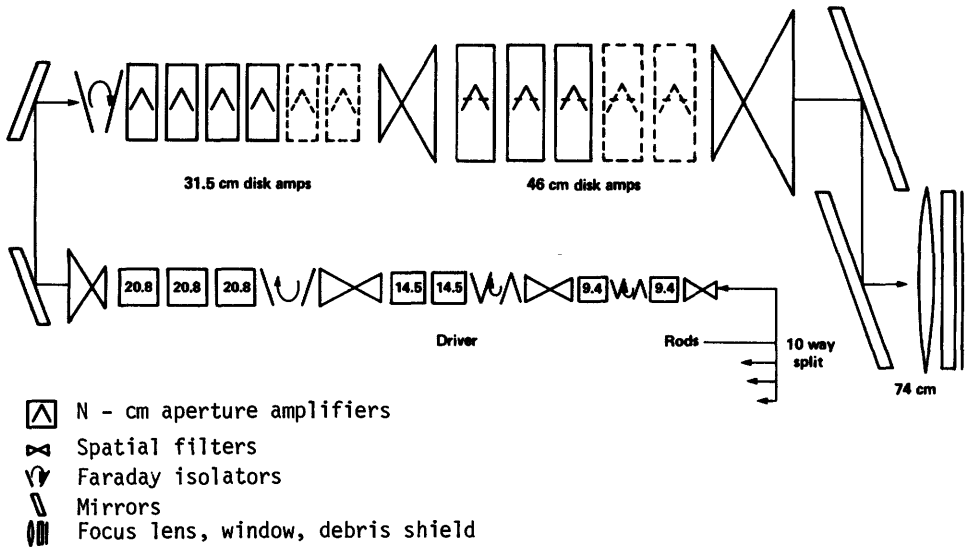

Fig. 16A1. A Nova Phase 1 amplifier chain. From J. A. Glaze, W. W. Simmons, R. O. Godwin, W. F. Hagen, J. F. Holzrichter, J. B. Trenholme, and W. E. Warren, "Nova glass laser fusion facility", ICF 80, Technical Digest of the Topical Meeting on Inertial Confinement Fusion, Optical Society of America, 1980, paper THF1, Fig. 1, p. 123.

threshold for coated optics. The variation of beam fluence (J/cm^2) with distance along the beam path is illustrated in Fig. 16A2.

Fig. 16A2. Variation of peak fluence with distance along the Nova laser chain for a 9.4 kJ, 1 ns laser pulse. The location of spatial filter lenses is indicated at the top of the figure. These lens surfaces will suffer damage if the peak fluence exceeds the indicated limits. The laser can be operated without damage at or below 9.4 kJ. The dots indicate the average fluence at various locations. From Energy and Technology Review, LLNL, December 1980, Fig. 3, p. 6.

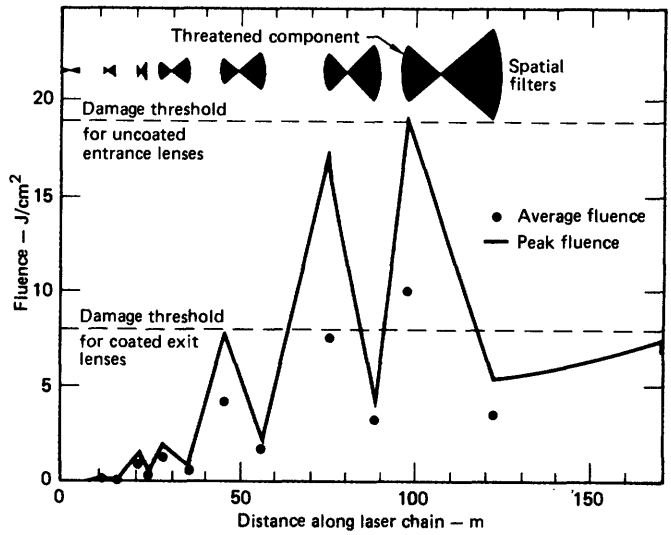

amplifiers

Figure 16A3 shows a partially assembled 46-cm amplifier. The amplifiers contain elliptical Nd-glass disks inclined at the Brewster angle to the beam to minimize reflection by the disks. The Brewster angle is defined by

$$\theta_B = \tan^{-1}\tilde{n} \qquad (16A1)$$

where $\tilde{n}$ is the refractive index of the glass. For example, if $\tilde{n} \simeq 1.5$, then $\theta_B \simeq 56°$. If the disks were thicker, it would take longer for them to cool off between pulses, and severe thermal stresses could cause cracking. Heat removal is a difficult problem, if rapid pulsing is desired.

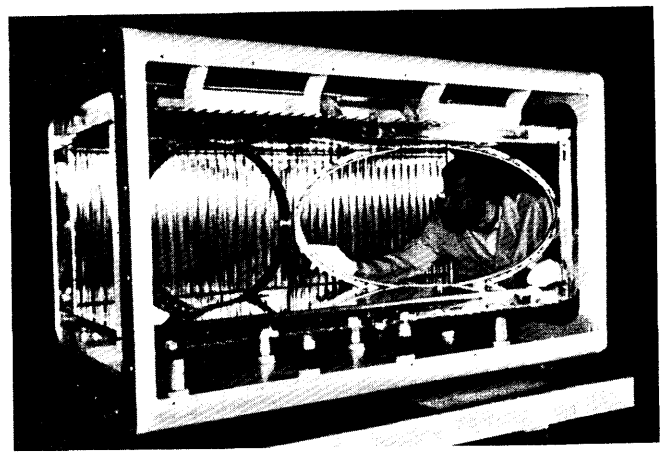

Fig. 16A3. A partially assembled 46-cm rectangular laser amplifier of the Nova system. Half disks will be inserted in the elliptical holders. Transverse flashlamps and their reflectors appear at the back of the amplifier head. The interior metal parts of the amplifier are insulated to 50 kV to prevent arc-over. Most of the metal parts shown are electroformed nickel; optical cavity interior parts are silver-plated for high reflectivity. From Energy and Technology Review, LLNL, December 1980, Fig. 7, p. 10.

The side walls of the rectangular amplifier box are lined with 80 flashlamps backed by silver-plated crenulated reflectors, which reflect light into the glass disks and minimize absorption by neighboring flashlamps. The flashlamps are xenon gas discharge tubes pulsed by capacitor banks. About 5-10 % of the electrical energy to the flashlamps emerges as light, and a fraction of that is absorbed by the Nd-glass disks in the proper wavelength region to excite the upper energy level of the laser. These excited atoms are de-excited by stimulated emission when the pulse of photons from the previous amplifier stage arrives. (The spatial length of a 1 ns laser pulse is 30 cm.)

parasitic oscillations

Figure 16A4 illustrates the path of a light ray internally reflected at the edges of a glass disk. Such light rays, created by spontaneous emission, may trigger unwanted stimulated emission, which depletes the population of excited atoms without contributing to the laser beam. To minimize such *parasitic oscillations*, the edges of the amplifier disks may be coated with a cladding

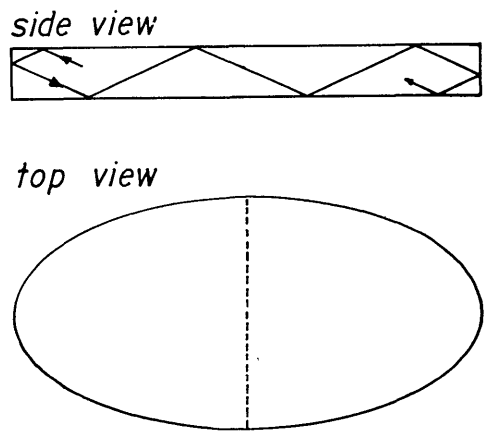

Fig. 16A4. Path of a light ray reflected internally from the edges of a glass amplifier disk.

material. If the cladding has the same index of refraction as the laser glass and absorbs the photons, instead of reflecting them, then the intensity of the parasitic oscillations will be unable to grow.

In large disks, cladding alone is not enough, and the disks are split at the middle (dashed line of Fig. 16A4), to further reduce the buildup of parasitic oscillations.

spatial filters

As the beam passes through amplifier stages, optical imperfections and self-focusing effects tend to make its intensity vary spatially over the beam cross section. At each stage of beam expansion, a spatial filter is used to reduce such spatial variations. Instead of being expanded directly with a diverging (concave) lens, the beam is focused through a pinhole. The non-parallel light associated with the intensity variations does not focus through the pinhole, but is scraped off at the edge of the pinhole. Thus, the pinhole collimators remove much of the spatial non-uniformity from the beam. The light rays passing through the pinhole expand to the desired larger beam diameter, where a convex lens makes them parallel for entry into the next amplifier stage. By removing intensity peaks and valleys, the spatial filters increase the *filling factor* (ratio of average beam intensity to peak beam intensity) to over 70 %.

If a beam expands from d_1 to d_2 in a spatial filter and then travels through an optical path of length L before entering the next filter, the optimum length of the first filter (distance between lenses) is

$$L_f = Ld_1/d_2 \quad . \tag{16A2}$$

The longest filter in the Nova chain has L_f = 23 m.

If the power flux around a pinhole is too large, its edges will be vaporized, and the resulting plasma may fill the hole and block the beam (self-closure).

The Nova design avoids this problem by careful choice of pinhole apertures and focal lengths. The spatial filters have f/20 lenses (focal length is 20 times beam diameter).

isolators

Light reflected from optics can go back into previous amplifier stages and be amplified flowing in the reverse direction. Such amplified pulses can cause damage to the optics, especially after being focused down to smaller diameters. Therefore, isolators are needed at each stage of expansion to prevent significant flow of light in the backwards direction.

Isolation may be accomplished using rotation of the plane of polarization or using a plasma shutter. When a high voltage is applied across a non-centro-symmetric crystal such as potassium dihydrogen phosphate (KDP), the plane of polarization of light passing through the crystal will be rotated. With polarized filters on each side of the crystal, it can be arranged to transmit light only during a brief interval ($\sim$ 10 ns) while the voltage is pulsed on.

Faraday rotation [Eq.(10G20)] can occur in most glasses. A strong axial magnetic field can be used to rotate forward-propagating light by 45° in a right-hand sense relative to the magnetic field. The plane of polarization of back-reflected light will then be rotated perpendicular to that of the initial beam, and can be rejected by a polarizing filter.

Since the large-diameter final beam would require a large, expensive magnet for a Faraday rotator, a plasma shutter is used instead. After the laser pulse has passed through the pinhole of the last spatial filter, a thin foil next to the pinhole is exploded by pulsing a high current through it. The resulting plasma flows across the pinhole with a velocity of 3 cm/μs, covering it before the reflected light from the target arrives. The plasma density $n \sim 1.5 \times 10^{27}$ m^{-3} is greater than the critical density, so the returning light is not transmitted. The plasma shutter is designed so that debris from the exploding foils does not reach the lenses, and the foil is automatically changed between shots.

glass properties

In a laser amplifier with small-signal gain g_0 and absorption coefficient α, the beam intensity I varies with position z as

$$\frac{dI}{dz} = \frac{g_0 I}{1 + \frac{I}{I_s}} - \alpha I \qquad (W/m^3) \qquad (16A3)$$

where I_s is the *saturation intensity*. For a high-intensity beam ($I >> I_s$), the solution of this equation is

$$I(z) = I_0 \exp(-\alpha z) + (g_0 I_s/\alpha)[1 - \exp(-\alpha z)] \qquad (16A4)$$

where I_0 is the intensity at z = 0. If $\alpha z << 1$, this reduces to

$$I(z) \simeq I_0 + g_0 I_s z \qquad (16A5)$$

which indicates a linear growth of intensity. The product $g_0 I_s$ represents the power which can be extracted per unit volume of amplifier. These equations apply to all types of lasers.

The index of refraction has a small variation with intensity, which may be represented by the equation

$$\tilde{n} = n_0 + n_2 I \ . \qquad (16A6)$$

This increase of $\tilde{n}$ with intensity can lead to self-focusing of laser light inside the glass at high intensities, and consequent damage to the glass. Self-focusing can be avoided by reducing the path length of the light in the glass (the disk thickness), reducing the beam intensity I, or by choosing glass with a low non-linear index n_2 .

Phosphate glass has been chosen for use in the Nova amplifiers, because of its high gain coefficient. Fluorophosphate and fluoroberyllate glasses have lower values of n_2 than phosphate glass, but they are difficult to manufacture.

frequency shifting

When Nd-glass laser light at 1.05 μm is passed through a KDP or similar crystal, a portion of the radiation emerging will be at twice the incident frequency (λ = 0.53 μm). Power conversion efficiencies around 80 % have been attained, and similar schemes are used to obtain light output at the third and fourth harmonics (λ = 0.35 μm and 0.26 μm). Several aspects of laser-pellet coupling improve with decreasing wavelength:

* higher absorption fraction f_a
* lower hot-electron temperature, so less preheat
* better radial heat transport to pellet surface, improving hydrodynamic efficiency η_h

Most target compression experiments have been done with Nd-glass lasers.

Because it is difficult to attain high pulse rates, long component lifetimes, and high efficiencies (>> 1 %) with Nd-glass lasers, they would not be economical ICF reactor drivers, but they are useful for high-power compression experiments.

16B. CO_2 Lasers

amplifiers

An electron-beam-controlled gas discharge amplifier is illustrated in Fig. 16B1. The gas might consist of 80 % CO_2 and 20 % N_2 at a total pressure of about 2 atm. Up to 90 % of the energy absorbed can be stored in vibrational states. Part of the vibrational energy of the N_2 molecules can be collisionally transferred to vibrational states of CO_2 molecules forming the upper levels of various laser transitions. The gas discharge lasts microseconds, but the laser beam energy is extracted in nanoseconds. Bleachable absorbers are used to control parasitic oscillations.

The gain-length product GL $\sim$ 5-7 for CO_2 amplifiers. Higher gains are prevented by parasitic oscillations, and lower gains are less efficient.

The oscillators and preamplifiers of the Antares system deliver 36 J pulses to each of the amplifier modules. Each circular module has a gas volume of about 3.2 m^3, with 12 beams around its circumference, as shown in Fig. 16B2. The input

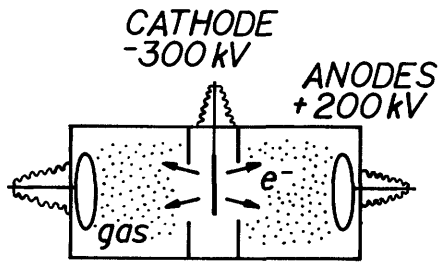

Fig. 16B1. A cold-cathode relativistic electron beam controlled gas discharge for a CO_2 laser. Two discharges are triggered by one cathode. The laser beam propagates perpendicular to the plane of the drawing.

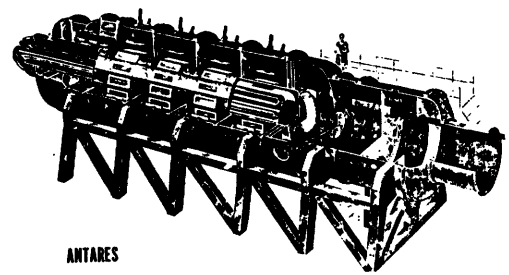

Fig. 16B2. One of the Antares amplifier modules. The central cylinder contains an electron-beam source, which controls the laser gas discharge. From R. B. Perkins, LASL-79-29 (1979), Los Alamos National Laboratory.

beams extract about 80 % of the energy stored in the upper laser levels as they make two passes through the module in 1 ns. The resulting 12 output beams provide a total energy of about 17 kJ per module, or 100 kJ for the six modules.

From the modules, the beams travel through long tubes to the target chamber building, which is shielded against 14 MeV neutrons, as illustrated in Fig. 16B3. Six modules are planned, but budget restrictions may reduce the final number.

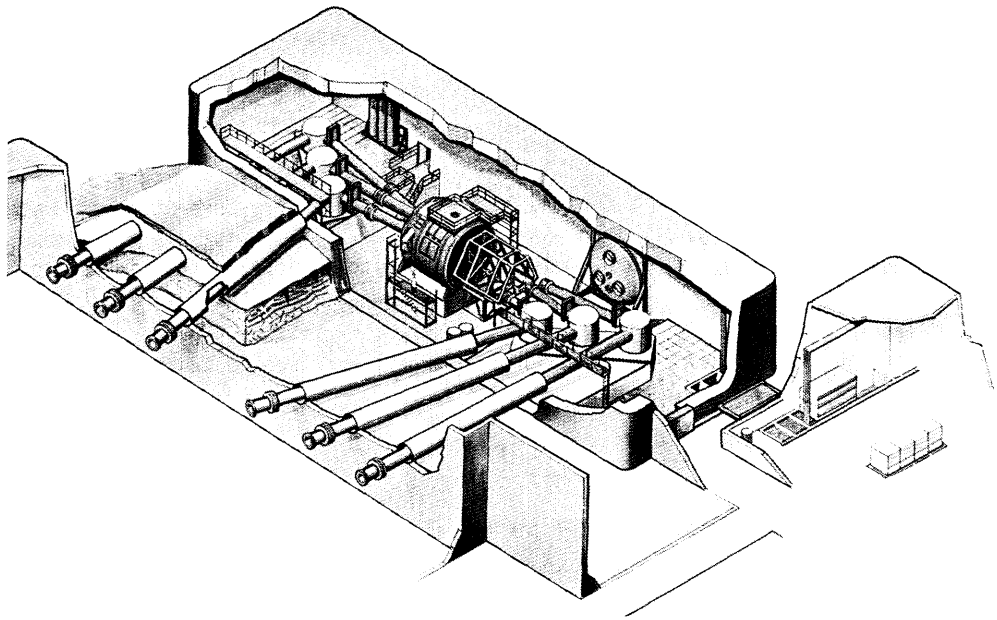

Fig. 16B3. The Antares 7 m diameter target chamber, building, and beam transport tubes. From R. B. Perkins, LASL-79-29 (1979), Los Alamos National Laboratory.

optics

Some type of window is needed to prevent CO_2 gas from flowing from the amplifiers into the beam transport tubes, where it would strongly attenuate the laser beams before they reached the target. The gas pressure in the tubes and chamber should be $\lesssim$ 0.1 Torr (13 Pa). Glasses do not transmit infrared radiation at 10.6 μm, so special windows are needed. The Antares amplifiers use 46 cm diameter polycrystalline NaCl windows (damage threshold $\sim$ 6 J/cm^2), exposed to fluences of 1-2 J/cm^2. Single-point diamond-machined copper disks are used for the turning and focusing mirrors.

For a 3 MJ laser system, the total area of the NaCl windows would be about 300 m^2. In order to avoid the expenses associated with producing and replacing so many salt windows, other options are being studied. One idea is to use a supersonic flow of gas to create the necessary pressure differential between the final amplifier and the target chamber. With such "gasdynamic windows" the gas pumping power required is about 20 MW/m^2 atm. Thus, with 20 m^2 aperture and 1 atm pressure, about 400 MW would be consumed.

power supplies

The Antares system uses 24 Marx generators (capacitors charged in parallel, then discharged in series to provide very high voltages). Each Marx generator stores 300 kJ at an open-circuit voltage of 1.2 MV, which discharges into the amplifier gas in 1-2 μs. If the pumping time could be extended to 4-5 μs without substantial energy loss by parasitic oscillations, then thyratrons and pulse transformers could be used (instead of the Marx generators) increasing the reliability of the pulsed system.

efficiency

The efficiency of multiple pass energy extraction with a single pulse is about 1-3 %. About 90 % of the energy stored in the CO_2 vibrational states can be extracted, but most of the energy is stored in the vibrational states of the N_2, and it takes 200 ns for effective collisional energy transfer from the N_2 to the CO_2. In order to use more of the stored energy, pulses can be sent through the CO_2-N_2 mixture at time intervals of about 200 ns. After several such pulses, much of the energy stored in the N_2 can be transferred to the CO_2 and extracted as stimulated emission. The early pulses can follow long paths, returning at the correct time to join the later pulses en route to the target. Efficiencies for CO_2 lasers with such *optical multiplexing* are expected to reach 5-10 %.

16C. Rare Gas Halide Lasers

characteristics

Rare gas halide laser combinations include KrF (248 nm), XeCl (308 nm), XeF (353 nm), and ArF (190 nm). These lasers, pumped by relativistic electron beam injection, have short radiative lifetimes (∿ 3 ns) so they cannot be pumped over a long period of time and then discharged suddenly, like Nd-glass and CO_2 lasers. Their short wavelengths are favorable for efficient coupling to targets. A KrF laser (0.248 μm) has attained an excited state production of over 20% of the input energy, and laser beam energies of 10 % of the input energy.

The excited states giving rise to stimulated emission are produced mainly by ion-ion recombination reactions, such as

$$Kr^+ + F^- \rightarrow KrF^* \quad . \tag{16C1}$$

From Eq. (16A3) the effective gain varies as

$$g \simeq \frac{g_0}{1 + I/I_s} - \alpha \quad , \tag{16C2}$$

illustrated in Fig. 16C1. High fluxes produce net absorption, instead of gain. The optimum extraction efficiency occurs at point A. For the KrF laser, $g/\alpha \sim 15$ are attainable at $I \sim 5$ MW/cm^2 (50 GW/m^2), with an extraction efficiency

(fraction of excited states utilized) about 50 %. This low output flux requires a large beam aperture. For example, if P = 10^{14} W, then A = 2000 m^2.

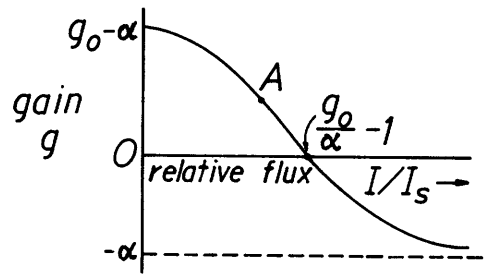

Fig. 16C1. Gain of a rare-gas halide laser vs. light flux.

The main problem with rare gas halide lasers is to get a lot of energy out in a short period of time (10-20 ns) for effective target compression. It is possible in principle to inject all the pump energy into the laser gas in the desired time, but it is very difficult to do so in practice. There are several other possibilities for attaining short pulse output:

* pumping a storage laser with the rare gas halide laser
* compression of a long pulse by backward wave Raman scattering
* pulse stacking
* pulse compression using polarization-sensitive optical time delay elements (H. E. Bates, ICF 80, p. 44).

pumping other lasers

In order to pump an energy storage laser with a rare gas halide laser, the laser wavelength must match the absorption bands of the storage medium, and its extraction efficiency should be high. One such possibility is a solid state laser consisting of Yttrium Lithium Fluoride containing Tm^{3+} ions. The $^1D_2$ level of the Tm^{3+} ions is close to the XeF pump laser energy, as illustrated in Fig. 16C2. The long radiative lifetime of the $^1D_2$ state (20 μs) permits effective energy storage. However, the lower laser level ($^3H_4$) also has a very long radiative lifetime (7 ms), so it tends to become overpopulated and to shut off the lasing action. Extraction efficiencies may be about 40 %, but overall efficiencies (final laser beam energy/input electrical energy) will probably be under 5 %, due to inefficiency of the XeF laser. Other combinations are under study.

backward wave Raman scattering

The energy states of a Raman scattering medium, such as methane, are illustrated in Fig. 16C3 at the left. Here ω_p represents the frequency of the

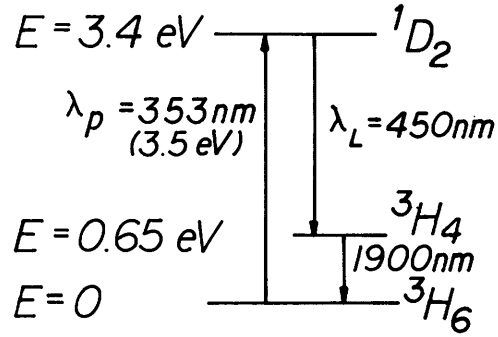

Fig. 16C2. Some energy levels of the Tm^{3+} ion. The XeF pump laser wavelength λ_p matches the energy transition from the ground state to the $^1D_2$ level, which decays by stimulated emission at the laser wavelength λ_L. Based on L. D. Pleasance, "Alternate laser fusion drivers", Proceedings of the Fifth Workshop on Laser Interactions with Matter, Plenum Press, NY, 1978, Fig. 9.

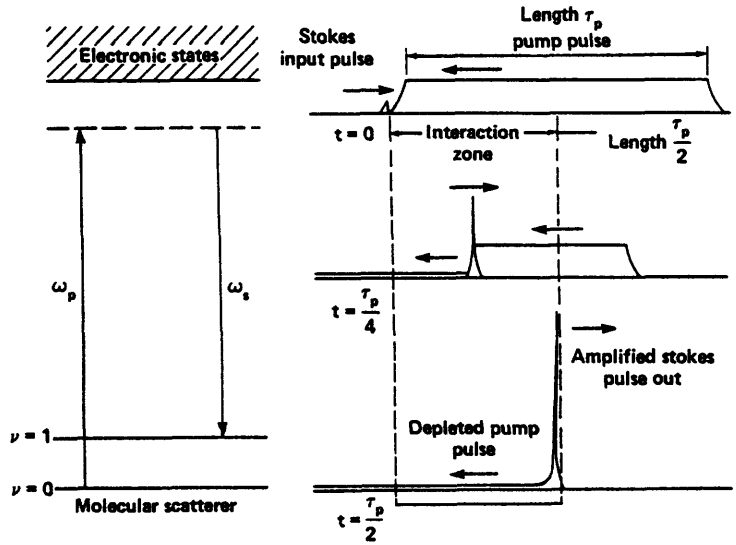

Fig. 16C3. Pulse compression and amplification by backward wave Raman scattering. Left: energy states of the Raman scattering medium, such as methane. Right: motion of short-pulse Stokes input beam to the right and longer pump pulse (from rare gas halide laser) to the left, with growth of the short-pulse Stokes wave as the two waves pass through each other. From L. D. Pleasance, "Alternate laser fusion drivers", Proceedings of the Fifth Workshop on Laser Interactions with Matter, Plenum Press, NY, 1978, Fig. 6.

"pump" wave, in this case a KrF laser beam (248 nm), and ω_s represents the frequency of the "Stokes" wave. From the diagram, it is apparent that

$$\omega_p = \omega_s + \omega_1 \qquad (16C3)$$

where ω_1 corresponds to the transition between the $\nu = 1$ and $\nu = 0$ states of the Raman scattering medium. When this resonance condition is satisfied, the two waves can interact strongly. A KrF laser beam with long pulse length τ_p can be injected into one end of the methane cell, and a weak, short-pulse Stokes wave at 268 nm can be injected from the other end, as shown at the right side of Fig. 16C3. As the waves pass through each other, energy from the pump wave is resonantly transferred to the Stokes wave, resulting in an amplified Stokes pulse and a depleted pump wave. The high-power, short-pulse Stokes wave can then be used for target compression. If the pulse length of the output Stokes pulse is τ_s, then the pump pulse has effectively been compressed by a factor of (τ_p/τ_s), with a slight frequency shift. Energy transfer efficiencies $\sim$ 80 % can be attained at $(\tau_p/\tau_s) \sim 5$, but efficiency decreases at higher pulse compression factors.

As the Stokes pulse amplitude grows, it can become the pump wave for a *second Stokes wave* at

$$\omega_2 = \omega_s - \omega_1 \quad . \qquad (16C4)$$

Although there is no pulse input at ω_2 to be amplified, there are some background oscillations at this frequency due to thermal noise, which can be amplified. Growth of the second Stokes wave steals energy from the primary Stokes wave ω_s, reducing the output pulse amplitude and energy transfer efficiency, especially at large pulse compression factors (τ_p/τ_s). At pulse compression factors (τ_p/τ_s) of 5, 10, and 20, second Stokes wave growth has limited the output efficiencies (Stokes pulse output/energy input) to values of about 75 %, 50 %, and 30 %. If the second Stokes wave growth could be inhibited by a selective absorber at ω_2, then higher efficiencies could be attained.

Metal vapors, such as Ba, Ca, and Pb, are also candidates for the Raman scattering medium, in place of methane. Their energy levels are more difficult to match, and the Stokes shift ω_1 is larger, so ω_s/ω_p is smaller, (less fractional energy transfer); but second Stokes generation is less than with methane.

Using Raman pulse compression, a KrF pulse with $\tau_p \sim 100$ ns could be compressed into a Stokes wave with $\tau_s \sim 10$-20 ns for target compression, with efficiency of 50-80 %.

pulse stacking

Pulse stacking is illustrated in Fig. 16C4. A short pulse from an oscillator and preamplifiers is divided into several paths by beamsplitters. For simplicity, only four paths are shown in the figure, but tens of paths may be used in practice. The four paths have different lengths, so the four initially simultaneous pulses arrive at the KrF amplifier in sequence, where they make two passes and grow in amplitude, Fig. 16C5c. Then the optical path lengths are adjusted to remove the optical delay, so the four large pulses are once again simultaneous, Fig. 16C5d. For example, with 50 beams, a 500 ns amplifier pulse could be compressed into a 10 ns output pulse for target compression.

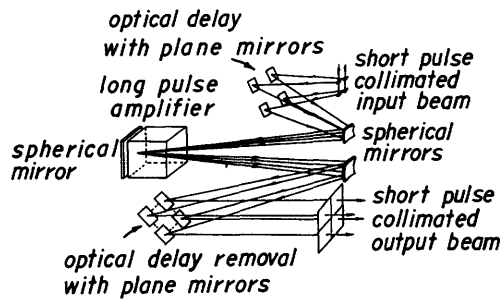

Fig. 16C4. A pulser stacker driver module. From R. A. Haas, L. G. Seppala, L. D. Pleasance, E. V. George, and W. F. Krupke, "KrF fusion laser system design. 1: General performance characteristics of stacker/Raman compressor laser systems", ICF '80 Topical Meeting on Inertial Confinement Fusion Technical Digest, Optical Society of America, 1980, paper TUF11, Fig. 2, p. 47.

It is also possible to use both backward wave Raman scattering and pulse stacking, in order to attain higher pulse compression factors. The energy conversion efficiencies of Raman compression, pulse stacking, and a hybrid of the two are illustrated in Fig. 16C6. The arrows indicate possible improvements attainable by suppression of the second Stokes wave.

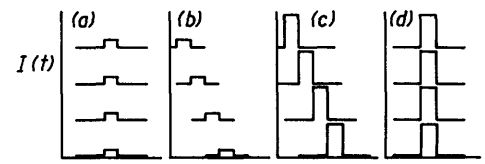

Fig. 16C5. Pulse shapes in the four beams of Fig. 16C4. (a) initially, (b) after optical time delay, (c) after amplification, (d) after second optical delay system.

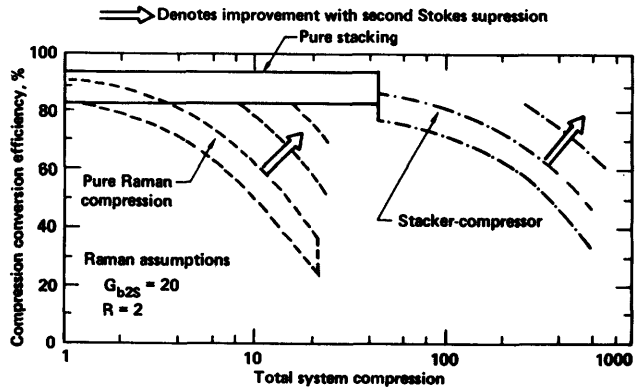

Fig. 16C6. Pulse compression efficiency vs. compression factor for Raman compression, pulse stacking, and a combination of the two. From R. A. Haas, "Review of KrF laser pulse stacking and compression techniques", ICF '80 Topical Meeting on Inertial Confinement Fusion Technical Digest, Optical Society of America, 1980, paper TUF7, Fig. 1, p. 43.

It appears feasible to use long pump times $\sim$ 1 μs with the KrF laser and to achieve 10-20 ns output pulses at driver efficiencies $\eta_d \sim$ 8-10 %.

16D. Other Lasers

Some characteristics of various laser systems under consideration for fusion drivers are listed in Table 16D1.

Table 16D1. Characteristics of some types of lasers. From L. D. Pleasance, "Alternate laser fusion drivers", Proceedings of the Fifth Workshop on Laser Interactions with Matter, Plenum Press, NY, 1978, Table 1.

Laser system	Wavelength (μm)	Typical energy (J)	Storage lifetime	Projected laser efficiency
HF	2.6	4000	10^{-8}	5%
Iodine	1.3	700	10^{-6}	<1%
Group VI	0.5, 0.7	<0.1	10^{-6}	1%
Solid state	0.3-1.1	<0.1	10^{-6}-10^{-3}	10%
Metal vapors	0.3-0.7	-	10^{-6}	10%
Rare gas halides	0.2-0.3	300	10^{-8}	5%
Rare gas excimers	0.15-0.18	10	10^{-8}	<1%

HF lasers

Hydrogen fluoride lasers are excited by the chemical reaction

$$H_2 + F_2 \rightarrow 2HF^* \qquad (16D1)$$

The Phoenix II device has three stages, with the final amplifier initiated by transverse injection of a 1.5 MeV electron beam. With gas pressures of 2100 Torr (0.28 MPa) of F_2 and 200 Torr (27 kPa) of H_2 and an active volume of 18 liters, a beam energy of 1.7 kJ can be extracted in a 60 ns pulse. When the input intensity is 4 MW/cm^2, about 90% of the available energy is extracted in the 2.6 μm laser beam. The broad bandwidth of the HF laser beam may reduce stimulated processes leading to production of suprathermal electrons (and associated preheat). The cost of a 1 MJ single-pulse HF laser facility is estimated to be about 40 $/J.

iodine lasers

Iodine lasers (1.315 μm) have demonstrated energy storage capability, and high-power, short-pulse operation. For example, the Asterix 3 device has delivered 1 TW to a target (300 J in 0.28 ns).

Chemically pumped iodine lasers have operated cw at high extraction efficiency. A metastable state of the O_2^* molecule is excited by chemical reaction of chlorine with hydrogen peroxide. Then the iodine is pumped by nearly-resonant energy transfer from the oxygen, via the reaction

$$O_2^*(^1\Delta) + I(^3P_{3/2}) \rightarrow O_2(^3\Sigma) + I^*(^2P_{3/2}) \qquad (16D2)$$

The energy stored in the O_2^* metastables is initially in equilibrium with the excited iodine atoms. When the iodine is de-excited by stimulated emission, there is a time delay before the rest of the energy stored in O_2^* molecules can be transferred to the iodine atoms. Using 10-20 beam passes through the amplifier, about 70 % of the stored energy could be extracted. Including energy expended for recycling the chemicals, overall efficiencies of up to 8 % might be attained by this system (Busch, ICF '80, p. 128).

Group VI Lasers

Group VI lasers include oxygen, sulfur, and selenium. These atoms have a couple of energy levels close to the ground state, then a large gap before the next energy level. For example, the $^1S_0$ and $^1D_2$ states of Se are about 3 and 1 eV above the ground state, Fig. 16D1, and the next state is at about 6 eV. The upper laser level (the $^1S_0$ state) which can be excited by absorption of ultraviolet radiation from another laser, has long radiative lifetime and good energy storage capability. Its stimulated emission cross section is low enough that amplified spontaneous emission is not a serious problem. Rare gas excimer lasers, which do not have such energy storage capability, have emission in the proper wavelength range for exciting Group VI lasers. A conversion of pump laser energy to Se laser output energy of 30 % has been measured.

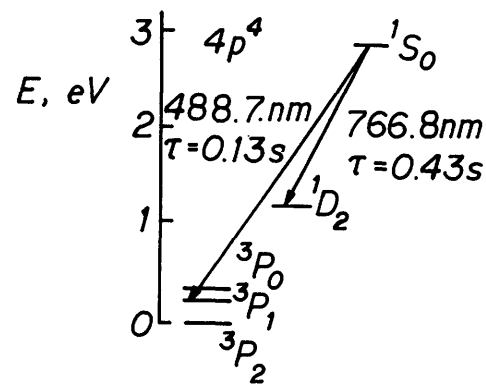

Fig. 16D1. Lower energy levels of Se I. From L. D. Pleasance, "Alternate laser fusion drivers", Proceedings of the 5th Workshop on Laser Interactions with Matter, Plenum Press, NY, 1979, Fig. 1.

As the pump intensity is increased, however, the excited state ($^1S_0$) population decreases, due to collisional deactivation by electrons, produced by photoionization. To reduce the electron population and energy, gases with high inelastic scattering cross sections (CO, N_2) or high attachment cross sections (SF_6) may be added. Low efficiency of the pump laser or fluorescence source is another major problem of Group VI lasers.

excimer lasers

An excimer is a molecule with stable excited states but an unstable ground state. Rapid dissociation of ground-state molecules prevents quenching of the laser output by accumulation of too many atoms in the lower laser level (*bottlenecking*). Excimer lasers do not have significant energy storage capability. They can be used with pulse compression techniques, or to pump energy storage lasers, such as Group VI lasers.

Excimers can be formed by processes such as

$$Xe^* + Xe^* \rightarrow Xe_2^* \quad . \tag{16D3}$$

Stimulated emission from Xe_2^* to the ground state results in dissociation of the molecule. The emission band-width is broad, so the gain is relatively low.

Efficiency is low, because much of the excitation appears as fluorescence radiation from states near the upper laser level rather than stimulated emission, and much of the stimulated emission is self-absorbed by the Xenon. (The absorption cross section is about 40 % of the stimulated emission cross section).

In addition to noble gas excimers, metal vapor excimers, such as Hg_2^*, also exist, but absorption coefficients of known excimers are too high for efficient laser operation.

solid state lasers

The Nd-glass lasers have low pulse repetition rates, due to thermal stress limitations, and low efficiencies, due to inefficient pumping with flashlamps. Improvements may be gained by using host materials other than glass or by using laser pumping.

With laser pumping the narrow linewidth permits selective pumping of levels not available with flashlamp pumping, and the high intensity makes it feasible to use storage media with shorter lifetimes. The pump laser must have high efficiency and match the solid state laser absorption band, as in the case of a Tm^{3+} ion (in a host medium of glass or YLiF) pumped by a XeF laser. The upper laser level ($^1D_2$) lifetime of 30 μs is long enough for efficient excitation of the pump laser, but the long lower state ($^3H_4$) lifetime will cause bottlenecking. Values of pumping and extraction efficiency of 10 % and 40 % could lead to an overall efficiency of about 4 % for this system.

Another possibility is xenon flashlamp pumping of a host medium with good thermal properties, such as MgF_2 with V^{2+} ions. The laser transition is from the $^4T_2$ level (2.3 ms lifetime) to the upper levels of the ground state manifold (group of energy levels), with a wavelength of 1.1 μm. Low-temperature operation could be used to avoid bottlenecking. Pulse repetition rates of several Hz and overall efficiencies of about 10 % might be attainable with the $V:MgF_2$ laser.

16E. Electron Beams

pulse formation

Production of relativistic electron beams (REB) requires an energy storage device, a pulse-forming line, a transmission line, and a diode where the electrons are emitted. The electrical energy is usually stored in a Marx generator, which consists of a group of capacitors charged in parallel, then reconnected in series by spark gap switches (Section 21E) and discharged into a pulse-forming line. For example, if twelve capacitors are each charged up to 100 kV and discharged in series, then the open-circuit output voltage of the Marx generator is 1.2 MV.

The current pulse from a Marx generator has a rise time $\tau \sim 1$ μs. A pulse-forming network can be used to shorten the final pulse length to $\tau \sim 20$-100 ns. A pulse-forming coaxial transmission line system is illustrated in Fig. 16E1(a). The output pulse amplitude is about half the input voltage. The *Blumlein* pulse-forming coaxial transmission line, Fig. 16E1(b), was devised to attain an output pulse amplitude equal to the input voltage. The input voltage initially charges the intermediate electrode (2) negative. When breakdown occurs across the switch S, the inner electrode (1) charges up negative, carrying a fast-rising negative pulse to the cathode. The charging inductance L_0 is small enough that the cathode and anode are at the same potential during charging, yet large enough to force most of the final current through the load R_L. A combination of a Marx generator and a Blumlein pulse-forming line is illustrated in Fig. 16E2. An insulating material may be placed between the concentric cylindrical electrodes of the transmission line to help prevent high-voltage breakdown.

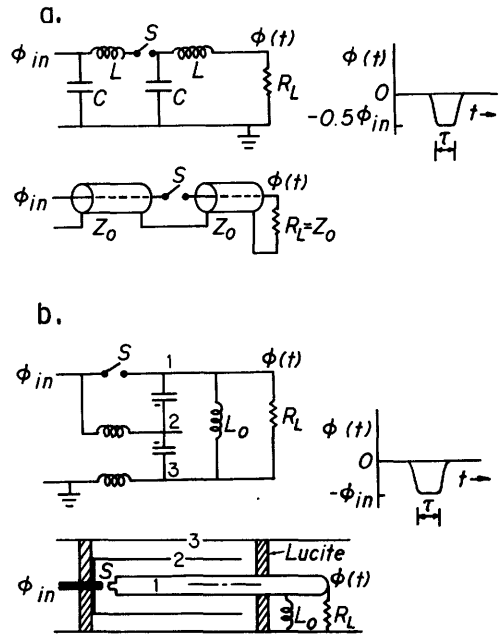

Fig. 16E1. Pulse-forming coaxial transmission lines. (a) a simple circuit, producing an output pulse with half the input voltage, (b) a Blumlein transmission line, consisting of three concentric cylinders, producing a full-voltage output pulse.

insulation

The insulation between the cylinders of a high-voltage line usually consists of vacuum, deionized water, oil, or an electronegative gas, such as SF_6. Because charged particles can flow across a vacuum and cause secondary emission, vacuum insulation is ineffective, unless supplemented by a magnetic field.

The maximum electric fields which water and oil can sustain are given approximately by the equations

$$E_+ = k_+ t^{-1/3} A^{-1/10}$$

$$E_- = k_- t^{-1/3} A^{-1/10} \qquad (16E1)$$

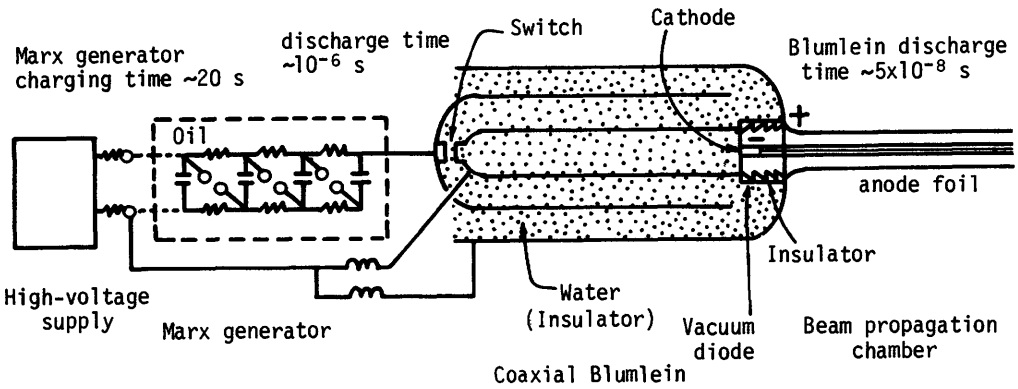

Fig. 16E2. Generation of a high-power relativistic electron beam. The capacitors of the Marx generator are charged up in parallel, then discharged in series by closing the spark gap switches ( ). The microsecond pulse is amplified and compressed by the coaxial Blumlein transmission line. A high current stream of electrons is emitted from the cathode by field emission when the high-voltage pulse arrives. Adapted from R. N. Sudan, "A decade of pioneering research in plasma studies at Cornell", Engineering: Cornell Quarterly 12, No. 3, 2-9 (1977), Fig. 1.

where the subscripts + and - refer to the positive and negative electrodes, t is the time that the field is greater than 63 % of the breakdown value (s), and A is the surface area of the electrode (m^2). For water, $k_+ = 1.2 \times 10^5$ V $m^{-4/5} s^{1/3}$ and $k_- \simeq 2k_+$; for oil, $k_+ = k_- = 2.0 \times 10^5$ V $m^{-4/5} s^{1/3}$. For example, if A = 0.1 m^2 and $t = 10^{-6}$ s, then $E_+ = 15$ MV/m in water and 25 MV/m in oil. For very short pulses ($\tau < 30$ ns) higher fields can be sustained (J. A. Nation, 1979).

The relative dielectric constant of water is $\varepsilon/\varepsilon_0 \simeq 81$, and for oil $\varepsilon/\varepsilon_0 \simeq 2.4$. The propagation velocity of an electromagnetic wave pulse through a dielectric is

$$v_g = (\varepsilon\mu_0)^{-\frac{1}{2}} = c(\varepsilon_0/\varepsilon)^{\frac{1}{2}} \qquad (16E2)$$

where c is the speed of light in vacuum.

The required length of a Blumlein pulse-forming line is

$$L \sim v_g(\tau/2) \qquad (16E3)$$

where τ is the pulse length. For example, if $\tau \simeq 50$ ns, the required length with water is $L \sim 1$ m, and with oil $L \sim 5$ m. The energy storage capacity of a medium also depends upon its dielectric constant, Eq. (1A10). A water dielectric can store about 150 kJ/m^3, and oil can store about 18 kJ/m^3.

Thus, water has a number of advantages, in comparison with oil:

* Water has a high dielectric constant, consequently
  short required lengths of pulse-forming lines
  high energy-storage capacity (for short pulses)
* Spilled water is easy to clean up.
* Water is inexpensive

A transmission line may be used to carry the high voltage pulse from the pulse-forming line to the diode, and an additional switch is often used to suppress prepulses, which could spoil diode operation.

High electric fields can also be sustained in a vacuum with the help of *magnetic insulation*. If the current through the center electrode is high enough, the associated self-magnetic field is strong enough to prevent electron motion from one electrode to the other, as illustrated in Fig. 16E3. Fields of over 1 MV/cm can be attained with such magnetic insulation. Since the diode chamber contains vacuum or gas at low pressure, water dielectrics must be contained by a vacuum window, which is prone to high voltage breakdown. If the pulse-forming transmission line uses magnetic insulation, the window problem can be avoided.

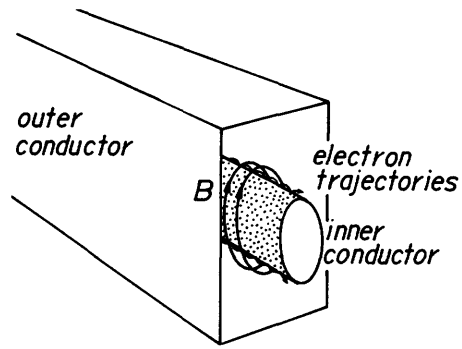

Fig. 16E3. Magnetic insulation. The azimuthal magnetic field B induced by electron flow along the inner conductor prevents most of the electrons from crossing the gap to the outer conductor, except at the head of the pulse, where B is weak.

diodes

The diode consists of a cathode and an anode separated by a short gap. In some cases the anode is a thin metal foil, through which the electron beam can pass with little energy loss. The beam current depends on the diode impedance, which is determined by the electrode shape and spacing, and by plasma motion within the gap. The diode impedance is typically 1-50 Ohm. In order to maximize the efficiency of pulse transmission, the impedance of various circuit elements (such as transmission line and diode) should be matched. The coaxial transmission line electrodes may be tapered in order to match different impedances at the two ends.

When the high voltage pulse arrives at the cathode, the cathode voltage rises in about 20 ns, and intense field emission occurs from microscopic *whiskers* on the cathode surface. Explosion of the whiskers produces a cathode plasma. The electron beam extracted from the plasma penetrates through the anode and propagates towards the target (or laser plasma). The electric field in the diode is about 50-100 MV/m (0.5-1 MV/cm), and the beam current density is typically about 10^4-10^5 A/m^2 (1 - 10 kA/cm^2). Up to 50 % of the stored electrical energy can be transferred to the beam.

Ionization of anode surface atoms produces an anode plasma (especially if an anode foil is used). The two plasmas move towards each other with velocities of 1-4x10^4 m/s (cathode plasma) and about 10^4 m/s (anode plasma), as in Fig. 16E4.

The electron beam current density is approximately

$$J_E \simeq 1.86(4\epsilon_0/9)(2e/m_e)^{\frac{1}{2}}\,\phi^{3/2}/x^2 \qquad (16E4)$$

where ϕ is the gap voltage and x is the plasma sheath thickness in the gap, [cf. Eq. (6F9)]. When the plasmas meet, the diode impedance drops to a low

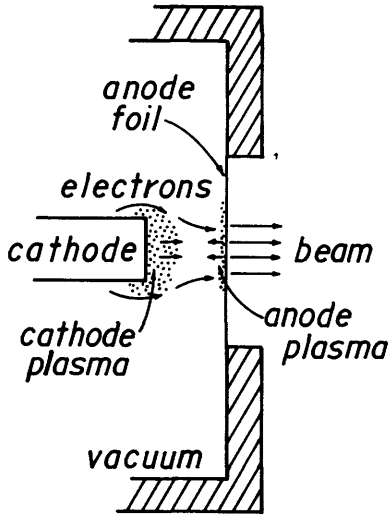

Fig. 16E4. A simple REB diode with an anode foil, showing the cathode and anode plasmas moving towards each other.

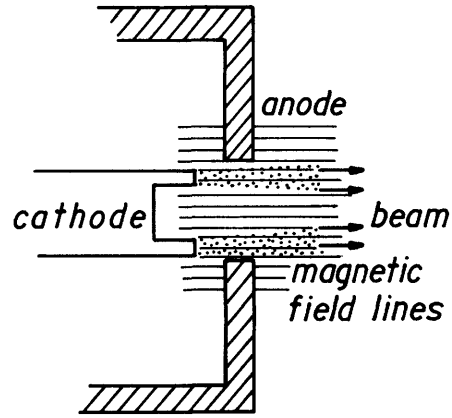

Fig. 16E5. A simple foilless diode. The applied magnetic field prevents most of the electrons from striking the anode.

value, because of the high plasma conductivity, reducing the voltage drop across the gap and the beam energy. Such *gap closure* limits the attainable pulse length of high-current beams to values around 1 μs, unless the plasma density is sufficiently low ($< 10^{20}$ m^{-3}).

Since anode foils have limited lifetimes, it is advantageous to use foil-less diodes. One type is illustrated in Fig. 16E5.

beam propagation

A relativistic electron beam is characterized by the dimensionless parameters

$$\nu \equiv Ne^2/4\pi\varepsilon_0 mc^2 = 2.8\times10^{-15}\ N \qquad (16E5)$$

$$\gamma \equiv \frac{1}{(1 - v^2/c^2)^{\frac{1}{2}}} \qquad (16E6)$$

where ν is a measure of the mutual repulsion of the electrons, N is the number of electrons in the beam per meter length, v is the electron speed, and c is the speed of light. Gamma is a measure of the beam's kinetic energy W, which is equal to

$$W = (\gamma-1)mc^2 = (0.511\text{MeV})(\gamma-1) \quad , \qquad (16E7)$$

Spatial focusing of the beam energy may be achieved by tapering the transmission line, and by focusing devices in the beam propagation region, such as plasma channels and strong magnetic fields.

If the electron beam propagates into a vacuum, mutual repulsion of the electrons leads to rapid spreading of the beam, and a decrease of the current density. When a low pressure gas is present, on the other hand, ions produced by ionization quickly neutralize the space charge of the beam, permitting the beam to propagate long distances, especially if a strong longitudinal or azimuthal magnetic guide field is provided.

When the beam is neutralized, its self-magnetic field pinches the beam to a small diameter. The self-magnetic field can hinder beam propagation when the beam current is above a critical value

$$I_{max} = 17000\ \gamma v/c \qquad (A) \quad , \qquad (16E8)$$

which is equivalent to the condition $v/\gamma = 1$. When the beam propagates through an isolated gas, the return current, which the beam induces in the opposite direction, partially cancels the beam current. Then it is possible to have $v/\gamma > 1$, although the net current is below I_{max}.

applications

Parameters of some powerful REB accelerators are listed in Table 16E1.

Table 16E1. Parameters of some accelerators producing powerful REB. PBFA can accelerate either electrons or light ions.

name	Aurora	Proto II	Particle Beam Fusion Accelerator		Angara V
			PBFA-I	PBFA-II	
location	Harry Diamond Laboratories, Washington, D.C.	Sandia Laboratories, Albuquerque, NM (SLA)	SLA	SLA	Kurchatov Institute, Moscow
year	1972	1977	1980	1984	1984
power (TW)	20	8	30	100	100
number of modules	4	8	36	72	∿48
purpose	weapons simulation	component development, propagation experiments	target compression & ignition		target compression & ignition
accelerating voltage (MV)	12	1.5	2.0	4.0	2.0
pulse length (nsec)	160	25-40	40	40	50
current (MA)	1.6	5	15	25	50
beam energy (MJ)	3	0.2	1.0	3.0	5
cost (M$)	15	1.5	14	40	∿50

A twin diode experiment for irradiating a target pellet is shown in Fig. 16E6. Fusion neutrons have been observed from such experiments. The parameters attained with electron beams are compared with those needed for an ICF reactor in Table 16E2. The current focusing requirement is the most formidable problem. If the diodes are close to the target, then blast damage will be severe, and if they are far away, then it is difficult to prevent beam expansion between the diodes and the target. If the required transport and focusing could be attained, target preheat by the relativistic electrons would still be severe. In view of these problems, REB's are not promising candidates for ICF target compression, in spite of their comparatively high efficiency and low cost.

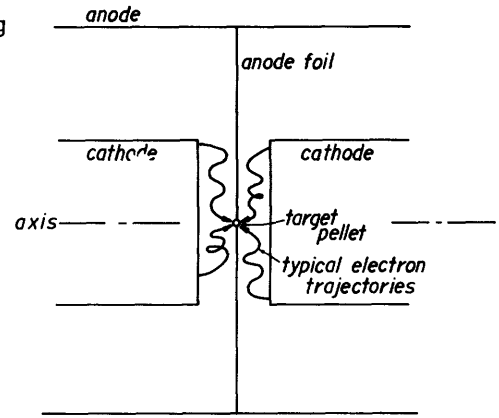

Fig. 16E6. A twin diode arrangement for focusing electrons onto a target pellet. The electric and self-magnetic forces cause the beam electrons to converge onto the pellet at the center.

However, there are other fusion research applications of electron beam accelerators: they are useful for plasma heating and confinement (Chapters 9 and 14), for excitation of high-pressure gas lasers (such as KrF lasers), and for development of free-electron lasers (Brau, 1981). They may also be used to compress metallic foils containing DT fuel.

Table 16E2. Parameters needed for electron-beam ignition of fusion pellets.

	needed	attained (in various devices, not simultaneously)
beam voltage	$\sim$ 1 MV	.1 - 10 MV
beam power	$\gtrsim$ 300 TW	20 TW
pulse length	$\lesssim$ 40 nsec	20-100 nsec
beam energy	$\sim$ 10 MJ	3 MJ
beam current	$\sim$ 300 MA	5 MA
current density at target	$\sim 10^{12}$ A/m^2	$\sim 10^{11}$ A/m^2

16F. Light Ion Beams

production

The energy storage, pulse shaping, and transmission lines for light ion beam production are the same as those for electron beam production, except that the polarity must be reversed at some point along the line. The Particle Beam Fusion Accelerator (PBFA) at SLA is designed to accelerate either electrons or light ions. The water-dielectric pulse-forming line has negative polarity (of the center conductor), as for electron beams. If the polarity of the pulse-forming line were reversed, it would have to be derated, because of the lower breakdown

fields of the positive electrode in water [$k_- \simeq 2k_+$ in Eq. (16E1)]. A polarity-reversing convolute section may be inserted into the transmission line to obtain positive polarity for ion beam production, with 90 % power transfer efficiency.

Several means are used for producing ion beams, including reflex tetrodes, magnetically-insulated diodes, and pinch-reflex diodes. The principle of a *reflex tetrode* is illustrated in Fig. 16F1. An axial magnetic field may be used to improve operation. Reflex tetrodes have attained output current densities around 3 kA/cm^2 (30 MA/m^2).

A *magnetically-insulated diode* is illustrated in Fig. 16F2. The transverse magnetic field is strong enough to suppress electron current flow across the

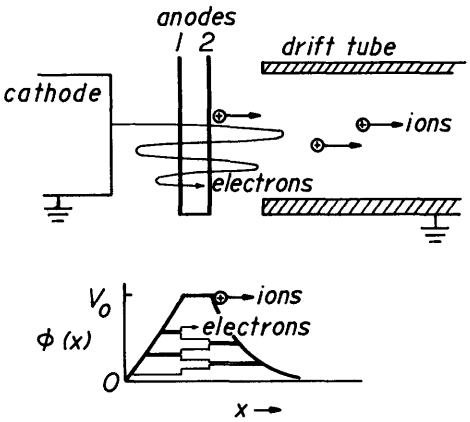

Fig. 16F1. A reflex tetrode ion beam generator, and the potential profile. Relativistic electrons from the cathode oscillate through the anode foils, producing ionization as they slow down. Anode foil (1) nearest the cathode is of a material which does not readily produce ions, such as polycarbonate or aluminized mylar, while foil (2) is of a material which produces copious light ions. These ions are accelerated into the drift tube, forming a high-current ion beam.

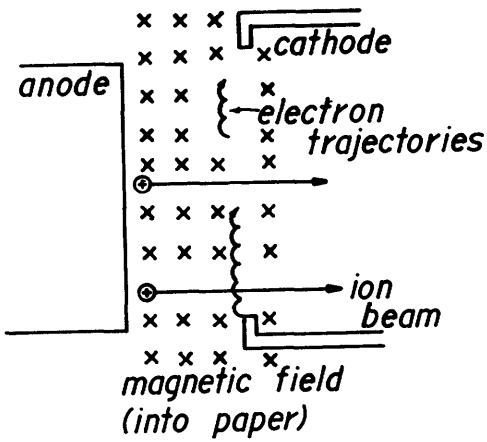

Fig. 16F2. Generation of an intense ion beam using a magnetic field to suppress electron flow from cathode to anode.

diode gap, but weak enough that the ion trajectories are only slightly curved. Thus, most of the current can be carried by the ions. Dielectric materials containing light ions (H, C, etc.) are included in the anode, in order to provide ion sources there. Electrostatic breakdown along the surface of the dielectric inclusions provides an anode plasma, from which the light ions are extracted. Hydrogen ions are the easiest to obtain. The magnetic field should be shaped so that electrons following field lines cannot easily cross the anode-cathode gap. Several geometries have been used successfully. Magnetically-insulated diodes with curved electrodes have produced focused ion beams with current densities over 10 MA/cm^2 (10^{11} A/m^2)and efficiency of 80 %.

At very high diode currents, the self-magnetic-field pinching force tends to choke off electron flow, so that much of the current is carried by ions, even without an external magnetic field. Such a *pinch-reflex diode* is illustrated in Fig. 16F3. The magnetic pinching force causes the electrons to move radially inwards as they reflex in and out of the anode foil. The curvature of the anode foil promotes some focusing of the beam, to attain higher current density than with a planar anode. Efficiencies of 60-70 % (ion current over total current) and current densities of 10 kA/cm^2 (100 MA/m^2) have been attained at the source, with focused values up to 300 kA/cm^2 (3 GA/m^2). It is easier for electron flow to neutralize the ion beam space charge in pinch-reflex diodes than in magnetically-insulated diodes. Space-charge neutralization is essential if the beams are to be transported over long distances to the target.

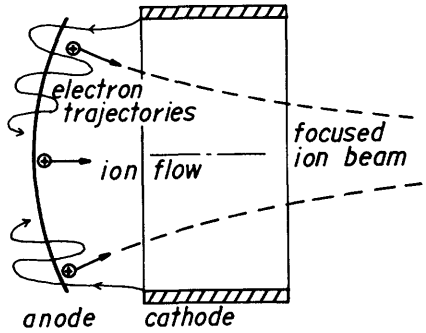

Fig. 16F3. A pinch reflex diode with curved anode.

focusing and transport

Three means are used to compress the ion beam power: geometric (ballistic) focusing, magnetic focusing, and time bunching. Geometric focusing is accomplished by using curved electrodes to direct the ions towards a focus point, as illustrated in Fig. 16F3. Magnetic focusing involves the use of specially shaped magnetic fields along the ion beam path, or self-pinching of beams which are charge-neutralized but not current-neutralized.

The concept of time bunching is to vary the energy given to various ions. If all the ions are emitted from the same location, then the ions emitted early in the pulse are given lower energies, and those emitted at the end of the pulse, the highest energies. The energies are controlled so that all the ions arrive at the target at about the same time. Thus, a pulse length of 100 ns at the ion source could be compressed to 20 ns at the target. Precise ramping of the diode voltage is difficult to attain, however.

Another means for time bunching is to use a plasma ion source, where the ions start out at different distances from the target. If the electrostatic potential profile is roughly parabolic in the plasma, with the ions farthest from the target receiving the highest energies, the ions from all locations will arrive at the target at nearly the same time. Such a potential profile can be produced, for example, by injection of electrons into a sphere, with formation of a virtual cathode inside the sphere, as illustrated in Fig. 16F4.

In order to minimize ion source damage by target pellet explosions, the sources will probably be separated from the target by distances of a few meters. The ion beams tend to expand as they travel from the sources to the target, so beam transport is a serious problem. If the chamber contains low-pressure gas, electrons from the gas can neutralize the ion beam space charge. A plasma channel may be formed from each beam source to the target by axial laser beams, and a gas discharge along the channel will create an azimuthal magnetic field which helps to contain the beams, as illustrated in Fig. 16F5. The plasma also provides return paths for the beam current, but spatial separation of the beam and return-current paths may result in large magnetic forces.

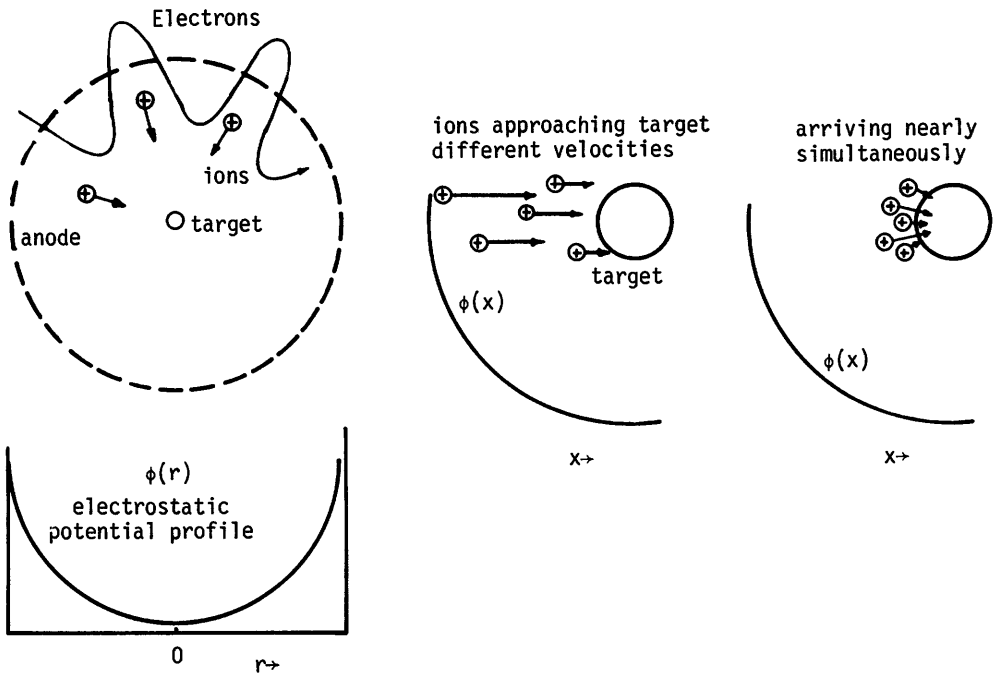

Fig. 16F4. Ionization and formation of a virtual cathode by reflexing electrons in a sphere (left), and the resultant acceleration of ions so that they arrive at the target almost simultaneously (center and right).

Particle Beam Fusion Accelerator (PBFA)

Some parameters of the PBFA-1 and PBFA-II devices were listed in Table 16E1. Figure 16F6 shows a possible PBFA-I experiment. Ion beams from 36 modules converge radially in the equatorial plane onto the target. During the conversion to PBFA-II the number of modules could be doubled by vertical stacking, as shown in Fig. 16F7, and the beam voltage could be increased from 2 MV to 4 MV. Experiments with PBFA and other devices will indicate whether light ion drivers can compress targets effectively. The PBFA-II experiment may demonstrate a fusion energy yield in excess of the energy input.

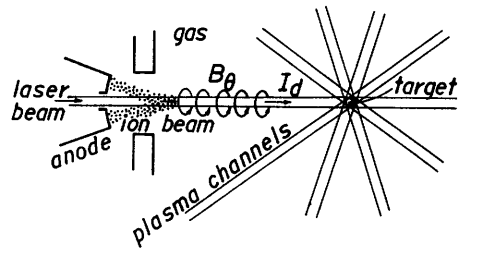

Fig. 16F5. Plasma channels for ion beam propagation to the target. Laser beams create ionized plasma channels. High-current discharges are produced by external circuits, not shown. The discharge currents I_d create strong azimuthal fields B_θ within each channel. Then the ion beams are injected through the magnetized plasma channels onto the target.

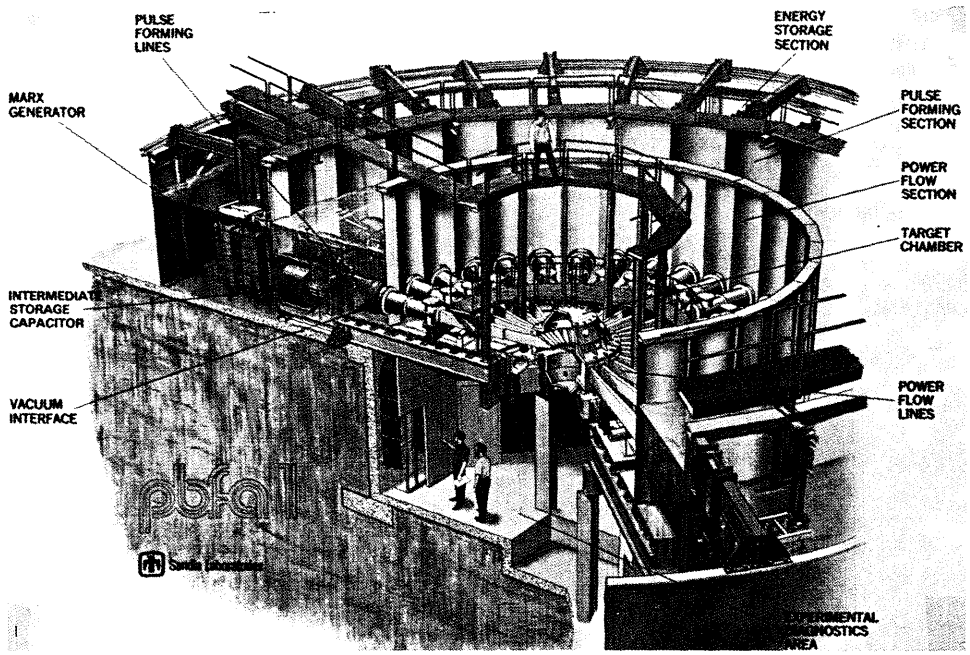

Fig. 16F6. The Particle Beam Fusion Accelerator (PBFA) at Sandia Laboratories.

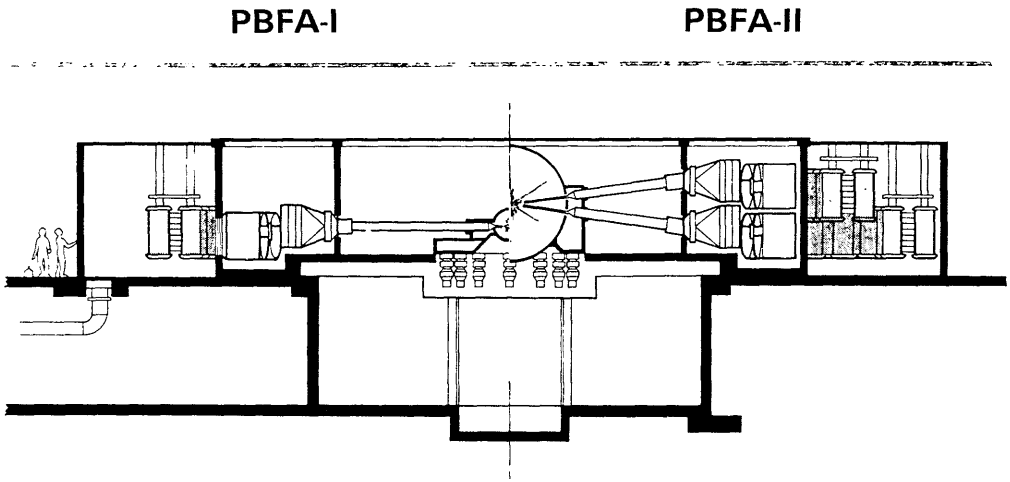

Fig. 16F7. The upgrading of PBFA-I to PBFA-II. Courtesy of Sandia Laboratories.

high average power systems

For reactors operating at repetition rates of about 10 Hz, the energy storage systems, pulse-forming lines, and ion sources must operate at high average powers. A rapid-pulsing Marx generator or high-voltage pulse transformer may be used for the energy storage system. The switching may be done with cooled, flowing-gas spark gaps, in order to attain the required 10^8 - 10^9 shot lifetimes. Injected plasma may be used in the ion sources instead of solid electrodes, in order to minimize electrode erosion rates. Ion bombardment of solid surfaces should be avoided.

In order to attain long lifetimes, components will typically be derated by factors of two or more below their single-shot values (voltages, charge transfer per switch, etc.).

The main problems of light ion beam drivers are focusing, transport, repetition rate, and lifetime. Some potential advantages of light ion beams, compared with laser beams, are

* *efficiency*: light ion beams ∿ 25 %, laser beams ∿ 5 %.
  Lower gain targets may be used.
  Less stored energy is required:
  light ion beams ∿ 10 MJ laser beams ∿ 50-100 MJ.
* *preheat*: Light ion beams probably produce less target preheat.
* *costs*: PBFA I & II costs are ∿ 10 $/J, while Nova costs are ∿ 1000 $/J.
  Estimated costs of future rapid-pulsing systems are (Brueckner et al, 1980, in 1980 $): light ion beams ∿ 70 $/J , laser beams ∿ 200 $/J.

16G. Heavy Ion Beams

required parameters

Target design calculations indicate that the following parameters are desirable:

pulse length ∿ 20 ns

energy input $\gtrsim$ 3 MJ

specific energy deposition ∿ 20 MJ/g

ion range in target $\rho_m R \sim 0.2$ g/cm^2 (0.02 kg/m^2)

where ρ_m is the target shell mass density. A typical target shell might contain an outer layer of lead, heated and expanding to a density $\rho_m \sim$ 2 g/cm^3 (2000 kg/m^3) and temperature T ∿ 200 eV. Ranges of various ions under these conditions are shown in Fig. 16G1.

We will speak of "uranium" ions, meaning any heavy ion with atomic number A ∿ 200. In order to attain the desired range with uranium ions, the maximum energy is about 10 GeV. The required number of incident ions is

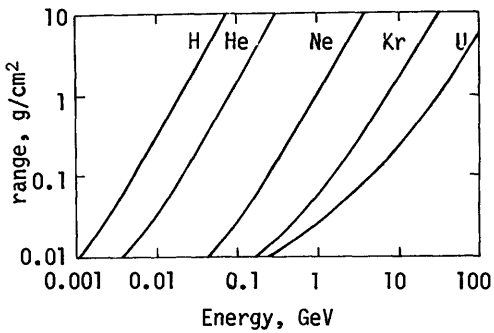

Fig. 16G1. Ion range vs. energy in lead at ρ_m = 2 g/cm^3, T = 200 eV. Courtesy of LLNL (Fig. 50-60-0378-0766, 11/79).

$$N = W_{in}/W_i \tag{16G1}$$

where W_{in} is the input energy and W_i is the energy of an ion. If W_{in} = 3 MJ and W_i = 10 GeV = 1.6×10^{-9} J, then N = 1.9×10^{15} ions. If the average ionic charge is q, then the average current is

$$I = Nq/\tau \quad . \tag{16G2}$$

Assuming singly-charged ions with $\tau \sim 20$ ns, we find $I \sim 15$ kA. The beam power $IW_i \sim 150$ TW for this case. Higher charge states, such as U^{++}, would require higher beam currents and increase beam space-charge problems. Another important beam parameter is emittance.

emittance

If the beam is propagating in the z direction, most of its momentum p will be in the p_z component, but there will be small components p_x and p_y leading to beam divergence. If all the beam ions had the same momenta, then the divergence angle α_x in the xz plane would be

$$\alpha_x \simeq \sin\alpha_x = p_x/p \tag{16G3}$$

since $(p_x/p) << 1$. Actually, the ions have a distribution of α_x, which varies with position x, as illustrated in Fig. 16G2. According to the Liouville theorem of statistical mechanics, the shape and orientation of the emittance contour may change as the beam propagates in the z direction, but the area enclosed tends to remain roughly constant, in the absence of collisions. The *emittance* of the beam is defined to be

$$\varepsilon_T \equiv C \int dx\, \alpha_x \tag{16G4}$$

where C is a constant and the integral represents the area enclosed by the outer emittance contour. Various values of C have been used in defining emittance. A similar diagram could be made for the α_y divergence vs. y position. If the beam has circular symmetry, then a plot of $\alpha \simeq p_r/p$ vs. radius r will suffice. We will use the definition of *normalized transverse emittance*

$$\varepsilon_T/\pi \simeq (p/m_i c)r\alpha = \gamma(v/c)r\alpha \tag{16G5}$$

where α is a typical value of divergence angle, r is the beam radius, m_i is the ion mass, c is the speed of light in vacuum, and γ was defined in Eq. (16E6).

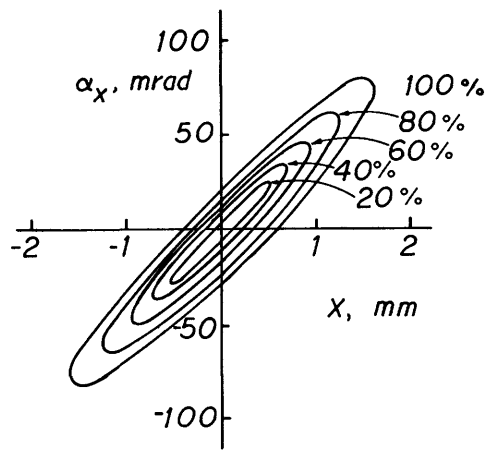

Fig. 16G2. A hypothetical emittance diagram for an ion beam. The fraction of the beam inside each contour is labelled as a percent. The "emittance" is proportional to the area inside the outer curve, which is on the order of 10 mrad-cm for this case. The numbers are for illustrative purposes only.

EXAMPLE PROBLEM 16G1

Consider a beam with radius b = 0.2 m at the reactor chamber wall being focused onto a target, as shown. Assume 10 GeV U^+ ions, total fusion power P_F = 3000 MWth, required fusion power flux at the wall F = 3 MW/m^2, and target radius r = 2.5 mm. Estimate the required beam emittance.

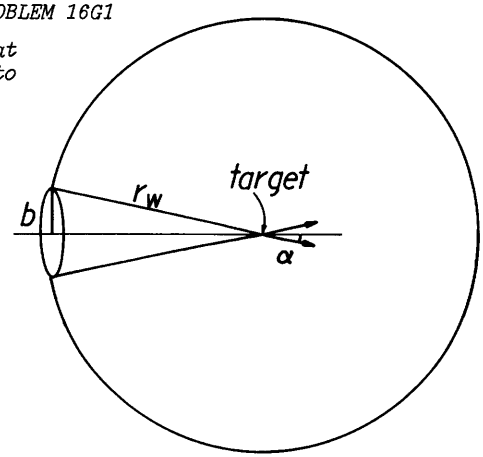

The power flux is related to the total power by

$$P_F = 4\pi r_w^2 F \qquad (16G6),$$

so the required wall radius is r_w = 9 m. [Various wall protection schemes (Section 16H) might permit smaller wall radii, at the expense of higher gas pressure in the chamber.] The focus angle is found from

$$\sin\alpha = b/r_w \qquad (16G7)$$

to be α = 22 mrad, For 10 GeV U^+ ions, v/c = 0.29 and γ = 1.045. From Eq.(16G5) ε_T/π = 1.7 mrad-cm.

Some typical parameters for a heavy ion beam fusion reactor are listed in Table 16G1. The two main accelerator schemes being considered are rf linacs and induction linacs.

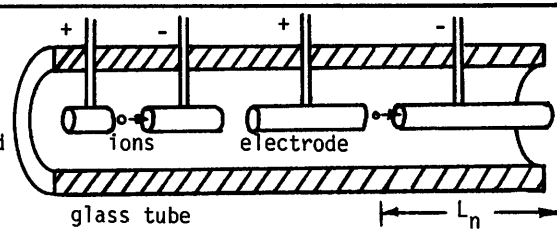

Fig. 16G3. Cutaway view of a Wideröe linac.

rf linacs

Radiofrequency linear accelerators (rf linacs) are of two main types: Wideroë and Alvarez. The *Wideröe linacs* use a glass chamber with a series of metal tube electrodes connected alternately to opposite poles of a radiofrequency voltage, Fig. 16G3. While the ions are drifting through the tubes, the rf voltage changes sign, so that the electric field is always pointing forwards when the ion bunch passes through an electrode gap. Thus, the ions receive a fixed voltage acceleration (such as 50 kV) as they pass through each gap, and the final beam energy is determined by the number of electrodes. As the ions accelerate, the drift tubes must be longer, in order to keep in phase with the applied rf voltage. If τ is the period of the rf voltage, then the length of the n-th cell should be

$$L_n = v_n\tau/2 = v_n/2f = v_n\lambda/2c \qquad (16G8)$$

where v_n is the ion velocity, f is the rf frequency, c is the speed of light in vacuum, and λ is the rf wavelength. [Wideröe linacs can also operate with $L_n = (v_n/c)\lambda/4.$] Ions with charge q receive an energy $q\phi$ in each gap, where ϕ is the rf voltage. If $v_n \ll c$, the ion velocity after passing through n gaps is

$$\tfrac{1}{2}m_i v_n^2 = nq\phi + W_0 \quad , \qquad (16G9)$$

$$v_n = [2(nq\phi + W_0)/m_i]^{\frac{1}{2}} \qquad (16G10)$$

where W_0 is the initial energy of ions entering the accelerator from the ion source or pre-accelerator.

For example, consider U^+ ions with W_0 = 100 keV, ϕ = 100 kV, and f = 1 MHz. When n = 1, $v_1 = 4.0\times10^5$ m/s and L_1 = 0.20m. When n = 30, $v_{30} = 1.6\times10^6$ m/s and L_{30} = 0.79 m. The required drift tube length increases roughly proportional to $n^{\frac{1}{2}}$ for large n. When L_n becomes very long, the beam can be injected into another chamber operating at higher rf frequency.

Table 16G1. Typical parameters of a heavy ion beam fusion reactor.

target radius	r_t	$\sim$ 2.5 mm
chamber radius	r_w	$\sim$ 3-10 m
total beam energy	W_b	$\sim$ 3 MJ
target energy gain	Q	$\sim$ 50-100
pulse repetition rate		$\sim$ 10 Hz
ion atomic number (such as U^+, A = 238)	A	$\sim$ 200
ion range in the target	$\rho_m R$	$\sim$ 0.2 g/cm^2 = 0.02 kg/m^2
ion energy	W_i	$\sim$ 10 GeV
number of ions in beam	N	$\sim 2\times10^{15}$
total charge of beam	Ne	$\sim$ 300 μC
pulse length	τ	$\sim$ 20 ns
average beam current	I	$\sim$ 15 kA
beam power	P_b	$\sim$ 150 TW
beam radius at target	r	$\sim r_t$
beam ion speed	v/c	$\simeq$ 0.29
	v	$\simeq 8.5\times10^7$ m/s
final beam length	$v\tau$	$\sim$ 2 m
beam emittance	ε_T/π	$\leq$ 2 mrad-cm
beam longitudinal momentum spread	$\Delta p_z/p$	$\simeq \pm$ 0.015

An *Alvarez linac* uses a cylindrical metal tube waveguide with radius b carrying a TM_{010} electromagnetic wave, meaning "transverse magnetic" with mode numbers 0, 1, and 0 in the r, θ, and z directions. This mode, with λ = 2.61b, has the electric field entirely in the z direction, strongest along the axis and zero at the walls as illustrated in Fig. 16G4. If b = 0.38 m, then λ = 1 m and f = 300 MHz. An ion with v/c = 0.1 would travel a distance of 0.2 m during one-half cycle of the wave. Ions would be accelerated forwards when the electric field is in the positive z direction and backwards when E is in the negative z direction.

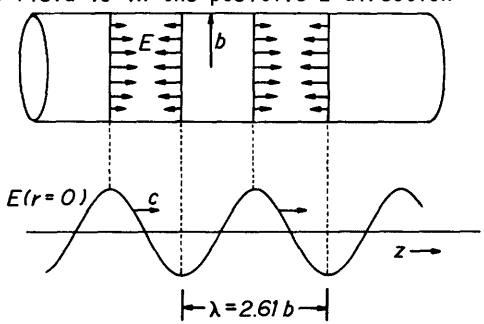

Fig. 16G4. Direction of the electric field for the TM_{010} mode in a cylindrical waveguide (top) and variation of axial electric field with distance along the chamber (bottom). The magnetic field is in the azimuthal direction (not shown), strongest at the walls and zero on the axis.

However, by placing drift tubes along the axis of the chamber, the ions can be shielded from the negative half-cycles of the travelling wave, and be exposed to only the positive half-cycles of the electric field, as illustrated in Fig. 16G5. In this case, a whole period of the wave should elapse during passage from one gap to the next, so the drift tube lengths are

$$L_n = v_n \tau = v_n/f = v_n \lambda/c \quad . \qquad (16G11)$$

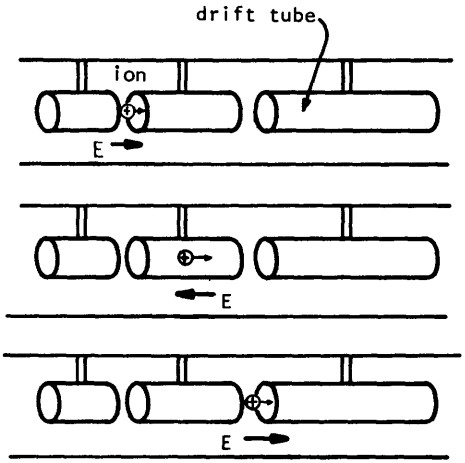

Fig. 16G5. Variation of electric field direction as an ion passes through a drift tube in an Alvarez linac.

The ion momentum increases linearly with the number of cells:

$$p_n = nqE_{av}\lambda \sin\delta \sin(\pi g_n/L_n)/c(\pi g_n/L_n) + p_0 \qquad (16G12)$$

where δ is the phase angle of the wave when the ions are at the center of the gap, g_n is the gap width between the drift tubes, p_0 is the initial momentum, and E_{av} is the average electric field strength over a cell length L_n (Livingood, 1961). Usually $g_n/L_n \sim 0.3$. Larger values decrease p_n, and smaller values are prone to high-voltage breakdown. The kinetic energy after n stages is

$$W_n = (m_i^2c^4 + p_n^2c^2)^{\frac{1}{2}} - m_ic^2 \simeq p_n^2/2m_i \quad \text{if } v^2 << c^2 \quad . \qquad (16G13)$$

In a Widerøe linac the resonant frequency is determined by matching a standing wave to the half-wavelength electrode structure, so it is independent of the tank size. In an Alvarez linac the wavelength and frequency are fixed by the tank size, with small tanks suitable for high frequencies.

Space charge effects prevent rf linacs from accelerating high currents, so a long-pulse, low-current beam is accelerated and then compressed in time to a short-pulse, high-current beam. For example, a 16 μs pulse of 1 A can be split into 16 1 A pulses, each 1 μs long. These pulses can be stacked side-by-side in a 4x4 array in a beam storage ring, so that the circulating current has a pulse length of 1 μs and a total current of 16 A. Then, the shortened pulse may be released to the next element of the accelerator. Time compression can also be accomplished by voltage ramping, similar to the method of time bunching for light ion beams. If I_0 is the initial current, N_t is the number of turns accumulated in each storage ring, N_r is the number of rings, and C is the bunch compression factor attained just prior to extraction from a ring, then the total attainable current is

$$I = I_0 N_r N_t C \quad . \qquad (16G14)$$

Pulse compression is illustrated in Fig. 16G6. The maximum nonrelativistic beam energy which can be stably contained in a single storage ring is

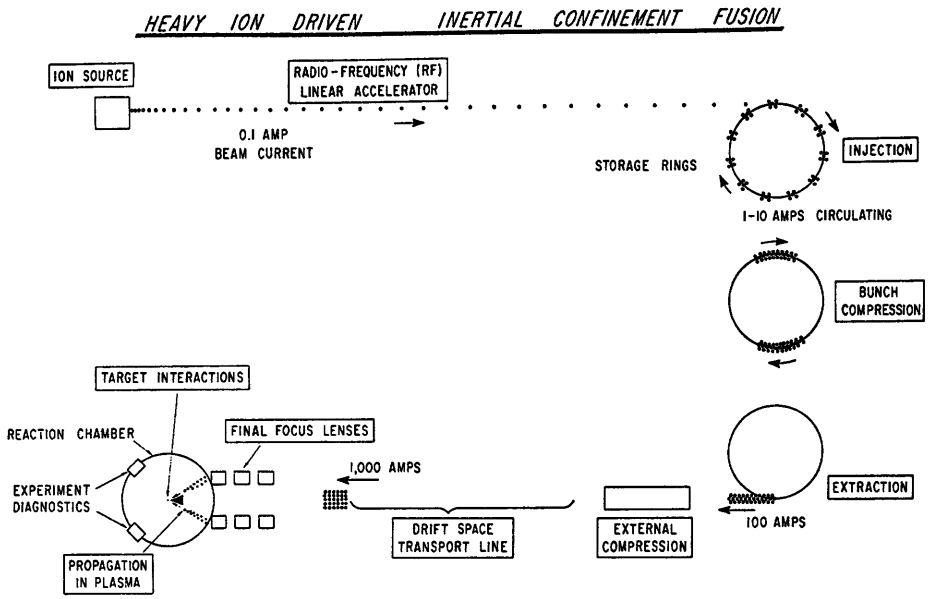

Fig. 16G6. A schematic illustration of compression of an rf linac pulse by means of storage rings. Courtesy of R. L. Martin, ANL.

$$W_s(MJ) \simeq 0.035\ \phi_G^2(\varepsilon_T/\pi)B_F \qquad (16G15)$$

where ϕ_G is the accelerator voltage (GV), the bunching factor B_F is the fraction of circumference occupied by the beam, and ε_T/π is in mrad-cm. The layout of a 10 MJ rf linac system for heavy ion beam fusion is shown in Fig. 16G7. The multiplier and accumulator rings are used for pulse compression. Several rf linacs have operated successfully with heavy ions, though at lower powers than needed for ICF.

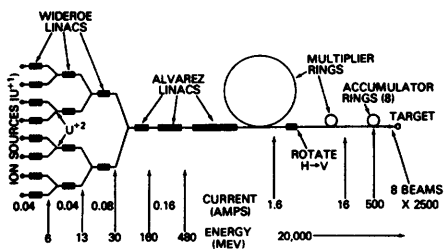

Fig. 16G7. Conceptual design in schematic form of a 10 MJ, 200 TW system developed at Brookhaven National Laboratory based on an RF linac/accumulator rings method. Multi-turn injection and bunching is employed in two intermediate "multiplier" rings. From T. F. Godlove, "Recent progress and plans for heavy ion fusion", IEEE Transactions on Nuclear Science NS-26, 2997-3001 (1979), Fig. 1.

induction linacs

A linear induction accelerator (LIA, or induction linac) uses a series of pulsed magnets to produce electric fields in accordance with the Maxwell equation $\vec{\nabla}\times\vec{E} = -\partial\vec{B}/\partial t$. The accelerator induces a voltage as if the ion beam were the secondary winding of a large transformer. The electrical pulse durations to the magnets must be on the order of microseconds in early stages to tenths of microseconds in the later stages, as shown for one design in Table 16G2. For this design, the efficiency (beam energy/input energy) is 9½ % at 1 Hz and 15½% at 10 Hz.

Table 16G2. Pulse power requirements for a 1 MJ, 210 μC linear induction accelerator producing 19 GeV U^{4+} ions (5 GV accelerating potential). From K. A. Brueckner et al, EPRI AP-1371 (1980), Table 4-2, p. 4-17.

Pulse Duration (μs)	Accelerator Power (TW)	Stored Energy (MJ)	Estimated Pulser Power (TW)
20-2.0	∿0.05	∿1	∿0.08
1.6	0.06	0.18	0.08
1.1	0.08	0.18	0.12
0.8	0.10	0.15	0.16
0.65	0.11	0.15	0.18
0.57	0.12	0.13	0.18
0.50	0.25	0.25	0.38
0.41	0.28	0.23	0.42
0.33	0.84	0.55	0.25
0.25	1.0	0.50	1.5
0.22	2.2	0.95	3.2
0.19	2.5	0.93	3.8
0.15	2.8	0.85	4.3
	10.4 TW	6 MJ	16 TW

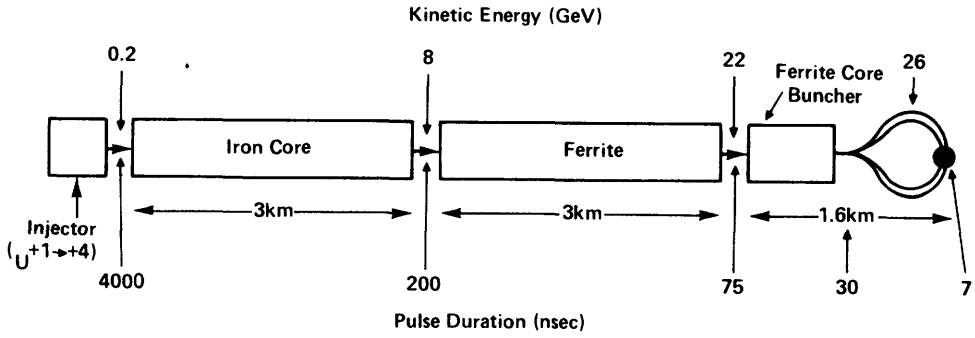

Fig. 16G8. Lawrence Berkeley Laboratory's preliminary conceptual design of a heavy ion pilot plant based on a linear induction accelerator (LIA). An injector consisting of a U^{+1} source, stripper ($U^{+1} \to U^{+4}$), and pulsed drift tube and induction modules (43 and 20 μs pulse duration) injects 14-MeV U^{+2} ions into the iron core LIA section. After 3 km the pulse length is 200 ns, allowing the use of ferrite core induction modules in the second 3-km section. A ferrite core buncher further compresses the beam longitudinally before splitting into 2, 4 or 8 beams for final transport to the target. From T. F. Godlove and D. F. Sutter, "The United States programme in heavy ion beam fusion", Plasma Physics and Controlled Nuclear Fusion Research 1978, Vol. III, IAEA, Vienna, 1979, Fig. 5, p. 217.

The layout of an induction linac is shown in Fig. 16G8. Several induction linacs have been operated successfully with electrons at currents of kA, and voltage ramping has been demonstrated, but experience with heavy ions is lacking.

design considerations

Induction linacs would need source currents of about 5 A, and rf linacs would need source currents $\sim$ 0.1 A. Sources for both appear to be attainable. The main problem associated with the sources and preaccelerators is to maintain high brightness of a beam at very low velocity. The rf linacs use reliable, high-efficiency rf power, but have low-current limitations and require many beam manipulations in order to achieve a compression factor $\sim 10^5$. Induction linacs can carry much higher currents easily, so they require many fewer beam manipulations, but they require Marx generators and water-insulated Blumlein pulse-forming lines, which are more complex than rf power.

Focusing of the beams will be accomplished with magnetic quadrupoles, Fig. 16G9, (and perhaps partly with electrostatic quadrupoles). The field shape tends to act like a lens, focusing the charged particles towards the beam axis. The maximum beam power which can effectively be focused by magnetic quadrupoles without excessive emittance growth is estimated to be

$$P = 2\times10^{15}\ (A/z)^{4/3}(B\varepsilon_T/\pi)^{2/3}(\gamma v/c)^{7/3}(\gamma-1) \quad \text{Watts} \quad , \qquad (16G16)$$

where ε_T/π is in rad-m ,
where A is the ion atomic number, z is its charge number (for U^+, A = 238 and z = 1), and B is the maximum field at the quadrupole pole tips (Tesla). This equation is illustrated in Fig. 16G10.

There are many instability mechanisms which must be considered, including charge density effects, waveform errors, structure effects, and bunch end effects. If some beam ions interact with the accelerator wall where the beam is split (septum), then the gas released may cause loss of more beam ions, releasing more gas, etc. Charge exchange between beam ions, such as

$$U^{4+} + U^{4+} \rightarrow U^{3+} + U^{5+} \qquad (16G17)$$

can cause loss of both the resultant ions, since the new q/m_i ratios are different from that of the beam.

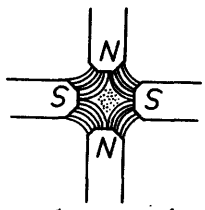

Fig. 16G9. The magnetic field lines of a magnetic quadrupole lens. Dots represent an ion beam travelling perpendicular to the plane of the drawing.

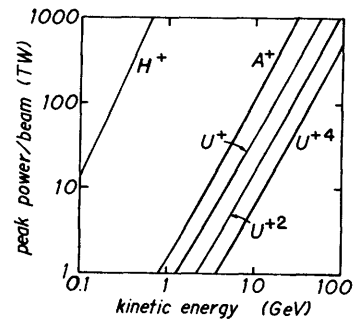

Fig. 16G10. Maximum peak power per beam line versus particle kinetic energy for several ion species and charge states, using $\varepsilon_T = 2$ cm·mrad and B = 4 T. Curves of this kind are derived from an equilibrium between the outward transverse force of the beam and the average external force due to periodic quadrupole focusing magnets. From T. F. Godlove and D. F. Sutter, "The United States programme in heavy ion beam fusion", Plasma Physics and Controlled Nuclear Fusion Research 1978, IAEA, Vienna, 1979, Fig. 1, p. 212.

Table 16G3. Design issues of rf linacs. (Many of these also apply to LIA). From R. L. Martin et al, "Argonne plans for a heavy ion fusion rf linac accelerator demonstration facility (phase zero)", ICF '80, Optical Society of America, 1980, p. 68.

Front end
- source and column characteristics, reliability
- rf capture, low β acceleration, current limitations
- stripping efficiency, charge selection, rematching, recapture (longitudinal emittance control)
- 6-D emittance growth
- transport limits of high space charge beams

Storage rings
- debunching
- injection (efficiency, emittance growth, effect of beam loss)
- beam lifetime—charge changing cross sections
- filling of both transverse phase planes (transfer from one ring to another with phase rotation)
- internal beam rf compression (beam handling above space charge limit)
- extraction efficiency, reliability (effects of beam loss)
- demonstration of adequate vacuum technology under operational conditions
- feasibility of single-pulse synchrotron acceleration (optional)

Extracted beam
- external compression—demonstration of acceptable dilution of longitudinal emittance
- provision of short pulse duration for transport, propagation, focusing, and deposition demonstrations
- demonstration of compression of successive pulses with ringing compressor for charge state telescoping
- transport—checking of instability theory (transport power limits)
- injection of beams into common beam line for telescoping
- splitting—demonstration of acceptable emittance dilution
- demonstration of survivability of splitter
- demonstration of multiple splittings (two or more in each plane)
- focusing on target spot—demonstration of ultimate achievement of expected emittance
- aberration corrections, chromatic and geometric, in the presence of space charges

The final focusing and transport to the target is an important problem. As the beam nears the target, it may break up into a number of small beamlets (the *filamentation instability*). In order to avoid filamentation, many beams ($N > 8$), a large initial beam radius ($r > 0.2$ m), and $p < 1$ Torr may be used (Godlove and Sutter, 1979). If the target chamber gas pressure is too high ($>> 1$ Torr), atomic collisions may cause excessive beam divergence. If the chamber is under a high vacuum, then the ion beam will not be neutralized, and space charge effects become dominant.

Some design considerations of rf linacs are listed in Table 16G3. Induction linacs have similar features, but do not require storage rings.

Other types of accelerators are also being considered. Rapid cycling synchrotrons may be developed for acceleration of heavy ions, in order to reduce the cost of utilizing full-energy rf linacs. Charge exchange losses would be increased, however, because of the increased accumulation time, and the average beam power capability would be lower. Another idea is to use diodes like those used for light ion beams to accelerate heavy ions, with time-of-flight bunching by

voltage ramping (Winterberg, 1979). The high-current capacity of radiofrequency quadrupole (RFQ) accelerators at low velocities may make them well-suited for the low-energy end of the accelerator train (Hansborough, Stokes, Swenson, and Wangler, 1980).

Due to funding limitations, experimental programs at ANL, BNL, and LBL have been limited to testing of front-end equipment, such as sources and accelerators up to about 10 MeV. Some potential advantages of heavy ion beam fusion are listed in Table 16G4.

Table 16G4. Potential advantages of heavy ion beam fusion.

effective coupling of beam energy to target
low required beam current (∿ 10 kA)
required beam parameters attainable with present technology
stiffness of heavy ion beams (eases final focusing problems)
high repetition rates attainable
satisfactory efficiencies (10 - 40 %)
high reliability

16H. Chambers

general considerations

Typical radiation environments in an ICF reactor chamber are indicated in Table 16H1. If the chamber radius is R = 5 m, the x-rays arrive at about 20 ns, the neutrons at about 100 ns, the alpha particles at about 400 ns, and the pellet debris at about 1 μs after explosion. Soft x-rays can cause intense wall surface heating, but hard x-rays tend to penetrate and cause less of a surface temperature rise.

Table 16H1. The radiation environment in ICF reactor chambers. From K. A. Brueckner et al, EPRI AP-1371 (1980), p. 5-8.

X-ray energy	0.1 to several keV
X-ray fraction of yield	2% to 15%
Pellet Debris	
light ions	H, D, T, He
heavy ions (examples)	Be, Li, C, O, Si, Fe, Au, Pb, W, Ta, U
Light ion debris energy	10 to several hundred keV
Light ion fraction of yield	5 to 20%
Heavy ion energy	10's to 1000's of keV
Heavy ion fraction of yield	0 to 20%
Neutron energy	Several MeV to 15 MeV
Neutron fraction of yield	70 to 80%
Total Yields	30 to 3000 MJ
Pulse rate	0.1 to 30 Hz

Figure 15A1 showed the main elements of a laser fusion reactor. Some problems to be considered in chamber design are listed in Table 16H2. If a reactor chamber can only be pulsed once per second and the driver is capable of 10 Hz operation, then it may be used to power 10 chambers, igniting pellets in one chamber after another. Laser beams could be switched to the 10 chambers with a

Table 16H2. Chamber design considerations.

blast protection
energy deposition and temperature rise
thermal stresses
shock waves and impact loading
surface damage
gas pressure control
low pressures needed for transmission of some laser and ion beams
vacuum pumping and vapor pressures of materials
pulse repetition rate
limited by drivers, gas pumping, re-establishing wall protection
targets
damage by overheating during injection may ruin cryogenic targets
high injection velocities ($\sim$ 1 km/s) may be needed
acceleration, tracking, and guidance technology needed
beam transmission and transport to target
absorption and scattering of laser beam energy
space charge effects (at low pressures) or instabilities (at high pressures) of light ion beams
stripping, scattering, and instabilities of heavy ion beams

large rotating mirror, and heavy ion beams could be switched magnetically into different chamber paths. This concept is not easily adapted to light ion beams, because the ion beam diodes need to be near the target. There are a variety of schemes for chamber wall protection, including dry walls, wetted walls, magnetically protected walls, protection by a falling liquid metal stream, and protection by a buffer gas.

dry walls

Unprotected metal walls are limited to low fusion energy yields or to large cavity radii. For example, the minimum cavity radius required to prevent melting of a stainless steel wall by pellet debris is shown as a function of the energy yield in Fig. 16H1. Additional limits are imposed by cyclic stresses induced in the walls.

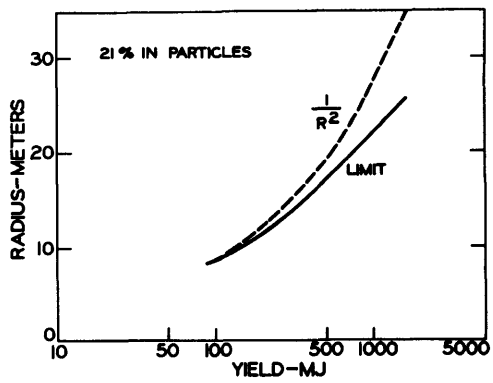

Fig. 16H1. Minimum cavity radius needed to prevent melting of a stainless steel wall by pellet debris, assuming that 21 % of the yield is in charged particle energy. From K. A. Brueckner et al, EPRI AP-1371 (1980), Fig. 5-5, p. 5-11.

If the metal wall is protected by a layer of graphite, erosion of the graphite becomes an issue, as illustrated in Fig. 16H2. Thus, for 100 MJ yields at a 30 Hz repetition rate, a cavity radius R > 7 m would be needed.

The energy fluence per pulse on the walls is

$$\text{fluence} = W_F/4\pi R^2 \qquad (16H1)$$

where W_F is the fusion energy yield. In order to keep the same wall erosion rates as in Fig.16H2, the radius $R \propto W_F^{\frac{1}{2}}$. Lowering the pulse repetition rate ν

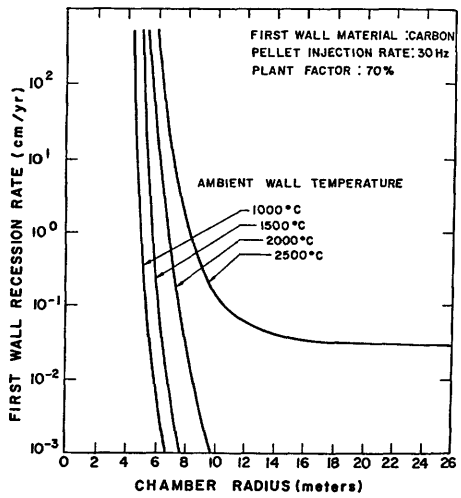

Fig. 16H2. Erosion rate of graphite due to a 100 MJ energy yield, 21 % of which is pellet debris (D, T, He, Si), for various possible operating temperatures of the graphite. From K. A. Brueckner, EPRI-AP-1371 (1980), Fig. 5-19, p. 5-28.

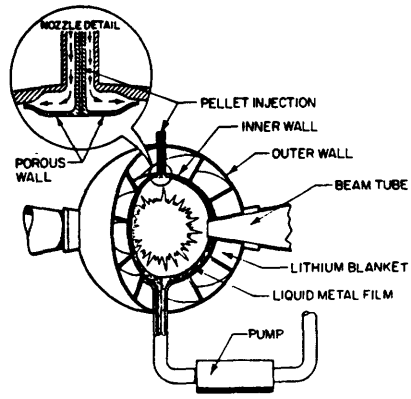

Fig. 16H3. A modified wetted-wall ICF reactor chamber. From J. H. Pendergrass, T. G. Frank, and I. O. Bohachevsky, "A modified wetted-wall inertial fusion reactor concept", Fourth ANS Topical Meeting on the Technology of Controlled Nuclear Fusion, October, 1980, and LA-UR-80-2891 (1980) Fig. 1.

would help decrease the average power flux and operating temperature, but would not affect the instantaneous temperature excursions during each pulse.

wetted walls

The wetted wall concept uses a thin film of liquid lithium covering the chamber wall. The lithium is vaporized by the blast energy, but the wall is not overheated or eroded away. The film must be replenished quickly between shots. One idea is to use porous metal walls through which the liquid lithium flows to replenish the film, but this limits the pulse repetition rate to about 1 Hz or less. Another idea is to use spray nozzles to replenish the lithium film more quickly, as illustrated in Fig. 16H3.

The pulse rate is also limited by the time it takes to remove most of the lithium vapor from the chamber after each shot. To permit effective penetration of infrared laser beams, the vapor density must be reduced to $n \lesssim 10^{23}$ atoms/m^3 before the next shot. One idea is to use supersonic vapor flow into a spray condenser below the chamber. Another idea, which may provide faster vapor removal, is to use condensation of the vapor onto the unvaporized lithium film with liquid flow downwards to a drain at the bottom. With spray nozzles and vapor condensation, pulse rates $\sim$ 10 Hz may be attainable.

Ablation of the lithium film produces a shock wave in the wall. The oscillatory hoop stresses, which damp out in less than 100 ms, limit the maximum energy yield which can be accommodated for a given chamber radius. For example, in a cylindrical chamber with R = 2 m and H = 6 m, yields of 150 MJ could be contained at pulse rates of 5 Hz, for an average thermal power of 750 MW.

Other design considerations include complete wall coverage, flow around beam ports, pumping power minimization, film stability, aerosol formation, and corrosion.

magnetically protected walls

Pellet debris can be deflected away from cylindrical chamber walls by use of an axial magnetic field, as shown in Fig. 16H4. The charged particles flow along the 0.2 T field to conical energy sinks at the ends of the chamber, where the energy may be spread out over a large area to minimize damage. This chamber concept prolongs first wall lifetime by minimizing charged-particle fluxes to the walls. Pulse repetition rates are not limited by replacement of a lithium film, and ion flow along the magnetic field to the energy sinks aids in rapid removal of pellet debris. The magnetic field also prevents charged particles from streaming out laser beam ports. A chamber with radius R = 2 m could accommodate 100 MJ yields at a rate of 10 Hz.

liquid metal streams

The pellet can be surrounded with liquid metal streams falling vertically downwards like a waterfall. This "High-Yield Lithium-Injection Fusion Energy" (HYLIFE) concept is illustrated in Figs. 16H5 and 16H6. The metal streams may be liquid lithium or a lithium-lead mixture.

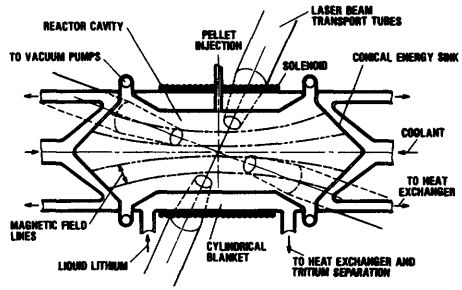

Fig. 16H4. A magnetically protected ICF reactor chamber. Courtesy of L. A. Booth, T. G. Frank, and I. O. Bohachevsky, Los Alamos National Laboratory.

The gaps between the jets allow venting of the high plasma pressure from the pellet debris and vaporized lithium. The lithium streams absorb virtually all of the x-ray and charged particle energy, and about 95% of the neutron energy, so that the stresses and neutron damage at the structural wall are greatly reduced. This effective absorption of the blast energy permits much higher yields to be contained than with other chamber concepts. Some parameters of the HYLIFE design are listed in Table 16H3. In addition to absorbing blast energy, the flowing lithium breeds tritium fuel for the reactor.

The final focusing mirrors of a laser driver are located 60m away from the chamber center, where the neutron flux is reduced to 40 kW/m^2 . Mirror

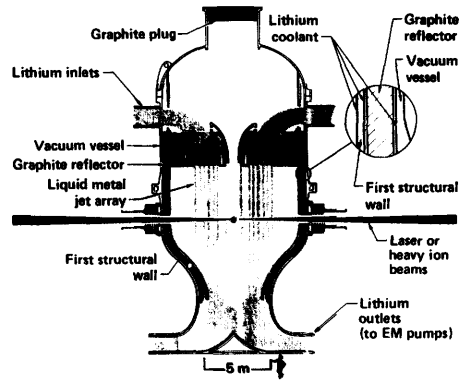

Fig. 16H5. A vertical cross section of the HYLIFE reactor chamber. From J. H. Pitts, "A consistent HYLIFE wall design that withstands transient loading conditions", 4th ANS Topical Meeting on the Technology of Controlled Nuclear Fusion, October 1980, and UCRL-84271 (1980), Fig. 1.

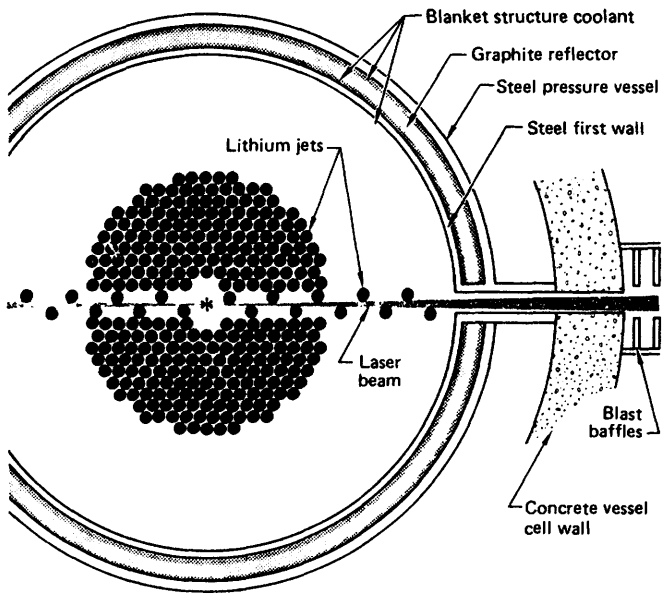

Fig. 16H6. The midplane of the HYLIFE chamber, showing the dense array of lithium jets. The laser beam and pellets enter the chamber horizontally through a portal formed by two rows of crossed jets. Most of the energy released by the explosions is absorbed in the flowing lithium. From M. J. Monsler, "The HYLIFE concept: electricity from laser fusion", Energy and Technology Review, LLNL, Oct. 1979, Fig. 4, p. 14.

Table 16H3. Parameters of the HYLIFE reactor design.

Fusion energy yield per pulse	2700 MJ
Repetition rate	1 Hz
Effective lithium thickness	1 m
Lithium jet diameter at midplane	20 cm
Lithium jet velocity at inlet	4.4 m/s
Lithium flow rate	160 m^3/s
Lithium pumping power	20 MW(e)
Lithium temperature (av)	770 K
Temperature rise in lithium per pulse	13 K
Tritium breeding ratio	1.0-1.7
Blanket energy multiplication	1.18
First wall radius	5 m
First wall neutron fluence with lithium	0.32 MW/m^2
(without lithium it would be	5.76 MW/m^2)
Chamber lifetime	30 years

lifetime is limited by nonuniform swelling induced by radiation damage. Flowing xenon gas is used to protect the mirrors from x-rays and pellet debris, as shown in Fig. 16H7.

Some technology issues of the HYLIFE concept are listed in Table 16H4.

gas-protected walls

The x-ray energy and charged particle energy incident on the chamber wall can be greatly reduced by filling the chamber with a high-Z gas at low pressure. (Low-Z gases like He are ineffective.) For example, the x-ray attenuation

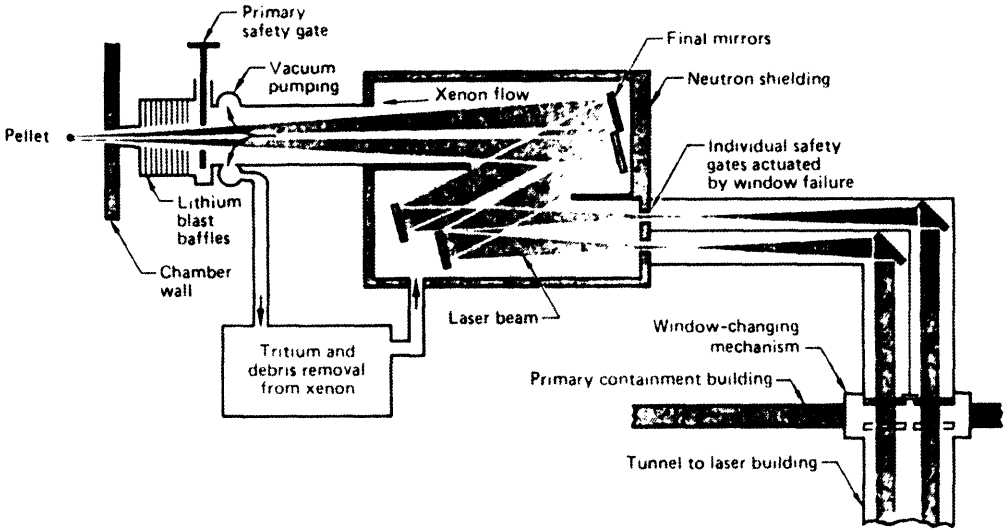

Fig. 16H7. Protection of laser mirrors by flowing xenon gas. The zigzag beam path minimizes neutron streaming towards the laser building. From M. J. Monsler, "The HYLIFE concept: electricity from laser fusion", Energy and Technology Review, LLNL, October 1979, Fig. 5, p. 15.

Table 16H4. Technology issues of the HYLIFE concept. Adapted from M. J. Monsler, Energy and Technology Review, LLNL, Oct. 1979, Table 3, p. 17.

* Beam transport
* Lithium fluid mechanics and chemistry
  - Stability of jets at Re = 2×10^6.
  - Response of liquid to energy deposition and momentum transfer of two-phase flow to wall.
  - Rate of condensation of vapor between pulses.
  - Removal of pellet materials from lithium.
* Materials
  - Erosion and corrosion rates of steels by lithium, including rate enhancement by impurities.
  - Fatigue strength of ferritic steels after neutron damage.
  - Effects of duty cycle and energy spectrum on pulsed neutron damage.
  - Lifetime of high reflectance optical coatings in neutron flux.
* Systems requiring demonstration
  - Tritium removal from lithium.
  - Pellet injection, pellet tracking, and beam pointing.

afforded by xenon in a chamber with R = 7 m is shown in Fig. 16H8. Good attenuation of low-energy x-rays is attained at gas pressures of 1-10 Torr (0.13 - 1.3 kPa). However, the gas tends to scatter and absorb the incident laser or heavy ion beams, so there is a limit on the allowable pressure. Light ion beams need plasma channels in gas at pressures $\sim$ 30 Torr (4 kPa) in order to propagate to the target with small divergence.

Energy absorbed in the gas creates a shock wave, which produces an overpressure at the chamber wall. If $R \lesssim 1$ m, the resulting stresses may be severe, but for $R > 1.5$ m the overpressure is less than 1 atm (10^5 Pa).

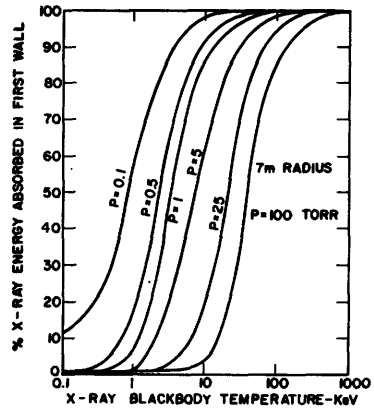

Fig. 16H8. Attenuation of x-rays by xenon gas, as a function of the x-ray blackbody temperature (representative of typical x-ray energies), for various gas pressures (1 Torr = 133 Pa) in a chamber with R = 7 m. From K. A. Brueckner et al, EPRI AP-1371 (1980) Fig. 5-6, p. 5-15.

comparisons

The attainable chamber pressures are limited by the vapor pressure of the metals (such as liquid lithium) at the operating temperatures, the means for removal of pellet debris and metal vapor, and the time $1/\nu$ available for restoring the chamber to the desired pressure, where ν is the pulse repetition rate (Hz). Low lithium and wall temperatures would provide low vapor pressures, but would also result in poor energy conversion efficiency η_e.

The approximate pressures needed at the start of each pulse for various reactor concepts, and the pressures typically attainable with various wall protection schemes are listed in Table 16H5. Heavy ion beam propagation requires low pressures for stability, but there may be a "window" at $p \sim 100$ Pa in some gases (such as N_2 and Ne) permitting transport of stripped ions in a "self-pinch" mode.

Laser beams could be used with almost any of the chamber schemes. Gas-protected walls are most likely for light ion beams. Heavy ion beam reactors can use dry walls, the HYLIFE concept, or possibly gas-protected walls, if adequate propagation can be attained.

Large energy yields (300 - 3000 MJ) require very large chamber radii with dry wall and wetted wall designs. Ion beam propagation is easiest if small wall radii ($R \lesssim 3$ m) can be used.

Approximate costs of various ICF drivers have been estimated (Brueckner et al, 1980) as follows, in 1979 $, including 40 % contingency and engineering:

cost (CO_2 laser) = 200 $W^{0.8}$ (M$)

cost (KrF laser) = 200 $W^{0.8}$ (M$)

cost (light ion beam = 75 $W^{0.8}$ (M$)

cost (heavy ion beam) = 400 $W^{0.4}$ (M$)

Table 16H5. Chamber pressure regimes.

needed	
laser beams	$\lesssim$ 100 Pa (1 Torr) (varies greatly with wavelength and type of gas)
light ion beams	$\sim$ 10 kPa (100 Torr)
heavy ion beams	$\lesssim$ 0.01 Pa (10^{-4} Torr) or $\sim$ 100 Pa (1 Torr) in N_2 or Ne
attainable	
dry walls	< 0.01 Pa (10^{-4} Torr)
magnetically protected walls	$\sim$ 0.01 Pa (10^{-4} Torr)
HYLIFE (700 K)	$\sim$ 0.01 Pa (10^{-3} Torr)
wetted walls	$\sim$ 0.1 Pa (10^{-3} Torr)
gas-protected walls	$\gtrsim$ 100 Pa (1 Torr)

where W is the beam energy (MJ). However, the beam focusing and transport problem is most severe for light ion beams.

Bibliography

general

K. A. Brueckner et al, "Assessment of drivers and reactors for inertial confinement fusion", EPRI AP-1371 (1980).

ICF '80 Topical Meeting on Inertial Confinement Fusion, Optical Society of America, IEEE, 1980.

B. A. Lengyel, *Lasers*, Second Edition, Wiley Interscience, New York, 1971.

G. H. Miley, Coordinator, Proceedings of the IEEE Minicourse on Inertial Confinement Fusion, (Montreal, June 1979), U. of Illinois Fusion Studies Laboratory, 1980.

Proceedings of the Fourth Topical Meeting on the Technology of Controlled Nuclear Fusion (King of Prussia, PA, 1980), DOE, 1981.

Topical Meeting on Inertial Confinement Fusion (San Diego, February, 1978), Optical Society of America, IEEE, New York, 1978.

C. Yamanaka, "Advances in inertial-confinement systems", *Nuclear Fusion 20*, 507-513 (1980).

laser systems

L. D. Pleasance, "Alternate laser fusion drivers", *Proceedings of the 5th Workshop on Laser Interactions with Matter, (Rochester, New York)*, Plenum Press, NY, 1980.

"The Nova laser fusion facility", *Energy and Technology Review*, LLNL, December 1980, p. 1-14.

electron beams

L. L. Alston, Editor, *High-Voltage Technology*, Oxford University Press, London, 1968. (breakdown and insulation)

C. A. Brau, "The free-electron laser: an introduction", *Laser Focus*, May 1981, 48-56.

H. H. Fleischmann, "High-current electron beams", *Physics Today*, May 1975, 35-43.

L. C. Marshall and H. L. Sahlin, Editors, Electrostatic and Electromagnetic Confinement of Plasmas and the Phenomenology of Relativistic Electron Beams, *Annals of the New York Academy of Sciences 251*, 1975.

G. Yonas, "Fusion power with particle beams", *Scientific American 239*, 50-61, November, 1978.

G. Yonas, J. W. Poukey, K. R. Prestwich, J. R. Freeman, A. J. Toepfer, and M. J. Clauser, "Electron beam focusing and application to pulsed fusion", *Nuclear Fusion 14*, 731-740 (1974).

F. Winterberg, "Production of dense thermonuclear plasmas by intense relativistic electron beams", *Proceedings of the International School of Physics "Enrico Fermi", Course XLVII*, Academic Press, New York, 1971, p. 370-401.

light ion beams

S. Humphries, Jr., Intense pulsed ion beams for fusion applications", *Nuclear Fusion 20,* 1549-1612 (1980).

W. L. Johnson, G. B. Johnson, and J. T. Verdeyen, "Ion bunching in electronic space-charge regions", *Journal of Applied Physics 47*, 4442-4447 (1976).

J. A. Nation, "High-power electron and ion beam generation", *Particle Accelerators 10,* 1-30 (1979).

D. D. Ryutov, "High-current electron and ion beam research and technology", *Nuclear Fusion 19,* 1685-1688 (1979).

G. Yonas, "Intense particle beams", *IEEE Transactions on Nuclear Science NS-26*, 4160-4165 (1979).

heavy ion beams

T. F. Godlove, "Recent progress and plans for heavy ion fusion", *IEEE Transactions on Nuclear Science NS-26,* 2997-3001 (1979).

T. F. Godlove and D. F. Sutter, "The United States programme in heavy ion beam fusion", *Plasma Physics and Controlled Nuclear Fusion Research 1978,* Vol. III, IAEA, Vienna, 1979, p. 211-223.

L. D. Hansborough, R.H. Stokes, D. A. Swenson, and T. P. Wangler, "The radio frequency quadrupole linac in a heavy-ion fusion driver system", *Proceedings of the 4th Topical Meeting on the Technology of Controlled Nuclear Fusion (King of Prussia, PA, 1980),* Department of Energy, 1981.

J. J. Livingood, *Principles of Cyclic Particle Accelerators,* D. Van Nostrand, Princeton, NJ, 1961.

E. Persico, E. Ferrari, and S. E. Segre, *Principles of Particle Accelerators,* W. A. Benjamin, New York, 1968.

R. G. Wilson and G. R. Brewer, *Ion Beams*, Wiley-Interscience, New York, 1973. (sources, focusing, transport, with applications to ion implantation).

F. Winterberg, "Generation of ultra-intense heavy ion beams for inertial confinement fusion", *Journal of Plasma Physics 21,* 301-315 (1979).

chambers

K. A. Brueckner, C. Hendrix, S. Jorna, R. E. Kidder, G. L. Kulcinski, J. Maniscalco, T. Martin, J. H. McNally, I. Smith, L. Smith, I. Sviatoslavsky, W. B. Thompson, "Assessment of Drivers and Reactors for Inertial Confinement Fusion", EPRI AP-1371 (1980).

J. Maniscalco, J. Blink, R. Buntzen, J. Hovingh, W. Meier, M. Monsler, and P. Walker, "Civilian applications of laser fusion", UCRL-52349 Rev. 1 (1978).

M. J. Monsler, J. Hovingh, D. L. Cook, T. G. Frank, and G. A. Moses, "An overview of inertial fusion reactor design", *Nuclear Technology/Fusion 1,* 302-358 (1981).

M. J. Monsler and W. R. Meier, "A conceptual design strategy for liquid-metal-wall inertial fusion reactors", *Nuclear Engineering and Design 63,* 289-313 (1981).

G. A. Moses and R. R.Peterson, "First-wall protection in particle-beam fusion reactors by inert cavity gases", *Nuclear Fusion 20,* 849-857 (1980).

Proceedings of the 4th Topical Meeting on the Technology of Controlled Nuclear Fusion, (King of Prussia, PA, 1980), DOE, 1981.

CHAPTER 17
OTHER FUSION CONCEPTS

17A. Radiofrequency Confinement

cavity modes and Q

Electromagnetic waves have been used to confine plasma in resonant cavities, using standing waves with large amplitudes of the oscillating electric field E and magnetic field B. Consider a cylindrical cavity with coordinates (r,θ,z). The cavity modes are designated *transverse electric* (TE) if $E_z = 0$, and *transverse magnetic* (TM) if $B_z = 0$. The modes are characterized by integer mode numbers m, n, and p in the θ, r, and z directions. The electric and magnetic fields will vary proportional to $\cos(m\theta)$ in the θ direction; the axial variations are

$$\text{TM mode: } E_z \propto \cos(p\pi z/d) \quad , \quad B_z = 0$$

$$\text{TE mode: } E_z = 0 \quad , \quad B_z \propto \sin(p\pi z/d) \tag{17A1}$$

where d is the cavity length; and the radial distributions will be Bessel functions characterized by the mode number n. The electromagnetic energy stored in the cavity is

$$U = \tfrac{1}{2} \int_{\text{volume}} d\vec{x}(\varepsilon_0 E^2 + B^2/\mu_0) \qquad (J) \quad . \tag{17A2}$$

By definition, let

$$Q \equiv \frac{\omega_0 U}{P} \tag{17A3}$$

where ω_0 is the cavity resonant frequency and P is the power loss to the walls. At steady state, P is equal to the applied rf power. The Q of the cavity is given by

$$Q = \frac{(\text{geometrical factor})(\text{cavity volume})}{(\text{volume of field penetration into walls})} = \frac{CV}{S\delta} \tag{17A4}$$

In this equation S and V are the cavity surface area and volume, the geometrical factor $C \sim 1$ depends on the cavity dimensions, and the *skin depth*

$$\delta = (2/\mu\sigma\omega)^{\frac{1}{2}} \qquad (17A5)$$

is the characteristic depth which the waves can penetrate into the metal cavity walls, where ω is the angular frequency of the wave, σ is the wall electrical conductivity, and μ is its permeability (for most nonferrous metals, $\mu = \mu_0$). For pure copper at $\omega = 10^{10}$ rad/s and room temperature ($\sigma = 6.0\times10^{7}\ \Omega^{-1}\ m^{-1}$) the skin depth $\delta = 1.6\times10^{-6}$ m. Thus, if $V/S \sim 0.1$ m, $Q \sim 6\times10^{4}$. Surface roughness tends to increase the effective area S and thus to reduce Q.

quasipotential wells

If the electron plasma frequency $\omega_{pe} < \omega$ (a low-density plasma), then the waves readily penetrate inside the plasma. In this case the effective force on the electrons $\vec{F} = -\vec{\nabla}\Phi$, where the quasipotential

$$\Phi = e^2E^2/4m\omega^2 \qquad (J) \quad . \qquad (17A6)$$

Plasma can be confined by cavity modes forming a potential well (a closed region where Φ is minimum), such as the TM_{011} mode (meaning m = 0, n = 1, p = 1), illustrated in Fig. 17A1. Low-density plasma confinement at $\omega_{pe} << \omega$ has been observed experimentally with this mode (Shelby and Hatch, 1972).

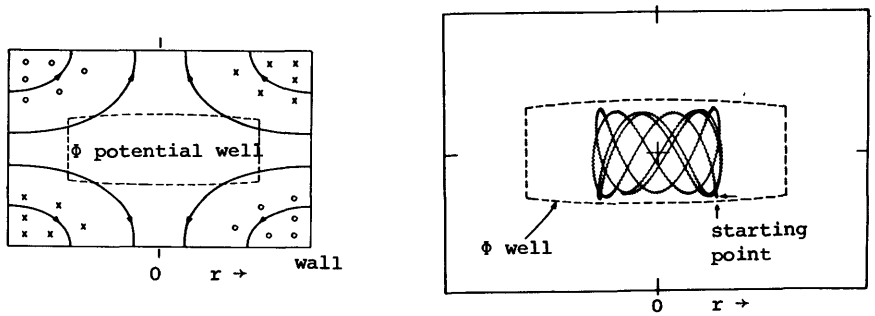

Fig. 17A1. Electric field (smooth curves) and magnetic fields (perpendicular to drawing) in the axial midplane of a cylindrical cavity with the TM_{011} mode (left), and a computer-simulated trajectory of an electron trapped in the Φ potential well (right). The collisionless trajectory was followed for 500 field periods. The dashed rectangle represents the boundary of the potential well, outside of which particles are not confined. From A. J. Hatch, Annals of the New York Academy of Sciences 251, 394-406 (1975), Fig. 1B and Fig. 2.

For the case of high-density plasmas ($\omega_{pe} > \omega$) the waves cannot penetrate into the plasma. If we approximate the plasma as a rigid sphere of radius a, then the confining force $\vec{F} = -\vec{\nabla}T$, where the quasipotential

$$T = \pi a^3(B^2/\mu_0 - 2\varepsilon_0 E^2) \quad (J) \tag{17A7}$$

The magnetic field of the wave tends to confine the plasma, but the electric field hinders confinement. One mode which produces a T quasipotential well is the TE_{012} mode, illustrated in Fig. 17A2. The magnetic field is altered by plasma diamagnetism, and the resulting plasma boundary is parallel to the cusp-shaped magnetic field lines. As the plasma forms, the resonant frequency of the cavity increases, and the rf generator must be able to track the increasing frequency. Plasma may form in other parts of the cavity, short-circuiting the desired fields and spoiling confinement. Plasma-wall interactions can also cause problems.

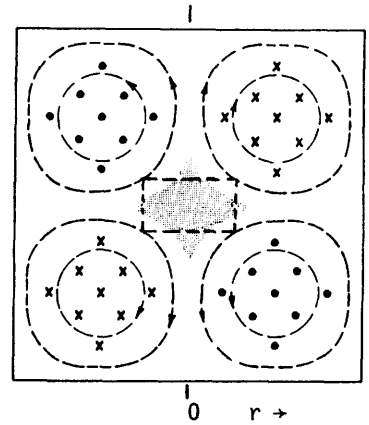

Fig. 17A2. The TE_{012} mode magnetic field lines (dashed circles) and electric field (perpendicular to the drawing). The small dashed rectangle represents the shape of the T quasipotential well in a vacuum, and the shaded region represents the plasma. From A. J. Hatch, in Microwave Power Engineering, Volume 2, Applications, Academic Press, New York, 1968, Fig. 3, p. 353.

power requirements

We can estimate the required energy density of the wave from the equation

$$(B^2/2\mu_0 + \varepsilon_0 E^2/2) \gtrsim p \quad , \tag{17A8}$$

where p is the plasma pressure. Then

$$U \sim pV \quad , \tag{17A9}$$

where V is the cavity volume. (If the fields were high near the plasma and low elsewhere, then U could be slightly lower than this value.) Combining this with Eq. (17A3), we find the required power input

$$P = \omega_0 U/Q \sim \omega_0 pV/Q \tag{17A10}$$

For a fusion reactor plasma with $n = 10^{20}$ m^{-3} and $T_e = T_i = 20$ keV, $p = nk(T_e + T_i) = 0.64$ MPa (6.4 atm). If $\omega_0 = 10^{10}$ rad/s, $Q = 6\times10^4$, and $V = 1$ m^3, then the required power for rf confinement is $P \sim 10^{11}$ W. Very high Q values (and low P) could be attained by using superconducting cavity walls, but it is not feasible to maintain the walls in the superconducting state (at $T \sim 10$ K) in the presence of a thermonuclear plasma. Any shielding or thermal insulation placed between the plasma and the superconducting wall would tend to absorb rf power and to spoil the cavity Q. An alternative for reducing the required rf power is to supply part of the confining pressure by other means, such as a high-pressure gas or a static magnetic field.

high-pressure discharges

Cord-shaped plasma discharges with lengths $L \sim 0.1$ m and radii $a \ll L$ have been produced in high-pressure gases ($p \sim 25$ atm) by intense rf power ($\lambda \sim 0.2$ m, $P \sim 10^5$ W). It is hypothesized that hot electrons are confined by a thin (~ 1 mm) *double layer* containing a strong outward electric field. The gas may be rotated to improve stability of the discharge. Electron temperatures up to 50×10^6 K (5 keV) have been observed in such cord discharges, but $T_i \ll T_e$ (Kapitza, 1979). The main problem is to heat the ions effectively, and to reduce their energy losses by heat conduction, convection, and charge exchange. A strong magnetic field is applied to reduce ion thermal conductivity, and magnetoacoustic wave heating is proposed for raising T_i. Convective heat transfer may be unavoidably rapid, however. If convective heat losses were not too large, and effective ion heating could be developed, then this scheme would have promise as a fusion reactor. The fusion-produced neutrons would be stopped by the high-pressure gas, which could be cycled directly through a gas turbine to drive an electrical generator.

17B. Radiofrequency Plugging

theory

Magnetic cusps have minimum-B magnetic wells and good MHD stability, but rapid plasma losses along magnetic field lines. These losses can be suppressed by radiofrequency (rf) plugging, which is usually done at applied frequencies ω near the ion cyclotron frequency ω_{ci}. The plugging will be *adiabatic* (no energy expended in heating the ions) if the following conditions are satisfied:

$$T_i \ll W_c = 70\, Z^{2/5} \left[\frac{m_i}{m_p}\right]^{3/5} E_0^{8/5}\, B_0^{-6/5}\, R_0^{2/5} \tag{17B1}$$

$$\bar{E} \equiv \frac{Z\, e\, E_0}{m_i \omega^2 R_0} = 5.2 \times 10^3 \left[\frac{m_i}{m_p}\right] \frac{1}{Z} \frac{E_0}{B_0^2 R_0} \ll 1 \quad , \tag{17B2}$$

$$\frac{\rho_i}{R_0} \ll 1 \quad , \tag{17B3}$$

where T_i is the temperature of the confined ions in eV, W_c is the critical energy in eV, E_0 is the rf electric field in the plasma in V/cm, B_0 is the static magnetic field at the rf electrodes in Gauss (1 Tesla = 10^4 Gauss), R_0 is the line cusp electrode radius in cm, Z is the particle charge in units of the proton charge, m_i is the ion mass, m_p is the proton mass, ω is the angular frequency of rf field, and ρ_i is ion Larmor radius. Condition (17B3) is usually satisfied in large devices. Computer simulations indicate that the required values of conditions (17B1) and (17B2) are

$$T_i/W_c = 1/50$$
$$\bar{E} \quad = 1/500 \quad . \tag{17B4}$$

Eliminating B_0 from Eqs. (17B1) and (17B2) with values from (17B4), we find

$$E_0 = 5000\ T_i/ZR_0 \quad . \tag{17B5}$$

For example, if the plasma consists of deuterons at $T_i = 2\times10^4$ eV and $R_0 = 1000$ cm, then the required field inside the plasma is $E_0 = 10^5$ V/cm. When the applied frequency $\omega \simeq \omega_*$ (the eigenfrequency of the electrostatic ion cyclotron mode), then the rf electric field E_0 excited inside the plasma is *stronger* than the vacuum field without the plasma (a coupling resonance), as illustrated in Fig. 17B1. Therefore, the applied electric field in the above example case could be somewhat lower than 10^5 V/cm.

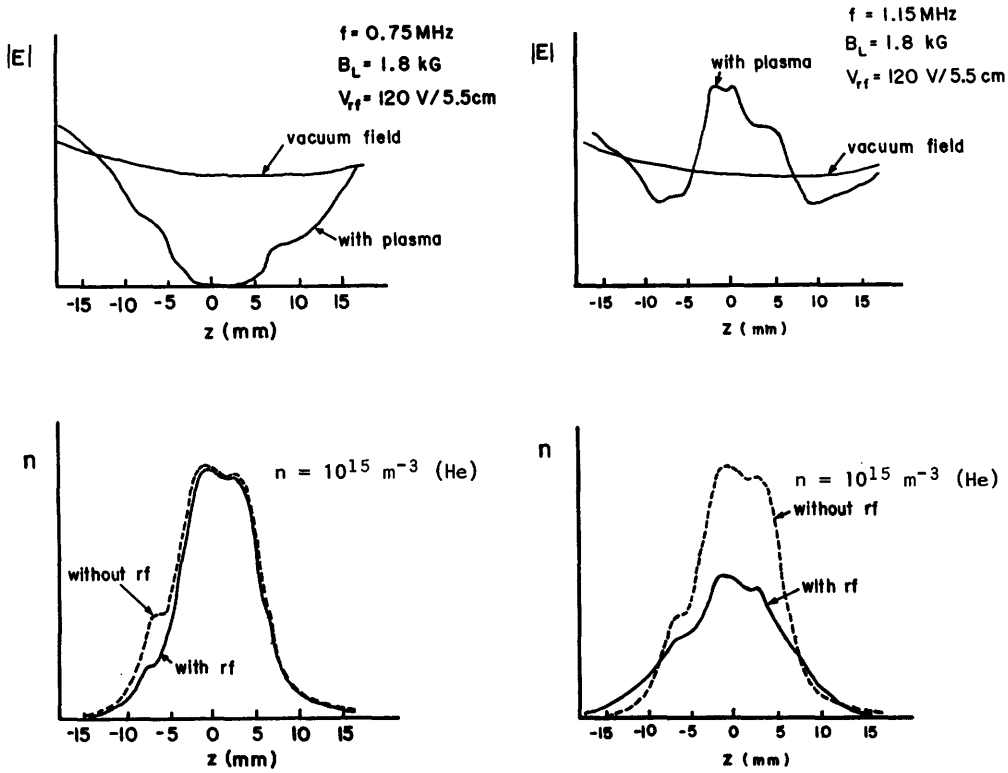

Fig. 17B1. Spatial distributions of rf electric field and ion density measured across the plasma sheet in a line cusp, with B = 0.18 T, electrode rf voltage = 120 V, and electrode gap = 5.5 cm. Left: f = 0.75 MHz ($\omega = 1.08\ \omega_{ci}$), and E is greatly reduced inside the plasma. Right: f = 1.15 MHz ($\omega = 1.66\ \omega_{ci} = \omega_*$), E is enhanced inside the plasma, and n is decreased in the cusp region by the rf plugging. Courtesy of T. Sato, Institute of Plasma Physics, Nagoya University.

If the rf plugging is *nonadiabatic*, ion heating occurs and more rf power is required. The effective quasipotential may be written

$$\psi_* = \frac{q^2 E_*^2}{4 m_i \omega_*^2} \tag{17B6}$$

where q is the ion charge, $E_* \simeq E_0 \omega_{ci}/\omega_{pi}$, and $\omega_{pi} = (nq^2/m_i\varepsilon_0)^{\frac{1}{2}}$ is the ion plasma frequency. The establishment of this quasipotential barrier reduces the ion loss flux by an amount

$$\alpha_i \equiv \frac{\text{ion loss rate with rf plugging}}{\text{ion loss rate without plugging}} = \exp(-\psi_*/T_i) \quad . \tag{17B7}$$

Experimental measurements of ψ_i are consistent with Eqs. (17B6) and (17B7), if E_*^2 is replaced by $E_*^{1.8}$ (Hiroe et al, 1978).

Since the eigenfrequency ψ_* is a function of (q/m_i), a given ion species may be selectively plugged, but the resonance is sufficiently broad that deuterons and tritons can probably be confined by the same rf frequency.

experiments

The TPD-III (Test Plasma Produced by Discharge) experiment is illustrated in Fig. 17B2. Applying rf voltage to the plugging electrode reduces the loss flux,

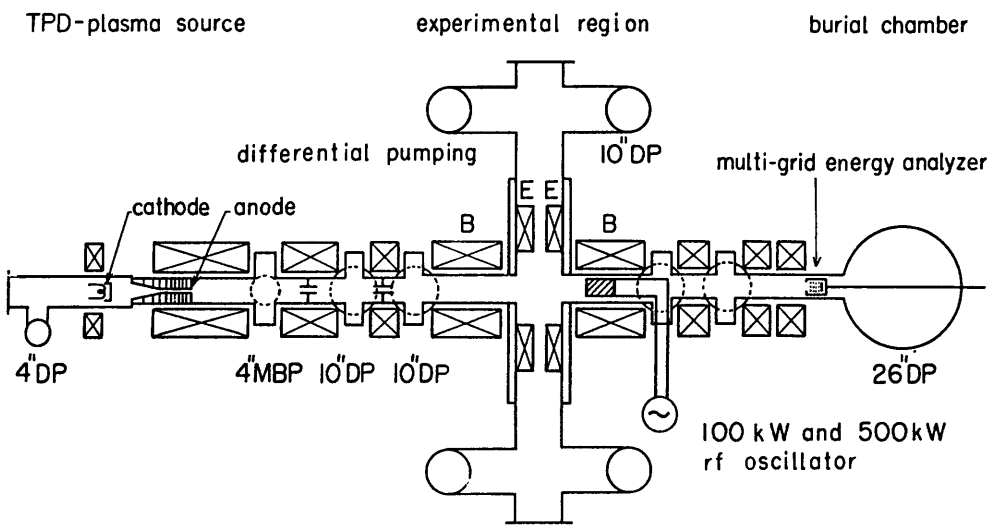

Fig. 17B2. The TPD-III experiment. Plasma flows from the TPD source (anode and cathode) at the left axially through the magnetic mirror B to the plugging electrode (cross-hatched). The loss flux passing through the electrode is measured with the multi-grid analyzer. DP = diffusion pumps. From T. Watari et al, The Physics of Fluids 21, 2076-2081 (1978), Fig. 1.

as shown in Fig. 17B3. Three different types of electrodes have been tried, as shown in Fig. 17B4. The rf voltage required to make α_i = 0.1 is shown as a function of plasma density for each of these electrodes in Fig. 17B5. The type 3 electrode induces plasma currents parallel to the magnetic field, resulting in the beneficial paramagnetic effect (Ohsawa et al, 1979).

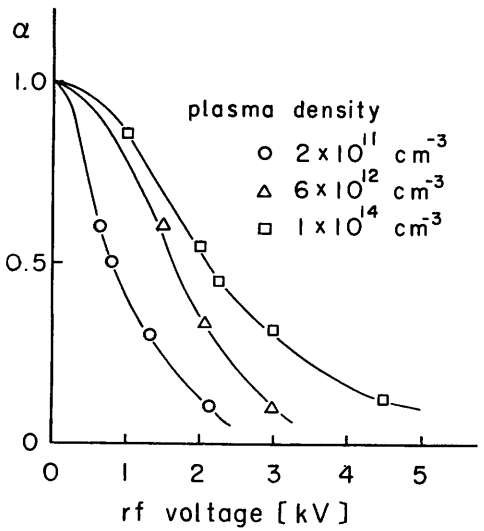

Fig. 17B3. Variation of plasma loss flux with applied rf voltage, at various plasma densities. From T. Watari et al, The Physics of Fluids 21, 2076-2081, (1978), Fig. 7.

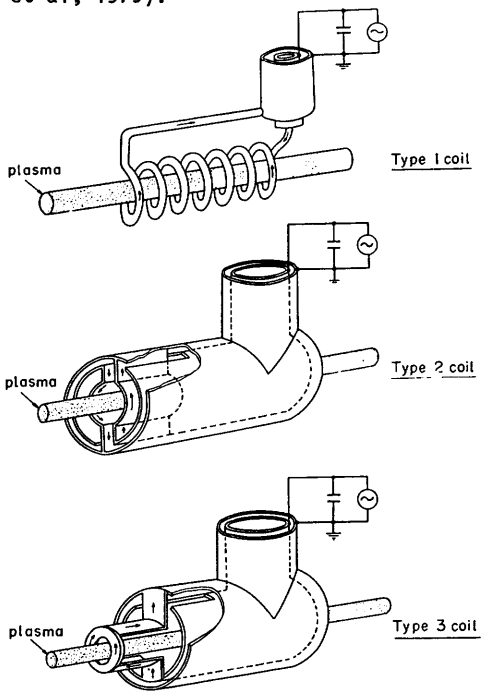

Fig. 17B4. Three types of plugging electrodes used in the TPD-III experiment. From T. Watari et al, The Physics of Fluids 21, 2076-2081 (1978), Fig. 3.

In another series of experiments on the TPD-III device, a spindle cusp magnetic field was used with rf plugging electrodes in the ring cusp and both point cusps. Laser beam impact on a polyethylene target produced a plasma with $n \sim 5\times10^{19}$ m^{-3}, $T_i \sim 30$ eV, $T_e \sim 10$ eV at $t \sim 10$ μs. The particle confinement time increased from 19 μs without plugging to 95 μs with rf plugging at 3 kV.

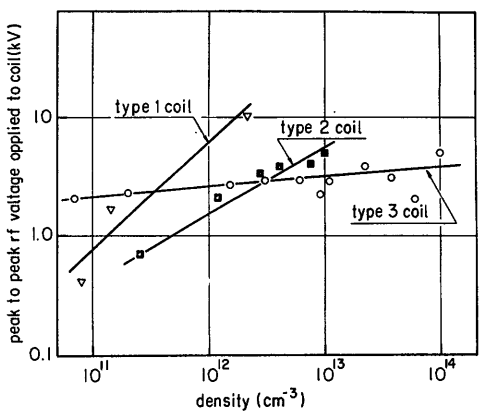

Fig. 17B5. The rf voltage required to make the loss reduction factor α_i=0.1 vs. plasma density, for the three types of plugging electrodes. From T. Watari et al, The Physics of Fluids 21, 2076-2081 (1978), Fig. 8.

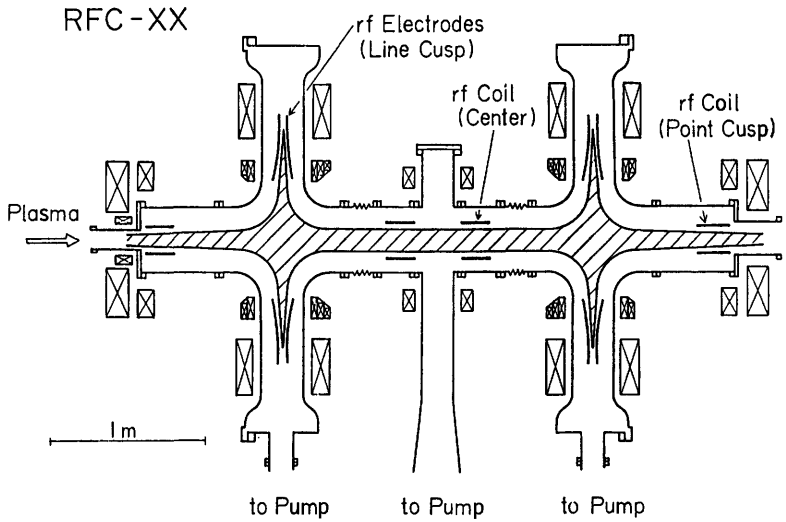

Fig. 17B6. The RFC-XX experiment. Plasma is injected from a TPD source at the right. Courtesy of the Institute of Plasma Physics, Nagoya University.

The RFC-XX (Radio Frequency Confinement - 20) experiment shown in Fig. 17B6 is a cusp-ended solenoid, with two ring cusps and two point cusps, all rf plugged. Some parameters of this experiment are listed in Table 17B1.

A conceptual rf-plugged reactor design is based on a cusp-ended solenoid like the RFC-XX, with the central section lengthened to 100 m. The ring cusp radii are about 15 m, in order to keep the plasma between the electrodes very thin, so that the rf fields can penetrate effectively. The magnetic fields are about twice those of RFC-XX, the rf electric field is about 10^5 V/cm, and the power gain ratio $Q \sim 5$. Such a reactor would have the advantages of axisymmetry (good drift orbits), good MHD stability (magnetic well and favorable curvature), impurity control via preferential plugging of fuel ions (D^+, T^+), and linear geometry (easy maintenance). However, many plasma physics questions remain to be answered, and technological problems may arise, like high-voltage breakdown and arcing of the electrodes.

Table 17B1. Parameters of the RFC-XX experiment.

length between point cusps	L	4 m
ring cusp radius	R	1 m
peak magnetic fields		
point cusp	B_z	3.9 T
ring cusp	B_r	2.0 T
magnetic field duration		3 s
rf plugging frequencies		20-60 MHz
maximum rf voltage		± 20 kV
rf power per electrode		1 MW
rf power duration		0.1 s
anticipated plasma parameters		
adiabatic plugging		
	n	10^{16}-10^{17} m^{-3}
	T_i	30 eV
	V	20 liters
nonadiabatic plugging		
	n	10^{18}-10^{19} m^{-3}
	T_i	300 eV
	V	60 liters
confinement time (theoretical)		10-100 ms
ion cyclotron resonance heating	n	10^{20} m^{-3}
	T_i	3 keV

17C. Electrostatic Confinement

Plasma can be confined by the electric fields of wire mesh grids. In one

scheme, ion guns shoot ions radially inwards into a hollow spherical wire mesh grid at a negative applied voltage, as shown in Fig. 17C1 (top). If the grid is 95 % open, then the grid current will be about 5 % of the total circulating current. Mutual repulsion of ions inside the grid causes formation of a virtual anode. Secondary electrons emitted at the inside of the grid (by ion bombardment) will be accelerated inwards by the virtual anode. As these electrons pass through the virtual anode and focus to the center of the sphere, their negative charge tends to form a potential well (virtual cathode), which traps ions, as shown in the potential profile. Under some conditions, the trapped ions accelerated inwards towards the center of the sphere would tend to form a second virtual anode there (dashed curve), trapping electrons, etc. Spherical focusing increases the ion density at small radii, as shown at the bottom of Fig. 17C1. Cylindrical and toroidal geometry may be used, as well as spherical geometry, and either electrons or ions may be injected.

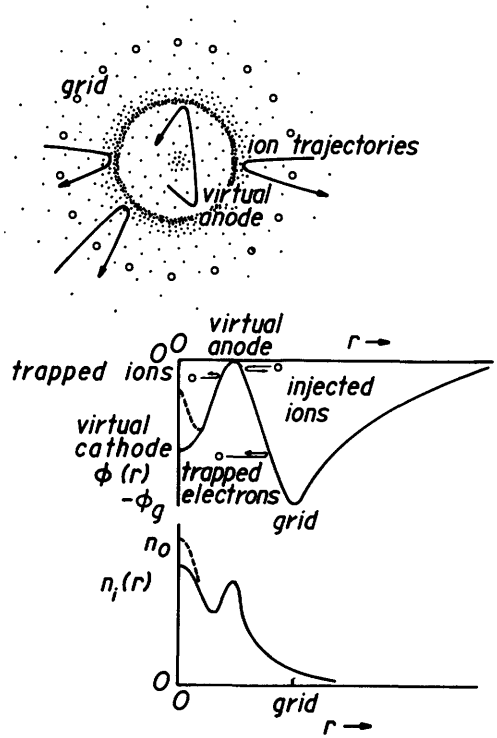

Fig. 17C1. Injection of ions (dots) into a hollow spherical wire mesh grid (top), the resulting electrostatic potential profile (middle), and radial distribution of electron density (bottom).

The following observations are consistent with the multiple-potential-well hypothesis:

* Theoretical studies (including angular momentum distribution) have found solutions of Poisson's equation with multiple potential wells (Cherrington, Verdeyen, and Swanson, 1975).
* Experimentally, injection of six 150 keV DT ion beams (each about 2 mm diameter) into a hollow spherical chamber with about 60 mA total beam current resulted in fusion reactions producing up to 10^{10} neutrons/s. This yield is consistent with the multiple-potential-well hypothesis, and not explained by simpler models (Hirsch, 1967).
* In the same experiment, collimated detectors measured radial variations of neutron emission and x-ray emission. The resulting curves had peaks like the $n_i(r)$ curve, Fig. 17C1.
* Similar (though less pronounced) peaks have been observed with direct measurement of $n_e(r)$ in cylindrical geometry by a laser heterodyne system (Meeker, Verdeyen, and Cherrington, 1973).
* The deflections of a probing electron beam in spherical geometry are consistent with the presence of multiple potential wells (Verdeyen, Cherrington, and Swanson, 1975).

Because they do not come in contact with the grid, the trapped ions and electrons have long confinement times, given approximately by Eq. (11E13) with no magnetic mirror (R = 1). If the grid voltage is 300 kV, then ions with $T_i \sim 20$ keV can be confined. The main problems are:

* attainment of high central ion densities n_0
* prevention of grid wire melting
* prevention of high-voltage breakdown.

If a high current is driven through the grid wires, the resulting magnetic field partially shields them from charged particle bombardment and inhibits high-voltage breakdown. The bombarding current is reduced, relative to the circulating current because the particles must now diffuse across the magnetic field to reach the grid. However, angular momentum imparted by the magnetic field reduces the spherical focusing effects. Magnetic shielding of the grid wires is equivalent to electrostatic plugging of a magnetic confinement system.

17D. Electrostatic Plugging

particle loss processes

Particle losses from magnetic cusps and mirrors can be reduced by applying strong electric fields along the magnetic field lines to reflect escaping ions and electrons, as illustrated for a spindle cusp in Fig. 17D1. A large negative voltage can be applied to the cathodes with the anodes grounded. (Alternatively, a high positive potential could be applied to the anodes, with the cathodes negative or grounded.) Plasma may be produced by

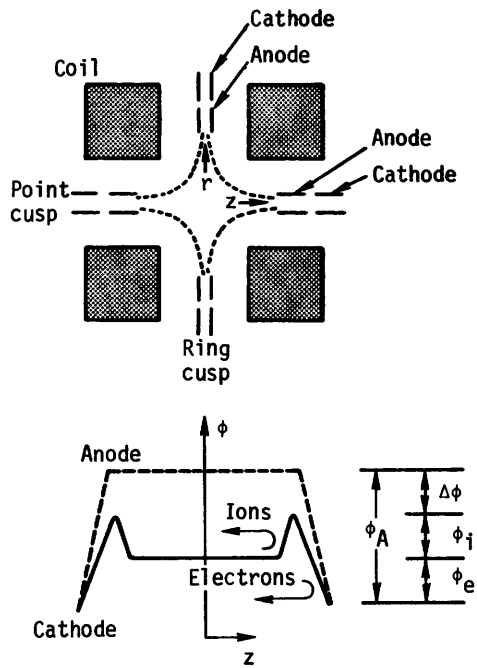

Fig. 17D1. Plugging electrodes and magnetic field lines (dashed curves) in a spindle cusp, and the corresponding axial variation of electrostatic potential in vacuum (dashed curve) and with plasma (smooth curve). Potential barriers ϕ_i and ϕ_e confront electrons and ions, with the applied voltage ϕ_A. The potential at the center of the anodes is depressed an amount $\Delta\phi$ by Debye shielding. From T.J. Dolan, "Design study of electrostatically plugged cusp fusion reactor", UCRL-52142 (1976), Figs. 2 and 3.

electron beam injection, ECRH, or other means. At first the potential profile is like the dashed curve of Fig. 17D1 and ions are easily lost along magnetic field lines, but electrons are confined. Then a charge imbalance develops, and the surplus negative charge drives the plasma potential negative, relative to the anodes, as shown by the smooth curve. This curve has the same shape as that for the tandem mirror, Fig. 11E1. Potential barriers ϕ_i and ϕ_e reflect ions and electrons. The potential surface in the anode regions is saddle-shaped, as

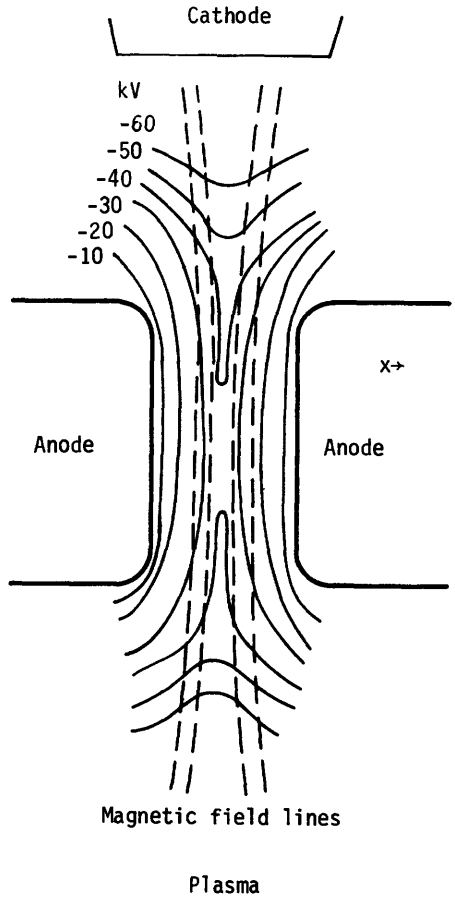

Fig. 17D2. Equipotential surfaces in the anode region, showing the saddle shape of the electrostatic potential $\phi(x,y)$. These contours are hypothetical voltages for the case in which the cathode potential is - 80 kV, the anodes are grounded, and $\Delta\phi$ = 35 kV. The width of the anode gap is exaggerated for clarity. From T. J. Dolan, UCRL-52142 (1976), Fig. 4.

illustrated in Fig. 17D2. Particle lifetimes $\tau_{\parallel}$ against escape over the electrostatic potential barriers are given approximately by Eq. (11E13), with R ≃ 1.

The electrons can also be lost by diffusion across the magnetic field. In a cusp system with only line cusps, such as a toroidal multipole cusp, with anode gap width 2b and plasma volume-to-surface-area ratio (V/S), the characteristic diffusion time is

$$\tau_{\perp} = \frac{\alpha \tau_{ei} b(V/S)}{\rho_b \rho_g} \qquad (17D1)$$

where τ_{ei} is the electron-ion Coulomb collision time, ρ_b and ρ_g are the electron Larmor radii at the plasma boundary [where $B^2/2\mu_0 = nk(T_e+T_i)$] and in the anode gap, and α is a numerical coefficient having a value $\alpha \sim 0.4$ if $T_e \sim T_i$ (Yushmanov, 1980). If instabilities occur, the effective value of τ_{ei} can be much shorter than the classical value.

The effective plasma radius r_p is approximately that radius where the plasma pressure equals the vacuum magnetic field pressure. For a sphere, $V/S \simeq r_p/3$, and for a large-aspect-ratio torus, $V/S \simeq r_p/2$. The increase of plasma radius with the number N of cusps in a toroidal multipole system is illustrated in Fig. 17D3. Thus, systems with large N tend to have larger values of r_p, (V/S), and $\tau_{\perp}$.

The cusp anode gaps must be kept narrow, to avoid severe Debye shielding effects (large $\Delta\phi$). Electrostatically-plugged mirrors would therefore have very small (V/S), so they are less useful than cusps.

Because the electric field in the anode regions is non-uniform, the $\vec{E}x\vec{B}/B^2$ drift velocity varies with x (Fig. 17D2). This shear of the electron drift velocity gives rise to the *diocotron* instability. At long-wavelengths the diocotron instability is stabilized by conducting walls (the anodes). The

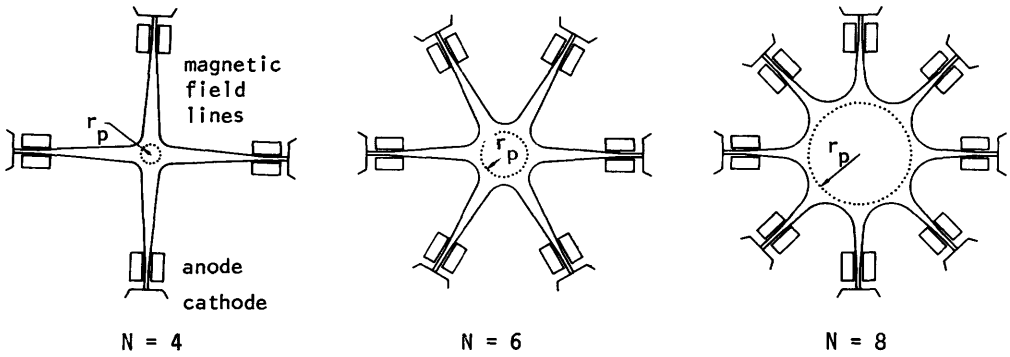

Fig. 17D3. Cross section of toroidal multipole cusps, showing magnetic field lines (smooth curves), plugging electrodes, and approximate radius of field-free plasma volume for cases of N = 4, 6, and 8 cusps. Magnet coils are not shown. From R. W. Moir, T. J. Dolan, and W. L. Barr, "Design of an electrostatic end-plugged plasma-confinement device", Proceedings of the Seventh Symposium on Engineering Problems of Fusion Research (Knoxville, 1977), © 1978 IEEE.

electron density n_A in the anode regions is limited by the short-wavelength diocotron instability to a value such that

$$\omega_{pe}^2/\omega_{ce}^2 \lesssim 0.2 \quad , \quad \text{or}$$

$$n_A \lesssim 0.2\varepsilon_0 B^2/m = (2\times10^{18}\ m^{-3})B^2 \qquad (17D2)$$

where ω_{pe} is the electron plasma frequency and ω_{ce} is the electron cyclotron frequency in the anode region.

The anode electron density n_A tends to be lower than the central plasma density n, because $nu_e \approx$ constant (steady-state continuity equation), and the electrons are accelerated as they enter the anode region. However, accumulation of cold electrostatically-trapped electrons in the anode region reduces this advantage.

power gain ratio

From Fig. 17D1, we see that

$$\phi_A = \Delta\phi + \phi_i + \phi_e \quad . \qquad (17D3)$$

For the usual case of narrow anode gaps, $\Delta\phi$ can be found from solution of a one-dimensional Poisson equation for an assumed electron density profile $n_e(x)$, where x is the direction perpendicular to the anode surface (Fig. 17D2). Then ϕ_i and ϕ_e can be calculated from the condition that the electron and ion loss rates are equal (steady state). Assuming $T_e \approx T_i = T$, the optimum temperature and barrier heights are approximately

$$\phi_e/T \simeq 9$$

$$\phi_i/T \simeq 7$$

$$T \simeq (\phi_A - \Delta\phi)/16 \quad , \tag{17D4}$$

and the maximum attainable reactor power gain ratio is

$$Q \lesssim 0.4(\phi_A - \Delta\phi)^{3/2}(n_{20})^{\frac{1}{2}} bB(V/S) \tag{17D5}$$

where ϕ_A and $\Delta\phi$ are in hundreds of kV, n_{20} is the central plasma density in units of 10^{20} m^{-3}, b is in mm, B is the gap magnetic field in Tesla, and (V/S) is in metres (Yushmanov, 1980). From the Poisson equation solution [assuming $n_A(x) \propto (1-x/b)^{\frac{1}{2}}$], it is found that $(\Delta\phi)^{\frac{1}{2}} \propto (n_{20})^{\frac{1}{2}} b$. Therefore, Q is optimized by maximizing $(\phi_A - \Delta\phi)^{3/2}(\Delta\phi)^{\frac{1}{2}}$, from which the optimum $\Delta\phi = \frac{1}{4}\phi_A$. The gap width b can be adjusted to attain this $\Delta\phi$. Then, the optimum Q is found to be

$$Q \lesssim \frac{0.1\phi_A^2 B(V/S)}{(1 + n_t/n_p)^{\frac{1}{2}}} \tag{17D6}$$

where ϕ_A is again in hundreds of kV, $n_A = n_p + n_t$, n_p is the density of central plasma electrons passing through the anodes, and n_t is the density of cooler electrons electrostatically trapped inside the anode potential peak of Fig. 17D1 (Yushmanov, 1980). For example, if $n_t/n_p \simeq 1$, ϕ_A = 300 kV, B = 10 T, and V/S = 2 m, then $Q \lesssim 4$.

experiments

Approximate parameters of some electrostatic plugging experiments are listed in Table 17D1. The spindle cusp experiments are limited by low values of (V/S). Multiple-cusp devices like Jupiter-2 offer the prospect of significantly longer confinement times.

Some potential advantages of electrostatically-plugged cusp reactors include reasonable $Q \sim 5$, simple coil geometry, possible steady-state operation (if impurity buildup is not severe), and low cyclotron radiation losses (since B is low inside the plasma). If very high plugging potentials could be sustained, then operation with advanced fuels might be feasible.

Potential problems of electrostatic plugging are:

* Nearly classical transport rates are needed in order to attain high Q. Significant enhancement of transport by sheath microinstabilities would be fatal. (Transport is nearly classical in past experiments.)
* The trapped electron density n_t in the anode regions tends to build up. A selective pumping mechanism is needed to remove the trapped electrons without spoiling confinement of passing electrons. It has been hypothesized that the diocotron oscillations may perform this function (Lavrent'ev, 1975).

*Table 17D1. Approximate parameters of some electrostatic plugging experiments. They all operate at neutral gas pressures $\lesssim$ 1 mPa (10^{-5} Torr), b $\sim$ 1-2 mm. * denotes predicted values.*

		KEMP-II	Jupiter-1M	ATOL	Jupiter-2
location		Quebec	Khar'kov	Moscow	Khar'kov
operational		$\sim$ 1975	$\sim$ 1975		
type		spindle cusp	spindle cusp	N=4 toroidal multipole cusp	linear set of ring cusps
B_r in line cusp	(T)	0.35	2.0	1-2	2.5
B_z in point cusp	(T)	0.5	6.6	(none)	5.
ring cusp radius	(m)	0.17	0.10	(major radius = 0.5 m)	$\sim$0.6
length between point cusps L	(m)	0.4	0.4	(minor radius to electrodes=0.25 m)	4.
ϕ_A	(kV)	2	6	20	25
n	(m^{-3})	4×10^{17}	3×10^{18}	3×10^{18}*	3×10^{19}*
τ_E	(ms)	$\sim$0.1	$\sim$1	$\sim$3*	$\sim$100*
T_i	(eV)	--	100-1000	100*	1000*
T_e	(eV)	$\sim$100	1000	1000*	2000*

* Alpha particle confinement is poor, so ignition is probably not feasible, unless the interior region is made adiabatic (such as by the addition of a toroidal field to a toroidal multipole cusp, as in the Tormac geometry).
* Impurities from the walls may tend to accumulate in the electrostatic potential well. If an impurity removal scheme is not available, then long-pulse operation, with periodic flushing and restarting may be necessary.
* Very high voltages must be sustained in the presence of intense radiation fluxes. Radiation shields will be needed between the plasma and the electrodes, and sets of electrodes at intermediate voltages will probably be needed to smooth out the potential gradients.

17E. Wall Confinement

A plasma may be heated to ignition by strong shock waves propagating axially in a coaxial shock tube, and then confined by the tube walls, with an azimuthal magnetic field providing thermal insulation, as illustrated in Fig. 17E1. The initial bias field is about 1 T, the final compressed field is on the order of 10 T, and the trapping coil field is about 15 T. The initial fill pressure is about 1-10 Pa (10 - 100 mTorr), and the final compressed plasma pressure is on the order of 30 MPa (300 atm).

The plasma pressure, greater than the magnetic field pressure ($\beta > 1$), is sustained by the tube walls. The total pressure ($2nkT + B^2/2\mu_0$) is fairly

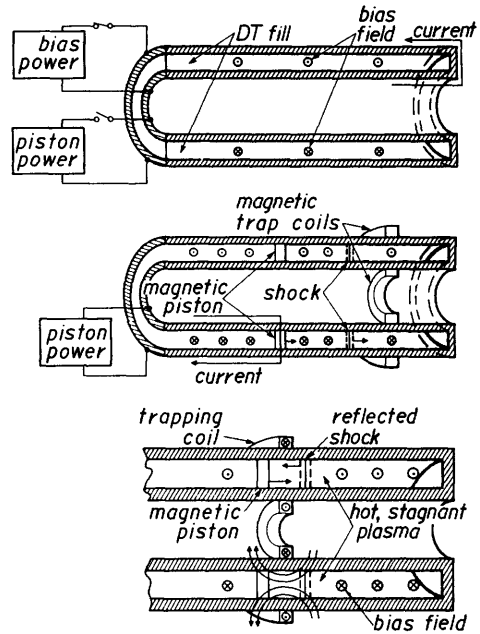

Fig. 17E1. A shock-heated reactor using wall confinement of plasma pressure. First a bias power supply produces a plasma with an embedded azimuthal field (top). Then the main power supply drives a sudden large current through the cylinders. The gas breaks down at the left end wall, creating a "magnetic piston" moving to the right, which drives a shock wave through the plasma, compressing it and the bias field (middle). After the shock wave has reflected from the end wall, it leaves a very hot, compressed plasma and bias field behind it. A trapping magnetic field is pulsed on where the piston meets the reflected shock wave (bottom), and the compressed plasma burns, confined by the walls and bias field. From F. F. Chen, EPRI ER-429-SR (1977), Part B, Fig. 1, p. 71.

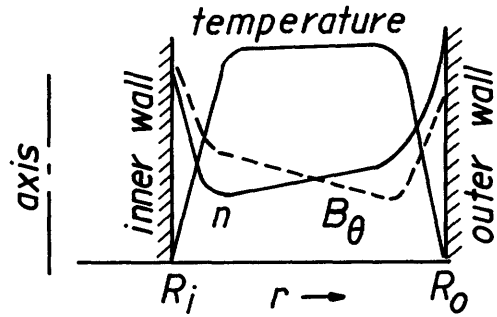

Fig. 17E2. Radial profiles of plasma density, temperature and azimuthal magnetic field. From R. A. Gross, Nuclear Fusion 15, 729-735 (1975), Fig. 2.

uniform, but varies in time. As the plasma moves towards the walls through the boundary layer magnetic field, surface currents are generated, which induce a self-magnetic field. Near the wall T decreases, and n and B increase, as illustrated in Fig. 17E2. The density and field gradients inhibit radial convection to the walls. The bremsstrahlung power loss ($\propto n^2T^{\frac{1}{2}}$) will be especially large near the plasma edge. Atoms sputtered off the walls will be ionized in the plasma edge, and very few will be able to penetrate to the hot plasma interior.

Experimentally, plasmas with keV ion temperatures have been produced. Plasma densities $n \sim 10^{22}$ m^{-3} have been confined for times ~ 50 μs, with nearly classical heat transport rates.

One-dimensional fusion burn calculations have been done for cases with confined plasma length L, outer radius $R_0 = 2$ L, and inner radius $R_i = L$. Fusion burn times of tenths of seconds are estimated. With L = 0.2 m, $W_{in} = 2$ MJ, a fusion energy output $W_F = 3.5$ MJ is predicted (a break-even case, $Q \sim 1.8$). With L = 0.5 m and $W_{in} = 47$ MJ, it is estimated that $W_F \sim 500$ MJ, ($Q \sim 11$). In this case, the energy fluences to the walls per pulse from alpha particles, neutrons, and heat are 13, 50 and 5 MJ/m^2, respectively. Such reactors would be simple and compact. The main questions are those of plasma behavior (such as heat transport),

reliable high-voltage high-power shock tube operation (6 MV, 100 TW), and plasma-wall interactions. Wall confinement is also used with multiple mirrors (Section 11G).

17F. Imploding Liner

To achieve $n\tau \sim 10^{21}$ m^{-3} s for a reactor, a confinement time of about 3 ms would suffice if the density were raised to 3×10^{23} m^{-3}. To confine this density at T = 20 keV with $\beta \sim 0.5$ requires a magnetic field of 50 T, which is higher than ordinary coils can produce, because the resulting stress exceeds their mechanical strength. However, such high magnetic fields can be produced by magnetic flux compression. Compression with a fast liner was described in Section 12A.

A slow liner-compression scheme (called "LINUS") is illustrated in Fig. 17F1. A compact toroidal plasma (such as a field-reversed theta pinch) with $r_s \sim 1.5$ m, L ~ 10 m, is injected into a cylinder containing a thick liquid-metal liner (Li or Li-Pb). When high-pressure (~ 14 MPa) helium gas is injected around the

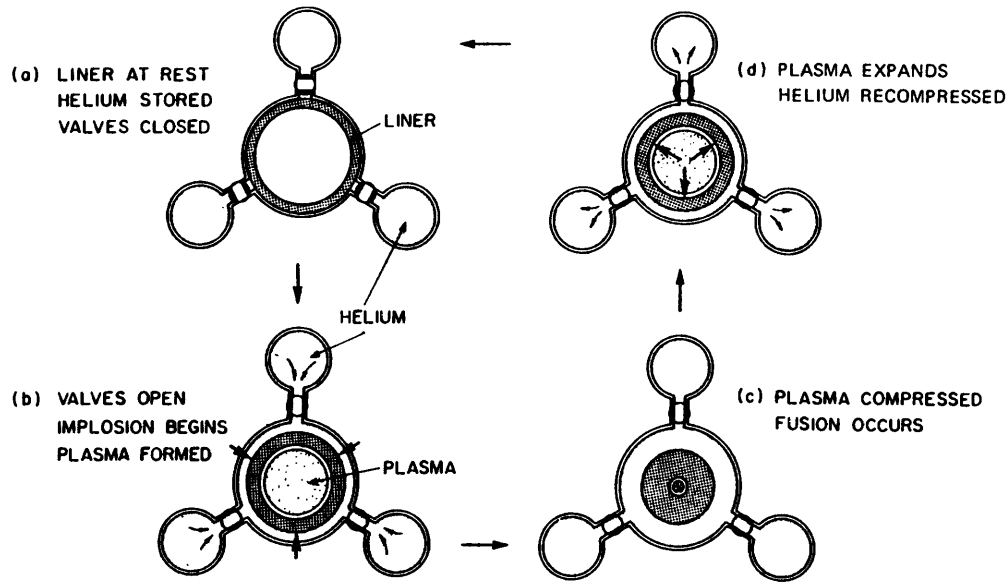

Fig. 17F1. Schematic end view of plasma compression by a slowly-imploding liner (LINUS). From C. C. Baker, G. A. Carlson, and R. A. Krakowski, Nuclear Technology/Fusion 1, 5-78 (1981), Fig. 38.

outside of the liner, the liner is compressed. The trapped magnetic field can only diffuse about 10 cm into the liner, during the 20 ms compression, and most of the magnetic flux is compressed to a flux density B ~ 60 T. At the same time, the plasma (with $\langle\beta\rangle \sim 0.5$) is radially compressed from about 1.5 m to about 0.1 m. The final pressure ~ 700 MPa (7000 atm) results in very high fusion power density during the 2 ms fusion burn period. A typical liner implosion trajectory is shown in Fig. 17F2. The fusion-product alpha particle energy heats the plasma, causing it to expand and drive the helium back into the storage containers. Thus part of the fusion energy is directly converted into mechanical energy, and a

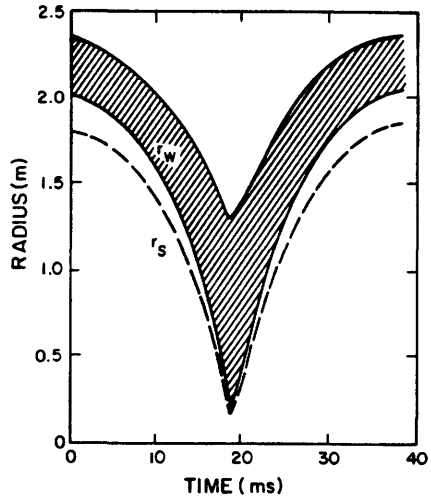

Fig. 17F2. A typical cylindrical liner implosion trajectory. The plasma separatrix radius (dashed curve) and liner inner and outer radii are shown as functions of time. From R. L. Miller and R. A. Krakowski, Proceedings of the 4th ANS Topical Meeting on the Technology of Controlled Nuclear Fusion (King of Prussia, PA, 1980), DOE, 1981, Fig. 2.

large electrical energy storage system is not needed.

In order to prevent the Rayleigh-Taylor instability (Section 8D) at the liner-plasma interface, the liner is rotated at a speed such that the centrifugal acceleration is greater than the inward acceleration at turnaround ($v_\theta^2/r > d^2r/dt^2$). The rotation is produced by injecting the liquid metal through nozzles pointed in the azimuthal direction around the outside of the cylinder (not shown in Fig. 17F1).

In order to prevent the Rayleigh-Taylor instability at the liner-helium interface, mechanical pistons are used. If the pistons travel radially inwards, then they may get out of phase with each other, resulting in an asymmetric compression. Using axial motion of annular pistons, as shown in Fig. 17F3, avoids this potential problem.

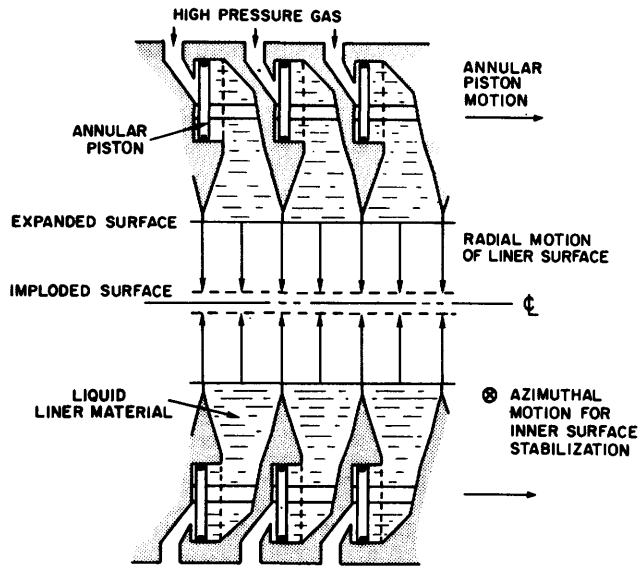

Fig. 17F3. Cutaway view of a LINUS stabilized implosion system. Annular pistons driven by high pressure gas move axially, causing radial motion of the free surface of the rotating liquid metal liner. From P.J. Turchi, D. L. Book, R. L. Burton, and A. L. Cooper, Journal of Magnetism and Magnetic Materials 11, 372-375 (1979), Fig. 1.

The gases are then pumped away, and another plasmoid is injected to begin a new cycle at a repetition rate of about 1 Hz. Part of the liquid-metal liner is continuously circulated to a steam generator for heat removal and electrical power production.

During radial compression from r_{s0} to r_s, the plasmoid length is expected to contract from ℓ_0 to ℓ, in accordance with the equation

$$\ell/\ell_0 \sim (r_s/r_{s0})^{2/5} \quad . \tag{17F1}$$

Thus, when $r_s/r_{s0} = 0.1$, ℓ/ℓ_0 will be about 0.4 .

A liquid metal liner driven by axial piston motion has demonstrated effective magnetic flux compression, and rotational stabilization has been verified by liquid metal liners driven electromagnetically. Repetitive pulsing and rotational stabilization have also been demonstrated using water liners.

Fusion burn calculations for various cases with input energies of 1 MJ per centimeter of liner indicate production of about 10^{21} neutrons per centimeter of plasma (about 3 MJ/cm) during fusion burn (Hamasaki and Book, 1980). [In view of Eq. (17F1), the final plasma length will probably be less than the liner length.] The direct recovery of plasma thermal energy to recompress the working fluid (helium) enables economic operation at much lower plasma energy gain ratios Q than other fusion systems. Net plant efficiencies $\eta \sim 0.27$ are estimated for fusion power plants using imploding liners (Miller and Krakowski, 1981).

Some potential advantages of imploding liner power plants are:

* Fusion power density is high, so the reactor is compact.
* Plasma heating is done with mechanical energy (compressed gas), which is recovered each pulse by direct conversion of plasma thermal energy, so a large electrical energy storage system is not needed.
* Plasma fuel is replenished each pulse, and impurity penetration during the short pulse is not a serious problem.
* The liner performs the functions of the first wall, breeding blanket, radiation shield, and coolant.

Uncertainties of the imploding liner concept include:

means of forming and injecting the plasmoid
plasma stability
attainable Q
reliability of mechanical parts
  shock wave damage and fatigue problems
  corrosion
time required for evacuation of exhaust gases

17G. Colliding-beam Mirror

High-energy ions can be injected into a magnetic mirror so that their trajectories pass through the mirror axis and precess around it, as illustrated in Fig. 17G1. The effective ion density is relatively high at the axis and low away from the axis. Near the axis the ions may undergo beam-beam fusion reactions. At energies of 1-2 MeV, the cross sections for charge exchange and Coulomb scattering are relatively much lower than at 10-100 keV, so the fusion probability p_f of the fast ions (Section 4F) is enhanced. The high ion energies make it possible to burn fuels which produce fewer neutrons, thus reducing structural activation.

Ion-ion scattering near the axis results in ion orbits which still pass through the axial region, because collisions near the axis do not impart significant angular momentum to the ions. Scattering collisions away from the axis can impart angular momentum and defocus the ions, but such collisions are less frequent, due

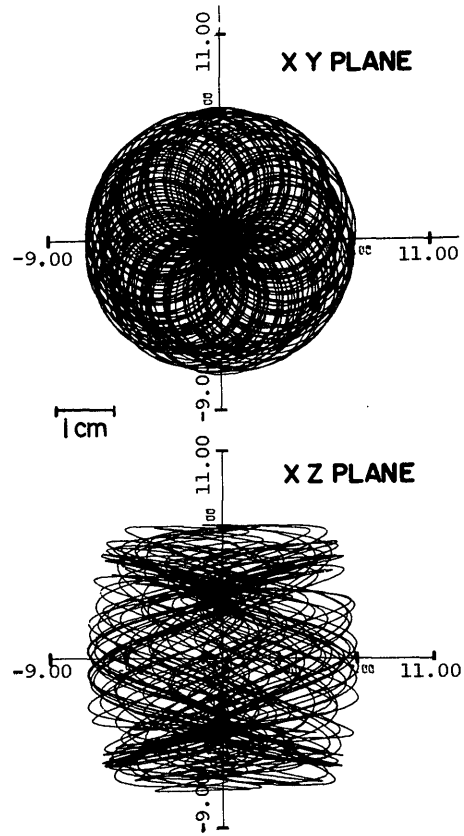

Fig. 17G1. Computer plot of the precessing orbit of a high-energy ion injected to pass through the axis of a magnetic mirror field. From B. C. Maglić, J. P. Blewett, A. P. Colleraine, and W. C. Harrison, Physical Review Letters 27, 909-912 (1971), Fig. 1.

to the lower densities away from the central region. The configuration of self-colliding orbits which intersect near the axis has been called a "Migma" (Greek for "mixture"). Neutral gas effects like charge exchange are detrimental, so pressures below 1 μPa (10^{-8} Torr) are desirable.

Electrons must be present to neutralize ion space charge, if significant ion densities ($> 10^{16}$ m^{-3}) are to be attained (Section 5G). Fusion reaction products, such as alpha particles and protons, are not well confined, and heating of the background plasma by them does not contribute to the desired ion orbit structure. Therefore, ignition will not occur, and the device functions as a low-gain power amplifier. Part of the escaping ion energy may be directly converted into electricity (Section 26G).

In the MIGMA-III experiment a 100 μA, 3 mm diameter beam of 1.2 MeV D_2^+ ions was injected into a magnetic mirror field at P ∿ 10 μPa (10^{-7} Torr). About 1 nA of the beam was dissociated near the axis, where B ∿ 3.3 T. The 0.6 MeV D^+ ions produced by dissociation near the axis were trapped by their smaller Larmor radii. Probe measurements indicated a narrow density peak (1-2 mm wide) with $n \sim 2 \times 10^{15}$ m^{-3}, which is consistent with the theoretical ion orbits. The trapped ion current (∿ 50 μA) had a decay time of about 2 s when the beam was turned off. A MIGMA-IV device is planned to attain higher densities by injecting higher currents at lower pressures.

The fusion power and power gain ratio Q in colliding-beam mirrors depend strongly on the attainable ion density n [or on $\beta = 2\mu_0 nk(T_e+T_i)/B^2$]. If $n = 10^{20}$ m^{-3} is desired, and B = 10 T, T_i (non-Maxwellian) ∿ 1 MeV, and $T_e \ll T_i$, then $\beta \sim .5$ is required. If such a high density can be attained, then one mirror cell might be able to produce $P_F \sim 1$ MW. Potential advantages of colliding-beam mirrors include burning "clean" fuels, direct conversion, compact size, and simple magnetic field.

Some potential problems are:

* Plasma instabilities may prevent buildup to high densities.

* If intense fusion reactions occur, plasma-wall interactions and recycling of neutral gas will increase chamber pressure, making the desired ultra-high vacuum difficult to maintain.
* Because of the low value of Q, the recirculating power fraction is high. Large values of the fusion probability p_f and energy conversion efficiencies would be needed to obtain net electrical power output.
* Capital costs may be high relative to the power output.

17H. Hypervelocity Impact

required parameters

Hypervelocity impact is a type of inertial confinement fusion (ICF). The idea is to accelerate small pellets (mass $\sim$ 1 gram) up to velocities > 10^5 m/s and shoot them at a solid target. Either the projectile or the target may contain DT fuel. During impact, intense compression and shock heating occur, igniting some of the fuel. If compression is great enough, a high energy gain ratio Q = (fusion energy)/(projectile kinetic energy) $\sim$ 50-100 may be attained.

The lower and upper bounds on fusion energy yield W_F are determined by the economics of power production and the maximum blast which can be contained at reasonable cost. The resulting estimates are 1 GJ $\lesssim W_F \lesssim$ 100 GJ. In order to keep the recirculating power fraction $\lesssim$ 30 %, the product of driver efficiency and energy gain should satisfy

$$\eta_d Q \gtrsim 10 \tag{17H1}$$

(cf Eq. 15B6). If $\eta_d \sim 0.2$, then $Q \gtrsim 50$ is needed.

If the compression is one-dimensional, a projectile velocity and energy of about 7×10^5 m/s and 50 MJ are needed. If the compression can be made nearly three-dimensional, then the minimum required velocity and energy are about 1.3×10^5 m/s and 12 MJ (Jarboe, in Fusion Impact Workshop Proceedings, 1979). These values are comparable to the shell implosion velocities needed for laser fusion, Example Problem 15B1. One idea for making the compression three-dimensional is illustrated in Fig. 17H1. The compressed region might reach values of density, temperature, and pressure of $n \sim 3\times10^{28}$ m^{-3}, T $\sim$ 10 keV, $p \sim 10^{14}$ Pa (10^9 atm), with confinement and burn lasting 5-10 ns. If the projectile velocity and kinetic energy are 2×10^5 m/s and 10 MJ, then the required projectile mass is about 0.5 gram.

Blast chambers were discussed in Section 16H. The flowing liquid metal (HYLIFE) scheme is well suited to large yields. A chamber with radius $\sim$ 10 m could probably contain yields up to 100 GJ, with pulses every few seconds.

accelerators

A rail gun is illustrated in Fig. 17H2. The force on the projectile is

$$F = \tfrac{1}{2}L'I^2 \tag{17H2}$$

where I is the current. For the rectangular geometry of Fig. 17H2, the inductance per unit length

$$L' \simeq K_{sh}\mu\, w/h \tag{17H3}$$

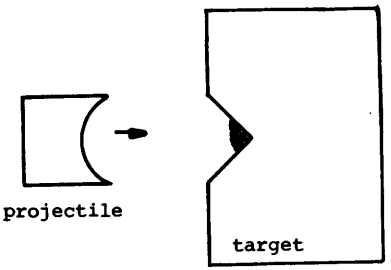

Fig. 17H1. Impact of a projectile on a target containing a conical hole produces a quasi-three-dimensional compression.

where μ is the effective magnetic permeability of the gun (if no ferromagnetic materials are present, $\mu = \mu_0$), and $K_{sh} \sim 0.5$ is given in Fig. 21B7. If $w \simeq h$, then $L' \simeq 0.4\ \mu H/m$. The allowable current I is limited by overheating and stresses in the projectile and rails. For example, the accelerating force must be less than the projectile yield stress times its area wh. If w = h, this gives

$$\tfrac{1}{2}L'I^2 < \sigma_y h^2 \qquad (17H4)$$

For a plastic projectile with $\sigma_y = 1.4 \times 10^9$ Pa, and h ≃ 0.01 m, $I \lesssim 0.8$ MA. For stability during acceleration, the projectile length ℓ should be at least half its transverse dimensions: $\ell \geq \tfrac{1}{2}w$, $\ell \geq \tfrac{1}{2}h$.

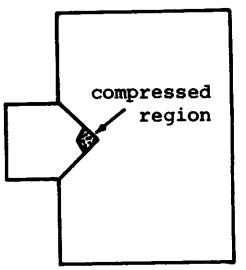

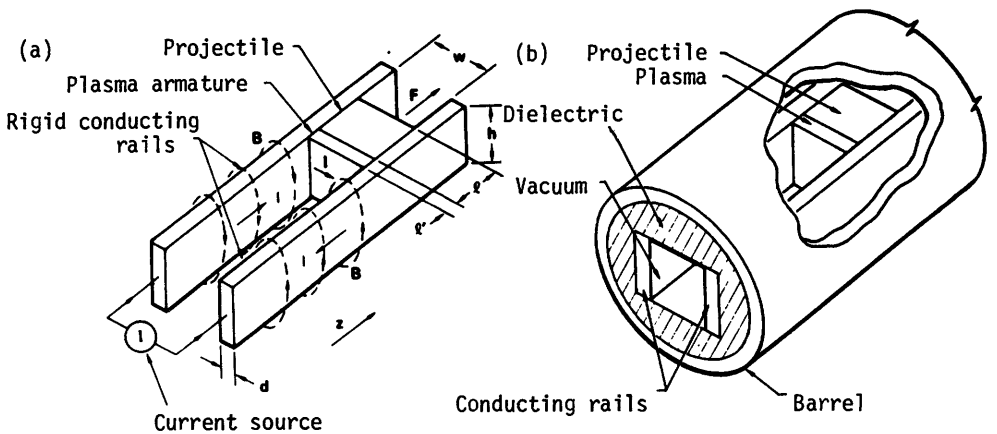

Fig. 17H2. A railgun accelerator, showing rails and projectile (a), and mounting of rails inside tube (b). The dielectric maintains the rail position and, with the rails, confines the plasma behind the projectile. From R. S. Hawke, LA-8000-C (1979), Fig. 1, p. 168.

If the rails are very long, I^2R power losses become excessive. Efficiency is improved by segmenting the rails into short lengths and driving each segment with a separate circuit.

The required accelerator length can be estimated from equating the work done Fz to the desired projectile energy

$$\tfrac{1}{2}L'I^2z = \tfrac{1}{2}mv^2 \qquad (17H5)$$

For example, if m = 1 gram, v = 2×10^5 m/s, L' = 0.4 μH/m, and I = 0.3 MA, then the accelerator length z = 1.1 km.

If metal projectiles are used, arcing between the projectile and the rails tends to cause "gouging" of the rails at high velocities, so it is preferable to drive a dielectric projectile with a plasma arc.

In some cases the projectile may be comprised of a "payload" and a "sabot" (French for "shoe", meaning a vehicle carrying the payload). At the end of acceleration, the payload would continue on to the target, and the sabot would be decelerated, and perhaps recycled. The velocities attainable with various input energies and accelerator lengths are shown in Fig. 17H3 for the case of a projectile with w=h=2ℓ=1 cm, I = 0.75 MA, total projectile mass = 1.23 gram. Thus, attainment of v ∿ 2×10^5 m/s requires input energy ∿ 100 MJ, and accelerator lengths ∿ 1 km. The projectile kinetic energy would be about 25 MJ, so the efficiency is about 25 %. If the payload mass were a fraction of the projectile mass, then the efficiency of energy transfer to the payload would be lower by the same fraction. Velocities attained experimentally are less than 10^4 m/s (10 km/s).

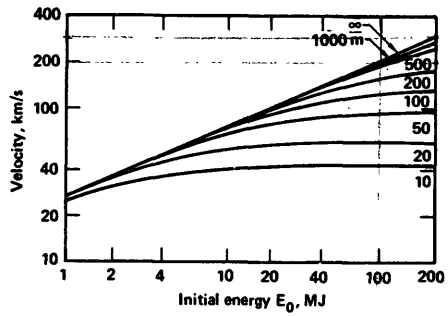

Fig. 17H3. Attainable projectile velocity vs. initial stored energy input to the accelerator, for various accelerator lengths, for a projectile with w = h = 1 cm, mass = 1.23 gram, I = 0.75 MA. From R. S. Hawke, LA-8000-C (1979), Fig. 2, p. 174.

A *travelling magnetic wave accelerator* involves a long solenoid comprised of many separate coils, which are pulsed one after the other to produce a travelling magnetic wave. If the projectile is a ferromagnetic cylinder, a conducting cylinder with diamagnetic currents, or a small superconducting coil, it will be carried along with the travelling wave by the magnetic field gradient force. Problems include prevention of projectile overheating and pellet guidance.

Other means of acceleration include two-stage light gas guns, a plasma impulse generator, acceleration by laser ablation, electrostatic accelerators, and a circular accelerator with magnetic levitation (Impact Fusion Workshop Proceedings, 1979). Pellet acceleration is also of interest for fueling magnetically confined plasmas (Section 25E).

Potential advantages of hypervelocity impact fusion are: effective conversion of kinetic energy into fusion energy, simple transport of macroparticles through small reactor chamber ports, and the possible availability of simple, efficient accelerators (not yet developed).

There are many uncertainties, including:

* physics of projectile target interaction, and attainability of effective 3-D compression
* ability of accelerators to attain $v \sim 2 \times 10^5$ m/s at high efficiency
* solution of engineering problems of accelerators, chambers, targets, and projectiles
* reliability of the reactor systems
* cost of accelerator research and development
* costs of targets and projectiles, and resulting electric power costs.

Alternate uses of impact fusion include breeding fissile fuel and destruction of radioactive wastes.

Bibliography

general

J. R. Roth, "Alternative approaches to plasma confinement", *IEEE Transactions on Plasma Science PS-6*, 270-295 (1978).

radiofrequency confinement

A. J. Hatch, "Properties of radiofrequency-confined plasmas, *Annals of the New York Academy of Sciences 251*, 394-406 (1975).

A. J. Hatch and M. Hasan, "Containment of plasmas in resonant-cavity fields", *Proceedings of the National Electronics Conference XXII*, 962-966 (1966).

P. L. Kapitza, "Free plasma filament in a high frequency field at high pressure", *Societ Physics JETP 30*, 973-1008 (1970).

P. L. Kapitza, "A thermonuclear reactor with a plasma filament freely floating in a high frequency field", *Societ Physics JETP 31*, 199-204 (1970).

P. L. Kapitza, "Plasma and the controlled thermonuclear reaction", *Science 205*, 959-964 (1979).

C. F. Shelby and A. J. Hatch, "Observation of radio-frequency confinement of a plasma", *Physical Review Letters 29*, 834-837 (1972).

radiofrequency plugging

S. Hiroe, T. Sato, T. Watari, S. Hidekuma, R. Kumazawa, K. Adati, T. Shoji, S. Kawasaki, A. Miyahara, K. Akaishi , Y. Kubota, N. Watanabe, and S. Miyake, "Experiment on nonadiabatic rf plugging in a cusped field", *The Physics of Fluids 21*, 676-681 (1978).

Y. Ohsawa, M. Inutake, T. Tajima, T. Hatori, and T. Kamimura, "Plasma paramagnetism in radio-frequency fields", *Physical Review Letters 43*, 1246-1249 (1979).

T. Sato, R. Kumazawa, K. N. Sato, T. Watari, S. Okamura, M. Ichimura, S. Hidekuma, T. Fukagawa, T. Aoki, T. Kawamoto, K. Adati, S. Hiroe, H. Obayashi, T. Hatori, T. Watanabe, K. Takayama, S. Okada, R. Yoshino, H. Saito, S. Sudo, and T. Sekiguchi, "Rf plugging of laser-produced plasma in a cusp field", *Plasma Physics and Controlled Nuclear Fusion Research (Innsbruck, 1978)*, IAEA, Vienna, 1979, Volume II, p. 401-410.

T. Watari, T. Hatori, R. Kumazawa, S. Hidekuma, T. Aoki, T. Kawamoto, M. Inutake, S. Hiroe, A. Nishizawa, K. Adati, T. Sato, T. Watanabe, H. Obayashi, and K. Takayama, "Radio-frequency plugging of a high density plasma", *The Physics of Fluids 21*, 2076-2081 (1978).

electrostatic confinement

R. L. Hirsch, "Inertial-electrostatic confinement of ionized fusion gases", *Journal of Applied Physics 38*, 4522-4534 (1967).
R. W. Hockney, "Formation and stability of virtual electrodes in a cylinder", *Journal of Applied Physics 39*, 4166-4170 (1968).
L. C. Marshall and H. L. Sahlin, Editors, "Electrostatic and Electromagnetic Confinement of Plasmas and the Phenomenology of Relativistic Electron Beams", *Annals of the New York Academy of Sciences 251*, (1975).
articles by:
J. T. Verdeyen, B. E. Cherrington, D. A. Swanson, and D. J. Meeker, p. 126-138
B. E. Cherrington, J. T. Verdeyen, and D. A. Swanson, p. 139-151
O. A. Lavrent'ev, p. 152-178
A. L. Gardner, D. M. Hatch, A. I. Y. Chan, and R. P. Evans, p. 179-189
E. H. Klevans, p. 190-212
T. Consoli, p. 322-345
C. W. Barnes, p. 370-380.
D. J. Meeker, J. T. Verdeyen, and B. E. Cherrington, "Measurement of electron density in a cylindrical inertial electrostatic plasma confinement device", *Journal of Applied Physics 44*, 5347-5355 (1973).
D. A. Swanson, B. E. Cherrington, and J. T. Verdeyen, "Potential well structure in an inertial electrostatic plasma confinement device", *The Physics of Fluids 16*, 1939-1945 (1973).

electrostatic plugging

Yu. S. Azovskii, V. I. Karpukhin, O. A. Lavrent'ev, V. A. Maslov, M. N. Novikov, and M. G. Nozdrachev, "Yupiter-1M single-gap electromagnetic confinement system", *Soviet Journal of Plasma Physics 6*, 142-146 (1980).
A. D. Komarov, O. A. Lavrent'ev, V. A.Potapenko, and I. A. Stepanenko, "Energy distributions of the plasma electrons and ions in an electromagnetic confinement system", *Soviet Physics Technical Physics 24*, 1060-1062 (1979).
O. A. Lavrent'ev, "Electrostatic and electromagnetic high-temperature plasma traps", *Annals of the New York Academy of Sciences 251*, 152-178 (1975).
V. P. Pashtukhov, "Classical transport in electrostatically plugged magnetic confinement systems", *Soviet Journal of Plasma Physics 4*, 311-316 (1978).
B. L. Stansfield, J. M. Larsen, B. Bergevin, P. Couture, and B. C. Gregory, "Density and lifetime measurements in the KEMP II electromagnetic trap", *Canadian Journal of Physics 54*, 1856-1861 (1976).
E. E. Yushmanov, "The influence of electron capture in gaps on the efficiency of magneto-electrostatic trap", *Nuclear Fusion 21*, 329-337 (1981).
E. E. Yushmanov, "The power gain factor Q of an ideal magneto-electrostatic fusion reactor", *Nuclear Fusion 20*, 3-8 (1980).
E. E. Yushmanov, "Charged-particle injection into an electrostatically plugged magnetic confinement device", *Soviet Journal of Plasma Physics 4*, 11-17 (1978).
Yu.G.Zalesskii, A. D. Komarov, O. A. Lavrent'ev, V. A. Naboka, N. I. Nozarov, V. A. Potapenko, and I. A. Stepanenko, "Plasma production in an electrostatically plugged mirror system by a microwave method", *Soviet Journal of Plasma Physics 5*, 532-534 (1979).

wall confinement

F. F. Chen, *Alternate Concepts in Controlled Fusion, Part B*, EPRI ER-429-SR (1977).
R. A. Gross, "Physics of a wall-confined fusion system", *Nuclear Fusion 15*, 729-735 (1975).
L. N. Kmetyk, "Thermonuclear burn in wall confined plasmas", *The Physics of Fluids 24*, 970-978 (1981).

liner compression

D. L. Book, R. L. Burton, A. L. Cooper, R. D. Ford, B. Hui, D. J. Jenkins, P. C. Liewer, A. E. Robson, P. J. Turchi, S. Hamasaki, N. A. Krall, L. Mascheroni, R. Shanny, E. L. Cantrell, R. A. Gerwin, I. Henins, T. R. Jarboe, R. C. Malone, J. Marshall, R. W. Moses, G. A. Sawyer, A. R. Sherwood, B. R. Suydam, and C. E. Swannack, "Experimental and theoretical liner fusion studies", *Plasma Physics and Controlled Nuclear Fusion Research (Innsbruck, 1978)*, Volume II, IAEA, Vienna, 1979, p. 93-102.
S. Hamasaki and D. L. Book, "Numerical simulation of the anomalous transport processes in radially compressed reversed-field configurations", *Nuclear Fusion 20*, 289-304 (1980).
R. L. Miller and R. A. Krakowski, "Assessment of the slowly-imploding liner (LINUS) fusion reactor concept", *Proceedings of the 4th ANS Topical Meeting on the Technology of Controlled Nuclear Fusion (King of Prussia, PA, 1980)*, DOE, 1981.
P. J. Turchi, D. L. Book, R. L. Burton, and A. L. Cooper, "Stabilized imploding liner research for high magnetic field plasma compression", *Journal of Magnetism and Magnetic Materials 11*, 372-375 (1979).

P. J. Turchi, A. L. Cooper, R. D. Ford, D. J. Jenkins, R. L. Burton, "Review of the NRL liner implosion program", in *Megagauss Physics and Technology*, Plenum Press, 1980, p. 375-386.
P. J. Turchi, A. L. Cooper, D. J. Jenkins, and E. P. Scannell, "A LINUS fusion reactor design based on axisymmetric implosion of tangentially injected liquid metals", NRL Memorandum Report 4388 (1981).

colliding-beam mirror

J. C. Ferrer, B. C. Maglich, M. G. Mazarakis, S. C. Menasian, J. E. Nering, C. W. Powell, J. R. Treglio, and A. R. Wittemore, "Observation of highly localized trapping of MeV deuterons into self-colliding orbit distribution ('Migma') and measurement of its density and confinement time", *Nuclear Instruments and Methods 157*, 269-277 (1978).

B. C. Maglić, J. P. Blewett, A. P. Colleraine, and W. C. Harrison, "Fusion reactions in self-colliding orbits", *Physical Review Letters 27*, 909-912 (1971).

B. C. Maglich, "Migmacell - a low-gain 'driven' fusion power amplifier", *Nuclear Instruments and Methods 151*, 1-27 (1978).

hypervelocity impact

R. S. Hawke, *Atomkernenergie-Kerntechnik 38*, 35 (1981).

R. N. Kostoff, A. T. Peaslee,Jr., F. L. Ribe, "Possible application of electromagnetic guns to impact fusion", LA-UR-80-3137 (1980).

A. T. Peaslee,Jr., Proceedings of the Fusion Impact Workshop, LA-8000-C (1979).

F. L. Ribe, A. T. Peaslee,Jr., "Evaluation of Impact Fusion Concepts", LA-UR-80-2612 (1980).

CHAPTER 18

FUSION ENGINEERING PROBLEMS

18A. Problem Areas

The purpose of this Chapter is to introduce various fusion engineering problems, which will be discussed in Chapters 19-29. The main components of a fusion reactor were illustrated in Fig. 1F1. Some fusion reactor design problem areas are listed in Table 18A1.

plasma

Plasma purity can be maintained by the use of a gas blanket, a magnetic divertor, or a pumped limiter (Chapter 25). Refueling may be done by gas puffing, beam injection, or pellet injection. Without plasma purity control, refueling and burn control, a fusion reactor would be limited to short pulse ($\lesssim$ 30 s) operation. The advantages of steady-state operation include:

* compatability with electrical power grid
* increased component and system reliability
* fatigue failures unlikely
* thermal and electrical energy storage requirements minimized.

On the other hand, short-pulsed reactors have potential advantages of not needing systems for burn control, fueling, and plasma purity control.

ICF targets, drivers, and chambers, described briefly in Chapters 15 and 16, will not be discussed further here.

vacuum

An ultrahigh vacuum is usually needed, in order to insure purity of the fuel gas. Elaborate outgassing, discharge cleaning, and gettering processes are used in most magnetic confinement experiments, in order to minimize concentrations of carbon, oxygen, and other impurities in the plasma.

The primary vacuum boundary can be located at the first wall, at the outside of the shield, or at the building wall. Locating the boundary at the first wall, as done in many experiments, would not be practical in the case of

Table 18A1. Fusion Reactor Design Problems. Numbers refer to chapters.

plasma		magnets	
production & heating	9	size & number of TF coils	
confinement & stability	8,11-17	location & type of OH, EF coils	
diagnostics	10	magnetic field calculations & coil forces	20
current drive	13	water-cooled coils	20
refueling	25	pulsed coils	21
burn control	13	superconducting magnets	22
purity	25	superconductors	
		cooling methods	
ICF targets, drivers, chambers	15, 16	stabilization	
		protection	
vacuum	19	cryogenics	23
chamber, joints, ports		thermal insulation	
		refrigeration	
pumps, gages, cryogenic fluids		environment	28
		tritium	
materials	24	inventory	
strength & ductility		containment	
fabrication & welding		activated structure	
thermal stress, creep, fatigue		materials selection	
surface erosion		stored energy	
radiation damage		lithium	
radioactivity (induced by neutron absorption)		magnets	
		stray magnetic fields	
compatibility with coolant		siting	
		decommissioning	
blanket & shield		materials shortages	
		economics	
heat removal	26	plant availability	18
coolant compatibility & pumping power		systems reliability	
thermal efficiency		quality assurance	
tritium breeding	27	redundancy & spare parts	
neutron multipliers		maintenance	
lithium		scheduled & unscheduled	
tritium inventory	26,28	module size	
energy multiplication	27	remote handling equipment	
radiation attenuation & streaming	27	cost of electricity	28
activation	28	fusion-fission hybrids	29

a reactor first wall. If the building is evacuated, then joints between reactor modules are simplified, atmospherical pressure loads are removed from the blanket-shield region (transferred to building walls). For example, the NASA Plum Brook facility, Sandusky, Ohio, has a 30 m inside-diameter building which can be evacuated to 10^{-6} Torr (0.1 mPa). Locating the vacuum boundary at the outside of the blanket-shield region protects the vacuum seals from intense radiation bombardment and makes them readily accessible, without requiring the whole building to be evacuated. In general, vacuum technology is well developed and adequate to meet the needs of fusion reactors.

materials

Materials problems are the main limitations of jet engines, fission reactors, and practically all areas of high technology, including fusion reactors. The reactor first wall (nearest to the plasma) will be subjected to a variety of forces (pressure, thermal, swelling, gravity, electromagnetic) in a very hostile environment (bombardment by ions, neutrons, x-rays, etc.). Consequently, there are many possible failure mechanisms, including overheating, embrittlement, fatigue, creep, swelling, erosion, and corrosion. A small leak from a single coolant tube (out of thousands of tubes) could force shutdown of the entire reactor. Chemical reactions between the coolants and structural materials can markedly shorten tube life. For example, traces of oxygen in a helium coolant can ruin tubes of some refractory metals.

blanket and shield

The blanket region of a DT reactor contains lithium as a liquid metal (Li or Li-Pb), as a molten salt (such as $2LiF\text{-}BeF_2$), or as a solid compound (such as Li_2O or $LiAlO_2$)which absorbs neutrons to produce tritium fuel (Table 1E1). It is important to minimize the amount of tritium held up in the blanket, for safety in case of accident. The neutron population may be increased by (n,2n) reactions, especially in ^7Li, Pb, and Be. The heat deposited in the blanket is removed by a coolant such as water, high-pressure helium, or a liquid metal. The coolant exit temperature should be high ($\gtrsim$ 700 K) in order to attain high steam cycle efficiency (converting thermal energy into electricity), yet not so high that corrosion, creep, or other materials problems drastically reduce tube lifetimes. Coolant channels are designed to remove heat effectively, with low tube stresses, few welds, and low coolant pumping power. Exothermic neutron capture reactions (n,γ) release additional energy in the blanket, giving neutron energy multiplication factors $M \sim 1.1\text{-}2$. (Fast fission reactions in fusion-fission hybrid blankets containing uranium can make $M \sim 10$). Typically about 99 % of the energy produced is deposited in the blanket region and removed by the blanket coolant.

The shield between the blanket and magnet coils further attenuates incident radiation so that the total attenuation factor for the blanket-shield region is $< 10^{-6}$. Ducts for vacuum pumping, plasma heating, and diagnostics should have several bends to minimize radiation streaming. The total thickness of the blanket-shield region is typically about 1-2 m.

magnets

Early tokamak designs had large numbers of toroidal field (TF) coils (16-32) to minimize ripple. Recent designs use fewer (6-12) TF coils, in order to improve access to the blanket and shield for maintenance. The ripple is reduced by making the coils extend out farther radially or by using small trim coils between the TF coils.

Most of the equilibrium field (EF) and ohmic heating (OH) coils are placed outside the toroidal field coils, to facilitate maintenance. A few low-power EF coils may be used inside the TF coils to facilitate plasma control, but they can be moved to permit blanket replacement.

Standard computer codes are available to compute magnetic fields and coil forces. Water cooled coils have been used in most toroidal fusion experiments, but their large power consumption makes superconducting coils desirable in many reactor designs. Large superconducting TF coils and mirror coils have been

developed for the Large Coil Test Facility and the MFTF experiment, respectively. Large coils with fields up to 12 T at the conductor can be built, and future developments may raise this to 15-20 T, subject to coil stress limitations. At high fields, the cost of the structural material exceeds that of the superconductor. Various stabilization techniques are used to prevent sudden loss of superconductivity from quenching the coil current. Protective circuitry is needed to prevent the energy dissipation during a coil quench from damaging the coil.

Techniques of cryogenic (low-temperature) insulation and refrigeration are well-developed and adequate for the needs of fusion reactors, but refrigeration efficiency and cost improvements would be helpful. A future shortage of helium may hinder wide-scale use of superconducting devices.

environment

Since the tritium fuel is radioactive, multiple barrier containment is used to minimize leakage into the air or water. The tritium inventory at the reactor is kept low (a few kg) in order to minimize the accidental release due to fire, earthquake, etc.

Reactor materials exposed to neutron bombardment can be selected to minimize the production of radioactive nuclides with long decay half-lives. Those materials with short half-lives ($\lesssim$ 3 years) can be allowed to decay for 30 years, and then recycled.

The greatest potential stored-energy hazard of a fusion reactor would be the chemical energy of a liquid lithium blanket, which could be released as heat during reactions with air, water, or concrete. To avoid this hazard, many reactor designs use other forms of lithium (such as Li-Pb and Li_2O) which are not as reactive.

The controversy over fission power plants will probably have adverse effects on siting requirements for fusion power plants. The costs of decommissioning the plant should be considered during plant design. Materials shortages (Nb, He, etc.) may add expense to the widespread deployment of fusion power.

economics

The availability of a power plant is defined as

$$availability = \frac{\text{(number of hours in a year that the generator is available)}}{\text{(total number of hours in a year)}} \tag{18A1}$$

If a plant has a low availability (due to forced shutdowns), then the cost of replacement power ($\sim$\$50000/hour for a 1 GWe plant) will make it uneconomical. Thorough quality assurance (QA) programs are needed for every system of a power plant during design, manufacture, and installation. Redundant systems are used in critical areas, such as coolant pumps.

Standardized procedures are available for estimating the capital cost of a fusion power plant and the resulting cost of electricity (COE). Such estimates indicate that fusion power costs can be comparable to costs of power from fission and fossil fuels. Fusion reactors may be used to breed fuel for fission reactors, with one fusion-fission hybrid supporting many fission reactors.

18B. Maintenance

The magnet coils and many other components will be designed to last the entire forty-year lifetime of the fusion power plant, but it is impossible to attain 100 % reliability. According to Murphy's Law, "If anything can go wrong, it will." Therefore, provisions for maintenance of every vital component are essential.

general principles

Maintenance should be planned during design of each component. The time required for each maintenance operation can be quantitatively estimated. Preventive maintenance can be used to replace parts before they fail. Cranes and transporters should have freedom of motion, unimpeded by cables, tubes, etc. Access to all components should be maximized to facilitate replacement or repair. All required operations should be simplified by careful design. For example, welded joints may be replaced by bolted joints, or bolted joints, by latches, to simplify disassembly. Standard (*generic*) connectors can be developed for electricity, coolants, cryogenic fluids, instrumentation, etc.

Contact ("hands-on") maintenance by people may be used where radiation levels are not too high ($\lesssim$ 0.5 mrem/hr), because it is faster than remote maintenance operations. Some operations can also be done by workers with partial shielding. Even though some operations may be done directly by workers, remote maintenance equipment should be capable of performing all the required maintenance operations.

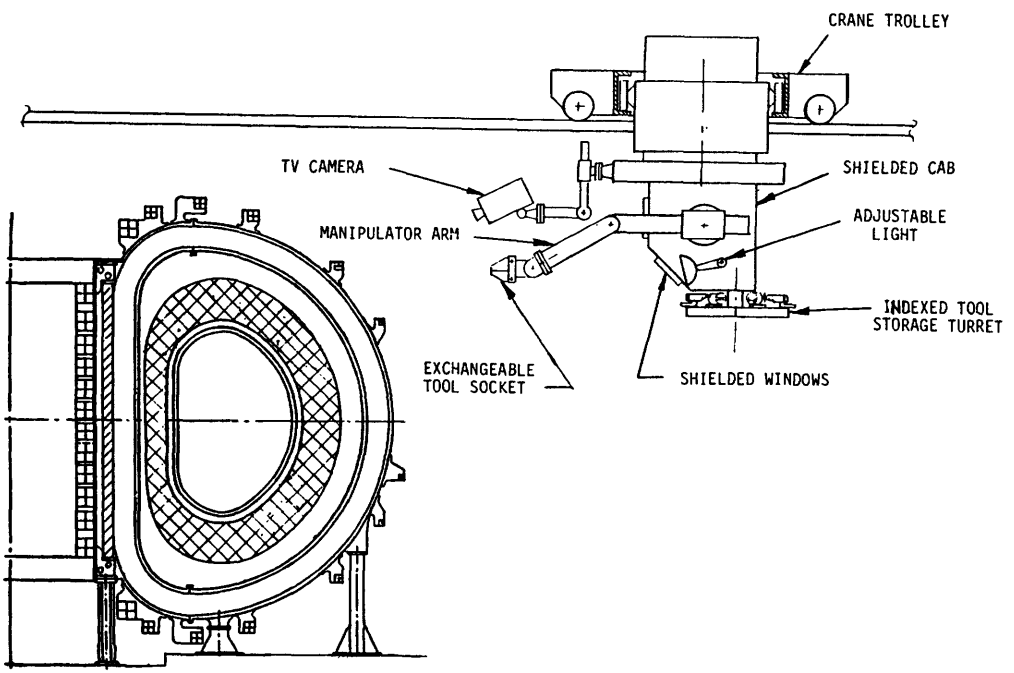

Fig. 18B1. A shielded crane cab. From M. Sniderman, "Fusion reactor remote maintenance study", EPRI ER-1046 (1979), Fig. A-2.

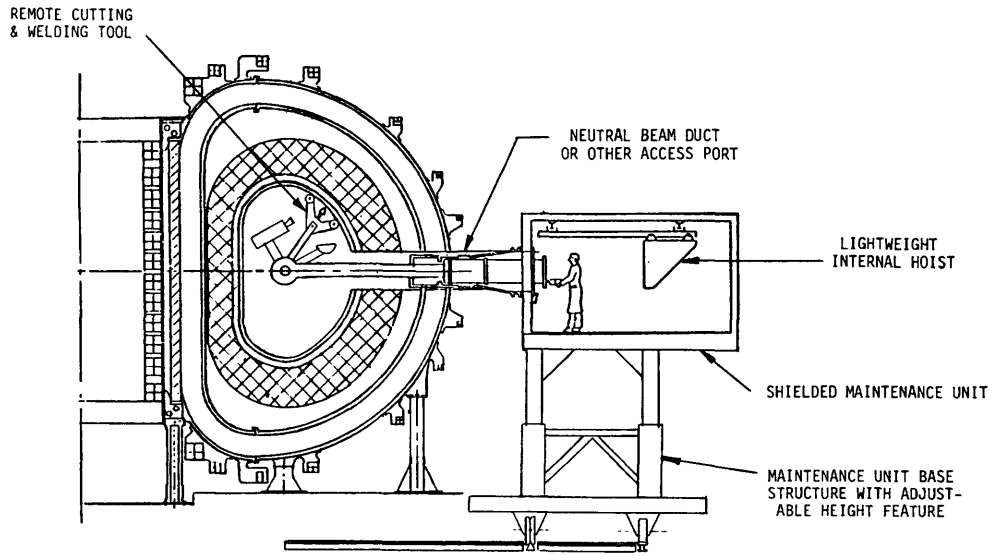

Fig. 18B2. A shielded mobile cutting and welding unit. From M. Sniderman, EPRI ER-1046 (1979), Fig. A-5.

Remote maintenance operations include:

* disconnection and reconnection of electrical power, coolant tubes, cryogenic fluid tubes, and instrumentation. Such operations may be done by a shielded crane cab, as illustrated in Fig. 18B1, or a similar unit rolling on the floor.
* opening and closing shield doors and vacuum seals and welds.
* going inside the reactor, inspecting the first wall, and replacing damaged sections, as illustrated in Fig. 18B2.
* transporting whole modules to the hot cell for repair, as illustrated in Fig. 18B3.
* replacing failed magnet coils.

A large air lock is needed between the reactor chamber and the hot cell, to prevent direct flow of contaminated gases from one room to the other. Other remote maintenance vehicles must be able to remove one which malfunctions at any stage of its performance. Automatic computer-controlled procedures can be developed for replacement of various components, to avoid operator errors. The number of required operations can be minimized by careful design. For example, many smaller coolant tubes can be combined into two large connections per module (inlet and outlet). Multiple vacuum zones are helpful in this regard. If the building is evacuated to 10^{-4} Torr (10^{-2} Pa), then welds or elaborate seals are not needed at the blanket-shield region. Minimizing the time required to shut-down and start up the plant also helps to reduce the total down time for maintenance.

scheduled and unscheduled maintenance

A fusion reactor first wall may be replaced periodically, to prevent failure. For example, a quarter of the blanket modules might be replaced every two

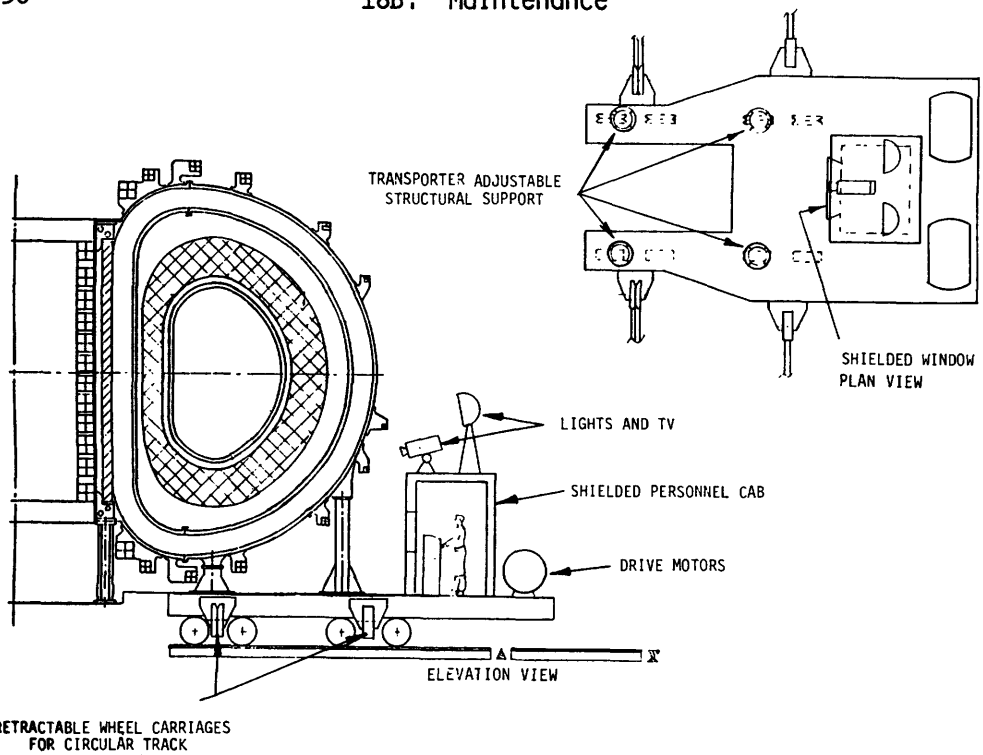

Fig. 18B3. A modular sector transporter. From M. Sniderman, EPRI ER-1046 (1979), Fig. A-4.

years. Large size modules are most efficient for replacement during scheduled maintenance. Annual scheduled maintenance is standard procedure for "balance of plant" (BOP) items, like the turbine-generator, and the reactor maintenance can be accomplished simultaneously. Scheduled maintenance typically takes about 4-6 weeks per year.

If a plant availability of 75 % is desired, and the scheduled maintenance takes 5 weeks, then about 8 weeks are available for unscheduled maintenance. Unscheduled maintenance is necessitated by any failure requiring plant shutdown. Small components which can be quickly replaced are desirable for unscheduled maintenance. For example, if a portion of the first wall failed, it might be possible to replace just that portion, instead of exchanging the whole module, which would presumably take longer. Inaccessible components, like EF coils underneath the reactor, should have redundant spares built in place. If one coil fails, then the extra one can be turned on. Adequate spare parts for all reactor components are essential. (To operate without them would be like driving a car without a spare tire.) A reasonable goal for wall or blanket failures is to replace the damaged section in about two weeks.

Some ideas on fusion reactor maintenance are summarized in Table 18B1. The realization of some of these ideas in specific reactor designs will be described in the following sections.

Table 18B1. Principles of fusion reactor maintenance. (These are all subject to cost limitations.)

Maximize component *reliability*, to reduce frequency of unscheduled maintenance.
Install *redundant* components for those which are difficult to replace.
Plan for maintenance during design.
Estimate maintenance *times* quantitatively.
Use *preventive* (scheduled) maintenance where practical.
Perform several scheduled maintenance operations *concurrently*.
Maximize *access* to all components.
Simplify all maintenance operations.
Minimize number of *connections*.
Use *contact* maintenance where feasible.
Develop remote maintenance *equipment* and computer-controlled automated operations.
Be able to *rescue* failed remote maintenance equipment quickly.
Replace *large* modules for scheduled maintenance, *smaller* components for unscheduled maintenance, when feasible, to save time.

18C. A Tokamak Reactor Design

For brevity, only the STARFIRE tokamak design will be described here. Some features of other designs, like NUWMAK, will be described in later chapters.

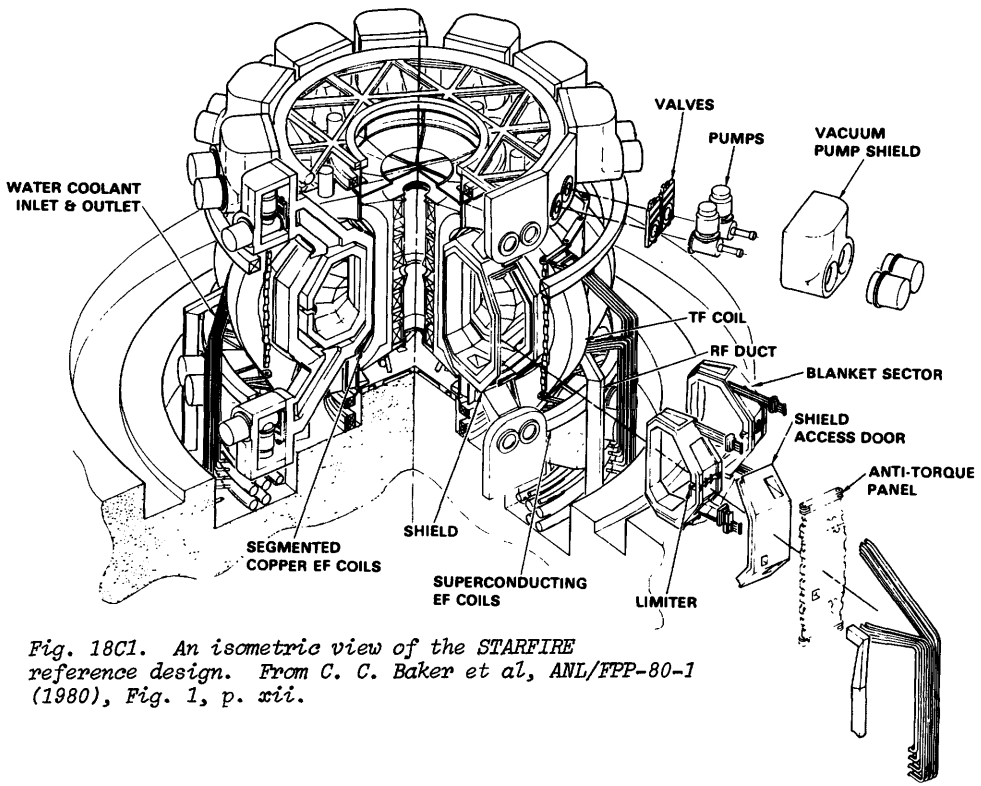

Fig. 18C1. An isometric view of the STARFIRE reference design. From C. C. Baker et al, ANL/FPP-80-1 (1980), Fig. 1, p. xii.

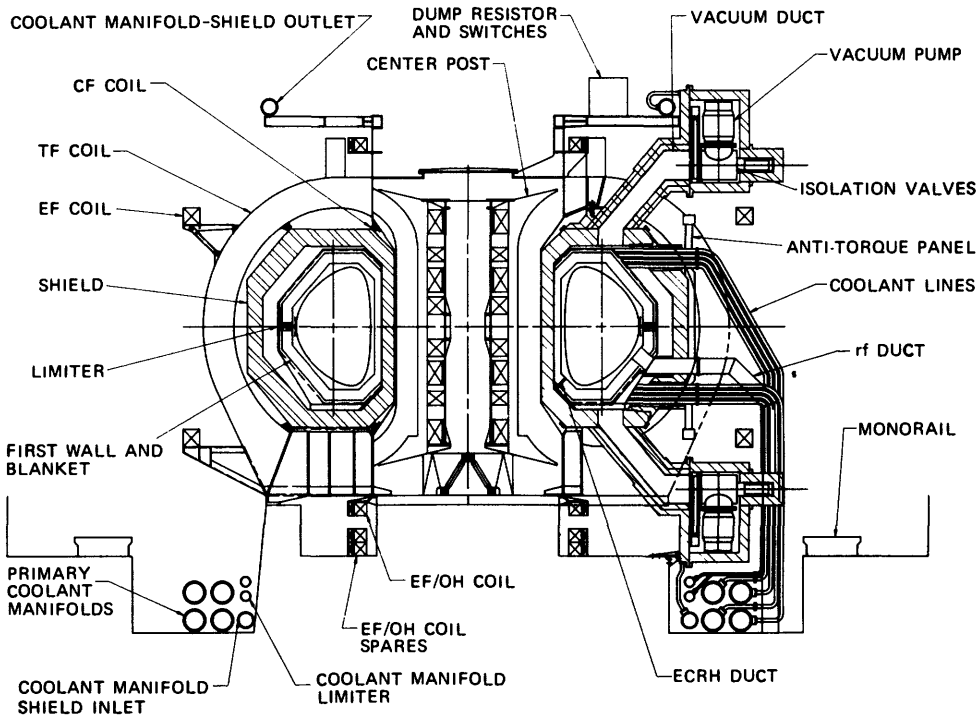

Fig. 18C2. Cross sectional view of the STARFIRE tokamak design. From C. C. Baker, G. A. Carlson, and R. A. Krakowski, Nuclear Technology/Fusion 1, 5-78 (1981), Fig. 10, p. 15.

STARFIRE design features

The STARFIRE reactor, illustrated in Figs. 18C1 and 18C2, is imagined to be the tenth plant in a series of commercial tokamak reactors. Some key features of this reactor design are:

* steady state operation, with lower hybrid rf current drive
* ECRH assisted startup
* pumped limiter for plasma purity control
* vacuum boundary at the shield, with mechanical seals
* modular design and remote maintenance
* all superconducting EF coils are outside the TF coils
* water-cooled, solid lithium compound breeder blanket with stainless steel structure
* low-Z beryllium coating on inside of first wall
* all materials outside the blanket can be recycled within 30 years
* less than 0.5 kg of vulnerable tritium inventory
* minimum radiation exposure to personnel
* conventional pressurized water/steam power cycle with no intermediate coolant loop and no thermal energy storage.

The plasma has a major radius of 7.0 m, a half-width of 1.94 m, and a vertical elongation of 1.6 . About 4000 MW of thermal power are developed by the reactor, producing 1440 MWe of electrical power, of which 240 MWe is recirculated to run the reactor and 1200 MWe is delivered to the power grid for sale. The main reactor parameters are summarized in Table 18C1.

Table 18C1. STARFIRE Major Design Parameters. From C. C. Baker et al, "STARFIRE - a Commercial Tokamak Fusion Power Plant Study", ANL/FPP-80-1 (1980), Table 2-2, p. 2-7.

Net electrical power, MW	1200
Gross electrical power, MW	1440
Fusion power, MW	3510
Thermal power, MW	4000
Gross turbine cycle efficiency, %	36
Overall availability, %	75
Average neutron wall load, MW/m^2	3.6
Major radius, m	7.0
Plasma half-width, m	1.94
Plasma elongation (b/a)	1.6
Plasma current, MA	10.1
Average toroidal beta	0.067
Toroidal field on axis, T	5.8
Maximum toroidal field, T	11.1
No. of TF coils	12
Plasma burn mode	Continuous
Current drive and heating method	66 MW rf at 1.6 GHz (lower hybrid)
Plasma startup	ECRH-assisted, limited OH coil
TF coils material	Nb_3Sn/NbTi/Cu/SS
Blanket structural material	Prime Candidate Alloy (PCA), an austenitic stainless steel
Tritium breeding medium	Solid breeder (α-$LiAlO_2$)
Wall/blanket coolant	Pressurized water (H_2O)
Plasma impurity control	Limiter and vacuum system supplemented by low-Z coating, enhanced radiation, and magnetic field margin
Primary vacuum boundary	Inner edge of shield

plasma

The average toroidal beta is 6.7 %, with $\bar{n}_e = 1.2 \times 10^{20}$ m^{-3}, $\bar{T}_e = 17$ keV (bars denote average values). Other plasma parameters are listed in Table 18C2. Plasma heating and current drive are both provided by lower hybrid frequency waves at 1.6 GHz. About 90 MW of rf power is available for startup, and then 66 MW is needed to sustain 10.1 MA of plasma current with a hollow current density profile.

The rf power enters through 12 rf ducts, one in each blanket segment. Each duct is 0.66 m by 0.78 m and carries an average power density of 15 MW/m^2. The required rf power is reduced by minimizing the required plasma current, generating the current density primarily in regions of low n_e, and transmission of a

Table 18C2. STARFIRE plasma parameters. From C. C. Baker et al, "STARFIRE - Commercial Tokamak Fusion Power Plant Study", ANL/FPP-80-1 (1980), Table 2-3, p. 2-14.

Parameter	Unit	Value
Major radius, R	m	7.0
Aspect ratio, A	--	3.6
Elongation, κ	--	1.6
Triangularity, d	--	0.5
Safety factor at limiter	--	5.1
Average beta, β		0.067
Maximum toroidal field at coil, B_m	T	11.1
Toroidal field at plasma center, B_0	T	5.8
Plasma current I_p	MA	10.1
Plasma volume, V_p	m^3	781
Average electron temperature, T_e	keV	17.3
Centerline electron temperature, T_{e0}	keV	22.5
Average ion temperature, T_i	keV	24.1
Centerline ion temperature, T_{i_0}	keV	31.3
Average fuel density, n_{DT}	m^{-3}	0.806×10^{20}
Center fuel density, n_{DT_o}	m^{-3}	1.69×10^{20}
Electron energy confinement time, τ_{Ee}	s	3.6
Power gain ratio, Q		39
Ion energy confinement time, τ_{Ei}	s	10
Particle confinement time, τ_p	s	1.8
Fractional helium concentration, N_α/N_{DT}	--	0.14
Fractional beryllium concentration, N_{Be}/N_{DT}	--	0.04
Fractional iodine concentration, N_I/N_{DT}	--	0.001
Fusion power, P_F	MW	3510 MW
Lower hybrid rf power to plasma, P_{rf}	MW	90
Average neutron wall load, P_{WN}	MW/m^2	3.6

narrow wave spectrum with a low toroidal refractive index. Compared with pulsed tokamaks, the rf current drive requires 12-15 % of the power output, but steady-state operation saves about 30 % on power costs, for a net savings of at least 15 %.

Five MW of ECRH heating produces an initial plasma in 10 ms with temperature of a few hundred eV and composition 96 % deuterium, 4 % tritium. The ECRH system stays on for 3 s, then the lower hybrid rf heating system is turned on low. The OH coil applies 25 V-s of induction to the plasma in 14 s to drive an initial current of 1-2 MA. Most of the required induction is supplied by the EF coils (180 V-s). When the plasma temperature reaches 1.4 keV, rf current drive becomes effective, and the rf power is increased to 45 MW and held constant for 250 s, while the temperature is about 6 keV and the current increases to 10 MA. The plasma density is maintained at about 10 % of its final value, to reduce the required rf power. Once the 10 MA current is established, the rf heating power is gradually increased to 90 MW over 15 s, and the DT plasma density is increased to its final value, but with 4 % tritium composition. Finally, the tritium fraction is slowly increased to 50 % over a period of about 17 min (about 5 % per minute increase in fusion power). The slow fusion power increase is needed to prevent large thermal transient problems in the first wall, blanket, and steam system. During startup iodine atoms are gradually added to the plasma to radiate away much of the alpha heating power, in order to control plasma temperature and beta. A maximum input power of about 250 MW is drawn from the grid during startup and 10 MJ of stored energy are needed for the OH coils.

The normal shutdown procedure is nearly the reverse of the startup procedure and takes about 24 minutes. Under emergency conditions, the shutdown can be greatly accelerated by injection of excess iodine (0.1 s) or by cutting off fuel and rf power (2.5 s).

limiter and vacuum system

A metal limiter running in the toroidal direction around the circumference of the torus (Fig. 18C2) defines the outer edge of the plasma. Some of the plasma diffuses across field lines and strikes the back side of the limiter, where it is neutralized and pumped away by a vacuum pumping duct. Of the helium ions striking the limiter, about 25 % are neutralized and pumped away, and 75 % are reflected back into the plasma, resulting in an equilibrium helium ion concentration about 14 % of the DT fuel ion concentration. The fuel ions striking the limiter have a lower pumping probability, so the tritium is effectively recycled many times into the plasma to attain high burnup fractions (summed over many cycles through the plasma). The metal limiter is coated with beryllium to avoid introducing high-Z impurities into the plasma. A 4 % Be concentration in the plasma tends to continually replace the Be coating, or even to increase its thickness. The main engineering concerns are the durability of the limiter to local plasma perturbations and the uniformity and redeposition rate of the beryllium coating on the limiter.

The vacuum duct opens into a plenum between the blanket and shield, and most neutrons streaming out the duct are stopped by the shield. The peak heat fluxes on the limiter of a few MW/m^2 are removed by water coolant at 4.2 MPa (600 psia). The 200 MWth removed from the limiter at T = 418 K is used for feed water heating in the steam system. The limiter is designed to withstand pressure forces and electromagnetic forces resulting from plasma disruptions.

The pumped limiter-reflector system is simple, easily maintained, inexpensive, and maintains satisfactory plasma purity, if it works as predicted. The main

physics question is how much of the plasma diffuses across field lines to reach the back side of the limiter. This concept will be discussed further in Section 25D.

first wall, blanket, and shield

A solid lithium ceramic compound α-$LiAlO_2$ is chosen as the breeding material in the STARFIRE design in order to eliminate the safety concern of using liquid lithium. In order to maintain a satisfactory breeding ratio, the lithium is enriched to 60 % ^6Li, and Zr_5Pb_3 is used as a neutron multiplier [producing (n,2n) reactions]. If Li_2O were used, a neutron multiplier would not be needed, but the high solubility of tritium in Li_2O would result in a high tritium inventory in the blanket. If liquid lithium were chosen as the breeding material, the tritium inventory could be kept low, but the potential for lithium reactions with air or water would be a serious hazard.

The structural material of the first wall and blanket is "prime candidate alloy" (PCA), a low-swelling titanium-modified Type 316 austenitic stainless steel. The STARFIRE blanket is illustrated in Fig. 18C3. The $LiAlO_2$ is in the form of 1 mm porous particles (comprised of 1 μm grains) sintered together with 2 mm holes running through for tritium removal by a low-pressure helium purge stream. Heat is removed by 15.2 MPa (2200 psi) pressurized water in 1.12 cm diameter PCA coolant tubes. Helium gas was also considered as a coolant, but it requires a higher coolant pumping power, permits neutron streaming along the helium tubes, and requires high temperature operation where tube corrosion becomes a serious problem.

The PCA is operated at temperatures below 670 K (400 C), which minimizes materials problems and tritium permeation rates into the water coolant. A low-Z beryllium coating on the plasma side of the first wall protects the plasma from contamination by high-Z wall atoms. Materials problems limit the first-wall to a maximum neutron power fluence of about 16 MW-yr/m^2, which corresponds to a lifetime $\sim$ 6 years at an average neutron power flux of 3.6 MW/m^2 and a 75 % availability.

The shield design criteria include:

* Protect magnet coils and other reactor components from excessive nuclear heating and radiation damage
* Keep the biological dose rate in the reactor building low enough to permit human entry 24 hours after shutdown ($\sim$ 1-2 mrem/h).
* Use materials which do not produce long-lived radioactive isotopes, so that they can be recycled after 30 years.

The shield on the inside of the torus (small R) contains alternate layers of W and B_4C to attenuate gamma rays and neutrons, respectively, with Fe-1422 structure. The thickness is only 54 cm, in order to minimize the plasma major radius R_0 so that the toroidal field B_0 at R_0 is maximized (fusion power $\propto B_0^4$). More space is available at the outside of the torus (large R). The shield there is 1.1 m thick and has three zones, containing (Ti + TiH_2 + H_2O), (Fe-1422 + B_4C) and (Fe-1422). The use of rf heating and a pumped-limiter have permitted heating and vacuum pumping ducts with several bends to be used, in order to reduce radiation streaming through the blanket and shield, which is a serious problem, especially with neutral beam injection heating, where large straight ducts would be necessary.

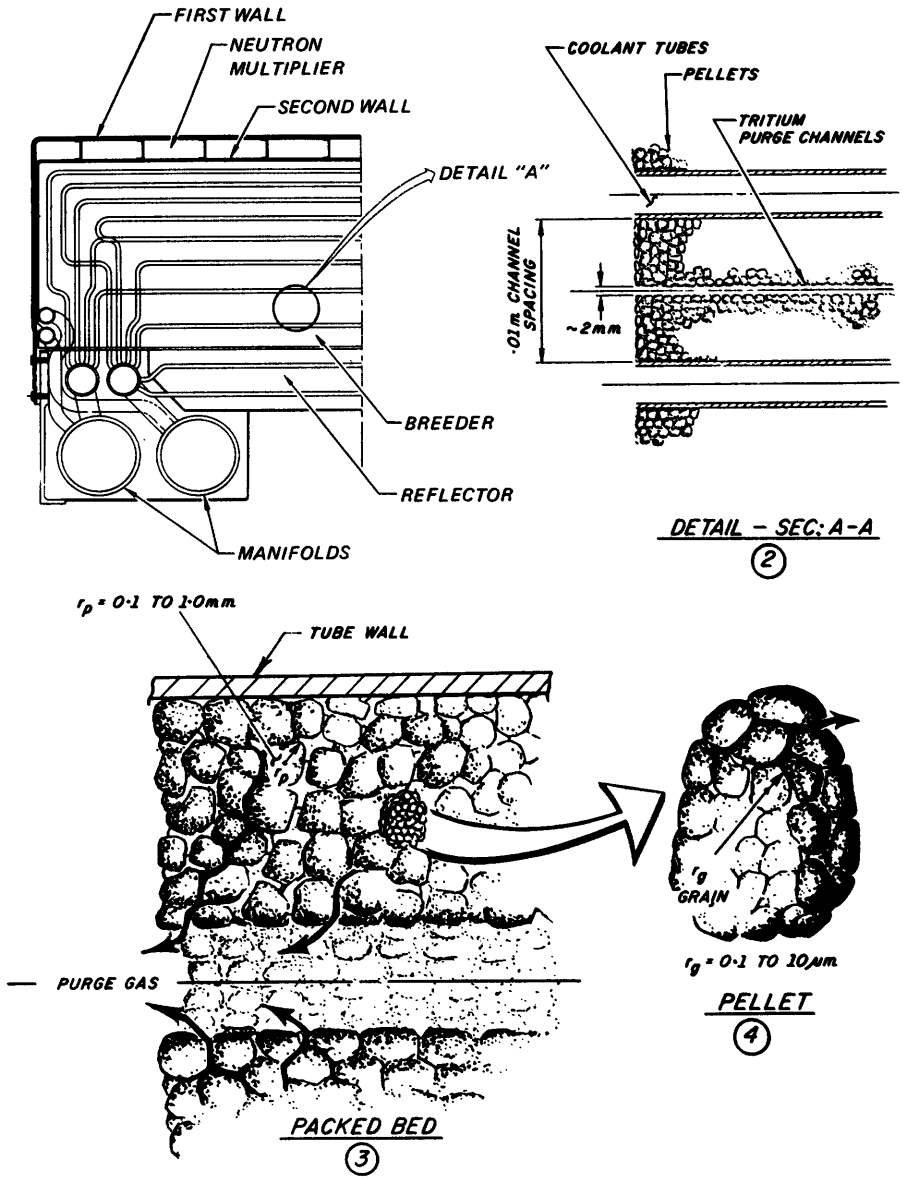

Fig. 18C3. Schematic diagram of STARFIRE blanket concept showing solid breeder microstructure with bimodal pore distribution and tritium removal scheme. From C. C. Baker et al, ANL/FPP-80-1 (1980), Fig. 2-9, p. 2-44.

The pressurized water coolant from the blanket flows to a steam generator, and the rest of the steam cycle is similar to that of a conventional pressurized water reactor (PWR) power plant. The net plant efficiency = 1200 MW/4000 MW = 30 % is limited by the low outlet temperature of the primary coolant. Other

fusion reactor designs (such as UWMAK-III) have attained higher plant efficiencies by using high-temperature cycles, but the resulting estimated cost of electricity (COE) has been higher, due to the high costs of advanced technology and exotic materials.

magnets

The twelve superconducting toroidal field (TF) coils, cooled by pool-boiling liquid helium at 4.2 K, extend to large major radii to reduce ripple and to permit radial removal of blanket modules. The inwards force of the TF coils is supported by a fiberglass-epoxy cylinder (support post, Fig. 18C2), which also contains the inner equilibrium field (EF) and ohmic heating (OH) coils in a common vacuum volume. Individual vacuum tanks surround each outer TF coil loop. To minimize recirculating power requirements, the EF and OH coils are also superconducting. They are located outside the TF coils for ease of maintenance. Their fields produce large overtuning moments (1.5×10^9 N-m) on the TF coils. The forces are sustained from the TF coil helium vessels to the vacuum tanks by cold-to-warm tiebars, and between coil vacuum tanks by intercoil shear panels (anti-torque panel, Figs. 18C1 and 18C2). Four water-cooled copper EF coils, called correction field (CF) coils, are located inside the TF coils, to control the plasma vertical position, but outside the shield, to minimize radiation damage and activation. They operate about 10 % of the time and consume a peak I^2R power of 2.3 MW. The magnet coils and shield are all designed to last the 40 year lifetime of the plant, but they can be replaced, if necessary. The EF and OH coils can be removed vertically, except for those underneath the reactor, for which spares are located below the coils.

environment

The thermal discharge from the STARFIRE reactor to the environment will be the same as from any other power plant with comparable efficiency and size. The main environmental hazards are tritium and activated PCA. The average discharge rate is about 9.5 m^3 (75 metric tons) of activated PCA per year. This is much less than the volume of high-level waste generated by a comparable LMFBR. The long-lived radioisotopes are mainly those of nickel and molybdenum. Other activated materials of the reactor have half-lives short enough to permit recycling after 30 years.

STARFIRE has vulnerable and non-vulnerable tritium inventories of 0.4 and 11.2 kg, respectively. The term "non-vulnerable" means that the tritium would not be released by an accidental rupture of containment. The tritium in the blanket must slowly diffuse out of the $LiAlO_2$, and that in storage is contained in multiple barriers which are very safe. Accidental release of the entire "vulnerable" inventory, having a radioactivity of about 4 MCi = 1.4×10^{17}Bq, would probably not result in grave danger to the public (cf. Fig. 28B5).

economics

The greatest uncertainty in estimating the cost of electricity (COE) is the plant availability. Many features of the STARFIRE design enhance plant availability:

* steady state operation with rf current drive
* comparative simplicity of the plasma purity control system (limiter/vacuum duct)
* vacuum boundary at the shield, and mechanical seals instead of welds
* service connections (such as coolant) all outside the shield
* optimized modular design

* superconducting EF coils outside the TF coils
* conservative TF coil design
* fully remote maintenance, permitting some repairs during reactor operation
* failed components immediately replaced, repairs done later in hot cell
* combination of functions for simplicity (such as TF coil dewar providing support for EF coils and shield)
* redundancy of components where maintenance would be difficult (such as EF coils trapped below the reactor).

Assuming that the goal of 75 % availability can be attained, the COE for STARFIRE is estimated to be about 35 Mill/kWh (1980 constant dollars) or 67 Mill/kWh (1986 current dollars). ("Constant dollars" and "current dollars" will be explained in Section 28E). These costs are comparable to those of electrical power from fission and fossil fuel plants.

18D. A Mirror Reactor Design

A reactor based on the tandem mirror concept will be described. Various other mirror and cusp confinement devices were described in Chapter 11.

WITAMIR-I

The Wisconsin Tandem Mirror (WITAMIR-I), shown in Fig. 18D1, has a central cell 165 m long, inboard thermal barriers (between the central cell and the end plugs) and Yin-Yang end plugs. Although it is linear instead of toroidal, its fusion power (3000 MWth) and nuclear plant volume (19,000 m^3) are nearly the same as those for the STARFIRE tokamak (3510 MWth and 23,000 m^3). (For purposes of comparison, most fusion reactor designs have net electrical power outputs $\sim$ 1 GWe).

Various parameters of the WITAMIR-I reactor are listed in Table 18D1. Some of the kinetic energy of ions leaking out the ends is directly converted into electricity with efficiency of 67 %, and a high coolant temperature results in a high

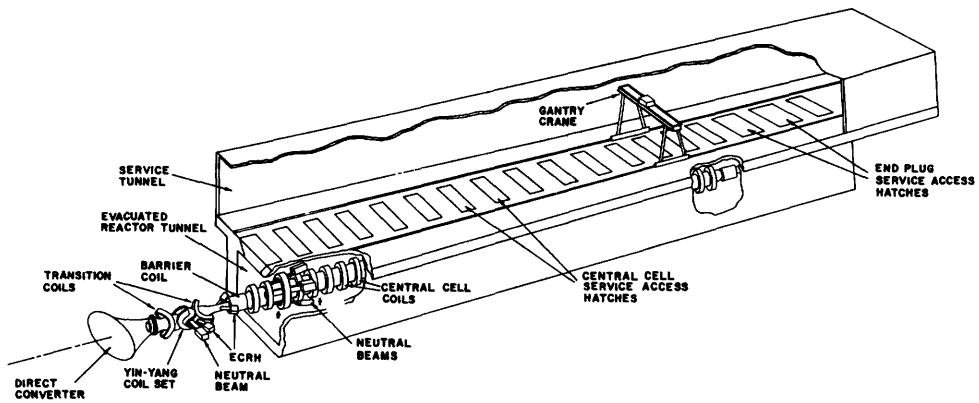

Fig. 18D1. Perspective view of WITAMIR-I tandem mirror reactor. From B. Badger et al, "WITAMIR-I, a University of Wisconsin Tandem Mirror Reactor Design", UWFDM-400 (1980), Fig. II-B-2, p. II-4.

efficiency (42 %) of converting thermal energy into electricity, so the net plant efficiency is high (39 %).

Only the barrier coil has a very high magnetic field (15 T), and its cylindrical shape alleviates structural support problems.

plasma

The axial variations of various plasma parameters are shown in Fig. 18D2. The barrier potential ϕ_b is a result of flux tube expansion from 14 T to 1.4 T and neutral beam charge-exchange pumping of ions from the barrier region (b). The presence of the barrier permits electrons in the plug region to be heated up to T_{ep} = 123 keV, while the electron temperature in the central cell is T_{ec} = 33 keV. The resulting potentials are found from Eqs. (11E28)-(11E30). Plasma parameters are summarized in Table 18D2.

The central cell contains DT fuel ions, but protons are injected into the end plugs, in order to minimize neutron production and coil shielding problems there. The assumed value β_c = 40 % in the central cell is higher than the theoretically predicted stable value of 25 %. The justifications for this optimistic assumption are uncertainties in the theory, experimental values exceeding theoretical predictions, and possible enhancement due to improvements in magnetic field design.

Table 18D1. General parameters of WITAMIR-I. From B. Badger et al, "WITAMIR-I, a University of Wisconsin Tandem Mirror Reactor Design", UWFDM-400 (1980), Table II-B-1, p. II-5.

Plasma Q		28
DT power		3000 MW_{th}
Net electrical output		1530 MW_e
Recirculating power fraction	ε	18%
Net plant efficiency	η	39%
Central cell length		165 m
Overall reactor length		250 m
Max. magnetic field - central cell		6.1 T
Max. magnetic field - barrier		15.0 T
Max. magnetic field - yin yang		8.1 T
Blanket material		HT-9
Neutron wall loading		2.4 MW/m^2
Blanket multiplication		1.37
Breeder material		$Pb_{83}Li_{17}$
Breeding ratio		1.07
Barrier pumping method (190 keV and 9.6 keV)		55.2 MW of NBI
ECRH power - barrier		33.2 MW (40 GHz)
- plug		16.4 MW (112 GHz)
Plug neutral beam power (500 keV)		18.2 MW

The arrangements of the neutral beams and ECRH units are shown in Fig. 18D3. The ECRH barrier heating enhances the barrier potential and power gain ratio Q. The potential barrier ϕ_c in one end is kept slightly lower than that in the other end, so that practically all of the ions leaking over the barrier go out the end where ϕ_c is lower. Therefore, the direct convertor is only needed at that end, and electrons are collected at the other end. (Direct convertors will be discussed in Section 26G).

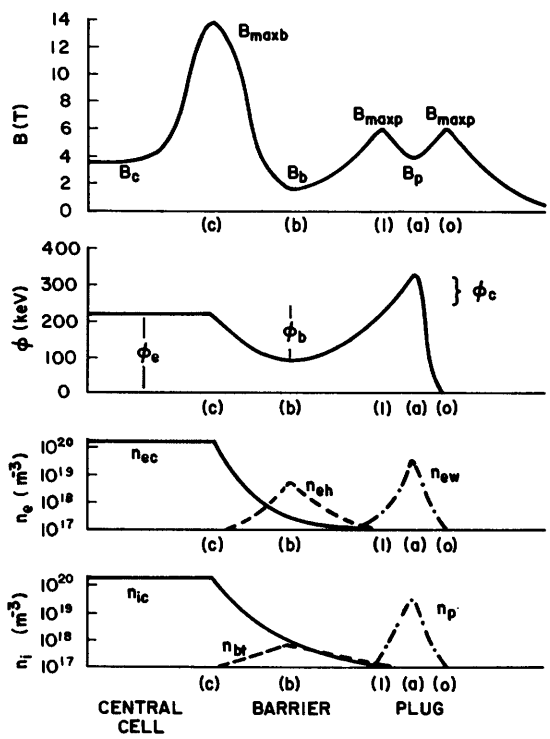

Fig. 18D2. Axial variations of magnetic field, electrostatic potential, and electron and ion densities in WITAMIR-I (not to scale). Only one end of the device is shown, since the parameters are symmetric about the midplane. From B. Badger et al, UWFDM-400 (1980), Fig. II-C-1, p. II-7.

Table 18D2. Plasma parameters of WITAMIR-I. From B. Badger et al, UWFDM-400 (1980), Table II-C-1, p. II-9.

Central Cell	
Magnetic field on axis	3.6 T
Density	1.5×10^{20} m^{-3}
Ion temperature	32.5 keV
Electron temperature	32.8 keV
Tritium burnup fraction f_b	21.6%
Potential, ϕ_c	102. keV
Beta, β_c	0.40
Plasma radius	0.72 m
$(n\tau)_{ic}$	7.8×10^{20} $m^{-3}s$
Barrier	
Magnetic field on axis	14.0 T
Average density	6.9×10^{18} m^{-3}
Ion temperature	32.5 keV
Mean hot electron energy, E_{eh}	270. keV
Passing electron fraction, F_{ec}	0.27
ratio of an ion density in barrier to density of passing ions there, g_b	2.0
Pumping fraction at low energy	0.95
Pumping fraction at high energy	0.05
Potential, ϕ_b	141. keV
Beta, β_b	0.235
Plasma radius average	0.59 m
Plug	
Maximum/minimum magnetic field on axis	6.0/4.0 T
Average density	2.7×10^{19} m^{-3}
Mean ion energy	905. keV
Electron temperature	123. keV
Potential, $\phi_c+\phi_e$	326. keV
Beta, β_p	0.64
Plasma radius	0.77 m
$(n\tau_{ip})$	9.8×10^{19} $m^{-3}s$

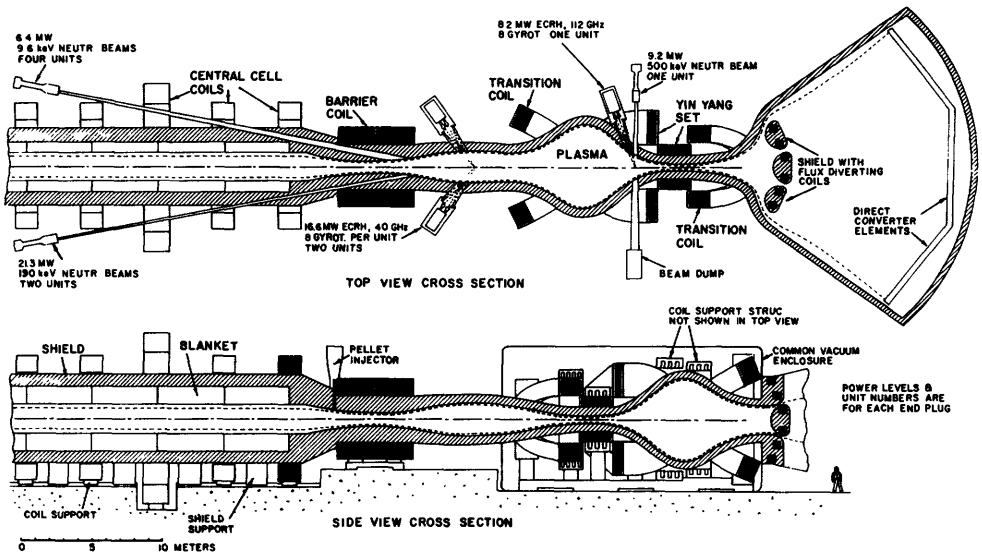

Fig. 18D3. Arrangement of the WITAMIR-I neutral beams and ECRH units. From B. Badger et al, UWFDM-400 (1980), Fig. II-C-2, p. II-8.

blanket and shield

A cross section of the blanket and shield is shown in Fig. 18D4, and the 9.75 cm diameter blanket tubes are shown in Fig. 18D5. HT-9 ferritic steel was chosen as the structural material because of its good radiation damage resistance. Weld zones are removed to at least 1 m behind the first wall, to avoid radiation damage. The blanket coolant is a flowing $Pb_{83}Li_{17}$ eutectic alloy, which also breeds tritium with a breeding ratio of 1.07 (tritium atoms produced per incident neutron) and provides a comparatively high blanket energy gain ratio M = 1.37. The large tubes permit a low coolant flow speed (0.13 m/s), which reduces pumping power and corrosion problems. The coolant inlet and outlet temperatures are 602 K (329 C) and 773 K (500 C). The lead provides (n,2n) reactions for neutron multiplication and has a low neutron capture cross section, and the HT-9 produces additional energy via (n,γ) reactions. The $Pb_{83}Li_{17}$ eutectic does not undergo violent reactions with water (as liquid lithium can), even at 770 K.

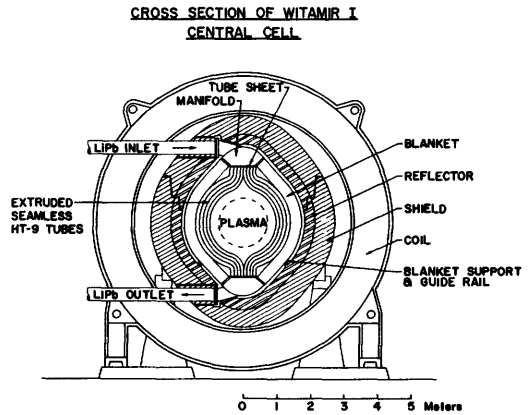

Fig. 18D4. Cross section of the WITAMIR-I central cell. From B. Badger et al, UWFDM-400 (1980), Fig. II-E-1, p. II-15.

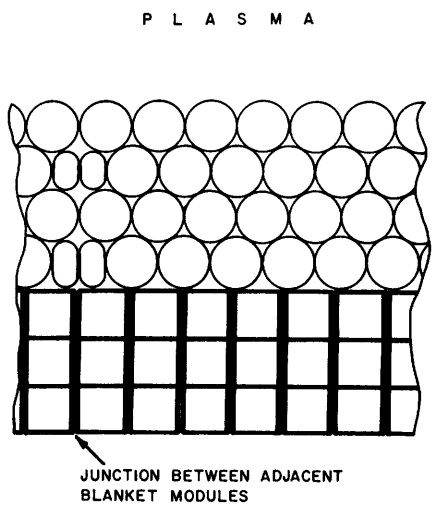

Fig. 18D5. Cross section of the WITAMIR-I blanket tubes, showing a junction between modules. From B. Badger et al, UWFDM-400 (1980), Fig. II-E-2, p. II-17.

The 0.73 m thick blanket region is surrounded by a 0.28 m water-cooled steel neutron reflector and a 0.6 m shield, containing alternate layers of Pb-steel-H_2O (to attenuate gamma rays), B_4C (to absorb neutrons), and steel-H_2O. Neutronics calculations indicate that the neutron damage to the magnet coils over 30 years of operation would not seriously degrade their performance.

Since most of the energetic ions go to the direct convertor, and the neutrons pass through the first wall (HT-9 tubes), the surface heat flux is quite low ($\sim$ 20 kW/m^2), even though the neutron wall loading is 2.4 MW/m^2. Therefore, thermal stresses will be much lower than in reactors (such as STARFIRE) with a high surface heat flux.

The vacuum seals are made at the outside of the shield, and the reactor tunnel is also partially evacuated during operation to about 9.3 kPa (70 Torr). Due to radiation damage, the blanket will need to be replaced about every four years. The magnets will be moved away axially to each side, the coolant will be drained out of the module, and then the blanket module will be lifted out vertically, as shown in Fig. 18D6. Only two coolant connections (and no welds) need to be broken on each module to remove it.

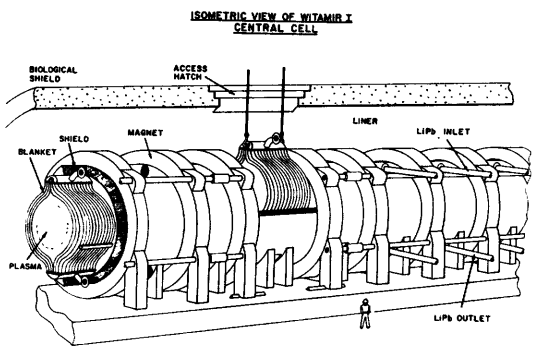

Fig. 18D6. Replacement of a blanket module in the WITAMIR-I central cell. From B. Badger et al, UWFDM-400 (1980), Fig. II-E-4, p. II-21.

environment and economics

The low solubility of tritium in the $Pb_{83}Li_{17}$ helps maintain low tritium concentrations in the blanket system. The quantities of tritium in the blanket system, fueling and exhaust system, and storage are 0.20 kg, 0.43 kg, and 2.1 kg, respectively. Thus the vulnerable inventory is comparable to that of STARFIRE, and the total inventory is considerably less. The central cell plasma is fueled by injection of frozen pellets (70 % T, 30 % D).

The radioactivity of the reactor (per unit thermal power) vs. time after shutdown is shown in Fig. 18D7. The dominant radioisotope is ^{55}Fe, which has a decay half-life of 3 years. At times over 40 years, the residual activity is due mainly

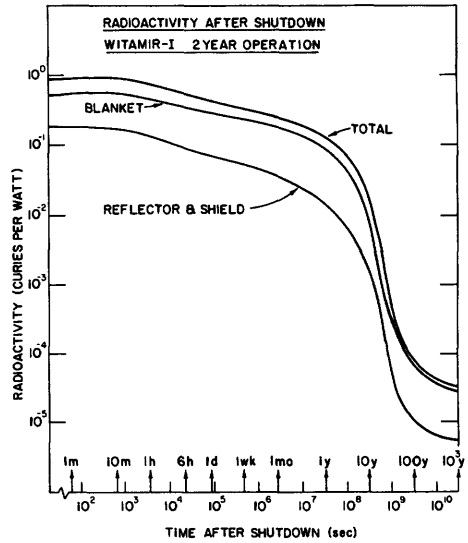

Fig. 18D7. Radioactivity of the WITAMIR-I reactor (relative to thermal power) vs. time after shutdown. From B. Badger et al, UWFDM-400 (1980), Fig. IX-B-2, p. IX-30.

to ^{93}Mo and ^{92}Nb. (Radioactivity will be discussed in Chapter 28).

The estimated COE for WITAMIR-I is 36 Mills/kWh (1980 constant dollars) or 76 Mills/kWh (1988 current dollars), which is almost the same as for STARFIRE (adjusted to 1988) and for NUWMAK, another tokamak reactor design. Of the reactor plant equipment costs, about 25 % is for the magnet, 23 % for the primary heat transport system (pumps, piping, steam generators, coolant cleanup system), 21 % for the plasma heating systems, 13 % for the shield, 5 % for the blanket, and the remainder for various other systems (fuel handling, auxiliary cooling, vacuum, maintenance, instrumentation, direct convertor, etc).

Some attractive features of the WITAMIR-I design are

* high Q
* steady state operation, few fatigue problems
* linear geometry, easy maintenance
* low first-wall heat flux, no plasma disruptions
* simple blanket design, high energy multiplication
* direct conversion of ion energy, high plant efficiency
* low neutron fluxes in barrier and end plug regions, where high-technology components are located
* no large ducts into central cell, so radiation streaming problems reduced.

The main physics uncertainties are: establishment of the thermal barrier, plasma stability, and attainable central cell beta. The main technological developments needed are the 18 MW, 500 keV neutral beam injectors and the 100 MW ECRH power system at reasonable costs ($\lesssim$ 2 \$/W).

The STARFIRE and WITAMIR-I reactor examples illustrate how various engineering problems are resolved in integrated system designs. The following chapters will discuss individual problem areas in greater detail. Many other fusion reactor designs are summarized by Baker, Carlson, and Krakowski (1981).

Bibliography

B. Badger, K. Audenaerde, J. B. Beyer, D. Braun, J. D. Callen, G. A. Emmert, J. M. Gilmore, N. Hoffman, J. Kesner, G. L. Kulcinski, D. C. Larbalestier, E. Larsen, X.-Z. Li, W. Maurer, C. W. Maynard, I. Ojalvo, M. Ortman, R. Perry, M. Ragheb, J. Santarius, J. Scharer, D. Schluderberg, K. Shaing, I. Sviatoslavsky, D. K. Sze, W. F. Vogelsang, A. White, P. Wilker, and T. Yang, "WITAMIR-I, a University of Wisconsin Tandem Mirror Reactor Design", UWFDM-400 (1980).

C. C. Baker, G. A. Carlson, and R. A. Krakowski, "Trends and Developments in Magnetic Confinement Fusion Reactor Concepts", *Nuclear Technology/ Fusion 1*, 5-78 (1981). Review paper.

C. C. Baker, M. A. Abdou, D. A. DeFreece, C. A. Trachsel, D. W. Graumann, et al, "STARFIRE - a Commercial Tokamak Fusion Power Plant Study", ANL/FPP-80-1 (1980).

G. M. Fuller, H. S. Zahn, H. C. Mantz, G. R. Kaletta, L. M. Waganer, L. A. Carosella, and J. L. Conles, "Developing maintainability for tokamak fusion power systems", COO-4184-6 (1978), Volumes I, II, and III.

R. A. Krakowski et al, "Reactor systems studies of alternative fusion concepts", *Plasma Physics and Controlled Nuclear Fusion Research (Brussels, 1980)*, IAEA, Vienna, 1981.

Proceedings of the 4th ANS Topical Meeting on the Technology of Controlled Nuclear Fusion (King of Prussia, PA, 1980), DOE, 1981.

M. Sniderman, "Fusion reactor remote maintenance study", EPRI ER-1046 (1979).

D. Steiner, W. R. Becraft, and P. H. Sager, "The engineering test facility", *Journal of Fusion Energy 1*, 5-14 (1981).

CHAPTER 19
VACUUM SYSTEMS

19A. Background

historical development

The notion that "Nature abhors a vacuum" can be traced back as far as Aristotle (384-322 BC). It was known in the Middle Ages that one must make a hole in the top of a wine barrel in order to let wine out a small hole in the bottom of the barrel. The first artificial vacuum was produced by Galileo (1564-1642) using a piston and cylinder. He stated that the maximum height to which water may be raised by suction is about 10 m (1638). Torricelli inverted a mercury-filled tube, and related the height of the column of mercury to the pressure of the atmosphere (about 1640). Pascal discussed the variation of pressure with altitude (1647), and Perier verified these predictions by carrying a mercury barometer up a mountain (1648).

The first successful vacuum pump was built in 1650 by Otto von Guericke. He demonstrated the force of the atmosphere in 1654 by putting two copper hemispheres together and pumping out air. Two teams of eight horses were unable to separate the hemispheres until air was readmitted.

Boyle (1627-1691) combined the vacuum pump and barometer, and obtained pressures less than .01 atm. He observed that the volume of a gas at constant temperature is inversely proportional to its pressure. Charles (1787) stated that at constant pressure the volume of a gas increases linearly with its temperature. In 1801 Dalton observed that the total pressure of a mixture of gases is equal to the sum of the partial pressures of the constituents.

In 1874 H. McLeod invented a mercury gage which could measure pressures down to about 10^{-3} Pa. Units of pressure are summarized in Table 19A1. The standard unit of pressure in the Systeme Internationale (SI) units is the Pascal (Pa), but the units of Torr (named after Torricelli) have been standard in vacuum technology for many years (760 Torr = 1 atm).

In 1892 Fleuss used an oil seal with a piston-cylinder pump (of the type invented by von Guericke) to obtain low pressures. In 1905 W. Kaufman and W. Gaede invented a rotary pump which could produce pressures of 10^{-3} Pa. In 1906 pressure gages were devised by Volge and by Pirani, based on the principle that the thermal conductivity of a gas is proportional to its pressure. These gages were effective

Table 19A1. Units of pressure. The standard unit in the Systeme Internationale (SI) is the Pascal, which is equal to 1 N/m^2.

conversion to Pa		conversion from Pa to other units
1 atm	= 1.01325×10^5 Pa	1 Pa = 9.86923×10^{-6} atm
1 dyne/cm^2	= 0.1 Pa	1 Pa = 10 dyne/cm^2
1 bar	= 10^5 Pa	1 Pa = 10^{-5} bar
1 lb/in^2	= 6894.7572 Pa	1 Pa = 1.450377×10^{-4} lb/in^2
1 Torr	= 133.3222 Pa	1 Pa = 7.500626×10^{-3} Torr
1 mm (Hg)	= 133.3222 Pa	1 Pa = 7.500626×10^{-3} mm (Hg)
1 mTorr	= 0.1333222 Pa	1 Pa = 7.500626 mTorr
1 micron	= 0.1333222 Pa	1 Pa = 7.500626 micron
1 inch (Hg) (@ 60°F)	= 3376.85 Pa	1 Pa = 2.96134×10^{-4} inch (Hg) (@ 60°F)
1 foot (H_2O) (@ 39.2°F)	= 2988.98 Pa	1 Pa = 3.34562×10^{-4} feet (H_2O) (@ 39.2 °F)
1 kg-force/cm^2	= 98066.5 Pa	1 Pa = 1.01972×10^{-5} kg-force/cm^2

in the range from 0.1 to 200 Pa.

During the period from 1910 to 1920 many advances were made. Gaede invented a rotary turbine molecular pump and also the mercury diffusion pump, and D. E. Buckley invented the ionization gage, which could measure pressures down to 10^{-6} Pa. In 1928 C. R. Burch introduced oil as a pumping fluid in diffusion pumps.

For many years it appeared that pressures below 10^{-6} Pa could not be obtained. Then in 1947 Nottingham discussed the limitation of ionization pressure gages by photoelectron emission from x-rays. Based on this theory Bayard and Alpert devised a new ionization gage in 1950 which could measure down to 10^{-8} Pa. Since then the development of cryogenic technology (Chapter 23) has added other improvements to vacuum technology.

need for ultra-high vacuum

An ultra-high vacuum ($p \lesssim 1$ mPa) is needed in fusion devices, in order to keep the fuel mixture of deuterium and tritium very pure. In a typical experiment the air is first pumped out of the chamber until a pressure $\sim 10^{-5}$ Pa (8×10^{-8} Torr) or lower is attained. Then the gas to be used for the experiment is admitted to the desired pressure (typically around 0.1 to 10 Pa). Finally, the gas is ionized and the resulting plasma is heated up to high temperatures, which increases its pressure by many orders of magnitude. If the initial vacuum pressure were 10^{-3} Pa and the filling pressure of experimental gas were 0.1 Pa, then it would have an impurity content of about 1% initially, which could cause large radiative power losses (Ch. 3). Plasma discharges gradually remove adsorbed impurities from the walls. In some experiments many days of operation elapse before the chamber becomes sufficiently clean.

The following sections will describe the equations for gas flow in vacuum, pumps, gages, chambers, and ultrahigh vacuum techniques.

19B. Viscous and Molecular Flow

types of flow

The mean free path of gas molecules between collisions is given by the equation

$$\lambda \simeq k_1/p \qquad (m) \qquad (19B1)$$

where p is the pressure (Pa) and the constant k_1 (Pa-m) has the following values: air = .0068, H_2 = .0141, He = .0195, N_2 = .00813, O_2 = .00916, Ar = .00933, Ne = .0149, water vapor = .0127. (There is a decrease in λ at low temperatures, due to intermolecular forces.) From Eq. (19B1) it is found that the mean free path of gas molecules in air at 1 Pa is about 7 mm. If these air molecules are flowing through a tube 3 mm in diameter, they will be colliding with the tube walls more frequently than with each other. Such a flow condition is called "molecular flow". On the other hand, if they are flowing through a tube 1 m in diameter, they will be colliding with each other more frequently than with the tube walls. This type of flow is called "viscous flow". The conditions for viscous and molecular flow can be expressed mathematically in terms of a characteristic dimension D, such as the tube diameter:

$$\begin{aligned} &\text{If } \lambda/D > 1. \quad \text{the flow is molecular} \\ &\text{If } \lambda/D < 0.01 \quad \text{the flow is viscous} \end{aligned} \qquad (19B2)$$

The ratio of λ/D is sometimes called the "Knudsen number". The "transition region" $.01 \lesssim \lambda/D \lesssim 1$ has characteristics of both types of flow.

At high flow velocities, viscous flow becomes turbulent flow. In terms of the gas viscosity η, mass density ρ, and flow velocity v, turbulent flow can be expected when the dimensionless Reynold's Number

$$Re = \frac{Dv\rho}{\eta} \gtrsim 2200 \; . \qquad (19B3)$$

(The average velocity of the fluid, v, should not be confused with the random velocities of the thermal motion of individual molecules, which are much larger.) For simplicity, we will consider only viscous and molecular flow.

throughput

Consider the case of two chambers at pressure p_1 and p_2 connected by a tube with length L and diameter D, as illustrated in Fig. 19B1. The gas flow rate past any plane perpendicular to the tube axis from the high-pressure chamber p_2 to the low-pressure chamber p_1 is called the "throughput" Q, and has units of Pa-m^3/s or Torr-litres/s (1 Pa-m^3/s = 1 Watt). The throughput may be calculated from the equation

$$Q = C(p_2 - p_1) = (p_2 - p_1)/Z \qquad (Pa\text{-}m^3/s) \qquad (19B4)$$

where C is called the "conductance" of the tube and has units of m^3/s (or L/s), and Z = 1/C is called the "impedance" of the tube, with units of s/m^3 (or s/L). This flow circuit is analogous to an electrical circuit: Q corresponds to current, Z to resistance, and (p_1-p_2) to the voltage difference across the resistance.

The throughput Q represents an energy flow rate, which may be expressed in terms of the number of molecules flowing past a given point per second:

$$Q = d(pV)/dt = d(nkTV)/dt$$
$$= kT\, d(nV)/dt = kT\, dN/dt \qquad (19B5)$$

where k is the Boltzmann constant, T is the gas temperature, dN/dt is the number of molecules flowing past per second. Therefore,

$$dN/dt = Q/kT \quad . \qquad (19B6)$$

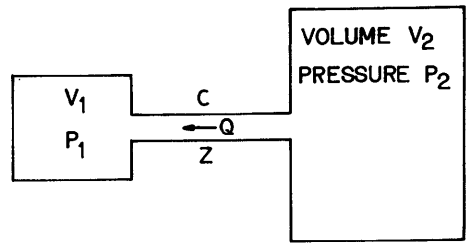

Fig. 19B1. Gas flow from a chamber at pressure p_2 to a chamber at a lower pressure p_1. The connecting tube has conductance C and impedance Z = 1/C. The gas flow rate is Q.

The average flow velocity v of a gas through a tube with area A is given by

$$v = Q/pA \qquad (19B7)$$

where p is the local pressure. The average speed of molecular thermal motion is

$$\bar{v} = (8kT/\pi m)^{\frac{1}{2}} \qquad (19B8)$$

where m is the mass of one gas molecule (kg). Usually $v << \bar{v}$.

EXAMPLE PROBLEM 19B1

N_2 gas at 293 K is flowing through a 0.1 m diameter tube at 1 Pa with throughput of 0.1 Pa-m^3/s. Find the average flow velocity, the average speed of thermal motion, the molecular flow rate, and the flow regime.

The area $A = \pi D^2/4 = .00785\ m^2$, so from Eq. (19B7) we find v = 12.7 m/s. From Eq. (19B8), with $m = 4.68 \times 10^{-26}$ kg for N_2, we find that $\bar{v}$ = 469 m/s. The molecular flow rate is found from Eq. (19B6) to be $dN/dt = 2.47 \times 10^{19}$ molecules/s. From Eq. (19B1) λ = 8.1 mm, so λ/D = 0.08, and the flow is in the transition region.

---

flow equations

The throughput of a pump is given approximately by the equation

$$Q = S_t(p_p - p_u) \qquad (19B9)$$

where S_t is the theoretical pumping speed (commonly called the pumping speed), p_p is the pressure at the pump, and p_u is the ultimate pressure attainable by the pump, limited by gases backstreaming from the pump. Pumping speeds have units of m^3/s (or L/s), as do conductances.

If the pump is connected to a chamber at pressure p by a tube with conductance C, as shown in Fig. 19B2, then

$$Q = C(p - p_p) \quad . \qquad (19B10)$$

If p_p is eliminated between these two equations, the throughput may be written

$$Q = \frac{S_t C}{(S_t + C)} (p - p_u) \quad . \qquad (19B11)$$

The rate of change of pressure in the chamber can be calculated from the equation

$$V\frac{dp}{dt} = \text{inflow} - \text{outflow} = Q_L - Q \qquad (19B12)$$

where Q_L is the leak rate. The leak rate has contributions from leakage through cracks, virtual leaks (gas trapped in internal cracks), outgassing of materials in the vacuum system, vapor pressures of materials in the vacuum system, and permeation of gases through the system walls and windows.

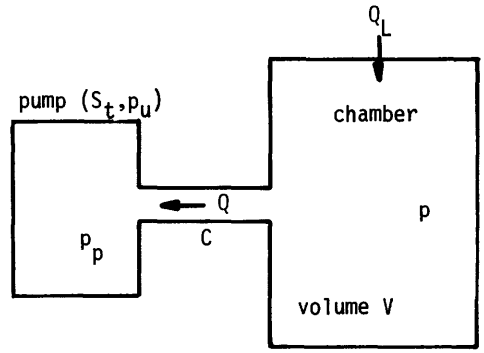

Fig. 19B2. Pumping a chamber at pressure p with a leak rate Q_L.

The above equations (19B4) - (19B12) apply to either viscous or molecular flow. If the conductance is known, the time variation of pressure and throughput can be calculated from these equations.

conductance

In the *viscous* flow regime, the conductance of a circular tube with diameter D (m) and length L (m) is found from the Poiseulle equation:

$$C = 1430(D^4 p_{av}/L)\ (\eta_{air}/\eta) \qquad (m^3/s) \qquad (19B13)$$

where p_{av} is the average pressure in the tube (Pa) [equal to $(p_1 + p_2)/2$ for the case of Fig. 19B1], η is the viscosity of the flowing gas, and η_{air} is the viscosity of air at 1 atm, 273K. Viscosities of common gases are listed in Table 19B1. For rectangular ducts with length L and cross sectional dimensions a and b, the conductance in the viscous regime is

$$C = 2070\ (Y p_{av} a^2 b^2/L)\ (\eta_{air}/\eta) \qquad (m^3/s) \qquad (19B14)$$

where Y is a function of the elongation ratio a/b with the values Y(1) = 1, Y(.6) = .90, Y(.4) = .71, Y(.2) = .42, Y(.1) = .23 (Roth, 1976, p. 76).

For the *molecular* flow regime case, consider the situation of Fig. 19B3. According to the kinetic theory of gases, the rate at which molecules pass through the hole from left to right is $n_1\bar{v}_1 A/4$, where n_1 and $\bar{v}_1$ are the density and average molecular speed (Eq. 19B8) of the gas on the left side of the wall. A similar relation holds for the gas flowing from right to left, so the net molecular flow rate from right to left is

$$dN/dt = An_2\bar{v}_2/4 - An_1\bar{v}_1/4 \quad . \qquad (19B15)$$

According to the ideal gas law,

$$p_1 = n_1 kT_1 \quad , \quad p_2 = n_2 kT_2 \quad . \qquad (19B16)$$

Table 19B1. Coefficients of viscosity of common gases at 1 atm, 273 K. At other temperatures, $\eta \approx \eta_0(T/273)^{\frac{1}{2}}$, where η_0 is the tabulated value. Data from A. Roth, Vacuum Technology, North Holland, New York, 1976, Table 2.9, p. 45; and reprinted with permission from CRC Handbook of Chemistry and Physics, 47th Edition 1966, p. F-39 to F-42. Copyright The Chemical Rubber Co., CRC Press, Inc.

gas	η_0, 10^{-7} Pa-s
air	170.8
argon	209.6
ammonia	91.8
carbon dioxide	139.0
chlorine	124.0
ethane	84.8
helium	186.0
hydrogen	83.5
krypton	232.7
methane	102.6
neon	297.3
nitrogen	166.6
oxygen	189.0
xenon	210.1
carbon monoxide	166.0
acetylene	93.5

Combining Eqs. (19B8), (19B15), and (19B16), the net flow rate is found to be

$$dN/dt = [p_2T_2^{-\frac{1}{2}} - p_1T_1^{-\frac{1}{2}}]A/(2\pi mk)^{\frac{1}{2}}, \tag{19B17}$$

assuming $m_1 = m_2 = m$. After a long time, equilibrium is reached, dN/dt goes to zero, and

$$p_1/p_2 = (T_1/T_2)^{\frac{1}{2}} \tag{19B18}$$

so that the colder chamber will be at a lower pressure. If the temperatures are nearly equal, on the other hand, the conductance can be found from Eqs. (19B4), (19B5), and (19B17) to be

$$C = Q/(p_2-p_1) = kT(dN/dt)/(p_2-p_1)$$
$$= A(kT/2\pi m)^{\frac{1}{2}}, \tag{19B19}$$

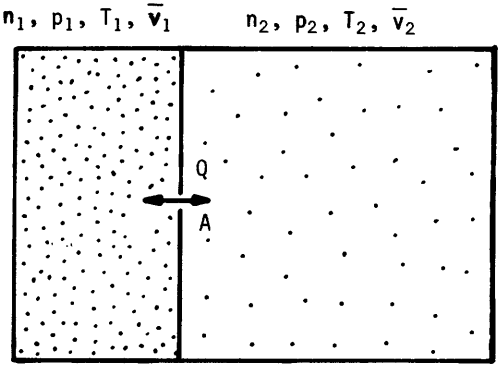

Fig. 19B3. Two gases separated by a wall with a small orifice with area A.

which is independent of pressure. For air at 293 K,

$$C = 116\ A \quad (m^3/s), \tag{19B20}$$

where A has units of m^2. The conductance of a circular tube with diameter D (m) and length L (m) for air at 293 K is

$$C = 122\ D^3/L(1 + 4D/3L) \quad (m^3/s). \tag{19B21}$$

As L goes to zero, $C = 3(122)D^2/4 = \pi(116)D^2/4 = 116A$. For a rectangular duct with sides a and b,

$$C = 309Ka^2b^2/L(a+b) \qquad (m^3/s) \quad , \tag{19B22}$$

where K is a function of (a/b), with K(1) = 1.11, K(.5) = 1.15, K(.33) = 1.20, K(.2) = 1.30, and K(.1) = 1.44 (Roth, 1976, p. 82).

Precise formulas have been derived for flow in the *intermediate* (transition) regime between viscous and molecular flow. However, for rough calculations, the approximation

$$C = C(\text{viscous}) + C(\text{molecular}) \tag{19B23}$$

may suffice, where the terms on the right are the conductivities for the viscous and molecular flow regimes. The error of this approximation does not exceed 13% for circular tubes.

If several conductances are connected in parallel, as shown in Fig. 19B4, the conductances add linearly, while for conductances in series (same figure), the conductances add reciprocally. (The flow impedances combine like electrical resistances). Conductances for complex shapes are given in the references. Conductances of various gases relative to air are listed in Table 19B2.

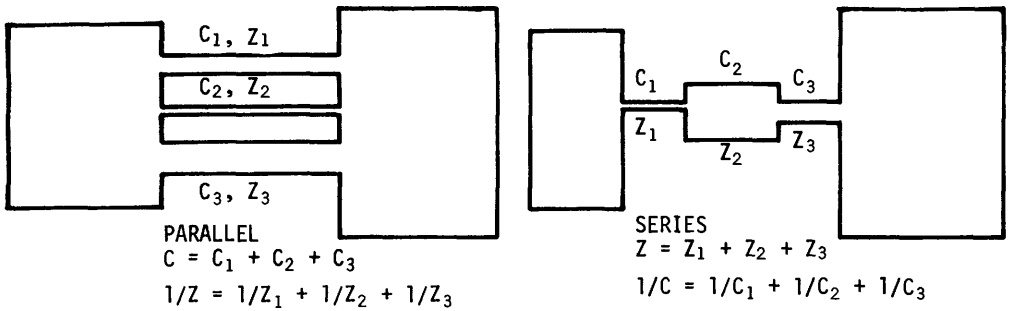

Fig. 19B4. Combinations of conductances in series and parallel.

Table 19B2. Conductances for various gases, relative to the conductance for air. From A. Roth, Vacuum Technology, North Holland, New York, 1976, Table 3.8, p. 121.

	C(gas)/C(air)	
gas	molecular flow	viscous flow
hydrogen	3.78	2.1
helium	2.67	0.93
water vapor	1.26	1.9
argon	0.85	0.82
CO_2	0.81	1.30
mercury vapor	0.38	-

pumpdown time

Eqs. (19B12) and (19B11) may be combined to give

$$dp/dt + \alpha p = Q_L(t)/V + \alpha p_u, \text{ where } \alpha \equiv S_t C/V(S_t + C). \tag{19B24}$$

If both sides are multiplied by $e^{\alpha t}dt$, the left side becomes equal to $d(pe^{\alpha t}) = dpe^{\alpha t} + \alpha pe^{\alpha t}dt$, so the equation may be integrated

$$\int_0^t d(pe^{\alpha t}) = \int_0^t dt' e^{\alpha t'}\left(Q_L/V + \alpha p_u\right) \tag{19B25}$$

to obtain

$$pe^{\alpha t} - p_0 = \int_0^t dt' e^{\alpha t'} Q_L(t')/V + p_u(e^{\alpha t}-1) \quad , \tag{19B26}$$

where p_0 is the initial pressure. We cannot proceed further unless the time variation of the leak rate is known. If the leak rate is assumed to be a constant equal to Q_0, then the time variation of pressure is found to be

$$p(t) = p_0 e^{-\alpha t} + (p_L + p_u)\,(1 - e^{-\alpha t}) \qquad \text{(Pa)} \tag{19B27}$$

where $p_L \equiv Q_0/\alpha V = Q_0(S_t + C)/S_t C$. Thus, the pressure tends to vary exponentially with a time constant

$$\tau = \frac{1}{\alpha} = \left[\frac{S_t + C}{S_t C}\right] V \quad \text{(s)} \quad . \tag{19B28}$$

Letting $t \to \infty$ in Eq. (19B27), we see that the ultimate pressure in the chamber is equal to $(p_L + p_u)$, which are the pressure limitations due to leakage and backstreaming from the pump.

EXAMPLE PROBLEM 19B2

A vacuum chamber with $V = 0.1\ m^3$, $T = 293\ K$, and $p_0 = .01\ Pa$ is connected to a pump with $S_t = 0.2\ m^3/s$ by a tube with $D = 0.1\ m$ and $L = 0.9\ m$. If there is a constant leakage of $10^{-7}\ Pa\text{-}m^3/s$ and the ultimate pressure of the pump is 10^{-6} Pa, find τ and the ultimate pressure.

From Eq. (19B1) $\lambda = 0.68$ m, so the flow is molecular. From Eq. (19B21), $C = .118\ m^3/s$, so $\alpha = S_t C/V(S_t + C) = .742/s$, $\tau = 1.3$ s, $p_L = Q_0/\alpha V = 1.35\times10^{-6}$ Pa, and $(p_L + p_u) = 2.4\times10^{-6}$ Pa.

In practice, however, such fast pumpdown times are rarely attained, because of higher leak rates, which gradually decrease in time, so that the pressure is in transient equilibrium, $p(t) \simeq p_L(t) + p_u$. The gradually decreasing leak rate is caused by gradual desorption of gas from surfaces, materials, and cracks. Water vapor is particularly tenacious, and does not desorb readily unless the chamber is heated.

Since the leakage term

$$p_L(t) = Q_L(t)(1/S_t + 1/C) \quad , \qquad (19B29)$$

either a small pumping speed or a small conductance can result in a high system pressure.

19C. Pumps

The main categories of vacuum pumps are mechanical pumps, jet pumps (diffusion pumps), ionization pumps, sublimation pumps (getters), cryosorption pumps, and cryogenic pumps.

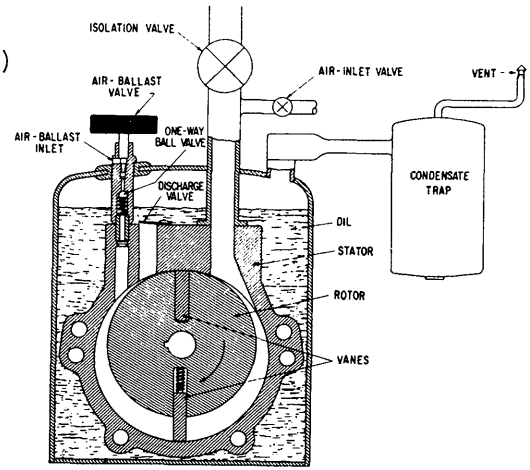

Fig. 19C1. A rotary vane mechanical pump. As the rotor turns, the spring-loaded vanes sweep the gas from the inlet port around to the outlet port, where it is squeezed out. From J. M. Lafferty, "Techniques of High Vacuum", General Electric Company Report 66-RL-3791 (1964), Fig. 7.

mechanical pumps

Early mechanical pumps used reciprocating pistons in cylinders, but such pumps have problems with vibrations, noise, and wear. Most mechanical pumps now are rotary pumps. A rotary vane pump is illustrated in Fig. 19C1. As the piston rotates, the vanes sweep the gas azimuthally around the outside from the inlet port to the exit port. Oil is used to attain a good seal between the vanes and the cylinder wall. Such mechanical pumps can typically evacuate a chamber down to about 0.1 Pa (0.0008 Torr).

Mechanical booster pumps of the Roots type (Fig. 19C2) can be used to augment other mechanical pumps. They are a type of gear pump, in which meshing gear teeth (two teeth per rotor) squeeze fluid out the exit. Because of their high throughput per unit cost, Roots blowers were selected for use in the Reversed Field Pinch Reactor design.

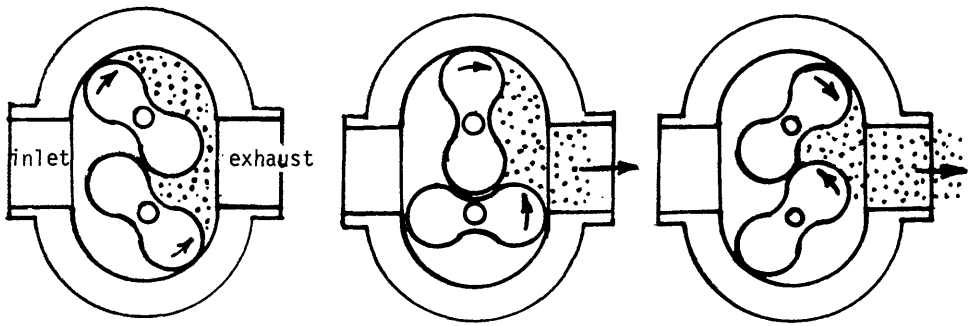

Fig. 19C2. Operation of a Roots mechanical booster vacuum pump. The rotating two-teethed gears sweep the gas around the outside of the chamber from inlet to outlet. Based on A. Guthrie, Vacuum Technology, Wiley, New York, 1963, Fig. 5.3b, p. 114.

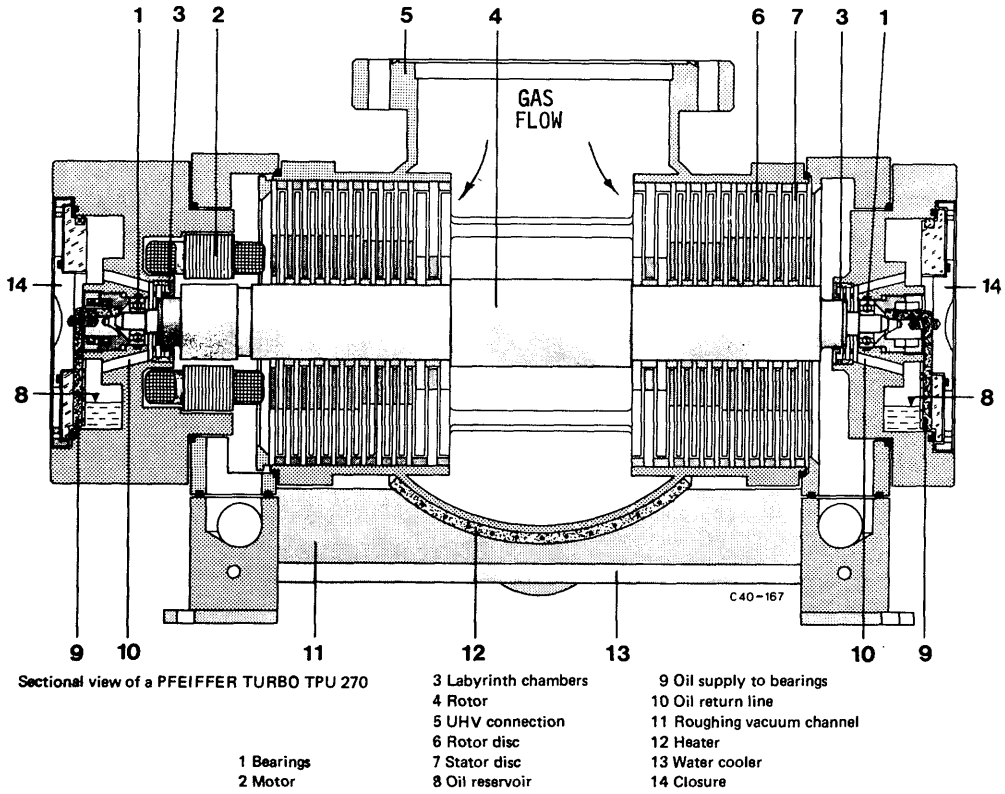

Fig. 19C3. Cutaway view of a turbomolecular pump. The rotor turns at a speed of 60,000 rpm (1000 Hz). Courtesy of Balzers Corporation, Hudson, NH.

A turbomolecular pump, illustrated in Fig. 19C3, is like the turbine of a jet engine. Rotor disks turning at high velocities impart momentum to the gas molecules, pumping them away from the vacuum chamber. Various types of turbomolecular pumps are available, with pumping speeds up to 4 m^3/s and ultimate pressures $p_u \leq 10^{-7}$ Pa. They have been selected for several fusion reactor designs. The low p_u is a significant advantage in comparison with other mechanical pumps. The turbine blade design is simpler than for steam turbines and jet engines, because the flow is molecular and the temperatures are much lower.

jet pumps

The basic principle of a jet pump is illustrated in Fig. 19C4. A high-velocity spray of fluid from a nozzle imparts momentum to surrounding fluid, moving the surrounding fluid through a tube. This principle is used for pumping water in a variety of applications (a pump must be provided for the primary stream), to

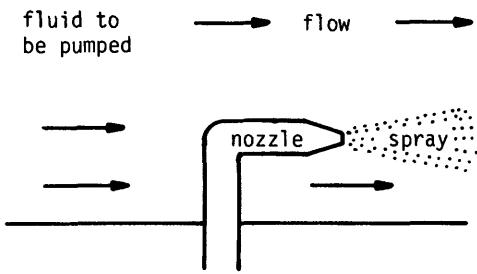

Fig. 19C4. A jet pump.

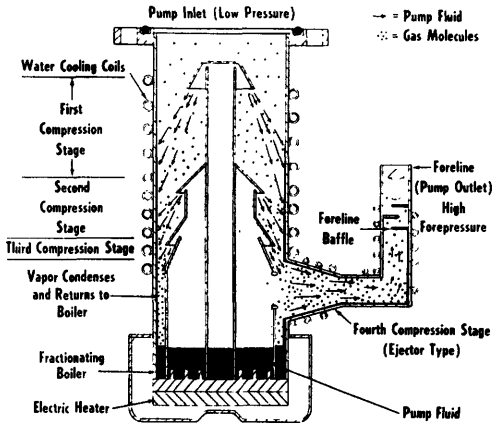

Fig. 19C5. A multistage oil diffusion pump, NRC Corporation. From J. M. Lafferty, "Techniques of High Vacuum", General Electric Company Report GG-RL-3791 (1964), Fig. 10.

create a vacuum in the condensers of steam turbines using a jet of steam to drive out air and water vapor, and in high vacuum systems to remove gases using a jet of hot oil vapor or mercury vapor. In high vacuum systems these jet pumps are called *diffusion pumps*.

A typical multistage diffusion pump is illustrated in Fig. 19C5. Oil (or mercury) is boiled in a tank at the bottom. The hot vapor rises through the central column and then sprays downward around the outside, pumping gases downward from the chamber above. Since diffusion pumps are only effective at pressures below about 1 Pa (.008 Torr), a mechanical pump is used in series with the diffusion pump to take the exhaust gases and pump them up to atmospheric pressure.

Diffusion pumps have the advantages of no moving parts, high pumping speeds, and low ultimate pressures. On the other hand, the pumping fluid can diffuse up into the chamber and contaminate its walls, so flow baffles and cold traps must be placed between the main chamber and the diffusion pump to prevent contamination. Cold traps not only prevent contamination due to the diffusion pump fluid, but also permit pressures many orders of magnitude below the room-temperature vapor pressure of the pump fluid to be attained. A typical cold trap is cooled with water, freon, or liquid nitrogen, with lower temperatures being more effective. Pump fluid condenses out in the trap, so that it does not reach the chamber. A U-bend cold trap and a chevron baffle are illustrated in Fig. 19C6.

ionization pumps

An ionization pump is illustrated in Fig. 19C7. Permanent magnets mounted outside the chamber create a strong magnetic field. A strong electric field parallel to the magnetic field is created by applying + 3 kV to the anode. When an electron-ion pair is created (by a cosmic ray, for example) the electron will oscillate back and forth through the hole in the anode, until it diffuses across the magnetic field and is lost to the anode. This *Penning discharge* is similar to that in a duoPIGatron ion source (Chapter 9). The oscillating electron has enough energy to ionize neutral gas atoms it collides with, creating more oscillating electrons. The ions thus formed are accelerated into the cathode and buried. In addition, an active metal such as titanium may be sputtered off the cathodes. The titanium atoms combine chemically with the gases being pumped and

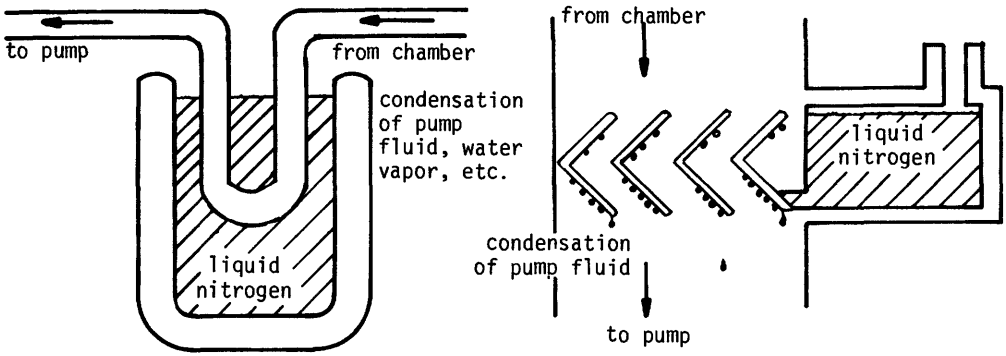

Fig. 19C6. A U-tube cold trap and a chevron baffle for prevention of pump fluid streaming into the vacuum chamber.

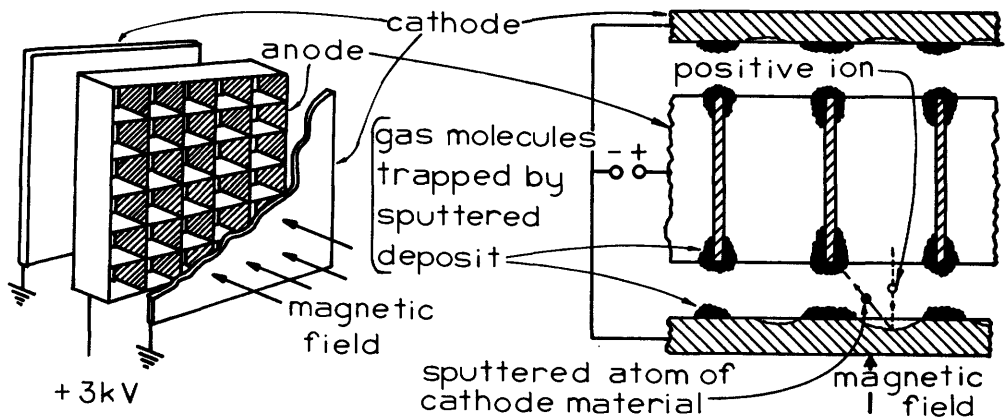

Fig. 19C7. Cutaway view of an ionization pump (left), and symbolic diagram of the effects of sputtering titanium from the cathode (right). The magnetic field of 0.15 T is produced by permanent magnets, which are not shown here. Drawing at right is from J. M. Lafferty, "Techniques of High Vacuum", General Electric Company Report 66-RL-3791 (1964), Fig. 13. Drawing at left is based on L. G. Carpenter, Vacuum Technology, American Elsevier, New York, 1970. Fig. 3.7, p. 28.

fasten them to the walls. Thus, there are two pumping mechanisms at work simultaneously: ionization of the neutral gases by the cloud of oscillating electrons, and chemical pumping by the sputtered titanium. Noble gases (helium, neon, argon, krypton, and xenon) are not affected by the chemical action of titanium. They can still be ionized and buried in the walls, but the pumping speed for noble gases is usually much lower than the pumping speed for chemically active gases. More complex electrode shapes have been devised (triode pumps) to enhance the pumping speed of noble gases.

The ionization or sputter-ion pump can attain pressures below 10^{-7} Pa (8×10^{-10} Torr), has no moving parts, and has no volatile fluid, so cold traps are not required. However, these pumps cannot operate until the chamber has been evacuated to pressures of about 1 Pa (0.008 Torr), so roughing pumps are needed

initially to pump the chamber down to a pressure where the ionization pump can be started. When the ion pump is started, the roughing pump can be turned off.

sublimation pumps

Sublimation pumps, or *getters*, use chemically active metals such as titanium and barium to adsorb gases chemically. Filaments of titanium may be heated in a vacuum chamber to boil off titanium vapor and deposit a thin film of it inside the chamber walls. This thin film of fresh metal has a high pumping speed for active gases, so it can produce a very low pressure in the chamber in a short time. However, after a period of minutes or hours, the titanium film becomes saturated, and more titanium must be deposited to renew the pumping effect. The saturation time is inversely proportional to the incident gas flux $n\bar{v}/4$, hence very short at high pressures. Thus, sublimation pumps are limited by the amount of titanium contained in the filaments or porous metal balls. Typical commercial elements are rated at tens to hundreds of hours operation at low heater current, or minutes at high current. (Commercial electronic tubes often use sublimation pumps in the form of active metal filaments which are "flashed", after the tube is sealed, to remove impurity gases and improve the vacuum, thereby prolonging the life of the thermoelectric filament. When you look at a vacuum tube you may see a silvery metallic deposit from the getter on the inside of the glass at the base of the tube.)

cryosorption pumps

A typical cryosorption pump is illustrated in Fig. 19C8. Zeolite pellets contained in a metal can are cooled by liquid nitrogen to 77 K or by liquid helium to 4 K. They strongly adsorb gases coming out of the chamber, and can pump a chamber down to pressures less than 1 Pa in a few minutes. When the desired pressure is attained, the cryosorption pump may be valved off and allowed to warm up. The adsorbed gases are then desorbed, building up a high pressure inside the can, which is vented by a relief valve, to prevent explosion. When the gases are desorbed, the pump can be cooled again and recycled. Cryosorption pumps at 77 K pump H_2 or He poorly, but pumps at 4 K pump all gases to $p \lesssim 10^{-6}$ Pa.

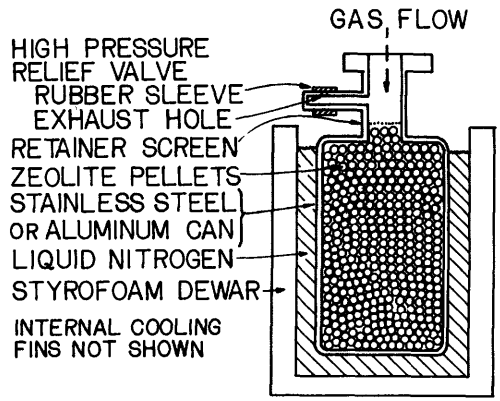

Fig. 19C8. Cutaway view of a cryosorption pump.

Cryosorption pumps are simple and relatively inexpensive, but they do require a cryogenic (low-temperature) fluid for their operation. They are often used to pump a chamber down to pressures where ionization pumps can be started.

cryogenic pumps

A cryogenic pump consists simply of a metal plate cooled to a very low temperature. At low temperatures the probability that a molecule striking the plate will stick to it is high, so that gases are readily adsorbed onto the plate, lowering the chamber pressure. The plate is usually cooled by liquid nitrogen (77 K) or by liquid helium (4 K). Lower pressures are attainable at the lower temperatures. To be effective, the cryogenic pump must be thermally insulated from the surroundings and from the plasma discharge, so

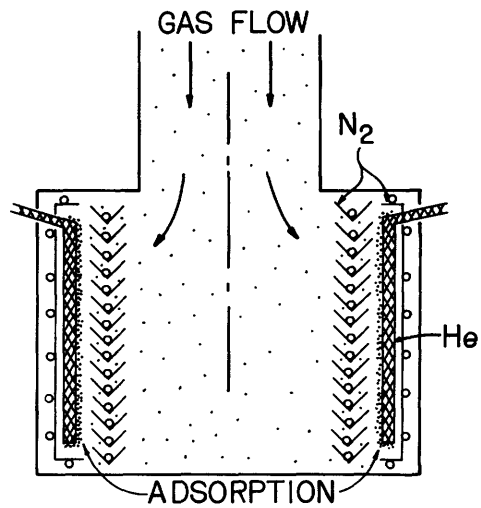

Fig. 19C9. A cryogenic pump. N_2 = liquid nitrogen cooled surfaces, He = liquid-helium-cooled surfaces. Without the radiation barriers, radiative heating would boil the liquid helium away too rapidly.

that the liquid coolant is not boiled away too rapidly (Fig. 19C9).

The pumping speed of a cryopump is roughly one-fifth the conductance of an orifice, Eq.(19B19). For deuterium at temperature T(K) with pump area A (m^2),

$$S_t \approx 89A(T/300)^{\frac{1}{2}} \quad (m^3/s). \qquad (19C1)$$

Various vacuum pumps are compared in Table 19C1.

Table 19C1. Typical operating ranges of various vacuum pumps. All except the first two require roughing pumps.

rotary vane mechanical	10^5 - 0.1 Pa	(760 - .0008 Torr)
cryosorption	10^5 - 0.1 Pa	(760 - .0008 Torr)
Roots blower	100 - 0.01 Pa	(0.8 - 8×10^{-5} Torr)
diffusion	1 - 10^{-6} Pa	(.008 - 8×10^{-9} Torr)
turbomolecular	1 - 10^{-6} Pa	(.008 - 8×10^{-9} Torr)
ionization	1 - 10^{-7} Pa	(.008 - 8×10^{-10} Torr)
sublimation	.01 - 10^{-7} Pa	(8×10^{-5} - 8×10^{-10} Torr)
cryogenic	.001 - 10^{-8} Pa	(8×10^{-6} - 8×10^{-11} Torr)

19D. Pressure Gages

Vacuum gages use many different phenomena to measure pressure: mechanical expansion, gravity, momentum transfer, viscosity, thermal conductivity, and ionization rates.

A *Bourdon tube* gage consists of a spiral tube of elliptical cross section connected to the vacuum to be measured and exposed to atmospheric pressure on the outside (Fig. 19D1). As the pressure in the tube is reduced, the tube curls up tighter, and the needle attached to the end of the tube indicates the pressure. Such gages are accurate down to about 1000 Pa (8 Torr).

Another type of mechanical vacuum gage uses a *diaphragm* with a reference vacuum on one side and the vacuum to be measured on the other side. Deflection of the diaphragm is amplified by mechanical linkage and displayed by a needle.

The use of gravity to measure pressure is familiar in mercury barometers and manometers. A more sophisticated version, called a *McLeod gage*, can measure pressures accurately down to 10^{-3} Pa (8×10^{-6} Torr) by compressing part of the

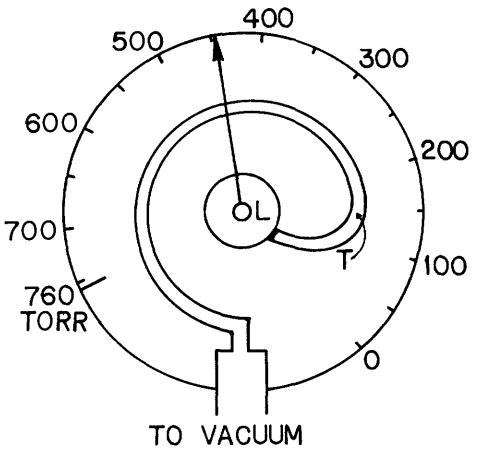

Fig. 19D1. A Bourdon tube vacuum gage. T = elliptical cross section tube. L = levers and gears (not shown) to amplify motion.

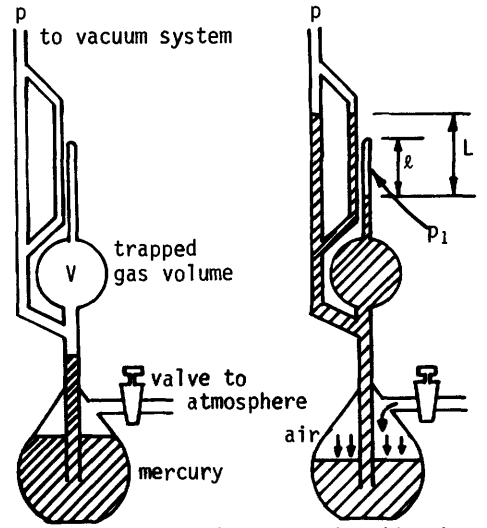

Fig. 19D2. A McLeod gage. Initially the volume V is at the same pressure p as the vacuum to be measured. When air is admitted through the valve, air pressure forces the mercury up the center tube into volume V. The trapped gas is compressed to a new pressure p_1 and volume Aℓ , where A is the cross-sectional area of the small tube. From G. Lewin, Fundamentals of Vacuum Science and Technology, Fig.5-1, p. 88. Copyright 1965 McGraw-Hill, New York. Used by permission of McGraw-Hill Book Company.

trapped gas and then comparing the pressure of the compressed gas with atmospheric pressure. The gas is trapped and compressed by a rising column of mercury, as illustrated in Fig. 19D2. By Boyles' Law, $pV = p_1 A\ell$. Furthermore, $p_1 - p = \rho gL$, where L is the height of the column of mercury supported by the pressure difference, ρ = density of mercury, g = acceleration of gravity. Therefore, $p = \rho gLA\ell/(V-A\ell)$. These gages are useful for calibration of other gages at 0.001-10 Pa, but they are slow and cumbersome, so other gages are employed for routine measurements.

A *thermocouple gage* is illustrated in Fig. 19D3. In the molecular flow regime, the thermal conductivity of a gas is proportional to its pressure. A heated filament can be cooled by conduction along its supports, by conduction through the gas, and by radiation. The support loss can be made negligibly small. If the filament is not too hot, the radiation loss will be much smaller than the heat transfer by conduction through the gas (down to a pressure of about 0.1 Pa). Then the temperature of the filament is controlled by the thermal conductivity of the gas, which is proportional to its pressure. A thermocouple mounted on the filament can be used to measure its temperature, which can be calibrated to give pressure readings of the gas. In some gages, two or three thermocouples are used in order to compensate for ambient temperature drift (the *Hastings gage*).

Alternatively, the filament resistance itself may be measured, since it increases with temperature. The resistance is measured with a "Wheatstone bridge", which compares the variable filament resistance with a reference resistance R_B at the same ambient temperature. Such a *Pirani gage* is shown in Fig. 19D4. Thermal conductivity gages are most useful between .1 Pa and 200 Pa (.0008 Torr and 1.5 Torr).

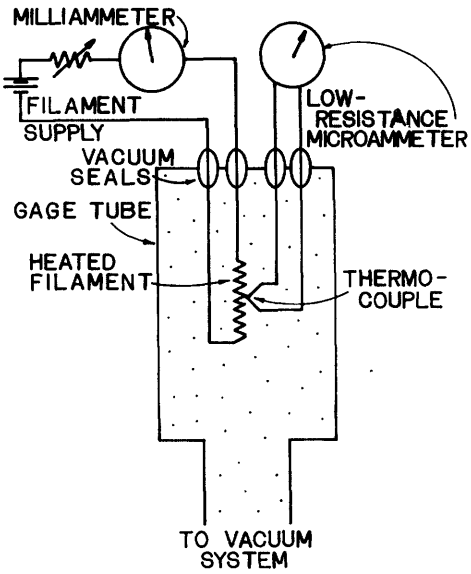

Fig. 19D3. Schematic diagram of a thermocouple gage tube and associated circuitry. The microammeter scale is calibrated in terms of pressure, with readings typically from .1 to 1000 milli-Torr (.013 to 133 Pa).

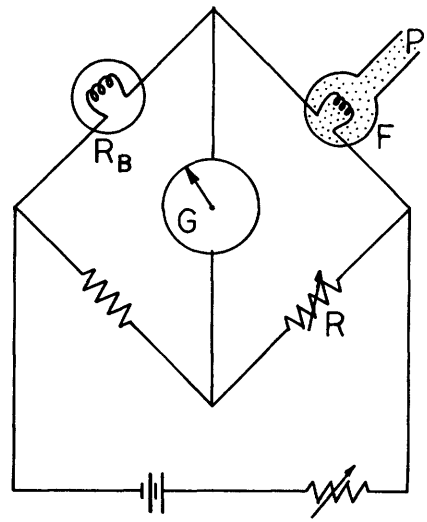

Fig. 19D4. Circuit diagram of a Pirani gage. Initially the current through the galvanometer G is balanced to zero by adjusting variable resistance R. When the pressure is changed in the gage tube, the temperature and resistance of the filament F change, causing a current to flow through the galvanometer, which can be calibrated in terms of system pressure. Based on J. M. Lafferty, "Techniques of High Vacuum", General Electric Company Report 64-RL-3791 (1964), Fig. 22.

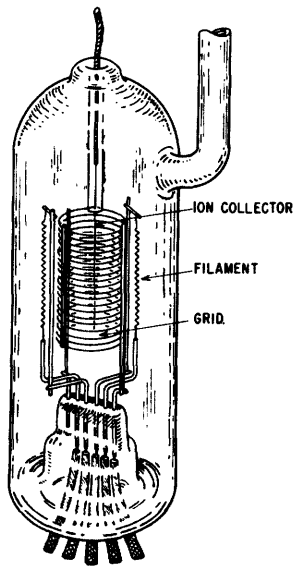

Fig. 19D5. Bayard-Alpert ionization gage. Typical voltages: filament = grounded, grid = + 150 V, ion collector = -45 V. From J. M. Lafferty, "Techniques of High Vacuum", General Electric Company Report 66-RL-3791 (1964), Fig. 24.

At pressures below 0.1 Pa, *ionization gages* are used. An ionization gage uses electrons from a hot filament to ionize some of the low-pressure gas atoms entering the gage. The ions are then collected by a negative electrode, and the ion current is linearly proportional to the gas pressure below about 0.1 Pa. A typical *Bayard-Alpert gage* tube is shown in Fig. 19D5. Electrons from the filament spiral in and out of the grid until they hit the grid wires. Some of these electrons produce ionization, and the ions are collected by the thin wire at the

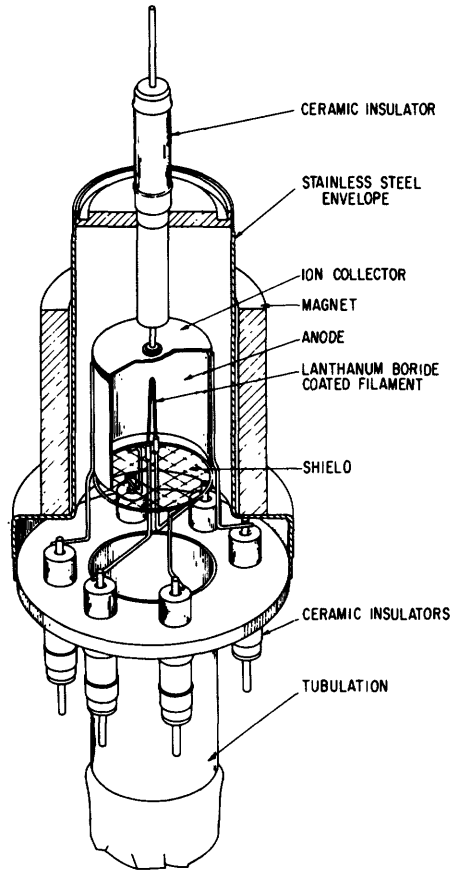

Fig. 19D6. A hot-cathode magnetron gage. The vertical magnetic field inhibits radial electron motion. From J. M. Lafferty, "Techniques of High Vacuum", General Electric Company Report 66-RL-3791 (1964), Fig. 25.

center. The ion collector has been made very small to minimize the effect of xray-produced photoelectrons from the ion collector, which would give a false current reading. At very low pressure (10^{-7} Pa) the ion currents are so low that very large electron currents from the filaments are needed. The filament requirements can be eased by the addition of a magnetic field to prolong the electron flight time. With a magnetic field of 250 Gauss (.025 Tesla), the ion currents are more than 10^4 times as large as without the magnetic field, and the pressure measurements can be extended down to about 10^{-11} Pa. Such a *magnetron* vacuum gage is illustrated in Fig. 19D6. In this case the filament is mounted at the center, and a positive anode surrounds it. The electrons spiral around the filament in the axial magnetic field, producing ionization, and the resulting ions are collected by the negative ion collector at the end. The ion collector and shield are negative relative to the cathode, to prevent axial electron losses.

Because thermal conductivity and ionization rates are different for different gases, gages relying on these phenomena must be calibrated for each gas to be used. Usually the gage is calibrated for air, and correction factors are calculated for other gases. For example, the calibration curves for a Pirani gage are shown in Fig. 19D7. Typical operating ranges of various pressure gages are listed in Table 19D1.

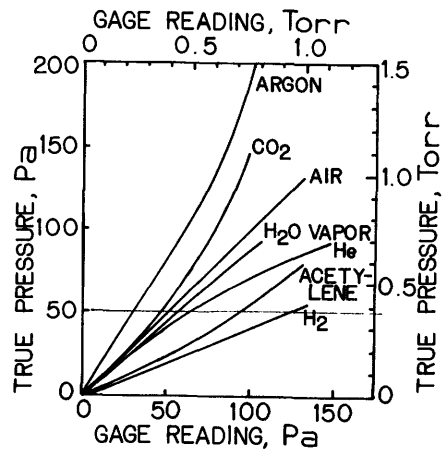

Fig. 19D7. Calibration curves for a Pirani gage. Adapted from A. Guthrie, Vacuum Technology, Wiley, New York, 1963, Fig. 6.7, p. 166.

Table 19D1. Typical operating pressure ranges of common pressure gages.

Bourdon	10^5 - 10^3 Pa	(760 - 8 Torr)
diaphragm	10^5 - 100 Pa	(760 - .8 Torr)
manometer (barometer)	10^5 - 100 Pa	(760 - .8 Torr)
McCleod	10 - 10^{-3} Pa	(8 - 8×10^{-6} Torr)
thermocouple, Pirani	200 - 0.1 Pa	(1.6 - 8×10^{-4} Torr)
Bayard-Alpert ionization	0.1 - 10^{-9} Pa	(8×10^{-4} - 8×10^{-12} Torr)
magnetron	0.1 - 10^{-11} Pa	(8×10^{-4} - 8×10^{-14} Torr)

19E. Chambers and Components

You are probably familiar with the experiment of boiling water in a metal can which has a screw-on lid. When the water is boiling you take it off the stove and screw on the lid. Then as the steam condenses inside, a vacuum is produced, and air pressure collapses the can. Vacuum chambers must be made strong enough so that they don't collapse from atmospheric pressure. There is a minimum thickness required to prevent buckling of vacuum vessels. For thin-walled cylindrical chambers, the ratio of the required thickness t to the chamber diameter D is a function of the chamber length L, as illustrated in Fig. 19E1. Design of vacuum vessels is discussed by Steinherz (1963). Stiffening rings can be added to permit the use of thinner walls.

Metal-to-metal joints can be made by soldering, brazing or welding. Soft solder is usually avoided, because of its higher vapor pressure. Silver brazing works well on small chambers of copper, brass, stainless steel, etc., but the brazing rod is expensive. Tungsten-inert-gas (TIG) welding is the best technique for stainless steel, which is the most common vacuum chamber material. A jet of argon or helium around the weld zone prevents oxidation of the weld.

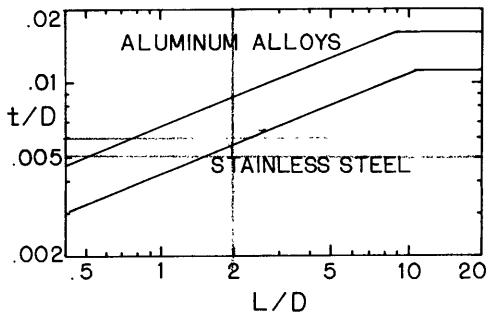

Fig. 19E1. Illustrative curves of the required ratio of vessel thickness to diameter for thin cylindrical vacuum chambers, as a function of the ratio of length to diameter. (These curves are for illustrative purposes only. For actual design work, consult the ASME Pressure Vessel Code.)

In designing welded joints, one should avoid *virtual leaks* and cracking from thermal stress. Virtual leaks are thin cracks on the inside of the chamber which can trap gases. When the chamber is pumped down to very low pressures, the gas molecules diffusing out of the crack can substantially raise the pressure. To prevent virtual leaks, it is best to run the weld around the inside of the chamber, instead of around the outside of the chamber, as illustrated in Fig. 19E2.

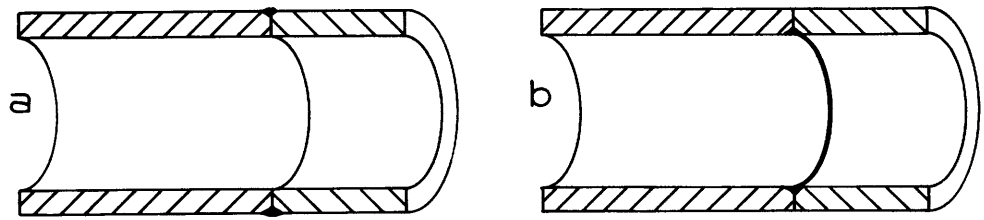

Fig. 19E2. Cutaway views of welds between two tubes. (a) Weld on outside, crack on inside may cause virtual leak. (b) Weld on inside, no virtual leak.

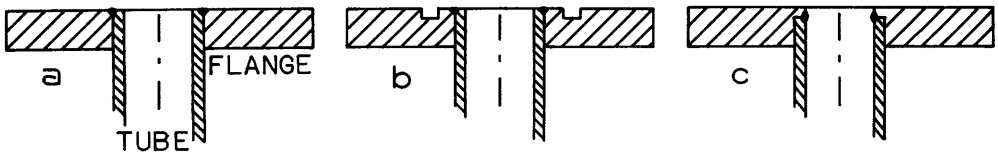

Fig. 19E3. Methods of welding a circular flange to a tube. (a) poor - warpage or cracking likely, (b) good - stress relief groove machined into flange, (c) good - thin ridge on inside of flange abuts tube.

Thermal stresses are caused by cooling of the heated weld zone. To avoid cracking or warping, the metal layer next to the weld should be thin, so that it reaches nearly the same temperature as the weld and cools with it. Some good techniques are illustrated in Fig. 19E3. Only a few aspects of vacuum chambers and seals are discussed here. A whole book has been written on vacuum sealing techniques (Roth, 1966).

In joining glass to metal, the thermal expansion of the two materials must be matched to prevent cracking of the glass as it cools. An alloy called *Kovar* has a thermal expansion coefficient nearly equal to those of some types of glass, so Kovar-to-glass seals are widely used (Fig. 19E4). The Kovar may be welded or brazed into the metallic chamber, but it is ferromagnetic. Other seals have been developed for applications where nonmagnetic materials are required.

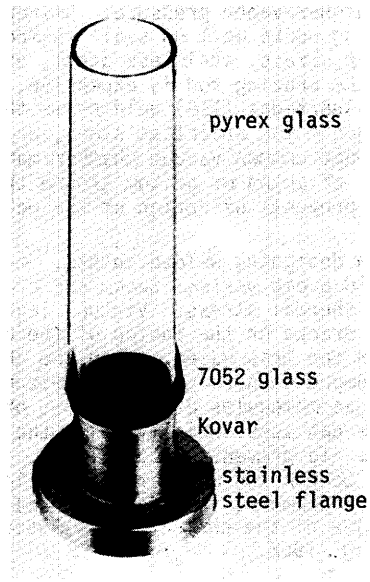

Fig. 19E4. A glass-to-metal seal. Courtesty of Thermionics Laboratory, Inc.

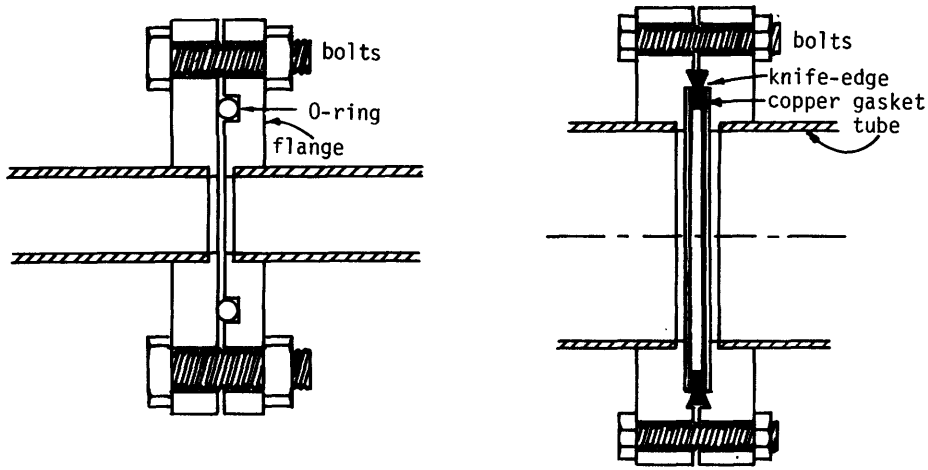

Fig. 19E5. Flange sealing techniques. An O-ring seal (left) and a bakeable metal seal (right).

Flange joints are usually sealed with elastomer O-rings (such as *viton*) or with metallic gaskets, as illustrated in Fig. 19E5. O-ring flanges are simpler and cheaper, but metallic gaskets are needed for ultrahigh vacuum systems ($p < 10^{-5}$ Pa), which require bakeout at high temperatures, because the O-rings have too high a vapor pressure at high temperatures ($T > 600$ K). Metallic gaskets are also needed for very low temperature (cryogenic) applications.

19F. Techniques

monolayers

Even the best vacuum equipment is useless if the proper techniques are not followed to insure cleanliness of everything inside the vacuum system. For example, outgassing from the miniscule amount of grease deposited by a single human fingerprint can be very significant in the ultrahigh vacuum range ($p \lesssim 10^{-5}$ Pa). This is true because the molecular density at 10^{-6} Pa is small (about 2.4×10^{14} m^{-3}) so that a fingerprint containing, say, 10^{16} molecules, can flood a 0.01 m^3 chamber with a lot of molecules compared to the number of gas molecules already present.

Ordinarily the walls of a vacuum chamber are covered with several layers of adsorbed gas molecules. (*Adsorption* refers to molecules sticking to the surface, while *absorption* refers to molecules penetrating into the wall.) Each layer one molecule thick is called a *monolayer*. The outer monolayers are weakly bound, and at equilibrium they are knocked off by thermal agitation as fast as they are reformed by adsorption. At a pressure of 10^{-4} Pa, the first monolayer would form on a perfectly clean surface in about 3 seconds. At 100 Pa, it would form in about 3 μs.

Each monolayer contains about 8×10^{18} molecules/m^2. If one monolayer is knocked off the wall of a fusion experiment by heat from the plasma, the influx of neutral atoms is substantial. At equilibrium during an experiment, each charge-exchange neutral leaving the plasma is replaced by an incident neutral refluxing off the

walls. It is important that these atoms be mostly hydrogen, so that impurity buildup does not cool the plasma too rapidly. One means of reducing the impurity influx is by thorough cleaning of the chamber walls. This cleaning can remove the oil, grease, oxides, etc. normally present on metallic surfaces.

cleaning

The following steps are often used to clean vacuum chambers. The surface should be mechanically polished before cleaning is begun.

1. *degreasing*. This is done by washing with detergent, followed by multiple rinses with hot water, cold water, and deionized water. Alternatively, a vapor degreaser may be used for small items. It consists of a heated bath of solvent, such as carbon tetrachloride, above which the parts to be cleaned are placed on a rack. The CCl_4 vapor condenses on the parts, dissolves the oils, and drips back down into the bath. Then the part is washed and rinsed.

2. *oxide removal* and *surface smoothing*. Acid etching or electropolishing removes oxides and some of the rough bumps normally present on a metallic surface. The decrease in surface roughness can lead to a reduction in the number of adsorbed gas molecules. For example, anodized aluminum can adsorb 100 times as many gas molecules as smooth polished aluminum can.

3. *rinsing*. To remove the acids, the surface is repeatedly rinsed using deionized water, then pure alcohol.

4. *bakeout*. After the chamber is assembled and pumped down, it is heated up to 400-700 K for many hours. The heat desorbs many of the molecules, such as water vapor, which would otherwise cling tenaciously to the surface.

5. *discharge cleaning*. Repeated plasma discharges are used to reduce the quantity of adsorbed gases.

Proper cleaning and bakeout are essential for the attainment of ultrahigh vacuum. Without such procedures the pressure will usually remain around 10^{-4} Pa for many days.

leak detection

Leaks can be detected by a variety of means. During initial pumpdown at high pressures, one can sometimes hear a hiss of air around the leak. The search can be aided by a stethoscope. Alternatively, one can pressurize the inside of the chamber and look for bubbles with a soap solution, or look for the deflection of smoke. Usually, however, leaks are much smaller than the gross leaks for which these procedures apply.

Leaks in glass systems can often be spotted by exciting the gas with a *Tesla coil*. The high voltage from the coil tip makes the gas glow, and the glow will be especially bright where air is leaking in through a crack. In metal systems with a glass section, the gas can be excited in the glass section, and acetone can be sprayed around the other sections. When the acetone hits the leak, the intensity or color of the glow will change.

Spraying acetone or helium can also be used in conjunction with a vacuum *pressure gage*, such as thermocouple gage or an ionization gage. When the fluid sprayed hits the crack, the gage needle will deflect one way or the other. (However, acetone fumes can be hazardous).

Helium mass spectrometers can be used in conjunction with spraying helium gas to look for leaks. This method is much more sensitive, as the detector only responds to helium. Such *leak detectors* are very convenient.

Another technique for leak detection is to spray a small amount of a *radioactive tracer gas* around possible leaks, and to detect this radioactive gas inside the chamber with an appropriate radiation detector.

Once the leak is located, if it is in a seal, the bolts may be tightened a little, to compress the gasket further. If this does not help, or if the leak is in a weld or joint, then the system must be opened up, rewelded, recleaned, pumped down, and baked out again. (This is a slow process, which is ample incentive to do it right the first time.) An exception is the case of a chamber where pressures below about 10^{-5} Pa are not required; in this case one can try to seal the leak with liquid sealant or with epoxy. Special epoxies have been developed with low vapor pressures, and they can be used temporarily to seal cracks in glass, for example.

diffusion

In addition to leakage and desorption effects, the ultimate pressure is limited by permeation of gases through the chamber walls. The constituents of air are listed in Table 19F1. Only the light gases, hydrogen and helium, have significantly high diffusion rates through most metals and glasses. Since helium is inert, it is not as likely to become chemically bound as hydrogen, and helium is about ten times as abundant as hydrogen in the air. Thus, in the ultrahigh vacuum region, the pressure may be limited by helium diffusion to around 10^{-10} Pa, with a wide variation from this number possible. We will not be concerned with this limitation, however, because vacuums of about 10^{-6} Pa are probably adequate for fusion reactors.

Table 19F1. Constituents of air (exclusive of water vapor). Reprinted with permission from CRC Handbook of Chemistry and Physics, 47th Edition, 1966, p. F-123. Copyright The Chemical Rubber Co., CRC Press, Inc.

	fraction of air
N_2	.78084 ± .00004
O_2	.20946 ± .00002
CO_2	.00033 ± .00001
Ar	.00934 ± .00001
Ne	18.18 ± .04 ppm
He	5.24 ± .004 ppm
Kr	1.14 ± .01 ppm
Xe	.087 ± .001 ppm
H_2	0.5 ppm
CH_4	2 ppm
N_2O	.5 ± .1 ppm

Problems

1. If Otto von Guericke's copper hemispheres had a diameter of 1 m, how large was the force holding them together? Express the number in N, lbs, and tons.

2. Two astronauts in a satellite orbiting station observe the pressure in their chamber ($V = 90\ m^3$) drops from 1.0×10^5 Pa to 0.987×10^5 Pa in 17 minutes, due to outflow through a small crack. Gas is not being added to the chamber from storage bottles. What is the effective conductance of the crack? At what time will the pressure be 0.90×10^5 Pa if the leak is not fixed? Assume constant conductance. [Hint: See Eqs. (19B12), (19B4).]

3. Air is flowing in a 5 cm diameter tube at $p = 100$ Pa, $T = 300$ K, with flow velocity $v = 0.3$ m/s. Find (a) the throughput, (b) the average molecular speed, (c) the molecular flow rate (d) the flow regime, (e) the tube conductance and pressure drop in a distance of 0.1 m.

4. A chamber of 0.05 m^3 volume at 77 K is connected through a 2 cm orifice to another chamber with 0.07 m^3 volume at 298 K and 10^{-4} Pa. What is the equilibrium pressure in the first chamber?

5. Two chambers, as in Fig. 19B1, are connected by a tube with 3 cm diameter and length 28 cm. The air pressure in one chamber is 0.1 Pa, and in the other chamber it is 0.002 Pa. (a) What kind of flow is occurring? (b) What is the throughput? (c) How many molecules are flowing through the tube per second? (d) What is the pumping speed at the entrance to the lower-pressure chamber (taking $p_u \approx 0$) ?

6. A pump with speed 0.08 m^3/s is connected to a large chamber with a tube 0.8 m long. When the pressure at the pump is 10^{-5} Pa (air), find the throughput and chamber pressure for tube diameters of (a) 1 cm, (b) 3 cm, (c) 10 cm, (d) 10 cm, but He gas instead of air. The pump ultimate pressure is 10^{-7} Pa.

7. A vacuum chamber with volume V at pressure p and temperature T is connected to two pumps with speeds S_1 and S_2 through tubes with conductances C_1 and C_2. Both pumps have the same ultimate pressure p_u. Find the equilibrium pressure corresponding to a constant leak rate Q_0 in terms of these parameters.

8. A pump with speed 0.1 m^3/s is connected to a 0.4 m^3 chamber by two 0.6 m long tubes in parallel. Tube diameters are 0.04 m and 0.07 m. The ultimate pump pressure is 10^{-6} Pa, and the leak rate is 10^{-5} Pa-m^3/s. (a) Find the equilibrium chamber pressure. (b) Find the equilibrium chamber pressure for the case in which the tubes are connected in series, instead of in parallel.

9. An accelerator is to be pumped every 3 meters with a pump connected through a conductance of 0.1 m^3/s. The ultimate pressure of the pumps is 10^{-8} Pa, and the pumping speed is 0.2 m^3/s. If a pressure of 3×10^{-8} Pa is desired, what is the maximum leak rate (including desorption) which can be tolerated in a 3-meter section?

10. A spherical chamber with R = 0.5 m initially has 10 monolayers of adsorbed gases on its interior. During the first 1000 s of bakeout, five of the monolayers are removed, and the gas temperature is about 500 K. What is the average throughput of desorbed gases to the pump during this period?

11. A stainless steel soup kettle 0.5 m in diameter and 0.7 m long is to be made into a vacuum chamber for a plasma experiment. The walls are 3 mm thick. Is the kettle safe, or does it need to have reinforcement? If the kettle were made of aluminum, how thick would the walls need to be?

12. A space colony is constructed in a large cylinder 3 km in diameter and 5 km long, which rotates to produce artificial "gravity". It contains air at 1 atm pressure. A meteor blasts a hole about 10 m in diameter in one wall, and the air begins to rush out the hole. How long does it take before the pressure has dropped to 0.95 atm? (Because $P_2 >> P_1$, the flow is "critical" or "choked", and the effective conductance C = 200 A.) $mr\omega^2 = mg \quad \tau = \frac{2\pi}{\omega} = 2\pi\sqrt{r/g} = 1.3$ min

13. A McLeod gage is used to calibrate a Pirani gage in air. The trapped gas volume V = 121 cm^3, the trapped gas tube area is 0.14 cm^2, the measured heights are L = 8.3 cm and ℓ = 6.1 cm. The density of mercury is 13.546 gm/cm^3, and the acceleration of gravity is about 9.806 m/s^2 (varies with altitude). The Pirani gage reads 0.17 Torr. Is it accurate? At the same true pressure, what would the Pirani gage read if the gas were argon?

Bibliography

L. G. Carpenter, *Vacuum Technology*, American Elsevier, New York, 1970.

N. T. M. Dennis and T. A. Heppell, *Vacuum System Design*, Willmer Bros. Limited, Birkenhead, England, 1968.

J. A. Dillon and V. J. Harwood, *Experimental Vacuum Science and Technology*, Marcel Dekker, New York, 1973.

G. W. Green, *The Design and Construction of Small Vacuum Systems*, Willmer Bros. Limited, Birkenhead, England, 1968.

A. Guthrie, *Vacuum Technology*, Wiley, New York, 1963.

M. A. Hoffman and A. S. Blum, "Cryotrapping vacuum pumping system design for a helium neutral beam injector", *Nuclear Technology/Fusion 1*, 275-284 (1981).

D. H. Holkeboer, D. W. Jones, F. Pagano, D. J. Santeler, *Vacuum Engineering*, Boston Technical Publications, Boston, 1967.

W. G. Homeyer, "Vacuum pumping concepts for ETF", *Fourth ANS Topical Meeting on the Technology of Controlled Nuclear Fusion (King of Prussia, PA, 1980)*, DOE, 1981.

R. R. LaPelle, *Practical Vacuum Systems*, McGraw-Hill, New York, 1972.

G. Lewin, *Fundamentals of Vacuum Science and Technology*, McGraw-Hill, New York, 1965.

J. F. O'Hanlon, *A User's Guide to Vacuum Technology*, Wiley, Somerset, NJ 1980.

M. Pirani and J. Yarwood, *Principles of Vacuum Engineering*, Reinhold, New York, 1961.

B. D. Power, *High Vacuum Pumping Equipment*, Williams Clows & Sons, London, 1966.

P. A. Redhead, J. P. Hobson, and E. V. Kornelsen, *Ultrahigh Vacuum*, Willmer Brothers Limited, Birkenhead, England, 1968.

R. W. Roberts and T. A. Vanderslice, *Ultrahigh Vacuum and its Applications*, Prentice-Hall, Englewood Cliffs, N.J., 1963.

A. Roth, *Vacuum Sealing Techniques*, Pergamon Press, Elmsford, N.Y., 1966.

A. Roth, *Vacuum Technology*, North Holland, New York, 1976.

H. A. Steinherz, *Handbook of High Vacuum Engineering*, Reinhold, New York, 1963.

H. A. Steinherz and P. A. Redhead, "Ultrahigh Vacuum", *Scientific American*, March 1962.

A. H. Turnbull, J. C. Rivere, and F. A. Vick, *An Introduction to Vacuum Technique*, Wiley, New York, 1964.

C. M. Van Atta, *Vacuum Science and Engineering*, McGraw-Hill, New York, 1965.

CHAPTER 20
WATER-COOLED MAGNETS

20A. Background

Since the magnetic rock lodestone was discovered near Magnes, Greece (now part of Turkey), the curious phenomena associated with this rock became known as "magnetism". Magnetism first came under intense scientific study in the early nineteenth century. Oersted observed the deflection of a compass needle by a current-carrying wire; Ampere studied the interaction of two current-carrying wires; and Faraday formulated a law of magnetic induction and observed the rotation of polarized light by a magnetic field. Electromagnetic field theory was further developed by Maxwell, who published his famous treatise on electricity and magnetism in the 1870's.

Interest in constructing high-field magnets increased around the turn of the century, following Fabry's analysis of high-field air-cooled solenoids. A water-cooled solenoid, which developed 5 Tesla and could operate for many minutes, was built by Deslandres and Perot in 1914. A field of 10 Tesla was produced at M.I.T. by Bitter in 1939. Higher fields were also produced during this period, but by pulsed magnets which sustained the field only a few milliseconds. In 1964 Bitter and Montgomery produced a field of 25 Tesla with a coil requiring 10 MW of electrical power and about 100 m^3 of cooling water per minute.

Technically, the *magnetic field* is denoted by $\vec{H}$ and the *magnetic induction* or *magnetic flux density* by $\vec{B}$, where $\vec{B} = \mu\vec{H}$, and μ is the permeability of the medium. However, B is often called the "magnetic field".

To confine a reactor plasma, the required average magnetic induction can be found from Eq. (8B6):

$$B \simeq [2\mu_0 nk(T_e + T_i)/\beta]^{\frac{1}{2}} \quad (T) \qquad (20A1)$$

For example, if $T_e + T_i = 2\times10^8$ K, $n = 2\times10^{20}$ m^{-3}, and $\beta = 0.1$, then B = 5.9 T. The peak field at the magnet coil conductor is usually significantly larger than the average field in the plasma region.

Water-cooled magnet coils require large amounts of electrical power and cooling water, but they offer some advantages, in comparison with superconducting magnets:

* no need for cryogenic insulation and refrigeration
* can be bolted together for easy disassembly and maintenance
* little danger from plasma disruptions
* can stand much higher neutron fluences.

The use of water-cooled tokamak toroidal field coils is discussed by Kalnavarns and Jassby (1979). Here we will discuss calculations of magnetic fields and coil forces (applicable to all types of magnets) and the power and cooling requirements of resistive water-cooled magnets, and then describe types of coil windings.

20B. Magnetic Field Calculations

basic equations

Let the vector $\vec{r}$ with components (x,y,z) represent the place where we want to calculate the magnetic field, and the vector $\vec{r}'$ with components (x',y',z') represent the location of a differential volume dV through which a current density J flows (Fig. 20B1). Then the vector $\vec{\rho} = \vec{r} - \vec{r}'$ points from dV to the place where we want to calculate the magnetic field, and its length is the distance between these two points. According to the Law of Biot-Savart, the differential magnetic field produced at $\vec{r}$ by the current density $\vec{J}$ flowing through dV is equal to

$$d\vec{B} = \mu_0 dV \, \vec{J} \times \vec{\rho} / 4\pi\rho^3 \quad \text{(Tesla)} \qquad (20B1)$$

where μ_0 is the permeability of free space. The total magnetic field at $\vec{r}$ is found by integrating over the entire volume where currents are flowing:

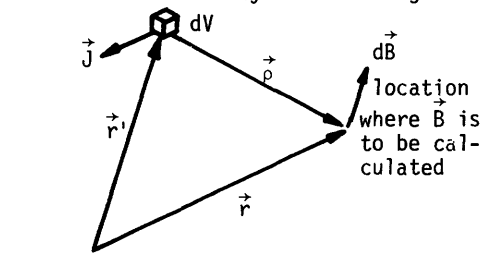

for filamentary currents:

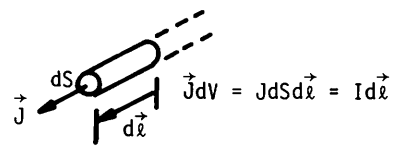

Fig. 20B1. Definitions of the vectors $\vec{r}$, $\vec{r}'$, and $\vec{\rho}$ for calculation of the magnetic field.

$$\vec{B}(r) = \int d\vec{B} = \frac{\mu_0}{4\pi} \int \frac{dV \, \vec{J} \times \vec{\rho}}{\rho^3} \quad \text{(T)} \quad . \qquad (20B2)$$

For the case of filamentary currents (thin wires), $\vec{J}dV = Id\vec{\ell}$ (Fig. 20B1), so this equation simplifies to

$$\vec{B}(r) = \frac{\mu_0 I}{4\pi} \int_{\text{wire}} \frac{d\vec{\ell} \times \vec{\rho}}{\rho^3} \quad \text{(T)} \quad , \qquad (20B3)$$

where the integration path is along the wire in the direction of current flow.

If magnetic materials, such as plain steel and soft iron, are nearby, the magnetic field will be distorted, and the results of these equations will be inaccurate. In calculating the total magnetic field at a point, the volume of integration of Eq. (20B2) should include both the magnet coils and the plasma, since plasma currents can be significant.

For the case in which the currents $\vec{J}$ vary in time, there is a slight delay between the time $\vec{J}$ changes at $\vec{r}'$ and the time when the effect is observed at $\vec{r}$, but this delay time is negligibly short for cases of interest, and we can use Eq. (20B2) to calculate $\vec{B}(\vec{r},t)$ corresponding to $\vec{J}(\vec{r}',t)$ as if the "action at a distance" were instantaneous.

For cases in which angular symmetry exists, it is sometimes easier to calculate B from the integral form of Ampere's Law (5B11) (ignoring the $\partial\vec{E}/\partial t$ term)

$$\oint d\vec{\ell}\cdot\vec{B} = \mu_0 \iint d\vec{S}\cdot\vec{J} = \mu_0 I(\text{enclosed}) \quad , \tag{20B4}$$

where $d\vec{S}$ is integrated over the surface bounded by the closed curve of the line integral $\oint d\vec{\ell}$. Use of Eqs. (20B2)-(20B4) will be clarified by a few examples.

The magnetic field may also be calculated from $\vec{B} = \vec{\nabla}\times\vec{A}$, where the magnetic vector potential $\vec{A}$ is defined by

$$\vec{A} = \frac{\mu_0}{4\pi}\int \frac{d\vec{V}\vec{J}}{\rho} = \frac{\mu_0 I}{4\pi}\int \frac{d\vec{\ell}}{\rho} \tag{20B5}$$

The direction of the magnetic field lines can be determined from the "right hand rule", Fig. 5B1.

straight wires

The magnetic field from a straight wire carrying a current I may be found from Eq. (20B3) using the geometry illustrated in Fig. 20B2. According to the Biot-Savart Law,

$$dB = \frac{\mu_0 I}{4\pi}\frac{d\vec{\ell}\times\vec{\rho}}{\rho^3} = \frac{\mu_0 I}{4\pi}\frac{d\ell\cos\theta}{\rho^2}$$

$$= \frac{\mu_0 I}{4\pi}\frac{d(r\tan\theta)\cos\theta}{(r/\cos\theta)^2} = \frac{\mu_0 I}{4\pi r}\cos\theta d\theta \tag{20B6}$$

since r is a constant. If the ends of the wire subtend angles θ_1 and θ_2, then

$$B(r) = \frac{\mu_0 I}{4\pi r}\int_{\theta_1}^{\theta_2} d\theta\cos\theta$$

$$= \frac{\mu_0 I(\sin\theta_2 - \sin\theta_1)}{4\pi r} \quad , \tag{20B7}$$

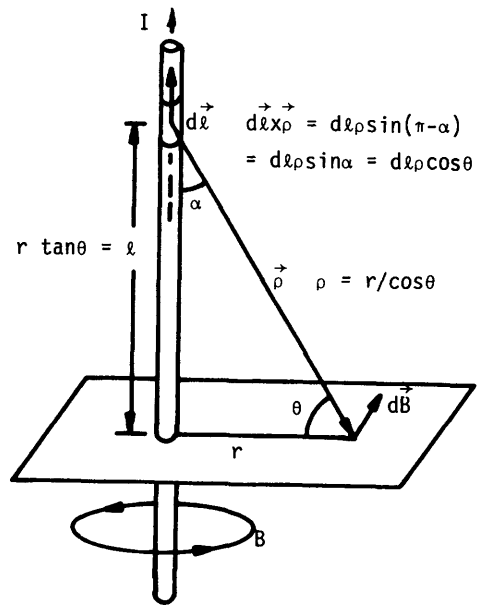

Fig. 20B2. Geometry for calculation of the magnetic field of a straight wire from the Biot-Savart Law.

with the magnetic field lines forming circles around the wire. For the special case of an infinitely long wire, $\theta_2 = \pi/2$ and $\theta_1 = -\pi/2$, so

$$B(r) = \mu_0 I/2\pi r \quad . \tag{20B8}$$

This result can also be derived from Eq. (20B4), using one of the circular field lines as the integration curve. Then Eq. (20B4) becomes

$$2\pi r B(r) = \mu_0 I \quad .$$

toruses and solenoids

Fig. 20B3 shows a torus with a wire coil wrapped around it. The torus is partially cut away to show the integration path for Eq. (20B4). If the torus has N turns of wire each carrying the same current I, then Eq. (20B4) reduces to

$$2\pi R B(R) = \mu_0 NI \quad , \quad B(R) = \mu_0 NI/2\pi R \quad . \tag{20B9}$$

(This equation is similar to Eq. 20B8 for a straight wire.) For values of R less than the radius where the coils are, there is no enclosed current, and B(R) = 0. For values of R outside the outer windings, the currents of the outer windings cancel the currents of the inner windings, the net enclosed current is again zero, and B(R) = 0. Let $L = 2\pi R$. In the limit as the major radius of the torus becomes infinitely large, its radius of curvature is infinitely large, and each section of the torus is like a section of a straight solenoid. Thus, we can deduce that the field in a long straight solenoid is

$$B = \mu_0 (N/L) I \tag{20B10}$$

where N/L is the number of turns per unit length. These results do not depend upon the shape of the cross sections of the torus or solenoid. The accuracy with which an actual toroidal field agrees with Eq. (20B9) depends upon how uniform and closely spaced the toroidal field windings are, and likewise for the solenoid. If there are few windings widely spaced, then better accuracy can be obtained by integrating Eq. (20B3) along the path of the windings.

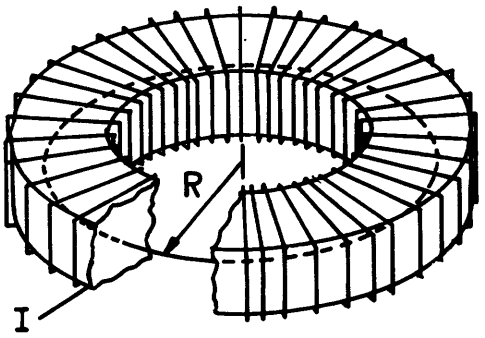

Fig. 20B3. A wire coil wrapped around a torus. The circle of radius R is the integration path for Eq. (20B4).

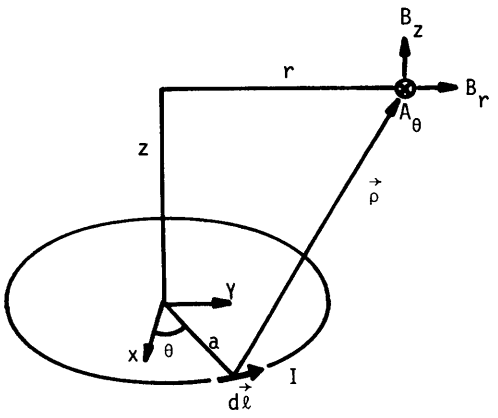

Fig. 20B4. Geometry for calculation of the magnetic field due to a circular loop of radius a located in the x-y plane and carrying a current I.

circular loops

In practice, toroidal and solenoidal magnetic fields are often produced by using a set of circular magnet coils. The resultant field may then be calculated by adding the fields of the individual coils, and each coil may be approximated as a set of circular loops. Therefore, the field produced by a circular loop of radius a carrying current I, as shown in Fig. 20B4, is of fundamental importance.

The resultant magnetic field has components in the r and z directions (cylindrical geometry). The Biot-Savart Eq. (20B3) cannot be integrated analytically for this case. However, Eq. (20B5) for the vector potential may be expressed in terms of "complete elliptic integrals"

$$K(k) \equiv \int_0^{\pi/2} d\theta/(1-k^2\sin^2\theta)^{\frac{1}{2}} \quad , \quad E(k) \equiv \int_0^{\pi/2} d\theta(1-k^2\sin^2\theta)^{\frac{1}{2}} \quad . \tag{20B11}$$

Values of these integrals are given in Table 20B1. If we let

$$k = \left[\frac{4ra}{z^2 + (r + a)^2}\right]^{\frac{1}{2}} \quad , \tag{20B12}$$

then the resulting equation for $\vec{A}$ has only a θ component, given by

$$A_\theta = \frac{\mu_0 I a^{\frac{1}{2}}}{2\pi r^{\frac{1}{2}}}\left[(\frac{2}{k} - k)K(k) - \frac{2}{k}E(k)\right] \tag{20B13}$$

(Shadowitz, 1975). After taking the curl of $\vec{A}$, the components of $\vec{B}$ are found to be

$$B_r = -\frac{\partial A_\theta}{\partial z} = \frac{\mu_0 I k z}{4\pi(ar^3)^{\frac{1}{2}}}\left[-K(k) + \frac{(1 - .5k^2)}{(1 - k^2)}E(k)\right]$$

$$B_z = \frac{1}{r}\frac{\partial}{\partial r} rA\theta = \frac{\mu_0 I k}{4\pi(ar)^{\frac{1}{2}}}\left[K(k) + \frac{(a + r)k^2 - 2r}{2r(1 - k^2)}E(k)\right] \quad . \tag{20B14}$$

The elliptic integrals can be computed using the IBM computer subroutine CEL2 or with polynomial approximations from Abramowitz and Stegun (1964).

For a point on the axis, the field components can be found by letting $r \to 0$ and using L'Hospital's rule, with the result that $B_r = 0$ and

$$B_z = \frac{\mu_0 I a^2}{2(a^2 + z^2)^{3/2}} \quad . \tag{20B15}$$

This result can also be obtained by direct use of Eq. (20B3) with Fig. 20B4 for the case of $r = 0$.

Table 20B1. Complete elliptic integrals. From Abramowitz and Stegun, 1964.

k^2	K(k)	E(k)	k^2	K(k)	E(k)
0.00	1.57080	1.57080			
0.01	1.57474	1.56686	0.51	1.86264	1.34559
0.02	1.57874	1.56291	0.52	1.87140	1.34051
0.03	1.58278	1.55895	0.53	1.88036	1.33538
0.04	1.58687	1.55497	0.54	1.88953	1.33022
0.05	1.59100	1.55097	0.55	1.89892	1.32502
0.06	1.59519	1.54696	0.56	1.90855	1.31979
0.07	1.59942	1.54293	0.57	1.91841	1.31451
0.08	1.60371	1.53889	0.58	1.92853	1.30919
0.09	1.60805	1.53483	0.59	1.93891	1.30383
0.10	1.61244	1.53076	0.60	1.94957	1.29843
0.11	1.61689	1.52667	0.61	1.96052	1.29298
0.12	1.62139	1.52256	0.62	1.97178	1.28748
0.13	1.62595	1.51843	0.63	1.98337	1.28194
0.14	1.63058	1.51428	0.64	1.99530	1.27635
0.15	1.63526	1.51012	0.65	2.00760	1.27071
0.16	1.64000	1.50594	0.66	2.02028	1.26501
0.17	1.64481	1.50174	0.67	2.03337	1.25926
0.18	1.64968	1.49753	0.68	2.04689	1.25346
0.19	1.65462	1.49329	0.69	2.06088	1.24759
0.20	1.65962	1.48904	0.70	2.07536	1.24167
0.21	1.66470	1.48476	0.71	2.09037	1.23568
0.22	1.66985	1.48047	0.72	2.10595	1.22963
0.23	1.67507	1.47615	0.73	2.12213	1.22351
0.24	1.68037	1.47182	0.74	2.13897	1.21732
0.25	1.68575	1.46746	0.75	2.15652	1.21106
0.26	1.69121	1.46309	0.76	2.17483	1.20471
0.27	1.69675	1.45869	0.77	2.19397	1.19829
0.28	1.70237	1.45427	0.78	2.21402	1.19178
0.29	1.70809	1.44983	0.79	2.23507	1.18518
0.30	1.71389	1.44536	0.80	2.25721	1.17849
0.31	1.71978	1.44088	0.81	2.28055	1.17170
0.32	1.72578	1.43637	0.82	2.30523	1.16480
0.33	1.73186	1.43183	0.83	2.33141	1.15779
0.34	1.73806	1.42727	0.84	2.35926	1.15066
0.35	1.74435	1.42269	0.85	2.38902	1.14340
0.36	1.75075	1.41808	0.86	2.42093	1.13600
0.37	1.75727	1.41345	0.87	2.45534	1.12845
0.38	1.76390	1.40879	0.88	2.49264	1.12074
0.39	1.77065	1.40411	0.89	2.53333	1.11286
0.40	1.77752	1.39939	0.90	2.57809	1.10477
0.41	1.78452	1.39465	0.91	2.62777	1.09648
0.42	1.79165	1.38988	0.92	2.68355	1.08794
0.43	1.79892	1.38509	0.93	2.74707	1.07912
0.44	1.80633	1.38026	0.94	2.82075	1.06999
0.45	1.81388	1.37540	0.95	2.90834	1.06047
0.46	1.82159	1.37051	0.96	3.01611	1.05050
0.47	1.82946	1.36560	0.97	3.15587	1.03995
0.48	1.83749	1.36064	0.98	3.35414	1.02859
0.49	1.84569	1.35566	0.99	3.69564	1.01599
0.50	1.85407	1.35064	1.00	∞	1.00000

EXAMPLE PROBLEM 20B1

A circular coil of radius 0.5 m carries a current of 100 kA. Find the magnetic field 0.4 m from the axis of the coil at a distance of 0.6 m from the plane of the coil.

(so $k^2 = .6837607$, $K = 2.05215$, $E = 1.25125$

Here a = 0.5, r = 0.4, and z = 0.6,) (interpolating). Then, from Eqs. (20B14) it is found that $B_r = 0.0025$ T and $B_z = 0.027$ T.

circular coils with rectangular cross sections

Instead of treating a circular coil with rectangular cross section as a collection of circular loops, one can use the method of Hart (1967), illustrated in Fig. 20B5. If we let $R_1 = r_1/r$, $R_2 = r_2/r$, $Z_1 = z_1/r$, and $Z_2 = z_2/r$,

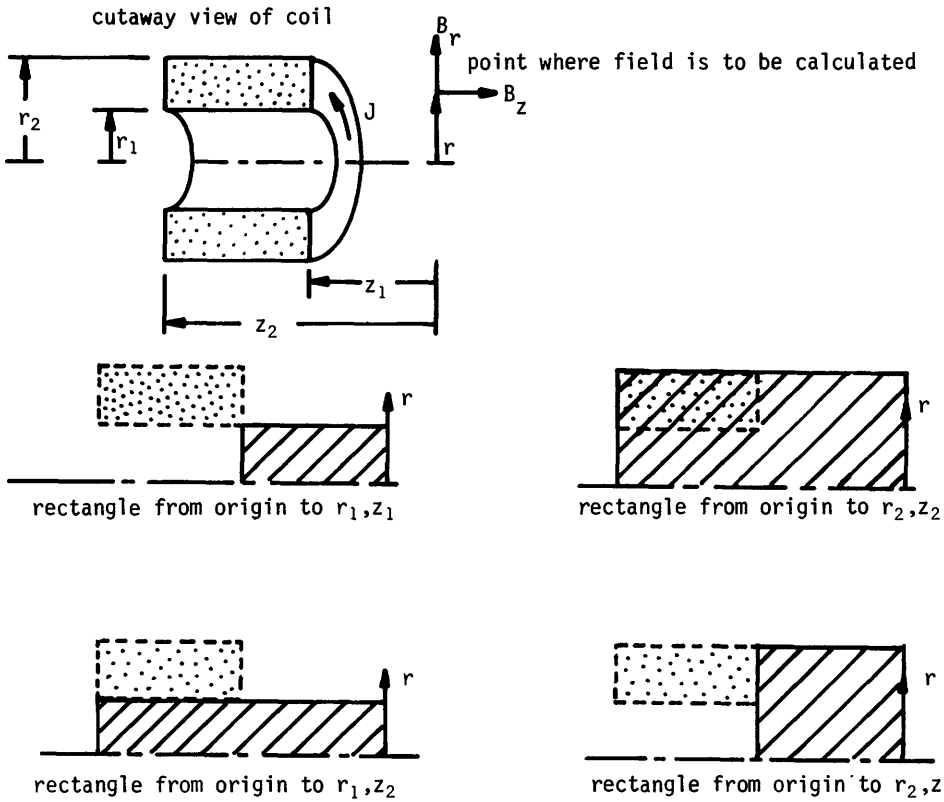

Fig. 20B5. Cutaway view of a circular coil with rectangular cross section. The field is to be calculated at a distance r from the axis. A function describing the field at r due to a rectangular coil extending from the origin to some point is known. The area of the coil can be represented as the sum of the rectangles: (0 to r_1, z_1) + (0 to r_2, z_2) - (0 to r_2, z_1) - (0 to r_1, z_2). Based on P. J. Hart, Universal Tables for Magnetic Fields of Filamentary and Distributed Circular Currents, American Elsevier, NY, 1967.

then the desired magnetic field components are found to be

$$B_r = 10^{-9}Jr[S_r(R_1,Z_1)+S_r(R_2,Z_2)-S_r(R_2,Z_1)-S_r(R_1,Z_2)]$$

$$B_z = 10^{-9}Jr[S_z(R_1,Z_1)+S_z(R_2,Z_2)-S_z(R_2,Z_1)-S_z(R_1,Z_2)] \qquad (20B16)$$

where J is the coil current density (A/m^2), r is in meters, and B_r, B_z are in Tesla. The functions $S_r(R,Z)$ and $S_z(R,Z)$ are shown in Figs. 20B6-20B8. More accurate values of these functions are tabulated by Hart (1967).

EXAMPLE PROBLEM 20B2

Find the field at a radius of 0.7 m for a coil with r_1 = 0.5 m, r_2 = 0.8 m, z_1 = 0.4 m, z_2 = 1.0 m, and $J = 10^7$ A/m^2.

The dimensionless variables are R_1 = .7142, R_2 = 1.143, Z_1 = .5714, and Z_2 = 1.429. From the tables of Hart (1967) it is found that

	$S(R_1,Z_1)$	$S(R_2,Z_2)$	$-S(R_2,Z_1)$	$-S(R_1,Z_2)$		net
S_r =	19.48	231.9	-171.45	-36.64	=	43.3
S_z =	-16.2	48.3	-11.13	+9.92	=	30.9

The resultant field components from Eqs. (20B16) are therefore B_r = .303 T, B_z = .216 T. Use of graphical data from Figs. 20B7-20B9 results in values of B_r and B_z which are within 10% of these correct values.

Accuracy is poorest for coils with very small cross sectional areas, because the S values are close in magnitude. For that case the circular loop approximation is better.

For the special case in which the field is to be calculated between the ends of the coil, as shown in Fig. 20B9, the coil can be divided into two sections, one on the right side and one on the left side. Then the B_r and B_z from the two sections can be added in accordance with the right hand rule to get the net fields. Since $S_r(R,0) = S_r(0,Z) = S_z(R,0) = S_z(0,Z) = 0$, the S functions are zero at the center points. The resulting equations are given at the bottom of the figure. The B_r contributions from the two segments have opposite directions, while the B_z contributions enhance each other.

Circular coils of arbitrary shapes may be represented as sums of rectangular sections.

Along the axis of the solenoid, $r \to 0$, and the S functions become infinite, so another method is used.

axial field of solenoid

A simpler formula can be derived for the field on the axis of a solenoid, as illustrated in Fig. 20B10.

Replacing I by Jdrdz in Eq. (20B15), we find the

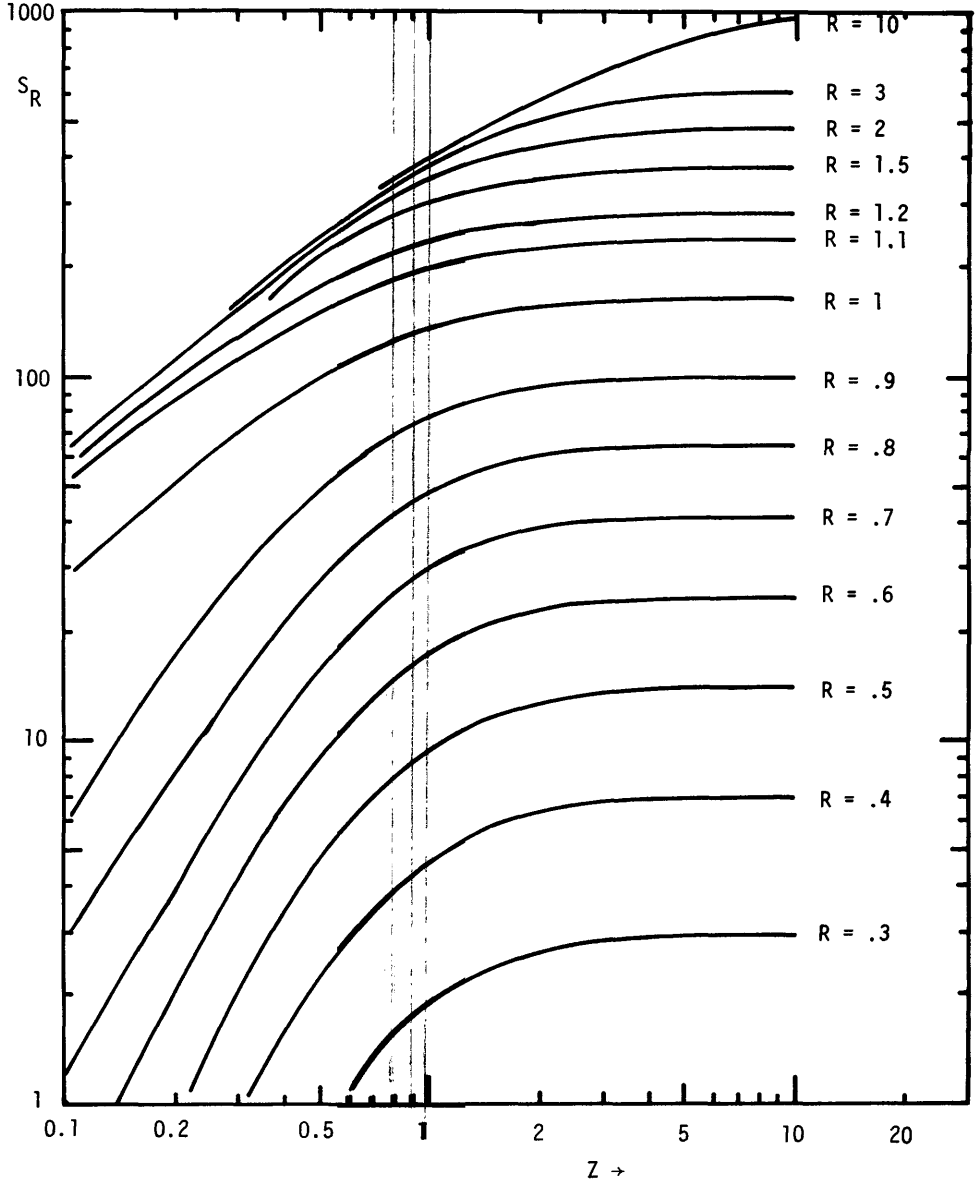

Fig. 20B6. S_R vs. Z for various values of R. Based on data of P. J. Hart, Universal Tables of Magnetic Fields of Filamentary and Distributed Circular Currents, American Elsevier, New York, 1967, Tables I-A and I-B.

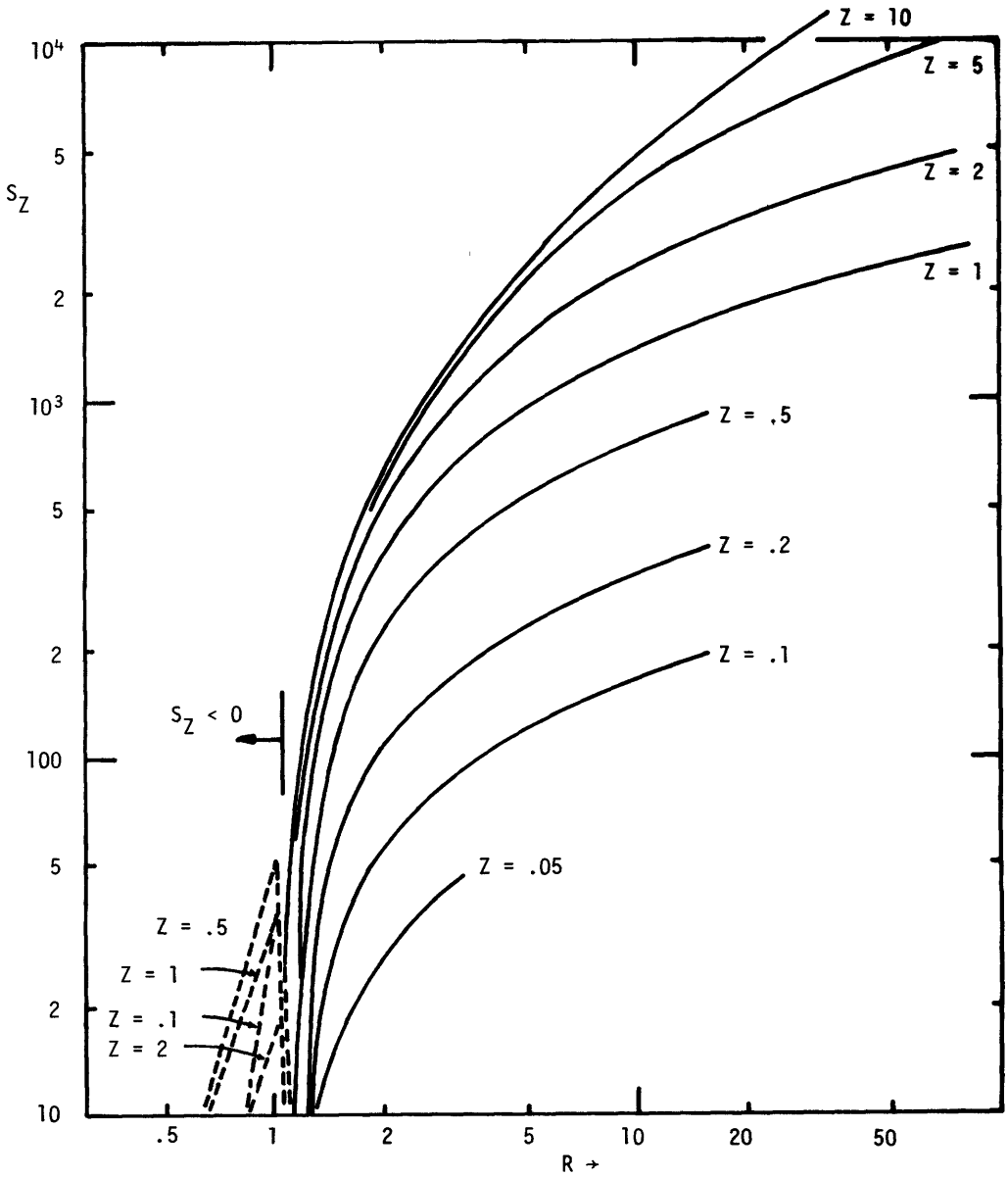

Fig. 20B7. S_z vs. R for various values of Z. For $R \lesssim 1.1$, the S_z values are negative (dashed curves). For R < 1.4 see Fig 20B8. Based on data of P. J. Hart, Universal Tables for Magnetic Fields of Filamentary and Distributed Circular Currents, American Elsevier, New York, 1967, Tables I-A and I-B.

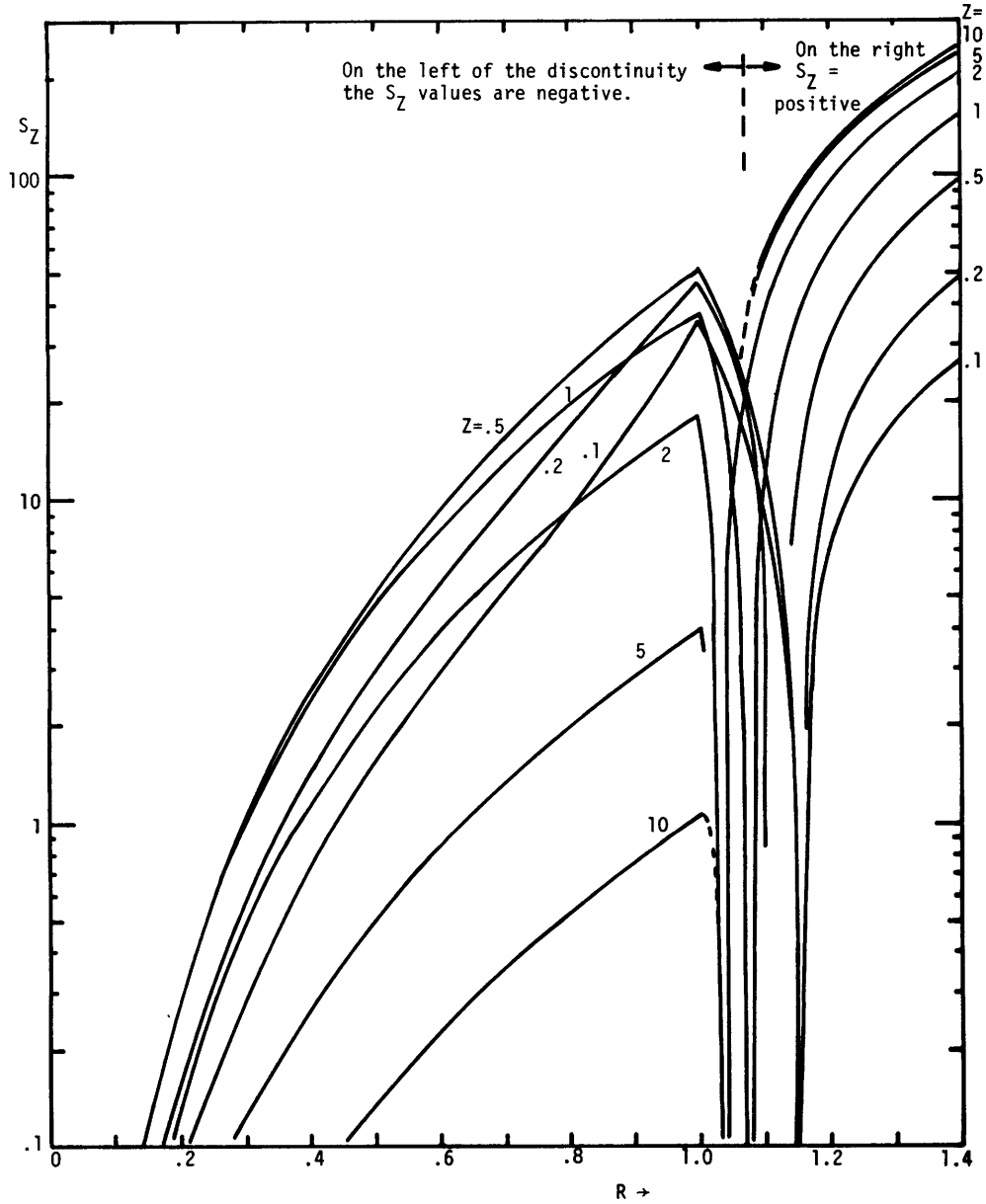

Fig. 20B8. Variation of S_z with R for various values of Z. For larger R, see Fig. 20B7. Based on data of P. J. Hart, Universal Tables for Magnetic Fields of Filamentary and Distributed Circular Currents, American Elsevier, New York, 1967, Tables I-A and I-B.

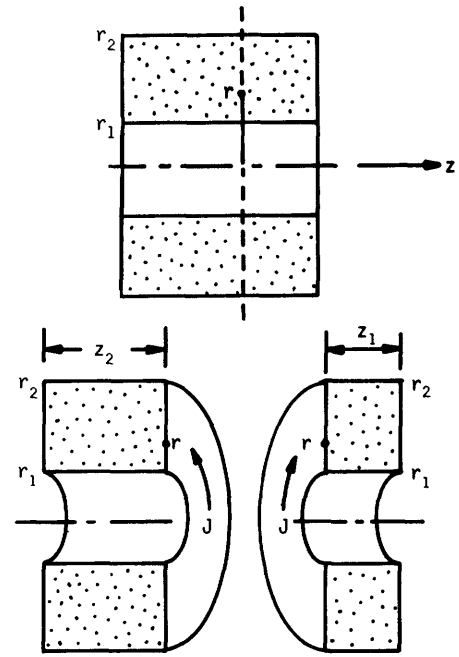

Fig. 20B9. Illustration of the use of Hart's method for the case in which the point where the field is to be calculated lies between the ends of the coil. From the right hand rule, it can be seen that B_r is positive for the left hand coil and negative for the right hand coil, while the B_z components are additive. Therefore,

$$B_r = 10^{-9}Jr\,[S_r(R_2,Z_2)-S_r(R_1,Z_2) - S_r(R_2,Z_1)+S_r(R_1,Z_1)]$$

$$B_z = 10^{-9}Jr\,[S_z(R_2,Z_2)-S_z(R_1,Z_2) +S_z(R_2,Z_1)-S_z(R_1,Z_1)]$$

for all values of r. Based on P. J. Hart (1967).

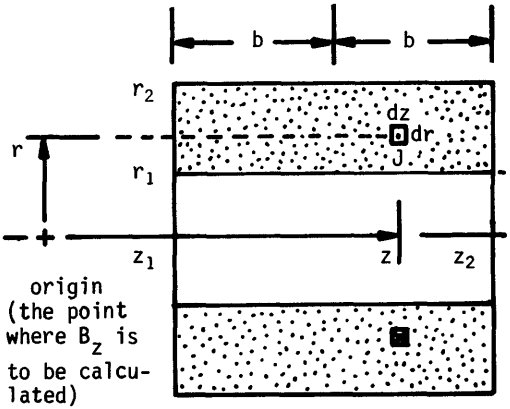

Fig. 20B10. Geometry for finding the field on the axis of a solenoid. If the field is to be calculated inside the solenoid, z_1 will be negative; and if B_z is to be found to the right of the solenoid, both z_1 and z_2 will be negative.

central field contribution of a loop at r,z to be

$$dB_z = \frac{\mu_0\, J dr dz\, r^2}{2(r^2+z^2)^{3/2}} \quad . \qquad (20B17)$$

The total field is the integral of dB_z over the coil area:

$$B_z = \frac{\mu_0\, J}{2}\int_{r_1}^{r_2} dr r^2 \int_{z_1}^{z_2} \frac{dz}{(r^2+z^2)^{3/2}}$$

$$= \frac{\mu_0\, J}{2}\left\{ z_2 \ell n\left[\frac{r_2+(r_2^2+z_2^2)^{\frac{1}{2}}}{r_1+(r_1^2+z_2^2)^{\frac{1}{2}}}\right] - z_1 \ell n\left[\frac{r_2+(r_2^2+z_1^2)^{\frac{1}{2}}}{r_1+(r_1^2+z_1^2)^{\frac{1}{2}}}\right]\right\} \text{(Tesla)}. \qquad (20B18).$$

At the *center* of the solenoid, $z_1 = -b$ and $z_2 = b$, so

$$B_z = \mu_0 Jb\, \ell n\left[\frac{r_2+(r_2^2+b^2)^{\frac{1}{2}}}{r_1+(r_1^2+b^2)^{\frac{1}{2}}}\right] \text{(Tesla)}. \qquad (20B19)$$

complex coil shapes

Some coils are not circular, however. Yin-Yang coils (mirror experiments) and helical windings (stellarators and torsatrons) require the use of sophisticated computer codes. The code MAFCO calculates the field due to any arbitrary three-dimensional current elements. It also has subroutines for handling circular loops, arcs, helices, and straight line segments (Perkins and Brown, 1966). To use MAFCO, one specifies the coordinates of the coil segments and the locations where the magnetic field is to be calculated. Then the program prints out the magnetic field components at all desired locations. The program can be directed to follow the path of any given magnetic field line and to print out the coordinates of its trajectory, permitting maps of magnetic field line paths to be made. An example of such a field line map can be seen in Fig. 11A2.

20C. Coil Forces

Massive structural supports must be provided to sustain the enormous forces produced by interaction of the magnet coil currents with the magnetic field. The basic equation for the differential force on a volume dV of conductor with current density $\vec{J}$ in a magnetic induction $\vec{B}$ is

$$d\vec{F} = \vec{J}x\vec{B}\ dV \quad \text{(Newton)}. \tag{20C1}$$

For thin wires, $\vec{J}dV$ may again be replaced by $Id\vec{\ell}$. The total force on a given volume of conductor is equal to the integral of $d\vec{F}$ over that volume.

long-parallel wires

The case of two long, parallel wires carrying currents I_1 and I_2 is illustrated in Fig. 20C1. With parallel currents, the wires attract each other, and with anti-parallel currents, they repel each other, hence, the saying "Like currents attract, unlike currents repel". This rule also holds for the case of two coaxial circular loops. (This is the opposite of the situation for electrostatic charges, where "Like charges repel, unlike charges attract".) Since $B_1 = \mu_0 I_1/2\pi r$

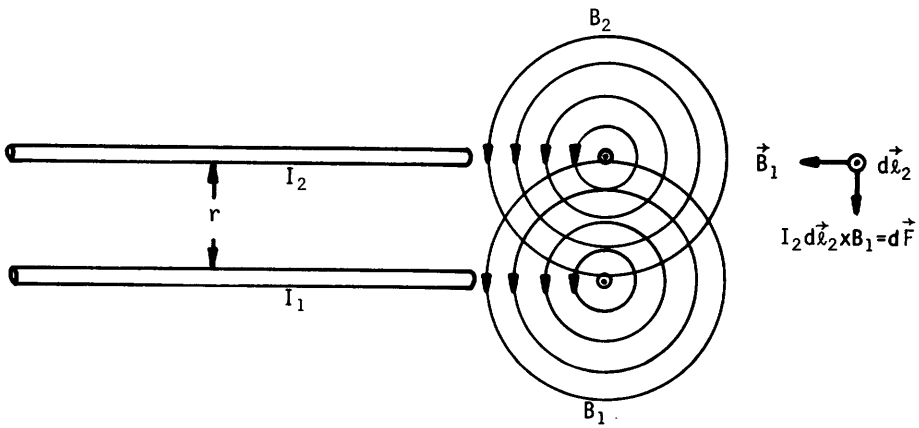

Fig. 20C1. Calculation of forces between two long, parallel wires.

(Eq.20B8), the magnitude of the force per unit length on wire 2 is

$$dF/d\ell = \mu_0 I_1 I_2/2\pi r \quad \text{(Newton/meter)} \quad . \tag{20C2}$$

The force per unit length on wire 1 has the same magnitude.

coaxial circular loops

For the case of two coaxial circular loops with equal radii a (Fig. 20C2), the B_z field produces radial forces on the coils, which create internal stress, but do not cause coil motion, since the net force on the coil as a whole is zero. The radial field B_r produces an axial thrust F_z, tending to pull the coils together, if they have like currents, or to push the coils apart, if they have opposite currents. The total force on a coil is

$$F_z = \int dF_z = I_2 B_{r1} \int d\ell_2 = 2\pi a I_2 B_{r1} \quad \text{(N)} \tag{20C3}$$

where B_{r1} may be evaluated from Eq. (20B14).

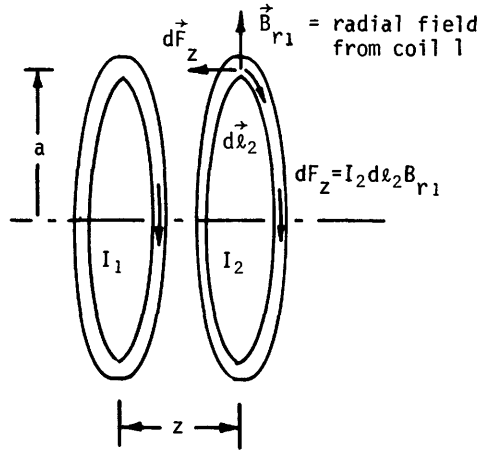

Fig. 20C2. Two coaxial circular current loops.

EXAMPLE PROBLEM 20C1

Two coaxial coils with radii of 1 m are separated by z = 1 m. If each coil has I = 1 MA, find the force between them.

For this case, it is found that $k^2 = 0.8$, $k = 0.8944$, $K = 2.257$, and $E = 1.178$. Then $B_r = 0.0697$ T, and $F = 4.38 \times 10^5$ N (98,400 lbs).

solenoids

The cross section of a long solenoid is illustrated in Fig. 20C3. Within the coil, $r_1 < r < r_2$, and

$$B(r) = B(r_2 - r)/\Delta r \quad , \tag{20C6}$$

assuming the current density to be uniform. Using Eq. (20C1), the outward force on the small segment of the free body diagram is found to be

$$F_r = \int_{r_1}^{r_2} dF_r = \int_{r_1}^{r_2} JB \, dV = J \int_{r_1}^{r_2} dr r d\theta dz B(r_2 - r)/\Delta r$$

$$F_r = \frac{JBr_1 \Delta r d\theta dz}{2} \left(1 + \frac{\Delta r}{3r_1}\right) \tag{20C7}$$

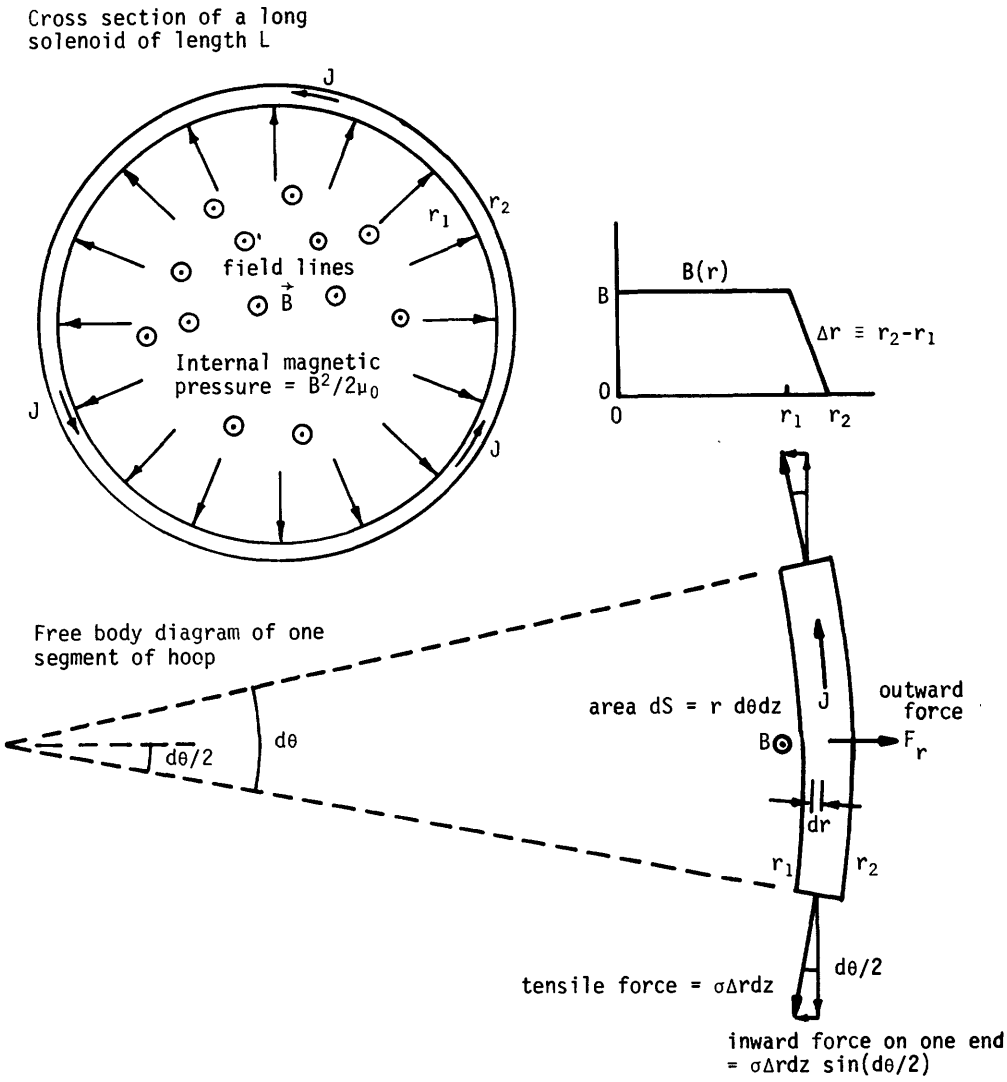

Fig. 20C3. The cross section of a long solenoid, radial variation of magnetic field, and free body diagram of one segment of the coil.

where r_2 was eliminated using $r_2 = r_1 + \Delta r$. Since the total coil current NI = JΔrL, Eq. (20B10) may be written

$$B = \mu_0(N/L)I = \mu_0 J\Delta r \quad . \tag{20C8}$$

If J is eliminated between Eqs. (20C8) and (20C7), the result is

$$F_r = (B^2/2\mu_0)r_1 d\theta dz(1 + \Delta r/3r_1) \quad (N) \; . \tag{20C9}$$

For very small Δr, this is equal to the magnetic pressure times the inner surface area. At equilibrium, the inward components of the tensile forces in the two ends of the segment must balance this outward force, and

$$(B^2/2\mu_0)r_1 d\theta dz(1 + \Delta r/3r_1) = 2\sigma\Delta r dz \sin(d\theta/2) \simeq \sigma\Delta r dz d\theta \ . \qquad (20C10)$$

The resultant average tensile stress is found to be

$$\sigma = (B^2/2\mu_0)\left(\frac{r_1}{\Delta r} + \frac{1}{3}\right) \quad (Pa). \qquad (20C11)$$

For example, if $r_1/\Delta r = 5$ and $B = 10$ T, then $\sigma = 212$ MPa (31,000 psi). This is near the yield stress of copper, which is about 280 MPa (40,000 psi).

force-reduced torsatron coils

Torsatron coils were illustrated in Fig. 14A6. For the case of a reactor, the forces on these coils could become enormous, but it is possible to minimize the forces by using a *force-reduced* coil geometry. The principle of force reduction is illustrated in Fig. 20C4. Long, straight, parallel conductors with currents in the same direction would have radially inward attractive forces between them. A solenoid, on the other hand, has radially outwards magnetic pressure forces. A long straight helix, then, has a combination of the radially inward and radially outward forces. If the pitch of the solenoid is properly chosen, the two radial forces cancel out, resulting in a "force-free" helical winding set.

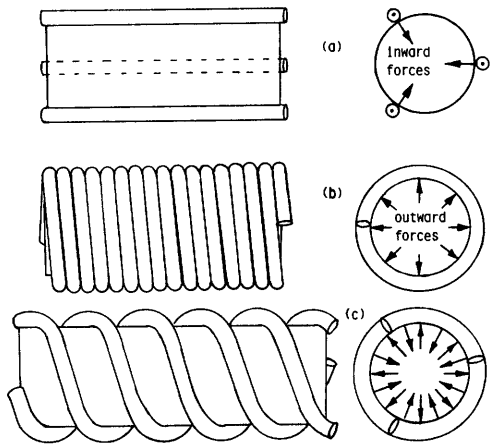

Fig. 20C4. Conductor configurations around a long, straight cylinder. (a) rods with parallel currents, (b) a solenoid, (c) helices. The helix has both the inward forces of the rods and the outward forces of the solenoid.

When the helical windings are bent into a torus, an additional vertical magnetic field is produced, resulting in coil forces. However, by adding a pair of large, circular coils around the outside of the torus to produce an opposite vertical field, the vertical field may be nearly cancelled out, again resulting in low coil forces. In one torsatron reactor design, the resultant coil forces are about 1/30 of what they would be without using the force-reduced geometry. In addition to nulling the vertical field of the helical coils, the vertical field coils transfer the radial forces to a convenient external structure and greatly reduce stray magnetic fields outside the reactor. (To optimize plasma confinement, it is desirable to shift the magnetic axis outwards a little, which can be accomplished with trim coils producing about 5% of the vertical field.)

For an $\ell = 3$ configuration, calculations of force-reduction and plasma confinement indicate that the optimum pitch angle is about 42°, and the optimum aspect ratio $R/a_c \sim 7$, where a_c is the minor radius of the helical windings. By proper selection of the number of field periods around the torus, the three helical windings can be connected end to end (electrically in series), so that they all

have the same current.

coil design considerations

Computer codes, such as FORCE (Henning, 1966), are used to calculate the forces at any point in a coil system. Since the toroidal field decreases with major radius, the azimuthal coil stress tends to be greatest at small R. Large toroidal field (TF) coils can be shaped to minimize bending stresses (Gralnick et al, 1979). The magnetic forces on TF coils tend to increase the coil radius (tensile strength), to decrease the major radius of the torus (due to attraction between coils), and to flip the coils over (due to interaction with poloidal fields). In designing structural elements to sustain coil forces, stress concentrations, cyclic fatigue, creep, and thermal stress must be taken into account (Chapter 24).

Slight deviations of the magnetic field from the desired shape, called *field errors,* can spoil plasma confinement. To minimize field errors, the following steps are taken:

* Coil winding is done very carefully to achieve the desired shape.
* Coils are aligned with great accuracy.
* Massive coil supports keep coil deflections within tolerable limits ($\sim$ mm).
* The coils may be connected in series electrically, to equalize their currents.
* Stray magnetic fields from current leads and nearby ferrous objects are carefully accounted for.

20D. Power and Cooling Water Requirements

relation of magnetic field to coil power

The power dissipated in a differential volume dV by a current density J_c (in the copper) is

$$dP = \eta J_c^2 dV \qquad \text{(Watts)} \qquad (20D1)$$

where η is the resistivity of the conductor (Ohm-m). For a uniform-current-density solenoid with packing fraction λ = (copper volume)/(coil volume), the total power required is

$$P = \int_{\substack{\text{volume}\\ \text{of copper}}} dP = \eta J_c^2 \cdot L\pi(r_2^2 - r_1^2)\lambda \qquad \text{(W)}, \qquad J_c = J/\lambda \qquad (20D2)$$

where L is the length of the solenoid. We can relate the power to the magnetic field by eliminating J between Eqs. (20B19) and (20D2). If we define dimensionless variables $\alpha = r_2/r_1$ and $\beta = L/2r_1$, the result may be expressed in the form

$$B_z = \lambda^{3/2}\mu_0 g(\alpha,\beta)(P/\eta r_1)^{\frac{1}{2}} \qquad \text{(Tesla)}, \qquad (20D3)$$

where

$$g(\alpha,\beta) \equiv \left[\frac{\beta}{2\pi(\alpha^2-1)}\right]^{\frac{1}{2}} \ln\left[\frac{\alpha+(\alpha^2+\beta^2)^{\frac{1}{2}}}{1+(1+\beta^2)^{\frac{1}{2}}}\right]$$

[This g is different from $G(\alpha,\beta)$ defined by Montgomery (1967). His $G(\alpha,\beta) = (4\pi/10)g(\alpha,\beta)$.] Values of $g(\alpha,\beta)$ are shown in Fig. 20D1. The maximum value $g_{max} = 0.142$ at $\alpha = 3$, $\beta = 2$. For copper

$$\eta = [1.68 + .0068(T-293)]\times10^{-8} \text{ Ohm-m.}$$
$$(270 < T < 400\,K) \qquad (20D4)$$

Taking $\lambda = 0.9$ and $T = 340$ K, the maximum value of B attainable in a uniform-current-density solenoid with rectangular cross section is

$$B_{max} = 0.9\mu_0 g_{max}(P/\eta r_1)^{\frac{1}{2}}$$
$$= 0.0011(P/r_1)^{\frac{1}{2}} \text{ (T)}.$$
$$P \simeq r_1(900B)^2 \text{ (W)}. \qquad (20D5)$$

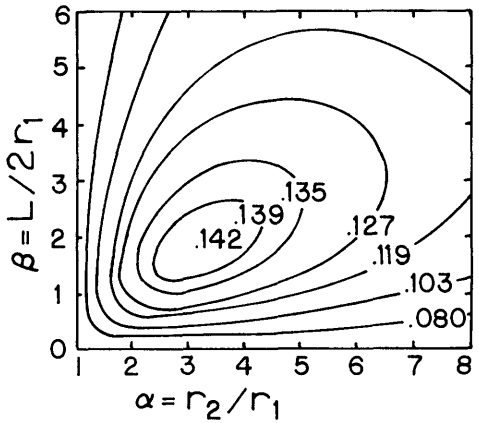

Fig. 20D1. Contours of constant $g(\alpha,\beta)$ plotted on the α-β plane. Based on data of D. B. Montgomery, Solenoid Magnet Design, Wiley, New York, 1969, Fig. 1.5.

For example, if we have 100 kW available for a coil with $r_1 = 0.1$ m, the optimum dimensions are $r_2 = 0.3$ m and $L = 4r_1 = 0.4$ m, and the maximum attainable field $B_{max} = 1.1$ Tesla. We can also invert Eqs. (20D3), (20D5) to find the required power to produce a given field in a coil with a given r_1. For example, if we want to produce $B = 10$ T in a coil with $r_1 = 3$ m, the required power $P \simeq 240$ MW. For a torus, many coils are needed. The required power becomes enormous if water-cooled copper magnets are used in fusion reactor designs with high fields and large coil radii.

The above analysis was restricted to uniform-current-density coils with rectangular cross section. By varying the current density and coil cross sectional shape, higher values of $g(\alpha,\beta)$ can be obtained. The highest g attainable is about 0.19. The value of B_{max} can also be increased by using cryogenic coolants, such as liquid nitrogen at 77 K, to lower the resistivity η.

cooling water

The thermal power removed by the coolant is

$$P = C\rho_m \Delta T(dV/dt) \qquad \text{(Watts)} \qquad (20D6)$$

where C is the specific heat of the coolant (J/kg-K), ρ_m is its mass density (kg/m^3), dV/dt is its volumetric flow rate (m^3/s), and ΔT is the temperature rise of the coolant as it passes through the coil. Equating this power removed to the power dissipated determines the required coolant flow rate. The volumetric flow rate is related to the average flow speed v in a given coolant channel by the equation

$$(dV/dt)_{channel} = A_w v \qquad (m^3/s) \qquad (20D7)$$

where A_w is the cross sectional area of the channel. Cooling water is usually

deionized to prevent mineral deposits from clogging channels and decreasing A_w.

The pressure drop of the coolant flowing through a tube of length L_c and diameter D depends upon the Reynold's Number

$$Re = Dv\rho_m/\mu \qquad \text{(dimensionless)}, \tag{20D8}$$

where μ is the fluid viscosity (Pa-s). The pressure drop may be written

$$\Delta p = fL_c\rho_m v^2/2D \qquad \text{(Pa)} \tag{20D9}$$

where the "friction factor" f is given as a function of Re in Fig. 20D2.

The pumping power required to produce a pressure rise Δp and flow rate dV/dt is

$$P_c = \Delta p(dV/dt)/\eta_p \qquad \text{(Watts)}, \tag{20D10}$$

where η_p is the pump efficiency.

The most commonly used coolant is water, because of its favorable properties and low cost. The properties of water at 293 K (20 C) are:

$$C = 4182 \text{ J/kg-K}$$
$$\rho_m = 998 \text{ kg/m}^3$$
$$\mu = .001002 \text{ Pa-s} \quad . \tag{20D11}$$

If an electrically conducting coolant is used, there is an additional pressure drop produced by the interaction of the coolant with the magnetic field, as will be discussed in Chapter 26.

EXAMPLE PROBLEM 20D1

A 100 kW magnet has 16 coolant passages, each 30 m long and 4.6 mm in diameter, connected in parallel. Find the required coolant flow rate, velocity, pressure drop, and pumping power, assuming a temperature rise of 60 K. For simplicity, ignore the slight variations of C, ρ_m, and μ with temperature, and assume that $\eta_p = 0.8$.

From Eq. (20D6) we find $dV/dt = 3.99\times10^{-4}$ m^3/s. Then, $(dV/dt)_{channel} = (dV/dt)/16 = 2.50\times10^{-5}$ m^3/s, and v = 1.50 m/s (from Eq. 20D7). From Eq. (20D8) Re = 6870, and f ≃ 0.035 (Fig. 20D2). The pressure drop is 2.56×10^5 Pa (37 psi) and the pumping power is 128 W (Eqs. 20D9, 20D10).

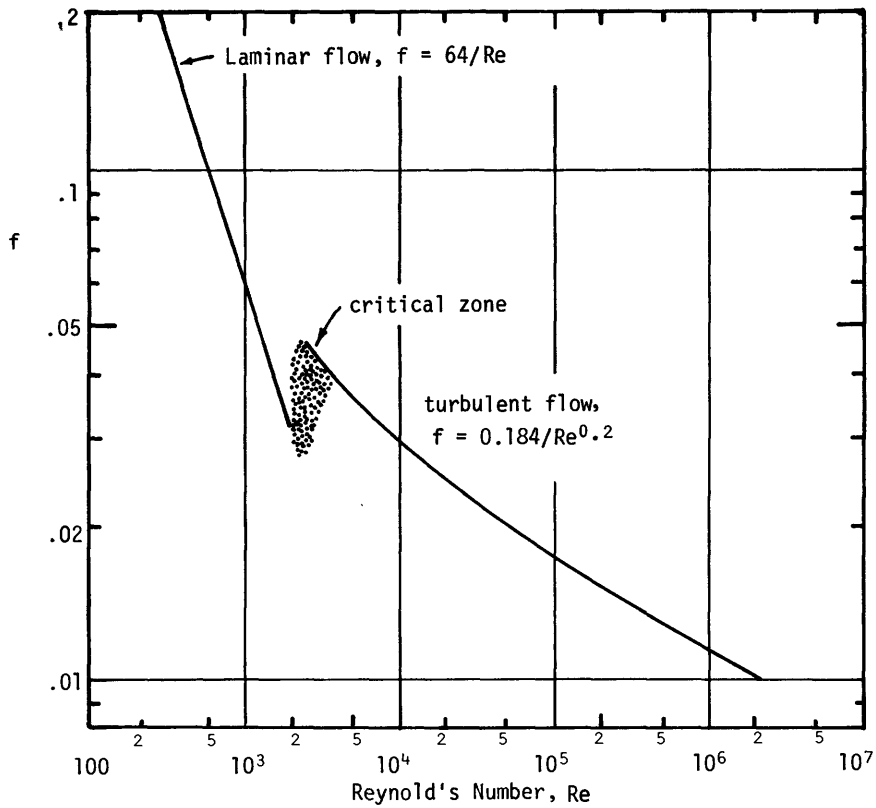

Fig. 20D2. Friction factor f vs. Reynold's Number, for smooth tubes. Based on data of M. El-Wakil, Nuclear Heat Transport, American Nuclear Society, LaGrange Park, IL, 1978, Appendix F.

20E. Coil Windings

There are three main types of magnet coil windings: hollow-conductor coils, tape-wound coils, and disk coils (Bitter coils). These are illustrated in Fig. 20E1. Hollow conductors are cooled by water flowing along the inside of the copper. They are often wound in "pancakes". The coolant in one pancake spirals radially inwards, then spirals back radially outwards. Epoxy between layers enhances mechanical strength of the coil.

Tape-wound coils are usually cooled by water flowing axially through small slots in the conductor or insulator. Windings are separated by insulation of plastic or synthetic fibers.

Bitter coils, named after Francis Bitter of the National Magnet Laboratory, may be cooled by radial flow through slots machined into the copper disks or by axial flow through holes drilled through both copper and insulator disks.

Hollow-conductor coils are probably most common, but higher fields can be attained with tape-wound coils and Bitter coils, because of their shorter coolant

flow paths. For example, Bitter coils produce $B_t \sim 12$ T in the Alcator C Tokamak.

For a given pump pressure and coolant channel size, the attainable volumetric flow rate can be determined from Eqs. (20D9) and (20D7) for one channel of a coil. Then, the heat which can be removed per channel is found using $(dV/dt)_{channel}$ in Eq. (20D6). If this heat removal power is equated to the heat dissipated per channel $\lambda\eta J^2 V_{ch}$, where V_{ch} is the coil volume to be cooled by that coolant channel, then the maximum safe value of current density J can be found.

The results of calculations of maximum safe currents are shown in Fig. 20E2.

The resistance of one segment of a hollow-conductor coil is given by

$$R_s = \eta L_c / A_c \quad \text{(Ohms)} \qquad (20E1)$$

where A_c is the cross sectional area of the copper in the conductor (m^2).

EXAMPLE PROBLEM 20E1

If the coil of Example Problem 20D1 is wound from the conductor with a = 8.64 mm and D = 4.66 mm, and the segments are connected in series, estimate the coil resistance at T = 320 K.

From Eq. (20D4), $\eta = 2.0\times10^{-8}$ Ohm-m. The coil conductor cross sectional area is $A_c = a^2 - \pi D^2/4 = 5.76\times10^{-5}$ m^2. From Eq. (20E1), we find $R_s = 0.0104$ Ohm, so the total resistance $R = 16R_s = 0.167$ Ohm.

Contact resistance in conductor joints can substantially increase R, unless the joints are carefully made. The conductor size can be chosen so that the coil resistance = (maximum power supply voltage)/(maximum power supply current), in order to fully utilize the supply capability. Various series-parallel connections of coil segments can be made to aid in impedance matching.

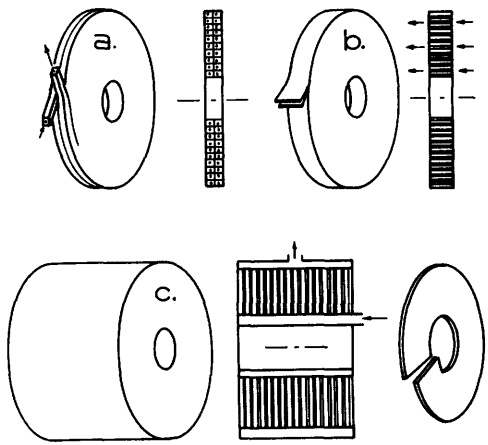

Fig. 20E1. Types of coil windings, (a) hollow conductor "pancake" coil, (b) tape-wound coil, (c) disk-wound Bitter magnet. In the Bitter magnet individual copper disks are slit, twisted, and joined together to form a spiral, with insulation between adjacent disks. Arrows denot coolant flow directions.

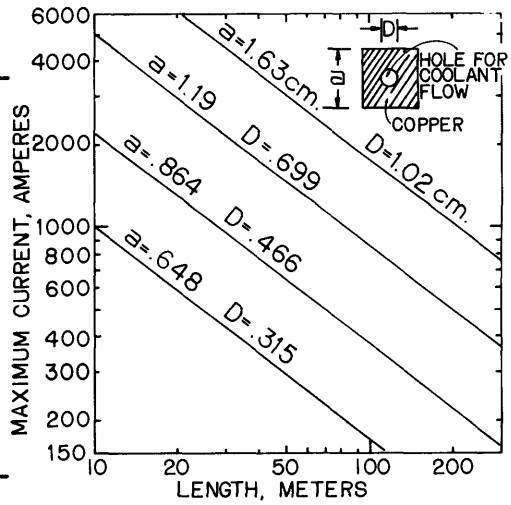

Fig. 20E2. Maximum safe current vs. length for various sizes of square, hollow copper conductors, assuming ΔT = 60 K, average conductor temperature = 313 K (40 C), and pressure drop = 4.14×10^5 Pa (60 psi). (It is possible for coils to fail at lower currents, due to clogged coolant channels, etc.)

During coil winding, epoxy, fiberglass, and sometimes stainless steel are used between layers of copper to provide electrical insulation and mechanical rigidity. Special brazing techniques have been developed to ensure good electrical conductivity and mechanical strength wherever two copper conductors must be joined together. These techniques are so good that poloidal field windings can be wound around a form, cut apart, slid under the toroidal field coils, and brazed back together (as was done on the PLT). It is more difficult to make good joints in aluminum.

Problems

1. How much power is required to generate a field of 6 T in a short solenoid with a 10 cm bore diameter?

2. A solenoid has inner and outer radii of 1.0 and 1.20 m, and it generates a magnetic induction of 4 T. Estimate the hoop stress in the conductor.

3. A solenoid has inner and outer radii of 1 and 2 m, and a length of 3 m. If 1 MW is available to power the coil, what is the maximum field which can be generated? Assume $\lambda = 0.9$.

4. A coil with $r_1 = 0.1$ m and optimum shape is to be wound with one of the conductors of Fig. 20E2, and connected to a power supply which provides up to 1000 A at 50 V. The coil segments will be pancake shaped and connected electrically in series. Which of the conductors provides the highest magnetic field, and what is that maximum field? [Hint $a^2 L_c(\text{total}) = \pi(r_2^2 - r_1^2)L$].

5. For the coil of problem 4, assume that the cooling water flows into 20 parallel segments of the coil. Estimate the length of each segment, the required flow rate, and pumping power, assuming that $\Delta T = 60$ K and $\eta_p = 0.8$.

6. A circular coil with $r_1 = 0.1$ m, $r_2 = 0.2$ m, and length = 0.1 m has 10x10 = 100 turns, with 1100 A of current in each turn. Estimate the field at r = 0.16 m one cm from the coil surface using Hart's method, and on the axis at the midplane. Then approximate the whole coil as a single loop, repeat the calculations, and compare results.

7. Using the facts that $B_r = -(\partial A_\phi/\partial z)$, and that $dE(k)/dk = [E(k)-K(k)]/k$, $dK(k)/dk = -K(k)/k + E(k)/k(1-k^2)$, derive Eq. (20B14) for B_r from (20B13).

8. Assume that the two coils shown in Fig. 20P1 have their currents in opposite directions, producing a spindle cusp field, and that the current in each turn is 300 A. Find the magnetic field at r = 0, z = -5 cm, and at r = 5, z = 0 cm,
(a) using Hart's method and the equation for the axial field of a solenoid;
(b) approximating each coil by a single loop.

9. Approximating each of the two coils of Fig. 20P1 as four circular loops, write a computer program to plot the path of the magnetic field line passing through the point $r_0 = .3$, $z_0 = -5$ cm. If z_0 and r_0 are the initial position, the location of the field line after travelling a distance ℓ along it is given by

$$z(\ell) = z_0 + \int_0^{\ell} d\ell B_z/B \quad ,$$

$$r(\ell) = r_0 + \int_0^{\ell} d\ell B_r/B.$$

The numerical integration should be done with a predictor-corrector or Runge-Kutta routine, with a step size of 1 mm. (See any text on numerical analysis.) Polynomial approximations of complete elliptic integrals are given in Abramowitz and Stegun, 1964.

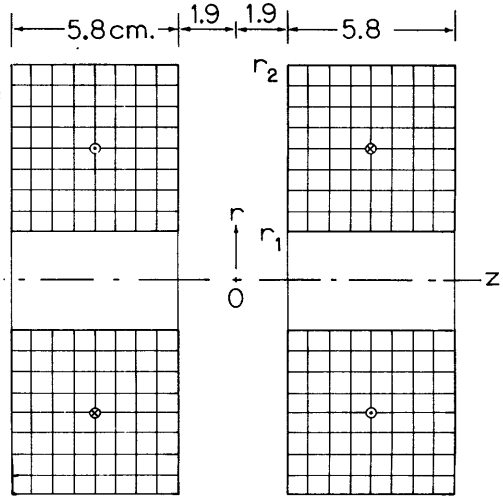

Fig. 20P1. Circular magnet coils wound from ¼ inch copper tubing. Inner radius $r_1 = 1.7$ cm; outer radius $r_2 = 7.5$ cm. Each coil has 8x8 = 64 turns of conductor. The current in each turn is 300 A, and the currents in the two coils are in opposite directions, as shown.

10. Estimate the force between the coils of Fig. 20P1.

11. Approximating each coil of Fig. 20P1 as a circular loop, calculate B_z along the axis and plot $B_z(z)$ from z = -10 to z = +10 cm. Scale the values using the result of Problem 8a.

12. A solenoid is to be constructed of pancake coils each two turns wide, with $r_1 = .15$ m and $r_2 = .45$ m, using the conductor with a = 1.19 cm, D = 0.699 cm (Fig. 20E2). Estimate (a) the number of turns and conductor length for each pancake coil, (b) the maximum safe current, coil resistance, and power required by one pancake at maximum current, (c) the required flow rate and coolant pumping power for each pancake, (d) the number of pancakes required for an optimum length solenoid, assuming a 2 mm gap between pancakes, (e) the total power required and maximum B_z produced by the optimum length solenoid.

13. Estimate the maximum safe current for a 50 m length of the conductor with a = .864, D = .466 cm by calculating the coolant flow rate and coil resistance, and compare with the value of Fig. 20E2. Assume $\Delta T = 60$ K, $\Delta p = 0.414$ MPa.

14. A tape-wound coil uses copper conductor with width w and thickness t (Fig. 20P2). Instead of machining coolant grooves into the copper, layers of the copper are separated by nylon monofilament spacers with diameter d, which are spaced azimuthally about 10d apart. If the average coil radius is r, estimate the resistance per turn of conductor, the power dissipated per turn at current I, and the required water flow speed to keep the water temperature rise to a given ΔT.

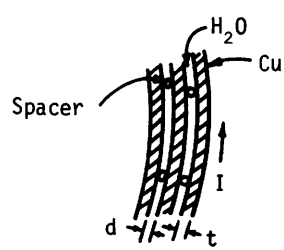

Fig. 20P2. Tape-wound coil.

Bibliography

background

W. Berkson, *Fields of Force, The Development of a World View from Faraday to Einstein,* Wiley, New York, 1974.

V. P. Kartsev, *Three Thousand Years of Magnets,* Mir Publishers, Moscow, 1975.

calculations

M. Abramowitz and I. A. Stegun, *Handbook of Mathematical Functions,* Applied Mathematics Series 55, National Bureau of Standards, Washington, DC, 1964.

H. Brechna, *Superconducting Magnet Systems,* Springer-Verlag, Berlin, 1973, Chapters 2 and 6.

D. R. Corson and P. Lorrain, *Introduction to Electromagnetic Fields and Waves,* Freeman, San Francisco, 1962.

S. L. Gralnick, I. U. Ojalvo, I. J. Zatz, and T. Balderes, "Compatibility consideration for zero moment tokamak toroidal field coils", *Nuclear Technology 45,* 233-243 (1979).

P. J. Hart, *Universal Tables for Magnetic Fields of Filamentary and Distributed Circular Currents,* American Elsevier, New York, 1967.

C. D. Henning, "FORCE - A Computer Program for Calculating Magnetic Forces Developed in Electromagnets", Proceedings of the Symposium on Engineering Problems of Controlled Thermonuclear Research, CONF-661016, 1966, p. 53.

W. A. Perkins and J. C. Brown, *MAFCO- A Magnetic Field Code for Handling General Current Elements in Three Dimensions,* UCRL-7744-Rev II, 1966.

A. Shadowitz, *The Electromagnetic Field,* McGraw-Hill, New York, 1975, Section 5.1.

magnet coils

D. L. Jassby, "TORFA, toroidal reactor for fusion applications", PPPL-1700 (1980).

J. Kalnavarns and D. L. Jassby, "Steady-state resistive toroidal-field coils for tokamak reactors", *Proceedings of the Eighth Symposium on the Engineering Problems of Fusion Research (San Francisco, 1979),* 148-153.

H. Knoepfel, *Pulsed High Magnetic Fields,* American Elsevier, New York, 1970.

H. Kolm, B. Lax, F. Bitter, and R. Mills, editors, *High Magnetic Fields,* Wiley, New York, 1962.

R. W. Moir and C. E. Taylor, "Magnets for open-ended fusion reactors", *The Technology of Controlled Thermonuclear Fusion Experiments and the Engineering Aspects of Fusion Reactors,* CONF-721111, USEAC, 1974, p. 853.

D. B. Montgomery, *Solenoid Magnet Design,* Wiley Interscience, New York, 1969.

D. H. Parkinson and B. E. Mulhall, *The Generation of High Magnetic Fields,* Plenum Press, New York, 1967.

K. E. Wakefield, "The Design of High Field, Air Core Magnets", Lecture 10 of *A Short Course in Fusion Power,* Princeton University Press, 1972.

CHAPTER 21

PULSED MAGNET SYSTEMS

21A. Introduction

The term "pulsed magnets" means that the current is supplied from a pulsed power source. Pulsed magnet systems consist of energy storage devices, switches, current transmission lines, and coils. Such systems can have higher coil currents and less severe cooling requirements than water-cooled dc magnets.

In the 1920's P. L. Kapitza produced magnetic fields up to 32 T using batteries and motor-generators, and T. F. Wall produced a field of 20 T, using a capacitor bank. The volumes of these intense fields were about 0.2-2 cm^3. Interest in large-volume pulsed magnetic fields was stimulated by the needs of the experimental fusion program in the 1950's. Since then, large capacitor banks (up to 10 MJ), high voltage switches, and cables have been developed; and ultrahigh fields have been generated using magnetic flux compression in single-shot experiments.

This Chapter will present the basic equations for RLC circuits and magnetic field diffusion; describe single-turn solenoids, energy storage systems, hardware and magnetic flux compression techniques; and then discuss component reliability.

21B. RLC Circuit Equations

A simple RLC circuit, representing a pulsed magnet system, is illustrated in Fig. 21B1. The capacitor C is charged up to a voltage V_0 with the switch S_1 open, and then S_1 is closed at t = 0. The problem is to determine the current I in the circuit as a function of time. Then the magnetic field produced by the coil can be calculated approximately using the methods of Chapter 20.

If q is the charge on the capacitor, then the voltage across the capacitor is q/C, the voltage drop across the resistance R is R(dq/dt), and the voltage drop across the inductance L is $L(d^2q/dt^2)$, assuming L to be a constant. (In an actual circuit, L will vary, because of phenomena such as plasma diamagnetism. However, a good estimate of the current can be obtained assuming L to be constant.) By Kirchoff's Law, the sum of the voltages around the circuit is zero, and

$$L(d^2q/dt^2) + R(dq/dt) + q/C = 0 \qquad (21B1)$$

The initial conditions are $q = CV_0$ and $dq/dt = 0$. This linear, homogeneous, second-order differential equation can be solved by using the operator notation $D = (d/dt)$, for which

$$(LD^2 + RD + 1/C)q = 0 \quad . \qquad (21B2)$$

The roots of this quadratic equation are

$$D = -a \pm i\omega \qquad (21B3)$$

where $a = R/2L$ and $\omega = [(1/LC) - a^2]^{\frac{1}{2}}$. For pulsed magnet circuits, the resistance is kept low, so the quantity in brackets is positive, and the solution is oscillatory. The general solution is therefore

$$q(t) = A_1e^{-at+i\omega t} + A_2e^{-at-i\omega t} \qquad (21B4)$$

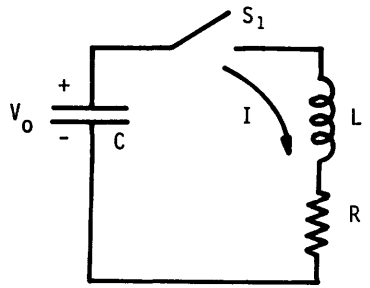

Fig. 21B1. Simple RLC circuit. Here R represents the total resistance of all the elements in the circuit, such as the capacitor, switch, transmission lines, headers, and magnet coil, and L represents the total inductance of all the circuit elements.

which may also be expressed in terms of trigonometric functions as

$$q(t) = A_3e^{-at}\cos\omega t + A_4e^{-at}\sin\omega t \quad . \qquad (21B5)$$

(This method of solving differential equations is described in most texts on differential equations. The Laplace transform method may also be used to obtain this solution.) From the initial condition $q(0) = CV_0$, it is found that $A_3 = CV_0$. From the other initial condition, $(dq/dt)_{t=0} = 0$, it is found that $A_4 = aA_3/\omega$. The current as a function of time is found from the relation $I(t) = -dq/dt$. The resulting expressions for charge and current are

$$q(t) = CV_0e^{-at}(\cos\omega t + (a/\omega)\sin\omega t) \qquad (21B6)$$

$$I(t) = (V_0/\omega L)\, e^{-at}\sin\omega t \quad . \qquad (21B7)$$

Thus I(t) is a damped sinusoid, as illustrated in Fig. 21B2. The maximum current and the time t_{max} when the current is maximum are found by setting $dI/dt = 0$, which gives

$$t_{max} = (1/\omega)\text{Arctan}(\omega/a) \qquad (21B8)$$

$$I_{max} = (V_0/\omega L)\exp(-at_{max})\sin(\omega t_{max}) \quad . \qquad (21B9)$$

If R, L, C, and V_0 are known, then t_{max} and I_{max} can be predicted. Conversely, if R and L are unknown, they can be calculated from measured values of t_{max} and

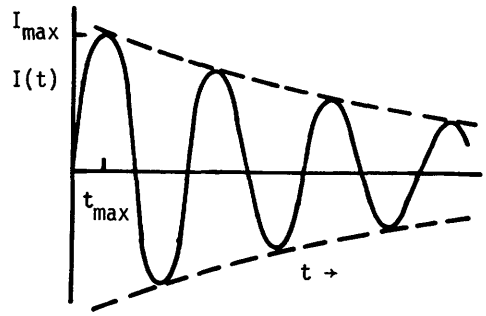

Fig. 21B2. Damped sinusoidal oscillation of current in an "undercritically damped" RLC circuit.

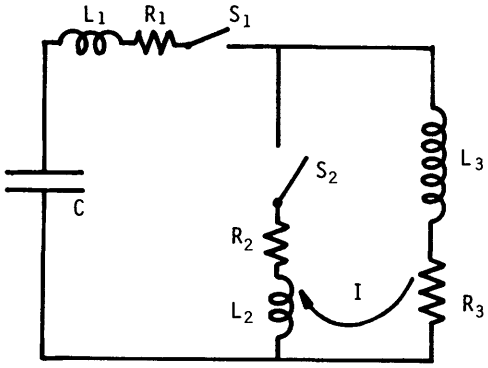

Fig. 21B3. A crowbar switch. In this circuit R_1 and L_1 represent the combined resistance and inductance of the capacitor, switch S_1, and other elements of the C-S_1 circuit. R_2 and L_2 represent the resistance and inductance of the S_2 circuit (the crowbar switch circuit), and R_3 and L_3 represent the combined resistance and inductance of the load circuit, including coil, header, transmission lines, etc.

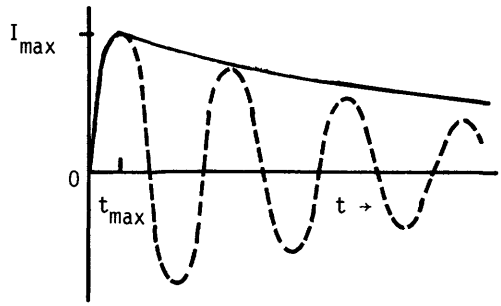

Fig. 21B4. Waveform of a crowbarred circuit. The dashed curve represents the damped sinusoid which would occur if the circuit were not crowbarred. There will be some ripples (not shown here) on the decay current, due to interaction of energy stored in L_2 and L_3. The ripples may be deleterious in some experiments.

I_{max}.

Usually it is desired to have the coil current rise up to a maximum value, then stay nearly constant at that value, instead of oscillating with the damped sinusoid wave form of Fig. 21B2. If a second switch S_2 is added to the circuit, as shown in Fig. 21B3, it can be closed when $I = I_{max}$, effectively short-circuiting coil L_3 at maximum current. Then the coil current gradually decays from its peak value with a time constant $[(L_2 + L_3)/(R_2 + R_3)]^{\frac{1}{2}}$, as shown in Fig. 21B4. The switch S_2 is called a *crowbar*.

resistance and inductance

In predicting the behavior of pulsed coil circuits, it is necessary to estimate the inductance and resistance of various circuit elements. Usually, the parameters of capacitors, cables, and switches are specified by the manufacturer. The dc resistance of conductors in general may be estimated from the equation

$$R = \int_0^{\ell} dx\eta/S \qquad \text{(OHM)} \qquad (21B10)$$

where S is the cross sectional area of the conductor (m^2), η is the resistivity of the metal (Ohm-m), and ℓ is the length (m) of the item considered. However, in pulsed operation, the current may not be distributed uniformly over the whole cross section of the coil, due to the skin effect (to be discussed).

The inductance of a uniform-current-density solenoid of length ℓ, inner radius r_1 (m), and outer radius r_2 with N turns can be found from the information given

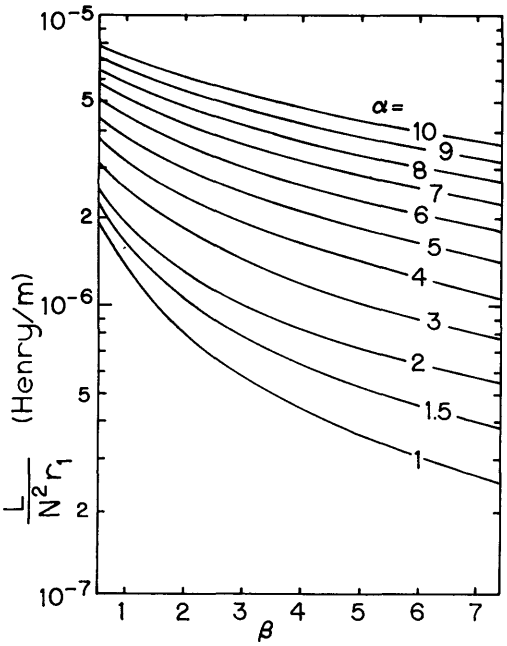

Fig. 21B5. Inductance of a uniform-current-density solenoid, as a function of $\beta = \ell/2r_1$ *for various values of* $\alpha = r_2/r_1$. *The inductance L is in Henry, N is the number of turns, and the solenoid length* ℓ *and radii* r_1 *and* r_2 *are in metres. From D. B. Montgomery, Reports on Progress in Physics 29, 69-104 (1963).* © *1963 The Institute of Physics.*

in Fig. 21B5 as a function of the dimensionless ratios $\alpha = r_2/r_1$ and $\beta = \ell/2r_1$.

The inductances of parallel plate and coaxial transmission lines are

$$L = \mu_0 s \ell K_{sh}/h \text{ (Henry)} \qquad (21B11)$$

$$L = \mu_0 \ell \ln(b/a)/2\pi \text{ (Henry)} \qquad (21B12)$$

where the dimensions (metres) are defined in Fig. 21B6. The factor K_{sh} is found from Fig. 21B7 as a function of the dimensionless ratio (s/h). Formulas for the inductances of more complex shapes are given by Knoepfel (1970).

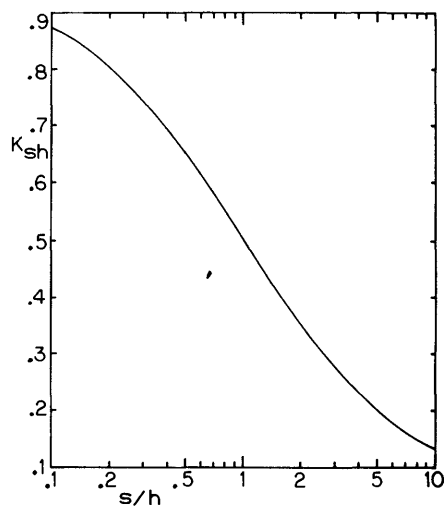

Fig. 21B7. Values of K_{sh} *as a function of (s/h) for the inductance of a parallel plate transmission line. If* $s/h \ll 1$, $K_{sh} \simeq 1$. *From H. Knoepfel, Pulsed High Magnetic Fields, American Elsevier, New York, 1970, Fig. A1.21, p. 323.*

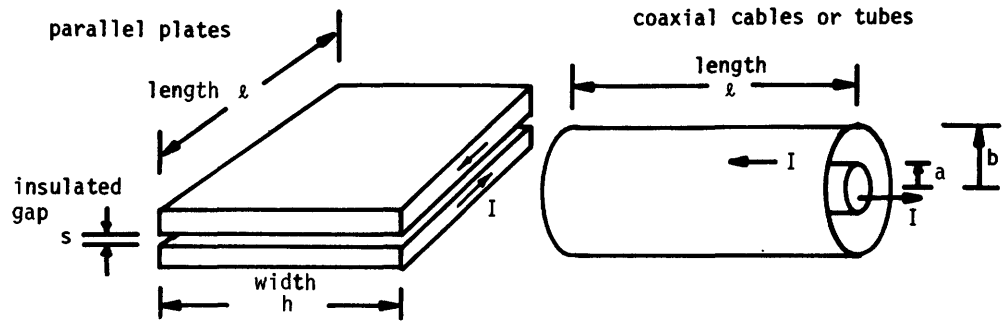

Fig. 21B6. Parameters of parallel plate and coaxial transmission lines.

21C. Distribution of $\vec{J}$ and $\vec{B}$

When a high current is pulsed through a conductor, the current begins in a thin layer at the metal surface and gradually spreads inwards. From the Maxwell equations and "Ohm's Law" (with $\vec{u} = 0$) it can be shown that the current density $\vec{J}$ and magnetic induction $\vec{B}$ both obey similar equations:

$$\frac{\partial \vec{J}}{\partial t} = \nabla^2 \vec{J}/\sigma\mu \qquad \sigma \equiv 1/\eta$$

$$\frac{\partial \vec{B}}{\partial t} = \nabla^2 \vec{B}/\sigma\mu \tag{21C1}$$

where σ is the conductivity of the medium (A/V-m), and μ is its permeability (Henry/m) (cf. Eq. 8D102). These equations are similar in form to the heat conduction equation $\partial T/\partial t = (K/c_v)\nabla^2 T$ in which T = temperature, K = thermal conductivity, and c_v is specific heat. Thus, the diffusion of current density and magnetic field into a conductor is analogous to the diffusion of heat into a solid, and many of the results for heat conduction may be applied to magnetic field diffusion. For magnetic field diffusion, the problem is complicated by the fact that the boundary condition at the edge of the conductor varies in time.

Typically, if the magnetic field at the edge of the conductor varies sinusoidally ($B \cong B_0 \sin\omega t$), then the depth which the magnetic field penetrates into the conductor is on the order of the "skin depth" δ, given by the equation

$$\delta = (2/\mu\sigma\omega)^{\frac{1}{2}} \quad (m) \tag{21C2}$$

as illustrated in Fig. 21C1.

For good conductors at high frequencies, this depth of penetration can be very small. For example, for copper at a frequency of 1 MHz, $\delta \cong 0.07$ mm, which indicates that the current density and magnetic field are located mainly in a very thin layer on the surface of the conductor.

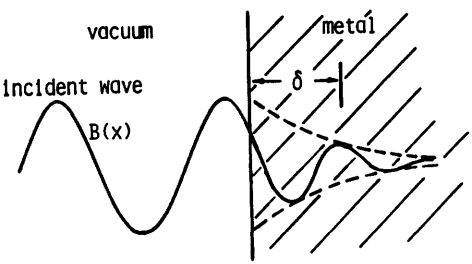

Fig. 21C1. Amplitude of a plane electromagnetic wave incident on a metallic conductor. The dashed curve shows the exponential decay of the amplitude, which occurs over a distance δ, called the "skin depth".

Order of magnitude estimates of magnetic field diffusion rates can be made by approximating the derivatives in Eqs. (21C1) as follows:

$$\partial B/\partial t \sim B/\tau$$

$$\nabla^2 B \sim B/\ell^2 \tag{21C3}$$

where τ and ℓ are the "characteristic diffusion time" and "characteristic

diffusion length". Then Eq. (21C1) simplifies to

$$1/\tau \sim 1/\sigma\mu\ell^2 \quad . \tag{21C4}$$

For a given conductor, we know σ and μ. If we specify a penetration distance ℓ, then we can find the approximate time τ that it takes for the magnetic field to penetrate, or vice-versa.

single-turn high-field solenoids

A single-turn solenoid can be simply a thick metal tube with an insulated slot. To sustain the large forces associated with high magnetic fields, the coil may be surrounded by a massive steel block (Fig. 21C2).

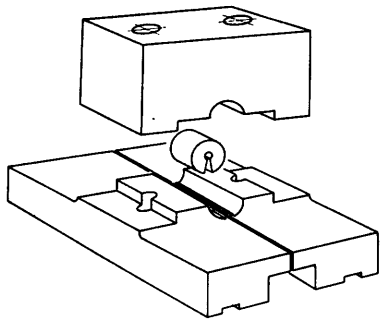

Fig. 21C2. A single-turn high-field coil surrounded by a steel block for structural support. From H. Knoepfel, "Very high magnetic fields generated in single-turn solenoids", Journal of Physics E: Scientific Instruments 5, 1133-1141 (1972), Fig. 8. © 1972 The Institute of Physics.

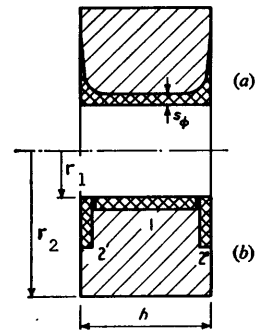

Fig. 21C3. Section through a thick, single-turn solenoid, showing distribution of magnetic field and current density, as characterized by the magnetic flux skin depth s_ϕ. (a) actual distribution, (b) approximation with three rectangular elements. From H. Knoepfel, Journal of Physics E 5, 1133-1141 (1972), Fig. 2. © 1972 The Institute of Physics.

The current density tends to be concentrated radially around the inside of the coil bore and axially near the ends of the coil, so the distributions of B found in Chapter 20 for uniform coil current density must be modified. We can define a magnetic flux skin depth

$$s_\phi \equiv \frac{\int_0^\infty dx\, B}{B_0} \quad , \tag{21C5}$$

where x is measured inwards from the coil surface and B_0 is the field at the surface. The distribution of s_ϕ in a one-turn solenoid is illustrated in Fig. 21C3a.

The actual coil current may be approximated by three elements (Fig. 21C3b) for rough calculations. The axial magnetic field distribution may be written

$$B_z(z) = K(z)\mu_0 I/h \tag{21C6}$$

where μ_0 is the permeability of free space, I is the coil current, h is the coil length, and K(z) describes the spatial variation. Values of K(z) for a few cases are shown in Fig. 21C4. There are significant departures from the field distributions of a uniform-current-density solenoid.

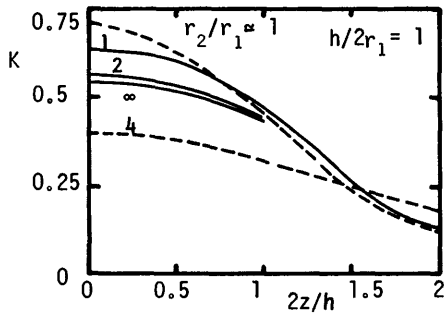

Fig. 21C4. Axial distribution of magnetic field in solenoids with $h = 2r_1$, for various ratios of outer to inner radius r_2/r_1. Smooth curves: single-turn solenoids. Dashed curves: solenoids with uniform current density. From H. Knoepfel, Journal of Physics E 5, 1133-1141 (1972), Fig. 4. © 1972 The Institute of Physics.

The attainable magnetic field and coil current are limited by coil stress and surface heating. The metals begin to yield at fields $B \lesssim B_y[r_2-r_1)/2r_1]^{\frac{1}{2}}$, where $B_y \simeq 25$ T for copper, brass, and steel, and $B_y \simeq 32$ T for tantalum. Melting occurs when $B > B_e/\theta^{\frac{1}{2}}$, where $\theta^{\frac{1}{2}} \sim 2$-3 depends upon the shape of I(t), and B_e is a characteristic field. For copper, brass, and steel, $B_e \simeq 90$-110 T, and for tantalum, $B_e \simeq 137$ T. Other refractory metals, such as Mo, W, and Nb, may also be used for high-field coils, but Mo and W have poor ductility. Since the conductivity σ decreases with increasing temperature, the diffusion equations (21C1) become nonlinear, especially at high fields and temperatures.

When the coil metal begins to yield, it will deform plastically. If the magnetic field and its duration are large enough, the coil may explode. The inner surface of a copper coil expands at a velocity $u \simeq 0.15\ B^{3/2}$(m/s) (valid for $B \gtrsim 150$ T). Thus, short current rise times ($\tau_{max} \lesssim 2$ μs) are needed for high fields, to produce the field before the coil is destroyed. At lower fields, severe stress cracking and fatigue may limit coil life to a few shots. Single shot coils have obtained fields of 100-200 T, and recoverable coils have attained fields up to 65 T for over 20 shots. Single-turn solenoid design and limitations are discussed by Knoepfel (1970 and 1972).

21D. Energy Storage Systems

For pulsed fusion experiments, such as theta pinches, the most common form of energy storage is in a capacitor bank. Capacitor banks have the following advantages over other types of energy storage: they store electrical energy, so conversion from another energy form is not necessary; the technology of capacitor banks is very well developed; and the energy can be released very rapidly, to produce shock heating.

The desirable features for capacitors are large energy stored per unit volume; long lifetime (about 10^6 shots); low self-inductance, to make I_{max} very large (Eq. 21B9); low resistance; and low cost. Some large capacitor banks are described in Table 21D1.

The Scyllac bank at Los Alamos National Laboratory can store about 10 MJ at 60 kV. The 60 kV capacitor developed for this bank is shown in Fig. 21D1.

Table 21D1. Large Capacitor Banks

location	stored energy $\frac{1}{2}CV_0^2$ (MJ)	V_0 (kV)	t_{max} (μs)	I_{max} (MA)
Garching, Germany	2.7	40	9.5	21
Naval Research Labs	2	20	16	17
Los Alamos	10	60	4	150

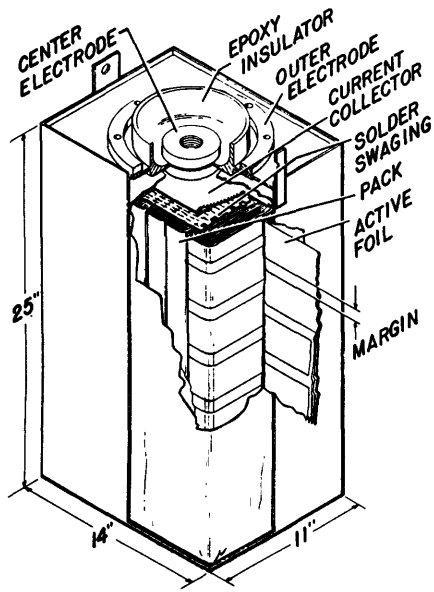

Fig. 21D1. The Scyllac 60 kV, 1.85 μF capacitor. From E. L. Kemp, "The final design of Scyllac", Proceedings of the Symposium on Engineering Problems of Fusion Research, LA-4250 (1969) Fig. 3, p. F1-8.

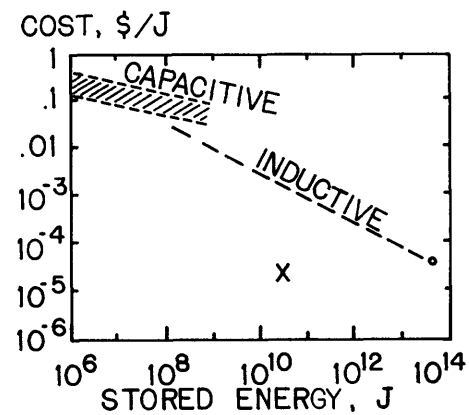

Fig. 21D2. Approximate energy storage system capital costs per Joule of stored electrical energy, as functions of stored energy. The datum o at 36 TJ is from J. D. Rogers, et al, LA-7885-MS (1979). The "x" represents mechanical energy storage in an optimized flywheel, capable of storing 10 MW-hr (3.6×10^{10} J) at a cost of 0.33 M$, from R. F. Post and S. F. Post, "Flywheels", Scientific American 229, 17 (1973), escalated to about 0.8M$ (1980 $).

Capacitive energy storage at V_0 = 60 kV costs about 30-40 ¢/J installed, so a 10 MJ bank costs about 3 M$. A capacitor bank for a fusion reactor requiring over 1 GJ of stored energy would cost more than 300 M$. By using lower voltages, such as 5 kV, the cost of capacitive energy storage may ultimately be reduced to about 10 ¢/J.

Development of inductive energy storage will result in substantial savings for large systems, as illustrated in Fig. 21D2. Large inductive energy storage systems will have applications for smoothing out daily electrical power demand fluctuations, for preventing instabilities of interconnected electrical power grids, for providing a "spinning reserve" of power to cope with sudden power source losses, for smoothing the output of solar electric power stations, and for pro-

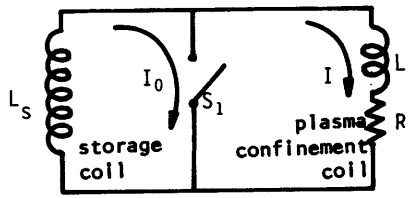

Fig. 21D3. Simplified circuit diagram of an inductive energy storage system for pulsing a current through a magnet coil.

Fig. 21D4. A 50 MJ homopolar generator of the TEXT energy storage system. The rotor turning azimuthally in an axial magnetic field generates a radial electromotive force, and drives a current, tapped by brushes on the shaft and rotor. Courtesy of W. F. Weldon, H. G. Rylander, and H. H. Woodson, The Center for Electromechanics, The University of Texas at Austin.

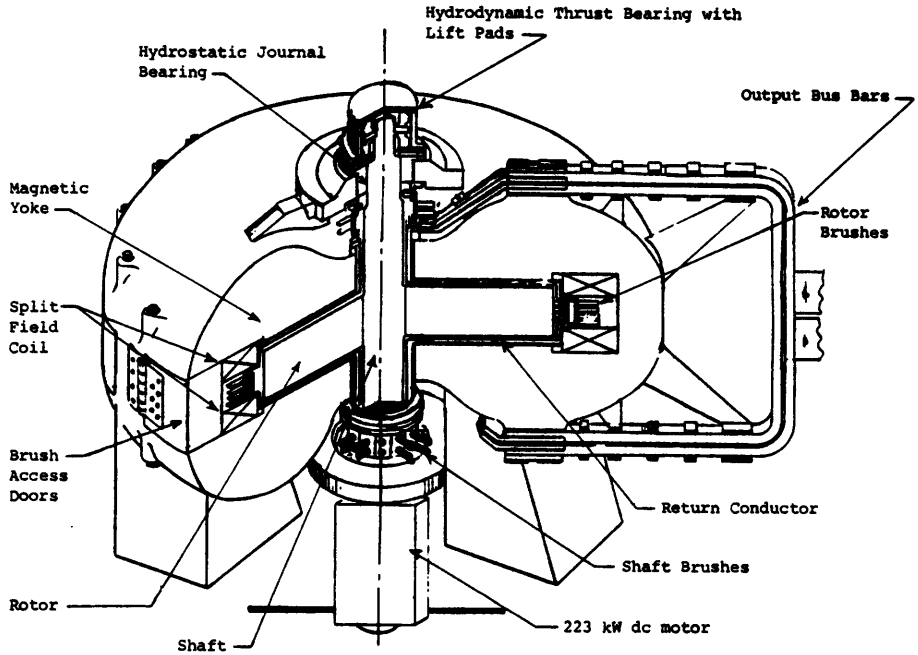

viding the energy to ignite pulsed fusion reactors. Pulsed fusion reactors will probably require about 0.1-10 GJ of stored energy.

A simple inductive energy storage system is shown in Fig. 21D3. A charging supply (not shown) builds up a high current I_0 in the storage inductor L_s with switch S_1 closed. The stored energy is $\frac{1}{2}L_sI_0^2$. When the switch S_1 is opened, a large voltage builds up and forces a current I to flow through the load coil L.

Design of the switch S_1 is a major problem. It is difficult to open a switch which is carrying a high current because the current tends to arc across the switch and continue flowing. Switches for this purpose can be fuses which melt, thin conductors which explode, vacuum tube interrupters, and superconductors which "go normal" (Change from zero resistivity to normal resistivity). For the simple circuit of Fig. 21D3, the fraction of energy transferred to the load coil is

$$\text{transfer efficiency} = \frac{\frac{1}{2}LI_{max}^2}{\frac{1}{2}L_sI_0^2} \leq \frac{L_sL}{(L_s + L)^2} \quad , \tag{21D1}$$

depending on the energy dissipated in R during the switch opening time. This efficiency has a maximum value of 25% when $L = L_s$. Much higher efficiencies (over 90%) can be attained by placing a capacitor bank in parallel with switch S_1. For optimum efficiency, the capacitor bank must be able to store half as much energy as the storage inductor. For large systems and slow discharge rates, high efficiencies can be obtained without the capacitors. Superconducting energy storage coils will be discussed briefly in Section 22G.

Batteries have been used to power magnet coils for some fusion experiments. Their relatively high internal resistance makes it difficult to attain very large currents in short pulses, so they are better suited to sustaining moderate currents for many seconds. Batteries tend to wear out after a few thousand heavy discharges and recharges, so they are unsuitable for reactors.

Flywheels rotating at high speeds can store energy densities around 0.2 MJ/kg or 500 MJ/m^3. They can be gradually charged up with a motor, then discharged suddenly through a generator to produce a pulse of high current. Flywheel-driven conventional dc generators at the Princeton Plasma Physics Laboratory provide 200 MW of direct current for about 3 seconds. Homopolar motor-generators, such as the one shown in Fig. 21D4, are well suited for coupling to flywheels. The rotor is just a conducting disk, which is much simpler than conventional dc generators requiring commutators.

Chemical energy is also used in producing high magnetic fields. Explosives may be used for magnetic flux compression (Section 21F).

21E. Switching and Transmission

Consider two spherical balls separated by a distance x, as shown in Fig. 21E1, with a high voltage between them. As the distance x is decreased, the point is finally reached where breakdown occurs, and current jumps across the gap like a lightning bolt. Such switches might be suitable for fusion experiments if many of them could be fired quickly and simultaneously, but it is impossible to move the balls fast enough. An alternative is to put a spark plug in the center of one ball, as shown in Fig. 21E2. When the spark plug fires, it creates a plasma in the gap, causing breakdown to occur. In this way the *spark gap* can be fired electrically with precision timing, instead of by mechanical motion of the spheres.

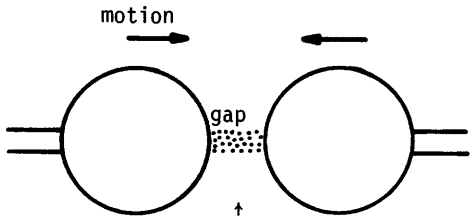

Fig. 21E1. A simple high-voltage switch actuated by decreasing the gap between two electrodes.

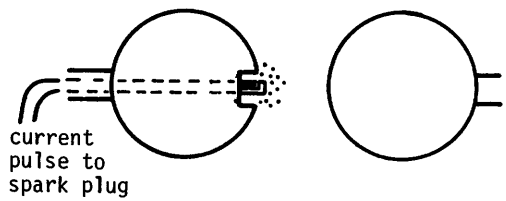

Fig. 21E2. A "spark gap" high voltage switch. Breakdown is initiated by triggering a spark plug near one electrode.

Further refinements have been added to improve timing and increase the useable lifetime of the switches. The spark gap developed for the LASL Scyllac experiment is shown in Fig. 21E3. It actually consists of two switches, which correspond to switches S_1 and S_2 in Fig. 21B3. Instead of just two balls, these switches have an additional ring in the middle to help the switches fire more rapidly. The time lag between firing various switches, which are supposed to fire

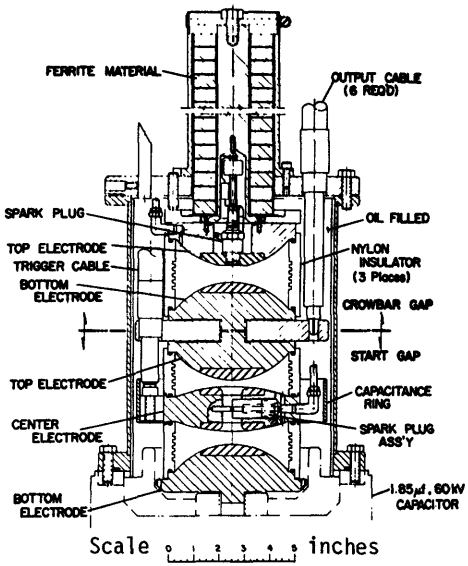

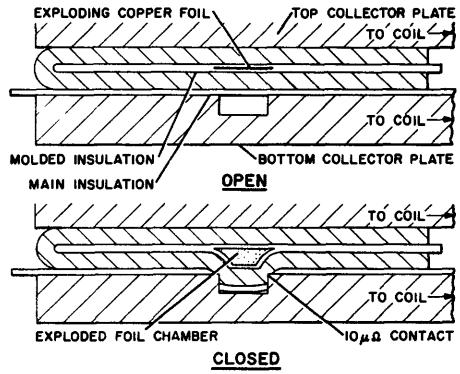

Fig. 21E4. Exploding foil low-resistance crowbar switch, developed for the Scyllac experiment at Los Alamos. From E. L. Kemp, LA-4250 (1969), Fig. 6, p. F1-9.

Fig. 21E3. The dual spark gap switch developed for the Scyllac experiment at Los Alamos. From E. L. Kemp, LA-4250 (1969), Fig. 5, p. F1-9.

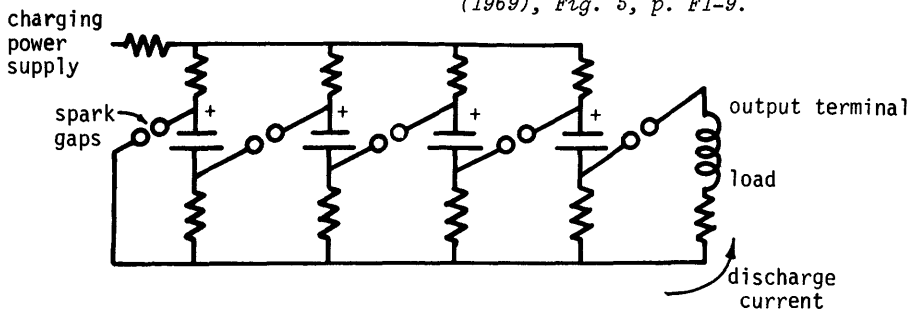

Fig. 21E5. The Marx technique for charging capacitors up to a voltage V_0 in parallel, then discharging them in series, so that a voltage of NV_0 appears across the load, where N is the number of stages (N = 4 in the diagram).

simultaneously, is called *jitter*. The rms jitter for the 3240 spark gaps of the Scyllac primary bank is about 10 ns. When the current is at its peak, the crowbar switches are triggered, allowing the coil current to keep flowing with a gradual decay. Additional explosive switches were developed to aid in crowbarring the discharge. In these switches a thin copper foil is exploded by pulsing a very high current through it. The explosion squeezes a thin aluminum plate through its insulation to make a low-resistance contact with the lower collector plate, as shown in Fig. 21E4.

To obtain very high voltage pulses, capacitors may be charged up in parallel to about 100 kV, and then rearranged and discharged in series. This technique, called *Marx charging*, is illustrated in Fig. 21E5. When the spark gaps are fired, they arrange the capacitors in series, resulting in the total output voltage being the sum of the voltages on the individual capacitors. Marx charging is used for producing relativistic electron beams (Chapter 16) and for some magnet coils.

Special low-inductance high-voltage coaxial cables were developed to carry the current from capacitors and switches to the coil header plates. The Scyllac system uses around 250 km of the cable shown in Fig. 21E6. Several layers of braids

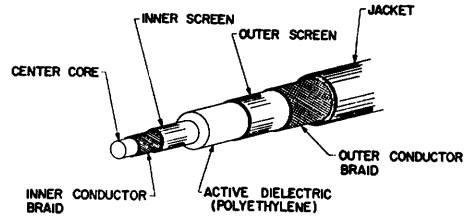

Fig. 21E6. The high voltage coaxial cable developed for the Scyllac experiment. From E. L. Kemp, LA-4250 (1969), Fig. 4, p. F1-8.

and screens are used to minimize electric potential gradients and dielectric fatigue, so that the cable can survive over 10^5 pulses without failure. Additional components for high voltage pulsed magnet circuits include collector plates, cable terminations and cartridges where the cables plug into the collector plates, the coils themselves, and protective circuitry to prevent damage to power supplies and capacitors in the event of a misfire.

21F. Magnetic Flux Compression

Since the magnetic field diffuses comparatively slowly into metallic conductors, as discussed in Section 21C, it may be compressed by moving the metallic walls inwards. One simple scheme for accomplishing flux compression is illustrated in Fig. 21F1. A magnetic field is established between two metallic plates by external coils or magnets. Then an explosive charge is detonated around the outside of the metallic plates, driving them together at a high speed. The magnetic field does not have time to penetrate into the metal plates, so it becomes compressed and squeezed through the slot into the circular coil. Now the flux density is very high, on the order of hundreds of Tesla. Such high fields can be used to compress plasma within the circular coil volume.

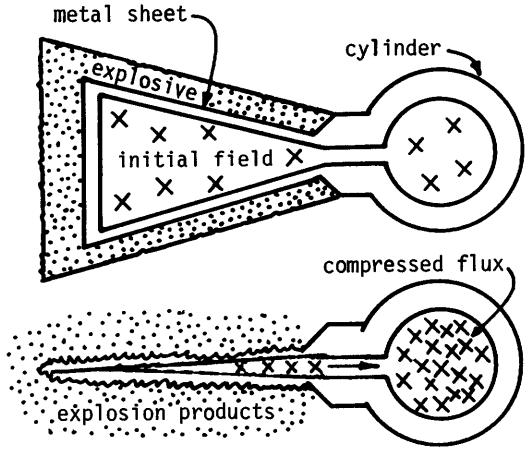

Fig. 21F1. The "bellows" type of magnetic flux compression.

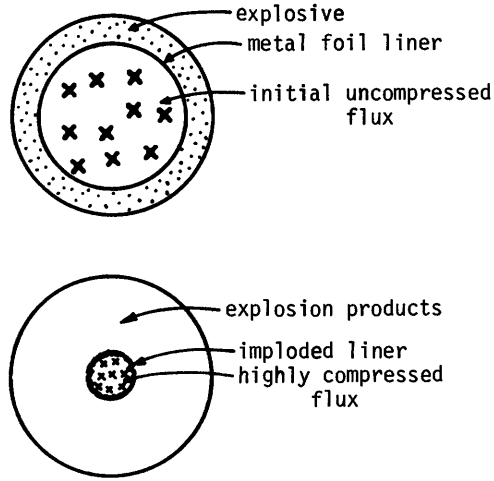

Fig. 21F2. Flux compression by an imploding metallic liner.

An alternate method of flux compression is to use an imploding metallic foil liner inside a coil system, as shown in Fig. 21F2. Fields of 1000 Tesla have been obtained by flux compression. A liner can be compressed by a rapidly rising magnetic field in the surrounding coil, by chemical explosive, or by a combination of both. Many of the high-field flux concentration experiments only last for one shot, because they self-destruct.

Several fusion reactor schemes have been proposed involving magnetic flux compression, including a fast liner reactor (FLR) and a slow liner driven by compressed gas (LINUS). The FLR would use implosion velocities of about 10^4m/s, with implosion times on the order of 10 μs. An initial plasma with $n = 10^{24}$ m^{-3}, $T_i = 0.2$ keV, and $B = 5$ T would be compressed up to $n = 10^{27}$ m^{-3}, $T_i = 10$ keV for a burn time of about 1 μs. Difficulties of this scheme include Rayleigh-Taylor instability of the liner, rapid replacement of the liner, production of the initial plasma, high stresses and fatigue failure of structure, and development of electrical insulators which will not fail under such a hostile environment.

The LINUS scheme was described in Chapter 17.

21G. Component Reliability

One of the major problems of pulsed magnet systems is component failures. Even if a given capacitor, switch, or cable has a very low failure probability, like 10^{-5} per shot, the overall failure probability for a large system with 10,000 components may be unpleasantly large. Let $f_j(t)dt$ be the failure probability of item j in the interval dt at time t. The probability that this item will fail between time 0 and time t is equal to $\int_0^t dt\, f_j(t)$. Therefore, the probability that it will *not* fail during this time period is equal to $[1 - \int_0^t dt\, f_j(t)]$. The "failure rate" r_j for item j is defined to be

$$r_j(t) = \frac{\text{failure probability per unit time at time } t}{\text{probability of } \textit{not} \text{ failing before time } t}$$

$$= \frac{f_j(t)}{1 - \int_0^t dt\, f_j(t)} \qquad (21G1)$$

In a pulsed plasma device, if the current fails in one coil segment, the plasma will be rapidly lost there, and confinement fails. If failure of any one component represents a failure of the entire system, the system is said to be a *series system*. This is like a string of electrical lights wired in series: if one bulb burns out, the whole string goes out.

For a series system with N components, the total failure rate is the sum of the individual failure rates r_j

$$r(t) = \sum_{j=1}^{N} r_j(t) \qquad (21G2)$$

The *estimated time to next failure (ETNF)* of an entire system is defined to be the reciprocal of the composite failure rate:

$$ETNF = 1/r(t) \quad . \qquad (21G3)$$

For some types of components, the failure rate is generally high for the first group of shots, while those with manufacturing defects are present. When the defective ones have been eliminated, the failure rate becomes fairly constant for a long time. Then, at very large numbers of shots, the failure rate rises again, because the parts are beginning to wear out. Such a failure rate curve, illustrated in Figure 21G1, is called a *bathtub curve* because of its shape. This type of failure rate might be expected from new cars, vacuum tubes, capacitors, cables, etc.

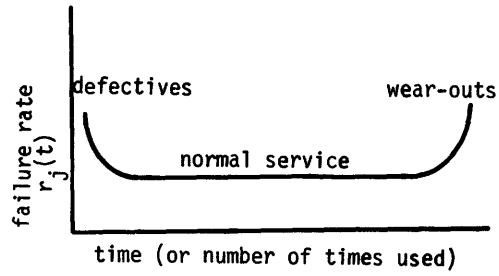

Fig. 21G1. The "bathtub" type of failure rate curve.

For components with a bathtub failure rate curve, the failure probability along the flat bottom portion of the curve is

$$f_j(t)\,dt = \lambda_j e^{-\lambda_j t}\,dt \quad . \qquad (21G4)$$

For this case, it is found from Eq. (21G1) that the failure rate is

$$r_j(t) = \lambda_j = \text{constant} \qquad (21G5)$$

For a series system composed of such components, then, the ETNF is

$$\text{ETNF} = \frac{1}{\sum_{j=1}^{N} \lambda_j} \quad . \qquad (21G6)$$

EXAMPLE PROBLEM 21G1

Estimate the ETNF for 100 identical capacitors with failure rates λ_j of 10^{-4} per shot and 600 identical cables with failure rates λ_j of 2×10^{-4}/shot, assuming that all these components are on the flat portion of a bathtub curve.

For this system,

$$\text{ETNF} = \frac{1}{100\ (10^{-4}/\text{shot}) + 600\ (2\times10^{-4}/\text{shot})} = 7.7 \text{ shots} \quad .$$

For a pulsed reactor operating at one pulse/s, an ETNF of about 3×10^6 shots would be needed in order to operate the reactor for a month without a misfire. Therefore, extremely low individual component failure rates would be needed. Such failure analyses may also be applied to other fusion research components, such as laser systems. In some cases the failure rates may not be described by the simple exponential function of Eq. (21G4), and the analysis is more complex (Boicourt, 1973).

Problems

1. A small theta pinch experiment has the following parameters:

one-turn aluminum coil
inside diameter = 3.0 cm
outside diameter = 5.0 cm
length = 20.2 cm

parallel plate transmission line (aluminum, $\eta = 2.8 \times 10^{-8} \Omega$-m)
width = 35.5 cm
length = 45.7 cm
thickness = 1.3 cm
insulation gap = 0.15 cm

capacitor
capacitance = 15.0 μF
inductance = 5 nH
resistance = negligible
charging voltage = 20 kV

switch (rail type spark gap)
inductance = 5 nH
assume resistance = 1 mΩ

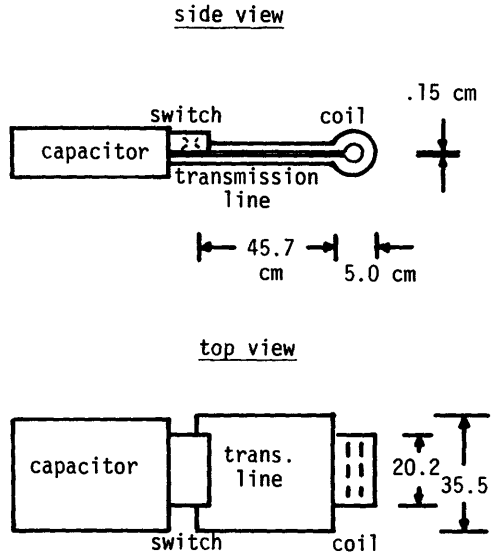

Fig. 21P1. Theta pinch experiment.

(a) Calculate the total circuit resistance and inductance.

(b) Find the maximum current in the coil, and the corresponding energy stored in the coil ($\frac{1}{2}LI^2$). What fraction of the original energy stored in the capacitor is this?

(c) Estimate the peak magnetic induction produced by the coil.

(d) Estimate the skin depth of the transmission line, and the magnetic field between the plates. (Hint: Use the line integral of Eq. 20B4 with the contour indicated in Fig. 21P2.)

(e) Estimate the magnetic pressure between the plates, and the instantaneous force tending to separate them. (Because the force is large, heavy insulated bolts are used to fasten the plates together. Although the instantaneous force may appear to create a dangerously high stress in the bolts, the total energy available is not enough to rupture them, if they are properly de-

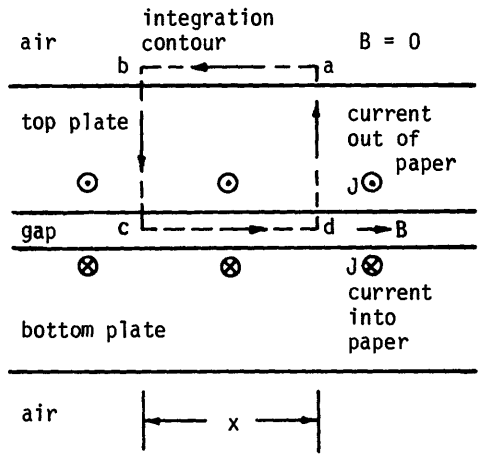

Fig. 21P2. Cross sectional view of parallel plate transmission line. The current density J is concentrated within a couple of skin depths of the inner surfaces. The magnetic field between the plates can be found by evaluating the contour integral in the limit of small x. In that case, $\int_d^a d\vec{\ell}\cdot\vec{B} = -\int_b^c d\vec{\ell}\cdot\vec{B}$, *since* $\vec{B}$ *is the same and the* $d\vec{\ell}$ *have opposite directions.*

signed.)

(f) How many coaxial cables, each with b = 1.23 cm and a = 0.4 cm, in parallel would give the same inductance as the parallel plate transmission line?

2. Verify the equations for I(t) and I_{max} in an RLC circuit.

3. A cylinder 10 cm in diameter is initially filled with a uniform magnetic induction of 0.7 T. Then a thin metallic liner is imploded by chemical explosives, and compressed to an inside diameter of 0.6 cm. What is the peak magnetic induction produced by this flux compression? If the liner is aluminum 1 millimeter thick, about how fast must the compression be to prevent the magnetic field from penetrating through the liner? (For nonferrous metals, $\mu \simeq \mu_0$).

4. A large capacitor bank system has 470 capacitors with failure rates of 2×10^{-6}/shot, 470 switches with failure rates of 3×10^{-6}/shot, and 2820 cables with failure rates of 4×10^{-6}/shot. Assuming that the components are used enough to get rid of defective items, but not yet near the end of life, estimate the approximate number of shots between failures.

5. If a second capacitor and switch, identical to the first ones, were added in parallel to the circuit of problem 1, what would the new maximum current and peak magnetic induction be? Assume that the transmission line and coil inductances and resistances remain the same.

6. Derive Eq. (21G5) from (21G1).

Bibliography

G. P. Boicourt, "The prediction of failures in C.T.R. systems", Fifth Symposium on Engineering Problems of Fusion Research, IEEE, New York, 1973, p. 308-313.

E. L. Draper, Jr., Editor, *Technology of Controlled Thermonuclear Fusion Experiments and the Engineering Aspects of Fusion Reactors*, CONF-721111, 1974.

Fourth Symposium on Engineering Problems of Fusion Research, IEEE Transactions on Nuclear Science, NS-18, No. 4, August, 1971.

V. P. Kartsev, *Three Thousand Years of Magnets*, Mir, Moscow, 1975.

H. Knoepfel, *Pulsed High Magnetic Fields*, American Elsevier, New York, 1970.

H. Knoepfel, "Very high magnetic fields generated in single-turn solenoids", *Journal of Physics E: Scientific Instruments 5*, 1133-1141 (1972).

H. Kolm, B. Lax, F. Bitter, and R. Mills, Editors, *High Magnetic Fields*, Wiley, New York, 1962.

D. B. Montgomery, *Solenoid Magnet Design*, Wiley, New York, 1969.

D. H. Parkinson and B. E. Mulhall, *The Generation of High Magnetic Fields*, Plenum, New York, 1967.

R. F. Post and S. F. Post, "Flywheels", *Scientific American 229, No. 6, 17* (1973).

P. J. Turchi, Editor, *Megagauss Physics and Technology*, Plenum Press, New York, 1980.

CHAPTER 22

SUPERCONDUCTING MAGNETS

22A. Superconductivity

domain of superconductivity

When H. K. Onnes (1911) was measuring the resitivity of metals at low temperatures, he discovered that the resistance of a sample of mercury dropped abruptly from 0.125 Ohm at 4.27 K down to less than 3×10^{-6} Ohm (which was the limit of his instrument) at about 4.22 K. Onnes named this condition *superconductivity*. Many other metals and alloys have been found to exhibit similar behavior: their resistance drops to zero when the temperature is lowered below a *critical temperature* T_c, which is different for each material.

Onnes also found that superconductivity can be destroyed by applying a sufficiently strong magnetic field, called the *critical magnetic field* B_c. The critical magnetic fields of materials known then were too low to be of interest for winding magnets, however.

In addition to the temperature (T) and magnetic field (B) limitations, there is also a limit on the current density J which may be flowing in the superconductor. The maximum value of J, called the *critical current density* J_c, is a function of T and B. Thus, there is a domain in T, B, J space within which the material is in the superconducting state, as illustrated in Fig. 22A1 for a few materials. If either T, B, or J becomes too large, superconductivity ceases, and the material returns to normal resistivity.

electron pairing

A metal can be pictured as a sea of mobile electrons flowing through a lattice of positive ions. The lattice ions vibrate back and forth, and the quantized lattice vibrations (phonons) may interact with the wave functions representing electrons. When one electron produces a phonon which is absorbed by a second electron, a mutual attraction between the electrons results, according to the BCS theory (Bardeen, Cooper, and Schrieffer, 1957). If this attraction is stronger than the mutual Coulomb repulsion, then the two electrons may become loosely bound together by repeated electron-phonon-electron interactions, even though they are separated by a large distance. Formation of such *Cooper pairs* is most probable

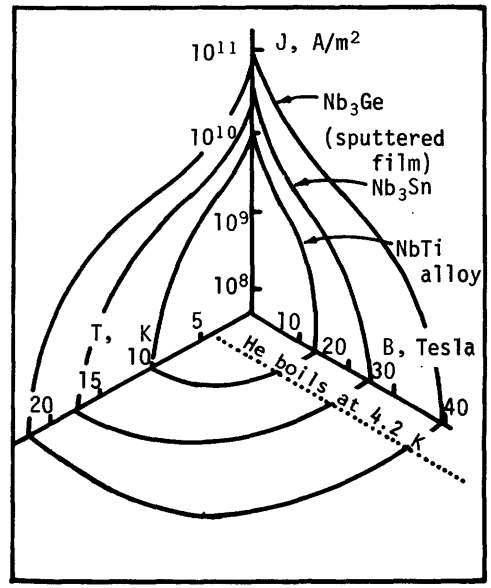

Fig. 22A1. Domains of superconductivity for several materials. The critical surfaces are shown as functions of temperature T, magnetic field B (upper critical magnetic field), and current density J. These materials are superconducting inside the critical surfaces, and they have normal resistivity outside the surfaces. From B. B. Schwartz and S. Foner, "Large-scale applications of superconductivity", Physics Today, July 1977, Fig. 2, p. 34.

for electrons having equal and opposite momenta and opposite spins. The separation between the paired electrons is much larger than the average distance between electrons. Many pairs of electrons overlap in the same spatial region, but the interactions between two paired electrons are much more important than their interactions with other electrons.

In an ordinary metal, electrons may be accelerated by an applied electric field and decelerated by collisions with the lattice. A balance between the acceleration and frictional forces determines the resistivity of the metal. In a superconductor, the paired electrons' interactions with the lattice affect only each other, without dissipation by the lattice. Then the frictional force is zero, and so is the resistivity.

Metals which have high conductivity at room temperature, such as copper, have weak electron-lattice interactions. The attraction of electron-lattice-electron interactions is not great enough to overcome Coulomb repulsion, so pairing cannot occur, and those metals cannot become superconducting.

energy gap

At zero Kelvin, with no applied magnetic field or current density, all electrons are paired. If energy is supplied to the metal, some of the Cooper pairs will be broken apart. For each pair split, the total electron system energy increases by an amount 2Δ, which is called the *energy gap*. Energy may be supplied by heat conduction, by applying an external magnetic field, by forcing a very large current density to flow through the metal, and by incident electromagnetic waves. If the added energy is large enough, all the Cooper pairs will be broken, and the metal will return to normal resistivity.

At T = 0 K, the energy gap is

$$2\Delta(0) \approx 3.5kT_c \qquad (22A1)$$

where k is the Boltzmann constant and T_c is the critical temperature. (The average energy of a diatomic molecule is 3.5kT.) As the temperature is raised, the presence of more unpaired electrons reduces the possible scattering states for the paired electrons, according to Pauli exclusion principle. The reduction of possible scattering states decreases the strength of the electron-phonon-electron interactions, reduces the attraction between electrons, and therefore

reduces the energy gap. Thus, as T increases, $\Delta \to 0$. The temperature where $\Delta = 0$ (and all electrons become unpaired) is, by definition, the critical temperature T_c.

The *coherence length* ξ is the spatial scale length over which the transition between a superconducting region and a normal region occurs. Thus, it is the approximate distance over which the density n_s of electrons in the superconducting state (the density of paired electrons) varies. It is also roughly equal to the average separation between any two paired electrons. In pure metals, $\xi \sim 1$ μm, but in impure metals, alloys, compounds, and metals with lattice defects, ξ can be much shorter, on the order of the electron mean free path.

diamagnetism

A superconductor tends to exclude an applied magnetic field from its interior, as was discovered by Meissner and Ochsenfeld (1933). This self-shielding effect was explained by London and London (1935).

The current density due to n_s superconducting electrons per m^3 moving with average velocity $\vec{v}$ is

$$\vec{J} = - n_s e \vec{v} \tag{22A2}$$

Moving particles have waves associated with them, with the DeBroglie wavelength λ and wavenumber k given by

$$\lambda = h/p, \quad k = 2\pi/\lambda = 2\pi p/h \tag{22A3}$$

where h is Planck's constant and p is the particle momentum. In a magnetic field, the momentum of a particle with mass m, velocity $\vec{v}$, and charge q is

$$\vec{p} = m\vec{v} + q\vec{A} \tag{22A4}$$

where $\vec{A}$ is the magnetic vector potential (Section 5B). Consider the case of a wave representing a Cooper pair, for which $m = 2m_e$, $q = -2e$. The phase difference between any two points along the wave is

$$\phi_b - \phi_a = - \int_a^b d\vec{\ell} \cdot \vec{k} = -(2\pi/h) \int_a^b d\vec{\ell} \cdot (2m_e \vec{v} - 2e\vec{A}) \tag{22A5}$$

where $d\vec{\ell}$ is a differential along the path from point a to point b. If we take the limit as $b \to a$, the result is

$$\vec{\nabla}\phi = -(4\pi/h)(m_e \vec{v} - e\vec{A}), \text{ or } \vec{v} = -h\vec{\nabla}\phi/4\pi m_e + e\vec{A}/m_e \tag{22A6}$$

Eliminating $\vec{v}$ between Eqs. (22A2) and (22A6), we get

$$\vec{J} = n_s e h \vec{\nabla}\phi/4\pi m_e - n_s e^2 \vec{A}/m_e. \tag{22A7}$$

Taking the curl of this equation , we find

$$\vec{\nabla}\times\vec{J} = -n_s e^2\vec{B}/m_e \quad , \tag{22A8}$$

since $\vec{\nabla}\times(\vec{\nabla}\phi) = 0$ by (F24) and $\vec{\nabla}\times\vec{A} = \vec{B}$ by (5B14). We can eliminate $\vec{J}$ using the Maxwell equation $\vec{J} = \vec{\nabla}\times\vec{B}/\mu_0$ (Eq. 5B8). Then

$$\vec{\nabla}\times(\vec{\nabla}\times\vec{B}/\mu_0) = -\nabla^2\vec{B}/\mu_0 = -n_s e^2\vec{B}/m_e \tag{22A9}$$

by virtue of Eq. (F30) and $\vec{\nabla}\cdot\vec{B} = 0$ (Eq. 5B6). If we let x be the direction perpendicular to the surface of a metal, then

$$d^2B/dx^2 = B/\lambda_L^2 \tag{22A10}$$

where

$$\lambda_L \equiv (m_e/n_s e^2\mu_0)^{\frac{1}{2}} = (\epsilon_0 m_e c^2/n_s e^2)^{\frac{1}{2}} = 5.3\times10^6 n_s^{-\frac{1}{2}} \quad . \tag{22A11}$$

If λ_L is constant, the solution of this equation for a thick metal is

$$B = B_0 e^{-x/\lambda_L} \tag{22A12}$$

where B_0 is the value of B at the surface x = 0. Thus, the magnetic field is attenuated exponentially in the metal over a distance λ_L, called the *London penetration depth.* [This penetration depth is comparable to the Debye length λ_D (Eq. 5F4) with kT_e replaced by $m_e c^2$.] For a typical case with $n_s \sim 10^{28}$ m^{-3} (less than one electron per atom in the superconducting state), $\lambda_L \sim 5\times10^{-8}$ m = 0.05 μm. Thus, the magnetic field is attenuated very close to the metal surface. (Some error is introduced into these equations when the separation of the Cooper pairs is greater than λ_L).

flux quantization

Consider the case of a superconducting region surrounding a normal region (Fig. 22A2). We can apply Eq. (22A5) to the integration path indicated by the dashed line. If we close the loop so that b coincides with a, then the phase difference must be an integer multiple of 2π:

$$2\pi n = (2\pi/h)\oint d\vec{\ell}\cdot(-2m_e\vec{J}/n_s e - 2e\vec{A}) \quad . \tag{22A13}$$

where n is an integer. By virtue of Stokes' Theorem (F10),

$$\oint d\vec{\ell}\cdot\vec{A} = \int d\vec{S}\cdot\vec{\nabla}\times\vec{A} = \int d\vec{S}\cdot\vec{B} = \Phi \tag{22A14}$$

where Φ is the magnetic flux enclosed by the integration path (Table 8B1). The current density is concentrated right at the boundary bewteen the normal and superconducting regions, so if the contour is drawn sufficiently far outside the

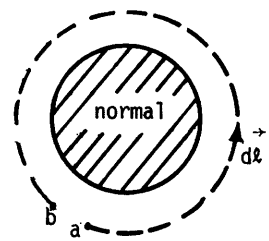

Fig. 22A2. Integration path around a normal region surrounded by a superconducting region.

boundary, the J term may be negligible. Then Eq. (22A13) reduces to

$$\Phi = n\Phi_0 \qquad (22A15)$$

where

$$\Phi_0 \equiv h/2e = 2.07\times10^{-15} \text{ Weber} \qquad (22A16)$$

is called a *fluxon*. Thus, the flux is quantized: the enclosed flux must be an integer number of fluxons. If the normal region is small, only one fluxon may be enclosed. Magnetic flux lines penetrating a superconductor tend to space themselves uniformly in a close-packed triangular lattice, as can be seen in Fig. 22A3.

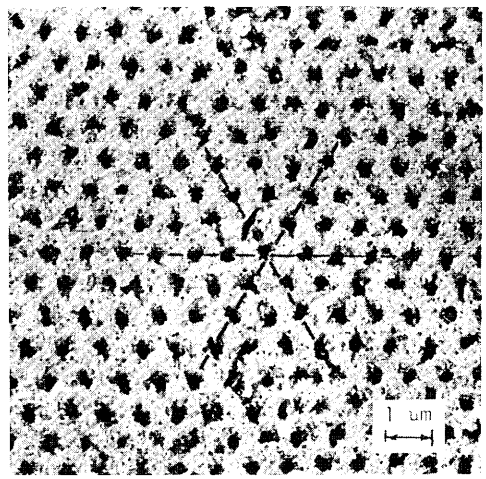

Fig. 22A3. Pattern of individual fluxons in a Type II superconductor. The pattern is revealed by allowing very small (500 Å) ferromagnetic particles to settle on the surface of a magnetized speciman (Pb-In alloy). The particles locate themselves where the magnetic flux intersects the surface. The photograph was obtained by electron microscopy of the deposited particles. Lines are drawn along the lattice directions. From H. Trauble and U. Essmann, Journal of Applied Physics 39, 4052 (1968).

Type I and Type II superconductors

Superconductors may be classified in two categories, depending upon the size of the coherence length ξ (average spacing between electron pairs) relative to the magnetic field penetration depth λ_L:

$$\xi > \sqrt{2}\,\lambda_L \quad \text{Type I}$$

$$\xi < \sqrt{2}\,\lambda_L \quad \text{Type II} \quad . \qquad (22A17)$$

Most pure metal superconductors are Type I. (Not all metals are superconductors.)

The critical magnetic induction above which Type I superconductors lose their superconductivity is given by

$$B_c = B_{c0}[1 - (T/T_c)^2] \ , \qquad (22A18)$$

where T is the temperature, T_c is the critical temperature (in the absence of a magnetic field), and B_{c0} is a constant. All Type I superconductors have low values of B_{c0}, as illustrated in Table 22A1 for a few metals, so they are unsuitable for winding magnet coils.

Table 22A1. Transition temperatures and magnetic flux density constants for some typical Type I metals. From A. C. Rose-Innes and E. H. Rhoderick, Introduction to Superconductivity, Pergamon Press, Oxford, 1969, Table 4.1, p. 46.

metal	T_c(K)	B_{c0}(T)
aluminum	1.2	0.010
lead	7.2	0.080
mercury α	4.2	0.041
β	4.0	0.034
tantalum	4.5	0.083
tin	3.7	0.031
zinc	0.9	0.0053

Niobium and vanadium are the only pure metals which are Type II superconductors. The discovery that Nb_3Sn wire can carry a high current density at B > 8 T (Kunzler et al, 1961) stimulated development of high-field magnets for fusion research and other applications.

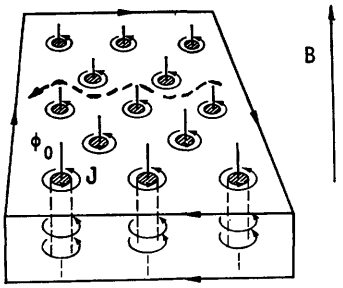

Fig. 22A4. Flow of vortex currents around fluxons ϕ_0. Each flux quantum ϕ_0 is in a local normal region, where the superconducting electron density n_s is very small (shaded regions), surrounded by circular vortex currents J. The outside of the metal has surface currents (large arrows) to maintain its diamagnetism. Additional superconducting internal currents may flow (dashed arrow) if an electric field is applied. From A. C. Rose-Innes and E. H. Rhoderick, Introduction to Superconductivity, Pergamon Press, Oxford, 1969, Fig. 12.3, p. 177.

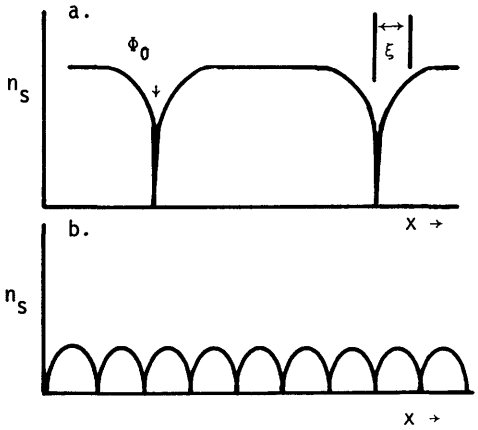

Fig. 22A5. One-dimensional variation of the density n_s of electrons in the superconducting state as a function of position x. (a) low flux density, (b) high flux density (near B_{c2}). Φ_0 denotes flux line location and ξ is the coherence length. When the flux lines are close together, their effects overlap, reducing n_s.

In Type II materials at low applied magnetic fields the magnetic field is excluded from the conductor, as in Type I materials. At the *lower critical magnetic field* B_{c1} the magnetic flux lines begin to penetrate into the metal. The flux lines (fluxons) carry a small normal core into the superconductor, similar to the normal region of Fig. 22A2. The positions of the fluxons can be photographed with an electron microscope, as shown in Fig. 22A3. Currents flow in circular vortices around each of the flux lines, as illustrated in Fig. 22A4. The existence of such Type II superconductors and their current vortices was predicted by Abrikosov (1957).

A one-dimensional plot of the superconducting electron density n_s vs. position in such a case is shown in Fig. 22A5. As the magnetic field is increased, the flux lines move closer together. Finally, at the *upper critical magnetic field* B_{c2} the overlapping of the effects of the flux lines reduces n_s to very small values, and superconductivity is lost. Thus, the condition for the flux density at the upper critical field may be written

$$B_{c2} \sim \Phi_0/(2\xi)^2 \qquad \text{(Tesla)}. \qquad (22A19)$$

critical current density in Type II materials

At very high magnetic fields, the critical current density is limited by the density n_s of electrons in the superconducting state. As n_s is decreased by overlapping of flux line effects, fewer electrons are available to carry the current.

At lower magnetic fields, where overlapping has a negligible effect on n_s, the Lorentz force limits the current which the material can carry. The fluxons tend to locate themselves along defects in the lattice, where their potential energy is lowest. The potential energy as a function of distance is illustrated in Fig. 22A6. The flux lines are said to be *pinned* to the defect locations. The Lorentz (JxB) force acting on current-carrying electrons tends to move these fluxons sideways from one lattice defect location to another. When the transverse current density (dashed arrow in Fig. 22A4) is high enough, the Lorentz force exceeds the pinning force of the potential barrier, and a fluxon can move from one location to the next. Such flux creep dissipates energy in the lattice (Anderson, 1962; Kim et al, 1963). The motion of many flux lines, called *flux jump*, may raise the local temperature above the critical temperature T_c, causing the material to become normal locally. To attain high critical current densities, it is desirable to minimize flux jumps, by having strong pinning forces in the material. One means for achieving this is by extensive cold-working, which increases the number of lattice defects. It has been said that the "worst lattice microstructures" produce the "best Type II superconductor properties".

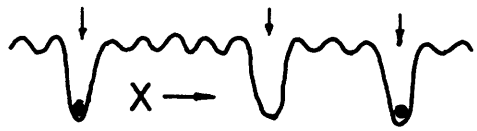

Fig. 22A6. One-dimensional variation of the potential energy of magnetic flux lines as a function of position in the metallic lattice. Arrows denote lattice defects, and dots denote pinned flux lines.

magnet coils

A superconducting material should have five properties in order to be satisfactory for winding magnets: high critical temperature T_c, high critical magnetic field B_{c2}, high critical current density J_c, commercial availability, and good mechanical properties, such as ductility. (Brittle conductors may be used if special fabrication techniques are employed.)

Type II superconductors, such as Nb_3Sn and NbZr, were used to build small magnets in the early 1960's, but the coils would often *quench* (transfer from the superconducting state to the normal state) unexpectedly. Since then, superconducting magnet technology has progressed to the point where large, high-field magnets can be built with less risk of failure. For example, the MFTF test coil (inside diameter 1.05 m) has been tested successfully with B > 7 T at the conductor.

22B. Superconductors

Conductors available commercially include NbTi, Nb_3Sn, and V_3Ga. Some properties of these materials are listed in Table 22B1. Niobium-zirconium was used in the 1960's, but it is now obsolete, having been replaced by NbTi, which has superior properties. Because of its good ductility, NbTi can be drawn into multiple thin filaments in a matrix of copper (Fig. 22B1) in order to help avoid quenching (Section 22C).

NbTi is not suitable for fields B > 8.5 T, unless the temperature is reduced below 4.2 K. (The NUWMAK tokamak design plans to use NbTi at 1.8 K to attain B = 12 T at the conductor.) V_3Ga has a higher current density than Nb_3Sn when B > 13 T, but it is also more expensive. Thus, NbTi is usually used for B < 8 T, Nb_3Sn for 8 < B < 13 T, and V_3Ga for B > 13 T. Nb_3Sn and V_3Ga are brittle and difficult to fabricate.

Before 1975 Nb_3Sn and V_3Ga were usually fabricated in tapes by reacting a thin layer of the brittle superconductor on a ductile substrate. Although such conductors have been used to wind many high-field coils (up to 17 T), they have some undesirable features:

* Their large ratio of width to thickness makes it difficult to wind coils which bend in more than one plane, such as Yin-Yang coils (Chapter 11).
* Tape conductors cannot be twisted or transposed like multifilamentary conductors can. They are highly diamagnetic, have large circulating currents, and are therefore prone to very large flux jumps. One plasma confinement experiment was a failure because its Nb_3Sn tape-wound coils were unable to attain even half the design fields without quenching.

Table 22B1. Parameters of common superconductors. From J. File, "Superconductivity as applied to fusion reactors", Lecture 11, A Short Course in Fusion Power, Princeton University, 1972, Table 11.1, p. 11.8.

type	T_c (K)	B_{c2}(T) at 4.2K	J_c(GA/m^2) at 4.2 K
Nb-33% Zr	10.7	8	.5 at B = 6 T
Nb-48% Ti	9.5	12.2	.8 at B = 7.5T
Nb_3Sn	18.2	24.5	5 at B = 10 T
V_3Ga	~15	21	4 at B = 10 T .2 at B = 20 T

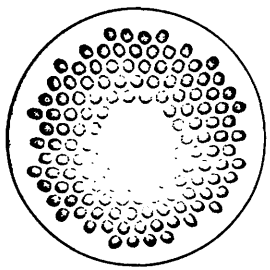

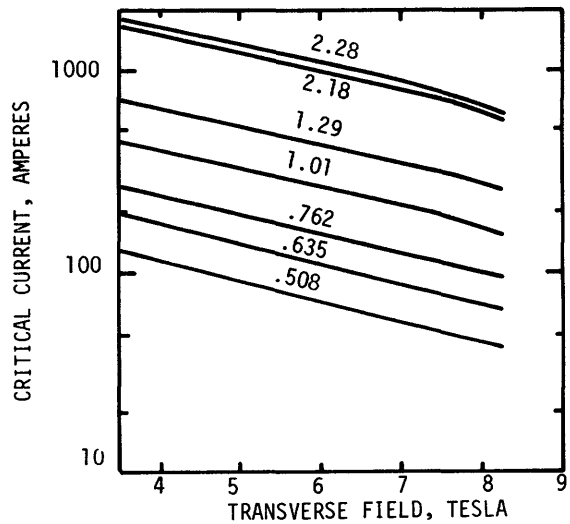

Fig. 22B1. Multifilamentary NbTi superconductors in a copper matrix (left) and critical current vs. magnetic field (right). Each wire contains 132 NbTi filaments and has a ratio of Cu:NbTi of 2.6:1. The numbers on the curves refer to the copper wire diameters (mm). Courtesy of the Magnetic Corporation of America, Waltham, MA.

Development of a process for producing multifilamentary Nb_3Sn conductors was a major advance in superconducting magnet technology. Nb filaments are extruded in a bronze matrix, and then the tin diffuses from the bronze into the Nb at elevated temperatures, producing a thin layer of Nb_3Sn. Such a conductor is illustrated in Fig. 22B2. A similar process has been devised for producing multifilamentary V_3Ga conductors. Although the Nb_3Sn is very brittle, the critical current density J_c actually increases slightly for strains below about 0.6%, as indicated in

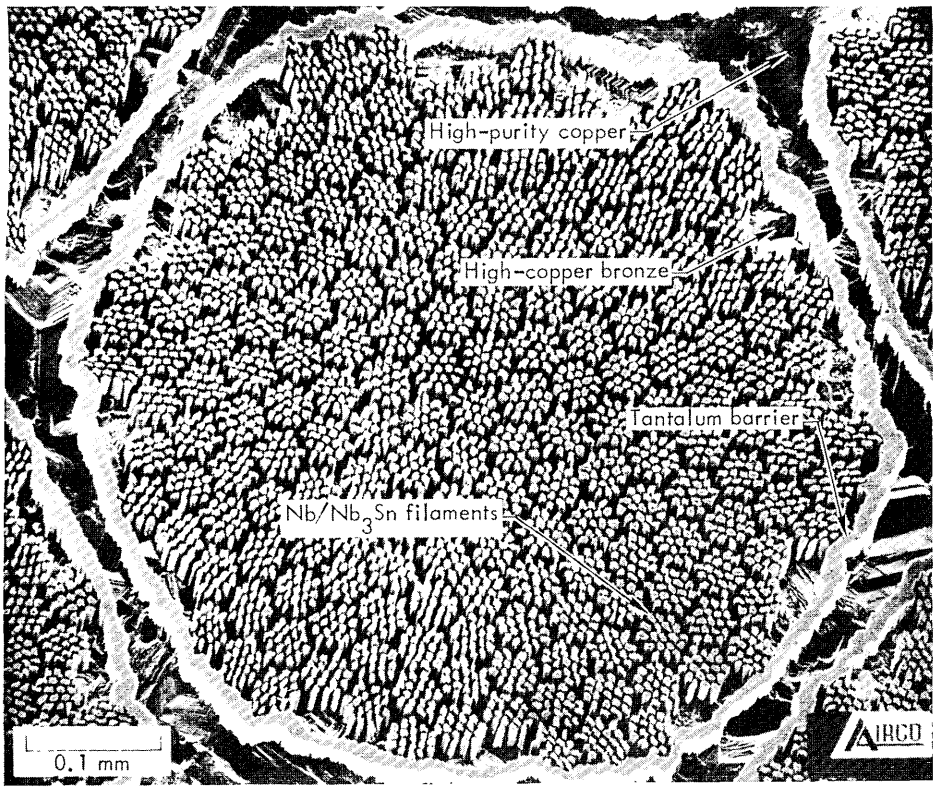

Fig. 22B2. Scanning electron micrograph of an etched section of Nb_3Sn conductor made with the external bronze technique by AIRCO, Inc. The tantalum liner surrounds a bronze matrix in which 3353 niobium filaments are embedded. The tin in the bronze has reacted with the niobium to form a layer of Nb_3Sn 1 to 2 μm thick. From Energy and Technology Review, December 1975, Fig. 5, p. 10. Courtesy of Lawrence Livermore National Laboratory and the US Department of Energy.

Fig. 22B3. Critical current I_c (normalized to the zero-strain value I_{co}) vs. strain for sample A-16 at various magnetic fields, including recovery from maximum strain when load is removed (dashed curves at bottom). From D. W. Deis et al, Advances in Cryogenic Engineering, Volume 24, Plenum, New York, 1978, Fig. 6, p. 322, and UCRL-79192 (1977).

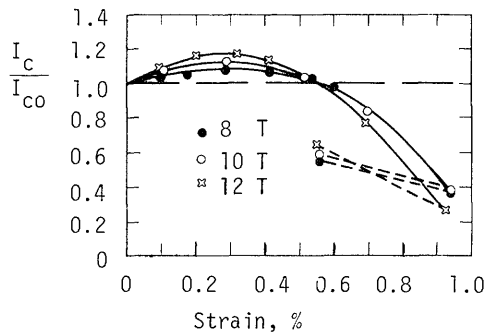

Fig. 22B3. This increase is probably due to the relief of residual compressive stresses in the conductor. Composite conductors capable of carrying 10 KA have been built by combining many conductors in parallel in a copper substrate.

Coils for B > 8 T are sometimes wound with NbTi on the outside and Nb_3Sn or V_3Ga in the high-field region on the inside of the coil. Water-cooled copper coil inserts may be used to attain higher fields (30 T has been attained in a 3 cm bore), or for regions exposed to high radiation levels.

The ideal current densities are not always attainable, however. In order to avoid quenches, superconducting coils must be stabilized.

Other conductors with superior properties may become available in the future. Properties of some materials under study are listed in Table 22B2.

Table 22B2. Some developmental superconductors. From J. File, "Superconductivity as applied to fusion reactors", A Short Course in Fusion Power, Princeton University, 1972, Table 11.2, p. 11.13.

material	T_c (K)	B_{c2} at 4.2 K	J_c(GA/m^2) at 4.2 K (B) in parentheses
NbN	~17	~20 (T)	
V_3Si	17	23.5	3 (4 T)
PbBi (glass)	8.6	12.5	.4 (5 T)
Nb_3Al	19	29.5	
$Nb_3(Al_{0.8}Ge_{0.2})$	20.7	40	3 (10 T) .15 (15 T, 16 K)
$V_2Hf_{0.5}Zr_{0.5}$	10	23	1 (13 T)

22C. Stabilization

need for stabilization

Various processes, such as flux jumps and conductor movement, can generate heat and make $T > T_c$ in a small region of superconductor, causing that region to go normal. When this occurs, the local resistance of the conductor goes from zero up to a finite value instantaneously. One might expect the finite resistance to lower the current, but any change in current develops a large voltage equal to L(dI/dt), where L is the coil inductance, and this voltage maintains the current nearly constant if the inductance is large. (The current will gradually decay with a time constant of L/R). Since a high current is flowing through a finite resistance, it dissipates heat at a rate $P = I^2R$ (W), heating up the surrounding conductor, too. This heating may drive the surrounding conductor normal, and the region of normalcy may spread rapidly throughout the entire coil. This rapid spread of the superconducting-to-normal transition is called a *quench*. In small magnets quenching can cause much of the liquid helium coolant to vaporize suddenly. The resulting overpressure could rupture the cryostat, if provisions for pressure-relief were not made. (A *cryostat* or *dewar* is an insulated container for low temperature devices, such as magnets.) If the magnet's stored energy is large, quenching could dissipate enough energy to melt part of the coil. Therefore, coils must be stabilized against quenching in order to attain their design fields, and they must be protected against the consequences of a quench, in case it occurs.

methods of stabilization

There are three main methods of stabilization:

* *cryogenic stabilization.* When normalcy occurs in the superconductor, its resistance suddenly becomes higher than that of the surrounding copper, so most of the current is shunted into the copper substrate. Thus, the overall resistance is lower than it would be if only superconductor were present, and less heat is generated. If the substrate has good thermal contact with the helium coolant, then the heat generated may be quickly transferred to the coolant without overheating surrounding areas, and a quench is avoided. This type of stabilization can occur when

$$\alpha_s = \frac{\text{(power dissipated)}}{\text{(power removed)}} = \frac{I^2 \eta \ell / A}{q\ S} \leqq 1 \ , \qquad (22C1)$$

where α_s is called the *Stekly number,* η is the resistivity of the conductor (Ohm-m); I is the current (A), A is the cross-sectional area of the conductor(m^2), ℓ is the length under consideration, S is the conductor surface area in contact with the helium coolant (m^2), and q is the maximum heat flux which the coolant can remove. For nucleate boiling in liquid helium $q \sim 4000\ W/m^2 = 0.4\ W/cm^2$. This type of stabilization relies on two phenomena: *current sharing* by the substrate and rapid *heat removal* by the coolant.

* *Adiabatic stabilization.* This method involves the use of superconductor *filaments* (Figs. 22B1, 22B2) which are so thin that the heat dissipated by a flux jump is too small to raise the temperature above T_c. The stability criterion for circular filaments is

$$dJ_s < \pi(\rho_m C_p T_0/\mu_0)^{\frac{1}{2}} \qquad (22C2)$$

where d is the filament diameter (m), J_s is the current density in the filament (A/m^2), ρ_m and C_p are the density (kg/m^3) and specific heat (J/kg-K) of the filament, μ_0 is the permeability of free space, and

$$T_0 \equiv - J_s(\partial J_s/\partial T)^{-1}_{B\,=\,\text{constant}} \ . \qquad (22C3)$$

Values of T_0 for NbTi and Nb_3Sn are shown in Fig. 22C1 as functions of B and T, Typically $\rho_m C_p \sim 1000\ J/m^3K$. If d $\sim$ 10 μm and $T_0 \sim 10$ K, then $J_s \lesssim 3\times10^{10}\ A/m^2$.

To prevent current loops from being induced between adjacent filaments as the field is increased, the filaments in a given substrate must be transposed (braided or twisted) with at least 4 transpositions occurring in a "critical length"

$$\ell_c = [2J_s d\ \eta/(dB/dt)]^{\frac{1}{2}} \qquad \text{(m)} \qquad (22C4)$$

where η is the substrate resistivity (Ω-m) and (dB/dt) is the time rate of change of the magnetic induction (T/s). Thus, a pulsed coil must have a short transposition length.

Adiabatic stabilization allows higher current densities than cryogenic stabilization, and it permits the field to be changed rapidly, provided that the trans-

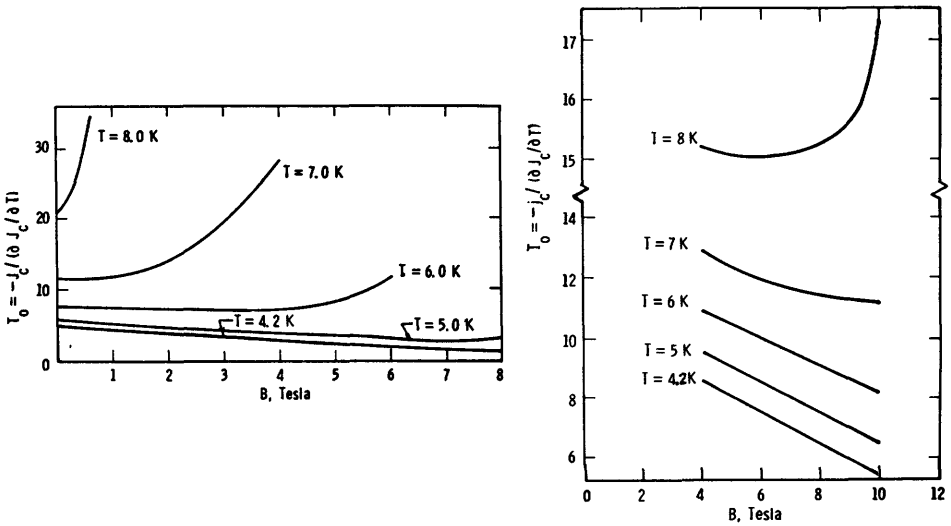

Fig. 22C1. Adiabatic stability parameters for NbTi (left) and Nb_3Sn (right) as functions of magnetic field and temperature. From B. R. Buncher et al, ORO-5153-1 (1976), Figs. 3.1.5 and 4.2.2.

position of filaments is adequate. Devices with pulsed coils use adiabatic stabilization. Epoxy may be used to prevent conductor motion.

* *dynamic stabilization.* Dynamic stabilization, used mainly with Nb_3Sn or V_3Ga tapes, relies on *magnetic damping* of flux jumps by the substrate material to reduce the heat generated, combined with *heat removal* by conduction. Two conditions must be met:

$$H_{\perp} < \pi(K_{cu}T_0/4\eta)^{\frac{1}{2}} \qquad \text{(A/m)} \qquad \text{(22C5)}$$

and

$$J_s < (\pi T_0 d_n K_s/\eta d_s^3)^{1/2} \qquad \text{(A/m}^2\text{)} \qquad \text{(22C6)}$$

where $H_{\perp}$ is the magnetic field (A/m) perpendicular to the ribbon (in the radial direction), K_{cu} and K_s are the thermal conductivities of the copper and superconductor (W/mK), η is the resistivity of the substrate (around 3×10^{-10} Ohm-m for copper), J_s is the current density in the superconductor (A/m^2), and d_n and d_s are the thicknesses of the normal conductor and superconductor ribbons (m). Since the Stekly number is greater than one, higher current densities may be achieved with dynamic stabilization than with cryogenic stabilization, but dynamic stabilization alone is not always reliable.

Use of materials with high heat capacities will minimize the temperature rise per Joule of heat added. Since liquid helium has a comparatively high latent heat of boiling, good contact between the helium and the conductors is helpful.

22D. Coil Protection

fault conditions

Fusion reactor coils will have stored energies on the order of GJ per coil. The coils must be protected against several possible fault conditions, including:

* *quench.* If a 1.5 GJ coil containing 70 tons of copper quenched and the entire energy were dissipated uniformly in the copper, then the coil temperature would rise to about 140 K, with little damage. If the energy were dissipated in a small region of the coil, however, the insulation or epoxy could overheat, and the copper could melt. Thus, it is desirable to ensure that the energy is either transferred to an external heat sink or dumped uniformly in the coil. The helium will be boiled and expelled from the dewar, which should be protected against rupture from overpressure.

* *broken circuit.* In this event, one or more arcs would occur between the broken ends of the conductor and the coil case, with an arc voltage on the order of 100 V. The arc could puncture a thin steel coil case, destroying the vacuum insulation and causing associated problems. The resistance of surrounding room-temperature structures is too high for much energy to be dumped into them.

* *short circuit to ground.* If the coil is grounded, a current-limiting resistor is usually inserted in the ground connection. This can limit the current to about 10 A, which will not cause too much damage.

* *coolant channel blockage.* If a normalcy occurred, inadequate heat removal could prevent recovery of superconductivity.

A comprehensive survey by BNL of superconducting magnet operational experience revealed that about 50% of existing systems had experienced some type of failure, such as hot spots and arcing, power lead failure, or conductor movement (Hsieh et al, 1978).

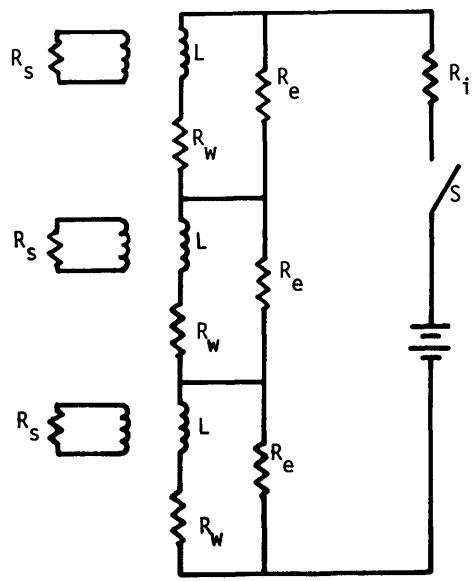

Fig. 22D1. Equivalent circuit of a coil protection system. L = coil inductance, R_w = coil winding resistance, R_e = external energy dump resistance, R_s = resistance of coil support structure, R_i = resistance of coil leads and power supply. Adapted from B. R. Buncher et al, ORO-5153-1 (1976), Fig. 3.3.10, p. 3-123.

protection circuitry

Protection circuitry can be passive (in place constantly) or active (actuated by switching devices). An example of a coil protection circuit is shown in Fig. 22D1. During normal operation the winding resistance R_w is zero, and current from the power supply flows through R_w and L. If a quench occurs, the current flows through the external resistances R_e, which can be massive ($\sim$ 10 ton) bars of iron, or water-cooled stainless-steel, and the switch can be opened. If the coil current is 10 kA and R_e = 0.1 Ohm, then 1000 Volts are developed across the insulation. If the inductance L = 30 H, then the current decays exponentially with decay time L/R = 300 s.

fault detection

In order to know where fault conditions exist, elaborate detection systems will be needed. Some parameter changes which can be monitored to identify various problems are listed in Table 22D1. It is not practical to put thousands of tem-

Table 22D1. Coil fault detection methods. From B. R. Buncher et al, ORO-5153-1 (1976), Fig. 3.3.13, p. 3-133.

Problem	Parameter Changes
Quench	Increased Coil Resistance Increased Local Temperature in Winding Increased Helium Heat Load Increased Coil Power Consumption Changing Magnetic Field Increased Voltage Across Coil Increased Helium Pressure Drop Changing Current Distribution between Coils
Ground Insulation Failure and Turn to Turn Short Circuit	Unbalanced Currents in the Array* Low Resistance to Ground Lower Capacitance to Ground Increased Local Temperature* * Occurs only when voltage appears across the coils
Open Coil Lead	Unbalanced Current in the Array Voltage Appears across Coil Increased Heat Load to Coil Structure Increased Currents in Neighboring Coils Changing Magnetic Flux in the Array Resistance Change in Conductor Currents Appear in External Resistor
Coil Movement	Coil Position Change
Coolant Pump Failure or Coolant Tube Rupture	Decreasing Helium Flow Rate Decreasing Helium Pressure Loss of Coolant Volume Coil Quench
Dewar Failure or Vacuum Pump Failure	Loss of Differential Pressure - Dewar to Atmosphere Increased Heat Load on Helium System
Refrigeration System Failure	Increased Helium or Nitrogen Temperature Increased Coil Temperature

perature-measuring devices in a coil. Local normalcies develop small increases in coil resistance, which are not easy to detect. (A single turn quench in a large coil would produce a voltage ∿ 30 mV.) Measurements of position, vibration, magnetic flux, pressure and flow can be done with standard equipment. Coil data will be computer-processed and interlinked with computer control of plasma heating and control systems.

The main conclusions of a magnet safety study are summarized in Table 22D2.

Table 22D2. Major conclusions of a magnet safety analysis. From S. Y. Hsieh, M. Reich, and J. R. Powell, "Safety issues for superconducting magnets", CONF-780508 (1978), Table 8, p. 901.

Large numbers of potential accident pathways can be visualized for fusion magnets. Quantitative estimation of probabilities is not yet feasible.
Very low failure rates will be required for fusion magnets.
Coil disruption accidents principally involve local conductor/reinforcement failure with subsequent spreading arcs.
Conductor arcs and failures should be considered as design basis accidents.
Most magnet energy must be dumped internally during a quench, due to voltage limitations.
Temperature will have to be relatively homogeneous during a quench, to prevent local mechanical yielding and/or electrical breakdown.
Electrical breakdown withstand capability will be very limited (<1000 Volts) if rigid reinforcement structure is used. (Reinforcement acts as a ground plane).
Organic insulators are probably not acceptable (H_2 release).
Capability to detect local hot spots (due to coolant channel blockage, etc.) is necessary. Large numbers of detectors will probably be required.

22E. Coil Design Considerations

Some coil design considerations are listed in Table 22E1. Several of these may require iteration, in order to satisfy overlapping criteria.

conductor design

The required coil energy $LI^2/2$ (L = inductance, I = current) is roughly equal to $VB^2/2\mu_0$, where $B^2/2\mu_0$ is the average magnetic energy density in the volume V corresponding to the coil. It is desired to have large I and small L, in order to have strong conductors, not too many turns to wind, and the ability to discharge the coil energy into the protective system in a reasonable length of time L/R_e. However, as the conductor size is increased, cryogenic stabilization becomes increasingly difficult, because the heat transfer area grows linearly with conductor size, while the current is proportional to the square of the conductor size. The conductor current in present large coils is typically ∿10 kA.

Large coils will use multifilamentary conductors and enough copper to provide cryogenic stabilization. This limits the attainable current density to

Table 22E1. Coil design considerations

magnetic analysis	magnetic field $\vec{B}(\vec{x})$, required number of Ampere-turns, inductances
conductor design	conductor current, stabilization, size, strain, AC (pulsed) losses, winding scheme, joints, availability, cost
coil protection	fault conditions, minimization of damage
heat removal	method, coolant channel configuration, coolant flow rate, pumping needs and stresses
structural design	forces and stresses under normal and fault conditions, thermal stresses, reduction of bending moments by adjusting coil shape, coil support structure, coil winding and clamping
cryogenics	heat loads, refrigeration requirements, dewar design
radiation damage	neutron and gamma ray doses to coil and structure, effects on properties such as resistivity of substrate

$J \sim 1\text{-}5$ kA/cm^2 (10-50 MA/m^2). Given the conductor current ($I \sim 10$ kA), the conductor cross sectional area is then fixed (a few cm^2).

The conductor strain, which can be estimated from stress calculations, is typically limited to values $\varepsilon \lesssim 0.3\%$ (Nb_3Sn), to avoid degradation of performance. In order to plan cryogenic refrigeration requirements and ensure stability, AC losses induced by pulsed ohmic heating fields must be calculated. Very large coils may be wound at the reactor site, instead of at a factory, due to shipping difficulty. Joints between superconductors have been made by soldering, clamping, or cold-welding. Cold-welding was used with the MFTF magnet conductor cores. Because the tiny superconducting filaments do not mate at joints, the current must flow through a thin layer of copper, resulting in a slight voltage drop and resistive heating.

heat removal

Several methods are available for heat removal:

* *pool boiling*. The coil may be immersed in a pool of liquid helium, with slots for helium flow through the windings. The boiling helium going up will be lighter than the nonboiling liquid helium coming down. If a helium reservoir is placed at the top of a tall chimney above the coil dewar, the difference in densities of the two channels creates a pressure difference, which drives natural convective flow. This method is used with the MFTF coil. Figure 22E1 shows the MFTF conductor, with coolant slots for free flow of helium through the coil.

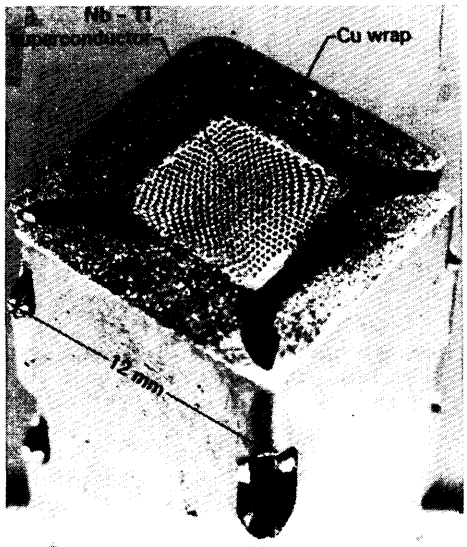

Fig. 22E1. The multifilamentary NbTi conductor for the MFTF magnet, with copper jacket and cooling slots, outside dimensions 12.4x12.4 mm. Courtesy of D. N. Cornish, Lawrence Livermore National Laboratory.

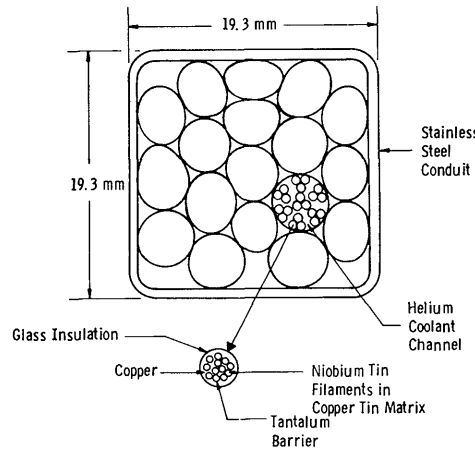

Fig. 22E2. Cross section of a niobium-tin conductor for a 12 Tesla TF coil. From B. R. Buncher et al, ORO-5153-1 (1976), Fig. 4.7.2, p. 4-83.

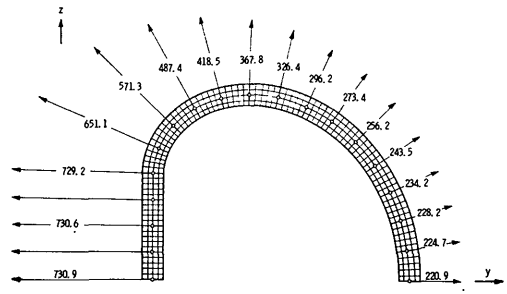

Fig. 22E3. The forces per unit length (arbitrary units) on the top half of a large TF coil, during normal operation. When one of the 16 TF coils quenches, then the forces on the other coils become skewed. From B. R. Buncher et al, ORO-5153-1 (1976), Fig. 4.3.4, p. 4-35.

* *forced two-phase flow cooling.* A pump is used to increase the flow rate of the helium. It can remove higher heat fluxes than natural convection, but the flow is prone to maldistribution and instabilities, so it is difficult to be confident of heat transfer predictions.

* *forced flow supercritical cooling.* In this case the coolant is not only pumped through the core, but also pressurized, so that boiling does not occur. This method provides good flow distribution, but the required pumping power adds extra heat to the helium, which must be removed by the refrigeration system. Figure 22E2 shows the cross section of a Nb_3Sn conductor designed for use in a 12 Tesla pancake-wound (Fig. 20E1a) TF coil, with coolant flow paths several hundred meters long.

structural design

Large coil design is dominated by stress considerations. Almost half the magnet cost and technical difficulty is associated with the coil structure. An example of the forces on a D-shaped TF coil is shown in Fig. 22E3. This shape is chosen to minimize bending moments on the coil during normal operation. When

Selecting the structural material and design stresses, several failure modes must be considered.

The design criteria developed by the MFTF group include:
* number of design stress cycles < 4 fatigue life (Chapter 24).
* design stress < smallest of
  (2/3) of yield stress (tension and combined stress)
  90% of yield stress (primarily bending stress)
  (1/3) tensile strength
  $(1/2)K_{IC}/(\pi a)^{\frac{1}{2}}$

where K_{IC} is the fracture toughness (Pa-$m^{\frac{1}{2}}$) and a is the flaw size (m). Stainless steels 304LN and 316LN were chosen for the MFTF magnet case and large TF test coils. Development of reliable welding techniques for coil structures is of particular concern. Structural materials problems are discussed by Henning and Dalder (1979).

Cryogenics and radiation damage problems will be discussed in Chapters 23 and 24.

22F. Large Coils

MFTF magnets

One MFTF Yin-Yang coil is shown in Fig. 22F1. Some of its parameters are listed in Table 22F1. The conductor was shown in Fig. 22E1. The arrangement of conductors and insulators in the 7.6 cm thick case is shown in Fig. 22F2. The stainless steel bladder, which serves as a form for injection of urethane thermal insulation, is indented to aid vacuum pumping. The natural convection helium flow rate is estimated to be 0.7 kg/s. At the estimated heat load of 350 W, this will result in less than 5% vapor bubbles at the top of the magnet (95% liquid).

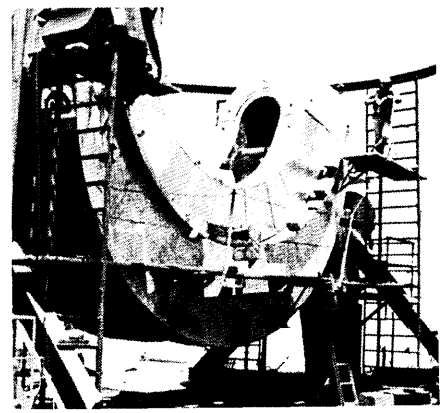

Fig. 22F1. One of the MFTF Yin-Yang coils. From LLNL Mirror Fusion Quarterly Report, April-June 1980, UCAR-10060-80-2, Fig. 41.

The external resistor is 0.17 Ohm, in order to keep the IR_e voltage less than 1000 V. The L/R_e time constant is then 69 s. If there were a 10 s delay before the quench detection circuit disconnected the power supply, then the conductor temperature rise in the absence of heat removal would be 200 K.

Large Coil Test Facility (LCTF)

The goal of the Large Coil Test Facility is to develop experience with large superconducting TF coils to assure performance, reliability, safety, and economy of future magnet systems. The facility consists of a torus of six large D-shaped TF coils, each from a different manufacturer, in a 13 m-high chamber at ORNL. A model of one of the coils is shown in Fig. 22F3. Some parameters of the six coils are listed in Table 22F2. The considerable variation in coil design will provide data on several different concepts of conductor design, cooling method, winding technique, and materials. The coils are tapered where they fit together against a bucking cylinder at the center of the torus. After testing the six 8-Tesla coils,

Table 22F1. Parameters of an MFTF Magnet. From C. D. Henning et al, "Mirror fusion test facility magnet", Proceedings of the Eighth Symposium on Engineering Problems of Fusion Research, San Francisco, 1979, Tables 1-4.

Magnet	
Maximum field	7.68 T
Central field	2.0 T
Mirror ratio	2.1
Mirror-to-mirror length	3.6 m
Major radius (mean)	2.5 m
Minor radius (mean)	0.75 m
Current	5775 A
Turns	1392
Stored energy	409 MJ
Conductor current density	3729 A/cm^2
Coil current density	2525 A/cm^2
Surface heat flux	.19 W/cm^2
Conductor length	50 km
Total weight	341,000 kg

Superconductor	
Critical current(4.2 K)	10 kA @ 7.5 T
Copper/Superconductor	1.7/1
Number of filaments	480
Filament diameter	0.20 mm
Twist pitch	180 mm
Conductor resistance ratio	150/1
Core size	6.5x6.5 mm

Stabilized conductor	
Maximum conductor field	7.68 T
Maximum conductor current	5775 A
Conductor operating temperature	4.5 K
Overall - Copper/ Superconductor	6.7/1
Stabilizer copper resistance ratio	220/1
Copper resistance at 4.5 K, 7.68 T	46 nΩ/cm
Helium cooled surface area	8.17 cm^2/cm
Required heat transfer rate	.19 W/cm^2
Overall size	12.4x12.4 mm

Thermal conditions in magnet	
Helium temperature at magnet inlet	= 4.36 K
Pressure at bottom of magnet	= 130 KPa (1.28 atm)
Saturation temperature at magnet inlet	= 4.52 K
Helium natural circulation rate	≃ 700 g/s
Heat load on magnet	≃ 350 W
Mean quality of helium at magnet outlet	< 5%
Minimum conductor transition temperature	= 4.98 K

Quench characteristics	
Coil inductance	= 11.0
Mutual inductance	= 1.2 H
Peak voltage	= 1,000 V
Quench-time constant	= 69 s
Peak conductor temperature after 100 seconds	< 200 K
Delay time	= 10 s
Propagation velocity	= 1.2 m/s
Quench resistor	= .17 Ω

the LCTF will be used to test large 12-Tesla coils.

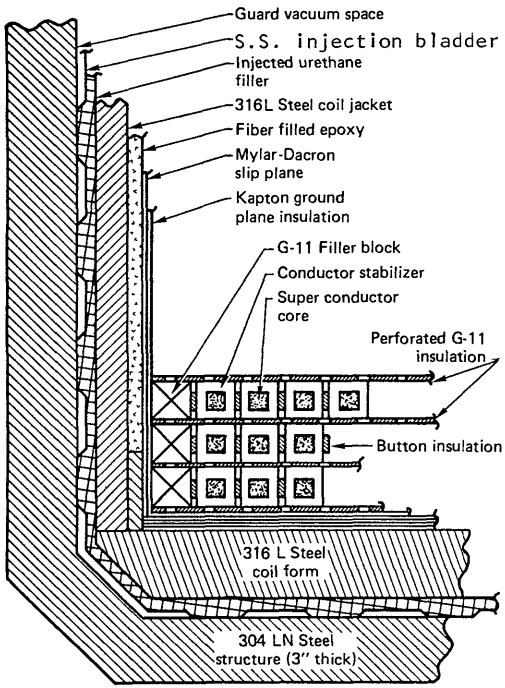

Fig. 22F2. Cross section of an MFTF coil. From C. D. Henning et al, (1979), Fig. 3.

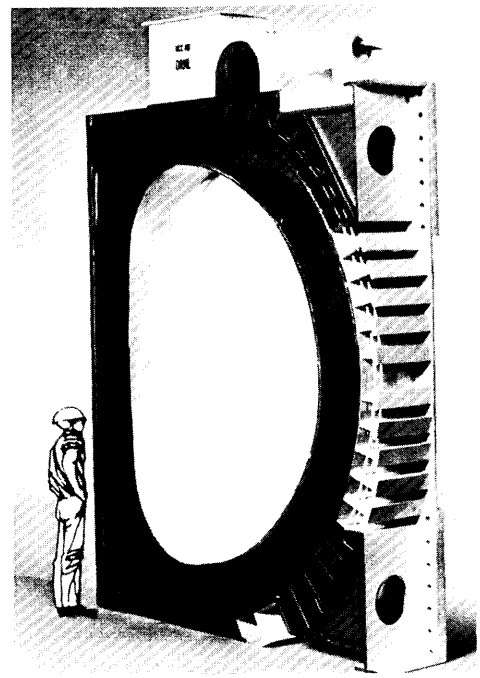

Fig. 22F3. Model of the General Dynamics coil for the LCTF. Courtesy of Oak Ridge National Laboratory.

Table 22F2. Parameters of the six large TF coils for the LCTF. All coils have a 2.5 by 3.5 m bore and produce a peak field of 8.0 Tesla at the inside of the coil. Each coil weighs about 40 tons.

	GD/CONVAIR	GENERAL ELECTRIC	WESTINGHOUSE	EURATOM	JAPAN	SWITZERLAND
Ampere-turns	6.6×10^6	7.0×10^6	7.4×10^6	6.6×10^6	6.8×10^6	6.0×10^6
Conductor current	10,200 A	10,450 A	17,800 A	11,000 A	10,210 A	13,000 A
Conductor material	NbTi	NbTi	Nb_3Sn	NbTi	NbTi	NbTi
Conductor configuration	Flattened cable in extended-surface copper bar	16 subelements, spiraled around copper core	Cable (insulated strands) in square conduit	22 subelements, spiraled around CrNi core, in rectangular conduit	Flattened cable in rough-surface copper bar	Square soldered-filled cable with coolant tube at center
Helium conditions	Pool boiling (4.2 K, 1 atm)	Pool boiling (4.2 K, 1 atm)	Supercritical, forced flow	Supercritical, forced flow	Pool boiling (4.2 K, 1 atm)	Supercritical forced flow
Winding	Edge wound in layers (14) on bobbin	Flat wound in pancakes (7) on bobbin	Laid in spiral grooves in 26 structural plates	Flat wound in pancakes (7) on forms	Edge wound in pancakes (20) on forms	Wound in pancakes (11) on bobbin
Structural material	304L stainless steel	316LN stainless steel	2219-T87 plates A286 bolts	316LN stainless steel	304L Stainless steel	316L/316LN stainless steel
Structure configuration	Fully welded case	Welded case with bolted closure	Grooved flat plates, bolted	Welded case, bolted closure	Welded case, bolted side plate closure	Bolted case

22G. Superconducting Magnetic Energy Storage

by R. W. Boom

University of Wisconsin

Superconducting magnetic energy storage (SMES), being developed by the University of Wisconsin and Los Alamos National Laboratory, can be used for several purposes:

* diurnal energy storage for peak shaving and load leveling by electric utility companies.
* energy supply for fusion reactor coils and heating systems
* stabilization of long-distance power transmission systems
* energy supply for high-energy particle accelerators.

Energy stored by a utility company during off-peak hours is discharged during peak demand hours. This *peak shaving* avoids the more expensive generation of peak power by oil-fired combustion turbines or by the inefficient older units typically relegated to intermittent generation.

Larger SMES diurnal storage units could replace intermediate load generation, as sketched in Fig. 22G1 [Boom et al (1981) and Eyssa et al (1981)]. The 1995 projected load curve for Wisconsin Electric Power Company shows that base load generation (the most efficient generators) could be increased from 3000 MW to 4000 MW and that the 350 MW of SMES discharged for 15 h would obviate the need for purchasing a new cycling coal generator costing $1000/kW in 1981 dollars. Credits for capital costs, fuel costs and spinning reserve could allow about $100 per kWh for the construction of an intermediate size SMES unit. SMES can be used for intermediate load because its storage efficiency is 95%. The other storage systems (batteries, pumped hydrostorage, and compressed air storage) are only 50% to 70% efficient and could not meet the intermediate use requirement. Such

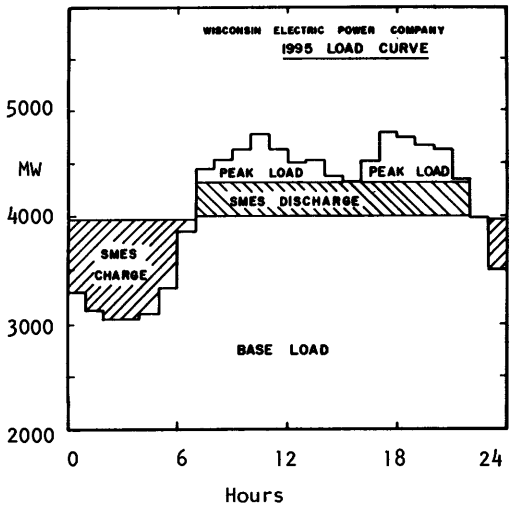

Fig. 22G1. Projected load curve for Wisconsin Electric Power C. (1995) with SMES discharging 350 MW for 15 hours and charging up to 930 MW for 9 hours.

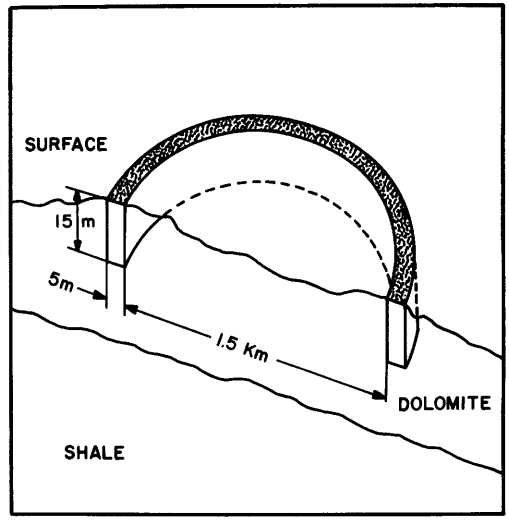

Fig. 22G2. Trench Sketch for 5000 MWh solenoid.

intermediate use is more properly called *load leveling* in contrast to smaller storage units for peak shaving.

Figure 22G2 is a sketch of the 5000 MWh unit trench sized for the intermediate use depicted in Fig. 22G1. Specifications are listed in Table 22G1. The solenoid is mounted in the surface trench so that the expanding magnetic forces can be contained by the in-situ rock without using a prohibitively large metallic structure. The forces are transmitted by epoxy-fiberglass struts from the 1.8 K coil turns to the rock at room temperature.

Table 22G1. Specifications of low aspect ratio unit. From Eyssa and Boom (1981).

Energy Stored	= 5000 MWh
Midplane Field	= 3.5 T
Maximum Field	= 6.8 T
Radius	= 757 m
Height	= 15 m
Number of Turns	= 108
Inductance	= 61 H
Current per Turn	= 768 kA (max)
Radial Force	= 2.8×10^{10} N
Average pressure on Rock	= 3.9×10^{5} N/m^2

The Los Alamos National Laboratory will utilize SMES as a stabilizing system on the west coast power transmission network as follows: There are two 500 kV, ac power transmission lines with a thermal rating of 3500 MW operated by the Bonneville Power Administration (BPA) System between the Pacific Northwest and southern California. System stability is affected by the relative weaknesses in the 900 mile long lines connecting the areas. In 1974, predicted negatively damped oscillations of about 3000 MW amplitude at 0.35 Hz were observed on the transmission lines. One means of preventing the oscillations is to apply a low amplitude, up to ± 5 MW, out of phase signal to the lines [Rogers et al (1979) and Rogers (1981)]. This is to be done with a 30 MJ, 5 kA, 2.8 T energy storage coil. The coil is interfaced to the transmission line through a converter and power transformers (similar to those in Fig. 22G3). Table 22G2 lists some of the coil characteristics. The SMES unit is to be

Table 22G2. BPA 30 MJ SMES coil. From Rogers, et. al. (1981).

Field, maximum	= 2.8 T
Winding	double pancake
Number of pancakes	= 40
Number of turns	= 920
Current	= 4.9 kA
Mean radius	= 1.53 m
Radial thickness	= 0.33 m
Height	= 1.21 m

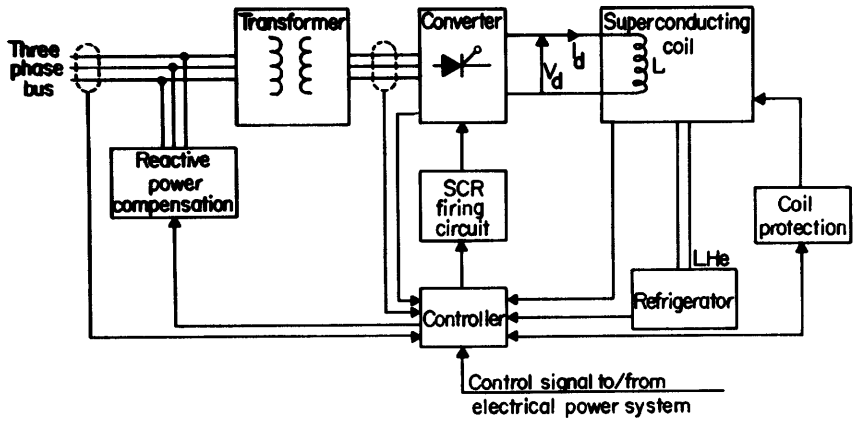

Fig. 22G3. Components of a large SMES. From J. D. Rogers et al, LA-7885-MS (1979), Fig. I-1.

installed at the Fite Substation, Tacoma, WA, and operated completely remotely over a microwave link from Portland, OR.

The conductor is a composite of NbTi and aluminum, 14 cm O.D. which would be rippled circumferentially as it is wound into a one-layer solenoid to be enclosed with a tight fitting vacuum insulated dewar of liquid helium. Rippling reduces strains from cool down and from magnetic forces. The helium would be subcooled at 1.8 K because of the quantum mechanical heat transmission superiority of He II as compared to HE I and because of the higher current capacity of NbTi at 1.8 K.

Components of a large SMES are illustrated in Fig. 22G3. A Graetz Bridge converts 3-phase ac current from the utility grid into dc for the storage solenoid, and vice-versa, during charging and discharging of the solenoid (Boom and Peterson 1972). The bridge circuitry is about 98.5 % efficient one way, enabling the SMES to attain a storage efficiency of 95 % or better. Power can be reversed in tens of milliseconds, compared with minutes for other types of storage.

Pulsed storage magnets for fusion research and for accelerators are similar to the BPA design described in Table 22G2. The main differences would be in pulsed energy discharge requirements. All such magnets would be low-loss magnets designed for maximum dB/dt without excessive eddy current and hysteresis losses.

Problems

1. Estimate the magnetic flux density B for the case of Fig. 22A3.

2. Estimate the order of magnitude of the coherence length of NbTi from its B_{c2}.

3. A superconducting magnet is to be wound from square conductors with side = a. The windings are to be grouped in square bunches (n turns) x (n turns), as shown in Fig. 22P1. The outside perimeter of the bunches is cooled by liquid helium. Show that the Stekly number for this case may be written $\alpha_s = nI^2\eta/4a^3q$, where q is the maximum heat flux for nucleate boiling (Hint: Consider the bundle as one conductor).

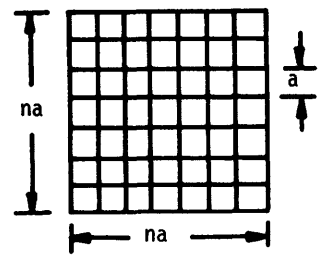

Fig. 22P1. A bunch of square conductors.

If $q = 0.4$ W/cm^2, $I = 50$ A, $a = 1$ mm, and $\eta = 3 \times 10^{-8}$ Ωcm, what is the maximum number of turns which can be grouped together and still have cryogenic stabilization?

4. Estimate the maximum allowable dB/dt for adiabatically-stabilized NbTi at 4.2 K and 3 T, assuming that the filament diameter is 7×10^{-5} m and that the transposition length is 1 cm.

5. For circular superconducting coils with rectangular cross section, it is sometimes desirable to find the coil dimensions which minimize the coil volume and conductor cost, while producing a given B in a given bore radius r_1. Defining $\alpha = r_2/r_1$ and $\beta = L/2r_1$, write Eq. (20B19) in the form $B_z = \mu_0 \lambda J r_1 f(\alpha,\beta)$, and express the coil volume in the form $V = r_1^3 v(\alpha,\beta)$. Find $f(\alpha,\beta)$ and $v(\alpha,\beta)$. For any given required r_1 and B_z and attainable λJ, the first equation determines the required value of f. Eliminating α algebraically in terms of f, show that

$$v = 2\pi\beta[(g^2-\beta^2)^2/4g^2 - 1] \quad , \quad \text{where } g \equiv e^{f/\beta}[1 + (1+\beta^2)^{\frac{1}{2}}] \; .$$

For any given required value of f, the minimum value of v can be found either by setting $dv/d\beta = 0$ and solving for β or by simply calculating v for several values of β. The required number of Ampere-meters of conductor can be found from $IL_t = \lambda JV$, where L_t is the total conductor length. Find the minimum conductor volume and required number of Ampere-turns to produce a central field B = 7 T in a bore diameter of 2 meters with cryogenic stabilization and $\lambda J = 20$ MA/m^2. What are the coil length and outer radius?

6. A large superconducting coil with inductance of 85 H carries a current of 9,000 A. If the protective circuit has a resistance of 0.7 Ohm, how long does it take to reduce the current to 100 A?

7. A tape conductor which is 1 cm wide and 0.15 mm thick carries a current of 300 A. If the average normal resistivity of the ribbon is three times that of pure copper, and the conductor is cooled only on the thin edges by liquid helium, calculate the Stekly number.

8. A coil with inductance of 1 H is charged up to full current, then its input leads are connected together by a superconducting switch (a *persistent switch*). If the current decreases by 0.2 % per month, what is the total resistance of the coil joints ?

Bibliography

superconductivity

J. Bardeen, "Theory of Superconductivity", Chapter 1 of *Superconductivity in Science and Technology*, M. H. Cohen, Editor, U. of Chicago Press, Chicago, 1968.

R. P. Feynman, R. B. Leighton, and M. Sands, *The Feynman Lectures on Physics*, Volume III, Addison-Wesley, Reading, MA, 1965, Chapter 21.

C. Kittel, *Introduction to Solid State Physics*, 5th Edition, Wiley, New York, 1976, Chapter 12.

M. S. Lubell, "Superconductivity and magnet technology", *Symposium on Energy Sources for the Future*, CONF-750733 (1975), p. 274-303.

A. C. Rose-Innes and E. H. Rhoderick, *Introduction to Superconductivity*, Pergamon Press, Oxford, 1969.

A. W. B. Taylor, *Superconductivity*, Wykeham, London, 1970.

historical developments

A. A. Abrikosov, *Soviet Physics JETP 5*, 1174 (1957).

J. Bardeen, L. N. Cooper, and J. R. Schrieffer, *Physical Review 108*, 1175 (1957).

J. E. Kunzler, E. Buehler, F. S. L. Hsu, and J. H. Wenick, *Physical Review Letters 6*, 89 (1961).

F. London and H. London, *Proceedings of the Royal Society (London) A155*, 71 (1935).

W. Meissner and R. Ochsenfeld, *Naturwissenchaften 21*, 787 (1933).

H. K. Onnes, *Communications of the Physics Laboratory of Leiden*, Numbers 119, 120, 122 (1911).

superconductors and stabilization

H. Brechna, *Superconducting Magnet Systems*, Springer-Verlag, New York, 1973.

M. S. Lubell, "State-of-the-art of superconducting magnets", *Cryogenics*, October, 1972, p. 340-355.

flux creep

P. W. Anderson, "Theory of flux creep in hard superconductors", *Physical Review Letters 9*, 309 (1962).

Y. B. Kim, C. F. Hempstead, and A. R. Strnad, "Flux creep in hard superconductors", *Physical Review 131*, 2486-2495 (1963).

coil development

B. Badger et al, "NUWMAK, A tokamak reactor design study", UWFDM-330, University of Wisconsin (1979).

B. R. Buncher et al, "Conceptual studies of toroidal field magnets for the tokamak experimental power reactors", ORO-5153-1 (1976).

D. Cornish, "Superconductivity and cryogenics for mirror fusion", *Eighth International Cryogenic Engineering Conference (Genoa, 1980)*.

D. N. Cornish, D. W. Deis, and J. P. Zbasnik, "Cold-pressure-welded joints in large multifilamentary NbTi superconductors", Proceedings of the Seventh Symposium on Engineering Problems of Fusion Research, Knoxville, 1977, and UCRL-79723 (1977).

D. N. Cornish, J. P. Zbasnik, R. L. Leber, D. G. Hirzel, J. E. Johnston, and A. R. Rosdahl, "MFTF test coil construction and performance", *IEEE Transactions on Magnetics MAG-15*, 530-533 (1979).

C. D. Henning and E. N. C. Dalder, "Structural materials for fusion magnets", Fifth International Conference on Structural Mechanics in Reactor Technology, West Berlin, 1979, and UCRL-81591 (1979).

C. D. Henning, A. J. Hodges, J. H. VanSant, R. E. Hinkle, J. A. Horvath, and R. E. Hintz, "The mirror fusion test facility magnet", *Proceedings of the Eighth Symposium on Engineering Problems of Fusion Research*, San Francisco, 1979.

S. Y. Hsieh, M. Reich, and J. R. Powell, "Safety issues for superconducting magnets", *Proceedings of the Third Topical Meeting on Controlled Nuclear Fusion*, CONF-750508 (1978), p. 890-902.

B. J. Maddock and G. B. James, "Protection and stabilization of large superconducting coil", *Proceedings of the Institute of Electrical Engineers (London) 115*, 543-547 (1968).

Proceedings of the 1980 Applied Superconductivity Conference, *IEEE Transactions on Magnetics MAG-17*, January 1981. Contains many articles describing the state of the art as of 1980.

Proceedings of the Fourth ANS Topical Meeting on the Technology of Controlled Nuclear Fusion (King of Prussia, 1980), DOE, 1981.

J. R. Roth, A. R. Holmes, T. A. Keller, and W. M. Krawczonek, "Performance of a 12-coil superconducting 'bumpy torus' magnet facility", Technology of Controlled Thermonuclear Fusion Experiments and the Engineering Aspects of Fusion Reactors, CONF-721111 (1974), p. 409-425.

B. B. Schwartz and S. Foner, "Large-scale applications of superconductivity", *Physics Today*, July 1977, p. 34.

energy storage

R. W. Boom, R. F. Bischke, G. E. McIntosh and Y. M. Eyssa; *7th International Conference on Magnet Technology*, Karlsruhe, Germany, March 30-April 3, 1981.

R. W. Boom and H. A. Peterson, *IEEE Transactions on Magnetics*, Vol. MAG-8, No. 3, September 1972.

Y. M. Eyssa, R. W. Boom, R. F. Bischke, K. T. Hartwig, G. E. McIntosh and S. W. Van Sciver; *16th Intersociety Energy Conversion Engineering Conference*, Atlanta, GA, August 9-14, 1981.

F. L. Ribe, R. A. Krakowski, K. I. Thomassen, T. A. Coultas, "Engineering study of a reference theta-pinch reactor (RTPR)", Special Supplement to Nuclear Fusion on *Fusion Reactor Design Problems*, IAEA, Vienna, 1974.

J. D. Rogers, *IEEE Transactions on Magnetics*, Vol. MAG-17, No. 1, January, 1981.

J. D. Rogers, H. J. Boenig, J. C. Bronson, D. B. Colyer, W. V. Hassenzahl, R. D. Turner and R. I. Schermer, *IEEE Transactions on Magnetics*, Vol. MAG-15, January, 1979.

J. D. Rogers, W. V. Hassenzahl, R. I. Schermer, "1-GWh diurnal load-leveling superconducting magnetic energy storage system reference design", LA-7885-MS, Volume I-VIII (1979).

CHAPTER 23
Cryogenics

23A. Introduction

The term "cryogen" was originated by H. K. Onnes from the Greek stems "cryo", which means "cold", and "genes", meaning "that which generates". Today, the term *cryogenics* refers to the physical, chemical, engineering, and industrial applications of phenomena at low temperatures, below about 123K (-150 C). The four common temperature scales are related by the equations

$$T(F) = 1.8\,T(C) + 32$$
$$T(R) = T(F) + 459.67$$
$$T(K) = T(C) + 273.15 \quad . \qquad (23A1)$$

Study of cryogenic phenomena is roughly one hundred years old. Early developments in production of liquid oxygen and nitrogen occurred in Europe in 1877-1890. James Dewar invented vacuum insulated flasks in 1892, and he liquefied hydrogen in 1898. Carl Von Linde and Georges Claude developed practical systems for the liquefaction of air in 1895 and 1902. H. K. Onnes liquefied helium (the last gas to be liquefied) in 1908 and discovered superconductivity in 1911. After the end of the First World War, production of industrial gases (such as oxygen and nitrogen) by cryogenic processes grew rapidly.

The first expansion engine for liquefying helium was built by P. Kapitza in 1934.

A comparatively economical process for producing liquid helium was developed by S. C. Collins in 1947, which facilitated expansion of research on low-temperature phenomena.

Large V-2 rockets fueled by liquid oxygen and alcohol were developed during the Second World War. Development of rocket technology was continued in the USSR and in the USA, leading to the launching of satellites and space flights. Cryogenics has now become an important industrial field with many practical applications, Table 23A1.

Cryogenic systems are essential to the success of neutral beam injection systems and superconducting magnets. Cryopumps, having the highest attainable pumping speed, prevent excessive influx of cold neutral gas from neutralizing cells into the confinement region. The cryogenic systems for magnets involve the

following considerations:

* *materials.* Materials must have suitable low-temperature mechanical, thermal, and electrical properties.
* *refrigeration.* For a reactor, heat loads of tens of kW must be removed at $T \sim 4$ K.
* *insulation.* Effective insulation must minimize conductive, convective, and radiative heat transfer.
* *structure.* The cryostat must sustain magnetic and gravity forces with a minimum of heat leakage.

Table 23A1. Applications of Cryogenic Technology

Industrial gas production and uses
- gases: O_2, N_2, CO_2, He, Ar, Ne, etc.
- steel refining (oxygen)
- prestressing of pressure vessels (liquid nitrogen)
- ammonia production (cryogenic systems)
- welding (argon or helium)

Food preservation
- dry ice production
- rapid-freezing with liquid nitrogen
- freeze drying processes

Biomedical applications
- preservation of tissue, blood, semen
- cryosurgery

Mechanical devices
- frictionless bearings and gyroscopes
- refrigeration processes

Electrical devices
- low-noise electronics and masers
- computers
- superconducting motors, generators, energy storage, transmission

Physics studies
- radiation damage
- neutron moderation
- bubble chambers
- low-temperature phenomena, such as superfluidity and superconductivity

Space technology
- rocket propulsion
- space simulation systems and vacuum chambers

Fusion Research
- superconducting magnet coils
- cryopanel vacuum pumping systems

23B. Properties of Materials At Low Temperatures

The properties of some materials change markedly at low temperatures. For example, some organic materials immersed in liquid nitrogen (at 77 K) become brittle and will shatter like glass when struck with a hammer.

mechanical properties

Some properties of interest (defined in Fig. 24D1) are yield stress, ultimate stress, percent elongation, impact energy, and modulus of elasticity. In general, the percent elongation and impact energy decrease at low temperatures as shown in Fig. 23B1 for elongation. In the early 1940's, several cargo ships unexpectedly broke apart and sank in the North Atlantic before it was discovered that their welds became brittle at low temperatures. Brittle materials usually perform better in compression than in tension. Because plastics are very brittle at low temperatures, thermal shock must be avoided during their cooling. For most materials the yield stress and ultimate stress increase slightly at low temperatures, as illustrated in Fig. 23B2 for ultimate stress. The modulus of elasticity usually remains about constant or increases slightly with decreasing temperature (except for some plastics, where a large increase occurs). If the magnet stresses are to be turned on and off, the possibility of low-cycle fatigue failure should be considered.

thermal properties

Pertinent thermal properties include specific heat, thermal conductivity, emissivity, and thermal expansion coefficient. The specific heats of most inorganic solids at low temperatures follow the Debye equation

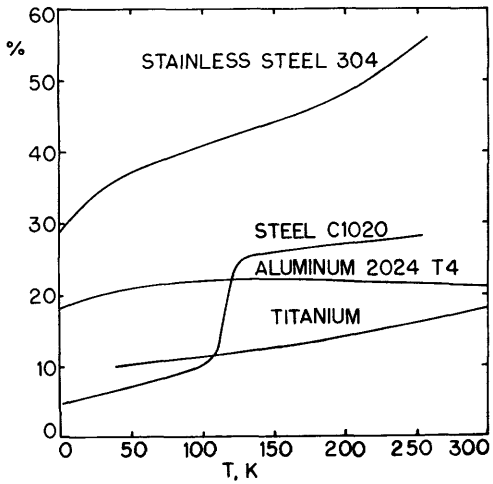

Fig. 23B1. Percent elongation of various metals as a function of temperature. Data from Cryogenic Systems, by R. Barron, Fig. 2-5, p. 21. Copyright 1966, McGraw-Hill Book Company, New York. Used by permission.

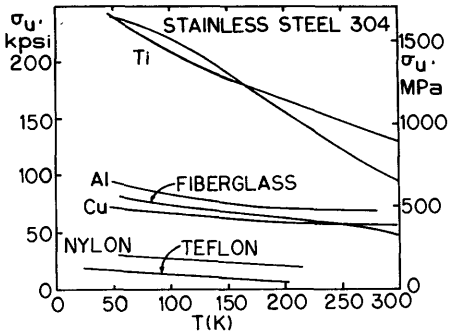

Fig. 23B2. Ultimate stress of various materials as a function of temperature. Data from Bell (1963), Scott (1959) and Vance and Duke (1962).

$$C = 9R\left(\frac{T}{\theta_D}\right)^3 \int_0^{\theta_D/T} \frac{dx\, x^4 e^x}{(e^x-1)^2} \quad , \tag{23B1}$$

where C is the specific heat at constant volume (J/mole K), R = 8.314 (J/mole K) is the universal gas constant, T is the material's temperature (K), and θ_D is the "Debye temperature", which is a constant for a given material. If this equation is divided by the molecular weight, C will be expressed in J/kg-K. The values of θ_D for various materials are shown in Table 23B1, and the ratio of C/R obtained from Eq. (23B1) is plotted as a function of (T/θ_D) in Fig. 23B3. At temperatures less than one-twelfth of θ_D Eq. (23B1) reduces to the approximate form

$$C/R = 233.8\ (T/\theta_D)^3 \ , \quad (T < .08\ \theta_D) \ . \tag{23B2}$$

The specific heat for stainless steel (18% Cr, 8% Ni) falls from 476 J/kg-K at room temperature to 159 J/kg-K at 77 K and 4.6 J/kg-K at 20 K.

The *enthalpy* of a material is defined by

$$h \equiv \int_0^T dT\, C + h_0 \quad \text{(J/kg)} \tag{23B3}$$

Table 23B1. Debye temperatures for various materials. From R. B. Scott, Cryogenic Engineering, Van Nostrand, Princeton, NJ, 1959, p. 328-329.

aluminum	390 K
copper	310 K
alpha-iron	430 K
gamma-iron	320 K
lead	86 K
lithium	430 K
nickel	375 K
titanium	350 K

where h_0 is the enthalpy at T = 0

The heat added per kg to raise the temperature from T_1 to T_2 is

$$W/M = \int_{T_1}^{T_2} dT\, C = h_2 - h_1 \qquad (23B4)$$

where W is the heat added (J), M is the mass of the material (kg), and h_2 and h_1 are the enthalpies at T_2 and T_1. Enthalpies of several materials are given in Table 23B2.

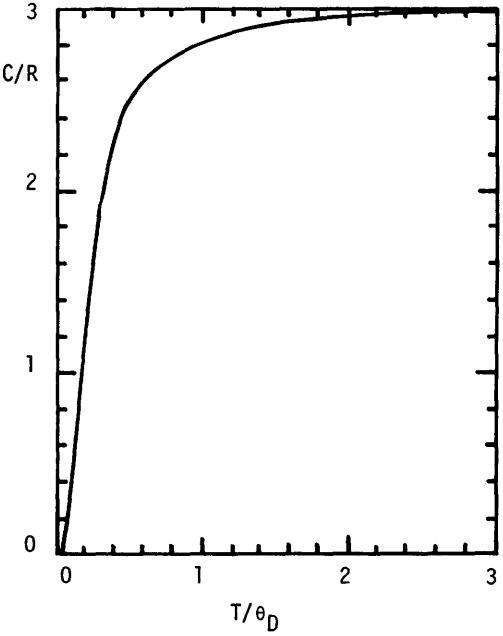

Fig. 23B3. Ratio of specific heat to universal gas constant R as a function of the ratio of temperature T to Debye temperature θ_D. From Cryogenic Systems, by R. Barron, Fig. 2-8, p. 28. Copyright 1966, McGraw-Hill, New York. Used by permission of McGraw-Hill Book Company.

Table 23B2. Enthalpies of various materials at low temperatures, J/g.

T,K	Cu	Al	Nb	Sn	Fe	Ni	C	Teflon
300	79.6	170.4	59.2	53.6	81.1	82.4	88.7	167.8
280	72.0	152.5	53.9	49.1	72.3	73.6	75.0	144.6
260	64.4	135.0	48.6	44.7	63.6	65.0	62.5	125.5
240	56.9	117.8	43.4	40.3	55.2	56.7	51.2	107.8
220	49.6	101.0	38.2	36.0	47.0	48.6	41.1	91.3
200	42.4	84.8	33.1	31.7	39.2	40.8	32.2	75.9
180	35.3	69.2	28.0	27.4	31.8	33.4	24.5	61.7
160	28.5	54.4	23.1	23.2	24.6	26.3	18.0	49.0
140	22.1	40.7	18.3	19.1	18.2	19.7	12.7	37.7
120	16.1	28.4	13.8	15.1	12.4	13.8	8.4	27.9
100	10.6	17.8	9.6	11.1	7.6	8.6	5.1	19.5
80	6.0	9.4	5.8	7.6	3.8	4.6	2.7	12.5
60	2.6	3.6	2.8	4.3	1.4	1.8	1.2	7.0
40	0.6	0.8	0.8	1.8	0.3	0.4	0.4	3.0
20	0.03	0.05	0.07	0.3	0.03	0.04	0.04	0.5
10	0.0024	0.005	0.007	0.02	0.005	0.007	0.003	0.05

EXAMPLE PROBLEM 23B1

A 1 GJ coil stabilized by aluminum at 10 K is not to exceed 100 K after a quench in which all the energy is distributed uniformly in the aluminum, ignoring heat absorption in superconductor and insulators. What is the required mass of aluminum?

For aluminum, the enthalpy difference $h_2 - h_1$ = 17,800 J/kg = W/M. Since $W = 10^9$ J, we find that M = 56,000 kg of aluminum.

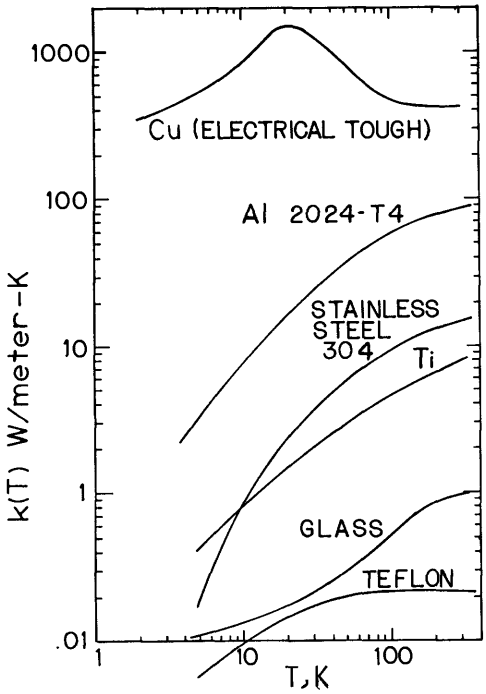

Table 23B3. Ratio of strength to thermal conductivity between room temperature and 90 K, relative to the ratio for 304 stainless steel. From Cryogenic Systems, by R. Barron, Table 7-5, p. 466. Copyright 1966, McGraw-Hill, New York. Used by permission of McGraw-Hill Book Company.

stainless steel 304	1.00
aluminum 2024-0	0.017
teflon	0.269
K Monel	0.68
Hastelloy C	0.606
nylon	0.957
glass fibers	3.63
mylar	5.67
Kel F oriented fibers	10.8
Dacron fibers	12.5

Fig. 23B4. Thermal conductivities of various materials. Data from Scott (1959), Barron (1966), and McClintock (1964). Cryogenic Systems by Barron, copyright 1966 by McGraw-Hill. Used by permission of McGraw-Hill.

Thermal conductivities vs. temperature for various materials are shown in Fig. 23B4. Structural materials extending between the coil and the cryostat (container) should have low thermal conductivity and high strength, so the ratio of yield stress to thermal conductivity is often used as a figure of merit. The mean value of these ratios between room temperature and 90 K, relative to the ratio for stainless steel 304, is given in Table 23B3 for various structural materials.

The linear thermal expansion is used to calculate thermal stresses, which arise from temperature gradients. Thermal expansion values for various materials are listed in Table 23B4, relative to the length of the material at 0 K.

The thermal emissivity is the ratio of the amount of heat radiated by a surface to that which would be radiated by a pure "black body". Values of thermal emissivity will be used in estimating radiative heat transfer between walls separated by a vacuum. The thermal emissivities of some common materials are given in Table 23B5.

electrical resistivity

Resistivities of Cu and Al, relative to the values at room temperature, are shown in Fig. 23B5. These values vary strongly with the impurity content, and the purity is sometimes spoken of in terms of the ratio of the resistivity at 293 K to that at 4.2 K, called the *residual resistivity ratio* (RRR), which is about 30 for the aluminum of Fig. 23B5. Values of RRR of several thousand can be obtained by careful refining, though at increased cost. The resistivities increase with applied magnetic field and with neutron irradiation fluence (Chapter 24).

Table 23B4. Thermal expansion of various materials. Data from R. B. Scott, Cryogenic Engineering, Van Nostrand, Princeton, NJ, 1959, Tables 10.5 and 10.6, p. 331, 333. Some interpolations are given here.

$[L(T) - L(0)]/L(0)$ (in units of 10^{-5})

Material	20 K	60 K	100 K	150 K	200 K	250 K	300 K
copper	0	10	44	105	178	256	339
aluminum	0	10	46	121	214	319	431
nickel	0	4	23	64	117	172	239
titanium	0	1	14	41	74	113	155
stainless 304	-1.1	2.8	30	85	151	225	304
yellow brass	0	15	57	130	214	303	397
polyester & fiberglass	3	21	49	99	159	223	291
nylon	10	81	217	443	716	1050	1450
teflon	45	200	410	717	1130	1747	2695

Table 23B5. Thermal emissivities of some common materials. Data from Scott (1959) p. 347 and Barron (1966) p. 38. © 1966 McGraw-Hill. Used by permission of McGraw-Hill.

material	at 77 K	room temperature
aluminum foil (bright)	0.018	0.03
copper (polished)	0.019	0.030
glass		0.94
304 stainless steel	0.061	0.150
titanium		0.11
silver	0.01	0.022
nickel	0.022	0.04

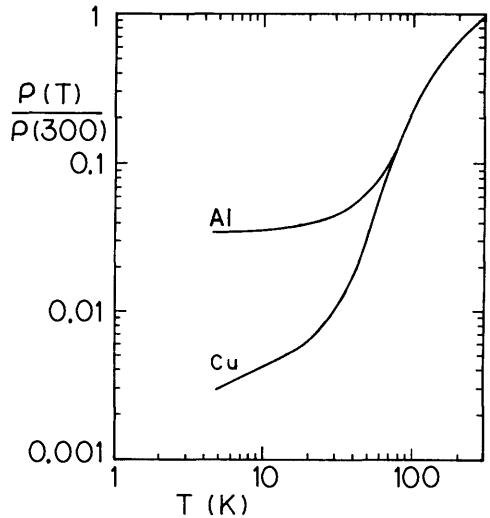

Fig. 23B5. Ratio of the electrical resistivities of Cu and Al at cryogenic temperatures to their resistivities at room temperature. Very pure samples would have lower resistivities. From Cryogenic Systems, by R. Barron, Fig. 2-13 p. 42. Copyright 1966, McGraw-Hill, New York. Used by permission of McGraw-Hill Book Company.

cryogenic liquids

At cryogenic temperatures ordinary gases become liquids or solids. Properties of some cryogenic fluids are listed in Table 23B6. The gases cannot be liquified above the "critical temperature", no matter how high a pressure is applied. Only about 1.3 ppm of ordinary helium is helium-3, the majority being helium-4. Helium-4 cannot be solidified at atmospheric pressure, but can be solidified at about 25 atm. Liquid helium has many unusual properties, such as superfluidity, which are described in the references.

Table 23B6. Properties of cryogenic liquids and water at 1 atmosphere. Data from Laquer (1973) Table 1 and Cryogenic Systems by R. Barron, Table 2-3, p. 38. Copyright 1966, McGraw-Hill, New York. Used by permission of McGraw-Hill Book Company

	helium-4	hydrogen	nitrogen	oxygen	water
boiling point (K)	4.2	20.3	77.4	90.2	373.2
melting point (K)	none	13.8	63.2	54.4	273.2
critical temperature (K)	5.2	33.2	126	155	645
properties at boiling temperature:					
density (kg/m^3)	125	71	800	1140	1000
heat of vaporization (MJ/m^3)	2.72	31.6	161.3	243	2257
specific heat c_p (kJ/kg-K)	4.56	9.76	2.04	1.70	4.22
thermal conductivity (W/m-K)	.0269	.118	.139	.148	.023

23C. Refrigeration and Liquefaction

Liquefaction refers to the process of condensing gases into liquids, while refrigeration refers to the process of heat removal from a substance. If superconducting magnets are cooled by liquid helium, then helium liquefaction will be necessary; if they are cooled by chilled helium vapor, then only refrigeration may be needed. Both processes are similar, however, in that they require cycles involving compression (with a temperature rise), cooling by a heat sink, and then expansion cooling (with or without condensation to the liquid phase), as illustrated in the simple diagram of Fig. 23C1.

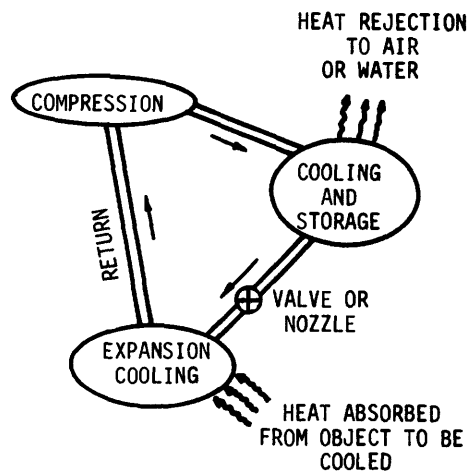

Fig. 23C1. A simple refrigeration cycle. Household refrigerators use this cycle with the fluid Freon. Cryogenic refrigerators use similar steps, but with additional measures to improve efficiency.

According to the *Joule-Thomson effect*, expansion of a gas lowers its temperature, provided that its initial temperature is below the *inversion temperature*. Gases like nitrogen and oxygen, which have inversion temperatures greater than room temperature, can be cooled by expansion at room temperature. On the other hand, hydrogen and helium have inversion temperatures of about 204 K and 40 K, so they require precooling to

below these temperatures if they are to be cooled by expansion. Such gases have been called "permanent gases" because of the difficulties encountered in attempting to liquefy them.

In liquefiers, the gas to be liquefied is usually the working fluid. It is precooled below the inversion temperature, and during expansion part of it condenses into the liquid state, forming a pool at the bottom of the expansion chamber. To cool and liquefy one mole of helium starting at 298.15 K, about 27.2 kJ of thermal energy must be removed. However, a much greater amount of energy must be expended by the machine to accomplish this amount of heat removal.

For liquefaction of helium, the precooling below the inversion temperature can be done either by evaporation of liquid hydrogen (which boils at 20.3 K) or by using heat exchangers with returning chilled helium vapor as the coolant. The latter method has the advantage of not requiring liquid hydrogen and a separate liquefier for it.

Ordinary expansion through a valve or nozzle is thermodynamically irreversible: heat energy is wasted in increasing the entropy, and cooling is inefficient. (Entropy is a ratio of energy to temperature, and it measures the amount of energy which is bound up in matter and unavailable for use). The expansion can be made more efficient by letting the gas expand gradually in an expansion engine, such as a cylinder-and-piston or a gas turbine. In such an engine the expansion becomes more nearly reversible or isentropic (constant entropy), and less thermal energy is trapped in entropy. Consequently, the amount of cooling produced by the expansion of a given quantity of gas is greatly increased. For this reason, expansion engines are often employed in cryogenic refrigeration and in liquefaction of permanent gases.

The Collins helium-liquefaction system is illustrated schematically in Fig. 23C2. In this system helium gas at room temperature and atmospheric pressure is compressed to about 14 atm, and then cooled in a series of heat exchangers with counterflowing chilled helium vapor. Any number of expansion engines may be used. For simplicity, only two are shown in the Figure. For this case, about 25% of the mass flow rate would be channeled through the first expansion engine, and about 50% through the second engine, leaving about 25% to pass through the Joule-Thomson expansion valve. About 12% of the mass flow condenses in the expansion chamber, and the remaining 13% vapor returns up through the heat exchangers, where it is joined by returning chilled vapor from the expansion engines.

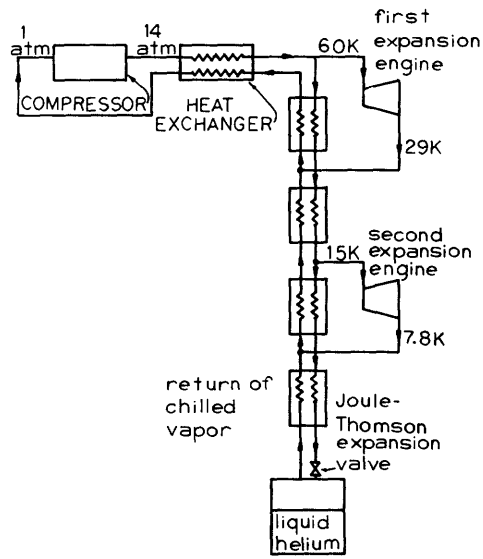

Fig. 23C2. The Collins system for helium liquefaction. Based on Cryogenic Systems, by R. Barron, Fig. 3-30, p. 122. Copyright 1966, McGraw-Hill, New York. Used by permission of McGraw-Hill Book Company.

In some refrigeration systems *regenerators* are used in place of heat exchangers. A regenerator is a heat storage device with a large internal surface area from which heat may be rapidly transferred to the working fluid. For example, a tube packed full of steel

wool could be used as a regenerator. A regenerator first receives heat from the hot fluid and then gives up this heat to the cold fluid. The two fluids flow through it alternately. Regenerators have the advantage of a low pressure drop, ease of construction, and a very large internal surface area per unit volume. They are limited by their low heat capacity (which may require rapid interchanging) and by the mixing of fluids from the two streams as they are interchanged. In practice, two regenerators may be used simultaneously, one for the hot fluid and one for the cold, and they may be rapidly interchanged to permit almost continuous flow of the two fluids.

For simplicity, only the Collins system has been illustrated here. Detailed analyses of the efficiencies of various types of heat exchangers, regenerators, expansion engines, and systems for refrigeration and liquefaction are given by Barron (1966).

23D. Insulation

Effective insulation must combat all three heat transfer mechanisms: conduction, convection, and radiation.

The thermal power flow by conduction along a body with cross sectional area A and length L is

$$P_{cond} = \frac{A}{L} \int_{T_1}^{T_2} dT\ k(T)\ \text{(Watts)}, \quad (23D1)$$

where k(T) is the thermal conductivity (W/metre-K), and T_1, T_2 are the temperatures at the endpoints of the body. To minimize the heat flow, one can use materials with low thermal conductivity, small cross sectional area A, or a long heat-flow path length L. Some values of $\int_4^T dT\ k(T)$ are given in Table 23D1.

Table 23D1. Thermal conductivity integrals $\int_4^T dT\ k(T)$ *in Watts/cm. From R. B. Stewart and V. J. Johnson, WADD Technical Report 60-56, Part IV, 1961.*

T, K	Electrical Tough Pitch Copper	(Pb) Brass	Aluminum 6063-T5	Stainless Steels	Glass
6	8.00	0.053	0.850	0.0063	0.00211
8	19.1	0.129	2.05	0.0159	0.00443
10	33.2	0.229	3.60	0.0293	0.00681
15	80.2	0.594	9.00	0.0816	0.0131
20	140	1.12	16.5	0.163	0.0200
25	208	1.81	25.8	0.277	0.0279
30	278	2.65	36.5	0.424	0.0368
35	345	3.63	48.8	0.607	0.0471
40	406	4.76	62.0	0.824	0.0586
50	508	7.36	89.5	1.35	0.0846
60	587	10.4	117	1.98	0.115
70	651	13.9	143	2.70	0.151
76	686	16.2	158	3.17	0.175
80	707	17.7	167	3.49	0.194
90	756	22.0	190	4.36	0.240
100	802	26.5	211	5.28	0.292
120	891	36.5	253	7.26	0.408
140	976	47.8	293	9.39	0.542
160	1060	60.3	333	11.7	0.694
180	1140	73.8	373	14.1	0.858
200	1220	88.3	413	16.6	1.03
250	1420	128	513	23.4	1.50
300	1620	172	613	30.6	1.99

EXAMPLE PROBLEM 23D1

A coil at 10 K is partially supported by a stainless steel tube with ID 7 mm, thickness 1 mm, and length 20 cm to an intermediate surface at 80 K. What is the heat flow into the coil along this tube?

From Table 23D1 the difference in conductivity integrals is 3.46 W/cm. The cross sectional area of the tube $A = \pi(r_2^2 - r_1^2) = 0.251\ cm^2$. Then from Eq. (23D1), $P_{cond} = (A/L)\int_{T_1}^{T_2} dT\ k = 0.043$ W.

Convection is reduced by dividing the gas into small cells (as in foam insulation) or by removing the gas (as in vacuum insulation). When both conduction and convection have been minimized, radiation may become the dominant heat transfer process.

The thermal power transferred radiatively from a spherical or cylindrical surface with area A_2, temperature T_2, and emissivity e_2 to another concentric surface with area A_1, temperature T_1, and emissivity e_1 is

$$P_{rad} = \frac{\sigma(T_1^4 - T_2^4)}{\frac{1}{A_1 e_1} + \frac{1}{A_2 e_2}(1-e_2)} \qquad (23D2)$$

where $\sigma = 5.67 \times 10^{-8}$ W/m^{2}K^4 is the Stefan-Boltzmann constant. To minimize radiant heat transfer, surfaces with low emissivity are used, and multilayer radiation barriers may be employed. For example, if $e_1 = e_2 = 0.90$, and if ten radiation shields with emissivity $e_s = 0.05$ are placed in between A_1 and A_2, then the radiant heat transfer rate P_{rad} drops to only 0.3% of what it would be without the shields.

Although Eq. (23D1) is only valid for simple cases of conductive heat transfer, it is convenient to define an "apparent mean thermal conductivity" k_{app} such that

$$P \simeq k_{app} A (T_2 - T_1)/L \qquad (23D3)$$

where P is the total heat flow from *all three* processes. This definition, although it is not rigorously accurate, facilitates comparison of k_{app} for various types of insulation, as illustrated in Table 23D2. The multiple-barrier insulation, which consists of alternate layers of reflective aluminum or copper foil and insulating substances, such as thin mesh or plastic or fiberglass, is clearly the best. Very thin sheets of aluminized mylar incorporate both the plastic and the reflector into one sheet. It has been found that k_{app} rises rapidly as the pressure is raised above 0.03 Pa. Holes about 5 mm diameter occupying about 5% of the sheet surface facilitate vacuum pumping without spoiling the insulation. As the number of layers of this "superinsulation" is increased, radiant heat transfer is drastically reduced, but when they are packed too tightly, conduction becomes significant. The optimum layer density is about 25 layers per cm. Compaction of the layers must be avoided, as it can increase k_{app} by an order of magnitude. One advantage of evacuated powders over superinsulation is ease of installation, especially around complex shapes; but the lower value of k_{app} provided by super insulation is probably worth the extra cost

Table 23D2. Apparent mean thermal conductivities for various types of insulation, between 300 K and 77 K. From Glaser et al (1967) and Vance and Duke (1962).

Material	(μW/cm-K)	mW/m-K
Foams, atmospheric pressure	300-400	30-40
Foams, evacuated	100-200	10-20
Powders, unevacuated	200-1000	20-100
Powders, evacuated ($p \lesssim 0.01$ Pa)	2-20	0.2-2
Multilayer reflective barriers, evacuated ($p \lesssim 0.01$ Pa)	0.1-2	0.01-0.2

of installation. Various types of multilayer insulation are reviewed by Glaser et al (1967).

The heat leak into liquid helium dewars can also be reduced by using *vapor shielding*. The vaporized helium from the inner vessel passes through a tube to cool an intermediate vessel as it escapes. In this way the temperature difference seen by the inner vessel is reduced, and boiloff may be reduced by about a factor of 4. High-current leads for superconducting magnets are usually vapor-shielded tubes.

23E. Cryostat Design

The vessels used to contain and insulate superconducting magnets are called *cryostats* or *dewars*. The main problem is to sustain the magnetic and gravity forces without introducing large heat leaks through the structure. Part of the structure may be at coil temperature (cold reinforcement) and part making the transition up to 77 K and 293 K (warm reinforcement). Cold reinforcement does not add to heat inflow during normal operation, but steels with good low-temperature properties must be used, and more metal must be cooled down initially. If much structural steel is involved, then using plain steel at room temperature may result in cost savings (Powell and Bezler, 1974).

The support for a large TF coil is shown in Fig. 23E1. The bucking cylinder at coil temperature sustains the centering forces, and thin kromarc spokes transmit gravity and lateral fault forces out to the dewar (at 77 K). The dewar is insulated from room temperature by foam plastic. The heat loads estimated for a torus consisting of 16 such TF coils, producing B = 12 T at the coils, are listed in Table 23E1. The losses in the pump are due to heat added in compressing the liquid helium coolant and overcoming frictional pressure drops.

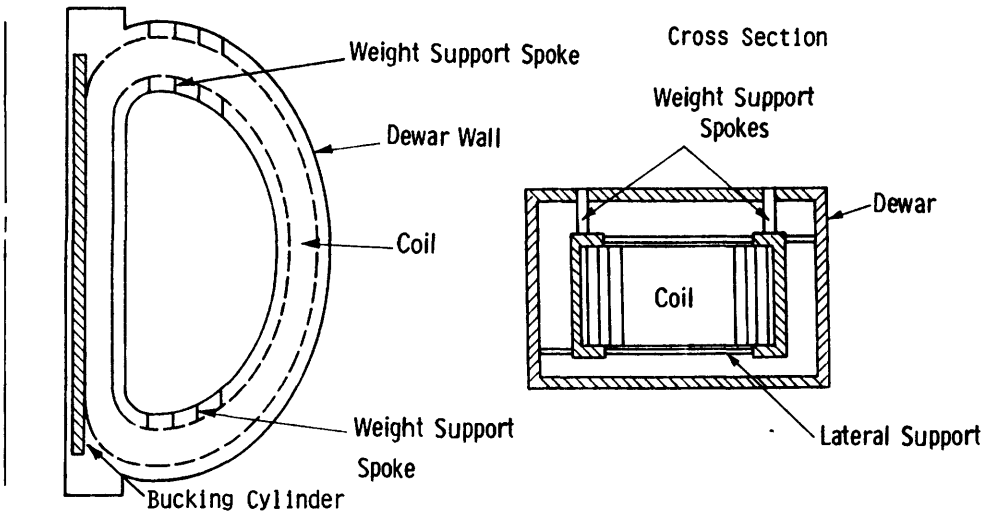

Fig. 23E1. Supports for a large toroidal field coil. The coil bore is about 7 m wide and 11 m high. From B. R. Buncher et al, ORO-5153-1 (1976), Fig. 3.4.4, p. 3-148.

23F. Cryogenic Systems

The vacuum vessel and liquid helium system of the Mirror Fusion Test Facility (MFTF) at LLNL are shown in Fig. 23F1. The coil stores up to 440 MJ of energy, and weighs nearly 300 tonnes. This Yin-Yang magnet will become one end plug of the MFTF-B Tandem Mirror experiment. Two 1.8 kW power supplies provide current to the coils, which would require about 1 GW of power if water-cooled copper coils were used instead of superconducting coils.

The magnet is supported by seven stainless steel struts, each 27 cm in diameter with 2.9 cm thick walls. At 5 K, the thermal conductivity of the stainless steel is less than 1 % of its room-temperature value, so less than 8 W of heat is conducted through each strut.

The 6 kA power leads consist of sixty 1.5 m-long copper tubes in a stainless steel tube, as illustrated in Fig. 23F2. Flowing helium vapor carries away most of the ohmic heating dissipated in the tubes. They are designed so that operation may be continued for 10 minutes after loss of helium vapor flow before a magnet current dump (dissipating the stored energy through an external 0.17 Ohm resistor) must be initiated.

Table 23E1. Helium refrigeration requirements for an array of 16 TF coils producing a peak field of 12 T at the coils. From B. R. Buncher et al, ORO-5153-1 (1976), Table 4.6.1, p. 4-65.

Structural Conduction		
Vertical Spokes	0.075	kW
Horizontal Spokes	2.941	kW
Residual Gas Conduction		
Dewar	0.472	kW
Vertical Spokes	0.036	kW
Horizontal Spokes	0.732	kW
Thermal Radiation		
Dewar	0.321	kW
Vertical Spokes	0.017	kW
Horizontal Spokes	0.355	kW
Nuclear Radiation		
Conductor	0.156	kW
Structure	0.260	kW
AC Losses		
Conductor	12.9	kW
Structure	3.2	kW
Joint Losses	17.3	kW
Losses in Pump ($\sim$ 50% efficiency pump)	29.2	kW
Total Thermal Load P_{th}	68.0	kW
Electrical Load $P_e \simeq 280\ P_{th}$	19	MW

The walls of the chamber and neutral beam tanks are lined with cryogenic pump panels to provide maximum vacuum pumping speeds. The cryogenic subsystems of the MFTF are listed in Table 23F1.

The estimated heat loads on the liquid helium and liquid nitrogen systems are listed in Table 23F2. The main helium refrigeration system will provide a capacity of 3075 W at 4.35 K steady state, in order to allow for additional heat loads from valves, transfer lines, etc. The system should be capable of liquifying 600 litres/hour (0.6 m^3/hour) of helium. The refrigeration mode is to be used during cool-down of the magnet, and the liquefaction mode, for refilling the supply dewars.

If the coil quenched, about 10 m^3 of liquid helium in the coil, cryopanels, and dewars might be vaporized, producing about 7000 m^3 of helium gas at room temperature. Inflatable bags are provided to contain some of this gas at atmospheric pressure until it can be purified, liquified, and recycled. The bags are anchored to concrete pads and protected by covers. The purification systems will include instruments to determine the concentrations of various impurities.

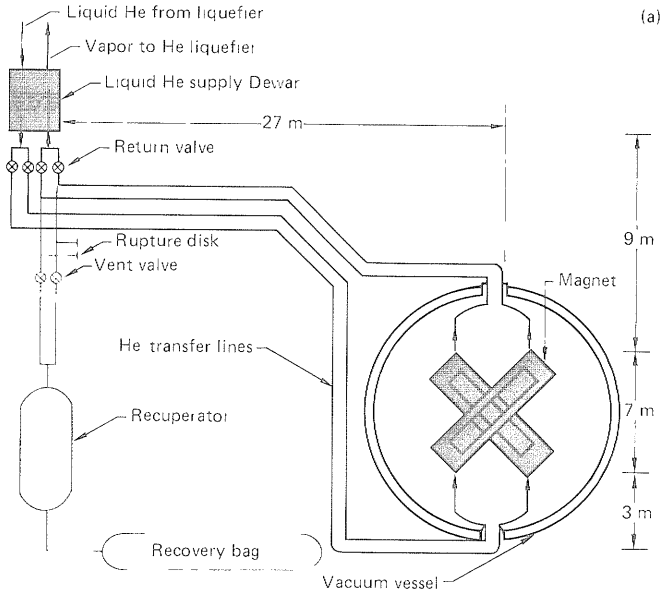

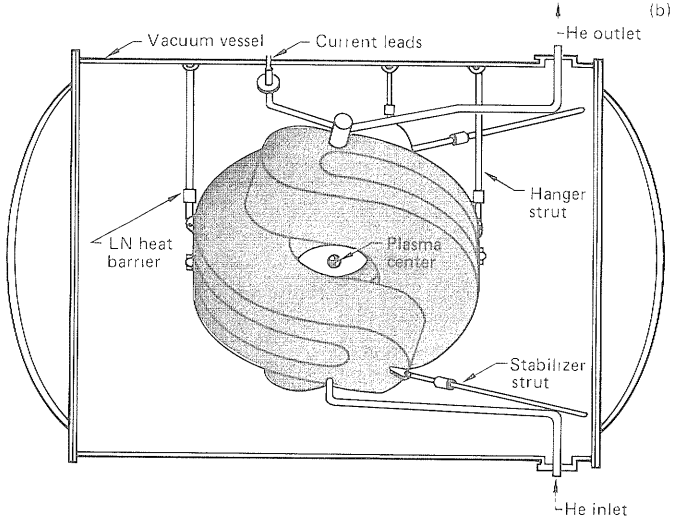

Fig. 23F1. The MFTF magnet, vacuum vessel, and liquid-helium flow system. (a) The magnet coils are oriented at a 45° angle with respect to the horizontal and positioned below the helium dewar, so that heat loads on the magnet will induce natural flow. If a magnet quench should occur, the return and supply valves would close, and the vent valves open to vent gaseous helium into a recovery bag. (b) Seven struts (not all shown) support the magnet in the vacuum vessel. Heat flow in the struts from the warm vessel wall is intercepted by liquid-nitrogen-cooled heat barriers. Gaseous helium flowing out the current leads intercepts heat flowing in through them. From J. H. Van Sant, Energy and Technology Review, May 1981, Fig. 1, p.15. Courtesy of LLNL.

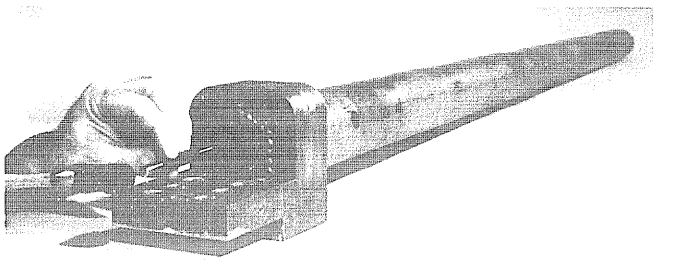

Fig. 23F2 (bottom of page). Vapor-cooled current lead for the MFTF magnet. Helium vapor flows through the 60 copper tubes, entering the bottom end at 5 K and leaving the top end at 30 K, while the lead is carrying 6000 A. The helium flow intercepts heat conduction in the lead from the warm end and is heated also by Joule heating. From J. H. Van Sant, Energy and Technology Review, May 1981, Fig. 3, p. 17. Courtesy of LLNL.

Table 23F1. Cryogenic subsystems of the MFTF experiment. From Sterbentz and Nelson (1979).

Helium Liquification/Refrigeration
1. Compressors
2. Cold boxes (liquifiers)

Helium Recovery
1. Low pressure storage bags
2. High pressure clean gas storage
3. High pressure dirty gas storage
4. Compressors (low pressure to high pressure storage)
5. Helium purification

Liquid Helium Storage
1. Liquid storage dewar (approximately 25,000 ℓ)
2. Cool down/accident valving and sensors

Helium Distribution
1. Transfer lines
2. Magnet supply dewar interface
3. Confinement vessels, dewar/ separation, interfaces,
4. Magnet vent return interface

Liquid Nitrogen Storage
1. Liquid storage dewar (approximately 400,000 ℓ)
2. Supply sensors

Liquid Nitrogen Distribution
1. Transfer lines
2. Valving and sensors
3. Magnet warm liner interfaces
4. Confinement vessels, dewar/ separators, interfaces

Auxiliary Systems
1. Magnet cooldown heat exchangers
2. Bypass system for cool gas return

Table 23F2. Estimated heat loads of the MFTF experiment. From Sterbentz and Nelson (1979).

heat loads at liquid helium temperature, W		
magnet coil		
radiation to case	160	
conduction to case	50	
instrumentation	70	
dissipation in coil joints	50	
support hangers	60	
supply lines	80	
leads	95	
total		565
cryopanels		1450
external piping		80
supply and storage dewars		100
external cryopumps		15
valves and valve box		100
reserve capacity		765
total		3075 W

heat loads at liquid nitrogen temperature, kW	
magnet	20
cryopanels	30
LN_2 subcooler	15
He refrigerator	7.7
He purifier	4.6
LHe dewar & piping	4
external cryopumps	1.6
LN_2 piping & valves	3.0
LN_2 storage tank	0.5
total	86.4 kW

The allowable rates of cooling the magnet and warming it up are limited by thermal stresses in the coil and support structure. Helium gas will be circulated through the coil from a liquid nitrogen heat exchanger for about five days to cool the coil down to 80 K. From 80 K to 15 K, the main liquefaction compressors will be used to cool the gas, and below 15 K, Joule-Thompson throttling will be employed. It will take about 4-5 days to cool the magnet from 80 K down to 4.2 K.

The cryogenic systems for a fusion reactor will be similar to the MFTF cryogenic systems, but larger. Thorough inspection and testing of all components and subsystems during assembly are essential, to ensure reliable operation.

Problems

1. Assume that the fiberglass support tubes of Fig. 23P1 have outer radius 28 cm, inner radius 27 cm and length 28 cm, and that the superinsulation is 1 cm thick with k = 10^{-4} W/m-K. The copper leads have a total cross sectional area of 0.1 cm^2 and lengths of 0.9 m. Assume that the thermal conductivity integral of the fiberglass is about twice that of glass, and that the coils may be considered to be all copper in estimating their mass and enthalpy. Estimate (a) the coil mass (read dimensions from sketch), (b) heat flow rate along the fiberglass support tubes, (c) heat flow rate along the coil leads, (d) heat leak rate through the superinsulation.

2. Estimate the heat which must be removed and the number of liters of liquid nitrogen which are boiled off in cooling 1 kg of copper from 300 to 80 K, and the how many liters of liquid helium are boiled off in cooling it from 80 K to 4.2 K. How many liters of nitrogen and helium will be consumed in cooling down the coils of problem 1, ignoring other losses ?

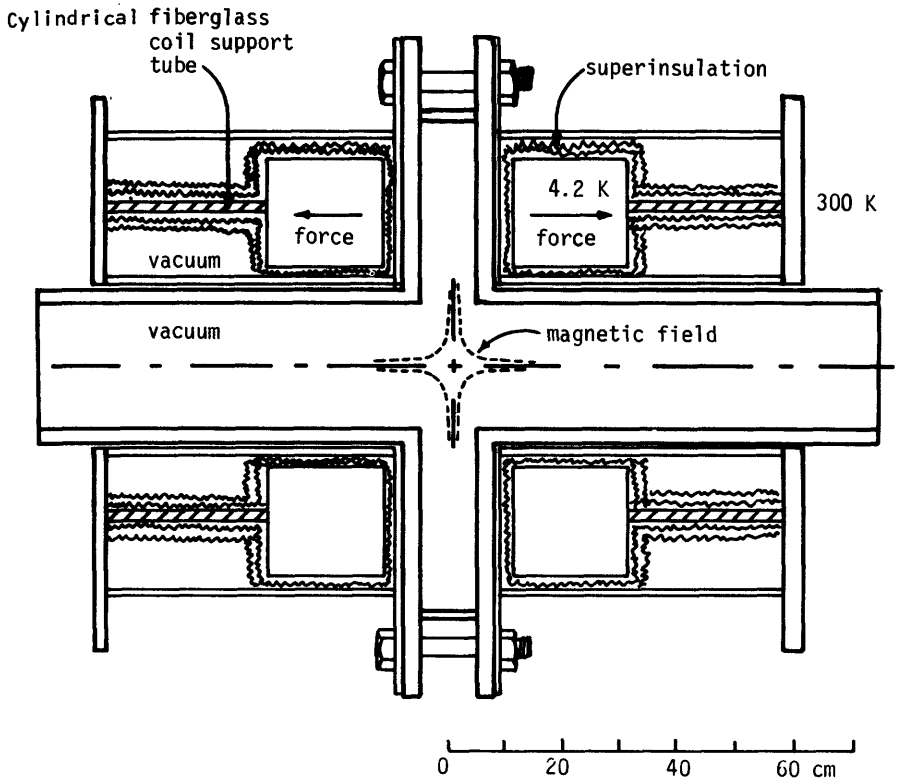

Fig. 23P1. The cryostat for a pair of spindle cusp magnet coils. The helium fill lines and coil current leads enter vertically from above (not shown).

3. How many liters of liquid helium will be boiled off per hour by a heat input of 1 kW? By the total heat input to the coils of Problem 1?

Bibliography

R. Barron, *Cryogenic Systems*, McGraw-Hill, New York, 1966.

J. H. Bell, Jr., *Cryogenic Engineering*, Prentice-Hall, Englewood Cliffs, NJ, 1963.

T. F. Durham, R. M. McClintock, and R. P. Reed, *Cryogenic Materials Data Handbook*, Office of Technical Services, Washington, DC, 1962.

J. File, "Superconducting Magnets and Cryogenic Systems", A Fusion Power Plant, MATT-1050, 1974, Ch. 13.

P. E. Glaser, I. A. Black, R. S. Lindstrom, F. E. Ruccia, and A. E. Wechsler, "Thermal Insulation Systems", NASA SP-5027, Washington, DC, 1967.

H. L. Laquer, *Cryogenics - the Uncommon Cold*, USAEC Technical Information Center, Oak Ridge, TN, 1973.

M. McClintock, *Cryogenics*, Reinhold, New York, 1964.

J. R. Powell and P. Bezler, "Warm Reinforcement and Cold Reinforcement Magnet Systems for Tokamak Fusion Power Reactors: A Comparison", Technology of Controlled Thermonuclear Fusion Experiments and the Engineering Aspects of Fusion Reactors, CONF-721111, USAEC, 1974, p. 358.

J. R. Roth, A. D. Holmes, T. A. Keller, and W. M. Krowcsonek, "Performance of a 12-Coil Superconducting 'Bumpy Torus' Magnet Facility", Technology of Controlled Thermonuclear Fusion Experiments and the Engineering Aspects of Fusion Reactors, CONF-721111, USAEC, 1974, p. 409.

R. B. Scott, *Cryogenic Engineering*, Van Nostrand, Princeton, NJ, 1959.

W. H. Sterbentz and R. L. Nelson, "Cryogenic aspects of the Mirror Fusion Test Facility", 8th Symposium on Engineering Problems of Fusion Research, (1979) IEEE, 1980.

R. W. Vance and W. M. Duke, Editors, *Applied Cryogenic Engineering*, Wiley, New York, 1962.

CHAPTER 24

MATERIALS PROBLEMS

24A. Introduction

"Materials is the queen technology of any advanced technical system. The economics eventually depend upon the materials, the reliability depends upon the materials, and safety depends upon the materials. I assure you that before we are through with fusion, the physicists will give way to the materials engineers as being the leading lights of fusion." (E. E. Kintner, 1975).

The United States Department of Energy (DOE) Fusion Reactor Materials Program is divided into four main categories: Damage Analysis and Fundamental Studies (DAFS), Alloy Development for Irradiation Performance (ADIP), Plasma Materials Interaction (PMI), and Special Purpose Materials (SPM). The topics included in these categories are summarized in Table 24A1. Basic research on behavior of metals (radiation effects, flow, fracture, etc.) comes under DAFS, while applied research to develop alloys with optimized properties comes under ADIP. The purpose of this Chapter is to describe briefly the main materials problems associated with fusion reactors. We will follow the order of Table 24A1, omitting a few topics.

24B. Damage Analysis and Fundamental Studies

Neutronics calculations will be discussed in Chapter 27. At a neutron wall loading of 1 MW/m^2, the 14.1 MeV neutron current is 4.43×10^{17} $m^{-2}s^{-1}$, and the total neutron flux is typically about 3.6×10^{18} $m^{-2}s^{-1}$. Methods for measuring neutron energy spectra were discussed in Section 10D. The neutron wall loading and flux may vary by more than a factor of two with poloidal angle in a tokamak.

damage production

Fast neutrons incident on matter can undergo various reactions: (n,n') (scattering), (n,2n), (n,α), (n,p), (n,γ), etc. The (n,α) and (n,p) reactions produce He and H gas atoms within the material, which can alter its properties. Thus, the atomic parts per million (appm) of He and H produced are measures of radiation damage via transmutations. Another measure of radiation damage is the displacements of lattice atoms caused by scattering of a fast neutron N, Fig. 24B1. The primary knock-on atoms P displace secondary knock-on atoms S, and so on. The

Table 24A1. Organization of the US DOE Fusion Reactor Materials Program. Based on DOE/ET-0032, Volumes 1-4 (1978).

Damage Analysis and Fundamental Studies (DAFS)

radiation environment characterization: neutron flux, energy spectrum, dosimetry
damage production: atomic displacements, He and H production, solid transmutation products, distributions of defects
damage microstructure evolution: motion of vacancies and interstitials, effects on mechanical behavior, models and correlations

Alloy Development for Irradiation Performance (ADIP)

analysis and evaluation: material property requirements, structural life predictions, test procedures, compatibility, fabrication
mechanical behavior: strength, ductility, fatigue, thermal creep
in-reactor deformation: changes in microstructure, swelling, irradiation creep

Plasma Materials Interaction (PMI)

plasma device characterization & wall interactions: particle fluxes, wall conditions, special surfaces, vacuum system, impurity effects
recycling of H, D, and T: reflection, gas trapping, diffusion, re-emission
impurity introduction: sputtering, chemical erosion, desorption, vaporization, blistering and flaking, unipolar arcing, synergistic effects
near-surface wall modifications: phase, alloy composition, microstructure, macrostructure, physical and mechanical properties, development of materials

Special Purpose Materials (SPM)

breeding materials: compatibility, physical properties, stability, tritium removal, breeding potential, MHD effects
coolants: properties, radiation stability, compatibility, neutronics, tritium removal, pumping power
materials for tritium service: permeation and barriers, interactions with organic materials, materials selection, fabrication, quality assurance
graphite and silicon carbide: applications, forms, limitations
heat-sink materials: applications, materials, problems
ceramics: applications, forms, problems
magnet materials: superconductors, structure, welds, insulation

knock-on atoms become interstitials I, and leave vacancies V behind where they had been. The first stage of damage begins when a primary knock-on atom is produced. This stage ends when the primary and other knock-on atoms have all slowed to energies below the displacement threshold energy (20-60 eV), so that no more knock-on atoms can be produced by the cascade from that neutron. In the second phase the motions are transformed into heat, and individual defects (vacancies and interstitials) are clearly defined. During the third stage, short-term annealing occurs: defect migration results in defects clustering together, annihilating each other (interstitial plus vacancy), or escaping from the region of interest. The configuration at the end of the third stage is called the *primary damage state.* Three types of defect clusters are illustrated in

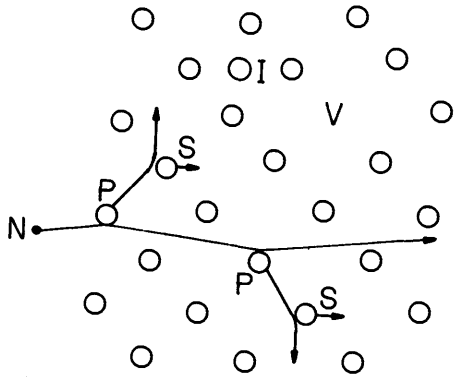

Fig. 24B1. Production of primary (P) and secondary (S) knock-on atoms by an incident fast neutron (N), resulting in interstitials (I) and vacancies (V).

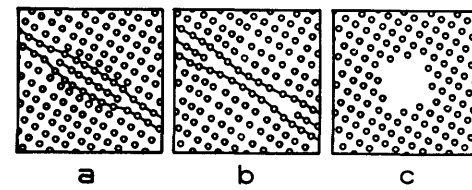

Fig. 24B2. The major types of defect clusters. (a) An interstitial dislocation loop, viewed on edge, forms by precipitation of interstitials into two-dimensional disks. (b) A vacancy dislocation loop forms similarly as vacancies precipitate into disk-shaped regions. (c) Cavities are three dimensional vacancy clusters with little strain at the cavity-lattice boundary. Based on F. W. Wiffen, "Radiation effects in structural materials for fusion reactors", Chapter 5 of Critical Materials Problems in Energy Production, Academic Press, New York, 1976, Fig. 2, p. 172.

Fig. 24B2. Cavities may be either empty voids, which shrink during annealing, or gas-filled bubbles, which swell during annealing.

The *molecular dynamics* method describes displacement cascades theoretically by integrating the equations of motion of the atoms in a small region after an atom has been displaced. This method, most useful for low energies of the primary knock-on atoms ($\lesssim$ 1 keV), can describe focussing and channeling of energy along various crystal planes.

The *binary collision approximation* method describes the trajectory of a knock-on atom as a series of isolated binary collisions in a discrete lattice. It can describe cascade development, sputtering, and backscattering, but loses accuracy at low energies. Continuum methods based on *transport theory* (Chapter 27) can also be applied to radiation damage studies.

The primary knock-on atom (PKA) energy spectra of a monoenergetic 14 MeV neutron source, a fusion reactor first wall, and a fission reactor are compared in Fig. 24B3. The PKA spectra of fusion neutrons have higher energies, so they produce more displacements per incident neutron.

The cross sections of (n,α) and (n,p) reactions grow rapidly at neutron energies of a few MeV, where there are few fission neutrons, so the gas generation rates produced by fusion neutrons are also much higher, in general, than those produced by fission neutrons. An exception is in alloys containing nickel, where the reactions

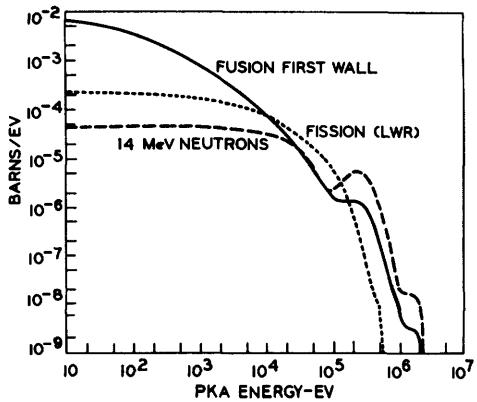

Fig. 24B3. Primary knock-on atom spectra for various neutron spectra incident on copper. From G. L. Kulcinski, CONF-750989 (1976) Volume I, pp. 17-43, Fig. 2.

Table 24B1. The displacement damage rate and gas production rates in typical fusion reactor materials, based on a time-averaged neutron wall loading of 1 MW/m^2 (14MeV current = 4.4×10^{17} neutrons/m^{2}s). Values in parentheses are helium production rates for a fast fission reactor (EBR-II). From Steiner (1975); Kulcinski (1976); and Gabriel, Bishop, and Wiffen (1978).

alloy	effective displacement threshold energy (eV)	displacement damage rate dpa/year	helium production rate appm/year	hydrogen production rate appm/year
SS 316	40	10-12	140-240 (5)	520-540
PE-16	40	12-15	160-240	780
Al	25	15	320-360	300
V-20 Ti	40	11	59	230
V	-	12	55-60 (0.3)	105
Nb	60	7	20-30 (1)	80-105
Mo	60	7-8	45-50 (2)	95-100
Be	-	-	3050	-
C	-	6	600-3000 (34)	-
B_4C	-	-	3600	-
$LiAlO_2$	-	-	15,500	-
SAP (Al+Al_2O_3)	-	14	410	780
SiC	-	-	1800	580
Al_2O_3	-	15	435	840

$$^{58}Ni + n \rightarrow {}^{59}Ni + \gamma \qquad (\sigma = 4.6\ b)$$
$$^{59}Ni + n \rightarrow {}^{56}Fe + \alpha \qquad (\sigma = 12.5\ b) \qquad (24B1)$$

can occur at thermal neutron energies.

If there are 1000 atomic displacements in a region containing a million atoms, then there are 10^{-3} displacements per atom (dpa). Using the neutron spectrum estimated for a typical fusion reactor, the number of dpa produced per year have been calculated for a variety of materials. The results of such calculations are shown in Table 24B1, along with estimated gas production rates, in atomic parts per million per year (appm/year). Under these conditions, each wall atom would be displaced many times a year. For comparison, helium production rates from fission reactors are given in parentheses. The figures in this Table increase linearly with neutron wall loading. They would vary somewhat with incident neutron energy spectrum and material compositions. The type of damage occuring depends partly on the ratio of appm(He) to dpa, which is much higher for fusion reactors than for fission reactors (Table 24B2).

Tritium diffusing through fusion reactor structure decays radioactively into helium. This effect can produce concentrations about 23 appm(He) in Nb, 11 appm(He) in V, but < 0.1 appm(He) in SS 316, for the conditions of Table 24B1.

Solid transmutation products are also produced by incident fast neutrons, as indicated for a few cases in Table 24B3.

Table 24B2. Ratio of appm(He) to dpa for a fast fission reactor (FFTF), a thermal fission reactor (HFIR), a Rotating Target Neutron Source of 14 MeV neutrons (RTNS-II), and a fusion reactor wall. The value for 316 SS in HFIR is high because of the reactions (24B1) in nickel. From Kulcinski (1976), Table 7.

	FFTF	HFIR	RTNS-II	fusion reactor
Nb	0.033	0.073	5.4	3.3
V	0.004	0.009	9.7	4.9
Mo	0.05	0.012		5.8
Al	0.11	0.31	63	24
316 SS	0.096	95	36	21

damage microstructure evolution

During bombardment self-interstitials and vacancies are produced in equal numbers. Later, as the interstitials and and vacancies gradually diffuse through the lattice, the interstitials are preferentially attracted to and trapped in dislocations (Fig. 24B2a), leaving an excess of free vacancies. The vacancies gradually form voids, and the net lattice distortion results in macroscopic swelling. At the same time, helium gas may accumulate in the cavities, increasing the amount of swelling.

Helium bubbles sometimes accumulate at grain boundaries, leading to intergranular fracture at low strain *(helium embrittlement)*. Other types of embrittlement will be discussed later.

Table 24B3. Solid transmutation rates in fusion reactor materials for a neutron wall loading of 1 MW/m^2. From Kulcinski (1976).

original metal	transmutation product	transmutation rate, appm/year
Al	Mg	400
	Si	40
SS 316	Mn	1200
	V	200
	Ti	50
V	Cr	130
	Ti	80
Nb	Zr	700
Mo	Tc	400
	Ru	30

As vacancies and self-interstitials recombine, lattice damage anneals out, especially at high temperatures. At the same time, more damage may be produced by incident neutrons. Thus, the lattice condition may depend on the *damage rate*, and not just on the total number of dpa produced. Significant annealing may occur during the time between reactor pulses.

The combination of both lattice damage (dpa) and gas production (appm of He) can produce swelling greater than expected for either phenomenon alone. Such *synergistic effects*, in which two or more processes combine nonlinearly, have been observed in other materials phenomena as well. Because synergistic effects involve several simultaneous phenomena with many parameters, they are difficult to model and predict.

Small changes in composition can make large changes in resistance to swelling and embrittlement, so there is hope that optimized alloys with favorable properties can be developed.

24C. Analysis and Evaluation

structural life predictions

Some material properties to be considered in the design of a fusion reactor first wall (nearest the plasma) are listed in Table 24C1. Failure of a structural component could be collapse, buckling, or fracture; or it could be simply a leak of coolant, tritium, or atmospheric pressure. Failure can be caused by stresses, radiation damage, surface bombardment, chemical reactions, and various combinations. Some sources of stress and failure mechanisms are listed in Table 24C2.

Table 24C1. Desired properties of first wall.

physical
- low mass density
- low vapor pressure

electrical
- resistant to unipolar arcing
- low conductivity (Ohmic-heated tokamaks)
- non-magnetic (not necessary)

chemical
- compatible with blanket and coolant
- low affinity for O,C,H,N
- permeable to tritium

neutronic
- low neutron cross sections, except (n,2n) cross section
- low transmutation rates
- short half-lives of transmutation products

thermal
- high thermal conductivity
- high melting point
- low vapor pressure
- low thermal expansion
- high heat capacity

mechanical
- high yield strength and ultimate strength
- good ductility
- resistant to crack growth
- high creep rupture strength
- good thermal stress parameter

radiation environment
- resistant to sputtering and blistering
- resistant to swelling
- resistant to embrittlement
- many data available

fabrication
- easy to form, machine, and weld
- welds durable under operating conditions

supply
- abundant domestic supply
- established industrial production
- cost not prohibitive

The required chamber wall thickness to withstand atmospheric pressure was illustrated in Fig. 19E1. Magnetic forces were described in Chapter 20, and coolant pressure stresses will be discussed in Chapter 26. Thermal stresses will be discussed here, and swelling, in Section 24E.

Table 24C2. Some components of structural life predictions. Adapted from DOE/ET-0032/1 (1978), p. 3-2.

sources of stress	*failure mechanisms*
gravity	embrittlement, brittle fracture
atmospheric pressure	fatigue
coolant pressure	thermal creep
magnetic forces	irradiation creep
thermal gradients	swelling
swelling	creep-fatigue interaction
	corrosion
	erosion
	overheating (loss of coolant)

thermal stress

If a metal rod is constrained at the ends (so that it cannot expand) and then heated up, a compressive thermal stress will be produced in the rod. The stress will be the same as if the rod were allowed to expand freely during heating, then compressed back to its original length. Similarly, thermal stresses can be created in other shapes, in nonmetals, and in any material containing a temperature gradient, since the material tends to expand different amounts in neighboring regions.

For a long tube with inner radius r, thickness Δr, and a temperature difference ΔT between the inner and outer walls, thermal stresses will be generated within the tube. If the tube is restrained at the ends, the azimuthal and axial stress components at the inner and outer radii are given by

$$\sigma_\theta(r) = \sigma_z(r) = \frac{-\alpha E \Delta T}{2(1-\nu)} \left(1 + \Delta r/3r\right)$$

$$\sigma_\theta(r+\Delta r) = \sigma_z(r+\Delta r) = \frac{\alpha E \Delta T}{2(1-\nu)} \left(1 - \Delta r/3r\right) \qquad (24C1)$$

where α is the thermal expansion coefficient (K^{-1}), E is the modulus of elasticity (Pa), ν is the Poisson ratio, which is 0.25-0.35 for most metals, and it is assumed that $\Delta r \lesssim 0.2\ r$. If the cylinder is not restrained at the ends, the maximum thermal stress near the free ends is about 1.25 times the stresses given by Eq. (24C1) with $\Delta r = 0$. These equations relate to cases in which boundary temperatures are fixed and there is no internal heat generation. Thermal stresses in fusion reactor components are discussed by Fraas and Thompson (1978).

The heat flux q/A through a wall with radius r (m), thermal conductivity k (W/m-K), temperature difference ΔT (K), and thickness Δr (m), is given by

$$q/A = k\Delta T/\Delta r \qquad (W/m^2) \ , \qquad (24C2)$$

if $\Delta r \ll r$. The average heat flux through a fusion reactor first wall may be written

$$q/A \simeq (\text{heating power} + \text{fusion power} - \text{neutron power})/(\text{wall area}) \ , \qquad (24C3)$$

since little of the neutron power P_n appears as heat in the first wall. By definition, $Q \equiv P_f/P_{in}$, where P_f and P_{in} are the fusion and input powers. For DT reactions, $P_n \simeq (4/5)P_f$, and Eq. (24C3) may be expressed in terms of P_n:

$$q/A \simeq (P_{in} + P_f - 0.8P_f)/A = (1/Q + 1/5)P_f/A$$

$$= \left(\frac{1}{4} + \frac{5}{4Q}\right)\frac{P_n}{A} \qquad (W/m^2) \qquad (24C4)$$

EXAMPLE PROBLEM 24C1

A fusion reactor with neutron wall loading $P_n/A = 2\ MW/m^2$ and $Q = 10$ has a first wall 0.5 cm thick made of stainless steel with $k = 20\ W/m\text{-}K$. If $E = 1.8\times10^{11}\ Pa$, $\alpha = 1.8\times10^{-5}\ K^{-1}$, and $\nu = 0.3$, estimate the magnitude of the thermal stress in the wall.

From Eq. (24C4) $q/A \simeq .75\ MW/m^2$, and from Eq. (24C2) $\Delta T \simeq 188$ K. If we approximate the toroidal reactor by a long cylinder with free ends, then the maximum thermal stress is approximately $1.25\alpha E\Delta T/2(1-\nu) = 544$ MPa (79,000 psi). For comparison, the yield strength of annealed SS 316 is about 240 MPa.

The thermal stress can be reduced by decreasing Δr (hence decreasing ΔT), by reducing the wall power flux, or by using materials with higher $k(1-\nu)/\alpha E$.

If we eliminate ΔT between Eqs. (24C1) and (24C2) for the case $\Delta r/r \ll 1$, we can express the ratio of the yield stress to the thermal stress as

$$\frac{\sigma_y}{\sigma_z} = \frac{\sigma_y}{\sigma_\theta} = \frac{M}{\Delta r(q/A)} \qquad (24C5)$$

where

$$M \equiv \frac{2(1-\nu)\sigma_y k}{\alpha E} \quad (W/m) \qquad (24C6)$$

is called the *thermal stress parameter*. Large values of M are desirable to permit large heat fluxes while keeping the thermal stresses $\sigma_\theta \simeq \sigma_z < \sigma_y$. Values of M vs. temperature for various materials are shown in Fig. 24C1.

The other stresses (Table 24C2) must be added to the thermal stresses to find the total stresses in the structure. Then the effects of the stresses on the various failure mechanisms can be estimated by comparison with experimental test data. Materials such as SS 316 can probably attain lifetimes of 5-10 MW-years/m^2 neutron fluence. The goal of the ADIP program is 40 MW-y/m^2.

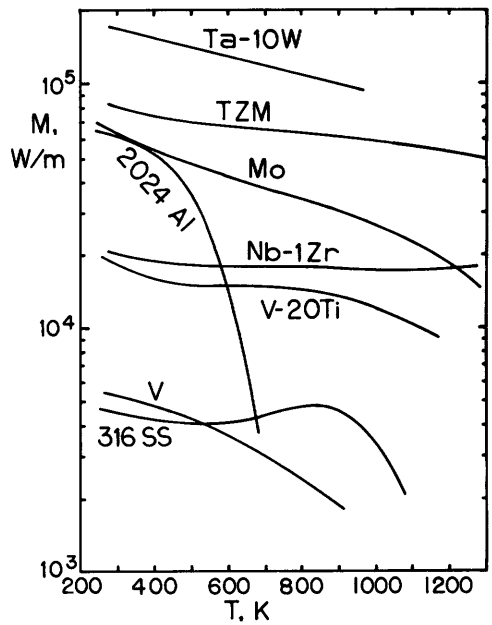

Fig. 24C1. Thermal stress parameter $M \equiv 2\sigma_y k(1-\nu)/\alpha E$ vs. temperature for various unirradiated materials. Based on data from B. Badger et al, "UWMAK-III, a noncircular tokamak power reactor design", EPRI ER-368 (1976), Table IX-B-4, p. 9-24.

test procedures

Preliminary studies and scoping tests are used to identify the most promising alloys, which have been grouped into five "paths":

A. austenitic alloys (such as stainless steel 316)
B. higher-strength Fe-Ni-Cr alloys
C. reactive and refractive metals and alloys (Nb, V, Ti, Zr, etc.)
D. innovative concepts (ceramics, fiber-reinforced composites, etc.)
E. ferritic/martensitic steels.

The most promising alloys in each group are studied in detail, with variations of parameters, in order to find the optimum combination. Finally, the optimum alloys will be extensively tested to provide the data needed for reliable predictions of structural lifetime. The main problem is that there is no suitable radiation source for fusion reactor materials testing. Some desirable radiation source features are:

high flux ($\gtrsim 10^{18}$ neutrons/m^{2}s)
energy spectrum similar to that expected for fusion reactor, to simulate reactor conditions: $\sim$ 10 dpa/year; $\gtrsim$ 100 appm(He)/year; appm(He)/dpa $\sim$ 10
large test volume, to accomodate many specimens
surface bombardment by charged particles and xrays
capability for either continuous or pulsed operation.

Fast fission reactors, mixed spectrum fission reactors, accelerator neutron generators, ion bombardment, and theoretical modeling are all being used to simulate the fusion reactor environment, but none of these is entirely satisfactory.

Table 24C3. Parameters of high energy neutron sources dedicated to fusion research.

parameter	*RTNS-II*	*FMIT*
location	LLL	HEDL
operational	1979	1983
target	rotating (5000 rpm), containing tritium	flowing liquid lithium
reaction	T(d,n)	Li(d,n)
neutron energy peak	14 MeV	10-20 MeV
beam	D^+	D^+
beam energy, MeV	0.4	35
beam current, A	0.15	0.10
target lifetime, hours	100	indefinite
beam size, cm	1	1x3
peak source strength (neutrons/s)	$4x10^{13}$	-
neutron flux, $m^{-2}s^{-1}$ (volume, cm^3)	10^{17}	10^{19} (10) 10^{18} (500)
dpa/week at peak flux	0.008	1.0

Fission reactors lack high-energy neutrons. Ion bombardment has different effects from neutron bombardment, and ions do not penetrate deeply beneath the surface. Accelerator neutron generators do not produce high fluxes over large test volumes. In the United States two high-energy neutron sources are dedicated to fusion research: the Rotating Target Neutron Source-II (RTNS-II) at LLL and the Fusion Materials Irradiation Test (FMIT) Facility at HEDL. Their parameters are listed in Table 24C3. The small test volumes available in these devices severelylimit the scope of the test program. An Engineering Test Facility (ETF) is needed for large-volume irradiation of reactor materials.

compatibility

Combinations of materials prone to chemical reactions are said to be "incompatible". Some combinations may be compatible at low temperatures, but incompatible at high temperatures. A few examples of compatibility problems are listed below:

* Plain steels rust when exposed to air and moisture.
* Liquid lithium and sodium react with air or water, posing fire hazards.
* Stainless steel is corroded by lithium at high temperatures ($\gtrsim$ 800 K). Aluminum additives help to suppress this corrosion. (The penetration rate of corrosion cracks caused by lithium in iron is greatly increased by applied stress. Creep strain may break protective corrosion-product coatings at the grain boundary interface.)
* Minute quantities of oxygen in He coolant at high temperatures (> 800 K) can cause problems with Nb and V structures.
* Some metals, such as Ta, are embrittled by hydrogen.
* Graphite is attacked by hydrogen to form methane at $500 \lesssim T \lesssim 1200$ K.

Virtually every structural material has some compatibility problems, which limit allowable coolants and temperature ranges.

Lithium can dissolve metal atoms from the structure and then deposit them somewhere else. Such *mass transfer* processes can cause clogging of coolant passages, overheating, and tube failure.

Tritium permeation and trapping in reactor materials are of particular concern, since it is desirable to minimize the radioactive inventory and the accidental release hazard (Chapter 28).

fabrication

Welding is the primary fabrication technique for structural components. Welds must be durable under operating conditions, whether at very high temperatures (first wall) or cryogenic temperatures. Welds may be more vulnerable to failure mechanisms (such as embrittlement) than the metals which are welded. The process of welding may introduce impurities, residual stresses, and variations in the microstructure. With some metals (Group V), welding must be done in vacuum or in very pure inert gases to avoid the detrimental effect of interstitial (O, C, N) pickup during welding. Brittleness of welds makes tungsten unsuitable for use as a structural material.

After the reactor is in operation, the structure will become radioactive from neutron bombardment. Damaged first-wall, blanket, and shield modules will probably be removed from the reactor and taken to the hot cell for repair or disposal. Fusion reactor maintenance was discussed in Section 18B.

24D. Mechanical Behavior

Several aspects of mechanical behavior, including yield strength, ductility, fatigue, and thermal creep are considered for various alloy compositions, microstructures, temperatures, and neutron fluences. A few common terms are defined in Fig. 24D1.

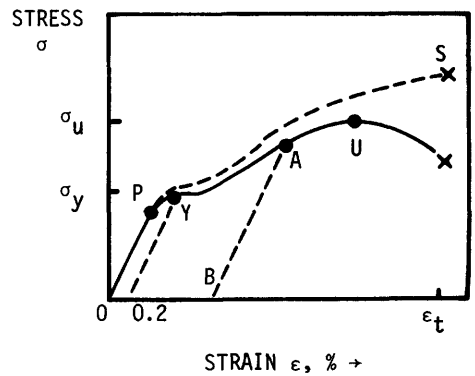

Fig. 24D1. Nominal (conventional) stress vs. strain for a tensile test of steel. Nominal stress = force divided by original cross sectional area, and strain = change in length divided by original length. Strain is linearly proportional to stress up to the proportional limit P. The modulus of elasticity (Young's modulus) E = dσ/dε along the linear portion of the curve. At the yield stress σ_y, plastic deformation begins, and the specimen no longer returns to its original length when the load is removed. For example, if the load were removed at point A, the strain would follow curve A-B. Ultimate stress σ_u is the peak conventional stress. The specimen cross sectional area decreases, so the "true stress" (force divided by actual area) continues to increase up to the point of failure (dashed curve O-P-S).

strength

Yield strengths of some structural alloys are shown as functions of temperature in Fig. 24D2 (100 MPa = 14,500 psi). Effects of irradiation-induced defect loops, voids, and precipitate particles tend to increase the yield strength. On the other hand, precipitation reactions which remove strengthening elements from solution tend to weaken alloys. At low temperatures ($T \lesssim 670$ K in stainless steels) the defect strengthening effect is dominant, and yield strengths increase with irradiation, but at high temperatures, the yield strengths may decrease with irradiation. In both cases, ductility is reduced by irradiation.

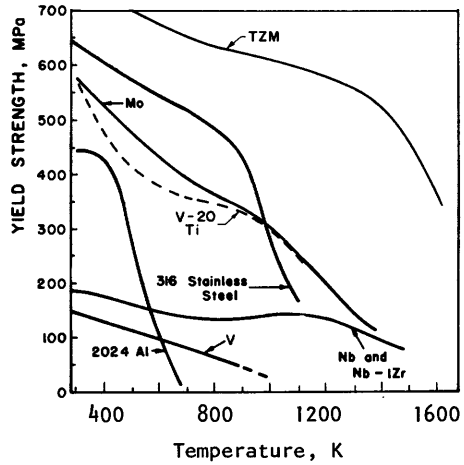

Fig. 24D2. Yield stress vs. temperature for various alloys. From B. Badger et al, "UWMAK-III, A noncircular tokamak power reactor design", EPRI ER-368 (1976), Fig. IX-B-3, p. 9-8.

ductility

Ductility refers to the ability of materials to stretch before they break. For example, a rubber band has good ductility. If the rubber band is immersed in liquid nitrogen, however, it loses its ductility and becomes very brittle, breaking without stretching. The rubber band may also be embrittled if it is immersed in certain chemicals or left out in the sun's rays. Thus, embrittlement may be caused by temperature changes, chemical changes, and radiation damage.

It is essential that a fusion reactor structure have adequate ductility, to bear high strain rates and high stresses without cracking. Local cracking could result in loss of vacuum chamber integrity, coolant leakage, or tritium leakage.

Ductility is measured in terms of the fractional elongation (strain) which a material can undergo up to its maximum stress *(uniform elongation)* or up to the point where it ruptures *(total elongation)*. The ETF components and fission reactor components are required to have at least 0.4% uniform elongation. Ductilities of various annealed, unirradiated alloys are shown as functions of temperature in Fig. 24D3.

The materials to be chosen must maintain ductility at all temperatures to which they will be exposed. For example, some materials (like irradiated Mo) may be ductile at operating temperatures, but become brittle when cooled down to room temperature. Temperature changes and inclusion pickup during welding tend to make welds brittle. Chemical attack can cause surface embrittlement and cracking.

Embrittlement caused by radiation damage from 0.1-5 MeV fission neutrons has been a severe problem of the LMFBR program. Extensive studies are being done in fast fission reactors like EBR-II, HFIR, and FFTF to define effects of neutron dose, irradiation temperature, helium production, etc. on the ductility of reactor materials, and to develop alloys which are resistant to embrittlement. An example of radiation-induced embrittlement of stainless steel is shown in Fig. 24D4. To maintain a total elongation of 1% in this material at temperatures around 670 K, it would be necessary to limit fission neutron fluence to less than 8×10^{25} neutrons/m^2 (approximately 0.7 MW-y/m^2 or 7 dpa).

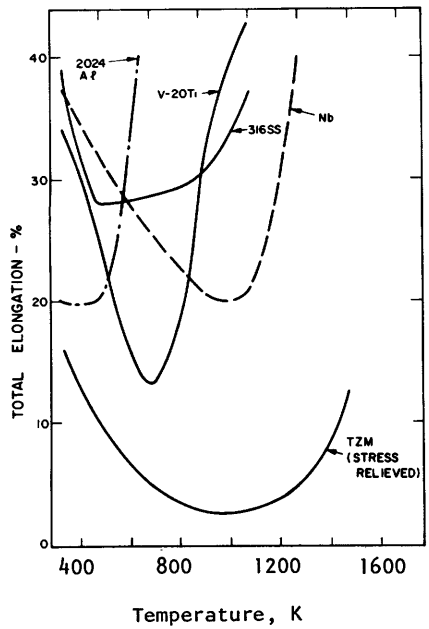

Fig. 24D3. Tensile ductilities of various annealed, unirradiated alloys vs. temperature. From B. Badger et al, "UWMAK-III, a noncircular tokamak power reactor design", EPRI ER-368 (1976), Fig. IX-B-4, p. 9-9.

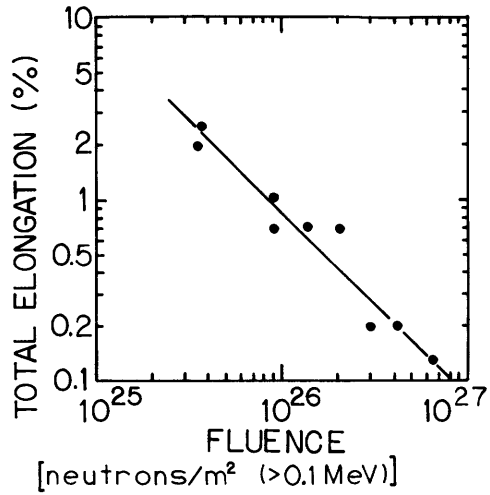

Fig. 24D4. Effect of neutron irradiation on ductility of stainless steel 304 creep tested to failure at 873 K. Irradiation in EBR-II at an initial stress of 190 MPA, at temperatures between 640 and 740 K. Ductility before irradiation was about 20%. From E. E. Bloom and J. O. Stiegler, pp. 451-467 in Irradiation Effects on Structural Alloys for Nuclear Reactor Applications, *ASTM-STP-484, Copyright 1971, American Society for Testing Materials, 1916 Race St. Philadelphia, PA, 19103. Adapted with permission.*

There are four principal types of radiation-induced embrittlement: hardening, DBTT shift, plastic instability, and helium embrittlement.

radiation hardening. An increase of ultimate tensile stress produced by irradiation, called radiation hardening, is accompanied by a reduction of uniform and total elongation. For example, Fig. 24D5a shows the stress-strain curves for Nb before and after irradiation at 730 K by fission neutrons. The ultimate stress increases from 180 MPa before irradiation to 450 MPa after irradiation (hardening). The uniform elongation decreases from about 25% before irradiation to about 5% after irradiation; and the total elongation decreases from 39% to 12%.

DBTT shift. For materials like ferritic (martensitic) steels and molybdenum, there are temperatures below which the ductility is very low, called the nil ductility temperatures (NDT) or ductile-to-brittle transition temperatures (DBTT). The DBTT is a function of alloy composition, microstructure, strain rate, and irradiation dose. During irradiation the DBTT shifts upwards, making the brittle regime more prevalent. Stress-strain diagrams for Mo illustrate this phenomenon in Fig. 24D5b. As with radiation hardening, the ultimate stress increases, but now there is very little ductility left: total elongation decreases from about

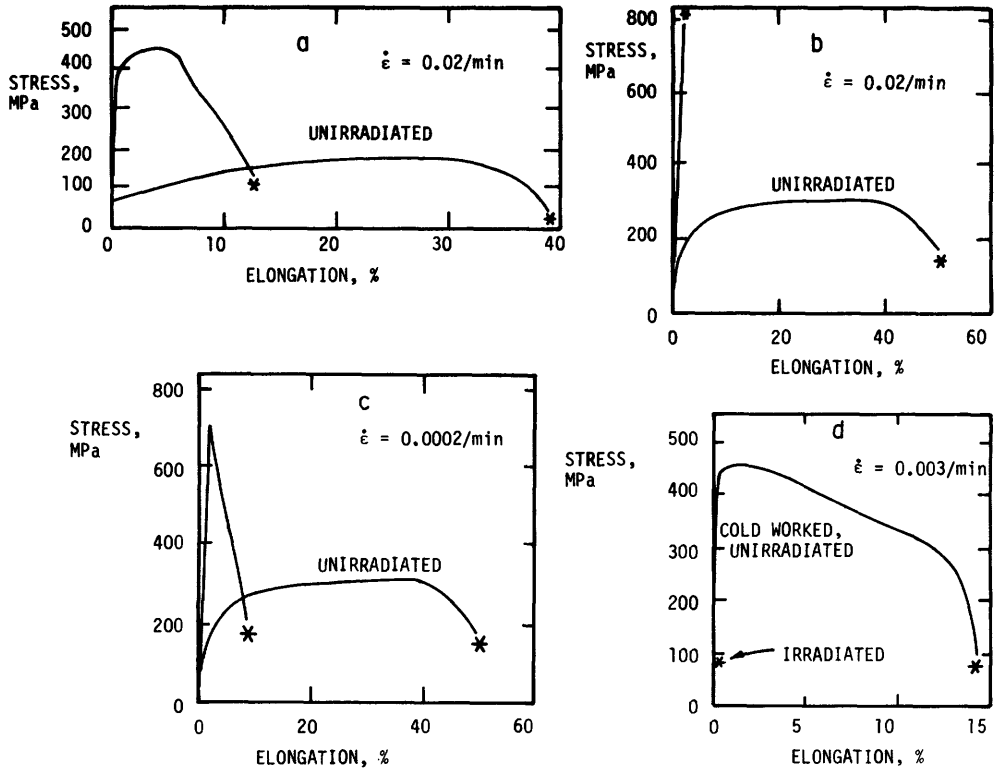

Fig. 24D5. Stress-strain curves illustrating the four types of radiation-induced embrittlement. (a) radiation hardening of Nb, (b) DBTT shift of Mo-0.5% Ti, (c) plastic instability of Mo-0.5% Ti, (d) helium embrittlement of Inconel 600. Cases (a), (b), and (c) were irradiated in EBR-II to 3×10^{26} neutrons/m^2 at 733 K, 698 K, and 698 K, respectively. Case (d) was irradiated in HFIR to 0.88×10^{26} neutrons/m^2 at 973 K after cold work, and acquired 1260 appm(He). Tensile tests were done at 673 K, except case (d) at 973 K. From F. W. Wiffen, ORNL/TM-5624 (1976), Figs. 8, 9, 12, 17.

50% to about 2% in this example.

The strain-rate (rate at which the specimen is stretched) has a significant effect on ductility and DBTT. For example, the specimen of Fig. 24D5b would retain about 8% ductility (Fig. 24D5c) if the strain rate were reduced to

.0002 min^{-1} (meaning that it takes 100 minutes to stretch the sample to 2% elongation). In effect, the DBTT increases with strain rate. The DBTT is also a function of irradiation temperature. If Mo is irradiated above 1070 K, no significant change in DBTT occurs.

Photographs of the microstructure for the two cases indicate dimples and high local deformation for the ductile case at low strain rate (above the DBTT) and a cleavage fracture, with no secondary cracking and little deformation for the brittle case at high strain rate (below the DBTT).

plastic instability. The irradiated curve of Fig. 24D5c illustrates the "plastic instability". After reaching maximum stress, the stress drops abruptly, ending in fracture with small total elongation.

For the case of metals with body-centered cubic (bcc) lattices irradiated at relatively low temperatures, a diamond-shaped pattern of light channels may be observed accompanying the plastic instability. (Mo, V, Nb, Fe, and Cr have bcc structure.) Once shear flow occurs along these channels, further flow may occur at lower stress.

Microstructures dominated by dislocation loops (Fig. 24B2) are susceptible to the plastic instability, while those with high concentrations of cavities (voids and bubbles) are not susceptible. Dislocation loops formed at low temperatures may join to form cavities at higher temperatures, inhibiting the plastic instability, so raising the temperature increases the ductility.

helium embrittlement. Helium produced during neutron irradiation migrates to grain boundaries, forming bubbles along the grain boundaries, and weakening the cohesion between grains. Thus, helium buildup promotes intergranular fracture, leading to rupture at low elongations, as illustrated in Fig. 24D5d. This problem is especially severe at high irradiation temperatures, where enhanced helium mobility permits rapid accumulation along grain boundaries.

Helium embrittlement is the most serious problem for stainless steels, nickel alloys, and aluminum alloys. Experimental modifications of alloy contents have reduced susceptibility to helium embrittlement, but not eliminated it. The roles of these four ductility-reduction mechanisms with various alloys are shown in Table 24D1.

Table 24D1. Mechanisms limiting the ductility of irradiated fusion reactor materials. This summary was developed from a very limited data base, so it is subject to revision. (Nb, Ta, and V alloys may also have DBTT shifts, but data are lacking.) From F. W. Wiffen, ORNL/TM-5624 (1976), Table 6.

alloy system	most severe restraint	secondary restraint
stainless steels and nickel-based alloys	He embrittlement	hardening
aluminum based alloys	He embrittlement	hardening
Mo and W based alloys	DBTT shift	plastic instability
Nb or Ta based alloys	plastic instability	hardening
V based alloys	hardening	He embrittlement

fatigue

If you pull on a tin can lid, you probably can't pull it apart, because your muscles cannot provide enough force. If you bend it back and forth a few times, however, it will gradually crack and break apart, even though the applied force is much lower than that required to pull it directly apart. Such crack growth and fracture during cyclic loading is called "fatigue". Fatigue has been the most difficult materials problem to overcome in aircraft wing design, bridge design, automobile engines, steam turbines, jet engines, pressure vessels, railroad wheels, and many other mechanical devices with cyclic stresses. On the order of a billion dollars is spent annually on fatigue research (Fong, 1979).

Fig. 24D6. Photograph of fatigue cracks (marked "C") emanating from a corrosion pit in low carbon steel. Magnification = 2200. Grain boundaries designated "G". From Dolan, Lazan, and Horger. Basic Concepts of Fatigue Damage in Metals, Fatigue, American Society for Metals, 1954, p. 6.

Chemical attack can cause stress corrosion fatigue. Changing temperatures can cause thermal stress fatigue, and so on. Fusion reactors will have stress changes every time the magnet coils are turned on or off, when the walls heat up or cool off during plasma burn or quench, when the vacuum chamber is evacuated or let up to air pressure, when the magnet coils are cooled down or warmed up, when the coolant flow rate is changed, and so on. In general, fatigue can cause failure at stresses less than expected for static loading, so it must be taken into account in any design involving cyclic stresses.

The surface of a metal normally has microscopic flaws in it, such as machining grooves, corrosion pits, weld defects, and, in the case of fusion reactor walls, damage from sputtering. When stress is applied, the local stress at cracks is much higher than the average stress on the whole piece of metal, and this local stress concentration may cause the cracks to grow (Fig. 24D6). With each stress cycle, the crack may propagate a little further, until the metal is so thin that it fractures.

Fatigue involves imperfections occurring on several different size scales (Fong, 1979, p. 729-747):

dislocation level	10^{-10} to 10^{-8} m	vacancies, interstitials, loops
subgrain level	10^{-8} to 10^{-6} m	slipbands, microvoids at grain boundaries
grain-size level	10^{-6} to 10^{-4} m	microcracks, voids
specimen level	10^{-4} to 10^{-2} m	cracks, pits, notches
component and structural level	> 10^{-2} m	welds, joints, cracks, misalignments

Fatigue crack growth rates depend upon many conditions, including
alloy composition
microstructure (grain size distribution, defects from cold-work, etc.)
irradiation and dpa
appm(He)
gases present in the crack, such as water vapor
temperature
stress amplitude, wave shape, and frequency.

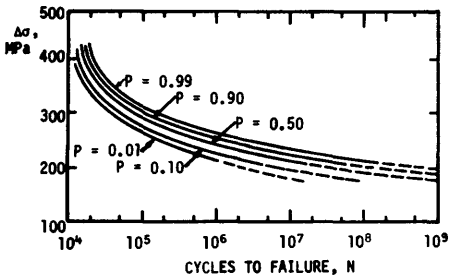

Fig. 24D7. Failure probabilities P for samples of 75S-T aluminum alloy at various cyclic stresses Δσ and numbers of stress cycles N, derived from fatigue tests of unnotched specimens. (100 MPa ≈ 15 ksi). From Dolan, Lazan, and Horger. Basic Concepts of Fatigue Damage in Metals, Fatigue, American Society for Metals, 1954, p. 17.

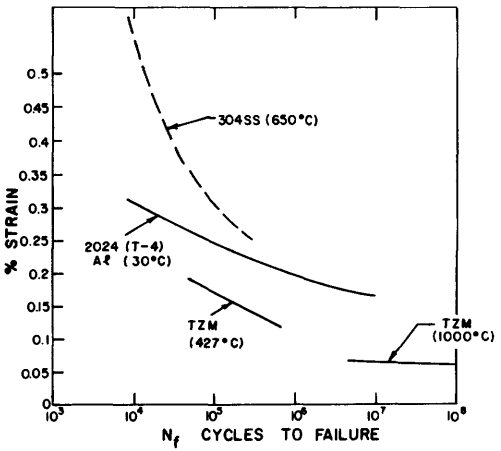

Fig. 24D8. Approximate "fatigue lives" of a few alloys. TZM is an alloy of Mo with 0.5% Ti, 0.08% Zr, and 0.03% C. From B. Badger et al, UWMAK-III, EPRI ER-368 (1976), Fig. IX-B-8.

If the applied stress is high, the crack propagates rapidly, and only a few stress cycles are needed to cause failure, as in the case of the tin can lid. If the applied stress is low, on the other hand, the crack propagates very slowly, and it may take millions of stress cycles to cause complete failure. This relation between applied stress and the number of cycles required to cause failure is illustrated in Fig. 24D7 for an unirradiated aluminum alloy. Sometimes such graphs are drawn with cyclic *strain* (instead of stress) vs. N (Fig. 24D8.) The stress or strain below which the failure probability is very low has been called the "fatigue life" or "endurance limit" of the material. However, such terminology could mislead design engineers into believing that the material is safe from failure at lower stresses.

Much more research is needed before service lives of cyclic fusion reactor components can be reliably predicted.

thermal creep

At temperatures $T \gtrsim .5T_m$, metals subject to constant stresses will gradually deform. This gradual yielding over long periods of time (1 - 10^4 hours) is called creep. If the stress is applied for a long enough time, the metal will ultimately rupture. The time to creep rupture is a function of stress, as shown in Fig. 24D9, and also a strong function of temperature. At low temperatures the creep rate is negligible, and creep rupture does not occur in unirradiated metals.

Fusion reactor components should be designed to function at least 10^4 hours (14 months) before creep rupture occurs. This means keeping stresses below about 160 MPa in 316 SS at 870 K.

Creep can also be induced by irradiation (Section 24E), and the required stresses for 316 SS may be a factor of two lower (about 80 MPa, or 40 MPa with a safety factor of two). Making the design stresses this low will not be easy.

24E. In-Reactor Deformation

Various changes in microstructure occur during irradiation:

* *enhanced diffusion.* During irradiation diffusional processes are accelerated, due to creation of many point defects and addition of vibrational energy to the lattice.
* *phase changes.* The presence of irradiation-produced defects can change the free energy of one phase relative to another, enabling phases to appear which would not appear in the absence of irradiation.
* *solute segregation.* One constituent element may be readily bound to point defects, like vacancies. As the defects flow to sinks, such as cavities, the element is carried along. Many atoms of that element may concentrate at the sink.
* *dissolution of precipitates.* Small precipitate particles may be broken up or disordered when interacting with collision cascades or moving dislocations.

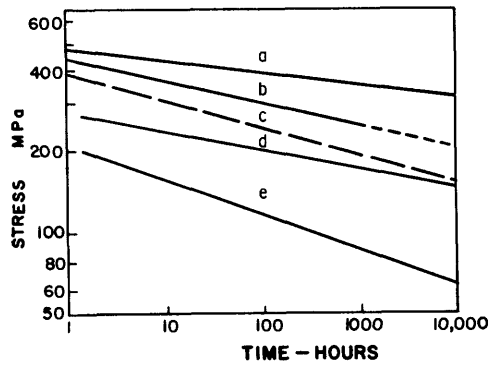

Fig. 24D9. Stresses causing thermal creep rupture of various alloys vs. time to rupture. (a) TZM at 1270 K, (b) 2024 Al (T-4) at 470 K, (c) Vanstar (10 Cr, 3 Fe, 1.3 Zr) at 970 K, (d) 316 SS at 870 K, (e) Nb-1 Zr at 1270 K. From B. Badger et al, UWMAK-III, EPRI ER-368 (1976), Fig. IX-B-7.

These changes in microstructure cause changes in dimensions (*in-reactor deformation)* and changes in mechanical behavior (hardening, embrittlement, etc.). Two types of dimensional changes occur: swelling and irradiation creep.

swelling

When vacancies precipitate as cavities, the corresponding interstitials create new lattice sites by precipitation at dislocations (Fig. 24B2a), and the macroscopic dimensions increase, resulting in swelling. Vacancy migration rates are high enough to promote void growth when the temperature $T > \frac{1}{4}T_m$, (T_m = melting temperature). As temperature increases, voids combine to form larger voids, spaced farther apart.

The amount of swelling depends upon several conditions:

* *alloy composition.* Slight changes in the nickel content of SS 316, for example, can change the amount of swelling by an order of magnitude.
* *metallurgical state.* Distributions of grain size, precipitates, and phase, and degree of cold work may all affect the amount of swelling. For example, cold worked SS 316 has less swelling than solution annealed SS 316.
* *temperature.* The amount of swelling generally increases with temperature.
* *displacements.* Swelling usually increases with the number of dpa.
* *helium.* Swelling increases with the concentration of He. Helium appears to promote void nucleation and growth.
* *other conditions.* Swelling may also depend on damage rates (dpa/s), applied stresses, ratio of dpa/appm(He), and reactor duty cycle.

Experimentally, the amount of swelling may be studied by measuring macroscopic dimension changes, differences between irradiated and unirradiated portions of a sample, change in mass density (by immersion in fluid), and with transmission electron microscopy (TEM) of microstructure. If the length of a specimen increased by $\Delta\ell/\ell = 1\%$ in every direction, then the volume would increase by ΔV such

that $(V+\Delta V)/V = (1.01)^3 = 1.0303$, and $\Delta V/V = 3.03\%$. Thus, for small swelling, the linear growth (percent) is roughly 1/3 the volumetric swelling (percent).

Figure 24E1 shows the swelling observed in 20% cold worked (CW) and solution annealed (SA) SS 316 in fission reactors. For this case helium increases swelling and cold working decreases swelling at low temperatures. In this experiment the average cavity diameters varied from about 15 nm (CW) and 30 nm (SA) at 700 K up to 100 nm (both cases) at 950 K for the samples irradiated in HFIR to 3000-4300 appm(He). Gradients of swelling magnitude produce internal stresses, just as gradients of temperature and thermal expansion produce thermal stresses.

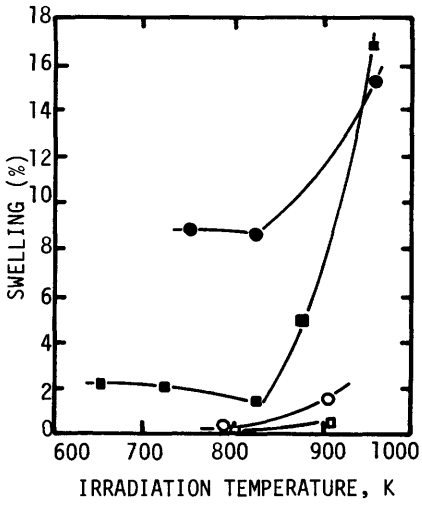

Fig. 24E1. Variation of volumetric swelling with irradiation temperature for annealed (circles) and 20% cold worked (squares) stainless steel 316 samples irradiated in fission reactors. Open squares and circles: irradiated to 31-37 dpa and about 15 appm(He) in EBR-II. Solid squares and circles: irradiated to 42-60 dpa and 3000-4300 appm (He) in HFIR. From P. J. Maziasz, F. W. Wiffen, and E. E. Bloom, "Swelling and microstructural changes in type 316 stainless steel irradiated under simulated CTR conditions", CONF-750989 (1976), p. I-259 to I-288, Fig. 2.

Solid transmutations can also lead to swelling, but the magnitude of the effect is usually much less. For example, transmutation of 1% of a Nb wall to Zr would produce a 0.2% volume swelling, and transmutation of 1% of a V wall to Cr would produce a 0.2% shrinkage.

irradiation creep

Change of elongation with time during static loading and irradiation, called *irradiation creep*, varies strongly with applied stress, but only weakly with temperature.

According to one theory of irradiation creep, the strain rate (rate of change of elongation) is given by

$$\dot{\varepsilon} \equiv \frac{d\varepsilon}{dt} = \frac{A\sigma^2 L}{\mu^2 bd}\ \nu_{climb} \qquad (24E1)$$

where A = a constant, σ = applied stress, L = average spacing between "obstacles" (barriers to motion of dislocations through the metal lattice), μ = shear modulus, d = average height of the obstacles, b = Burgers vector, and ν_{climb} is the dislocation climb velocity. The dislocation climb velocity is roughly proportional to the damage rate (dpa/s) so strain rate should vary almost linearly with damage rate and irradiation flux.

The variations of creep strain rate with damage rate and with applied stress are shown in Fig. 24E2. The linear variation with damage rate and quadratic variation with stress are consistent with Eq. 24E1. These experiments were done with ion bombardment instead of neutron irradiation, due to lack of high-flux 14 MeV neutron sources.

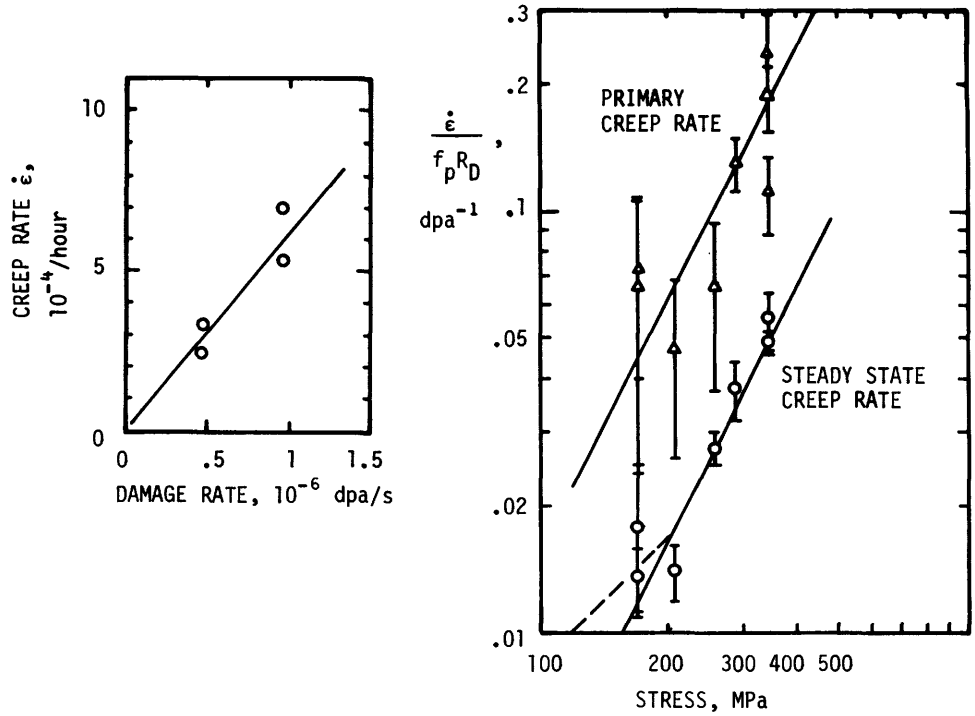

Fig. 24E2. Effects of damage rate and stress on creep rate. The left hand graph is for nickel irradiated by 4 MeV protons at 820 K, 100 MPa, after 40 hours. From R. J. McElroy, J. A. Hudson, and R. S. Nelson, "Irradiation creep during a 4 MeV proton irradiation", CONF 750989 (1976), p. II-72 to II-83. The right hand graph is for nickel irradiated by 22 MeV deuterons or 70 MeV alpha particles at 497 K, 1.3-3x10^{-7} dpa/s. The strain rate $\dot{\varepsilon}$ (s^{-1}) is normalized to the damage rate R_D (dpa/s) and a particle factor f_p, which accounts for the difference between deuterons and alpha particles. From P. L. Hendrick et al, "Ion-simulated irradiation-induced creep of nickel", CONF 750989 (1976), p. II-84 to II-117.

24F. Hydrogen Recycling

Here "hydrogen" includes all three isotopes H, D, and T. The term *recycling* refers to the processes by which hydrogen gas atoms leave the walls and return to the plasma.

* *reflection* (also called backscattering). During its interaction with wall atoms, an incident atom or ion may re-emerge from the wall.
* *spontaneous desorption* (also called thermal desorption). Hydrogen atoms adsorbed on the wall surface may leave the surface as they recombine into H_2 molecules.
* *stimulated desorption* (also called gas sputtering). Atoms adsorbed on the surface or absorbed near the surface may be ejected by incident ions, atoms, electrons, or photons.

Recycling is important because it determines the rate at which hydrogen atoms

are incident on the plasma. This rate affects the ionization and charge exchange rates, and thus influences the plasma density and temperature. High recycling rates tend to increase plasma density and decrease ion temperature. During a long plasma pulse, each hydrogen atom recycles from the wall many times.

reflection

Reflection coefficients have been calculated using the Monte Carlo technique (Section 27C), and measured experimentally. The results may be expressed in terms of the *Linhard reduced energy*

$$\varepsilon = \frac{32.5\ m_2 W_1}{(m_1+m_2)Z_1 Z_2 (Z_1^{\frac{1}{2}} + Z_2^{\frac{1}{2}})^{2/3}} \quad \text{(dimensionless)}, \tag{24F1}$$

where W_1 is the incident particle energy (monoenergetic) or temperature (Maxwellian) expressed in keV, m_1 and Z_1 are the incident particle mass and nuclear charge number, and m_2, Z_2 are the target atom mass and nuclear charge number.

Let θ be the angle between the incident particle velocity and a normal to the surface. Cases with normal incidence ($\theta = 0$), with a $\cos\theta$ distribution of incident particles, and with an isotropic distribution of incident particles have been studied. Experimental measurements for the case of monoenergetic ions at normal incidence are in fair agreement with theoretical predictions. For the cosine distribution, which probably best represents a fusion plasma, the theoretical values of particle reflection coefficient (number of reflected particles per incident particle) are fit approximately by the equation

$$r_n \simeq 0.35 - 0.2 \log_{10}\varepsilon \qquad (0.01 < \varepsilon < 10) \tag{24F2}$$

For the cosine case, values outside this range are not available. The theoretical results for most target materials studied agree fairly well with Eq. (24F2), but r_n for Be is about a factor of 2 lower than the Equation. Values for the normal incidence case are lower than Eq. (24F2), and values for the isotropic distribution case are slightly higher (Haggmark and Biersack, 1979). Values of the "energy reflection coefficient" (energy reflected divided by incident energy) have also been calculated for the three angular distribution cases.

EXAMPLE PROBLEM 24F1

Assume that deuterons with temperature 1 keV are incident on an aluminum surface with cosine angular distribution. Estimate the fraction of the deuterons which are trapped in the surface.

For this case, $m_1 = 2$, $m_2 = 27$, $Z_1 = 1$, $Z_2 = 13$, and $W_1 = 1$. From Eq. (24F1) we find $\varepsilon = 0.841$, and from (24F2), $r_n \simeq 0.36$. The fraction trapped is $(1 - r_n) = 0.64$.

---

spontaneous desorption

Incident energetic particles not reflected will be implanted inside the wall. From there they may gradually diffuse back to the surface and be desorbed. The time it takes for them to re-emerge from the surface is the sum of the times for diffusion and desorption. Spontaneous desorption of hydrogen occurs via molecular recombination on the surface, so the recombination rate determines the time delay

before desorption. Thus the spontaneous desorption flux may be limited either by diffusion or by recombination, whichever is the slower process. Let c(x,t) be the hydrogen atom concentration (atoms/m^3), where x is the distance from the surface and t is the time. The spontaneous desorption flux may be written

$$(\text{spontaneous desorption flux}) = Kc^2(0,t) \quad (\text{atoms}/m^2 s), \qquad (24F3)$$

where K is a recombination rate paramater (m^4/s), which can be estimated from Eq. (28B18). The resulting values of K are shown as functions of 1000/T in Fig. 24F1, where T is the surface temperature (K). Energy must be supplied for hydrogen to enter *endothermic* metals like Al and Fe, but energy is released when hydrogen enters *exothermic* (reactive) metals like Ti and Zr. This energy of solution makes K very low for exothermic metals.

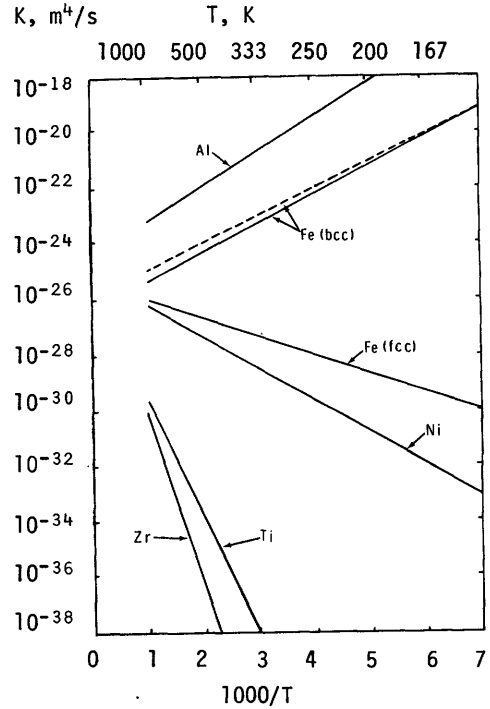

Fig. 24F1. Surface recombination coefficient K vs. inverse temperature for various metals. Dashed curve: experimentally measured values. From M. I. Baskes, "A calculation of the surface recombination rate constant for hydrogen isotopes on metals", Journal of Nuclear Materials, 92, 318-324 (1980) Fig. 3.

The concentration c(0,t) can be determined by solving a diffusion equation of the form

$$\frac{\partial c}{\partial t} = \frac{\partial}{\partial x}\left[D \frac{\partial c}{\partial x}\right] + S(x,t) \qquad (24F4)$$

where D is the diffusion coefficient and S(x,t) is the volumetric source of hydrogen atoms from implantation. (If a strong temperature gradient is present, a term proportional to $\partial T/\partial x$ is also needed in this equation.) Thus, a slow diffusion rate can keep c(0,t) low, and limit the spontaneous desorption rate. The diffusion coefficient varies with temperature T as

$$D = D_0 \exp(-E_d/T) \qquad (24F5)$$

where D_0 is a constant for any given metal, E_d is the "activation energy for diffusion", and T is expressed in energy units. (Values of D_0 and E_d are given in Table 28B3.)

stimulated desorption

The gas flux emitted from the surface by stimulated desorption is proportional to the incident fluxes causing the desorption, including energetic ions, neutrals, electrons, and photons. If the bombarding particles mainly knock atoms out of the surface, then the stimulated desorption flux is also proportional to c(0,t). If the bombarding particles act mainly to accelerate the rate of diffusion to the surface, then the stimulated desorption flux is proportional to $(\partial c/\partial x)_{x=0}$.

Thus, according to these two models, the flux emitted by energetic incident ions is

$$\text{(stimulated desorption flux)} = \begin{cases} A\Gamma_i c(0,t) & \text{(gas sputtering)} \\ A_1\Gamma_i(\partial c/\partial x)_{x=0} & \text{(accelerated diffusion)} \end{cases} \quad \text{(24F6)}$$

where Γ_i is the incident ion flux, and A, A_1 are constants. The constant A may be expressed in terms of an effective desorption cross section $\sigma_d(m^2)$ and incident ion mean range λ as

$$A \sim \sigma_d \lambda/4 \quad \text{(24F7)}$$

where $\lambda/4$ is taken as the maximum depth from which stimulated desorption is effective. Rough experimental measurements indicate values of $\sigma_d \sim 10^{-19}$-10^{-20} m^2 but accurate data are lacking. Accelerated diffusion is discussed by Hotston (1980).

The above estimates of spontaneous and stimulated desorption ignore the possible buildup of monolayers of adsorbed gas on the wall surface. If several monolayers are present, then atoms could be more easily knocked off, and stimulated desorption rates would be much higher (much larger values of σ_d would be measured). At equilibrium, gas atoms would leave the surface as fast as others arrived, and the number of adsorbed monolayers could be calculated from their binding energies and the surface temperature. Under transient conditions, however, no equations or data are available yet for calculating the number of monolayers present as a function of temperature, species, incident fluxes, etc.

The recycling situation is further complicated by chemical reactions of hydrogen with oxygen, carbon, and metals; by surface films; and by trapping of hydrogen in lattice defects with binding energies of eV.

applications

Wall models incorporating recycling processes are used to describe

* boundary conditions for transport codes describing various plasma confinement experiments (tokamaks, EBT, etc.).
* variation of plasma density with time in gettered (sublimation pumped) and ungettered tokamak discharges.
* operation of tokamaks for many discharges with hydrogen, then switching to deuterium. For the first few discharges, hydrogen coming out of the walls dominates the discharge.
* pressure rise with time after the end of a plasma discharge, due to hydrogen coming out of the walls.
* neutral gas - wall interactions in divertors, limiters, and beam dumps.
* effect of neutral beam injection on plasma density.
* time variation of gas trapping efficiency as a metal saturates with gas.

Recycling models suffer from oversimplicity, which is necessitated by a paucity of data. Nevertheless, there have been some consistencies between model predictions and experimental observations in most of the above areas (Vernickel et al, 1980).

Plasma-wall interactions involve not only recycling of hydrogen, but also contamination of the plasma by impurity atoms from the walls.

24G. Impurity Introduction

physical sputtering

Incident ions (or atoms) may eject atoms from wall surfaces, by either primary or secondary collisions (Fig. 24G1). The average number of wall atoms ejected per incident ion, called the *sputtering yield* S, varies with wall material, incident ion type, energy, angle of incidence, and surface conditions. For the case of light ions at normal incidence, the sputtering yield may be represented in terms of a universal formula

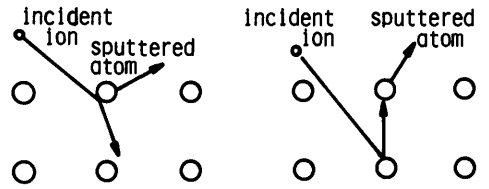

Fig. 24G1. Physical sputtering of surface atoms by incident ions. Wall atoms may be ejected by primary collisions (left) or by secondary collisions (right).

$$S = 0.0064\, m_2 \gamma^{5/3} E^{\frac{1}{4}} \left(1 - \frac{1}{E}\right)^{7/2}, \quad (1 < E \lesssim 30),\ (m_1/m_2 \leq 0.4) \qquad (24G1)$$

$$\gamma \equiv \frac{4m_1m_2}{(m_1+m_2)^2} \qquad (24G2)$$

where m_1 and m_2 are the incident ion and wall atom mass numbers (m_2 = 27 for aluminum),

$$E \equiv W/W_{th} \qquad (24G3)$$

W is the incident ion energy, W_{th} is the "threshold energy" given by

$$W_{th} = \frac{W_B}{\gamma(1-\gamma)} \qquad (24G4)$$

and W_B is the surface binding energy of the wall atoms. The variation of sputtering yield with normalized energy E given by Eq. (24G1) is compared with data points for a wide variety of wall atoms and incident ions in Fig. 24G2. Agreement is satisfactory for $E \lesssim 30$. Values of the threshold energy W_{th} for various cases are listed in Table 24G1.

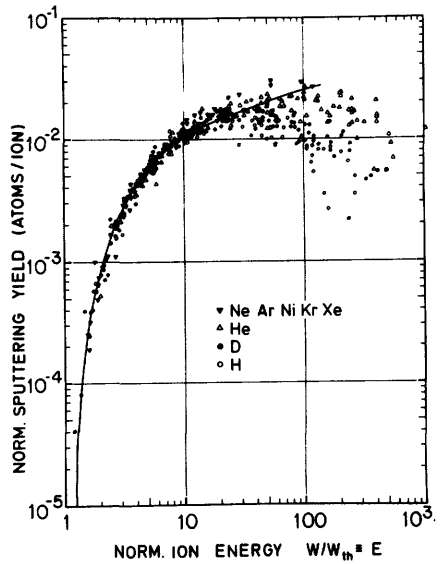

Fig. 24G2. Sputtering yield vs. normalized energy E, for various wall materials and incident ions. Smooth curve is from Eq. (24G1). From J. Roth, J. Bohdansky, and W. Ottenberger, "Data on low energy light ion sputtering", Max-Planck-Institut für Plasmaphysik Report IPP 9/26 (1979), Fig. 40.

If Eq. (24G1) is integrated over a Maxwellian distribution of incident particle energies, the resulting sputtering yield has the form shown in Fig. 24G3 as a function of incident ion temperature. Some Maxwellian-ion sputtering yields are listed in Table 24G2 for various species and temperatures.

For cases in which the ions are not normally incident, the sputtering yield increases with angle of incidence (measured from the normal), as illustrated in Fig. 24G4 for nickel. Thus the sputtering yield for ions incident with a distribution of angles (such as a cosine distribution) would be *larger* than for the

Table 24G1. Values of the threshold energy W_{th} (eV) for various ions and wall atoms. From J. Roth, J. Bohdansky, and W. Ottenberger, "Data on low energy light ion sputtering", Max-Planck-Institut für Plasmaphysik Report IPP 9/26 (1979), Table 34.

Ion / Target	H	D	He^3	He^4
Al	53	34		20.5
Au	184	94	60	44
Be	27.5	24		33
C	9.9	11		16
Fe	64	40		35
Mo	164	86	45	39
Ni	47	32.5		20
Si	24.5	17.5		14
Ta	460	235		100
Ti	43.5			22
V	76			27
W	400	175		100
Zr				60

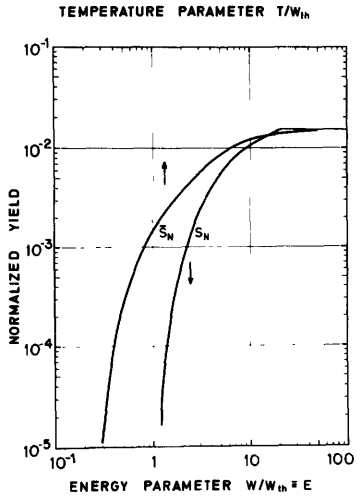

Fig. 24G3. Sputtering yields $\bar{S}_N$ from Maxwellian ions and S_N from monoenergetic ions vs. normalized temperature or energy. From J. Roth, J. Bohdansky, and W. Ottenberger, "Data on low energy light ion sputtering", Max-Planck-Institut für Plasmaphysik Report IPP 9/26 (1979), Fig. 43.

case of normal incidence described by Eq. (24G1) and Figs. 24G2 and 24G3.

The angular distribution of sputtered wall atoms has also been studied. Most of the atoms are emitted at angles between 0° and 60° on the side away from the incident ion. There is little backscattering, and few atoms are emitted at angles $> 60^\circ$.

Sputtering yields have been measured for a variety of alloys and compounds, including stainless steel, Al_2O_3, BeO, B_4C, Inconel, SAP (sintered aluminum powder), SiC, SiO_2, TaC, Ta_2O_5, TiC, WC, and ZrC. Sputtering may preferentially deplete one element of a compound or alloy.

Sputtering by heavy atoms, such as Ni^+ striking a Ni wall, produces very large yields, exceeding 1 at high energies (keV). Sputtering yields for 14 MeV neutrons are on the order of $1\text{-}4\times10^{-5}$ atoms/neutron for Nb, Au, and Cu. Neutrons can sputter atoms from both sides of a wall, in contrast to ions, which do not penetrate.

The density n_w of wall atoms may be found from Eq. (2B8). The wall surface erosion rate by sputtering from various fluxes ϕ_j (particles/m^2s) with sputtering yields S_j is given by

$$\frac{dx}{dt} = \frac{1}{n_w} \sum_j \phi_j S_j \qquad \text{(m/s)}, \qquad (24G5)$$

where the summation is over the various ion species j.

Table 24G2. Predicted sputtering yields for Maxwellian ions on various materials. S_z represents self-sputtering. Subscripts 1 and 2 represent the two elements of a compound, in order. For BeO, S_{z1} represents sputtering by Be and S_{z2}, by O. From D. L. Smith, Journal of Nuclear Materials 75, 20-31 (1978), Table 4. Research performed at ANL.

Material	T_i(eV)	S_D	S_T	S_{He}	S_{z1}	S_{z2}
Be	60	0.0187	0.0280	0.0546	0.1571	
	200	0.0224	0.0337	0.0858	0.3142	
	1000	0.0140	0.0210	0.0742	0.3899	
B	60	0.0105	0.0160	0.0297	0.1040	
	200	0.0140	0.0210	0.0508	0.2365	
	1000	0.0096	0.0145	0.0492	0.3716	
C	60	0.0081 .0101	0.0121	0.0220	0.0851	
	200	0.0115	0.0173	0.0401	0.2113	
	1000	0.0086	0.0130	0.0427	0.3999	
Al	60	0.0108 .0136	0.0164	0.0260	0.2088	
	200	0.0204	0.0307	0.0598	0.6383	
	1000	0.0227	0.0341	0.0959	2.221	
Si	60	0.0077	0.0116	0.0182	0.1518	
	200	0.0149	0.0223	0.0429	0.4685	
	1000	0.0172	0.0259	0.0715	1.695	
Ti	60	0.0046	0.0072	0.0109	0.1482	
	200	0.0107	0.0162	0.0285	0.4753	
	1000	0.0159	0.0238	0.0595	2.036	
V	60	0.0041 .0052	0.0063	0.0096	0.1372	
	200	0.0096	0.0144	0.0251	0.4409	
	1000	0.0145	0.0217	0.0536	1.910	
Fe	60	0.0047 .0060	0.0072	0.0109	0.1695	
	200	0.0114	0.0171	0.0292	0.5478	
	1000	0.0183	0.0275	0.0660	2.438	
Nb	60	0.0012 .0017	0.0022	0.0035	0.0964	
	200	0.0044	0.0068	0.0110	0.3153	
	1000	0.0093	0.0140	0.0303	1.494	
Mo	60	0.0014 .0020	0.0025	0.0038	0.1078	
	200	0.0049	0.0075	0.0120	0.3526	
	1000	0.0103	0.0155	0.0333	1.674	
W	60	0.0001	0.0004	0.0009	0.0829	
	200	0.0016	0.0030	0.0049	0.2743	
	1000	0.0060	0.0092	0.0176	1.342	
BeO	60	0.0094	0.0143	0.0257	0.0694	0.1371
	200	0.0134	0.0201	0.0467	0.1561	0.3603
	1000	0.0101	0.0151	0.0497	0.2402	0.7834
B_4C	60	0.0095	0.0145	0.0268	0.0932	0.1067
	200	0.0129	0.0194	0.0464	0.2140	0.2565
	1000	0.0091	0.0136	0.0459	0.3433	0.4518
BN	60	0.0095	0.0144	0.0259	0.0875	0.1190
	200	0.0135	0.0203	0.0470	0.2082	0.3050
	1000	0.0102	0.0152	0.0501	0.3595	0.6225
MgO	60	0.0088	0.0132	0.0219	0.1631	0.1062
	200	0.0152	0.0227	0.0469	0.4849	0.3020
	1000	0.0147	0.0220	0.0656	1.522	0.8186
Al_2O_3	60	0.0072	0.0107	0.0177	0.1500	0.0865
	200	0.0123	0.0185	0.0382	0.4492	0.2460
	1000	0.0120	0.0180	0.0534	1.447	0.6668

Material	T_i (eV)	S_D	S_T	S_{He}	S_{z1}	S_{z2}
SiC	60	0.0071	0.0106	0.0175	0.1547	0.0626
	200	0.0122	0.0183	0.0377	0.4662	0.1710
	1000	0.0118	0.0177	0.0528	1.5369	0.4112
SiO_2	60	0.0071	0.0106	0.0175	0.1547	0.0855
	200	0.0122	0.0183	0.0377	0.4662	0.2430
	1000	0.0118	0.0177	0.0528	1.5369	0.6589
TiO_2	60	0.0057	0.0087	0.0138	0.2025	0.0652
	200	0.0108	0.0163	0.0319	0.6370	0.1908
	1000	0.0119	0.0179	0.0505	2.494	0.5657
ZrO_2	60	0.0032	0.0052	0.0079	0.2130	0.0362
	200	0.0074	0.0112	0.0202	0.6897	0.1097
	1000	0.0101	0.0151	0.0391	3.099	0.3688
Nb_2O_5	60	0.0032	0.0051	0.0079	0.2132	0.0357
	200	0.0077	0.0117	0.0207	0.6920	0.1092
	1000	0.0113	0.0169	0.0426	3.150	0.3803

EXAMPLE PROBLEM 24G1

A given plasma has ion fluxes to its steel walls of 4×10^{19} $m^{-2}s^{-1}$ of D-T ions, 3×10^{19} $m^{-2}s^{-1}$ of alpha particles, and 10^{18} $m^{-2}s^{-1}$ of iron ions. If the effective temperature of the particles striking the wall is 200 eV, estimate the wall erosion rate and the wall atom flux into the plasma. Assume that the steel behaves like iron.

From Table 24G2, the Maxwellian sputtering yields for DT, alphas, and iron ions are 0.014, 0.029, and 0.548, respectively. Then the flux of wall atoms into the plasma is

$$\sum_j \phi_j S_j = 2.0\times10^{18} \text{ atoms/m}^2\text{s}.$$

The mass density and atomic weight of iron are 7870 kg/m^3 and 0.05585 kg/mole, so from Eq. (2B8) we find $n_w = 8.49\times10^{28}$ atoms/m^3. The wall erosion rate is then

$$dx/dt = 2.36\times10^{-11} \text{ m/s} = 0.74 \text{ mm/year}.$$

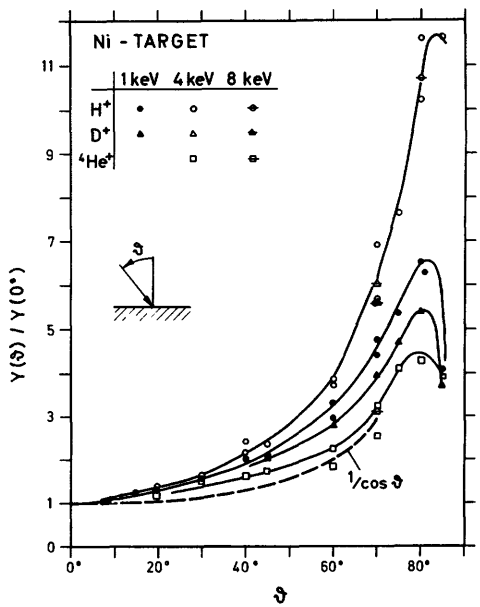

Fig. 24G4. Sputtering yield of nickel vs. angle of incidence of H^+, D^+, and $^4He^+$ ions. From H. L. Bay and J. Bohdansky, Applied Physics 19, 421-426 (1979), Fig. 3.

In most fusion reactor designs, wall erosion by sputtering can be reduced below this value, and erosion is not as serious a problem as impurity influx. However, local "hot spots" of high particle fluxes occur at limiters and divertor entrances, where sputtering damage may be severe. Sputtering damage in ICF reactors may be significant if the target pellets contain heavy elements.

physichemical sputtering

When oxygen ions strike a metal surface, chemical reactions may occur, which alter the effective sputtering yields. Similar effects may occur for impact of carbon, nitrogen, and hydrogen ions and formation of carbides, nitrides, and hydrides at the wall surface. Various chemical films may be formed, which have different sputtering rates from the original wall material. The term *physichemical sputtering* refers to sputtering where both kinetic energy and chemical binding energy affect the sputtering yield.

chemical erosion

In some cases, chemical effects alone may cause wall erosion, even at low incident kinetic energies. For example, hydrogen isotopes incident on graphite can produce hydrocarbons like methane and acetylene, and consequently erode the wall. Chemical erosion (also called chemical sputtering) of graphite reaches a maximum at $T \sim 870$ K, with a peak yield of about 0.08 C atoms lost per incident hydrogen ion, Fig. 24G5. The chemical erosion rate of graphite is typically less than its physical sputtering rate for $T \lesssim 570$ K or $T \gtrsim 1170$ K.

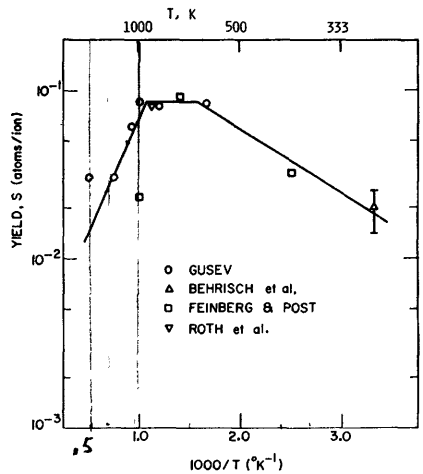

Fig. 24G5. Temperature dependence of sputter yields for 1-10 keV protons incident on carbon. Courtesy of W. M. Stacey, Jr.

desorption

Light impurities like C, N, H_2O, and O are frequently adsorbed on chamber walls. Surface impurities come from

* residual gases present in the chamber
* redeposition of sputtered atoms
* segregation to the surface of impurities present in the wall material.

Baking out the vacuum chamber helps to remove most of the adsorbed monolayers. Plasma discharges are often repeated for days on large experiments to clean the chamber walls. Plasma particles and photons striking the walls may produce stimulated desorption to remove impurities. Loosely bound molecules have the highest yield for any kind of desorption. Since loosely bound molecules are removed by bakeout, the apparent stimulated desorption yields decrease with increasing bakeout temperature.

Cross sections for stimulated desorption on the order of 10^{-19}-10^{-20} m^2 and higher have been measured for impact of H^+ and Ar^+ ions on various adsorbed residual gases. For the case of one monolayer coverage, this corresponds to gas sputtering yields around 0.5 to 10 atoms per ion.

Electron-impact desorption typically has yields on the order of 0.01 to 0.1 molecules per incident electron for electron energies of 0.1 to 5 keV. Stimulated desorption by photons typically has yields of 10^{-3} molecules per photon or less, so it is not likely to be significant in comparison with ion-impact desorption,

except at very high photon fluxes. Cooling a tokamak wall to 77 K greatly reduces the desorption and influx of oxygen (Marmar et al, 1979).

Although plasma discharges for cleaning chamber walls generally do not raise the wall temperature much, the transient wall temperature in high-density pulsed fusion reactors can become high enough that vaporization is significant.

vaporization

The energy required to remove an atom from the surface of a metal, called the heat of sublimation ΔH, is typically 5-10 eV. The equilibrium vapor pressure of a metal is given approximately by the equation

$$p = p_0 \exp(-\Delta H/T) \quad , \qquad (24G6)$$

where p_0 is a constant and T is the temperature (in energy units). This relation is shown in Fig. 24G6 for some elements.

The surface evaporation flux is given approximately by the equation

$$\phi_n = 2.6\times10^{24}\ \alpha p/(AT)^{\frac{1}{2}} \quad (\text{atoms/m}^2\text{s}), \qquad (24G7)$$

where $\alpha \simeq 1$ is the sticking coefficient, p is the vapor pressure (Pa), A is the atomic weight (g/mole), and T is the temperature (K). The wall erosion rate is

$$dx/dt = \phi_n/n_w \quad (\text{m/s}) \quad . \qquad (24G8)$$

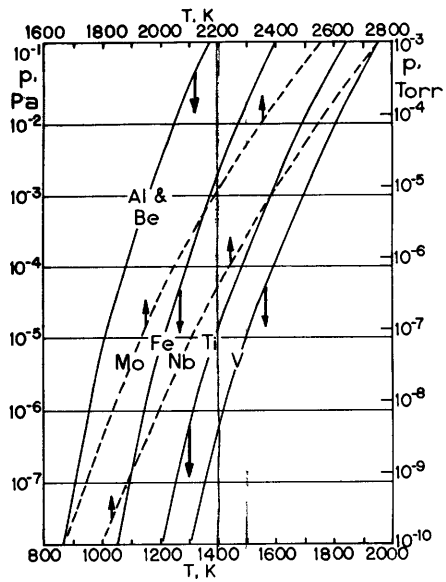

Fig. 24G6. Equilibrium vapor pressures for various wall materials. For dashed curves read top temperature scale. From R. E. Honig and D. C. Kramer, RCA Review 30, 285 (1969).

EXAMPLE PROBLEM 24G2

If one tried to operate a vanadium wall at 1600 K, what would the wall erosion rate be?

For vanadium the mass density and atomic weight are 6110 kg/m^3 and 0.05094 kg, so $n_w = 7.21\times10^{28}$ atoms/m^3. From Fig. 24G6, $p = 1.3\times10^{-4}$ Pa. From Eq. (24G7) we find $\phi_n = 1.2\times10^{18}$ atoms/m^{2}s, and from Eq. (24G8), $dx/dt = 1.7\times10^{-11}$ m/s = 0.54 mm/year. This would be unacceptably high, so lower operating temperatures would be required.

The above estimate is for a constant wall temperature. For a pulsed reactor, there will be a peak temperature at the end of each pulse when the plasma energy dumps onto the wall. If a total energy W(J) is dumped onto a surface area S(m^2) during a brief time interval τ, then the surface temperature rise is

$$\Delta T = 2W/S(\pi c_p k \rho_m \tau)^{\frac{1}{2}} \quad (K), \tag{24G9}$$

where ρ_m is the density (kg/m^3), c_p is the specific heat (J/kg-K) and k is the thermal conductivity (W/m-K). The consequent number of wall atoms evaporated by the pulse is approximately

$$\Delta n/S \simeq 0.1\ \tau \phi_n\ (T_{max}) \qquad (atoms/m^2), \tag{24G10}$$

where $\phi_n(T_{max})$ is the evaporation rate at the peak temperature. Some pertinent thermal properties of various materials are listed in Table 24G3. For plasma energy dumps with $\tau > 0.1$ s in tokamak reactors, evaporation will not be a serious problem, unless the energy is concentrated on a small area. The above equations may underestimate the evaporation, however, if the thermal conductivity is reduced by oxide films, cracks, etc.

blistering and flaking

When energetic helium ions strike the first wall, they penetrate to a given depth and come to rest. Irradiation by monoenergetic ions thus produces a build-up of helium atoms at a depth corresponding to the range of the incident particles.

Table 24G3. Thermal properties of various materials. From R. Behrisch, "First-wall erosion in fusion reactors", Nuclear Fusion 12, 695 (1972).

		V	Nb	Mo	C	SS 304
Z, atomic number		23	41	42	6	(18% Cr, 8% Ni)
A, atomic mass (gm/mole)		50.94	92.9	95.94	12	
ρ_m, mass density (kg/m^3)		5870	8570	9010	2250	7900
n_w, atomic density (10^{28} atoms/m^3)		6.93	5.56	5.65	11.3	8.6
T_m, melting temperature (K)		2192	2688	2883	3925 (vap.)	1400
ΔH, heat of sublimation (eV/atom)	300 K	5.33	7.5	6.83	8.2-10.4	
	500 K	5.27	7.43	6.78		
	1000 K	5.16	7.28	6.63		
	1500 K	4.96	7.14	6.48		
	2000 K	4.75	6.97	6.3		
k, thermal conductivity (W/meter-K)	500 K	33.1	56.7	130	80-100	19
	1000 K	38.6	64.4	112	49-64	
	1500 K	44.7	72.1	97	40-50	
	2000 K	50.9	79.1	88	30-40	
c_p, specific heat (J/kg-K)	500 K	500	280	254	1200	500
	1000 K	640	300	290	1670	
	1500 K	700	330	330	1800	
	2000 K	850	370	380	2000	

If the irradiation dose is high enough, these atoms coalesce to form bubbles. The gas pressure in the bubbles and shear stresses in the metal may cause plastic deformation of the surface skin to form visible blisters. Once the blister is formed, the skin tends to overheat, and increased gas pressure from additional helium bombardment may cause the blister to rupture. The ruptured blisters cause wall erosion and plasma contamination.

Blistering can also be caused by hydrogen ion bombardment (including deuterons and tritons), but hydrogen ions have much higher solubilities and diffusivities in metals, so they can usually diffuse back out of the metal before the pressure builds up in the blisters. On active metals like Ti and Zr, hydrogen can form hydride layers which may flake off.

The effect of wall temperature on blister formation is illustrated in Fig. 24G7. Exfoliation of blisters and wall erosion are most severe in the temperature range $0.3 < T/T_m < 0.5$. Above 0.5 the increased diffusivity of helium allows the gas to escape, forming a porous surface structure in the metal (Fig. 24G7d).

The blister skin thickness t is roughly equal to the theoretical ranges of the helium ions. The bubble height h and radius r are related to the gas pressure p and metal yield strength σ_y approximately by the equation

$$\frac{(r^2+h^2)}{h} = \frac{4\sigma_y t}{p} \qquad (24G11)$$

The yield strength and gas pressure are practically independent of bombardment energy. As the energy is increased, the skin thickness t increases and the bubble size (r and h) also increase.

The critical pressure for blister formation is given by

$$p_{cr} = \frac{4\sigma_y t^2}{3r^2} \quad . \qquad (24G12)$$

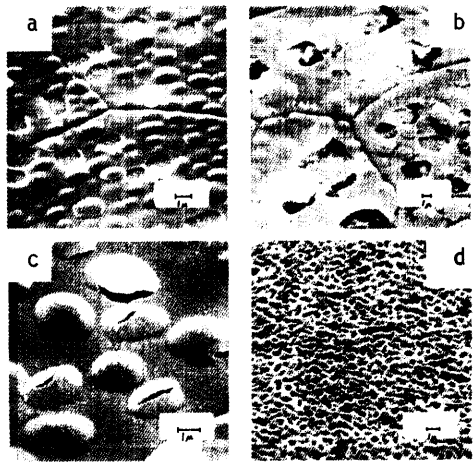

Fig. 24G7. Blistering of molybdenum surfaces after bombardment with 36 keV He^+ ions. (a) $T/T_m = 0.1$, (b) $T/T_m = 0.3$, (c) $T/T_m = 0.4$, (d) $T/T_m = 0.6$, where T is the wall temperature and T_m is the wall melting temperature. From S. K. Erents and G. M. McCracken, Radiation Effects 18, 191 (1973).

For a given incident ion energy, t and r vary little with wall temperature, but σ_y decreases with increasing temperature. Therefore, less pressure is required for blister formation at high temperatures. The critical gas concentration (He atoms/wall atom) for blistering decreases almost linearly from about 0.5 at $T/T_m = 0.1$ to 0.1 at $T/T_m = 0.6$, where T is the wall temperature and T_m is the wall melting temperature.

As the total dose is increased at constant energy, the blister density (number of blisters per m^2) increases, but the average blister size changes little. When

the blisters are fully grown, or when they overlap, then exfoliation begins. In some cases several layers of blisters may be eroded away.

The data of Fig. 24G7 are for monoenergetic ion bombardment at normal incidence, where the helium gas tends to accumulate at a depth equal to the ion range. In a fusion reactor, three factors tend to broaden the helium distribution:

* The angular distribution of the incident alphas tends to produce varied ranges.
* Not all alphas will hit the wall with 3.5 MeV energy. Some will slow down to lower energies first.
* The surface will also be eroded away by sputtering, so that the old helium will become closer to the receding surface, and the new helium will be implanted further into the wall.

The angular distribution of 3.5 MeV alpha particles striking a typical tokamak wall has been calculated. The implantation profiles corresponding to that angular distribution are shown in Fig. 24G8 for various wall materials. Blistering can occur when the critical helium concentration occurs inside the metal before it occurs at the surface. Blistering and flaking may be a problem in cases where sputtering rates are low, most of the alphas are at 3.5 MeV, and the alpha flux is high. If the alpha flux is low, if the alphas are more uniformly distributed in energy, or if sputtering rates are high, then blistering is not likely to be a serious problem.

unipolar arcs

Arcs were discussed briefly in Chapter 6. Small arcs between the plasma and walls or limiter can constitute a significant source of impurities. The arcs can occur when the plasma potential near the wall $\phi \gtrsim 15$ V positive with respect to the wall. Such a positive potential could arise as a sheath potential (Fig. 5F2) resulting from rapid electron flow

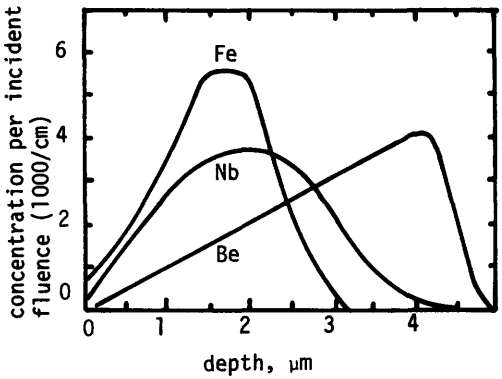

Fig. 24G8. Helium implantation vs. depth for 3.5 MeV alphas in Fe, Nb, and Be, using an angular impact distribution calculated for a given tokamak geometry. From W. Bauer et al, Nuclear Fusion 19, 93-103 (1979), Figs. 5, 6, 7.

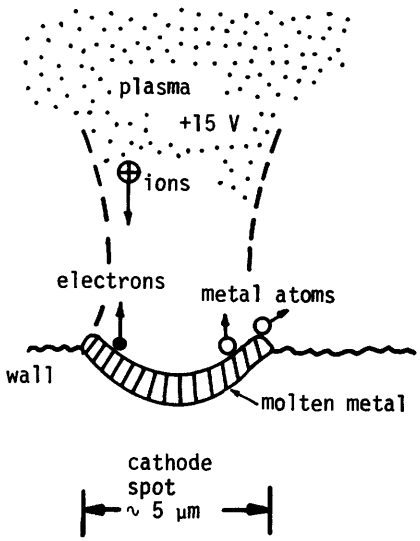

Fig. 24G9. A unipolar arc. Plasma ions hitting the wall heat up the cathode spot and cause thermionic and secondary electron emission. Most of the current is carried by the electrons. The surface of the cathode spot melts, and metal atoms are ejected by vaporization and sputtering.

along magnetic field lines to the walls in an adjacent region, or as the result of electric fields parallel to the walls generated within the plasma. In a *unipolar arc* the plasma is the anode. A cathode spot with a diameter of a few μm forms on the chamber wall or limiter, as illustrated in Fig. 24G9.

A current flow I > 10 A is required to maintain the arc, and the current density $J \sim 10^9 - 10^{12}$ A/m^2. In vacuum arcs about 8% of the current is carried by the ions, but such measurements have not been made in unipolar arcs in strong magnetic fields. An electron return current flows to the walls in an adjacent region over an area on the order of 1 cm^2. The cathode spot moves along the wall in a direction opposite to the $\vec{J}x\vec{B}$ force (*retrograde* motion) with a velocity on the order of 100 m/s.

The cathode spot temperature may exceed 3000 K, and metal atoms are rapidly lost by vaporization and sputtering, forming a crater in the wall surface. In metals with low melting points, droplets of metal may be sprayed out the sides of the crater by the arc plasma pressure. On the order of 0.02 - 0.1 wall atoms are lost per unit charge flowing in the arc. If this value were 0.05 and the arc current were 30 A, then about 10^{19} atoms/s would be lost from the wall. If a plasma with $n = 3\times10^{19}m^{-3}$ and volume V = 1 m^3, a single arc of this size could produce an impurity fraction of 1% in 30 ms. Some of the metal ions acquire kinetic energies of tens of eV.

The small scratches and fern-like projections attributed to arcing have been observed in many tokamaks and other plasma experiments. It appears that arcing in tokamaks occurs mainly during the buildup of plasma current and during plasma disruptions.

Arcing could be combatted by segregating the wall into insulated cells, with areas too small for collection of the return current, but this appears to be impractical. Materials selection involves determining which materials are resistant to arcing and have low atom loss rates per unit of charge flow, with strong preference to low-Z elements, since larger impurity fractions of low-Z elements are tolerable in the plasma. Arcing may also be inhibited by use of gas blankets or divertors (Chapter 25) to reduce the plasma density and temperature near the wall, thus reducing the potential for arcing. [The electric field at the wall is proportional to $(n_e T_e)^{\frac{1}{2}}$.]

synergistic effects

When two or more phenomena act simultaneously on the wall surface, interactions between the phenomena may produce *synergistic effects*, meaning that the net impurity release rate is not simply a linear sum of the individual process rates. For example:

* The physichemical sputtering process is a combination of both physical and chemical effects.
* Gas desorption rates are influenced by diffusion rates (affected by radiation damage) and by surface conditions (affected by sputtering, etc.)
* Photon and ion irradiation may cause the skin of blisters to overheat and rupture.
* Impurity release from blistering may be reduced if the sputtering rate is high.

In fact, almost all the phenomena occurring at the wall are influenced in some way by other phenomena. Experimental measurements usually concentrate on one bombarding species at one energy and angle. The combined effects of many species, energies, and angles may be significantly different.

24H. Near-Surface Wall Modifications

The wall is modified by exposure to the plasma (sputtering, etc.). It may also be deliberately modified by controlled processes to minimize damage during plasma bombardment. In addition to impurity introduction and wall surface erosion, bombardment may also weaken the wall's structural integrity by processes like erosion of grain boundaries and crack growth. The near-surface wall modifications may be grouped into five main categories:

phase changes

Phase changes may result in surface films, such as oxides, carbides, and hydrides. The changes of thermal conductivity can result in flaking. A phase change can also occur internally, such as a strain-induced austenitic-martensitic transformation in stainless steels. This transition changes the steel's mechanical properties and makes it vulnerable to hydrogen cracking.

alloy composition changes

The composition of an alloy may be modified near the surface by three processes:

* *nuclear transmutations*. Both gaseous and solid transmutants are produced, as discussed previously.
* *preferential sputtering*. Elements with high sputtering yields will be preferentially removed from the surface of an alloy. This also depends upon relative diffusion rates of the alloy constituents towards the surface.

* *diffusion and surface segregation*. Various impurities, like carbon, gradually diffuse to the surface, where they are desorbed or sputtered away. In stainless steel, the chromium normally segregates to the surface as an oxide. In a reducing environment (hydrogen) the chromium may be depleted by reduction and solution. The resulting loss of chromium could make the near-surface properties of the wall more like those of an iron-nickel alloy.

microstructural changes

Ion bombardment produces many vacancies, interstitials, and dislocation loops in the first 10 nm of the surface, in addition to the neutron-induced radiation damage. These defects can lead to internal stresses, swelling, creep, recrystallization and grain growth, and tritium trapping in the near-surface region.

macrostructural changes

Macrostructural changes include nonuniform erosion, cracking, and changes in surface shape.

* *nonuniform erosion and redeposition*. The particle fluxes in toroidal devices vary with poloidal angle, and so does the wall erosion rate. The metallic impurities may be redeposited at other locations on the walls, building up flakes.
* *cracking*. Cracks may be initiated by phase changes, hydrogen implantation, helium production, and neutron damage. Cracks grow under cyclic stresses (fatigue), especially in the presence of chemically active elements. Crack growth may lead to leaks and to reduced heat transfer, which increases the surface temperature.
**topological changes*. Blistering and exfoliation leave the surface scarred as in Fig. 24G7. Sputtering can leave the surface pitted like a honeycomb. These changes in the surface and near-surface regions reduce sputtering reflux and heat transfer.

property changes

Many properties near the surface will be affected by the wall modifications, including:

* *physical properties:* electrical and thermal conductivity, emissivity, density, optical reflectivity, radioactivity, work function, and magnetic permeability.
* *mechanical properties:* ductility, creep rate, crack growth rates.

materials development

Various materials, surface treatments, and special coatings are being considered to provide low surface erosion rates, low average Z, long wall life, and low tritium inventory. Ideas under consideration include:

* *armor.* Expendable tiles or curtains of graphite or similar materials may be placed between the wall and the plasma.
* *sputtering.* The ratio of critical impurity concentration for ignition to sputtering yield is one figure of merit for wall surface materials (Fig. 24H1). Usually low-Z materials are superior, in spite of their high sputtering yields, because of their much higher allowable concentrations in the plasma. Thus, Be, BeO, C, B_4C, and similar coatings are of interest. If the plasma edge temperature is low, however, the sputtering rates for high-Z materials may be so low that they are satisfactory.
* *blistering.* Highly porous surfaces are resistant to blistering. High porosity may be produced initially by various metallurgical processes, including coating techniques, powder metallurgy, and irradiation. However, the durability of the porosity is uncertain.
* *arcing.* We can use the ratio of the critical impurity concentration to the erosion yield due to arcing as a figure of merit for materials. As for sputtering, low-Z materials have better values, by about a factor two orders of magnitude, than high-Z materials.

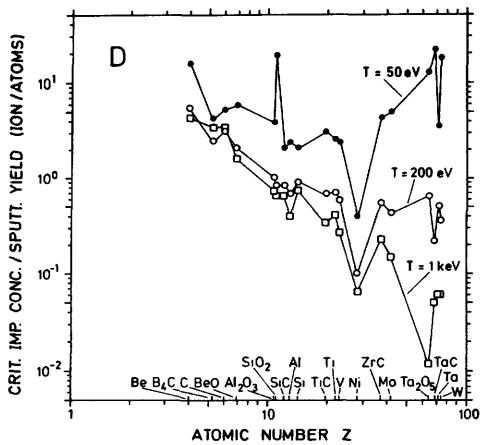

Fig. 24H1. Sputtering figure of merit (critical impurity concentration divided by sputtering yield) vs. atomic number, for deuterons at various temperatures. From R. Behrisch, "Surface erosion from plasma materials interaction", Journal of Nuclear Materials 85 & 86 1047-1061 (1979), Fig. 8a.

Plasma-surface interactions and experimental methods for surface studies are reviewed by McCracken and Stott (1979).

24J. Special Purpose Materials

Selection of breeding materials and coolants will be discussed in Chapter 26, and tritium problems will be discussed in Chapter 28.

graphite and silicon carbide

One potential application of graphite and silicon carbide is a radiatively cooled first wall liner, as illustrated in Fig. 24J1. Other applications are

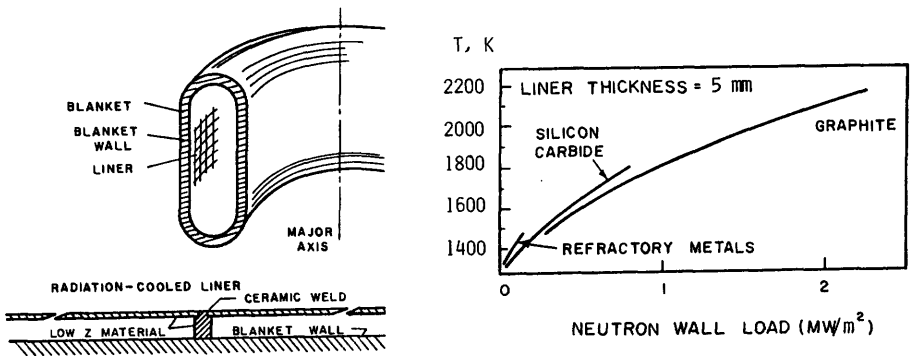

Fig. 24J1. Sketch of a fusion reactor first wall with radiation-cooled liner (left) and the probable surface temperature of the liner as a function of neutron wall load (right). From G. H. Miley, "Overview of fusion research and development", Proceedings of the First IEEE Minicourse on Fusion, Edited by G. H. Miley, U. of Illinois Fusion Studies Laboratory, 1976, p. 1-51.

listed in Table 24J1. Graphite has good thermal shock resistance, neutron reflection and moderation capability, high-temperature stability, and low atomic number. Silicon carbide is not quite as good, but has better stability under neutron irradiation up to its maximum use temperature (about 1700 K).

During neutron irradiation graphite first shrinks, then swells, as shown in Fig. 24J2. Thus, the useful life of graphite at 1270-1670 K (1000-1400 C) is limited to an irradiation fluence producing about 10-20 dpa. A fission neutron fluence of 1.4×10^{25} neutrons/m^2 corresponds to 1 dpa. For 14 MeV neutrons, the fluence required to produce 1 dpa is probably lower. Graphite cloths and fibers have withstood fast fission neutron fluences of 10^{26} neutrons/m^2 and remained intact.

The various forms of graphite may have markedly different properties. For example, the stress limit of bulk graphite is about 15-25 MPa, while that of pyrolitic graphite is about 250 MPa. It may be possible to make high quality graphite from coal in the future, instead of from petroleum coke, as it is now.

heat-sink materials

Heat-sink materials are needed for limiters, wall armor, beam dumps, calorimeters, divertor targets, and direct convertors. Heat-sinks may be water-cooled copper or radiatively-cooled refractory materials. Desirable properties are high melting temperature, high thermal conductivity, good radiation resistance, and (for pulsed devices) high heat capacity.

The maximum heat fluxes which various materials can tolerate for a 0.5 s pulse are shown in Table 24J2. Thermal fatigue limits for multiple pulses are somewhat lower. Other materials under consideration include Ta-10% W, TiC, TiB_2. Ta-10% W was chosen for the limiter of the Doublet III tokamak because of its good thermal shock resistance. Although Ta reacts with hydrogen, it was estimated that these reactions would not be a serious problem for the anticipated cyclic temperature and alternate vacuum-hydrogen atmospheres.

Table 24J1. Applications and potential problem areas for graphite and SiC. From "Special purpose materials", The Fusion Reactor Materials Program Plan, DOE/ET-0032/4 (1978), Table 3.D.1.

	Application	Material	Critical properties: Degassing	Sputtering	Thermal shock	Radiation stress	Compatability	Swelling	Thermal conductivity	He generation
1.	First-wall liner	G, SiC, C/C, F	A	A	B	B	B	A	A	
2.	First-wall coating	SiC, PyC	A	A	B	B	A	A		B
3.	Limiter	G, SiC, C/C	B	A	A	B	B	A	B	
4.	Beam stop	G, SiC, C/C	B	A	A	B	B	A	B	
5.	Moderator/reflector	G				B	B	B	B	
6.	Shielding	B_4C in G				B		B		A
7.	Thermal insulation	F					B	B		

G = Bulk graphite.
SiC = Silicon carbide.
C/C = Carbon/carbon composite.
F = Fibrous graphite (cloth).
PyC = Pyrolytic carbon

A Very important.
B Moderately Important

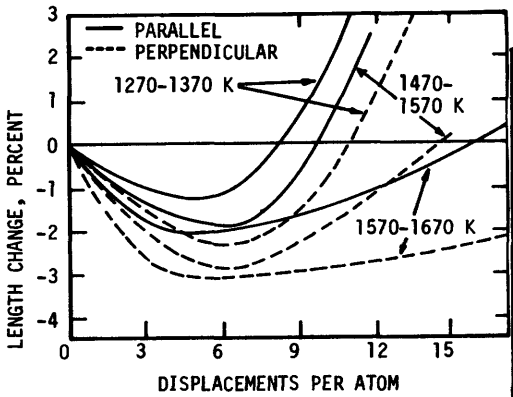

Fig. 24J2. Length changes of type 9640 graphite parallel and perpendicular to the direction of molding as functions of the number of dpa. From G. L. Kulcinski, "Radiation damage: the second most serious obstacle to commercialization of fusion power", CONF-750989 (1976) Fig. 11, p. I-48.

Table 24J2. Thermal shock limits (MW/m^2) of some materials for a 0.5 s pulse, assuming one-dimensional heat flow. From DOE/ET-0032/4 (1978), Table 3.F.2. Based on work by G. Lewin, J. Schivell, and M. Ulrickson, PPPL.

material	surface melting	surface cracking
OFHC copper	52	31
Tungsten	94	69
Molybdenum	70	48
Pyrolytic graphite	130	197
ATJ graphite	53	68
Boron carbide	19	3
Silicon carbide	28	3
Aluminum	22	9

Table 24J3. Applications of ceramics and plastics in fusion reactors, typical operating environments, and candidate materials. Temperatures are during full power operation, and fluences are estimated for 100% duty factor. From CONF-760558 (1976), p. 5 and DOE/ET-0032/4 (1978), p. 3-60.

	typical peak annual fluences, neutrons/m^2	typical peak temperatures, K	typical candidate materials
1. insulators for rf heating systems	3×10^{23}	500	Al_2O_3, $MgAl_2O_4$, $Y_3Al_5O_{12}$
2. implosion-heating first wall	3×10^{26}	1200	$MgAl_2O_4$, $Y_3Al_5O_{12}$, Si_3N_4
3. low-Z first walls or liners	3×10^{26}	1000	SiC, Al_2O_3, B_4C, $MgAlO_4$, Si_3N_4
4. neutral beam injector insulators	3×10^{23}	500	glass, Al_2O_3, BeO, SiO_2
5. direct convertor insulators	3×10^{22}	400	Al_2O_3, Si_3N_4, AlN
6. toroidal current breakers	3×10^{26}	1100	Al_2O_3 powder in metal tube, enamel, anodization plus pressurized O-ring
7. magnet coil insulators			
7.1 severe environment			Si_3N_4, Y_2O_3, $MgAl_2O_4$, $Y_3Al_5O_{12}$, castable aluminum silicates, glass
7.2 mild environment			any of the above, plus MgO, mica, epoxy/fiberglass, Mylar, Vespel, and Kapton.

ceramics

Ceramics and plastics are highly susceptible to radiation damage, yet they are essential to fusion reactor operations. Some applications and typical operating environments are listed in Table 24J3, along with candidate materials.

The problems associated with these applications are listed in Table 24J4, with an indication of their degree of severity.

Under EBR-II fission neutron irradiation to about 3 dpa (3×10^{25} neutrons/m^2), Al_2O_3 and Beo swell about 2% (volume), but $Y_3Al_5O_{12}$, $MgAl_2O_4$, Y_2O_3, Si_3N_4, Si_2ON_2, and SiAlON swell less than 0.5%. Irradiation to about 3 dpa in EBR-II at 1000 K produced little degradation of dielectric breakdown strength in Al_2O_3 and $Y_3Al_5O_{12}$. However, these irradiations are only about two months' exposure in a first wall environment with a 1 MW/m^2 neutron wall loading. Sputtering and ionizing radiation could also cause breakdown along the surface of insulators.

Table 24J4. Problem areas for the various applications of ceramics. The numbers 1-7 refer to the previous table. From "Special Purpose Materials", DOE/ET-0032/4 (1978), Table 3.E.1.

Problem	Severe	Moderate	Slight	None
Swelling	2,3,1	7.1	6,7.2	4,5
Bulk dielectric strength	2,4,5,7.1	1	6,7.2	3
Surface dielectric strength	4,5,1,7.1	2,7.2	6	3
Bond integrity	2,6a,3,1,7.1	4,5	7.2	
Mechanical properties	2,7.1	4,5,3,1,7.2	6	
Gas/solid reactions	2,4b,3,1		6,5	7.0
Degradation in thermal conductivity	2,3,1			7.0,6,4,5
DC polarization (electrolysis)	4,5	6	2	7.0,3,1
Thermal stresses	2,4,5,3,1		6,7.0	
Ion sputtering	3,1	6,4,2	5	7.0
Blistering	1,3	2,4,6	5	7.0
Bulk resistivity	4,1	2,5,7.1	6,7.2	3
Thermal stability	2,5,3,1	6		4,7.0
Loss tangent	1			2,3,4,5,6,7.0
Radiation damage	2,4c,3,1	6,5,7.1	7.2	
Fabrication	1,2,6,4,3d,7.1	5	7.2	

[a] If vacuum wall.

[b] Cs vapor.

[c] Irradiation-induced surface flashover.

[d] Strongly design-dependent.

Ceramics are subject to thermal stress, creep, and fatigue problems, compounded by the fact that most of them are brittle even before irradiation. Irradiation degrades thermal conductivity of Al_2O_3 by about a factor of two after irradiation in EBR-II to about 8 dpa at 1000 K. Sustained dc electric fields can cause polarization, resulting in a drop in resistivity of ceramics by several orders of magnitude. Neutron irradiation can cause a significant degradation of the "loss tangent", which relates to power loss in rf windows by radio waves.

Most of the ceramics applications have fabrication difficulties related to their large size, unusual configuration or materials, or need for very high quality. Ceramics problems are reviewed by Clinard (1979).

superconducting magnet materials

Materials problems for advanced superconducting magnets include development of superconductors, structures, and insulation.

* *high-field superconducting composites.* Multifilamentary, high-current composite conductors of Nb_3Sn, V_3Ga, or newer superconductors are under development for production of fields with $B \gtrsim 12$ T.

For radiation damage levels of 10^{-5} to 0.01 dpa, resistivities of Cu and Al increase to unacceptably high values, as shown in Fig. 24J3. Most of the resistivity increase accumulated at 4 K may be annealed out by warming the coils to room temperature, however.

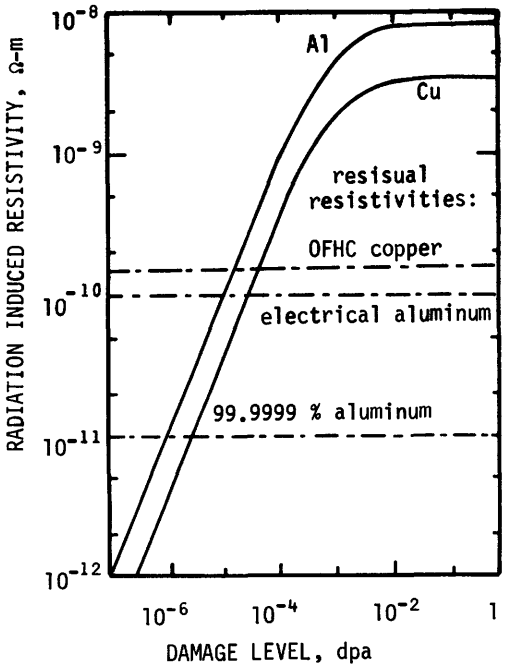

Fig. 24J3. Radiation-induced resistivities of aluminum and copper. From G. L. Kulcinski, CONF-750989, Volume I, p. I-61, Fig. 15.

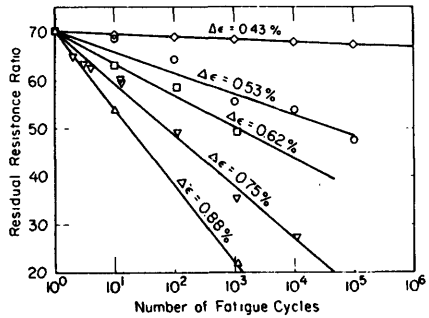

Fig. 24J4. Degradation of residual resistivity ratio, R(295 K)/R(9 K), of the copper stabilizer in a commercial NbTi conductor with number of cycles of cyclic strain, for various values of strain range. From F. R. Fickett, R. P. Reed, and E. N. C. Dalder, Journal of Nuclear Materials 85 & 86, 353-360 (1979), Fig. 7.

Radiation damage effects on NbTi are slight, but the critical current and critical temperature of Nb_3Sn and similar compounds drop off at fluences around 10^{-3} dpa ($3x10^{22}$ neutrons/m^2). Adequate shielding can avoid this problem.

In pulsed coils, the cyclic strain increases the resistivity of the stabilizer, as shown in Fig. 24J4. This problem can be avoided by keeping the strain low, which requires stiff structural materials.

* *structural materials and welds.* Many structural materials are brittle at 4 K, including carbon steels, alloy steels, titanium alloys, ferritic and martensitic stainless steels, and magnesium alloys. Nickel alloys and superalloys are ferromagnetic at 4 K and expensive. Austenitic stainless steels have been used for most cryogenic structural applications, but weld strength and ductility are major problems. Because the neutron fluence through superconducting coils is very low, radiation damage is not a problem. Copper alloys are acceptable, but not as good as austenitic stainless steels.

* *nonconducting composite structures.* Pulsed magnetic fields induce eddy current dissipation in metallic structures, adding to the heat load on the refrigeration system (ac losses in Table 23E1). A nonconducting composite structure, such as epoxy-fiberglass, would eliminate this problem. However, the low modulus of elasticity of the epoxy-fiberglass composite would permit high conductor strains, causing degradation of the stabilizer conductivity (Fig. 24J4). Use of strong, stiff fibers such as graphite, boron, and Kevlar-49 (Du Pont Co.) is under study.

* *magnet insulation.* Aluminized Kapton and Mylar, used as superinsulation in dewars, may be seriously degraded by neutron and gamma irradiation. Their properties during low temperature irradiation are not well known. Eddy-current heating in aluminized plastic superinsulation may produce unacceptable heat loads

for pulsed coils. Inorganic insulators are being considered, but they are brittle and may not be durable under stress.

Problems

1. Assume that a stainless steel wall may be represented as iron for a sputtering estimate, and that the plasma edge temperature is 1000 eV. Calculate the wall erosion rate (mm/year) due to a total ion flux of 10^{20} ions/m^2s, of which 95% are D-T ions, 5% are alpha particles, and .07% are wall atoms.

2. If the reactor of problem 1 is a torus with R = 10 m, a = 3 m, and the plasma density is 2×10^{20} fuel ions/m^3 (constant), estimate the rate at which Fe impurities build up as a result of sputtering, assuming that the impurities are perfectly confined. How long does it take to build up an impurity fraction of 10^{-3}?

3. Estimate the evaporation rate (mm/year) for a Ti wall at 1400 K. $\rho_m = 4540$ kg/m^3

4. If 0.1 MJ of plasma energy is dumped on 1 m^2 of a 1000 K vanadium reactor wall in 0.1 ms, estimate the peak temperature, number of atoms evaporated by the thermal spike per m^2, and the wall thickness loss.

5. Vanadium has a linear expansion coefficient of 7.9×10^{-6}/K, a modulus of elasticity of 1.3×10^{11} Pa. Assume Poisson's ratio is 0.3. If the reactor has Q = 12, P_n = 2.2 MW/m^2 (maximum), and the wall temperature is approximately 1000 K, estimate the peak thermal stress in a 5 mm wall.

6. A SS 316 wall (annealed) undergoes a wall loading P_n = 1.9 MW/m^2 (total flux = 6.9×10^{18} neutrons/m^2s) for 2 years. Estimate the displacement damage (dpa), total helium production (appm) and total Mn production (appm). Estimate the volumetric swelling, assuming swelling is linearly proportional to appm (He). What would the corresponding linear expansion be? Assume wall temperature = 773 K.

7. A wall with P_n = 1.9 MW/m^2 has a graphite armor plate in front of it. What would be the dimensional change of the graphite at 1700 K parallel and perpendicular to the molding direction after 1 year?

8. If the first wall neutron flux is 7×10^{18} neutrons/m^2s, what attenuation factor must the blanket and shield provide to avoid significant damage to Nb_3Sn coils over a 20 year lifetime?

Bibliography

general

R. E. Gold, E. E. Bloom, F. W. Clinard, Jr., D. L. Smith, R. D. Stevenson and W. G. Wolfer, "Materials technology for fusion: current status and future requirements", *Nuclear Technology/Fusion 1*, 169-239 (1981). Review Paper.

damage analysis and fundamental studies

J. W. Corbett and L. C. Ianniello, Editors, *Radiation-Induced Voids in Metals*, US Atomic Energy Commission Office of Information Services, CONF-710601 (1972).

"Damage Analysis and Fundamental Studies", The Fusion Reactor Materials Program Plan, DOE/ET-0032/2 (1978).

T. A. Gabriel, B. L. Bishop, and F. W. Wiffen, "Calculated atom displacement and gas production rates of materials using a fusion reactor first wall neutron spectrum", *Nuclear Technology 38*, 427-433 (1978).

G. L. Kulcinski, "The newest frontier in radiation damage research -- laser fusion reactors", Proceedings of the Third Topical Meeting on the Technology of Controlled Nuclear Fusion, CONF-780508 (1978), Volume 1, p. 598-610.

G. L. Kulcinski, "Radiation damage: the second most serious obstacle to commercialization of fusion power", Volume 1, *Radiation Effects and Tritium Technology for Fusion Reactors*, CONF-750989 (1976), pp. 17-43.

L. K. Mansur and M. H. Yoo, "Advances in the theory of swelling in irradiated metals and alloys", *Journal of Nuclear Materials 85 & 86*, 523-532 (1979).

G. R. Odette, "Modeling of microstructural evolution under irradiation", *Journal of Nuclear Materials 85 & 86*, 533-545 (1979).

D. R. Olander, *Fundamental Aspects of Nuclear Reactor Fuel Elements*, Technical Information Center, Energy Research and Development Administration TIE-26711-P1 (1976), Chapters 6, 7, 8, 17, 18, 19.

"RTNS-II Utilization Plan", DOE/ET-0066 (1978).

J. A. Spitznagel, F. W. Wiffen, and F. V. Nolfi, "Microstructures developed in 'simulated' fusion irradiations", *Journal of Nuclear Materials 85 & 86*, 629-646 (1979).

J. A. Sprague and D. Kramer, Editors, *Effects of Radiation on Structural Materials*, Special Technical Publication 683, American Society for Testing and Materials, Philadelphia, 1979, pp. 5-232.

D. Steiner, "The technological requirements for power by fusion", *Nuclear Science and Engineering 58*, 107-165 (1975).

J. S. Watson and F. W. Wiffen, Editors, *Radiation Effects and Tritium Technology for Fusion Reactors*, CONF-750989 (1976), Volumes 1 and 2.

F. W. Wiffen, "Radiation effects in structural materials for fusion reactors", Chapter 5, *Critical Materials Problems in Energy Production*, Academic Press, New York, 1976.

F. W. Wiffen, J. H. DeVan, and J. O. Stiegler, Editors, Proceedings of the First Topical Meeting on Fusion Reactor Materials, *(Journal of Nuclear Materials 85 & 86)*, North Holland, Amsterdam, 1979, Chapters 9, 10, 11.

alloy development for irradiation performance

"Alloy Development for Irradiation Performance", The Fusion Reactor Materials Program Plan, DOE/ET-0032/1 (1978).

"Assessment of titanium for use in the 1st wall/blanket structure of fusion reactors", Electric Power Research Institute EPRI ER-386 (1977).

B. Badger et al, "NUWMAK, a tokamak reactor design study", University of Wisconsin Report UWFDM-330 (1979), Chapter IX (discussion of Ti alloy properties).

B. Badger et al, "UWMAK-III, a noncircular tokamak power reactor design", EPRI ER-368 (1976), Chapter IX (discussion of Mo alloy properties).

E. E. Bloom, "Mechanical properties of materials in fusion reactor first-wall and blanket systems", *Journal of Nuclear Materials 85 & 86*, 795-804 (1979).

R. W. Conn, "Tokamak reactors and structural materials", *Journal of Nuclear Materials 85 & 86*, 9-16 (1979).

J. H. DeVan, "Compatability of structural materials with fusion reactor coolant and breeder fluids", *Journal of Nuclear Materials 85 & 86*, 249-256 (1979).

A. P. Fraas and A. S. Thompson, "ORNL fusion power demonstration study: fluid flow, heat transfer, and stress analysis considerations in the design of blankets for full-scale fusion reactors", ORNL/TM-5960 (1978).

J. T. Fong, Editor, *Fatigue Mechanisms*, Special Technical Publication 675, American Society for Testing and Materials, Philadelphia, 1979.

R. E. Gold and D. L. Harrod, "Refractory metal alloys for fusion reactor applications", *Journal of Nuclear Materials 85 & 86*, 805-815 (1979).

S. D. Harkness and B. Cramer, "A review of lifetime analyses for tokamaks", *Journal of Nuclear Materials 85 & 86*, 135-145 (1979).

J. J. Holmes and J. L. Straalsund, "Irradiation sources for fusion materials development", *Journal of Nuclear Materials 85 & 86*, 447-451 (1979).

R. H. Jones, B. R. Leonard, Jr., A. B. Johnson, Jr., "Assessment of titanium alloys for fusion reactor first-wall and blanket applications", EPRI AP-1433 (1980).

T. Lyman, Editor, *Metals Handbook*. 8th Edition, American Society for Metals, Metals Park, Ohio, 1975.

F. V. Nolfi, Jr., and C. Y. Li, "The application of simulation experiments to fusion materials development", *Nuclear Technology 38*, 405-414 (1978).

J. A. Sprague and D. Kramer, Editors, *Effects of Radiation on Structural Materials*, Special Technical Publication 683, American Society for Testing and Materials, Philadelphia, 1979, pp. 235-679.

J. S. Watson and F. W. Wiffen, Editors, *Radiation Effects and Tritium Technology for Fusion Reactors*, CONF-750989 (1976), Volumes 1 and 2.

F. W. Wiffen, J. H. DeVan, and J. O. Stiegler, Editors, Proceedings of the First Topical Meeting on Fusion Reactor Materials, *(Journal of Nuclear Materials 85 & 86)*, North Holland, Amsterdam, 1979, Chapters 4, 6, 9, 11, 12.

F. W. Wiffen, "The effects of CTR irradiation on the mechanical properties of structural materials", ORNL/TM-5624 (1976).

F. W. Wiffen, P. J. Maziasz, E. E. Bloom, J. O. Stiegler, and M. L. Grossbeck, "The behavior of type 316 stainless steel under simulated fusion reactor irradiation", *The Metal Science of Stainless Steels*, Proceedings of a Symposium (Denver, 1978), The Metallurgical Society of AIME.

plasma materials interaction

W. Bauer, K. L. Wilson, C. L. Bisson, L. G. Haggmark, and R. J. Goldston, "Alpha transport and blistering in tokamaks", *Nuclear Fusion 19*, 93-103 (1979).

R. Behrisch, "Evaporation for heat pulses on Ni, Mo, W, and ATJ graphite as first wall materials", *Journal of Nuclear Materials 93 & 94*, 498-504 (1980).

R. Behrisch, "Fusion -- first wall problems", Chapter 3, *Critical Materials Problems in Energy Production*, Academic Press, New York, 1976.

R. Behrisch, "Surface erosion from plasma materials interaction", *Journal of Nuclear Materials 85 & 86*, 1047-1061 (1979).

M. J. Davis, "Material surface modification for first wall protection", *Journal of Nuclear Materials 85 & 86*, 1063-1072 (1979).

L. G. Haggmark and J. P. Biersack, "Monte Carlo Studies of light ion reflection from metal surfaces", *Journal of Nuclear Materials 85 & 86*, 1031-1036 (1979).

E. S. Hotston, "A current induced diffusion model of gas sputtering", *Journal of Nuclear Materials 88*, 279-288 (1980).

B. Juttner, M. Laux, J. Lingertat, P. Pech, P. Siemroth, and H. Wolff, "Arc tracks in the T-10 tokamak", *Nuclear Fusion 20*, 497-500 (1980).

W. Köpperdörfer, "A simple model describing hydrogen re-cycling in fusion experiments and its influence on discharge behavior", *Nuclear Fusion 19*, 1319-1325 (1979).

E. S. Marmar, D. Overskei, H. Helava, K. I. Chen, J. L. Terry, and H. W. Moos, "The effects of wall temperature on light impurities in Alcator", *Nuclear Fusion 19*, 485-488 (1979).

G. M. McCracken, "Recycling and surface erosion processes in contemporary tokamaks", *Journal of Nuclear Materials 85 & 86*, 943-949 (1979).

G. M. McCracken and P. E. Stott, "Plasma-surface interactions in tokamaks", *Nuclear Fusion 19*, 889-981 (1979).

"Plasma Material Interaction", The Fusion Reactor Materials Program Plan, DOE/ET-0032/3 (1978).

R. Prater, R. Stambaugh, J. Wesley, D. Bhadra, K. Matsuda, and L. Rovner, "Fusion experimental power reactor (EPR) design tasks", EPRI AP-1347 (1980), Chapter 6, "Wall Regeneration".

J. Roth, J. Bohdansky, and W. Ottenberger, "Data on low energy light ion sputtering", Max-Planck-Institut für Plasmaphysik Report IPP 9/26 (1979), to be published.

D. L. Smith, "Physical sputtering model for fusion reactor first-wall materials", *Journal of Nuclear Materials 75*, 20-31 (1978).

H. Vernickel, B. Behrisch, B. M. U. Scherzer, and F. Wagner, Editors, *Plasma Surface Interactions in Controlled Fusion Devices*, North-Holland, Amsterdam, 1980. (also published as *Journal of Nuclear Materials 93 & 94*, 1980.) Conference Proceedings, 870 pages of articles.

F. W. Wiffen, J. H. DeVan, J. O. Stiegler, Editors, Proceedings of the First Topical Meeting on Fusion Reactor Materials, *(Journal of Nuclear Materials 85 & 86)*, North Holland, Amsterdam, 1979, Chapters 11, 13, 14.

special purpose materials

F. W. Clinard, Jr. "Ceramics for applications in fusion systems", *Journal of Nuclear Materials 85 & 86*, 393-404 (1979).

F. W. Clinard, Jr., "Electrical insulators for magnetically confined fusion reactors", Chapter 4, *Critical Materials Problems in Energy Production*, Academic Press, New York, 1976.

F. W. Clinard and M. M. Cohen, Chairman and Coordinator, Proceedings of the Meeting on CTR Electrical Insulators, CONF-760558 (1978).

F. R. Fickett, R. P. Reed, and E. N. C. Dalder, "Structures, insulators and conductors for large superconducting magnets", *Journal of Nuclear Materials 85 & 86*, 353-360 (1979).

W. J. Gray, "Neutron irradiation effects on carbon and graphite cloths and fibers", *Nuclear Technology 40*, 194-207 (1978).

G. Hopkins, G. C. Trantina, and J. Corelli, "Ceramic materials for fusion reactors", EPRI AP-1702 (1981).

V. A. Maroni and E. H. Van Deventer, "Materials considerations in tritium handling systems", *Journal of Nuclear Materials 85 & 86*, 257-269 (1979).

"Special Purpose Materials", The Fusion Reactor Materials Program Plan, DOE/ET-0032/4 (1978).

F. W. Wiffen, J. H. DeVan, and J. O. Stiegler, Editors, Proceedings of the First Topical Meeting on Fusion Reactor Materials, *(Journal of Nuclear Materials 85 & 86)*, North-Holland, Amsterdam, 1979, Chapters 5, 7, 8.

CHAPTER 25
PLASMA PURITY AND FUELING

25A. Impurities

impurity effects

Impurities affect practically every aspect of plasma behavior, including:

Coulomb collision processes
runaway electrons
neutral beam trapping
radiation losses
plasma resistivity and ohmic heating
current density and magnetic field distributions
onset of disruptive instability (tokamaks)
transport coefficients and confinement times
fuel ion density and fusion power density.

Impurities inhibit neutral beam penetration. Impurity enhancements of radiative and ionization power losses tend to lower T_e, while impurity enhancement of plasma resistivity and ohmic heating tends to increase T_e. The variation of T_e and conductivity affect the current density distribution, magnetic field topology, and plasma stability.

Heavy impurities, such as tungsten, emit intense line radiation even in a hot plasma core, so only small density fractions ($\lesssim 10^{-4}$) are tolerable. Light impurities, such as carbon and oxygen, will be completely stripped in a hot plasma core, so their main contribution to core radiation losses is enhancement of bremsstrahlung. Reduction of edge plasma temperature by line radiation from impurities can be beneficial, in that a cooler edge plasma may produce less wall erosion and impurity influx (Section 24G).

Methods of estimating radiative power loss and power gain ratio Q were described in Chapters 3 and 4. The effect of impurities on reactor Q is indicated in Fig. 25A1. These curves show the maximum allowable impurity concentrations for a given Q, or, conversely, they indicate the maximum possible Q for a given impurity concentration, even if confinement is perfect (zero conduction and convective heat losses).

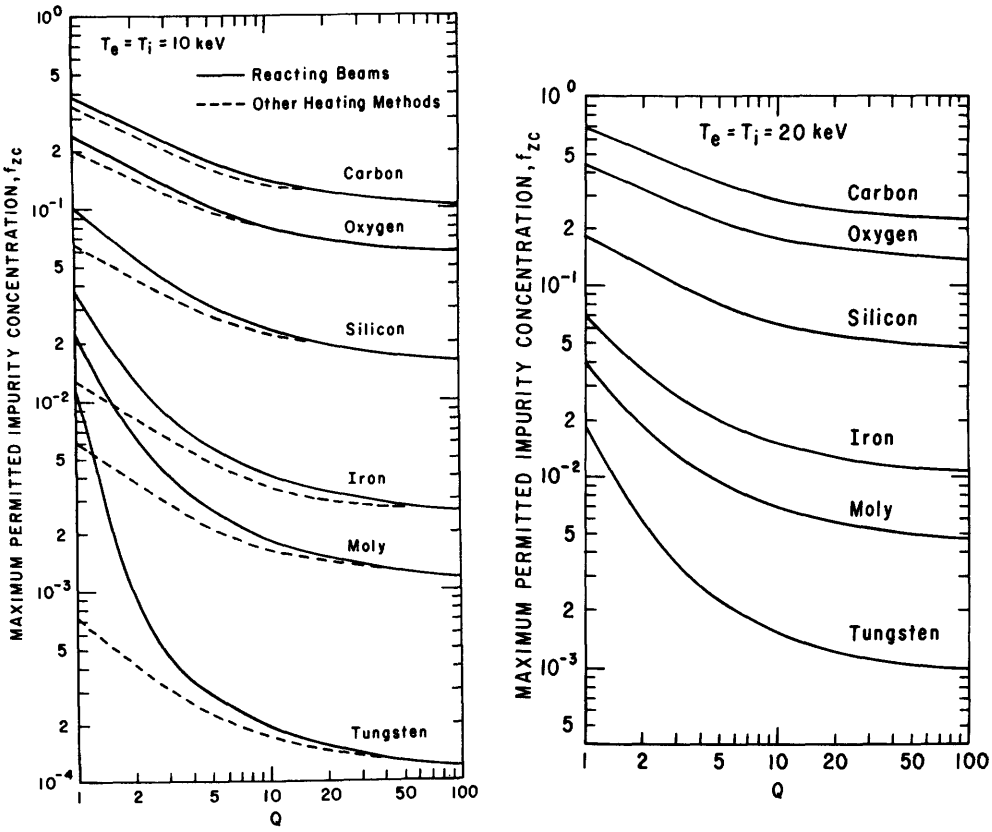

Fig. 25A1. Maximum allowed concentrations of various impurity species for attaining given Q values in a D-T plasma, using 200 keV deuteron beam heating. The dashed curves are for other heating methods, such as rf heating. From R. V. Jensen, D. E. Post, and D. L. Jassby, "Critical impurity concentrations for power multiplication in beam-heated toroidal fusion reactors", Nuclear Science and Engineering 65, 282 (1978), Figs. 3, 4. Published by ANS.

Large values of Q represent ignition. The ignition requirements for an ideal plasma are summarized in Fig. 25A2. For a real plasma with transport losses, the allowable impurity fractions for ignition are lower. Thus, the plasma impurity control system should have the goal of keeping impurity fractions for low-Z elements (O, C, N) $\lesssim 10^{-2}$, for intermediate-Z elements (V, Fe) $\lesssim 10^{-3}$, and for high-Z elements (Mo, W) $\lesssim 10^{-5}$. (If only one or two impurity species were present, slightly higher values might be tolerable.)

impurity concentrations

We will make a rough estimate of the equilibrium concentration of a single species of impurity sputtered from the walls in a steady-state reactor. The particle conservation equation for an impurity with density n_z, confinement time

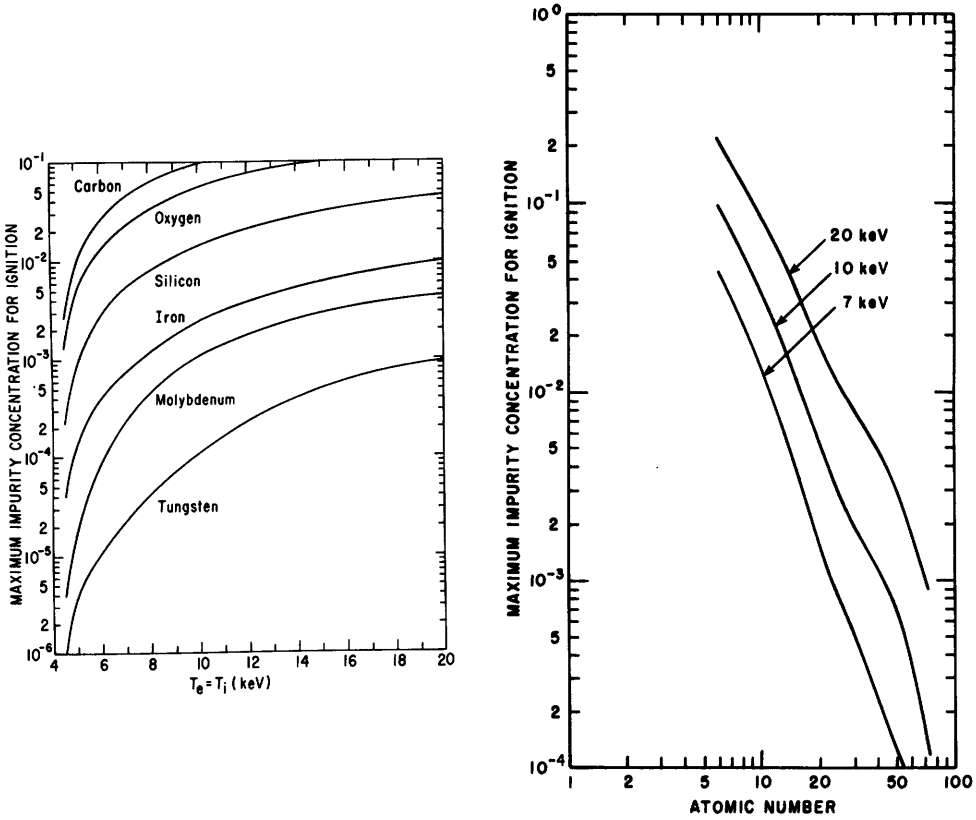

Fig. 25A2. Maximum allowed impurity concentration for ignition of a D-T plasma vs. temperature for various impurity species, and vs. atomic number for various temperatures, assuming zero nonradiative energy losses. From R. V. Jensen, D. E. Post, and D. L. Jassby, Nuclear Science and Engineering 65, 282 (1978), Figs. 5, 6. Published by ANS.

τ_z, and reflection coefficient R_z is

$$V(dn_z/dt) = \text{(production rate by sputtering)} - \text{(net flow rate to walls)}$$

$$= n_i V S_i/\tau_i + n_\alpha V S_\alpha/\tau_\alpha + n_z V S_z/\tau_z - n_z V(1-R_z)/\tau_z \qquad (25A1)$$

where V is the plasma volume (m^3), n and τ are volume averaged densities and confinement times, S are sputtering yields, and the subscripts i and α represent fuel ions and alpha particles. At equilibrium

$$\frac{n_z}{n_i} = \frac{\tau_z(S_i/\tau_i + n_\alpha S_\alpha/n_i\tau_\alpha)}{1 - S_z - R_z} \qquad (25A2)$$

Consider the case of a plasma with pressure $p = \beta B^2/2\mu_0$ limited by the attainable value of β. For simplicity we will assume p = constant and $T_e = T_i = T_\alpha = T_z = T$. Then

$$(n_e + n_i + n_\alpha + n_z)kT = p = \text{constant} \equiv 2n_0kT. \tag{25A3}$$

where $n_i = n_e = n_0$ when $n_\alpha = n_z = 0$. By quasineutrality

$$n_i + 2n_\alpha + Zn_z = n_e \tag{25A4}$$

where Z is the impurity charge number.

EXAMPLE PROBLEM 25A1

Estimate the steady-state Be impurity fraction and the reduction of DT fusion power density for the case of walls coated with Be, if the edge plasma temperature T = 200 eV, $R_z = 0.05$, and $n_\alpha/n_i = 0.1$. Assume $\tau_z = \tau_\alpha = \tau_i$.

From Table 24G2 we find S_i = (average of D and T) = 0.028, S_α = 0.086, and S_z = 0.314. From Eq. (25A2), $n_z/n_i = 0.058$. This is well below the maximum concentration for ignition (Fig. 25A2). From quasineutrality (25A4) $n_e = n_i + 2n\alpha + 4n_z = n_i[1 + 2(.1) + 4(.058)] = 1.432\ n_i$. From Eq. (25A3), $(n_i + n_e + n_z + n_\alpha)kT = p_0 = 2n_0kT$, $n_i(1 + 1.432 + 0.058 + 0.1) = 2n_0$, $n_i/n_0 = 0.772$. $P_f/P_{f0} = (n_i/n_0)^2 = 0.60$. Thus the fusion power density would be 60% of its value without impurities.

---

helium accumulation

Helium "ash" produced by DT fusion reactions displaces fuel ions in a pressure-limited plasma. If a fraction R_α of the alpha particles incident on the walls is reflected back into the plasma, then the alpha particle conservation equation (4A3) becomes

$$dn_\alpha/dt = \tfrac{1}{4}n_i^2\langle\sigma v\rangle_{DT} - n_\alpha(1-R_\alpha)/\tau_\alpha \tag{25A5}$$

We will use this equation to estimate how fast the ash accumulates when none is removed (when $R_\alpha = 1$), and to estimate the equilibrium concentration of helium attainable for various ash removal efficiencies $(1-R_\alpha)$.

For simplicity, assume $n_z = 0$. Let $f_\alpha \equiv n_\alpha/n_0$. From Eqs. (25A3) and (25A4) we find

$$n_i = n_0 - 3n_\alpha/2 = n_0(1 - 3f_\alpha/2) \tag{25A6}$$

With $R_\alpha = 1$, Eq. (25A5) becomes

$$df_\alpha/dt = A_1(1 - 3f_\alpha/2)^2 \tag{25A7}$$

where

$$A_1 \equiv n_0\langle\sigma v\rangle_{DT}/4 \quad .$$

If $f_\alpha(0) = 0$, the solution is

$$f_\alpha(t) = A_1 t/(1 + 3A_1 t/2) \quad . \tag{25A8}$$

The reduction of fusion power density due to alpha particle accumulation is

$$P_f(t)/P_{f0} = (n_i/n_0)^2 = (1 - 3f_\alpha/2)^2 = (1 + 3A_1 t/2)^{-2} \quad . \tag{25A9}$$

A more general solution of Eq. (25A5) will be described in Problem 2 at the end of the Chapter.

EXAMPLE PROBLEM 25A2

If helium ash is not removed from a pressure-limited plasma with $n_o = 10^{20}$ m^{-3} and $T = 20$ keV, how long does it take for the helium accumulation to reduce the fusion power density by a factor of two?

Solving Eq. (25A9) for t, we find

$$t = [(P_{f0}/P_f)^{\frac{1}{2}} - 1] \; / \; (3A_1/2) \quad . \tag{25A10}$$

For this case $A_1 = 0.0106$ s^{-1} and $P_{f0}/P_f = 2$, so $t = 26$ s.

Thus, if helium ash is not removed, fusion burn will be quenched in tens of seconds, even if no other impurities are present.

equilibrium helium concentration

For simplicity, we will again assume $n_z = 0$. For small values of burnup fraction, Eq. (4D7) reduces to

$$f_b \simeq n_i \tau_i \langle\sigma v\rangle_{DT}/2 \quad , \qquad (f_b << 1) \quad . \tag{25A11}$$

The equilibrium solution of Eq. (25A5) may be written

$$n_\alpha/n_i = a \equiv n_i \langle\sigma v\rangle_{DT} \tau_\alpha/4(1-R_\alpha) = f_b \tau_\alpha/2\tau_i(1-R_\alpha) \quad . \tag{25A12}$$

The helium concentration may also be expressed in terms of n_0, with the result

$$f_\alpha \equiv n_\alpha/n_0 = a/(1 + 3a/2) \quad . \tag{25A13}$$

The reduction in fusion power density caused by the helium alone (ignoring effects of other impurities) is

$$P_f/P_{f0} = (n_i/n_0)^2 = (1 - 3f_\alpha/2)^2 = (1 + 3a/2)^{-2} \quad . \tag{25A14}$$

In order to keep $P_f/P_{f0} \geq \frac{1}{2}$, we must have $a \leq 2(2^{\frac{1}{2}}-1)/3 = 0.28$. (The case $P_f/P_{f0} = \frac{1}{2}$ corresponds to $n_\alpha/n_0 \simeq 20$ %.) For example, if $(\tau_\alpha/\tau_i) \simeq 1$ and we desire $f_b \simeq 0.1$, then we need $R_\alpha \leq 0.82$. Attainable values of R_α will be estimated for one method of impurity removal in Section 25D. Usually, several species of impurities will be present at once.

Table 25A1. Modes of fusion reactor operation

short-pulse mode. ($t \lesssim 30$ s)	Fusion burn occurs until impurity buildup quenches it. Impurity control and refueling are minimal or non-existent. Recirculating power fraction is high, and rapid pulsing creates problems like fatigue. (pinches, ICF, early tokamaks)
long-pulse mode. ($t \gtrsim 30$ s)	Impurity control and refueling prolong plasma burn. (tokamaks).
steady-state operation	Very effective impurity control and refueling. Plasma current (tokamaks) sustained by rf or other means. (mirrors, stellarators, maybe EBT)

modes of operation

With regard to impurity control and fueling, three modes of reactor operation may be distinguished (Table 25A1). Even in the short-pulse mode, low impurity fractions are needed initially to obtain ignition.

Impurities from the walls will be ionized near the edge of the plasma. From there they tend to diffuse inwards and accumulate near the plasma center, according to simple diffusion theory. However, several phenomena tend to inhibit such accumulation, and various techniques have been suggested to exploit these phenomena for impurity control (Table 25A2).

The impurity species can be partially selected by using low-Z liners or coatings. For example, if a small fraction of Be atoms were injected with the DT fuel, then Be^+ ions would be deposited on the wall, continuously regenerating a Be coating.

25B. Divertors

types of divertors

A divertor is a device which bends the outer magnetic field lines away from the plasma and leads them to a separate external chamber. The outer layers of plasma flow along these diverted field lines to the outer chamber, where the plasma deposits its energy via several processes, including impact on a neutralizer plate (target), collisions with neutral gas, and radiation. The cooled plasma recombines into neutral gas, which can be pumped away by vacuum pumps. Thus, the outer layers of plasma are continuously removed, cooled, neutralized, and pumped away by the divertor.

There is a bounding magnetic surface, called the *separatrix*. Plasma inside the separatrix is confined, and plasma in the *scrape-off region* outside the separatrix flows into the divertor. Divertors may divert the toroidal magnetic flux, the poloidal flux, or a small bundle of flux, as illustrated in Fig. 25B1.

Divertors can perform two useful functions: (1) If plasma is rapidly removed from the scrape-off region, then the first wall bombardment is reduced, thus

Table 25A2. Phenomena and techniques of impurity control.

PHENOMENA	
density gradient force	A positive dn_i/dr makes impurities tend to diffuse outwards.
temperature gradient force	A negative dT_i/dr makes impurities tend to diffuse outwards.
ion-impurity frictional force	When the parallel ion flow velocity is in the right direction, the ion-impurity frictional force makes impurities tend to diffuse outwards.
electric field force	An outward electric field inhibits inward flow of impurities, as in magnetic mirrors.
centrifugal force	In a rotating plasma, the centrifugal force tends to make impurities move outwards.
radiative cooling	Cooling of edge plasma by line radiation lowers wall sputtering rates. Low-Z elements are preferable for radiative cooling, because high-Z impurities also cause line radiation from the hot plasma core.
TECHNIQUES	
wall modification	Honeycomb surfaces, low-Z coatings or liners, bakeout, discharge cleaning, gettering.
discharge dynamics	The plasma current may be controlled to avoid plasma contact with walls, especially during the initial breakdown phase, when divertors may not be effective.
divertors	Outer layers of plasma are channeled to another chamber, cooled, neutralized, and pumped away.
neutral gas blanket	Neutral fuel gas between the plasma and wall enhances density- and temperature-gradient forces, reduces sputtering rates, blocks flight of wall atoms into the plasma, and provides a source of new fuel. However, the high density at the plasma edge may lead to instability.
impurity injection	Impurity gases may be deliberately injected to enhance radiative cooling of the plasma edge.
gas flow	Azimuthal gas flow may lead to outward flow of impurities via the ion-impurity frictional force.
neutral beam injection	Neutral beam injection may induce desirable ion-impurity frictional forces. Low-energy neutral beam injection may produce a "cool plasma mantle", with a positive fuel ion density gradient (similar to gas blanket, but lower density).
limiter-reflectors	Limiter-reflectors around the plasma periphery may scrape off edge plasma and neutralize it. High-speed vacuum pumps would then remove some of the neutralized gas.
selective rf plugging	If impurities have substantially different charge-to-mass ratios than fuel ions have, then rf waves may be selectively absorbed by one species. (a) Fuel ions can be selectively confined in open magnetic systems or in divertor throats. (b) Heating impurities might enhance their diffusion rates.

reducing the sputtering rate (an *unload* divertor). The sputtering problem is transferred to the divertor chamber. If the plasma can be cooled before it hits the divertor chamber walls or collection plates, then the overall sputtering problem can be reduced. (2) Impurities sputtered off the walls have a high probability of being ionized in the scrape-off region and swept into the divertor chamber, so that they cannot enter the central plasma region (a *screening* divertor).

A given divertor will perform both functions to some extent. Both functions are enhanced by making the scrape-off region thick.

The effectiveness of a divertor may be described in terms of the reduction of wall bombardment or in terms of reduction of impurity flow into the plasma.

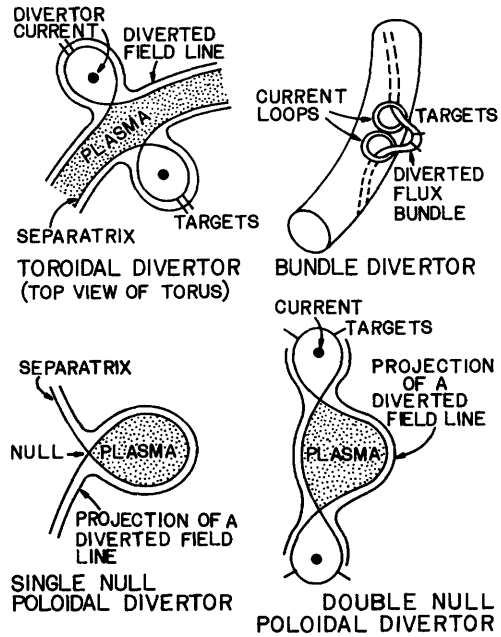

Fig. 25B1. Toroidal, poloidal, and bundle divertors. The poloidal divertor sketches represent cross sections of toruses. (Not all currents shown.) From G.H. Miley, Editor, Proceedings of the First IEEE Minicourse on Fusion, U. of Illinois Fusion Studies Laboratory, 1976, p. 1-34.

plasma flow

Plasma flow in a double-null tokamak poloidal divertor is illustrated in Fig. 25B2. Divertor coils are designed and wound carefully in order to avoid introducing too much magnetic field ripple in the confinement region. The exact location of the separatrix depends upon plasma current distribution, and a poloidal divertor may not be effective during start-up, when plasma current is low. The plasma could become contaminated with impurities by contact with the walls during this period. Plasma crossing the separatrix may flow along the magnetic field to the target, or diffuse across the field to the walls. Since the toroidal field $B_t \gg B_p$, the ions travel a long way in the toroidal direction (out of the plane of the drawing) while going a short poloidal distance towards the target. At the null point the poloidal field $B_p = 0$, but $B_t \neq 0$. To simplify the description of divertors, the scrape-off region and flow channel may be approximated by a long straight rectangle, as illustrated in Fig. 25B3.

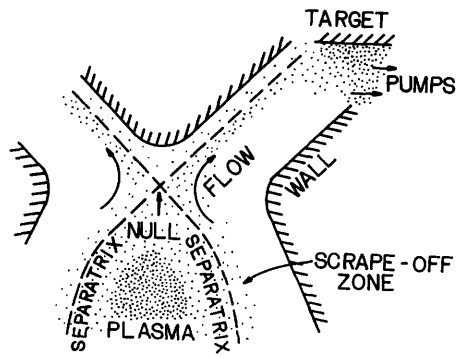

Fig. 25B2. The upper half of a double-null tokamak poloidal divertor (coils not shown). Plasma crossing the separatrix may flow along the magnetic field to the target, or diffuse across the field to the walls.

Variations of magnetic field strength along the ion path (Fig. 25B3) can cause

mirror reflection of some ions. The longest confinement time $\tau_{\parallel}$ of ions along the magnetic field is therefore approximately τ_{ii}, the ion-ion collision time.

The shortest ion confinement time along the magnetic field is the flow time at the ion sound speed L/c_s, where L is the ion flow path length (mostly in the toroidal direction) and $c_s \simeq [(kT_e + \gamma_i kT_i)/m_i]^{\frac{1}{2}}$, [$\gamma_i$ is in Eq. (5D16)].

Thus $$L/c_s \lesssim \tau_{\parallel} < \tau_{ii} \quad . \qquad (25B1)$$

Various mirror microinstabilities are expected to make $\tau_{\parallel}$ closer to the lower limit, L/c_s. The minimum and maximum values of diffusion coefficients $D_{\perp}$ across the magnetic field are neoclassical and Bohm values:

$$D_{NC} < D_{\perp} \lesssim D_B \quad . \qquad (25B2)$$

Turbulence may raise $D_{\perp}$ close to the upper limit. Let $\vec{\Gamma} = n\vec{u}_i$ be the ion particle flux. We can separate $\vec{\nabla}\cdot\vec{\Gamma}$ into components along the magnetic field and perpendicular to the field:

$$\vec{\nabla}\cdot\vec{\Gamma} = \vec{\nabla}_{\parallel}\cdot\vec{\Gamma}_{\parallel} + \vec{\nabla}_{\perp}\cdot\vec{\Gamma}_{\perp}$$
$$\simeq \frac{nu_{\parallel}}{L} - \frac{\partial}{\partial x}\left(D_{\perp}\frac{\partial n}{\partial x}\right) \qquad (25B3)$$

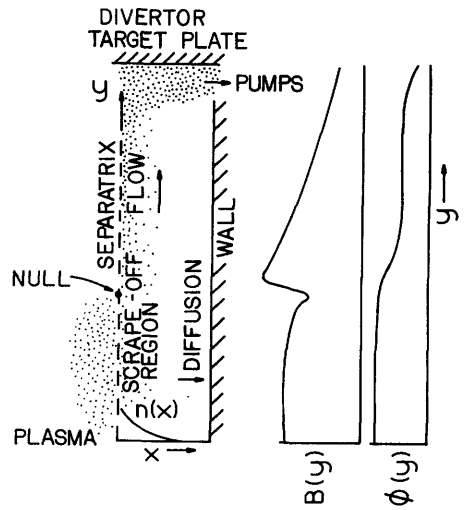

Fig. 25B3. Simplified representation of scrape-off region and flow region (not to scale). The x coordinate represents distance across the magnetic flux surfaces from the separatrix towards the wall, and the y coordinate represents distance along the poloidal flux surfaces towards the target. Typical variations of total magnetic field strength and electrostatic potential in the y direction are shown at the right.

where n is the ion density, and $u_{\parallel}$ is the ion parallel flow velocity. By definition, $\tau_{\parallel} \equiv L/u_{\parallel}$. Since the ion temperature in the scrape-off region is not high enough to produce significant ionization by ions, the steady-state ion continuity equation (5D1) reduces to

$$\frac{n}{\tau_{\parallel}} - \frac{d}{dx}\left(D_{\perp}\frac{dn}{dx}\right) = nn_n\langle\sigma_e v_e\rangle - n^2\langle\sigma_r v\rangle \quad . \qquad (25B4)$$

If we make the simplifying assumptions that

* $D_{\perp} \simeq$ constant

* recombination is negligible

then this equation can be written

$$\frac{d^2n}{dx^2} = \frac{n}{\lambda^2} \qquad (25B5)$$

where

$$\lambda^2 \equiv D_{\perp}\tau_{\parallel}(1 - n_n\langle\sigma_e v_e\rangle\tau_{\parallel})^{-1} \quad . \qquad (25B6)$$

If λ = constant, $n(0) = n_0$ at the separatrix, $n(x_w) \simeq 0$ at the walls, and $\lambda << x_w$, then the solution is

$$n(x) \simeq n_0 e^{-x/\lambda} \quad . \tag{25B7}$$

Thus, for large x_w, the thickness of the plasma density profile is roughly equal to λ. A thick plasma is more effective than a thin plasma at ionizing wall-originated impurity atoms before they can reach the separatrix. The plasma is thinnest if no ionization occurs (if $n_n \langle \sigma_e v_e \rangle \approx 0$). If ionization is significant, the plasma thickness λ increases. Large diffusion coefficients and long parallel flow times both tend to make the plasma in the scrape-off zone thick.

EXAMPLE PROBLEM 25B1

Estimate the plasma thickness in the scrape-off zone, assuming the minimum parallel flow time and maximum diffusion rate, for a deuterium plasma with $n_0 = 10^{19}$ m^{-3}, $n_n = 10^{17}$ m^{-3}, $L = 100$ *m*, $T_e = 0.3$ *keV*, $T_i = 1$ *keV*, $x_w = 0.5$ *m, and* $B = 4$ *T in the scrape-off region.*

For this one-dimensional case, $\gamma_i = 3$, $c_s = 4 \times 10^5$ m/s, $\tau_{\parallel} = 2.5 \times 10^{-4}$ s. From Eq. (8F14), $D_B = T_e/16eB = 4.7$ m^2/s. Fig. 3D1 $\rightarrow \langle \sigma_e v_e \rangle = 3 \times 10^{-14} m^3 s^{-1}$. Then, from Eq. (25B6), $\lambda = 0.07$ m. If n_n were smaller, λ would be reduced by a factor of two. In fact, n_n will vary with x and y. The above analysis assuming λ = constant is inexact, but gives an approximate estimate of the plasma thickness. Neoclassical diffusion would decrease λ, but mirror trapping would increase $\tau_{\parallel}$ and λ. For this case the radiative recombination rate is about 10^{-5} of the ionization rate, so neglect of recombination is well justified.

For a more accurate description of the scrape-off zone, the spatial variation of the neutral density should be calculated, including recycling from the wall (Section 24F), ionization, etc. Spatial variations of T_e and T_i can be estimated from energy conservation equations, including cooling by charge exchange and radiation during flow towards the target.

The variation of electrostatic potential is described by equations similar to those of Section 5F, but with added terms for ionization and secondary electron emission from the target. These additional phenomena tend to broaden the sheath and reduce the sheath potential fall, thus reducing the sputtering yield.

Intense cyclotron radiation from the plasma will tend to ionize sputtered impurities in the scrape-off region, reducing their chance of penetrating across the separatrix, and thus enhancing the screening efficiency of the divertor.

Divertors are being simulated in detail by two-dimensional computer codes, taking into account plasma flow, diffusion, ionization, charge exchange, recombination, frictional forces, radiative cooling, reflection, adsorption-desorption, secondary emission, and sputtering. Many species, ionization states, and their interactions must be taken into account. Values of diffusion coefficients and thermal conductivities for various species are assumed, which introduces uncertainty to the results. If few of the ions reach the walls by diffusion and few wall-originated neutrals reach the separatrix, then a simple zero dimensional

model of the scrape-off zone may be used to estimate T_e, T_i, and the charge-exchange neutral flux striking the wall (Mense and Emmert, 1979).

divertor target and pumping

The divertor target for a reactor will probably have heat loads of several MW/m^2, so overheating is a potential problem. Unless the plasma has cooled substantially, sputtering will also be a serious problem. Sputtered target metal atoms may become ionized in the sheath and accelerated back into the target, causing self-sputtering with high yield. Honeycomb shape surfaces have been proposed to catch many of the sputtered atoms. If the temperatures are reduced to very low values ($\lesssim$30 eV), then the sheath potential accelerating the ions may be below the sputtering threshold (Table 24G1), and sputtering rates will be low. A low sheath potential is also desirable to prevent unipolar arcing in the target and chamber walls.

High vacuum pumping speeds may be needed to handle the gas load from a fusion reactor divertor exhaust. The heat flow is typically hundreds of MW. If this is to be carried by low-energy particles striking the target (to reduce sputtering), then the particle flow rate must be very large.

EXAMPLE PROBLEM 25B2

A fusion reactor has 200 MW of heat flowing into the divertor, which has a total target area of 100 m^2. If half the energy is carried by ions, the average particle energy is to be 50 eV, and the target and wall temperatures are about 800 K, estimate the required vacuum pumping speed and cryopanel area to keep the target region at p = 0.1 Pa(8×10^{-4} Torr).

The required ion flow rate is

$$\dot{N}_i = P_i/\langle W_i\rangle = (10^8 \text{ J/s})/(50 \text{ eV/ion})(1.6\times10^{-19} \text{ J/eV}) = 1.25\times10^{25} \text{ ions/s} \quad .$$

The neutrals will be at the wall temperature. From Eq. (19B6),

$$Q = \dot{N}kT = 1.4 \times 10^5 \text{ J/s} \quad .$$

If the cryopumps are located very close to the target plates, the conductance will be very large. Then from Eq. (19B11), with $p_u \ll p$ and $C \gg S_t$, we find $S_t = Q/p = 1.4\times10^6$ m^3/s. For deuterium at 800 K, the pumping speed of a cryogenic pump panel is $S_t \simeq 145$ A [Eq. (19C1), at 800 K]. Thus, the required cryopanel area would be $A = 10^4$ m^2. Such a large pump area would probably be unfeasible.

To alleviate the pumping problem, we can
*reduce the heat load to the divertor, and increase heat flow to the first wall. This would increase first wall sputtering rates.
*allow higher energy per particle hitting the divertor target. This would increase divertor target sputtering rates.
*allow higher pressure near the target. This would increase neutral gas flow across the separatrix, tending towards the gas blanket concept.

tokamak divertors

Since tokamaks work best at small aspect ratios ($R_0/a \lesssim 4$) there is not enough room for a toroidal divertor. A toroidal divertor would also destroy the axisymmetry, which aids confinement. Tokamak divertors are usually poloidal divertors or bundle divertors. Figure 25B4 shows the divertors of the DIVA, T-12, and DITE tokamaks. The thicknesses of the scrape-off layers are 1-2 cm, 0.5-1 cm, and 7 cm respectively in these devices. When the divertor coil currents are increased above a critical value, the plasma becomes unstable. The radiative power loss in DIVA and DITE is reduced by a factor of 2-4 by operation of the divertors. The energy confinement time was increased by a factor of about 2.5 in DIVA.

The Poloidal Divertor Experiment (PDX) is illustrated in Fig. 25B5. The divertor coils can be used in four configurations: (1) off, circular plasma, (2) D-shaped plasma, (3) inverted D-shaped plasma, (4) rectangular plasma with four null points (shown in Figure). Some parameters of PDX are listed in Table 25B1. Divertor efficiencies will improve with size in larger machines.

other divertors

The torsatron magnetic field configuration provides a natural helical poloidal divertor, as shown in Fig. 25B6. An ℓ=2 torsatron (or "heliotron") also has favorable flux surfaces and built-in divertor. Since EBT devices have large aspect ratios and do not have axisymmetry, toroidal divertors are appropriate for them. A toroidal divertor on the Model C Stellarator succeeded in reducing the oxygen impurity content of the plasma from 5 % to 0.05 %.

A divertor adds complexity, increases cost, and makes maintenance more difficult, so alternate means of impurity control are desirable.

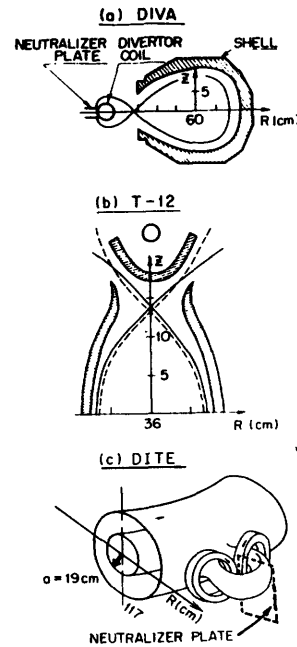

Fig. 25B4. Tokamak divertors. (a) the DIVA single-null poloidal divertor, (b) the T-12 double-null poloidal divertor, (c) the DITE bundle divertor. From Y. Shimomura and H. Maeda, "Divertor experiments for controlling plasma-wall interactions", Journal of Nuclear Materials 76 & 77, 45-48 (1978), Fig. 1.

Table 25B1. Parameters of PDX, with divertor operating.

minor radius	a	0.47	m
major radius	R	1.45	m
toroidal field	B_t	2.4	T
plasma current	I_p	0.5	MA
plasma temperature	T		
0.3 MW ohmic heating		1-2	keV
6 MW neutral beams for 0.5 s		2-6	keV
plasma density	n	$0.4\text{-}3\times10^{20}$	m^{-3}
plasma beta	β	2-5	%
energy confinement time	τ_E	0.1	s

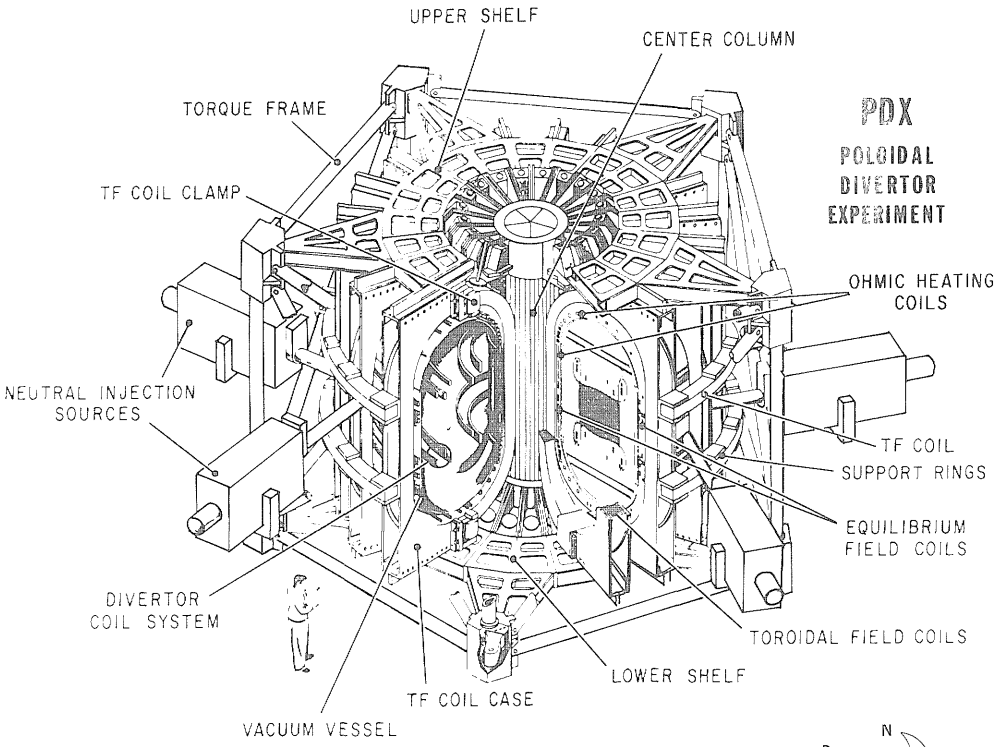

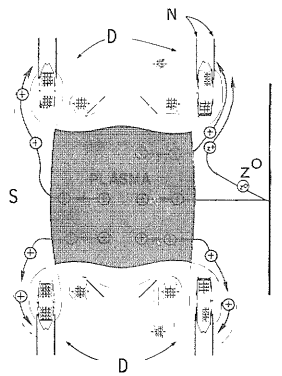

Fig. 25B5. The Poloidal Divertor Experiment (above) and a cross section of the divertor region (right).
N = neutralizer plates
D = divertor region
S = scrape-off region
z^o = sputtered impurity atom

Courtesy of PPPL.

25C. Neutral Gas Blankets

Neutral gas incident on a dense plasma will be ionized in a thin layer at the plasma edge. A plasma layer of thickness L and density n will be impermeable to neutral atoms from the walls if

$$nL >> 3\times10^{18}\ m^{-2} \quad , \tag{25C1}$$

(Lehnert, 1973). Admitting cold neutral gas around the outside of the plasma will form a cool, high-density plasma layer, called a *neutral gas blanket* or *cool plasma blanket*. For example, if the layer thickness $L \sim 0.1$ m, then a neutral gas density $n_n \gtrsim 3\times10^{20}\ m^{-3}$ is needed to make the plasma layer impermeable. At a wall temperature of 500K, this density would correspond to a gas pressure $P \gtrsim 2$ Pa (16 mTorr).

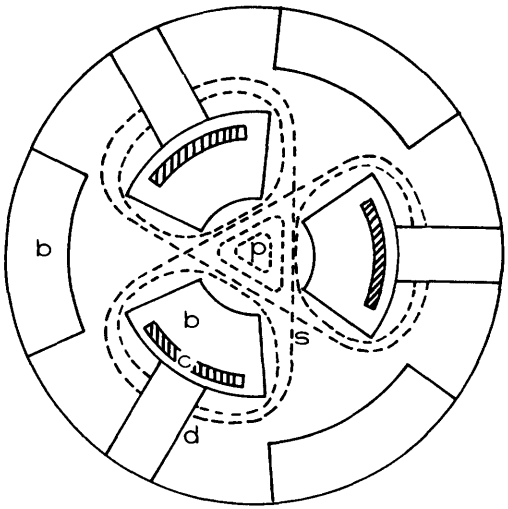

Fig. 25B6. Cross section of an ℓ = 3 torsatron reactor. c = magnet coils, b = blanket and shield, p = plasma region, dashed lines = magnet flux surfaces, s = separatrix, d = divertor collector plates.

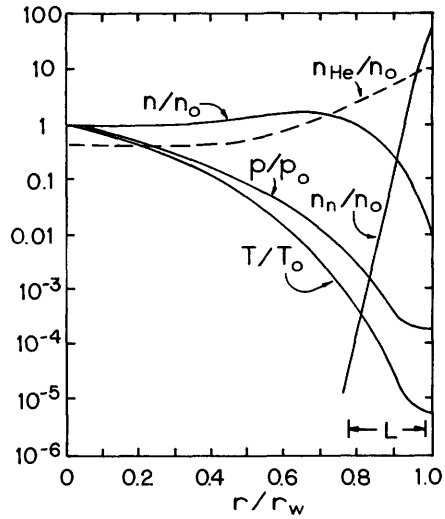

Fig. 25C1. Hypothetical radial variations of plasma density, helium density, pressure, temperature, and neutral gas density n_n, (relative to the central values of plasma density n_0, temperature T_0, and pressure p_0) for the neutral gas blanket concept. The thickness of the "impermeable" edge layer is indicated by L.

Hypothetical density, temperature, and pressure profiles for a neutral gas blanket are illustrated in Fig. 25C1. The shape of p(r) is determined mainly by the J×B force. Near the walls, the high-resistivity cold plasma will conduct only a small current density J, so the pressure gradient

$$\vec{\nabla}p = \vec{J}\times\vec{B} \qquad (25C2)$$

is small, and the pressure profile is nearly flat. Multigroup transport codes and Monte Carlo codes (Chapter 27) have been developed to calculate neutral atom density profiles. The neutral gas density n_n drops off rapidly away from the walls, but reaches an equilibrium value, limited by recombination, in the plasma core. Near the walls the neutral gas contributes significantly to the total pressure.

For a reactor, the parameters might be $T_0 \sim 15$ keV, $n_0 \sim 2\times10^{20}$ m^{-3}, $p_0 = 2n_0kT_0 \sim 1$ MPa = 10 atm, with values at the wall $T_w \sim 0.1$ eV, $P_w \sim 100$ Pa = 0.8Torr, plasma density peak $n_{max} \sim 3\times10^{21}$ m^{-3}, neutral density $n_n \sim 10^{22}$ m^{-3} (corresponding to a neutral gas pressure $p_n \sim 100$ Pa = 0.8 Torr at 700 K).

The density and temperature profiles are determined by various transport processes (Chapter 8). The temperature gradient force causes the helium ion density to increase with radius.

When the plasma is impermeable to neutral penetration, the driving forces for ballooning and flute instabilities inside the plasma are greatly reduced.

Impermeability, however, makes penetration of neutral atom beams for plasma heating difficult, so injected neutral atom beams would be trapped near the outside of the plasma, not at the center. The resulting density spike (not shown in Fig. 25C1) might cause instability. The impermeability condition also requires high plasma density and pressure, which might not be attainable in small low-beta systems.

Magnetically stabilized arcs have operated with central densities around 3×10^{21} m^{-3} and temperatures around 10 eV, with the temperature dropping off to about 0.05 eV at the wall. The surrounding gas pressure was about 10 Pa. Such arc experiments are similar to the gas blanket scheme, although the central temperature is much lower than it will be in a reactor, and the plasmas were much more permeable to neutral atom penetration. The high plasma densities and low impurity levels attained in the Alcator tokamaks indicate that gas blanket effects may be active there. However, the concept remains to be tested in a large device.

Some advantages and problems of the neutral gas blanket concept are summarized in Table 25C1. If the problems can be overcome, this technique is highly desirable for impurity control and refueling. For example, the magnet coil system could be simpler and smaller than for a reactor with a divertor.

Table 25C1. Advantages and problems of the neutral gas blanket concept.

advantages
reduced sputtering and arcing
reduced impurity penetration
refuelling by inward diffusion
helium density minimum in plasma core
problems
high pressures
possible instability
incompatible with neutral beam heating
high equilibrium alpha particle density

25D. Other Impurity Control Techniques

impurity injection

Controlled amounts of low-Z impurity gases, like neon, may be added to the plasma to enhance line radiation cooling of the edge regions. Because the ions are fully stripped in the plasma core, the core radiation losses would not be increased as much as the edge losses. The increased radiation loss also helps to limit the equilibrium plasma temperature, if transport scaling does not provide a sufficiently low value.

gas flow

Each ion species has a flow pattern where the vertical gradient and curvature drift is followed by return flow along a magnetic field line. Species with different charges will have different flow velocities, and the collisional friction forces between species will alter their drift motion. Normally the outward motion of hydrogen and inward motion of impurities would be enhanced by friction between them. If the relative velocity of hydrogen and impurities can be reversed, however, then the inward impurity flow and outward hydrogen flow may be reversed. One means of changing the relative velocity is to inject hydrogen gas azimuthally at one poloidal position and remove it with vacuum pumping at the diametrically opposite position. Such *impurity flow reversal* was demonstrated with the ISX-A tokamak.

neutral beam injection

Neutral beam injection in the direction of the plasma current (*co-injection*) results in better confinement and heating than injection in the opposite direction (*counter-injection*). Impurity flow reversal can be induced by co-injection under certain circumstances (Stacey and Sigmar, 1979). The required neutral beam currents are near those planned for large tokamaks.

pumped limiters

The STARFIRE tokamak reactor design employs two limiter-reflectors extending toroidally around the torus and occupying less than 5 % of the wall area. If a particle just missed a limiter, it would make half a revolution poloidally and q/2 revolutions toroidally before encountering the other limiter, where q is the safety factor (Table 8B1). Thus, the distance travelled is

$$L = 2\pi R(q/2) \quad . \tag{25D1}$$

For the STARFIRE design R = 7 m, q = 3.6, and L = 80 m. The limiters define a scrape-off region similar to that defined by the separatrix of divertors. The plasma thickness in the scrape-off region is estimated from Eq. (25B6) to be $\lambda \sim 7$ cm, assuming Bohm diffusion and free flight. Vacuum pumping ducts are placed immediately behind the limiters, so that part of the neutralized gases may be pumped away (Fig. 25D1).

The peak power incident on the limiters is

$$P_{lim} = (P_{ext} + P_{\alpha}) - (P_{rad} + P_{cx} + P_{ioniz}) \tag{25D2}$$

where P_{ext} is the external heating power (rf waves in the case of STARFIRE), P_{α} is the fusion alpha power, P_{rad} is the power radiated from the plasma core and edge regions, P_{cx} is the power flowing to the walls by charge exchange, and P_{ioniz} is the power expended in ionizing neutrals and ions. To reduce P_{lim} to acceptable values, P_{rad} is increased by admitting controlled amounts of impurity gas (such as 0.1 % Xe) to the plasma. The peak heat flux flowing poloidally onto the limiters is estimated to be $q_0 \simeq 7$ MW/m^2. However, this heat is at grazing incidence on the front of the limiter, affording larger areas and greatly reducing the heat flux encountered by the metal. The maximum heat flux encountered by the limiter is at the "leading edge", where q has dropped off to about 4 MW/m^2 (Fig. 25D1).

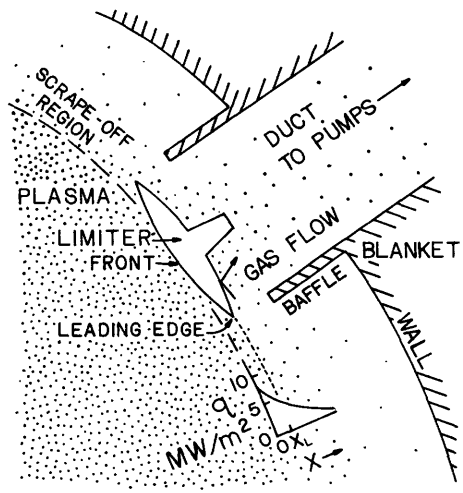

Fig. 25D1. A pumped limiter for impurity control in a tokamak reactor. The "leading edge" is set back to a power flux q = 4 MW/m^2. The vacuum duct may be zig-zagged (not shown) to reduce neutron streaming.

Let R_L, R_V, and R_W be the reflection coefficients of the limiter, vacuum duct, and wall, for alpha particles. Alpha particles reflected from the limiter have a probability a_p of returning directly to the plasma, a probability a_v of entering the vacuum duct, and a probability a_w of hitting the walls ($a_p + a_v + a_w = 1$). Thus, the total reflection probability for alpha particles is

$$R_\alpha = R_L(a_p + a_w R_w + a_v R_v) \qquad (25D3)$$

Initially the reflection coefficients from clean surfaces might be low, but at steady state the surfaces become saturated with gas, and helium atoms will leave the surface almost as fast as they arrive, due to thermal and stimulated desorption processes. Therefore, $0.95 \lesssim R_L \leq 1$, and $0.95 \lesssim R_W \leq 1$. Since atoms are pumped away in the duct, its effective reflection coefficient may be lower, however. Typical values might be $a_p \sim 0.4$, $a_v \sim 0.4$, $a_w \sim 0.2$, $R_V \sim 0.5$, $R_L \sim R_W \sim 0.97$. For these values, the net alpha particle reflection probability is $R_\alpha \sim 0.77$. This means that about 23 % of the alpha particles leaving the plasma would be pumped away. This value is comparable to the required values of R_α estimated from Eq. (25A14). An optimum design would maximize a_v and minimize R_V.

The problems of the limiter-reflector concept are the high limiter heat loads and impurity sputtering rates. Low-Z coatings (Be) are envisioned to avoid high-Z contamination. Enhanced radiation is used to cool the plasma radiatively, reducing the heat carried by particles to the limiter. A high toroidal field is employed to sustain higher plasma pressures, so that acceptable fusion power densities may be attained even in the presence of substantial impurity fractions (He, Be, and Xe). The magnetic field and coils are much simpler than for a divertor system, permitting easier maintenance and lower cost.

The last impurity control concept, rf plugging, was discussed in Chapter 17.

25E. Fueling

Possible fueling methods include gas blankets, plasma guns, neutral beam injection, cluster injection, and pellet injection.

gas blankets

The inverted density profile and steep temperature gradient associated with a gas blanket promote outward diffusion of helium ash and inward diffusion of fuel ions.

When hydrogen gas was admitted to the Alcator tokamak plasma, the new ions quickly flowed into the plasma core, instead of slowly diffusing inwards, as predicted by neoclassical theory. Such rapid penetration without disruption bodes well for plasma fueling by gas blankets.

The Ringboog experiment operates at higher densities than conventional tokamaks: gas pressures of 1-10 Pa and central plasma densities of $0.8\text{-}2.5 \times 10^{21}$ m^{-3} are observed at plasma currents of 5-20 kA, with electron temperatures of a few eV. The configuration appears stable at low currents, but becomes unstable at

high currents. Hydrogen line radiation plays a dominant role in the energy balance of high-density regions. The observed particle fluxes agree with highly-collisional transport theory. Theoretical predictions indicate certain parameter ranges in which gas-blanket fueling of reactors is feasible. The conditions of reactor gas blankets will lie in between those of present tokamaks and those of the Ringboog device.

plasma guns

Plasma guns can produce plasmas containing many particles ($> 10^{21}$ per shot) with MJ of energy at efficiencies over 50 %. Gun plasmas can sometimes penetrate across magnetic field lines into toroidal confinement systems. Some gun plasmas have very low impurity content. Let S_i be the volume-average fuel ion source (ions/m^3s) and V be the plasma volume (m^3). Since each fuel ion undergoing fusion produces $W_{DT}/2$ of energy, the fusion power may be written

$$P_F = f_b S_i V W_{DT}/2 \quad (W) , \tag{25E1}$$

where f_b is the burnup fraction. The required fuel ion source is

$$S_i V = \frac{2P_F}{f_b W_{DT}} \quad (\text{ions/s}) . \tag{25E2}$$

For example, if a reactor produces P_F = 3.3 GW (thermal) and has a burnup fraction f_b = 0.05, then the required fueling rate is $S_i V = 5 \times 10^{22}$ ions/s. If plasma guns produced 10^{21} particles per blob, and half of those particles had adequate penetration into the confinement system, then about 100 plasma blobs per second would be needed to sustain the reactor.

However, there is little experience with injection of gun plasmas into large toroidal experiments, such as tokamaks. It is uncertain whether the plasma blobs could penetrate far enough into high density plasmas to produce the desired fueling profile.

neutral beam injection

Neutral beam injection was described in Section 9E. The required beam current for fueling a reactor is

$$I = eS_i V = 2eP_F/f_b W_{DT} \quad (A) . \tag{25E3}$$

For the example with P_F = 3.3 GW and f_b = 0.05, the required current is I = 8 kA. If the beam energy were 200 kV, the beam power would be 1.6 GW. This enormous power requirement illustrates the inefficiency of trying to fuel a reactor with neutral beam injection: it is difficult to achieve high Q = (fusion power)/(input power) if neutral beams are used for fueling. Two familiar examples of neutral beam fueling are the simple mirror attaining $Q \lesssim 1$ (Section 4E) and beam-driven toroidal reactors attaining $Q \lesssim 3$ (Section 4F). High Q could be attained with an ignited reactor using low-energy ($\sim$ 10 keV) neutral beam fueling, if shallow penetration were adequate. Neutral beam fueling is technologically feasible and demonstrated, but neutral beam injectors are complex and expensive.

cluster injection

The term *cluster* refers to a tiny droplet of solid hydrogen (H_2, D_2 or T_2) containing less than a million molecules. A cluster injection system involves the following components:

* *source*. Typical clusters of 10^3-10^6 molecules are formed by expanding H_2 in a nozzle cooled at 20-40 K. Beams with 100 Ampere-equivalent current have been produced.
* *ionizer*. The clusters are ionized and their size is adjusted to contain on the order of 100 molecules.
* *accelerator*. The clusters are accelerated up to MeV energies (1-100 keV/atom) by a high voltage electrode gap.
* *drift tube*. The accelerated clusters flow through a drift tube to the plasma confinement region.

The solid H_2 crystals have densities of 2.2×10^{28} molecules/m^3, mass densities of 73.6 kg/m^3, and intermolecular binding energies of about 10^{-2} eV (Van der Waals forces). The small ratio of charge to mass permits cluster injection across the magnetic field. Clusters may also be neutralized by passing them through a gas cell, as with neutral beam production. When the clusters impinge on the plasma, electron impact ionization increases their charge, and they split apart, because the Coulomb repulsion is greater than the intermolecular binding energy. Non-ionizing collisions with ions transfer kinetic energy to the crystal lattice, which is responsible for about 10-20 % of the total fragmentation. Surface evaporation also removes molecules, but at a slower rate than fragmentation.

The particle deposition per unit length in a uniform plasma is represented approximately by the expression

$$dN/dx \simeq C\beta^2 x \exp[-(\beta x)^{1.9}/1.9] \qquad (25E4)$$

with

$$\beta \equiv 5.8 \times 10^{-8} (Bn/E_0)^{\frac{1}{2}} \quad (m^{-1}) \quad , \qquad (25E5)$$

where x is the distance into the plasma (m), B = magnetic field (T), n = plasma density (m^{-3}), and E_0 = energy per unit mass of injected particles (eV/u), and u represents atomic mass units (for deuterium M = 2 u). Equation (25E4) is valid for $E_0 < 50$ keV/u. The maximum deposition occurs at $L_0 = 1/\beta$. For example, if $E_0 = 10^4$ eV/u, B = 4 T, and $n = 10^{20}$ m^{-3}, then $L_0 = 0.09$ m. If E_0 is small, then L_0 will be small and penetration will be poor. If E_0 is too large, then the injection power will be large and the reactor Q will be low, as with neutral beam injection.

pellet injection

production

Pellets of solid deuterium or tritium with diameters of 1-10 mm may be suitable for fueling reactors, if they can be accelerated to a velocity adequate for penetration. Solid hydrogen pellets may be produced by two methods. A jet of liquid hydrogen forced through a nozzle may be broken up into droplets, which freeze if they are injected into a vacuum. Alternately, solid hydrogen may be

extruded through an orifice and then cut with a laser beam or arc into tiny cylinders.

acceleration

A variety of means have been considered for acceleration of the pellets, including electrostatic accelerators, electromagnetic accelerators, ablation, centrifugal acceleration, and light gas guns.

It is difficult to get the pellets to hold a large electrostatic charge without breaking apart, because of the very low strength of solid hydrogen. Very high voltages (>10 MV) and long accelerators would be required to accelerate 1 mm pellets up to the required velocities (several km/s), so electrostatic accelerators appear to be impractical.

Electromagnetic accelerators have been proposed to accelerate a sabot (carrier) holding a pellet. At the end of the accelerator the carrier would be separated from the pellet. The pellet would go into the plasma and the carrier would be caught. Accelerators, like rail guns (Section 17H), could operate with acceptable lengths (<100 m), but have not been developed for pellet fueling.

A laser or electron beam incident on one side of a pellet could ablate away part of the pellet surface, accelerating the pellet away from the beam. The ablation must be done gradually, to avoid shock waves which would fracture the pellet. However, in laser fusion experiments it has been observed that when a pellet is illuminated by a single laser, a spherical cloud quickly surrounds the pellet, ablating it on all sides so that acceleration away from the beam is impeded.

A pellet may be accelerated by placing it in a rotating arm, like throwing a baseball. The pellet velocity attainable is ultimately limited by the strengths of the arm and pellet to less than 5 km/s, and the velocities attained are less than 1 km/s.

Light gas guns have accelerated two-gram pellets up to velocities of 12 km/s, but the pellets were not solid hydrogen, which is more fragile. Velocities over 1 km/s have been attained with solid hydrogen pellets by Milora and Foster (1979). It is difficult for such guns to attain high pulse repetition rates, however.

interaction with plasma

When a pellet is injected into a plasma, the outer surface of the pellet is ablated away, forming a large cloud of neutral gas around the pellet. The radius of the cloud may be up to 100 times as large as the radius of the pellet. The outer edge of the cloud is ionized and heated by the plasma, and heat transported to the pellet continues to ablate its surface as it penetrates into the plasma. This neutral gas shielding permits the pellet to penetrate much farther into the plasma than it would if the plasma interacted directly with the pellet surface. The plasma at the outer edge of the gas cloud may also distort the local magnetic field, providing further shielding. Electrons hitting the pellet could charge it up negatively to repel other electrons, but the attainable pellet voltage is probably much less than the surrounding plasma electron temperature, so electrostatic self-shielding is probably a small effect.

Let f be the ratio of the number of atoms in the pellet to the number of ions in the plasma. Then for a spherical pellet

$$f = \frac{(4/3)\pi r_p^3 n_s}{\langle n \rangle V} \qquad (25E6)$$

where r_p is the pellet radius (m), n_s is the atomic density of the pellet (m^{-3}), $\langle n \rangle$ is the volume-average plasma density (m^{-3}) and V is the plasma volume (m^3). For solid hydrogen, $n_s = 4.4 \times 10^{28}$ m^{-3}. Values of $f \gtrsim 1$ may disrupt plasma confinement, so values of $f \sim 0.1$-0.5 are likely to be used. Smaller values of f would correspond to small r_p, which would not penetrate well into the plasma.

Assuming $n \propto [1 - (r/a)^2]$ and $T_e \propto [1 - (r/a)^2]^2$ a neutral gas shielding model of pellet lifetime gives the following estimate of the velocity required to penetrate a distance ℓ (measured from the plasma edge) into a plasma with radius a (m):

$$u = aM^{-1/3}(fV)^{-5/9}\langle n \rangle^{-2/9}\langle T_e \rangle^{1/6} G[\langle T_e \rangle, (\ell/a)] \quad \text{(m/s)} \quad , \qquad (25E7)$$

where M = molecular weight of fuel (u) (for D_2, M = 4), $\langle T_e \rangle$ is the volume-averaged electron temperature (eV), and the function G is plotted in Fig. 25E1. If $(\ell/a) = 0.2$, the pellet is ablated away by the time it reaches $(r/a) = 0.8$. For $(\ell/a) \gtrsim 0.5$, the following approximate equation is valid

$$u \simeq 4100\, a(fV)^{-5/9} M^{-1/3} \langle n \rangle^{-2/9} \langle T_e \rangle^{1.7} (\ell/a)^3 \quad \text{(m/s)} \qquad (25E8)$$

EXAMPLE PROBLEM 25E1

Deuterium pellets are injected into a plasma with a = 1.3 m, $\langle n \rangle = 10^{20}$ m^{-3}, V = 300 m^3, $\langle T_e \rangle$ = 10 keV. If f = 0.3 and penetration to (r/a) = 0.7 is desired, what is the required pellet velocity, according to the neutral gas shielding model?

For this case, $(\ell/a) = 0.3$, and $G = 8 \times 10^7$. From Eq. (25E7), we find u = 900 m/s. The approximate Eq. (25E8) is not valid, and would give an answer almost twice as large.

Solid hydrogen pellets have been injected into some tokamaks with $\langle n \rangle \sim 10^{19} m^{-3}$, $\langle T_e \rangle \sim 300$ eV. Pellet lifetimes, typically hundreds of microseconds, were in fair agreement with predictions of this neutral gas shielding model.

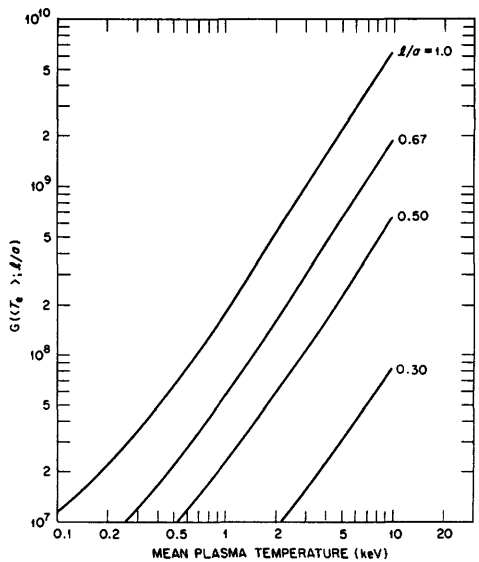

Fig. 25E1. Variation of G with $\langle T_e \rangle$ for various (ℓ/a). From S.L. Milora and C.A. Foster, IEEE Transactions on Plasma Science PS-6, 578-592 (1978), Fig. 6. © *1978 IEEE.*

summary

The main problem with all fueling methods is attaining adequate penetration into a reactor plasma. It is not yet clear how much penetration is

necessary. Penetration into the outer 10-20 % of the plasma may prove adequate if transport processes move the fuel rapidly inwards without disrupting confinement. Fueling with high-energy neutral beams would result in low Q values. Pellet injection has been done successfully in low-pressure plasmas. The fueling situation will be clarified by experiments on large tokamaks.

Problems

1. A steady-state reactor with aluminum walls has n_α/n_i = 12 %, plasma edge temperature = 60 eV, and R_Z = 0.2 for aluminum. Assuming equal particle confinement times for all species, estimate the fractional concentration of aluminum and the reduction of fusion power density. Is this aluminum concentration enough to prevent ignition at 10 keV?

2. In Eq. (25A7) we assumed that all alphas were reflected (R_α = 1) so that the last term of Eq. (25A5) dropped out. In this problem we will consider the general case ($R_\alpha < 1$). Let $\theta \equiv (1-R_\alpha)t/\tau_\alpha$, and $A \equiv n_0\langle\sigma v\rangle_{DT}\tau_\alpha/4(1-R_\alpha)$. Show that Eq. (25A5) may be written

$$df_\alpha/d\theta = A(1 - 3f_\alpha/2)^2 - f_\alpha \quad .$$

Assuming that $f_\alpha(0) = 0$, show that

$$f_\alpha(\theta) = \frac{3A+1}{4.5A} - \frac{(6A+1)^{\frac{1}{2}}}{4.5A}\tanh\left[\tanh^{-1}\frac{3A+1}{(6A+1)^{\frac{1}{2}}} + \frac{(6A+1)^{\frac{1}{2}}\theta}{2}\right]$$

Estimate f_α at t = 30 s for a reactor with R_α = 0.9, $n_0 = 10^{20}$ m^{-3}, T = 15 keV, τ_α = 5 s.

Take the limit as $\theta \to \infty$ to find the equilibrium concentration f_∞, and evaluate f_∞ for the above case.

3. A deuterium plasma has the following parameters at the separatrix: L = 120 m, $n = 10^{19}$ m^{-3}, T_i = 2 keV, T_e = 1 keV, B = 5 T. If x_w = 0.6 m and $n_n = 1.3\times10^{17}$ m^{-3} estimate the plasma thickness in the scrape-off region.

4. As n_n is increased to large values, λ^2 changes sign and becomes negative. How does the solution of Eq. (25B5) change? What does the new solution look like? What is happening physically in this case?

5. A divertor target region is to be kept at p = 0.2 Pa, and its walls are at 700 K. Two-thirds of the transported energy is carried by ions, and the average energy per ion is to be 60 eV. The divertor target area is 130 m^2, and 300 MW of heat flow into the divertor. Estimate the required vacuum pumping speed and cryopanel area.

6. The steady-state continuity equation for impurities in the scrape-off region may be written

$$dn_Z/dx \simeq - b(x)n_Z \quad ,$$

$$b(x) \equiv n(x)\langle\sigma v\rangle_{tot}/u$$

where $\langle\sigma v\rangle_{tot}$ is the total rate coefficient for attenuation of impurities by ionization and charge exchange, n is the plasma density, n_z is the impurity density, and u is the impurity velocity. (Since the impurities are flowing from the wall in the -x direction, $u < 0$ and $b < 0$.) Assuming that the rate coefficients are constant in the scrape-off region and that the density follows Eq. (25B7), we can write $b \simeq b_0 e^{-x/\lambda}$. Show that the fraction of impurity atoms penetrating to the separatrix (x = 0) is

$$\frac{n_z(0)}{n_{zw}} \simeq \exp\{\lambda b_0[1 - \exp(-x_w/\lambda)]\}$$

where n_{zw} is the impurity concentration at the wall. Evaluate $n_z(0)/n_{zw}$ for the case of 5 eV Be atoms with $x_w = 0.15$ m, $\lambda = 0.07$ m, $n_0 = 5\times10^{18}$ m^{-3}, and $\langle\sigma v\rangle_{tot} = 10^{-13}$ $m^3 s^{-1}$.

7. Assume that the average energy per particle in the scrape-off zone of Fig. 25D1 is constant, so that the particle flux is proportional to the energy flux. If x_L is the position of the leading edge of the limiter, show that the approximate fraction of particles hitting the limiter on the plasma side is $a_p \simeq 1 - \exp(-x_L/\lambda)$. If $q_0 = 7$ MW/m^2 at the limiter boundary and $q = 4$ MW/m^2 at the leading edge, how large is a_p? How large is $(a_v + a_w)$? Assuming $a_v = a_w$, $R_L = R_w = 0.95$, and $R_v = 0.5$, estimate R_α for this case. If $\tau_\alpha = \tau_i$ and $f_b = 0.05$, estimate the equilibrium value of f_α.

8. Show that the maximum value of $Q = P_F/P_{in}$ for a reactor fueled by neutral beam injection is $Q \leq f_b W_{DT}/2W_0$. Evaluate this expression for a case with edge-fueling by 80 keV neutral beams and burnup fraction of 4 %.

9. If the pellet of Example Problem 25E1 had $u = 10^4$ m/s, how far could it penetrate? What is its radius?

Bibliography

impurities

V. A. Abramov, "Impurities in tokamaks: sources, effects and control", *Nuclear Fusion 20*, 225-229 (1980) (report on conference).

A. Gibson, "Impurity behavior in real and simulated tokamak plasmas", *Journal of Nuclear Materials 76 & 77*, 92-102 (1978).

R. J. Hawryluk, S. Suckewer, and S. P. Hirschman, "Low-Z impurity transport in tokamaks", *Nuclear Fusion 19*, 607-632 (1979).

T. S. Hsu, Editor, "Tokamak impurity report", DOE/ET-0001 (1977).

R. V. Jensen, D. E. Post, and D. L. Jassby, "Critical impurity concentrations for power multiplication in beam-heated toroidal fusion reactors", *Nuclear Science and Engineering 65*, 282-289 (1978).

E. S. Marmar, J. E. Rice, and S. L. Allen, "Confinement of injected silicon in the alcator-A tokamak", *Physical Review Letters 45*, 2025-202c (1980).

divertors

A. V. Bazaeva, V. E. Bykov, A. V. Georgievskij, I. N. Golovin, A. O. Kaminskij, L. V. Mikhajlovskaya, V. G. Peletminskaya, and V. N. Pyatov, "Magnetic configuration of a poloidal divertor tokamak", *Nuclear Fusion 20*, 83-90 (1980).

P. J. Harbour and M. F. A. Harrison, "An analysis of the exhaust of a fusion reactor to a divertor target by collisionless processes", *Nuclear Fusion 19*, 695-701 (1979).

A. T. Mense and G. A. Emmert, "Simulation of poloidal divertors in one-dimensional tokamak transport codes", *Nuclear Fusion 19*, 361-372 (1979).

A. T. Mense, G. A. Emmert, and J. D. Callen, "Mirror microinstabilities in divertors", *Nuclear Fusion 15*, 703-707 (1975).

Y. Seki, Y. Shimomura, K. Maki, M. Azumi, and T. Takizuka, "Numerical calculations of helium ash enrichment and exhaust by a simple divertor", *Nuclear Fusion 20*, 1213-1226 (1980).

S. Sengoku, M. Azumi, Y. Matsumoto, H. Maeda, and Y. Shimomura, "Effects of metal impurity re-cycling in the scrape-off plasma of a large tokamak", *Nuclear Fusion 19*, 1327-1332 (1979).

Y. Shimomura and H. Maeda, "Divertor experiments for controlling plasma-wall interactions", *Journal of Nuclear Materials 76 & 77*, 45-48 (1978).

gas blankets

D. Anderson, M. Lisak, and H. Wilhelmsson, "Anomalous heat transport through a cold turbulent plasma blanket", *Nuclear Fusion 19*, 1522-1528 (1979).

B. Lehnert, "Stability of plasmas penetrated by neutral gas", *Nuclear Fusion 13*, 781-791 (1973).

J. H. Marable and E. M. Oblow, "The application of neutron transport codes to the transport of neutrals in plasmas", *Nuclear Science and Engineering 61*, 90-97 (1976).

J. A. Markvoort, "The effect of thermo-electric forces on the density profiles in a thermonuclear plasma surrounded by a cold blanket", *Nuclear Fusion 19*, 401-497 (1979).

F. C. Schüller, W. J. Goedheer, L. Th. M. Ornstein, F. Englemann, and T. J. Schep, "Cold blanket studies in Jutphaas", Proceedings of the Fusion Fueling Workshop, CONF-771129 (1978), pp. 75-82.

G. K. Verboom and J. Rem, "The temperature profile in a thermonuclear reactor", *Nuclear Fusion 13*, 69-79 (1973).

other impurity control techniques

J. N. Brooks, "The impurity control methods for tokamak fusion power reactors", Proceedings of the Third Topical Meeting on the Technology of Controlled Nuclear Fusion, CONF-780508 (1978), Volume 2, pp. 873-882.

J. N. Brooks, C. C. Baker, H. C. Stevens, and C. A. Trachsel, "The impurity control system for the STARFIRE commercial tokamak", ANL/FPP/TM-127 (1979), pp. 12-15.

K. H. Burrell, S. K. Wong, and T. Amano, "Analysis of the impurity flow reversal experiment", *Nuclear Fusion 20,* 1021-1036 (1981).

P. B. Parks, K. H. Burrell and S. K. Wong, "Impurity transport in tokamak plasmas containing momemtum sources", *Nuclear Fusion 20,* 27-34 (1980).

W. M. Stacey, Jr., and D. J. Sigmar, "Impurity control by neutral-beam injection", *Nuclear Fusion 19,* 1665-1673 (1979).

fueling

C. T. Chang, L. W. Jorgensen, P. Nielsen, and L. L. Lengyel, "The feasibility of pellet re-fueling of a fusion reactor", *Nuclear Fusion 20,* 1021-1036 (1980).

F. S. Felber, "Fueling moving ring field-reversed mirror reactor plasmas", *Nuclear Technology 50,* 119-123 (1980).

W. A. Houlberg, H. C. Howe, and S. E. Attenberger, "Deuterium and tritium fueling in an ETF/INTOR plasma with divertor", ORNL/TM-7124 (1980).

A. T. Mense, W. A. Houlberg, S. E. Attenberger, and S. L. Milora, "Effects of fueling profiles on plasma transport", *Nuclear Fusion 19,* 1473-1489 (1979).

S. L. Milora, "Review of Pellet Fueling", *Journal of Fusion Energy 1,* 15-48 (1981).

S. L. Milora and C. A. Foster, "A revised neutral gas shielding model for pellet-plasma interactions", *IEEE Transactions on Plasma Science PS-6,* 578-592 (1978).

S. L. Milora and C. A. Foster, "Pneumatic hydrogen pellet injection system for the ISX tokamak", *Review of Scientific Instruments 50,* 482-487 (1979).

P. B. Parks, "Magnetic field distortion near an ablating hydrogen pellet", *Nuclear Fusion 20,* 311-320 (1980).

R. Prater, R. Stambaugh, J. Wesley, D. Bhadra, K. Matsuda, and L. Rovner, "Fusion experimental power reactor (EPR) design tasks", EPRI AP-1347 (1980),

"Proceedings of the Fusion Fueling Workshop", CONF-771129 (1978), (contains papers on plasma guns, cluster beams, neutral beams, gas blankets, and pellet injection).

CHAPTER 26
BLANKETS

26A. Introduction

energy conversion efficiencies

Since the revenues generated by a power plant are proportional to its efficiency, it is important to attain high efficiency. Plants with high efficiency also discharge less "waste heat" to the environment than those with lower efficiencies. The waste heat rejected to the environment by a power plant is equal to $(1 - \eta)P_{th}$, where η is the plant efficiency (Chapter 4) and P_{th} is the thermal power output.

Heat engines are the most likely means for conversion of fusion power into electricity. A fraction of the charged particle energy may be directly converted into electricity (Section 26G), but the majority of the fusion power will be extracted as thermal energy. Magnetohydrodynamic (MHD) generators, thermoelectric convertors, and thermoionic convertors are not economically competitive with heat engines.

A simplified diagram of a conventional steam cycle coupled to a fusion reactor blanket is shown in Fig. 26A1. The primary coolant may be liquid metal, helium gas, pressurized water, or molten salt. Alternatively, a closed cycle helium turbine may be used, as illustrated in Fig. 26A2. The helium may be heated directly in the blanket or indirectly by a liquid metal primary coolant in an intermediate heat exchanger.

The "thermal efficiency" of Chapter 4 is the product of heat engine efficiency η_{he} and generator efficiency η_g:

$$\eta_t = \eta_{he}\eta_g \qquad (26A1)$$

Generators convert mechanical energy into electricity with efficiencies $\eta_g \simeq 98$ %. Heat engines (like turbines)

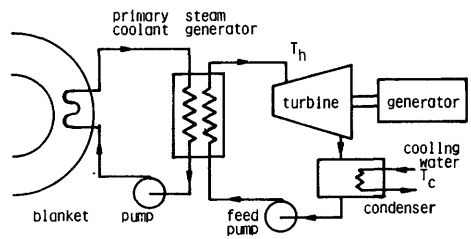

Fig. 26A1. A conventional steam cycle coupled to a fusion reactor blanket.

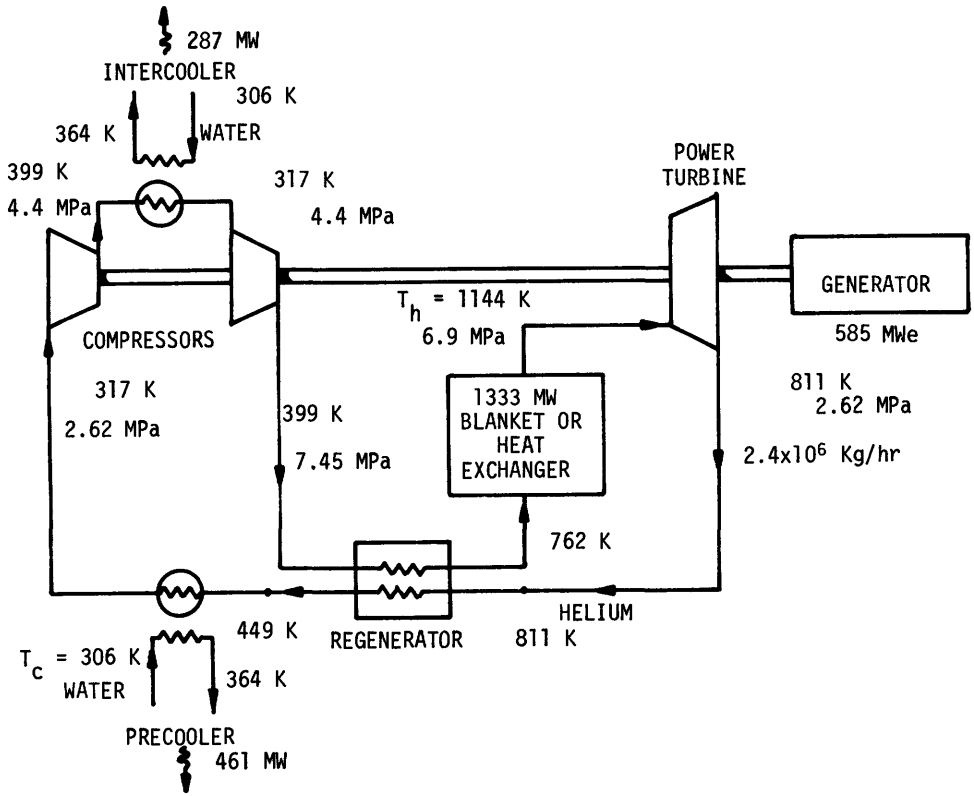

Fig. 26A2. A closed cycle helium gas turbine system for converting thermal energy into electricity. The intercooler and regenerator improve the cycle efficiency to 43.9 %. Adapted from B. Badger et al, "UWMAK-III, a noncircular tokamak power reactor design", EPRI ER-368 (1976), Fig. 20, p. 10-43.

convert thermal energy into mechanical energy with efficiencies less than the Carnot efficiency

$$\eta_{he} < \eta_c \equiv 1 - T_c/T_h \quad , \tag{26A2}$$

where T_h is the "hot" temperature of the cycle (the turbine inlet temperature) and T_c is the "cold" temperature (the cooling water temperature). Conventional steam cycles attain $\eta_t \sim 0.64\ \eta_c$. Gas turbines operate at much higher T_h, but attain smaller fractions of η_c, as illustrated in Fig. 26A3.

Helium gas turbine systems require use of high-temperature materials in order to attain high efficiencies. At $T \gtrsim 900$ K, minute quantities of oxygen in the helium rapidly attack metals like vanadium and niobium. A molybdenum alloy, TZM, would probably be compatible with helium at higher temperatures, with operating lifetimes perhaps as long as 2 years at 1270 K. High heat rejection temperatures T_c in some gas turbine cycles would reduce cooling tower costs, and the absence

Table 26A1. Blanket design problems. Numbers in parentheses refer to chapters or sections of this book.

materials limitations
- structure and special purpose materials (24)
- breeding materials and coolants (26B)

heat removal
- heat transfer (26C)
- coolant tube stresses (26D)
- pressure drop, pumping power (26E)
- coolant channel configuration (26F)

neutronics (27)
- breeding
- energy multiplication
- radiation attenuation

environment and economics (28)
- tritium
- structure activation
- fire and other hazards
- materials resource limitations
- costs

ease of maintenance (18B)

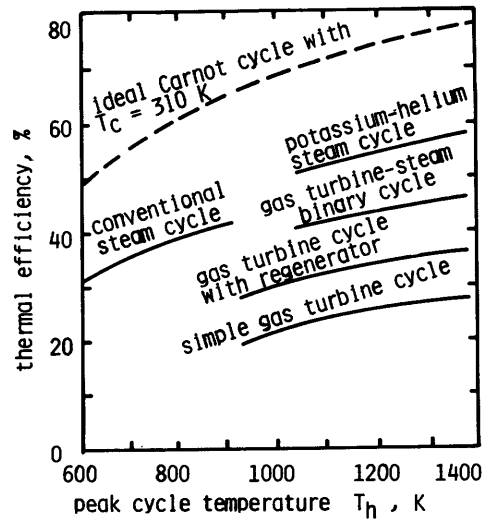

Fig. 26A3. Approximate efficiencies attainable with various thermal conversion systems. Based on data of A. P. Fraas, ORNL-TM-4999 (1975), Fig. 16.

of a steam cycle would remove a major pathway of tritium leakage. The UWMAK-III gas turbine system efficiency is considerably above the "gas turbine cycle with regenerator" curve of Fig. 26A3, due to special features, such as intercooling.

The "gas turbine-steam binary cycle" means that the precooler of Fig. 26A2 is replaced by a steam generator driving a steam turbine, as in Fig. 26A1. Large potassium vapor turbines have not yet been developed, but offer potentially high efficiency when coupled with steam cycles.

In general, high peak temperatures result in higher energy conversion efficiencies. Therefore, it is desirable to use high coolant temperatures in the blanket, if materials limitations permit. Calculation of heat engine efficiencies is described by El-Wakil (1978b), and fusion energy conversion systems are described by Miley (1976).

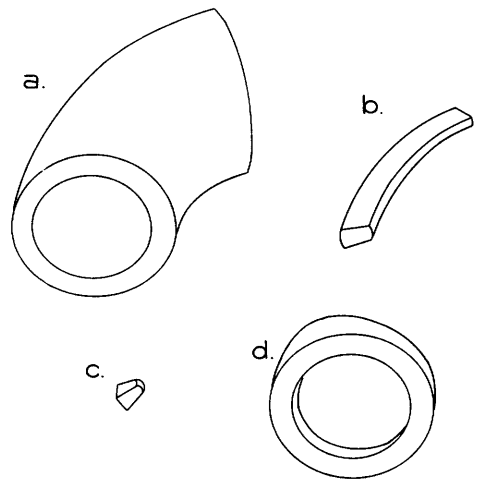

Fig. 26A4. Shapes of possible blanket modules and segments for a toroidal fusion reactor. From A. P. Fraas, ORNL-TM-4999 (1975), Fig. 20.

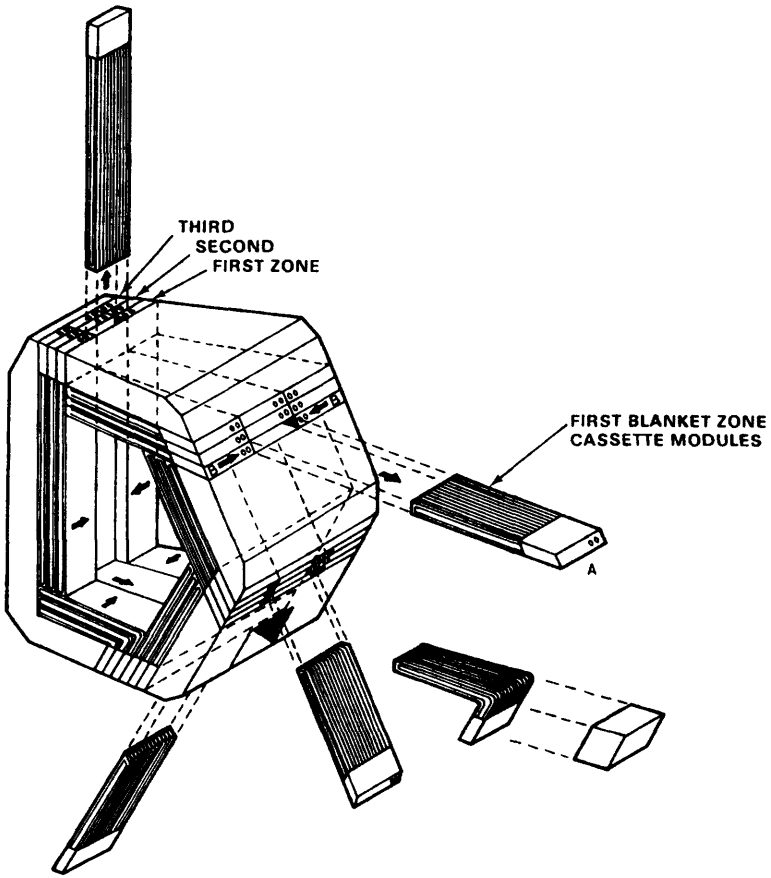

Fig. 26A5. Cassette blanket removal. First the five middle cassettes (A) would be removed. Next, the outer cassettes (B) are moved sideways to the open space, and then outwards. From D. Steiner et al, "ORNL Fusion Power Demonstration Study: Interim Report", ORNL/TM-5813 (1977).

blanket design problems

Some problem areas of fusion reactor blanket design are listed in Table 26A1. Materials problems limit the attainable values of coolant temperature and T_h. Since the structure will become radioactive, remote maintenance is necessary, and blanket design will aim at simplifying disassembly, repair, and reassembly procedures.

Some possible shapes for blanket modules are illustrated in Fig. 26A4. The large segment (a) would be difficult to move in and out of toroidal field coils, and very heavy. Longitudinal segments like (b) would reduce pumping power of liquid metal coolants, allowing the coolant to flow mainly along magnetic field lines, but they would be difficult to remove and reassemble. Small segments like (c) would be easy to remove and replace, but it would be time-consuming and expensive to replace many of them. Segments like (d), or slightly larger, are the most popular shape for blanket modules. A cassette blanket

module, Fig. 26A5, permits easy replacement of the first blanket zone (nearest) the plasma). Other module shapes were illustrated in Chapter 18.

26B. Blanket Materials

Some potential fusion reactor blanket materials are listed in Table 26B1. Not all combinations of breeding materials, structural materials, and coolants are compatible, however. For example, liquid lithium reacts violently with water, so use of water coolant with a liquid lithium blanket would be hazardous. The total thickness of the blanket plus shield is typically 1 - 2 m.

neutron multipliers

The Be(n,2n) reaction has high cross sections and can significantly increase the supply of neutrons to the blanket. However, Be has resource limitations, high helium generation rates, and toxicity. Lead has lower (n,2n) cross sections.

Table 26B1. Some tritium breeding materials, structural materials, and coolants considered for use in fusion reactor blankets.

neutron multipliers
- Be
- Pb

breeding materials
- Li
- $Li_{17}Pb_{83}$ eutectic
- $Li_{62}Pb_{38}$ eutectic
- Li_2O
- $LiAlO_2$
- Li_2BeF_4 (FLIBE)

structural materials
- 316 SS
- Nb-1%Zr
- Ni alloys & superalloys
- V alloys
- Ti alloys
- Mo alloys
- ferritic steel

coolants
- liquid metals
  - Li
  - Na
  - K
- water
- helium
- molten salts
- flowing Li_2O particles

breeding materials

* *lithium.* Natural lithium (7.5 % ^6Li, 92.5 % ^7Li) produces tritium by fast neutron interactions with ^7Li and by thermal neutron capture in ^6Li. Lithium has melting and boiling temperatures T_m = 450 K and T_b = 1600 K. About 5 % expansion occurs during melting.

Breeding ratios up to 1.6 (tritium atoms/incident neutron) can be attained, depending on the amount of structural material and the thickness of the blanket (Chapter 27). Tritium may be continuously removed from a slowly circulating lithium blanket. (Methods of tritium processing will be discussed in Chapter 28.)

In order to avoid excessive corrosion and mass transfer problems with lithium, path A alloys (stainless steels) will be limited to temperatures $T \lesssim 770$ K, and path B alloys (higher-strength Fe-Ni-Cr alloys) will have lower temperature limits. Path C alloys (Mo, V, Nb, Zr, Ti) may be able to operate with lithium at temperatures over 1100 K, but concentrations of impurities, such as oxygen, must be very low. Aluminum alloys are incompatible with lithium.

A diagram of melting temperature vs. atomic % lithium in Li-Pb mixtures is shown in Fig. 26B1. At T $\gtrsim$ 770 K, Pb attacks Fe-Cr-Ni alloys via solution corrosion.

* *solid lithium compounds.* Solid lithium compounds available include Li-Pb mixtures, Li_2O, and others. Breeding ratios up to 1.6 can be attained by Li-Pb mixtures, and up to 1.4 with Li_2O.

Lithium oxide is a solid compound with melting temperature ($\sim$ 1840 K), molecular weight 0.02988 kg/mole, and mass density 2013 kg/m^3. Solid lithium compounds have low thermal conductivities, but they are much less corrosive than pure lithium, and may operate at temperatures of 700-950 K, depending on structural materials and coolant.

Tritium may be removed by flowing helium gas, or it may be allowed to build up until the breeding compound is removed from the blanket and reprocessed.

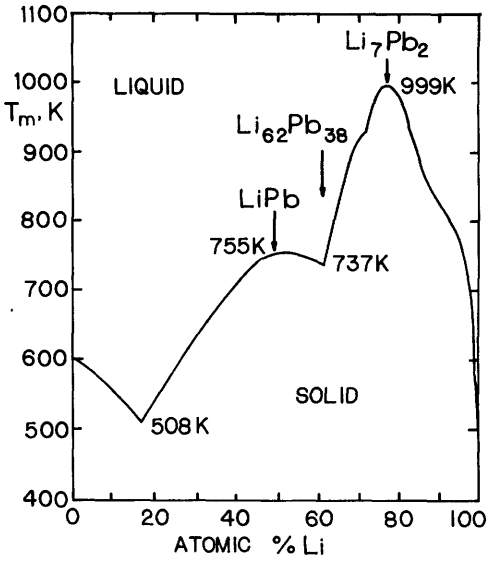

Fig. 26B1. Melting temperature of Li-Pb mixtures and compounds as a function of atomic percent lithium. Based on B. Badger et al, "NUWMAK, a tokamak reactor design study", UWFDM-330 (1979), Fig. VII-B-1, p. VII-6.

* *molten salts.* The molten salt LiF-BeF_2 (called "FLIBE") has a high heat capacity (2.4 J/kg-K at 810 K), but a comparatively low thermal conductivity (1.0 W/m-K at 810 K). Its melting temperature is over 637 K, and varies with composition. This salt has good chemical stability and resistance to radiation damage in the liquid state. It is compatible with Mo, Nb, and Ni alloys at all temperatures where their strength is adequate (up to about 970 K). It may be used with 316 SS up to 920 K, if a corrosion control chemical is added. The concentration of tritium fluoride (TF) must also be controlled. The breeding ratio of FLIBE with a PE-16 structure (an alloy of Ni-Fe-Cr) was estimated to be less than 1.07. Since many neutrons are lost out various ports and do not enter the blanket, this breeding ratio is only marginally satisfactory. The main problems associated with FLIBE are its high melting point, low thermal conductivity, and low breeding ratio.

* *reactors with no tritium breeding.* If the catalyzed DD fuel cycle (Chapters 1 and 4) is used, tritium breeding materials are unnecessary, and blanket design is considerably simplified.

coolants

* *liquid metals.* Liquid metals have high thermal conductivities and heat capacities. They can carry high heat fluxes at high temperatures and low pressures.

The use of lithium both as breeding material and blanket is attractive in its simplicity, but causes a number of problems: (1) Lithium is chemically very active and poses compatibility problems (discussed above). (2) The heat transfer capability of lithium is reduced by magnetic fields. (3) high pumping

powers may be needed to move lithium coolant across the magnetic field (Section 26F). (4) The resultant high pressures create high stresses in the coolant ducts. (Section 26E.) These problems are alleviated by the use of Li_{17} Pb_{83} in large tubes in the WITAMIR-I design (Section 18D).

If K were boiled in the blanket, then K vapor could easily flow out through the magnetic field to complete the cycle without additional MHD pressure drop. The latent heat of vaporization would help maintain a constant temperature in the blanket. One boiling-K blanket design producing 1000 MWth required only about 2 MW of pumping power. If the pumping power and compatibility problems of liquid metals are resolved, they can be used as coolants with any of the breeding materials.

* *helium*. Helium coolant is compatible with many alloys, nonradioactive, unaffected by the magnetic field, is conducive to easy tritium extraction, and has a well-developed technology in the High-Temperature Gas-Cooled Reactor (HTGR) program. Pressures of about 5 MPa (50 atm) are needed to obtain good heat transfer properties, and about 5-10 MW/m^3 may be removed from the blanket by helium.

Impurities in the helium are inevitable: they may come from the breeding materials, steam generator, seals, etc. Trace amounts of oxygen are especially active. Path A and B alloys (austenitic stainless steels and nickel alloys) will probably be compatible with helium up to about 970 K, because of the protective oxide films formed on them. Path C alloys (refractory and reactive metals) may be limited to $T \lesssim 870$ K by oxygen attack.

Since helium has low thermal conductivity and heat capacity, high flow rates and large coolant ducts are necessary. Neutron streaming out the ducts is a shielding problem. Pumping powers for helium can be quite large, from 1 - 10 % of the reactor thermal power.

* *molten salts*. Because of their high boiling points and low vapor pressures, molten salt coolants can be contained at low pressures. Turbulent flow is required for effective heat removal. Molten salts are affected little by magnetic fields, but the small voltages developed by their motion may cause chemical breakdown of some compounds and increased corrosion problems. Some characteristics of various molten salt coolants are listed in Table 26B2.

"Heat Transfer Salt" (HTS) composed of 53 % KNO_3, 40 % $NaNO_2$ and 7 % $NaNO_3$ has been widely used for heat transport. It is compatible with Path A and B alloys from 420-810 K, but it is probably not compatible with Path C alloys. Hydroxides may be compatible with Ni and Mo alloys below 870 K, but in general they are very corrosive and unsuitable for blanket coolants. Chlorides are more corrosive than FLIBE, and corrosion data on carbonates are incomplete. Tritium removal would be feasible from chlorides and fluorides, but difficult from the other salts.

* *water*. A blanket may be cooled by pressurized water or by boiling water, as in PWR's and BWR's. A boiling-water blanket will be described in Section 26G. Water has excellent heat-transfer properties and low required pumping power. It is also a good neutron moderator. It is compatible with Path A and B alloys, but not with Path C alloys. Reactions with lithium would be hazardous. Compatibility with solid lithium compounds is uncertain. Tritium removal is difficult.

* *solid lithium oxide*. Flowing Li_2O particles might be used as both breeding material and coolant. Such a system would operate at low pressures, simplify structural design, and have easy tritium removal, but poor heat transfer.

Table 26B2. Features of some molten salt coolants. From "Special purpose materials", DOE/ET-0032/4 (1978), Table 3.B.3.

Type of salt	Melting Temperature K	Advantages	Disadvantages
KNO_3-$NaNO_3$-$NaNO_2$	410	Low melting point; inexpensive; compatible with stainless steel	Radiolytic decomposition; reaction with Li and C.
NaOH-KOH-LiOH	430	Low melting point; inexpensive; radiation stability	Corrosive; reaction with Li
Carbonates	670	Inexpensive; compatible with stainless steel	Radiolytic decomposition; reaction with Li; high melting point
LiF-BeF_2	730	Compatible with stainless steel; radiation stability; limited reaction with Li	High melting point; limited beryllium availability
Chlorides	370-720	Low melting point; radiation stability; limited reaction with Li; possibility of nonionic bonding	Corrosive

There is little experience in use of solid materials for heat transport. Water reacts with lithium to form lithium hydroxide, which is corrosive. Radiation stability of Li_2O is uncertain. If particles disintegrated or sintered together, the flow characteristics might be degraded. Electrostatic forces build up deposits that clog pipes. Uneven flow might result in voids developing in the blanket, with subsequent neutron leakage. At high velocities severe erosion occurs in bends.

Some properties of various coolants are listed in Table 26B3.

structural materials

The cyclic strain $\Delta\varepsilon$ required to cause failure at N_f cycles of fatigue may be represented approximately by an equation of the form

$$\Delta\varepsilon \simeq 3.5\ \varepsilon_f N_f^{-0.12} \qquad (26B1)$$

where ε_f varies with material and temperature. Values of ε_f for various materials at typical operating temperatures are given in Table 26B4, along with various other properties of interest.

Operating temperatures may be limited either by structural strength or by compatibility. Some operating temperature limits are given in Table 26B5.

26C. Heat Transfer Processes

radiation

A radiatively-cooled low-Z armor may be placed between the first wall and the plasma, to avoid plasma contamination by wall atoms. The armor may consist of ceramic or graphite tiles or a graphite curtain.

The armor will reach a temperature at which its cooling rate by infrared radiation to the first wall equals its heating rate from the plasma. Some heat is also reradiated from the first wall back to the armor. If the wall and armor are nearly flat and parallel, the net heat flow per m^2 from the armor to the wall is

$$q/A = \frac{\sigma(T_a^4 - T_w^4)}{\frac{1}{e_a} + \frac{1}{e_w} - 1} \quad (W/m^2) \quad , \tag{26C1}$$

where T_a and T_w are the armor and wall temperatures (K), e_a and e_w are their emissivities, and $\sigma = 5.670 \times 10^{-8}$ W/m^2K^4 is the Stephan-Boltzmann constant. Spectral emissivities of various materials are given in Table 26C1.

Table 26B3. Some properties of coolants. From G. H. Miley, Fusion Energy Conversion, American Nuclear Society, LaGrange Park, IL, 1976, Table 5.2.

	Lithium	Sodium	Potassium	H_2O (1 atm)	Flibe	Helium (60 atm)
Temperature, T (K)	1100	1000	1000	373	1200	1200
Density, ρ_m (kg/m^3)	450	780	676	960	1840	2.5
Viscosity, μ (Pa-s)	2.5×10^{-4}	1.8×10^{-4}	1.36×10^{-4}	2.84×10^{-4}	3×10^{-3}	5×10^{-5}
Kinematic Viscosity, $\nu(\frac{m^2}{s})$	5.5×10^{-7}	2.34×10^{-11}	2.01×10^{-7}	2.96×10^{-7}	1.6×10^{-6}	2.0×10^{-8}
Specific Heat, c_p (J/kg-K)	4.2×10^{3}	1.3×10^{3}	1.1×10^{3}	4.19×10^{3}	2.4×10^{3}	5.2×10^{3}
Thermal Conductivity k(W/m-K)	65	59	34	0.7	1.0	0.4
Electrical Conductivity, σ (A/V-m)	2×10^{6}	5×10^{6}	1.8×10^{6}	low	3.94×10^{2}	low
Prandtl Number, $Pr \equiv \frac{\mu c_P}{k}$	0.017	0.0040	0.0045	1.7	7.2	0.65

*Table 26B4. Properties of structural alloys. *(Thermal conductivity is for Al-2024, not Al-2219. Electrical resistivities are for 321 SS and V, not 316 SS and V-20Ti). From "Assessment of titanium for use in the 1st wall/ blanket structure of fusion power reactors", EPRI ER-386 (1977), Tables 1, 2, 4, 5.*

	Titanium		Aluminum	Stainless Steel	Vanadium	Niobium	Molybdenum
	Ti-6Al-4V	Ti-6242	2219	316	V-20Ti	Nb-1Zr	TZM
atomic weight, g/mole	45.9	47.6	29.3	∿56	50.3	92.9	95.95
melting temperature, K	1941	1922	930	∿1700	2170	2920	2890
mass density, kg/m^3	4400	4540	2830	8030	5800	8600	10200
atomic density, 10^{28} atoms/m^3	5.8	5.8	5.8	8.6	6.9	5.6	6.4
Electrical Resistivity ($\mu\Omega$ - m)							
370 K	1.74	1.79	0.039	0.78*	0.24*	0.17	0.08
670 K	1.86	2.20	0.008	1.00*	0.44*	0.31	0.17
1070 K	1.84	1.98	--	1.22*	0.66*	0.43	0.28
Thermal Conductivity W/m•K							
370 K	8	8	152*	18	20	43	115
670 K	12	12	181*	22	25	48	105
1070 K	16	16	-	25	30	56	98
Coefficient of Thermal Expansion 10^{-6} K^{-1}							
370 K	9.1	7.9	22.4	16.8	8.5	7	5.2
670 K	10	9.3	25.5	18.1	9.6	7.4	5.8
1070 K	10.4	10.2	-	19.2	10.4	7.8	6.2
Heat Capacity J/kg•K							
370 K	543.4	480.7	961.4	459.8	∿502	271.7	668.8
670 K	668.8	647.9	1128.6	543.4	∿560	284.2	710.6
1070 K	877.8	1011.6	--	627	∿643	301	794.2
Fatigue Strain Parameter ε_f	0.74	0.79	0.38	0.37	0.57	0.36	0.28
At temperature T(K)	670-770	670-770	470	670-770	670-770	1270	1270

Table 26B5. Maximum temperatures for compatibility of coolant and structure. From D. L. Kummer, "The relationship between material properties and the economics of fusion power", Journal of Nuclear Materials 85 & 86, 47-56 (1979). All temperatures are in Kelvin.

Working Fluid/ Coolant	Stainless Steel	Nickel Base	V	Nb	Ti
Liquid Lithium	770	720	1070	1270	1070
Helium	970	1020	<620	<620	670
Molten Salt	920	970	<570	<570	<570
H_2O	∿670	∿720	<570	<570	<620 (a)

(a) No pertinent data; number cited is based on similarity to zircaloy.

EXAMPLE PROBLEM 26C1

Given graphite armor with 0.63 MW/m² of power deposited on it and radiated to a plain steel wall at 770 K, what is the equilibrium temperature of the side of the graphite armor facing the wall?

From Table 26C1, $e_a \simeq 0.8$, $e_w \simeq 0.8$. Solving Eq. (26C1) for T_1, we find that $T_1 = 2030$ K. - [Taking $Q \sim 10$, Eq. (24C4) gives $P_n/A = 1.7$ MW/m², and Fig. 24J1 also yields $T_1 \simeq 2030$ K.] Thermal expansion could make armor support difficult.

Table 26C1. Approximate emissivities of smooth materials in the temperature range 300-1000 K. Emissivities increase with temperature and with surface roughness.

aluminum, unoxidized	0.1 ± 0.05
oxidized	0.3 ± 0.2
stainless steel, nickel alloys, refractory alloys	0.4 ± 0.3
graphite, ceramics, plain steel, heavily oxidized metals	0.8 ± 0.1

A similar equation applies to the case of other high temperature surfaces cooled by radiation, such as grids. However, Eq. 26C1 must be modified to include shape factors for surfaces which are not planar and parallel (Chapman, 1960).

convection

Convective heat transfer from a hot surface at temperature T_s to a fluid at temperature T_f is described by "Newton's Law of Cooling",

$$q/A = h\,(T_s - T_f) \qquad (W/m^2) \qquad (26C2)$$

where h is called the *convective heat transfer coefficient* or *film coefficient* and has units of W/m^2K. This equation does not accurately represent what is happening on a microscopic scale at the surface, but it permits evaluation of the net heat flow, provided that the correct value of h is used. Usually h is expressed in terms of dimensionless quantities called the *Reynolds Number* Re, the *Prandtl Number* Pr, and the *Nusselt number* Nu, defined as

$$Re \equiv Dv\rho_m/\mu \qquad (26C3)$$

Table 26C2. Various convective heat transfer correlations for turbulent flow ($Re \gtrsim 3000$). *For noncircular channels, replace D by* $D_e = \frac{4(\text{flow area})}{(\text{wetted perimeter})}$.

From M. M. El-Wakil, Nuclear Heat Transport, American Nuclear Society, 1978, Eqs. (9-22), (9-29), (9-40), (9-41), (10-2), (10-3), (10-4).

nonmetallic coolants (He, H_2O, molten salts, etc.)

$Nu = 0.023(Re)^{0.8}(Pr)^{0.4}$ where Re and Pr are evaluated at the fluid bulk temperature T_f.

For high velocity gas coolants with Mach number $M \gtrsim 1$, Re and Pr should be evaluated at the "adiabatic wall temperature", T_{fa}, defined by $T_{fa} \equiv T_f[1 + .45(\gamma-1)M^2]$ where $\gamma \sim 1.4$ is the ratio of specific heats.

liquid metal coolants

Constant heat flux along channel: $Nu = 7 + 0.025\ (RePr)^{0.8}$
Uniform wall temperature along channel: $Nu = 5 + 0.025\ (RePr)^{0.8}$

$$Pr \equiv c_p\mu/k \tag{26C4}$$

$$Nu \equiv hD/k \tag{26C5}$$

where D is a characteristic dimension, such as the diameter of a tube, v is the average fluid velocity, ρ_m and μ are the density and viscosity of the fluid, and c_p and k are its heat capacity and thermal conductivity. If Nu is known, h can be calculated from Eq. (26C5). Usually Nu is expressed as a function of Re and Pr by means of empirical equations or graphs, which are called *correlations*. The usual procedure for obtaining h is to calculate Re and Pr for the given fluid conditions (which depend on temperature), to use the appropriate correlation for Nu, and then to calculate h from Eq. (26C5). Some correlations of interest for fusion reactor blanket design are given in Table 26C2 and by Kays (1966).

conduction

Steady state heat flow by conduction through a region of several materials may be written in the form

$$q/A = \frac{\Delta T}{R_1 + R_2 + \ldots} \quad (W/m^2) \tag{26C6}$$

where ΔT is the overall temperature difference and R_1, R_2, ... are the thermal resistances of the various layers. This equation is analogous to the electrical circuit equation $I = \phi/R$, where I is the current, ϕ is the voltage, and R is the sum of the electrical resistances. For heat conduction, the thermal resistances may be calculated from the equations

$$R = r_q \ln(r_0/r_i)/k \qquad \text{cylindrical layer} \tag{26C7}$$

$$R = \Delta x/k \qquad \text{planar layer} \tag{26C8}$$

where r_q is the radius where q/A is to be found, r_0 and r_i are the outer and inner radii of the cylindrical layer, k is the thermal conductivity of the layer, and Δx is the thickness of a planar layer.

The electrical circuit analogy of Eq. (26C6) may be extended to include the thermal resistances of convection boundary films, which are given by

$R = r_q/hr$ cylindrical surface, with convection occurring at radius r (26C9)

$R = 1/h$ planar surface . (26C10)

EXAMPLE PROBLEM 26C2

Consider the case shown in Fig. 26C1, consisting of a double-layer tube with a hot fluid at temperature T_0 on the inside and a cool fluid at temperature T_4 on the outside. Find the heat flow q/A_3 (at radius r_3), and find T_2.

Here $r_q = r_3$. If L is a given length along the tube, $A_3 = 2\pi r_3 L$. Call the convective heat transfer coefficients h_{01} at r_1 and h_{34} at r_3, and call the thermal conductivities k_{12} between r_1 and r_2, and k_{23} between r_2 and r_3. The thermal resistances are given by Eqs. (26C7) and (26C9), so Eq. (26C6) becomes

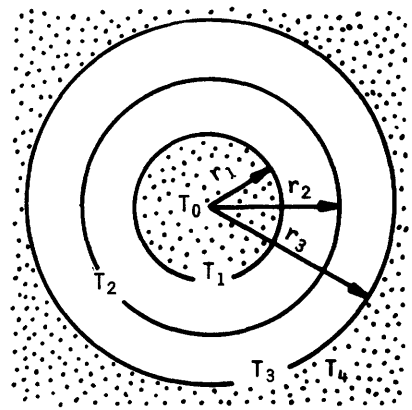

Fig. 26C1. A double-walled tube with inner radius r_1 and outer radius r_3 in contact with fluids at temperatures T_0 and T_4.

$$q/A_3 = \frac{T_0 - T_4}{(r_3/h_{01}r_1)+r_3\ln(r_2/r_1)/k_{12}+r_3\ln(r_3/r_2)/k_{23}+1/h_{34}} \quad (26C11)$$

The temperature at an intermediate point such as r_2 can now be found by rewriting Eq. (26C6) for heat transfer between T_0 and T_2, with $r_q = r_2$:

$$q/A_2 = \frac{T_0 - T_2}{(r_2/h_{01}r_1)+r_2\ln(r_2/r_1)/k_{12}} \quad (26C12)$$

where $A_2 = 2\pi r_2 L$. The value of q from Eq. (26C11) is used in this equation, and the resulting equation may be solved for T_2 :

$$T_2 = T_0 - \frac{r_3(T_0-T_4)[r_2/h_{01}r_1 + r_2\ln(r_2/r_1)/k_{12}]}{r_2[r_3/h_{01}r_1+r_3\ln(r_2/r_1)/k_{12}+r_3\ln(r_3/r_2)/k_{23}+1/h_{34}]} \quad (26C13)$$

The case of planar layers is simpler, because all the areas are equal, and the thermal resistances are simply $\Delta x/k$ or $1/h$.

26D. Coolant Tube Stresses

Coolant tubes will have stresses induced by gravity, coolant pressure, thermal gradients, and perhaps swelling and magnetic forces. Assuming that the tube thickness is much less than its radius ($t/r << 1$), the temperature drop across a tube wall with thickness t(m) is

$$\Delta T \simeq (q''t + q''' t^2/2)/k \quad (K), \tag{26D1}$$

where $q'' \equiv q/A$ is the heat flux through the surface of the tube (W/m^2), q''' is the heat deposited internally by nuclear radiation (W/m^3), and k is the thermal conductivity of the tube (W/m-k).

Stress is actually a tensor quantity with nine components. Here we will use a scalar stress approximation for simplicity. Combining Eq. (26D1) with Eq. (24C1), the thermal stress is

$$\sigma_{th} \simeq \frac{\alpha E}{2k(1-\nu)} [q''t + q''' t^2/2] = \frac{\sigma_y}{M} [q''t + q''' t^2/2] \quad (Pa) \quad , \tag{26D2}$$

where E is the modulus of elasticity (Pa), ν is the Poisson ratio, σ_y is the yield strength (Fig. 24D2), and M is the thermal stress parameter (Fig. 24C1).

The hoop stress due to internal pressure may be estimated from the equation

$$\sigma_h \simeq (pr/t)\left(1 + \frac{t}{2r}\right) \tag{26D3}$$

where p is the pressure difference across the tube wall (Pa), and r is the tube radius (m). [This is similar to Eq. (20C11) for the hoop stress in solenoid magnet coils.] If the pressure stress and thermal stress are dominant, then the total stress

$$\sigma \simeq \sigma_h + \sigma_{th} \tag{26D4}$$

The hoop stress becomes very large at small t, and the thermal stress is great at large t. There is a value of t for which the total stress is a minimum.

EXAMPLE PROBLEM 26D1

A stainless steel 316 tube with r = 2 cm, $q'' = 0.5$ MW/m^2, T ≃ 770 K, $E = 1.9\times10^{11}$ Pa, $\nu \simeq 0.3$, contains helium at 6 MPa(60 atm). Internal heat generation is negligible. How large is the minimum total stress?

From Table 26B4, $\alpha \simeq 18.4\times10^{-6}$/K, k ≃ 23 W/m-K, by interpolation. From Eqs. (26D2), and (26D3) we find

$$\sigma_{th} \simeq 5.4\times10^{10}t \quad (Pa)$$

$$\sigma_h \simeq 1.2\times10^{5}/t \quad (Pa) \quad .$$

These stresses and the total stress are plotted as functions of t in Fig. 26D1. The minimum total stress is about 160 MPa (24 ksi) at t = 1.5 mm. For SS 316 at 770 K, the stress should be kept below 100 MPa, so a redesign would be necessary. For example, a different structural material, having a better thermal stress parameter (Fig. 24C1) could be used instead of SS 316, or q'' could be reduced.

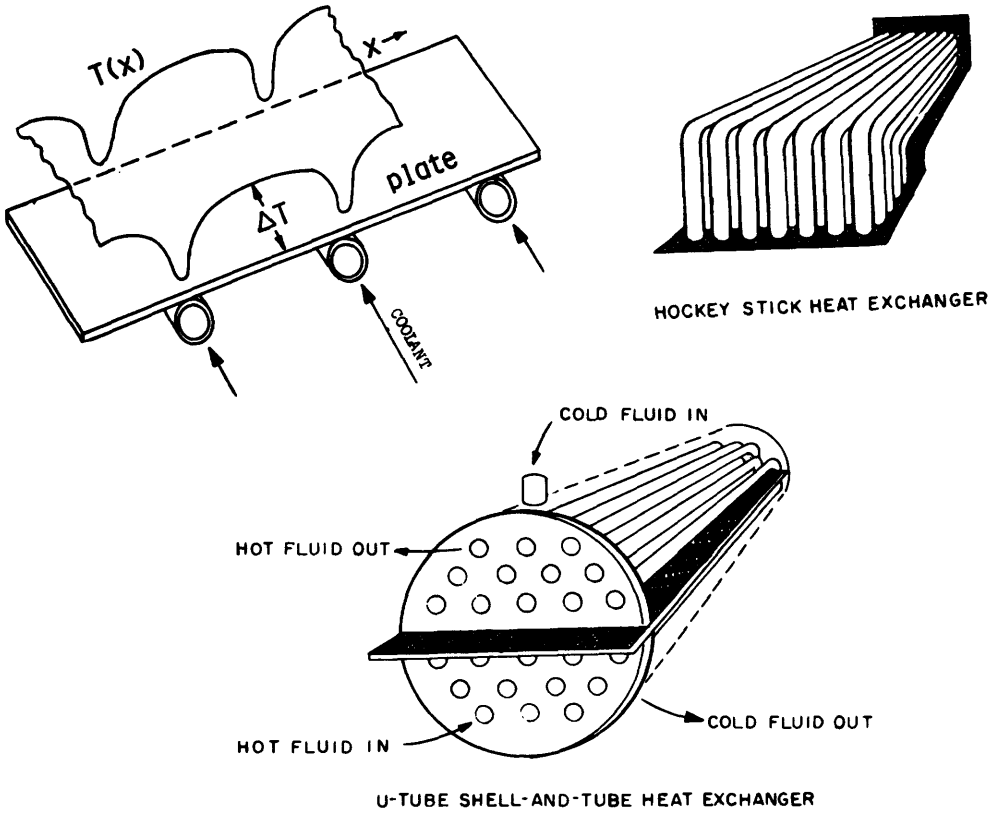

Fig. 26D2. Examples of situations which give rise to thermal stress problems. From A. P. Fraas, ORNL-TM-4999 (1975), Fig. 22.

Some coolant tube configurations giving rise to severe thermal stresses are shown in Fig. 26D2. Round tubes welded to a flat plate cause low-temperature regions in the plate, as shown in the sketch. The steep temperature gradients are accompanied by high thermal stresses. Thermal expansion and contraction during startup and shutdown cause severe bending stresses in the short straight sections of a hockey stick heat exchanger. The temperature difference on the hot and cold sides of a U-tube shell-and-tube heat exchanger induce shear stresses in both the shell and the end plates (headers).

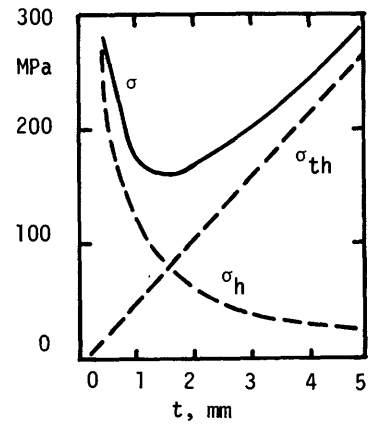

Fig. 26D1. Thermal stress, hoop stress, and total stress vs. tube thickness for the case of Example Problem 26D1.

Rectangular coolant channels are not as strong as circular tubes, because rectangular channels have bending stresses, while circular tubes have mainly

tensile stress, if the pressure is higher on the inside. If the pressure is higher on the outside of the tube, then there is a danger of creep buckling. Stress problems of some blanket designs are discussed by Fraas (1975) and by Fraas and Thompson (1978).

26E. Coolant Flow Rate and Pumping Power

flow rates

If boiling does not occur, the required coolant mass flow rate $\dot{m}$ (kg/s) may be found from the equation

$$P = \dot{m} c_p \Delta T \qquad (W) \tag{26E1}$$

where P is the heat to be removed (W), c_p is the coolant specific heat (J/kg-K), and ΔT is the coolant temperature rise (K) as it flows through the given blanket region.

The average coolant flow velocity v_c is related to $\dot{m}$ by the equation

$$\dot{m} = \rho_m A_c v_c \qquad (kg/s) \tag{26E2}$$

where ρ_m is the coolant mass density (kg/m^3) and A_c is the coolant channel cross sectional area (m^2). The volumetric flow rate is

$$A_c v_c = \dot{m}/\rho_m \qquad (m^3/s) \quad . \tag{26E3}$$

EXAMPLE PROBLEM 26E1

For helium at p = 6 MPa (60 atm) and T = 800 K, ρ_m = 3.6 kg/m^3 and c_p = 5200 J/kg-K. If ΔT = 100 K, estimate the required mass flow rate, volumetric flow rate, and velocity of such helium for a reactor with P = 1 GW and 20 m^2 total duct area.

From Eq. (26E1), we find $\dot{m}$ = 1920 kg/s. From Eq. (26E3), the volumetric flow rate is $A_c v_c$ = 533 m^3/s, and v_c = 27 m/s.

For comparison, typical flow rates for various coolants to remove 1 GW with ΔT = 100 K are shown in Tables 26E1. Attempting to lower the flow rate by raising ΔT can exacerbate thermal stress problems, but $\Delta T \sim 300$ K are used in some designs.

pressure drop and pumping power

For electrically *nonconducting* coolants, the pressure drop in a coolant tube with length L_c and diameter D is given by the equation

$$\Delta p = f L_c \rho_m v_c^2 / 2D \qquad (Pa) \quad , \tag{26E4}$$

where f is the friction factor (Fig. 20D2).

For *conducting* coolants, the pressure drop is much larger, because flow across the magnetic field does work in generating electrical voltage and current. The MHD pressure drop is given approximately by the equation

Table 26E1. Required flow rates for various coolants in a 1 GWth reactor with a temperature rise of 100 K.

coolant	ρ_m (kg/m^3)	c_p (J/kg-K)	$\dot{m}$ (kg/sec)	$A_c v_c$ (m^3/sec)
Li	450	4100	2430	5.4
Na	770	1300	7700	10.
K	606	940	10600	17.5
NaK	703	890	11200	16.
Li_2BeF_4	183	2400	4200	23.
He(60 atm, 800 K)	3.6	5200	1920	540
H_2O	900	4100	2430	2.7

$$\Delta p = \int_0^{L_c} dx\ v_c B_\perp^2 \sigma C/(1+C) \simeq L_c v_c B_\perp^2 \sigma C/(1+C) \qquad (26E5)$$

where σ is the electrical conductivity of the fluid (A/V-m), $C = 2\sigma_w t/\sigma D$ is the "conductivity ratio", σ_w is the tube wall electrical conductivity (A/V-m), t = tube wall thickness (m), and $B_\perp$ is the component of the magnetic induction (T) perpendicular to the coolant flow direction. This equation is valid for large values of the *Hartmann number*

$$Ha = B_\perp D(\sigma/\mu)^{\frac{1}{2}} \qquad (26E6)$$

where μ is the viscosity of the fluid (Pa-s).

The pumping power required to force a fluid through a channel with pressure drop Δp is

$$P = \Delta p \dot{m}/\rho_m \eta_p = \Delta p A_c v_c/\eta_p \quad (W) \quad , \qquad (26E7)$$

where η_p is the pump efficiency.

EXAMPLE PROBLEM 26E2

A 2.5 GWth reactor uses lithium coolant at T ~ 1100 K with ΔT = 100 K, flowing at 3 m/s for distances of 3 m in and out across an average magnetic field of 4 T in Nb-1Zr tubes with diameter 30 cm, thickness 0.2 cm. The pump efficiency is 90 %. Estimate the MHD pressure drop, number of coolant tubes, and the pumping power.

From Table 26B3 $\sigma = 2\times10^6$ A/V-m, and from Table 26B4 $\sigma_w \simeq 2.3\times10^6$ A/V-m (reciprocal of resistivity). Then C = 0.0153. From Table 26B3 $\mu = 2.5\times10^{-4}$ Pa-s, so Ha = 1.1×10^4, and Eq. (26E5) may be used. Using L_c = 3 m in this equation,

Table 26E2. Typical pumping powers required for coolant flow 3 m radially in and 3 m radially out of a 3.5 T magnetic field in a 1 GW_{th} reactor. From A. P. Fraas, ORNL-TM-4999 (1975), Table 6, p. 85.

	Li	boiling K	He	Li_2BeF_4
v_c, m/sec	4.6	3 (vapor=72)	46	4.3
total area required for inlet and outlet ducts, m^2	2.0	3.7	38	1.0
electrical resistivity μΩcm	40.0	80.0	very high	1.5
MHD pressure drop psi/m	222.0	74.0	0	0.0054
non-MHD pumping power, MW	0.6	0.1	15	0.7
MHD pumping power, MW	43.0	1.45	0	0.47
total pumping power, MW	43.6	1.55	15	0.7

the pressure drop flowing inwards is $\Delta p = 4.3$ MPa. An equal pressure drop occurs for the outward flow, so the total MHD pressure drop is $\Delta p = 8.6$ MPa.

From Table 26E1, $A_c v_c = 13.5\ m^3/s$. The area of one tube $\pi D^2/4 = 0.0707\ m^2$, so 64 tubes are needed. From Eq. (26E7), the required pumping power is P = 129 MW, or about 5 % of the reactor thermal power.

Similar estimates for various coolants are compared in Table 26E2. If a non-conducting layer were used on the coolant ducts for liquid metals, the MHD pumping power could be greatly reduced. Then the friction factor in Eq. (26E4) would become a function of Ha (Miley, 1976, Fig. 5.14). However, it is difficult to prevent the insulating layer from flaking off at $T \gtrsim 480$ K.

power flux limitations

The allowable power flux on the first wall may be limited by several different problems:

* convective heat transfer capability of coolant
* pumping power
* stresses
* radiation damage
* materials compatibility at higher temperatures.

At high flow rates across a magnetic field, the voltage induced in molten salts may be high enough (around 1 V) to cause chemical breakdown and enhanced corrosion. Estimates of the maximum attainable neutron wall loads for various cases are shown in Fig. 26E1.

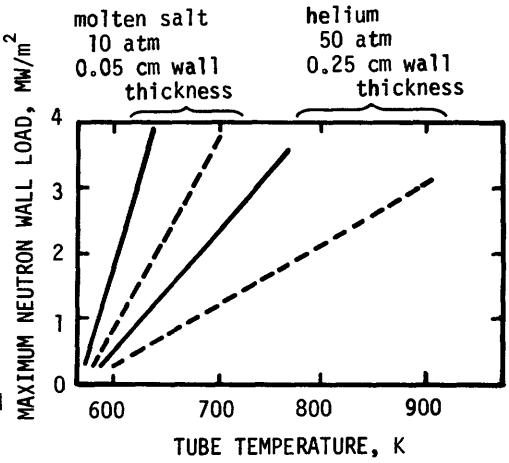

Fig. 26E1. Maximum attainable neutron wall load (MW/m²) vs. maximum allowable tube temperature, for helium and molten salt coolants with and without divertors. Assumptions: coolant inlet temperature = 570 K, 2.5 cm diameter stainless steel tubes, turbulent flow. Dashed curves = no divertor (surface heat flux equal to 25 % of neutron wall load), smooth curves = divertor (surface heat flux = 12.5 % of neutron wall load). From D. L. Kummer, Journal of Nuclear Materials 85 & 86, 47-56 (1979), Fig. 3.

Lower neutron wall loads may be needed to reduce the coolant pumping powers. The ratio of pumping power to heat removed is an important figure of merit in blanket design.

26F. Blanket Designs

coolant flow configurations

Blankets may be of three general types: flowing blanket; pressurized tubes carrying the coolant; or pressurized modules with coolant flowing around clad rods or spheres of solid breeding material (Li_2O or Li-Pb mixture), as illustrated in Fig. 26F1. Some coolant channel design considerations are listed in Table 26F1.

flowing blanket designs

For lithium, the pumping power can be reduced by directing the flow mainly along magnetic field lines. A lithium-cooled blanket design with TZM structure (a Mo alloy) is illustrated in Fig. 26F2. The coolant flows along the magnetic field through the manifold to each cell, then around the U-shaped cell (37 cm wide) and back out. There is a 10 cm stagnant zone in the center of each cell to insulate hot exit lithium from cooler incoming lithium. Thermal recirculation is a major design problem, because of the high thermal conductivity of lithium. Use of $\Delta T \sim 330$ K, large coolant ducts (0.5 m) and low flow velocity (0.39 m/s in ducts, 0.01 m/s in cells) results in a total pressure drop of 0.8 MPa and pumping power of 2 MW. See also the WITAMIR-I blanket, Section 18D.

pressure tube designs

In general, coolant tubes will be spaced close together near the first wall, where heat deposition is greatest, as illustrated in Fig. 26F1. This configuration may be used with any type of breeding material: Li, solid compounds, or FLIBE.

If Li is used for breeding and circulated within the blanket, then the coolant tubes could be placed at the back of the blanket, away from the first wall.

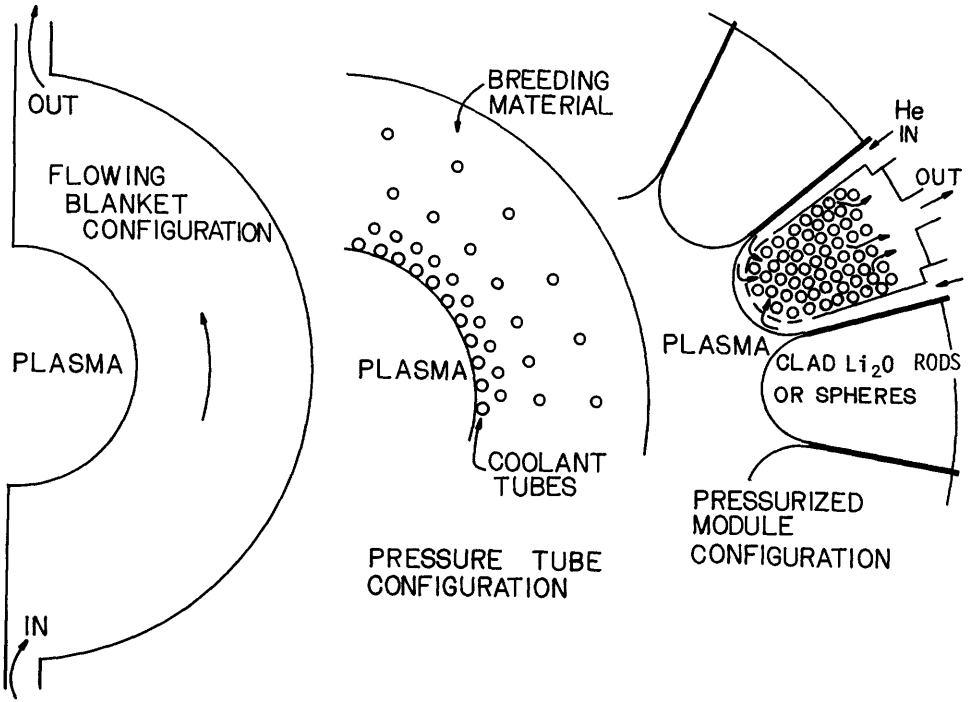

Fig. 26F1. Coolant flow configurations, simplified for clarity.

Various compromises are made in choosing coolant temperature, pressure, and tube size. High outlet temperatures are needed for good thermal conversion efficiency, but detrimental to strength and compatibility. Large coolant ΔT's through the blanket permit lower flow rates and pumping powers, but create thermal stress problems. High helium coolant pressures decrease the required velocities, but increase duct stresses. Large tube diameters decrease the number of tubes and welds needed, but increase hoop stress. Thin tubes have high hoop stresses, and thick tubes have high thermal stresses.

Helium and water are the most popular coolants for pressure tube designs. Trace amounts of oxygen in helium make it incompatible with many structural materials at high temperatures. Water requires much less pumping power than helium, but it may react with breeding materials if a tube leak develops, and tritium removal is more difficult from water than from helium.

Design of tube manifolds and headers is a major problem. Tube joints are vulnerable to thermal stress problems, as in Fig. 26D2. Coolant tubes leaving a module should be few in number and simple to disconnect for remote maintenance (Simple connections are not yet available for liquid metals, molten salts, or high-pressure coolants). With helium coolant, there is danger of neutron streaming out the helium ducts.

The NUWMAK tokamak reactor design uses $Li_{62}Pb_{38}$ breeding material cooled by boiling water in pressure tubes at 570 K, 8.6 MPa (1250 psi). The phase change of the water helps to keep the tubes near the boiling temperature, and phase changes of the $Li_{62}Pb_{38}$ melting and freezing in the blanket provide 140 kJ/kg of

Table 26F1. Coolant channel design considerations.

temperature distribution
- Maximize coolant outlet temperature to attain high energy conversion efficiency.
- Keep first wall cool.
- Keep breeding material hot enough for rapid diffusion of tritium, yet cool enough to avoid sintering (solid compounds).
- Match heat removal to heat deposition.
- Avoid hot spots.
- Minimize thermal resistances of coolant tubes.
- Design to keep thermal stresses within safe limits.
- Keep temperatures within compatibility and stress limits.

pumping power
- Minimize pressure drop and pumping power.

stress
- Allow for differential thermal expansion.
- Estimate thermal stresses, pressure stresses, gravity stresses.
- Avoid creep buckling.
- Avoid thermal strain fatigue and stress corrosion fatigue, especially at joints.

tritium removal
- If tritium is to be removed by coolant stream, use high permeability tubes.
- If tritium is to be removed by a separate purge stream, use low permeability coolant tubes.

neutronics
- Design for a small void fraction in the blanket, in order to minimize blanket thickness and coil size.
- Avoid neutron streaming out coolant ducts (helium).
- Design for small structure fraction, to maximize breeding ratio.
- Avoid creating long-lived radioisotopes.

maintenance
- Design for high reliability, over 10^5 hours between tube failures.
- Design for quick disconnection of coolant tubes and easy reassembly.
- Allow blanket breeding material and coolant to be drained, if feasible.

material supply
- Try to use materials which have abundant domestic supply, easy fabrication, reliable welds, and low cost.

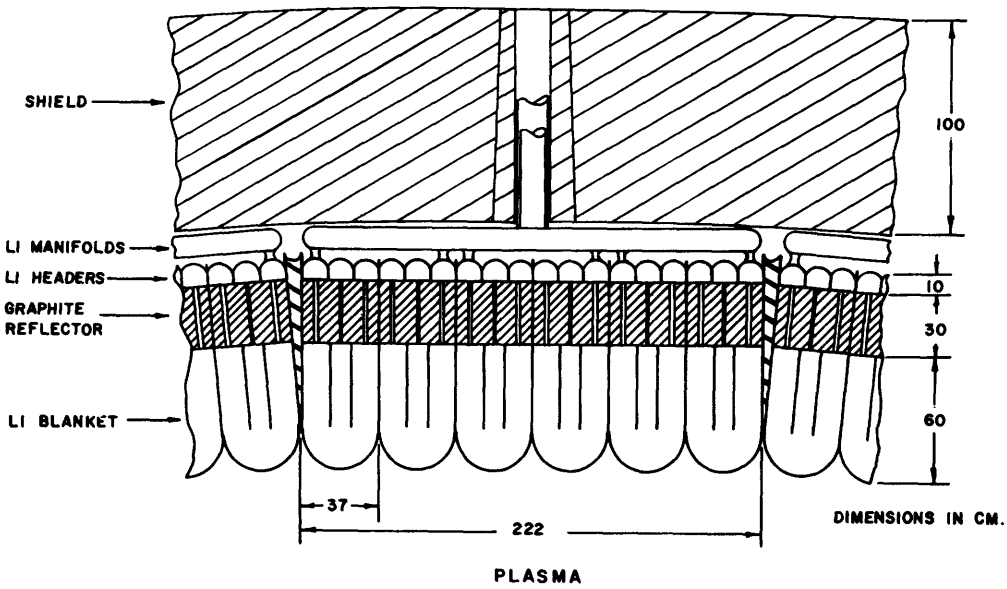

Fig. 26F2. Toroidal cross section of the UWMAK-III outer blanket. From B. Badger et al, "UMWAK-III, a noncircular tokamak power reactor design", EPRI ER-368 (1976), Fig. VI-B-1, p. 6-8.

thermal energy storage (latent heat of fusion), maintaining the blanket near the melting temperature (737 K, Fig. 26B1). The coolant tubes for this blanket are shown in Fig. 26F3. The nearly constant temperature helps to reduce thermal strain fatigue problems, and the thermal energy storage keeps the steam system running during plasma down time between burn periods. Volumetric changes of the Li_{62} Pb_{38} during melting and freezing could cause stress problems. Tritium diffusion into the cooling water system is impeded by using a double-wall coolant tube design, which also helps prevent water from reaching the $Li_{62}Pb_{38}$. The use of a Ti alloy structure reduces blanket radioactivity, and its low operating temperature increases the structural lifetime, in comparison with other designs.

The STARFIRE blanket (Section 18C) uses water coolant pressurized to 15.2 MPa (2200 psi), so boiling does not occur in the blanket. The primary coolant (pressurized water) carries the heat to a steam generator, as in Fig. 26A1. The NUWMAK and STARFIRE energy conversion systems are analogous to those of boiling water reactor (BWR) and pressurized water reactor (PWR) fission reactors, respectively.

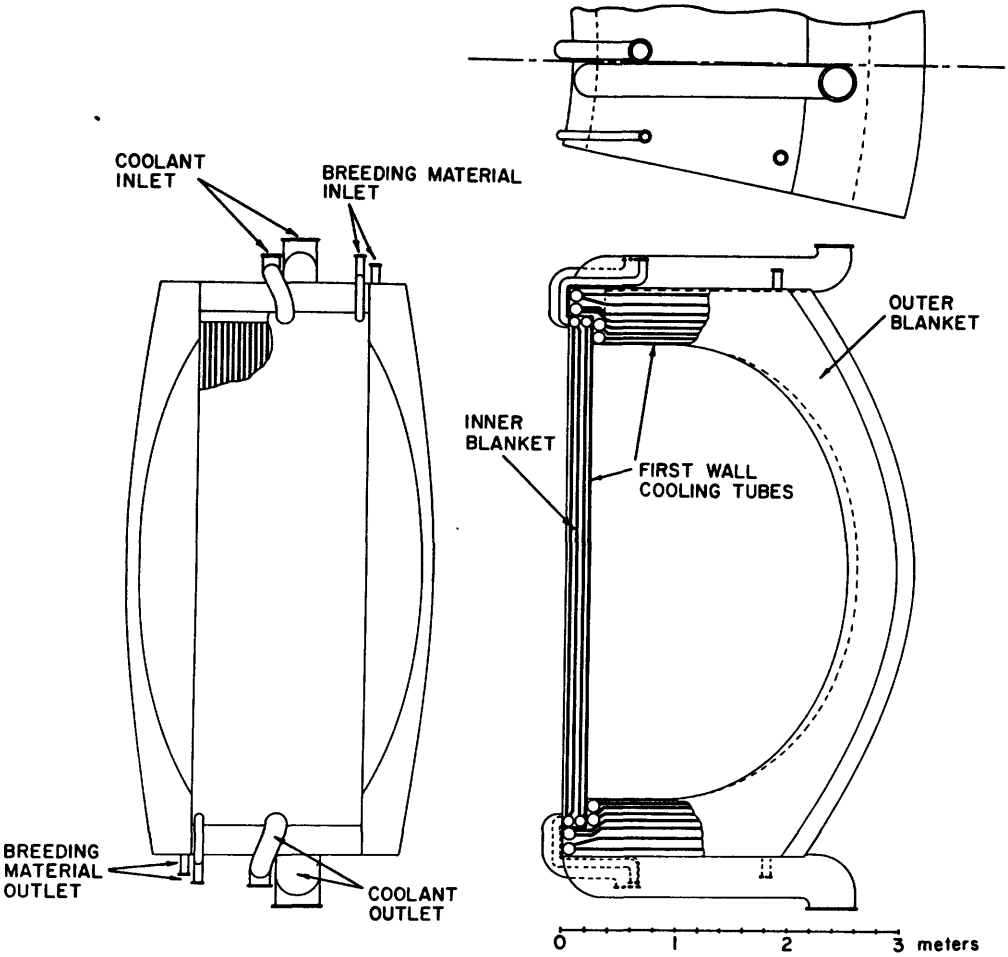

Fig. 26F3. The NUWMAK blanket design. From B. Badger et al, "NUWMAK, a tokamak reactor design study", UWFDM-330 (1979), Fig. VII-C-1, p. VII-10.

pressurized module designs

Pressurized module designs are useful with solid breeding materials cooled by He. An example is the use of Mo-clad Li_2O spheres, as shown in Fig. 26F4. The helium flows first to the first wall, to keep it cooler, then radially outwards

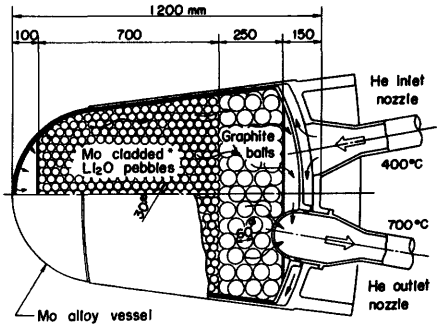

Fig. 26F4. Cutaway view of a blanket module containing pebbles of Li_2O and graphite. From A. P. Fraas, ORNL-TM-4999 (1978), Fig. 15.

between the spheres. The large void fraction around the spheres makes a thicker blanket region necessary than for the case of a compact blanket.

Another pressurized module design uses cylindrical tubes of Li_2O clad in SiC tubes with 5 MPa helium coolant flowing across the outside of the tubes. Helium exit temperatures about 1100 K may be attainable. The Li_2O tubes are hollow, with a helium purge stream flowing inside to remove tritium. In this way the tritium can be separated from the main coolant circuit and turbines.

In a comparison of pressure tube and pressurized module designs with helium coolant, it was found that the pressurized module concept offered higher helium outlet temperature, higher thermal conversion efficiency, and lower pumping power, but the pressurized tube concept afforded a lower void fraction in the blanket.

If the blanket materials can attain a high breeding ratio, it is not necessary to surround the plasma completely with a breeding blanket. For example, in UWMAK-III a lithium blanket was used on the outside of the torus, but only a shield for the magnet coils was needed on the inside of the torus.

The best first-wall coolants are H_2O and D_2O. Heavy water is more expensive, but tritium recovery from D_2O requires much less processing than from H_2O, since much larger fractions of D than of H are tolerable in the tritium fuel stream.

26G. Direct Energy Conversion

principles

The power leaving a fusion reactor in the form of charged particles is

$$P_{ch} = P_F\left(\frac{1}{Q} + \Psi_R\right) \qquad (W) \quad , \tag{26G1}$$

where P_F is the thermal fusion power (W), Q is the power gain ratio, and Ψ_R is the radiation power parameter (Fig. 4C2). For a DT reactor, $\Psi_R \leq 0.2$, and for a catalyzed DD reactor, $\Psi_R \leq 0.62$. Thus if $Q \sim 10$, the charged particle power may be up to 30 % of the fusion power in a DT reactor and up to 70 % in a catalyzed DD reactor. This charged particle power flows out the ends of a mirror machine, where it can be converted directly into electricity. Direct conversion might be used with charged particles flowing into the divertor of a toroidal reactor. However, the average particle energies would be much lower and particle fluxes much higher than in mirrors, so direct convertors would be more difficult to use with toroidal reactors.

The simplest direct conversion scheme would be a metal plate intercepting a stream of energetic positive ions. If the plate were biased at a high positive voltage (slightly less than the ion energy) and electrons were removed from the beam, then the ions impinging on the plate would produce an electrical current at that high voltage: their kinetic energy would be converted directly into electrical energy.

There are four main steps in direct conversion systems:

* *expansion*. The plasma is expanded by flowing along a diverging magnetic field to reduce its power flux to $\lesssim 1$ MW/m^2 and increase its Debye length to $\gtrsim 1$ cm, so that the self-shielding effect will not prevent proper grid operation.

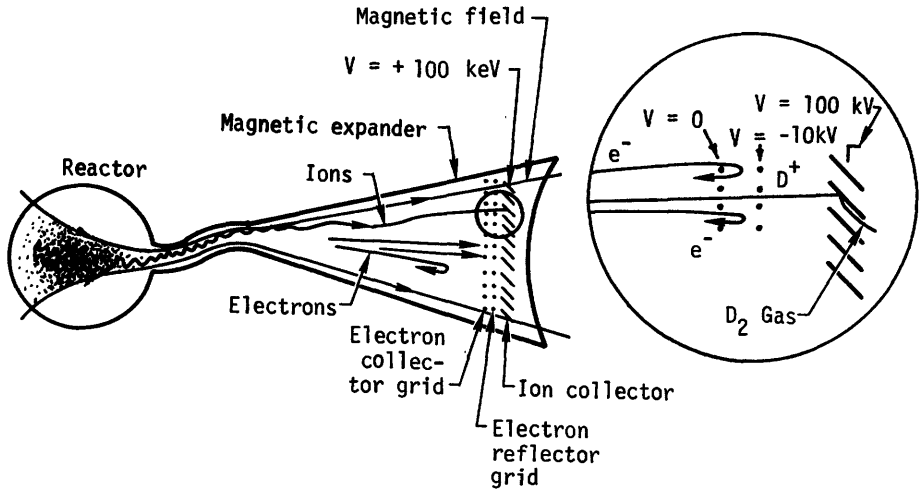

Fig. 26G1. Expansion and separation of plasma streaming out of a fusion reactor into a direct convertor. From R. W. Moir, W. L. Barr, and G. A. Carlson, UCRL-76051 (1974), Fig. 4.

* *separation.* The electrons must be removed from the plasma, so that only ions are incident on the positive high voltage collectors. This is the most difficult stage.
* *collection.* The ions strike the high-voltage collectors, and are neutralized.
* *conversion.* If more than one collector voltage is used, the output powers at various voltages are converted to the desired common voltage. This stage can be accomplished by solid state devices with very high efficiency.

The expansion and separation stages are illustrated in Fig. 26G1. Electrons are repelled back into the plasma by the negative electron-reflector grid and collected by the grounded electron collector. Most of the ions pass on through these grids to the ion collector, where they deposit their energy and are neutralized. The newly-formed neutral atoms constitute a substantial gas throughput, which must be removed with a very high pumping speed to keep the residual gas pressure in the direct convertor $p \lesssim 2$ mPa (1.5×10^{-5} Torr). Otherwise, losses of fast ions by charge exchange would be excessive. Cyropanels will probably be needed, since other vacuum pumps do not have high enough pumping speeds.

plasma direct convertors

An experimental two-stage "venetian blind" collector is illustrated in Fig. 26G2. High-energy ions pass directly through to the second collector (at high positive voltage V_2) while intermediate-energy ions are caught by the first collector (at intermediate voltage V_1) as they curve around during reflection. Low energy ions may be reflected by the first collector and returned to the plasma. The average efficiency predicted for this two-stage collector, for incident ion energies of 330-1000 eV, is 69 %, and the average measured efficiency is 65 %.

For a reactor with high power fluxes, high voltages and a spread of ion energies, the efficiency of a two-stage collector would be about 59 %. With

additional thermal conversion of collector heat into electricity at about 40 % efficiency, about 74 % of the ions' energy could be converted into electricity. (Neutron energy and radiation would still have conversion efficiencies ∿ 40 %.) Additional collection stages would provide slightly higher direct conversion efficiencies, but would add complexity and cost.

The maximum power flux which can be handled by venetian blind direct convertors is about 1 MW/m^2. A single-stage convertor has been run continuously at 0.7 MW/m^2 for many hours, attaining about 77 % efficiency with a 100 keV monoenergetic ion beam.

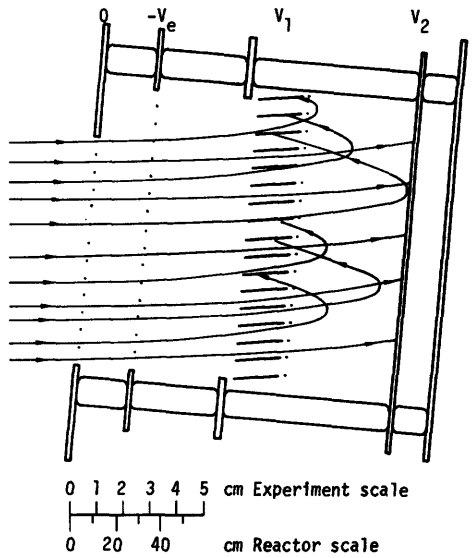

Fig. 26G2. A two-stage "venetian blind" direct convertor. From R. W. Moir, W. L. Barr, and G. A. Carlson, UCRL-76051 (1974), Fig. 5. A grounded grid is followed by an electron repulsion grid ($-V_e$) and two collector grids (V_1, V_2).

beam direct convertors

Direct conversion is also needed in the process of generating neutral atom beams for plasma heating. In order to keep the total area of neutral beam ports low, high beam power densities must be achieved. There will not be much room for expansion of the un-neutralized beam ions, so beam direct convertors will have to handle higher power densities than plasma direct convertors, and separation of electrons is difficult. The beams can be kept narrow enough that the electrons can be repelled by biasing a close-fitting electrode to a high negative potential. The Debye length is very short where $n_e \simeq n_i$, but near the repeller $n_e \ll n_i$, and the shielding effect is slight.

A beam direct convertor is shown in Fig. 26G3. Ions incident from the left will spread radially (space-charge blowup) and strike the conical collectors. The resultant neutral gas flow is pumped by cyropanels. The suppressors act to repel electrons, like the electron reflecting grid V_e of the plasma direct convertor. A water-cooled tube is used,

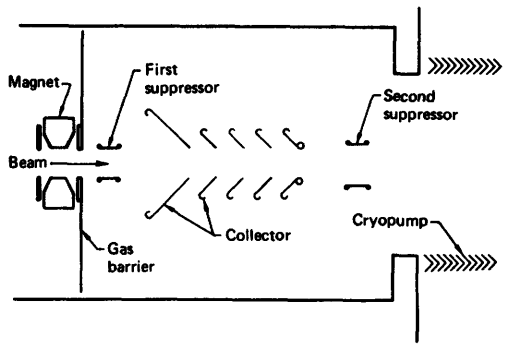

Fig. 26G3. An experimental beam direct convertor. Either electrostatic or magnetic suppression can be used to repel electrons. The tank is 0.91 m in diameter. From W. L. Barr, R. W. Moir, and G. W. Hamilton, "Tests of high-power direct conversion on beams and plasma", Proceedings of the 8th Symposium on Engineering Problems of Fusion Research, IEEE, 1979, Fig. 1. © 1979 IEEE.

because grid wires would melt. Alternatively, the magnet at the left may be used to reflect incident electrons. Successful development of magnetic suppression would permit larger beam diameters to be handled than with electrostatic suppression.

Such a beam direct convertor has operated at 0.7 MW/m^2 with a hydrogen beam for 0.5 s. The beam consisted of 100 keV H^+ (1.4 A), 67 keV H_2^+ (0.04 A), 50 keV H^+ (0.24 A), and 33 keV H^+ (0.11 A). The peak power efficiency of the beam direct convertor was about 61 % with electrostatic suppression, 39 % with magnetic suppression. Increasing neutral gas pressure caused a drop of efficiency during the pulses, in spite of cryopumping.

Plasma energy may also be converted directly into electricity by magnetic induction: plasma expansion against a magnetic field induces currents in the magnet coils. Various energy conversion concepts are discussed by Miley (1976).

26H. Fuel Production

Heat and electricity from fusion reactors can be used to produce hydrogen from water. High temperature steam produced in a fusion reactor blanket may be split into hydrogen and oxygen via high-temperature electrolysis (HTE), as illustrated in Fig. 26H1. At temperatures over 1600 K, over 50 % of the fusion energy may be converted into H_2 fuel energy, assuming 40 % efficiency for production of electricity in the steam cycle.

The fusion reactor blanket might consist of two types of modules: one for production of high-temperature process heat (steam or CO_2) and the other for tritium breeding and electrical power production. A process heat module is shown in Fig. 26H2. Either the pressurized module or the pressure tube configuration may be used, with ceramic rods or balls cooled by steam or CO_2 at temperatures of 1500-2000 K. A water-cooled outer shell at about 650 K is insulated from the interior by MgO fibers. The attainable temperature will depend upon materials problems, such as thermal strain fatigue. Most high-temperature materials have poor ductility.

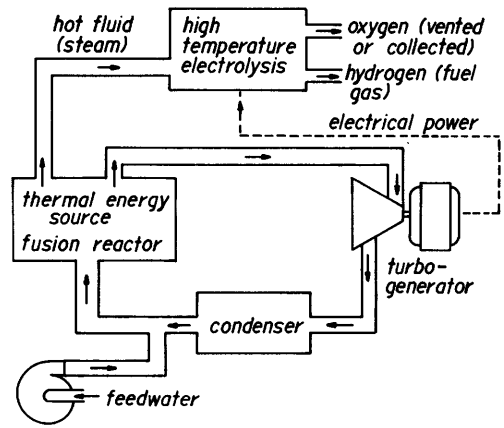

Fig. 26H1. Use of a high-temperature fusion reactor blanket for production of electricity, high-temperature steam, and hydrogen by high temperature electrolysis. From J. A. Fillo et al, BNL-24906 (1978), Fig. 1.

The hydrogen produced by HTE may be burned directly as fuel or used in production of other synthetic fuels. For example, hydrogen can triple synfuel production from coal. Fusion reactor waste heat could be used to distill alcohol. Other applications of fusion power were indicated in Fig. 1F2.

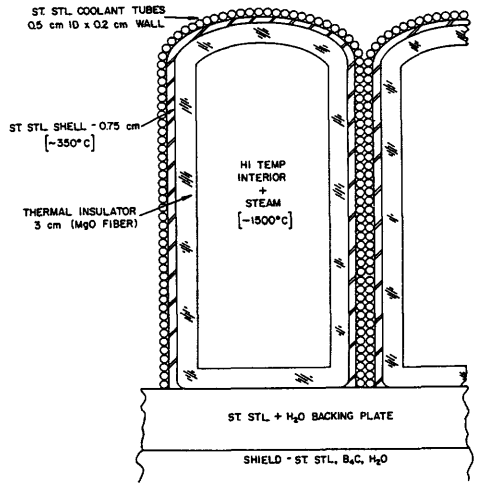

Fig. 26H2. Cross section of a blanket module for production of high-temperature steam to be used in high-temperature electrolysis. From J. A. Fillo et al, BNL-24625 (1978), Fig. 3.

Problems

1. Estimate the waste heat released by a 3 GWth fusion power plant operating with a conventional steam cycle (no direct conversion) at a peak cycle temperature of 700 K, assuming Q = 10, η_{in} = 0.7, M = 1.2. (Hint: Find η using equations from Chapter 4.)

2. Show that the ratio of first wall heat power (charged particles and radiation) to neutron wall loading is $(P_{ch} + P_{rad})/P_n = (0.25 + 1.25/Q)$. A given reactor has Q = 10, P_n/A = 1.5 MW/m^2, steel walls with T_w = 700 K, e_w = 0.7, and radiatively-cooled SiC armor tiles with e_a = 0.85. Estimate the temperature of the SiC on the wall side.

3. Helium at 6 MPa, 1200 K flows with v_c = 10 m/s through a tube with D = 0.05 m, and receives a power flux of 0.1 MW/m^2 through the tube walls. What is the tube inner wall temperature? (For this case the Mach number M << 1.)

4. A TZM tube outer wall temperature is not to exceed 1100 K. The inner wall temperature is maintained at 1000 K by a coolant at 6 MPa. The tube inner diameter is 0.04 m and the thickness is 2 mm. What is the maximum allowable heat flux through the outside of the tube? What are the thermal and hoop stresses in the tube, assuming internal heat generation is negligible? (Figures 24C1 and 24D2 will be useful.)

5. If a reactor is cooled entirely by tubes of the kind in problem 3, and other pressure drops are negligible, what would the ratio of pumping power to thermal power be?

6. A SS 316 coolant tube with t = 3 mm, D = 10 cm carrying liquid Li at 800 K is to remove 2 MW from the blanket with a temperature rise of 140 K. Pump efficiency is 80 %. The average value of B^2 perpendicular to the 15-meter long channel is 20 T^2. What are the velocity and pumping power?

Bibliography

general

A. P. Fraas, "Comparative study of the more promising combinations of blanket materials, power conversion systems, and tritium recovery and containment systems for fusion reactors", ORNL-TM-4999 (1975).

G. H. Miley, *Fusion Energy Conversion*, American Nuclear Society, Lagrange Park, IL, 1978.

D. Steiner, "The technological requirements for power by fusion", *Nuclear Science and Engineering 58*, 107-165 (1975).

blanket materials

"Assessment of titanium for use in the 1st wall/blanket structure of fusion power reactors", EPRI ER-386 (1977).

"Special purpose materials", The Fusion Reactor Materials Program Plan, DOE/ET-0032/4 (1978).

V. A. Maroni, E. J. Cairns, and F. A. Cafasso, "A review of the chemical, physical, and thermal properties of lithium that are related to its use in fusion reactors", ANL-8001 (1973).

heat transfer, stress, pumping power

A. J. Chapman, *Heat Transfer*, Macmillan, New York, 1960.

M. M. El-Wakil, *Nuclear Heat Transport*, American Nuclear Society, LaGrange Park, IL, 1978a.

A. P. Fraas and A. S. Thompson, "ORNL fusion power demonstration study: fluid flow, heat transfer, and stress analysis considerations in the design of blankets for full-scale fusion reactors", ORNL/TM-5960 (1978).

W. M. Kays, *Convective Heat and Mass Transfer*, McGraw-Hill, 1966.

blanket designs

B. Badger et al, "NUWMAK, a tokamak reactor design study", UWFDM-330 (1979), Chapter VII.

B. Badger et al, "UWMAK-III, a noncircular tokamak power reactor design", EPRI ER-368 (1976), Chapters 6, 10.

E. L. Draper, Jr., Editor, *Technology of Controlled Thermonuclear Fusion Experiments and the Engineering Aspects of Fusion Reactors*, CONF-721111 (1974).

G. D. Morgan, C. A. Trachsel, B. A. Cramer, D. A. Bowers, and D. L. Smith, "First wall and blanket design for the STARFIRE commercial tokamak power reactor"; and D. L. Smith, R. G. Clemmer, and J. W. Davis, "Assessment of solid breeding blanket options for commercial tokamak reactors", in ANL/FPP/TM-127 (1979), pp. 16-26.

J. R. Powell and C. T. Eterno, Editors, "Proceedings of the Third Topical Meeting on the Technology of Controlled Nuclear Fusion", CONF-780508 (1978), Chapter 4.

J. R. Powell, J. A. Fillo, B. G. Twining, and J. J. Dorning, Editors, "Proceedings of the magnetic fusion energy blanket and shield workshop", ERDA-76/117/1 and ERDA-76/117/2 (2 volumes) (1976).

energy conversion

W. L. Barr, R. W. Moir, and G. W. Hamilton, "Tests of high-power direct conversion on beams and plasma", Proceedings of the 8th Symposium on Engineering Problems of Fusion Research, to be published (1980).

L. A. Booth, Chairman, "Fusion energy applied to synthetic fuel production", CONF-770593 (1977).

M. M. El-Wakil, *Nuclear Energy Conversion*, American Nuclear Society, LaGrange Park, IL, 1978b.

J. A. Fillo et al, "Hydrogen production from fusion reactors coupled with high temperature electrolysis", BNL-24625 (1978).

J. A. Fillo et al, "Fusion energy for hydrogen production", 10th Symposium on Fusion Technology, Padua, Italy, 1978 and BNL-24906 (1978).

R. W. Moir and W. L. Barr, " 'Venetian blind' direct energy converter for fusion reactors", *Nuclear Fusion 13*, 35-45 (1973).

L. Rovner et al, "Study of chemical production utilizing fusion neutrons", GA-A15371 UC-20d (1979).

S. Shioda and K. Maeda, "MHD gas turbine energy conversion for mirror fusion reactors", *Nuclear Fusion 19*, 508-514 (1979).

R. T. Taussig, "High thermal efficiency, radiation-based advanced fusion reactors", EPRI ER-544 (1977).

CHAPTER 27
NEUTRONICS

27A. Introduction

goals

The main goals of neutronics calculations are listed in Table 27A1. If many neutrons are lost through ports in the chamber walls (such as neutral beam injection ports), then the effective breeding ratio will be reduced by approximately the ratio of blanket area to total surface area of the chamber. If $R_B > 1$, then more tritium fuel is produced than is consumed, and the amount of tritium on hand increases with time (Chapter 28). Fusion-fission hybrids may also breed U^{233} or Pu^{239} (Chapter 29).

The blanket energy gain is used in calculating reactor power balance. Typical values of M are 1.1 to 1.2 without beryllium, 1.5-1.7 with beryllium, and $M \sim 10$ with fast fission of U^{238}. The value of M has a strong influence on net electrical power output (Chapter 4) and on reactor economics.

In calculating nuclear heating, it is usually assumed that the energy lost by a neutron from a collision is deposited at the point of the collision. If gamma rays are emitted, their paths are calculated to determine where their energy is deposited. The power deposition per unit volume at each point is used as the starting point for thermal-hydraulics calculations.

The radiation reaching the magnet coils must be attenuated by a factor of

Table 27A1. Predictions of neutronics calculations.

breeding ratio R_B = number of tritium atoms produced per DT fusion neutron.
blanket energy gain M = total energy deposited in blanket by neutrons (including neutron capture reactions) divided by neutron kinetic energy.
nuclear heating = power deposited per unit volume at each point in the first wall, blanket, shield, and coils.
radiation attenuation (neutrons and gammas).
radiation streaming through ducts and cracks.

structure activation by neutron absorption.
radiation damage to materials: number of displacements per atom per year (dpa/year), and hydrogen and helium gas production rates via (n,p), and (n,α) reactions.
corrosive element production by nuclear reactions.

about 10^{-7}, in order to keep nuclear heating of the coils and radiation damage to the coil copper, superconductor, and insulation satisfactorily low. Materials which are good neutron moderators and absorbers, such as B_4C and borated water, are needed to stop the neutrons; dense, high-Z materials, such as iron and lead, are needed to stop the gammas. The required thickness of the blanket plus shield is roughly 1 - 2 m.

Predictions of the residual radioactivity induced in the structure are needed for estimating dose-rates to workers, for remote maintenance planning, and for planning the final decommissioning of the reactor and subsequent disposal of radioactive wastes. Use of high-purity materials with short half-lives can significantly reduce the maintenance and waste disposal problems (Chapter 28).

Calculations of radiation damage and transmutations are needed to predict structural lifetimes.

methods

Two main methods are used in neutronics analyses: neutron transport theory and Monte Carlo. Neutron transport codes solve the Boltzmann transport equation for the motion of particles (neutrons or gammas) through the blanket-shield, in order to find the neutron flux distribution as a function of position, energy, and angle. We will speak here of neutrons, keeping in mind that the same equations, after slight modifications, also apply to gamma rays.

The Monte Carlo technique uses a random-number generator to make decisions (like flipping a coin) about the interactions of a single neutron, based on the probabilities of various phenomena; and it keeps track of the entire history of that neutron: where it has collisions, the scattering angles, how much energy is deposited at each point, and where it is finally absorbed. After simulating thousands of neutron histories, a Monte Carlo code averages the results to determine how much energy is deposited at each point in the blanket, and so on for the other predictions of Table 27A1.

Both of these methods rely on extensive libraries of nuclear cross section data: cross sections for scattering, absorption, (n,2n) reactions, etc. as functions of neutron energy and scattering angle, for all the elements present in the wall, blanket, coolant, and shield. Use of up to 300 neutron energy groups requires very large data tables. Special computer codes are used to manipulate the cross section data and organize it in the desired form for a given computation.

After brief descriptions of transport theory and the Monte Carlo technique, some examples of neutronics calculations will be discussed.

27B. Transport Theory

Boltzmann equation

Blanket calculations often consider a steady-state case in one-dimensional cylindrical geometry. For the purpose of illustrating the transport theory method, a simpler slab geometry will be considered here. The independent variables are x, the spatial coordinate; E, the neutron energy; and μ, the cosine of the angle between the neutron velocity vector and the x direction. It is customary to replace the distribution function $f(x,\mu,E)$ with a "flux distribution function" $\phi(x,\mu,E) \equiv vf(x,\mu,E)$, where v is the neutron speed. The forces of gravitational, electric, and magnetic fields on a neutron (or gamma ray) are negligible, and the

term $(F_j/m)(\partial f/\partial v_j)$ drops out of the Boltzmann equation (3D3). The transport equation is a conservation equation for the number of neutrons in the differential volume element $dx\,d\mu\,dE$ at x, μ, and E. It may be expressed in words as

(Change due to neutron flow) = (Scattering in from other angles and energies)
+ (Source of neutrons)
- (Removal of neutrons) . (27B1)

All terms in this equation have units of neutrons/m^3s (or neutrons/cm^3s).

The removal term is equal to the total rate for neutron interactions,

$$\text{(Removal rate of neutrons)} = \Sigma_t(x,E)\phi(x,\mu,E) \quad ,$$

$$\Sigma_t(x,E) \equiv \sum_j n_j(x)\sigma_{tj}(x,E) \equiv \textit{macroscopic total cross section} \tag{27B2}$$

where n_j is the atomic density of species j, and σ_{tj} is the total neutron cross section of species j. (Here "species" means the different isotopes present in the first wall, blanket, or shield.)

Since $v_x = \mu v$, the "change due to neutron flow" term $v_x(\partial f/\partial x)$ [Eq. (3D3)] may be written $\mu(\partial\phi/\partial x)$.

The rate at which neutrons from volume element $dx\,d\mu'dE'$ scatter into volume element $dx\,d\mu\,dE$ is written in the form $\phi(x,\mu',E')\Sigma(x,E'\to E,\mu'\to\mu)\,dE'd\mu'$. The inscattering term in Eq. (27B1) is the integral of this rate over all E' and solid angles $d\Omega'$. Since $d\Omega' = d\mu'd\phi'$, where ϕ' is the azimuthal angle, Eq. (27B1) may be written in the form

$$\mu(\partial\phi/\partial x) = \int_0^{2\pi} d\phi' \int_0^{\infty} dE' \int_{-1}^{1} d\mu'\ \phi(x,\mu',E')\Sigma(x,E'\to E,\mu'\to\mu) + S(x,\mu,E)$$

$$- \Sigma_t(x,E)\phi(x,\mu,E) \quad , \tag{27B3}$$

where $S(x,\mu,E)$ represents an arbitrary neutron source term.

For charged particles, the Lorentz force term $q\vec{E} + q\vec{v}\times\vec{B}$ was dominant in the Boltzmann Eq. (5C3), and collisional effects were minimal. For neutrons, on the other hand, the Lorentz force is negligible, and collisional interactions (inscattering and removal terms) are dominant. Thus, the same equation takes on radically different forms in the two cases. The Boltzmann equation has a similar form in cylindrical geometry, but with added complexity from the effects of curvature.

Legendre expansion

Let μ_0 be the cosine of the angle between $\vec{v}$ and $\vec{v}'$, where $\vec{v}$ and $\vec{v}'$ are the velocities of a neutron before and after scattering. Then the macroscopic inscattering cross section may be written $\Sigma(x,\mu_0, E'\to E)$, since its angular dependence is solely a function of μ_0. It is convenient to represent the scattering cross section in terms of a series of Legendre polynomials:

Table 27B1. Properties of Legendre Polynomials $P_\ell(\mu)$.

differential equation:

$$(1-\mu^2)(d^2P_\ell/d\mu^2) - 2\mu(dP_\ell/d\mu) + \ell(\ell+1)P_\ell = 0$$

values of P_ℓ:

$$P_0(\mu) = 1, \quad P_1(\mu) = \mu, \quad P_2(\mu) = (3\mu^2-1)/2, \quad P_3(\mu) = (5\mu^3-3\mu)/2, \text{ etc.}$$

Recurrence relation:

$$P_{\ell+1}(\mu) = [(2\ell+1)\mu P_\ell(\mu) - \ell P_{\ell-1}(\mu)]/(\ell+1)$$

Orthogonality condition:

$$\int_{-1}^{1} d\mu\, P_\ell(\mu)P_m(\mu) = \begin{cases} 0, & \ell \neq m \\ 2/(2\ell+1), & \ell = m \end{cases}$$

Expansion Theorem: Any continuous function $F(\mu)$ in the domain $(-1,1)$ may be represented as a series of Legendre Polynomials.

$F(\mu) = \sum_{\ell=0}^{\infty} a_\ell P_\ell(\mu)$, where the coefficients a_ℓ are given by

$$a_\ell = \frac{2\ell+1}{2} \int_{-1}^{1} d\mu F(\mu)P_\ell(\mu)$$

Addition Theorem: If μ_0 is the cosine of an angle between two vectors having polar angles θ and θ' and azimuthal angles ϕ and ϕ' relative to a given coordinate system, then

$$P_\ell(\mu_0) = P_\ell(\mu)P_\ell(\mu') + 2\sum_{m=1}^{\ell} \frac{(\ell-m)!}{(\ell+m)!} P_\ell^m(\mu)P_\ell^m(\mu')\cos m(\phi-\phi') \quad ,$$

where $\mu = \cos\theta$, $\mu' = \cos\theta'$, and the functions $P_\ell^m(\mu)$ are "Associated Legendre Polynomials".

$$\Sigma(x,\mu_0,E'\to E) = \sum_{\ell=0}^{L} \Sigma_\ell(x,E'\to E)P_\ell(\mu_0) \tag{27B4}$$

where Σ_ℓ are the expansion coefficients. Some properties of Legendre polynomials are listed in Table 27B1. In the Expansion Theorem $L = \infty$, but accuracy is usually satisfactory with $L = 3$ or 5. The transport Eq. (27B3) becomes

$$\mu(\partial\phi/\partial x) = \int_0^{2\pi} d\phi' \int_0^{\infty} dE' \int_{-1}^{1} d\mu'\, \phi(x,\mu',E') \sum_{\ell=0}^{L} \Sigma_\ell(x,E'\to E)P_\ell(\mu_0)$$

$$+ S(x,\mu,E) - \Sigma_t(x,E)\phi(x,\mu,E) \quad . \tag{27B5}$$

The integration over ϕ' may be carried out after using the Addition Theorem of Table 27B1 for $P_\ell(\mu_0)$. Thus,

$$\int_0^{2\pi} d\phi' \; P_\ell(\mu_0) = 2\pi P_\ell(\mu)P_\ell(\mu') \tag{27B6}$$

since $\int_0^{2\pi} d\phi' \cos m(\phi-\phi') = 0$. Equation (27B5) becomes

$$\mu(\partial\phi/\partial x) = 2\pi \int_0^{\infty} dE' \int_{-1}^{1} d\mu' \; \phi(x,\mu',E') \sum_{\ell=0}^{L} \Sigma_\ell(x,E'\to E)P_\ell(\mu)P_\ell(\mu')$$

$$+ S(x,\mu,E) - \Sigma_t(x,E)\phi(x,\mu,E) \quad . \tag{27B7}$$

If the flux and source terms in Eq. (27B7) are also represented in terms of series of Legendre polynomials, and if the resulting equation is multiplied by $P_k(\mu)d\mu$ and integrated from -1 to 1, then the "spherical harmonics" form of the Boltzmann equation is obtained. The spherical harmonics method, also called the *P_L approximation*, has been used successfully to solve some radiation transport problems; but for fusion reactor blanket design, it has not been as popular as the discrete ordinates method.

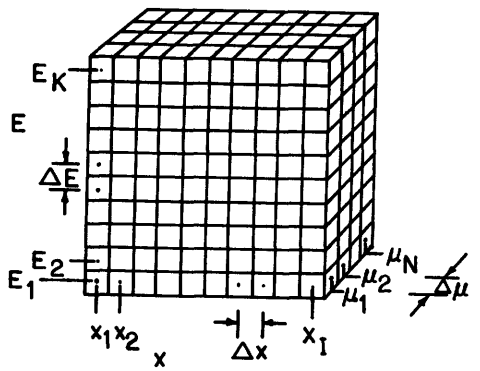

Fig. 27B1. Division of the space (x,μ, E) into I discrete spatial positions x_i, N discrete angular values μ_j, and K discrete energy groups E_k. For the specific case shown, I = 10, N = 4, and K = 10. The flux is to be found at the center of each of the 400 little cubes.

discrete ordinates method

The *discrete ordinates* method involves dividing up the spatial, angular, and energy regions into discrete locations x_i, μ_j, E_k separated by intervals Δx, $\Delta\mu$, ΔE, as illustrated in Fig. 27B1. The discrete ordinates equation is formally derived by integrating the Boltzmann equation (27B7) over the volume of one of the little cubes of Fig. 27B1. For simplicity, we will use a less rigorous approach here.

Since the Boltzmann equation is a neutron conservation equation, it must hold for each little cube of Fig. 27B1. Thus, Eq. (27B7) may be written separately for each cube, denoted by (x_i, μ_j, E_k) or simply (i,j,k). The summation sign may be moved to the left of the integral signs. Then the integrals over dE' and dμ' may be replaced by summations over k' and j'. For example

$$\int_{-1}^{1} d\mu' \; \phi(x,\mu',E')P_\ell(\mu') \simeq \sum_{j'=1}^{N} \phi(i,j',k')P_\ell(j')\Delta\mu(j')w(j') \tag{27B8}$$

where w(j') are weighting factors appropriate to the numerical approximation of the integral. The simplest value of w(j') is 1, which approximates the curve by a series of rectangles. Greater accuracy can be obtained by approximating the curve with a series of straight line segments (the trapezoidal approximation) with a series of parabolic segments (Simpson's Rule), or with a Gaussian quadrature formula. (With Gaussian quadrature, the $\Delta\mu(j')$ vary.)

The derivative of ϕ appearing in Eq. (27B7) may be replaced by the finite difference approximation.

$$\partial\phi(i,j,k)/\partial x \simeq [\phi(i+1,j,k) - \phi(i,j,k)]/\Delta x \tag{27B9}$$

or a similar alternative.

The discrete ordinates version of Eq. (27B7) for one little cube may now be written

$$(\mu_j/\Delta x)[\phi(i+1,j,k) - \phi(i,j,k)] = S(i,j,k) - \Sigma_t(i,k)\phi(i,j,k)$$
$$+ 2\pi \sum_{j'=1}^{N} \sum_{k'=1}^{K} \sum_{\ell=0}^{L} \Delta\mu(j')\Delta E(k')w(j')w(k')\phi(i,j',k')\Sigma_\ell(i,k'\to k)P_\ell(j)P_\ell(j') \quad . \tag{27B10}$$

Except for the fluxes, the parameters of this equation are all known. The flux, or its derivative, will be known along a boundary (such as x_1). In the original S_N method, the weighting factors w were derived assuming that the flux varies linearly between neighboring locations. In more recent versions other weights have been used to improve accuracy and convergence, and some quantities may be evaluated at the edges of the little cubes of Fig. 27B1, as well as at their centers.

Equations of the form (27B10) are written at every point where the flux is to be found, and the resulting set of linear, algebraic equations must be solved simultaneously. In principle, the equations could be written in matrix form and the matrix inverted to determine the fluxes. In practice, however, the inversion of an enormous matrix is too time-consuming, so the equations are solved iteratively. Initial values of ϕ are assumed at all locations. Then each equation of the form (27B10) is solved for a new value of $\phi(i,j,k)$ in terms of the present values at all the other points. The order of calculations should correspond to the direction of neutron motion. For example, if the neutrons start off at x_1 with high energy in the forward direction, then the calculations would start off at x_1, high energy, large μ. Solving for the new fluxes at every point in the volume of Fig. 27B1 constitutes one *iteration*. After many iterations, the values of the fluxes will usually converge to the desired solution.

The term "S_N approximation" means that N angular intervals are used. For example, a P_3 S_8 approximation uses N = 8 angular intervals and has L = 3 in the Legendre expansion of the scattering cross section. A typical blanket calculation might use on the order of 100 spatial points (I = 100) and 100 energy groups (K = 100). The discrete ordinates method is used to calculate gamma fluxes, using on the order of 30 gamma energy groups. It may also be adapted to two or three spatial dimensions, with a great increase in computer time.

If the angular dependence is dropped from the Boltzmann equation (by taking L = 0, N = 1), then the "multigroup diffusion equations" are obtained. This loss of angular resolution reduces the accuracy of the results, so the multigroup diffusion equations are not used much for blanket-shield design.

Once the neutron flux is known, the reaction rates r for neutron absorption, tritium breeding, energy deposition, etc. may be calculated using equations of the form

$$r_q(x) = 2\pi \int_{-1}^{1} d\mu \int_{0}^{E_{max}} dE\ \phi(x,\mu,E)\Sigma_q(x,E) \qquad \text{(reactions/m}^3\text{sec)}$$

$$\simeq 2\pi \sum_{j=1}^{N} \sum_{k=1}^{K} \Delta\mu(j)\Delta E(k)w(j)w(k)\ \phi(i,j,k)\Sigma_q(i,k) \quad , \qquad (27B11)$$

where $\Sigma_q \equiv \sum_j n_j\sigma_{qj}$ is the macroscopic cross section for reaction type q, and the w's are again weighing factors for numerical integrations.

Some sources of error in neutron transport calculations are listed in Table 27B2. Convergence, roundoff, and human error can be made negligible. The overall probable error of the results can be estimated by combining the probable errors due to truncation, model, and data. The spatial details of a blanket are poorly represented by a one-dimensional transport model, but they can be taken into account with the Monte Carlo technique.

Table 27B2. Sources of error in neutron transport calculations.

Convergence error can be made very small by using a large number of iterations.
Roundoff error is usually negligible on modern computers with many significant digits.
Human error can be minimized by thorough checking of programs, and by having the same set of calculations done independently by two or more groups of researchers, using different codes.
Truncation error arises from using a finite number of increments I, N, K, L to approximate continuous varibles. Methods of estimating this error are well developed.
Model error arises from representing the blanket by an idealized model. For example, helium coolant tubes might be represented by a uniform void fraction and a uniform structure fraction.
Data error arises from uncertainty in nuclear cross sections, typically a few percent.

27C. The Monte Carlo Method

decisions

The Monte Carlo method simulates a large number of individual particle trajectories, and then averages the results to determine the desired quantities, such as breeding ratio and energy deposition. We will again consider neutrons, keeping in mind that the technique applies equally well to gamma rays.

To simulate a given neutron's history, a series of questions are posed, and the answer to each question is decided statistically. For example, if only two choices were available, and if they had equal probability, we could flip a coin to decide. In practice, many choices are available, and they have probabilities determined by factors such as nuclear scattering cross sections. Instead of flipping a coin, a "random number generator" is used. The random number generator is a computer algorithm (procedure) to generate decimal fractions randomly and uniformly between 0 and 1.

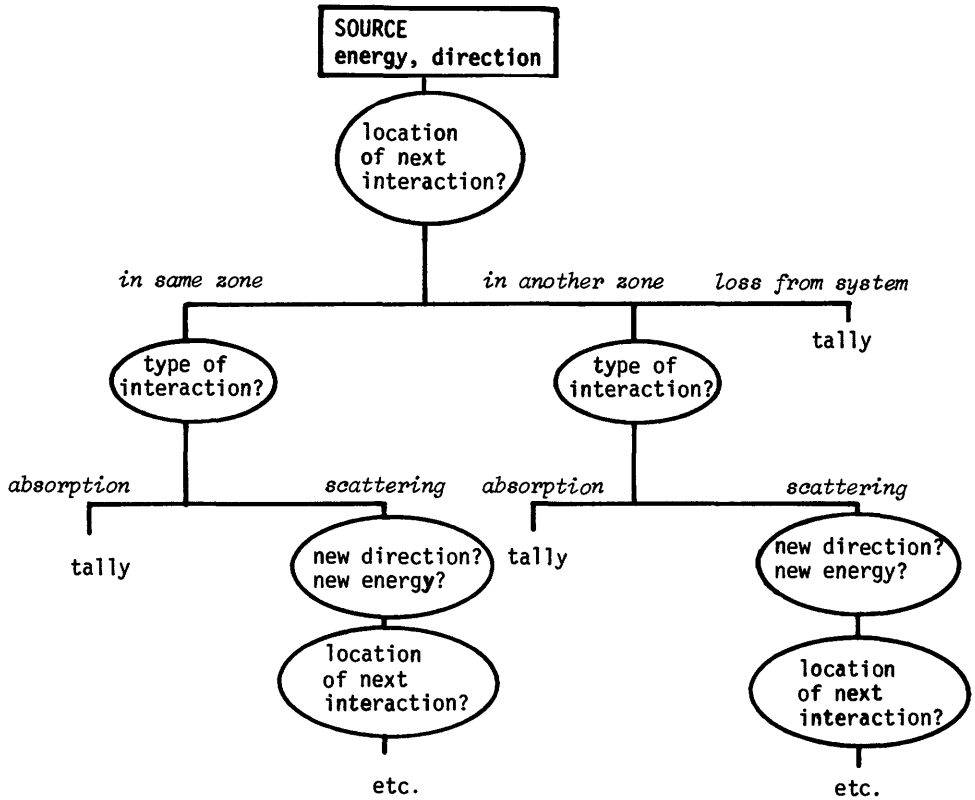

Fig. 27C1. Flow chart for decision-making in the Monte Carlo method.

The random number is compared with the probability of an event to decide whether or not it occurs. For example, if the probability of an event were 0.300, we could decide that the event will occur if the random number is less than 0.300, and that it will not occur if the random number is greater than 0.300.

A flow chart for Monte Carlo neutron simulations is shown in Fig. 27C1. For example, we will consider the case of a monoenergetic beam of neutrons entering a slab of thickness L at angle θ_0, as illustrated in Fig. 27C2.

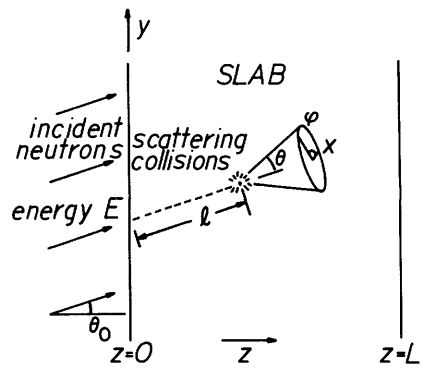

Fig. 27C2. A beam of neutrons incident on a single-zone slab. It is desired to know the numbers of neutrons absorbed at each point in the slab, the number transmitted through the slab, and the number backscattered out of the slab. The axes have been chosen so that the initial velocity of the neutrons lies in the y-z plane.

location of next interaction

The probability that a neutron travels a distance ℓ without having an interaction is equal to $\exp(-\ell/\lambda)$, where $\lambda = 1/\Sigma_t$ is the neutron mean free path (Eq. 2B37). Therefore, the probability that a neutron *does* have an interaction within distance ℓ is

$$P_{int}(\ell) = 1 - \exp(-\ell/\lambda) \tag{27C1}$$

which is plotted in Fig. 27C3. In order to decide how far the neutron goes before it has an interaction, we can equate $P_{int}(\ell)$, which ranges between 0 and 1, to a random number N_r between 0 and 1. Then, solving for ℓ/λ, we find that

$$\ell/\lambda = -\ln(1-N_r) = -\ln N_r' \tag{27C2}$$

where $N_r' \equiv (1-N_r)$ is also a random number. For example, if the $N_r' = 0.386$, this equation decides that the neutron travels a distance of 0.952 mean free paths before its first collision. The z distance of travel is equal to $\ell\cos\theta_0$. If the z distance travelled is greater than L, then the neutron has escaped from the slab. If not, it has a collision within the slab.

type of interaction

Consider a case in which four types of neutron interactions can occur:

Σ_{el} elastic scattering

Σ_{in} inelastic scattering (*Inelastic* means that the target nucleus absorbs energy internally during the collision and is raised to an excited nuclear energy level, usually followed by gamma emission.)

Σ_{2n} (n,2n) reactions

Σ_γ radiative capture (*Radiative capture* refers to neutron absorption by a nucleus, followed by gamma decay of the new nucleus.)

The following algorithm could be used to decide which type of interaction occurs:

$$\text{if } 0 \leq N_r \leq \frac{\Sigma_{el}}{\Sigma_t} \quad \text{elastic scattering}$$

$$\text{if } \frac{\Sigma_{el}}{\Sigma_t} < N_r \leq \frac{(\Sigma_{el}+\Sigma_{in})}{\Sigma_t} \quad \text{inelastic scattering}$$

$$\text{if } \frac{(\Sigma_{el}+\Sigma_{in})}{\Sigma_t} < N_r \leq \frac{(\Sigma_{el}+\Sigma_{in}+\Sigma_{2n})}{\Sigma_t} \quad (n,2n) \text{ reaction}$$

$$\text{if } \frac{(\Sigma_{el}+\Sigma_{in}+\Sigma_{2n})}{\Sigma_t} < N_r \leq 1 \quad \text{radiative capture}$$

(27C3)

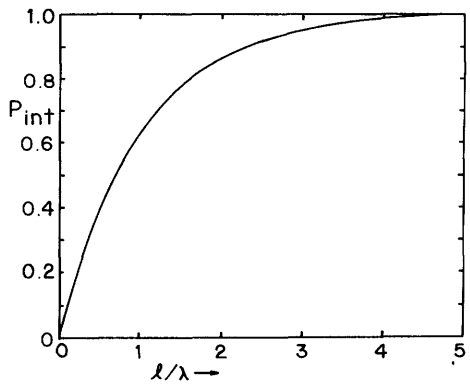

Fig. 27C3. A graph of the equation $P_{int}(\ell) = 1 - \exp(-\ell/\lambda)$.

where $\Sigma_t \equiv \Sigma_{el} + \Sigma_{in} + \Sigma_{2n} + \Sigma_\gamma$. If scattering occurs, the scattering angle and new energy are chosen using random numbers (described below). If an (n,2n) reaction occurs, the second neutron trajectory must be traced later on. (This case was omitted from Fig. 27C1.) If radiative capture occurs, then the gamma energy deposition must be calculated.

new direction and energy

Nuclear collision scattering angles are usually calculated in the *center of mass* (COM) coordinate system. The position $\vec{r}_c$ of the center of mass is defined to be

$$(m+M)\vec{r}_c = m\vec{r} + M\vec{R} \qquad (27C4)$$

where m and M are the neutron and target nucleus masses, and $\vec{r}$ and $\vec{R}$ are their position vectors, as illustrated in Fig. 27C4. The velocity of the center of mass is found by differentiating Eq. (27C4) with respect to time:

$$\vec{v}_c = (m\vec{v} + M\vec{V})/(m+M) = (\vec{v} + A\vec{V})/(1+A) \quad , \qquad (27C5)$$

where $\vec{v}$ and $\vec{V}$ are the velocities of the neutron and target nucleus and A = M/m. The COM coordinate system has its origin at the COM, so it moves relative to the fixed ("laboratory") coordinate system with a velocity $\vec{v}_c$.

Let $\sigma(\psi,E)d\psi$ be the cross section for a neutron with energy E to scatter into a differential angle $d\psi$ at ψ, where ψ is measured relative to the COM coordinate system. The total scattering cross section is $\sigma(E) = \int d\Omega'\sigma(\psi',E)$ where $d\Omega'$ is a differential solid angle. The probability of scattering through an angle less than ψ is equal to

$$P(\psi,E) = \frac{\int_{\psi'=0}^{\psi} d\Omega'\sigma(\psi',E)}{\int_{\psi'=0}^{\pi} d\Omega'\sigma(\psi',E)} = \frac{\int_0^{\psi} 2\pi\sin\psi'd\psi'\sigma(\psi',E)}{\int_0^{\pi} 2\pi\sin\psi'd\psi'\sigma(\psi',E)} \qquad (27C6)$$

The scattering angle is found by equating $P(\psi,E)$ to a random number and solving Eq. (27C6) for ψ. This can be accomplished on a computer by tabulating $P(\psi,E)$ vs. ψ and E, then inverting the table and interpolating to get the value of ψ corresponding to any given E and $P(\psi,E) = N_r$. For the simple case in which scattering is equally probable in all directions (*isotropic scattering*) in the COM system, the equation for ψ simplifies to

$$\psi = \cos^{-1}(1 - 2N_r) \quad . \qquad (27C7)$$

For example, if $N_r = 0.215$, then the COM scattering angle $\psi = 55.2$ degrees.

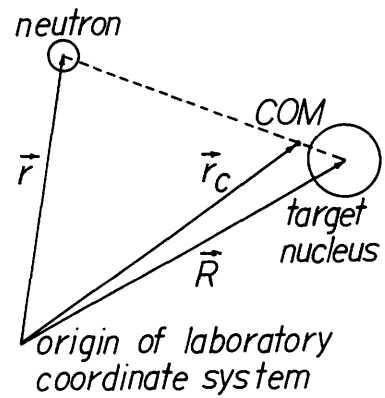

Fig. 27C4. Location of the center of mass (COM).

Consider the case of *inelastic scattering*, in which the target nucleus receives an excitation energy ε. If E was the initial neutron energy, the final neutron energy E' is given by

$$\frac{E'}{E} = \frac{1}{(A+1)^2}\left[1 + A^2\left(1 - \frac{\varepsilon}{E}\right) + 2A\cos\psi\left(1 - \frac{\varepsilon}{E}\right)^{\frac{1}{2}}\right] \quad , \tag{27C8}$$

and the neutron scattering angle θ measured in the laboratory system is found from the equation

$$\cos\theta = \frac{1 + A\cos\psi\left(1 - \frac{\varepsilon}{E}\right)^{\frac{1}{2}}}{\left[1 + A^2\left(1 - \frac{\varepsilon}{E}\right) + 2A\cos\psi\left(1 - \frac{\varepsilon}{E}\right)^{\frac{1}{2}}\right]^{\frac{1}{2}}} \quad , \tag{27C9}$$

(Schaeffer, 1973).
The kinetic energy imparted to the target nucleus is equal to $(E - E' - \varepsilon)$. For *elastic scattering*, $\varepsilon = 0$ in these equations.

All values of the azimuthal scattering angle ϕ (Fig. 27C2) are equally probable, so ϕ is distributed uniformly between 0 and 2π:

$$\phi = 2\pi N_r \quad . \tag{27C10}$$

If (α,β,γ) are the original *direction cosines* of the neutron velocity relative to the x, y, and z axes, the new direction cosines are given by

$$\alpha' = \alpha\cos\theta + \gamma\alpha\frac{\sin\theta\cos\phi}{(1-\gamma^2)^{\frac{1}{2}}} - \beta\frac{\sin\theta\sin\phi}{(1-\gamma^2)^{\frac{1}{2}}}$$

$$\beta' = \beta\cos\theta + \gamma\beta\frac{\sin\theta\cos\phi}{(1-\gamma^2)^{\frac{1}{2}}} + \alpha\frac{\sin\theta\sin\phi}{(1-\gamma^2)^{\frac{1}{2}}}$$

$$\gamma' = \gamma\cos\theta - (1-\gamma^2)^{\frac{1}{2}}\sin\theta\cos\phi \quad , \tag{27C11}$$

except for the case $(1-\gamma^2) \ll 1$, where

$$\alpha' = \sin\theta\cos\phi \quad , \quad \beta' = \sin\theta\sin\phi \quad , \quad \gamma' = \gamma\cos\phi \quad . \tag{27C12}$$

may be used for better accuracy (Schaeffer, 1973).

Having calculated the new neutron energy E' and direction (α',β',γ'), we are ready to return to the starting point of the flow chart, Fig. 27C1, and ask whether the neutron escapes from the slab or has another collision. The new path length ℓ is calculated from Eq. (27C2), and so on until the particle escapes from the slab or is absorbed. (Gamma rays are also "killed" if their energy falls below some chosen value, to save computer time by not tracking low-energy gammas.)

tallying

For the case in which several isotopes are present, the algorithm Eq. (27C3) is further divided up according to the macroscopic cross sections for each isotope,

so it determines both the type of interaction and the species of the target nucleus. The slab (or cylinder, in the case of a fusion reactor blanket) is divided up into small spatial regions, and each region is assigned several "bins" in the computer program, to count the number of times a neutron has various types of interactions in that region (such as tritium breeding) and the amount of energy deposited in that region. For example, if a neutron loses 1.2 MeV in an interaction in the spatial region between x = 55 cm and x = 60 cm, then 1.2 MeV is added to the energy deposition bin for that region. If part of this energy is emitted as a gamma ray, however, the gamma ray should be tracked to see where its energy is deposited, and some of the 1.2 MeV may go into other bins.

After tallying case histories of thousands of neutrons, the numbers in the bins are analyzed to determine the desired quantities, such as energy deposition vs. radius and tritium breeding ratio per incident neutron. The required number of neutron histories which must be run is determined from the desired accuracy by a statistical error analysis.

error estimates

Some parameters used in statistical error analysis are defined in Table 27C1.

Consider the problem of determining the fraction of neutrons which are transmitted through a given slab of blanket material. In ordinary Monte Carlo calculations without "splitting" (discussed below), each neutron penetrating through the slab adds one count to the tally, and those which don't penetrate add zero, so the data points x_j are all either 0 or 1.

EXAMPLE PROBLEM 27D1

In a given Monte Carlo simulation with N = 80 neutron histories, 4 neutrons penetrated through the slab. Find the fractional penetration, and estimate the standard error of this value.

Here we have 4 data points with $x_j = 1$ and 76 data points with $x_j = 0$. The mean value is $\bar{x} = 4/80 = 0.05$, which is the simulation estimate of the true fractional penetration μ. The standard deviation of the sample is found from the equation of Table 27C1 to be $s = \left[\frac{80(4)-16}{80(79)}\right]^{\frac{1}{2}} = 0.2193$. We make the customary approximation that $\sigma \simeq s$, and find that $\sigma_{\bar{x}} \simeq 0.2193/(80)^{\frac{1}{2}} = 0.0245$. Then, we can use the consequence of the Central Limit Theorem to estimate the probable error of $\bar{x}$. It is 68 % probable that the experimental value $\bar{x}$ is within $\pm$ 0.0245 of the true value μ. This may be called the "standard error" of $\bar{x}$. Thus, we estimate that $\mu = 0.050 \pm 0.0245$, which is a relative error of about 49 %.

Such a large relative error would make the results practically worthless. To avoid such difficulties, we need to plan ahead to make N large enough to ensure the desired level of accuracy. For example, if we increased N to 800 in the above example, and if 39 neutrons penetrated the slab, then the revised estimate would be $\mu = 0.0488 \pm 0.0076$, or a relative error of 16 %. If we further increased N to 8000 and observed 394 neutrons penetrated, the estimate would become $\mu = 0.04925 \pm 0.00242$, a relative error of 4.9 %.

Table 27C1 Parameters used in statistical error analysis.

individual data points	$x_1, x_2, x_3, \ldots x_j, \ldots x_N$	
number of data points in sample	N	
mean value of data	$\bar{x} = \frac{\Sigma x_j}{N}$	where summation is from 1 to N.
true value sought, to which $\bar{x}$ is an approximation	μ	(The value of μ is a secret known only to Mother Nature)
sample variance (variance of data about $\bar{x}$)	$s^2 \equiv \frac{\Sigma(x_j-\bar{x})^2}{N-1} = \frac{N\Sigma(x_j)^2 - (\Sigma x_j)^2}{N(N-1)}$	
standard deviation of sample	s	(x_j relative to $\bar{x}$)
standard deviation (of data about μ)	σ	(x_j relative to μ)
standard deviation of the mean	$\sigma_{\bar{x}} = \sigma/N^{\frac{1}{2}}$	($\bar{x}$ relative to μ)
error	$\varepsilon = \lvert\bar{x} - \mu\rvert$	
probability that error is less than z	$P(\varepsilon<z)$	

ESTIMATION OF PROBABLE ERROR

Central Limit Theorem: If N is large ($N \gtrsim 30$), the distribution of $\bar{x}$ about μ is closely approximated by a normal (Gaussian) distribution with standard deviation $\sigma_{\bar{x}}$.

Consequence: $P(\varepsilon<z) = \text{erf}(z/2^{\frac{1}{2}}\sigma_{\bar{x}})$ (Error function: Appendix E)

Example: It is 68.3 % probable that $\varepsilon < \sigma_{\bar{x}}$ (the standard error)
It is 95.4 % probable that $\varepsilon < 2\sigma_{\bar{x}}$.
It is 99.7 % probable that $\varepsilon < 3\sigma_{\bar{x}}$.

RELATION BETWEEN s AND σ (Burlington and May, 1970)

If N = 5, it is 90 % probable that $.73 < (s/\sigma) < 2.65$.
If N = 10, it is 90 % probable that $.77 < (s/\sigma) < 1.73$.
If N = 20, it is 90 % probable that $.81 < (s/\sigma) < 1.41$.
If N = 30, it is 90 % probable that $.84 < (s/\sigma) < 1.30$.

number of case histories needed

For the simple situation in which the data are either 0 or 1, $\Sigma(x_j)^2 = \Sigma x_j$, and the expression for s may be simplified to the form

$$s = \left[\frac{N\bar{x}(1-\bar{x})}{N-1}\right]^{\frac{1}{2}} , \tag{27C13}$$

so the standard error estimate yields

$$\frac{\sigma_{\bar{x}}}{\mu} \simeq \frac{s}{N^{\frac{1}{2}}\bar{x}} = \left[\frac{1-\bar{x}}{\bar{x}(N-1)}\right]^{\frac{1}{2}} . \tag{27C14}$$

which gives the same error estimates obtained above, namely 49 %, 16 %, and 4.9 % respectively. For large N and small $\bar{x}$, the relative error reduces to

$$\frac{\sigma_{\bar{x}}}{\mu} \simeq \left[\frac{1}{N\bar{x}}\right]^{\frac{1}{2}} \qquad \text{or} \quad N = \left(\frac{\mu}{\sigma_{\bar{x}}}\right)^2 \frac{1}{\bar{x}} \tag{27C15}$$

We can use this formula to estimate the number of histories required for a given degree of accuracy ($\sigma_{\bar{x}}/\mu$), if we have an estimate of $\bar{x}$ (or of μ). For example, if we expect $\bar{x} \simeq 0.003$ we want a relative error of less than 5 %, then the required value is $N = 1/(.05)^2\bar{x} = 1.3 \times 10^5$ neutron histories. This large value illustrates the main limitation of ordinary Monte Carlo methods: study of improbable phenomena requires excessively large numbers of case histories. To get around this difficulty, a number of "variance reduction" techniques have been devised to decrease the probable error without increasing N.

variance reduction techniques

The main types of variance reduction techniques are:

* *statistical tallying.* Instead of counting each particle as 0 or 1, the particle is given a variable weight W_j, which may be split up and deposited in many bins during the particle history. For example, if the probability of absorption during a given collision is 0.12, then $0.12W_j$ is deposited in the absorption bin at that point, and $0.88W_j$ continues the history. In the slab penetration problem, each neutron flight path could be extended to the exit boundary to estimate the penetration probability at that step, and the corresponding fractional penetration weight tallied and subtracted from the particle weight.
* *importance functions.* An "importance function" is a means for increasing the number of particles in a spatial, angular, or energy region of interest. (The region of interest in the slab penetration problem is the spatial region near the exit boundary). To conserve particles, $N_g W_g$ = constant, where N_g is the number of particles in a group g and W_g is their weight. For example, if the number of particles in a given region is doubled, then their weights must be halved. (This is called *splitting.*)
* *avoidance of gaming.* Every time a random number N_r is used to make a decision, the variance of the data is increased, and so is $\sigma_{\bar{x}}$. It is thus desirable to get a maximum amount of information from a Monte Carlo program with a minimum of random-number decisions. Reducing the use of random-number decisions is called "avoidance of gaming".

Some techniques for variance reduction are listed in Table 27C2. Systematic sampling should not be used in more than one decision, in order to avoid possible errors due to correlations of two non-random decisions. In shielding problems with thick slabs, many splitting planes may be placed in the slab, to keep the number of particles roughly constant through the slab, while greatly decreasing their individual weights. Thus, for the case in which N = 1000 and $\mu = 0.002$, instead of 2 particles emerging from the slab, one might have over 1000 particles emerging with an overall average weight of about 0.002. For this case, the probable error is greatly reduced in comparison to the case of 2 neutrons emerging. In spite of the advantages of variance reduction techniques, their use complicates the program and should be avoided if ordinary Monte Carlo can do an adequate job (for example, when $\bar{x}$ is not small).

Table 27C2. Variance reduction techniques used with Monte Carlo simulation of radiation transport.

avoidance of gaming
- statistical tallying of fractional weights.
- statistical estimation of fractional penetration, backscatter, etc.
- systematic sampling = using an ordered cycle to replace N_r at one point in the program. For example, if there are N = 100 cases, the values replacing N_r could be 0.005, 0.015, 0.025, ..., 0.995 .

importance functions
- source biasing = artificially increasing the number of incident particles going in the desired direction or having the desired energy (with a corresponding reduction of their weights).
- path-length biasing = artificially decreasing the flight path lengths (to increase the number of interactions in a given region) or increasing the flight path lengths (to increase the number penetrating through the region), with a corresponding adjustment of particle weights.
- splitting = artificially doubling the number of particles entering a given region, while halving their weights.
- Russian Roulette = "killing" some of the particles in regions of little interest, and increasing the weights of the remaining particles. (opposite of splitting.)

A sample ordinary Monte Carlo program for estimating neutron penetration, absorption, and reflection in a slab is listed by Schaeffer (1973).

For one-dimensional problems and two-dimensional problems with simple geometry, transport theory is probably faster and more accurate than Monte Carlo. However, for complex two- and three-dimensional problems, transport theory is too cumbersome, and Monte Carlo must be used. For example, estimation of the radiation streaming out a neutral beam injection port is best done with the Monte Carlo method.

27D. Blanket and Shield Designs

To illustrate blanket neutronics studies, we will describe the Princeton Reference Design (PRD), an early tokamak reactor study. This design has a blanket of FLIBE with PE-16 structure (43 % Ni, 39 % Fe, 18 % Cr) cooled by helium, and a shield of concrete (90 %) and SS 305 (5 %).

flux distribution and neutron balance

Figures 27D1 and 27D2 show the variations of neutron and gamma fluxes with position and energy in the PRD blanket and shield. The fluxes were calculated in cylindrical geometry with the ANISN discrete ordinates code, P_3-S_8 approximation, with 52 neutron energy groups and 21 gamma energy groups. The discontinuity near r = 440 cm corresponds to the boundary between the blanket (r = 360 to 440 cm) and the shield (r = 445 to 500 cm). The neutron flux is attenuated by about 10^{-6} between the first wall (r = 360 cm) and the magnet coils outside the shield.

The neutron production and absorption in various elements and spatial regions are shown in Table 27D1. On the average, 0.280 secondary neutrons are produced in the blanket by (n,2n) reactions per incident neutron. Of the 1.280 neutrons

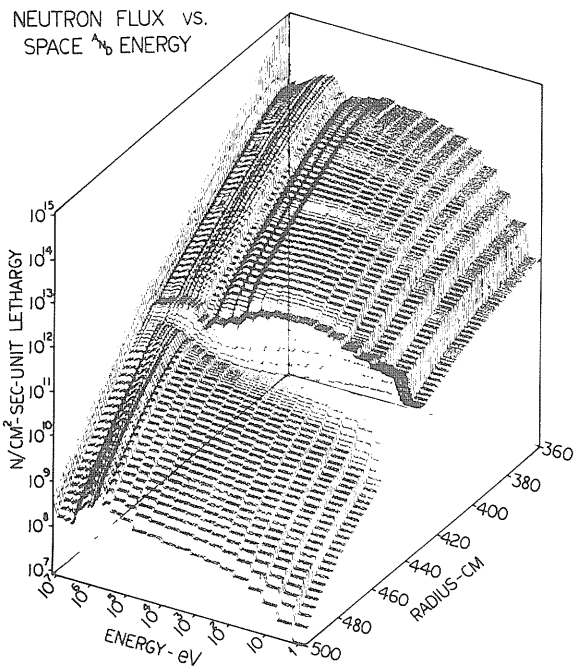

Fig. 27D1. Variation of neutron flux with position and energy in the PRD blanket and shield. From R. G. Mills, Editor, "A fusion power plant", MATT-1050 (1974), Fig. 10.5. (Research at PPPL is supported by Princeton University and DOE under Contract #DE-AC02-76-CH03073 .)

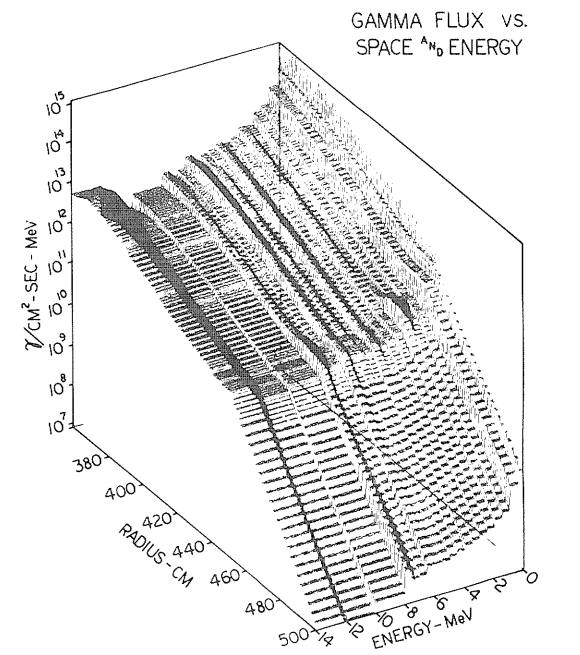

Fig. 27D2. Variation of gamma flux with position and energy in the PRD blanket and shield. From R. G. Mills, Editor, MATT-1050 (1974), Fig. 10.9.

Table 27D1. Neutron production and absorption reactions in a tokamak reactor blanket and shield, per incident neutron. [The fluorine (n,2n) reaction was not incorporated in the neutron balance]. From R. G. Mills, Editor, MATT-1050 (1974), Tables 10.6 and 10.7.

Neutron production by (n,2n) reactions

Zone Number	Fe	Cr	Ni	Li-6	Li-7	Be	F	Sum
2	.024201	.006275	.001352	.0	.0	.0	.0	.031828
3	.007021	.001794	.000382	.000550	.005035	.109665	.018732	.124447
4	.002435	.000614	.000129	.0	.0	.0	.0	.003178
5	.002106	.000526	.000110	.000252	.002183	.065049	.007945	.070226
6	.000748	.000185	.000038	.0	.0	.0	.0	.000971
7	.000705	.000173	.000035	.000116	.000955	.036983	.003387	.038967
8	.000117	.000028	.000006	.0	.0	.0	.0	.000151
9	.000060	.000014	.000003	.000025	.000196	.010017	.000668	.010315
10	.000006	.000002	.000003	.0	.0	.0	.0	.000011
All	.037399	.009611	.002058	.000943	.008369	.221714	.030732	.280094

Neutron loss by absorption reactions

Zone Number	Fe	Cr	Ni	Li-6	Li-7	Be	F	Sum
2	.021592	.010600	.043341	.0	.0	.0	.0	.075533
3	.009189	.004666	.019458	.269370	.001048	.012482	.041053	.357266
4	.004528	.002370	.009513	.0	.0	.0	.0	.016411
5	.005220	.002782	.010666	.282892	.000537	.008273	.027899	.338269
6	.002599	.001409	.005076	.0	.0	.0	.0	.009084
7	.003391	.001849	.006340	.282286	.000314	.005084	.017368	.316632
8	.000883	.000485	.001555	.0	.0	.0	.0	.002923
9	.000602	.000325	.001026	.135383	.000126	.001466	.005042	.143970
10	.000565	.000205	.000644	.0	.0	.0	.0	.001414
All	.048569	.024691	.097619	.969931	.002025	.027305	.091362	1.261502

available (per incident neutron), 1.2615 are absorbed in the blanket, and 0.0185 neutrons leak into the shield.

tritium breeding

The tritium breeding reactions for the PRD blanket are summarized in Table 27D2. If all the neutrons emitted by fusion were trapped in the blanket and shield, the breeding ratio would be 1.067 tritium atoms per neutron. Neutron loss through beam injection ducts, pumping ports, etc., reduces the effective breeding ratio below this value. The FLIBE used in the PRD has a lower breeding

Table 27D2. Tritium production in the PRD blanket, per incident neutron. From R. G. Mills Editor, MATT-1050 (1974), Table 10.8.

Zone	Be	Li-7	Li-6	Total
2	.0	.0	.0	.0
3	.001996	.048669	.269238	.319903
4	.0	.0	.0	.0
5	.000814	.026913	.282809	.310536
6	.0	.0	.0	.0
7	.000334	.014497	.282238	.297069
8	.0	.0	.0	.0
9	.000063	.003742	.135369	.139174
10	.0	.0	.0	.0
All	.003207	.093821	.969654	1.066682

ratio than lithium and solid lithium compounds. The tritium breeding ratios attainable in blankets of Li, Li_2O, and Li_7Pb_2 are shown in Fig. 27D3 as functions of the volume percent of stainless steel structure.

energy deposition

The energy deposition in a blanket and shield may be calculated from the flux distribution, using tabulated "Kinetic Energy Released in Materials" (KERMA) factors. The resulting nuclear heating in the PRD is shown in Fig. 27D4. The total power produced in the blanket and shield is 4562 MW. Of this, 2752 MW is from thermalization of fusion neutrons, and 1810 MW is produced by additional nuclear reactions. Therefore, the blanket energy gain M = 4562/2752 = 1.66 for the PRD. This high value of M is due to (n,2n) reactions in beryllium. Typically, M ∿ 1.2 in blankets without Be.

radiation damage

Figure 27D5 shows some indicators of radiation damage to the structure of the PRD as functions of radius. These values are useful in estimating structural component lifetime.

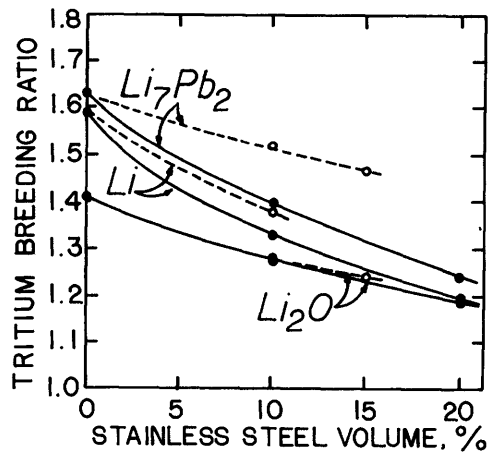

Fig. 27D3. Attainable breeding ratio vs. volume percent of stainless steel structure, for blankets of Li, Li_7Pb_2, and Li_2O, assuming full density. (The same breeding ratios could be attained with a given void fraction by making the blanket thicker.) Solid circles: without water, 15 v/o He in Li_7Pb_2 and Li_2O. Open circles: with 10-15 v/o water and 0-5 v/o He in Li_7Pb_2 and Li_2O. Breeder blanket= 0.8 m; 50% SS + 50% B_4C shield =0.2 m. From J. C. Jung, "The neutronic performance of candidate tritium breeding materials", Special Purpose Materials, Annual Progress Report, DOE/ET-0095 (1979), Fig. 1.1.7.

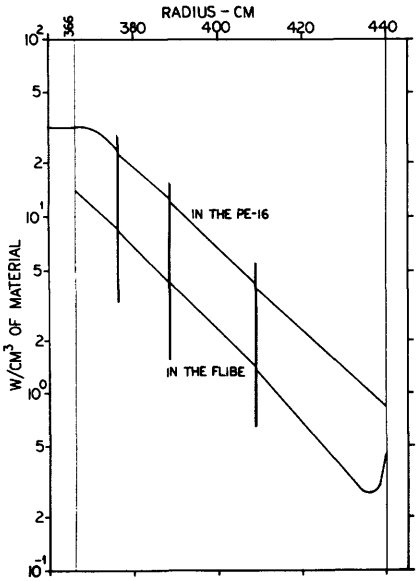

Fig. 27D4. Nuclear heating vs. radius in the PRD blanket. From R. G. Mills, Editor, MATT-1050 (1974), Fig. 10.16.

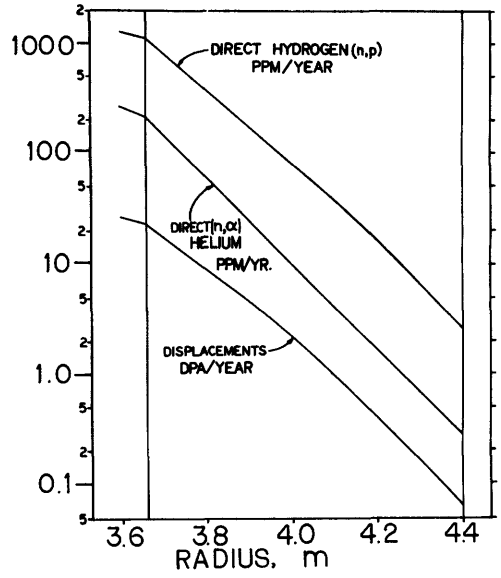

Fig. 27D5. Annual production of hydrogen, helium, and displacements per atom as a function of position in the PRD blanket. From R. G. Mills, Editor, MATT-1050 (1974), Fig. 10.18.

Decay heat from induced radioactivity in the PRD is shown as a function of time after shutdown in Fig. 27D6.

benchmark calculations

In order to compare the accuracy of various computational methods, a "benchmark" calculation of tritium breeding in a fusion reactor blanket was done by several different laboratories, using various computer codes. The blanket model used in this analysis is shown in Fig. 27D7. The resultant breeding ratios calculated by various methods are shown in Table 27D3. There is good agreement between the Monte Carlo result and the discrete ordinates codes' results.

neutron streaming

Neutron streaming through fusion reactor ports and ducts is a major problem of shield design. Figure 27D8 shows the calculational model used for a Monte Carlo study of neutron streaming through a tokamak neutral beam injection duct.

The goal of this study is to find out how much the predictions of nuclear heating and radiation damage to the magnet coils increase when duct streaming is taken into account. The blanket consists of stainless steel 316, lithium, and graphite, and the shield contains SS 316, water, boron, and lead. The neutron wall loading is 1 MW/m^2, which represents 4.4×10^{17} neutrons/m^2 sec . First the ANISN discrete ordinates code was run, to predict radiation attenuation, nuclear heating and radiation damage with no duct streaming. Then the MORSE Monte Carlo code was run to study streaming through the duct.

Because the fraction of neutrons streaming out the duct and penetrating to detector positions 1-5 is very small, ordinary "forward" Monte Carlo would be too time-consuming. Instead, the solution of the "adjoint" Boltzmann transport equation (Hansen and Sandmeier, 1965) was simulated. Source angular biasing was used to direct more neutrons and gammas through the duct, and path length stretching, nonabsorption weighting, splitting, and Russian roulette were also used to reduce variance.

The increase in nuclear heating and radiation damage caused by neutron and gamma streaming out the duct is summarized in Table 27D4. It is clear that duct streaming is the main source of nuclear heating and radiation damage to the coils at the detector positions chosen. Detailed Monte Carlo studies of this type will be indispensible in fusion reactor designs.

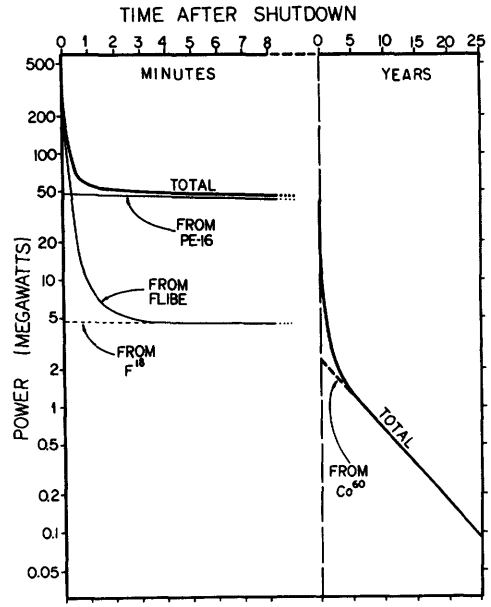

Fig. 27D6. Decay heat vs. time after shutdown, for the PRD. From R. G. Mills, Editor, MATT-1050 (1974), Fig. 10.20 .

Distances in cm	0		150		200		200.5		203.5		204				264		294		300
Origin	Plasma		Vacuum		Nb		94% Li 6% Nb		Nb		20 cm	94% Li 6% Nb	20 cm		C		94% Li 6% Nb		
Zone Number	1		2		3		4		5			6			7		8		
Region Number	1		2		3		4		5		6	7	8		9		10		
Material	A		B		C		D		C			D			E		D		
Number of Intervals Per Zone	1		1		3		6		3			30			15		3		
Thickness	150		50		0.5		3		0.5			60			30		6		

Fig. 27D7. Configuration of the "bench-mark" blanket model. Intervals in each zone are of equal step length. There are 62 intervals altogether. From D. Steiner, "Analysis of a bench-mark calculation of tritium breeding in a fusion reactor blanket: the United States contribution", ORNL-TM-4177 (1973), Fig. 1.

Table 27D3. Summary of bench-mark calculations of tritium breeding ratio, per source neutron. All methods used the same cross section data. From D. Steiner, ORNL-TM-4177 (1973), Table 5.

Laboratory	Method of Calculation	Code Used	Breeding in ^{7}Li	Breeding in ^{6}Li	Total Breeding
BNL	Discrete Ordinates P_3-S_4	ANISN	0.512	0.883	1.395
LASL	Discrete Ordinates P_3-S_4	DTF-IV	0.507	0.888	1.395
LASL	Discrete Ordinates P_3-S_8	DTF-IV	0.522	0.891	1.413
LASL	Discrete Ordinates P_3-S_{12}	DTF-IV	0.529	0.892	1.421
ORNL	Discrete Ordinates P_3-S_4	ANISN	0.518	0.933	1.451
ORNL	Discrete Ordinates P_3-S_8	ANISN	0.522	0.934	1.456
ORNL	Discrete Ordinates P_3-S_{12}	ANISN	0.527	0.932	1.459
ORNL	Discrete Ordinates P_3-S_{16}	ANISN	0.526	0.932	1.458
ORNL	Monte Carlo	MORSE	0.523 ± 0.003	0.932 ± 0.003	1.455 ± 0.004

Table 27D4. The ratio of nuclear heating and radiation damage predicted by the MORSE Monte Carlo code (including duct streaming) to the values predicted by the ANISN discrete ordinates code (ignoring streaming), for the Tokamak geometry of Fig. 27D8. Only the "true track length estimator" data are shown here. From R. T. Santoro, J. S. Tang, R. G. Alsmiller, Jr., and J. M. Barnes, Nuclear Technology 37, 65-72 (1978), Tables II, III, V.

detector position:	1	2	3	4	5
nuclear heating					
neutron	182	12	30	44	26
gamma	16	2	9	125	115
atomic displacement rate (displacements/ atom-year)					
SS 316	95	5	26	20	35
Nb	66	3	23	15	32
Cu	60	4	26	18	32
Al	36	2	30	26	31
helium gas production					
SS 316	6336	150	64	173	16
Nb	7384	200	54	160	15
Cu	6222	120	40	158	15
Al	6250	160	55	155	16
number of particle histories N (10^5) used in calculation	2	2	4	3.4	6

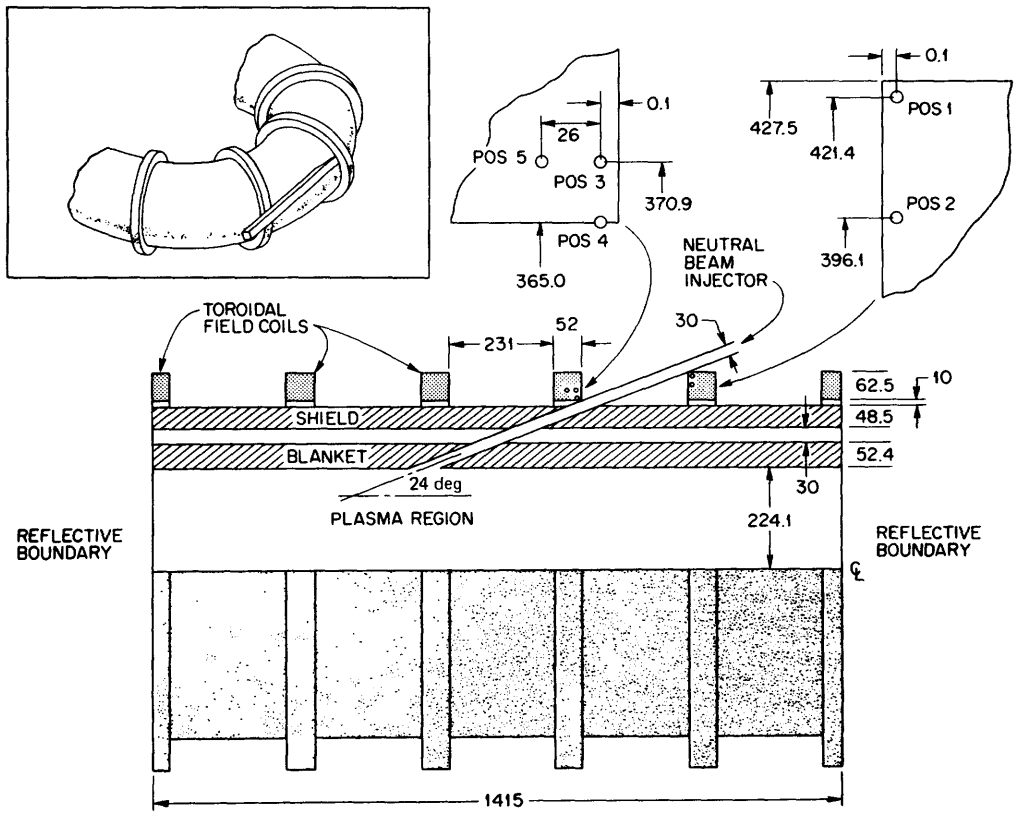

Fig. 27D8. Illustration of the geometry and detector locations used for a Monte Carlo simulation of neutron streaming out through a Tokamak neutral beam injection port. Dimensions are in cm. The detector positions 1, 2, 3, 4, and 5 represent points where the neutron flux is to be tallied by the Monte Carlo program. From R. T. Santoro, J. S. Tang, R. G. Alsmiller, Jr., and J. M. Barnes, "Monte Carlo analysis of the effects of a blanket-shield penetration on the performance of a tokamak fusion reactor", Nuclear Technology 37, 65-72 (1978), Fig. 1.

Problems

1. Legendre polynomials: (a) Show that $P_3(\mu)$ satisfies the basic differential equation. (b) Derive $P_4(\mu)$ using the recurrence relation.

2. Derive the equation for the Legendre expansion coefficients a_ℓ. (Hint: multiply the expansion theorem by $P_M(\mu)d\mu$ and integrate, using the orthogonality condition.)

3. Given $\Sigma(x,\mu_0,E'\to E) = S(x,E'\to E)(1 + a\mu_0 + b\mu_0^2)$, calculate the expansion coefficients $\Sigma_\ell(x,E'\to E)$ of the expansion (27B4).

4. A 1 MeV neutron is incident at x = 0, y = 0, z = 0 on a slab with the following parameters: $\Sigma_{n,2n} = .001\ cm^{-1}$, $\Sigma_{in} = .02\ cm^{-1}$, $\Sigma_{el} = .410\ cm^{-1}$, $\Sigma_a = .030\ cm^{-1}$, L = 10 cm, isotropic scattering, A = 30, and angle of incidence $\theta_0 = 30°$ (in y-z plane, as in Fig. 27C2). Track the neutron history with the Monte Carlo technique, and determine the location (x,y,z) where it has its second collision, using the following random numbers in order of appearance: .5149, .7830, .2365, .4482, .3389, .7124, ... [In the equation for path length, use $N'_r = .5149$].

5. Estimate the number of ordinary Monte Carlo neutron histories needed for a calculation of magnet coil heating with 10 % accuracy, if the attenuation factor is to be 10^{-6}.

6. Given the masses of ten apples chosen randomly from an orchard: (190, 205, 187, 212, 220, 171, 203, 194, 213, 192 grams), estimate the mean apple mass for the orchard, and the probability that your estimate is close to the true mean value within certain limits. If you weighed 30 apples from the same orchard altogether, and the mean and standard deviation were 196 and 8.2, what could you say about the true mean value?

7. Using ordinary Monte Carlo, how many neutron histories would be needed to achieve the accuracy stated for ^7Li in Table 27D3 ?

BIBLIOGRAPHY

transport theory

G. I. Bell and S. Glasstone, *Nuclear Reactor Theory*, Van Nostrand Reinhold, New York, 1970.

M. Clark, Jr. and K. F. Hansen, *Numerical Methods of Reactor Analysis*, Academic Press, New York, 1964.

G. E. Hansen and H. A. Sandmeier, "Neutron penetration factors obtained by using adjoint transport calculations", *Nuclear Science and Engineering 22*, 315 (1965).

E. Inönü and P. F. Zweifel, *Developments in Transport Theory*, Academic Press, New York, 1967.

J.-C. Jung, "A computational method for neutron transport problems in toroidal geometry", *Nuclear Science and Engineering 65*, 130-140 (1978).

N. M. Schaeffer, *Reactor Shielding for Nuclear Engineers*, TID-25951, AEC Technical Information Center, Oak Ridge, 1973.

A. M. Weinberg and E. P. Wigner, *The Physical Theory of Neutron Chain Reactors*, University of Chicago Press, Chicago, 1958.

Monte Carlo techniques

L. L. Carter and E. D. Cashwell, *Particle-Transport Simulation with the Monte Carlo Method*, TID-26607, 1975.

E. D. Cashwell and C. J. Everett, *A Practical Manual on the Monte Carlo Method for Random Walk Problems*, Pergamon Press, New York, 1959.

M. Clark, Jr. and K. F. Hansen, *Numerical Methods of Reactor Analysis*, Academic Press, New York, 1964.

R. T. Santoro, J. S. Tang, R. G. Alsmiller, Jr., and J. M. Barnes, "Monte Carlo analysis of the effects of a blanket-shield penetration on the performance of a tokamak fusion reactor", *Nuclear Technology 37*, 65-72 (1978).

N. M. Schaeffer, *Reactor Shielding for Nuclear Engineers*, TID-25951, AEC Technical Information Center, Oak Ridge, 1973.

mathematics

G. Arfken, *Mathematical Methods for Physicists*, Second Edition, Academic Press, New York, 1973.

R. S. Burlington and D. C. May, Jr., *Handbook of Probability and Statistics with Tables*, Second Edition, McGraw-Hill, New York, 1970.

J. E. Freund, *Modern Elementary Statistics*, Third Edition, Prentice-Hall, Englewood Cliffs, N.J., 1967.

D. L. Harnett, *Introduction to Statistical Methods*, Addison-Wesley, Reading, PA, 1970.

L. A. Pipes and L. R. Harvill, *Applied Mathematics for Engineers and Physicists*,

M. R. Spiegel, *Theory and Problems of Calculus of Finite Differences and Difference Equations*, McGraw-Hill, New York, 1971.

blanket and shield calculations

H. Bachmann, U. Fritscher, F. W. Kappler, D. Rusch, H. Werle, and H. W. Wiese, "Neutron spectra and tritium production measurements in a lithium sphere to check fusion reactor blanket calculations", *Nuclear Science and Engineering 67*, 74-84 (1978).

B. Badger et al, "NUWMAK, a tokamak reactor design study", UWFDM-330 (1979), Chapter VIII.

F. Beranek and R. W. Conn, "Neutron moderation in inertial confinement fusion pellets and effects on damage and radioactive inventory", *Nuclear Technology 47*, 406-411 (1980).

J. Chao, B. B. Mikic, and N. E. Todreas, "Neutronic performance of fusion reactor blankets with different coolants and structural arrangements", *Nuclear Technology 45*, 113-120 (1979).

J.-C. Jung, "A comparative study of tritium breeding performance of lithium, Li_2O, and Li_7Pb_2 blankets in a tokamak power reactor", *Nuclear Technology 50*, 60-82 (1980).

R. G. Mills, Editor, *A Fusion Power Plant*, MATT-1050 (1974), Chapter 10.

J. R. Powell, J. A. Fillo, B. G. Twining, and J. J. Dorning, Editors, Proceedings of the Magnetic Fusion Energy Blanket and Shield Workshop, ERDA-76/117/1 and ERDA-76/117/2 (CONF-760343), 1975.

Proceedings of the 4th ANS Topical Conference on the Technology of Controlled Nuclear Fusion (King of Prussia, PA, 1980), DOE, 1981.

R. T. Santoro, V. C. Baker, and J. M. Barnes, "Neutronics and photonics calculations for the Tokamak Experimental Power Reactor", *Nuclear Technology 37*, 274-295 (1978).

R. T. Santoro, R. A. Lillie, R. G. Alsmiller, Jr., and J. M. Barnes, "Shielding calculations for the Tokamak Fusion Test Reactor neutral beam injectors", *Nuclear Technology 47*, 412-420 (1980).

D. Steiner, "Analysis of a bench-mark calculation of tritium breeding in a fusion reactor blanket: the United States contribution", ORNL-TM-4177 (1973).

CHAPTER 28

ENVIRONMENT AND ECONOMICS

28A. Introduction

Environmental and cost requirements will be the final basis for comparison between solar, fission, and fusion power sources. Some interactions of a power plant with the environment are illustrated in Fig. 28A1. Most of these apply to all types of power plants using heat engines (solar, fission, fusion, and fossil fuel). Environmental considerations for fusion reactors are listed in Table 28A1.

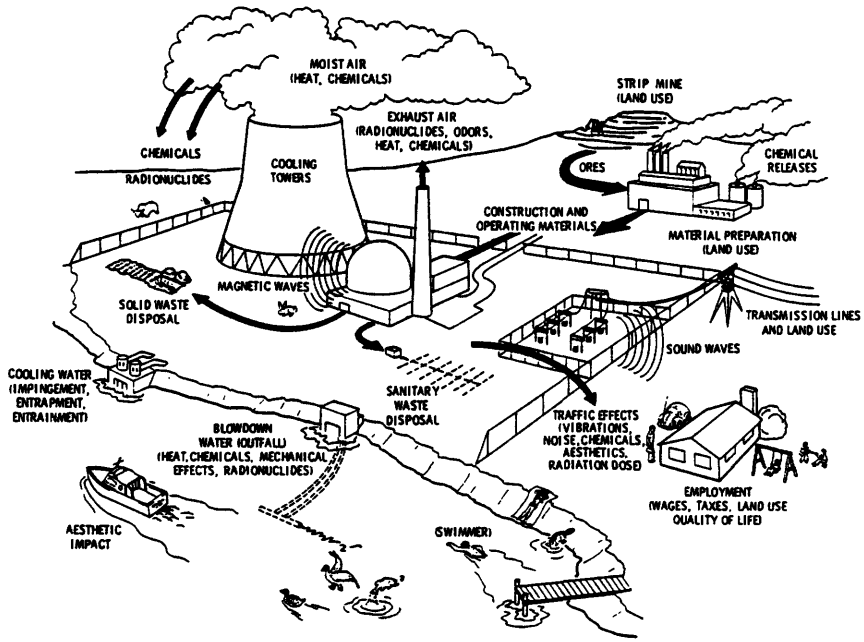

Fig. 28A1. Interactions of a power plant with the environment. From J. R. Young, "An environmental analysis of fusion power to determine related R&D needs", BNWL-2010 (1976).

Table 28A1. Environmental and other considerations of fusion power plants.

routine tritium releases	effects of stray magnetic fields
disposal of activated structure	plant decommissioning
accidental releases	proximity to
tritium	industry
activated structure	population centers
chemical discharges	transportation facilities
thermal discharge to water and air	natural hazards (earthquakes, floods, etc.)
stored energy release	effects on local economic and social conditions
liquid metal fire	aesthetic impact
magnet coils	
radioactive afterheat	
atmospheric pressure on chamber	

28B. Tritium

biological hazard

If N_0 atoms of a radioactive element are present at time t = 0, the number N present at any later time is

$$N = N_0 e^{-\lambda t} \quad , \tag{28B1}$$

where

$$\lambda = \ln 2 / t_{\frac{1}{2}} \quad \text{(Bq)} \tag{28B2}$$

is the *decay constant*, and $t_{\frac{1}{2}}$ is the *half-life* (s). When $t = t_{\frac{1}{2}}$, $N = \frac{1}{2}N_0$, hence the name "half-life". The *activity* of a radioisotope is

$$\text{Activity} = N\lambda \quad \text{(Bq)} \tag{28B3}$$

where the unit Becquerel (Bq) represents disintegrations per second. Units of radioactivity are defined in Appendix A. Some radiological aspects of tritium are described in Table 28B1.

The *biological half-life* refers to the time during which half of the tritium is eliminated from the body. A person typically receives an annual dose of about 0.1 rem from natural background radiation (cosmic rays, etc.), which is comparable to the dose from ingestion of 1 Ci of tritium.

Tritium is one of the least hazardous radionuclides. It is not concentrated in the food chain. Its aqueous forms (T_2O, THO, TDO) are more hazardous than its gaseous forms (T_2, TH, TD). Aqueous forms do not disperse as readily as gaseous forms, and they can enter tissue more easily.

If gaseous TH, TD or T_2 came in contact only with skin, it would pose little hazard, because its maximum energy beta particles cannot even penetrate the exterior dead skin layer (an energy of 70 keV is required for penetration). However, if the TH, TD or T_2 is inhaled, it may become THO, TDO, or T_2O and stay in the body in aqueous form, with danger to the body. Thus, it is usual to assume conservatively that all of the tritium released is in aqueous form, for which the MPC is about 2000 times smaller than for gaseous tritium.

The *biological hazard potential* (BHP) represents the quantity of air or water which would be required to dilute a radioisotope to a safe concentration. For a

Table 28B1. Radiological aspects of tritium, $T \equiv {}^{3}_{1}H$.

abundance = about 10 kg in the earth's upper atmosphere

atomic mass = 3.01605 u = 5.00835×10^{-27} kg

beta decay: $T \rightarrow {}^{3}_{2}He + \beta + \bar{\nu}$. ($\beta \equiv$ electron , $\bar{\nu} \equiv$ antineutrino) .

half-life $t_{\frac{1}{2}}$ = 12.3 years

decay constant $\lambda = 1.787 \times 10^{-9}$ Bq

beta energy: maximum = 18.5 keV

average = 5.7 keV

activity of 1 kg(T) = 9.64 MCi = 3.57×10^{17} Bq

biological half-life in humans $\simeq$ 10 days

dose from ingestion of 1 Ci(T) $\sim$ 0.070 rem = 0.7 mGy

maximum permissible body burden = 1 mCi = 3.7×10^{7} Bq

maximum permissible concentration (MPC) assuming continuous exposure:

THO or T_2O in air	0.2 μCi/m^3 = 7.4 kBq/m^3
THO or T_2O in water	3 mCi/m^3 = 11 MBq/m^3

[These MPC are from the U.S. Nuclear Regulatory Commission, Code of Federal Regulations, Title 10, Chapter 1, Part 20 (1978). Higher MPC apply to the case of workers exposed only 40 hours/week.]

Inventory of a 1 GWe DT fusion power plant $\sim$ 10 kg(T) $\simeq$ 100 MCi

biological hazard potential (BHP) $\equiv$ inventory/MPC
for DT reactors:
BHP(air, continuous exposure) $\sim 5 \times 10^{14}$ m^3(air) for a 1 GWe plant
BHP(water, continuous exposure) $\sim 3 \times 10^{10}$ m^3(water) for a 1 GWe plant.

DT fusion reactor, the tritium BHP would be $\sim 5 \times 10^{14}$ m^3(air). Tritium inventories and BHP of DD fusion reactors would be much smaller. For comparison, the BHP of plutonium isotopes in a 1 GWe LMFBR is about 2×10^{19} m^3 (air), and the BHP of ^{131}I from a 1 GWe fission reactor (via the grass-cow-milk pathway) is about 6×10^{20} m^3 (air).

production rate

The rate of tritium consumption is

$$\text{Consumption rate} = P/W'_{DT} \qquad \text{(atoms/s)} \tag{28B4}$$

where P is the reactor thermal power (including blanket reactions),

$$W'_{DT} = 1.6 \times 10^{-13}(3.5 + 14.1\ M) \qquad \text{(J)} \quad , \tag{28B5}$$

and M is the blanket energy gain (Chapter 4). Typically $M \simeq 1.2$, and $W'_{DT} \simeq 3.2\times10^{-12}$ J. For example, if P = 2.5 GWth, then the tritium consumption rate = 7.8×10^{20} atoms/s, which corresponds to a mass consumption rate of 0.34 kg(T)/day.

By definition, the breeding ratio R_B = (production rate)/(consumption rate). If $R_B = 1.2$ in the above example, then tritium would be produced at the rate of 9.4×10^{20} atoms/s = 0.41 kg/day. At the same time, the tritium is decaying radioactively with a time constant $\lambda = 1.79\times10^{-9}$ Bq. If N is the total number of tritium atoms in the system, its rate of change is given by the equation

$$dN/dt = R_B P/W'_{DT} - P/W'_{DT} - \lambda N \quad . \tag{28B6}$$

Taking $N = N_0$ at $t = 0$, the solution of this equation is

$$N/N_0 = (1/x)(1 - e^{-\lambda t}) + e^{-\lambda t} \tag{28B7}$$

where

$$x \equiv \frac{W'_{DT}\lambda N_0}{P(R_B-1)} \quad . \tag{28B8}$$

This equation may also be solved for t, with the result

$$t = \frac{1}{\lambda} \ln\left[\frac{1-x}{1 - xN/N_0}\right] \quad (s) \quad . \tag{28B8}$$

If $R_B > 1$, the quantity of tritium on hand will increase with time. Let t_2 be the time at which $N/N_0 = 2$ (the "doubling time"). If $x \ll 1$, the logarithm terms can be expanded in Taylor series to obtain

$$t_2 = (x/\lambda)(1 + 3x/2 + \ldots) \quad (s) \quad . \tag{28B9}$$

For comparison, we will estimate the doubling time for fuel in *fission* breeder reactors. Since the decay rates of ^{239}Pu and ^{233}U are negligibly small, we may set $\lambda \simeq 0$ in Eq. (28B6) and find

$$N/N_0 = 1 + Pt(R_B - 1)/N_0 W \quad ,$$

$$t_2 = N_0 W/P(R_B - 1) \quad (s) \quad , \tag{28B10}$$

where $W \simeq 200$ MeV $= 3.2\times10^{-11}$ J is the energy released per fission.

EXAMPLE PROBLEM 28B1

Estimate the fuel doubling times of (a) a 2.5 GWth fusion reactor with 10 kg of T, (b) a 2.5 GWth fission breeder with 10^4 kg of fuel, assuming both have $R_B = 1.2$.

(a) For the fusion reactor $N_0 = 10$ kg/$(5.008\times10^{-27}$ kg/atom) $= 2.00\times10^{27}$ atoms(T). Then $x = 2.29\times10^{-2}$, and $t_2 = 1.32\times10^7$ s = 5.1 months.

(b) For the fission reactor, $N_0 = 10^4$ kg/(238 u)$(1.66\times10^{-27}$ kg/u) $= 2.53\times10^{28}$ atoms. From Eq. (28B10), we find $t_2 = 1.62\times10^9$ s = 51 years.

The mass flow rate $\dot{m}$ of tritium through a fusion reactor plasma is

$$\dot{m} = (\text{consumption rate})m_t/f_b = Pm_t/W'_{DT}f_b \quad (\text{kg/s}) \quad , \qquad (28B11)$$

where m_t is the mass of one tritium atom (kg), and f_b is the burnup fraction (Eq. 4D7). For a 2.5 GWth reactor with $f_b = 0.05$, $\dot{m} \simeq 7.8\text{x}10^{-5}$ kg/s = 6.8 kg/day.

tritium inventory

There are three incentives for keeping the reactor tritium inventory low:

initial cost ($\sim$ 1-2 M$/kg)
embrittlement of structure (if tritium concentration $\gtrsim$ 100 appm)
tritium release rates to environment.

The environmental consideration is the most restrictive, making tritium concentrations of 1-10 appm or less desirable in the blanket.

EXAMPLE PROBLEM 28B2

A 2.5 GWth DT fusion reactor has a wall surface area of 2500 m^2 and the blanket contains a layer of Li 0.8 m thick. If the blanket contains 3 appm(T), what is the blanket portion of the tritium inventory (kg)?

The density of lithium is about 450 kg/m^3 (Table 26B3), and the atomic weight of lithium is 6.939x10^{-3} kg/mole, so its atomic density is found from Eq. (2B8) to be n = 3.906x10^{28} atoms/m^3. The lithium volume is 2000 m^3, so the total number of lithium atoms is 7.8x10^{31}. The number of tritium atoms is then 2.34x10^{26}, and the tritium inventory in the blanket is 1.17 kg.

The tritium inventory for the NUWMAK tokamak reactor is illustrated in Table 28B2. The 21.4 kg(T) corresponds to an activity of about 206 MCi. If a six-hour supply were deemed adequate, the inventory would be reduced to 6.85 kg, having an activity of 66 MCi.

Table 28B2. Tritium inventory of the NUWMAK reactor, with cold gas blanket fueling. From B. Badger et al, "NUWMAK, a tokamak reactor design study", UWFDM-330 (1979), Table X-A-2, p. X-5.

Fueling System	
Cryopumps (4 hr. cycle time)	1.6 kg
Storage (1 day's supply, 91.8% duty factor)	19.4 kg
Purification System	
Distillation Columns	0.34 kg
Blanket	
$Li_{62}Pb_{38}$ eutectic	0.088 kg
Processing of breeder	0.01 kg
Reactor Coolant	
Coolant (H_2O)	Negligible
TOTAL	21.4 kg

routine releases

Tritium may flow out of the reactor through the following pathways:

vacuum pumping system
coolant system
blanket tritium removal system (if separate from coolant)
permeation through chamber walls.

Secondary containment will be provided around the vacuum system and chamber walls.

If all the heat rejected from a 2.5 GWth fusion reactor operating at 80 % load factor and 40 % thermal conversion efficiency were carried by once-through condenser water with ΔT = 10 K, then the required condenser volumetric flow rate is found from Eqs. (26E1) and (26E3) to be $A_c v_c$ = 29 m^3/s. If this water carried 0.3 mCi/m^3 of tritium (one-tenth of the MPC), about 750 Ci/day would flow out in the cooling water.

The limits on tritium release to the air will probably require a dose at the site boundary of less than 0.005 rem/year. For typical atmospheric conditions (dilution factor $\chi/Q = 10^{-5}$), this means that the releases to the air must be kept to about 40 Ci/day.

On a global scale, if each fusion reactor emitted 10 Ci/day into the air plus 500 Ci annually during maintenance, then 1000 such plants would emit about 4 MCi/year. This would result in worldwide doses of 4,000 to 20,000 man-rem/year. Cosmic rays also produce about 5.5 MCi/year of tritium in the stratosphere.

The effects of long-term low-level exposure to radiation are under debate. According to the "linear hypothesis", the effects are linearly proportional to the integrated population dose (man-rem). If this hypothesis is correct, then extremely low individual doses would still have significant ill effects upon a few individuals in a large population. According to the "quadratic hypothesis", the effects are proportional to the square of the dose. If this hypothesis is correct, then individuals exposed to very low doses would have no significant ill effects, even if a very large population were exposed.

tritium permeation rates

Consider the case of tritium permeation through a wall of thickness x_1 with tritium pressures p_1 on one side and p_2 on the other, with $p_2 < p_1$. Let c(x) denote the tritium atom concentration within the wall.

Usually, molecular recombination must occur before the tritium can leave the wall. At low driving pressures p_1, surface molecular recombination may be the tritium flow rate-limiting process. At high pressure p_1, or with fluids (such as liquid metals) capable of carrying atomic tritium on the p_2 side, diffusion through the wall is the rate-limiting process. These two cases are illustrated in Fig. 28B1.

The concentration at x = 0 may be estimated from Sievert's Law

$$c(0) = S p_1^{\frac{1}{2}} \quad (\text{atoms}/m^3) \quad , \tag{28B12}$$

where S is the "solubility" of tritium in the given metal ($\text{atoms}/m^3 Pa^{\frac{1}{2}}$).

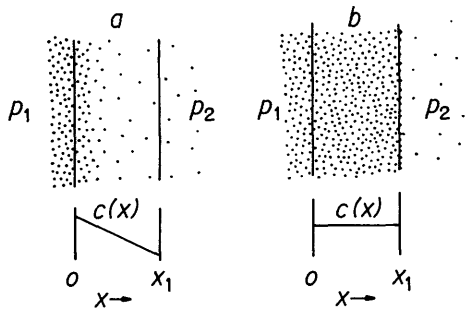

Fig. 28B1. Distribution of tritium atom concentration c(x) within a tube wall. (a) permeation rate limited by diffusion in wall, (b) permeation rate limited by surface recombination.

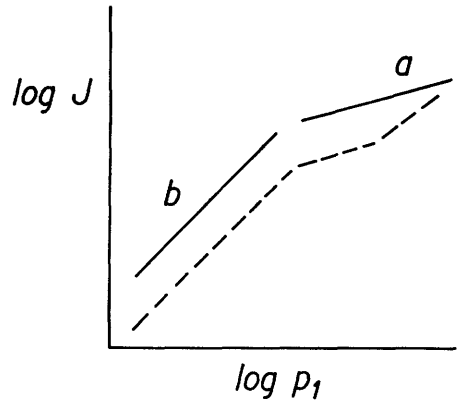

Fig. 28B2. Variation of tritium permeation rate J (atoms/m²s) with driving pressure p_1 for (a) diffusion-limited flow, (b) surface-recombination-limited flow. The dashed curve illustrates the effect of oxide surface films. Based on Zarchy and Axtmann (1978), Fig. 3.

For the case of *recombination-limited flow*, the maximum flow rate may be estimated from

$$J = Kc^2(x_1) \leq Kc^2(0) = KS^2p_1 \quad (\text{atoms/m}^2\text{s}) \quad , \tag{28B13}$$

where the surface recombination coefficient K was given in Fig. 24F1 for a few metals.

For the case of *diffusion-limited flow*, the concentration at $x = x_1$ may also be estimated from Sievert's Law

$$c(x_1) = Sp_2^{\frac{1}{2}} \quad (\text{atoms/m}^3) \quad . \tag{28B14}$$

Using Fick's Law for the diffusion flow rate, we obtain Richardson's Equation:

$$J = -D(dc/dx) \simeq -D[c(x_1) - c(0)]/x_1 = DS(p_1^{\frac{1}{2}} - p_2^{\frac{1}{2}})/x_1 \quad (\text{atoms/m}^2\text{s}) \quad , \tag{28B15}$$

where D is the diffusion coefficient (m^2/s). The product DS is called the "permeation coefficient" or "permeability". The variation of J with p_1 is illustrated in Fig. 28B2. The diffusion and solubility coefficients may be expressed in terms of the wall temperature T(K)

$$D \simeq D_0\exp(-E_d/kT) \quad (\text{m}^2/\text{s}) \tag{28B16}$$

$$S \simeq S_0\exp(-E_s/kT) \quad (\text{atoms/m}^3\text{Pa}^{\frac{1}{2}}) \quad , \tag{28B17}$$

where E_d and E_s are activation energies for diffusion and solution, k is the Boltzmann constant, and D_0 and S_0 are constants. Some values of these constants for ordinary hydrogen in various metals are given in Table 28B3. Diffusion rates are inversely proportional to the square root of the isotopic mass, so $D_0(T) \simeq 0.58D_0(H)$. Values of the permeability DS of hydrogen in various metals are shown in Fig. 28B3.

Table 28B3. Diffusion and solubility coefficients of hydrogen in various metals. There is considerable scatter among experimental measurements, so some values of S_0 and D_0 may have large errors (∿ 50 %). These data are from M. I. Baskes, "A calculation of the surface recombination rate constant for hydrogen isotopes on metals", Journal of Nuclear Materials 92, Table 1, p. 322, 1980; J. L. Cecchi, Journal of Vacuum Science and Technology 16, (1979) 58-70; and W. G. Perkins, Journal of Vacuum Science and Technology 10, 543-556 (1973).

metal	S_0 10^{23} atoms/$m^3Pa^{\frac{1}{2}}$	E_s eV	D_0 $10^{-7}m^2/s$	E_d eV
Ni	9.7	0.16	4.0	0.41
Fe(bcc)	6.3	0.28	0.78	0.08
Fe(fcc)	14.0	0.32	6.7	0.47
Al	5.6	0.66	110.0	0.43
Ti	4.7	-0.50	18.0	0.54
Zr	20.0	-0.63	4.2	0.41
Mo	4.2	0.22	4.8	0.39
304 SS	1.1	0.061	4.7	0.56
Inconel 625	2.2	0.13	7.6	0.50
Cu	4.8	0.40	11.0	0.40

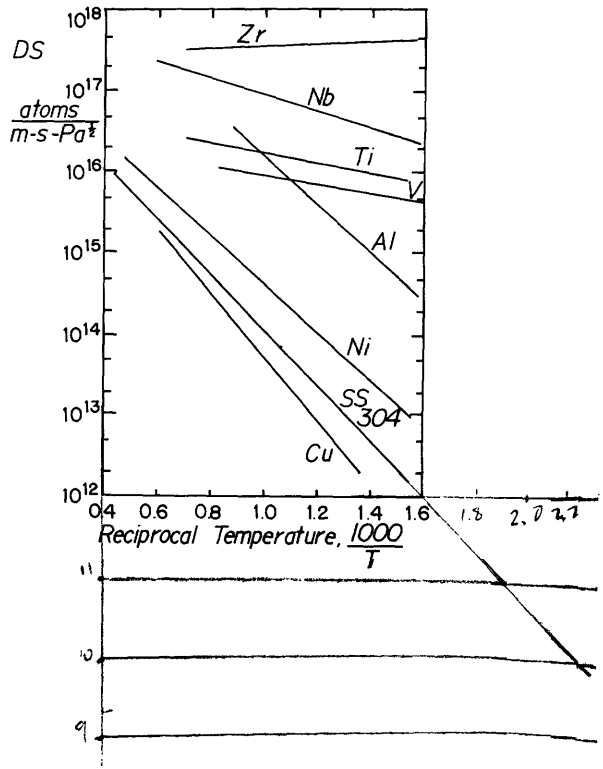

Fig. 28B3. Permeation coefficient vs. reciprocal temperature, for H in various metals. T is in Kelvin. Adapted from A. P. Fraas, ORNL-TM-4999 (1975), Fig. 34.

$DS \approx 2 \times 10^{9}$

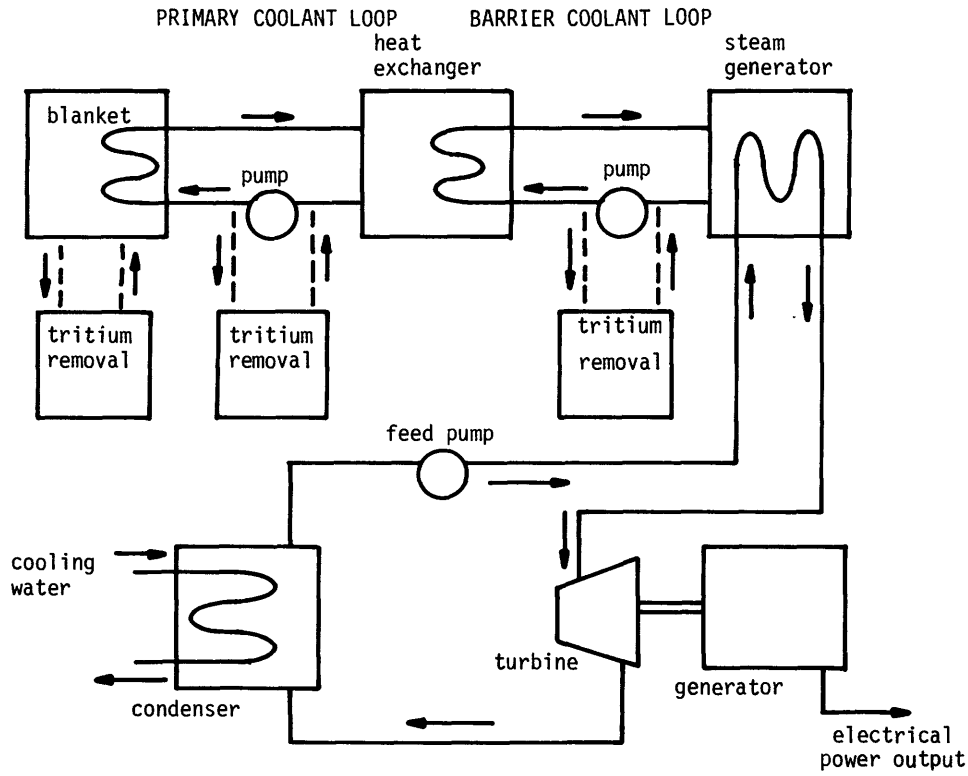

Fig. 28B4. Flow diagram for a system using an intermediate "barrier" coolant loop to reduce tritium leakage into the steam system.

An approximate expression for the surface recombination coefficient is

$$K \simeq (8/MT)^{\frac{1}{2}}(c_1\alpha/S_0^2)\exp[(2E_s - E_x)/kT] \quad (m^4/s) \tag{28B18}$$

where M is the atomic weight (u) of the metal,

$\alpha \simeq 0.5$ is the sticking coefficient, $c_1 = 2.60\times10^{24}\ K^{\frac{1}{2}}u^{\frac{1}{2}}/Pa\text{-}s\text{-}m^2$,

and

$$E_x = \begin{cases} E_s + E_d, & \text{if } E_s + E_d > 0 \\ 0 & \text{otherwise.} \end{cases} \tag{28B19}$$

(Baskes, 1980).

EXAMPLE PROBLEM 28B3

A steam generator with total tube surface area 2000 m^2 has Ni tubes 2 mm thick at 800 K, with a partial pressure of 10^{-5} Pa tritium on the primary coolant side and a negligible tritium pressure on the steam side. Estimate the leakage of tritium (Ci/day) into the steam system.

From Eq. (28B18), $K \simeq 4.8 \times 10^{-28}$ m^4/s.

28B. Tritium

From Eqs. (28B16), (28B17) we find DS = 9.5×10^{13} atoms/m^{3}s-Pa$^{\frac{1}{2}}$ for hydrogen, or 5.5×10^{13} for tritium. (The value from Fig. 28B3 is DS $\simeq$ 7×10^{13} atoms/m^{3}s-Pa$^{\frac{1}{2}}$). From Eq. (28B15) with $p_2^{\frac{1}{2}} << p_1^{\frac{1}{2}}$ we find J = 8.7×10^{13} atoms/m^{2}s. [From Eq. (28B13), J $\leq$ 4.4×10^{13} atoms/m^{2}s, so the flow is recombination-limited.] The total atom flow rate JA = 8.7×10^{18} atoms/s, which represents an activity of λJA = 1.6×10^8 Bq/s = 360 Ci/day.

Due to parameter uncertainties, such estimates are highly uncertain. Oxide films may reduce permeation rates by orders of magnitude (dashed curve, Fig. 28B2). Low-permeation tube coatings are under development. If necessary, an intermediate "barrier" coolant loop may be used to reduce tritium leakage into the steam generator, as shown in Fig. 28B4. The intermediate coolant could be a fluid with good compatibility and a low fire hazard, such a molten nitrate-nitrite salt. Use of an intermediate loop, however, would increase capital costs and lower steam temperature and thermal efficiency.

tritium recovery systems

Tritium can be removed from the vacuum system by cryogenic distillation or by diffusion through permeable membranes. Tritium removal from the blanket and coolant, however, is more difficult, because of the need to keep the partial pressure of T_2 very low. (In Example Problem 28B3, a pressure $p_1 = 10^{-5}$ Pa led to an excessive release rate.)

There must be a tritium removal system for the coolant. There may also be a direct tritium removal system for the blanket (such as a "purge stream" of He). Some techniques for recovery of tritium from the blanket and coolant are listed in Table 28B4. Recovery from liquid metals depends upon their temperature. At high temperatures tritium diffuses rapidly (Eq. 28B16).

With a closed cycle helium turbine system (Fig. 26A2) the cooling water is at low temperatures, so tritium permeation coefficients would be comparatively low, and higher partial pressures would be allowable than with steam generators.

accidental tritium release

If an entire 100 MCi inventory were released as HTO from a fusion reactor under the worst atmospheric conditions [no thermal plume rise; very stable atmosphere (Pasquill F); mean wind = 1 m/s, dry deposition velocity = 1 cm/s], the area receiving a "prompt" (within 60 days) lethal dose would be around 0.1 km^2, Fig. 28B5. If less than one-fourth of the inventory escaped, no prompt fatalities would occur.

Because the bulk of the tritium inventory is locked in segmented, isolated systems, it is unlikely that more than about 10 % of the tritium inventory would be released by a single accident. The tritium released into the air would probably be in gaseous form, rather than HTO, so it would tend to diffuse and disperse more rapidly than HTO. Tritium gas, being much lighter than air, tends to rise as it spreads out. These beneficial effects were ignored in the calculations of Fig. 28B5. Thus, it is extremely unlikely that the "worst case" accident could occur. Even if it did occur, evacuation of the danger area ($\sim$ 1 km^2 downwind) could probably prevent prompt fatalities. For DD reactors, the tritium inventory and hazard would be much less.

Table 28B4. Some tritium recovery techniques. From J. S. Watson, ORNL-TM-4022 (1972), and A. P. Fraas, ORNL-TM-4999 (1975).

liquid lithium blanket or coolant
1. permeation through metal window (such as Nb) into vacuum system or flowing gas: Good at high temperatures (> 1200 K), poor at low temperatures (< 800 K).
2. solid sorbent (Y, Zr): Not good at high temperatures, because of T_2 leakage from regenerators and large regenerator size.
3. cold trap: Residual T_2 solubility too high, so trapping is ineffective.
4. gas sparging: Ineffective, due to unfavorable equilibria.

liquid metal coolants (Na, K)
1. solid sorbents (yttrium or zirconium): operate at about 470 K. One tank is used while the other is being regenerated by heating and flushing with inert gas (He or A).
2. cold traps: Large volume traps required, equilibrium T_2 pressures not very low.

molten salt blanket or coolant (such as FLIBE)
1. stripping column (salt spray tower): Oxidizing agent must be added to gas (to keep T_2 pressure low) and causes corrosion problems.
2. diffusion into He coolant stream: Permeation rates limited by film resistance (oxide films on heat exchanger tubes).

solid blanket compounds (such as Li-Pb, LiO_2)
1. diffusion into coolant stream (such as He): Requires good porosity of compounds and high temperature (to attain good permeation rates), and compound sintering must be avoided.
2. diffusion into vacuum system: Same limitations.

helium gas coolant
1. oxidation-dehydration: An oxidizer (such as O_2 at very low pressure) is added to the helium, to produce T_2O (or other similar compound). Then the T_2O is removed with a dessicator or cold trap. Compatible with stainless steel tubes, but not with reactive metals (like Nb) because of corrosion.
2. diffusion into vacuum: only if high pressures of T_2 are allowable (as with closed cycle gas turbine or very effective permeation barrier coatings on steam generator tubes).
3. solid sorbents: Same limitations as diffusion into vacuum.

minimum attainable T_2 pressures (approximate)

lithium blanket, metal window	10^{-8} Pa
molten salt blanket, stripping column	10^{-3} Pa
potassium coolant, solid sorbent	10^{-7} Pa
potassium coolant, cold trap	10^{-5} Pa
helium coolant, solid sorbent	10^{-2} Pa

28C. Other Radioisotopes

production

Let n represent the densities of various isotopes (atoms/m^3), λ represent their decay constants (Bq), σ represent their neutron absorption cross sections

(m^2), and ϕ represent the neutron flux (neutrons/m^2s). Consider the case in which isotope B is produced by neutron absorption in isotope A and by radioactive decay of isotope C. Then the rate of change of the density of B is given by

$$dn_B/dt = (\text{production from A}) + (\text{production from C}) - (\text{loss by radioactive decay}) - (\text{destruction by neutron absorption})$$

$$= n_A\sigma_A\phi + \lambda_C n_C - \lambda_B n_B - n_B\sigma_B\phi \quad . \qquad (28C1)$$

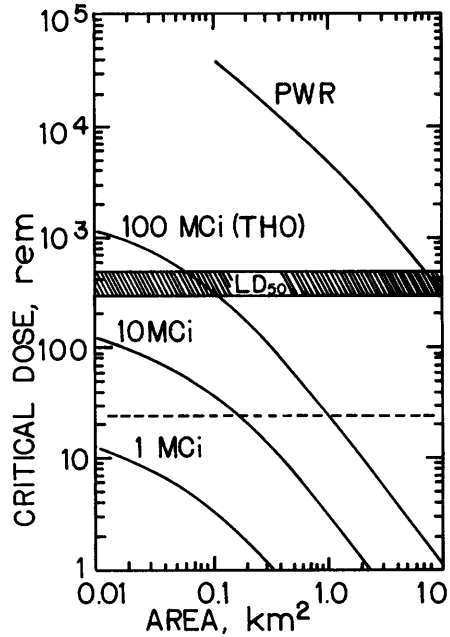

Fig. 28B5. Critical dose to bone marrow vs. area receiving that dose for "worst possible case" accidents of a fission reactor (PWR), of fusion reactors with various tritium (THO) releases. A dose of 25 rem is considered an emergency (dashed line). "Critical dose" means 100 % of the dose delivered in the first seven days plus half the dose delivered from days 8 to 30. The LD_{50} is the dose fatal within 60 days to half those exposed, in the absence of heroic medical measures. From J. P. Holdren, Science 200, 168-180 (1978), Fig. 4. Copyright 1978 by the American Association for the Advancement of Science.

Here $\sigma_A\phi$ and $\sigma_B\phi$ represent values averaged over the neutron energy spectrum. Let the initial density of B be n_{B0}. The solution of this equation is

$$n_B(t) = n_{B0}e^{-\alpha t} + \sigma_A\phi e^{-\alpha t}\int_0^t dt' n_A(t')e^{\alpha t'} + \lambda_C e^{-\alpha t}\int_0^t dt' n_C(t')e^{\alpha t'} \quad . \qquad (28C2)$$

where

$$\alpha \equiv \lambda_B + \sigma_B\phi \quad .$$

For simplicity, we will consider the special case where $n_C\lambda_C$ is negligible and n_A is constant. If neutron irradiation ends at time t_1, the density of B at later times is

$$n_B(t > t_1) = [n_{B0}e^{-\alpha t_1} + (n_A\sigma_A\phi/\alpha)(1 - e^{-\alpha t_1})]\exp[-\lambda_B(t-t_1)] \quad . \qquad (28C3)$$

The *activity* of B is $\lambda_B n_B$.

To illustrate the calculation of radioisotope production, we will consider the decay chains of vanadium, Fig. 28C1. Natural vanadium consists of 0.25 % ^{50}V and 99.75 % ^{51}V.

The isotope $^{48}_{21}Sc$ is produced by the reaction chain

$$^{51}_{23}V + n \rightarrow ^{52}_{23}V \rightarrow ^{48}_{21}Sc + ^{4}_{2}He \qquad (28C4)$$

and it decays by beta emission to $^{48}_{22}Ti$ with a half life of 1.83 days. (The compound nucleus ^{52}V also has several other modes of decay, the most probable being emission of two neutrons.)

ACTIVATION CHAIN 1

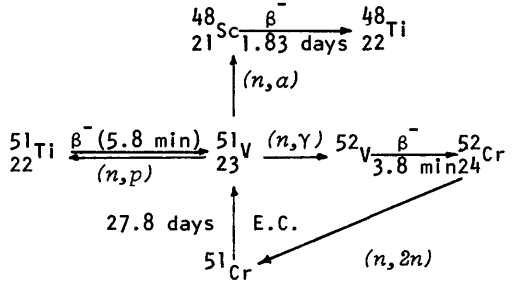

ACTIVATION CHAIN 2

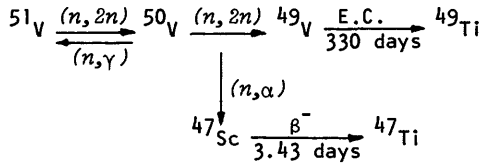

Fig. 28C1. Neutron activation chains for vanadium. From D. Steiner and A. P. Fraas, Nuclear Safety 13, 353-362 (1972).

EXAMPLE PROBLEM 28C1

The density of natural vanadium is 7.212×10^{28} atoms/m^3, and the cross section for reaction (28C4) is about 0.2 barn. Assume that the average neutron flux is 10^{18} $m^{-2}s^{-1}$ in a given blanket region containing 10 m^3 of V. The reactor operates continuously for 30 days, then shuts down. Find the activity of the ^{48}Sc one week after shutdown, assuming that its initial density is zero, its neutron absorption cross section is negligible, and that the density of ^{51}V is roughly constant.

For this case $n_A = 0.9975(7.212\times10^{28}) = 7.194\times10^{28}$ m^{-3}, and $\sigma_B = 0$. The decay constant of ^{48}Sc is $\lambda_B = \ln 2/t_{\frac{1}{2}} = 0.379$/day, so $\alpha = 0.379/\text{day} = 4.38\times10^{-6}s^{-1}$. From Eq. (28C3), with $t_1 = 30$ days, $(t-t_1) = 7$ days, $n_{B0} = 0$, $\sigma_A = 2\times10^{-29}$ m^2, we find $n_B = 2.31\times10^{22}$ m^{-3}. The activity of ^{48}Sc at that time is $\lambda_B n_B V = 1.01\times10^{18}$ Bq = 27 MCi, where V is the volume of that blanket region.

Similar calculations have been done for the various other elements and activation chains in the NUWMAK reactor Ti-6Al-4V first wall, with the result shown in Fig. 28C2. At early times the ^{48}Sc activity is dominant, but at very long times, the ^{14}C and ^{26}Al activities are dominant. Long-term activities of some candidate wall materials are compared in Fig. 28C3. Of those shown, V-20Ti is clearly the best, but the industrial capacity and materials data base for V alloys are not yet well developed. Titanium alloys with low Al content (<2%) are under development.

afterheat and biological hazard

The afterheat of the NUWMAK reactor vs. time after shutdown is shown in Fig. 28C4. The afterheat of an early tokamak design using 316 SS structure is also shown for comparison. The afterheat of NUWMAK 1 hour after shutdown is about 0.15 % of the 2097 MW of thermal power, or 3 MW. After 1 month, it has dropped to about 0.4 MW.

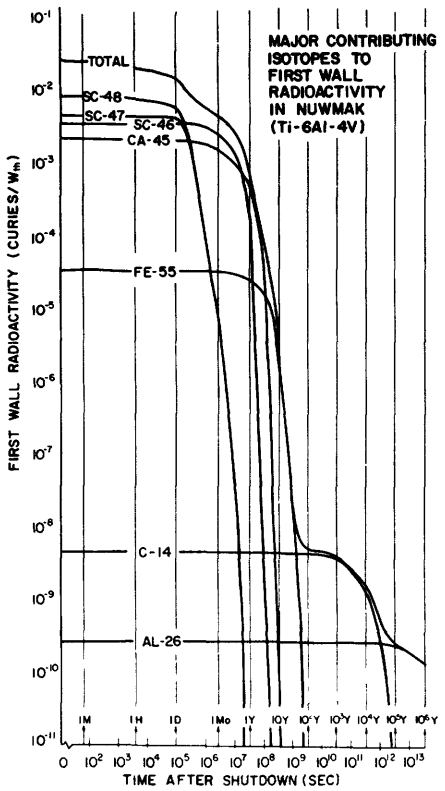

Fig. 28C2. Activity of the NUWMAK first wall (Ti-6Al-4V) vs. time after shutdown following 1 year of operation. The contributions of various isotopes are indicated. From B. Badger et al, "NUWMAK, a tokamak reactor design study", UWFDM-330 (1979), Fig. VIII-F-5, p. VIII-59.

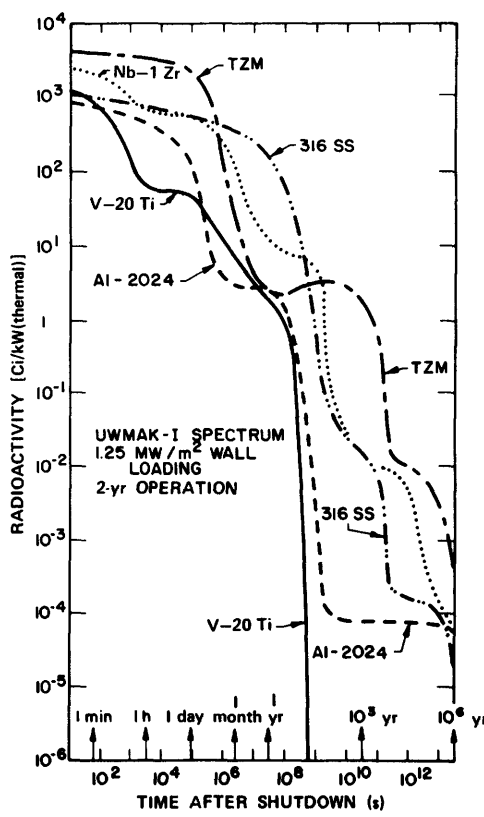

Fig. 28C3. Activities vs. time after shutdown for five different structural alloys, using the neutron spectrum from UWMAK-I. From B. Badger et al, "A Wisconsin tokamak reactor design, UWMAK-I", UWFDM-68 (1973).

The biological hazard potentials vs. time after shutdown have shapes different from the afterheat curves, because the various isotopes involved have different MPC. The BHP (water dilution) of various power plants are shown in Fig. 28C5 vs. time after shutdown. Assuming underground storage for solid wastes, it is appropriate to consider water dilution, instead of air dilution. The NUWMAK curve (not shown) would lie close to the UWMAK-I curve and slightly below it. The LMFBR actinide curve is for 1 % release, so the total release curve would be a factor of 100 higher than shown here. The LWR and LMFBR fission reactors have high BHP at times over 100 years, and so do the PPPL and UWMAK-III fusion reactor designs. The BNL design BHP is initially low, but doesn't drop off at long times, due to the long half-life of ^{26}Al (7.4×10^5 years) produced by the $^{27}Al(n,2n)$ reaction. The ORNL-DEMO and UWMAK-I BHP drop off to low values at long times, as does the NUWMAK BHP (not shown).

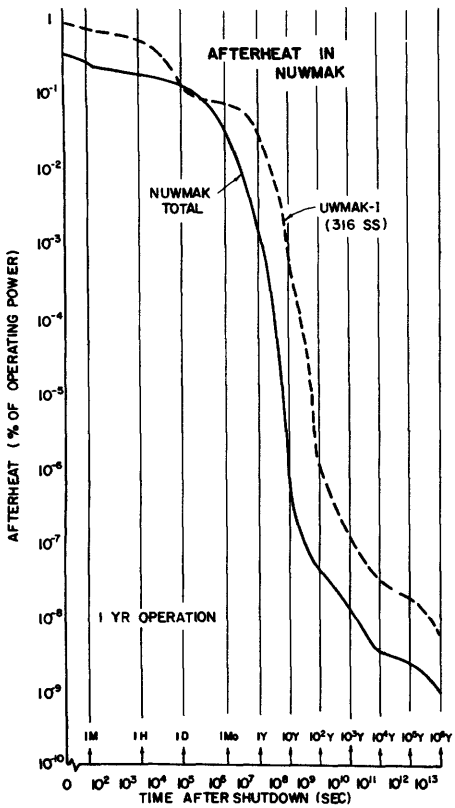

Fig. 28C4. Afterheat of the NUWMAK and UWMAK-I tokamak reactors vs. time after shutdown. From B. Badger et al, UWFDM-330 (1979), Fig. VIII-F-3, p. VIII-56.

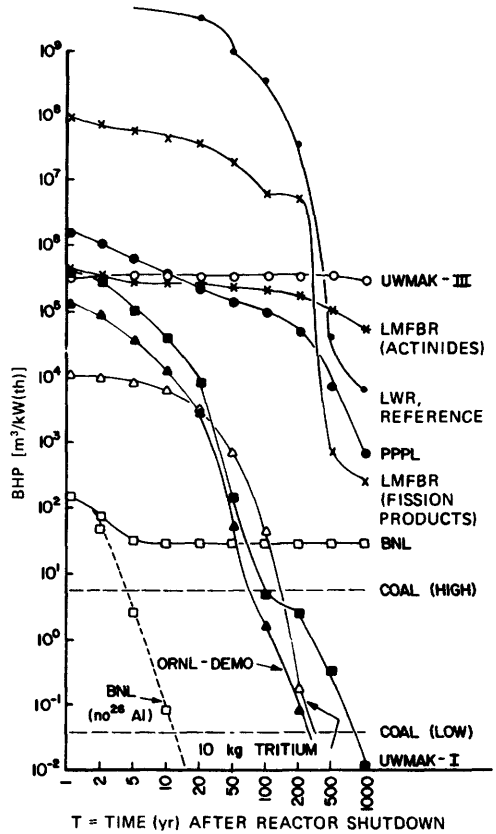

Fig. 28C5. Biological hazard potential (water dilution) as a function of time for various power-generating systems. The UWMAK-I Tokamak uses stainless steel; the BNL design uses Al, Al_2O_3, $LiAlO_2$, and C; the PPPL design uses PE-16 alloy, and UWMAK-III uses TZM alloy and C. Variations in organic composition of coal cause the wide spread shown. From T. E. Botts and J. R. Powell, Nuclear Technology 37, 129-137 (1978), Fig. 3.

disposal

Fusion reactors will require periodic wall replacement and other maintenance. The dose rate will be too high for human contact, so remote handling equipment must be developed.

First wall and blanket segments will be highly radioactive. Nonvolatile solids, like Nb, V, Al, and stainless steel, may be stored at the plant site. Blanket fertile materials, like Li and Li_2BeF_4, can be recycled into fusion reactors, after processing to remove impurities. Other radioactive wastes will be disposed of at the end of the reactor life, when the plant is decommissioned. A fusion reactor waste management flow chart is shown in Fig. 28C6.

Decommissioning can consist of either entombment on site or complete removal and cleanup. Entombment on site is much cheaper, but may leave the site

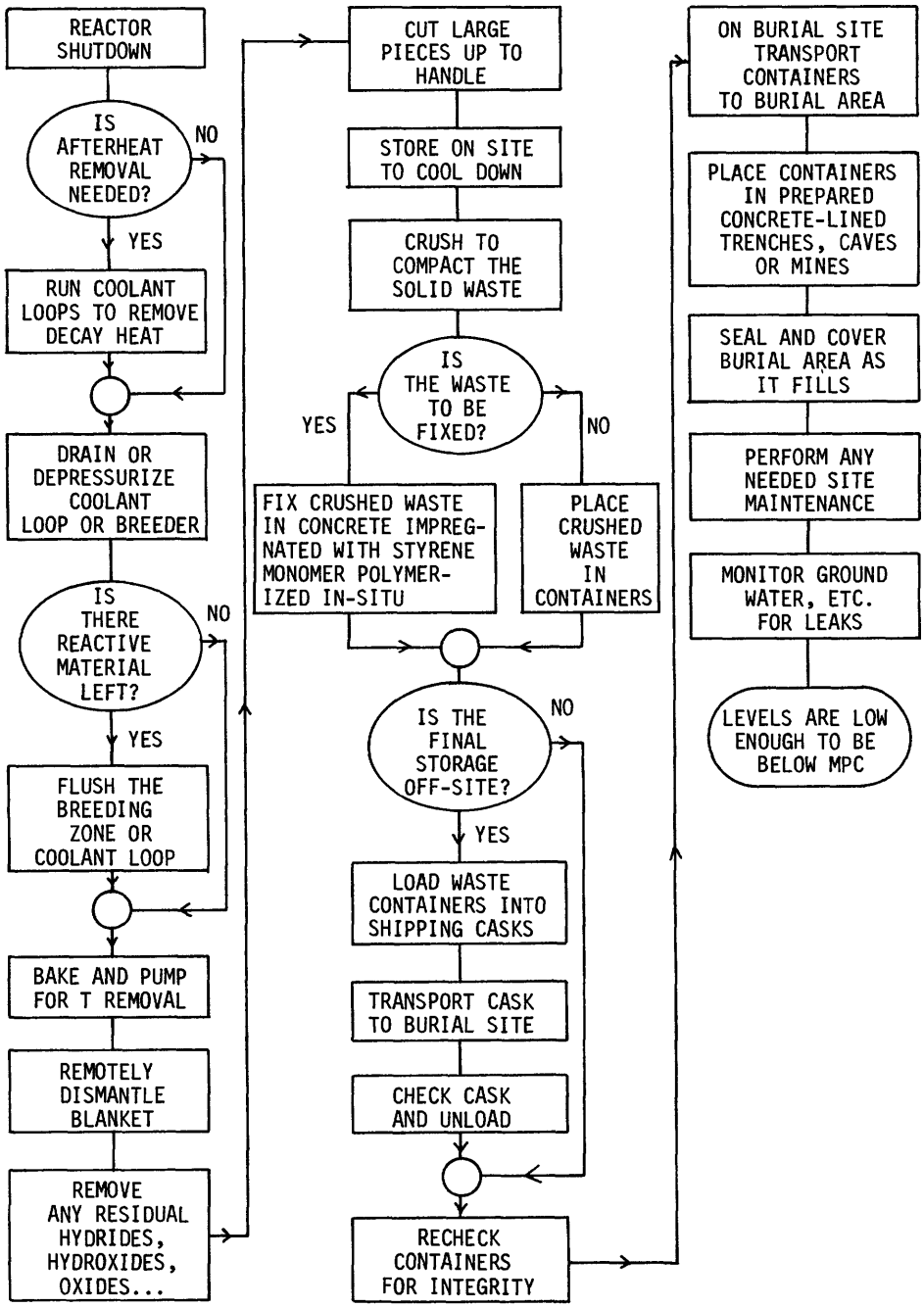

Fig. 28C6. A generalized fusion reactor waste management flow chart. From T. E. Botts and J. R. Powell, Nuclear Technology 37, 129-137 (1978), Fig. 1.

unsatisfactory for other use. The cost of decommissioning should be considered during reactor plant design.

On-site entombment costs are typically on the order of 10 M$, while complete removal may cost an order of magnitude more. Estimated radiation releases, waste burials, doses, land use, and transportation requirements for various 1 GWe power plants are compared in Table 28C1.

Table 28C1. Estimated radiation releases, waste burials, and other environmental effects of 1 GW_e power plants. From J. R. Young, "An environmental analysis of fusion power to determine related R&D needs", BNWL-2010 (1976).

Unit Environmental Impact (Per GW-yr or GWe)	*Fossil*	*Solar*	*LWR*	*LMFBR*	*HTGR*	*Fusion*
Releases in 2040						
Heat (10^{12}Btu)	58.0	44.0	66.8	44.0	51.2	44.0
Radionuclides						
Tritium (Curies)	0	0	33,300	1,400	36,800	1,400
Krypton (Curies)	0	0	3,480	2,080	4,370	0
Xenon (Curies)	0	0	48.5	0	0	0
Plutonium (Curies)	0	0	0.20	0.16	0.08	0
Transuranics (millicuries)	0	0	1.06	0.16	0.01	0
Other (Curies)	0	0	0.168	0.004	0.020	0
Nonradioactive Materials						
SO_2(10^3Tons)	15.7	0	0.034	0.034	0.034	0.034
NO_x (10^3 Tons)	36.0	0	0.076	0.076	0.076	0.076
Chlorine (Tons)	27.0	20.0	47.1	23.4	32.9	23.4
Radioactive Waste Burials						
High-Level (Ft^3)	0	0	69	69	63	0
Other (Ft^3)	0	0	42,000	42,000	7,500	20,000
Radiation Doses (man-rem)						
General Public	0	0	32.5	5.2	32.0	3.2
Employees	0	0	600	440	490	600
Plutonium Discharged (Metric Tons)	0	0	0.53	2.4	0.00004	0
Truck Shipments	0	0	191	111	62	56
Railroad Shipments	33,750	0	30	75	27	0
Land Use (Sq. Mi.)	3.0	10.0	1.30	0.67	1.0	0.63
Material Use						
U_3O_8 and ThO_2 (10^3 Metric Tons)	0	0	0.230	0.030	0.163	0
Coal (10^6 Tons)	4.0	0	0	0	0	0
D_2O (Metric Tons)	0	0	0	0	0	0.066

recycling

If the structural radioactivity decays to low values after times on the order of 30 years, it will be feasible to store the materials on site and then reprocess them. Vanadium and titanium alloys are likely candidates for recycling.

One study estimated the dose to a machinist working 8 hours/day, 260 days/year at distances of 2-10 m from a 1 m sphere of recycled metal. To keep the machinists annual dose below 0.5 rem, the required decay times of the metal were about 50 years for 316 SS (UWMAK-I), 70 years for PE-16 (PRD), and less than 1 year for Al and Al_2O_3 (BNL), (Botts and Powell, 1978).

Enrichment of various isotopes, which do not become radioactive, leads to shorter required decay times and reduced long-term activity, but the costs depend upon developments in isotopic enrichment technology. Fusion reactor neutrons may also be used to transmute actinide wastes from fission reactors.

28D. Hazards and Materials Shortages

hazards

In addition to hazards from radioactivity, there are various forms of stored energy present in fusion reactors, which may cause fire or structural failure, as indicated in Table 28D1. The greatest hazard is the potential for a lithium-air or lithium-water reaction, if lithium is used. Other liquid metal coolants (Na, K) have similar fire hazards. Avoiding the use of liquid metals would reduce the fusion reactor stored energy by two orders of magnitude.

The large magnetic field energy could cause structural failure or local coil melting, but these dangers can be avoided by proper design (Section 22D). Radioactive afterheat will be removed by coolant flow, to avoid overheating the blanket structure. The afterheat problem is much less severe than for fission reactors.

The stray magnetic field outside the reactor may affect the health of humans and animals. It would be very expensive to put magnetic shielding (such as soft iron) around the entire reactor, but it is probably feasible to shield the control room. The stray magnetic fields associated with an early tokamak reactor design and a simple mirror reactor are illustrated in Fig. 28D1 as functions of distance from the reactor. The biological effects of exposure to magnetic fields are being studied to determine what field strength is safe. Pulsed fields are more hazardous than steady fields.

Table 28D1. Approximate values of stored energies in a 1 GWe fusion power plant. Based on "Fusion power: an assessment of ultimate potential", WASH-1239 (1973) and information from J. P. Holdren (1980).

	GJ
chemical energy, if blanket is liquid lithium (lithium-air or lithium-water reactions)	50,000
thermal energy in coolant	
if lithium	1,000
if helium	100
magnetic field energy	200
radioactive afterheat, first hour (depends on choice of materials)	50
nuclear energy of fusion plasma (complete burnup is impossible)	50
mechanical energy of atmospheric pressure on vacuum chamber	10
thermal energy of plasma	1

materials shortages

We will consider the materials requirements for construction of 1000 fusion power plants, each producing 2.5 GWth (1 GWe). This would provide about 8 % of the estimated 30 TW demand in the year 2020 (Table 1B3). Estimates of materials requirements, based on various fusion reactor designs, are listed in Table 28D2. (If fusion reactors were to produce 80 % of the world's power, instead of 8 %, then the required tonnages

would be an order of magnitude larger than shown in the Table, but such a rapid conversion to fusion power is probably not feasible.)

The "early designs" would have potential problems with supply of Be and V, in addition to the elements marked *. The UWMAK-III design study cites Li, Mo, Nb, and Ni as potential problems. The NUWMAK study cites Co, Nb, and W as severe problems, because of lack of adequate supply in the USA. Demand for Nb will soar as superconducting motors, generators, and transmission lines are introduced. Unless large-scale recycling of materials is adopted, materials shortages will limit many industries, including construction of fusion power plants.

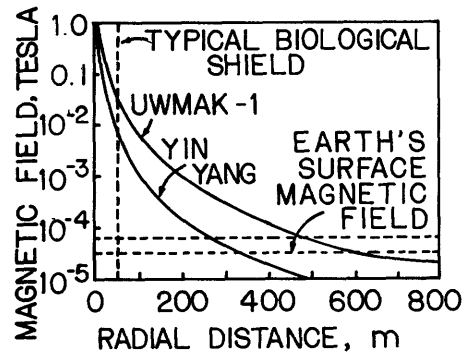

Fig. 28D1. Variation of stray magnetic field with radial distance from Tokamak and mirror fusion reactors. From J. R. Young, BNWL-2010 (1976).

Table 28D2. Estimates of materials requirements (millions of metric tons) for 1000 fusion power plants of various types (2.5 GWth each), and estimated reserves. From: G. L. Kulcinski, Energy Policy 2, 104 (1974); B. Badger et al, "UWMAK-III, a noncircular tokamak power reactor design", EPRI ER-368 (1976). B. Badger et al, "NUWMAK, a tokamak reactor design study", UWFDM-330 (1979).

element	early designs	UWMAK-III	NUWMAK	1970 US reserves	1970 world reserves
Al	0.6	2.4	2.2	13	3000
B	0.8	0.47	2.2	33	66
Be	0.12	0	0	0.018	0.38
C	2.	0	1.1	10	large
Co *	0	0.003	0.068	?	?
Cr *	2	1.1	0.35	small	370
Cu *	2	0.98	1.2	74	310
F	1	0	0	9	62
Fe	10	60	56	8500	180,000
He *	0.3	0.07	0.05	1.2	?
K	0.02	0	0	42	30,000
Li *	1	0.24	0.063	6	180
Mg	0	0	0.008	?	?
Mn	0.2	0.46	0.053	0	590
Mo *	0.2	4.1	0	3-4(1976)	6.5
Na	0	1.0	0	large	large
Nb *	0.8	0.06	0.075	0.005	7.8
Ni *	1.5	0.67	0.044	0.14	24
Pb *	11	1.8	2.8	39	85
Sn *	0.2	0	0	0.009	6
Ti	0.8	0.05	1.3	23	134
V	0.5	0	0.12	0.1	26
W *	0	0	1.04	?	?
Zr	0.002	0.01	0.0015	0.06	25

* Serious shortages of these elements would exist even if no fusion power plants were built.

helium

Helium is a vital, nonrenewable resource. Helium consumption in the USA in 1975 was for:

cryogenics, 34 % (Table 23A1)
purging and pressurizing, 18 %
welding, 16 %
controlled atmospheres and breathing mixtures, 12 %
other uses, 20 % .

Future development of the following sophisticated technologies relies on helium: fusion reactors; HTGR's; laser-based missile defense systems; propulsion for new transport systems; refrigeration for military aircraft; MHD generators; and superconducting motors, generators, transmission lines, and energy storage systems. For example, the following cumulative demands through the year 2050 are estimated for just three of these new technologies: (Gcf = billion cubic feet)

fusion reactors:	>	$1.4 \times 10^9 m^3$	(> 50 Gcf)
transmission lines:		$12.0 \times 10^9 m^3$	(425 Gcf)
energy storage:		$1.5 \times 10^9 m^3$	(54 Gcf)
sum		$15.0 \times 10^9 m^3$	(530 Gcf)

These needs alone are larger than what is available. Helium constitutes about 0.3 % of "helium-rich" natural gas. Helium can also be recovered from air, of which He constitutes about 5 ppm, but extraction from air requires 800 times as much energy as extraction from natural gas. About 96 % of the world's known helium-rich natural gas is located in the USA, and the US helium reserves are rapidly dwindling (Fig. 28D2). Fields now being exploited for natural gas, representing about 85 % of the 1977 measured reserves, will be essentially exhausted in 20-30 years. Only 20 % of the helium present in the natural gas consumed in the USA in 1977 was stored or used: the other 80 % was wasted!

summary

Some potentially good and bad environmental effects of fusion reactors are summarized in Table 28D3.

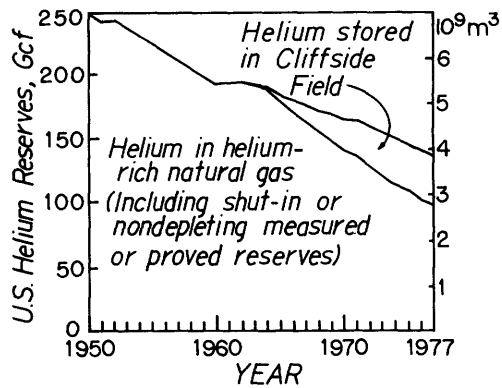

Fig. 28D2. Known US helium reserves at beginning of each year, from 1950 to 1977. The density of helium at 1 atm, 293 K is about 0.166 kg/m^3, so 10^9 m^3 (He) would have a mass of about 166,000 metric tons. The helium content of "potential gas reserves" in the USA is about 160-310 billion cubic feet (4.5 to 8.8x10^9 m^3). From R. M. Drake, Jr., Chairman, Helium Study Committee, Helium: a Public Policy Problem, National Academy of Sciences, Washington, DC, 1978.

Table 28D3. Summary of environmental effects of fusion reactors, in comparison with fission power plants. Adapted from J. R. Young, BNWL-2010 (1976).

adverse	increased use of some scarce materials.
unknown	biological effects of long-term exposure to low magnetic fields.
unchanged	assured fuel supply, waste heat released, radioactive structure.
better	safety against accidental criticality, prompt criticality, and loss-of-coolant accidents.
	reduction of safeguard concerns (regarding nuclear weapons production)
	lower routine chemical releases, since fusion does not involve as extensive mining, milling, enrichment, fabrication, and reprocessing systems.
	no fission product high-level radioactive wastes.
	lower BHP of radioisotopes

28E. Economics

electrical power cost

A standard accounting procedure for estimating fusion power costs is described by Schulte, Willke, and Young (1978). The main parameters are defined in Table 28E1. The cost of electricity is estimated from the formula

$$COE = 1000[C_c(fcr) + (C_{o\&m} + C_{scr} + C_f)(1 + E)^P]/PC(PAF) \quad (mills/kWh), \quad (28E1)$$

where 1 mill = 10^{-3} \$. Standardized values of E and fcr are assumed, in order to facilitate comparison of various reactors. There are two modes of analysis:
* *current dollar mode*. This includes effects of inflation, taking E = 0.05 and fcr = 0.15 .
* *constant dollar mode*. This ignores effects of inflation, taking E = 0 and fcr = 0.10.

Values of F_{IDC} and F_{EDC} for computing C_{tr} are listed in Table 28E2. Typical costs of components are listed by Schulte et al (1979).

The standard cost account numbers and items are illustrated in Table 28E3 for the case of the NUWMAK reactor design. The reactor plant equipment is about 63 % of the direct capital cost, structures and site facilities are about 15 %, and turbine plant equipment is about 14 %. Each of the entries in this table is broken down into several categories. For example, major categories of Account 22, Reactor Plant Equipment, are listed in Table 28E4 for the NUWMAK case. Each of these categories may be comprised of several items. For example, Account 22.01.03, Magnets, is comprised of

22.01.03.01 TF magnets	51.1710 M\$
22.01.03.02 Ohmic heating and superconducting vertical field coils	16.2820
22.01.03.03 Cryogenic vertical field coils	4.4910
22.00.03.04 Trimming coils.	6.4100

The items are further broken down into individual cost components, as illustrated in Table 28E5 for Item 22.01.03.01, TF Magnets.

For NUWMAK, the total capital cost is 2.33 times the direct capital cost. The net electric power output of NUWMAK is 660 MWe, so the capital cost per kWe is 1968.162 M\$/660,000 kWe = 2982 \$/kWe.

Table 2 E1. Parameters determining the cost of electricity. Based on S. C. Schulte, T. L. Willke, and J. R. Young, PNL-2648 (1978).

direct capital cost	C_{dc}	= equipment, land, buildings, materials and labor, except for fuel and scheduled component replacement
indirect capital cost	C_{ic}	= engineering, management, construction = 0.35 C_{dc} (by assumption)
time-related costs	C_{tr}	= interest during construction (IDC) and escalation during construction (EDC) due to inflation = $(F_{IDC} + F_{EDC})(C_{dc} + C_{ic})$ where F_{IDC} and F_{EDC} are given in Table 28E2.
total capital cost	C_c	= $C_{dc} + C_{ic} + C_{tr}$ = 1.35 C_{dc} $(F_{IDC} + F_{EDC})$
annual operating and maintenance cost	$C_{o\&m}$	= salaries, support services, fuel handling, etc. = 0.02$(C_{dc} + C_{ic})$ (by assumption)
annual scheduled component replacement cost	C_{scr}	= major items (> 10^4 \$), such as first wall replacement
annual fuel cost	C_f	= materials consumed (D, T, breeding material, cladding, neutron multipliers, etc.) and offsite processing and disposal.
plant capacity	PC	= (8760 hours/year)(design net electrical power output, kW)
plant availability factor	PAF	= $(8760 - T_s - T_u)/8760$, where T_s and T_u are the annual scheduled and unscheduled outage times (hours).
annual escalation rate	E	= rate of inflation of costs of goods and services = 0.05 for "current dollar" estimates = 0 for "constant dollar" estimates
annual fixed charge rate	fcr	= cost of capital, depreciation, interim replacement, property insurance, and taxes = 0.15 for "current dollar" estimates = 0.10 for "constant dollar" estimates
construction period	P	= time it takes to build the power plant (years)

EXAMPLE PROBLEM 28E1

Assuming that the annual times for scheduled and unscheduled maintenance on NUWMAK are six weeks and four weeks, estimate the cost of electricity (current dollars).

With T_s = 1008 hours and T_u = 672 hours, we find PAF = 0.808 (Table 28E1), and PC = 5.782×10^9 kWh/year. Using values of costs from Tables 28E1 and 28E3 in Eq. (28E1), we find

Table 28E2. Values of F_{IDC} and F_{EDC} vs. construction period P. From Schulte, Willke, and Young (1978).

P, years	CONSTANT DOLLAR MODE (E = 0, assumed cost of capital = 0.05/year) F_{IDC}	F_{EDC}	CURRENT DOLLAR MODE (E = 0.05/year, assumed cost of capital = 0.10/year) F_{IDC}	F_{EDC}
4	.081	-0-	.191	.122
5	.108	-0-	.251	.155
6	.129	-0-	.316	.190
7	.152	-0-	.388	.225
8	.170	-0-	.466	.261
9	.192	-0-	.551	.299
10	.221	-0-	.644	.338

$$COE = \frac{1000[1968.162\times10^6(0.15) + (22.793 + 3.988 + 0.449)\times10^6(1.05)^8]}{5.782\times10^9(0.808)} = 71.8 \frac{mills}{kWh}.$$

If we devise an approximate rule-of-thumb for estimating the COE (current dollars) in the form

$$COE \simeq K\,(1.1)^P\, C_{dc}/P_e \qquad (mills/kWh) \qquad (28E2)$$

with C_{dc} in M$ and P_e in MWe, we find values of the adjustable parameter K for the NUWMAK, STARFIRE, and WITAMIR-I designs of 26.2, 26.3, and 26.2, respectively.

cost scaling

The cost of various first wall and blanket structural materials is indicated in Table 28E6. Stainless steel is the cheapest, and vanadium is the most expensive, but vanadium has less long-lived radioactivity, and it may be able to operate at higher peak coolant temperatures, depending on choice of coolant. The effect of coolant temperature on the cost of electricity is illustrated in Fig. 28E1. There is little benefit to be derived from coolant temperatures over 920 K with a steam system, because the turbine inlet temperature is limited to about 820 K in order to attain a long turbine lifetime. Because of its higher cost, the V structure must operate at about 100 K higher temperature than the SS structure to attain the same COE. Compatibility limits of these metals with various coolants were described in Table 26B5. V and Nb may require use of liquid metal coolants to attain high temperatures.

Cost scaling studies indicate that the electrical power cost increases by about 1 mill/kWe for every

* increase in blanket structure cost of 50 $/kg
* decrease in peak coolant temperature by 25 K (stainless steel, 670 K < T < 770 K)
* decrease in peak coolant temperature by 43 K (vanadium, 770 K < T < 920 K).

Table 28E3. Standard cost accounts (SWY) with values for NUWMAK. From B. Badger et al, UWFDM-330 (1979).

Acct. No.	Description		Cost, M$
20	Land and land rights		2.500
21	Structures & site facilities		106.824
	Design allowance (10%)		10.682
	Contingency (10%)		10.682
	Spare parts (0.5%)		0.534
22	Reactor plant equipment		404.495
	Design allowance (20%)		80.899
	Contingency (10%)		40.450
	Spare parts (2%)		8.090
23	Turbine plant equipment		98.035
	Design allowance (10%)		9.803
	Contingency (10%)		9.803
	Spare parts (1%)		0.980
24	Electric plant equipment		38.000
	Design allowance (10%)		3.800
	Contingency (10%)		3.800
	Spare Parts (0.5%)		0.190
25	Miscellaneous plant equipment		11.000
	Design allowance (10%)		1.100
	Contingency (10%)		1.100
	Spare parts (1%)		0.110
26	Special materials		1.300
	TOTAL DIRECT COSTS	C_{dc} =	844.177
91	Construction facilities		
	Equipment of Service (15% of C_{dc})		126.627
92	Engineering and construction		
	Management service (15% of C_{dc})		126.627
93	Owner's costs (5% of C_{dc})		42.210
	TOTAL INDIRECT COSTS	C_{ic} =	295.464
94	Interest during const. (P = 8 years)		
	F_{IDC} (current dollar) = 0.466		531.073
93	Escalation during const. (P = 8 years)		
	F_{EDC} (current dollar) = 0.261		297.477
	TOTAL TIME RELATED COSTS	C_{tr} =	828.520
	TOTAL CAPITAL COST	C_c =	1968.162
40 to 47	Operation and Maintenance	$C_{o\&m}$ =	22.793
50 to 51	Scheduled Component Replacement	C_{scr} =	3.988
02 to 03	Annual Fuel Cost	C_f =	0.449

Table 28E4. The main categories of Account 22, Reactor Plant Equipment, for the NUWMAK design. From B. Badger et al, UWFDM-330 (1979).

Acct. No.	Description	Cost $x10^6$	% of Total RPE
22.01.01	Blanket/first wall	10.77	2.66
22.01.02	Shield	63.038	15.58
22.01.03	Magnets	78.354	19.37
22.01.04	Supplemental heating	36.000	8.90
22.01.05	Primary structure & support	0.9284	0.23
22.01.06	Reactor vacuum systems	20.030	4.95
22.01.07	Power supply switching & energy storage	47.170	11.66
22.01.08	Impurity control	0.750	0.19
22.02.01	Primary coolant system	46.990	11.62
22.02.02	T_2 extraction from blanket	0.374	0.09
22.03.01	Magnet cooling (refrigeration)	34.740	8.59
22.03.02	Shield and structure cooling	0.200	0.05
22.03.03	Vacuum system cooling	3.410	0.84
22.03.04	Power supply cooling	0.300	0.07
22.04	Radwaste treatment/ disposal	5.500	1.36
22.05	Fuel handling/air detritiation	23.441	5.80
22.06	Other reactor plant equipment	17.500	4.33
22.07	Instrumentation and control	15.000	3.71
	Total Reactor Plant Equipment	404.4954	100%

For stainless steel, there is an optimum first wall neutron power flux of about 2 MW/m^2. At higher fluxes, the wall must be replaced too frequently, and at lower fluxes, the electrical power output is low.

The variation of power cost with first wall life is illustrated in Fig. 28E2 for vanadium and stainless steel walls at different temperatures. There is a strong incentive for developing alloys with long wall lifetimes.

A reliability of less than one failure per year is needed. If the structure fails and a 1 GWe reactor is shut down for repairs, the utility must pay about 0.4 M$/day for replacement power to supply its customers. Speedy remote maintenance is also very important. Ideally, the components should all be designed to last 30 years, but this may not be feasible for the first wall.

Table 28E5. Cost components of Item 22.01.03.01, TF Magnet, for the NUWMAK design. From B. Badger et al, UWFDM-330 (1979).

	Unit Cost ($/kg)	Quantity (Tonnes)	Cost ($x10^6)
1. NbTi superconductor	50	58.2	2.91
2. Aluminum Stabilizer	10	212	2.12
3. Conductor Fabrication	40	270.2	10.808
4. Fabricated Al Structure	30	384	11.52
5. Fiberglass Epoxy	10	23	0.23
6. Fabricated Micarta Spacers	15	34	0.51
7. Dewar (TF)	40	85	3.40
Dewar (Central Support)	40	15	0.60
8. Aluminum Shield	20	192	3.84
9. Superinsulation	$100/m^2	2000 m^2	0.20
10. Epoxy Struts	15	9.5	0.143
11. Central Support Structure	30	113	3.390
12. Motorized Carriages	$0.5x10^6 each	8	4.000
13. Assembly & Erection	$12.5/man-hr	6x10^{5}man-hr	7.500
			51.171

Total mass of TF coil is 1125.7x10^3 kg.

Average unit cost of conductor $58.6/kg.

Avg. unit cost of coil system $45.45/kg.

Table 28E6. Estimated costs of various first wall and blanket structural materials (1977 $). From D. L. Kummer, Journal of Nuclear Materials 85 & 86, 47-56 (1979), Table 3.

Material	Raw Material Cost $/kg (1977 $)	Fabrication Cost $/kg	Fabricated Part Cost $/kg
Austenitic Stainless Steel	7	22	29
Titanium Alloys	22	34	56
Niobium Alloys	77	39	116
Vanadium Alloys	125	59	184
Molybdenum Alloys	107	62	169

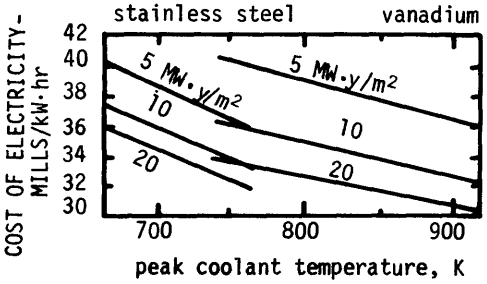

Fig. 28E1. Effect of peak coolant temperature on cost of electricity (constant $) of a hypothetical tokamak reactor for stainless steel and vanadium structures with various lifetimes. From D. L. Kummer, Journal of Nuclear Materials 85 & 86, 47-56 (1979), Fig. 2.

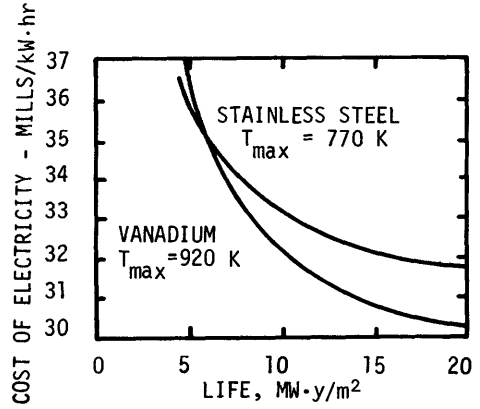

Fig. 28E2. Estimated cost of electricity (constant $) vs. wall life for stainless steel and vanadium structures in a hypothetical tokamak reactor. From D. L. Kummer, Journal of Nuclear Materials 85 & 86, 47-56 (1979), Fig. 5.

Problems

1. A sealed bottle containing initially pure tritium is stored for 1 year. If permeation through the bottle is negligible, what fraction of the gas will be helium at the end of the year?

2. A fusion reactor has a breeding ratio of 1.07, a burnup fraction of 4.3 %, a tritium inventory of 21 kg, and it produces 4.7 GWth of power. How long will it take to double the tritium inventory ? What is the tritium mass flow rate through the reactor ? How many kg(T) are consumed daily ?

3. A reactor has a blanket of Li_2O spheres with total volume 520 m^3 and a void fraction of 47 %. In order to keep the tritium in the blanket below 100 MCi, what average fraction of tritium (appm) is tolerable in the Li_2O spheres ? (Ignore tritium in the helium coolant and cladding.)

4. Repeat Example Problem 28B3 for the case in which the tubes are Cu instead of Ni.

5. Derive Eqs. (28C2) and (28C3) by solving the appropriate differential equations.

6. The cross section for the $^{51}V(n,p)$ reaction is 0.2 barn. For the case of Example Problem 28C1, estimate the ^{51}Ti activity 10 minutes after shutdown. (Its half life is given in Fig. 28C1.) Ignore neutron absorption in ^{51}Ti.

7. Estimate the cost of electricity from NUWMAK using a constant dollar mode analysis.

8. If the cost of the NUWMAK magnets increased to 150 M$, what would the new cost of electricity (current dollars) be ? At the original magnet cost, how much would a reduction in shield cost to 10 M$ reduce the COE (current dollars) ?

Bibliography

general

Proceedings of the Fourth ANS Topical Meeting on the Technology of Controlled Nuclear Fusion (King of Prussia, PA, 1980), DOE, 1981.

tritium

R. Axtmann, A. S. Zarchy, and E. J. Lightfoot, "Assessment of transport barriers to tritium migration through fusion reactor materials", EPRI AP-1696 (1981).

M. I. Baskes, "A calculation of the surface recombination rate constant for hydrogen isotopes on metals", *Journal of Nuclear Materials 92*, 318-324 (1980).

P. A. Finn, R. G. Clemmer, V. A. Maroni, and C. Dillow, "Tritium handling and vacuum considerations for the STARFIRE commercial tokamak reactor", ANL/FPP/TM-127 (1979), pp. 27-31.

R. L. Hirsch and W. L. Rice, "Nuclear fusion power and the environment", *Environmental Conservation 1*, 251-262 (1974).

J. P. Holdren, "Fusion energy in context: its fitness for the long term", *Science 200*, 168-180 (1978).

J. P. Holdren, T. K. Fowler, and R. F. Post, "Fusion power and the environment", UCRL-76911 (1975).

E. M. Larsen, S. I. Abdel-Khalik, and M. S. Ortman, "Tritium pathways and handling problems in a laser fusion reactor", *Nuclear Technology 41*, 12-26 (1978).

T. E. McKone and W. E. Kastenberg, "Calculation of radiological dose due to release of tritium oxides from controlled thermonuclear reactors", *Nuclear Technology 40*, 170-184 (1980).

M. S. Ortman, E. M. Larsen, and S. I. Abdel-Khalik, "A study of the tritium handling systems in magnetic and inertial confinement fusion reactors with and without tritium breeding", *Nuclear Technology/Fusion 1*, 255-274 (1981).

J. R. Powell and C. T. Eterno, Editors, *Proceedings of the Third Topical Meeting on the Technology of Controlled Nuclear Fusion*, American Nuclear Society, CONF-780508 (1978), Chapter 9.

D. Steiner and A. P. Fraas, "Preliminary observations on the radiological implications of fusion power", *Nuclear Safety 13*, 353-362 (1972).

V. G. Vasil'ev, "Chemical systems for obtaining tritium in thermonuclear power generation", *Soviet Atomic Energy 48*, 1-8 (1980).

G. S. Was and L. M. Lidsky, "Cyclic purging for low-temperature solid fusion reactor blanket operation", *Nuclear Technology 43*, 289-300 (1979).

J. S. Watson, "A summary of tritium handling problems in fusion reactors", ORNL-TM-4022 (1972).

A. S. Zarchy and R. C. Axtmann, "Limitations on tritium transport through fusion reactors", *Nuclear Technology 39*, 258-265 (1978).

other radioisotopes

D. H. Berwald and J. J. Duderstadt, "Preliminary design and neutronic analysis of a laser fusion driven actinide waste burning hybrid reactor", *Nuclear Technology 42*, 34-50 (1979).

T. E. Botts and J. R. Powell, "Waste management considerations for fusion power reactors", *Nuclear Technology 37*, 129-137 (1978).

R. W. Conn, K. Okula, and A. W. Johnson, "Minimizing radioactivity and other features of elemental and isotopic tailoring of materials for fusion reactors", *Nuclear Technology 41*, 389-400 (1978).

hazards and materials shortages

B. Badger et al, "UWMAK-III, a noncircular tokamak power reactor design", EPRI ER-368 (1976), Chapter 12.

B. Badger et al, "NUWMAK, a tokamak reactor design study", UWFDM-330 (1979), Chapter XIII.

R. M. Drake, Jr., Chairman, Helium Study Committee, *Helium: a Public Policy Problem*, National Academy of Sciences, Washington, DC, 1978.

"Fusion power: an assessment of ultimate potential", WASH-1239 (1973).

W. E. Kastenberg and D. Okrent, "Some safety considerations for conceptual tokamak fusion power reactors", EPRI ER-546 (1978).

M. S. Kazimi and R. W. Sawdye, "Radiological aspects of fusion reactor safety: risk constraints in severe accidents", *Journal of Fusion Energy 1*, 87-101 (1981).

J. R. Powell and C. T. Eterno, Editors, Proceedings of the Third Topical Meeting on the Technology of Controlled Nuclear Fusion, CONF-870508 (1978), Chapter 11.

economics

B. Badger et al, "NUWMAK, a tokamak reactor design study", UWFDM-330 (1979), Chapter XIV.

D. J. Bender and G. A. Carlson, "System model for analysis of the mirror fusion-fission reactor", UCRL-52293 (1977).

G. M. Fuller, "Fusion reactor first wall/blanket systems analysis, tokamak concepts", EPRI ER-582 (1977).

D. L. Kummer, "The relationship between material properties and the economics of fusion power", *Journal of Nuclear Materials 85 & 86*, 47-56 (1979).

S. C. Schulte, W. E. Bickford, C. E. Willingham, S. K. Ghose, and M. G. Walker, "Fusion reactor design studies - standard unit costs and cost scaling rules", PNL-2987 (1979). Lists standardized costs estimates for various fusion reactor components.

S. C. Schulte, T. L. Willke, and J. R. Young, "Fusion reactor design studies-standard accounts for cost estimates", PNL-2648 (1978).

W. M. Stacey, Jr. and M. A. Abdou, "Tokamak fusion power reactors", *Nuclear Technology 37*, 29-39 (1978).

CHAPTER 29
Fusion-Fission Hybrids

29A. Need

depletion of fissile fuel supplies

In 1990 the installed nuclear electric generating capacity in the USA will be about 200 GWe. Each 1-GWe light-water reactor (LWR) burns most of the ^{235}U and a little of the ^{238}U from about 5600 tons of U_3O_8 ("yellow cake") during its 30-year lifetime. Natural uranium is 99.27% ^{238}U and only 0.72% ^{235}U, so the present reactors are only using a small fraction of the uranium. The cumulative consumption of U_3O_8 for LWR's in the USA after 1990 is shown in Fig. 29A1, along with estimates of the U_3O_8 resources available in the USA. It appears that these resources may be fully committed before 2030, unless we develop other nuclear fuels, such as ^{239}Pu and ^{233}U. The worldwide situation is similar.

Since zero-energy neutrons can cause fission of ^{235}U, it is called *fissile*. Only neutrons with energies above 0.6 MeV can cause fission of ^{238}U, and it is not feasible to produce a chain reaction with ^{238}U alone. However, neutron absorption in ^{238}U can result in formation of fissile ^{239}Pu, a suitable reactor fuel, via the reactions

$$^{238}U(n,\gamma)^{239}U \xrightarrow[23\ min]{\beta} {}^{239}Np \xrightarrow[2.3\ days]{\beta} {}^{239}Pu \qquad (29A1)$$

where β represents beta emission with the given half life and γ indicates gamma ray emission. Since fissile fuel can be bred from ^{238}U by neutron absorption, ^{238}U is called *fertile*. Similarly, the fissile isotope ^{233}U, which has negligible natural abundance, can be produced from fertile ^{232}Th by the reactions

$$^{232}Th(n,\gamma)\ {}^{233}Th \xrightarrow[22\ min]{\beta} {}^{233}Pa \xrightarrow[27.4\ days]{\beta} {}^{233}U\ . \qquad (29A2)$$

Although the amount of ^{235}U available is limited, the reserves of the fertile isotopes ^{238}U and ^{232}Th are vast (Table 1C1).

fissile fuel production

Efficient conversion of fertile isotopes into fissile fuels requires high-flux sources of neutrons, such as liquid metal fast breeder reactors (LMFBR's), fusion-fission hybrids, and electronuclear breeders.

Electronuclear breeders produce neutrons by spallation when GeV proton beams strike solid targets. Because of the accelerator's high capital cost and low current, the fissile fuel thus produced will be very expensive, resulting in electricity costs much higher than from fission breeders or fusion-fission hybrids (Kostoff, 1979).

A fusion-fission hybrid is a fusion reactor with fertile isotopes in the blanket. The fusion neutrons may be used for several applications: breeding fissile fuel; inducing fission reactions to produce additional power; and transmutation of radioactive wastes via neutron absorption. Radwaste transmutation requires very high neutron fluxes, but it may be feasible for some isotopes, such as actinide elements. The hybrid blanket can be designed to maximize fissile fuel breeding, or to maximize the blanket energy gain M (defined in Table 4C1). The optimum design, which minimizes the cost of electricity from the entire system (hybrid reactor plus fission reactors fueled by it), may tend toward either extreme, depending upon the market price of fissile fuel. (If fissile fuel is very expensive, breeding should be maximized.)

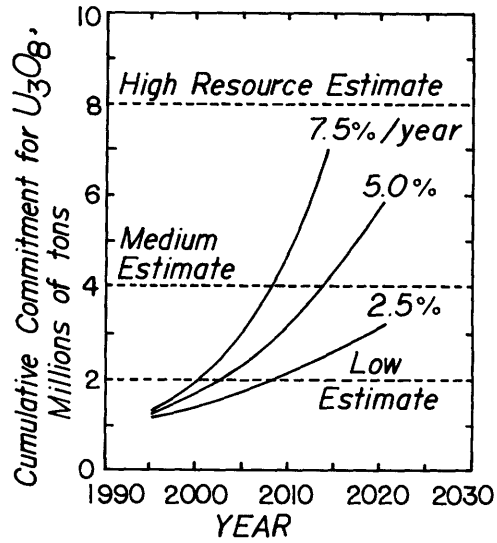

Fig. 29A1. Cumulative commitment for U_3O_8 in the United States, as a function of time, for 32 % efficient LWR's with various growth rates. From R. W. Werner, "Cumulative fuel commitment for light water reactors. Is there a 'uranium crunch' ? The fusion-fission fuel factory can help", UCRL-81600 (1978).

comparison with fusion and fission

A fusion reactor needs $Q \gtrsim 10$ to be economical, but a fusion-fission hybrid may be economical with $Q \sim 2$. The lower Q permits operation with shorter confinement times, which may relax the required values of some of the following parameters: plasma size, magnetic field, neutral beam injection energy, and energy conversion efficiency. Hybrids may be a useful intermediate step along the path to "pure" fusion reactors.

Fusion-fission hybrids and LMFBR's are compared in Table 29A1. Environmental concerns and associated costs will be important in determining which type of power system is preferable.

Table 29A1. Comparison of fusion-fission hybrids with LMFBR's.

potential advantages relative to LMFBR's

A critical mass is not needed.
No fissile fuel is needed for startup.
Fuel doubling times are months (compared to about 15 years for LMFBR's).
One hybrid can provide fuel for many LWR's.
Power density is lower, so fuel element design is easier.
Hybrids have less afterheat, so a loss of coolant accident (LOCA) is less severe.
Hybrids do not need to generate power "on-line". They can operate intermittently to produce fissile fuel.
Hybrids accelerate the development of fusion power.
Hybrids may have lower fission product inventories and lower fissile fuel inventories.

potential disadvantages relative to LMFBR's

Hybrids are less developed; costs are uncertain.
Hybrids have large tritium-handling requirements.
Machine design is more complex, so maintenance is more difficult.

29B. Blanket Design

considerations

Some problems to be considered in design of a hybrid blanket are listed in Table 29B1. Conformity to plasma and coil geometries is the same as for fusion reactors. Low power densities are uneconomical, and high power densities create structural and cooling problems, especially during a loss-of-coolant accident (LOCA).

Table 29B1. Hybrid blanket design considerations.

thermomechanical

conformance to plasma & coil shapes
maximum surface coverage
structural loads & lifetime
heat removal, normal operation and loss-of-coolant accident (LOCA)
low coolant pumping power
minimum structural material
low first-wall temperature
easy remote handling & component replacement
containment of fission fragments & tritium
tritium removal & inventory

other

materials compatibility
hazards (fire, toxic materials)
cost

neutronic

average power density $\sim$ 100 W/cm^3 (lower values less economical, much higher values difficult to cool)
adequate tritium breeding ratio ($T \sim 1.1$)
large fissile breeding ratio F
large blanket energy gain M
low-cross-section structural material
blanket subcritical under all conditions
neutron multiplier
fuel management scheme (fissile inventory, residence time)
radiation damage effects
afterheat

Hybrid blankets may be characterized by three parameters: the blanket energy gain M, the tritium breeding ratio T (tritium atoms bred per neutron incident on blanket), and the fissile fuel breeding ratio F (net fissile atoms bred per neutron incident on the blanket). To attain large values of M, T, and F, the neutron population can be increased with (n, 2n), (n, 3n), and (n, f) reactions, and neutron losses can be minimized by careful selection of structural configurations and materials. To increase wall lifetime, the first wall can be kept below the blanket temperature by cooling with water. (D_2O softens the neutron spectrum less than H_2O, and low-pressure water requires less structure than high-pressure water.)

The requirement for subcriticality limits the allowable buildup of plutonium in the blanket. The fuel management scheme is also limited economically: leaving fissile fuel in the blanket too long delays revenue which could be gained, so the utility in effect pays interest on unremoved fissile fuel. Irradiations longer than about one year result in an economic penalty, so fuels which can attain high "burnup" (atomic fraction consumed by nuclear reactions) are probably not needed (Bender and Carlson, 1977).

neutron interactions

Many nuclear reactions occur simultaneously in addition to those listed in Eqs. (29A1) or (29A2). For example, the isotope chains associated with ^{232}Th interactions are shown in Fig. 29B1. It is undesirable for ^{233}Pa to capture neutrons, because this reduces the quantity of ^{233}U produced and also depletes the neutron supply. A flowing blanket material can allow separation of Pa and decay outside the reactor, away from the neutron flux. When a 14 MeV neutron enters ^{232}Th or ^{238}U, the numbers of secondary neutrons produced by first collisions are about the same in the two cases, when (n, 3n), (n, 2n) and (n, f) reactions are all considered (Fig. 29B2). However, the secondary neutrons in the .5-5 MeV range can produce far more fissions in ^{238}U than in ^{232}Th, so the neutron multiplication occurring in ^{238}U is much greater than that in ^{232}Th and (T+F) is greater for ^{238}U.

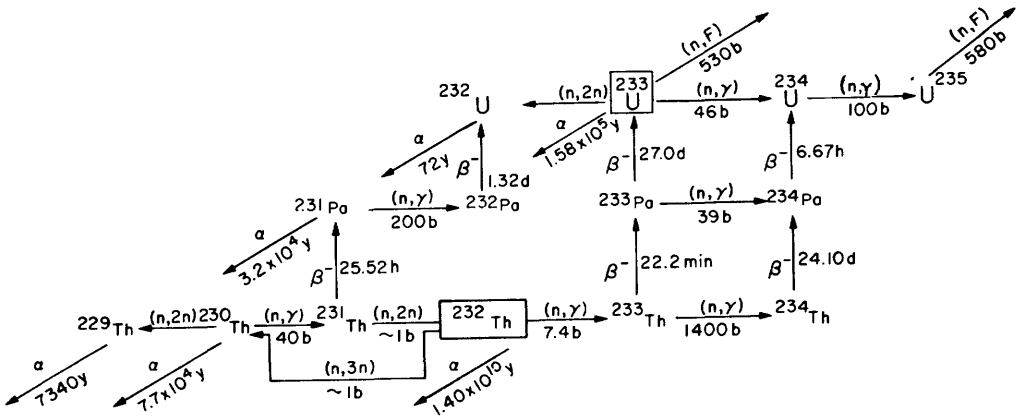

Fig. 29B1. Isotopic chain for the $^{232}Th/^{233}U$ fuel cycle. Cross sections for capture of 14 MeV neutrons are given in barns (b). From R. A. Krakowski, D. J. Dudziak, T. A. Oliphant, K. I. Thomassen, G. E. Bosler, and F. L. Ribe, "Prospects for converting ^{232}Th to ^{233}U in a linear theta-pinch hybrid reactor (LTPHR)", ERDA-4, 249-323 (1974).

Estimates of T, F, and M for 14 MeV neutrons incident on infinitely thick homogeneous blankets of various materials are shown in Table 29B2. It is apparent that ^{238}U is a better neutron and energy multiplier than ^{232}Th, that Be is better than Pb, and that, in an infinite homogeneous medium, natural Li is better than either ^{6}Li or ^{7}Li alone. Use of multi-region blankets can increase the values of T, F, and M, but absorption in structural materials decreases them.

fuel forms

The uranium or thorium fuels may be in solid form (plates, cylinders, or spheres) or in liquid form (molten salts or aqueous solutions). Conventional fuel fabrication technology uses rods. Balls could be continuously removed by gravity flow through the blanket, as in a pebble bed reactor, and could be dumped into coolant tanks in the event of a LOCA. Liquid-fuel blankets with Li- and fertile-fuel-bearing salts would have lower values of (T+F) and M, but the flowing salts may be chemically processed continuously outside the blanket to remove fission fragments, tritium, fissile fuels, and neutron absorbers. Because of low after-heat in liquid-fuel blankets, a LOCA would be less dangerous than with solid fuels. Hybrid blanket materials selection is discussed by Rose et al (1979).

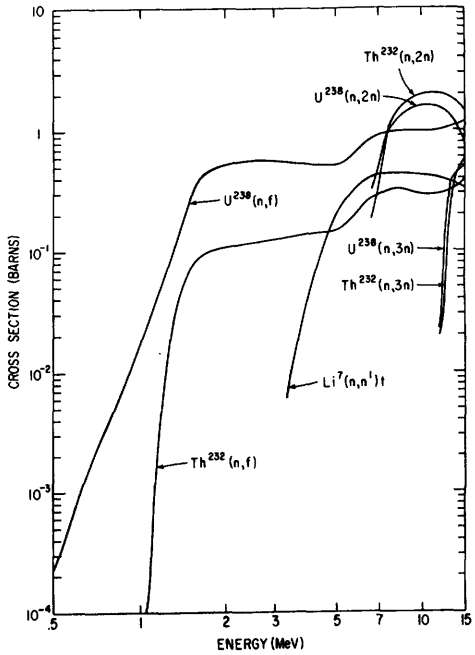

Fig. 29B2. Some neutron cross sections pertinent to hybrid reactors, as functions of neutron energy. From F. H. Tenney et al, "A systems study of tokamak fusion-fission reactors", PPPL-1450 (1978), p. 459.

Table 29B2. Results calculated for 14 MeV neutrons incident on infinitely thick single-region blankets. From R. W. Moir, "The fusion-fission fuel factory", Fusion Technology, Editor E. Teller, Academic Press, to be published.

blanket material	T	F ^{239}Pu	F ^{233}U	M
^{238}U	0	4.18	0	14.1
Natural U	0	5.0	0	21.3
^{232}Th	0	0	2.49	3.59
^{6}Li	1.08	0	0	1.17
^{7}Li	0.89	0	0	0.87
Natural Li (7.56% ^{6}Li)	1.90	0	0	1.16
^{238}U + 7.6% ^{6}Li	1.1	3.1	0	13.7
^{232}Th + 16% ^{6}Li	1.1	0	1.3	3.48
^{9}Be + 5% ^{6}Li	2.72	0	0	1.56
^{9}Be + 5% ^{232}Th	0	0	2.66	2.10
Pb + 5% ^{6}Li	1.74	0	0	1.28
Pb + 5% ^{232}Th	0	0	1.58	1.49

cost goals

If the purpose of the hybrid is primarily to sell fissile fuel for use in fission reactors, the cost of that fuel should be competitive with prices of fissile fuels produced by other means, such as gaseous diffusion enrichment of ^{235}U from natural uranium, centrifuge enrichment, and ^{239}Pu produced in LMFBR's. According to one estimate, the value of fissile fuels in the early 1990's will be 47-63 $/gram [1980 dollars, adjusted from Tenney et al (1978), p. 22].

Another way of estimating economic goals for hybrids is to consider the hybrid plus the fission reactors it supports as a complete system, as if they were sited at a common location (the nuclear park model). Then only the cost of electricity produced by the system is important, and the electricity must be competitive with that produced by LMFBR's, LWR's, and fossil fuel plants, which will probably be ~ 40 mills/kWh (1980 dollars). At the turn of the century with 500 GWe at 80% capacity factor in the USA, each mill/kWh decrease in the price of electricity represents an annual savings of 3.5 billion dollars.

29C. Tokamak Hybrids

large tokamaks

A Princeton study considered the three-region blanket shown in Fig. 29C1, with a neutron multiplier, burner region, and scavenger region. The first wall ("radiation shield" in Fig. 29C1) is cooled by low-pressure water. The multiplier region has U-7% Mo alloy fuel (0.3% ^{235}U) occupying 44% of the volume, SS-316 pressure tubes (8%), helium coolant (32%), and void (16%). The pressure tubes have 80 mm OD and 2 mm walls, and hollow fuel cylinders have 62 mm OD and 22 mm ID.

The first burner and third burner regions have 80% molten salt, 5% SS-316 and 15% helium coolant, and the central burner region is 85% graphite and 15% molten salt. The molten salt is 52 mole% BeF, 47.75% LiF, and 0.25% PuF_3. The lithium is depleted to 0.1% ^6Li in this region to avoid thermal neutron capture and enhance the Pu fission rate.

The scavenger region consists of 70% molten salt, 20% graphite, 5% SS-316 and 5% helium coolant. The salt is 52% BeF and 48% LiF, with the lithium enriched to 15% ^6Li, to produce tritium from neutrons leaking out of the burner region. Neutronics calculations were done using the ANISN discrete ordinates code with a P_3S_8 approximation.

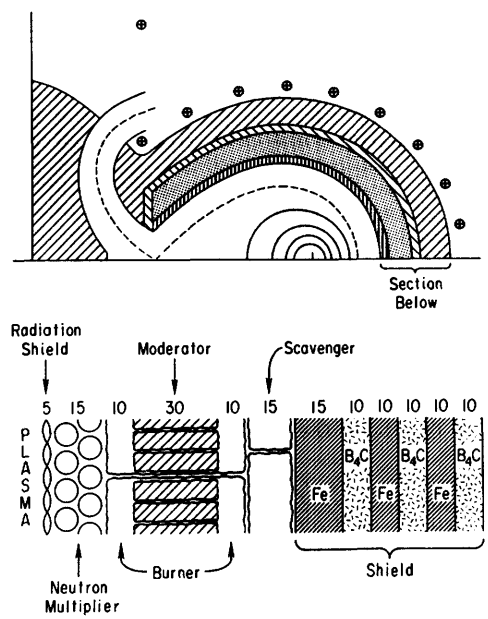

Fig. 29C1. Cross section of single-null Tokamak hybrid reactor (top) and blanket regions (bottom). The numbers indicate the region thicknesses (cm). Double-null configurations were also studied. From F. H. Tenney et al, PPPL-1450 (1978), p. 53.

The reactor parameters are related to six basic parameters: the minor plasma radius a, the distance h from the major axis of the torus to the TF coil shield, the electron temperature T_e, the neutral beam injection energy W_0, the ratio of beam density to plasma density n_h/n_e, and the gross electrical power P_g. The ranges studied are:

$$a = 1.2 \text{ to } 4.0 \text{ m}$$
$$h = 2.5 \text{ to } 8.0 \text{ m}$$
$$T_e = 6 \text{ to } 18 \text{ keV}$$
$$W_0 = 150 \text{ to } 300 \text{ keV}$$
$$n_h/n_e = 0.0 \text{ to } 0.3$$
$$P_g = 1 \text{ to } 10 \text{ GW}_e$$

The main constraints on the allowable parameters are:

(1) The current density $J \leq 1.25$ kA/cm^2 in the ohmic heating coils.
(2) The confinement time needed to achieve the specified plasma conditions must be attainable according to the scaling law chosen. (There is some uncertainty as to which scaling law is correct.)
(3) The plasma current $I > 1$ MA, in order to confine alpha particles.
(4) The blanket energy gain ratio is in the range $8 < M < 27$.
(5) The area required for neutral beam injectors must not exceed the wall area available.
(6) The hybrid must produce more electricity than it consumes.
(7) The plasma parameters are derated if the neutral beams cannot penetrate to the center.
(8) The plasma pressure is reduced to satisfy MHD stability requirements.

The resultant costs of electricity for optimum hybrids with P_g = 1, 3, and 6 GWe are shown in Fig. 29C2 as functions of the price of fissile fuel. The straight line indicates the cost of electricity from LWR's at the given fuel price. For example, if fissile fuel costs 60 \$/g, then the optimum hybrids with 1, 3, and 6 GWe could produce electricity for about 35, 29, and 22 mills/kWh, respectively, and the cost from LWR's would be about 30 mills/kWh. For this case a 3 GWe hybrid would be economical, while a 1 GWe hybrid would not. The "nuclear park" model for the 3 GWe case would occur at the intersection of the 3 GWe curve and LWR curve, fixing the prices of fissile fuel and electricity at about 45 \$/g and 29 mills/kWh. Various confinement time scaling laws and plasma pressure profiles shift the hybrid curves up or down, but do not greatly affect their shape. The optimum configurations generally have the highest allowable $n\tau$, and the minimum allowable W_0 for which beam penetration is adequate. Power costs for a double null divertor are slightly lower than for a single null divertor, but the single-null configuration might work better in practice, because of its longer flow channels.

Consider the following three cases of fissile fuel costs:

case A: f = 25.0 \$/g
case B: f = 87.5 \$/g
case C: f = 175.0 \$/g

The parameters of the resulting optimum hybrid 3 GWe reactors are listed in Table 29C1. For case A, fissile fuel is cheap, and it is most economical to burn it in the hybrid blanket and maximize M. For case C, fissile fuel is very expensive,

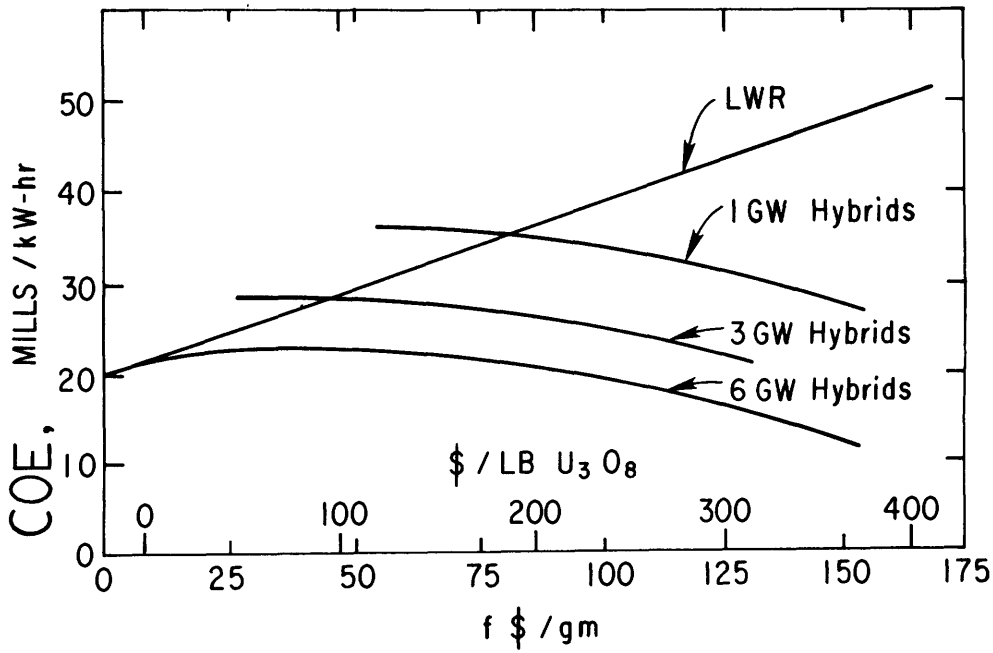

Fig. 29C2. Electrical power cost vs. fissile fuel cost for fusion-fission hybrids and LWR's. From F. H. Tenney et al, PPPL-1450 (1978), Fig. 2, p. 7.

and it is important to maximize F and the quantity of Pu which can be sold. Case B is intermediate between these two extremes. Maximizing fusion power density in case A results in high beam injection power and n_h/n_e, but low plasma volume, magnet size, and capital cost.

Finding an economic optimum configuration requires multidimensional analysis with many independent parameters, including
costs of downtime for maintenance (scheduled and unscheduled),
costs of fuel reprocessing,
costs of waste management and decommissioning, and
effects of changes in M (power swing) during the fuel cycle,
in addition to the plasma and materials parameters. However, fairly wide parameter variations are possible around the optimum, with only slight increases in power cost. The power cost is most sensitive to the shapes of the plasma density and temperature profiles, confinement time scaling laws, and interest rates. All cases display a similar economy of scale: Large reactors produce much cheaper power. Industrial parks could be built around one or two large hybrid reactors, including several LWR's and various industries using process heat.

small beam-driven tokamaks

A Westinghouse-EPRI group has studied small tokamaks in the two-component torus (TCT) mode ($Q \sim 1.3$) and in the beam-driven thermonuclear (BDTN) mode ($Q \sim 2$). The TCT hybrid, described in Table 29C2, is much smaller than the tokamak hybrids of Table 29C1. The BDTN reactor would have a

Table 29C1. Physical Parameters of Three Optimum Hybrids Rated at 3000 MWe. From F. H. Tenney et al, PPPL-1450 (1978), p.331-332.

Reactor Parameters	Case A	Case B	Case C	
fissile fuel cost	25	87.5	175	$/g
major radius R_0	10.83	15.72	16.07	m
minor radius a	2.435	2.940	2.912	m
aspect ratio R_0/a	4.45	5.35	5.52	
plasma volume	1267.	2682.	2690.	m^3
wall area	1129.	1922.	1948.	m^2
plasma density n_e	0.50	1.13	1.08	$10^{20}m^{-3}$
temperature T_e	7.0	6.1	6.5	keV
$n\tau$	0.56	7.61	6.57	$10^{20}m^{-3}s$
n_h/n_e	0.041	0.001	0.002	
β pressure ratio	1.29	0.99	0.95	%
beam energy W	150.0	168.0	157.0	keV
beam power	344.1	164.6	178.4	MW
fusion power	409.8	985.3	1087.0	MW
wall load	0.2905	0.4106	0.4467	MW/m^2
burnup	0.480	0.242	0.157	%
batch lifetime	7.68	3.53	2.17	yr
energy multiplication	23.64	9.86	8.91	
average Pu inventory	7494.	2800.	2422.	kg
gross Pu bred	1941.	2681.	2855.	kg/yr
net Pu sold	0.0	1988.	2336.	kg/yr
U inventory	978.0	1666.	1668.	Mg
net power	2144.00	2419.	2406.	MW
capacity factor	69.7	69.1	68.9	%
annual output	13.10	14.65	14.53	TWhr
Annual Revenue	500.83	709.08	837.16	M$
price of electricity	38.22	36.67	29.48	$/MW-hr
electric power	2144.00	2419.00	2406.00	MWe
electricity revenue	500.53	537.14	428.31	M$
capacity factor	69.73	69.12	68.94	%
price of plutonium	25.00	86.50	175.00	$/g
plutonium production	0.0	1987.70	2336.30	kg
plutonium revenue	0.0	171.94	408.85	M$
Annual Charges	500.72	709.31	836.05	M$
fixed charges	420.79	494.87	501.57	M$
wall replacements	0.43	1.04	1.14	M$
maintenance	19.65	21.98	21.80	M$
salt processing	1.00	1.00	1.00	M$
fuel cycle	58.84	190.42	311.68	M$
Capital Items	3316.54	3299.10	3343.81	M$
magnets	244.14	493.90	509.35	M$
wall and structure	140.63	209.21	213.80	M$
injectors	126.60	64.09	67.23	M$
invariant	50.00	50.00	50.00	M$
balance of plant	891.95	891.95	891.95	M$
indirect charges	653.99	769.12	779.55	M$
interest during construction	481.34	566.07	573.75	M$
Cost of Capacity (including inventory)				
electricity	1428.00	1477.00	1525.00	$/kWe
plutonium	--	1242.00	1083.00	$/(kg/yr)

Table 29C2. Parameters of a TCT hybrid reactor. From R. P. Rose et al, "Design study of a fusion-driven tokamak hybrid reactor for fissile fuel production", EPRI ER-1083 (1979), Table 9-1.

Plasma major radius, R_0 (meters, m)	4.45
Plasma minor radius (half-width), a(m)	0.90
Plasma aspect ratio (=R_0/a), A	4.89
Vertical elongation ratio of plasma, b/a = K	1.60
Horizontal first wall radius, (m) (inner/outer)	1.15/1.20
Plasma volume (m^3)	125
First wall area (m^2)	245
Toroidal magnetic field on magnetic axis, B_t(T)	4.25
Toroidal magnetic field at magnet coil, B_m (T)	10.5
Toroidal discharge plasma current, I_p(MA)	3.5
Plasma safety factor, q	2.5
Average electron density, $\bar{n}_e$ (cm^{-3})	1.0×10^{14}
Plasma temperature, $\bar{T}_e = \bar{T}_i$ (keV)	6.5
Density - confinement time product, $\bar{n}_e \tau_E$ (cm^{-3} s)	9×10^{12}
Neutral beam injection energy, W_b (keV)	200
Neutral beam mean-free-path, λ_t (m)	0.54
Neutral beam power, P_b (MW)	380
Beam pressure/plasma pressure, Γ	0.92
Plasma pressure/pressure of poloidal magnetic field, β_p	3.7
Fusion power/injected beam power, Q_b	1.25
Fusion power density, P_f (MW/m^3)	3.8
Total neutron production (n/s)	1.7×10^{20}
Neutron loading at first wall, (MW/m^2)	1.55
Bulk - plasma composition (% T)	82
Thermonuclear reactions (% total)	4
Total thermal power (MW)	855
Total neutron power (MW)	380
Power Dissipation of Divertor, P_{DBC} (MW)	335
Power Dissipation to First Wall, (MW)	140
Impurity Control	Liquid lithium coated, nested chevrons & external pumping
Pulse duration (seconds, s)	50-100
Time interval between pulses (s)	10-15

larger size than the TCT, giving better access, higher Q, and higher burnup fraction than the TCT; but the TCT has a higher neutron production rate and wall loading, lower required plasma current, lower required $n_e \tau_E$ (by a factor of 6), and higher tolerable impurity fraction than the BDTN reactor. More recent designs have higher values of β and Q, hence more favorable economics.

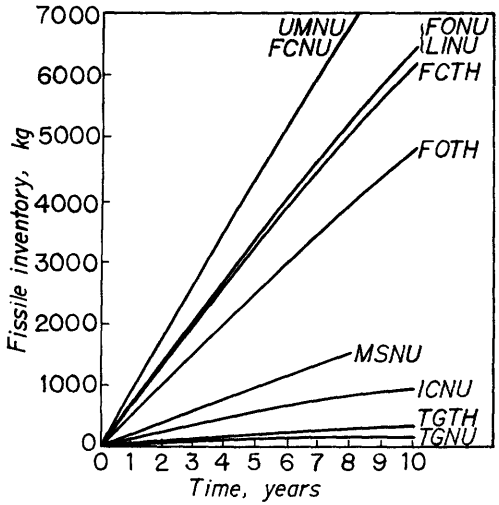

Fig. 29C3. Fissile fuel inventory vs. time for various fuel lattices.

FC = fast carbide
NU = natural uranium
UM = uranium-molybdenum
FO = fast oxide
LI = lithium
TH = thorium
MS = molten salt
IC = intermediate carbides
TG = thermal graphite

From R. P. Rose et al, EPRI ER-1083 (1979), Fig. C-13.

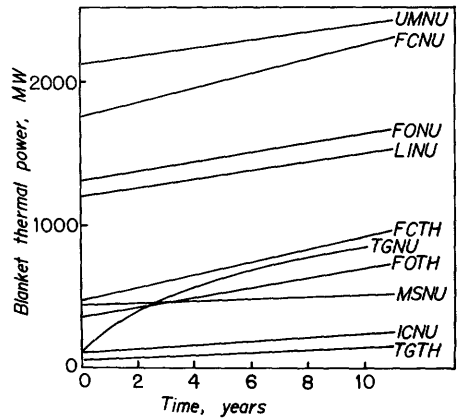

Fig. 29C4. Blanket thermal power vs. time for various fuel lattices. Same nomenclature as previous figure. From R. P. Rose et al, EPRI ER-1083 (1979), Fig. C-14.

Liquid metal coolants were found to have excessive MHD pressure drops in the small flow channels between fuel rods, so helium coolant was chosen for the blanket. From a comparison of various fuels using fast, intermediate, and thermal neutron spectra, it was found that the thermal lattices produce more power and fuel *per kg of U or Th* in the blanket, but the fast lattices produce more *total* power and fuel. The fissile fuel inventory and blanket thermal power vs. time for various fuel lattices are shown in Figs. 29C3 and 29C4.

For the TCT hybrid reactor, substantial cost savings could be achieved by successful development of:

low-cost superconducting cables
in-line direct convertors for the neutral beam injection system
bundle divertors.

29D. Mirror Hybrids

A helium-cooled submodule for a mirror hybrid blanket is shown in Fig. 29D1. Three fuels were studied: UC, U-7% Mo, and ^{232}Th. Although M and F increase with fission zone thickness, T decreases, so the maximum thickness is that for which the fraction of fusion neutrons intercepted by the blanket (blanket coverage) times T just exceeds one. A decrease in blanket coverage requires a

decrease in fission zone thickness, strongly reducing M and F. The neutronics results for the three fuels are shown in Fig. 29D2 as functions of neutron exposure, MW-yr/m^2. Exposures are limited primarily by economic penalties for leaving the bred fissile fuel in the blanket, and secondarily by radiation damage to fuel, cladding, and pressure vessel. The U-Mo fuel gives the best results for this blanket configuration.

Fig. 29D3 shows the estimated fissile fuel costs for the U-Mo blanket as a function of fertile fuel burnup. The optimum is at about 1% burnup (4 MW-yr/m^2 exposure), which is about the radiation damage limit for this fuel. Fig. 29D4 shows the variation of estimated fissile fuel costs and electrical power costs (1976 $)as a function of the reactor power gain ratio Q (defined in Chapter 4). Increasing Q results in a dramatic improvement in costs. Although simple mirror reactors would have Q $\lesssim$ 1, tandem mirrors and field-reversed mirrors may be able to achieve Q $\sim$ 10.

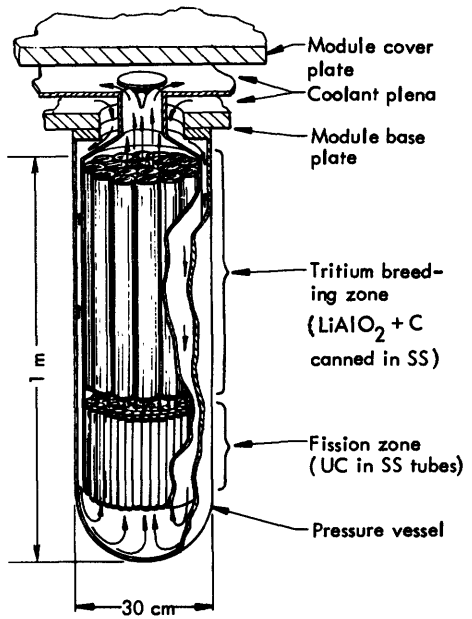

Fig. 29D1. A submodule for a mirror hybrid blanket. From R. W. Moir et al "Progress on the conceptual design of a mirror hybrid fusion-fission reactor", UCRL-51797 (1975), Fig. 6-3.

For the U-7% Mo case, each DT source neutron incident on the blanket generates 2.4 neutrons by fast fission of ^{238}U, 0.26 neutrons by (n, 2n) reactions, 0.24 neutrons by (n, 3n) reactions, for a total of 3.9 neutrons. Of these 3.9 neutrons, 1.8 are absorbed by ^{238}U to breed ^{239}Pu, 1.14 are absorbed by ^{6}Li to produce T, 0.68 cause fission of ^{238}U, 0.29 are captured in the structure, and 0.02 leak out of the blanket (Moir, 1981).

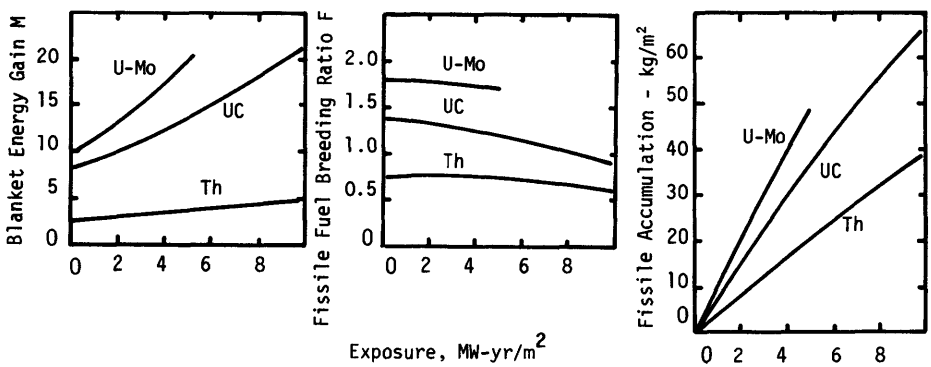

Fig. 29D2. Comparison of performance vs. exposure for blankets fueled with UC, U-7% Mo, and Th. From J. D. Lee, "Blanket design for the mirror fusion/fission hybrid reactor", CONF-760733 (1976), Fig. 14, p. 34.

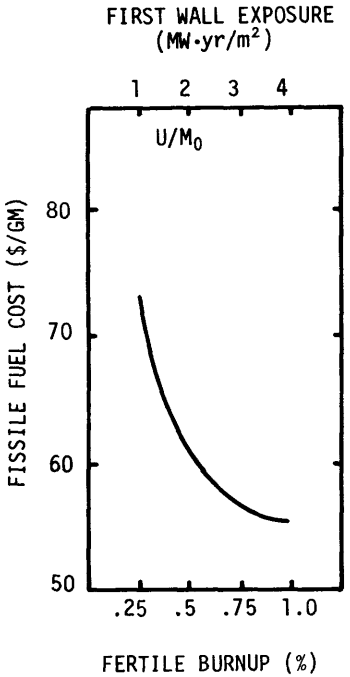

Fig. 29D3. Fissile fuel cost vs. fertile fuel burnup or first wall exposure. From D. J. Bender, "Mirror hybrid reactor optimization studies", CONF-760733 (1976), Fig. 8, p. 41.

Some parameters of the hybrid with the U-Mo and Th blankets are listed in Table 29D1. Significant improvements will be realized if higher Q values are attained by tandem mirrors or field-reversed mirrors. The U-Mo and Th hybrids provide fuel for about 7 and 14 fission reactors, respectively.

Uranium silicide (U_3Si) may be better than U-Mo fuel. The neutronics performance of a U_3Si-fueled blanket with LiH tritium-breeding material is shown in Fig. 29D5 for the case of *depleted* uranium, containing 0.25% ^{235}U (in contrast to natural uranium, which has 0.72% ^{235}U). (Great amounts of depleted uranium have been produced as "tails" of the ^{235}U enrichment process at gaseous diffusion plants.)

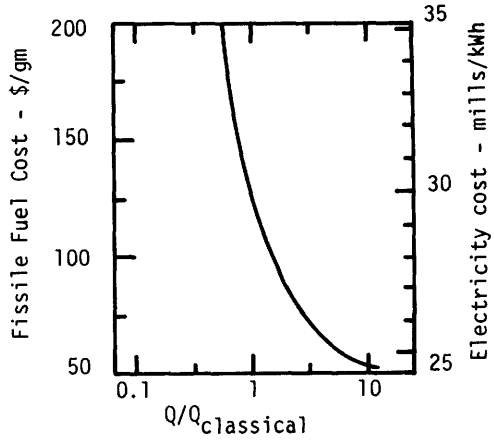

Fig. 29D4. Variation of fissile fuel cost and electrical power cost with power gain ratio Q. (For this reactor, $Q_{classical} \approx 0.7$). From D. J. Bender and G. A. Carlson, "System model for analysis of the mirror fusion-fission reactor", UCRL-52293 (1977), Fig. 3.5 .

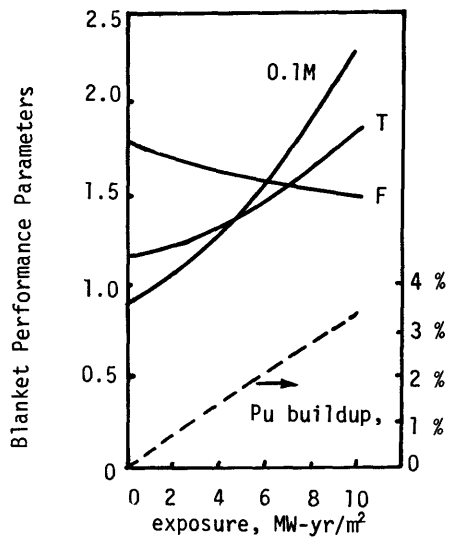

Fig. 29D5. Blanket performance vs. exposure for U_3Si blanket. From J. D. Lee, "Nuclear design of the LLL-GA U_3Si blanket", UCRL-80588 (1978), Fig. 6.

Table 29D1. Comparison of mirror hybrid reactor systems using natural U and Th fuels. From Moir (1981) and Bender (1976).

hybrid reactor parameters	U-7% Mo fuel	Th fuel
magnetic mirror ratio	2.50	2.75
injection energy W (keV)	100	100
magnetic field at coil (T)	8	12
Q	0.68	0.75
fusion power (MW)	470	1500
first wall flux (MW/m^2)	1.3	4.2
average blanket thermal power (MW)	4220	3340
electrical output (MW)	1040	-40
capacity factor	0.75	0.73
length between mirrors (m)	15	15
fissile output (kg/yr)	2360	2590
average value of M	11.1	2.8
blanket coverage	0.86	0.77
fertile burnup (%)	1.0	0.5
blanket exposure ($MW-yr/m^2$)	4.1	9.2
fuel power density (W/cm^3)	150	110
peak to average electrical output	1.13	no output
thermal convertor reactor type	LWR	HTGR
conversion ratio	0.5	0.8
fissile fuel requirements (kg/MWe-yr)	0.333	0.185
installed capacity (GWe)	8.13	14.0
economics (1976 $)		
capital cost of hybrids (G$)	2.3	3.3
capital cost of fission reactors ($/kWe)	750	750
nuclear park electric costs (mills/kWh)	24.8	25.3
fixed charges	19.7	20.5
fuel cycle	4.3	4.0
operation and maintenance	0.8	0.8
effective fissile fuel costs ($/g)	55	127
effective average capital costs for nuclear park ($/kWe)	935	985

other types of hybrids

With regard to neutronics and thermomechanical considerations, these mirror hybrid blankets could be used with Tokamaks, and vice-versa. Other types of hybrids, such as inertial confinement fusion (ICF) devices, can use similar blankets. One laser fusion hybrid uses (n, 2n) reactions in Pb as a neutron multiplier with Th fuel (Ragheb et al, 1979). The main differences between various types of fusion-fission hybrid reactors are

* steady-state vs. pulsed operation
* average neutron power flux at wall
* power gain ratio Q
* capital costs of plasma confinement and heating systems
* fusion fuel and fissile fuel types,

29E. Catalyzed DD Hybrids

advantages

A catalyzed DD hybrid reactor does not need to breed tritium in the blanket, so more neutrons can be used to breed fissile fuel. Potential advantages of a semicatalyzed DD hybrid with a molten salt blanket are summarized in Table 29E1. ("Semicatalyzed" means that the tritium produced by DD reactions is burned in the plasma, but the ^{3}He produced is not.)

Table 29E1. Comparison of a molten-salt-blanket semicatalyzed DD hybrid with a DT hybrid. From M. J. Saltmarsh, W. R. Grimes, and R. T. Santoro, "An optimization of the fission-fusion hybrid concept", ORNL/PPA-79/3 (1979).

advantages of DD

Tritium breeding is not necessary.
- More neutrons are available for breeding.
- More neutron captures in structure are allowable.
  - pressurized water cooling of first wall
  - longer first-wall life
- Structural separation of first wall and breeding regions makes replacement of components easier.

On-line reprocessing of molten salt:
- lower inventories of fissile fuel and fission fragments
- less decay heat after shutdown
- lower reprocessing costs ($\sim$ 1 \$/g vs. $\sim$ 20 \$/g for solid fissile fuels at 1% enrichment).

disadvantages of DD

DD reactors require better plasma confinement $n\tau$
Corrosion problems
Molten salt technology is not yet developed on a commercial scale.

neutronics

The blanket regions of a hypothetical DD reactor are listed in Table 29E2. Neutronics analysis indicates that for each neutron incident on the blanket, 0.026 extra neutrons are produced in the first wall, 0.019 in the structure, and 0.159 in the salt, for a total of 1.204 neutrons. Of these 1.204 neutrons, 0.101 are absorbed in the first wall, 0.989 in the salt, 0.1 in the structure, and the rest are absorbed in the reflector or coolant or lost by leakage. As a result, $M \simeq 1.5$ and $F \simeq 0.85$, so the effective value of F for 80% blanket coverage is about 0.7 .

advantage of ^{233}U fuel

The ratio of fission to fusion power is

$$P_{fis}/P_{fus} = \frac{200\ F}{12.5(1-C)(1+\alpha)} \qquad (29E1)$$

where 200 MeV is the energy released by fission, 12.5 MeV is released by semicatalyzed DD fusion (per neutron released), F is the fissile breeding ratio of the hybrid ($F \sim 0.7$ for the molten salt DD hybrid), C is the conversion ratio of

Table 29E2. DD hybrid blanket regions. From M. J. Saltmarsh, W. R. Grimes, and R. T. Santoro, ORNL/PPA-79/3 (1979), Table C1.

Zone	Description	Outer radius (cm)	Thickness (cm)	Remarks
1	Plasma	100	100	Half of the neutrons have 2.45 MeV, and half, 14.1 MeV.
2	Vacuum	150	50	
3	First wall	151	1	SS-316
4	Coolant	151.5	0.5	Water
5	Structure	152.5	1	SS-316
6	Salt	194.5	42	$NaF \cdot BeF_2 \cdot ThF_4$ (71-2-27 mole %)
7	Structure	195.5	1	SS-316
8	Reflector	235.5	40	Graphite
9	Structure	236.5	1	SS-316
	Shield			Simulated by 20 % reflectivity

the fission reactor (the average number of fissile atoms produced in the fission reactor per fuel atom consumed) and α is the capture-to-fission ratio (ratio of neutron cross sections for radiative capture and fission in the fission reactor fuel).

Use of ^{233}U fuel has the advantage that it may be burned in HTGR's with $C \simeq 0.85$ and $\alpha \simeq 0.1$, while ^{239}Pu would probably be burned in LWR's with $C \simeq 0.6$ and $\alpha \simeq 0.3$. Thus, $P_{fis}/P_{fus} \simeq 69$ for ^{233}U fuel and 22 for ^{239}Pu fuel. For a given hybrid reactor power, the fission power which can be generated with ^{233}U fuel is about three times as large as that which can be generated with ^{239}Pu fuel. If the fission reactors are all the same power, then about three times as many reactors can be fueled by one hybrid with ^{233}U as with ^{239}Pu.

economics

The hybrid may be characterized by the parameters N, the number of fission reactors fueled by it, and C_{HB}/C_{LWR}, the allowable ratio of hybrid capital costs to LWR (or HTGR) capital costs. For example, if $C_{HB}/C_{LWR} = 2$, then hybrids costing 2.1 times the cost of an LWR would be uneconomical, while hybrids costing 1.9 times the cost of an LWR would be profitable. Large values of N and C_{HB}/C_{LWR} indicate that the hybrids have good chances of being economical. Let the parameter δ be defined by the equation

$$COE = C_0(1 + \delta) \qquad (29E2)$$

where COE is the actual electrical power cost (mills/kWh) and C_0 is what the power cost would be if the fuel were free. Thus, $\delta/(1+\delta)$ is the fraction of the power cost due to the fuel cycle cost.

If $C_0 = 20$ mills/kWh, then the value of fissile fuel $f = 300\delta$ (\$/g) for ^{239}Pu and $f = 975\delta$ (\$/g) for ^{233}U. For typical values $0.1 < \delta < 0.3$, these fuel costs are $30 < f < 100$ \$/g for ^{239}Pu and $100 < f < 300$ \$/g for ^{233}U. (Saltmarsh et al, 1979).

The numbers of fission reactors fueled by one hybrid are shown in Fig. 29E1 as functions of $Q' \equiv \eta_{in}Q$ (defined in Table 4C1) for various types of hybrids. The

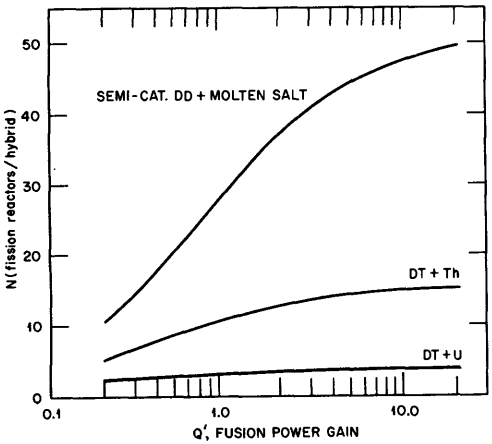

Fig. 29E1. The number N of fission reactors fueled by one hybrid as functions of fusion power gain $Q' = \eta_{in}Q$, for DD hybrids with molten salt blankets, for DT hybrids with Th blankets, and for DT hybrids with U-7%Mo blankets. From M. J. Saltmarsh, W. R. Grimes, and R. T. Santoro, ORNL/PPA-79/3 (1979), Fig. 8.

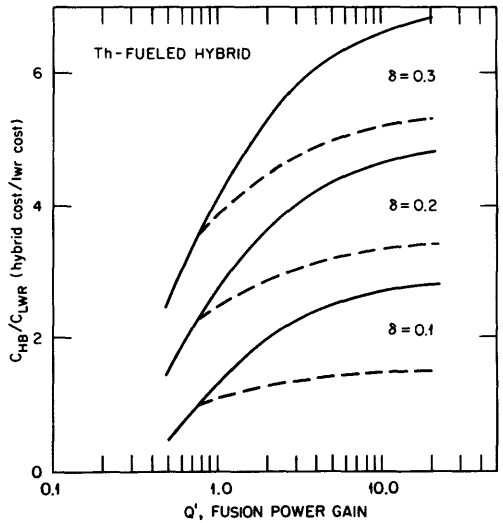

Fig. 29E2. The allowable capital costs for Th-fueled DT hybrids (relative to LWR capital cost) vs. fusion power gain $Q' = \eta_{in}Q$, for various values of δ (defined in Eq. 29E2). Smooth curves refer to on-line operation, dashed curves represent off-line operation. From M. J. Saltmarsh, W. R. Grimes, and R. T. Santoro, ORNL/PPA-79/3 (1979), Fig. 7.

semicatalyzed DD hybrid with molten salt blanket is superior to DT hybrids with either a Th blanket or a U-7% Mo blanket. The acceptable capital costs of hybrids are shown in Figs. 29E2 and 29E3 for DT hybrids with Th blankets and DD hybrids with molten salt blankets. Again the DD hybrid is superior. Thus, if the disadvantages cited in Table 29E1 can be overcome, DD hybrids with molten salt blankets may produce very economical electrical power.

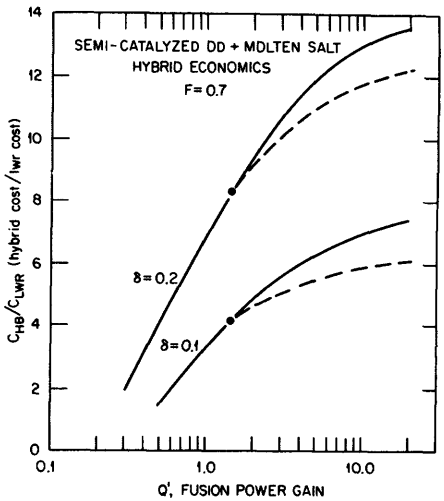

Fig. 29E3. The allowable capital costs for semicatalyzed DD hybrids with molten salt blankets (relative to LWR or HTGR capital cost) vs. fusion power gain $Q' = \eta_{in}Q$, for two values of δ (defined in Eq. 29E2). Smooth curves are for on-line operation of the hybrid, dashed curves are for off-line operation. From M. J. Saltmarsh, W. R. Grimes, and R. T. Santoro, ORNL/PPA-79/3 (1979), Fig. 9.

Bibliography

D. J. Bender, "Mirror hybrid reactor optimization studies", CONF-760733, 37-44 (1976).

D. J. Bender and G. A. Carlson, "System model for analysis of the mirror fusion-fission reactor", UCRL-52293 (1977).

R. W. Conn, F. Kantrowitz, and W. F. Vogelsang, "Hybrids for direct enrichment and self-protected fissile fuel production", *Nuclear Technology 49*, 458-468 (1980).

W. E. Kastenberg, D. Okrent, et al, "Some safety studies for conceptual fusion-fission hybrid reactors", EPRI ER-548 (1978).

R. N. Kostoff, "Status and prospects of advanced fissile fuel breeders", CONF-790103 (1979).

R. A. Krakowski, D. J. Dudziak, T. A. Oliphant, K. I. Thomassen, G. E. Bosler, and F. L. Ribe, "Prospects for converting ^{232}Th to ^{233}U in a linear theta-pinch hybrid reactor (LTPHR)", ERDA-4, 249-323 (1974).

J. D. Lee, "Nuclear design of the LLL-GA U_3Si blanket", UCRL-80588 (1978).

J. D. Lee, "Blanket design for the mirror fusion/fission hybrid reactor", CONF-760733, 27-35 (1976).

L. M. Lidsky, "Fission-fusion systems: hybrid, symbiotic and augean", *Nuclear Fusion 15*, 151-173 (1975).

R. W. Moir, "The fusion-fission fuel factory", *Fusion Technology*, editor E. Teller, Academic Press, to be published, 1981.

R. W. Moir et al, "Progress on the conceptual design of a mirror hybrid fusion-fission reactor", UCRL-51797 (1975).

Proceedings of the 4th ANS Topical Meeting on the Technology of Controlled Nuclear Fusion (King of Prussia, PA, 1980), DOE, 1981.

M. M. H. Ragheb, S. I. Abdel-Khalik, M. Youssef, and C. W. Maynard, "Lattice Calculations and three-dimensional effects in a laser fusion-fission reactor", *Nuclear Technology 45*, 140-152 (1979).

R. P. Rose et al, "Design study of a fusion-driven tokamak hybrid reactor for fissile fuel production", EPRI ER-1083 (1979), (2 volumes).

M. J. Saltmarsh, W. R. Grimes, and R. T. Santoro, "An optimization of the fission-fusion hybrid concept", ORNL/PPA-79/3 (1979).

K. R. Schultz, "Materials implications of fusion-fission reactor designs", *Journal of Nuclear Materials 85 & 86*, 29-36 (1979).

K. R. Schultz, G. A. Backus, C. B. Baxi, J. B. Dee, E. A. Estrine, R. Rao, and A. R. Veca, "Mirror hybrid reactor blanket and power conversion system conceptual design", CONF-760733 (1976).

K. F. Schoepf and A. A. Harms, "The synergetics of the catalytic D-D-fusion-fission breeder", *Nuclear Fusion 19*, 5-19 (1979).

F. H. Tenney, C. G. Bathke, W. G. Price, Jr., W. H. Bohlke, R. G. Mills, E. F. Johnson, A. M. M. Todd, C. H. Buchanan, and S. L. Gralnick, "A systems study of Tokamak fusion-fission reactors", PPPL-1450 (1978).

R. W. Werner, "Cumulative fuel commitment for light water reactors. Is there a 'uranium crunch' ? The fusion-fission fuel factory can help", UCRL-81600 (1978).

M. Z. Youssef, R. W. Conn, and W. F. Vogelsang, "Tritium and fissile fuel exchange between hybrids, fission power reactors, and tritium production reactors", *Nuclear Technology 47*, 397-405 (1980).

CHAPTER 30

THE FUTURE

30A. Experimental Progress

The progression of fusion research experiments in the United States towards the reactor regime is illustrated in Fig. 30A1. Only a few larger devices are shown. Similar progress is occurring in other countries around the world. Although only tokamaks, mirrors, and laser fusion experiments are shown in the Figure, many other confinement concepts are under study (Chapters 11-17), and some of the alternate concepts may ultimately be superior to the main line approaches.

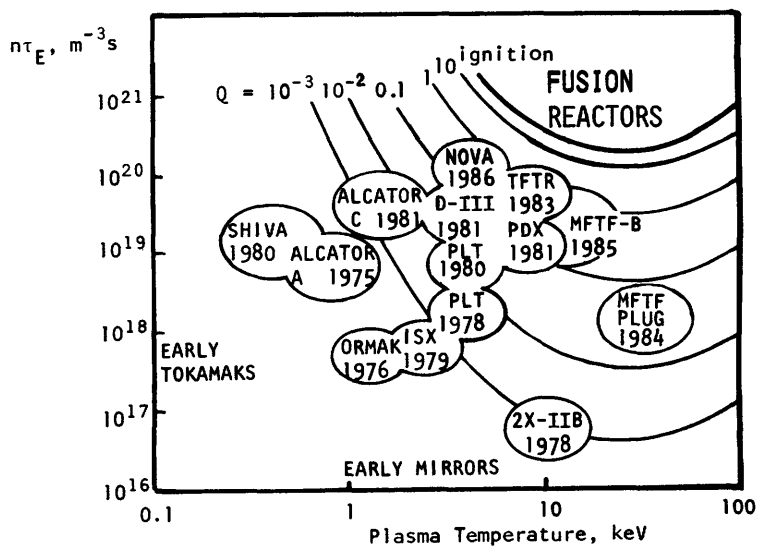

Fig. 30A1. Energy confinement parameters $n\tau_E$ and temperatures of various tokamak, mirror, and laser fusion experiments.

30B. Remarks

To illustrate various philosophies and opinions on the future of fusion research, some remarks by research leaders are quoted here.

Fusion, the Ultimate Energy

Edwin E. Kintner Associate Director for Fusion Energy, Office of Energy Research
United States Department of Energy

Of all the potential energy resources, fusion is the least developed and yet has the greatest implications for the future of the human race. Fusion is the energy of the sun and stars, the fundamental energy of the universe. The energy we create by burning fossil fuels was, of course, first produced by fusion energy in the sun. Fusion is the last known physical process by which energy can be created. Its fuel supply is inexhaustible and widely available. The environmental effects of fusion are such that it can be considered, either as to combustion waste products or radioactive waste products, as ecologically acceptable for all time and all places. Fully developed, fusion could be a flexible energy resource -- one which could generate electricity as well as portable fuels like hydrogen, which could then in turn be used to produce synthetic fuels from fossil sources.

So, if all these things are true, why aren't we using fusion today ? The most important reason is that fusion is probably the most difficult technical challenge ever undertaken by man. If we are to use the energy of the sun and the stars, we have to create and control the conditions of the sun and the stars here on earth. Even that is not enough, because we have then to learn how to engineer that first physical knowledge into practical plants and systems. The technology problems of materials, superconducting magnets, plasma heating devices, and the like are less sophisticated, but perhaps more difficult. In short, we have to learn a great deal more than we know about the fourth state of matter -- plasmas -- and then translate that new knowledge into practice.

We are making gratifying progress. We have already created temperatures three times those in the center of the sun, temperatures high enough to cause fusion reactions to take place at a power producing rate. We have already confined plasmas at a combination of density and magnetic field insulation within a factor of three of that required for net power production. We expect to close that gap of a factor of three with the Alcator C device at MIT this year. And the TFTR project, which we confidently believe will produce net fusion energy for the first time, is already half way through its design and construction at Princeton.

Two years ago, the question within the fusion community was whether scientific feasibility could be achieved. In the last two years, that question has been answered affirmatively for all but the most pessimistic. There no longer seems to be remaining doubt in the fusion community that man can, using only his intelligence, and with materials and devices already known, produce net fusion energy on the surface of the earth. The achievement has profound implications for the future.

But as so often happens in translating scientific knowledge into practical economic usefulness, the most expensive and time-consuming stages are ahead. We reached this point with expenditure of approximately $2 billion of fusion research in this country, but we estimate it will take four or five times that much before fusion has reached economic practicality. And that is the rub! No

society, no nation, has ever committed to a program so expensive and so long range for a non-military purpose. What we are asking is that today's citizens provide the resources and the effort to develop a technology whose economic usefulness will not be significant for at least two decades at best. I think this is our biggest challenge in fusion. We can, we now know, answer the scientific and technical questions, but there is still a doubt as to whether that moral commitment can be made.

Paths of Fusion Research

Stephen O. Dean President, Fusion Power Associates

Until the late 1960's there was very little evidence that the conditions of density, temperature and confinement required for net fusion energy production could be achieved in any of the approaches then under study. There were hopes, of course, and many ideas. Perhaps most importantly, there was enthusiasm and a growing cadre of smart people who would dedicate their careers to finding solutions to many difficult physics and engineering problems.

The decade of the 1970's has seen the development of more sophisticated theories, a substantial amount of experimental data and the construction, operation, and modification of a variety of facilities with capabilities of producing plasmas in the physics regime relevant to fusion reactors. Most importantly, the 1970's has seen the emerging of the first approach to fusion which, from a physics point-of-view, is guaranteed to be able to achieve the conditions of net energy release -- the tokamak. Experiments like Alcator at MIT, ORMAK at Oak Ridge, and PLT at Princeton demonstrated empirically the scaling laws for confinement as a function of plasma size and density at very respectable temperatures of about 1 keV. Then, using neutral beam heating, the scaling law was verified in the PLT to temperatures of 6.5 keV, well in excess of the ideal ignition temperature of 4 keV required for fusion reactions to become self-sustaining. Based on the emerging physics principles of the tokamak, the Tokamak Fusion Test Reactor (TFTR) is under construction, with a 1982 completion target. This facility is conservatively designed to achieve, using deuterium-tritium fuel, the simultaneous conditions of density, temperature, and confinement required for energy breakeven.

The decade of the 1970's has also seen the emergence of a new field of fusion research -- inertial confinement. The new organizations and the people who are developing the science and technology of this approach have brought enhanced life and vigor to fusion research as a whole. The spirit of friendly competition which has emerged between the magnetic and inertial communities has helped to sharpen the issues of fusion engineering, development, and the search for useful applications.

The progress and promise in fusion have not been limited to tokamaks within the magnetic confinement program and lasers within inertial confinement. The magnetic mirror has emerged as the major alternative to the tokamak; and particle beam drivers, as the alternative to the laser driver. The details of magnetic mirror geometry are still evolving, as are the different types of particle beams (electron, light ion, heavy ion) and inertial pellet designs. Indeed, a variety of interesting concepts have emerged, and each has its own group of enthusiasts.

Some people ask questions such as, "How can we afford to pursue so many approaches ?" Such questions, while honestly motivated, miss the essential unity of fusion science and engineering. Most, if not all, of what is learned in one area benefits the activities in the other areas. It is through this variety that the principles of fusion science become firmly established, the engineering problems get properly posed, and the required technology emerges. The trade-offs in funding and timescales required by finite budgets are part of the normal management process for any development and should not be viewed as dilemmas unique to fusion research.

In some government circles a "Let's wait and see" attitude has existed when it comes to questions such as how much effort should be put into engineering development, how much industrial participation should there be, and how much effort should be put into studies of potential applications. To delay increased effort in these areas, in hopes that a clearer path to fusion is about to emerge is, I believe, a great mistake. For one thing, scientific progress in fusion has been and is directly related to technology advances and to the insights and guidance acquired from conceptual studies of fusion reactors. In addition, these areas must be developed well in advance of when they are needed; otherwise fusion progress will grind to a halt just when it is ready to capitalize on its accomplishments. Building up the engineering skills and organizations needed for fusion development is the best way to ensure that systematic progress continues to be made toward our ultimate goal: the sustained, controlled released of practical quantities of fusion energy.

The Future of Fusion Research

Tihiro Ohkawa — Vice President
General Atomic Company

The variety of confinement schemes under investigation and the increasing sophistication of both plasma diagnostics and device engineering have made fusion a particularly vibrant field of research. The rapidly growing data base has made possible more realistic assessments of the reactor prospects of the alternate approaches, and these assessments will, to a large extent, dictate the future course of fusion research. The program will inevitably narrow the choice of confinement schemes as the reactor demonstration phase is approached. Further, it will focus primary attention upon a small number of devices, each of which will be aimed toward answering specific questions needed for reactor design.

While the bulk of the resources will be channeled toward solving the engineering and technology obstacles to fusion power, the scientific questions will remain the key to the pace of progress in the foreseeable future. For, despite the considerable advances in understanding achieved to date, the history of the program leaves little doubt that many surprises lie in store for us as increasingly reactor-like plasmas are produced.

The Future of Tokamak Research

Harold P. Furth Princeton Plasma Physics Laboratory

During the 1980's, the scientific and technical feasibility of a power-producing tokamak reactor will become increasingly obvious. The economic viability of such a reactor will remain controversial, however. If an experimental tokamak reactor is built, the very process of confronting the detailed engineering problems of fusion-power production for the first time is likely to sharpen criticism of the tokamak approach -- and possibly of fusion research in general.

During this period, a key decision will have to be made: whether to concentrate on perfecting the tokamak reactor, or on substituting an alternate fusion reactor approach. On the basis of the present-day experimental picture, I would expect that an investment of inventiveness and effort in the tokamak area will yield the best returns in terms of the realization of a practical first-generation power reactor.

If fusion research can successfully approach initial commercialization, around the turn of the millenium, I would then expect that the combination of intensified interest, clarified physical understanding, and evolved technology will ultimately lead to far better fusion reactor concepts than any we have yet discerned.

The Future of Mirror Fusion

T. Kenneth Fowler Lawrence Livermore Laboratory

In the 1980's, magnetic fusion research will enter a new phase. Whereas the decade of the 1960's was devoted to basic plasma physics and the 1970's to the emergence of the tokamak, mirror and other successful confinement concepts, in the 1980's a large effort must be devoted to engineering development of these concepts toward practical power plants. The precursor to this engineering thrust will be physics results from the major scaling experiments, first for the tokamak (TFTR, in 1982), followed around 1984 by the tandem mirror (the MFTF-B, a tandem mirror upgrade of the Mirror Fusion Test Facility now under construction at the Lawrence Livermore Laboratory).

Much of the engineering technology associated with the particular confinement concepts -- superconducting magnets, neutral beams, cryopumping, etc. -- is being developed in the course of constructing the TFTR and the MFTF. Beyond that, it will be necessary to develop the so-called "blanket" in which neutrons breed tritium and deposit their energy as heat, and to do this in integrated systems that can provide a basis for designing successful commercial reactors in the future. Because fusion is a young science with many possible applications, it will be important not to narrow the choices too early. Thus it is planned to carry out engineering development simultaneously for the tokamak, mirror, and other promising concepts as they emerge. Fortunately, because of the similarity of technologies for different magnetic concepts, retaining N options will not

cost N times as much as one. Even so, embarking on the costly engineering development phase will require roughly twice the present level of effort. Whether or not this increased financial support is provided will be the determining factor on the rate of magnetic fusion progress in the 1980's.

It will, of course, be essential to maintain a strong scientific program in parallel with the engineering development of magnetic fusion. In the 1980's, scientific research will probably concentrate on two areas. First, more than ever before, it will be necessary to obtain quantitative agreement between experiment and theory and to provide an accurate basis for the design of large facilities in the future. This will require more accurate computer modeling of processes already understood quantitatively, and improved and more extensive diagnostics in the experiments. This will occur first for the more mature concepts, tokamaks and mirrors, with a strong focus on the TFTR and MFTF. The second area of research emphasis will be the further improvement of existing concepts and the generation of new ideas. This will involve new theoretical concepts and new experiments, at first in smaller facilities, with a strong emphasis on reducing the cost and complexity of reactors. For example, for the tandem mirror concept there will be a concerted effort to simplify the "end plug" magnet design, possibly by devising stable axisymmetric geometries (see Fig. 11E8). Improved confinement aimed at advanced fuel cycles (D-D etc.) will also be an important goal.*

In the longer term, the pace of fusion development beyond the 1980's will depend mainly on the number and size of the intermediate steps required. For the tandem mirror concept, it is hoped that a single DT-burning tandem mirror facility (called MNS) will be the only step required between the MFTF-B and a demonstration reactor that could then be completed by the turn of the century. Any iterative development steps required to improve the power generating system could be carried out in stages in the MNS by replacing sections of the modular center cell. Another mirror concept, the Field Reversed Mirror (FRM), could perhaps be developmed even faster, depending on a number of scientific factors not yet well understood (notably, MHD stability). The reason is that the FRM can in principle lead to compact systems at very high beta and high power density. Conceptual studies carried out at Livermore together with the Pacific Gas and Electric Company and others have shown that an attractive FRM power plant could be based on a linear array of self-contained modules producing as little as 10 MW of electrical output. Smaller plants based on this concept could be deployed sooner, in order to gain valuable on-line experience in the course of developing fusion power.

---

* B. G. Logan, A. A. Mirin, M. E. Rensink, and T. K. Fowler, "Calculation of the Fusion Power Gain for a DD Tandem Mirror Reactor", Fizika Plazmy, Vol. 4, pp. 542-550, May/June 1978. (English translation in Soviet Journal of Plasma Physics, Vol. 4, pp. 301-305, May 1978.)

Some Comments on Inertial Confinement Fusion (ICF)

Gerold Yonas Sandia Laboratories, Albuquerque

ICF represents an extremely challenging scientific and technological goal for a fairly large multi-disciplinary segment of the technical community, which is located primarily within the national laboratories. The program derives its fundamental optimism from the knowledge that the basic concept of imploding matter to achieve ignition by compressional heating has already been accomplished in the hydrogen bomb. The central questions of ICF are whether a laboratory device to drive the implosion can be made large and powerful enough to ignite a small fuel mass and whether that ignitable fuel mass can be small enough to lead to a practical application. Secondary issues are whether that device can be engineered to act as a practical ignition system in a power plant, whether the fuel pellets can be mass produced at a low enough cost, and whether a target chamber can be devised which can sustain the repetitive loading.

During the 1980's the U.S. program will confront the primary scientific question of fuel ignition at Lawrence Livermore National Laboratories using the Nova glass laser, which will operate through frequency conversion at sub-micron wavelengths, and at Sandia National Laboratories using the PBFA 100 TW pulsed power driver. PBFA is being constructed to couple its energy output to either multiple light ion beam diodes or a single imploding foil. In both cases the goal is to deliver $\sim$ 100 TW and $\sim$ 1 MJ to a pellet. This important step is being supported by the defense programs with the Department of Energy for both near term nuclear weapons applications and the potential long term energy application. Since funding for ICF research is limited, principal emphasis is being given to vital demonstration of ignition as a pre-requisite to further enhancement of the tasks that deal with the long term engineering issues. In spite of this, enough effort has been devoted to system considerations to show that the low cost and relatively high efficiency of light ion accelerators could make them suitable candidates for energy applications.

The most fundamental question in ICF is whether we can produce a stable and symmetric enough implosion without deleterious preheat of the fuel to achieve ignition at fuel densities $\sim$ 1000 times that of a solid. Pulsed power devices can provide the required MJ energies but have not as yet been able to demonstrate the required power concentration. It is thought that 10^{13} - 10^{15} W/cm^2 will have to be directed onto a few mm radius pellet, and this can be accomplished only through many successive space and temporal stages in power concentration. With lasers, power concentration is trivial, but providing sufficient energy within limited budgets, and coupling light with matter without producing excessive preheat are difficult. Using pulsed power to deliver 10^{14}W is within our reach at a relatively low cost (although not without rather dramatic advances in switching, power conditioning, and concentration), but achieving power intensity levels of 10^{13} - 10^{14} W/cm^2 requires further improvements in ion diodes. Using light ions we must improve the combination of intensity and directionality of ion diodes by at least another factor of 10. This may be done by a three-fold reduction in beam divergence, and this may require both higher mass ions (carbon or He rather than protons) and higher voltage accelerators (10 - 15 MV rather than 2 - 3 MV). It is also necessary to develop large area, uniform sources of dense plasma suitable for supplying the ion flow. Multiple plasma discharges are currently in use but other plasma sources may be needed to obtain the required required plasma uniformity, purity and density.

Even if ignition and the first low gain experiments are accomplished within close proximity of low divergence ion diodes or with direct electrical contact to an imploding foil, the task of developing a reactor will require the further achievement of efficient beam transport over distances of several meters. The only methods proposed to accomplish this are propagation of intense ion beams in preformed plasma channels or propagation of neutralized ion beams in vacuum. Both methods will introduce additional complexity and further bound the parameter space available for ignition. Nevertheless, it is reasonable to expect that if ignition can be achieved with pulsed power devices, enhanced emphasis on solving the additional questions related to reactors will follow.

APPENDIX A. SYSTEME INTERNATIONALE (SI) UNITS

Basic Units

	abbreviation	*measure of*
Ampere	A	current
candela	cd	luminous intensity
Kelvin	K	temperature
kilogram	kg	mass
metre	m	length
mole	mol	amount of substance
radian	rad	plane angle
second	s	time
steradian	sr	solid angle

Derived Units

		equal to	*measure of*
Becquerel	Bq	$= s^{-1}$	radioactive decay
Coulomb	C	= A-s	charge
Farad	F	= A-s/V	capacitance
		= C/V	
		$= C^2/J$	
Gray	Gy	= J/kg	absorbed dose
Henry	H	= V-s/A	inductance
		$= J/A^2$	
		= Wb/A	
Hertz	Hz	$= s^{-1}$	frequency
Joule	J	= N-m	energy
		$= kg\text{-}m^2/s^2$	
		= W-s	
Newton	N	$= kg\text{-}m/s^2$	force
		= J/m	
Ohm	Ω	= V/A	resistance
Pascal	Pa	$= N/m^2$	pressure or stress
		$= J/m^3$	
Sievert	Sv	= J/kg	dose equivalent
Tesla	T	$= Wb/m^2$	magnetic flux
		$= V\text{-}s/m^2$	density
Volt	V	= W/A	voltage
		= J/C	
Watt	W	= J/s	power
		= V-A	
Weber	Wb	= V-s	magnetic flux

Prefixes

10^{18}	Exa	E	10^{-2}	centi	c
10^{15}	Peta	P	10^{-3}	milli	m
10^{12}	Tera	T	10^{-6}	micro	μ
10^{9}	Giga	G	10^{-9}	nano	n
10^{6}	Mega	M	10^{-12}	pico	p
10^{3}	kilo	k	10^{-15}	femto	f

energy — *Joule*

Btu (international)	1055.1	
calorie (international)	4.1868	
electron volt, eV	1.60219 x	10^{-19}
kilo-electron-Volt, keV	1.60219 x	10^{-16}
Mega-electron-Volt, MeV	1.60219 x	10^{-13}
erg		10^{-7}
foot-pound-force	1.3558	
kilowatt-hour	3.6000 x	10^{6}
ton TNT	4.20 x	10^{9}
Tera-Watt-year, TWy	3.1536 x	10^{19}
quad (Q) (10^{15} Btu)	1.055 x	10^{18}
ton of coal (Bituminous)	2.95 x	10^{10}
barrel of oil (42 US gallons)	6.2 x	10^{9}
cubic metre natural gas (35.3 Ft^3)	3.85 x	10^{7}
ton of oil (1000 kg)	4.194 x	10^{10}
cubic metre liquified natural gas	2.01 x	10^{10}
associated with atomic mass unit	1.4924 x	10^{-10}

power — *Watt*

Btu/h (international)	0.29307
horsepower, hp (550 ft-lb_f/s)	745.7
horsepower, hp (electrical)	746.0

mass — *kilogram*

pound-mass (avoirdupois)	0.45359
slug	14.594
ton (metric)	1000.0
ton (short)	907.18
ton (long)	1016.0
atomic mass unit, u	1.660566 x 10^{-27}

length — *metre*

Angstrom Å	10^{-10}
foot, ft	0.30480
micron	10^{-6}
inch	0.0254
mil, 10^{-3} inch	2.540 x 10^{-5}
mile (US statute)	1609.3
mile (nautical)	1852.0
yard	0.91440

Appendix A. SI Units

time	*seconds*
day	86400
year	3.1536×10^{7}
month	2.628×10^{6}
minute	60
hour	3600

area	*square metres*
barn	10^{-28}
square foot, ft^2	0.092903

volume	*cubic metres*
cubic centimetre, cm^3	10^{-6}
litre	10^{-3}
cubic foot, ft^3	0.028317
gallon (US liquid)	3.7854×10^{-3}

velocity	*metres per second*
ft/s	0.30480
ft/h	8.4667×10^{-5}
mile/h (US statute)	0.44704

force	*Newtons*
dyne	10^{-5}
pound-force	4.4482
poundal	0.13826
kilogram-force	9.80665

density	*kilogram/m^3*
pound-mass/ft^3	16.0185
gram/cm^3	1000.0

pressure or stress	*Pascal*
atmosphere, 760 Torr	1.01325×10^{5}
bar	10^{5}
dyne/cm^2	0.100000
foot of water	2.98893
kilogram-force/mm^2	9.80665×10^{6}
kilogram-force/cm^2	9.80665×10^{4}
millimetre (Hg)	133.322
torr	133.322
pound-force/ft^2	47.880
pound-force/in^2, psi	6894.76
ksi	6.89476×10^{6}

temperature	*Kelvin*
Celsius, C	C + 273.15
Fahrenheit, F	(F + 459.67)/1.8
Rankine, R	R/1.8
eV	11604.85

charge	*Coulomb*
stattcoulomb, esu	3.33564×10^{-10}
Faraday	9.6487×10^{4}

current	*Ampere*
esu, current	3.3356×10^{-10}
emu, current	10.000

electromotive force	*Volt*
statvolt	299.79
emu of potential	10^{-8}

magnetic flux	*Weber*
Maxwell	10^{-8}

magnetic flux density	*Tesla*
Gauss	10^{-4}

inductance	*Henry*
emu, inductance	10^{-9}
esu, inductance	8.98758×10^{11}

magnetic field	*Ampere/m*
Oersted	79.577

resistance	*Ohm*
emu, resistance	10^{-9}
esu, resistance	8.98758×10^{11}

capacitance	*Farad*
emu, capacitance	10^{9}
esu, capacitance	1.11265×10^{-12}

radioactivity

Curie (decay rate)	3.7×10^{10} Bq
Roentgen (radiation dose)	2.57976×10^{4} C/kg
rad (absorbed radiation dose)	0.01 Gy
rem ("Roentgen-equivalent-man")	(0.01)QF Gy
QF (quality factor)	1 for betas (electrons), x rays 2-5 for thermal neutrons 5-10 for fast neutrons (~10 MeV) 10 for protons 20 for alpha particles

other

degree (angle)	0.0174533 radians
Btu/ft^2-h (heat flux)	3.152 W/m^2
Btu/ft^2-h-F (heat transfer coefficient)	5.674 W/m^2-K
Btu/ft-h-F (thermal conductivity)	1.731 W/m-K
Btu/lb-F (specific heat)	4187 J/kg-K

APPENDIX B. FUNDAMENTAL CONSTANTS

nuclear masses (to find atomic masses, add Zm_e)

atomic number Z	mass number A	particle	mass (u)	mass (kg)	percent abundance
0	0	electron,e	.0005485801	9.109534×10^{-31}	
0	1	neutron, n	1.00866452	1.674954×10^{-27}	
1	1	proton,p,H	1.00727644	1.672649×10^{-27}	99.985
1	2	deuteron,D,^{2}H	2.013553	3.343468×10^{-27}	0.0153
1	3	triton,T,^{3}H	3.015501	5.007438×10^{-27}	
2	3	^{3}He	3.014933	5.006495×10^{-27}	0.00013
2	4	^{4}He, α	4.001503	6.644760×10^{-27}	99.99987
3	6	^{6}Li	6.013470	9.985764×10^{-27}	7.42
3	7	^{7}Li	7.014354	1.164780×10^{-26}	92.58
4	9	^{9}Be	9.009986	1.496168×10^{-26}	100
5	10	^{10}B	10.010757	1.662352×10^{-26}	19.78
5	11	^{11}B	11.018857	1.829754×10^{-26}	80.22
6	12	^{12}C	11.996709	1.992133×10^{-26}	98.89
6	13	^{13}C	13.000059	2.158746×10^{-26}	1.11

other constants

Boltzmann constant	$k = 1.38066 \times 10^{-23}$ J/K
speed of light in vacuum	$c = 2.99792 \times 10^{8}$ m/s
electronic charge	$e = 1.60219 \times 10^{-19}$ C
Avogadro constant	$N_A = 6.02204 \times 10^{23}$
Planck constant	$h = 6.62618 \times 10^{-34}$ J-s
Stefan-Boltzmann constant	$\sigma = 5.67032 \times 10^{-8}$ W $m^{-2}K^{-4}$
permittivity of free space	$\varepsilon_0 = 8.85419 \times 10^{-12}$ F/m
permeability of free space	$\mu_0 = 4\pi \times 10^{-7}$ H/m
energy associated with 1 u	= 931.481 MeV
molecular density at 1 Pa, 273.15 K	$= 2.6516 \times 10^{20}$ molecules/m^3
acceleration of gravity at sea level, 45 degree latitude	$g = 9.8062$ m/s^2

APPENDIX C. INTEGRALS

n	$\int_0^\infty dx\, x^n e^{-\alpha x^2}$	$\int_{-\infty}^\infty dx\, x^n e^{-\alpha x^2}$	$\int_0^\infty dy\, y^{\frac{n-1}{2}} e^{-\alpha y}$
0	$\frac{\pi^{\frac{1}{2}}}{2\,\alpha^{\frac{1}{2}}}$	$\frac{\pi^{\frac{1}{2}}}{\alpha^{\frac{1}{2}}}$	$\frac{\pi^{\frac{1}{2}}}{\alpha^{\frac{1}{2}}}$
1	$\frac{1}{2\alpha}$	0	$\frac{1}{\alpha}$
2	$\frac{\pi^{\frac{1}{2}}}{4\alpha^{3/2}}$	$\frac{\pi^{\frac{1}{2}}}{2\alpha^{3/2}}$	$\frac{\pi^{\frac{1}{2}}}{2\alpha^{3/2}}$
3	$\frac{1}{2\alpha^2}$	0	$\frac{1}{\alpha^2}$
4	$\frac{3\pi^{\frac{1}{2}}}{8\alpha^{5/2}}$	$\frac{3\pi^{\frac{1}{2}}}{4\alpha^{5/2}}$	$\frac{3\pi^{\frac{1}{2}}}{4\alpha^{5/2}}$
5	$\frac{1}{\alpha^3}$	0	$\frac{2}{\alpha^3}$
6	$\frac{15\pi^{\frac{1}{2}}}{16\alpha^{7/2}}$	$\frac{15\pi^{\frac{1}{2}}}{8\alpha^{7/2}}$	$\frac{15\pi^{\frac{1}{2}}}{8\alpha^{7/2}}$

APPENDIX D. IMPORTANT PLASMA EQUATIONS

Maxwell equations (simplified for plasmas)

$$\vec{\nabla}\times\vec{E} = -\partial\vec{B}/\partial t \qquad (5B7)$$

$$\vec{\nabla}\times\vec{B}/\mu_0 = \vec{J} + \varepsilon_0\partial\vec{E}/\partial t \qquad (5B8)$$

$$\vec{\nabla}\cdot\vec{E} = \rho/\varepsilon_0 \qquad (5B5)$$

$$\vec{\nabla}\cdot\vec{B} = 0 \qquad (5B6)$$

Coulomb collisions

$$\tau_e = 7.5\times10^{15}T_{ek}^{3/2}/nL \quad \text{s} \qquad (2E52)$$

$$\tau_i = 7.5\times10^{15}T_{ik}^{3/2}(m_i/m_e)^{\frac{1}{2}}/Z^4nL \quad \text{s} \qquad (2E53)$$

$$\nu_{ei} = 6.7\times10^{-17}nZ^2L/T_{ek}^{3/2} \quad \text{s}^{-1} \qquad (2E57)$$

Pressure

$$p = n_ekT_e + n_ikT_i + \ldots \quad \text{Pa} \qquad (2D5)$$

$$\vec{\nabla}(p + B^2/2\mu_0) = (\vec{B}\cdot\vec{\nabla})\vec{B}/\mu_0 \quad \text{Pa/m} \qquad (8B6)$$

Fusion power

DT: $\langle P_f\rangle \simeq 1.1\beta_*^2B^4$ MW/m^3 $(8 \leq T_{ik} \leq 25$ keV) (2D18)

cat. DD: $\langle P_f\rangle \simeq 0.027\beta_*^2B^4(30/T_{ik})^{\frac{1}{2}}$ MW/m^3 $(15 \leq T_{ik} \leq 70$ keV) (2D19)

rms beta: $\beta_* \equiv \dfrac{\langle p^2\rangle^{\frac{1}{2}}}{B^2/2\mu_0}$ (8B10)

Reaction rate

$$r = n_1n_2\langle\sigma v\rangle \quad \text{m}^{-3}\text{s}^{-1} \qquad (2B19)$$

Lengths

$$\lambda_D \simeq (\varepsilon_0kT_e/ne^2)^{\frac{1}{2}} \quad \text{m} \qquad (5F4)$$

$$\rho_e = (2m_ekT_e)^{\frac{1}{2}}/eB \quad \text{m} \qquad (7B2)$$

$$\rho_i = (2m_ikT_i)^{\frac{1}{2}}/qB \quad \text{m} \qquad (7B2)$$

$$\lambda_1 = \langle v_1\rangle/n_2\langle\sigma v\rangle \quad \text{(mean free path)} \quad \text{m} \qquad (2B37)$$

Frequencies

$\omega_{pe} = (ne^2/m_e\epsilon_0)^{\frac{1}{2}} = 56.4\ n^{\frac{1}{2}}$	rad/s	(5E8)
$\nu_{pe} = \omega_{pe}/2\pi = 9.0\ n^{\frac{1}{2}}$	Hz	
$\omega_{ce} = eB/m_e$	rad/s	(9F1)
$\nu_{ce} = \omega_{ce}/2\pi = 28.0\times10^9\ B$	Hz	(9F2)
$\omega_{ci} = eB/m_i$	rad/s	(9F1)
$\nu_{ci} = \omega_{ci}/2\pi = 7.63\times10^6\ B$	Hz	(9F2)
$\nu_{LH} = 0.148n^{\frac{1}{2}}[1 + 1.03\times10^{-19}n/B^2]^{-\frac{1}{2}}$	Hz	(9F2)

Velocities

$v_A = B/(\mu_0 n m_i)^{\frac{1}{2}}$	m/s	(5E34)
$v_{te} = (kT_e/m_e)^{\frac{1}{2}}$	m/s	(13D7)
$c_s \simeq (3.3kT/m_i)^{\frac{1}{2}}$	m/s	(15B7)
$v = (2W/m)^{\frac{1}{2}}$ if $v \ll c$	m/s	

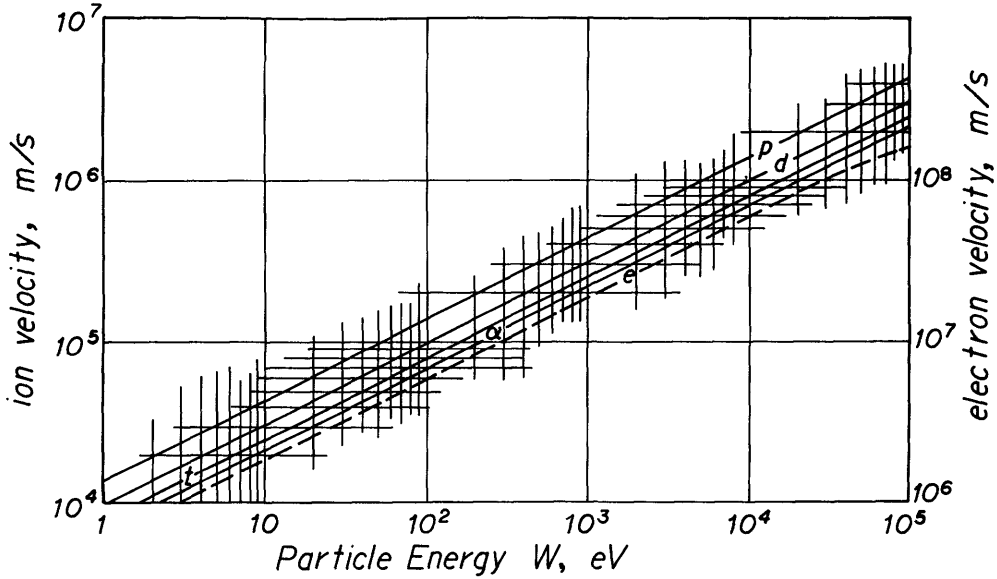

Fig. D1. Velocity of ions and electrons vs. energy. p = protons, d = deuterons, t = tritons (or ^{3}He), α = alpha particles (^{4}He); e = electrons (scale at right).

APPENDIX E. THE ERROR FUNCTION

Reference: M. Abramowitz and I. A. Stegun, Handbook of Mathematical Functions, National Bureau of Standards, Applied Mathematics Series 55, Washington, D. C., 1964, Ch. 7.

$$\mathrm{erf}(z) = \frac{2}{\sqrt{\pi}} \int_0^z dy \, \exp(-y^2) \tag{E1}$$

$$\mathrm{erf}(-z) = -\mathrm{erf}(z) \tag{E2}$$

for small z:

$$\mathrm{erf}(z) = \frac{2}{\sqrt{\pi}} \left(z - \frac{z^3}{3 \cdot 1!} + \frac{z^5}{5 \cdot 2!} - \frac{z^7}{7 \cdot 3!} + \frac{z^9}{9 \cdot 4!} - \ldots \right) \tag{E3}$$

for large z:

$$\mathrm{erf}(z) = 1 - \frac{e^{-z^2}}{z\sqrt{\pi}} \left(1 - \frac{1}{2z^2} + \frac{1 \cdot 3}{(2z^2)^2} - \frac{1 \cdot 3 \cdot 5}{(2z^2)^3} + \ldots \right) \tag{E4}$$

z	erf(z)	z	erf(z)
0	0		
.05	.056 372	1.05	.862 436
.10	.112 463	1.10	.880 205
.15	.167 996	1.15	.896 124
.20	.222 703	1.20	.910 314
.25	.276 326	1.25	.922 900
.30	.328 627	1.30	.934 008
.35	.379 382	1.35	.943 762
.40	.428 392	1.40	.952 285
.45	.475 482	1.45	.959 695
.50	.520 500	1.50	.966 105
.55	.563 323	1.55	.971 623
.60	.603 856	1.60	.976 348
.65	.642 029	1.65	.980 376
.70	.677 801	1.70	.983 790
.75	.711 156	1.75	.986 672
.80	.742 101	1.80	.989 091
.85	.770 668	1.85	.991 111
.90	.796 908	1.90	.992 790
.95	.820 891	1.95	.994 179
1.00	.842 701	2.00	.995 322

APPENDIX F. VECTOR RELATIONS

$\vec{A} = A_x\hat{x} + A_y\hat{y} + A_z\hat{z}$, where $\hat{x}$, $\hat{y}$, and $\hat{z}$ are unit vectors.

Scalar or dot product of two vectors: $\vec{A}\cdot\vec{B} = A_xB_x + A_yB_y + A_zB_z$. (F1)

Vector or cross product:

$$\vec{A}\times\vec{B} \equiv \begin{vmatrix} \hat{x} & \hat{y} & \hat{z} \\ A_x & A_y & A_z \\ B_x & B_y & B_z \end{vmatrix} = (A_yB_z - A_zB_y)\hat{x} + (A_zB_x - A_xB_z)\hat{y} + (A_xB_y - A_yB_x)\hat{z} = -\vec{B}\times\vec{A} \quad (F2)$$

Differential operator Del: $\vec{\nabla} \equiv \hat{x}\frac{\partial}{\partial x} + \hat{y}\frac{\partial}{\partial y} + \hat{z}\frac{\partial}{\partial z}$ (F3)

Gradient of scalar: $\vec{\nabla}\phi \equiv (\partial\phi/\partial x)\hat{x} + (\partial\phi/\partial y)\hat{y} + (\partial\phi/\partial z)\hat{z}$ (F4)

Divergence of vector: $\vec{\nabla}\cdot\vec{A} = (\partial A_x/\partial x) + (\partial A_y/\partial y) + (\partial A_z/\partial z)$ (F5)

Curl of vector:

$$\vec{\nabla}\times\vec{A} = \begin{vmatrix} \hat{x} & \hat{y} & \hat{z} \\ \frac{\partial}{\partial x} & \frac{\partial}{\partial y} & \frac{\partial}{\partial z} \\ A_x & A_y & A_z \end{vmatrix} = [(\partial A_z/\partial y) - (\partial A_y/\partial z)]\hat{x} + [(\partial A_x/\partial z) - (\partial A_z/\partial x)]\hat{y} + [(\partial A_y/\partial x) - (\partial A_x/\partial y)]\hat{z} \quad (F6)$$

Laplacian of scalar: $\nabla^2\phi = (\partial^2\phi/\partial x^2) + (\partial^2\phi/\partial y^2) + (\partial^2\phi/\partial z^2)$ (F7)

Laplacian of vector:

$$\nabla^2\vec{A} = \left(\frac{\partial^2 A_x}{\partial x^2} + \frac{\partial^2 A_x}{\partial y^2} + \frac{\partial^2 A_x}{\partial z^2}\right)\hat{x} + \left(\frac{\partial^2 A_y}{\partial x^2} + \frac{\partial^2 A_y}{\partial y^2} + \frac{\partial^2 A_y}{\partial z^2}\right)\hat{y} + \left(\frac{\partial^2 A_z}{\partial x^2} + \frac{\partial^2 A_z}{\partial y^2} + \frac{\partial^2 A_z}{\partial z^2}\right)\hat{z} \quad (F8)$$

Theorems

Divergence Theorem

$$\int_{\text{volume}} d\vec{x}\ \vec{\nabla}\cdot\vec{A} = \int_{\text{surface}} d\vec{S}\cdot\vec{A} \quad (F9)$$

Stokes' Theorem

$$\int_{\text{surface}} d\vec{S}\cdot\vec{\nabla}\times\vec{A} = \oint_{\substack{\text{boundary}\\ \text{curve}}} d\vec{\ell}\cdot\vec{A} \quad (F10)$$

$$\int_{\text{volume}} d\vec{x}\ \vec{\nabla}\times\vec{A} = \int_{\text{surface}} d\vec{S}\times\vec{A} \quad (F11)$$

$$\int_{\text{surface}} d\vec{S}\times\vec{\nabla}\phi = \oint_{\substack{\text{boundary}\\ \text{curve}}} d\vec{\ell}\ \phi \quad (F12)$$

Appendix F. Vector Relations

Identities

$$\vec{\nabla}p(\psi) = \frac{dp}{d\psi}\vec{\nabla}\psi \tag{F13}$$

$$\vec{A}\cdot(\vec{B}\times\vec{C}) = \vec{B}\cdot(\vec{C}\times\vec{A}) = \vec{C}\cdot(\vec{A}\times\vec{B}) \equiv (\vec{A}\vec{B}\vec{C}) \tag{F14}$$

$$(\vec{A}\times\vec{B})\cdot(\vec{C}\times\vec{D}) = (\vec{A}\cdot\vec{C})(\vec{B}\cdot\vec{D}) - (\vec{A}\cdot\vec{D})(\vec{B}\cdot\vec{C}) \tag{F15}$$

$$\vec{A}\times(\vec{B}\times\vec{C}) = (\vec{A}\cdot\vec{C})\vec{B} - (\vec{A}\cdot\vec{B})\vec{C} = -(\vec{B}\times\vec{C})\times\vec{A} \tag{F16}$$

$$(\vec{A}\times\vec{B})\times(\vec{C}\times\vec{D}) = (\vec{A}\vec{B}\vec{D})\vec{C} - (\vec{A}\vec{B}\vec{C})\vec{D} = (\vec{A}\vec{C}\vec{D})\vec{B} - (\vec{B}\vec{C}\vec{D})\vec{A} \tag{F17}$$

$$\vec{\nabla}(\phi+\psi) = \vec{\nabla}\phi + \vec{\nabla}\psi \tag{F18}$$

$$\vec{\nabla}\cdot(\vec{A}+\vec{B}) = \vec{\nabla}\cdot\vec{A} + \vec{\nabla}\cdot\vec{B} \tag{F19}$$

$$\vec{\nabla}\times(\vec{A}+\vec{B}) = \vec{\nabla}\times\vec{A} + \vec{\nabla}\times\vec{B} \tag{F20}$$

$$\vec{\nabla}(\phi\psi) = \phi\vec{\nabla}\psi + \psi\vec{\nabla}\phi \tag{F21}$$

$$\vec{\nabla}\cdot(\phi\vec{A}) = \phi\vec{\nabla}\cdot\vec{A} + \vec{\nabla}\phi\cdot\vec{A} \tag{F22}$$

$$\vec{\nabla}\times(\phi\vec{A}) = \phi\vec{\nabla}\times\vec{A} + \vec{\nabla}\phi\times\vec{A} \tag{F23}$$

$$\vec{\nabla}\times\vec{\nabla}\phi = 0 \tag{F24}$$

$$\vec{\nabla}\cdot(\vec{\nabla}\times\vec{A}) = 0 \tag{F25}$$

$$\vec{\nabla}\cdot(\vec{A}\times\vec{B}) = \vec{B}\cdot(\vec{\nabla}\times\vec{A}) - \vec{A}\cdot(\vec{\nabla}\times\vec{B}) \tag{F26}$$

$$\vec{\nabla}\times(\vec{A}\times\vec{B}) = (\vec{B}\cdot\vec{\nabla})\vec{A} - (\vec{A}\cdot\vec{\nabla})\vec{B} + \vec{A}(\vec{\nabla}\cdot\vec{B}) - \vec{B}(\vec{\nabla}\cdot\vec{A}) \tag{F27}$$

$$(\vec{A}\cdot\vec{\nabla})\vec{B} \equiv A_x\frac{\partial\vec{B}}{\partial x} + A_y\frac{\partial\vec{B}}{\partial y} + A_z\frac{\partial\vec{B}}{\partial z} \tag{F28}$$

$$\vec{\nabla}(\vec{A}\cdot\vec{B}) = (\vec{A}\cdot\vec{\nabla})\vec{B} + (\vec{B}\cdot\vec{\nabla})\vec{A} + \vec{A}\times(\vec{\nabla}\times\vec{B}) + \vec{B}\times(\vec{\nabla}\times\vec{A}) \tag{F29}$$

$$\vec{\nabla}\times(\vec{\nabla}\times\vec{A}) = \vec{\nabla}(\vec{\nabla}\cdot\vec{A}) - \nabla^2\vec{A} \tag{F30}$$

Cylindrical Geometry

$$\vec{\nabla} = \hat{r}\frac{\partial}{\partial r} + \frac{\hat{\phi}}{r}\frac{\partial}{\partial\phi} + \hat{z}\frac{\partial}{\partial z} \tag{F31}$$

$$\vec{\nabla}\psi = \hat{r}\frac{\partial\psi}{\partial r} + \frac{\hat{\phi}}{r}\frac{\partial\psi}{\partial\phi} + \hat{z}\frac{\partial\psi}{\partial z} \tag{F32}$$

$$\vec{\nabla}\cdot\vec{A} = \frac{1}{r}\frac{\partial}{\partial r}(rA_r) + \frac{1}{r}\frac{\partial A_\phi}{\partial\phi} + \frac{\partial A_z}{\partial z} \tag{F33}$$

$$\vec{\nabla}\times\vec{A} = \left(\frac{1}{r}\frac{\partial A_z}{\partial\phi} - \frac{\partial A_\phi}{\partial z}\right)\hat{r} + \left(\frac{\partial A_r}{\partial z} - \frac{\partial A_z}{\partial r}\right)\hat{\phi} + \left(\frac{1}{r}\frac{\partial}{\partial r}(rA_\phi) - \frac{1}{r}\frac{\partial A_r}{\partial\phi}\right)\hat{z} \tag{F34}$$

$$\nabla^2\psi = \frac{1}{r}\frac{\partial}{\partial r}r\frac{\partial\psi}{\partial r} + \frac{1}{r^2}\frac{\partial^2\psi}{\partial\phi^2} + \frac{\partial^2\psi}{\partial z^2} \tag{F35}$$

$$\nabla^2\vec{A} = \left[\nabla^2A_r - \frac{1}{r^2}\left(A_r + 2\frac{\partial A_\phi}{\partial\phi}\right)\right]\hat{r} + \left[\nabla^2A_\phi - \frac{1}{r^2}\left(A_\phi - 2\frac{\partial A_r}{\partial\phi}\right)\right]\hat{\phi} + \nabla^2A_z\hat{z} \tag{F36}$$

$$(\vec{A}\cdot\vec{\nabla})\vec{B} = \left[A_r\frac{\partial B_r}{\partial r} + \frac{A_\phi}{r}\frac{\partial B_r}{\partial\phi} + A_z\frac{\partial B_r}{\partial z} - \frac{1}{r}A_\phi B_\phi\right]\hat{r}$$

$$\left[A_r\frac{\partial B_\phi}{\partial r} + \frac{A_\phi}{r}\frac{\partial B_\phi}{\partial\phi} + A_z\frac{\partial B_\phi}{\partial z} + \frac{1}{r}A_\phi B_r\right]\hat{\phi}$$

$$\left[A_r\frac{\partial B_z}{\partial r} + \frac{A_\phi}{r}\frac{\partial B_z}{\partial\phi} + A_z\frac{\partial B_z}{\partial z}\right]\hat{z} \tag{F37}$$

APPENDIX G. TABLE OF SYMBOLS

by J. J. Browning

symbol	*name*	*units*	*Chapter*
A	aspect ratio		18
A	atomic mass number	u	1
$\vec{A}$	magnetic vector potential	T-m	5
A_c	coolant channel cross sectional area	m^2	26
A_c	area of wire loop	m^2	10
A_e	variable in Eq.(13E1)	J^2/m^2	13
A_p	area of probe	m^2	10
A_p	plug ion mass	u	11
A_{point}	effective loss area of two point cusps	m^2	11
A_{ring}	loss area of ring cusp	m^2	11
A_w	cross sectional area of cooling water channel	m^2	20
A_s	spectral line constant	m^3	10
A_ϕ	toroidal component of magnetic vector potential	T-m	8
$d\vec{A}$	differential cross sectional area	m^2	2
a	plasma edge radius	m	7
a_p	probability that an alpha particle reflected from the limiter returns directly to the plasma		25
a_v	probability that an alpha particle reflected from the limiter enters the vacuum duct		25
a_w	probability that an alpha particle reflected from the limiter hits the wall		25
$\vec{B}$	magnetic induction (magnetic flux density)	T	20
B	magnitude of $\vec{B}$	T	1
$\dot{B}$	rate of change of B	T/s	12
B_{avg}	average magnetic induction in circle of radius r	T	7
B_c	critical magnetic field	T	22
B_{c1}	lower critical field	T	22
B_{c_2}	upper critical field	T	22
B_F	linac bunching factor		16
B_i	initial reverse bias field	T	12
B_k	component of $\vec{B}$ parallel to wave propagation direction	T	10
B_m	maximum magnetic induction	T	11
B_{mid}	value of B at mirror midplane	T	14
B_p	poloidal magnetic field	T	7
B_{res}	value of B at cyclotron resonance layer	T	14
B_t	toroidal magnetic field	T	7
B_v	vertical magnetic field	T	7
B_{vac}	magnetic field in vacuum	T	11
B_θ	azimuthal magnetic field	T	6
δB	magnetic field perturbation	T	14
b	impact parameter	m	2
b	Burgers vector, Eq.(24E1)		24
C	bunch compression factor of a linac		16
C	capacitance	F	1
C	conductance of a tube	m^3/s or L/s	19
C	conductivity ratio in Eq. 26E5		26
C	conversion ratio of fission reactor		29
C	geometrical factor in Eq. 17A4		17
C	specific heat at a constant volume	J/mole-K	23
C	specific heat of a coolant Eq. 20D6	J/kg-K	20
C_c	total capital cost	$	28
C_{dc}	direct capital cost	$	28
C_f	annual fuel cost	$	28
C_{ic}	indirect capital cost	$	28
C_m	heat capacity	J/kg-K	1
$C_{o\&m}$	annual operating and maintenance cost	$	28
C_{scr}	annual scheduled component replacement cost	$	28
C_{tr}	time-related costs	$	28
C_0	power cost with free fuel	mills/kWh	29
c	speed of light	m/s	1
c_s	ion sound speed	m/s	5
c	concentration	$atoms/m^3$	24
c_p	specific heat	J/kg-K	23
D	atomic energy level		16
D	diffusion coefficient	m^2/s	8

Appendix G. Table of Symbols

D	operator notation for d/dt		21
D	tube diameter	m	19
DDn	$D(d,n)^3He$ reaction		1
DDp	D(d,p) T reaction		1
D_B	Bohm diffusion coefficient		25
D_h	helical diffusion coefficient		14
D_{NC}	neoclassical diffusion coefficient		25
$D_\perp$	diffusion coefficients perpendicular to $\vec{B}$		5
D_0	constant in Eq. 28B16	m^2/s	28
d	Triangularity		18
d	deuteron		1
E	annual escalation rate		28
E	electric field	V/m	1
$\vec{E}$	electric field defined by Eq. 17B2	V/cm	17
E	modulus of elasticity	Pa	24
E	neutron energy	J	27
E	parameter defined by Eq. 24G3		24
E	complete elliptic integral		20
E_{av}	average electric field over a cell length	V/m	16
E_c	critical electric field	V/m	13
E_d	activation energy for diffusion	eV	24
E_I	ionization energy of atomic hydrogen	eV	14
E_0	energy per unit mass of injected particles	eV/u	25
E_0	rf electric field in the plasma	V/cm	17
E_s	activation energy for solution	eV	28
E_s	average energy carried away per electron-ion pair	J	14
e	electronic charge	C	3
e	electrons (subscript)		2
e	emissivity		23
e_s	radiation shield emissivity		
erf	error function (Appendix E)		2
e^-	electron		3
F	field-reversal ratio, Eq. 12D4		17
F	fissile fuel breeding ratio		29
$\vec{F}$	magnitude of $\vec{F}$		1
F_{EDC}	factor of escalation during construction		28
F_{IDC}	factor of interest during construction		28
F_p	average power flux on walls (Eq. 2D4)	W/m^2	2
$F_{\nabla p}$	pressure gradient force	N	15
$\vec{F}$	force	N	5
$\vec{F}_{pm}$	pondermotive force	N	15
f	"friction factor", Fig. 20D2		20
f	mass fraction		15
f	ratio of number of atoms in a pellet to the number of ions in a plasma (Eq. 25E6)		25
f_a	fractional absorption		15
f_b	burnup fraction		4
f_c	fraction of fusion energy carried by charged particles		4
fcr	annual fixed charge rate		28
f_d	fraction of recirculated electrical energy going to the driver		15
f_e	fraction of the alpha energy given to the electrons		4
f_i	fraction of alpha energy given to plasma ions		2
f_i	ion velocity distribution function		8
f_j	failure probability of item j		21
f_k	distribution function of species k	$m^{-6}s^3$	5
f_M	Maxwellian Distribution Function (Eq. 2A7)	$m^{-6}s^3$	2
f_n	fraction of fusion energy carried by neutrons		4
f_p	fuel ion density/n_e, Eq. 13F9		13
f_r	fraction of charged-particle energy retained in the plasma for heating		4
f(r)	radial variation of temperature		4
f_t	fraction of particles which are trapped		7
f_t	fraction of the beam power trapped in the plasma		11
f_α	$\equiv n_\alpha/n_0$, Eq. 25A6		25
$(\frac{df}{dt})_{col}$	rate of change of f due to collisions	$m^{-6}s^2$	5
G	energy gain ratio for ICF target pellet (dimensionless)		15
G	Function in Eq. (11E16)		11
G	Function in Eq. (25E7), Fig. 25E1		25

G	gravitational constant	$J\text{-}m/kg^2$	1
G	perveance of diode	$Am^{-2}V^{-3/2}$	6
G_k^2	numerical coefficient in Eq. 13B4		13
GL	gain-length product		16
$\vec{g}$	acceleration of gravity	m/s^2	5
g_a, g_b	degeneracy factors of states a and b		3
g_b	ratio of ion density to density of passing ions		18
g_n	gap width between drift tubes of a linac	m	16
g_0	small-signal gain	m^{-1}	16
H	Hamiltonian H	J	11
H	neutral atom of hydrogen, deuterium, tritium		3
H	Coulomb collision function Eq. 2E39		2
Ha	Hartmann number		26
H^+	proton		3
ΔH	heat of sublimation	eV	24
$H_\perp$	magnetic field perpendicular to coil winding	A/m	22
$\vec{H}$	magnetic field	A/m	20
h	convective heat transfer coefficient or film coefficient Eq. (26C2)	W/m^2k	26
h	enthalpy, Eq. (23B3)	J/kg	23
h	Planck's constant	J-s	3
h	width of parallel plates	m	
I	current	A	1
I	detector signal		10
I	function in Eq.(11E17)		11
I	intensity of laser beam	W/m^2	15
I	moment of inertia	Js^2	1
I_d	discharge current	A	16
I_i	random ion current or ion saturation current	A	10
I_{in}	current in the inner helical conducter	A	14
I_{kj}	rate coefficient for ionization of n_{kj}	m^3s^{-1}	3
I_ℓ	modified Bessel Functions of order ℓ, Eq. (14A4)		14
$I_{m,opt}$	optimum maximum plasma current	A	12
I_{out}	current in the outer helical conductor	A	14
I_p	beam current needed to sustain each plug	A	
I_p	pinch current	MA	12
I_s	saturation intensity	W/m^2	16
I_0	normalizing factor (determined by a specified toroidal current)		12
$\dot{I}_0$	rate of change of initial current	A/s	12
i	fuel ions (subscript)		2
J	longitudinal invariant	s^{-1}	7
$\vec{J}$	current density	A/m^2	2
J_E	electron beam current density	A/m^2	16
J_{beam}	neutral beam current density	A/m^2	13
J_c	critical current density	A/m^2	22
J_m	Bessel Functions of order m, Eq. (12D2)		12
J_p	poloidal current density	A/m^2	8
$\vec{J}_p$	polarization current density	A/m^2	7
J_t	toroidal current density	A/m^2	8
j	charge state of an ion		3
j_m	$\equiv j_m(kr)$ Spherical Bessel Functions (Eq. 12C4)		12
K	$\equiv b/a$ = elongation p. 386		13
K	magnetic helicity (T^2m^4)		12
K	complete elliptic integral		20
K	recombination rate parameter, Eq. (24F3)	m^4/s	24
K	spatial variation of B in a pulsed solenoid		21
K_c	fraction of cyclotron radiation which is absorbed in walls and not reabsorbed in the plasma.		3
K_{IC}	fracture toughness	$Pa\text{-}m^{\frac{1}{2}}$	22
K_{sh}	factor in Eq.(21B11)		21
k	Boltzmann constant	J/K	2
k	spring constant	J/m^2	1
$\vec{k}$	vector pointing in the direction of wave propogation	m^{-1}	5
k	wave number = $\lvert\vec{k}\rvert$	m^{-1}	8
k_{app}	apparent mean thermal conductivity	W/m-K	23
k_R, k_L	vectors of the right and left circularly polarized waves	m^{-1}	10
k	thermal conductivity	W/m-K	23
k_1	gas collision constant, Eq. (19B1)	Pa-m	19

k_+, k_-	constants for the maximum electric fields an insulator can sustain at the positive and negative electrodes, $V\ m^{-4/5}\ s^{1/3}$		16
L	Coulomb logarithm, Table 2E1		2
L	inductance	H	1
L	ion flow path length	m	25
L	left-hand circularly polarized wave, Eq. (5E33)		5
L	length of cylinder	m	2
L	length of a mirror cell	m	14
L	plasma length	m	9
L	spacing between obstacles	m	24
L_f	optimum length between filters or distance between lenses	m	16
L_{ii}, L_{ie}	Coulomb logarithms for ion-ion and ion-electron collisions, Eqs. (11E7), (11E8)		11
L_n	length of the n-th cell of an rf linac	m	16
L_p	characteristic scale length corresponding to spatial derivative of p_e Eq. (5D11)	m	5
L_s	shear length	m	8
L_s	storage inductor	H	
L_u	characteristic scale length corresponding to spatial derivative of u_e, Eq. (5D11)	m	5
$\dot{L}$	rate of change of inductance	H/s	12
L'	inductance per unit length	H/m	17
L_Q	external circuit inductance	H	12
ℓ	beam duct length	m	9
ℓ	characteristic diffusion length	m	21
ℓ_a	characteristic attenuation length of beam intensity	m	15
ℓ_c	critical length, Eq.(22C4)	m	22
$d\vec{\ell}$	differential path length	m	5
M	magnetic mirror ratio		14
M	blanket energy gain ratio		4
M	mass	kg	4
M	molecular weight	kg/mole	2
M	thermal stress parameter, Eq.(24C6)	W/m	24
$\dot{M}$	mass flow rate	kg/s	15
ΔM	excess mass	kg	1
m	mass	kg	1
m	poloidal mode number		8
m_h	mass of central hot region heated to ignition	kg	15
m_i	ion mass	kg	2
m_j	mass of species j	kg	5
m_p	proton mass	kg	2
m_r	reduced mass	kg	2
m_*	field particle mass	kg	2
m_0	particle rest mass	kg	1
N	number of angular intervals in S_N approximation		27
N	number of turns of a coil		20
N	number of particles		16
N	number of electrons in the beam per unit length	m^{-1}	16
N	number of degrees of freedom		9
N_A	Avogadro Number	mol^{-1}	2
N_t	number of turns accumulated in a storage ring		16
N_D	Debye number		5
N_k	population of region k		1
N_a	number of target atoms per target molecule		2
N_r	number of rings in a linac		16
N_r	random number		27
Nu	Nusselt number, Eq(26C5)		26
n	particle density	m^{-3}	2
n	neutron		1
n	toroidal mode number		8
n	variable parameter, Eq.(15D4)		15
n_A	electron density in the anode regions	m^{-3}	17
n_D	deuteron density	m^{-3}	4
n_T	triton density	m^{-3}	4
n_a	density of particles of species a	m^{-3}	11
n_b	unattenuated beam density	m^{-3}	9

n_b	ion density at point b	m^{-3}	11
n_b^*	electron density at point b	m^{-3}	11
n_c	cutoff density	m^{-3}	5
n_c	plasma density of a central cell	m^{-3}	11
n_{e0}	electron density at x=0	m^{-3}	6
n_i	ion density	m^{-3}	3
n_{kj}	density of atoms or ions of species k and ionization state j	m^{-3}	3
n_n	neutral atom density	m^{-3}	3
n_p	density of central plasma electrons passing through an anode	m^{-3}	17
n_p	plasma density of end plug cells	m^{-3}	11
n_s	surface plasma density	m^{-3}	14
n_s	atomic density of pellet, Eq.(25E6)	m^{-3}	25
n_t	trapped electron density	m^{-3}	17
n_t	total heavy particle density	m^{-3}	3
n_3	density of ^3He	m^{-3}	4
$\bar{n}$	average density	m^{-3}	13
$\bar{n}_{crit}$	critical density in tokamaks	m^{-3}	13
$\tilde{n}$	refractive index		5
n_*	field particle density	m^{-3}	2
P	probability function		27
P	construction period	years	28
P	magnetic pitch	m	12
PAF	plant availability factor		28
P_B	bremsstrahlung radiation power density	W/m^3	3
PC	plant capacity	hrs/yr	28
P_C	cyclotron radiation power density	W/m^3	3
P_D	dielectric recombination power density	W/m^3	3
P_{DBC}	power dissipation of divertor	MW	29
P_F	total fusion power	W	2
P_L	line radiation power density	W/m^3	3
P_R	radiative recombination power density	W/m^3	3
$\underline{\underline{P}}_R$	ring pressure tensor Eq.(14D4)	Pa	14
P_{abs}	laser power absorbed	W	15
P_{br}	bremsstrahlung power density	W/m^3	10
P_{ch}	power leaving a fusion reactor as charged particles	W	26
P_{cond}	thermal power conduction	W	23
P_{cx}	power lost by charge exchange	W/m^3	5,25
P_e	net electric power	kWe	28
P_{ext}	total external heating power	W	4
P_f	fusion power density	W/m^3	2
$<P_f>$	volume averaged power density	W/m^3	2
P_g	gross electrical power	GW	29
P_h	alpha heating power	W	4
P_i	external heating power to ions	W	4
P_{int}	probability that a neutron has an interaction Eq.(27C1)		27
P_{ioniz}	power expended in ionization	W	25
P_{lim}	power incident on a limiter	W	25
P_{loss}	power lost	W	15
P_ℓ	Legendre Polynomials Table 27B1		27
P_m^n	Associated Legendre Function Eq.(12C4)		12
P_{oh}	ohmic heating power	W	13
P_{pump}	pump beam power	W	11
Pr	Prandtl Number Eq.(26C4)		26
P_{rad}	total radiation power density	W/m^3	3
P_s	power scattered	W	10
P_w	total energy consumption rate of the world	W	1
P_α	fusion alpha power	W	25
$P_{\alpha\beta}$	components of pressure tensor,Eq.(5D7)	Pa	5
P_μ	microwave power	W	14

P_0	beam power	W	9
P_0	incident laser beam power	W	16
p	pressure	Pa	2
$\vec{p}$	momentum	kg-m/s	2
p_a	abalation pressure	Pa	15
p_{cr}	critical pressure for blister formation	Pa	24
p_k	average per-capita energy consumption rate of region k	W/person	1
p_L	pressure due to leakage	Pa	19
p_n	ion momentum in the n-th cell of linac	kg m/s	16
p_u	ultimate pressure attainable by pump	Pa	19
$\dot{p}$	dissipation of wave momentum	kg/m^2s^2	13
$\delta\vec{p}$	change in momentum per collision	kg m/s	2
Q	throughput	$Pa\text{-}m^3/s$	19
Q	power gain ratio		4
Q	cavity quality Eq.(17A3)		17
Q_L	leak rate	$Pa\text{-}m^3/s$	
Q_e	heat generation by collisions	W/m^3	5
Q_i	heat generation by collisions	W/m^3	5
Q_{ei}	electron-ion energy exchange rate	W/m^3	14
Q_k	radiation power parameter for species k	$W\cdot m^3$	3
Q_{ve}	heat generation by viscous forces	W/m^3	5
Q_{vi}	heat generation by viscous forces	W/m^3	5
q	particle charge	C	1
q	safety factor, Table 8B1		8
$\vec{q}_e$	electron heat-flux vector	W/m^2	5
$\vec{q}_i$	ion heat-flux vector	W/m^2	5
q_1, q_2	charges	C	1
q''	heat flux through the surface of a tube	W/m^2	26
q'''	heat deposited internally by nuclear radiation	W/m^3	26
q_*	field particle charge	C	2
R	major radius	m	7
R	fuel radius at the end of compression	m	15
R	mirror ratio,Eq.(7D12)		7
R	resistance	Ω	6
R	right-hand circularly polarized wave		5
R	universal gas constant	J/mole-K	23
R_B	breeding ratio, Eq.(28B8)		28
R_L	reflection coefficient of a limiter		25
R_V	reflection coefficient of a vacuum duct		25
R_c	curvature radius	m	7
Re	Reynolds Number, Eq.(26C3)		26
R_{eff}	effective plug mirror ratio, Eq.(11E9)		11
$\vec{R}_{ei}$	rate of momentum transfer from electrons to ions	Pa/m	5
R_h	radius of heated fuel region	m	15
R_{kj}	rate coefficient for recombination of n_{kj}	m^3/s	3
R_m	effective mirror ratio Eq.(7E23)		7
R_s	resistance of a segment of a hollow-conductor coil	Ω	20
R_p	plug mirror ratio, Eq.(11E5)		11
R_w	reflection coefficient for wall		25
R_w	winding resistance	Ω	22
R_z	reflection coefficient of impurities		25
R_α	total reflection coefficient for alpha particles		25
R_α	range of fusion product alpha particles	m	15
R_0	plasma major radius	m	7
ΔR	thickness of a layer containing particular atoms	m	15
ΔR_0	initial thickness of a thin spherical shell of fuel	m	15
r	distance between charges	m	1
r	reaction rate per unit volume	reactions/m^3s	2
$r_j(t)$	"failure rate" of item j, Eq.(21G1)		21

r_n	particle reflection coefficient		24
r_p	plasma radius	m	4
r_p	radius of fuel pellet	m	25
r_q	reaction rate of reaction type q, Eq.(27B11)	reactions/m^3s	27
r_w	wall radius	m	2
Δr	banana width	m	8
S	cross sectional area of a conductor	m^2	21
S	wave power flux	W/m^2	14
S	solubility	atoms/m^3-$Pa^{\frac{1}{2}}$	28
S	cavity surface area	m^2	17
S	volumetric source of hydrogen atoms from implantation	$m^{-3}s^{-1}$	24
S	magnetic Reynolds Number, Eq.(8D105)		8
S	atomic energy level (1st)		16
S	sputtering yield		24
S_T	injected particle source of tritons		4
S_e	sources of electron energy	W/m^3	8
S_i	source of ion energy	W/m^3	8
S_n	source of particles	$m^{-3}s^{-1}$	8
S_t	theoretical pumping speed	m^3/s	19
S	neutron source	$m^{-3}s^{-1}$	27
S_r	functions for calculating magnetic field by Harts method		20
S_z	functions for calculating magnetic field by Harts method		20
S_3	injected particle source for ^3He	$m^{-3}s^{-1}$	4
dS	differential surface area	m^2	5
S_0	constant in Eq.(28B17)		28
s	standard deviation of sample		27
s	insulated gap width	m	21
s_ϕ	magnetic flux skin depth	m	21
s^2	sample variance		27
$d\vec{s}$	differential path length	m	1
T	temperature	K	1
T	tritium breeding ratio		29
T_A	annulus electron temperature	keV	14
T_{OX}	fraction of incident power converted from ordinary to extraordinary mode		14
T_a	temperature of central-cell particles of species a	keV	11
T_a	armor temperature	K	26
T_b	effective burn temperature	keV	4
T_{ep}	plug electron temperature	keV	11
T_{ek}	electron temperature in keV	keV	2
T_{es}	temperature of suprathermal electrons	keV	15
T_s	annual scheduled outage time	hrs	28
T_u	annual unscheduled outage time	hrs	28
T_w	wall temperature	K	8
T_ϕ	"torque"	W/m^5	13
T_0	adiabatic stability parameter, Eq.(22C3)		22
t	time	s	2
t	pulse length	s	9
t_2	doubling time, Eq.(28B9)	s	28
t	thickness of a tube	m	26
t	triton		1
$t_{\frac{1}{2}}$	half-life	s	28
t_1	time to slow down to thermal energy	s	4
U	potential energy	J	8
U	ionization potential of a gas	eV	3
U	stability parameter	m/T	14
U	electromagnetic energy stored in a resonant cavity	J	17
U_a, U_b	energies of states a and b	J	3
U_i	potential barrier retarding ion escape	keV	11
U_{opt}	optimum bank voltage	V	12
u	atomic mass unit (Appendix A)		1
$\vec{u}$	relative velocity	m/s	2

u_b	beam velocity	m/s	13
u_{bc}	threshold beam velocity	m/s	13
$u_{e\theta}$	azimuthal drift velocity of electrons	m/s	
u_f	final velocity	m/s	15
u_{ir}	radial drift velocity of ions	m/s	8
$u_{i\theta}$	azimuthal drift velocity of ions	m/s	8
u_j	velocity of species j	m/s	5
$\bar{u}$	average speed	m/s	15
V	plasma volume	m^3	2
V	cavity volume	m^3	17
V_p	plug plasma volume	m^3	11
V_s	surface plasma volume	m^3	14
v	speed	m/s	1
v_A	Alfven velocity	m/s	5
$\vec{v}_E$	drift velocity from electric field	m/s	7
v_{Te}	electron thermal velocity	m/s	15
$\vec{v}_b$	beam velocity	m/s	2
$\vec{v}_c$	center-of-mass velocity	m/s	2
$\vec{v}_c$	drift velocity of centrifugal force	m/s	7
$\vec{v}_d$	drift velocity	m/s	7
v_{de}	electron diamagnetic drift velocity	m/s	8
v_{di}	ion diamagnetic drift velocity	m/s	8
v_g	group velocity	m/s	5
$\vec{v}_g$	drift velocity of gravitational force	m/s	7
v_{min}	velocity of ions at the collector of a grid	m/s	10
$\vec{v}_{pi}$	polarization drift of ions	m/s	7
$\vec{v}_{pe}$	polarization drift of electrons	m/s	7
v_r	radial drift velocity	m/s	13
v_{rot}	rotational velocity	rad/s	7
v_{te}	electron thermal velocity	m/s	13
$\vec{v}_\phi$	phase velocity	m/s	5
$\vec{v}_{\nabla B}$	magnetic field gradient drift velocity	m/s	7
$<\vec{v}>$	average velocity	m/s	2
$\vec{v}_*$	field particle velocity	m/s	2
v_0	quiver velocity, Eq.(15C9)	m/s	15
$d\vec{v}$	$dv_x dv_y dv_z$		2
δv	tangential velocity	m/s	15
W	kinetic energy	J	1
W	photon energy	J	3
W	energy flows *per pulse* J of a pulsed reactor or *per unit time* W of steady state reactor		4
W_B	surface binding energy	J	24
W_{DD}	energy of catalyzed DD reaction	MeV,J	4
W_{DT}	energy of DT reaction	MeV,J	4
W_F	potential energy of the plasma	J	8
W_L	average energy at which plug ions are lost	keV	11
W_d	driver beam energy incident	J	15
W_d	deuteron kinetic energy	J	2
W_f	fusion energy	J	4
W_f	turbulent energy density	Pa	13
W_g	gross electrical energy output	eV	4
W_{in}	energy input to heat or sustain plasma	J	4
W_j	energy released by reaction	J	2
W_k	internal kinetic energy content of the plasma	keV	12
W_{nc}	remaining charged-particle energy available to heat the plasma, DDn reactions	J	4
W_{pc}	remaining charged-particle energies available to heat the plasma, DDp reactions	J	4
W_s	maximum energy stored in a single storage ring of a linac	GJ	16
W_s	potential energy of the plasma surface	J	8
W_t	triton kinetic energy	J	2
W_{th}	plasma thermal energy	J	4
W_v	potential energy of the vacuum magnetic field around the plasma	J	8

W_{th}	threshold energy	J	24
W_w	wave energy	J	8
$W_{\alpha 0}$	initial fusion product alpha energy	J	4
$\bar{W}_a$	mean energy of escaping particles	keV	11
$W_{L/L}$	liner energy per unit length	GJ/m	12
W_{rf}	rf power dissipated	W	13
W_ν	photon energy	keV	10
$<W>$	average kinetic energy	J	2
$<W_\perp>$	average energy perpendicular to a magnetic field	J	7
W_0	neutral atom beam injection energy	keV	4
δW	energy change due to a single collision	J	2
w_c	energy required per unit mass to compress fuel to the desired density	J/kg	15
w_f	fusion energy released per unit mass burned	J/kg	15
w_f	Fermi energy	J/kg	15
w_h	energy per unit mass needed to heat the central fuel up to ignition temperature	J/kg	15
x	Saha Equation parameter Eq.(3E4)		3
x	plasma sheath thickness in cathode gap	m	16
x	extension of spring	m	1
x	variable defined in Eq.(28B8)		28
x	velocity ratio, Eq.(13E1)		13
x_c	critical velocity ratio or dimensionless critical velocity Eq.(13E2)		13
$d\vec{x}$	differential volume dxdydz	m^3	1
Y	a function of the elongation ratio a/b, Eq.(19B14)		19
Y	yield of activated atoms		15
Y_m	maximum neutron yield		12
Y_n	yield of neutrons		15
y_a	parameter in Eq.(11E15)		11
Z	Atomic number		2
Z	major axis perpendicular to the plane of a torus		8
Z_{eff}	effective value of Z for the plasma		3
Z	"imedance" of a tube	s/m^3 s/L	19
$<Z>_k$	average values of ionic charge		3
$<Z^2>_k$	average values of ionic charge squared		3
α	angle, Fig.2E4	rad	2
α	divergence angle	rad	16
α	absorption coefficient, Eq.(16A3)	m^{-1}	16
α	fraction of the maximum possible turbulent energy density, W_f		13
α	inverse pitch of the helix	rad/m	12
α	capture-to-fission ratio		29
α	thermal expansion coefficient	K^{-1}	24
α	variable in Eq.(19B24)	s^{-1}	19
α	variable in Eq.(28C2)	s^{-1}	28
α	first Townsend coefficient	m^{-1}	6
α	an alpha particle		1
α	power absorption coefficient	m^{-1}	14
α	sticking coefficient		24
α_i	ion loss flux ratio		17
α_m	loss cone angle	rad	7
α_s	Stekly number		22
α_w	modulation of the helical winding	rad	14
$\bar{\alpha}$	average value of α (first Townsend coefficient)	m^{-1}	6
α_0	initial pitch angle between $\vec{v}$ and $\vec{B}$	rad	7
β	Maxwellian parameter, Eq.(2A7)	s^2/m^2	2
β	parameter in Eq.(25E5)	m^{-1}	25

β	ratio of plasma pressure to magnetic field pressure		8
β_A	beta of the annulus		14
β_D	plasma energy fraction, Eq.(12D9)		12
β_b	value of beta in the barrier cells		11
β_c	plasma beta in central cell		18
β_p	poloidal beta		8
β_p	value of beta in the end plugs		11
β_t	toroidal beta		8
$<\beta>$	average beta Eq.(8B9)		8
$\hat{\beta}$	peak beta Eq.(8B8)		8
β^-	beta particles (electrons)		15
β_*	rms beta Eq.(8B10)		8
Γ	particle flux	$m^{-2}s^{-1}$	11
$<\Gamma_x>$	spatially-averaged particle flux	$m^{-2}s^{-1}$	14
γ	imaginary part of frequency ω	s^{-1}	5,8
γ	gamma rays		1
γ	parameter in Eq.(24G2)		24
γ	ratio of total energy to rest mass energy		1,16
γ	secondary emission yield		6
γ_e	electron specific heat ratio		5
γ_i	ion specific heat ratio		5
γ_i	secondary emission coefficient (second Townsend coefficient)		6
Δ	distance of magnetic axis shift	m	13
Δ_m	half-width of magnetic islands	m	8
δ	half-width of a ring gap	m	11
δ	skin depth of field penetration	m	17,21
δ	phase angle	rad	16
δ	parameter in Eq.(29E2)		29
δ	toroidal field ripple		13
δ_A	half-width of the annulus	m	14
ε	fractional error		27
ε	Linhard reduced energy		24
ε	exitation energy	J	27
ε	recirculating energy fraction		4
ε	inverse aspect ratio		7
ε	permittivity	F/m	1
ε_T	emmitance of a beam	rad-m	16
ε_f	fatigue strain parameter Eq.(26B1)		26
ε_g	grid transparency		10
ε_h	helical field ripples		14
ε_t	modulations of toroidal field		14
$\varepsilon_{xx}\varepsilon_{yy}$ ε_{zz}	dielectric tensor components		15
$\underline{\underline{\varepsilon}}$	dielectric tensor		5
$\dot{\bar{\varepsilon}}$	strain rate	s^{-1}	24
ε_0	permittivity of free space	F/m	1
$\Delta\varepsilon$	cyclic strain		26
ζ	displacement	m	8
ζ	variable in Eq.(13C3)		13
η	resistivity	Ω-m	9,21
η	gas viscosity	kg/m-s	19
η	fraction of ion beam neutralized by charge exchange		9
η	plant efficiency		4
η_C	Carnot efficiency, Eq.(26A2)		26
η_a	fraction of beam energy absorbed by the target		15
η_g	generator efficiency		26
η_c	coupling efficiency		15
η_d	driver efficiency		15
η_{dc}	efficiency of a direct convertor		4
η_e	efficiency of converting thermal into electrical energy		4
η_h	hydrodynamic efficiency		15
η_{he}	heat engine efficiency		26
η_{in}	energy input fraction		4
η_p	pump efficiency		20
η_t	efficiency of converting thermal energy to electricity with a heat engine		4
η_{tr}	energy transfer efficiency		15
η_μ	microwave transmission efficiency		14
η_3	compound efficiency ($\varepsilon\eta_e\eta_{in}$)		4

$\eta_{\parallel}$	parallel resistivity	Ω-m	9
$\eta_{\perp}$	perpendicular resistivity	Ω-m	9
Θ	pinch parameter Eq.(12D3)		12
θ	angle	rad	2
θ	poloidal angle	rad	7
θ	characteristic time for self-heating of plasma	s	4
θ_B	Brewster angle	rad	16
θ_D	"Debye temperature"	K	23
θ_i	beam injection angle relative to $\vec{B}$	rad	11
θ_{min}	minimum scattering angle	rad	2
θ_m	modulation angle of plane of polarization	rad	10
θ_p	Faraday rotation angle produced by plasma	rad	10
θ_{rot}	angle of rotation	rad	10
ι_I	transform due to the plasma current	rad	14
ι_h	transform due to the helical windings	rad	14
ι	rotational transform angle	rad	8
κ	Elongation		18
Λ	parameter in Eq.(13A8)		13
λ	wavelength	m	3
λ	DeBroglie wavelength	m	22
λ	packing fraction Eq.(20D2)		20
λ	decay constant	Bq	28
λ	variable in Eq.(25B6)	m	25
λ_D	Debye length	m	2
λ_L	London penetration depth	m	22
λ_a	attenuation length	m	9
λ_{av}	value of λ_a at average values of n_e and T_e	m	9
λ_e	electron mean free path	m	2
λ_i	ion mean free path	m	2
λ_j	failure rate parameter Eq.(21G4)		21
λ_p	wavelength of surface perturbation	m	15
λ_s	wavelength of scattered radiation	m	10
λ_1	mean free path of particles 1	m	2
λ_0	wavelength from an atom at rest	m	10
$\delta\lambda_z$	magnitude of Zeeman splitting	m	10
λ/D	Knudsen Number Eq.(19B2)		19
μ	ion viscosity	Pa-s	11
μ	permeability of a medium	H/m	20
μ	shear modulus Eq.(24E1)	Pa	24
μ	cosine of the angle between neutron velocity and x-direction		27
μ	true value sought		27
μ_m	magnetic moment	J/T	7
$\mu_{\perp i}$	ion and electron mobilities perpendicular to $\vec{B}$		5
$\mu_{\perp e}$			
ν	frequency	Hz	3
ν	Poission ratio		24
ν	variable parameter Eq.(13A1)		13
ν	electron beam parameter Eq.(16E5)		16
ν	pulse repetition rate	Hz	16
ν_{climb}	dislocation climb velocity		24
ν_{ci}	ion cyclotron frequency	Hz	9
ν_{ce}	electron cyclotron frequency	Hz	9
ν_{eff}	effective collision frequency for detrapping		13
ν_{ei}	electron-ion momentum-transfer collision frequency	Hz	2
ν_{en}	electron-neutral momentum transfer collision frequency	Hz	5
ν_{in}	ion-neutral momentum transfer collision frequency	Hz	5
ν_{jk}	momentum transfer collision frequency between species j and k	Hz	5
ν_{LH}	Lower Hybrid frequency	Hz	9

ν_U	Upper Hybrid frequency	Hz	9
ν_{*e}	ratio of electron collision frequency to electron bounce frequency		8
ν_{*i}	ratio of ion collision frequency to ion bounce frequency		8
ν_h^* ν_t^*	ratios of effective collision frequency for detrapping to bounce frequency for helical ripples and toroidal mirrors		14
ξ	streaming parameter (drift parameter) Eq. (13E10)		13
$\vec{\xi}$	displacement	m	8
ξ	coherence length	m	22
π	variable, Fig. 9E8		9
$\underline{\underline{\Pi}}_{\alpha\beta}$	anisotropic part of the pressure tensor, Eq. (5D8)		5
ρ	target mass density	kg/m^3	2
ρ	charge density	C/m^3	5
ρ	Larmor radius	m	7
ρ_i	ion Larmor radius	m	7
ρ_e	electron Larmor radius	m	7
ρ_m	mass density	kg/m^3	5
ρ_s	density of solid DT fuel at atmospheric pressure	kg/m^3	15
ρ_θ	poloidal gyroradius of electrons	m	8
ρ_0	initial liner density	g/cm^3	12
Σ	macroscopic cross section for neutron attenuation	m^{-1}	15
Σ_{el}	elastic scattering macroscopic cross section	m^{-1}	27
Σ_{in}	inelastic scattering macroscopic cross section	m^{-1}	27
Σ_ℓ	expansion coefficients in Eq. (27B4)		27
Σ_t	macroscopic total cross section	m^{-1}	27
Σ_γ	radiative capture macroscopic cross section	m^{-1}	27
Σ_{2n}	(n, 2n) reaction macroscopic cross section	m^{-1}	27
Σ_0	radiation barrier parameter, Eq. (12D8)		12
σ	tensile stress	Pa	20
σ	conductivity	A/Vm	5
σ	standard deviation of data about μ		27
σ	cross section	m^2	2
σ_d	desorption cross section	m^2	24
σ_{el}	elastic scattering cross section	m^2	3
σ_h	hoop stress	Pa	26
σ_{th}	thermal stress	Pa	26
σ_u	ultimate stress	Pa	24
$\sigma_{\bar{x}}$	standard deviation of the mean		27
σ_{xx}, σ_{yy} σ_{zz}	conductivity tensor components, Eq. (5E9)	A/Vm	5
σ_y	yield stress	Pa	17
σ_z	axial stress component	Pa	24
σ_θ	azimuthal stress component	Pa	24
σ_{01}	cross section for reionization of neutrals	m^2	9
σ_{10}	cross section for neutralization by charge exchange	m^2	9
$\underline{\underline{\sigma}}$	conductivity tensor Eq. (5E10)	A/Vm	5
$\langle\sigma v\rangle$	reaction rate parameter	m^3s^{-1}	2
$\langle\sigma v\rangle_{cx}$	charge exchange rate coefficient	m^3s^{-1}	3
$\langle\sigma_e v_e\rangle$	rate for ionization of neutrals by electrons	m^3s^{-1}	3
$\langle\sigma_i v_i\rangle$	rate for ionization of neutrals by ions	m^3s^{-1}	5
$\langle\sigma_r v\rangle$	recombination rate	m^3s^{-1}	5
$d\sigma$	differential Coulomb scattering cross section	m^2	2
τ	confinement time	s	1
τ	logarithm of poloidal field energy ratio		12
τ_A	Alfven transit time	s	8
τ_E	energy confinement time	s	3
τ_{Ee}	energy confinement time for electrons	s	4
τ'_{Ee}	nonradiative electron energy confinement time	s	3
τ_{Ei}	ion energy confinement time	s	3
τ_R	resistive diffusion time	s	8
τ_a	collision time of central-cell particles of species a	s	11
τ_b	fuel burn time	s	4

τ_c	period of rotation about a magnetic field line	s	7
τ_e	characteristic collision time for electrons	s	2
τ_{eq}	equilibration time	s	2
τ_{he} τ_{hi}	variables in Eq. (13B12)	s	13
τ_i	self-collision time for ions	s	2
τ_{ie}	ion-electron collision time	s	2
τ_{ii}	ion-ion collision time	s	11
τ_{opt}	optimum current rise time	s	12
τ_p	particle confinement time	s	2,8
τ_p	pulse length	s	16
τ_s	sawtooth pulse length	s	13
τ_s	pulse length of Stokes wave	s	16
τ_s	time for fuel pellet to disassemble	s	15
τ_α	particle confinement time for alpha particles	s	3
τ_1	collision time for species 1	s	2
$\tau_\perp$	characteristic diffusion time across $\vec{B}$	s	17
$\tau_\perp$	deflection time	s	2
$\tau_\parallel$	slowing-down time	s	2
Υ	quasipotential	J	17
Φ	magnetic flux	Wb	8
Φ	flux surface invariant Eq. (7D14)	Wb	7
Φ	quasipotential	J	17
Φ_0	fluxon	Wb	22
Φ_0	initial bias flux	Wb	12
ϕ	angle	rad	2
ϕ	toroidal angle	rad	7
ϕ	electrostatic scalar potential or voltage	V	5
ϕ	phase of electromagnetic wave	rad	10
ϕ_A	applied voltage	V	17
ϕ_A	electrostatic analyzer voltage	V	10
ϕ_G	accelerator voltage in a linac	GV	16
ϕ_b	potential valley constituting a thermal barrier to electron flow between central cell and end plug	V	11
ϕ_b	power supply voltage	V	6
ϕ_c	potential barrier height	kV	11
ϕ_m	potential at the maximum magnetic field	V	11
ϕ_n	surface evaporation flux	$m^{-2}s^{-1}$	24
ϕ_p	plasma potential	V	10
ϕ_t	potential drop between electrodes	V	6
ϕ_0	accelerating voltage	V	10
$\hat{\phi}$	unit vector in toroidal direction		8
χ_e	electron thermal conductivity	$m^{-1}s^{-1}$	8
$\underline{\underline{\chi}}$	thermal conductivity tensor	$m^{-1}s^{-1}$	5
Ψ_R	fraction of fusion energy leaving the plasma as charged particles		4
ψ	angle	rad	22
ψ_p	poloidal flux	Wb	8
ψ_r	magnetic flux in the r direction	Wb	8
ψ_s	separatix	Wb	8
ψ_t	toroidal flux	Wb	8
ψ_z	magnetic flux in the z-direction	Wb	8
ψ_*	effective quasipotential	keV	17
Ω_A	hot electron precession frequency	Hz	14
Ω_{eff}	variable defined by Eq. (14D22)	Hz	14
$d\Omega$	differential solid angle	Sr	2
ω	angular frequency	rad/s	1
ω	wave frequency	rad/s	5
ω_{LH}	Lower hybrid frequency	rad/s	5
ω_U	Upper hybrid frequency	rad/s	5
ω_b	bounce frequency	rad/s	7
ω_{ce}	electron cyclotron frequency	rad/s	5
ω_{ci}	ion cyclotron frequency	rad/s	5
ω_{ia}	ion acoustic wave frequency	rad/s	15
ω_j	eigenvalues of Eq. (8D38)		8
ω_p	frequency of "pump" wave	rad/s	16
ω_{pi}	ion plasma frequency	rad/s	5

ω_{pe}	electron plasma frequency		
	frequency	rad/s	5
ω_r	real part of frequency ω	rad/s	5
ω_s	frequency of "Stokes" wave	rad/s	16
ω_t	transverse electromagnetic wave frequency	rad/s	15
ω_0	cavity resonant frequency	rad/s	17
ω_*	drift wave frequency	rad/s	8,11
$\sim$	on the order of		2
$\perp$	perpendicular (subscript)		2
$\parallel$	parallel (subscript)		2
$< >$	average		3
$\{ \}$	differential operator notation		8
$\vec{\nabla}$	gradient operator (Appendix F)	m^{-1}	5,6
∇^2	Laplacian operator	m^{-2}	7

APPENDIX H. ABBREVIATIONS

by J. J. Browning

		chapter number
ADIP	Alloy Development for Irradiation Performance	24
AEC	Atomic Energy Commission	12
AI	Atomics International Corp.	
ANL	Argonne National Laboratory	9
ANS	American Nuclear Society	9
appm	atomic parts per million	24
APS	American Physical Society	
ARE	aspect ratio enhancement	14
ASME	American Society of Mechanical Engineers	
ASTM	American Society for Testing Materials	24
ATC	Adiabatic Toroidal Compressor	9
bbl	barrels	1
bcc	body-centered cubic	24
BCS	Bardeen, Cooper, Schrieffer	22
BDTN	beam-driven thermonuclear	29
BFM	Bessel Function Model	12
BHP	biological hazard potential	28
BNL	Brookhaven National Laboratory	16
BOP	balance of plant	18
BPA	Bonneville Power Administration	22
BWR	Boiling Water Reactor	26
CAP	capita	1
CICADA	Central Instrumentation Control and Data Acquisition System	10
CF	correction field	18
C mode	collisional mode	14
COE	cost of electricity	18
COM	center of mass (coordinate system)	27
CT	compact toroid	12
CTR	controlled thermonuclear reactions	
CTR	controlled thermonuclear research	
CW	cold worked	24
cw	continuous wave	10
DAFS	Damage Analysis and Fundamental Studies	24
DBTT	ductile-to-brittle transition temperature	24
DCLC	drift cyclotron loss cone	11
DEMO	Demostration Reactor	
DOE	Department of Energy (USA)	9
dpa	displacements per atom	24
DT	Deuterium-Tritium	1
EBR	Experimental Breeder Reactor	
EBT	Elmo Bumpy Torus	11
ECH	electron cyclotron heating	
ECRH	Electron Cyclotron Resonance Heating	9
EDC	escalation during construction	28
EF	equilibrium field	13
EPR	Experimental Power Reactor	
EPRI	Electric Power Research Institute	4
ERDA	Energy Research and Development Administration	
ETF	Engineering Test Facility	24
ETNF	estimated time to next failure	21
FED	Fusion Engineering Device	
FFTF	Fast Flux Test Facility	24
FINTOR	Frascati-Ispra-Naples-Torus	
FIR	Far-infrared	10
FLIBE	LiF-BeF_2	26
FLR	fast liner reactor	21
FMIT	Fusion Materials Irradiation Test Facility	24
FR	fundamental resonance	14
FRD	IAEA Workshop on Fusion Reactor Design	
FRM	field-reversed mirror	11
GA	General Atomic Company	
Gcf	billion cubic feet	28
GE	General Electric Corp.	
GMB	glass microballoon	15
GNP	Gross National Product	1
HBM	high beta model	12
HCN	Hydrogen Cyanide	10
HEDL	Hanford Engineering and Development Laboratory	
HFIR	High Flux Isotope Reactor	24
HFITR	High-Field Ignition Test Reactor	
HTE	high-temperature electrolysis	26
HTGR	High-Temperature Gas-Cooled Reactor	26
HTS	"Heat Transfer Salt"	26
HYLIFE	"High-Yield Lithium-Injection Fusion Energy"	10
IAEA	International Atomic Energy Agency	9
ICF	inertial confinement fusion	1

ICRF	Ion Cyclotron Range of Frequencies	9
ID	inside diameter	
IDC	interest during construction	28
IEEE	Institute of Electrical and Electronic Engineers	1
INESCO	International Nuclear Energy Systems Corporation	
INTOR	International Tokamak Reactor	13
ISX	Impurities Study Experiment	
ITR	Ignition Test Reactor	
JET	Joint European Torus	
KERMA	"Kinetic Energy Released in Materials"	27
KFA	Kernforschungsanlage Jülich	
LASL	Los Alamos Scientific Laboratory (now called Los Alamos National Laboratory)	12
LBL	Lawrence Berkeley Laboratory	9
LCTF	Large Coil Test Facility	22
LHH	Lower Hybrid Resonance Heating	
LIA	Linear Induction Accelerator	
LLL	Lawrence Livermore Laboratory (now called LLNL)	
LLNL	Lawrence Livermore National Laboratory	1
LMFBR	Liquid metal fast breeder reactor	1
LOCA	loss-of-coolant accident	29
LTE	local thermodynamic equilibrium	3
LWR	light-water reactor	29
MDAC	McDonnell Douglas Astronautics Company	
MFECC	Magnetic Fusion Energy Computer Center (at LLNL)	
MFR	Magnetic Fusion Reactor	
MFTF	Mirror Fusion Test Facility	11
MGF	Motor-Generator Flywheel	
MHD	Magnetohydrodynamic	5
MIRICLE	"mirrored ions closed-loop electrons"	14
MIT	Massachusetts Institute of Technology	1
M mode	mirror mode	14
MPC	maximum permissible concentration	28
MTF	Mock-up Test Facility	
NATO	North Atlantic Treaty Organization	1
NASA	National Aeronautics and Space Administration	18
NBI	neutral beam injection	
NBT	Nagoya Bumpy Torus	14
NDT	nil ductility temperature	24
NRC	Nuclear Regulatory Commission	
NTIS	National Technical Information Service, Springfield, VA 22161	
NYU	New York University	
OD	outside diameter	
OFE	Office of Fusion Energy	
OH	ohmic heating	13
OHTE	Ohmic Heated Toroidal Experiment	12
O mode	ordinary mode	14
ORMAK	Oak Ridge Tokamak	
ORNL	Oak Ridge National Laboratory	
OTEC	Ocean thermal electric conversion	1
PBFA	Particle Beam Fusion Accelerator	16
PCA	prime candidate alloy	18
PDX	Poloidal Divertor Experiment	13
PF	poloidal field	17
PKA	primary knock-on atom	24
PLT	Princeton Large Torus	9
PMI	Plasma-Materials Interactions	
PNL	Pacific Northwest Laboratory	
ppb	parts per billion	
ppm	parts per million	1
PPPL	Princeton Plasma Physics Laboratory	9
PRD	Princeton Reference Design	27
PS	Paramagnetic Spheromak	12
PWR	pressurized water reactor	
QA	quality assurance	
REB	relativistic electron beams	14
RECE	Relativistic Electron Coil Experiments	14
RF	radiofrequency, same as rf	
rf	radiofrequency	8
RFC-XX	Radio Frequency Confinement-20	17
RFP	Reversed Field Pinch	12
RFQ	radiofrequency quadrupole	16
rms	root mean square	2
RRR	residual resistivity ratio	23
RTNS	Rotating Target Neutron Source	24
RTPR	Reference Theta Pinch Reactor	
SA	solution annealed	24

SAI	Science Applications, Inc.	
SAP	sintered aluminum powder	24
SB	"superbananas"	14
SBS	stimulated Brillouin scattering	15
S/C	superconducting	
SI	Systeme Internationale	
SLA	Sandia Laboratories, Albuquerque	16
SMES	Superconducting magnetic energy storage	22
SMH	Standard Mirror Hybrid	
SNR	signal-to-noise ratio	10
SPM	Special Purpose Materials	24
SR	second harmonic resonance	14
SR	Stress-rupture	
SRS	stimulated Raman Scattering	15
SS	stainless steel	24
SSCF	Stress/Strain controlled fatigue	
SSPS	Solar satellite power stations	1
STEC	Solar thermal electric conversion	1
SURMAC	Surface Magnetic Confinement	14
TCT	two-component torus	29
TEM	transmission electron microscopy	24
TE	transverse electric	17
TF	toroidal field	12
TF	tritium fluoride	26
TFR	Torus Fontenay-aux-Roses	10
TFTR	Tokamak Fusion Test Reactor	9
TIG	Tungsten Inert Gas	19
TM	transverse magnetic	17
T mode	toroidal plasma mode	14
TMR	Tandem Mirror Reactor	
TMX	Tandem Mirror Experiment	11
TN	thermonuclear	
TNS	"The Next Step"	
TORMAC	Toroidal Magnetic Cusp	11
TP	tensile properties	
TPD	Test Plasma Produced by Discharge	17
TRACT	triggered reconnection adiabatically compressed torus	12
TSTA	Tritium Systems Test Assembly	
UCLA	University of California - Los Angeles	
UTRC	United Technologies Research Center	
UW	University of Wisconsin	
UWMAK	name of University of Wisconsin tokamak reactor designs	9
VUV	vacuum ultraviolet spectroscopy	10
WITAMIR	Wisconsin Tandem Mirror	18
X mode	extraordinary mode	14

APPENDIX I. ANSWERS TO PROBLEMS

by L. C. Cadwallader, M. D. Carter } Chapters 1-10
J. P. Head } Chapters 19-28

Chapter 1

1. 0.78 TW food energy; 6.2 TW for agriculture
2. DDn energy yield = 3.268 MeV
   DDp energy yield = 4.032 MeV
3. (a) 0.0151 $/MJ
   (b) 0.717 $/MJ
   (c) 0.0139 $/MJ
   (d) 14.50 $/MJ
   (e) 0.521 $/MJ
4. 192 kg of D_2, 5648 m^3 of H_2O
5. ~ 353 liters gasoline
6. 5.0 GJ, 99 Henrys
7. $W = (P_0/\lambda)(e^{\lambda t}-1) \rightarrow t = 50$ years after 1980, depletion in year 2030

Chapter 2

1. $\langle v_x^3 \rangle = 0$
   $\langle v_x^4 \rangle = 3(kT/m)^2$
2. (a) $\Delta n_1/n_1 = 2.2\times10^{-7}$
   (b) $\Delta n_1/n_1 = 9.0\times10^{-8}$
3. (a) $\sigma = 1.33$ mb $= 1.33\times10^{-31}$ m^2
   (b) I = 16 μA
4. (a) $P_f = 5.69\times10^5$ W/m^3
   (b) 3.42×10^{16} neutrons/m^3s
   (c) p = 2.48 MPa
5. Intermediate step: $\langle \sigma v \rangle_b =$

$$2\pi(\beta_2/\pi)^{3/2} \int_0^\infty dv\, v^3 \exp[-\beta_2(v_b^2 + v^2)] \cdot \int_0^\pi d\theta \sin\theta \exp[2\beta_2 v v_b \cos\theta].$$

   Let $x = \cos\theta$.
6. $\bar{x} = \frac{1}{n\sigma}$
7. (a) $\lambda = 6.054\times10^9$ m
   (b) $\lambda = 3.20\times10^7$ m
   (c) fraction of T consumed = 0.0488
8. $F_i = [2\langle\sigma v\rangle_{DHe} + \langle\sigma v\rangle_{DDn} W_{DDn} + \langle\sigma v\rangle_{DDp} W_{DDp}]/8(kT_i)^2$.

   Max $F_i = \frac{5.2\times10^{-6} m^3}{J^2\ s}$ at 55 keV

   B = 3.7 T
   r_w = 3.1 m
9. $n_B/n_p = 1/3$; p = 18 MPa
10. $dW/dt = (9.63\times10^{-13}W)_{electrons} + (1.45\times10^{-13}W)_{ions}$,
    fraction to ions = 13 %.
11. (a) $n = 6.24\times10^{18} m^{-3}$
    (b) before equilibration,
    T_i = 13.33 keV
    T_e = 66.67 keV
    after equilibration,
    T = 40 keV
    (c) $\tau_e \simeq 0.032$ s, $\tau_i \simeq 0.15$ s .
    Thermalization will be completed in a few times τ_e or τ_i, respectively.
    (d) $\tau_{eq} \simeq 40$ s (using $T_e \simeq 40$ keV)

Chapter 3

1. $\lambda_{en} = 13$ m
   $\lambda_{ne} = 1.3$ mm
   $L = 11.6 \rightarrow \nu_{ei} = 7.8\times10^6\ s^{-1}$

$$\frac{n_i}{n_t} = \frac{10^{19}}{1.1\times10^{19}} = .909$$

   Saha eq. $\rightarrow \frac{n_i}{n_t}$ <<< 1, so plasma is not in thermal equilibrium.
2. charge exchange and ionization.
   λ = 2.1 cm
   fraction having charge exchange = 80 %
3. $t = 1n2/n_e[(\sigma v)_{(H+H)} + (\sigma v)_{(H+H^+)} + (\sigma v)_{(H_2^+)}]$

   (a) t = 0.03 s
   (b) t = 1.4 s
4. 2.1×10^{21} photons/m^2s
   1.7×10^{18} ionizations/m^3s
   λ = 21 km
5. fraction neutralized
   $\simeq 1 - \exp(-n_{H_2}\langle\sigma v\rangle \dot{x}/v) = 15$ %
6. $W_i \gtrsim 160$ keV
7. (a) 2.59 eV
   (b) 0.54 eV
8. $n_h/n = \langle\sigma_r v_e\rangle/[\langle\sigma_e v_e\rangle + \langle\sigma_i v_i\rangle]$
   $= 1.5\times10^{-8}$
   Agrees with Fig. 3E2.

9. (a) yes ($n_e t \simeq 1.2\times10^{19}$ m^{-3}s)

   (b) line = 2580 W/m^3
   radiative recombination = 1310 W/m^3
   dielectronic recombination = 58 W/m^3
   hydrogen bremsstrahlung = 2650 W/m^3
   oxygen bremsstrahlung = 1440 W/m^3
   total = 8040 W/m^3

(c) 5.4×10^{16} m^{-3}

   (d) oxygen Z_{eff} = 1.56
   aluminum Z_{eff} = 1.14

   (e) T_e = 20 keV

10. (a) T ≃ 83 keV
    (b) T ≃ 25 keV

11. T_e = 45 keV, D = 4×10^{22}
    $K_c P_c = 4.6\times10^4$ W/m^3

12. 13 s

Chapter 4

1. f = 20 %
2. $n\tau_E = 1.75\times10^{21}$ s/m^3
3. $\varepsilon \simeq 0.238$, Q = 68.1, W_{net} = 2500 MJ/pulse
4. Q = 2.41, ε = 0.64
5. $n\tau_E = 1.09\times10^{20}$ s/m^3
6. (a) p = 5.48 MPa
   (b) $n_e = 2.75\times10^{20}$m^{-3}
   (c) η = 0.205
   (d) f_b = 0.255
7. ε = 0.152, $\tau_B \simeq 14.7$ ms, f_B = 0.141
8. P_{net} = 1090 MW$_e$, ε = 0.253, η = 0.261
9. p_f = 1.83 %. From Fig. 4F1,
   Q ≃ 1.5, p_f = 1.8 %
10. $\langle P_{rad}\rangle = 1.1\times10^4$W/m^3,
    $P_{rad} = 5.5\times10^3$W/m^3 at $\langle n\rangle$, $\langle T\rangle$.
11. (a) n_e = 0.39
    (b) M = 16.2
    (c) breakeven Q = 245
    $n\tau_E = 1.50\times10^{21}$s/m^3
    power plant Q = 1718,
    $n\tau_E = 1.05\times10^{22}$s/m^3

Chapter 5

1. $\eta_\parallel = 3.7\times10^{-8}$ Ω-m, $\partial B/\partial t \simeq 0.92$ T/s
2. $n_0 = 1.18\times10^{14}$m^{-3}
3. See Tanenbaum, pages 188-191 or Chen, pages 213-214.
4. $\frac{dN_i}{dt} \simeq 1.1\times10^{14}$ ions/s
5. (a) 2300 V
   (b) potential at plug is higher
   (c) kinetic energy = 2300 eV
6. fully ionized $D_\perp = \frac{\nu_{ei}(kT_e + kT_i)}{m_e\omega_{ce}^2}$

   weakly ionized $D_\perp = \frac{\nu_{in}\nu_{en}(kT_e + kT_i)}{m_e\omega_{ce}^2\nu_{in} + m_i\omega_{ci}^2\nu_{en}}$
7. See Eqs. (15C3) - (15C8).
8. $\lambda \to \infty$ ($k \to 0$): $v_g \to 0$, $v_\phi \to \infty$.
   $\lambda \to 0$ ($k \to \infty$): $v_g^2 \to \frac{3kT_e}{m_e}$, $v_\phi^2 \to \frac{3kT_e}{m_e}$
9. $\omega_{pe} = 6.53\times10^8$ rad/s, ν = 104 MHz

Chapter 6

1. (a) $u_e = 1.56\times10^4$ m/s
   (b) $\langle v_e\rangle = 6.51\times10^5$ m/s
   (c) $\nu_{en} = 8.46\times10^8$ s^{-1}
   (d) $\bar{\alpha} = 3.08$ m^{-1}
   (e) $\langle\sigma_e v_e\rangle = 5.2\times10^{-19}$ m^3/s
2. ϕ_t = 12 kV
3. (a) at L = 0.01 m, breakdown does not occur (pL too small).
   (b) at L = 1 m, $\phi_t \simeq 470$ V
4. B_θ = 0.8 T
   F/V = 2.04×10^7 N/m^3
   $\nabla p = 2.04\times10^7$ Pa/m = 20.4 MPa/m
   = 2.0 atm/cm
5. I ≃ 0.06 A
   L ≃ 2.4 mm

Chapter 7

1. [Differentiate solutions to obtain (7A1)-(7A3). Then show that they satisfy the initial conditions, noting that
$v_{rot}\cos\theta = v_{yo} + F_x/qB$
$v_{rot}\sin\theta = v_{xo} - F_y/qB$]

2. $\vec{v}_d$ = 0.01 m/s west.

3. $\vec{v}_c = 8.33\times10^3$ m/s in the z direction.

4. Negative z direction. $E_y = 10^4$ V/m.

5. (a) $x(t) = -4.253\times10^{-4}[\cos(2.398\times10^7 t + 1.374) - 0.1961]$
$y(t) = 4.253\times10^{-4}[\sin(2.398\times10^7 t + 1.374) - 0.9805] - 2000\ t$

(b) $x(t) = -5.004\times10^{-4}[\cos(2.397\times10^7 t) - 1]$
$y(t) = 5.004\times10^{-4}[\sin(2.397\times10^7 t) - 2000\ t$

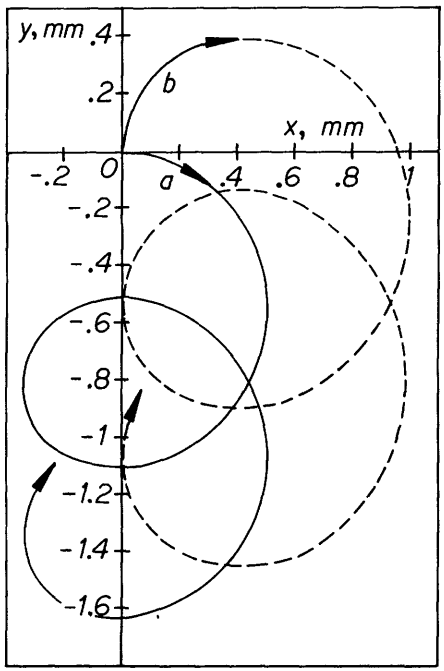

by R. N. Ballou

6. (a) $F = 6.4\times10^{-16}$ N
(b) z = 0.25m
(c) z = 0.25m, same as (b)

7. 3.2 T, 105 T.

8. Fraction lost = $1-\cos\theta_L$ = 0.155

9. r = 1 m
θ = 5 radians = 287°
z = 7.8 mm

Chapter 8

1. iota = 2.51 rad = $2\pi/2.5$ After going around 5 times, the angle of rotation is 4π radians, so the field line returns to its starting point.

2. T_i = 1.55 keV

3. p = 3.93 atm, E = cB = 2.998×10^8 V/m (3MV/cm).

4. $\langle\beta\rangle = (1/3)\,\hat{\beta} = 1/3$

5. $\psi_p = \int_0^R dR 2\pi R\,(\frac{1}{R}\frac{\partial\psi}{\partial R}) = 2\pi\psi$

6. (a) $\partial^2 z/\partial x^2 = 2$, $\frac{\partial^2 z}{\partial y^2} = 2$ stable

(b) $\frac{\partial^2 z}{\partial x^2} = 2 - 24x^2$ stable at x = 0

(c) $\frac{\partial^2 z}{\partial y^2} = -2$ unstable

(d) $\frac{\partial^2 z}{\partial x^2} = 12x^2 - 6$ unstable at x = 0

7. $\delta\int d\ell/B = 2\pi R_2/B_2 - 2\pi R_1/B_1$
$= 2\pi(R_2^2 - R_1^2)/B_0R_0 > 0$, unstable.

8. (a) $\beta \lesssim 0.04$, Eq. (8D72).
(b) R_0 = 7.4 m
a = 1.85 m
(c) B = 7.93 T
B_t = 7.89 T
B_p = 0.79 T
(d) $I = 2\pi aB_p/\mu_0$ = 7.3 MA
(e) $W = 1.25\times10^{10}$ J

9. $\omega_{pe} = 1.78\times10^{10}$ rad/s
$\frac{\omega}{k} = v = 1.88\times10^7$ m/s
λ = 6.6 mm
$\gamma = 9.3\times10^{10}$/s

10. $v_{de}(a) = 2.16\times10^4$ m/s
λ = 5.66 mm

11. (a) $\tau_e = 4.1$ μs
$\nu_{*e} = 1.01$
$K_{11} = 0.235$
$K_{22} = 1.37$
$D = 5.6\times10^{-3}$ m^2/s
$\chi_e = 3.3\times10^{16}$m^{-1}s^{-1}

(b) $D = 0.096$ m^2/s
$\chi_e = 2.9\times10^{17}$m^{-1}s^{-1}

(c) $D = 3.8$ m^2/s
$\chi_e = 1.1\times10^{19}$ m^{-1}s^{-1}
plateau regime

(d) $\tau'_{Ee} = .555a^2/[0.9D + 3.6\chi_e/n_0]$
$= 0.32$ s, neoclassical
$\tau'_{Ee} = .017$ s, pseudoclassical
$\tau'_{Ee} = 7.1\times10^{-4}$ s, Bohm

12.
$$\tau'_{Ei} = \frac{\int_0^1 dx\, x(1 - .9x^2)^2}{\int_0^1 dx\, x(1 - .9x^2)^2 n_n \langle\sigma v\rangle},$$

$x \equiv r/a$

$\tau'_{Ei} = 1.8\times10^{-4}$ s, not dependent on a

Chapter 9

1. (a) $P = 0.45$ MW/m^3
(b) $P = 0.014$ MW/m^3
2. (a) $T_{\parallel} = 1$ keV, $T_{\perp} = 3$ keV
(b) $T_{\parallel} = T_{\perp} = 2.08$ keV
3. $T_1/T_0 = (B/B_0)^{4/5} \rightarrow T = 2.41$ keV
4. $T_1/T_0 = 1.35$
5. 1.1 %
6. $W_0 > 400$ keV, Fig. 9E1
$\eta_{D^+} \simeq 3$ %
$\eta_{D^-} \simeq 60$ %
7. $p \simeq 63$ Pa
8. beam divergence angle $\simeq 0.9°$
9. 1 MHz : couple to ν_{ci} at $B \sim 0.13$ T
100 MHz : couple to ν_{LH} at $B \sim 0.24$ T
10 GHz : couple to ν_{ce} at $B \sim 0.36$ T

Chapter 10

1. $n_i \simeq 5.8\times10^{16}$m^{-3}, $T_e \simeq 0.87$ eV
2. $\partial B/\partial t = 2.8\times10^3$ T/s
3. $$J_t(r) \simeq J_z(r) = \frac{B_{p0}}{\mu_0}\frac{2a + r}{(a + r)^2}$$
4. $\phi = \pm 57$ V, (Sign depends on direction of B_0 relative to direction of windings.)
5. $T_i = 5.2$ keV
6. $\phi = -0.7$ kV
7. $T_i \simeq 89$ eV
8. $n \simeq 3.2\times10^{22}$ m^{-3}
9. $T_e = 0.87$ keV
10. $n_e = 2.1\times10^{16}$ m^{-3}
11. $n_0 = 3.2\times10^{22}$ m^{-3}
12. $\theta_{rot} \simeq 0.25$ rad $= 14°$

Chapter 19

1. 7.96×10^4 N, 1.79×10^4 lb$_f$, 8.94 tons
2. $C_{eff} = 1.15\times10^{-3}$ m^3/s,
$t_2 = 2.28$ hours
3. (a) $\dot{Q} = 0.0589$ Pa-m^3/s
(b) $\bar{v} = 468$ m/s
(c) dN/dt = 1.42×10^{19} molecules-air / second
(d) viscous
(e) $C = 8.53$ m^3/s,
$(p_2 - p_1) = 0.00691$ Pa
4. 5.08×10^{-5} Pa
5. (a) molecular
(b) $Q = 1.01\times10^{-3}$ Pa-m^3/s
(c) dN/dt = 2.49×10^{17} molecules/s
(d) $S_t = 0.505$ m^3/s
6. (a) $Q = 7.92\times10^{-7}$ Pa-m^3/s,
$p = 5.29\times10^{-3}$ Pa
(b) $Q = 7.92\ 10^{-7}$ Pa-m^3/s,
$p = 2.12\times10^{-4}$ Pa
(c) $Q = 7.92\times10^{-7}$ Pa-m^3/s,
$p = 1.61\times10^{-5}$ Pa
(d) $Q = 7.92\times10^{-7}$ Pa-m^3/s,
$p = 1.23\times10^{-5}$ Pa

7. $p(\infty) = p_u + p_L$, $p_L \equiv Q_0/\alpha V$,

$$\alpha V \equiv \frac{S_1 C_1}{S_1 + C_1} + \frac{S_2 C_2}{S_2 + C_2}$$

8. (a) $p(\infty) = 2.39 \times 10^{-4}$ Pa
(b) $p(\infty) = 1.10 \times 10^{-3}$ Pa

9. $Q_0 = 1.33 \times 10^{-9}$ Pa-m^3/s

10. $Q_{avg} = 8.68 \ \ 10^{-4}$ Pa-m^3/s

11. Stainless steel is safe for the vacuum chamber, $(t_{min})_{Al} = 3.8$ mm

12. t = 32.0 hours

13. No. True p = 0.59 Torr, so the gage is factor of 0.29 low. In argon, a calibrated Pirani gage would read 0.38 Torr, but the given Pirani gage would read 0.29 (0.38) = 0.11 Torr.

Chapter 20

1. P = 1.5 MW

2. $\sigma \simeq 34$ MPa = 4.9 ksi

3. g = 0.134, B = 1.07 T

4. $R = 2.03 \times 10^{-9} \Omega\text{-m}^4/a^4(1 - \pi D^2/4a^2)$

a =	0.00648	.00864	.01190	.01630 m
D =	0.00315	.00466	.00699	.01020 m
R =	1.414	.4723	.1389	.0415 Ω

$I_{max} = \frac{50V}{R}$ = 35 106 360 1200 A

Therefore, a = 0.0163 m conductor is best.
$\lambda = 0.692$
B = 0.56 T

5. $L_{seg} = 18.9$ m
$dV/dt = 8.29 \times 10^{-6}$ m^3/s per channel
v = 0.101 m/s
$\Delta p = 570$ Pa
$P_C = 0.12$ W per channel

(Pumping power would be much higher for small diameter tubes and long flow paths.)

6. At r = 0.16 m, 1 cm from surface:

	B_r	B_z (T)
Hart (20B16)	0.31	0.114
single loop (20B14)	0.287	0.106

on axis at midplane:

single loop (20B15)	0	0.461
Eg. (20B19)	0	0.450

7. --

8. At r = 0, z = -0.05 m :

	B_r	B_z
Hart	0	0.212
single loops	0	0.241

at r = 0.05 m, z = 0

Hart	0.0852	0
single loops	0.052	0

9. Good luck !

10. Hart: $B_r \simeq 0.010$ T, F ≃ 55 N
single loops: $B_r \simeq 0.015$ T, F ≃ 82 N

11. See graph.

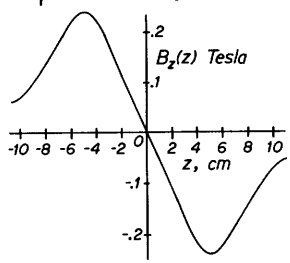

12. 2x25 turns per pancake; L = 95.0 m
I = 870 A; R = 0.0186 Ω;
P = 14.0 kW per pancake; v = 1.46 m/s
P_C = 30 W; 23 pancakes; P = 0.32 MW
B_z = 1.24 T;

13. v = 1.53 m/s; f = .033; P = 6540 W
R = 0.017 Ω; I = $(P/R)^{\frac{1}{2}}$ = 614 A
Fig. 20D4 → I ≃ 640 A

14. $R = 2\pi rn/wt$; $P = (\eta 2\pi r/wt)I^2$ per turn
$v = I^2 \eta/wtC\rho_m \Delta T d(1 - \pi/40)$

Chapter 21

1. (a) $R_{tot} = 1$ mΩ, $L_{tot} = 16.6$ nH
(b) 5.86×10^5 A, W = 721 J, $W/W_0 = .24$
(c) If current density were uniform, B ≃ 3.6 T. (Fig. 21C4 is not valid, because it is for h/2r = 1 case.) For a long solenoid, $B \simeq \mu_0 NI/L = 3.6$ T.
(d) $\delta = 0.15$ mm, $B = \mu_0 I/h = 2.1$ T
(e) P = 1.76 MPa, $F = 2.84 \times 10^5$ N
(f) 42 cables

2. --

3. $B_z = 194$ T, $\tau \lesssim 50$ μs

4. ETNF = 73 shots

5. $I_{max} = 9.96 \times 10^5$ A, $B_{max} = 6.1$ T

Chapter 22

1. $B = 0.0052$ T
2. $\xi = 6.5$ nm
3. $n < (4qa^3/I^2\eta) = 21$
4. $\ell_c > 0.04$ m, $T_0 \simeq 4$,
   $J_s \simeq 2.5\times10^9$,
   $(dB/dt) \leq 0.066$ T/s
5. $f(\alpha, \beta)$

$$= \beta \ln\left[\frac{\alpha + (\alpha^2 + \beta^2)^{\frac{1}{2}}}{1 + (1 + \beta^2)^{\frac{1}{2}}}\right]$$

$v(\alpha,\beta) = 2\beta\pi(\alpha^2 - 1)$

$$v(g,\beta) = \left[\left(\frac{g^2 - \beta^2}{2g}\right)^2 - 1\right] 2\pi\beta$$

$g \equiv e^{f/\beta}[1 + (1 + \beta^2)^{\frac{1}{2}}]$

$V_{min} = 6.5\ m^3$ at $\beta = 0.8$

$IL_t = 1.3\times10^8$ A-m

$L = 1.6$ m, $r_2 = 1.52$ m

6. $t = 546$ s $= 9.1$ min
7. $\alpha_s = 45$
8. $R = 7.7\times10^{-10}\ \Omega$

chapter 23

1. (a) m = 578 kg per coil
   (b) 25 W per coil
   (c) 1.8 W per coil
   (d) 3.9 W per coil, A = 1.32 m^2 per coil.
2. for 300 K to 80 K, W = 7.36×10^4 J removed, 0.46 L of liquid N_2

   for 80 K to 4.2 K, W = 6×10^3 J removed, 2.21 L of liquid He

   for 578 kg x 2 coils, 532 L of LN_2. 2540 L of LHe.
3. at input of 1 kW, boiloff = 1320 L/hr

   for problem 23-1, boiloff = 81L/hr

Chapter 24

1. $dx/dt = 0.98$ mm/yr
2. $dn_{imp}/dt = 1.78\times10^{18}$ atoms/m^3-s

   $\Delta t = 0.112$ s
3. $dx/dt = 0.11$ mm/yr
4. $T_{peak} = 1937$ K
   $\Delta n/s = 7.45\times10^{15}$ atom/m^2
   $\Delta x = 1.08\times10^{-13}$ m
5. 92 MPa or 13 ksi
6. 41.8 dpa, 722 appm (He), 4560 appm (Mn)
   $\Delta v/v \simeq 1.72$ %, $\Delta\ell/\ell \simeq 0.57$ %
7. $\sim$ 15 dpa
   parallel $\Delta\ell/\ell = -0.2$ %
   perpendicular $\Delta\ell/\ell = -2.4$ %
8. unattenuated fluence $= 4.4\times10^{27}$ neutrons/m^2
   attenuation $\lesssim 7\times10^{-6}$ needed.
   Damage to stabilizer may require smaller attenuation ($\sim10^{-7}$).

Chapter 25

1. $n_{Al}/n_i = 0.028$
   $P_f/P_{f0} = 0.53$
   ignition prevented
2. $A = 1.76\times10^{-3}$
   $f_\alpha(\theta = 0.6) = 7.89\times10^{-4}$
   $f_\infty = 1.75\times10^{-3}$
3. $\lambda = 0.082$ m
4. At high n_n, $\lambda^2 < 0$. Let $h \equiv -\lambda^2$.
   Then $d^2n/dx^2 = -n/h^2$.
   Curvature of n(x) changes sign, due to ionization of neutral gas.

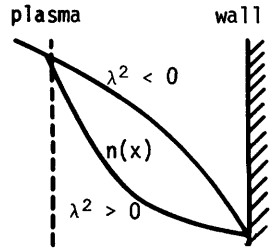

density profiles in scrape-off region

5. $Q = 2.01 \times 10^5$ Pa-m^3/s
   $S_t = 10^6$ m^3/s
   $A = 7390$ m^2

6. $u = -1.03 \times 10^4$ m/s
   $b_0 = -48.3$ m^{-1}
   $n_z(0)/n_{zw} = 0.050$

7. $a_p = 3/7$, $(a_v + a_w) = 4/7$
   $R_\alpha = 0.801$, $f_\alpha = 0.106$

8. $Q \simeq 4.4$

9. $G = 8.92 \times 10^8$
   $\ell/a = 0.58$, $\ell = 0.75$ m
   $r_p = 3.7$ mm

Chapter 26

1. $(1 - \eta)P_{th} = 2.24$ GW (th)

2. $q/A = 0.563$ MW/m^2, $T_a = 2000$ K

3. $Nu = 63.9$, $T_s = 1400$ K

4. $(q/A)_{max} = 4.67$ MW/m^2

   $\sigma_{th} = 97$ MPa, $\sigma_h = 60$ MPa

5. $P/q = f\rho_m v_c^3/8\eta_p(q/A) = 8.3 \times 10^{-5}$

6. $v_c = 0.962$ m/s, $C = 0.028$,
   $P = 148$ kW

Chapter 27

1. (b) $P_4(\mu) = (1/8)(35\mu^4 - 30\mu^2 + 3)$

2. $a_\ell = \frac{2\ell + 1}{2} \int_{-1}^{1} d\mu F(\mu) P_\ell(\mu)$

3. $\Sigma_0(x,E' \to E) = S(x,E' \to E)(1+b/3)$
   $\Sigma_1(x,E' \to E) = S(x,E' \to E)(a)$
   $\Sigma_2(x,E' \to E) = (2b/3)S(x,E' \to E)$

4. $\ell_1 = 3.294$ cm
   $\alpha_0 = 0$
   $\beta_0 = 0.5$
   $\gamma_0 = 0.866$
   $x_1 = x_0 + \alpha_0\ell_1 = 0$
   $y_1 = y_0 + \beta_0\ell_1 = 0.72$ cm
   $z_1 = z_0 + \gamma_0\ell_1 = 1.247$ cm
   elastic scattering
   $\psi = 58.2°$
   $E' = 0.9705$ MeV
   $\theta = 56.60°$
   $\phi = 161.35°$
   $\alpha' = -0.267$, $\beta' = -0.4097$
   $\gamma' = 0.8722$
   $\ell_2 = 2.347$ cm
   $x_2 = x_1 + \alpha'\ell_2 = -0.627$ m
   $y_2 = y_1 + \beta'\ell_2 = 0.241$ cm
   $z_2 = z_1 + \gamma'\ell_2 = 1.438$ cm
   both collisions within slab

5. $N = 10^8$ histories

6. $\bar{x} = 198.7$ grams, $s = 14.7$. It is 90% probable that $8.5 < \sigma < 19.1$. Take $\sigma \simeq 19.1$, then $\sigma_{\bar{x}} \simeq 6.0$.

   It is 61% probable that $\mu \simeq 198.7 \pm 6.0$

   It is 86% probable that $\mu \simeq 198.7 \pm 12.0$

   It is 90% probable that $\mu \simeq 198.7 \pm 18.0$

   If $s = 8.2$, then it is 90% probable that $6.3 < \sigma < 9.76$. Take $\sigma \simeq 9.8$. Then $\sigma_{\bar{x}} = 1.8$.

   It is 61% probable that $\mu \simeq 196 \pm 1.8$

   It is 86% probable that $\mu \simeq 196 \pm 3.6$

   It is 90% probable that $\mu \simeq 196 \pm 5.4$

7. $N = 2.77 \times 10^4$ histories.

Chapter 28

1. 5.48 % will be He atoms.

2. $t_2 = 1.46$ yrs, 14.5 kg/day

3. 93 appm He

4. From Eq.(28B15) $J = 4.4 \times 10^{12}$m^{-2}s^{-1}, but from Eqs.(28B13) and (28B18), $J \leq 1.49 \times 10^{12}$m^{-2}s^{-1}, so flow is recombination-limited.
   $\lambda JA = 12$ Ci/day.

6. 1.18×10^8Ci $= 4.36 \times 10^{18}$ Bq

7. COE = 34.4 mills/kWh

8. 79.7 mills/kWh, 5.82 mills/kWh

In the paperback edition

Volume I: Principles includes pages 1-272

Volume II: Experiments includes pages 273-549

Volume III: Technology includes pages 550-855

by H. J. Stansfield
J. J. Browning

A

B

C

D

E

F

G

H

I

J

K

L

N

O

P

Q

R

T

Y

Z

SUBJECT INDEX

by R. N. Ballou

A

B

C

D

E

F

G

H

I

M

Q

R

S

T

U

V

W

X

Y

Z

ABOUT THE AUTHOR

Tom Dolan received his PhD in Nuclear Engineering from the University of Illinois in 1970. In 1970-71 he studied plasma physics at the Novosibirsk State University and Institute of Nuclear Physics, USSR. Since then he has taught at the University of Missouri-Rolla, developing courses in fusion which became the basis of this book. He has participated in fusion research programs at Lawrence Livermore National Laboratory, Los Alamos National Laboratory, Oak Ridge National Laboratory, INRS-Energie (Universite du Quebec, Varennes), and taught at the National Tsing Hua University, Taiwan, Republic of China.

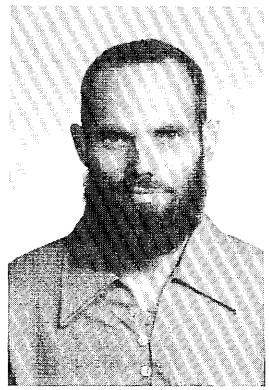

ISBN 0-08-025565-5